

PROCEEDINGS OF SPIE



SPIE—The International Society for Optical Engineering

Laser Applications in Microelectronic and Optoelectronic Manufacturing IV

Jan J. Dubowski
Henry Helvajian
Ernst W. Kreutz
Koji Sugioka
Chairs/Editors

25-27 January 1999
San Jose, California

Sponsored by
AFSOR—U.S. Air Force Office of Scientific Research
SPIE—The International Society for Optical Engineering

20000124 130



Volume 3618

DISTRIBUTION STATEMENT A
Approved for Public Release
Distribution Unlimited

DWG QUALITY INSPECTED 1

REPORT DOCUMENTATION PAGEForm Approved
OMB No. 0704-0188

Public reporting burden for this collection of information is estimated to average 1 hour per response, including the time for reviewing instructions, searching data sources, gathering and maintaining the data needed, and completing and reviewing the collection of information. Send comments regarding this burden estimate or any other aspect of this collection of information, including suggestions for reducing this burden to Washington Headquarters Service, Directorate for Information Operations and Reports, 1215 Jefferson Davis Highway, Suite 1204, Arlington, VA 22202-4302, and to the Office of Management and Budget, Paperwork Reduction Project (0704-0188) Washington, DC 20503.

PLEASE DO NOT RETURN YOUR FORM TO THE ABOVE ADDRESS.

1. REPORT DATE (DD-MM-YYYY) 15-07-1999		2. REPORT DATE Final Technical Report		3. DATES COVERED (From - To) 01-01-1999 - 31-12-1999	
4. TITLE AND SUBTITLE Laser Applications in Microelectronic and Optoelectronic Manufacturing IV				5a. CONTRACT NUMBER	
				5b. GRANT NUMBER F49620-99-1-0078	
				5c. PROGRAM ELEMENT NUMBER	
				5d. PROJECT NUMBER	
6. AUTHOR(S) Jan J. Dubowski Henry Helvajian Ernst W. Kreutz Koji Sugioka				5e. TASK NUMBER 2301/AX	
				5f. WORK UNIT NUMBER	
7. PERFORMING ORGANIZATION NAME(S) AND ADDRESS(ES) Society of Photo-Optical Instrumentation Engineers PO Box 10 Bellingham, WA 98227-0010				8. PERFORMING ORGANIZATION REPORT NUMBER 3618	
9. SPONSORING/MONITORING AGENCY NAME(S) AND ADDRESS(ES) AFOSR/NEO Air Force Office of Scientific Research 8011 Randolph St., Room 0732 Arlington, VA 22203-1977				10. SPONSOR/MONITOR'S ACRONYM(S) AFOSR	
				11. SPONSORING/MONITORING AGENCY REPORT NUMBER	
12. DISTRIBUTION AVAILABILITY STATEMENT Approved for Public Release					
13. SUPPLEMENTARY NOTES ISBN 0819430889					
14. ABSTRACT This proceedings contains papers on the following topics: Laser Nanotechnology; Fundamental Processes and Diagnostics of Laser Ablation; Ultrashort Pulse Laser Processing; Laser-induced Modification of Surface and Subsurface Properties of Materials; Innovative Laser Technology for Industrial Applications; Laser Surface Cleaning and Crystallization; Laser Microfabrication and Micromachining; Novel Methods and New Tools for Photon Processing; Pulsed Laser Deposition, Nanoclusters, Tribological and Diamond Films.					
15. SUBJECT TERMS Laser, Microelectronic, Optoelectronic					
16. SECURITY CLASSIFICATION OF:			17. LIMITATION OF ABSTRACT	18. NUMBER OF PAGES 534	19a. NAME OF RESPONSIBLE PERSON Marshall Weathersby
a. REPORT Non-Classified	b. ABSTRACT	c. THIS PAGE			19b. TELEPHONE NUMBER (Include area code) (360) 676-3290



PROCEEDINGS OF SPIE
SPIE—The International Society for Optical Engineering

Laser Applications in Microelectronic and Optoelectronic Manufacturing IV

Jan J. Dubowski
Henry Helvajian
Ernst W. Kreutz
Koji Sugioka
Chairs/Editors

25–27 January 1999
San Jose, California

Sponsored by
AFSOR—U.S. Air Force Office of Scientific Research
SPIE—The International Society for Optical Engineering

Published by
SPIE—The International Society for Optical Engineering



Volume 3618

SPIE is an international technical society dedicated to advancing engineering and scientific applications of optical , photonic, imaging, electronic, and optoelectronic technologies.



The papers appearing in this book comprise the proceedings of the meeting mentioned on the cover and title page. They reflect the authors' opinions and are published as presented and without change, in the interests of timely dissemination. Their inclusion in this publication does not necessarily constitute endorsement by the editors or by SPIE.

Please use the following format to cite material from this book:

Author(s), "Title of paper," in *Laser Applications in Microelectronic and Optoelectronic Manufacturing IV*, Jan J. Dubowski, Henry Helvajian, Ernst W. Kreutz, Koji Sugioka, Editors, Proceedings of SPIE Vol. 3618, page numbers (1999).

ISSN 0277-786X
ISBN 0-8194-3088-9

Published by
SPIE—The International Society for Optical Engineering
P.O. Box 10, Bellingham, Washington 98227-0010 USA
Telephone 360/676-3290 (Pacific Time) • Fax 360/647-1445

Copyright ©1999, The Society of Photo-Optical Instrumentation Engineers.

Copying of material in this book for internal or personal use, or for the internal or personal use of specific clients, beyond the fair use provisions granted by the U.S. Copyright Law is authorized by SPIE subject to payment of copying fees. The Transactional Reporting Service base fee for this volume is \$10.00 per article (or portion thereof), which should be paid directly to the Copyright Clearance Center (CCC), 222 Rosewood Drive, Danvers, MA 01923. Payment may also be made electronically through CCC Online at <http://www.directory.net/copyright/>. Other copying for republication, resale, advertising or promotion, or any form of systematic or multiple reproduction of any material in this book is prohibited except with permission in writing from the publisher. The CCC fee code is 0277-786X/99/\$10.00.

Printed in the United States of America.

Contents

- ix *Conference Committee*
- xi *Introduction*

SESSION 1 LASER NANOTECHNOLOGY

- 2 **Interferometric lithography for nanoscale fabrication (Invited Paper)** [3618-02]
S. H. Zaidi, S. R. J. Brueck, Univ. of New Mexico
- 9 **Optical nanoprobes for SNOM based on laser technology (Poster Presentation)** [3618-05]
V. P. Veiko, N. B. Voznessenski, I. B. Smirnov, A. I. Kalachev, D. I. Ivanitski, St. Petersburg Institute of Fine Mechanics and Optics (Russia); J. M. Voronin, S.I. Vavilov State Optical Institute (Russia); M. Wolf, K. Meteva, Bremen Institute for Applied Beam Technology (Germany)
- 17 **Atom projector: basic concept, construction, and applications (Poster Presentation)** [3618-52]
N. M. Sovetov, A. V. Nikonov, D. A. Grigor'ev, A. V. Khobotov, V. A. Moskovsky, E. V. Naumova, Saratov State Technical Univ. (Russia)

SESSION 2 FUNDAMENTAL PROCESSES AND DIAGNOSTICS OF LASER ABLATION

- 26 **Laser-induced electronic bond breaking and structural changes on semiconductor surfaces (Invited Paper)** [3618-07]
K. Tanimura, J. Kanasaki, Nagoya Univ. (Japan)
- 37 **Pulse-width influence on laser-induced desorption of positive ions from ionic solids (Invited Paper)** [3618-08]
R. M. Williams, K. M. Beck, A. G. Joly, Pacific Northwest National Lab.; J. T. Dickinson, Washington State Univ.; W. P. Hess, Pacific Northwest National Lab.
- 45 **Mechanistic studies and applications of laser-induced desorption from metal surfaces (Invited Paper)** [3618-09]
J. Bosbach, D. Martin, F. Stietz, T. Wenzel, F. Träger, Univ. Kassel (Germany)
- 53 **Direct mesoscopic simulation of melting and evaporation (Invited Paper)** [3618-10]
T. Yabe, Tokyo Institute of Technology (Japan)
- 61 **Optical detection of laser plasma interaction during laser ablation** [3618-11]
M. H. Hong, Y. F. Lu, National Univ. of Singapore
- 71 **Emission spectra and particle ejection during visible laser ablation of graphite for diamondlike coatings** [3618-50]
J. J. Chang, W. McLean, E. P. Dragon, B. E. Warner, Lawrence Livermore National Lab.
- 81 **Spectroscopic energy characterization of laser-induced titanium plume (Poster Presentation)** [3618-66]
S. S. Chu, M. Ye, C. P. Grigoropoulos, Univ. of California/Berkeley

SESSION 3 ULTRASHORT PULSE LASER PROCESSING

- 90 **Vibrational excitation and relaxation processes in insulators initiated by ultrashort mid-infrared laser pulses (Invited Paper)** [3618-12]
R. F. Haglund, Jr., R. Cramer, D. R. Ermer, M. R. Papantonakis, H.K. Park, O. Yavas, Vanderbilt Univ.
- 102 **Material processing of dielectrics with femtosecond lasers (Invited Paper)** [3618-13]
D. Ashkenasi, A. Rosenfeld, Max-Born-Institut für Nichtlineare Optik und Kurzzeitspektroskopie (Germany)
- 114 **Micromachining with ultrashort laser pulses** [3618-14]
J.-X. Zhao, B. Hüttner, A. Menschig, DLR (Germany)
- 122 **Second harmonic of Ti:sapphire femtosecond laser as a possible tool for pointlike 3D optical information recording (Poster Presentation)** [3618-54]
N. M. Bituryn, A. I. Korytin, S. V. Muraviov, Institute of Applied Physics (Russia);
A. M. Yurkin, Institute of Minerals and Petrography (Russia)

SESSION 4 LASER-INDUCED MODIFICATION OF SURFACE AND SUBSURFACE PROPERTIES OF MATERIALS

- 132 **Photoinduced and grating alignment of polyimide using excimer lasers for liquid crystal displays (Invited Paper)** [3618-16]
C. J. Newsome, M. O'Neill, Univ. of Hull (UK); G. P. Bryan-Brown, Defense Evaluation and Research Agency (UK)
- 141 **Three-dimensional microscopic modifications in glasses by a femtosecond laser (Invited Paper)** [3618-17]
K. Miura, J. Qiu, T. Mitsuyu, ERATO (Japan); K. Hirao, ERATO (Japan) and Kyoto Univ. (Japan)
- 152 **Fiber Bragg grating writing by interferometric or phase mask methods using high-power excimer lasers** [3618-18]
E. E. Mayer, D. A. Gillett, S. V. Govorkov, Lambda Physik, Inc.
- 161 **Modification in optical fibers using high-intensity femtosecond lasers** [3618-19]
S.-H. Cho, Keio Univ. (Japan) and RIKEN—Institute of Physical and Chemical Research (Japan);
H. Kumagai, K. Midorikawa, RIKEN—Institute of Physical and Chemical Research (Japan);
M. Obara, Keio Univ. (Japan) and RIKEN—Institute of Physical and Chemical Research (Japan)
- 170 **Laser-induced nonthermal surface modification of aluminum** [3618-20]
D. P. Taylor, H. Helvajian, The Aerospace Corp.
- 182 **Time- and space-resolved imaging and numerical simulation of laser zone texturing of Ni-P disk substrates** [3618-22]
S. Chen, M. Ye, C. P. Grigoropoulos, Univ. of California/Berkeley
- 191 **Semiconductor laser array fabricated by Nd:YAG laser-induced quantum well intermixing** [3618-21]
J. J. Dubowski, G. Marshall, Y. Feng, P. J. Poole, C. Lacelle, J. E. Haysom, N. Charbonneau, M. Buchanan, National Research Council Canada

- 198 **Thermal and optical properties of semitransparent ceramics: laser-induced high-temperature modifications** [3618-23]
O. G. Tsarkova, S. V. Garnov, V. I. Konov, E. N. Lubnin, General Physics Institute (Russia); F. Dausinger, Univ. Stuttgart (Germany)
- 205 **Laser texturing processes by reflected light detection (Poster Presentation)** [3618-55]
W. J. Wang, Y. F. Lu, M. H. Hong, National Univ. of Singapore
- 213 **Fabrication of true 3D microstructures in glass/ceramic materials by pulsed UV laser volumetric exposure techniques (Poster Presentation)** [3618-59]
P. D. Fuqua, S. W. Janson, W. W. Hansen, H. Helvajian, The Aerospace Corp.
- 221 **Planarization of hexagonal-GaN(0001) by KrF excimer-laser ablation followed by hydrochloric acid treatment (Poster Presentation)** [3618-73]
T. Akane, K. Sugioka, RIKEN—Institute of Physical and Chemical Research (Japan); H. Ogino, H. Takai, Tokyo Denki Univ. (Japan); K. Midorikawa, RIKEN—Institute of Physical and Chemical Research (Japan)

SESSION 5 INNOVATIVE LASER TECHNOLOGY FOR INDUSTRIAL APPLICATIONS

- 230 **Laser applications in the electronics and optoelectronics industry in Japan (Invited Paper)** [3618-24]
K. Washio, NEC Corp. (Japan)
- 240 **Advanced-laser processing of photonic and microelectronic components at Photonics Research Ontario (Invited Paper)** [3618-25]
P. R. Herman, G. Goodno, X. Gu, J. B. Kalbfleisch, J. Long, M. Lukacs, R. S. Marjoribanks, R. J. D. Miller, M. Nantel, S. Ness, A. Oetl, Photonics Research Ontario and Univ. of Toronto (Canada)
- 251 **Excimer laser micromachining: a 15-year perspective (Invited Paper)** [3618-26]
M. C. Gower, Exitech, Ltd. (UK)
- 262 **Laser welding of functional and constructional ceramics for microelectronics** [3618-27]
H. Exner, A.-M. Nagel, Laserinstitut Mittelsachsen e.V. (Germany)
- 269 **Concurrent in-line inspection system for CO₂ laser drilling machine (Poster Presentation)** [3618-60]
M. Kato, N. Araki, Matsushita Research Institute Tokyo, Inc. (Japan); K. Isaji, H. Karasaki, Matsushita Industrial Equipment Co., Ltd. (Japan)

SESSION 6 LASER SURFACE CLEANING AND CRYSTALLIZATION

- 278 **Laser surface cleaning of electronic materials (Invited Paper)** [3618-28]
Y. F. Lu, W. D. Song, Y. Zhang, Y. W. Zheng, National Univ. of Singapore
- 290 **Excimer laser cleaning for microelectronics: modeling, applications, and challenges (Invited Paper)** [3618-29]
M. Meunier, X. Wu, F. Beaudoin, E. Sacher, Ecole Polytechnique de Montréal (Canada); M. Simard-Normandin, Nortel (Canada)

- 302 **Transient temperature measurement of amorphous silicon thin films during excimer laser annealing** [3618-30]
S. Moon, M. Lee, Univ. of California/Berkeley; M. Hatano, K. Suzuki, Hitachi, Ltd. (Japan); C. P. Grigoropoulos, Univ. of California/Berkeley
- 310 **Correlation between power density fluctuation and grain size distribution of laser-annealed polycrystalline silicon** [3618-31]
K. Suzuki, M. Saitou, M. Takahashi, N. Hayashi, T. Terabayashi, Hitachi, Ltd. (Japan)
- 320 **Lattice strain in excimer-laser-crystallized poly-Si thin films** [3618-32]
H. Okumura, A. Tanikawa, K. Sera, F. Okumura, NEC Corp. (Japan)

SESSION 7 LASER MICROFABRICATION AND MICROMACHINING

- 330 **Laser direct writing of circuit elements and sensors (Invited Paper)** [3618-33]
A. Piqué, D. B. Chrisey, Naval Research Lab.; R. C. Y. Auyeung, SFA, Inc.; S. Lakeou, Univ. of the District of Columbia; R. Chung, Geo-Centers, Inc.; R. A. McGill, Naval Research Lab.; P. K. Wu, Southern Oregon Univ.; M. T. Duignan, Potomac Photonics, Inc.; J. Fitz-Gerald, Naval Research Lab.; H. D. Wu, SFA, Inc.
- 340 **Microstructuring of materials by pulsed-laser focusing and projection technique** [3618-34]
H. Exner, B. Keiper, P. Meja, Laserinstitut Mittelsachsen e.V. (Germany)
- 348 **High-accuracy micromachining of ceramics by frequency-tripled Nd:YAG lasers** [3618-35]
D. Hellrung, L.-Y. Yeh, F. Depiereux, A. Gillner, R. Poprawe, Fraunhofer-Institut für Lasertechnik (Germany)
- 357 **UV laser ablation of ultrathin dielectric layers** [3618-36]
K. Rubahn, J. Ihlemann, Laser Lab. Göttingen e.V. (Germany); F. Balzer, Stanford Univ.; H.-G. Rubahn, Max-Planck-Institut für Strömungsforschung (Germany)
- 363 **Micromachining of glass materials by laser-induced plasma-assisted ablation (LIPAA) using a conventional nanosecond laser** [3618-37]
J. Zhang, K. Sugioka, K. Midorikawa, RIKEN—Institute of Physical and Chemical Research (Japan)
- 370 **Laser direct dry etching of GaAs/AlGaAs multilayer (Poster Presentation)** [3618-62]
S.-K. Park, C. Lee, Inha Univ. (Korea); E.-K. Kim, Korea Institute of Science and Technology
- 378 **Maskless laser-induced deposition of Cu film patterns from copper formate (Poster Presentation)** [3618-63]
J.-K. Kim, C. Lee, Inha Univ. (Korea)

SESSION 8 NOVEL METHODS AND NEW TOOLS FOR PHOTON PROCESSING

- 388 **Overview of the user program for the Jefferson Lab free-electron laser (Invited Paper)** [3618-39]
H. F. Dylla, Thomas Jefferson National Accelerator Facility

- 396 **High-power ultraviolet all-solid-state laser for industrial applications [3618-40]**
C. Mehlmann, T. Schröder, P. Klopp, R. Koch, U. Stamm, Lambda Physik GmbH (Germany);
D. Basting, Lambda Physik, Inc.
- 403 **Efficiency increase for laser structuring using mask projection [3618-41]**
K. Jasper, P. Berger, H. Hügel, Univ. Stuttgart (Germany)
- 413 **Microstructuring with 157-nm laser light [3618-74]**
H. Endert, M. Kauf, E. E. Mayer, M. J. Scaggs, J. Fair, D. Basting, Lambda Physik, Inc.
- 418 **Electrical and optical properties of ITO films deposited by excimer-laser-assisted EB method (Poster Presentation) [3618-64]**
T. Yano, M. Yoneda, T. Ooie, M. Katsumura, Shikoku National Industrial Research Institute (Japan); Y. Suzuki, T. Shikama, Takamatsu National College of Technology (Japan)
- 425 **Reliability and lifetime of UV excilamps pumped by glow, barrier, and capacitive discharges (Poster Presentation) [3618-65]**
V. F. Tarasenko, High-Current Electronics Institute (Russia); E. B. Chernov, Tomsk State Univ. (Russia); M. V. Erofeev, A. N. Panchenko, V. S. Skakun, E. A. Sosnin, High-Current Electronics Institute (Russia)

SESSION 9 PULSED LASER DEPOSITION, NANOCLOUDS, TRIBOLOGICAL AND DIAMOND FILMS

- 434 **Condensation of vapor and nanoclusters formation within the vapor plume produced by nanosecond-laser ablation of Si, Ge, and C (Invited Paper) [3618-43]**
B. S. Luk'yanchuk, General Physics Institute (Russia); W. Marine, UMR/CNRS (France);
S. I. Anisimov, Landau Institute for Theoretical Physics (Russia); G. A. Simakina, General Physics Institute (Russia)
- 453 **Pulsed laser deposition of nanocomposite thin films for photonic applications (Invited Paper) [3618-45]**
C. N. Afonso, J. Solis, R. Serna, J. A. Gonzalo, J. M. Ballesteros, Instituto de Optica (Spain);
J. C. G. de Sande, Univ. Politécnica de Madrid (Spain)
- 465 **Semiconductor nanocrystallite formation using inert gas ambient pulsed laser ablation and its application to light-emitting devices (Invited Paper) [3618-46]**
T. Yoshida, Y. Yamada, N. Suzuki, T. Makino, Matsushita Research Institute Tokyo, Inc. (Japan);
T. Orii, S. Onai, Univ. of Tsukuba (Japan)
- 475 **Advances in pulsed laser deposition growth of nitride thin films (Invited Paper) [3618-47]**
F. E. Fernández, M. Pumarol, A. Martínez, W. Jia, Y. Wang, E. Rodríguez, H. A. Mourad, Univ. of Puerto Rico
- 487 **Pulsed laser deposition of high-quality tribological coatings (Invited Paper) [3618-48]**
G. Radhakrishnan, P. M. Adams, D. M. Speckman, The Aerospace Corp.
- 495 **Pulsed-laser-deposited amorphous diamond and related materials: synthesis, characterization, and field emission properties (Invited Paper) [3618-49]**
V. I. Merkulov, D. H. Lowndes, L. R. Baylor, G. E. Jellison, Jr., A. A. Puretzky, D. B. Geohegan, Oak Ridge National Lab.

- 504 **Pulsed laser deposition of Ti: sapphire thin films using high-speed rotating target (Poster Presentation) [3618-67]**
Y. Nakata, H. Uetsuhara, S. Goto, N. Vasa, T. Okada, M. Maeda, Kyushu Univ. (Japan)
- 512 **Crystallinities and light-emitting properties of nanostructured SiGe alloy prepared by pulsed laser ablation in inert background gases (Poster Presentation) [3618-68]**
T. Yoshida, Y. Yamada, N. Suzuki, T. Makino, Matsushita Research Institute Tokyo, Inc. (Japan); T. Orii, K. Murakami, Univ. of Tsukuba (Japan); D. B. Geohegan, D. H. Lowndes, Oak Ridge National Lab.; M. J. Aziz, Harvard Univ.
- 520 **Properties of boron-carbon-nitrogen ternary thin films synthesized by pulsed laser deposition (Poster Presentation) [3618-71]**
Z. M. Ren, Y.-F. Lu, Z. H. Mai, National Univ. of Singapore; B. A. Cheong, S. K. Chow, J. P. Wang, T. C. Chong, Data Storage Institute (Singapore)
- 529 *Addendum*
- 532 *Author Index*

Conference Committee

Conference Chairs

Jan J. Dubowski, National Research Council Canada
Henry Helvajian, The Aerospace Corporation
Ernst W. Kreutz, Technical University Aachen (Germany)
Koji Sugioka, RIKEN—The Institute of Physical and Chemical Research (Japan)

Program Committee

Glenn H. Chapman, Simon Fraser University (Canada)
Paul B. Corkum, National Research Council Canada
Douglas B. Chrisey, Naval Research Laboratory
J. Thomas Dickinson, Washington State University
Peter E. Dyer, University of Hull (UK)
Daniel J. Ehrlich, Revise, Inc.
Eric Fogarassy, CNRS (France)
James A. Greer, PVD Products Inc.
Bo Gu, Resonetics, Inc.
James S. Im, Columbia University
Tomoji Kawai, Osaka University (Japan)
Vitaly I. Konov, General Physics Institute (Russia)
Paul Leiderer, University of Konstanz (Germany)
Thomas K. Lippert, Los Alamos National Laboratory
Douglas H. Lowndes, Oak Ridge National Laboratory
Glenn Ogura, Resonetics, Inc.
Tatsuo Okada, Kyushu University (Japan)
Michael Reichling, Freie Universität Berlin (Germany)
Mordechai Rothschild, MIT Lincoln Laboratory
Chandrasekhar Roychoudhuri, University of Connecticut
Nikolaus Schwentner, Freie Universität Berlin (Germany)
Michael Stuke, Max-Planck-Institut für Biophysikalische Chemie (Germany)
Rongfu Xiao, Hong Kong University of Science and Technology

Session Chairs

- 1 Laser Nanotechnology
Carmen N. Afonso, Instituto de Optica (Spain)
Henry Helvajian, The Aerospace Corporation
- 2 Fundamental Processes and Diagnostics of Laser Ablation
David Ashkenasi, Max-Born Institut (Germany)
Richard F. Haglund, Jr., Vanderbilt University
- 3 Ultrashort Pulse Laser Processing
Koji Sugioka, RIKEN—Institute of Physical and Chemical Research (Japan)

- 4 Laser-induced Modification of Surface and Subsurface Properties of Materials
Ernst W. Kreutz, Institute for Laser Technologies (Germany)
Andrew C. Tam, IBM Almaden Research Center
- 5 Innovative Laser Technology for Industrial Applications
Jan J. Dubowski, National Research Council Canada
- 6 Laser Surface Cleaning and Crystallization
Wayne P. Hess, Pacific Northwest National Laboratory
Frank Traeger, Universität Kassel (Germany)
- 7 Laser Microfabrication and Micromachining
Malcolm C. Gower, Exitech, Ltd. (UK)
Yongfeng Lu, National University of Singapore
- 8 Novel Methods and New Tools for Photon Processing
Peter R. Herman, University of Toronto (Canada)
- 9 Pulsed Laser Deposition, Nanoclusters, Tribological and Diamond Films
Michel Meunier, Ecole Polytechnique de Montréal (Canada)
James S. Horwitz, Naval Research Laboratory

Introduction

The conference on Laser Applications in Microelectronic and Optoelectronic Manufacturing (LAMOM-IV) was a three-day event included in the framework of the Microengineering/Manufacturing program at Photonics West '99. A steadily increasing attendance at the laser processing of materials conferences organized in San Jose since 1995 (see *Proceedings of SPIE* volumes 2403, 2703, 2991, and 3274), proves that there is a need for a forum where fundamental aspects of the rapidly progressing field of laser-matter interaction and emerging laser applications in device manufacturing can be discussed on a regular basis. The focus on microelectronic and optoelectronic applications distinguishes LAMOM from other high-power laser applications conferences. Representatives from Canada, Germany, Japan, Korea, Puerto Rico, Russia, Singapore, Spain, the U.K., and the U.S. attended LAMOM-IV.

Topics covered at the 1999 conference were laser nanotechnology, fundamental processes and diagnostics of laser ablation, ultrashort-pulse laser processing, modification of surface and subsurface properties of materials, innovative technologies for industrial applications, surface cleaning and crystallization, microfabrication/micromachining, novel methods and new tools for photon processing, pulsed laser deposition, and nanocluster formation. These topics were discussed over the course of nine sessions where the stage was set by leading experts from each field. Most of the papers presented at the meeting are included in the conference proceedings. We hope these will be useful not only for the attendees, but will serve as a useful reference for those who are interested in the application of lasers as tools for manufacturing of microelectronic and optoelectronic devices and who wish to follow closely the exciting developments taking place in the area of lasers and laser processing of materials.

We would like to thank the members of the program committee, invited speakers, and all the participants for making LAMOM-IV a successful meeting. Our thanks are also due to the SPIE technical personnel for helping in the organization of the meeting.

We acknowledge the U.S. Air Force Office of Scientific Research for the financial support provided to this conference.

**Jan J. Dubowski
Henry Helvajian
Ernst W. Kreutz
Koji Sugioka**

SESSION 1

Laser Nanotechnology

Interferometric Lithography for Nanoscale Fabrication

Saleem H. Zaidi and S. R. J. Brueck^{a,b}

Center for High Technology Materials, University of New Mexico, Albuquerque, NM 87106

ABSTRACT

Interferometric lithography (IL) techniques provide a demonstrated, low-cost, large area nanoscale patterning capability with feature resolution to ~ 50 nm. Combining IL with anisotropic etching (both by reactive-ion etching and by KOH wet etching) and with 3-D oxidation techniques provides a suite of techniques that accesses a broad range of Si nanostructures (as small as 10 nm) over large areas and with good uniformity. Optical characterization includes measurements of reflectivity for a wide range of 1D grating profiles, and Raman scattering characterization of Si nanostructures. Three regimes are found for the Raman scattering: bulk (to linewidths of ~ 200 nm), resonant enhanced (~ 50 nm linewidths) and asymmetry and splitting (linewidths < 20 nm).

Keywords: interferometric lithography, Si nanoscale structures, Si quantum wires, Si photoluminescence

I. INTERFEROMETRIC LITHOGRAPHY

We have investigated interferometric lithography (IL) as a cost-effective alternative towards nanoscale patterning. IL techniques have been demonstrated to produce uniform nm-scale structures over large areas at low cost. The period for IL is $\lambda/2\sin\theta$, where 2θ is the intersection angle between the two exposing laser beams. There is no constraint on the feature dimension, only the period. Nonlinear response of photoresist and other processing techniques allow linewidths as small as 10 nm, limited only by the uniformity and process control. For readily available laser sources from 0.488- to 0.193- μm at $\theta=75^\circ$, this translates into periods ~ 0.25 -0.1 μm with linewidths of < 0.12 -0.05 μm .

Single exposure interferometric grating fabrication has a long history^{1,2} Figure 1 shows a typical experimental configuration in which an expanded and collimated laser beam is incident on a Fresnel mirror (FM) arrangement mounted on a rotation stage³ for period variation. The mirror and sample stages have tilt & tip adjustments, the sample stage is equipped with in-plane rotation adjustment as well. The interference between two beams one directly incident on the wafer on one side of the FM and the second reflected from the mirror mounted on the other side of the FM, results in a periodic pattern $\lambda/2\sin\theta$, where θ can be precisely varied by the computer-controlled rotation stage. Grating patterns are first formed in photoresist (PR) followed by a pattern transfer to the underlying substrate. Figure 2 shows examples of 360- and 250-nm period photoresist gratings fabricated on a bottom-ARC-coated Si wafer. These structures were fabricated with laser exposure at $\lambda=355$ nm (third harmonic of a YAG laser) in Shipley 505-A positive photoresist. The grating linewidths were ~ 180 - and 130-nm respectively at a thickness of ~ 500 nm⁴. At smaller periods, photoresist collapse⁵ and horizontal thinning during the development process limit the achievable aspect ratios and force the use of thinner (~ 100 -200 nm) PR films.

Single exposure IL is limited in its applicability to 1-D grating structures, more useful patterns are formed using multiple exposures either with a simple 2-beam configuration, or using multiple laser beams. Figure 3 shows the simplest examples of 2-D patterns consisting of posts and vias formed in Shipley 508 positive and Ultra i-300 negative photoresists, respectively, by two orthogonal IL exposures in the same level of resist. Multiple exposure interferometric lithography (MEIL) techniques⁶ appropriately combined with a synthesis procedure offer a cost-effective alternative to conventional optical lithography in nm-scale regime. A major limitation of these methods remains the overall periodic character of the patterns; this can be addressed by mix-and-match with optical lithography or by imaging interferometric lithography. In either case, development of an understanding and process for matching multiple exposures is a critical step in the development of these capabilities.

^a brueck@chtm.unm.edu

^b Also Departments of Electrical and Computer Engineering and Physics and Astronomy

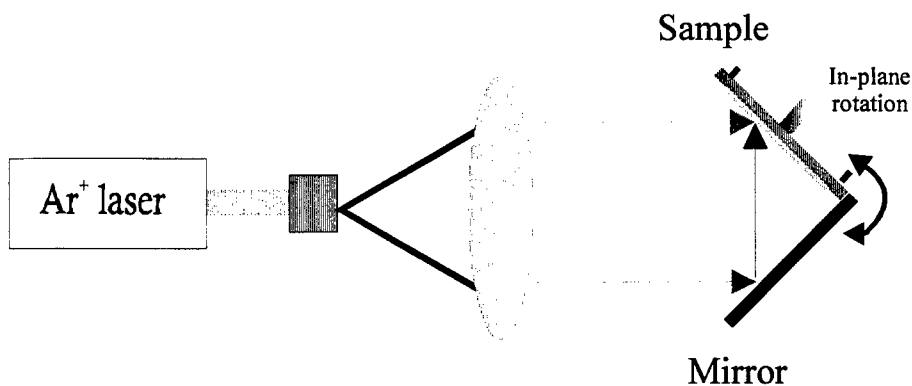


Figure 1 Typical experimental configuration for interferometric lithography.

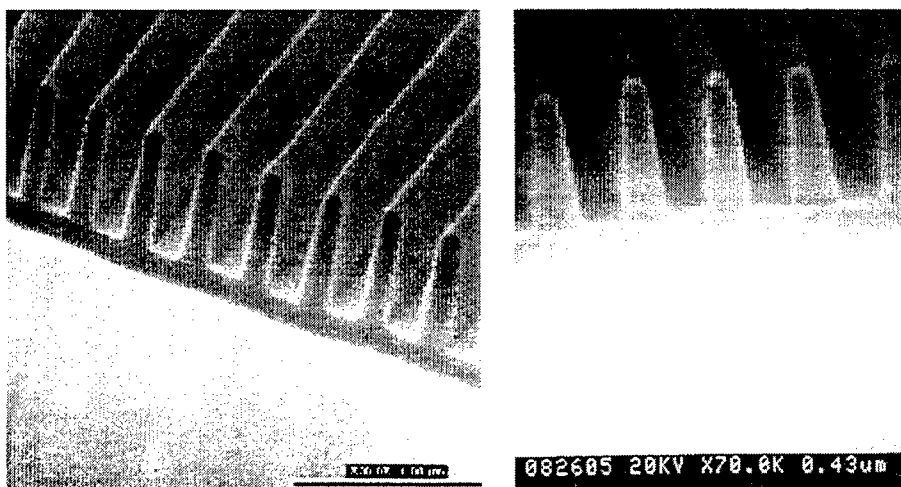


Figure 2 Cross-sectional photoresist profiles of a 360-nm (left), and 250-nm (right) pitch gratings.

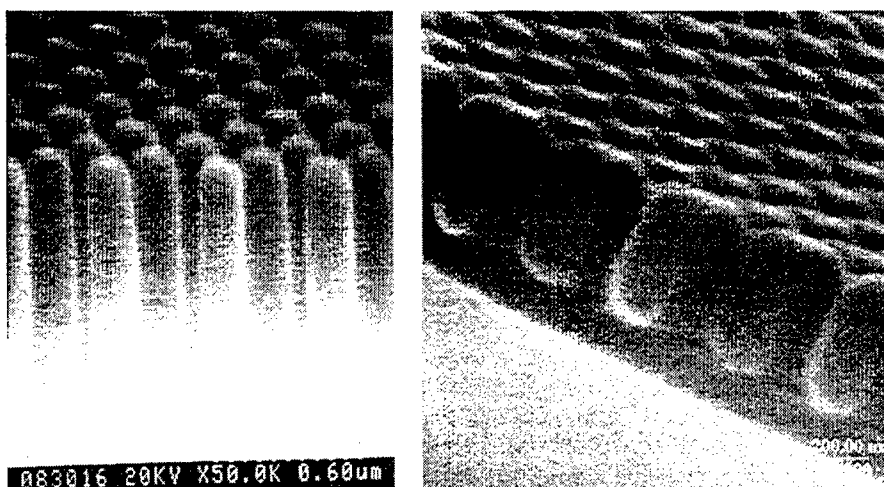


Figure 3 Cross-sectional profiles of a 500-nm (left), and 360-nm (right) pitch posts and vias formed in positive and negative photoresist, respectively.

II. Si NANOSCALE FABRICATION

Si is the dominant microelectronics material. Its nanoscale material properties in the 1- to 100-nm size range is of interest due to a continuing trend in IC manufacturing of reducing device dimensions with the twin aims of increased packing density and

higher speed. We have applied IL techniques to form nanoscale linewidth features in Si using wet- and reactive-ion-etching and thermal oxidation techniques. Optical properties of Si in nanoscale regime were evaluated using reflectance, Raman scattering, and photoluminescence measurements. Some results are presented below. More detailed accounts are presented elsewhere.^{7,8}

II.1 Reflectance measurements of 1-D gratings

We have investigated spectral reflectance response of 1-D Si gratings as a function of profile, linewidth, and height. Figure 4 shows three rectangular-profiled gratings formed in (110) Si using wet-chemical etching. The grating periods are 1.0-, 0.5- and 0.3- μm with linewidths ~ 0.33 , 0.13 and 0.05 μm respectively. All of the gratings were 1- μm high. Figure 4 shows normal incidence spectral reflectance response of these structures in 0.3-0.8- μm range. It is seen that the reflectance of these nanoscale linewidth structures is a strongly dependent on incident polarization. For linewidths > 50 nm, the gratings act as

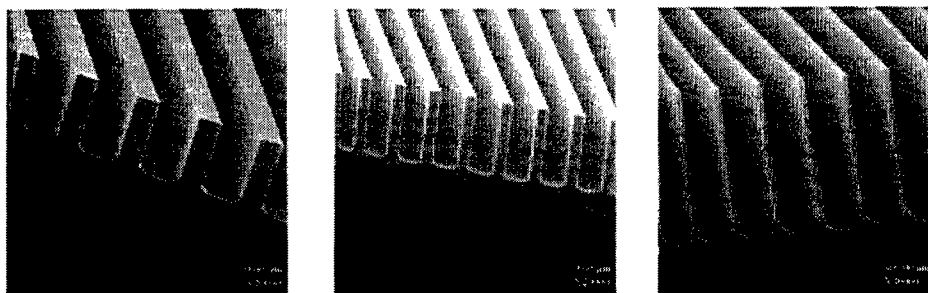


Figure 4 Cross-sectional profiles of 1.0- (left), 0.5- (middle), and 0.3- μm (right) period gratings etched 1- μm deep in (110) Si.

color filters with spectral linewidths ~ 50 nm. As linewidths are reduced below ~ 50 nm, the reflectance response is characterized by a uniform low, or high reflection. At 300-nm pitch period, there are no-diffraction orders, therefore, energy lost in zero-order is absorbed by the Si surface. The narrow-band reflectance response has been observed only in rectangular profiles. For a triangular profile structure as shown in Fig. 6, a polarization-independent broad band reduced reflectance response is observed (Fig. 6). The absorptive grating structure in Fig. 6 has a period of 0.44 μm , depth of ~ 0.6 μm , and linewidth variation of ~ 20 -200 nm from top-to-bottom. These reflectance measurements demonstrate that sub- μm , nanoscale-linewidth Si grating structures can either be designed for a narrow-band color filters, or broadband absorptive behavior. Extension of these 1-D structures to 2-D post, or via patterns is straightforward.

II.2 Raman Scattering and Photoluminescence Measurements

Reflectance measurements provide useful information for grating linewidths > 50 nm. As linewidths are reduced below 50 nm, Raman scattering (RS) measurements provide precise information about crystalline dimensions. Si structures in sub-

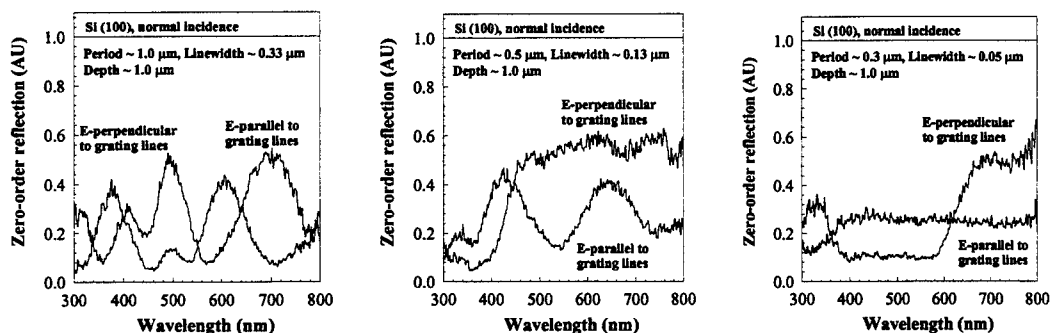


Figure 5 Normal incidence spectral reflectance measurements of gratings shown in Fig. 4.

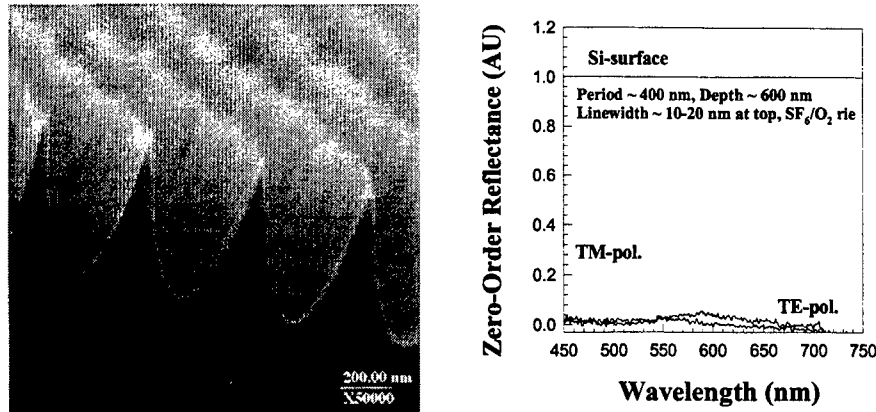


Figure 6 Cross-sectional profile of a 0.44- μm period structure (left), and its spectral response (right).

50 nm range are fabricated using controlled thermal oxidation of Si grating structures. Figure 7 shows example of $\sim 10\text{-}20$ nm linewidth Si grating and wire structure embedded in thermally grown oxide. For the wall structure, the grating depth is ~ 1.0 μm , and period ~ 1.0 μm , for the wire structure, period is ~ 0.75 μm , and wire diameter $\sim 10\text{-}20$ nm. The wires were formed by application of IL, etching and oxidation techniques to Si films in an insulator (SOI) configuration.

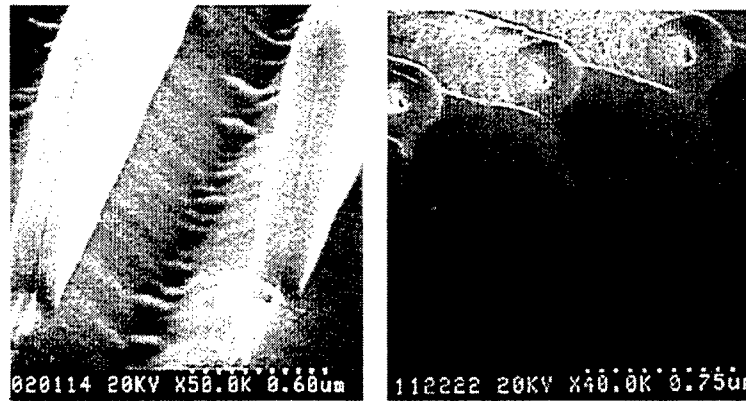


Figure 7 Cross-sectional profiles of Si walls (left), and wires (right) embedded in thermally grown oxide.

We have evaluated Si response as grating linewidths are systematically reduced to $\sim 5\text{-}10$ nm. Three behavioral regimes have been identified: a) for >200 nm linewidths, RS response is identical to bulk Si, b) for Si linewidths $\sim 50\text{-}100$ nm, RS signal enhancement by as much as two orders of magnitude over bulk, and c) for linewidths < 10 nm, a splitting of bulk Raman peak. Figure 8 shows Raman scattering response of $\sim 50\text{-nm}$ linewidth Si structures at a pitch of ~ 380 nm, bulk Si RS response under identical conditions is also plotted for reference. It is observed that enhanced Raman signal is symmetric, and independent of incident light polarization. Figure 9 shows RS response from $\sim 10\text{-nm}$ diameter wall, and wire structures, again in each case bulk Si RS measurement under identical conditions is also plotted for reference.. The splitting of the Raman peak for walls and wires reflects Si bandgap variation, and is usually accompanied by room temperature photoluminescence (PL) as is reflected in increased background signal. Also notice that the two Raman peaks for wall structure have lower frequency than the bulk Si, whereas for wires, the bulk mode is split into a higher and lower frequency component. This may be attributed to stress effects related to Si/SiO₂ interface. We have also carried out room temperature

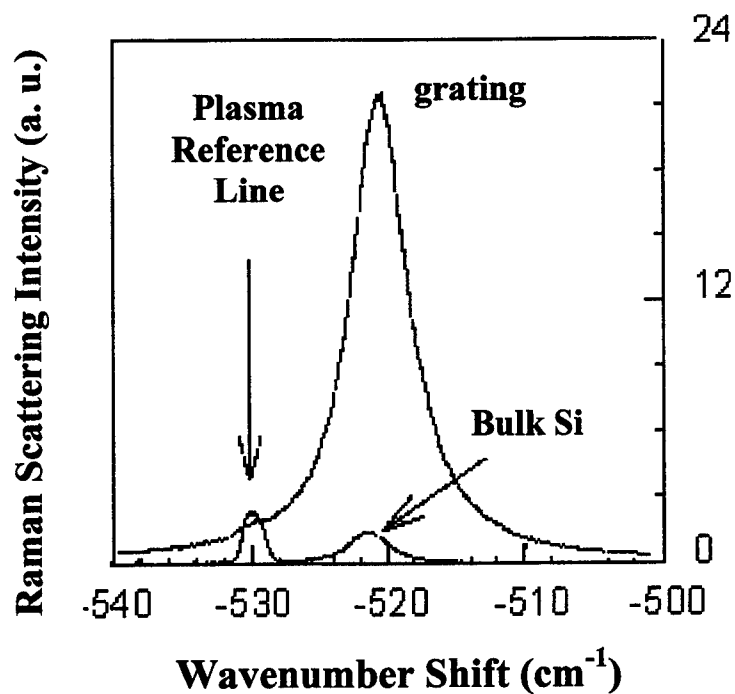


Figure 8 Raman scattering enhancement from ~ 50 -nm linewidth, 380-nm period grating structure.

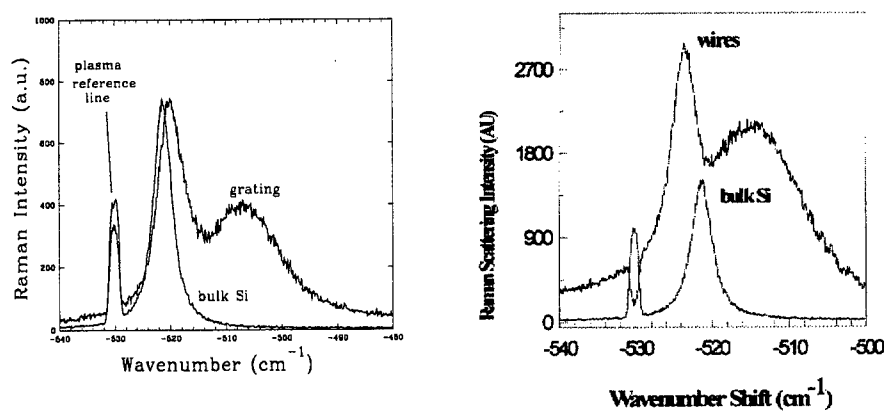


Figure 9 Raman scattering measurements of Si walls (left), and wires (right) embedded in thermally grown oxide.

PL measurements of Si wall and wire structures, Figure 10 shows the PL response of wall and wire structures at 257-nm laser excitation. It is seen that the wall PL has a maxima at ~ 500 nm, whereas wire PL is characterized by a strong peak at ~ 700 nm, and a much weaker broad peak at ~ 350 nm.

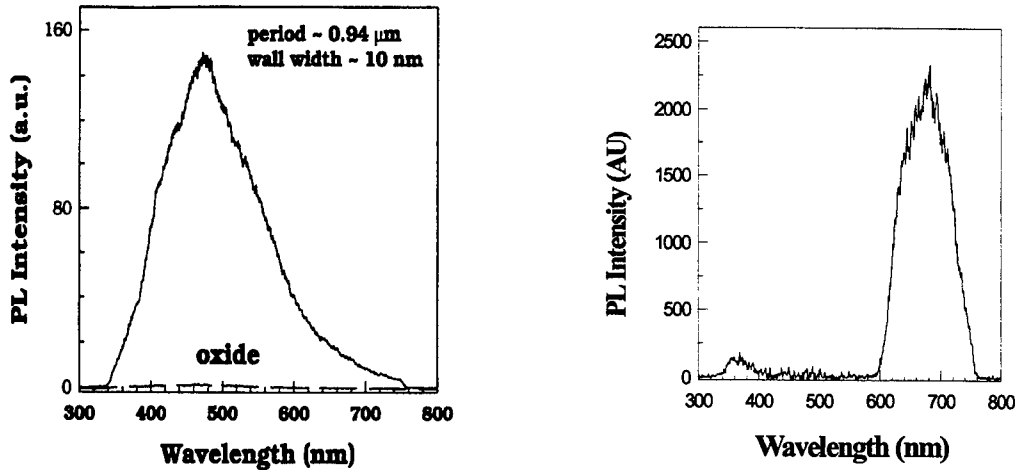


Figure 10 Room temperature PL measurements of Si walls (left), and wires (right) embedded in thermally grown oxide.

These measurements demonstrate that Si behavior undergoes dramatic change as its linewidth is reduced from ~ 100 - 10 nm. Even though the room temperature PL is weak, it still shows the potential for improved Si-based optoelectronics technology. Finally, the IL techniques used to form these structures are low-cost, applicable to large areas, and compatible with existing microelectronics technology.

III. DEVICE APPLICATIONS

The nanoscale IL based technology has extensive application base. We have investigated integration of grating structures in MSM photodetectors, light emitting diodes, and field effect transistor devices. Other applications include super-conducting transistors, photonic crystals, etc. Figure 11 shows photoresponse of MSM photodetectors at $\lambda=633$ nm. These Cr/Si interdigitated photodetectors were formed on p-type Si substrate. Nanoscale linewidth grating patterns were formed between metal fingers using a mix and match approach with optical lithography. For comparison, planar detectors were also formed on the same p-type wafers, and subjected to same processing conditions. It is seen that current response of grating devices has been improved by a factor of 2. Increased current response is attributed to improved absorption of the grating structure.

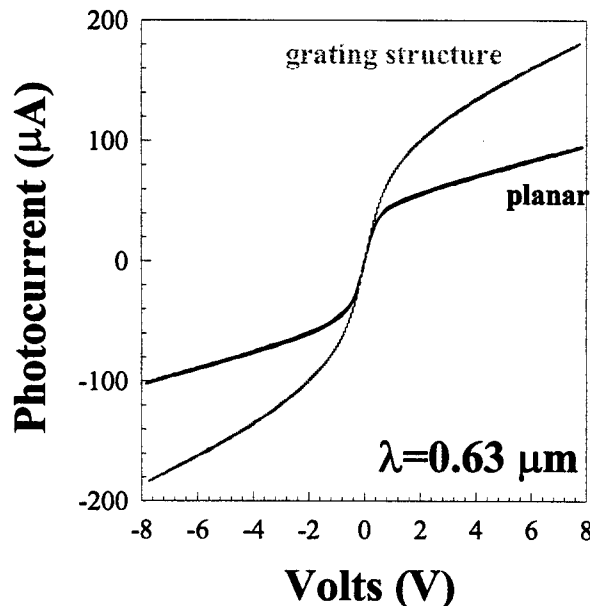


Figure 11 Photo-current enhancement due to grating structure in MSM configuration..

IV. SUMMARY

Interferometric lithography coupled with anisotropic etching and 3D oxidation provide a suite of powerful techniques for the fabrication of large-area arrays of Si nanostructures. Examples include ~ 10- to 20-nm free-standing Si walls and wires surrounded by oxide. Optical characteristics of these structures include pattern dependent reflectivity (artificially structured dielectrics), changes in the Raman scattering spectra for sub-100 nm structures, and photoluminescence for structures of ~ 10 nm and smaller. There are significant device applications for these structures. Initial photodetector results show significant improvement over unstructured devices.

ACKNOWLEDGEMENTS

Support for this work was provided by the Air Force Office of Scientific Research and by the Defense Advanced Projects Agency. Helpful discussions with A.-S. Chu and the technical assistance of Andrew Frauenglass are gratefully acknowledged.

REFERENCES

- ¹ L. F. Johnson, G. W. Kammlott, and K. A. Ingersoll, "Generation of Periodic Surface Corrugations," *Appl. Opt.* **17**, 1165-1181 (1978).
- ² E. H. Anderson, V. Boegli, M. L. Schattenberg, D. Kern, and H. I. Smith, "Metrology of Electron-Beam Lithography Systems using Holographically Produced Reference Samples," *J. Vac. Sci. Technol.* **B 9**, 3606-3611 (1991).
- ³ Saleem H. Zaidi and S. R. J. Brueck, "High Aspect Ratio Holographic Photoresist Gratings," *Appl. Opt.* **27**, 2999 (1988).
- ⁴ Saleem H. Zaidi, S. R. J. Brueck, F. M. Schellenberg, R. S. Mackay, K. Uekert, and J. J. Persoff, "Interferometric Lithography Exposure Tool for 180-nm Structures," *SPIE* **3048**, 248-254 (1997).
- ⁵ X. Chen, Z. Zhang, S. R. J. Brueck, R. A. Carpio and J. S. Petersen, "Process Development for 180-nm Structures using Interferometric Lithography and I-Line Photoresist," *SPIE* **3048**, 309-318 (1997).
- ⁶ Saleem H. Zaidi and S. R. J. Brueck, "Multiple Exposure Interferometric Lithography," *Jour. Vac. Sci. Technol.* **B11**, 658-666 (1993).
- ⁷ Saleem H. Zaidi, An-Shiang Chu and S. R. J. Brueck, "Optical Properties of Nanoscale, One-Dimensional Silicon Grating Structures," *Jour. Appl. Phys.* **80**, 6997-7008 (1996).
- ⁸ Saleem H. Zaidi and S. R. J. Brueck, "Photoluminescence of Manufactured 1-D Crystalline Si Gratings," *Opt. Commun.* **135**, 264-268 (1997).

Optical nanoprobes for SNOM based on laser technology

Vadim P. Veiko, Nikolay B. Voznessenski, Igor B. Smirnov, Alexey I. Kalachev, Dmitry I. Ivanitski

St.-Petersburg State Institute of Fine Mechanics and Optics (Technical University), Sablinskaya ul., 14, St.-Petersburg, Russia, 197101

Juriy M. Voronin

S.I. Vavilov State Optical Institute, Birjevaja ul., 12, St.-Petersburg, Russia, 199134

Michael Wolf, Krassimira Meteva,

Bremen Institut for Applied and Beam Technology, Klagenfurter Strasse 2, D - 28359 Bremen, Germany

Telephone: +49 421 218 01, Telefax: +49 421 218 5063

ABSTRACT

Optics with resolution within the wavelength – scanning near-field optical microscopy (SNOM) – is highly important science field nowadays. Main parameters of the SNOM – resolution, contrast, energetical efficiency are defined by optical probes characteristics: aperture size or curvature radius of the sharp, geometry, material etc. Fabrication and testing of optical probes in nanometric scale of size are described in the paper. For fabrication of near-field probes the laser many-steps drawing and chemical etching of single- and multimode optical fibers is realized. Investigation of far-field light distribution and theoretical reconstruction of near field carried out the testing of probes.

Keywords: nanoprobes, near-field optics, superresolution, SNOM tips fabrication

1. INTRODUCTION.

A great amount of tasks concern small and extra small elements and structures namely photomasks and compact optoelectronic devices, nanopowder particles, nanosubstrates, tools for micro and laser surgery, biomolecules, viruses, etc. In all these cases the urgency of the use of optical research methods is doubtless. However it is evident that the far-field optical microscopy offers no direct imaging technique in nanometric scale and it is necessary to take alternate means such as electron scanning microscopy techniques. Some of tasks in question accommodate the use of the latter methods but there are cases in which their application is hardly reasonable and even impossible. This concerns objects which cannot be observed with the use of electron irradiation for example biological objects accommodating only visual electromagnetic field effects, being investigated in vivo, interesting only by their optical properties, etc. So visual optics is still the reasonable choice but with request of new opportunities.

Most common today is the use of aperture probes for transmission microscopy, either in illumination or in collection mode. However, many samples or substrates are opaque, so that working in reflection is necessary. The reflected light can be collected by optics close to the tip, or by the fiber probe itself, in which case often uncoated fiber tips are used.

Let us underline that nanooptical probes work as electromagnetic (radio) antennas and evidently many general laws valid for them. As for example reciprocity theorem etc., which gives grounds for thoughts. The most important element of the SNOM, as of any scanning microscope is the probe itself.

Further author information -

V.P.V.: E-mail: veiko@lastech.ifmo.ru

N.B.V.: E-mail: vnb@aco.ifmo.ru

M.W.: E-mail: info@oskar.bias.uni-bremen.de

Resolving power of the SNOM is determined mainly by dimensions of the near-field optical probe and the distance from the surface of the specimen to be scanned.

To obtain an image in the SNOM with resolution higher than the diffraction limit, it is necessary to satisfy a few conditions:

- to be able to fabricate in conducting film an aperture with a diameter less than 10–50 nm,
- aperture have to be located at the very tip of the conical light guide in order it could be brought close to any point of a rough surface at a distance less than size of the probe,
- to reduce light losses during passage through the aperture in possible degree.

The most perfect optical probe was used by E.Betsig et al¹. The tip was fabricated from a single mode optical fiber in a device for drawing micropipettes with laser heating. The choice of the drawing regime ensured that tips were obtain reproducibly, with a smooth cone coming at the very end of the tip. When the fiber is broken, a microarea perpendicular to the fiber axis will be formed at the apex of the tip. Nanoaperture is formed by coating the sides of the tapered region with 100–150 nm of opaque Al, leaving the flat endface as a transitive aperture. Apertures from 20 to 500 nm in diameter can be made. The main advantage of a probe based on a drawn optical fiber is that practically all luminous flux can be conducted to the aperture. Authors successfully used such apertures to obtain an image with resolution of about 12 nm and a signal intensity almost five orders of magnitude larger then in other papers.

Light conducting insulating tips made from optical fiber are used in PSTM as light detectors for extracting photons from evanescent field, that exists at the boundary of optical media with different refractive indices in the presence of total internal reflection. The exponential character of the drop in the evanescent field cause tunneling of photons into the extreme point of the tip.

Tips for the PSTM are very often produced by chemical etching in hydrofluoric acid single- and multimode graded-index optical fiber with a core diameter of 5–20 μm and a cladding diameter of 100–200 μm . Depending on the acid concentration, the time and the processing methods of the etching tips are obtained in the form of a truncated cone, a paraboloid of rotation or a cylinder with radius of curvature of 25–100 nm^{2,4}.

The tetrahedral tip with surface plasmons is used as a light emitting probe for the SNOM⁵. It has no aperture as an element for the confinement of light and the techniques of scanning tunneling microscopy and the SNOM can be combined with the same probing tip. The bulk of this tip consists of one corner of a triangular glass fragment of microscope cover glass. It is coated with a 50 nm thick vacuum deposited gold film. An incoming plane wave is first transformed to surface plasmons and than to the linear plasmons traveling along the edge of the pyramid towards the tip. The linear plasmons excites a local plasmon on a metal grain on the tip. In the image of the specimen silver grains are distinguished from gold grains in the transmission SNOM with edge resolution of 1 nm.

Direct control geometry of tips and apertures are usually produces by electron and optical microscopes. Light emitting and collection properties of the nanoprobe are studied by special apparatus in near and far fields.

2. GENERAL REQUIREMENTS TO OPTICAL NANOPROBES CONSTRUCTION

Optical probe in any case independent of the SNOM mode work as an antenna for optical waves and only electrodynamics (field) theory can explain all peculiarities of the probe in the range of $a < \lambda$ size. That is why it is possible to find many analogies with extrashort radio waves antennas. In some cases a probe works as radiating (emitting) antenna, in other cases as a detecting (collecting) antenna.

As it is clear from the principal of the SNOM its spatial resolution and contrast of image depends not from the wavelength λ but from the probe (aperture) size.

Let us note that the most important condition of the real work of the probe with the size $a \ll \lambda$ in both modes of the probe (emitting and collecting) is the presence in their near-field zone more optically dense media.

Any optical antenna should satisfy the next constructive requirements:

- 1) aperture (probe tip) size should be about 5–50 nm,

2) aperture should place at the tie of sharp-only in this case it is possible to bring it near to the surface to the distance $l \sim 5-10$ nm,

3) in case of aperture probes the material of the aperture (diaphragm) should be opaque and depth of light penetration $\delta = \frac{1}{\alpha}$ (α — extinction coefficient) should be less than the aperture size a : $\delta < a$.

The ideal aperture would be the small hole in the thin high conductivity metallic film. Only in this case the light penetration depth δ will be less the geometrical size of aperture a and physical size of the probe will be a little bit more than a . But real metals usually have small conductivity at the optical frequencies. This requirement limits the lowest aperture diameter, because it can not be much less then h . In other case it will work like attenuating waveguide and will have the small transparency. To reduce a we have to use the film coating, smoothly decreasing to the end of edge of aperture. Probably it is the example of good compromise between maximal h and minimal a .

4) The optical transparency or energetical efficiency $\Theta = \frac{P_a}{P_f}$ of the probe is the next important question.

Parameter Θ depends firstly on the diameter of aperture a and secondly from the length l of a conical part l_c of an aperture tip (especially in the zone where diameter of optical fiber d is less than the wavelength λ , $d < \lambda$) and from the shape of this part l_c .

From the optical wave-guides theory, only the main (zero) mode can propagate through the optical fiber with diameter d less than λ . But in this case electromagnetic field goes out from the boundaries of fiber especially where $d < \lambda$. The energetical efficiency (optical transparency) of the first near-field probes was about 10^{-6} . The problem of increasing of the probe optical transparency is one of the most important now.

3. LASER TECHNOLOGY FOR THE PROBE FABRICATION

We have developed the special laser set-up and process installation for the OA fabrication based on laser-mechanical method on action⁶. The idea of this kind of action lies in laser heating during mechanical forces action which accompanies strain, rotation, twisting, bending and other mechanical movements. In this specific case we like to organize the fiber drawing and process during laser heating.

Laser heating comparing with other techniques can provide important advantages for the process:

- the smallest size of heating zone, and
- the minimal inertia of the heating process (to reduce l_c down to λ and less)
- high technological purity.

To realize the fiber-drawing out process usually it is enough to strain and some times to rotate fiber for homogeneity of temperature distribution across the fiber cross-section.

The laser-drawing out set-up scheme is presented in the fig. 3.

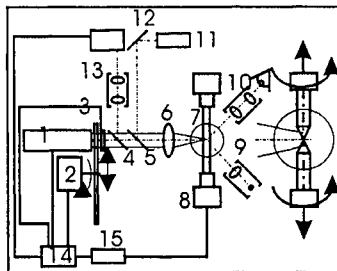


Fig. 3. Scheme of laser set-up for fibers drawing out: 1- CO₂-laser, 2-attenuator, 3-shutter, 4-5 - light-splitting plates, 6-lens, 7-processed sample (optical fiber), 8-electrical motors, 9-illuminator, 10-optical microscope, 11-He-Ne laser, 12-mirror, 13-pyrometer, 14-computer, 15-controller.

The CO₂-laser was chosen for a heating of a fiber-glass. Wavelength of the laser provides an effective absorptency of the light ($\lambda = 10.6 \mu\text{m}$) due to high extinction coefficient $\sim 10^5\text{--}10^6 \text{ sm}^{-1}$ and low reflectance — $R \sim 10\text{--}20 \%$.

The CO₂-laser radiation going through attenuator focuses on to the surface of the fiber cladding. For the homogeneous irradiation it is possible to use a rotation of fiber or some optical devices (thermophysically time of temperature leveling $\tau \sim r^2/a$ across the fiber with diameter $125 \mu\text{m}$ is less than 1 sec.).

We have used different mechanical devices with various direction of forces putting (vertical and horizontal) and with various character of loading (static and dynamic).

Forces of strain was measured by dynamometers, speed of drawing out by tachometer and lengthening by micrometer.

To control the shape of the fiber during the drawing out process the most important parameter is a temperature of a heating zone which directly influences on the viscosity of fiber. That is why to measure temperature was necessary. The high speed path radiation optical micropyrometer was used for this purposes, which described earlier⁷. Main parameters of them are: spectral band — $5.7\text{--}8.7 \mu\text{m}$, temperature range — $200\text{--}2000^\circ\text{C}$, size of registered zone — $0.5\text{--}5 \mu\text{m}$, time of measuring — 0.1 s , accuracy of measurements — $\pm 10 \text{ K}$.

The program of the loading was given by the controller and have had the different scenarios.

All these devices should to permit us to control the process in very delicate zone, where diameter of fiber d and the length of the tip l_c about and less than wavelength λ ($d, l_c < \lambda$, and we are interested in control of $d(l)$).

Important differences of the process in nanometric scale of dimensions are in two main areas: 1) strong influence of small forces (for example, very small residual stresses in the fiber due to drawing out from the hank can lead to the curvature of the end of the tip at the very last moment of drawing out (look fig.) etc.), and 2) hard requirements to the stability and accuracy of the process mechanical and energetical parameters (laser power, fiber temperature, mechanical dimensions, optical parameters, etc.) and to a purity of an environment.

The most important parameters of the process are:

- temperature of fiber T ,
- speed v and force F of drawing out,
- time of strain t_0 and of break fiber T_B beginning on the curve the temperature (more correctly, on the curve of viscosity, depending of temperature),
- length of heating zone l_h and lengthening Δl of fiber, and some others.

Qualitative curves of temperature T , straining forces F and lengthening U during drawing out process of fiber under the laser heating are given at the fig. 4.

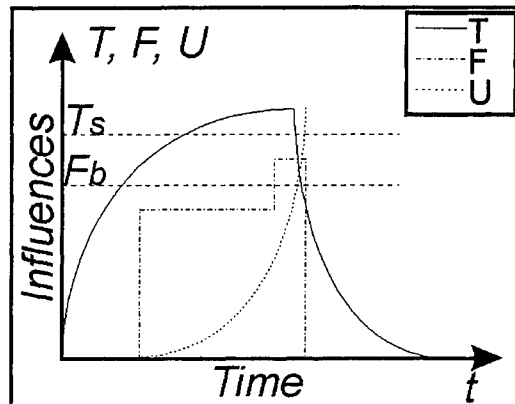


Fig.4. Qualitative characteristics of drawing out of fiber process.

By changing the T , F , v , t_0 , t_b etc. it is possible to control of aperture d , l . Some of parameters like T and U can be used to arrange the feedback for drawing out process. The most complicated task to control shape of the tip $d(l)$, or $r(l)$, which is characterized by many parameters: curvature of the tip end $\frac{d^2r}{dl^2}$, or angle of the tip, etc. Some photographs of typical experimental tips, drawing out under the laser heating are presented at the fig. 5.

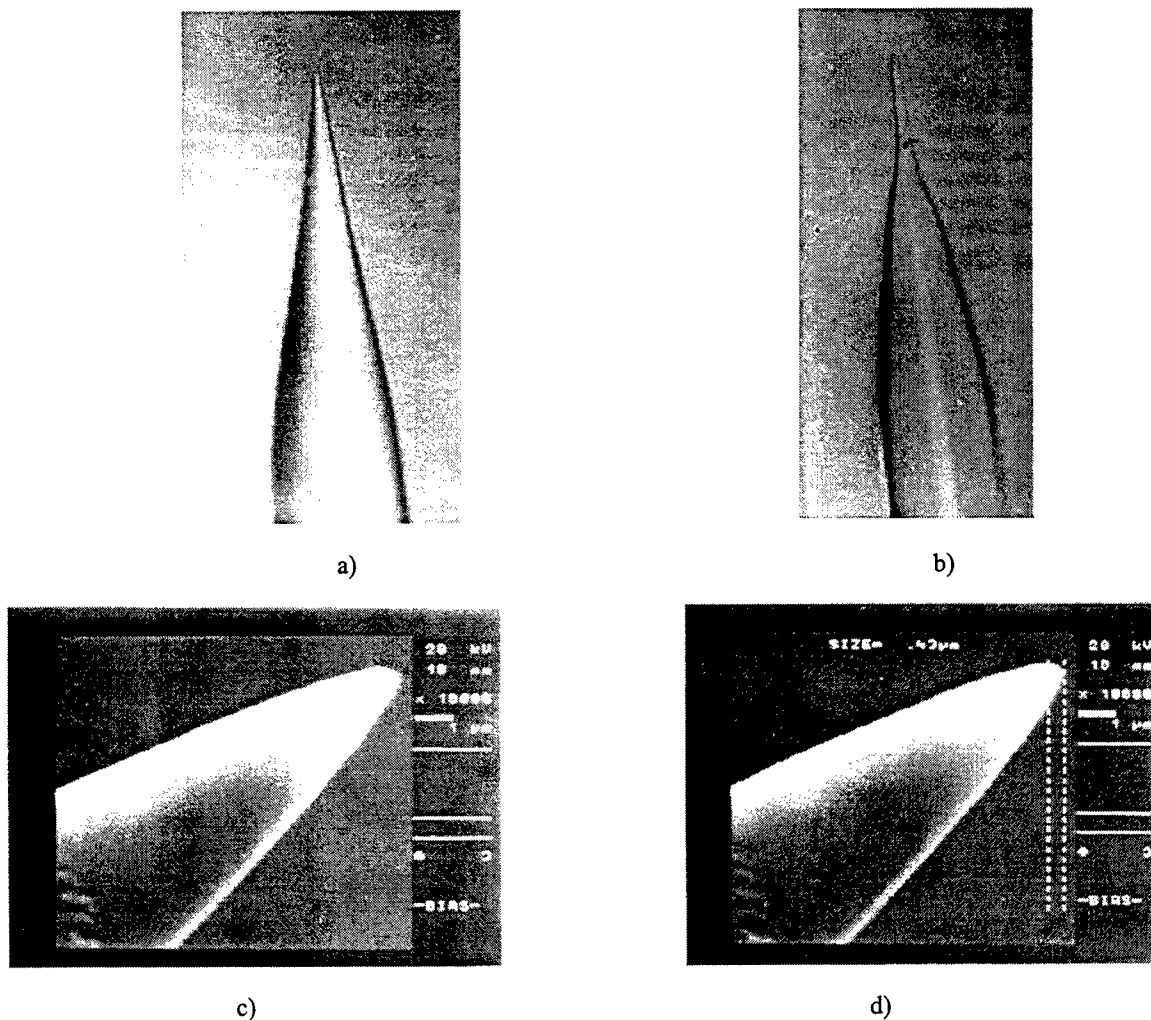


Fig.5. Photographs of nanoprobes fabricated by laser drawing out set-up: a) and b) made by an optical microscope with magnification of $200\times$, c) and d) made by an electron microscope with magnification of $10000\times$. Length of nanoprobes 320 (a) and 300 (b) μm and tips end diameters less than 400 nm. It is possible to obtain various kinds of shapes – conical (a) or pseudoparabolic (b).

In Tunneling Scanning Optical Microscope (TSOM) as a rule chemically etched fiber tips are used. For manufacturing such tips we used a single-mode gradient optical fiber with cladding diameter 125 μm and core diameter 13 μm . Instead of fluoride acid dangerous for human health we used 25-50% NH_4F water solution. The end of the fiber was immersed into solution for 3-10 hours and during this time the level of solution being slowly decreased. The fig.6 shows a general view of one of the manufactured tips at two different magnifications. In the fig.6b the apex of the core can be seen which had as usual curvature radii of 0.1-0.05 μm . Such tips had been used for imaging in the laboratory prototype TSOM in S.I.Vavilov State Optical Institute.

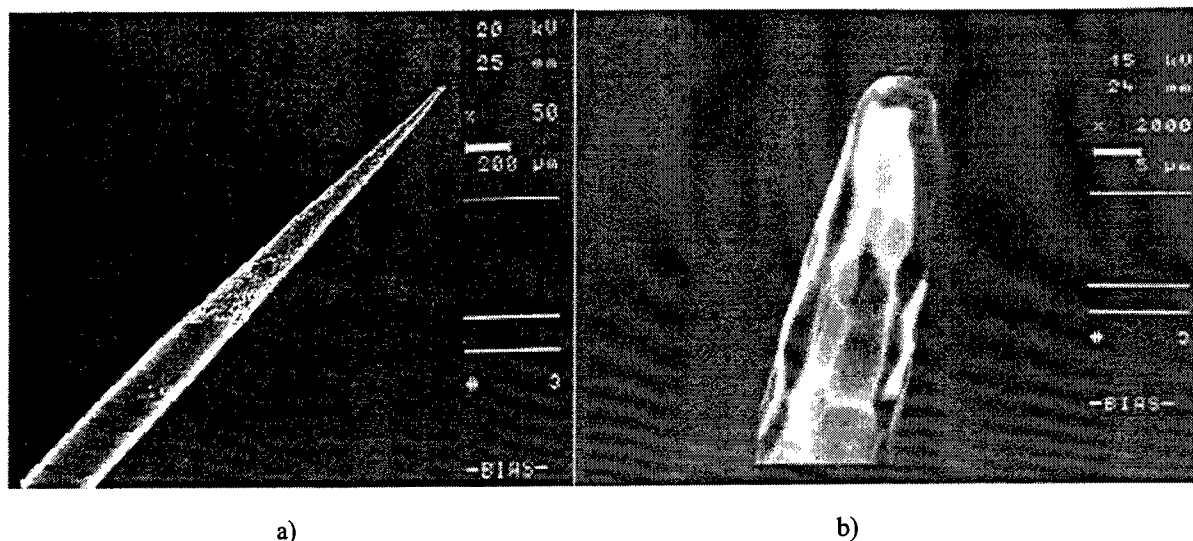


Fig.6 SEM images of an etched optical fiber tip at different magnifications: a – $50\times$, b – $2000\times$. In fig. b) a small part of the core can be seen on the top of the fiber.

4. A THEORETICAL RECONSTRUCTION OF PROBE SHAPE AND DIMENSIONS BY THE FAR-FIELD PARAMETERS

The reconstruction of OA from the registered far-field light is possible if we take into account the Babinet's principle. Being applied to the light passing through a subwavelength sized hole it substantiates that there is some information about the shape and sizes of the secondary source enclosed in the far-field distribution. Some time ago Chr. Obermüller and Kh. Karrai⁸ had investigated the possibilities of far-field registration in order to define the aperture of a secondary light source in submicron scale. This task leads to a generally formulated problem of investigating an arbitrary separate subwavelength sized optical object by its far-field diffracted light processing. In this case the shape recognition with great lack of information meets great troubles and requires a preliminary mathematical extension of the registered part of the diffracted field distribution in order to grasp nanometric dimensions and anything differing from a simple circle.

The theoretical and mathematical problems come from the difficulties of far- and near-field phenomena representation in one model in terms of linear reversible equations. The suggested mathematical modeling is based on the superposition of solutions of Maxwell's equations enclosing linearly polarized vector plane waves in real and complex forms as functions of spatial frequencies corresponding both to the propagating and evanescent light.

The use of vector representation of the light complex amplitude leads to effective reversible calculation procedures for rigorous far-field intensity distribution simulation because it makes possible to use the digital Fourier transform to calculate all the components of the light vector and consequently the intensity. The registered far-field radiation is the angular intensity distribution with respect to angles of diffraction and that is why it should be transformed into the complex amplitude. This transformation leads to the loss of phase which fortunately may be taken as a constant. But the knowledge of the incident light polarization must be taken into account. As it is often noted the polarization status remains without any change inside the fiber as well as while scattering on the aperture. Therefore the vector amplitude of the registered light may be described on the basis of a taken mathematical representation of plane waves.

For the restored parameters of the OA model we obtain a matrix expression which says that a set of Fourier transforms should be performed to obtain the elements of a matrix S' defining the restored shape and sizes of the model. Of course S' may differ greatly from the matrix of initial parameters S because of the lack of direct information about the near-field distribution. The difference increases as a subwavelength sized hole diminishes further. This comes from that the share of propagating waves in the whole mathematical spectrum extremely diminishes as the spatial frequencies of the propagating waves occupy a small interval. To improve the task of restoration of the secondary light source parameters an additional mathematical procedure is required.

The task of more detailed definition of the input distribution may be solved with the use of its continued Fourier spectrum. The process of continuation itself usually is being built as the process of recognition of the input with a sequence of feedback procedures. The real examples of such kind deal either with the analytical continuation of the spectrum on the basis of the sample theorem⁹ or with various iterative procedures¹⁰. The suggested procedure involves a step of polynomial expansion which is realized as Zernike polynomial extrapolation with new approach to calculation of polynomials beyond their orthogonality region with high accuracy. This step gives a set of orthogonal polynomial expansion coefficients which form a numerical model of the visible part of the spectrum strongly related with the model of the invisible one. After that a new iterative procedure of superresolution may be taken for numerical continuation of the invisible part of the spectrum.

The suggested concept of relation between near- and far-field distributions has been applied to a binary model of a secondary light source with circular, elliptical and rectangular apertures. The taken apertures offer to show not only the opportunities of size recognition but the profile as well. Figures 7-9 and 10-12 display the numerical model of near-field intensity distributions and restored distributions for certain secondary sources, all of these distributions having the boundary profile closer to the initial shape of a source aperture after several iterations.

During calculations it was found that simple smallest shapes may be restored with exclusively high accuracy which may help to organize a very stable process of SNOM optical probes estimation.

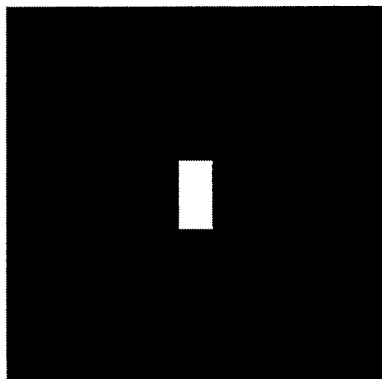


Fig. 7 Rectangle $90 \times 180 \text{ nm}^2$

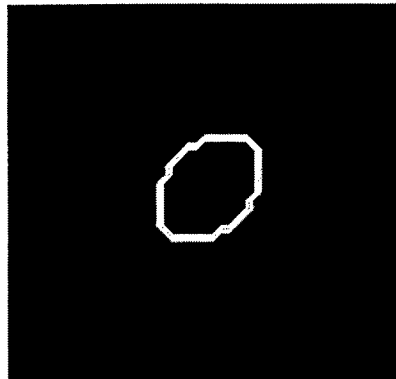


Fig. 10 Ellipse $180 \times 240 \text{ nm}^2$

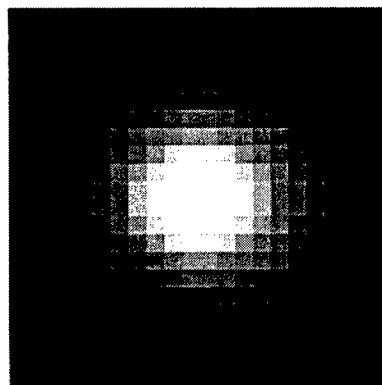


Fig. 8 Reconstruction without continuation

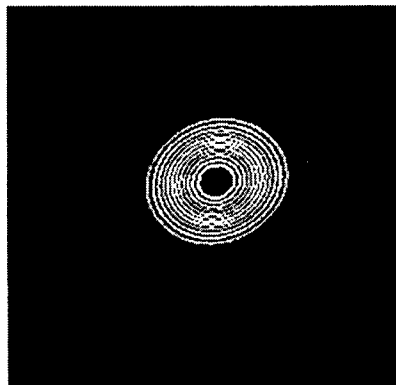


Fig. 11 Reconstruction without continuation

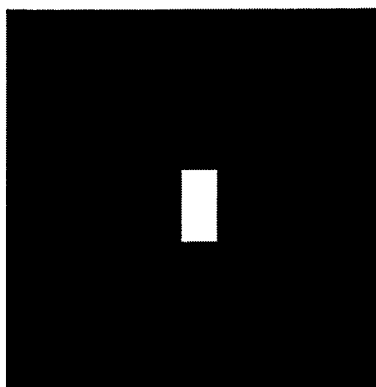


Fig. 9 Reconstruction after 12 iterations

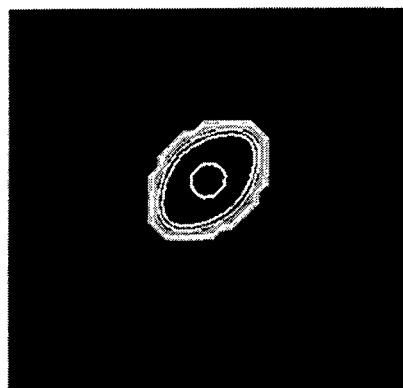


Fig. 12 Reconstruction after 10 iterations

5. CONCLUSION

The problem of stable fabrication of SNOM probes is being characterized by sufficient difficulties of successful forming nanosized tips with taking account of a variety of dynamics, thermal, residual stresses, chemical, etc. factors and ensured control as well. The presented practical and theoretical approaches promise to obtain an effective combined technique based on various ideas of modern technology and optical superresolution in particular.

6. ACKNOWLEDGEMENTS

The authors are very grateful to Prof. Meshkovsky for granting of a drawing-out machine, to Dr. V. Chouyko for the help in experiments, to Prof. M.N. Libenson and Dr. E. Jakovlev for useful discussions. The work was supported in part by the project «Integration of higher education with basic research» funded by the President of the Russian Federation.

7. REFERENCES

1. Courjon D., Sarayedine K., Spajer M., *Opt. Com.*, 1,2, pp. 23-28, 1989.
2. Moechman H.M., Griffith J.E., Filas R.W., *Rev. Sci. Instr.*, 8, pp. 2538-2540, 1994.
3. T.Saiki, S.Mononobe, M.Ohtsu, *Appl.Phys.Lett.* 68 (19), pp. 2612-2614, 1996.
4. J.Koglin, U.C.Fischer, H.Fuchs, *Phys.Rev.* B55, 12, pp. 7977-7984, 1997.
5. Salomon L.D., Fornel F., Goudonet J. P., *J. Opt. Soc. Am.*, 12, pp. 2009-2015, 1991.
6. V.P.Veiko, V.A.Chuiko, M.P.Tokarev. «Laser-mechanical methods of optical fiber treatment for number of microoptical components fabrication», *Proceedings SPIE*, v.2383, Miniaturized Systems with Microoptics and Micromechanics, pp. 224-233, 1995.
7. V.P.Veiko, E.B.Jakovlev, A.K.Kromin. «Laser fabrication on MOC based on laser heating of glass and glass-like materials», *Proceedings SPIE*, v.1992, Miniature and Microoptics, pp.159-167, 1993.
8. Chr. Obermüller and Kh. Karrai «Far-field characterization of diffracting circular apertures», *Appl. Phys. Lett.*, Vol. 67, No. 23, pp. 3408-3410, 1995.
9. Harris J.L. «Diffraction and Resolving Power», *J. Opt. Soc. Am.*, Vol. 54, No. 7, pp. 931-936, 1964.
10. Bates R.H.T. and McDonnell, *Image Restoration and Recognition*, Chs. 2-3, Oxford: University Press, 1986.

Atom projector: basic concept, construction and applications

Nickolay M. Sovetov*, Anatoly V. Nikonov, Dimitry A. Grigor'ev,

Andrey V. Khobotov, Victor A. Moskovsky, Elena V. Naumova

Saratov State Technical University, Politekhnikeskaya 77,

Saratov, Russia, 410054

ABSTRACT

The problems of the atom beam formation and its application to the micro- and nanoelectronic manufacturing are considered. The method introducing a useful information into the structured atom beam and focusing this beam is described. This method named the atom projection is relevant to atom optics. Negative detuned laser radiation field controls the beam. Features of the cooling, structuring, information input, focusing processes are discussed. The scheme of the plant using the focused neutral atom beam as a tool to process surface is designed. This plant named atom projector forms structured cool atom beam with adjustable density distribution. The atom beam cross-section and the processed area are shaped according to the desired profile. The scheme of the atom projector and the functions of its units are described. The spatial resolution of processing and the resolution of surface analysis are evaluated to be about 10 nm and 1 nm correspondingly. Presented process is maskless, in-situ, with high output rating. The atom projector can be applied for the manufacturing, analysis and in-line reconstruction of the IC as well as for basic researches of matter. Authors consider the nanoelectronic chip manufacturing as the most perspective application for the atom projector.

Keywords: nanoelectronic manufacturing, nanotechnology, nanostructure, atom beam, atom optics, Doppler cooling

1. INTRODUCTION

The development of novel generation of IC is connected with their components scaling to small dimensions. In solid-state structures with nanoscales the quantum properties of electron are exhibited, and one can find application for such effects as the interference of electron waves, the resonance tunneling, the single electron tunneling or the coulomb blockade and others. Presently, a number of switching, storing and amplifying electronic devices with unique characteristics are developed¹. For example, the switching frequencies of resonant tunneling and quantum interference transistors are more than 100 times higher the ones of the best silicon transistors; based on single-electron tunneling transistors single-chip memory with the capacity of 1012 bits can be arranged within about 6 cm².

It is supposed that such components will revolutionize electronics as first chips. But these inventions are suppressed, because industrial technologies for nanostructure manufacturing are not developed yet. Various nanotechnologies progress rapidly: the scanning tunneling microscopy, the atom lithography², chemical methods et cetera. Some traditional microelectronic manufacturing technologies are improved and adapted for the nanostructure fabrication. But overwhelming majority of such up-to-date plants fit to laboratory conditions only. While using charged particles, due to space-charge forces the rate of nanostructure fabrication is extremely low. Therefore, increasing attention is paid to the nanotechnologies using neutral atoms for processing. The atom control by resonant laser field seems to be perspective, because forces are rather strong in this case. The idea of practical application of laser radiation forces to atom manipulation is attractive for investigators for a long time from Ashkin's paper³ up to date^{4,5,6,7}. Our group has been developing the disclosed technology since 1989 year. It is designed for precision processing in a broad sense - from the atom deposition on a substrate to the depth-controllable implantation.

* Correspondence: Email: sovetov@altavista.net; WWW: <http://members.xoom.com/sovetov/>

2. ATOM PROJECTION.

The technique of atom projection and the description of field configurations corresponding to all sections of the presented plant were disclosed in detail earlier⁸. Also the mathematical model of atom ensemble dynamics and the results of the computer modeling of the atom beam formation at first two sections of plant were presented ibidem. Here we consider the concept of atom projection in brief only.

One can divide the process of atom projection into the three stages: the stage of the monochromatization and the separation of the original atom stream - the preparing stage, the stage of the beam cross-section formation - the structuring one and the stage of the beam focusing - the compression stage.

The atom projection is based on the following phenomena. In a standing wave formed by quasiresonant laser radiation the dipole (gradient) force manipulates the atoms. If the laser frequency is detuned below the resonance, i.e. if the detuning is negative, the atoms are attracted toward the wave antinodes. Another useful phenomenon- the laser cooling caused by the counter-propagating negative detuned radiations.

At the presented scheme the laser beams of two types are used, they are named the manipulating and the cooling ones. The manipulating radiation has the low intensity and the small frequency detuning, the dipole force is rather great in this case and the cooling is weak. The cooling radiation has the high intensity and the significant detuning.

Let's start from the preparing stage. Suppose the original atom flow to be rather spatially uniform near the axis. Proposed configuration of the manipulating field is presented on Fig.1. The standing wave formed by the manipulating radiations is three-dimensional, so the potential structure for atoms is three-dimensional too. The laser beams are denoted by the wave vectors \vec{k}_i . The atoms concentrate near antinodes corresponding to potential wells (Fig.2). For more effective manipulation the atoms are cooled at the bottoms of these potential wells continuously. The cooling field configuration is three-dimensional too. To spread the energy range of coolable atoms and to erase a potential structure of the cooling field this radiation is frequency swept. The sweep band is matched to the atom beam temperature. Let's take the detunings so as the standing wave formed by the manipulating radiations to drift. The species of conveyor for atoms is realized. This is the task of the preparing stage, i.e. the preparing stage forms the latticed cool atom beam with low velocity.

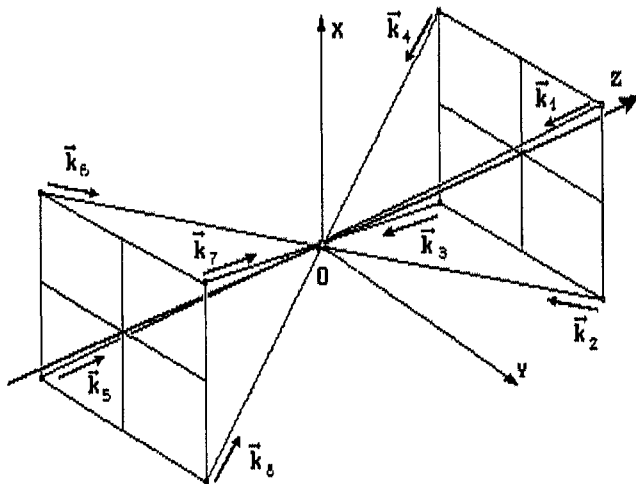


Fig.1. Configuration of the manipulating field at the preparing stage.

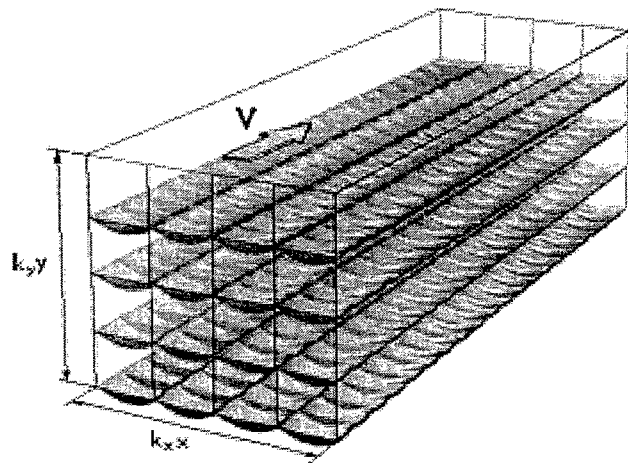


Fig.2. The skeleton potential structure for atoms at the preparing stage.

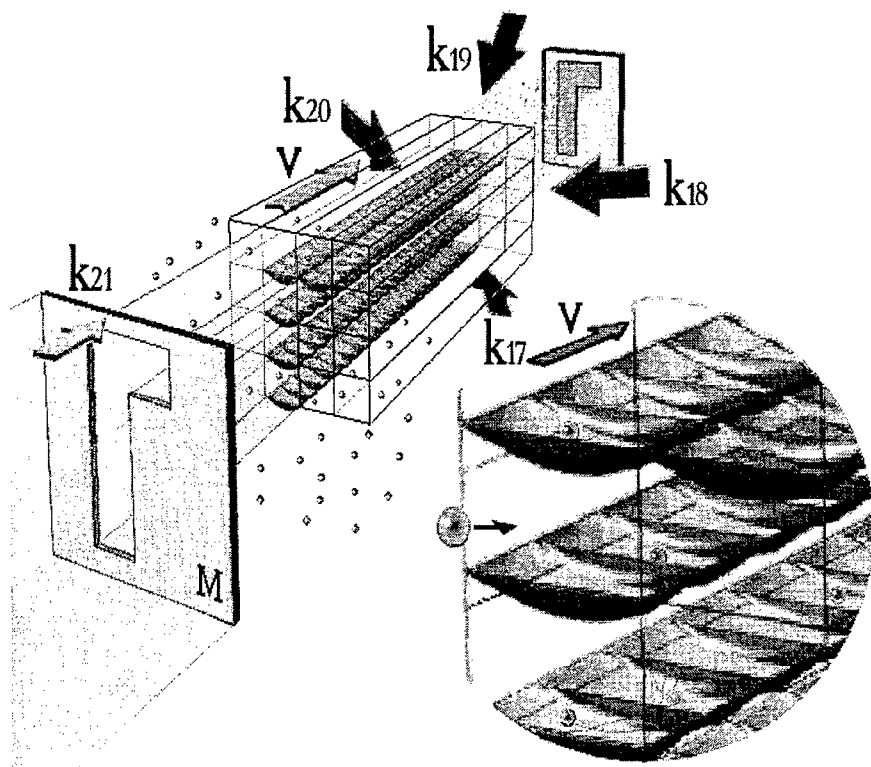


Fig.3. Configuration of the manipulating field and the «atom conveyor» at the structuring stage.

Then the manipulating field with another configuration (Fig.3) acts on this drifting atom lattice at the structuring stage. The co-propagating laser radiation has specified intensity distribution, for example, it may be cut out by the mask. Within the exposed pattern of cross section the field has a structure similar to the conveyor, at the masked area a head "laser wind" blows. This head "wind" cuts out the certain "belts" of the conveyor. The desired pattern is projected in the atom beam like so. At the structuring stage the cooling field configuration is analogous to the preparing stage's one, but the sweep band is narrowed according to the atom temperature lowering. So the preparing stage forms the atom beam with latticed internal structure and the cross-section pattern specified by the mask. At this stage the translation velocity of the atom beam keeps the same. Resulted beam is well collimated and cooled.

At the following stage the field has rather complicated structure disclosed earlier⁸. The potential for atoms has no longitudinal structure, its cross structure represents square cells scaling down along longitudinal axis. This field structure makes the "conveyor belts" to converge homocentrically (Fig. 4). So the atom beam is focused, and the cross-section pattern of the atom beam formed at the structuring stage is scaled. Simultaneously the atoms are accelerated along the "conveyor belts", leave off the interaction with the field due to Doppler effect, and then atoms continuing inertial motion get at the processed surface.

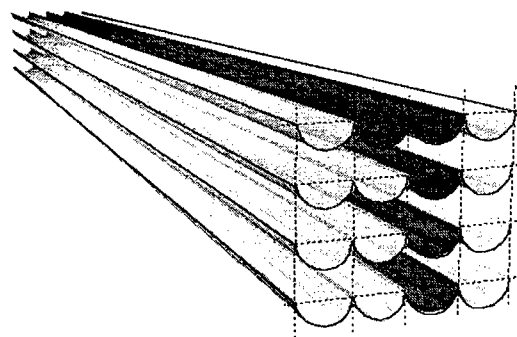


Fig.4. The skeleton potential structure at the compression stage.

3. THE SCHEME OF THE ATOM PROJECTOR.

The plant based on presented technique was named the atom projector. Some quantitative characteristics mentioned below were computed for helium, but theoretically atom projector allows manipulating atom beams of other substances.

This paper presents the atom-optical system of the plant only, the auxiliary systems (vacuum, antivibrating, mechanical systems et cetera) are not described here, only several most important parameters of the auxiliary systems are mentioned below.

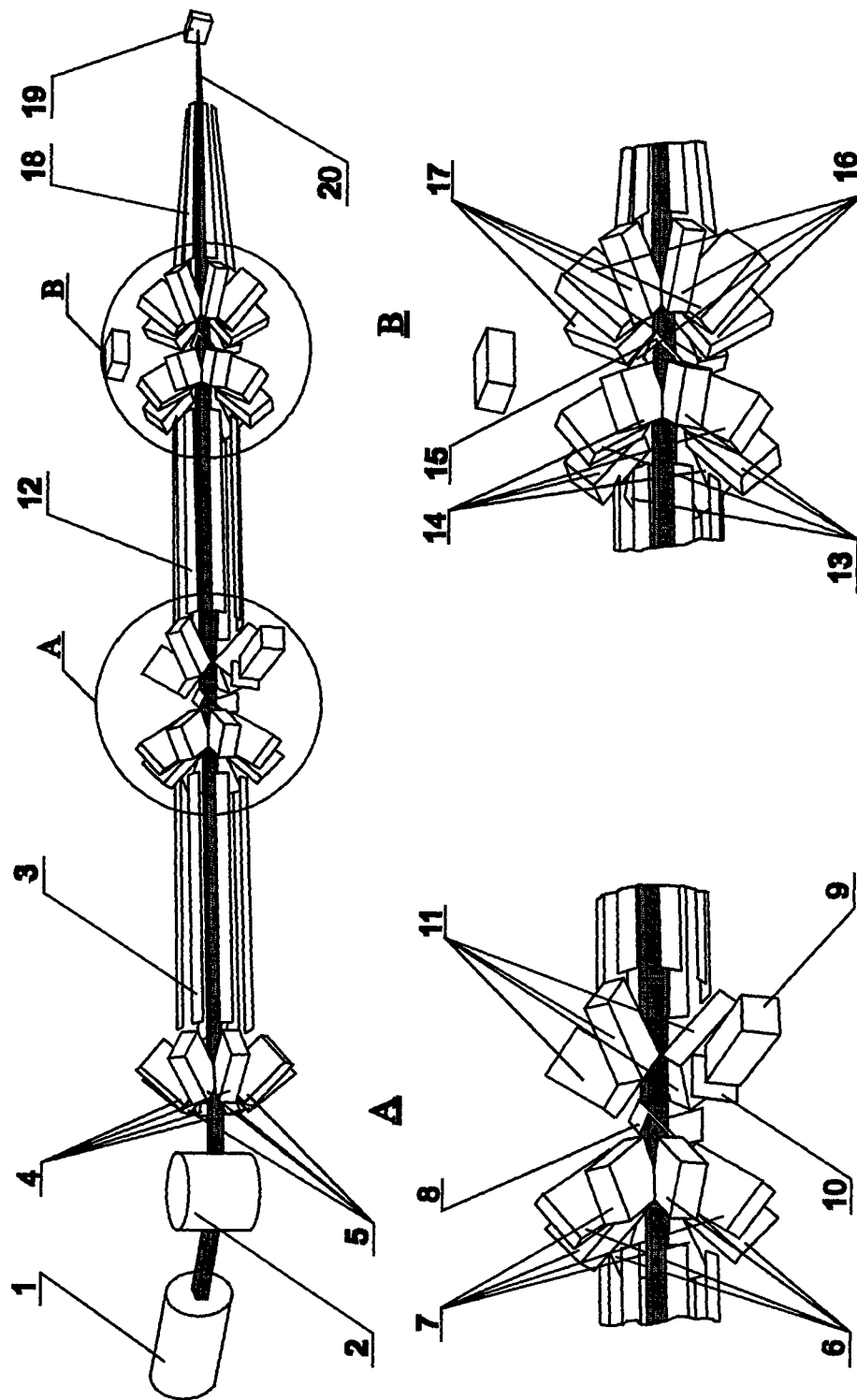


Fig. 5. The atom projector scheme: the neutral atom source 1; the optomagnetical separator 2; the preparing section: the mirrors 3 forming the manipulating and cooling fields (the plane-parallel axicon), the sources 4 of the co-propagating coherent manipulating radiation, the sources 5 of the co-propagating cooling radiation, the source 6 of the counter coherent manipulating radiation, the sources 7 of counter cooling radiation; the microchannel mirror - filter 8; the structuring section: the source 9 of the co-propagating manipulating radiation, the mask 10, the sources 11 of the co-propagating cooling radiation, the mirrors 12 forming the manipulating and cooling fields (the plane-parallel axicon), the sources 13 of the counter coherent manipulating radiation, the sources 14 of the counter cooling radiation; the microchannel mirror - filter 15; the compression section: the sources 16 of the co-propagating manipulating radiation, the sources 17 of the co-propagating cooling radiation, the mirrors 18 forming the manipulating and cooling fields (the pyramidal axicon); the processed microobject 19; the atom beam 20.

In the working chamber of the plant the vacuum system should support the pressure less than 10^{-6} torrs with the leakage rate about 500 litre/sec. The antivibrating system should prevent the transversal oscillations more than 0,1 microns for the frequencies more than 50 kilohertz.

3.1. The neutral atom source

At the neutral atom source 1 (see Fig.5) the original stream of ions is formed by the ion source. As an ion source the abnormal or normal glow discharge device with the plate voltage 0,5 - 1,5 kilovolts working on helium - argon mixture at the pressure 10^{-2} - 10^{-3} torrs can be used. Such ion source creates sufficient monochromatic ion stream. However as an ion source some other standard devices can be applied also.

Then a low-energy electron cloud neutralizes the ion stream. Such neutralization is estimated to distort atom trajectories and energies less than others do. The neutralized atom stream passes through the optomagnetical separator 2 (Fig.5) eliminating electrons, ions and not interacted atoms from excited atoms of a working substance. Thus, only excited atoms meeting the Doppler resonance condition³ at the preparing section are selected.

3.2. The preparing section

The selected neutral atom stream moves to the input of the preparing section. This section main task is to cool atom beam near the low velocity V_0 and to structure it uniformly. The preparing section consists of the mirrors 3 (see Fig.5) forming the manipulating and cooling fields (the plane-parallel axicon), the sources 4 of the co-propagating manipulating radiations, the sources 5 of the co-propagating cooling radiations, the sources 6 of the counter-propagating manipulating radiations, the

sources 7 of counter-propagating cooling radiations. The laser sources of the preparing section form linearly polarized plane waves. For the field to fill out the working zone of the channel more uniformly, over the wave front the amplitude of each laser beam is modulated in the triangular form by the inhomogeneous - reflecting mirrors in the input of the axicon 3 as shown on Fig. 6. Overlapping codirectional laser beams form running wave, which is homogeneous over the wave front. Triangular amplitude distribution matches not only amplitudes but also phases of various waves of the same name (the cooling or manipulating ones), those fill up an axicon interior. It avoids phase and amplitude abrupt changes, when an unavoidable insignificant shift of the laser beams took place. Some other wave front modulations are acceptable as well as the triangular one. So, the better uniformity and periodicity of the laser field are achieved.

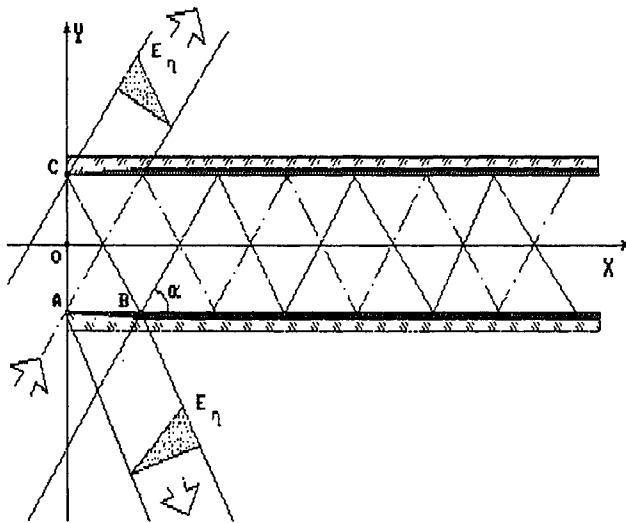


Fig.6. The formation of laser beams with triangle amplitude distributions over the wave fronts and their overlap scheme.

The axicon mirrors 3 reflects the laser beams from the sources 4 and 6, thus and so they form the three-dimensional interference periodic pattern (Fig.2, Fig.3) in the form of lattice. This lattice with fixed structure is drifting along the axis Oz with the velocity V_0 . The small

detuning between the contradirectional beams causes the uniform movement of this three-dimensional standing wave. The lattice cross-section represents close-fitting square cells with the pitch depending on the declination of the manipulating beams to the channel axis. As mentioned above, the minims of the potential structure of the manipulating field represent the drifting three-dimensional lattice too. This lattice moves along the channel axis with a low velocity evenly. The manipulating field is designed to concentrate atoms near these drifting minima by a dipole force, so as to form the structured beam. Depending on the possible filling of this lattice by atoms is evaluated to be about 5-10%. More compact filling is undesirable, so as to avoid interaction between atoms at the compression section. The axicon mirrors 3 reflect the laser beams from the sources 5 and 7, so the cooling field fills up a space of the preparing section uniformly. To intensify the interaction with the manipulating field, atoms are cooled over the velocity of the wells drifting continuously with velocity V_0 . To avoid the formation of the additional potential structure by the cooling field and to widen the temperature

range of controllable atoms, the cooling field is frequency-swepted². The various modes of sweeping not causing the additional motion of atoms over wells may be designed.

Due to the interaction with the field of the preparing channel, the excited atoms are cooled² and localized in potential wells of the three-dimensional interference periodic pattern driven with the velocity V_0 . The organized atom beam passes through the orifices of the mirror - filter 8 to the structuring section. Some atoms interact with laser field not effectively. They are reflected by the microchannel plate 8 and leave the interaction area.

3.3. The structuring section

The structuring section includes the source 9 (see Fig.5) of the co-propagating manipulating radiation, the mask 10, the sources 11 of the co-propagating cooling radiation, the mirrors 12 forming the manipulating and cooling fields (the plane-parallel axicon), the sources 13 of the counter-propagating radiations, the sources 14 of the counter-propagating cooling radiation. At the structuring section the co-propagating manipulating radiation of the source 9 passes over the mask 10, which transparent areas represent the scaled copy of the substrate areas to be processed. The radiation of the sources 9 and 13 reflected by the axicon mirrors 12 forms the three-dimensional interference pattern, exposure of its cells corresponds to the mask pattern. This interference pattern drifts along the axis Oz with the constant velocity V_0 . At "not lightened" areas the cellular field structure is absent, and the counter-propagating radiation destroys the atom beam structure, these atoms fall into vacant cells of the "lightened" area or return to the ground state and can not interact. Thus, the useful information is projected into the neutral atom beam. At the output of the structuring stage, the atom beam has the cross distribution according to the desired layout and the internal beam structure rests uniform. The mirror - filter 15 placed between the preparing and structuring sections reflects co-propagating radiation to absorber and eliminates atoms left interaction. The mirror- filter 15 is analogous to the mirror - filter 2 dividing the preparing section and the structuring one.

3.4. The compression section

The main purpose of the compression section is to focus the atom beam with the least distortion of the information projected into the beam. This section consists of the sources 16 (see Fig.5) of the co-propagating manipulating radiations, the sources 17 of the co-propagating cooling radiations, the mirrors 18 forming the manipulating and cooling fields (the pyramidal axicon). The configuration of the compression section is designed to generate the converging potential structure for atoms. For this purpose the axicon 18 of the compression section is not plane-parallel, as for the previous two sections, but pyramidal. Its form and also an absence of counter-propagating manipulating radiation result in the field structure representing homocentric converging square tubes without longitudinal structure. The potential structure of each tube has the axial symmetry, the potential minima coincide to the tube axis. To keep the information more completely the transverse interference pattern of the compression section input is matched with the pitch of the beam structure at the structuring section. At the compression section neutral atoms are kept inside converging channels of the field and are accelerated (due to absence of the counter-propagating radiation). The longitudinal atom velocity is rising gradually, at the output of the compression section this velocity can exceed the velocity of drift at the previous sections in 5-6 times. The energy of the accelerated atoms is more than 100 electronvolts. Varying the parameters of the accelerating field at the compression section one can vary the atom beam energy in broad band. Due to this feature the plant can execute different operations (from the degassing to the implantation).

With atom velocity increasing, the intensity of atom- field interaction is reduced, atoms hold off the interaction gradually, and their motion becomes inertial, then being moving the same directions the atoms drift to the substrate 20 mechanically. It is also important, that the atom velocity and the equivalent energy have great increase before the effective interaction hold-off. So with the atoms returning from the excited state to the ground one, the uncompensated emitted quantum of energy does not influence on atom trajectory and on the resolution consequently.

Precomputations show the presented plant resolution 6-8 nm that exceeds the resolution of up-to-date methods at least in the order of magnitude.

4. CHARACTERISTICS AND APPLICATIONS OF THE ATOM PROJECTOR.

Main technical applications of the atom projector correspond to levels of atom beam energies. At up-to-date level of laser

engineering the following operations are achievable (listed in order of the beam energy increasing):

- the degassing, purification and the preparing of a surface, the modification of its properties;
- the atom lithography with the resolution about 5-10 nm;
- the controlled growth of microcrystals by deposition on substrate of atom stream with strictly specified spatial and energy distributions;
- the high-resolution maskless one-stage processing of microstructures (from the atom deposition on substrate to the etching of upper layers according to the specified layout, the in-line reconstruction of defective structures);
- the non-destructive topological and chemical surface monitoring with high spatial and spectral resolutions and a lowered level of electrostatic disturbance;
- the layer-by-layer scanning quantitative and qualitative analysis of surface, the parallel defectoscopy;
- the atom microscopy with resolution about 1-2 nm;
- the depth-controllable implantation of atoms with the specified concentration distribution over the cross section of the processed object;
- the acceleration of neutral atoms.

Summing up we specify features of the atom projection:

- the spectral purity and high level of the organization of the manipulated atom beam;
- the atom velocity distribution is very narrow;
- the beam energy is adjustable in a broad band easily;
- the transverse distribution of the atom beam is controlled by rather simple projection technique;
- the high compression of the atom beam (to be matched with the analogues ion beam the intensive atom beam is corresponding to the $I = 1.7 \text{ A}$).

All these features allow to hope for the development of new, effective processing and analysis of microobjects. Listed advantages appear in technological process as:

- the high efficiency. For example, the rate of coating etching is estimated to be about $3 \mu/\text{sec}$ (with the sputtering coefficient 0.1 atom/particle, the density- 20 g/cm^2 , the 10%- filling of potential well pattern), the spraying rate of complete conducting structure is $0.5 - 1.5 \mu/\text{sec}$;
- possibility to manufacture the micro- and nano-scaled structures with complex layouts including three-dimensional nanoneuroelements;
- the minimum of steps for complex chip manufacturing;
- the high reproducibility of structure parameters with the minimum of in-process transfers and with nanometer resolution;
- the simplicity of residual contamination removal;
- the reliability of defect diagnostics;
- the in-line reconstruction of produced structures;
- the chip manufacturing in-situ;
- the universality of the processing.

Main design parameters of the disclosed plant:

- a) the area processed simultaneously- $200 \times 200 \mu$,
- b) the number of element channels per the area processed simultaneously - 9000000,
- c) the resolution- from 1-2 nm to 10 nm (for different operations),
- d) the positioning precision - 6 nm.

According to preliminary estimations, the universality of this plant and the possibility of processing in-situ allow to decrease the number of operations in 3 times, the necessary number of plants - in 7 times and to reduce number of the staff in comparison with modern industrial technologies.

The atom projector was designed for micro- and nanoelectronic manufacturing, but it should be applied for scientific research in different areas, for example, in surface investigations, atom physics and spectroscopy, molecular chemistry, biology, crystallography.

The authors suppose that with paying due attention to the presented plant and its development, it will be one of practical laser nanotechnologies in the XXI century.

7. ACKNOWLEDGMENTS

Authors are grateful to Lepilova T.D. for her support in this paper preparing.

REFERENCES

1. В.Е. Борисенко, "Наноэлектроника- основа информационных систем XXI века," Соросовский образовательный журнал 5, pp. 101-105, 1997 (in Russian).
2. R. J. Celotta, J. J. McClelland, *US.Patent* 5,360,764.
3. Ashkin, *Sci. Amer.* **226**, No. 2, pp. 63-78, 1972.
4. S. Chu, "Laser trapping of neutral particles", *V mire nauki* 4, pp. 41-47, 1992 (in Russian).
5. V.G. Minogin., Yu.V. Rozhdestvenski, "Stable localization of atoms in standing light wave field," *Opt. Commun.* **64**, No.2, pp. 172-174. 1987.
6. В.Г. Миногин., В.С. Летохов, *Давление лазерного излучения на атомы*, "Nauka", Moscow, 1986.-226 p. (in Russian).
7. V.I. Balykin, "Laser optics of neutral atom beams", *Izv. AN SSSR. Ser. Phys.* **52**, No.6, pp. 1073-1080, 1988 (in Russian).
8. N.M. Sovetov, A.V. Nikonov, D.A. Grigor'ev, V.A. Moscovsky, E.V. Naumova, "Laser controlled moving atom structures for microelectronics," *Proc. SPIE* 2991, pp.274-284, San Jose, California, USA, 1997

SESSION 2

Fundamental Processes and Diagnostics of Laser Ablation

Laser-induced electronic bond breaking and structural changes on semiconductor surfaces

Katsumi Tanimura* and Jun'ichi Kanasaki

Dept. of Physics, Nagoya Univ. Furo-cho, Chikusa, Nagoya 464-8602, Japan

ABSTRACT

We review the bond breaking and structural changes on clean surfaces of Si(111)-(7x7) and of InP(110)-(1x1) induced by ns- and fs-laser irradiation with fluences below thresholds of melting and ablation. Atomic imaging of the irradiated surface by scanning tunneling microscopy (STM) has shown that the bond breaking of adatoms of Si(111)-(7x7) is induced by an electronic process to form adatom vacancies mostly at individual adatom sites. Si atoms in the electronic ground state are desorbed with a peak translational energy of 0.06 eV, as a direct consequence of the bond breaking. On the other hand, STM images of the irradiated InP(110)-(1x1) surfaces have revealed the preferential removal of the top-most P atoms, with significant formation yields of vacancy strings consisting of several adjacent vacancies on the quasi-one dimensional P rows. The isolated In vacancies are also formed, but with a much smaller yield. For both surfaces, bond breaking takes place at intrinsic sites of the surface structures, and the efficiency is strongly site-sensitive, resonantly wavelength-dependent, and highly super-linear with respect to the excitation intensity. The electronic bond breaking is shown originate from non-linear localization of excited species in surface electronic states.

Keywords: Laser-induced desorption, electronic excitation, semiconductor surfaces, scanning tunneling microscopy,

1. INTRODUCTION

Extensive studies have been carried out on the interaction of laser light with solid surfaces, motivated from both applications in material processing and basic research on light/matter interactions¹⁻². The interaction results in phenomena full of variety, depending on wavelength and the power of laser light, and on the basic properties of surfaces of materials. Even for semiconductor surfaces, several qualitatively different phenomena are induced, depending on a wide range of fluence from a few hundreds of $\mu\text{J}/\text{cm}^2$ to a few J/cm^2 of ns lasers. As demonstrated clearly, the surfaces of semiconductors start to be melted upon laser irradiation above certain thresholds of fluence, which depend of the wavelength, pulse width, and basic properties of substance.³ For laser fluences above the melt threshold, sublimation from laser-induced molten layers takes place leading to desorption of constituent atoms,⁴ and surface reconstruction are often induced by rapid melting followed by rapid recrystallization.⁵ At more intense-fluence regime, the interaction of laser pulses with surface results in ablation, in which dense plasma is formed to cause ejection of high energetic ions and atoms. On the other hand, desorption of constituent atoms from semiconductor surfaces is induced even for fluence range much below the thresholds of melting and ablation. It has been shown that electronic processes are primarily involved in surface structural changes associated with desorption of constituent atoms for low-fluence regime.⁶⁻¹¹ Recent developments in experimental techniques, e.g. sophisticated methods of high-sensitive detection of desorbed species and direct atomic imaging⁸⁻¹¹ of the irradiated surfaces have enabled us to study the surface atomic processes induced by electronic mechanisms from a more microscopic point of view.

Surfaces of tetrahedrally bound semiconductors generally show drastic reconstruction and/or relaxation, where bonding properties differ significantly from those in bulk.¹² Consequently, surface electronic states with quasi two-dimensional nature are formed which are characteristic of reconstruction and relaxation. The Si(111)-7x7 surface is a typical example of a reconstructed surface on which extensive studies have been carried out both experimentally and theoretically. The atomic structure of this surface is well described by the dimer-adatom-stacking-fault (DAS) model,¹³ with a unit cell consisting of 12 adatoms, 42 first-layer atoms and 9 dimers. The surface electronic states have also been studied by photoelectron spectroscopy (UPS),¹⁴ inverse-photoelectron spectroscopy,¹⁵ scanning tunneling spectroscopy,¹⁶ and theoretical calculation.¹⁷ The other example of the surface studied extensively is the {110} surface of III-V compound semiconductors, which crystallize in the cubic zincblende structure. With this {110} surfaces of semiconductors no reconstructions are

* Correspondence: Email: tanimura@edu3.phys.nagoya-u.ac.jp; Telephone:+81 52 789 3552; Fax:+81 52 789 2933

induced but the surface atoms relax significantly from a bulklike termination.¹² As a result of this relaxation, the cation-anion zigzag chains become tilted with the anions being raised. Thus, the surface structure is quasi-one dimensional rather than two-dimensional. The accumulating knowledge of semiconductor surfaces provides the basis on which we can study the laser-induced electronic processes of structural changes and desorption.

Recently, it has been demonstrated that a laser-induced electronic process removes adatoms of the Si (111)-(7x7).¹⁰ This electronic bond breaking on Si(111)-(7x7) has shown quite different features from those known through laser annealing studies. Subsequent studies on InP(110)-(1x1) surfaces have shown that the similar electronic mechanism holds for bond breaking of In and P atoms incorporated into the intrinsic 1x1 structure, although some features are different depending on basic properties of the surfaces.¹¹ The purpose of this paper is to review laser-induced structural changes by the electronic mechanism on these typical semiconductor surfaces.

2. LASER-INDUCED ELECTRONIC BOND BREAKING ON Si(111)-(7x7)

Laser-induced effects on silicon surfaces were studied extensively for understanding the mechanism of laser annealing in this material. For fluences above melt threshold, structural changes of Si(111)-7x7 surface were induced to result in new reconstructions forming c-(4x2) and (2x2) structures on the surface.⁵ The structural transformation was attributed to the laser annealing involving rapid melting followed by rapid re-crystallization. Sublimation of constituent atoms from the laser-induced molten layer is also induced. Time-of-Flight (TOF) spectra of Si atoms under the irradiation of laser pulses with fluences of 1-2 J/cm² showed that the translational energy of desorbed Si atoms increased with increasing fluence.⁴ The fluence-dependent translational energy was regarded as a consequence of the melting of the surface region. The atomic processes on Si(111)-7x7 we discuss here show essentially different features from those reported previously in the laser-annealing study. First of all, the fluence of laser pulses used for exciting surfaces is smaller by an order of magnitude than those used previous studies. Also, the structural changes revealed by direct atomic imaging by STM and characteristics of desorption of constituent atoms show significant difference from those in laser annealing. Below we survey important features of the process induced by irradiation of laser pulses at fluences below the melting threshold.

2.1. Features revealed by STM observation

Ishikawa et al. have studied the changes in atomic structures of Si(111)-7x7 surface irradiated with 500-nm dye-laser pulses with a fluence of about 100 mJ/cm², which is below the thresholds of melting and of ablation.⁸ They found that adatom vacancies were newly formed, while keeping the 7x7 structure essentially unchanged. The atomic images of the irradiated surfaces showed no trace of surface melting and no indication of forming intermediate structures, which could be formed under more intense-laser irradiation.⁵ Their statistical analysis of the laser-induced adatom-vacancy formation revealed an interesting feature that the removal of adatoms took place with strongly site-dependent efficiency. In the DAS model of Si(111), 12 adatoms in a unit cell are not completely equivalent; a triangle composed of six adatoms is located on the subunit containing the second-layer atoms with stacking fault with respect to the third-layer atoms, but the other is on the subunit lacking the staking fault.¹³ Also, the sites of adatoms comprising a triangle can be classified into two sites; the adatoms at the corner of the triangle, corner adatoms, and the rest, center adatoms, show different properties.¹⁸⁻²⁰ Ishikawa et al. have found that adatom vacancies at the center-adatom site are formed by about three times more efficiently than at the corner adatom site. This preferential removal of center adatoms holds for irradiation with different fluences; the ratio of number of vacancies at the center-adatom site relative to that at the corner adatom site remains almost constant irrespective of laser fluence. On the other hand, essentially no difference was detected in the relative ratio of the yields of adatom vacancies whether they are on the faulted half or unfaulted half.

Kanasaki et al. have studied the yield of adatom vacancies formed by repeated irradiation of laser pulses as a function of the number m of laser shots (or dose) at a given fluence Φ .¹⁰ Their result for 600-nm excitation is shown in Fig.1, where the total number n_t of laser-induced adatom vacancies, (a), and the ratio of vacancies at corner-adatom sites relative to those at center-adatom sites, (b), are plotted as a function of m . It is clear in the figure that n_t increases in proportion to m up to the concentration of about 10 %, with keeping the ratio of about 0.3 constant. Since the ratio of 0.3 does not depend on m , the site-dependent yield of adatom-vacancy formation is not due to any accumulated effects under repeated irradiation, but is a direct consequence of the process, which takes place within each laser pulse. Results similar to those shown in Fig.1 were obtained for irradiation at various fluences and at different wavelengths from 400 to 700 nm.¹⁰ The site-dependent yield of the adatom-vacancy formation with a ratio of about 0.30 was the case for all of these different excitation conditions. Therefore, the site-sensitive yield is a characteristic of the final step of bond breaking process, independent of excitation wavelengths.

Based on the linear relation between n_L and m , they determined the efficiency η of adatom-vacancy formation per single shot of a laser pulse with a given Φ . In Fig.2, the magnitudes of η 's thus determined for 500-nm excitation are plotted as solid circles as a function of Φ . The efficiency shows a super-linear dependence on the excitation intensity. Similar measurements of η 's at different excitation wavelengths have shown that the magnitude of η depends strongly on the

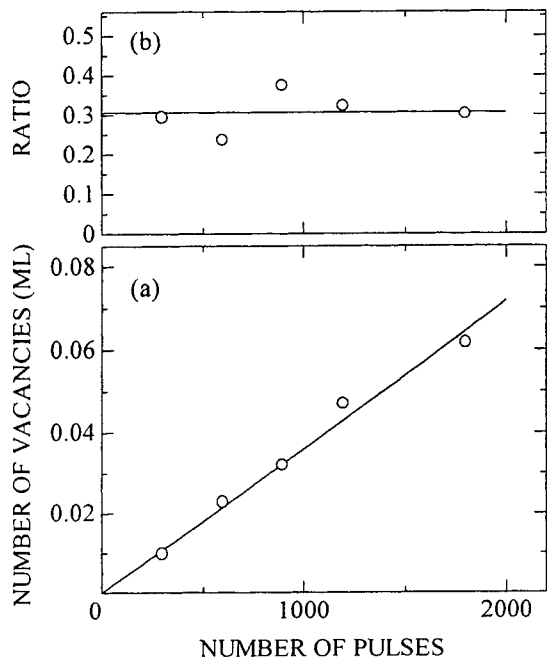


FIG. 1. The concentration of laser-induced adatom vacancies (a), and the ratio of the number of vacancies formed at the corner-adatom site relative to that at the center-adatom site (b), as a function of the number of 600-nm laser pulses with a fluence of 23 mJ/cm² (from Ref.10).

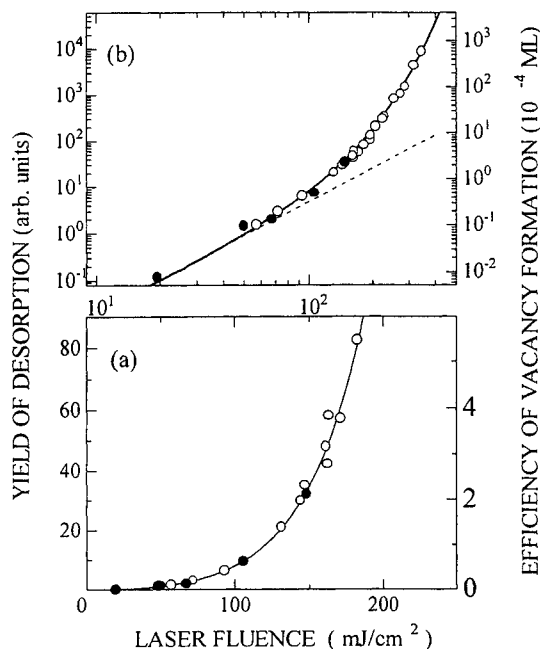


FIG. 2. Fluence dependence of the yield of Si-atom desorption (open circle) and efficiency of adatom-vacancy formation (solid circle) induced by irradiation with a single shot of a 500-nm laser pulses in (a), linear scale, and in (b), logarithmic scale. Solid curves are the best-fit curve of the formula of the two-hole localization mechanism (from Ref.10)

wavelength for surface excitation. Thus, the bond breaking of adatoms on Si(111)-(7x7) induced by laser pulses with fluence far below melt threshold is characterized by the efficiency which is site-dependent, wavelength-dependent and highly super-linear with respect to the excitation intensity. The result that no trace of melting is detectable in STM images is indicative of the electronic mechanism of the bond breaking of adatoms.

2.2. Desorption of Si atoms induced by the electronic bond breaking of adatoms

The laser-induced bond breaking on Si(111)-7x7 surfaces have been studied also by detecting desorbed species with high sensitivity. From the results of STM measurements, it has been shown that adatoms are removed at a rate of 10⁻⁴ monolayer or less per pulse. When neutral atoms are the main desorbed species, we need to use a method with high sensitivity for detecting these small amounts of atoms. Kanasaki et al. have applied the resonance-ionization spectroscopy (RIS), in which neutral atoms are excited first to an excited level and then ionized by an intense laser pulse.^{10, 21} By tuning the wavelength of the laser light for ionization, desorbed atomic species are identified. Also, by changing the time delay between the laser pulse for exciting the surface and the one for ionizing neutral atoms, one can determine the kinetic energy distribution of desorbed atoms from the resulting TOF spectra. Figure 3 shows the TOF spectra of Si atoms desorbed from a 7x7 surface irradiated with 532-nm laser pulses with fluences of 84 and 245 mJ/cm².²¹ In the measurements, ns-laser pulses tuned to the ³P₀-³P₁ transition energy (4.928 eV) of Si atoms were used for ionization. This means that the desorbed species by laser irradiation to the 7x7 surface is mainly Si atoms in the electronic ground state. Si ions were not detected for the fluence range studied (below 400 mJ/cm²). The TOF spectra measured for two fluences show the same peak flight time and the same distribution; velocity distribution of desorbed Si atoms is not dependent on the fluence. This contrasts to the case of laser annealing, where the peak translational energy of desorbed Si atoms increases with increasing fluence of excitation-

laser pulse.⁴ Therefore, the fluence-independent velocity distribution also indicates that desorption of Si atoms from this 7x7 surface induced by irradiation with laser pulses of the fluence below 400 mJ/cm² is not related to surface melting.

In Fig.2, the yield of Si-atom desorption for 500-nm excitation, measured at a time delay giving the peak intensity, is shown by open circles as a function of the fluence of excitation laser pulses. It is evident that the yield of desorption and the efficiency of bond breaking determined by STM study show the same super-linear dependence on the fluence. The result demonstrates clearly that desorption of Si atoms is the direct consequence of bond breaking of adatoms from the 7x7 surface. A power law cannot describe the yield shown in Fig.2; a log-log plot does not give a single straight line. It depends on almost the square of the fluence at low fluence region, while the dependence becomes almost exponential at higher intensities.

Spectroscopic studies of laser-induced desorption of Si atoms from the Si(111)7x7 surface have been carried out to identify the electronic transitions which are responsible for the Si-atom desorption.^{10,21} Because of the super-linear behavior of the desorption yield, the usual definition of the efficiency is not applicable. Instead, Kanasaki et al. introduced a practical definition of the 'desorption efficiency' to be the desorption yield at a fixed laser fluence of 150 mJ/cm². Measurements of desorption efficiency thus defined has revealed a strong peak at 2.0 eV in the desorption efficiency as a function of photon energy. In the Si crystal, there exist no such peaks at 2.0 eV in the absorption coefficient. Therefore, this result suggests that the optical absorption associated with the bulk electronic transitions is not effective for the Si-atom desorption. Alternatively, possible optical transitions involving surface electronic states have been examined in the light of experimental and theoretical results of the surface electronic structures of Si(111)-7x7 surface.¹⁴⁻¹⁶ One can find two possible surface transitions around 2.0 eV. The one is the transition from the surface band (S₂) composed of the rest-atom dangling bond to the band (U₂) of the unoccupied adatom back-bond orbital, and the other is from the band (S₃) composed of the occupied adatom back-bond orbital to the band (U₁) of the unoccupied adatom dangling bond orbital. The peak energy of desorption enhancement agrees well with the energies of the surface electronic transitions mentioned above. Based on this consideration, it has been concluded that laser-induced electronic transitions within the surface electronic state are responsible for the Si-atom desorption.

An alternative assignment may be argued that the peak of 2.0 eV in the desorption efficiency is related to the two-photon absorption transition in the bulk electronic states, based on the fact that the direct band gap of Si crystals is 4.185 eV,²² about the twice of the peak energy in the desorption efficiency spectrum, and on the feature of the nearly quadratic dependence of the yield of desorption at weak fluence regime. In order to examine this alternative, the desorption of Si atoms was studied for the surface excited with 266-nm laser pulses, the photon energy (4.66 eV) of which is above the direct band gap.²³ The Si atoms in the electronic ground state were emitted as the major product under this excitation, and the super-linear dependent change of the yield with respect to the excitation intensity was observed, similarly to those for ns-laser excitation in visible region. This result excludes definitely the alternative assignment of the 2.0-eV peak in the desorption efficiency.

As seen in Fig.3, velocity distribution of Si atoms desorbed from the surface is not dependent on fluence of ns-laser pulses. The velocity distribution of Si atoms desorbed under 266-nm excitation was essentially the same as those obtained for excitation with ns-laser pulses in the visible region. Kanasaki et al. have studied the desorption induced by fs laser pulses of 403 and 269 nm, and found the same velocity distribution of Si atoms as that in ns-laser excitation.²³ The yield of desorption shows a similar super-linear dependence on the fluence of fs lasers to that for ns lasers. Therefore, TOF spectra of desorbed Si atoms are characterized by a given velocity distribution and the same peak flight time, neither of which depend on wavelengths, fluences and temporal widths of laser light. This feature indicates clearly that the final step of the bond breaking which governs the energy partition to Si atoms is common for any type of excitation. It implies that the same

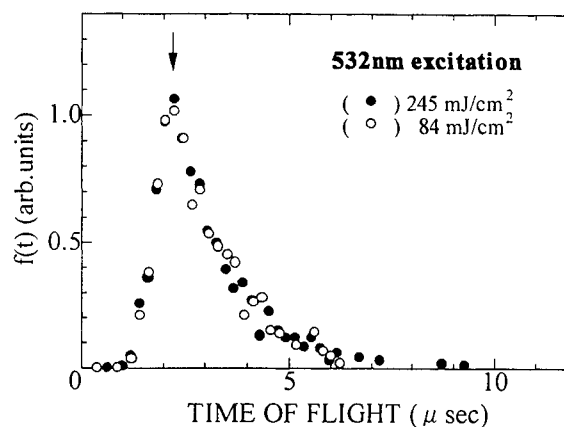


FIG. 3. Time-of-Flight spectra of Si atoms desorbed from Si(111)-(7x7) irradiated by 532-nm laser pulses of fluence of 84 mJ/cm² (open circle) and of 245 mJ/cm² (solid circle), respectively. The yield of desorption changes as much as three-orders of magnitudes for the two fluences (From Ref.21)

localized excited state (the reactive state) is formed at adatom sites with a formation yield, which is dependent on several characteristics of excitation laser light.

In order to have deeper insight into the bond breaking process, the number density $N(\epsilon)$ of atoms with translational energy ϵ has been evaluated from TOF spectra.²³ In this evaluation, a phase space factor of v^2 was taken into account (v is the speed),²⁴ to compare experimental data with consequences of a one-dimensional model which will be discussed later. The result is shown in Fig.4. The distribution shows a steep increase after an onset energy of about 0.02 eV (shown by the arrow) to form a peak at 0.06 eV, associated with the high-energy tail up to 0.6 eV. Although the peak flight time of 2.05 μ s in TOF spectra corresponds to the translational energy of 0.15 eV, the peak translational energy of 0.06 eV in $N(\epsilon)$ is obtained after the phase-factor correction, which enhances significantly number densities at low-energy parts.²⁴ Since the amount of Si atoms desorbed by one pulse is at most 10^{-4} ML, any effects of gas-phase collision after desorption can be neglected.²⁵ Therefore, the energy distribution seen in Fig.4 is characteristic of the bond breaking process at the surface.

2.3. Possible mechanisms of electronic bond breaking of adatoms on Si(111)-(7x7)

Based on the results described above, it is reasonable to conclude that the structural change of Si(111)-7x7 surface induced by laser irradiation below thresholds of melting and ablation originates from an electronic process where surface excited states are involved. Since the desorption is caused by the removal of Si atoms at individual adatom sites on the 7x7 structure, localization of these photo-generated species, which are delocalized two-dimensionally, onto particular adatom sites is included as an important step in the desorption process. The super-linear dependence of the yield of Si-atom desorption on fluence of excitation-laser pulses shown in Fig. 2 indicates that multiple photo-excited species are involved in the localization process.

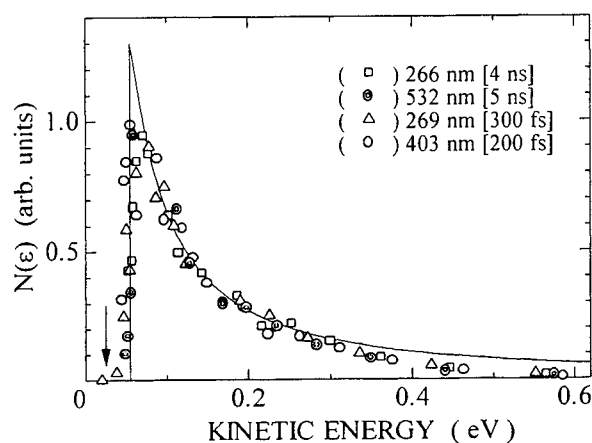


FIG. 4. Translational energy distribution of Si atoms desorbed by the laser-induced electronic bond breaking of adatoms of Si(111)-(7x7). Surface excitation was made at 300 K with laser pulses of different characteristics in wavelengths, fluences and temporal widths. Data for different types of laser light are normalized to the same peak height (From Ref. 23).

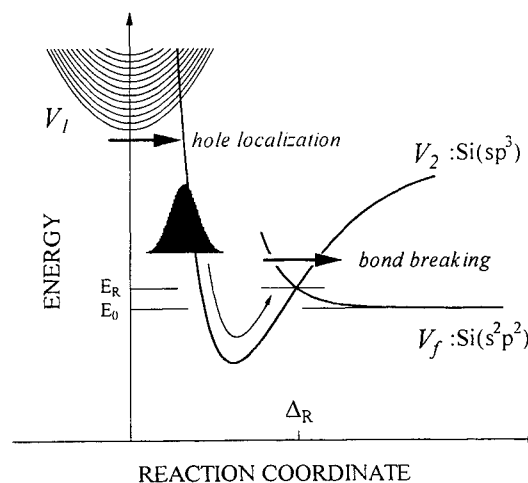


FIG. 5. Schematic of the model of phonon kick process following two-hole localization at adatom sites. Adiabatic potentials V_1 , V_2 , and V_f show the state of the second hole staying in the free state in addition to the first localized hole, that of two-hole localized, and that of the final state of the bond breaking (From Ref.23).

Several models have been proposed for the electronic mechanism of bond breaking and structural changes on semiconductor surfaces. Among them, the two-hole localization mechanism studied by Sumi²⁶ can explain most of important features of the electronic processes on Si(111)-(7x7). He formulated the rate of the two-hole localization onto a particular lattice site by considering that it is the crucial step of desorption of atoms from semiconductor surfaces. It has been assumed reasonable that successive localization of two holes is more probable than simultaneous localization. It implies that a single

hole can be first localized at a lattice point by some mechanisms. The rate P of the two-hole localization can be approximated well by the simple expression of $P = A\{\exp(n_h) - 1\}^2$ where n_h is the density of photo-generated holes relative to the effective number of free-hole state in the surface valence state at a given temperature. For weak excitation, which gives $n_h \ll 1$, the rate is proportional to the square of n_h , while for intense excitation it increases exponentially. This enhancement of the localization rate at intense-excitation regime has been attributed to the increase in the average kinetic energy of the holes due to the degenerate Fermi distribution, which makes localization of the second hole by overcoming the Coulomb barrier effective.

The quantity n_h and the excitation intensity characterized by fluence Φ can be correlated as

$$n_h = \sigma(\tau/\omega)n_0\Phi \quad (1)$$

with a cross section σ of the optical transition, the normalized density of surface valence states n_0 , the lifetime of photo-excited holes τ , and temporal width ω of excitation-laser pulses, when $\tau \ll \omega$. Then, the yield of desorption which is proportional to P is given by

$$Y = Y_0 \{\exp(C\Phi) - 1\}^2, \quad (2)$$

where Y_0 is a constant and $C = \sigma(\tau/\omega)n_0$. The experimental results of the bond breaking efficiency and yield of Si-atom desorption were compared with this equation with Y_0 and C being fitting parameters. The solid curve of Fig.2 is the best-fit curve of Eq.(2) to experimental results; Eq.(2) describes almost perfectly the results for a whole range of fluence of the excitation-laser pulses. The results taken for other wavelengths from 700 to 400 nm can be fitted by Eq.(2) as well.²¹ The fact that Eq.(2) explains satisfactorily the super-linear feature of the yield may indicate that the bond breaking of adatoms is governed by the rate of the sequential two-hole localization process.

The two-hole localization mechanism assumes the first-hole localization on the surface. Since the adatom-vacancy formation is not related at all to pre-existing defects on the surface, an intrinsic process of the first-hole localization has to be assumed. The self-trapping is a typical of the intrinsic carrier localization. A criterion of localization by the self-trapping mechanism of a single carrier in the phonon field has been shown to be $E_{LR} > B$,²⁷ where E_{LR} is the lattice relaxation energy which represents the energy gained by the lattice relaxation, and B is the delocalization energy measured as a half of the width of the band. In contrast to the valence electronic state of Si crystal showing a large B , some of occupied surface states on Si(111)-(7x7) show much narrower bandwidths. According to UPS studies, the widths of the S_1 and S_2 bands are much narrower than other surface bands. Although no information on E_{LR} is available for the localization of a single hole on a surface atomic site of the Si(111)7x7 surface, holes generated in these bands have certainly an advantage for localization by the self-trapping mechanism over other competing de-excitation channels. On the other hand, the S_3 band composed of the adatom back-bond orbital shows a strong dispersion and broader width. Therefore, the localization of holes in the S_3 band has a larger energy cost, which would reduce the effectiveness of holes generated in this band for Si-atom desorption. In fact, no enhancement of the desorption efficiency has been detected around 3 eV where transition from S_3 to U_2 is expected.

Experiments²⁸ and ab initio calculations¹⁷ have shown a significant charge delocalization of dangling bond state of the adatoms, which results in a bonding interaction between adatoms and the Si atoms directly below them. Therefore, upon hole localization at adatom sites, bonding property of the adatom may be affected seriously to weaken the bond. Successive localization of the second hole at the site where the first hole is localized may induce finally the bond breaking of adatoms.

The bond weakening of adatoms upon hole localization may induce a strong adatom vibration normal to the surface. Defect reactions induced (or enhanced) by transiently generated violent lattice vibration (phonon kick) upon the carrier localization at defect sites are well documented in semiconductors.²⁹ This phonon-kick mechanism has been proposed to be responsible for the bond breaking and desorption of adatoms from the surface.²³ In this case of bond breaking, however, "defect sites" are the first-hole localized sites, and the violent vibration leading to the bond breaking is induced only upon the second-hole localization along the reaction coordinate Q_R of vibrational motion of adatoms normal to the surface. This process is schematically portrayed in Fig.5, where a group of parabolas denoted by V_1 represents the state of the second hole staying in the free state with the first-hole localized, V_2 the state of two-hole localized, and V_f the final state of the bond breaking, respectively. In the bond breaking process, the adatom electronic state of a perturbed sp^3 -like configuration is finally transformed into the free-atom s^2p^2 state in V_f . It has been assumed that this electronic transition, a key of the bond breaking, takes place on V_2 at a critical point R with energy E_R and a distortion Δ_R on Q_R .

The phonon-kick process can be described as follows; the packet formed on the coordinate with a mean total energy $E_i \geq E_R$ passes the critical point n times with the energy $E \leq E_i$ during relaxation, induces the transition with a probability P at each passage, and is dissipated finally. The Si atoms desorbed by the packet with E have ε given by $\varepsilon = E - E_0$, where E_0 is the energy of V_i measured from the bottom of V_2 . The number density $N(\varepsilon)$ is determined by the product of n and P , both of which are dependent on E . As a crude guide of the dependence, n is inversely proportional to E when a simple damping oscillator is assumed for the packet. And, when P is evaluated by Landau-Zener formula³⁰ of

$$P_{LZ} = \{1 - \exp(-2\pi T^2 / \hbar v_R |F_R|)\}, \quad (3)$$

where T is the transition matrix element, F_R the change of the energy separation of the surfaces at R and v_R the velocity of the packet at R, respectively, it takes the largest value for $v_R = 0$, with a sharp cut off for $E \leq E_R$. For $E > E_R$, P decreases with increasing E .

In view of this model, the peak energy of 0.06 eV in $N(\varepsilon)$ shows that E_R is higher by about 0.06 eV than E_0 . A sharp cutoff is in fact observed $E < E_R$, and $N(\varepsilon)$ decreases with increasing ε as expected from the dependence of both n and P on E . The highest energy of E_i which determines the highest ε is estimated to be about 0.6 eV + E_0 . The solid curve in Fig.1 is the energy distribution calculated by this simple model of $N(\varepsilon) = nP_{LZ}$ with assuming v_R to be proportional to $(E - E_R)^{1/2}$ and a constant E_i . It describes the overall features of the experimentally determined energy distribution of Si atoms, although it includes some discrepancies, which can be solved by more sophisticated theoretical analysis.

3. LASER-INDUCED ELECTRONIC BOND BREAKING ON InP(110)-(1x1)

The laser interaction with surfaces of III-V semiconductors has also been studied extensively. Because of the properties of easier decomposition by heat below melting temperature, the important roles of thermal mechanism of laser-induced heating have often been emphasized. Nevertheless, there are growing experimental evidences that indicate electronic mechanisms of the surface structural changes. In the studies by means of highly sensitive detection methods of desorbed species, electronic mechanism has been proposed, and the defects on the surface have been ascribed to the active sites for the removal by electronic processes.^{6,7} Time-resolved photoelectron spectroscopy and scanning electron microscope have been used to demonstrate a photon-activated process of Ga island formation on GaAs(110).³¹ In this photodecomposition, Ga and As atoms at kinks on cleavage steps have been considered as the active sites for the electronic process. Whether terrace atoms, namely the intrinsic sites of the reconstructed structure, are removed by the electronic process was an interesting open question, although some theoretical suggestions have been made. Recent STM study for laser-irradiated InP(110)-(1x1) surfaces has revealed that the P and In atoms in the intrinsic sites of the surface are indeed removed by an electronic mechanism.¹¹

3.1 Features of structural changes revealed by STM observation

The {110} surface of typical III-V compound semiconductor is characterized by the tilted cation-anion zigzag chains associated with surface relaxation. The electronic states of the surface are characterized by three distinct surface optical transitions in the photon-energy range above bulk band gap. For InP(110)-(1x1), these are peaked at 2.6-2.75, 3.04-3.1, and 3.6 eV, respectively.¹² Kanasaki et al. has excited cleaved surfaces of InP with laser pulses photon energies of which fall in resonance to one of these peaks, and examined the surface structural changes by using STM. Figure 6 presents a STM image acquired with a positive tip-bias voltage (+2.5V) for a cleaved surface after irradiation with 3000 shots of 460-nm laser pulses with 22 mJ/cm² of fluence.¹¹ In the image, which represents the structure of P atoms on this surface, we evidently see several dark spots newly generated after laser irradiation. These spots in the image correspond to the single vacancy and vacancy strings consisting of different numbers of neighboring vacancies. In STM images acquired with a negative tip-bias voltage for the same surface, which represents the structure of In

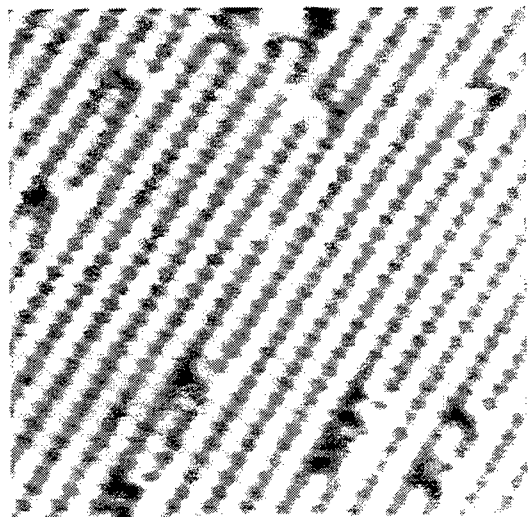


FIG. 6. A STM image showing vacancies of P atoms induced by irradiation with 3000 shots of 460-nm laser pulses on InP(110)-(1x1). Vacancy strings consisting of a few neighboring vacancies are formed with significantly enhanced yields (From Ref.11).

atoms on this surface, newly generated dark spots were also found. However, the spots are mainly in the form of the single vacancy, and the total number of In vacancies generated by laser irradiation is about 1/4 to that of P vacancies. These results demonstrate clearly that P and In atoms on the terrace, namely the intrinsic sites of the reconstructed structure, are removed by the bond breaking induced by laser irradiation, with keeping (1x1) structure essentially un-changed. The estimated surface temperature with the formula in Ref. 32 was at most 450 K for the fluence of 22 mJ/cm², far below the melting temperature. In fact, any changes characteristic of thermal effects,³³ like formation of P₂ and In-In bonds on the surface, could not be detected after irradiation. Therefore, it has been concluded that these single vacancies and vacancy strings are formed by electronic process on the surface. The more quantitative examination of the vacancy formation process below is certainly consistent with this conclusion.

Kanasaki et al. have also studied formation of single vacancy and vacancy strings with different lengths as a function of number m of laser shots (or dose) under a given fluence of laser pulses. The fractions of numbers of vacancies with respective forms relative to the total number of surface-atomic sites surveyed are portrayed as a function of m in Fig.7. The initial concentration of vacancies on a cleaved surface is at most 0.2%. It increases up to a few percent of the surface sites after irradiation. In the growth of the P vacancies, it is evident that dimer vacancies and vacancy strings are formed with significantly enhanced yields than those expected from statistics of random distribution of vacancy formation. Therefore, the results shown in Figs.6 and 7 indicate clearly that the P atoms located at neighboring sites of the vacancies are preferentially removed by laser irradiation to form vacancy strings with longer lengths. The preferential removal of P atoms nearest to the single vacancies leads to the formation of dimer vacancies with expense of numbers of single vacancies. Therefore, decrease in the growth rate of the single vacancies is naturally expected with increasing m . However, an interesting feature seen in Fig.7 is that the growth rate of total number of vacancies also shows a tendency of saturation for the concentration as low as a few percent. This feature contrasts strongly to the bond breaking of adatoms on Si(111)-(7x7), where the growth rate of adatom vacancies is constant up to about 10 % of the surface defect concentration. Therefore, the electronic process of bond breaking on InP(110) includes a new factor, which has not been considered in the case of Si(111) surface.

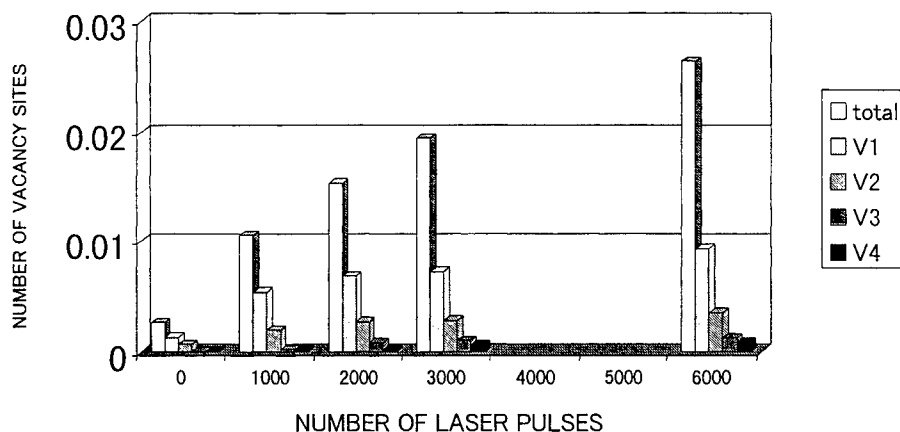


FIG. 7. A histogram of the number of laser-induced single vacancies, V_1 , the dimer vacancies, V_2 , trimer vacancies, V_3 , and tetramer vacancies, V_4 , and total number of P vacancies on InP(110)-(1x1) as a function of number of laser shots of 460 nm laser pulses with fluence of 30 mJ/cm² (From Ref.11).

3.2 Possible mechanism of electronic bond breaking and vacancy-strings formation

In the study of the formation of vacancy strings on InP(110)-(1x1), a simple rate equation model has been formulated.¹¹ When the rate g_0 of bond breaking of a P atom from the intrinsic site with concentration N_0 is introduced, then the concentration V_1 of the single vacancy is determined by the equation; $dV_1/dt = g_0N_0 - g_1V_1$, where g_1 is the rate of bond breaking at the site nearest to the single vacancy to form the dimer vacancy. A similar equation is hold for the concentration

V_j of the vacancy string consisting of j vacancies; $dV/dt = g_{j-1}V_{j-1} - g_jV_j$. When we define the total number of vacancy sites to be $V = \sum_j V_j$, V satisfies the following simple equation;

$$\frac{dV}{dt} = g_0 N_0 \quad (4)$$

In Fig.8, the magnitude of V is plotted as a function of m ; it shows a linear growth at very low dose region, while it tends to be saturated for higher doses. Since the fraction of the total number of vacancies formed is still in the range of a few percent, the decrease of the number of active sites can be ignored. It follows that the main factor, which leads to the saturation of the rate of vacancy formation, is concerned with the rate g_0 . The rate g_0 , which includes the all effects in the process from localization of photo-generated species to bond breaking, is then dependent strongly on the small number of vacancies formed on the surface.

For obtaining deeper understanding of the vacancy formation process, the magnitude of g_0 was determined as a function of laser fluence, based on the linear region of V vs. m curves. The result is shown in Fig.9. It is evident that g_0 thus determined is strongly super-linear as a function of fluence, similarly to the case of electronic bond breaking of adatoms on Si(111)-(7x7). The solid curve in the figure is the best fit to the equation derived in the two-hole localization mechanism of the bond breaking. It describes the experimentally determined dependence satisfactorily, indicating an important role of this process on InP(111)-(1x1) surfaces. In the vacancy string formation via two-hole localization, the first hole is localized on the site nearest to a single vacancy, and the second hole is localized at the site where the first hole is localized. Since the probability of the two-hole localization is dependent strongly on the density of holes, small reduction in the density leads to the significant reduction of the probability, and hence the rate of vacancy formation. It implies that the lifetime of holes on the surface is dependent on the concentration of the vacancies.

For ns-laser pulses, the density n_h of holes is given by Eq.(1). When we consider the trapping of the holes at sites near the vacancies to be an effective de-excitation channel of the holes, then τ can be expressed as

$$1/\tau = 1/\tau_0 + \sum_j \sigma_j V_j, \quad (5)$$

where σ_j represents the cross-section of hole trapping at the nearest sites of vacancy strings consisting of j vacancies. When it is assumed for simplicity that $\sigma_j = \sigma_0$ for any forms of vacancies, then the total number of vacancy sites defined above determines the lifetime. The growth of V is, then, expressed as

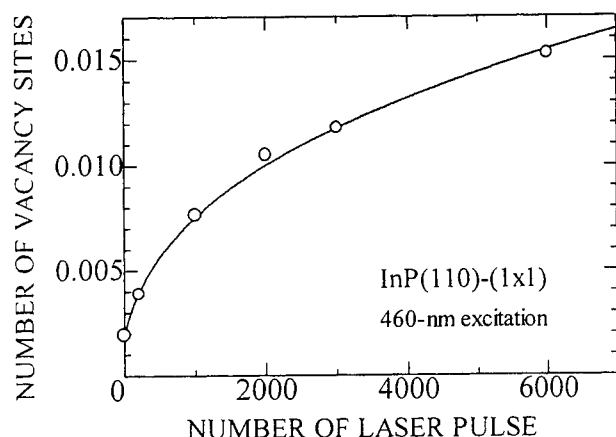


FIG. 8. Does dependence of the total number of P vacancy sites on InP(110)-(1x1) induced by irradiation of laser pulses of fluence of 30 mJ/cm². The solid curve in the figure is the result of numerical calculation of the model assuming the two-hole localization as the bond breaking mechanism (From. Ref.11).

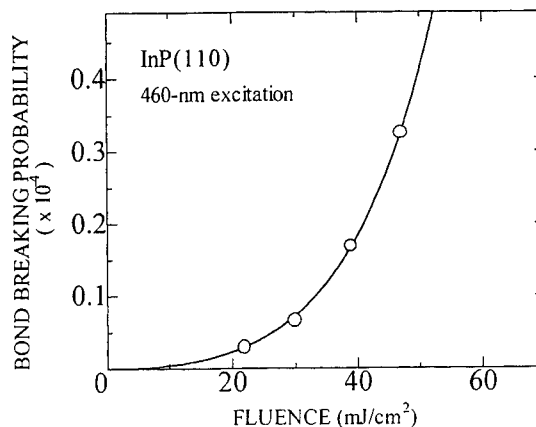


FIG. 9. Dependence of the bond-breaking probability for P atoms at the intrinsic surface site as a function of laser fluence. The solid curve is the best-fit curve of the formula derived from the two-hole localization mechanism (From Ref.11).

$$\frac{dV}{dt} = A[\exp\{\sigma n_0 \tau_0 \Phi / \omega(1 + \tau_0 \sigma_0 V)\} - 1]^2 N_0 \quad (6)$$

The solid curve in Fig.8 is the numerically solved result of this equation with A , $\sigma n_0 \tau_0 / \omega$ and $\tau_0 \sigma_0$ as parameters. It describes satisfactorily the characteristic feature of the growth curve of V as a function of dose. The growths of vacancies at different fluences were fitted as well with changing only the magnitude of Φ in Eq.(6). Also, the growth characteristics of single vacancies and vacancy strings were well described by the equation, $dV/dt = g_{j-1}V_{j-1} - g_j V_j$, with the expression of g_j of two-hole localization mechanism. Based on the results and analysis, it has been concluded that the efficient formation of vacancy strings is due to the preferential condensation of holes at neighboring sites of vacancies.

Thus, the bond breaking of surface atoms in intrinsic surface sites of InP(110)-(1x1) has been described well by the electronic mechanism assuming the two-hole localization. An interesting feature on this surface is that the lifetime of holes, more generally the excited species, is dependent of the small concentration (less than a few %) of defects on the surface. This feature substantiates the important role of the holes generated in the surface-specific electronic bands on the bond breaking process; it is unlikely that the lifetime of holes in bulk electronic states is affected by such a small amount of surface defects.

4. SUMMARY

We have surveyed recent results of laser-induced structural changes on Si(111)-7x7 and on InP(110)-(1x1) under the excitation below ablation and melt thresholds. Direct imaging of the irradiated surface by STM and measurement of kinetic-energy distributions of desorbed Si atoms have substantiated that the bond breaking of adatoms on Si(111)-(7x7) is induced by an electronic mechanism. A resonant enhancement of the desorption efficiency at 2.0 eV, revealed by excitation spectroscopy, can be attributed to surface optical transitions. The analysis of non-linear dependence of the desorption yield on fluence of excitation has suggested strongly the crucial role of the two-hole localization in the desorption process. Translational energy distribution of desorbed Si atoms has been described satisfactorily by the phonon-kick process following the two-hole localization. The electronic bond breaking of P atoms in the intrinsic surface structure of InP(110)-(1x1) can also be described well by the two-hole localization mechanism. However, the process on InP(110) shows an interesting feature of the efficient vacancy-string formation on P rows on the surface. This feature, together with saturation of the growth rate of vacancies with concentration as low as a few %, shows strong contrast to the case of similar electronic bond breaking of adatoms on Si(111)-(7x7) where growth rate of vacancies is constant up to the vacancy level of 10 %. The difference can be ascribed to the nature of the surface electronic states between the two systems; occupied surface bands of Si(111)-(7x7) show rather local nature, while the band of InP(111)-(1x1) shows quasi one-dimensional nature with relatively wide dispersion inducing effective transfer. Thus, for both surfaces, experimental results suggest strongly the important roles of the surface excited states in the electronic process of bond breaking on semiconductor surfaces.

ACKNOWLEDGMENTS

Support of this work by Grant-in-Aid for Scientific Research by the Ministry of Education, Science, Sports, and Culture of Japan is gratefully acknowledged. The work was also supported in part by the Murata Science Foundation.

REFERENCES

1. M. Von Allmen and A. Blatter, *Laser-Beam Interaction with Materials; physical principle and applications*, Springer-Verlag, Berlin, 1987.
2. *Laser-Induced Material Modifications*, edited by P. J. Kelly, a special volume of Opt. Eng. **28**, 1989.
3. D. von der Linde, "Ultrashort Interaction in Solids", *Ultrashort Laser Pulses*, edited by W. Kaiser, Topics in Applied Physics, Vol. **60**, pp. 113-182, Springer, Berlin, 1988.
4. B. Stritzker, A. Pospieszczyk, and J. A. Tagle, "Measurement of lattice temperature of silicon during pulsed laser annealing", Phys. Rev. Lett. **47**, pp. 356-358, 1981.
5. R. S. Becker, J. A. Golovchenko, G. S. Higashi, and B. S. Swartzentuber, "New reconstructions on silicon (111) surfaces", Phys. Rev. Lett. **57**, pp. 1020-1023, 1986.
6. J. Kanasaki, A. Okano, K. Ishikawa, Y. Nakai, and N. Itoh, "Dynamical interaction of surface electron-hole pairs with surface defects", Phys. Rev. Lett. **70**, pp. 2495-2498, 1993.
7. B. Dubreuil and T. Gilbert, "Soft laser sputtering of InP(100) surface", J. App. Phys. **76**, pp. 7545-7551, 1994.
8. K. Ishikawa, J. Kanasaki, K. Tanimura, and Y. Nakai, "Site-sensitive yield of atomic emission induced by laser

- irradiation on Si(111)-7x7 surface", Solid State Commun. **98**, pp. 913-916, 1996.
9. Jun Xu, S. H. Overbury, and J. F. Wendelken, "Selective laser removal of the dimer layer from Si(100) surfaces revealed by scanning tunneling microscopy, Phys. Rev. B **53**, pp. R4245-R4248, 1996.
 10. J. Kanasaki, T. Ishida, K. Ishikawa, and K. Tanimura, "Laser-induced electronic bond breaking and desorption of adatoms on Si(111)-(7x7)", Phys. Rev. Lett. **80**, pp. 4080-4083, 1998.
 11. J. Kanasaki, N. Mikasa, and K. Tanimura, "Formation of vacancy strings by laser-induced electronic processes on InP(110)-(1x1)", to be published.
 12. W. Monch, *Semiconductor surfaces and interfaces*, Springer, Berlin, 1995.
 13. K. Takayanagi, Y. Tanishiro, M. Takahashi, and S. Takahashi, "Structural analysis of Si(111)-7x7 by UHV-transmission electron diffraction and microscopy", J. Vac. Sci. Technol. A **3**, pp. 1502-1506, 1985.
 14. R.I.G.Uhrberg, G.V.Hansson, J.M.Nicholls, P.E.S.Persson, and S.A.Flodstrom, "Photoemission study of the surface and bulk electronic structures of Si(111) 7x7 and Si(111) $\sqrt{3} \times \sqrt{3}$:Al", Phys. Rev. B **31**, pp. 3805-3810, 1985.
 15. J. M. Nicholls and B. Reihl, "Adatom electronic structure of the Si(111) 7x7 surface", Phys. Rev. B **36**, pp. 8071-8074, 1987.
 16. R.J.Hamers, R.M.Tromp, and J.E.Demuth, "Surface electronic structure of Si(111)-(7x7) resolved in real space", Phys. Rev. Lett. **56**, pp. 1972-1975, 1986.
 17. I. Stich, K. Terakura, and B. E. Larson, "First-principles finite-temperature characterization of dynamics of the Si(111)-7x7", Phys. Rev. Lett. **74**, pp. 4491-4494, 1995.
 18. R. Wolkow and Ph. Avouris, "Atom-resolved surface chemistry using scanning tunneling microscopy", Phys. Rev. Lett. **60**, pp. 1049-1052.
 19. H. Uchida, D. Huang, F. Grey, and M. Aono, "Site-specific measurement of adatom binding energy differences by atom extraction with the STM", Phys. Rev. Lett. **70**, pp. 2040-2043, 1993.
 20. B. C. Stipe, M. A. Rezaei, and W. Ho, "Site-specific displacement of Si adatoms on Si(111)-(7x7)", Phys. Rev. Lett. **79**, pp. 4397-4400, 1997.
 21. J. Kanasaki, T. Ishida, K. Iwata, and K. Tanimura, "Spectroscopic study of laser-induced desorption of Si atoms from Si(111)-(7x7)", to be published.
 22. D. E. Aspnes and A. A. Studna, "Direct observation of the E_0 and $E_0 + \Delta_0$ transitions in silicon", Solid State Commun. **11**, pp. 1375-1378, 1972.
 23. J. Kanasaki, K. Iwata, and K. Tanimura, "Translational energy distribution of Si atoms desorbed by laser-induced electronic bond breaking of adatoms on Si(111)-(7x7)", Phys. Rev. Lett. in print.
 24. F. M. Zimmermann and W. Ho, "Velocity distributions of photochemically desorbed molecules", J. Chem. Phys. **100**, pp. 7700-7706, 1994.
 25. I. NoorBatcha and R. R. Lucchese, "Monte Carlo simulation of gas-phase collision in rapid desorption of molecules from surfaces", J. Chem. Phys. **86**, pp. 5816-5824, 1987.
 26. H. Sumi, "Theory of laser sputtering by high-density valence-electron excitation of semiconductor surfaces", Surf. Sci. **248**, pp. 382-410, 1991.
 27. M. Ueta, H. Kanzaki, K. Kobayashi, Y. Toyozawa, and E. Hanamura, *Excitonic Processes in Solids*, Springer Series in Solid State Sciences, Vol. **60**, Springer, Berlin, 1986.
 28. W. Daum, H. Ibach, and J. M. Muller, "Adatom vibrations on Si(111) reconstructed surfaces", Phys. Rev. Lett. **59**, pp. 1593-1596, 1987.
 29. H. Sumi, "Dynamical defect reactions induced by multiphonon nonradiative recombination of injected carriers at deep levels in semiconductors", Phys. Rev. B **29**, pp. 4616-4630, 1984.
 30. L. D. Landau and E. M. Lifshits, *Quantum Mechanics*, Pergamon Press, New York, 1956.
 31. J. P. Long, S. S. Golenberg, and M. N. Kabler, "Pulsed laser-induced photochemical decomposition of GaAs(110) studied with time-resolved photoemission spectroscopy using synchrotron radiation", Phys. Rev. Lett. **68**, pp. 1014-1017, 1992.
 32. P. Baeri and S. U. Campisano, "Heat flow calculation", *Laser annealing of semiconductors*, edited by J. M. Poate and J. W. Mayer, pp. 75-109, Academic, New York, 1982.
 33. F. Proix, A. Akremi, and Z. T. Zhong, "Effects of vacuum annealing on the electronic properties of cleaved GaAs", J. Phys. C **16**, pp. 5449-5463, 1983.

Pulse-Width Influence on Laser Induced Desorption of Positive Ions from Ionic Solids

Richard M. Williams^{*a}, Kenneth M. Beck^a, Alan G. Joly^a, J. Thomas Dickinson^b, Wayne P. Hess^{†a}

^aPacific Northwest National Laboratory¹, EMSL, MS K8-88, P.O. Box 999, Richland, WA 99352

^bDepartment of Physics, Washington State Univ., Pullman, WA 99164

ABSTRACT

We have compared the desorption of positive ions, including Mg^+ and MgO^+ , from ionic magnesium oxide (MgO) single crystals following pulsed laser excitation using either nanosecond (3 ns, 266 nm) or femtosecond (~ 300 fs, 265 nm) sources. Following optical excitation, desorbed ions are rapidly extracted and mass analyzed using standard time-of-flight techniques. Ion yields and velocities are determined as a function of laser fluence. The threshold similarity is a surprising result, as sub-band gap nanosecond pulses are only likely to excite defect states efficiently (via linear excitation), while the ultrahigh peak-power femtosecond pulses could in principle induce multiphoton and avalanche excitation. We argue that at least in this specific case, the important factor appears to be merely the number of photons and not the pulse duration. However, it is observed that femtosecond excitation yields considerable H^+ and less interference from impurity alkali ions than does nanosecond excitation. The source of the protons is presumably the hydroxylated MgO surface.

Keywords: MgO , Magnesium Oxide, Laser Ablation, Laser Induced Desorption, Ultrafast Laser, Ionic Solids, Ionic Crystals, Wide Bandgap Insulators, Ultrafast Processes, Multi-photon processes.

1. INTRODUCTION

Environmental samples are often difficult to analyze for possible contamination, requiring sophisticated analytical techniques. Some of these techniques rely upon laser ablation as a primary means of vaporization and/or ionization. They include matrix-assisted laser desorption/ionization (MALDI) and laser ablation mass spectrometry (LAMMS). Generally, nanosecond lasers have been used as the irradiation source for laser desorption and ablation, however many of the key processes (i.e. electron/hole-pair recombination, trapping, electron/phonon interactions, etc.) involved in laser/solid interactions occur on a sub-nanosecond time-scale. An important first step in optimizing methods based on laser desorption/ablation lies in the understanding of these fundamental processes. The goal of this research effort is to study how these important aspects are involved in energetic desorption of ions from surfaces during and after laser/solid interactions, where the solid material is usually an environmentally relevant wide-band gap material, such as magnesium oxide, calcium carbonate or sodium nitrate. This paper will present a comparison between the amount and type of desorption products that result when the temporal pulse duration of the UV desorption laser is varied by up to four orders of magnitude and as a function of laser fluence.

Previous work by Dickinson et al.¹⁻³ has shown that positive ion desorption can occur from a variety of wide-band gap materials when irradiated with photons that have less than bandgap energies (MgO has an approximate band gap energy of 7.9 eV). It was shown that primarily Mg^+ desorbed from cleaved or abraded MgO when irradiated with 248 nm (5 eV) photons from a 30 ns excimer laser pulse. In addition, the kinetic energy distributions were determined by measuring the

^{*} Associated Western Universities Postdoctoral Research Associate.

[†] Correspondence: Email: wayne.hess@pnl.gov; WWW: <http://www.emsl.pnl.gov:2080/homes/csd/epl/index.html>, Telephone: 509 376 9907; Fax: 509 376 6066

¹ Pacific Northwest National Laboratory is operated for the U.S. Department of Energy by Battelle under Contract DE-AC06-76RLO 1830.

velocity profiles of mass filtered desorption products using a quadrupole mass spectrometer in a time-of-flight mode. Those results showed that translational kinetic energies up to 20 eV were attainable, even though the photon energies are significantly less (5 eV). An emission model was postulated involving the photo-ionization of defect states (F and F⁺ centers) located nearby and directly beneath an isolated "adion" (e.g., Mg²⁺) along with trapping and re-trapping of photo-generated conduction band electrons during the 30 ns pulse. An important result of this model is that it accurately recovers the high order fluence dependence of the total ion yield that is measured experimentally by relying upon a series of subsequent linear absorption events involving these defect states (which readily absorb 5 eV photons). To further support this hypothesis experiments were performed on surfaces which had been purposely damaged (abraded) and it was shown that while the power dependence of the ion yield remained nearly the same, the total yield increased by more than an order of magnitude. The large translational kinetic energy is presumed to be the result of a coulombic "kick" experienced by the desorbing positive ions as the local environment directly beneath them is emptied of charge neutralizing electrons (as a result of the photo-ionization). Similar results were shown to occur on a number of other ionic crystals (e.g., CaCO₃, CaHPO₄•2H₂O, NaNO₃, and Na_{0.9}Cs_{0.1}NO₃).⁴ Fluences employed in all of this work ranged from 10 mJ/cm² up to 770 mJ/cm².

The desorption of a variety of positive ions from MgO and other insulators (SrF₂ and CaF₂) following UV nanosecond laser excitation was also reported by Kreitschitz et al.⁵ over a fluence range of 17 – 425 mJ/cm² at 193 nm (6.4 eV). In addition to Mg⁺ and Mg²⁺, Kreitschitz et al. detected both MgO⁺ and O⁺ using their time-of-flight apparatus (presumably similar to the apparatus described here). One significant observation made by Kreitschitz, is the variation in the yield of different ionic species as a function of laser fluence. It was found that at the lowest fluences MgO⁺ is the dominant desorption product, as the fluence is increased Mg⁺ then Mg²⁺ and O⁺ appear in the mass spectra while the percentage of MgO⁺ decreases. The decrease in the molecular ion yield is rationalized in terms of dissociation within a dense energetic expanding plasma generated by the laser pulse. Kinetic energy of the desorbing ions is inferred⁵ and found to be as high as several hundred eV at the higher fluences; an expanding plasma description is invoked to explain these high kinetic energies. Finally, Kreitschitz et al. suggest that measuring the relative ion yields and ion kinetic energies represents a measure of the dynamic plasma environment (including interactions with the nanosecond laser pulse itself) and not the local surface environment during the desorption process itself.

Previous work has shown that a number of interesting phenomena are involved with the desorption/detection process, more importantly however is that a large number of difficult questions remain unanswered. The focus of our current research effort is to measure desorption products under two very different pulsewidth conditions in hope of elucidating some of the processes involved in this complex system. The first set of experiments presented explore the desorption products using a 3 ns, 266 nm (4.66 eV) laser source. These results provide a "bridge" to previous work by Dickinson et al. and Kreitschitz et al., and establish a baseline for comparison to ultrafast desorption experiments which comprise the second set of experiments described here. Ultraviolet (265 nm) sub-picosecond pulses are employed as an irradiation source and desorption products are measured as a function of fluence. Several important differences in the nature of the laser/solid interaction exist and should be noted.

The first reflects the difference in intensity (W/cm²). The measurements described in this study employ fluences ranging from 1 to 40 mJ/cm², however the corresponding values of intensity differ by up to 10⁴ between nanosecond and femtosecond sources. It is generally accepted that at these fluences, sub-bandgap nanosecond pulses cannot produce conduction band (CB) electrons (via non-resonant 2-photon excitation) of sufficient quantity to broadly influence laser desorption. The reason for this is the relatively rapid relaxation of the few CB electrons generated via multiphoton absorption. Petite et al.⁶ have shown that CB density in MgO decreases with a decay time of 50 ps following multiphoton excitation using a fs UV source. This suggests that the slow production rate of CB electrons in the nanosecond case is completely offset by the rapid relaxation of these electrons, presumably to the valence band (ref. 6 was only sensitive to the density of CB electrons and could not determine the exact fate of the relaxing CB electrons). However, an increase in pulse intensity of 10⁴ would increase the production rate of CB electrons by eight orders of magnitude, additionally, the relaxation of the CB electrons is now negligible compared to the excitation time scale. Under this scenario it is likely that a high degree of electronic excitation could exist during and immediately following the subpicosecond pulse. In hopes of quantifying this we have performed simple calculations⁷ solving the differential equations describing the excitation and relaxation schemes, as described by Stuart et al.⁸ On the basis of these equations we conclude that CB densities of ~ 10¹⁷ CB e/cm³ may exist following excitation. Stuart et al. suggest that ultrashort-pulse damage in wide-bandgap materials occurs when the CB electron density reaches a critical value between 10¹⁹ and 10²¹ CB e/cm³. Clearly short pulse excitation explores a new aspect of laser/solid interactions. In MgO, the pulsewidth has a significant influence upon the ion mass spectra.

The second important difference between nanosecond and femtosecond excitation lies in the influence (or lack thereof) that the excitation laser pulse has on the desorbing species. An expansive set of literature exists which describes nanosecond desorption/ablation products resulting from the laser-pulse/ablation-plume interaction rather than describing intrinsic desorption/ablation processes. The obvious reason for this is the time-scale involved for the material being ejected from the surface; neutral (or ionic) atoms or molecules can travel microns away from the surface during the laser pulse, these

"gas-phase" species can then undergo further modification (i.e. ionization, photofragmentation, acceleration) if sufficient electron densities and temperatures are generated in the plume. The overall result of the pulse/plume interaction is to complicate the interpretation of the measurable quantities and great effort has gone into understanding these interactions in addition to the already complex laser/solid interactions. In general, employing lasers with a pulse duration of less than a picosecond removes the pulse/plume interaction from the analysis and thereby reduces the study to only the laser/solid interaction. For example, a magnesium atom possessing 1 eV of translational energy (directed normal to the surface) can travel a maximum of 0.8 nm from the surface in 300 femtoseconds (this assumes zero acceleration time, including a realistic acceleration would *significantly* reduce the distance traveled). An important question, yet to be answered for this system, involves the time-scale over which the species desorb.

The remaining sections of this paper will cover the experimental apparatus, time-of-flight results showing varied speciation depending upon the pulsewidth and fluence dependence, and finally a discussion of the results with proposed future experimental directions.

2. EXPERIMENTAL

A portion of the experimental apparatus which consists of an ultrahigh vacuum (UHV) chamber, ion detection electronics and laser systems is schematically shown in Fig. 1. The UHV chamber is fitted with a variable temperature sample manipulator (capable of stepper motor actuated X,Y,Z translation and rotation about the sample surface), Wiley-McLaren time-of-flight mass spectrometer (TOF-MS), quadrupole mass spectrometer (QMS), Auger Electron Spectrometer (AES), Low Energy Electron Diffraction (LEED) optics and laser access windows. The base pressure of the vacuum system was maintained at 4×10^{-10} Torr. In a typical experiment, a freshly cleaved (in air) sample of synthetically grown single crystal MgO (100) is mounted on the sample holder, no attempt was made to select a particular crystallographic orientation with respect to the laser polarization vector. The samples are held tightly against an encapsulated, stainless-steel button-heater using tungsten clips while a type-K thermocouple junction is positioned to register the temperature of the crystal surface. The samples are heated, in vacuum, to approximately 575–600 K for > 24 hours in an *attempt* to desorb water adsorbed to the cleaved surface prior to mounting in vacuum (discussed further below).

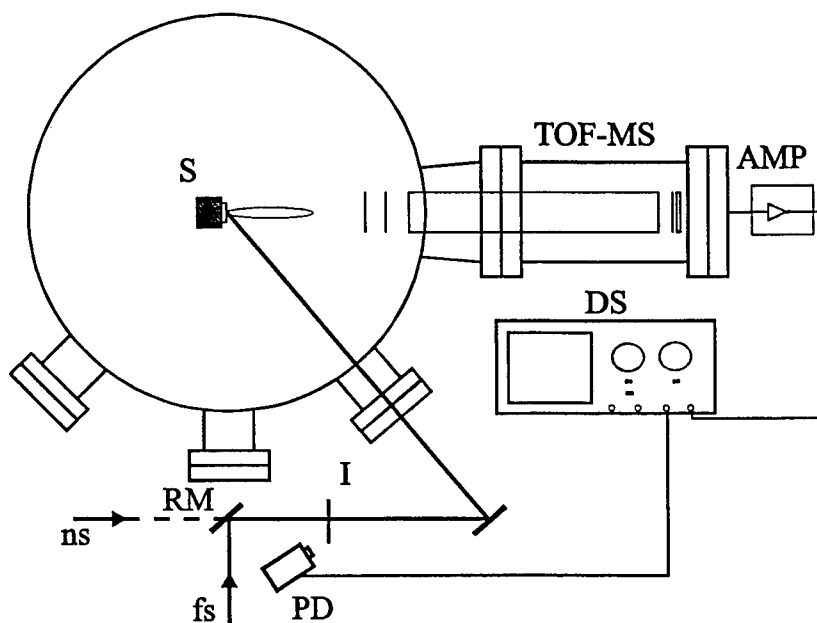


Figure 1. Schematic representation of the experimental apparatus for acquiring time-of-flight spectra of desorbing ionic species following laser irradiation of the sample. The nanosecond (ns) or femtosecond (fs) beam is directed toward the chamber, through an iris (I), via a removable mirror (RM). A negative potential (–400 VDC), between the grounded sample holder and the first grid, extract the ions into the Wiley-McLaren type TOF-MS. Ion pulses are detected, amplified and subsequently averaged using a digital oscilloscope (DS) that is triggered by a scattered laser light signal from a fast photodiode.

The freshly cleaved and baked samples are irradiated with UV laser pulses which illuminate the sample at an angle of incidence of 60 degrees which respect to the surface normal. Positive ions are extracted and accelerated into the Wiley-McLaren TOF-MS and detected with a dual element micro-channel plate multiplier/anode assembly. The anode output is amplified (20 dB gain) and averaged (typically 2500 laser pulses) using a digital oscilloscope (1 GS/s). Mass calibration of the TOF-MS is accomplished by recording the time-of-flight spectrum of a known compound. In this case, a small amount of nitric oxide (NO) is introduced into the chamber and the UV nanosecond laser is focused in front of the sample-holder assembly producing, through non-resonant multi-photon ionization, NO^+ . Two different laser systems are employed in this experiment, providing either nanosecond or subpicosecond pulses.

The nanosecond laser is a commercially available Nd:YAG system utilizing a Q-switched diode pumped solid-state oscillator which seeds a flashlamp pumped amplifier producing pulsewidths of 3 ns (FWHM) at the fundamental (1064 nm) wavelength. The repetition rate of the laser can be varied from single-shot to 100 Hz, but is fixed at 20 Hz for this work. The temperature stabilized second harmonic output (532 nm) is frequency doubled into the UV (266 nm) in BBO, yielding pulse energies 0.25 – 5.0 mJ/pulse. Pulse energies are varied by adjusting the flashlamp energy while the beam diameter/fluence is defined by an iris. The Nd:YAG laser is designed to produce a “top-hat” output spatial profile regardless of flashlamp pulse energy. The apertured beam is qualitatively uniform across its profile as it impinges upon the sample; although the spatial profile is expected to undergo some transformation as a result of the apodization from the iris.

Femtosecond UV pulses are produced in an amplified Titanium-sapphire (Ti:sapphire) based laser system operating at a fundamental wavelength of 795 nm. A cw pumped, mode-locked Ti:sapphire oscillator, producing < 100 fs pulsewidths at a repetition rate of 82 MHz, is used to seed the Ti:sapphire amplifier (pumped at 20 Hz by the frequency doubled output of a Q-switched Nd:YAG laser) which increases the energy of the femtosecond pulses to ~10 mJ/pulse in a regenerative and linear double-pass amplifier arrangement while maintaining pulsewidths ~ 130 fs. The spectral and temporal characteristics of the laser system are monitored using a grating spectrometer fitted with a CCD detector and a single-shot second harmonic autocorrelator, respectively. The amplified output is doubled and tripled in KDP crystals producing up to 1.1 mJ/pulse at 265 nm (as measured using a calibrated pyroelectric joulemeter). Variable attenuation of the ultrafast UV pulse energy is accomplished by adjusting the polarization angle of the residual fundamental pulse (after doubling) with respect to the polarization of the doubled beam prior to sum-frequency generation in the tripling crystal. The ultrafast beam is directed to the chamber through an iris (thereby defining the fluence illuminating the sample) in a similar arrangement as the nanosecond beam (no focusing lens is used). The temporal duration of the UV pulse used for excitation has been determined to be less than 300 fs FWHM assuming a gaussian pulse profile.

3. RESULTS/DISCUSSION

3.1. Subpicosecond, 265 nm, Desorption Products from MgO

Figure 2 displays the time-of-flight spectrum of MgO recorded following subpicosecond exposure. The sample was baked (~600 K) in vacuum (base pressure during heating < 10^{-9} Torr) for several days. Multiple experiments (both nanosecond and ultrafast) have been done and the results are reproducible from sample to sample. This reproducibility indicates that a unique surface morphology is not responsible for the differences between nanosecond and femtosecond induced ion emission observed here. The fluence in Fig. 2 is approximately 2 mJ/cm² where the illuminated surface area is roughly 0.16 cm². Several notable peaks are present in the time-of-flight spectrum using ultrafast excitation. First, the H^+ peak indicates the MgO surface could possibly contain a significant quantity of hydroxylated sites. A hydroxylated surface may result from dissociative adsorption of water on the in-air cleaved surfaces prior to mounting and baking in the vacuum assembly. Recent synchrotron X-ray photoemission studies of the reaction of water with MgO(100) at 300 K by Liu et al.⁹ conclude that water dissociatively adsorbs on MgO at defect sites initially and subsequently on terrace sites present on cleaved surfaces forming a hydroxylated surface on which additional waters may physisorb. Figure 2 also displays a peak at 4.75 microsecond that has been assigned by Kreitschitz et al.⁵ as Mg^{2+} in time-of-flight experiments. However, in our spectrum we note the absence of Mg isotope peaks (for masses 25 and 26) which should be present if this peak is to be unequivocally assigned to Mg. An additional small feature in Fig. 2 found at an arrival time of ~ 5.3 μs may be due to O^+ and/or OH^+ although this feature has not been thoroughly investigated.

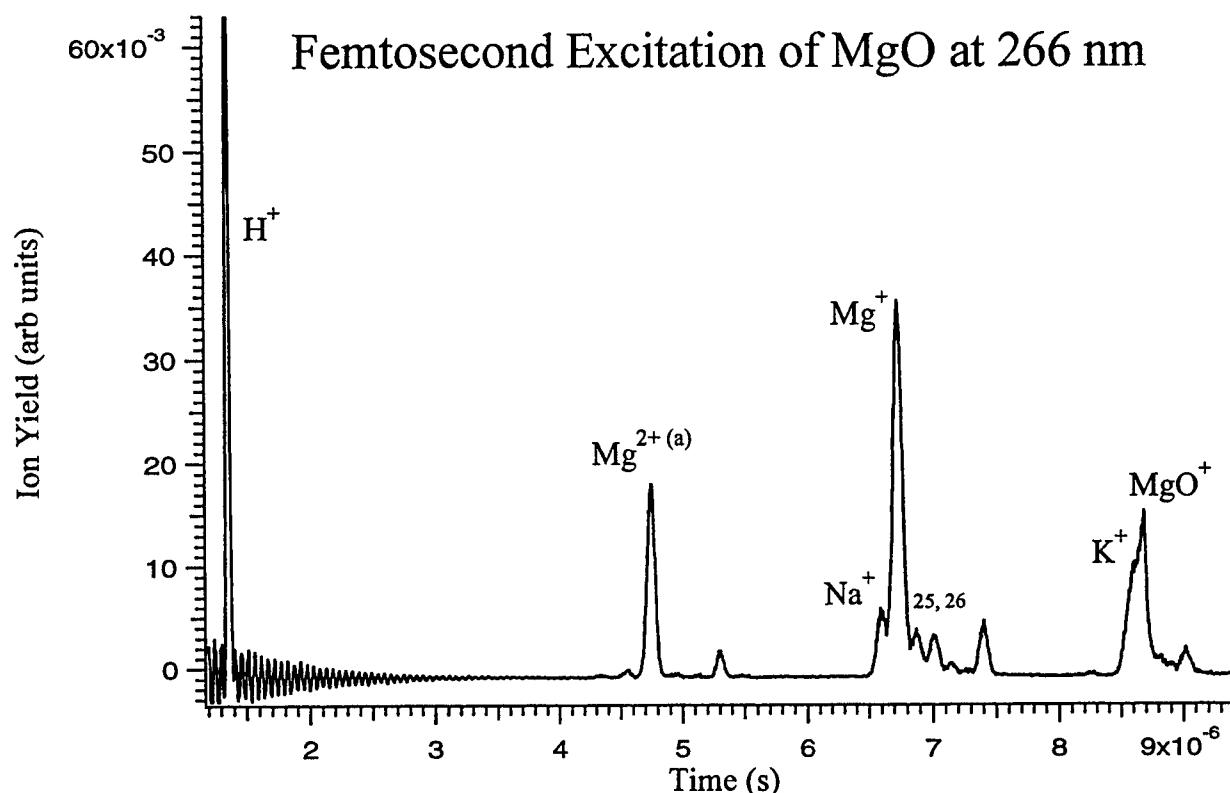


Figure 2. Time-of-flight spectrum of MgO after irradiation with ultraviolet femtosecond pulses. The dominant features include peaks assigned to H^+ , Mg^+ , and MgO^+ . The peaks assigned as Na^+ and K^+ are believed to be due to alkali metal present either on the surface or in the sample itself. (a) This peak has been assigned previously by Kreitschitz et al. NIMB 78, (1993) 327.

In addition to the observation of H^+ in the mass spectra, there are two clusters of peaks which are of interest. The first is located between 6.5 and 7.2 microseconds. The earliest peak may be assigned as Na^+ which is present in all spectra. This is likely due to contamination either from the MgO surface or the crystal itself. Next, there are three peaks at masses 24, 25 and 26. These may be assigned as the Mg^+ peaks arising from the three naturally occurring isotopes of magnesium. Finally, there is a smaller contribution from MgO^+ which occurs at about 8.5 microseconds. The early time shoulder may be assigned to K^+ , also a likely contaminant. Small impurity concentrations, of alkali metals, on the order of several ppm are readily observed in UV nanosecond desorption from a variety of materials.¹⁰

Figure 3 depicts the femtosecond power dependence for the integrated Mg^+ peaks (all isotopes). The power dependence is found to be approximately 5.4. No power dependence is reported for MgO^+ due to the interference from the nearby potassium peak. The initial nanosecond power dependence for Mg^+ , determined in quadrupole mass spectrometry experiments, is approximately 4.0 (although the nanosecond ion yield power dependence is more complex than that given by a simple power law).² The difference between the initial ion yield curves may indicate the an additional process contributes to ion emission under femtosecond excitation. Indeed, we find that the initial detection threshold for desorption is roughly an order of magnitude smaller than that reported for nanosecond excitation.² We note however, that femtosecond and nanosecond ion thresholds are not different by several orders of magnitude as might be expected if a multiphoton absorption description were invoked for both nanosecond and subpicosecond exposure. This strongly suggests a similar "initiation" step exists that depends upon fluence and not irradiance. Hattori et al.¹¹ have reported similar results for neutral Ga atom laser induced desorption. In that work, absorption through adion defects was suggested as the reason for the lack of flux dependence on the observed threshold. As mentioned in the Introduction section, Dickinson has proposed a model for Mg^+ desorption involving Mg^+ adions positioned directly atop F-centers (oxygen vacancy occupied by 2 electrons); this model is based upon the photoionization and trapping of electrons in or near the adion defect. The similar nature of the observed fluence thresholds for the two different pulse durations suggests that, if Dickinson's model is correct, this "shuffling" of

electrons beneath the adion defect can be induced by both nanosecond and femtosecond pulses. Further work, including time-resolved measurements of desorption, are necessary to test this model.

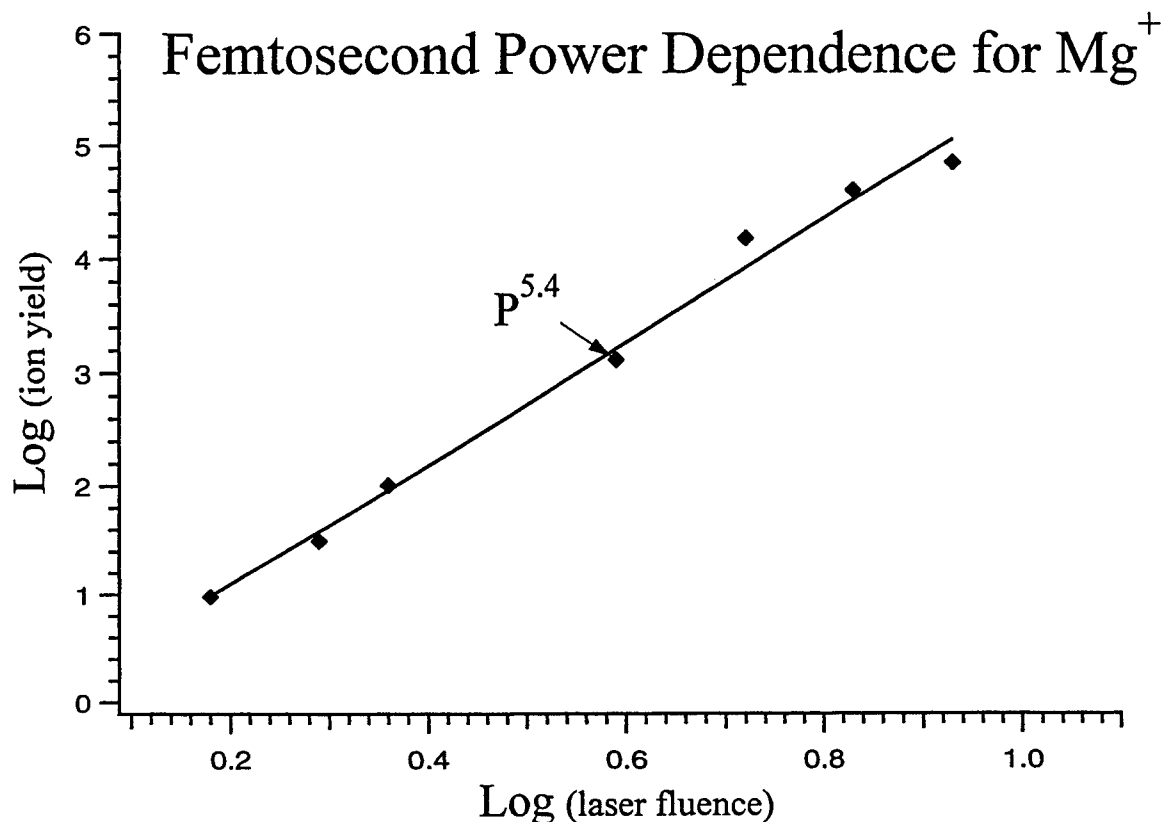


Figure 3 depicts the power dependence for the Mg^+ as a function of ultrafast excitation fluence. The observed power dependence of about 5.4 is greater than that determined in nanosecond experiments² and suggests that an additional channel may contribute in femtosecond laser desorption.

3.2. Nanosecond, 266 nm, Desorption Products from MgO

Figure 4 depicts a time-of-flight mass spectrum from MgO recorded using UV nanosecond irradiation at a fluence of 40 mJ/cm^2 . The major features are tentatively assigned as Na^+ , Mg^+ , Al^+ , K^+ , MgO^+ , Mg_2^+ , and Mg_2O^+ . As in the ultrafast case the presence of alkali metals is indicative of bulk or surface contamination. In contrast to the ultrafast case however, the alkali metals appear to be enhanced with nanosecond excitation, causing additional difficulty in the unambiguous assignment of the spectrum. Furthermore, in the nanosecond spectra the width of the features is considerably broader and also shifts to shorter time at higher powers. These effects obscure the mass peaks attributed to Mg^+ and MgO^+ making the analysis more complicated. Still, there are several notable differences between the nanosecond and femtosecond irradiation products. First of all, no H^+ is seen after ultraviolet nanosecond excitation at these fluences. This implies that the H^+ products arise from a multiphoton excitation mechanism enhanced by the use of the ultrashort pulse. The increased width of the ion distributions in the nanosecond regime likely results from electrostatic interactions between the particles (positive ions) themselves and perhaps the surface. In addition, the charge state of the surface is also unknown; it is possible that the surface may become charged (either positive or negative). Ermer et al.¹² have studied the photoelectron emission from MgO which accompanies positive ion emission following 248 nm (30 ns pulsewidth) irradiation and it is suggested that complex coulombic interactions exist between the desorbing positive ions and the photoelectrons.

Nanosecond Excitation of MgO at 266 nm

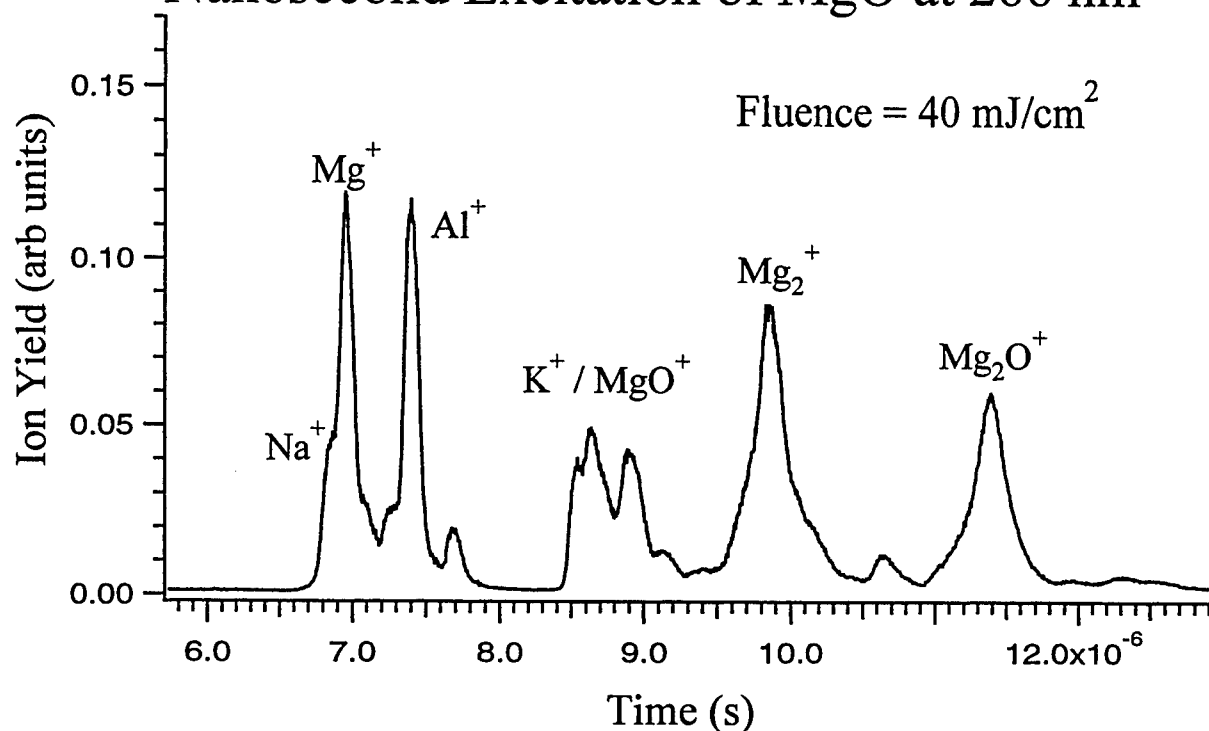


Figure 4. A time-of-flight mass spectrum from MgO recorded using 3 ns, 266 nm laser pulses at a fluence of 40 mJ/cm^2 .

4. CONCLUSION

Desorption products from in-air cleaved MgO samples have been measured, and their fluence dependence characterized, following both nanosecond and femtosecond ultraviolet laser irradiation. The mass spectra show significant differences for the nanosecond or femtosecond sources. In addition to Mg^+ , species such as H^+ are found following femtosecond exposure while some MgO^+ is detected. And finally, the observed threshold suggests that the ion desorption mechanism is dominated by defect photoabsorption. Future extensions of this work will include a more detailed investigation of the desorption phenomenon by employing time-resolved pump-probe type experiments to determine the nature of electronic excitation which eventually leads to ionic desorption. Additionally, plans are underway to study the ionic desorption products from CaCO_3 , and LiF (both positive and negative species) using a Laser Ablation and Ion-Trap Mass Spectrometer.

ACKNOWLEDGMENTS

This work is supported by the U.S. Department of Energy Office of Basic Energy Sciences (including Grant No. DE-FG03-98ER14864), Chemical Sciences Division. The research described in this paper was performed at the W. R. Wiley Environmental Molecular Sciences Laboratory, a national scientific user facility sponsored by the Department of Energy's

Office of Biological and Environmental Research and located at Pacific Northwest National Laboratory. Pacific Northwest National Laboratory is operated for the U.S. Department of Energy by Battelle under Contract DE-AC06-76RLO 1830.

REFERENCES

- 1.) J.T. Dickinson, J.-J. Shin, and S.C. Langford, "The role of defects in laser induced positive ion emission from ionic crystals," *Appl. Surf. Sci.* **96-98**, pp. 316-320, 1996.
- 2.) D.R. Ermer, J.-J. Shin, S.C. Langford, K.W. Hipps, and J.T. Dickinson, "Interaction of wide band gap single crystals with 248 nm excimer laser radiation. IV. Positive ion emission from MgO and NaNO₃," *J. Appl. Phys.* **80**, pp. 6452-6466, 1996.
- 3.) J.T. Dickinson, S.C. Langford, J.J. Shin, and D.L. Doering, "Positive Ion Emission from Excimer Laser Excited MgO Surfaces," *Phys. Rev. Lett.* **73**, pp. 2630-2633, 1994.
- 4.) J.T. Dickinson, "Low Fluence Laser Desorption and Plume Formation from Wide Bandgap Crystalline Materials," in *Experimental Methods in the Physical Sciences-Laser Ablation and Desorption*, Vol. 30, J.C. Miller and R.F. Haglund, eds. Academic Press, New York, 1998, pp. 139-172.
- 5.) O. Kreitschitz, W. Husinsky, G. Betz, and N.H. Tolk, "Laser induced desorption of ions from insulators near the ablation threshold," *Nucl. Instr. and Meth.* **B78**, pp. 327-332, 1993.
- 6.) G. Petite, P. Daguzan, S. Guizard, and P. Martin, "Conduction electrons in wide-bandgap oxides: a subpicosecond time-resolved optical study," *Nucl. Instr. and Meth.* **B107**, pp. 97-101, 1996. P. Martin, S. Guizard, Ph. Daguzan, G. Petite, P. D'Oliveira, P. Meynadier, and M. Perdrix, "Subpicosecond study of carrier trapping dynamics in wide-band-gap crystals," *Phys. Rev. B* **55**, pp. 5799-5810, 1997.
- 7.) A more comprehensive analysis of this work will be submitted for publication at a later date.
- 8.) B.C. Stuart, M.D. Feit, S. Herman, A.M. Rubenchik, B.W. Shore, and M.D. Perry, "Nanosecond-to-Femtosecond laser-induced breakdown in dielectrics," *Phys. Rev. B* **53**, pp. 1749-1761, 1996.
- 9.) P. Liu, T. Dendelewicz, G. E. Brown Jr., G. A. Parks, "Reaction of water with MgO(100) surfaces. Part I: Synchrotron X-ray photoemission studies of low-defect surfaces," *Surf. Sci.* **412/413**, pp. 287-314, 1998.
- 10.) D.P. Taylor, W.C. Simpson, K. Knutsen, M.A. Henderson, and T.M. Orlando, "Photon stimulated desorption of cations from yttria stabilized cubic ZrO₂ (100)," *Appl. Surf. Sci.* **127-129**, pp. 101-104, 1998.
- 11.) K. Hattori, A. Okano, Y. Nakai, and N. Itoh, "Laser-induced electronic processes on GaP (110) surfaces: Particle emission and ablation initiated by defects," *Phys. Rev. B* **45**, pp. 8424-8436, 1992.
- 12.) D.R. Ermer, S.C. Langford, and J.T. Dickinson, "Interaction of wide band gap crystals with 248 nm excimer laser radiation. V. The role of photoelectronic processes in the formation of a fluorescent plume from MgO," *J. Appl. Phys.* **81**, pp. 1495-1504, 1997.

Mechanistic studies and applications of laser-induced desorption from metal surfaces

J. Bosbach, D. Martin, F. Stietz^{*}, T. Wenzel, and F. Träger
Fachbereich Physik, Universität Kassel,
Heinrich-Plett-Str. 40, D-34132 Kassel, Germany

ABSTRACT

This article presents an overview of recent mechanistic studies of laser-stimulated desorption from rough metal surfaces and, as an application, describes novel experiments that exploit thermal desorption to fabricate small silver particles with an extremely narrow size distribution. Such systems are of great interest in catalysis or integrated optics and many other fields.

Keywords: Laser-induced desorption, nonthermal desorption mechanism, rough metal surfaces; clusters; nanoparticles

1. INTRODUCTION

Laser-induced desorption processes have been studied extensively in the last decade, quite often with emphasis on well-defined single crystal surfaces of different metals. Today, *rough* metal surfaces such as films of different topography or supported metal particles are of particular interest since they interact with laser radiation in very special ways¹. On an atomic scale, such surfaces are often composed of a large number of binding sites with low coordination numbers like adatoms on terraces, steps or kinks. Such "defects" can be regarded as building blocks of surface roughness. Electronic excitations that are *localized* at these sites can be driven by an incident light field and are associated with resonances which reflect the properties of each binding site. These localized excitations are important in promoting desorption but also, for example, in resonantly enhancing optical second harmonic generation. Of course, other electronic excitations, in particular non-localized surface plasmon-polaritons, i.e. collective oscillations, can also be stimulated. In fact, the localized resonances play their most essential role if they spectrally overlap with the plasmon. In such cases the localized single-electron excitations are driven with very high rate because of the well-known pronounced enhancement of the electric field that accompanies the collective resonance².

This article presents an overview of recent mechanistic studies of laser-stimulated desorption from metals and, as an application, describes novel experiments that exploit such processes to tailor small silver particles with an extremely narrow size distribution, systems which are of great interest in catalysis or integrated optics, to mention only two examples.

Surfaces with large roughness, i.e. atoms with different binding sites of low coordination number, have been prepared by deposition of metal atoms on dielectric single crystal surfaces held at low temperature. For this purpose alkali metals adsorbed on quartz served as model systems. The deposited atoms nucleate into small particles, with the surface defects acting as nucleation centers, processes known as Volmer-Weber growth mode in thin film epitaxy. The alkali metal clusters, if generated at low temperature, in fact offer the desired considerable number of surface sites with low coordination numbers. It turns out that their surface roughness cannot only be prepared reproducibly but also be diminished by annealing at different substrate temperatures and increased intentionally by depositing additional atoms. Thus, the surface topography can be influenced on an atomic scale, and, by growing particles of different size, varied in the nanometer regime. The above mentioned applied studies were carried out on small silver particles which nucleate with

^{*} Correspondence: E-mail: stietz@physik.uni-kassel.de; WWW: <http://www.physik.uni-kassel.de/exp1>; Telephone: +49 561 804 4501, Fax: +49 561 804 4518

high number density on, for example, quartz substrates by a combination of homogeneous nucleation and the above mentioned Volmer-Weber growth.

2 MECHANISTIC STUDIES OF LASER-INDUCED DESORPTION

The experimental arrangement used for the studies described here basically consists of an ultrahigh-vacuum system with the sample, two lasers for stimulating desorption and photo-ionizing the desorption products, and a time-of-flight mass spectrometer. The quartz substrate could be cooled to 80 K and heated to about 750 K for cleaning and annealing. A thermal beam of metal atoms with well-defined constant flux was generated in order to deposit a predetermined coverage of atoms onto the surface. Most of the experiments were carried out at low coverage, i.e. under conditions where the clusters are well separated and far from growing together. Since their number density is constant during growth, the coverage, i.e. the number of deposited atoms per cm^2 , and the average particle size are related to each other. For example, at a typical defect density of the quartz surface of $10^{10}/\text{cm}^2$ the coverage of $5.6 \cdot 10^{14}$ atoms/ cm^2 (about one monolayer of Na) corresponds to a mean cluster radius of 8 nm. After preparation and characterization by optical spectroscopy the samples were irradiated with the fundamental or higher harmonics of a Nd:YAG laser at $\lambda = 1064, 532, 355$ and 266 nm in order to stimulate desorption. The pulse duration was about 7 ns at a repetition rate of 10 Hz. Laser fluences ranging from 0.1 up to $150 \text{ mJ}/\text{cm}^2$ were used. At a distance of 20 mm in front of the sample the detached species were ionized with the light of an excimer laser operating at $\lambda = 193$ or 248 nm and subsequently passed the time-of-flight spectrometer. By varying the delay time between the two laser pulses used for desorption and ionization the kinetic energy distributions of the desorption products could be determined. Data were taken for different fluences, frequencies and polarizations of the light used for desorption but also in dependence of the cluster size and, as explained above, for different surface roughness. The incident light fluence was kept as low as sufficient signal-to-noise ratio allowed so that only subtle changes of the surface morphology were induced. Desorption studies under such conditions of low reaction rate open the door to correlate the desorption behavior with details of the electronic and geometric structure of different binding sites of the surface. Furthermore, light intensities not sufficient to remove large quantities of material per laser pulse ensure that gas phase collisions of the detached species can be avoided and their genuine kinetic energy distribution determined.

At this point, one may ask how desorption experiments can distinguish between detachment of atoms from different binding sites. For this purpose, measurement of the total number of desorbed atoms or molecules, the kinetic energy distributions of the released species and the dependence of the desorption signal on the number of fired laser pulses as a function of laser wavelength and fluence have turned out to be very useful. Furthermore, it is essential to distinguish between thermal and non-thermal desorption. Thermal desorption is characterized by an exponentially growing rate and an increase of the average velocity of the detached species with increasing laser fluence. Conversely, the desorption rate increases linearly with fluence in non-thermal reactions and the kinetic energy is independent of fluence (as long as multi-photon processes can be excluded).

The most important experimental results can be summarized as follows: if desorption is stimulated with laser light of $\lambda = 355$ nm two distinct maxima can be observed in the kinetic energy distribution. They are located at $E_{\text{kin}} = 0.16$ and 0.33 eV. If the coverage is varied, the amplitudes of the two maxima change. Their positions, i.e. the most likely values of the kinetic energies, however, remain constant. For $\lambda = 266$ and 532 nm, only atoms with kinetic energies of around $E_{\text{kin}} = 0.16$ eV are detected. For both wavelengths the positions of the maxima do not depend upon the fluence (if kept low) and polarization of the laser light. The integral desorption rate depends linearly on the fluence of the light stimulating desorption. In contrast, very different results are obtained if the measurements are repeated with laser light of $\lambda = 1064$ nm. For this wavelength desorption can only be observed for large fluences above approximately $40 \text{ mJ}/\text{cm}^2$ and for large coverages exceeding $9.0 \cdot 10^{15}$ atoms/ cm^2 . The desorption rate of the ejected atoms increases exponentially, and their kinetic energy rises as a function of fluence.

As explained above, the surface roughness has been gradually reduced by heat treatment of the samples. The results of these studies are as follows. If the temperature rises by about 30 K, the peak at $E_{\text{kin}} = 0.16$ eV disappears; if the increase is chosen to be larger than 50 K the maximum at $E_{\text{kin}} = 0.33$ eV also vanishes. Obviously, the two maxima exhibit different "annealing" behavior.

Desorption of atoms with light of $\lambda = 266, 355$ and 532 nm and low fluences obviously constitutes a non-thermal reaction. This is supported by the shape of the kinetic energy distributions of the detected atoms, the absolute energies of 0.16 and 0.33 eV as well as by their independence of the laser fluence. Also, the transition from non-thermal to thermal desorption can be followed. It is reflected in the transition from a linear to an exponentially growing dependence of the desorption rate as a function of laser fluence and a change of the kinetic energy distributions. For laser light with $\lambda = 1064$ nm, on the other hand, the measured kinetic energy distributions are always characteristic of thermal bond breaking and desorption is only observed if the fluence is about two orders of magnitude larger as compared to the other wavelengths.

As mentioned above, the measured kinetic energies are independent of particle size and light intensity in the non-thermal fluence regime. The two values actually remain constant under variation of all experimental parameters. We conclude that both values of $E_{\text{kin}} = 0.16$ and 0.33 eV constitute *fingerprints* of the metal surface. The different annealing behavior indicates that desorption of atoms takes place from well defined and different binding sites that predominantly exist at low temperature. Since both non-thermal signals disappear upon heating, these sites must have low coordination numbers. The electronic wavefunctions not being totally delocalized at these "defects", the electron-phonon-coupling is reduced in strength making possible desorption with finite probability.

Since light of $\lambda = 355$ nm stimulates desorption with a bimodal kinetic energy distribution whereas a single maximum is observed if the cluster surface is irradiated with light of $\lambda = 532$ nm, desorption with the two energies seems to be characterized by different wavelength dependencies which provide evidence of specific electronic properties of the binding sites. Unfortunately, the resonances associated with the defect sites of the metal surface are not known and the electronic and geometric signatures of special surface sites embedded in the kinetic energies of the desorbed atoms cannot be readily observed with standard surface science tools like photoemission. Thus, the sites responsible for desorption cannot be identified unambiguously at present. Still, measurements with different polarization of the laser light give some hints from where the atoms might be detached. The maximum at $E_{\text{kin}} = 0.16$ eV could be due to adatoms desorbed from terraces of the particle surface.

The experimental results allow us to suggest a desorption mechanism following the Menzel-Gomer-Redhead scenario (see e.g.³). Laser light is absorbed and, depending on the applied wavelengths of $\lambda = 266, 355$ or 532 nm, initially populates different electronic levels. The energy balance of the desorption reaction indicates that each of these excitations is followed by rapid relaxation into a lower-lying intermediate state, i.e. the absorbed photon energies are only partially converted into the kinetic energies of the liberated atoms or needed to supply the binding energy of a surface atoms of about 0.7 eV⁴. The intermediate state being antibonding, the atoms are accelerated away from the surface and gain kinetic energy E_A . The value of E_A depends upon the lifetime of the repulsive state which in turn determines the released kinetic energy. For $\lambda = 1064$ nm, on the other hand, the antibonding state cannot be reached. As a result, the absorbed photon energy can only be converted into heat causing thermal desorption. Further information on laser-induced desorption of metal atoms can be found in the literature⁵⁻⁹

Another interesting issue is that aggregates like dimers, trimers etc. can be desorbed with laser light. In order to detect such species, "soft" ionization must be accomplished to prevent dissociation of the desorbed molecules and unambiguously identify their masses. This has been realized here by using laser light with $\lambda = 248$ nm for ionization of Na_2 . The corresponding photon energy lies only little above the dissociation threshold of Na_2 and guarantees minimal fragmentation. Again, the particle size and the laser fluence were varied systematically. We find that laser-induced desorption of Na dimers is not only readily detectable but also takes place with surprisingly large rate. Under certain experimental conditions the rate of dimers desorbed per laser pulse can by far surmount the rate of atoms. For laser light of $\lambda = 532$ nm the measured kinetic energy distributions are characteristic of thermal bond breaking. Furthermore, the experimental data prove that desorption of Na_2 with $\lambda = 355$ and low fluences ($\phi < 8$ mJ/cm²) is non-thermal, the constant value of the most likely kinetic energy being $E_{\text{kin}} = 0.06$ eV. It is independent of coverage, i.e. particle size, and, as mentioned above, of the light intensity. The transition from non-thermal to thermal desorption as a function of laser fluence can also be identified. It is reflected in the change from a linear to an exponential dependence of the integral desorption rate and simultaneous modifications of the kinetic energy distributions. The large number of dimers that can be released with laser radiation indicates that Na_2 constitutes a highly stable subunit of the metal surface that can be detached without falling apart into individual atoms. In fact, two special binding sites from which the dimers are removed can be distinguished experimentally. For further details the reader is referred to recent publications¹⁰⁻¹³.

3 SIZE MANIPULATION OF METAL PARTICLES BY LASER-INDUCED DESORPTION

Nanoparticles exhibit very special properties which are not only different from the bulk but also depend upon the particle size and shape². In principle, this allows one to tailor make novel materials with special characteristics. Unfortunately, however, the size dependent features are obscured in most cases, since fabrication of small particles usually results in a mixture of different sizes^{2,14,15}. This does not only make it difficult to correlate certain properties to well defined particle radii but also prevents extensive use in future technological applications like, for example, novel catalytic converters with optimized selectivity^{16,17}, thin film technology^{18,19} or magnetic disk drives²⁰.

Therefore, preparation of nanoparticles of well defined size on support materials has long been a key issue in cluster science^{18,19}. In the past, a variety of attempts have been made to synthesize such systems by, for example, generating charged clusters in the gas phase with methods like gas aggregation or ion sputtering followed by mass-separation and soft landing on the substrate. The main drawbacks of these methods, however, are the restriction to clusters with at most 20 atoms^{21,22}, the very small amount of generated particles and a disproportionate experimental effort. Relatively large particles, on the other hand, can be generated with high size uniformity using lithographic techniques, methods which are, however, restricted to structures larger than about 20 nm¹⁷.

Here, we describe a novel experimental technique for fabrication of metallic nanoparticles of predetermined size and with very high size uniformity. The method is based on laser-induced thermal desorption and offers the following combination of advantages: little technical effort, generation of a large number of particles in parallel, no restriction to certain size ranges, fabrication of almost monodisperse particles, i.e. distributions with standard deviations of about 10 %. The principle is as follows, Figure 1.

Metal clusters are prepared by deposition of atoms and subsequent surface diffusion and nucleation on the substrate surface. The initial widths of the resulting size distributions are about 40 % of the mean particle diameter. Subsequently, the given distribution is narrowed by irradiating the clusters with pulsed laser light. Since the absorption cross section depends on the particle size², the frequencies of the incident laser radiation can be chosen such that only particles in certain size intervals of the distribution absorb light efficiently. During decay of the stimulated electronic excitation the absorbed photon energy is rapidly converted into heat. The heated clusters evaporate atoms and selectively shrink in size. As a consequence, the distribution alters. To accomplish the size manipulation the well-known surface plasmon resonance which is red-shifted as a function of particle radius in the size regime considered here can be exploited most profitably. The distribution narrows dramatically if two appropriately chosen laser wavelengths λ_1 and λ_2 are applied: Irradiation with λ_2 causes removal of the smallest particles and firing of laser pulses with λ_1 results in shrinking of the particles larger than the mean size. This process

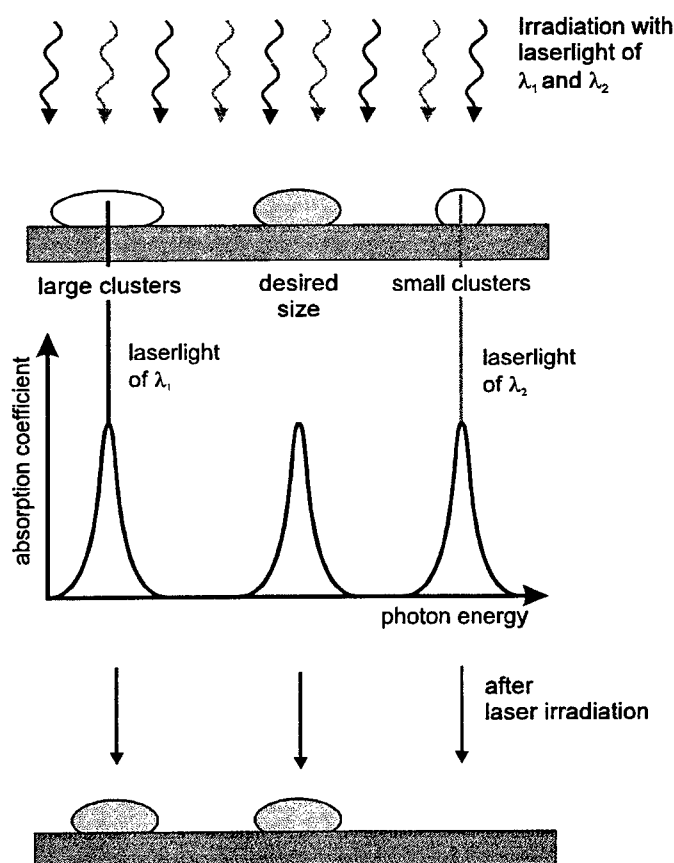


Figure 1: Schematic representation of the experimental method used to narrow the size distribution (top) of metal nanoclusters on dielectric substrates with pulsed laser light. After laser irradiation only particles of the desired size remains on the surface. For details see text.

automatically comes to an end if the clusters have shifted out of resonance due to the size change and do not interact with the laser light anymore.

In order to demonstrate that this method can be used for producing particles with an extremely high size uniformity, Ag clusters were grown under ultrahigh vacuum conditions on quartz substrates as explained above. The surface and cluster morphology were characterized in situ by scanning force microscopy (SFM) and optical spectroscopy. The distribution was determined from the SFM images and resembles a Gaussian with a rather large width of $\sigma^* = \sigma/\langle d \rangle = 0.40$. σ is the standard deviation of all particle diameters. Determination of the size distribution is based on measurements of the dimensions of several hundred clusters in many SFM images.

After imaging, the particles were irradiated with light pulses generated by a Nd:YAG laser. The pulse duration was 7 ns and the repetition rate 10 Hz. Subsequently, the particles were again characterized with scanning force microscopy and optical spectroscopy.

Figure 2 illustrates the influence of laser irradiation of the clusters with 6000 laser pulses of $\lambda = 355$ nm and, subsequently, with 6000 pulses of $\lambda = 532$ nm. The average particle diameter was found to decrease from $\langle d \rangle = 12$ to 10 nm²³. This is accompanied by a drastically improved size uniformity. The width of the size distribution has been reduced by 70 % and now amounts to as little as $\sigma^* = 0.13$. It should be pointed out that the distribution narrows strongly during the first 1000 laser pulses of each applied wavelength and changes only little upon further laser irradiation. The repetition rate of the laser pulses being 10 Hz, the narrowing process is completed after only few minutes.

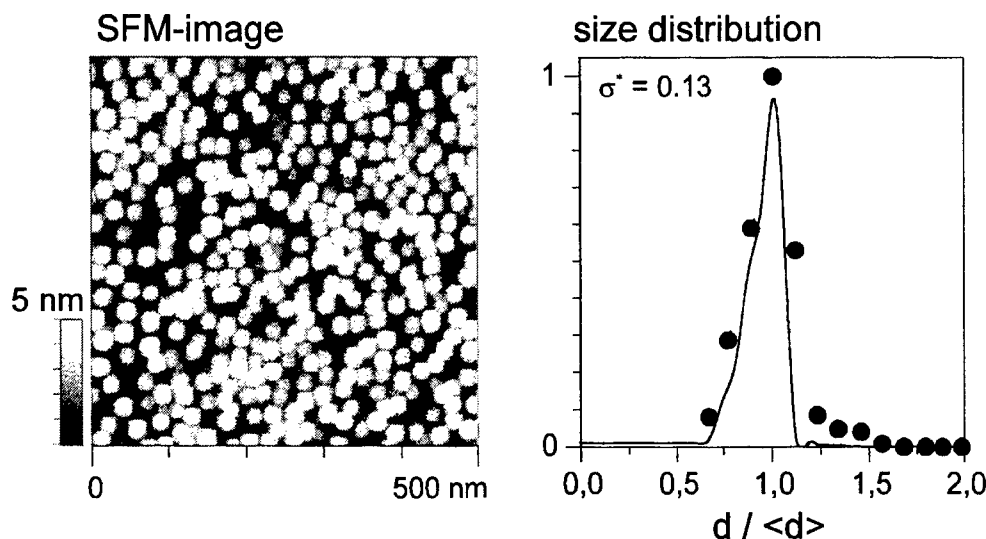


Figure 2: SFM image (left) of silver nanoclusters after irradiation with 6000 laser pulses of $\lambda = 355$ nm and, subsequently, with 6000 pulses of $\lambda = 532$ nm. The average particle diameter was found to decrease from $\langle d \rangle = 12$ to 10 nm. This is accompanied by a drastically improved size uniformity. The width of the size distribution (right) has been reduced by 70 % and now amounts to as little as $\sigma^* = 0.13$. The solid line is the result of theoretical modeling of the narrowing process and describes the experimental data (full circles) very well.

The drastic narrowing of the size distribution is also reflected in the optical spectra of the Ag particles, Figure 3. They are dominated by two maxima which arise from the excitation of surface plasmon-polaritons in the direction of the long ((1,1)-mode) and short ((1,0)-mode) axis of the particles. Their energetic positions reflect the mean size and shape of the clusters². The width is determined by homogeneous broadening arising from the finite decay time of the plasmon^{2,24}

and an inhomogeneous contribution due to the above mentioned dependence of the plasmon frequency on the particle diameter. For particles as grown the (1,1)-mode has a rather large width of $\Delta E = 0.92$ eV. After laser irradiation with $\lambda = 355$ and 532 nm, the resonance position is shifted to higher energy, consistent with the reduction of the mean size of the silver particles. Due to the drastic decrease of the width of the size distribution, the shift is accompanied by a pronounced reduction of inhomogeneous broadening. The width converges to the homogeneous linewidth of the plasmon resonance and now amounts to as little as $\Delta E = 0.35$ eV. The measured spectra demonstrate impressively that the size manipulation is in fact accompanied by tailoring of the optical properties of the nanoparticles.

The size manipulation and narrowing has also been modeled theoretically in order to ensure optimization of the narrowing process with as little experimental effort as possible. The absorption coefficient, temperature rise and evaporation rate have been calculated as a function of cluster size. For computation of the absorption coefficient electrodynamic theory was used^{2,25}. The temperature rise was determined by solving the heat diffusion equation and the resulting evaporation rate during each laser pulse was calculated using the Arrhenius equation. In fact, the theoretical size distribution obtained after applying the two wavelengths of $\lambda = 532$ and 355 nm in subsequent manipulation steps agrees almost perfectly with the measured distribution and also reproduces the value of the standard deviation of $\sigma^* = 0.13$, Figure 2. We emphasize, that this value compares very favorably to results obtained by deposition of size selected metal cluster ions ($\sigma^* \sim 0.3$)²¹, lithographically designed nanoparticles¹⁷ or nanostructure arrays grown on specially prepared substrates ($\sigma^* < 0.2$)²⁶. Moreover, size distributions of metal particles with standard deviations below $\sigma^* = 0.20$ have not been reported previously for the size range considered here, i.e. for metal particles with diameters of around $d = 10$ nm. Details of the model will be described elsewhere.

4 CONCLUSIONS

In conclusion, we have shown that the very special geometric and electronic properties of rough metal surfaces can be investigated by laser-induced desorption with its inherent surface specificity. Undoubtedly, the detailed characterization of the different binding sites and their electronic resonances is a great challenge. To this end, scanning tunnelling and atomic force microscopy, for example, of single crystal surfaces containing adatoms that represent roughness could be helpful. Furthermore, desorption experiments with continuously tunable laser radiation will be of great value.

Our experiments further illustrate the feasibility of controlled fabrication of monodisperse metallic nanoclusters on substrate surfaces through laser-stimulated narrowing of broad size distributions. The applied method relies on the size dependence of the absorption coefficient of metal nanoparticles. It can be applied to a wide range of desired cluster sizes as long as the frequencies of the optical absorption lines shift monotonously as a function of size. The gradient of this red or blue shift and the difference $\Delta\lambda$ of the used laser wavelengths determine the remaining width of the size distributions. Even if the plasmon resonance of the particles, however, is located far away from available laser photon energies the overall d^3 -increase of the optical absorption coefficient can be exploited to narrow the distributions. The ability to fabricate monodisperse metal nanoparticles of predetermined sizes opens up the possibility of examining the chemical and physical

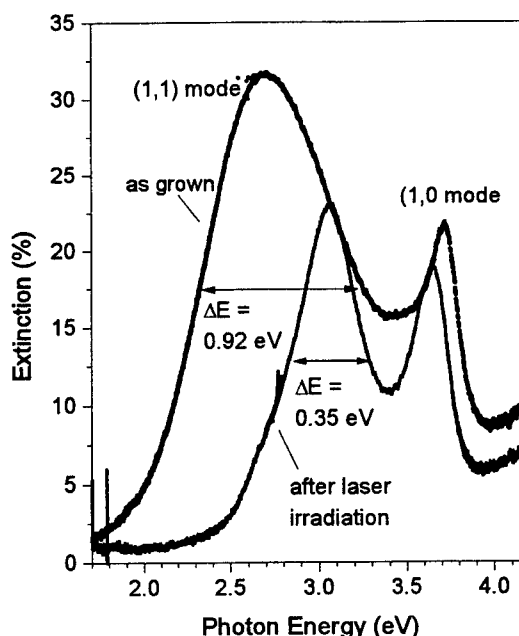


Figure 3: Optical spectra of silver nanoclusters measured with p-polarized light before and after narrowing of the particle size distribution with laser light.

properties of clusters in novel experiments and correlate them to well defined sizes. The particles can also be covered with a protective layer to incorporate them in a variety of devices, for example, in linear and non-linear optical components.

ACKNOWLEDGEMENTS

Financial support by the Deutsche Forschungsgemeinschaft and the Fond der Chemischen Industrie is gratefully acknowledged. T.W. thanks the Otto-Braun-Fond for a scholarship.

REFERENCES

1. F. Träger: in *Atomic Physics Methods in Modern Research*, Lecture Notes in Physics **499**, p. 423; editors K. Jungmann, J. Kowalski, I. Reinhard, F. Träger, Springer (1997)
2. M. Vollmer, U. Kreibig: *Optical Properties of Metal Clusters*, Springer Ser. Mat. Sci. **25** (1995)
3. *Desorption Induced by Electronic Transitions, DIET VI*, Nucl. Instrum. Meth. Phys. Res. B **101** (1995)
4. M. Vollmer, F. Träger, "Atom desorption energies for sodium clusters", Z. Physik D **3**, 291 (1986)
5. W. Hoheisel, M. Vollmer, F. Träger, "Desorption of metal atoms with laser light – mechanistic studies", Phys. Rev. B **48**, 17463 (1993)
6. T. Götz, M. Bergt, W. Hoheisel, F. Träger, M. Stuke, "Non-thermal laser-induced desorption of metal atoms with bimodal kinetic energy distribution", Appl. Phys. A **63**, 315 (1996)
7. I. Lee, T.A. Callcott, E.T. Arakawa, "Desorption studies of metal atoms using laser-induced surface plasmon excitation", Phys. Rev. B **47**, 6661 (1993)
8. A.M. Bonch-Bruевич, T.A. Vartanyan, Yu.N. Maksimov, S.G. Przhibel'skii, V.V. Khromov, "Photodesorption and work function study of long living states on metal surfaces", Surf. Sci. **307-309**, 350 (1994)
9. F. Balzer, R. Gerlach, J.R. Manson, H.-G. Rubahn, "Photodesorption of Na atoms from rough Na surfaces", J. Chem. Phys. **106**, 7995 (1997)
10. J. Viereck, M. Stuke, F. Träger, "Laser-induced desorption of Na-dimers", Appl. Phys. A **64**, 149 (1997)
11. J. Viereck, M. Stuke, F. Träger, "Non-thermal kinetic energy distributions of desorbed Na-dimers", Surf. Sci. **377-379**, 687 (1997)
12. T. Götz, M. Bergt, W. Hoheisel, F. Träger, M. Stuke, "Laser ablation of metals: the transition from non-thermal processes to thermal evaporation", Appl. Surf. Sci. **96-98**, 280 (1996)
13. F. Stietz, M. Stuke, J. Viereck, T. Wenzel, and F. Träger, "Observation of strong optical absorption at the surface of small particles", Surf. Sci. Lett. **389**, L1153 (1997)
14. H. Brune, "Microscopic view of epitaxial metal growth: nucleation and aggregation", Surf. Sci. Rep. **31**, 121 (1998)
15. C.R. Henry, "Surface studies of supported model catalysts", Surf. Sci. Rep. **31**, 231 (1998)
16. M. Valden, X. Lai, D.W. Goodman, "Onset of Catalytic Activity of Gold Clusters on Titania with the Appearance of Nonmetallic Properties", Science **281**, 1647 (1998)
17. G.A. Somorjai, "New model catalysts (platinum nanoparticles) and new technique (SFG and STM) for studies of reaction intermediates and surface restructuring at high pressure during catalytic reactions", Appl. Surf. Sci. **121/122**, 1 (1997)
18. *Proceedings of the Science and Technology of Atomically Engineered Materials*, edited by P. Jena, S.N. Khanna, B.K. Rao, World Scientific Publishing, Singapore, New Jersey, London, Hongkong (1995)
19. *Proceedings of ISSPIC 8, Small Clusters and Inorganic Particles*, ed. H.H. Andersen, Copenhagen 1996; Z. Phys. D **40**, 1-578 (1997)
20. A.E. Berkowitz in *Magnetic Properties of Fine Particles*, ed. J.L. Dormann and D. Fiorani, North Holland, Amsterdam (1992)
21. K. Bromann, C. Felix, H. Brune, W. Harbich, R. Monot, J. Buttet, K. Kern, "Controlled deposition of size-selected silver nanoclusters", Science **274**, 956 (1996)
22. W.-D. Schneider, H.-V. Roy, P. Fayet, F. Patthey, B. Delley, C. Massobrio, in *Cluster Assembled Materials*, edited by K. Sattler, Materials Science Forum **232**, Trans Tech Publications, Switzerland, Germany, UK, USA, 1996

23. The diameters of the particles as shown in the SFM images are overestimated due to the finite radius of the SFM tip ($r \approx 12$ nm). However, the actual mean diameter $\langle d \rangle$ of the clusters could be derived from the Ag coverage measured by a quartz crystal microbalance and the known cluster density to be $\langle d \rangle = 12$ nm.
24. T. Klar, M. Perner, S. Grosse, G. von Plessen, W. Spirkel, J. Feldman, "Surface-plasmon resonances in single metallic nanoparticles", *Phys. Rev. Lett.* **80**, 4249 (1998)
25. C.F. Bohren, D.R. Huffman: *Absorption and Scattering of Light by Small Particles*, Wiley, New York (1983)
26. H. Brune, M. Giovanni, K. Bromann, K. Kern, "Self-organized growth of nanostructure arrays on strain-relief patterns", *Nature* **394**, 451 (1998)

Direct Mesoscopic Simulation of Melting and Evaporation

Takashi Yabe¹

Department of Energy Sciences, Tokyo Institute of Technology, Yokohama 226, Japan

ABSTRACT

We have succeeded for the first time to simulate dynamic phase transition from metal to vapor. This success is due to the CIP(Cubic-Interpolated Pseudoparticle/Propagation) method that can treat solid, liquid and gas together and can trace a sharp interface with almost one grid. For these types of problems such as welding and cutting processes, we need to treat topology and phase changes of the structure simultaneously. Furthermore, the grid system aligned to the solid or liquid surface has no meaning and sometimes the mesh is distorted and even broken up. The CIP method developed by the author does not need adaptive grid system and therefore removes the problems of grid distortion caused by structural break up and topology change. In this paper, we will give a brief introduction of the CIP method, then report here the application to laser-induced evaporation and welding process. In the former case, aluminum is evaporated well after the laser beam ended and evaporation occurs with a large angle to the target normal leading to large debris. In the latter case, a deep penetration welding of SUS304 by YAG laser has been successfully replicated the experiments and the simulation clarifies the formation mechanism of keyhole.

Keyword: Laser Cutting, Laser Welding, Simulation, Phase Transition, Unified Solver, CIP, Coronet, Milk-Crown

1 INTRODUCTION

Recent high technology requires new tools for combined analysis of materials in different phase state, e.g., solid, liquid and gas. A universal treatment of all phases by one simple algorithm is essential and we are at the turning point of attacking this goal. For these types of problems such as welding and cutting processes, we need to treat topology and phase changes of the structure simultaneously. In freezing, condensation, melting and evaporation, the grid system aligned to the solid or liquid surface has no meaning and sometimes the mesh is distorted and even broken up.

Toward this goal, we take Eulerian-approach based on CIP¹⁻⁴ method developed by the author. The CIP method does not need adaptive grid system and therefore removes the problems of grid distortion caused by structural break up and topology change. The material surface can be captured almost by one grid throughout the computation. Furthermore, the code can treat all the phases of materials from solid state through liquid and two-phase state to gas without restriction on the time step from high-speed.

In this paper, we shall present the strategy of the CIP method to these problems and show three typical examples which are related to laser-cutting, laser-welding. Although the last example is the coronet formation and is not directly related to the laser processing, it demonstrates the importance of interaction between liquid surface and ambient gas and will be important also in laser processing.

2. UNIVERSAL TREATMENT

2.1 Hydrodynamic Equations

In order to solve all the materials in a universal form, we must find an appropriate equation for solid, liquid and gas. We use full hydrodynamic equations for these materials, which can be written in a form :

¹Correspondence : E-mail : yabe@es.titech.ac.jp ; WWW:<http://ciprus2.es.titech.ac.jp> ; Telephone:+81-45-924-5535 ;
Fax:+81-45-924-5536

$$\frac{df}{dt} \equiv \frac{\partial f}{\partial t} + (\mathbf{u} \cdot \nabla) \mathbf{f} = \mathbf{g}, \quad (1)$$

where $\mathbf{f}=(\rho, \mathbf{u}, T)$ and $\mathbf{g}=(-\rho \nabla \cdot \mathbf{u}, -\nabla p / \rho + Q_v, -P_{TH} \nabla \cdot \mathbf{u} / \rho C_v + Q_E)$, where ρ is the density, \mathbf{u} the velocity, p the pressure, T the temperature, Q_v represents viscous, stress terms and surface tension etc., and Q_E includes viscous heating, heat conduction and heat source. Here C_v is the specific heat for constant volume and we defined $P_{TH} = T(\partial p / \partial T)_\rho$.

It is illustrative to give an explicit expression of P_{TH} in special cases. For ideal fluid, it becomes pressure since p is linearly proportional to T , while for two-phase flow if the pressure is given by the Clausius-Clapeyron relation,

$$p = p_0 \exp\left(-\frac{L}{RT}\right), \quad P_{TH} = T\left(\frac{\partial p}{\partial T}\right) \propto L \quad (2)$$

where R is the gas constant and therefore P_{TH} is proportional to latent heat L and P_{TH} represents the latent heat release owing to the increase of volume followed by the increase of fraction of gas in two phase flow. For more general equation of state, C_v and P_{TH} can be calculated analytically or numerically throughout all phases.

The CIP method solves the equations like Eq.(1) by dividing those into non-advection and advection phases as given in previous papers. A cubic-interpolated profile propagates in space in the advection phase and then nonadvection phase is calculated by finite difference method. As shown in the previous papers, we can trace even shock waves correctly with the CIP method although it uses fluid equations written in a non-conservative form or in primitive Euler representation. It is well known at present that the primitive Euler scheme is the best suited for multi-phase boundary but unfortunately no other modern schemes except for the CIP method have succeeded to use the primitive Euler representation to treat shock waves in multi-media.

2.2 Universal Solver

Since we are treating hydrodynamic equations in a non-conservative form, it is easy to extend it to include both incompressible and compressible fluids. Let us consider again the origin of the difficulty. In the gas phase where density is sufficiently low, the pressure is in proportion to the density. Therefore, we may solve the density first in Eq.(1) and then after temperature is obtained, we use EOS(equation of state) like that shown in Fig.1. However, near the solid density, the pressure rises very sharply. If we use the same procedure there, the pressure can change easily by 3-4 orders of magnitude even with small error of density around few tens of percent. Therefore, the strategy to solve the density first is broken in this area. This is the reason why the universal treatment of solid, liquid and gas has been a difficult task. In attacking this problem, the physicist in incompressible fluid invented an interesting technique. We will translate the strategy they used from a different view point and reconsider the technique. If the pressure is very sensitive to the density, we had better solve pressure at first. If we have a way to solve pressure at first, then we get density very accurately at the solid density. Since the pressure is proportional to density in the gas phase, this strategy does not harm the solution there either. Then how to realize this strategy? Our method starts with the thermodynamic relation:

$$\Delta p = \left(\frac{\partial p}{\partial \rho}\right)_T \Delta \rho + \left(\frac{\partial p}{\partial T}\right)_\rho \Delta T \quad (3)$$

where $\Delta p = p^{n+1} - p^*$ and $*$ represents a profile after advection. The same expression is used for ρ and T . Therefore, if $\Delta \rho$ and ΔT are predicted by the continuity equation and energy equation, Δp can be obtained since $(\partial p / \partial \rho)$, $(\partial p / \partial T)$ are already given from EOS. The advantage of the CIP is the separate treatment of the non-advection term. We should note that this merit is quite important to get the final result. Then we obtain the equation^{3,5} for p^{n+1}

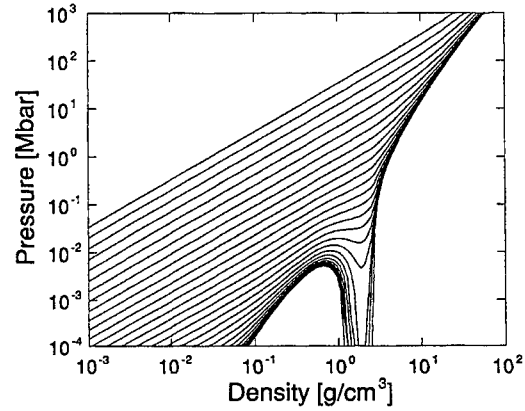


Figure 1. Equation of state of aluminum. Each line represents isotherms.

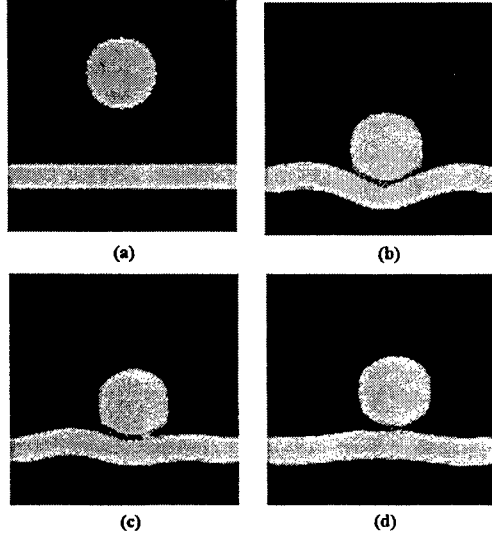


Figure 2 Example of elastic-plastic flow. The system is described by 100×100 Cartesian fixed grid and only 10 grids are used for the width of plate. Plate and ball are moving through fixed grid system. Black part is filled with air and also calculated.

We note again that this property is a consequence of the separate treatment of advection and non-advection terms, otherwise the continuity of $\nabla p / \rho$ is not guaranteed and a large density can not be traced.

Before going into the application, we should mention that the scheme can easily include the stress calculation in equation of motion as shown by the example in Fig.2 since the CIP can capture the material surface by one grid point.

3. APPLICATIONS

We have developed a numerical scheme to solve dynamics of solid, liquid and gas together. By this scheme, we are able to attack the elastic-plastic behavior of solid interacting with liquid and gas. In this section, we shall give some typical examples demonstrating the potentiality of the scheme.

3.1 Laser-Induced Evaporation

Figure 3 shows melting and evaporation of aluminum under the illumination of laser light, where the density changes from 2.7 to $10^{-4} \text{ g.cm}^{-3}$. Aluminum solid is treated as an elastic-plastic material initially and then changes to liquid and vapor during

$$\nabla \left(\frac{1}{\rho^*} \nabla p^{n+1} \right) = \frac{p^{n+1} - p^*}{\Delta t^2 (\rho C_s^2 + \frac{P_{TH}^2}{\rho C_v T})} + \frac{\nabla \cdot \mathbf{u}^*}{\Delta t} \quad (4)$$

where $C_s^2 = (\partial p / \partial \rho)_T$.

It is very important to note that in Eq.(4), ρ is inside the derivative on the lefthand side. At the interface between materials having large density difference, the continuity of acceleration $\nabla p / \rho$ is very important because the denominator ρ can change by several orders of magnitude in one grid. Equation (4) guarantees the continuity of $\nabla p / \rho$ at the discontinuity. By this procedure, we can treat all the material at once by simply changing its equation of state.

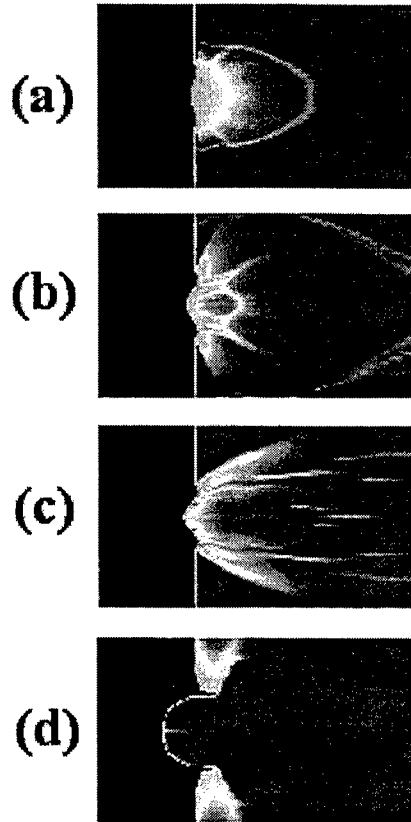


Figure 3. Density contour of aluminum illuminated by laser light. Time sequence is (a)40, (b)90, (c)290 nsec with elastic-plastic effect. Filamentary structure explains the experimental results.(d) is done without elastic-plastic effect.

phase transition. This change is simply realized by the equation of state. This example shows the high ability of the code to describe a sharp interface and to be robust enough to treat both compressible and incompressible fluid simultaneously.

The experiment was performed at the Institute of Laser Engineering, Osaka University regarding the x-ray source development⁶: a YAG laser of 650 mJ in 8nsec is used to obliquely illuminate an aluminum slab target with an angle of 45 degree to the target normal. Final crater depth and shape agree quite well with the simulation⁵ and seems to be anomalous because the cutting speed is $100\mu\text{m}/8\text{nsec}=10^6\text{cm}\cdot\text{sec}^{-1}$ if this crater should have been created during laser pulse. Since the speeds of sound wave and elastic wave inside aluminum are order of $10^5\text{cm}\cdot\text{sec}^{-1}$, the cutting speed is much larger than these speeds. Is this speed physically possible? It is interesting to note that the crater is not formed during the laser pulse, but it develops gradually in the time scale of several 100 ns well after the laser pulse ended as shown in Fig.3. The very high temperature plasma more than a few tens of eV produced by the 8 ns laser pulse and most of them expands from the target. However, some of them still stay near the target for long time after the laser pulse because of recoil force from expanded plasmas and act as heat source to melt aluminum metal in the time scale of several 100 ns.

When the plasma temperature becomes less than melting temperature around 290 nsec (the time is measured from the laser peak), the stress of aluminum whose strength is 0.248 Mbar and yield strength is 2.2976 kbar is recovered and no distortion occurs after that time. This yield stress is quite important to determine the final crater size. Without elastic-plastic effect, the crater develops further even after 490 ns and the depth becomes more than $300\mu\text{m}$ as shown in Fig.3(d) although less difference is seen at the beginning around 90 ns.

The plasma heated crater formation leads to other interesting phenomena. Since the plasma acts not only as heat source but also as pressure source, the dynamic expansion of evaporated material at later time is strongly modified. Since a high pressure region is just in front of the evaporation surface, the vapor is forced to flow bypassing through a narrow channel between the metal surface and this pressure source. Therefore, the vapor preferentially flows toward a circumference with a large angle to the target normal. This effect is the exactly the same as that obtained in the experiment. Figure 4 shows a distribution of debris from the targets. The histogram is the experimental result and it was drawn from 2000 shots accumulated. The distribution was obtained using an interference microscope by measuring the thickness of aluminum piled-up on the glass plate with an accuracy of $0.01\mu\text{m}$ and then getting volume combined with the area measured by a microscope. The estimated error in the distribution is a few tens of percent and is small enough to compare with the simulation result. Clearly there exist two peaks around 0 and 75 degree. As in Fig.3, the plasma expands being directed normally to the target at early time $t<90\text{ ns}$ and this expansion is a bulk part of the laser-heated plasma. As already stated, this expansion causes recoil force to the hot plasma surrounding aluminum surface. This main part of the expansion creates a peak at 0 degree. The triangles in Fig.4 show the distribution calculated from the time integration of mass flow ρu up to $t=90\text{ ns}$. At an early stage $t<90\text{ ns}$, no peak appears around 75 degree. On the other hand, the expansion at later stage $t>90\text{ nsec}$ is limited to the sideward direction as stated before and creates the peak at 75 degree. Therefore accumulated distribution up to 490 ns shown by circles in Fig.3 increases mainly at 75 degree.

Simulation also predicts further interesting behavior. The expansion at $t<40\text{ nsec}$ is quite uniform because its temperature is quite high a few tens of eV. The experiment supports this result and the debris around 0 degree is very fine and indistinguishable with an optical microscope. On the other hand, the simulation result at $t=290\text{ nsec}$ shows some filamentary streams flowing from the surface. The experiment also supports this result and the debris at 75 degree consists of 1 to $20\mu\text{m}$ sized particles. Since the simulation is two-dimensional axisymmetric, we cannot estimate the particle size but we can suggest the origin of the filaments.

3.2 Welding and Keyhole

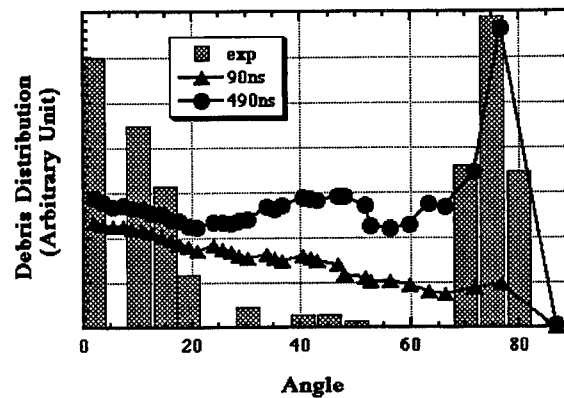


Figure 4. Debris distribution. 0 degree corresponds to the target normal. The histogram shows the experimental result, while circles and triangles show the accumulated mass from the simulation at 490 ns and 90 ns, respectively.

Welding is another interesting application of the code. Although the keyhole dynamics in deep penetration welding has been well investigated experimentally, no one has succeeded to simulate the process. Therefore, conventional theoretical speculation on how keyhole is created has not yet been confirmed. In order to do this simulation, we need some assumption on absorption process. As is well known, in the metal, conduction electron behaves as free electron and absorbs laser energy through collision with lattice. If we introduce the conductivity of the metal σ , then reflectivity is given by Hagen-Rubens formula

$$R = 1 - \sqrt{\frac{2\omega}{\pi\sigma_0}} \cos\theta \quad (5)$$

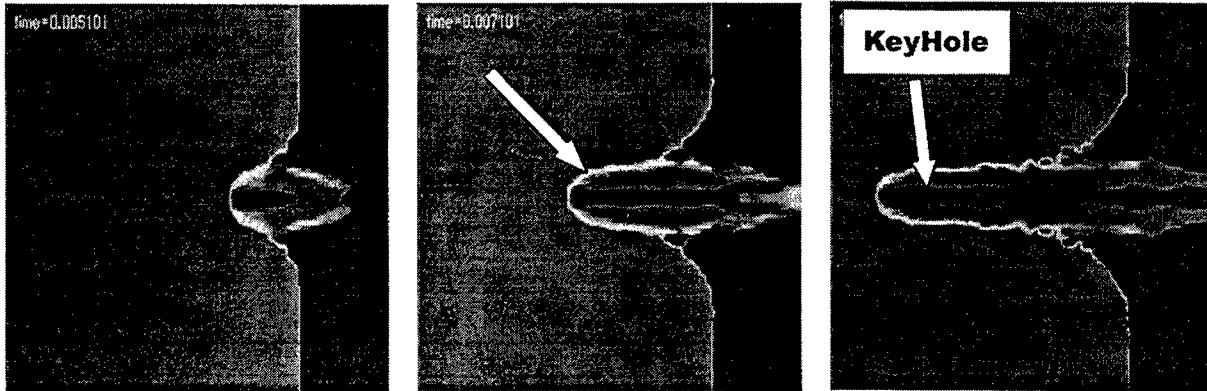


Figure 5. Two-dimensional axisymmetric simulation of laser welding. Density contour at 5,7,10 msec.

where ω and θ are the angular frequency and incident angle of laser light. If the laser frequency becomes larger than collision frequency, Drude's model for conduction electron

$$\sigma = \frac{\sigma_0}{(1 - i\omega\tau)}$$

is required and then absorption rate approaches $1/\sigma_0$ scaling instead of $(1/\sigma_0)^{1/2}$ scaling in Eq.(5). This transition is critical for YAG laser, but we still use Eq.(5) and set the absorption rate scaled from the absorption data of CO₂ laser of SUS.

When the metal is heated above the evaporation temperature, it will start to expand continuously. This is important inside keyhole because the evaporated vapor will not easily escape from the keyhole and density there can be quite high. The ablation mass flux dm/dt is determined from thermal conduction and can be fixed like

$$dm/dt = \rho_{ab} V_{ab}.$$

Since the generated pressure is $p = \rho_{ab} V_{ab}^2$ which is estimated to be $(dm/dt)^2 / \rho_{ab}$, the pressure is very sensitive to ablation density. Therefore, it is important to know the realistic value of density inside the keyhole. Adding to this, if very high-density vapor exists inside the keyhole, the ablation process is not as same as the ablation into vacuum and dm/dt may become a function of ambient density. Even if we accept that dm/dt is constant, V_{ab} should be much smaller for the expansion into dense gas rather than into vacuum, although many people have assumed that the ablation velocity V_{ab} is roughly $(T/m)^{1/2}$ and this value is about 10^5 cm/sec. Thus, quite a high-density matter may exist inside keyhole.

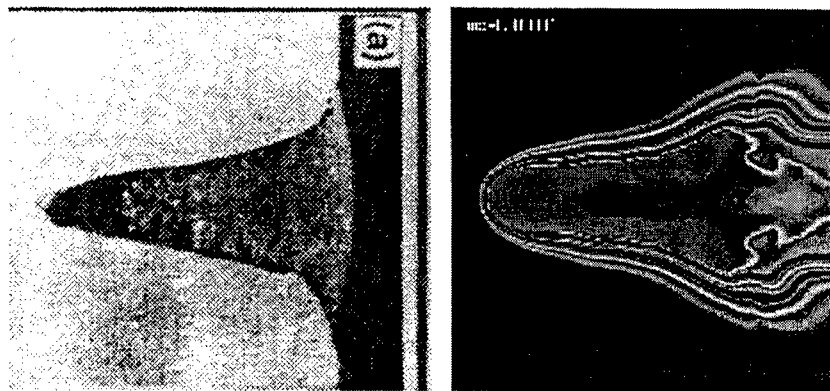


Figure 6. (Left) Cross sectional view of welded structure obtained in experiment. (Right) Temperature contour at 10 msec in the same simulation as in Fig.5.

This high-density matter can affect the absorption process. What happens when density gradually decreases from the solid density to vapor. When the density gradually decreases, at some density inter-atomic distance becomes large enough and conduction electrons no longer exist. Then absorption by conduction electrons disappears and thereby laser beam becomes transparent through this material. In the following simulations, we shall investigate the effect of ambient gas in deep penetration welding.

We have done welding simulation replicating experiments done by Katayama and Matsunawa⁷ at Osaka University. Laser is YAG laser and its peak power is 5kW, the pulse rises linearly until 5msec and gradually decreases down to 4kW at 10 msec. Spatial profile is Gaussian and its diameter is 0.8 mm where the intensity is reduced to $1/e^2$ of the peak. The irradiated material is SUS304. In the simulation, each ray of laser light has been traced as straight line and absorption is calculated depending on the incident angle. We neglect the absorption by plasma since it is proportional to square of laser wavelength and is negligible for YAG laser.

Figure 5 shows density contour at 5,7,10 msec. It is seen that evaporation occurs near the cylindrical axis and a keyhole is created. In such a deep penetration welding, keyhole plays an important role. We compared this result with experimental one in Fig. 6, which shows simulation result of the temperature at 10msec and cross sectional view of welded structure obtained in the experiment. Together with density contour at 10 msec in Fig. 5, the simulation result seems to agree well with experimental result.

Interestingly, in the experimental result, large bubble is observed at the bottom of the welded structure which corresponds to the left end of melted zone in Fig. 6. The simulation also suggests that some instability takes place during evaporation process. This can be attributed to Kelvin-Helmholtz instability on the melted surface because vapor is flowing through a narrow channel of keyhole with high speed and thus inducing wave on the surface. Thus keyhole is sometimes disconnected as shown in the right figure of Fig. 5 and thus causing bubble trapping inside the melted zone.

In this simulation, the each ray has been traced and is reflected at the surface by number of times. During these reflections, laser beam is absorbed according to Hagen-Rubens formula with incident angle calculated by normal vector of density gradient and the direction of laser at each reflection point. As already stated, we must define the surface of some

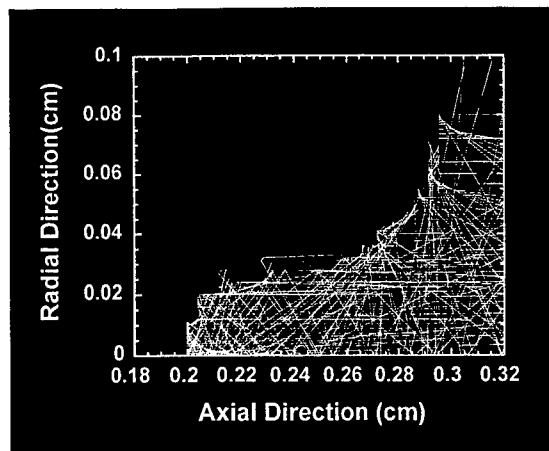


Figure 7. Typical ray traces calculated in the simulation.

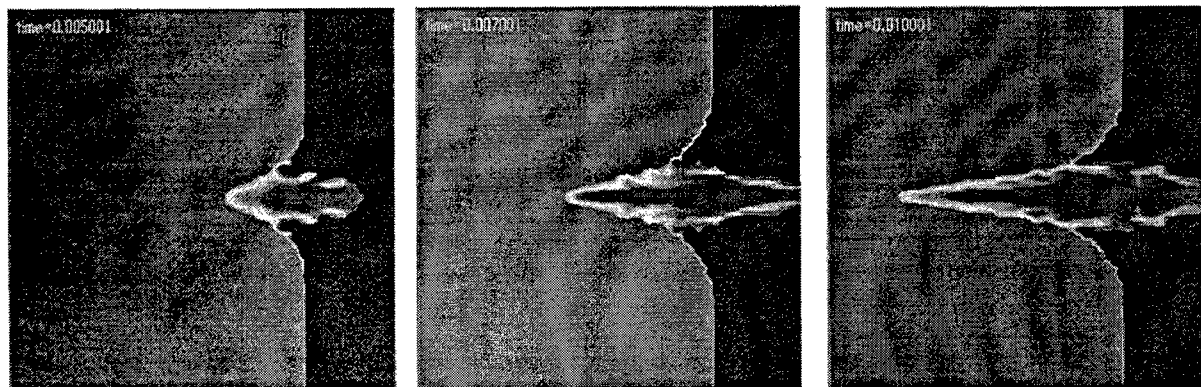


Figure 8. Two-dimensional axisymmetric simulation of laser welding without ray tracing. Density contour at 5,7,10 msec.

density below which no conduction electrons exist and no absorption occurs. From number of simulations, we have chosen 6.0 g/cm^3 as this critical density. The tip of white arrow in the center figure of Fig. 5 shows this density. Therefore, below this density laser beam is assumed to be transparent and moves as a straight line. Typical results of ray tracing are shown in Fig. 7. Therefore, laser light in circumference of beam is focused into the central axis of keyhole by channeling. The

simulation shows that this channeling is quite important to create keyhole. Figure 8 shows the result without ray tracing but laser light propagated straightforwardly from right to left with no reflection. In this case, the amount of laser light around the axis rapidly decreases when keyhole depth increases and thus vapor sufficient to create keyhole will not be generated.

3.3 Coronet Formation

Simulation of the coronet or "milk-crown" has long been a dream in computational physics. Several interface capturing schemes have been proposed to attack this problem. Although the present-day technique is already close to this goal, nobody reported the three-dimensional coronet formation before except for several two-dimensional works pioneered by Harlow, in which instability and therefore break-up of ring leading to coronet was not simulated. This is because the coronet is not merely a consequence of a free surface problem but we must solve surrounding gas as well. This requires a special treatment at the complex boundary of the coronet in which density ρ changes by 1000 times. In solving pressure p , it is quite a difficult task to guarantee the continuity of force $(\nabla p)/\rho$ across the complex interface having very large density ratio without special boundary condition there.

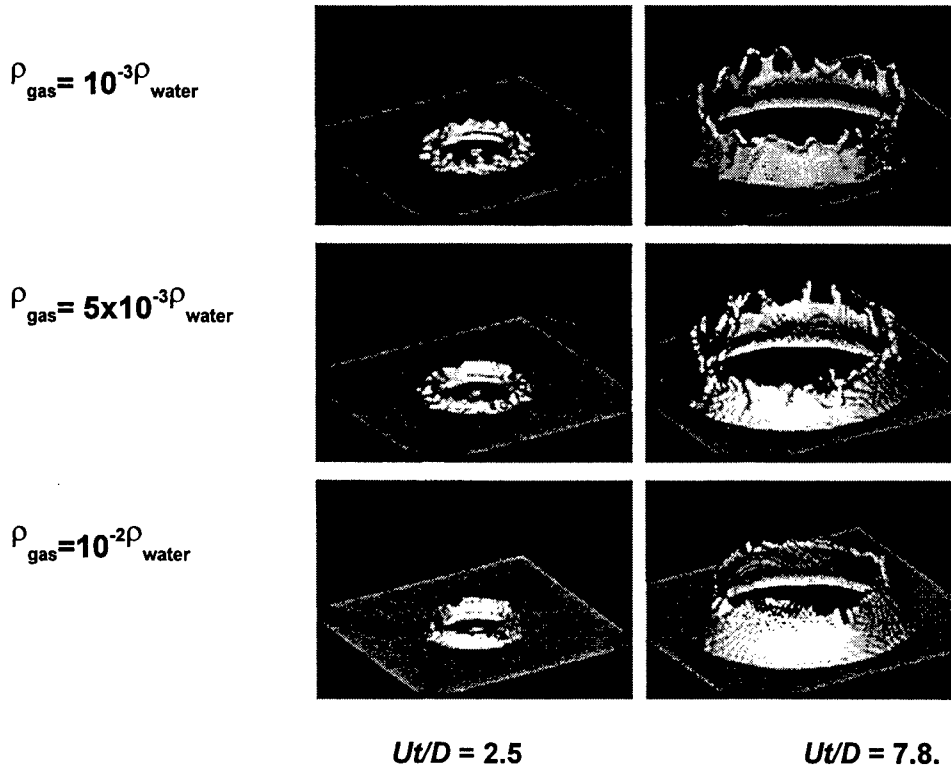


Fig.9. Water surface plot for various ambient gas at $Ut/D=2.5$ and 7.8 . $100 \times 100 \times 34$ Cartesian fixed grids are used.

Figure 9 shows an iso-surface contour of density in which 100×100 (horizontal) $\times 32$ (vertical) fixed equally spaced grids are used with $D/16$ grid spacing where D is the diameter of water drop. A thin water film of $D/4$ thick is placed on a solid plate and a water drop impacts from the top at a speed of U and $Re=UD/\nu=8000$. We solved air as well as water and the density ratio at the interface is almost 1000 as already mentioned. From the simulation, we can estimate the deceleration of the radial-expanding motion to be $a=1.472U^2/D$ after $t=1.375 D/U$ and from typical wavelength $0.42D$ ($kD=16$) of the irregularity along the rim during deceleration we get the growth rate of $\gamma_{RT} = (ak)^{1/2} = 4.85U/D$ for the R-T (Rayleigh-Taylor) instability. This growth rate seems to be sufficient to account for the evolution of the irregularity because of $\gamma_{RT} \Delta t = 3.93$ during the deceleration time $\Delta t = 0.812 D/U$. At $t=1.87 D/U$, the deceleration is largely reduced

and from this time on, because of the lack of the instability, laminar belt of the coronet begins to develop just below the ornament.

Since the computer capability is limited, we can check the validity of the theory only by changing some parameters, for example the gas density ρ_{gas} . Since the gas density is 1000 times less than water, it may not contribute to the evolution of the coronet. Surprisingly, it sensitively changed the evolution as shown in Fig.9. Interestingly, unstable wavelength became longer when gas density was increased. Although the gas density comes into the growth rate as the Atwood number $= [(\rho_{\text{water}} - \rho_{\text{gas}})/(\rho_{\text{water}} + \rho_{\text{gas}})]^{1/2}$, it is too small already to change the number even for denser gas of $\rho_{\text{gas}}/\rho_{\text{water}}=0.01$. If the instability was caused by the K-H (Kelvin-Helmholtz) instability, the growth rate is $\gamma_{\text{KH}} = k|U|(\rho_{\text{water}}\rho_{\text{gas}})^{1/2}/(\rho_{\text{water}} + \rho_{\text{gas}})$, where U is the relative velocity between gas and water, and can be affected by the ambient gas density by a factor of 3 for 10 times difference of density. However, the growth rate was larger for denser gas and contradicts with the simulation result. Therefore, we need to find a new instability mechanism explaining the dependence on the ambient gas.

This instability of expanding rim of this kind may occur also at the rim of crater generated by laser-illumination. If this instability leads to the debris formation, then ambient gas pressure may change the debris size as occurred in the coronet formation.

4. SUMMARY

We have proposed a new tool to attack the simultaneous solution of all the materials. The success of the code is due to a high ability of tracing sharp interface even with fixed grid and flexibility of extension to various materials and physics. The code has been applied to two typical subjects related to laser-matter interaction. One is laser-induced cutting of aluminum with a very short high power laser. The other is laser welding with a long-pulse low power laser. Both results show quite good agreement with experiments and give interpretation to cutting and keyhole creation processes.

REFERENCES

- (1) H.Takewaki, A.Nishiguchi and T.Yabe, 'The Cubic-Interpolated Pseudo-Particle (CIP) Method for Solving Hyperbolic-Type Equations' *J. Comput. Phys.* **61**, pp.261-, 1985.
- (2) T.Yabe *et al.*, "A Universal Solver for Hyperbolic Equations by Cubic-Polynomial Interpolation", *Comput.Phys.Commun.* **66**, pp.219-, 1991.
- (3) T.Yabe and P.Y.Wang,, "Unified Numerical Procedure for Compressible and Incompressible Fluid", *J.Phys.Soc.Japan* **60**, pp.2105-, 1991.
- (4) T.Yabe and F.Xiao, "Simulation Technique for Dynamical Evaporation Processes", *Nucl Eng. & Design* **155**, pp.45-, 1995.
- (5) F.Xiao *et al.*, "An Efficient Model for Driven Flow and Application to GCB", *Comput. Model. & Sim. Eng.* **1**, pp.235-, 1996.
- (6) T.Yabe *et al.*, "Anomalous Crater Formation in Pulsed-Laser-Illuminated Aluminum Slab and Debris Distribution", *Research Report NIFS (National Institute for Fusion Science) Series, NIFS-417*, May (1996).
- (7) S.Katayama *et al.*, "Pulse Shape Optimization for Defect Prevention in Pulsed Laser Welding of Stainless Steels", *ICALEO* (1993) p.487.

Optical detection of laser plasma interaction during laser ablation

M. H. Hong, Y. F. Lu

Laser Microprocessing Laboratory, Department of Electrical Engineering and
Data Storage Institute, National University of Singapore,
10 Kent Ridge Crescent, Singapore 119260

ABSTRACT

Laser plasma interaction during pulsed laser ablation is investigated by ultrafast phototube detection. There are two peaks in an optical signal with the first peak attributed to laser scattering and the second one to plasma generation. As laser fluence increases, the second peak rises earlier to overlap with the first one. The signal is fitted by different distribution functions for the laser scattering and the plasma generation. Peak amplitude and its arrival time, full width at half maximum (FWHM), starting time and termination time of the distributions are studied for different laser fluences and detection angles. Laser pulse is mainly scattered from the plasma during the laser ablation. Peak amplitude of the laser scattering increases but its FWHM decreases with laser fluence. Angular distribution of the peak amplitude can be fitted with $\cos^n \theta$ ($n=4$) while detection angle has no obvious influence on the FWHM. In addition, FWHM and peak amplitude of the plasma increase with laser fluence. However, its starting time and peak arrival time reduce with laser fluence. Time interval between plasma starting and scattered laser pulse termination is proposed as a quantitative parameter to characterize laser plasma interaction. Threshold fluence for the interaction can be estimated to be 3.5 J/cm^2 for KrF excimer laser ablation of silicon. For laser fluence above 12.6 J/cm^2 , the plasma and scattered laser pulse distributions tend to saturate.

Keywords: Laser ablation, laser light scattering, laser plasma interaction.

1. INTRODUCTION

Pulsed laser ablation of solid materials has been widely used in the applications of thin film deposition and materials microprocessing in the last decade.¹⁻³ For laser fluence higher than the ablation threshold of target, the laser beam evaporates and ionizes the target materials. It creates a plasma plume above the target surface. The plasma generated by the laser ablation at a high laser fluence results in a shielding effect to the later part of the laser pulse and in turn reduces the laser energy coupling with the target surface. Since the coupling between the incident laser beam and the substrate becomes strongly nonlinear with the onset of the plasma formation,⁴ it complicates the laser interaction with the materials. Therefore, to have a better understanding of the laser interaction with the plasma within the laser pulse is very important to control and optimize the laser processing. However, the plasma is very small at the end of the laser pulse with its size less than a few hundred microns. It is one of the major obstacles to perform plasma diagnostics by an aided probe beam detection.⁵ Recently, several research groups studied the plasma shielding effect by measurement of transmitted and reflected laser pulse profiles.⁵⁻⁸ H. Schmidt et. al. drilled a $5 \sim 15 \text{ }\mu\text{m}$ hole on a polymer (PMMA) substrate and measured laser pulse behind the sample during pulsed laser irradiation.⁶⁻⁷ They found that at a short time delay after the starting of the laser pulse, the transmitted laser light started to decrease significantly and its pulse duration was truncated at a high laser fluence. In another study, the reflected laser light from a brass disc during pulsed laser ablation was measured.⁸ It was found that the reflected laser pulse was shorter at a higher laser fluence due to plasma scattering of the incident laser beam. Though these studies had investigated plasma absorption of the incident laser energy, the transmitted and reflected measurement only qualitatively considered the laser pulse profiles and did not offer more information on laser plasma interaction. In this work, an ultrafast phototube is used to detect scattered laser signal and plasma signal at the same time. Angular distributions of the signal profiles at different laser fluences are also studied. Time interval between plasma starting and laser pulse termination is defined as laser plasma interaction time and used as a quantitative parameter to characterize their interaction.

M.H. Hong: E-mail: dsihmh@dsi.nus.edu.sg; Telephone: 65-8748409; Fax: 65-7776619

Y. F. Lu: E-mail: eleluyf@nus.edu.sg; Telephone: 65-8742118; Fax: 65-7791103

2. EXPERIMENT

Figure 1 shows the experimental setup for the detection of the scattered laser light and the plasma induced by the laser ablation. A KrF excimer laser (Lambda Physik LPX 100) was used as a light source. The laser beam has a wavelength of 248 nm and a pulse duration around 23 ns. The laser beam was re-directed by a mirror and focussed by a quartz lens which has a diameter of 50 mm and a focal length of 150 mm. Laser fluence was changed in a range from 0.2 to 16.7 J/cm² by varying laser pulse energy. A p-type (100) Si substrate was used as the sample which was placed in air with its surface perpendicular to the incident laser beam. An ultrafast phototube (Hamamatsu R1328U-53) with the photocathode diameter of 1 cm was used to detect the scattered laser light and the plasma at the same time. Its spectral response is from 185 to 650 nm. The phototube rise time and fall time are 60 and 55 ps, respectively. The optical signal recorded was sent to a digital oscilloscope (Tektronix TDS 520) which has a time resolution of 2 ns. The synchronous output of the laser controller was also sent to the oscilloscope as a trigger signal for the signal detection. The digitized signal was then sent to a PC for data storage and further processing. A narrowband interference filter which only allows 248 nm laser light passing through was inserted in front of the phototube to distinguish the scattered laser light from the plasma. The position of the phototube was kept at 6 cm away from the laser spot on the sample. The angular distributions were measured at detection angles for the phototube center with respect to the substrate normal as 15°, 30°, 45°, 60°, 75° and 90° respectively. For the detection angle of 90°, the phototube center was in the same level of the substrate surface and the optical signals were sensed from the upper half of the phototube. Laser plasma interaction during Nd:YAG laser (wavelength: 532 nm, pulse duration FWHM: 7 ns) ablation of silicon and copper is also detected by slightly modifying the experimental setup.

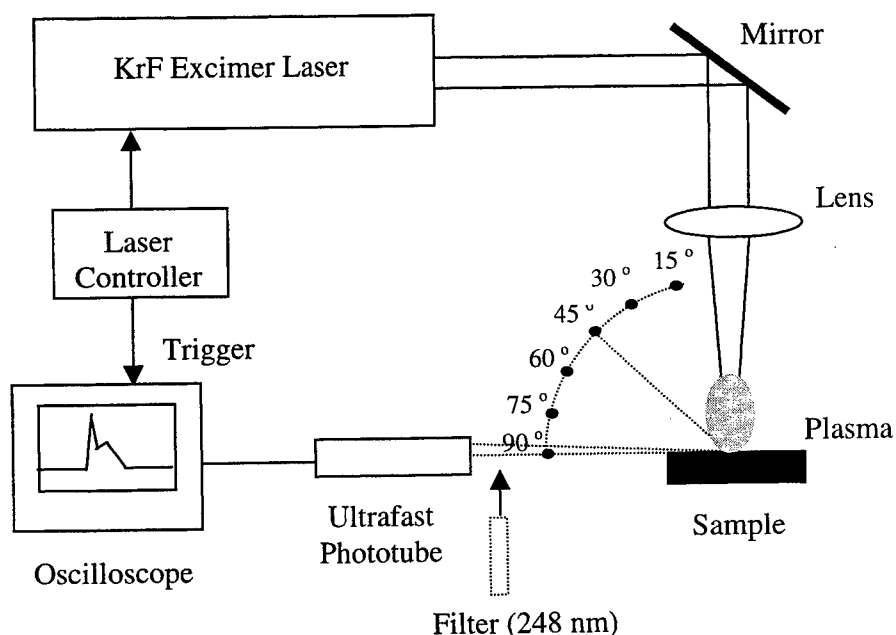


Figure 1 Experimental setup for the detection of the scattered laser light and the plasma induced by the laser ablation.

3. RESULTS AND DISCUSSION

Figure 2 shows the optical signals detected by the ultrafast phototube during the KrF excimer laser ablation of silicon at a detection angle of 90° and laser fluences of 3.3, 5.8 and 9.8 J/cm² respectively. Since these fluences are much higher than silicon ablation threshold of 1.1 J/cm², there is plasma generation due to the laser ablation.⁹ It can be found that all the signals detected have two peaks which have different distributions. It can also be observed that these profiles are different

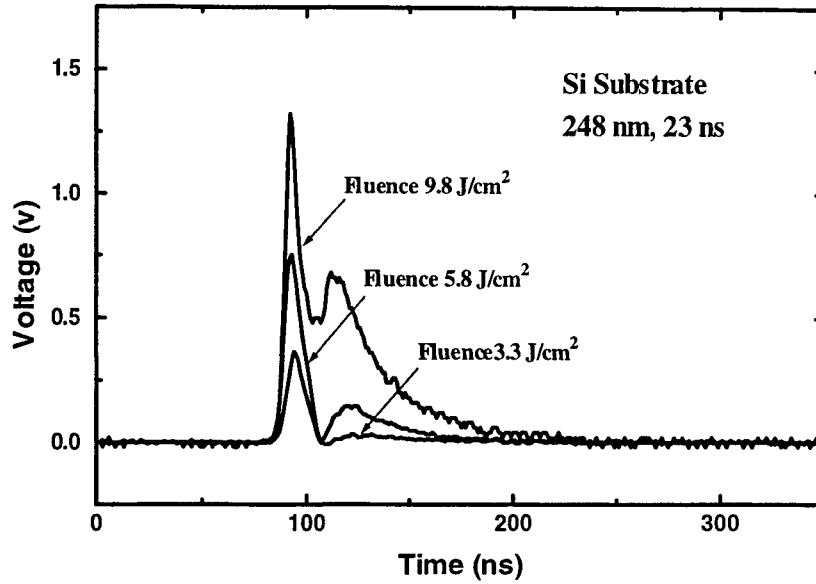


Figure 2 Optical signals detected by the ultrafast phototube during the excimer laser ablation of silicon at a detection angle of 90° and laser fluences of 3.3, 5.8 and 9.8 J/cm^2 .

for various laser fluences. The peak amplitudes increase with the laser fluence. Meanwhile, the second peak moves to the left and overlaps with the first one at a laser fluence higher than 5.8 J/cm^2 . In order to distinguish the nature of these two peaks, the 248 nm filter was inserted in front of the phototube. The second peak disappeared for the optical signal passing through the filter, as shown in Fig. 3 (a). It is clear that the first peak is attributed to the laser light which arrives at the phototube during the laser ablation. Since the phototube is not placed inside the reflection path of the laser beam, the optical signal obtained is the laser light scattered from the substrate and the plasma generated during the laser pulse. Therefore, it can be concluded that the first and second peaks in the detected optical signals are related to laser scattering and plasma generation respectively.

To analyze the peak distributions, the optical signals were deconvoluted into two different profiles. Since the laser light is in a form of pulse, it is fitted by the following equation:

$$f_1(t) = A \times [1 - \exp(-\frac{t-t_0}{\tau_1})]^p \times \exp(-\frac{t-t_0}{\tau_2}) \quad (1)$$

where A , p , t_0 , τ_1 and τ_2 are fitting parameters. Figure 3 (a) shows the curve fitting of the scattered laser light which was detected with the filter in front of the phototube at a detection angle of 90° and a laser fluence of 9.8 J/cm^2 . It is clear that equation (1) can be used to fit the experimental measurement very well. In addition, laser ablation of solid materials produces a plasma which has a strongly forward-peaked distribution along the direction normal to the substrate surface. Due to collisions among ablated species in the early stage of materials evaporation, laser ablation behaves like a nozzle source. Besides the plasma plume expansion, there is a large center-of-mass motion. Time-of-flight (TOF) spectrum of the plasma is often described as a shifted Maxwell-Boltzmann distribution:^{10, 11}

$$f_2(t) = \frac{B}{t^4} \times \exp\left[-\frac{(m/2kT_0)(L_f - v_d t)^2}{t^2}\right] \quad ,$$

or

$$f_2(t) = C \times t^{-4} \times \exp[-b_1 \times t^{-2} + b_2 \times t^{-1}] \quad (2)$$

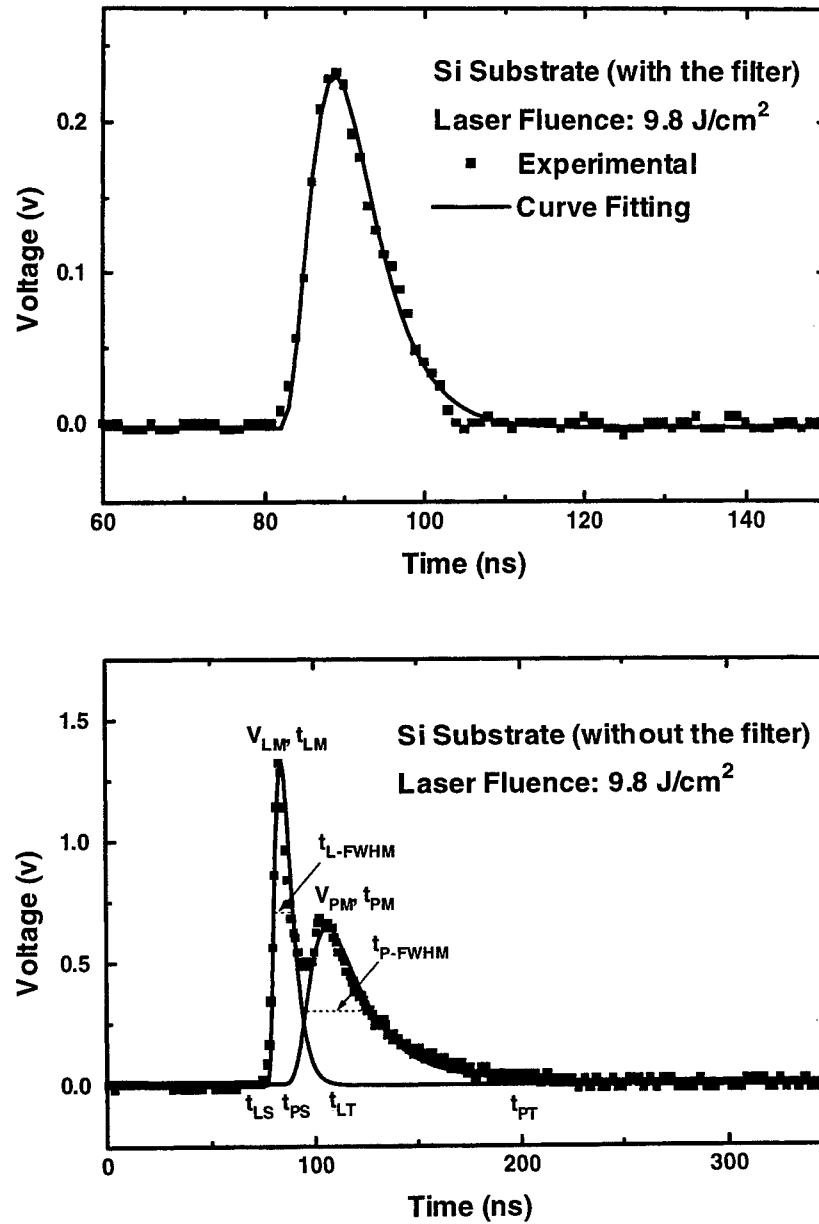


Figure 3 Curve fitting for the optical signals detected (a) with and (b) without the filter in front of the phototube at a detection angle of 90 ° and a laser fluence of 9.8 J/cm².

where $b_1 = mL_f^2/2kT_o$ and $b_2 = mv_dL_f/kT_o$. B and C are fitting parameters, m is the mass of the ablated species, k is the Boltzmann constant and T_o represents the characteristic temperature of the distribution. L_f stands for the plasma flight distance from the substrate surface and v_d is the center-of-mass velocity. The above equations were used to fit the optical signal in Fig. 2 for the laser fluence of 9.8 J/cm². The curve fitting result is shown in Fig. 3 (b). Peak amplitude V_{iM} , peak arrival time t_{iM} , FWHM t_{i-FWHM} , starting time t_{iS} and termination time t_{iT} of the profiles are applied to characterize the scattered laser light and the plasma distributions. The sign i denotes L or P for the scattered laser light and the plasma respectively.

When the laser light irradiates on a solid surface, it is scattered in all directions. The distribution of the scattered laser light is a function of the incident angle θ_i , scattering angle θ_s , laser wavelength λ and incident laser energy P_i . It also depends on the substrate surface characteristics. According to Rayleigh-Rice vector perturbation theory, the scattered laser light energy can be expressed as:¹²

$$dP_s = \frac{16\pi^2}{\lambda^4} \times P_i \times \cos \theta_i \times \cos^2 \theta_s \times Q \times S(f_x, f_y) \times d\Omega_s, \quad (3)$$

where Q is a reflectivity factor which depends on the substrate materials. $S(f_x, f_y)$ is the two-dimensional energy spectral density function in terms of the sample surface spatial frequencies f_x and f_y . $d\Omega_s$ is the differential solid angle to the laser irradiated spot. In this study, equation (3) can be simplified as:

$$P_s = D \times P_i \times \cos^2 \theta_s, \quad (4)$$

where D is a constant to P_i and θ_s if the surface morphology does not change during the laser irradiation. It is clear that the laser light energy scattered from the substrate surface is proportional to the incident laser energy and the cosine square of the scattering angle.

During laser ablation, the substrate endures the surface melting, materials evaporation and plasma generation within the laser pulse. Besides the solid surface, the melted substrate surface and the plasma generated also contribute to the scattering of the incident laser light. Figure 4 shows the laser pulse peak amplitude for the total and substrate scattering versus the laser fluence during the excimer laser ablation of silicon at a detection angle of 90° . The peak amplitude of the total scattering increases with the laser fluence and tends to saturate at a laser fluence of 12.6 J/cm^2 . For a laser fluence of 0.2 J/cm^2 , there is no plasma generation and surface morphology change under the laser irradiation. The total laser scattering is only attributed to the solid substrate. Based on equation (4) and assuming there were no incident laser energy loss due to plasma absorption and surface morphology change, its peak amplitude is used to calculate the substrate scattering for the laser fluence up to 16.7 J/cm^2 . Compared with the experimental result of the total scattering, it can be found that the substrate scattering plays a minor role in the laser scattering at a high laser fluence. As to the melted surface, it has been reported that the surface reflectivity increases about 10 % during the laser melting of the Si substrate.¹³ Therefore, it can be concluded that the plasma generated during the laser ablation is a dominant factor for the laser scattering. Since there are

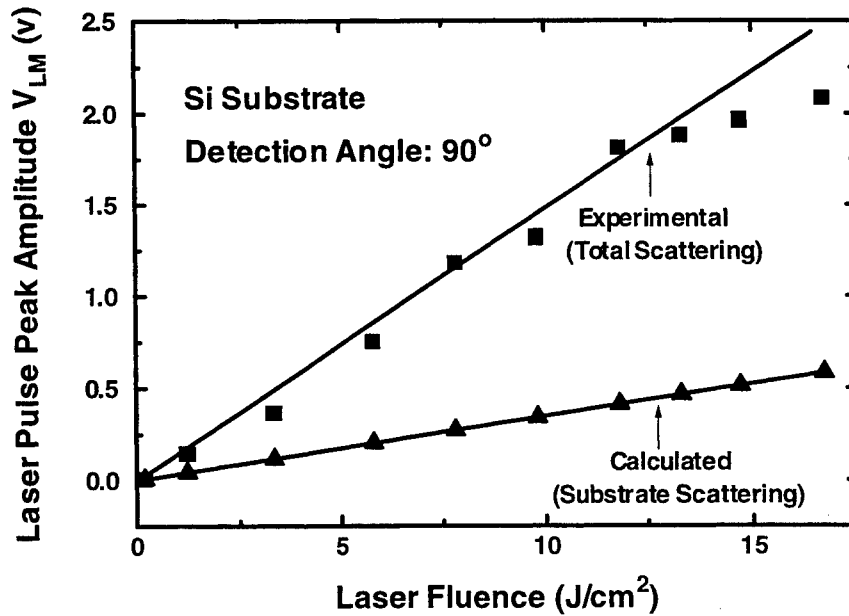


Figure 4 Laser pulse peak amplitude of the total and substrate scattering versus laser fluence during the excimer laser ablation of silicon at a detection angle of 90° .

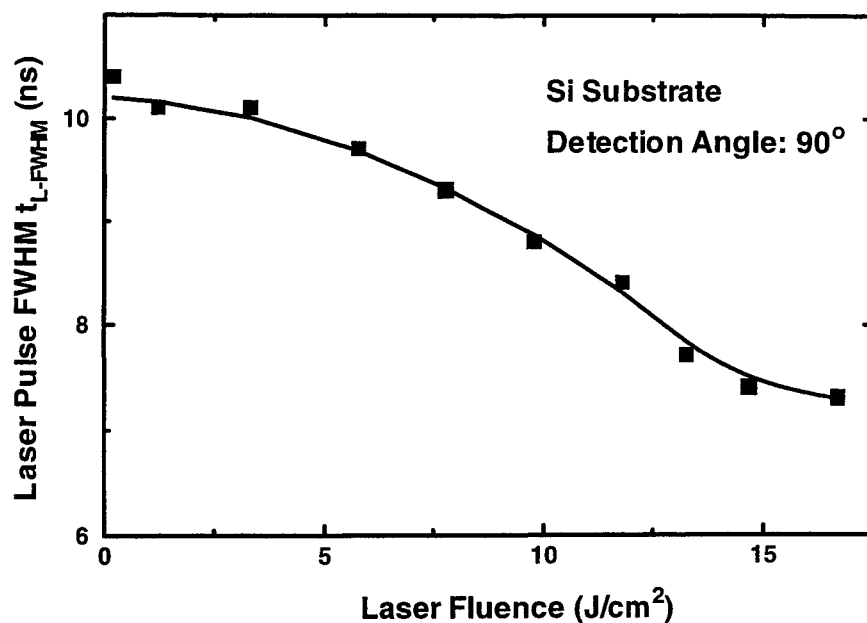


Figure 5 FWHM of the scattered laser pulse versus the laser fluence during the excimer laser ablation of silicon at a detection angle of 90°.

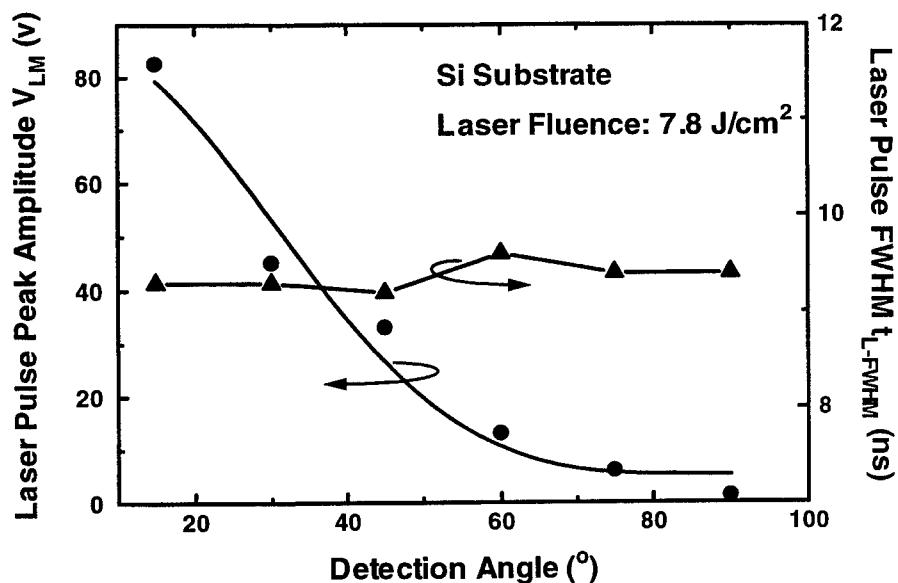


Figure 6 Angular distributions of the scattered laser pulse peak amplitude and FWHM during the excimer laser ablation of silicon at a laser fluence of 7.8 J/cm².

many ablated species in the plasma, the incident laser light is scattered to different directions by the species in the laser pulse duration. It leads to more scattered laser light arriving at the phototube. As the laser fluence increases further, the plasma density increases greatly which will reflect back more laser light and cause the saturation of the scattered laser light.

Figure 5 shows the FWHM of the scattered laser light versus the laser fluence during the excimer laser ablation of silicon at a detection angle of 90°. When the laser fluence is higher than 5.8 J/cm², the laser pulse duration is shorter. It is

different from the laser pulse scattered from the substrate surface which has the same pulse duration as the incident laser light. The truncation of the scattered laser pulse implies that the plasma generation shields the later part of the incident laser pulse passing through the plasma onto the substrate surface. It causes the weaker laser coupling with the substrate. As shown in Fig. 6, angular distribution of the peak amplitude of the scattered laser light is measured during the excimer laser ablation of silicon at a laser fluence of 7.8 J/cm^2 and detection angles of 15° , 30° , 45° , 60° , 75° and 90° respectively. It is clear that the peak amplitude has a narrow angular distribution which can be well fitted by a function of $\cos^n \theta$ with the best n value as 4. This is because the plasma is flying forward at a speed up to 10^4 m/s from the explosive ablation.¹⁴ It is different from the angular distribution of the laser light scattered from the substrate surface as $\cos^2 \theta$ expressed in equation (4). The angular distribution of the scattered laser light also confirms that the plasma scattering plays the dominant role for the laser light scattering in the laser pulse duration. It can also be found from Fig. 6 that the FWHM of the scattered laser pulse does not have obvious change at different detection angles.

Figure 7 shows the plasma peak amplitude versus the laser fluence during the excimer laser ablation of silicon at a detection angle of 90° . The plasma peak amplitude increases greatly with the laser fluence. It tends to saturate at a laser fluence of 12.6 J/cm^2 . It is because the higher laser fluence generates a denser plasma which enhances the shielding effects. The weaker laser interaction with the substrate in turn limits the plasma generation and saturates the peak amplitude. The dependence of the peak amplitude on the laser fluence is similar to that of the laser ablation rate.⁹ This is because the plasma intensity is proportional to the concentrations of ablated materials during the laser ablation. The plasma intensity normalized to the laser beam area can be used to represent the laser ablation rate.⁸ Figure 7 also shows the plasma peak arrival time versus the laser fluence. It can be observed that the arrival time reduces with the higher laser fluence and also tends to saturate at the laser fluence of 12.6 J/cm^2 due to the strong plasma shielding effect. By setting the differential of equation (2) as zero, the peak arrival time can be calculated as:

$$t_m = \frac{-b_2 + \sqrt{b_2^2 + 32b_1}}{8}$$

Since L_f is in millimeter order and v_d about 10^4 m/s , b_2 is much larger than b_1 . The above equation can be simplified as:

$$t_m = L_f / v_d \quad (5)$$

The shorter peak arrival time is attributed to the higher plasma velocity at a higher laser fluence. The maximum center-of-mass velocity of the plasma distribution can be easily obtained from the saturation of the peak arrival time.

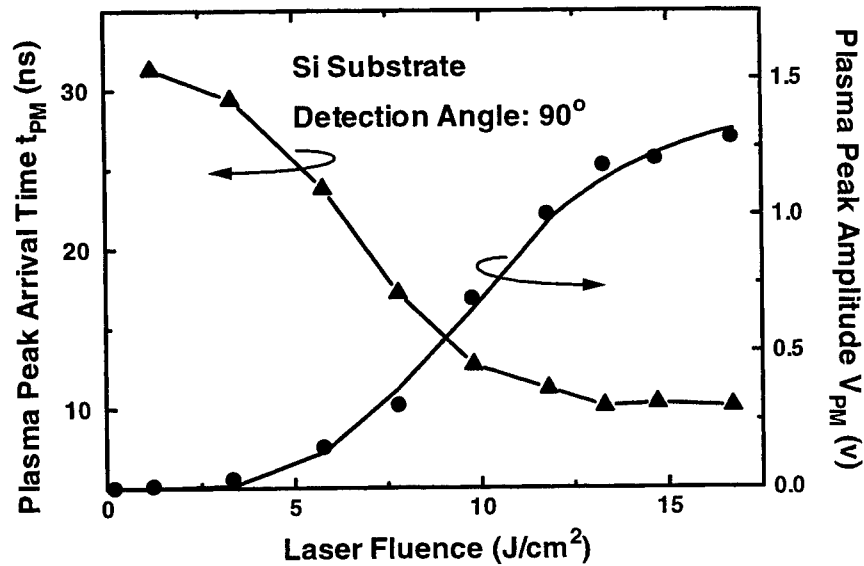


Figure 7 Plasma peak amplitude and its arrival time versus the laser fluence during the excimer laser ablation of silicon at a detection angle of 90° .

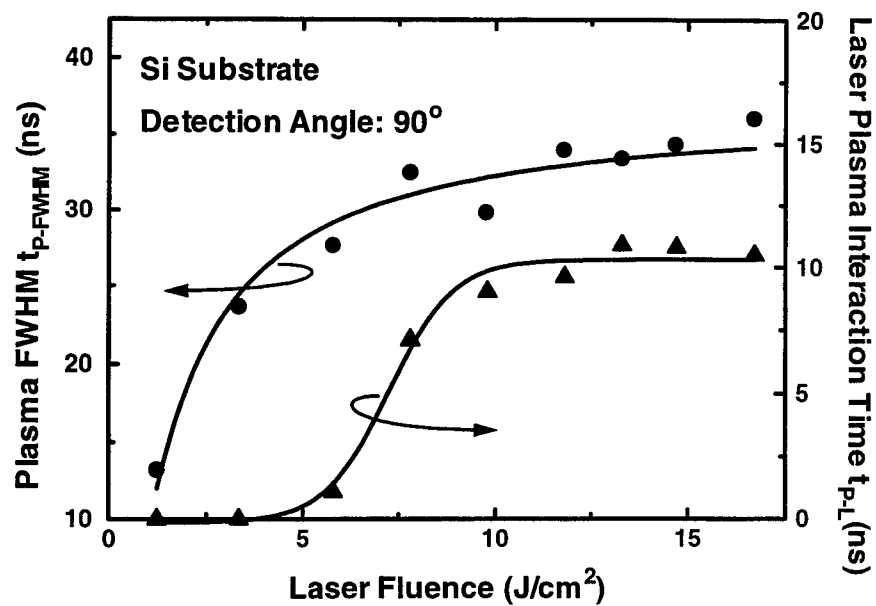


Figure 8 Plasma FWHM and laser plasma interaction time versus the laser fluence during the excimer laser ablation of silicon at a detection angle of 90°.

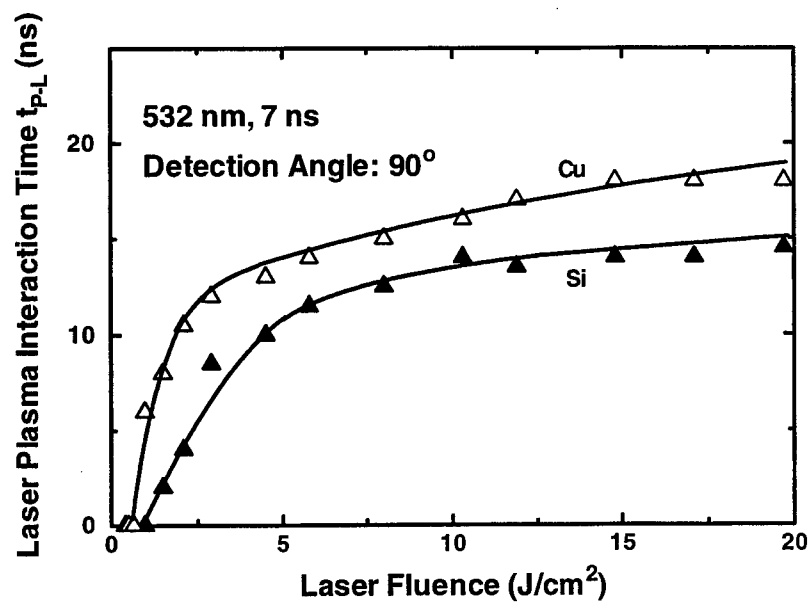


Figure 9 Laser plasma interaction time versus the laser fluence at a detection angle of 90° during Nd:YAG laser ablation of silicon and copper substrates.

Figure 8 shows the FWHM of the plasma profile distribution versus the laser fluence at a detection angle of 90° . It increases greatly with the laser fluence and tends to saturate at the laser fluence of 12.6 J/cm^2 . The higher laser fluence for the laser ablation generates the higher density plasma. It enhances the collisions among the ablated species and absorbs the more incident laser light which increases the FWHM of the plasma. Because of the strong plasma shielding effect at a laser fluence above 12.6 J/cm^2 , the FWHM increase is also saturated. The plasma interaction with the incident laser light is often characterized by the qualitative analyses of the transmitted and reflected laser pulse profiles. To obtain a quantitative parameter for their interaction, time interval between the plasma starting and the laser pulse termination is proposed as an interaction time between the laser and the plasma. If the interaction time t_{p-L} is larger than zero, it means that the plasma has been generated before the laser pulse terminates. In the optical signal, the plasma profile overlaps with that of the scattered laser light. The laser interaction with the plasma occurs. It can be observed from Fig. 8 that the plasma has generated at a laser fluence of 1.3 J/cm^2 while the interaction time is zero. It implies that the plasma is generated after the laser pulse terminates and does not have any chance to absorb the incident laser light. For the laser fluence higher than 5.8 J/cm^2 , the interaction time is above zero. It means that the laser interaction with the plasma exists in a duration of 1.5 ns. By the numerical fitting of the experimental result, the threshold fluence of the laser plasma interaction by setting the interaction time as zero can be estimated as 3.5 J/cm^2 . It can also be observed from Fig. 8 that the interaction time increases with the laser fluence up to 12.6 J/cm^2 . Though the plasma generated has a shielding effect to the incident laser light, the plasma density is not high enough to completely block the laser irradiation on the substrate surface. However, as the laser fluence increases higher than 12.6 J/cm^2 , the interaction time tends to saturate due to the high plasma density. Figure 9 shows the laser plasma interaction time versus the laser fluence at a detection angle of 90° during Nd:YAG laser (wavelength: 532 nm, pulse duration FWHM: 7 ns) ablation of silicon and copper substrates. It can be found that the interaction time increases with the laser fluence and tends to saturate at laser fluences above 4.8 J/cm^2 for copper and 8.2 J/cm^2 for silicon. Threshold laser fluences for the laser plasma interaction can also be estimated from Fig. 9 as 0.6 J/cm^2 for copper and 1.0 J/cm^2 for silicon, respectively. It implies that copper is more easily ablated by the laser than silicon. It can also be found that the threshold fluence for Nd:YAG laser ablation of silicon is lower than that for KrF excimer laser ablation. It is due to the shorter laser pulse duration for the Nd:YAG laser than that of the excimer laser.

4. CONCLUSIONS

Laser plasma interaction during pulsed laser ablation is studied by optical measurement of the scattered laser signal and the plasma signal at the same time. The optical signals are deconvoluted into a pulse distribution for the scattered laser light and a drifted Maxwell-Boltzmann distribution with a center-of-mass velocity for the plasma. It is found that the plasma scattering plays a dominant role in the laser scattering during the laser ablation. Its peak amplitude is angularly distributed as a function of $\cos^4 \theta$ and increases with the laser fluence, while its FWHM reduces with the laser fluence and does not show obvious dependence on the detection angle. In addition, the plasma FWHM and the peak amplitude increase with the laser fluence due to higher plasma density at a higher laser fluence, while the plasma starting time and its peak arrival time reduce with the laser fluence. For the laser fluence higher than 5.8 J/cm^2 during KrF excimer laser ablation of silicon, the plasma profile overlaps with that of the scattered laser pulse. The laser plasma interaction time is characterized quantitatively. The threshold laser fluence to have the interaction is estimated to be 3.5 J/cm^2 . For laser fluence below the threshold fluence, there is no laser plasma interaction. With the laser fluence in a range from 3.5 to 12.6 J/cm^2 , the interaction exists and the interaction time increases greatly with the laser fluence. For the laser fluence higher than 12.6 J/cm^2 , the dense plasma saturates the laser plasma interaction time. Due to a shorter pulse duration, Nd:YAG laser interaction with the plasma generated starts and saturates at much lower laser fluences than the excimer laser. The threshold fluences of the laser plasma interaction are 0.6 J/cm^2 for Cu and 1.0 J/cm^2 for Si. Their interaction tends to saturate for laser fluences above 4.8 J/cm^2 for Cu and 8.2 J/cm^2 for Si.

REFERENCES

1. R.K. Singh and J. Narayan, "Pulsed-laser evaporation technique for deposition of thin films: Physics and theoretical model", *Phys. Rev. B*, **41**, pp. 8843-8859, 1990.
2. Y.F. Lu, Y. Aoyagi, M. Takai and S. Namba, "Laser surface cleaning in air: Mechanisms and Applications", *Jpn. J. Appl. Phys.* **33**, pp. 7138-7143, 1994.
3. M.C. Gower, "Excimer lasers: current and future applications in industry and medicine", *Laser Processing in Manufacturing*, Chapman and Hall, London, 1993, pp. 189.

4. D. Bäuerle, *Laser Processing and Chemistry*, Springer-Verlag, New York, 1996, pp. 181.
5. K.H. Song and X. Xu, "Mechanisms of absorption in pulsed excimer laser-induced plasma", *Appl. Phys. A.* **65**, pp. 477-485, 1997.
6. J. Ihlemann, A. Scholl, H. Schmidt and B. Wolff-Rottke, "Nanosecond and femtosecond excimer-laser ablation of oxide ceramics", *Appl. Phys. A.* **60**, pp. 411-417, 1995.
7. H. Schmidt, J. Ihlemann, B. Wolff-Rottke, K. Luther and J. Troe, "Ultraviolet laser ablation of polymers: spot size, pulse duration, and plume attenuation effects explained", *J. Appl. Phys.* **83**, pp. 5458-5468, 1998.
8. X. Mao and R. E. Russo, "Observation of plasma shielding by measuring transmitted and reflected laser pulse temporal profiles", *Appl. Phys. A.* **64**, pp. 1-6, 1997.
9. M.H. Hong, Y.F. Lu, W.D. Song, D.M. Liu and T.S. Low, "Audible acoustic wave real-time monitoring in laser processing of microelectronic materials", *SPIE* **3184**, pp. 148-157, 1997.
10. Q.Z. Qin, Z.H. Han and H.J. Dang, "An angle-resolved time-of-flight mass spectrometric study of pulsed laser ablated Ta_2O_5 ", *J. Appl. Phys.* **83**, pp. 6082-6088, 1998.
11. A. Cavalleri, K. Sokolowski-Tinten, J. Bialkowski and D.von der Linde, "Femtosecond laser ablation of gallium arsenide investigated with time-of-flight mass spectroscopy", *Appl. Phys. Lett.* **72**, pp. 2385-2387, 1998 .
12. J.C. Stover, *Optical Scattering Measurement and Analysis*, McGraw-Hill, New York, 1990, pp. 60.
13. G.E. Jellison, Jr., D.H. Lowndes, D.N. Mashburn and R.F. Wood, "Time-resolved reflectivity measurements on silicon and germanium using a pulsed excimer laser heating beam", *Phy. Rev. B.* **34**, pp.2407-2415, 1986.
14. M.H. Hong, Y.F. Lu, T.M. Ho, L.W. Lu and T.S. Low, "Fast ICCD imaging of KrF excimer laser induced titanium plasma plumes for silicon metallization", *Appl. Surf. Sci.*, to be published.

Emission spectra and particle ejection during visible-laser ablation of graphite for diamond-like coatings^{*}

Jim J. Chang, William McLean, Ernest P. Dragon and Bruce E. Warner
Lawrence Livermore National Laboratory, P.O. Box 808, M/S L-463, Livermore, CA 94550

ABSTRACT

We have investigated the emission spectra of a carbon plume generated from graphite by a visible pulsed laser for diamond-like coatings (DLC). The laser utilized was a 300-watt class copper vapor laser with a pulse duration of ~40 ns. To better understand the laser-target interaction, we have visualized plume dynamics near the graphite surface via Schelieren method. We found that the laser ablation process was accompanied with explosive material ejection during pulsed laser deposition (PLD). The ejection of material started at about 500 ns after the onset of laser pulse and lasted for about 10 μ s. The material ejection is very directional and introduced large amount of micro particulates in the DLC film. We have found that the use of a random phase plate to smooth the laser intensity profile effectively eliminated this ejection of material with additional advantage of higher coating rate. The spectra in the visible and UV of the plume emission were analyzed to correlate with DLC quality and coating rate. We have characterized the carbon plasma based on emissions from C, C₂, C⁺ and C⁺⁺ for laser peak intensities between 0.1 - 5 GW/cm². We have produced high-quality DLC with its coating rate optimized at laser peak power densities between 0.5 GW/cm² and 0.8 GW/cm². The kinetic energy of C⁺ was estimated to be ~20 eV at this optimized coating condition. We found that greater C⁺ kinetic energy at higher laser intensity does not necessarily produce better DLC. This process optimization enabled us to demonstrate a coating rate as high as 2000 μ m-cm²/hr. The C₂ swan-band emission from the plume was most pronounced in the optimized coating condition and was used as a process diagnostic tool.

Keyword: Pulsed laser deposition, laser ablation, diamond-like coatings, laser plasma.

1. INTRODUCTION

Thin film formation by pulsed laser deposition (PLD) has been routinely demonstrated at the laboratory scale for many elements and compounds. One of the distinct advantages of the PLD process is the near stoichiometric transfer from the ablation target to the desired substrate, a feature that is often difficult to achieve with conventional coating technologies such as magnetron sputtering or electron beam evaporation. However, PLD has only recently gained prominence in the deposition of diamond-like coatings (DLC) and high T_c superconductors¹⁻⁴. DLC deposited by the vapor phase of carbon are amorphous and have many good properties⁵. They are hard coatings with low friction, transparent in the IR, electrically insulating, and chemically inert. Since the DLC are prepared without hydrogen using PLD, they have a higher density and index of refraction than the hydrogenated DLC obtained by plasma deposition processes.

In order for processes based on PLD to progress from bench top experiments to commercialization, a number of key issues must be resolved. The principle limitations of current PLD technology are low deposition rate (i.e., typically 10 μ m-cm²/hr)^{6,7}, inclusion of micro particles in the film, and the difficulty in producing uniform coatings over large areas. In order to make the PLD for DLC more economically viable, we have investigated the laser-target interaction and the characteristics of the ablated carbon plume for process optimization. As a result, we have greatly improved the quality of our DLC with very low level of micro particle inclusions. A significant increase in coating rate has also been achieved in our laboratory, over 2000 μ m-cm²/hr. In this paper, we report the dynamics of laser ablation of graphite using a high-power pulsed visible laser. The measurements of laser-target interaction and plume emission spectra are also compared with the coating results.

^{*} This work was performed under the auspices of U.S. Department of Energy by Lawrence Livermore National Laboratory under contract No. W-7405-Eng-48

2. EXPERIMENTAL APPARATUS

In this investigation, we used a 300-W class copper vapor laser in a master-oscillator-power-amplifier configuration⁸. The laser repetition frequency can be varied from below 1 Hz to greater than 5 kHz by adjusting the timing between the oscillator and the amplifier. Both of the copper laser green (511-nm) and yellow (578-nm) outputs were used for this work. The ratio of green/yellow in the output was typically 2:1. The pulse duration of the laser output was ~40 ns FWHM with a base-to-base pulse width of ~60 ns. The laser beam was focused to the graphite target by an achromatic lens located adjacent to a vacuum deposition chamber. The laser beam was aligned to the 1-inch-diameter graphite rod such that the ablated carbon plume is at 45 degrees from the incident beam, as illustrated in Fig. 1. The carbon plume generated by the laser moved toward directly to the sample port. The substrate to be coated was mounted within the sample port with a distance to the graphite surface of 7.6 cm. The laser peak intensity on the target could be varied from 0.1 GW/cm² to 5 GW/cm² by adjusting the laser power but maintaining a constant spot size. The vacuum chamber was typically kept a base pressure of 5×10^{-8} Torr. The pressure rose to $\sim 10^{-6}$ Torr during PLD process.

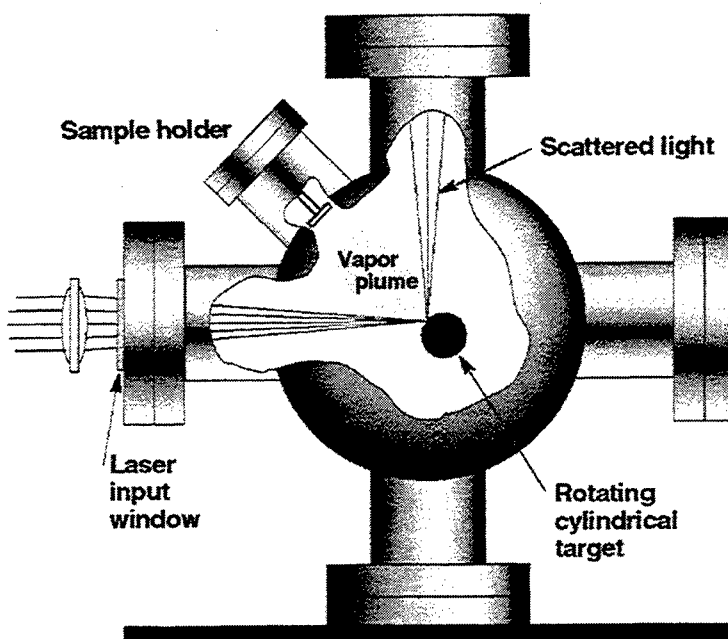


Fig. 1 The schematic of a PLD chambers; a high-purity graphite rod with 1" diameter is used as the target for producing DLC.

We used a 0.275-meter spectrometer with an optical multichannel analyzer (OMA) to measure the plume emissions. The OMA had a gated intensifier with 10-ns resolution to resolve the temporal development of the plume spectra. The schematic drawing of the setup is shown in Fig. 2a. The graphite rod rotated at approximately 1 RPS inside the deposition chamber. It could also be moved axially to keep a relatively fresh surface for laser ablation. The emission of the carbon plume was magnified and imaged to the entrance slit of the OMA. The plasma spectra were resolved spatially along the plume axis by moving the plume image relative to the entrance slit of the spectrometer. The width of the entrance slit was typically set at 10 μm for most of our measurements. The spectrometer was equipped with 300, 600 and 1200 l/mm gratings all blazed at 500-nm.

We used Schelieren technique to visualize the dynamics of carbon plume and material ejection during laser ablation. The schematic of the setup is illustrated in Fig. 2b. A frequency-doubled Q-switched Nd:YAG laser with an output of 10-ns green pulse (532nm) was collimated and used as a probe laser to illuminate the plume. The

YAG laser beam was spatially filtered to obtain a smooth and uniform beam profile. By adjusting the delay between the copper laser and the probe laser, we were able to visualize the dynamic of the laser-target interaction with 10-ns resolution. The knife-edge placed near the focus of the image lens was used to produce a Schelieren image. A 532-nm line filter was used to prevent both the plasma emission and the scattered copper laser light from entering the CCD camera.

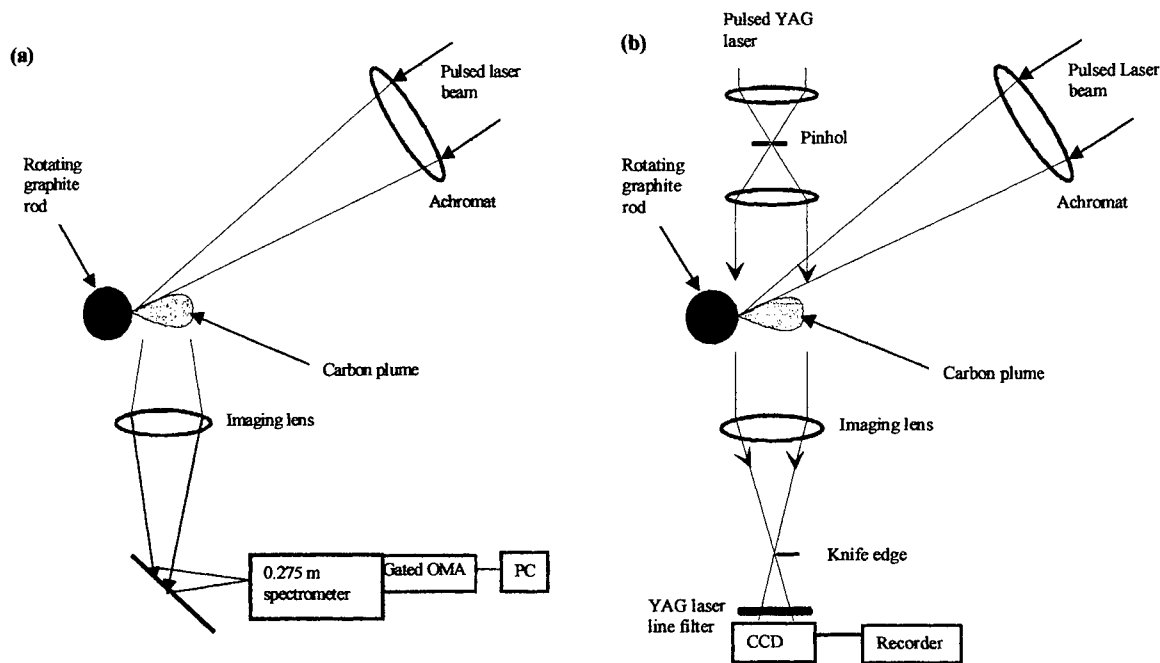


Fig. 2 (a) The setup for measuring emission spectra of the carbon plume. The graphite rod is placed in a vacuum deposition chamber. The plume is magnified and imaged into the entrance slit of the spectrometer. (b) The Schelieren setup for visualizing laser-target interaction using a 10-ns pulsed YAG laser.

2. CARBON PLUME AND EJECTION OF MICRO PARTICULATES

Figure 3 illustrates a sequence of Schelieren images near the target during laser ablation with various delays. These images were produced with a laser peak intensity of $\sim 2 \text{ GW/cm}^2$ on the target. Note that a laser intensity of 1 GW/cm^2 is equivalent to 40 J/cm^2 in this work. The carbon-plume produced by the 40-ns laser pulse was only visible during the initial 200 ns by the Schelieren technique. However, noticeable material ejection from the target was found to start at $\sim 500 \text{ ns}$ after the onset of laser pulse. This explosive material ejection lasted for $\sim 10 \mu\text{s}$ as illustrated in Fig. 3(c) & 3(d). Based on a sequence of Schelieren images, we estimate that the average speed of the ejected particles is approximately 400 m/sec . The temperature of the ejected material is estimated to be $2500 \text{ K} - 3000 \text{ K}$ based on their blackbody-radiation profile measured between 400 nm and 800 nm . It's worth noting that this explosive ejection of material was very directional as shown in Fig. 3(c) & 3(d). It is quite different from a melt splashing during laser machining of metals, which typically has a wide ejection angle⁹. The highly directional material ejection led to large amount of undesirable macro particulates in the DLC film. Singh has suggested that subsurface superheating induced micro explosion is the main cause of material ejection during laser ablation of superconducting material ($\text{YBa}_2\text{Cu}_3\text{O}_7$). The laser induced subsurface superheating, however, is not likely to occur on graphite because of its high absorption coefficient and high thermal conductivity¹¹. Although the physical mechanism responsible for this material ejection is still not well understood, we found that it's a direct result of a non-uniform laser intensity profile (i.e., existence of a few hot spots) on the target.

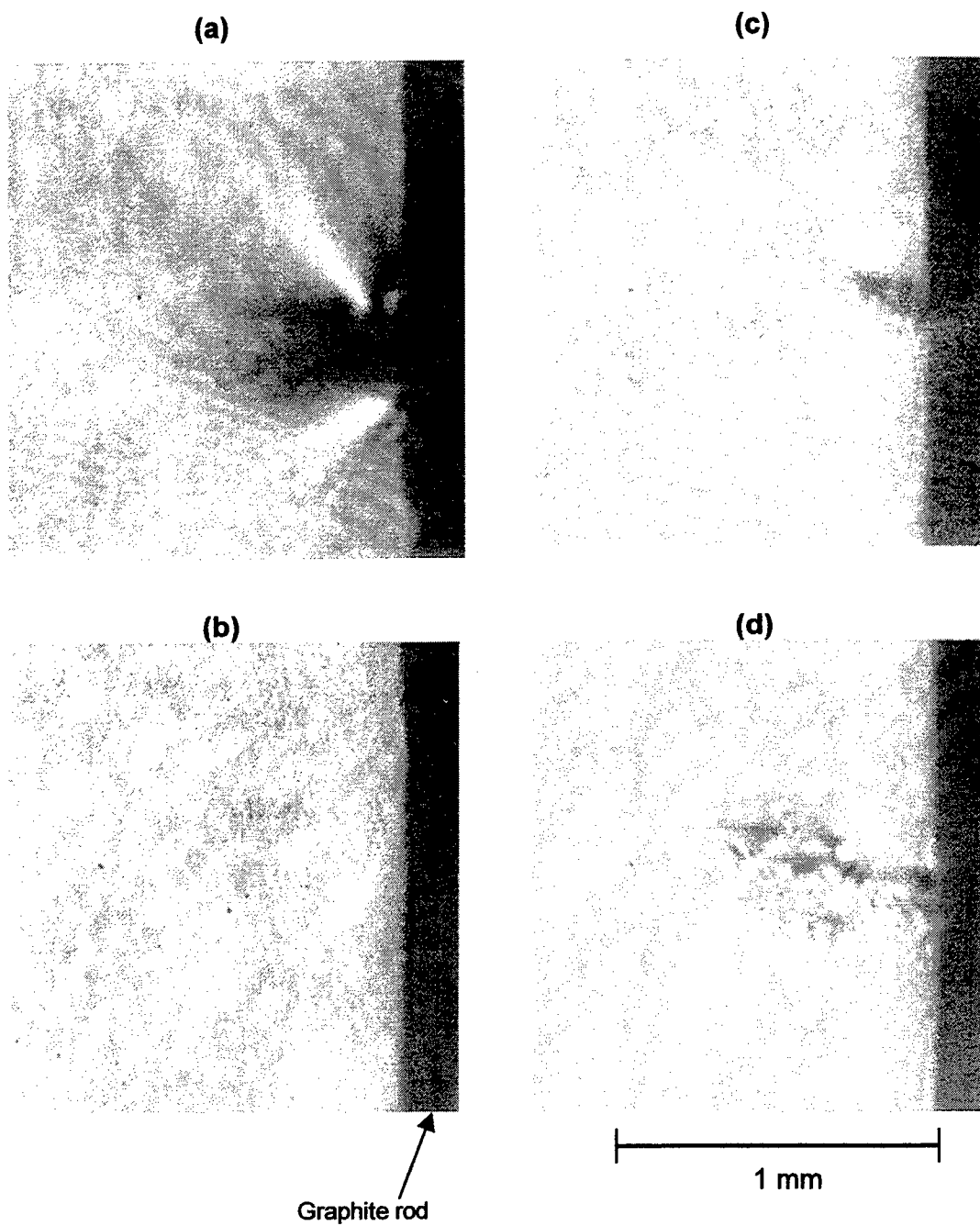
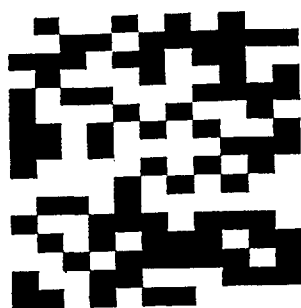
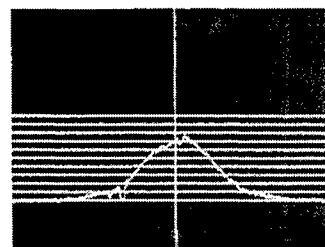
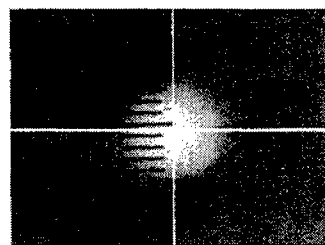


Fig. 3 The Schlieren images of laser ablation (a) and material ejection (c & d) at different delays after the onset of laser pulse; (a) 50 ns, (b) 400 ns, (c) 1 μ s, (d) 3 μ s. The 40-ns laser pulse came from left.

One of the methods to smooth the intensity profile of a laser focal spot is to use a random phase plate (RPP)¹². A RPP has many phase-delay elements on its surface with specifically designed patterns to achieve a desired laser intensity profile. The phase-delay elements preferably have a thickness of $n\lambda/2$ in order to create a phase π shift, where λ is the wavelength of the laser and n is the index of refraction of the phase-delay elements. A typical phase-plate pattern is illustrated in Fig. 4a where the delay elements are denoted by the darkened areas. This design is used in conjunction with a focusing lens to convert a circular laser beam to a focal point in the shape of an ellipse with a 400-micron major axis. The illuminated area becomes circular when this ellipse is projected onto a flat surface at an angle of incident of 45 degrees. The effect of inserting the RPP in front of a lens can be seen by examining the spatial intensity profile of the focus spot on the target, as illustrated in Fig. 4(b). With the addition of a RPP, the laser intensity profile on the target becomes gaussian-like with the elimination of hot spots that previously existed. The smoothing of the laser intensity profile using a RPP effectively eliminated any detectable material ejection from the graphite target, as examined by Schelieren images. As a result, the DLC produced with a RPP had significant fewer included particles. The resulting particle density is typically 2-8 particles within 40 μm by 40 μm areas with particle sizes of 50 ± 10 nm wide and 200 ± 50 nm height. This nanoparticle formation is believed mostly a result of condensation during the fast expansion of vapor plume¹³. The use of a RPP also



(a)



(b)

Fig. 4 (a) A typical pattern of phase-delay elements on a random phase plate. (b) The intensity profile of the laser focal spot with a RPP in front of a focusing lens ($f = 0.5$ meter). The spot size is ~ 400 μm (FWHM).

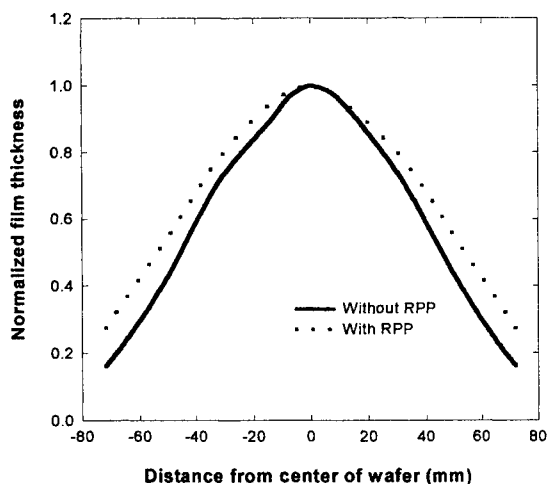


Fig. 5 The DLC deposition profiles on a silicon wafer with and without the use of a RPP .

increased the film deposition rate on a silicon substrate by as much as 50-60%. The spatial distribution of deposition thickness, as shown in Fig. 5, illustrates a more uniform film growth when use a RPP. The film deposition profile, which is typical represented by a cosin law in PLD, is improved from $\cos^{7.5} \theta$ to $\cos^{5.3} \theta$, where θ is the angle measured from the target surface normal. These improved features make PLD of DLC easier to scale up with greatly improved film quality.

3. EMISSION SPECTRA OF A CARBON PLUME

In this investigation, the spectra of the ablated carbon plume was measured mainly between 220 to 600 nm from direct emissions of C_2 dimer, C neutral, and C ions. The emission spectra were recorded at various time delays and downstream positions from the target. With a 1200 l/mm grating, we measured the C_2 Swan-band emission ($d^3\Pi_g \Rightarrow a^3\Pi_u$) near the target surface. The measured spectra illustrated in Fig. 6 shows the plume emission from 20 ns to 120 ns relative to the onset of the laser pulse. It is interesting to note that the initial broad band radiation is not necessarily greater at higher laser intensity, as shown in Fig. 6(a) and 6(c). The signal strength of the C_2 Swan band ($\Delta v = -1$), however, declines significantly as laser intensity increases from 0.8 GW/cm^2 to 4 GW/cm^2 . We believe that the higher plasma temperature and electron density of the carbon plume at higher laser intensity lowers the possibility of C_2 formation (i.e., The C_2 dissociation energy is $\sim 6 \text{ eV}$). The stronger C^+ and C^{++} emissions shown in Fig. 6(c) and 6(d) manifest a higher electron density and temperature. It's worth noting that the line broadening of the C^+ emission at 0.8 GW/cm^2 is more pronounced than that at 4 GW/cm^2 , especially later in time (i.e., 90 ns). This may be a result of slower plasma expansion at lower laser intensity. Figure 7 illustrates the plume emission in the UV range, which includes C, C^+ , and C^{++} emissions at 247.8 nm, 251.2 nm, and 229.7 nm, respectively. The higher C^{++} emission resulting from higher plasma temperature at greater laser intensity is clearly shown in Fig 7 (c) and (d). The laser threshold for generating detectable ionic emission from ablation is found to be $\sim 0.1 \text{ GW/cm}^2$.

The temporal development of C, C^+ , and C^{++} emission illustrated in Figures 6 and 7 are plotted relative to the laser pulse, as shown in Fig. 8. It indicates that the ionic emission peaks near the end of laser pulse, when the carbon plume has the highest plasma temperature. The C and C_2 emissions, however, only start to appear at the end of

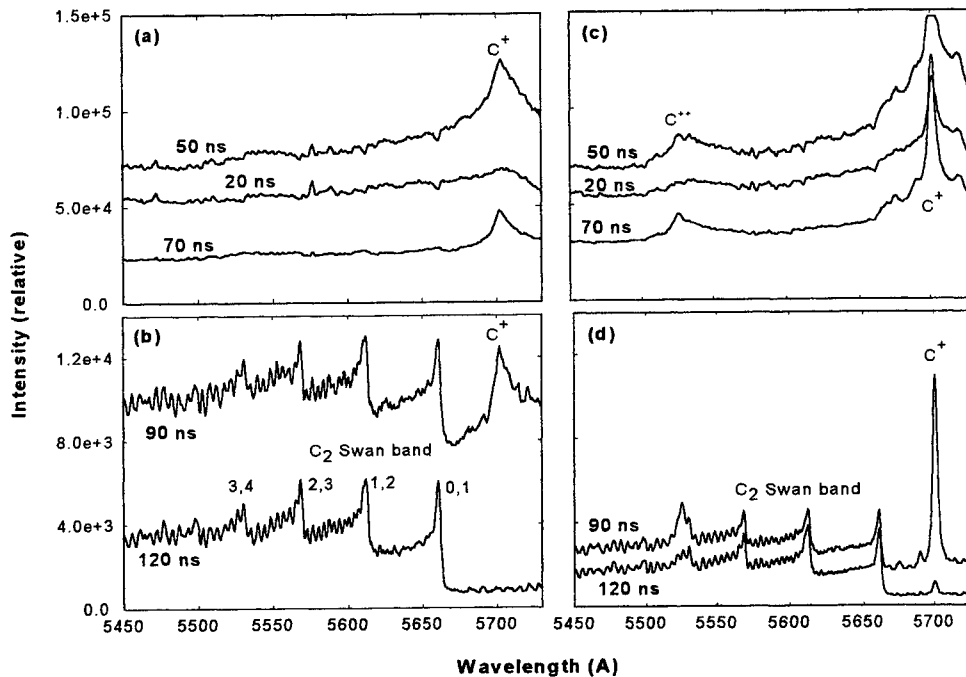


Fig. 6 Plume emission spectra near the target surface; the spectra were taken from 20 ns to 120 ns after the onset of laser pulse. The laser peak power was 0.8 GW/cm^2 (a & b) and 4 GW/cm^2 (c & d). Note that the vertical scales are the same between (a) & (c) and between (b) & (d).

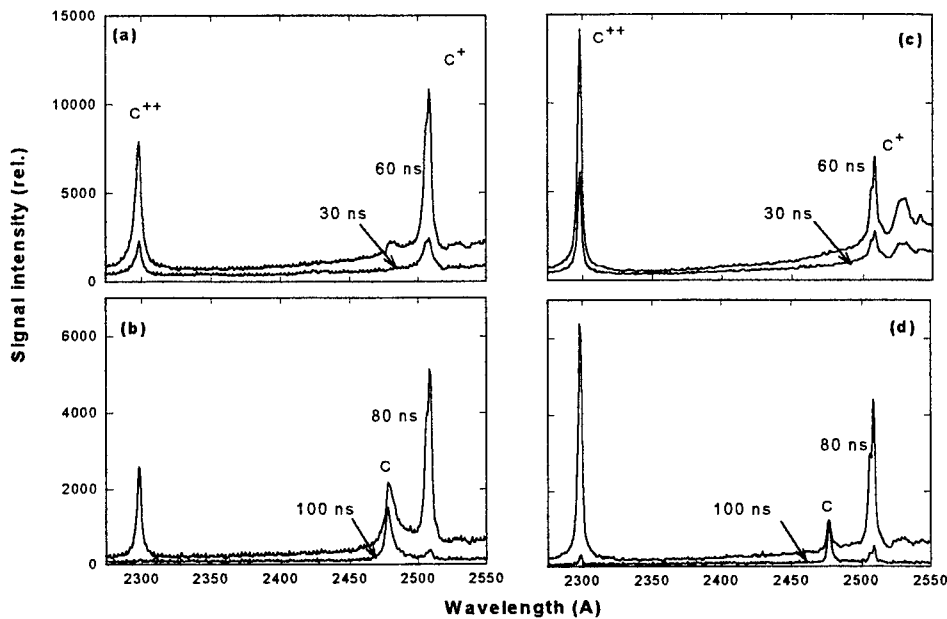


Fig. 7 Plume emission spectra near the target surface; the spectra were taken from 30 ns to 100 ns after the onset of laser pulse. The laser peak power was 0.8 GW/cm^2 (a & b) and 4 GW/cm^2 (c & d).

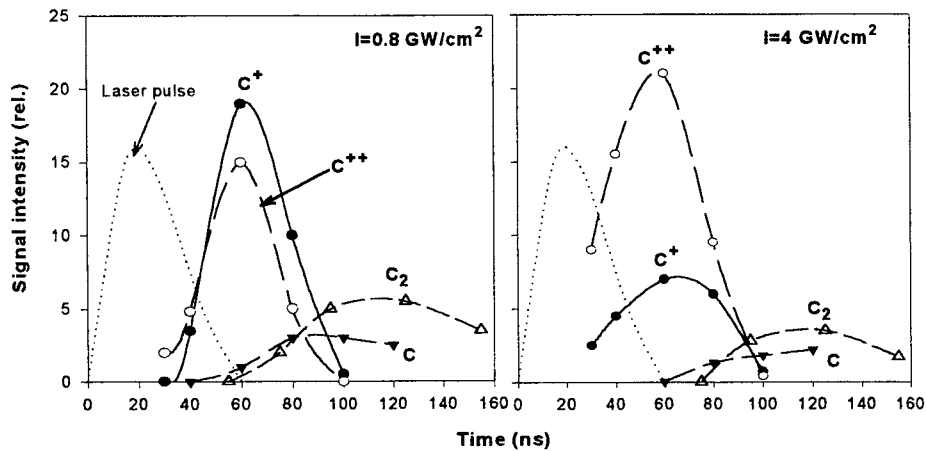


Fig. 8 The temporal development of carbon-plume emission near the graphite target at two laser peak intensities.

laser pulse. They reach their peaks at 100 -130 ns, when most of the ionic species have moved away from the target surface. Note that the C^{++}/C^+ ratio increases significantly as the laser intensity increases from 0.8 GW/cm^2 to 4 GW/cm^2 .

Figure 9 illustrates the spatial distribution of the emission along the plume axis at 100 ns. As illustrated in Fig 9a, the emission at a laser intensity of 0.5 GW/cm^2 is dominated by C and C_2 emission. We found that the Swan-band emission is strongest at this laser intensity. It's worth noting that the C_2 Swan band decays quickly (i.e., its radiative lifetime is $\sim 110 \text{ ns}$) as it moves away from the target. The spectra of the carbon plume become mostly neutral and ionic emissions as the laser intensity increases to 2 GW/cm^2 , as shown in Fig. 9(b). The temporally and spatially resolved emission measurement of the carbon plume enabled us to map the plume expansion after laser pulse. Figure 10 illustrates the spatial distribution of C, C^+ , and C^{++} based on their emission at 247.8 nm, 426.7 nm, and 272.5 nm, respectively. Note that the 247.8-nm and 272.5-nm emission were detected by their 2nd order as

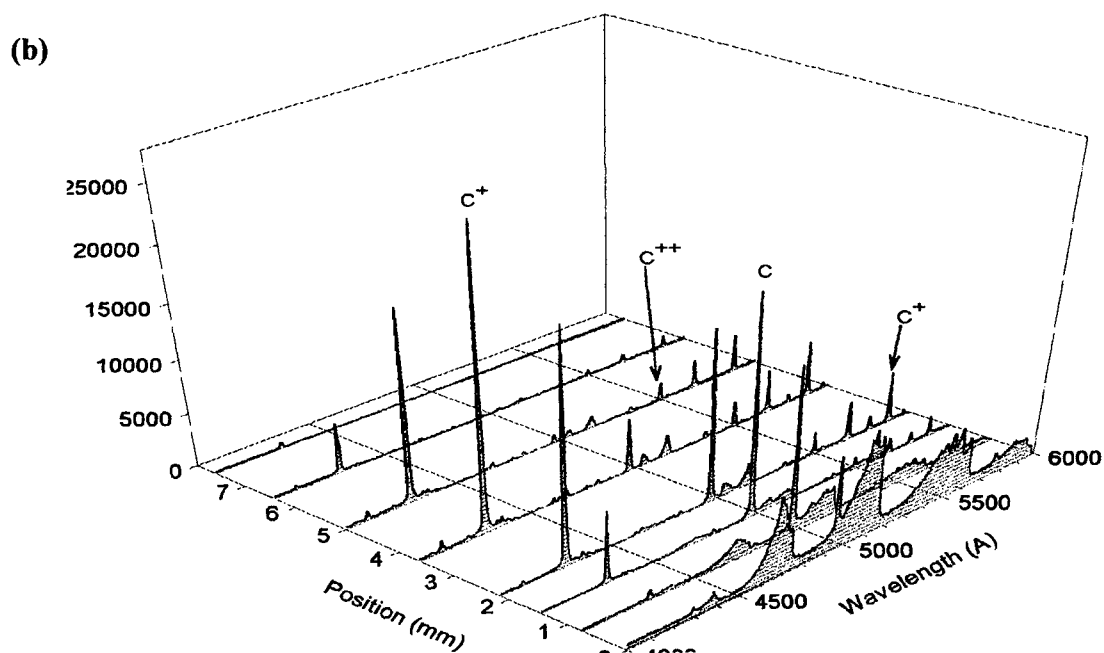
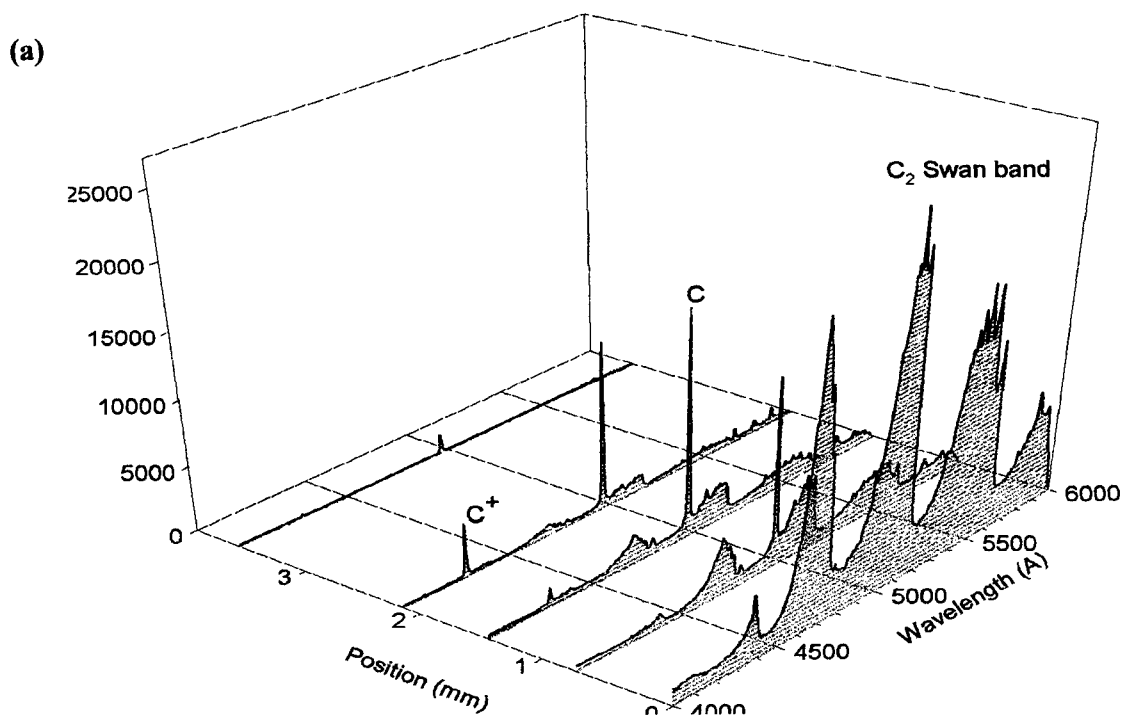


Fig. 9 The spatial distribution of plasma emission from laser ablated carbon plume; the spectra were taken at 100 ns after the onset of laser pulse with laser peak intensities of (a) 0.5 GW/cm^2 and (b) 2 GW/cm^2 . The "Position" is the distance from the target.

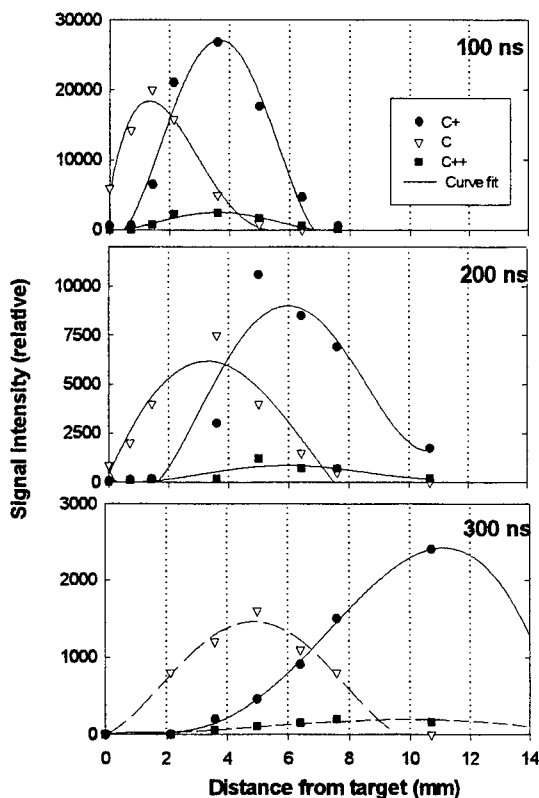


Fig. 10 The spatial distribution of plume emission from C, C⁺, and C⁺⁺ at 100 ns, 200 ns, and 300 ns after the onset of laser pulse.

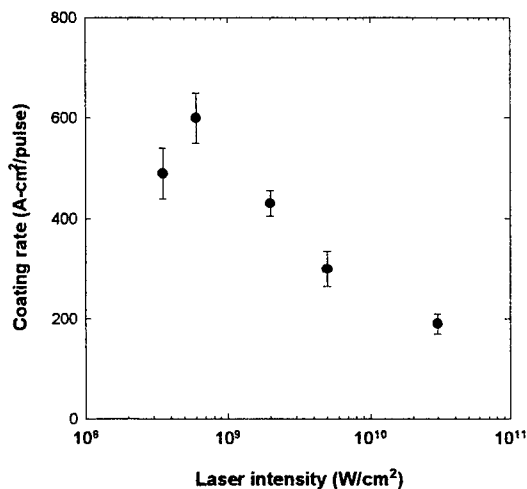


Fig. 11 The DLC coating rate vs. laser peak power on a silicon substrate.

shown in Fig. 9. The delay of the OMA was varied from 100 ns to 300 ns after the onset of the laser pulse. This figure clearly indicates that C⁺ and C⁺⁺ move jointly as a result of the Coulomb force in the ionized plume. The C neutrals lag behind the ionized particles with a slower speed. Based on this time-of-flight measurement, the kinetic energies of C neutral and C ions at a laser peak power of 2 GW/cm² are estimated to be 20 eV and 76 eV, respectively. The kinetic energies of C and C ions decrease to 15 eV and 20 eV, respectively, as the laser intensity is reduced to 0.5 GW/cm². It's worth noting that the ratio of C⁺⁺/C⁺ remains about the same as the plume expands.

4. DEPOSITION RESULTS

The elimination of micro particulates using a random phase plate has enabled us to produce high quality DLC on polished Si (100) substrate. We have measured the coating rate of DLC at various laser intensities as plotted in Fig 11. It's found that the peak coating rate occurs at a laser peak intensity of 0.5-0.8 GW/cm². According to our measurements of plume emission, the variation of coating rate with laser intensity correlates to the intensity of the C₂ Swan-band emission. The reduction of coating rate at higher laser intensities is believed to be a result of plasma absorption. The plasma ignition threshold for carbon plume is similar to aluminum¹⁴, which is measured to be ~2 GW/cm²¹⁵. No significant difference in DLC properties was measured at these laser intensities. The increase of ion kinetic energy from 20 eV to 76 eV as laser intensity increases from 0.5 – 2 GW/cm² has no noticeable effect on the coating quality.

Figure 12 shows Elastic Electron Loss Spectroscopy (EELS) spectra performed on the resultant material and on a graphite substrate. Typically there are three predominant features in an EELS DLC spectra. The elastic electron scattering peak is at the incident electron energy 500 eV. There is a peak ~6.6 eV below the incident energy which represents energy lost to the π -bonds of graphite (at 494 eV). The third feature is an unsolved broad plasma loss peak 30-40 eV below the incident energy. The lack of a π - π^* feature as compared to the graphite spectra indicates a DLC film¹⁶. With Atomic Force Microscopy (AFM) to measure surface roughness, we have determined a surface roughness of less than 10 nm with a 400-nm thick DLC. We have produced some films with RMS surface roughness as low as a few nanometers.

CONCLUSION REMARKS

The PLD of DLC with visible laser light has been demonstrated with a 300-W copper laser running at 4.4 kHz. We have observed that explosive material ejection during laser ablation of graphite starts at ~500 ns after the onset of

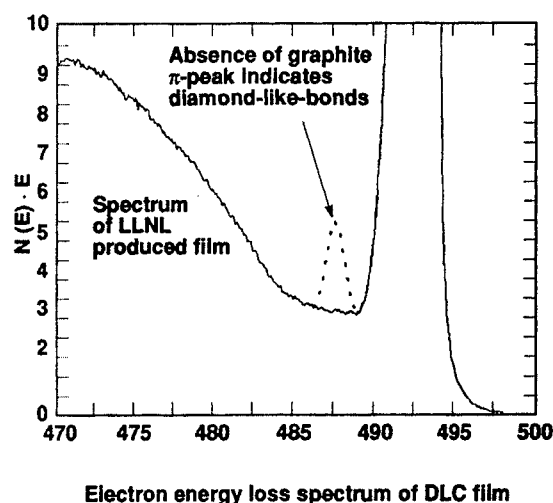


Fig. 11 Electron energy loss spectrum of the DLC film produced with a copper laser.

laser pulse. The material ejection lasts for about 10 μ s that leads to large amount of particle inclusion in the DLC film. Although the physical mechanism of this material ejection is still not well understood, we found that it's a result of non-uniform laser intensity profile on the target. With the use of a RPP to smooth the laser focal spot, we essentially eliminate the explosive material ejection. Additional advantages of using a RPP for PLD is a 50-60% increase of coating rate and a more uniform DLC film thickness.

It's found that the optimized coating rate for DCL is at a laser peak intensity of 0.5-0.8 GW/cm². Our investigation on plume emission spectra indicates that the coating rate correlates to the emission of C₂ Swan band. The kinetic energy of C⁺ for the optimized coating rate is estimated to be ~20 eV based on a time-of-flight measurement. We found that higher kinetic energy of C⁺ at higher laser intensities does not necessarily produce a better DLC quality. By optimizing the coating process base on our findings, we have demonstrated a coating rate of 2000 μ m-cm²/hr. This rate is ~100 times greater than any other known laser technology.

REFERENCES

1. J. Cuomo, D. Pappas, J. Bruley, and J. Doyle, *J. Appl. Phys.*, **70**, p.1706, 1991.
2. D. Pappas, K. Saenger, J. Bruley, W. Krakow, J. Cuomo, T. GU, and R. Collins, *J. Appl. Phys.*, **71**, p.5675, 1992.
3. F. Muller, K. Mann, and P. Simon, *SPIE*, **1858**, p.464, 1993.
4. F. Qian, R. Singh, S. Dutta, and P. Pronko, *Appl. Phys. Lett.*, **67**, p.3120, 1995.
5. J. Angus and C. Hayman, *Science*, **241**, p.913, 1988.
6. B. Baren, J. Dubowski, and D. Norton, *Mat. Res. Soc. Symp. Proc.*, **285**, p. 263, 1993.
7. B. Baren, J. Dubowski, and D. Norton, *Mat. Res. Soc. Symp. Proc.*, **285**, p. 355, 1993.
8. J. Chang, *Appl. Optics*, **32**, p.5230, 1993.
9. B. Yilbas, *J. Laser Application*, **7**, p.147, 1995.
10. R. Sing, D. Bhattacharya, and J. Narayan, *Appl. Phys. Lett.*, **57**, p.2022, 1990.
11. R. Sing, D. Bhattacharya, and J. Narayan, *Appl. Phys. Lett.*, **62**, p.483, 1992.
12. S. Dixit, I. Thomas, B. Woods, A. Morgan, M. Henesian, P. Wegner, and H. Powell, *Appl. Optics*, **32**, p.2543, 1993.
13. D. Geohegan, A. Puretzky, G. Duscer, and S. Pennycook, *Appl. Phys. Lett.*, **72**, p.371, 1998.
14. M. Shannon and X. Mao, paper presented at the OSA Annual Meeting, Portland, Oregon, 1995.
15. J. Chang, and B. Warner, *Appl. Phys. Lett.*, **69**, p.473, 1996.
16. P. Murry and D. Peeler, *J. Elec. Mater.*, **23**, p.855, 1994.

Spectroscopic Energy Characterization of Laser-Induced Titanium Plume

Schubert S. Chu, Mengi Ye, and Costas P. Grigoropoulos*

Dept. of Mechanical Engineering, Univ. of California at Berkeley, Berkeley, CA 94720

ABSTRACT

A titanium target was ablated by a KrF excimer laser with fluences varying from 4 to 8 J/cm² in an argon filled environment with pressures ranging from vacuum to 1 torr. The effects of laser fluence and background gas pressure on the kinetic energies of the ablated species were investigated by temporally and spatially resolved emission spectroscopy. The maximum surface temperatures were calculated by an one-dimensional conduction model. Experimentally obtained surface temperatures from the kinetic energy of the ejected plume were one order of magnitude higher than the calculated temperatures. This discrepancy is most likely due to the absorption of laser energy by the plasma that is formed early in the pulse. Temporally resolved imaging with 10 ns gate width was also employed to reveal the evolution of the ablated plume against the background gas. Separation of slower and faster components were observed for pressures above 50 mTorr, and angular concentration of titanium in the plume was determined.

Keywords: Pulsed Laser Deposition, Laser Ablation, Emission Spectroscopy, Titanium, Optical Time-of-Flight

1. INTRODUCTION

In the last few decades, Pulsed laser deposition (PLD) of thin films has evolved into a well recognized technique for a wide range of materials and in a variety of devices. One key parameter in determining the quality of the film deposited by PLD is the kinetic energy of vaporized atoms. Adatoms with greater kinetic energy have higher mobility once they reach the substrate and consequently tend to form a more crystalline film¹. There has been increased interest in the deposition of titanium based thin film by PLD since titanium based thin films have a great range of uses in microelectronic devices, optics, and tribology^{2,3,4,5}.

Optical methods such as emission time-of-flight (TOF) measurements are attractive for determining the energy and the extent of ionization of the ablation plume for several reasons. First, these methods are non-intrusive. With fast detectors, it is possible to obtain time-resolved spectroscopic information on the nanosecond scale. Furthermore, emission spectroscopy can effectively distinguish between different neutral and ionized species. This work employed emission time-of-flight and imaging techniques to investigate laser ablated titanium plumes.

2. EXPERIMENTAL SETUP

A schematic diagram of the experimental setup is shown in Fig. 1. The laser used in this experiment is a Lumonics Index 210 KrF ($\lambda=248$ nm) excimer laser with a FWHM pulse width of 20 ns. In order to ensure uniform laser intensity on the target, a tunnel-type homogenizer was used in the beam delivery system. The focused spot size on the titanium target was 0.34 mm \times 0.05 mm yielding fluences ranging from 4 to 8 J/cm². A polycrystalline titanium target of 99.99% purity polished to 0.02 μ m was mounted inside a stainless steel high vacuum chamber on a rotational feedthrough which was set to rotate at 0.7 Hz in order to avoid deep drilling. The pressure inside the chamber was manually controlled by filling the chamber with high purity (99.99%) argon to vary between $< 10^{-6}$ torr to 760 torr.

* Correspondence: Email: cgrigoro@me.berkeley.edu; WWW: <http://www.me.berkeley.edu/lt/ltl.html>; Telephone: (510)642-2525; Fax: (510) 642-6163

The emission from the plume was detected by two different methods. Spectrally-integrated and temporally-gated images of the plume were captured via a Princeton Instruments ITE 576 intensified CCD (ICCD) camera with 576×384 pixels. Although the minimum gate width for this ICCD is 5 ns, a gate width of 10 ns was used to maximize the intensity while maintaining good temporal resolution. Since the majority of titanium line emission are in the UV range, a Nikkor 105 mm/f4.5 UV photo lens was used in conjunction with the ICCD. With the 105 mm UV lens installed, the spatial resolution of the combined imaging system is 100 μ m, and the sensitive spectral range is between 300 nm and 850 nm. In order to precisely

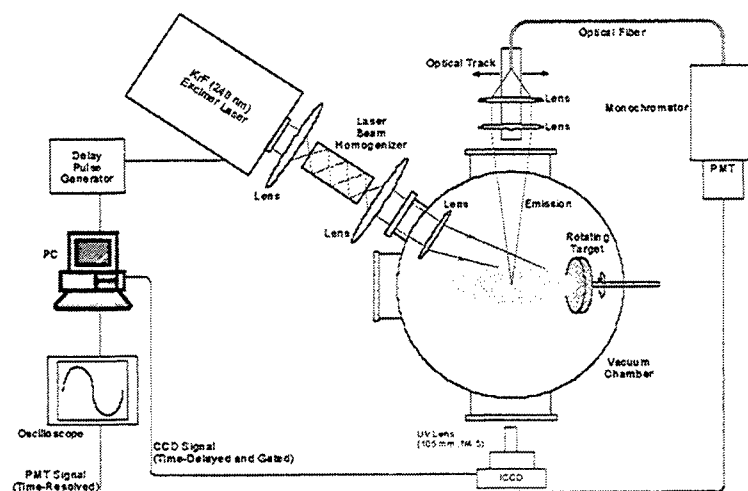


Figure 1 Experimental Setup

synchronize the firing of the excimer laser and the delay in the gating of the ICCD, a Stanford Research DG535 programmable pulse generator with variable delay was used to trigger both the laser and the ICCD. The timing jitter of the imaging system was 3 ns under this configuration.

Spectrally resolved TOF data were acquired by imaging the plume via a $f = 150$ mm quartz UV lens to a magnification of 3.12 X. A fused silica optical fiber with an 1.6 mm aperture was placed on the image plane and mounted on a micrometer stage so that different locations of the plume can be probed. The aperture of the optical fiber is aligned with the centerline of the plume, and therefore detects the time-of-flight of species traveling axially above the surface along the centerline. The spatial resolution of this setup is 300 μ m. The other end of the optical fiber is connected to a McPherson Model 2035 monochromator with an 1800 grooves/mm grating installed. The variable slits of the monochromator were adjusted so that spectral resolution of the monochromator is 0.3 nm. The 399.86 nm emission line from neutral titanium was monitored. This emission line corresponds to $3d^2 4s^2 a^3 F_4 - 3d^2 4s^1 4p^1 y^3 F_4^o$ transition. A Hamamatsu R928 photomultiplier tube (PMT) with 2.2 ns rise time was mounted on the exit slit of the monochromator to monitor the transient emission intensity from the plume. The PMT signals were digitized by a HP 54510 250 MHz digital oscilloscope and then downloaded to a PC. Since the cutoff frequency of the PMT signal is inversely proportional to the termination impedance, a 50 Ω termination was used to avoid distortion in the temporal profile of the emission signal. In order to enhance the signal-to-noise, accumulations of 20 to 500 signals were used for each data point. The synchronization for this part of the experiment was done by using the pulse generator to trigger the excimer, and a photodiode which detects the excimer beam then was used to trigger the digital oscilloscope.

3. NUMERICAL MODEL FOR SURFACE TEMPERATURE

The maximum surface temperatures were calculated for the range of fluences used in this experiment. The details of the model were previously published^{6,7} and summarized here.

The metal surface reflectivity, R , is given by:

$$R = \frac{(n-1)^2 + k^2}{(n+1)^2 + k^2} \quad (1)$$

where n and k are the real and imaginary parts of the index of refraction, respectively. The values used for n and k for the calculation for the rate of titanium vaporization were 1.24 and 1.21. The absorption coefficient, α , is given by:

$$\alpha = \frac{4\pi k}{\lambda} \quad (2)$$

where λ is the wavelength of the laser used for ablation. In this case, $\lambda = 248$ nm. The energy absorbed by the target, Q , at a depth, z , below the surface and at time t after the laser pulse, is then described by:

$$Q(z, t) = (1 - R)I(t)\alpha \exp(-\alpha z) \quad (3)$$

The heat transfer in the target was approximated as a one-dimensional semi-infinite conduction problem since the thermal penetration depth is orders of magnitude smaller than the dimensions of the laser spot. The conduction equation takes the form of:

$$\rho(T)C_p \frac{\partial T}{\partial t} = \frac{\partial}{\partial z} \left(K(T) \frac{\partial T}{\partial z} \right) + Q \quad (4)$$

The boundary condition was set as $\left. \frac{\partial T}{\partial z} \right|_{z=0} = 0$, and the initial target temperature was set to be equal to the ambient temperature. All other heat losses to the ambient by conduction, convection and radiation were neglected.

4. RESULTS

A typical emission TOF signal from the PMT is show in Fig. 2. The lifetime, τ , of an emission line is given by:

$$\tau = A^{-1} \quad (5)$$

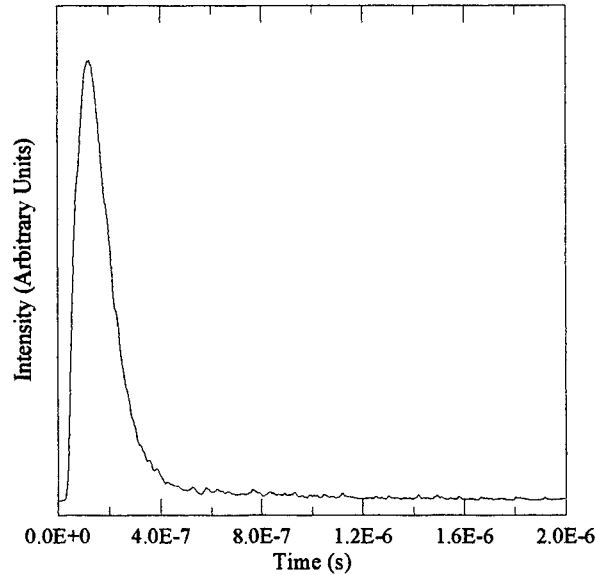


Figure 2 Typical TOF signal

where A is the transition probability. The value of the transition probability for spontaneous emission for $3d^2 4s^2 \alpha^2 F_4 \rightarrow 3d^2 4s^1 4p^1 y^3 F_4^o$ transition is $0.39 \times 10^8 \text{ s}^{-1}$ ⁸. Accordingly, the lifetime of the 399.86 nm emission line is 25 ns. However, the emission of this wavelength is detectable even beyond 2 μs . The prolonged detection of line emission is the result of re-excitation of atoms through collisions with other atoms in the plume. Since the likelihood of collisions is proportional to the concentration of atoms, therefore the maximum emission intensity at a particular location in the plume corresponds to the peak concentration. The fluences used in this experiment were well above the threshold for vaporization and sufficient for the formation of a Knudsen⁹. Hence the intensity signal of the ablated titanium follows the full-range Maxwellian distribution for a density-sensitive detection device given by¹⁰.

$$f(x, t) = \frac{Cx}{t^4} \exp \left[-\frac{m}{2k_B T_s t^2} (x - v_c t)^2 \right] \quad (6)$$

where k_B is the Boltzmann constant, T_s is the surface temperature, m is the mass of the atom, v_c is the center of mass velocity, and C is a constant. An x - t diagram can be constructed by plotting the location versus the time corresponding to the peak emission signal detected at that particular location. The most-probable velocity is then found by taking the slope of this curve. Figure 3 shows the x - t curves for neutral titanium ablated at several different laser fluences under vacuum. Since the locations present the distance above the target surface on the centerline of the plume, the velocities derived from the slopes are therefore the most-probable axial centerline velocities. Since collisions occur in the plume, and the plume expands laterally, the centerline velocity can be expected to decrease. The decrease in centerline velocity is more significant for the lower fluence as shown in Fig. 3.

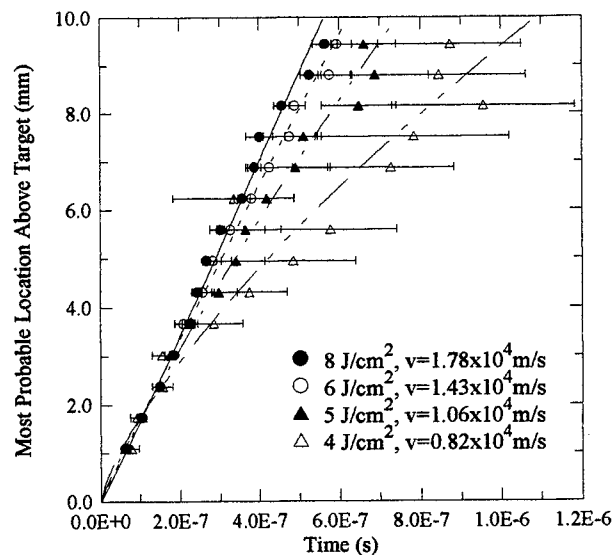


Figure 3 Effects of ablating laser fluence on the most probably centerline velocity of neutral titanium. The velocities shown are average values.

In the presence of the Knudsen layer, the surface temperature is given by:

$$k_B T_s = \frac{(mv_p^2 / 2)}{(\eta T_k / T_s)} \quad (7)$$

where $\eta T_k / T_s$ is equal to 2.52 for the centerline ($\theta = 0^\circ$) of a monatomic plume¹⁰. The experimentally obtained surface temperature and calculated maximum surface temperature are plotted in Fig. 4. The experimentally obtained values are at least an order of magnitude greater than the calculated values. This can be attributed to the formation of plasma early in the laser pulse, which was not accounted for by the either analysis. The vaporization model may overstate the surface temperature since the absorption of laser energy by the plasma⁹ is not accounted for. However, the overstatement may be more severe with the Knudsen layer analysis because the high velocities measured were likely the result of redistribution of velocities due to

collisions in the plasma. The exact mechanisms of laser absorption and the acceleration of atoms have not been clearly determined at the present time.

The effects of the background argon pressure on the centerline velocity is shown in Fig. 5. The background pressure suppresses plume expansion and consequently enhances collisions within the plume. This is evident in the decrease in centerline velocity and as will be seen later, the overall increase of emission intensity.

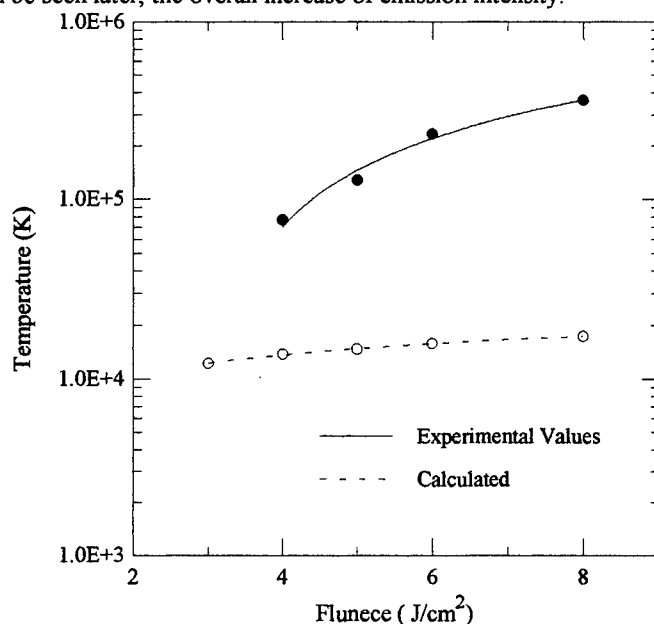


Figure 4 Experimentally obtained surface temperature using Eq. (7) and calculated surface temperature.

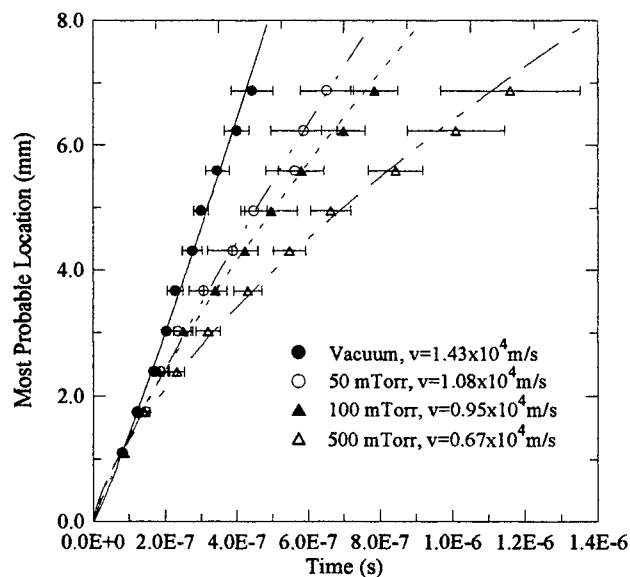


Figure 5 Effects of background argon pressure on the most-probable center-line velocity. $\Phi = 5 J/cm^2$. The velocities shown are average values.

Spectrally-integrated and temporally resolved images of plumes were obtained under background argon pressures ranging from vacuum to 1 Torr. Some selected images are shown in Fig. 6. At pressures above 50 mTorr, a separation of faster and slower moving components in the plume was observed. Similar results were also observed by Wood et. al.¹¹ in ablation of silicon. The intensity of the emission was also greater with higher background pressure as a result of greater number of collisions. The location at which the separation occurs was closer to the target surface at higher pressures. Additional imaging also revealed that the threshold for the separation to occur varied with the laser fluence and therefore evaporative flux. Thus it is reasonable to suggest that this occurrence may be determined the number of collisions and hence characterized by the Knudsen number.

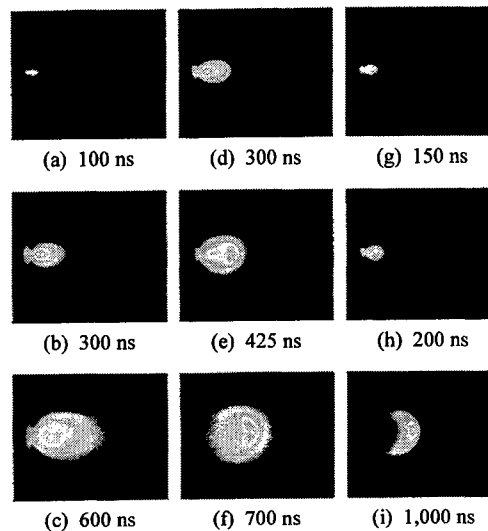


Figure 6 Spectrally integrated images with 10 ns gating in normalized pseudocolor. All were taken at $\Phi = 5 \text{ J/cm}^2$. (a)-(c) were under vacuum. (d)-(f) $P = 100 \text{ mTorr}$. (g)-(i) $P = 1 \text{ Torr}$.

Figure 7 shows the angular concentration distribution as measured from the emission intensities from the gated images. This distribution takes on the $\cos^4\theta$ shape and was observed for all background pressures. Analysis which took into account the existence of a Knudsen layer suggested that the Knudsen layer Mach number is unity¹⁰. This was the reason for using the value for $\eta T_k/T_s$ in calculating surface temperature from the velocities obtained experimentally. However, this analysis did not consider the absorption of laser energy by the plasma which may aid in explaining the unusually high temperature.

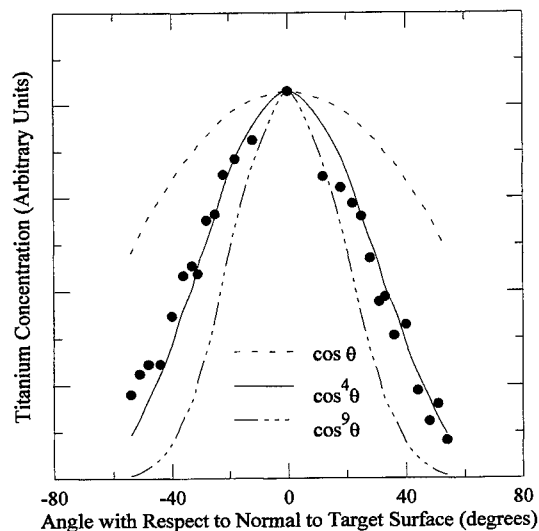


Figure 7 Angular distribution of titanium concentration in the plume. The experimental data follow a $\cos^4\theta$ distribution which indicates that $M_k = 1$. The $\cos^9\theta$ distribution corresponds to $M_k = 2^{10}$.

5. CONCLUSIONS

Optical time-of-flight measurements were performed for fluences ranging from 4 to 8 J/cm² and various background argon pressures. Maximum surface temperatures were calculated and were an order of magnitude lower than the temperatures derived from the experimentally obtained velocities. The likely reason for the discrepancy is the absorption of the laser by the plasma which forms early in the laser pulse. Optical emission imaging revealed a separation of slower and faster components in the plume. The separation was likely a result of collisions and related to a particular Knudsen number since the occurrence depends on fluence and background pressure. Angular distribution of concentration in the plume were also determined from emission imaging and followed a $\cos^4\theta$ distribution.

REFERENCES

1. M. Ohring, *Materials Science of Thin Films*, Academic Press, Boston, 1992.
2. J. E. Sundgren, "Structure and Properties of TiN Coatings," *Thin Solid Films*, **128**, pp.21-29, 1985.
3. J. Hems, "Barrier Layers: The Advantages of Titanium Nitride," *Semiconductor International*, **13**, pp. 100-102, 1990.
4. J. Narayan, "Epitaxial Growth of TiN Films on (100) Silicon Substrates by Laser Physical Vapor Deposition," *Applied Physics Letters*, **61**, pp. 1290-1292, 1992.
5. E. Valkonen, T. Karlsson, B. Karlsson, and B. O. Johansson, "Selective Transmission of Thin TiN-Films," Proceedings. SPIE Thin Film Technology Conference, Geneva, Switzerland, **401**, pp. 375-381, 1983.
6. X. Zhang, S. S. Chu, J. R. Ho, and C. P. Grigoropoulos, "Excimer Laser Ablation of Thin Gold Films on a Quartz Crystal Microbalance at Various Argon Background Pressures," *Applied Physics A*, **64**, pp. 542-552, 1997.
7. J. R. Ho, C. P. Grigoropoulos, J. A. C. Humphrey, "Gas Dynamics and Radiation Heat Transfer in the Vapor Plume Produced by Pulsed Laser Irradiation of Aluminum," *Journal of Applied Physics*, **79**, pp.7205-7215, 1993.
8. W. L. Wiese, and J. R. Fuhr, "Atomic Transition Probabilities for Scandium And Titanium," *Journal of Physical and Chemical Reference Data*, **4**, pp.263-353, 1975.
9. J. Hermann, A. L. Thomann, C. Boulmer-Leborgne, B. Dubreuil, M. L. De Giorgi, A. Perrone, A. Luches, and L. N. Mihailescu, "Multistage Plasma Initiation Process by Pulsed CO₂ Laser Irradiation of a Ti Sample in an Ambient Gas," *Journal of Applied Physics*, **73**, pp. 1091-1099, 1993.
10. R. Kelly and R. W. Dreyfus, "Reconsidering the Mechanisms of Laser Sputtering with Knudsen-Layer Formation Taken into Account," *Nuclear Instruments and Methods in Physics Research B*, **32**, pp. 341-348, 1988.
11. R. F. Wood,, K. R. Chen, J. N. Leboeuf, A. A. Puretzky, and D. B. Geohegan, , "Dynamics of Plume Propagation and Splitting during Pulsed-Laser Ablation," *Physical Review Letters*, **79**, pp. 1571-1574, 1997.

SESSION 3

Ultrashort Pulse Laser Processing

Vibrational Excitation and Relaxation Processes in Insulators Initiated by Ultrashort, Mid-Infrared Laser Pulses

R. F. Haglund Jr.,* R. Cramer,[†] D. R. Ermer, M. R. Papantonakis, H. K. Park[‡] and O. Yavas*

Department of Physics and Astronomy and
W. M. Keck Foundation Free-Electron Laser Center
Vanderbilt University, Nashville, TN 37235

ABSTRACT

Ultrashort-pulse lasers are increasingly being used for laser-induced surface modification, texturing and marking of insulators. Ultrashort pulses interacting with insulators in the vibrational infrared produce a number of novel effects of potential utility in materials processing and analysis applications, including the creation of microbumps, microdimples, generation of hydrodynamic instabilities, and creation of smooth ablation craters. This paper describes recent results in the study of ultrashort-pulse laser interactions with surfaces when the irradiation is in the 2-10 μm range. The laser source was a tunable, free-electron laser (FEL) with 1-ps micropulses spaced 350 ps apart in a macropulse lasting up to 4 μs , with an average power of up to 3 W. This unusual pulse structure makes possible novel tests of the effects of resonant vibrational excitation, controlling the ratio of absorption depth to thermal diffusion length, and desorption and ionization by resonant excitation. The mechanisms underlying these effects, including vibrational excitation and relaxation dynamics, as well as their implications for materials-modification strategies, are discussed with reference to recent experimental examples.

Keywords: ablation, infrared, shock waves, vibrational resonance, desorption-ionization processes, surface instability

1. INTRODUCTION

Ultrashort-pulse lasers are increasingly being used to create specific surface modifications in metals, semiconductors and insulators. Solid-state chirped-pulse amplifier systems, with fundamental wavelengths in the near infrared, couple laser light into electronic material excitations, either by a multiphoton absorption process or by one-photon transitions on laser harmonics.¹ The relaxation of electronic excitation into vibrational modes can produce efficient ablation and other desirable surface modifications with little collateral damage because the laser energy is deposited on a time scale much shorter than thermal diffusion times. Little is known, however, about how ultrashort pulses interact with insulators at wavelengths in the vibrational infrared. Moreover, in many simple molecular crystals and in organic materials with strong infrared-active vibrational bands, ablation or desorption with as little electronically-excited photochemistry as possible is especially interesting.

In previous work, we have reported on the phenomenology of surface modifications induced by picosecond mid-infrared laser pulses in such model materials as calcium carbonate, sodium nitrate and fused silica. Our results show distinct changes in surface morphology, in ablation plume emission and in photoacoustic deflection as one ranges over wavelengths in the near-ultraviolet, visible, near- and mid-infrared.² The infrared results were obtained with a tunable free-electron laser that can directly excite vibrational modes of the O-H defects and the fundamental $\nu_2 - \nu_4$ asymmetric stretch mode of the

* Correspondence: Email: richard.haglund@vanderbilt.edu; WWW: <http://optics1.phy.vanderbilt.edu>; Telephone 615-322-7964; Fax: 615-343-7263.

[†] Present address: Ludwig Institute for Cancer Research, 91 Riding House Street, London W1P 8BT, United Kingdom

[‡] Present address: IBM Manufacturing Technology Center, Code 2106, 1798 N.W. 40th Street, Boca Raton, FL 33431

* Present address: Center for Materials Science at Extreme Conditions, Osaka University, 1-3 Machikaneyama, Toyonaka, Osaka 560-8531, JAPAN

carbonate group (nitrate group in sodium nitrate), the SiO stretch of fused silica, and the O-H, C-H, C-N and C-O stretching vibrations in molecular crystals used as matrices for mass spectrometry of biomolecules. The morphology of surface damage is consistent with thermomechanical fracture at visible and near ultraviolet wavelengths, while in the infrared the mechanism is much more consistent with surface melting and vaporization, even for single shot modifications. In addition, the plume spectra show that the absorbed photon energy exits through different channels for infrared *vis á vis* visible or ultraviolet laser light. These studies – the first of their kind using tunable, high-power mid-infrared radiation – call into question analyses based solely on pulse duration, and suggest that the wavelength, intensity and fluence of the laser pulse can all play distinctive roles in determining the mode of excitation and the pathways to surface modification, ablation, desorption and ionization.

In this paper, we highlight recent results shedding light on the dynamics of excitation and relaxation of insulating materials during and after irradiation by tunable, ultrashort pulses from a mid-infrared laser. The three salient examples we consider in detail include

- contrasting phenomenology in ablation initiated by resonant and non-resonant excitation of calcium carbonate;
- tuning absorption depth to thermal diffusion length to achieve controlled melting and vaporization in silica, and
- infrared-laser-induced desorption and ionization of biological macromolecules embedded in microcrystallites.

We describe the physical basis of these results using as a model system the anharmonic quantum oscillator, guided by what is known of the optical response of these materials in the mid-infrared. The experimental results suggest not only an extremely rapid generation of internal excitation for molecular vibrations well above the Debye frequency, but also a shift in the wavelength at which the most efficient energy deposition is achieved. The concept of coupled oscillators may explain some of the most puzzling aspects of our recent studies of surface melting, instability, desorption, ionization, and evaporation.

2. FREE-ELECTRON-LASER SOURCE

The mid-infrared laser source used in our experiments was a free-electron laser (FEL) in which light emitted by a relativistic electron beam moving through a spatially periodic magnet array called a *wiggler* is amplified by classical electromagnetic-field effects.³ The wavelength λ_{FEL} of the FEL is related to the energy of the electron beam and the parameters of the wiggler magnets by

$$\lambda_{\text{FEL}} = \frac{\lambda_w}{2\gamma^2} (1 + \kappa^2) \quad (1)$$

where λ_w is the wiggler spatial period; γ is the ratio of the electron-beam energy to the electron rest energy; and κ is a magnetic-field-dependent quantity of order unity. Thus the FEL wavelength can be varied continuously over a wide range by changing either the wiggler magnetic field or the electron-beam energy.

The Vanderbilt free-electron laser delivers a pulse train comprising some $2 \cdot 10^4$ 0.7-1.0-ps micropulses in a 4- μ s macropulse, with an interpulse spacing of 350 ps.⁴ This micropulse structure is determined by the choice of electron accelerator and rf generation system; in the Vanderbilt FEL, this is an S-band klystron operating at 2.865 GHz. Typical macropulse energies are in the range 30-120 mJ. The FEL beam as delivered to the user laboratories exhibits a diffraction-limited TEM₀₀ spatial profile; the pulse width of the micropulses is essentially transform-limited. An electro-optic switch can be used to slice a short pulse train (≥ 50 ns) from the macropulse with a contrast ratio of order 160:1. Tuning the FEL from one frequency to another in a narrow range ($\pm 10\%$) around a central frequency is generally accomplished by adjusting the wiggler magnetic field; larger adjustments of frequency require returning the electron-beam energy and sometimes inserting a new mirror set in the broadband optical cavity to optimize the laser gain.

3. INFRARED LASER-INDUCED SURFACE MODIFICATIONS

During recent years, we have carried out intensive studies of laser-induced surface modifications in materials with both electronic and vibrational excitation channels. This research has provided new insights into laser ablation, laser-induced structural phase transformations induced by hydrodynamic processes, and infrared desorption and ionization processes. Here we present a sample of these various aspects of our experimental results in the context of specific desirable surface modifications which can be achieved using a picosecond laser source.

3.1. Surface Modifications with Ultrashort-Pulse-Laser Sources

Lasers have been used almost since their invention for modifying surfaces of materials, whether by accident or design. A number of important applications are now completely industrialized, such as the use of large carbon dioxide lasers for cut-

ting and welding applications, and the widespread deployment of continuous-wave Ar⁺ and very long-pulse Nd:YAG lasers in medicine. For metals and semiconductors, the surface modifications achieved in such applications as shock hardening, annealing and welding were governed by the thermal properties of the materials, and hence near- and mid-infrared lasers were typically used. Until recently, however, virtually all lasers used for surface modification in insulators — ablation, structuring, lithography — were nanosecond lasers operating in the visible or near-ultraviolet. Excimer lasers have been particularly prominent in cutting, structuring and lithographic applications because of their small focal spot size, high average power and the useful photochemical effects which were observed in their interaction with materials.

The advent of two new classes of lasers is changing that picture substantially, however. One of these classes comprises fixed-frequency solid-state laser systems using the chirped-pulse amplifier principle. There is now a whole family of ultrashort-pulse (typically 100-200 fs) lasers at wavelengths in the near-infrared and harmonics thereof. These lasers initiate surface modifications by electronic excitations, and, since the laser energy is deposited in a time scale short compared to electron-lattice coupling times, they often do substantially less thermal damage than lasers operating at longer pulse durations because the deposited energy is spatially confined largely to the absorption volume. These lasers operate over a range of pulse repetition frequencies and energies, ranging from tens of nanojoules per pulse for lasers operating at 80-100 MHz repetition frequencies, to many mJ or more in single pulses for lasers operating at pulse repetition rates of a few Hz.

The other newcomer to the materials-modification arena, free-electron lasers operating in the mid-infrared range, were first considered for biomedical applications because they operate in the range in which are found all the important biochemical vibrational bands for O-H, C-H, C-N, and C-C bonds. As average powers have increased, however, these lasers can now be considered for high-throughput, cost-effective materials modification. Among the possible uses which have been considered are subsurface micromachining, pulsed laser deposition of organics, and lithographic applications. These lasers have long macropulse trains — even quasi-continuous operation under some circumstances — with pulse repetition frequencies in the range from tens of MHz to a few GHz, and average powers as high as 300 W. The combination of ultrashort micropulses, with durations substantially less than typical electron-phonon coupling times, and high average power opens a different regime of potential surface modifications.

The most interesting surface modifications for many applications areas are all non-equilibrium processes. As we shall see, the wavelength tunability of the free-electron laser source makes it possible to prepare an unusual family of non-equilibrium processes than those normally encountered in ultrashort-pulse fixed-frequency lasers. And while the large capital investment required to construct free-electron lasers may not make them routine industrial tools, it is very possible that the FEL can be a useful tool for process optimization with the idea that once one knows where in frequency space to go, it may well be possible to construct an appropriate, specialized solid-state laser system to do the same job.

The processes which are important in mid-infrared excitation and relaxation are seen schematically in Figure 1. Following photoexcitation of electronic or vibrational modes, either of the perfect solid or of defects, the energy resides initially in strongly localized, highly anharmonic modes. The second stage in laser-induced desorption or ablation is marked by a competition between localized and delocalized relaxation processes for the absorbed energy. Desorption of an atom or molecule can occur if the localization process wins out by retaining the absorbed energy at a single site for longer than a few vibrational periods — long enough for the bond to be broken and the atom or molecule to begin to move away from its former "home." Radiative recombination, because of its long lifetime (typically a nanosecond or more), is rarely the major channel of energy dissipation for high local density of electronic or vibrational excitation. These non-radiative processes may include:

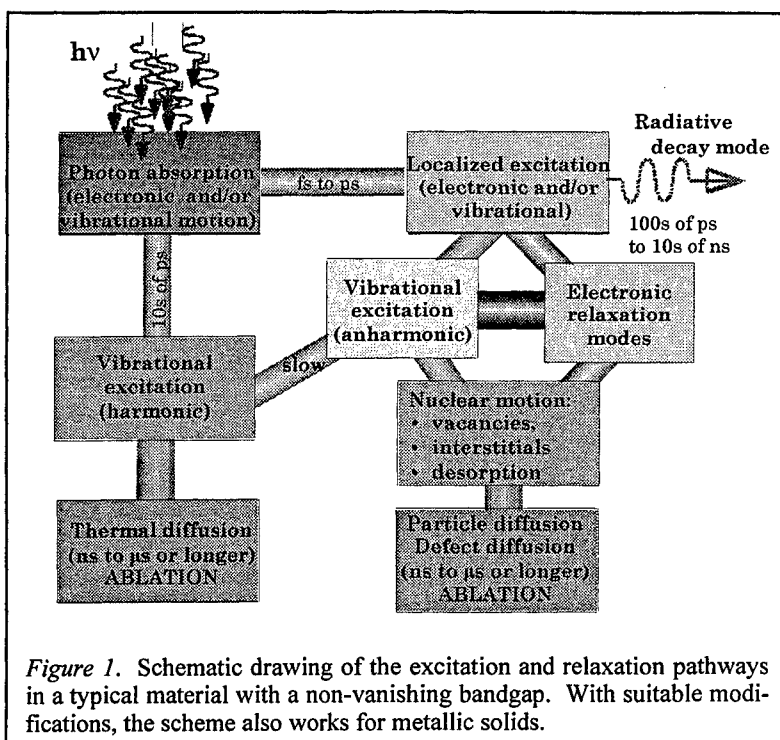


Figure 1. Schematic drawing of the excitation and relaxation pathways in a typical material with a non-vanishing bandgap. With suitable modifications, the scheme also works for metallic solids.

- (1) Conversion of electronic energy to harmonic, vibrational energy by electron-phonon scattering;
- (2) Conversion of electronic excitation energy to configurational energy;
- (3) Conversion of electronic energy from one configuration coordinate to another; and
- (4) Conversion of localized, anharmonic vibrational energy to delocalized, harmonic vibrational energy (heat).

If the localization condition is satisfied, any of these processes may lead to desorption or ablation; however, if localization does not occur at the surface, other radiationless relaxation processes may simply return the system to its ground state. In the case of vibrational excitation, the resonant, anharmonic modes may couple either slowly or rapidly to the harmonic vibrational modes which constitute the phonon bath states.

The first of these processes is the only mechanism relevant to electronic relaxation in metals, except in excitation of surface plasmons or small metallic clusters; it also plays a critical role in laser-excited semiconductors. An electronic excitation in an ionic insulator generally takes the form of creating a hole on the anion; if that excitation leads to the creation of an exciton, electronic excitation energy is converted into *configurational energy* of the exciton, and the evolution of such a new configuration is followed on a *reaction coordinate*. That configurational energy can be used to produce a new configuration; for example, an exciton might be converted into a vacancy-interstitial defect pair. Finally, it is also possible for vibrational energy in one degree of freedom, such as vibration in a particular bond, to be converted into a different vibrational mode. It is this process which we want to explicate in the ensuing paragraphs.

3.2. Ablation dynamics in CaCO_3

Molecular and organic crystals have strong vibrational absorption bands which can be excited without ever leaving the electronic ground state. We have found that picosecond laser pulses tuned to the resonant frequency of these infrared-active bands can produce extremely efficient, yet simultaneously gentle, ablation and material removal in such molecular crystals as carbonates and nitrates.

As a model materials system, we consider ablation in the molecular crystal calcium carbonate. Calcium carbonate and its isoelectronic cousin sodium nitrate, have infrared-active vibrational bands around $7\text{ }\mu\text{m}$ wavelength. Calcite, the crystalline form of calcium carbonate (CaCO_3), occurs naturally in the mineral form used in these experiments. It is a widely used optical material and is a basic unit of biominerals and hard tissues. Each CO_3 group forms a triangular cluster whose plane is perpendicular to the optic axis, making the crystal anisotropic and birefringent. Calcium carbonate is transparent in the visible, but has an OH absorption peak near $3.3\text{ }\mu\text{m}$, which is probably due to waters of hydration, and an absorption peak near $7\text{ }\mu\text{m}$ arising from the overlapping asymmetric stretching modes of the carbonate group. Cleaved calcite is a rhombohedron, in which the optic axis makes equal angles with each face (45.5°). Samples were cleaved from a natural but optically clear single crystals (Edmund Scientific, Barrington, NJ) and irradiated without further preparation, either in air or in vacuum.

When one irradiates these crystals at fluences of a few $\text{J}\cdot\text{cm}^{-2}$, one observes striking differences in the ablation phenomenology, depending on whether is on or off the vibrational resonance, *even for the FEL's train of ultrashort pulses*, as illustrated in Figure 2. Figure 2 (top) shows a scanning electron micrograph of a calcite surface irradiated by a single FEL laser pulse at $\lambda = 3.2\text{ }\mu\text{m}$, well off the resonant wavelength. The surface morphology of the ablation crater bespeaks an explosive thermomechanical event, probably initiated at a defect. The debris from the ablation event typically has the appearance of microcrystallites with the same rhombohedral structure as the parent CaCO_3 crystal. Irradiation under vacuum near the resonant wavelength of the calcite at $7.0\text{ }\mu\text{m}$, in contrast, produces the

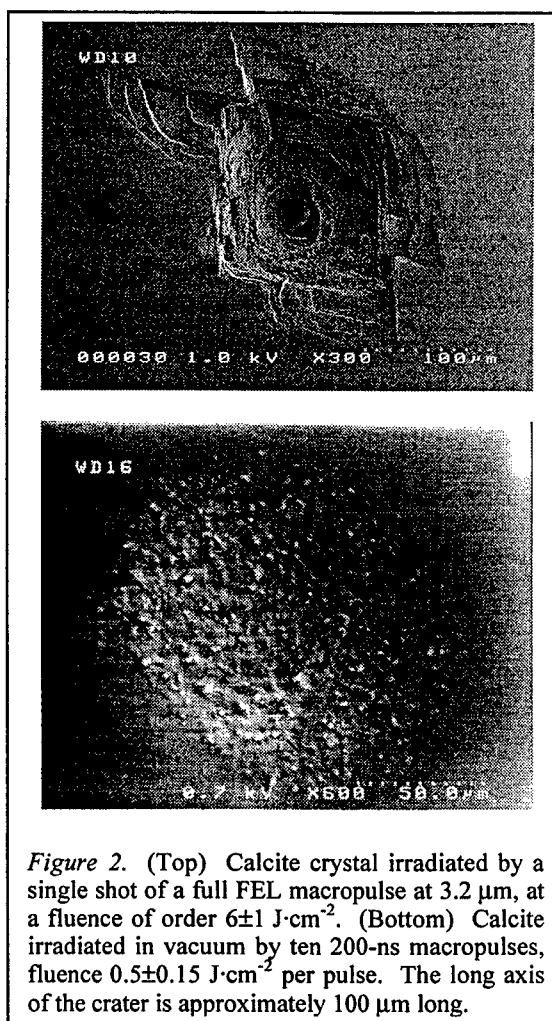


Figure 2. (Top) Calcite crystal irradiated by a single shot of a full FEL macropulse at $3.2\text{ }\mu\text{m}$, at a fluence of order $6\pm 1\text{ J}\cdot\text{cm}^{-2}$. (Bottom) Calcite irradiated in vacuum by ten 200-ns macropulses, fluence $0.5\pm 0.15\text{ J}\cdot\text{cm}^{-2}$ per pulse. The long axis of the crater is approximately $100\text{ }\mu\text{m}$ long.

result shown in Figure 2 (bottom). There is a smooth ablation crater, somewhat deeper at the center where the beam intensity is highest. If one scans the crater with an atomic-force microscope in tapping mode, the spherical pebbles in the ablation crater are loosely attached to the surface, easily moved about by the AFM tip. This suggests that these crystalline fragments have in fact been melted, and undergone a phase transition due to the strong laser absorption.⁵

As we have shown elsewhere⁶ using a surface-plasmon-resonance detector to measure the shock waves produced by calcite ablation in air, ablation off the vibrational resonance produces a nearly spherical shock wave, while ablation on resonance yields nearly planar shock waves. The apparently less explosive, more nearly planar material removal indicated by the lowest curve in the case of 7.0 μm irradiation of calcite is consistent with scanning electron microscopy and the emission spectra of the plasma plume. In this regard, the shock front produced by FEL front-side ablation with ultrashort pulses resembles the rear-side ablation seen in irradiation of calcite by Nd:YAG lasers (1064 nm), while the off-resonance FEL ablation more nearly resembles the front-side ablation of calcite by the ns Nd:YAG laser.⁷ This indicates that both wavelength and pulse duration, not pulse duration alone, can have a strong effect on the laser-surface interaction. Since no electronic excitation is involved here, it also indicates that the key difference in the ablation phenomenology must have something to do with the transfer of vibrational energy between the initial anharmonic excitation and the harmonic phonon modes ("bath states"). The dynamics involved in this process is the critical physics issue to be resolved in laser-surface interactions in the mid-infrared.

Relatively little is known about the dynamics of these energy-transfer processes. To measure the relaxation time for resonant vibrational excitation in calcite, we used a standard delay-line configuration to separate out a small fraction of the FEL macropulse, and measured the reflectivity of calcite in air as a function of the delay between this weak probe beam and the remaining pump beam of the FEL. Figure 3 shows the reflectivity as a function of pump-probe delay time for a calcite sample, again measured in air, at a wavelength of 7.1 μm . The strong peak at the center is the autocorrelation peak; if one assumes a Gaussian pulse, the measured pulse width should be divided by a factor of $\sqrt{2}$ in order to obtain the true width. This result gives a 0.9 ps pulse duration for the FEL pulse. The long tail, or slow relaxation time, of this pulse is probably due to the fact that there is a thermal buildup as each successive micropulse strikes the target; since the measurement was carried out with the full FEL macropulse, a considerable thermal background can build over a few microseconds. As one might expect, the measured relaxation time for the reflectivity, presumably mirrored in the optical absorption, is on the order of 8-10 ps. This time scale is consistent with the few extant measurements of vibrational relaxation times primarily for chromophores in liquids, as we shall discuss in Section 4; however, the measurement may mix several different relaxation processes.

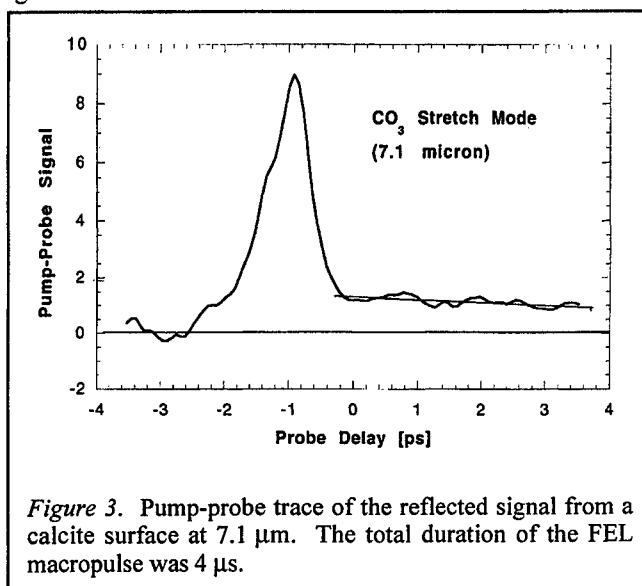


Figure 3. Pump-probe trace of the reflected signal from a calcite surface at 7.1 μm . The total duration of the FEL macropulse was 4 μs .

In summary, our studies of mid-infrared laser ablation show that vibrationally resonant excitation of solids built up from molecular crystal groups produces significantly lower energy deposition thresholds and reduced energy going into shock waves and other unproductive interactions with the materials. Ion emission spectra from calcium carbonate on and off the vibrational resonance likewise indicate that much less energy is going into highly excited atomic and ionic systems than is observed with ultraviolet, visible or near-infrared lasers. We believe this is because much more of the absorbed light goes into strong vibrational excitation and less into gas-phase excitation in the laser plume.

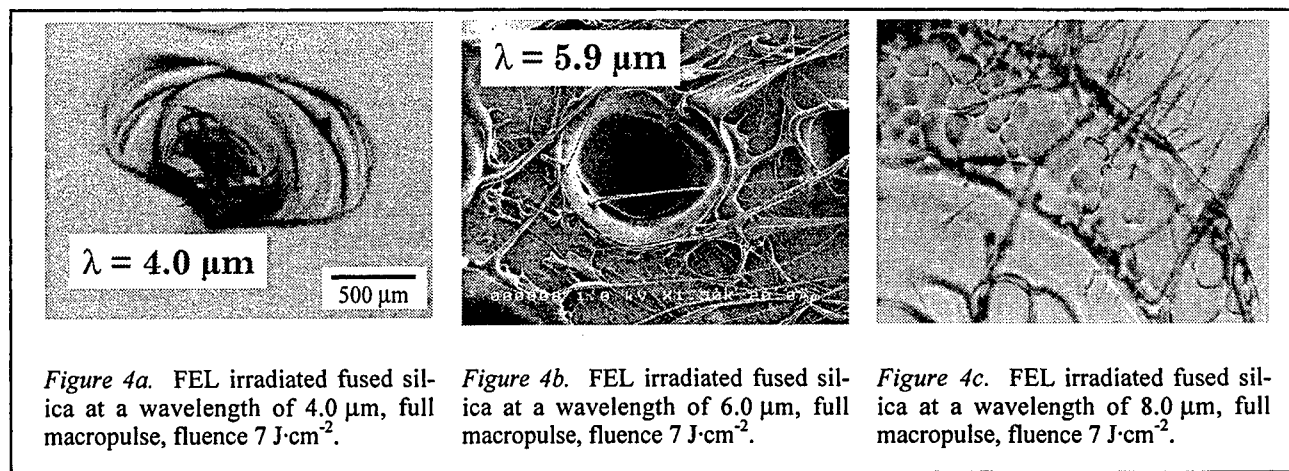
3.3 Surface modification of fused silica

Some of the most important possibilities for surface modification with ultrashort-pulse lasers arise because, once the laser pulse becomes comparable to or less than thermal diffusion times in a given material, modification can become practically independent of thermal effects. In our studies of surface modifications to dielectrics using the free-electron laser, we have observed such features as reproducible micron-size surface dents or protrusions, laser-induced transitions to polymorphic phases, and even the creation of a flexible glass "wool" with sub-100-nm-diameter fibers.

The utility of being able to separately determine absorption depth and total laser energy deposited in the material has recently been exploited in experiments using the Vanderbilt FEL, the former by changing wavelength and the latter by controlling the length of the FEL macropulse. This degree of control has made it possible to study the complex hydrodynamics

resulting from ultrafast melting and quenching of insulators. In the experiments reported here, we used silica glass as a model material. The experiments were conducted using commercial, uv-grade fused silica samples (ESCO, Oak Ridge, New Jersey, USA) as purchased without further treatment. Surface-modification experiments in the wavelength range from 3 to 9 μm were carried out in air using the FEL. The fluence in each case was calculated from the focal-spot size measured by scanning electron micrographs of the sample surface after single-macropulse irradiation. The absorption spectrum for fused silica exhibits a broad absorption band which begins around 4.0 μm ; it is due to the Si-O stretch, and peaks at around 9.6 μm , after rising through almost five orders of magnitude.⁸

At wavelengths in the range from 1 to 5 μm , far from the Si-O stretching vibration the dominant absorption mechanism in wide bandgap materials such as fused silica results from the excitation of harmonic vibrations (heat); in this regime, the thermal diffusion length is much less than the optical absorption depth. The low spatial density of absorbed laser energy causes thermomechanical fracture and subsurface boiling. Consequently, reproducible ablation craters were not obtained at these wavelengths, as in previous studies of laser ablation of calcite in the same wavelength region. However, unlike the calcite where fracture is nearly localized in the laser irradiated area due to the brittleness of the material and the presence of cleavage planes, in case of fused silica large pieces exceeding the laser spot diameter in size are cleaved off the surface, pro-



ducing ablation craters of random shape (Fig. 4a).

As the FEL wavelength is varied in the range from 6 to 9 μm , resonant, vibrational excitation of the Si-O stretching mode increasingly becomes the dominant absorption mechanism and the shorter absorption depth and greater volumetric deposition of laser energy causes surface melting of fused silica, as seen in the smaller features of the ablation craters in Figures 4b and 4c. At short macropulse durations, this leads to the confinement of the laser energy near the central focus of the laser spot, enabling the formation of microdimples [not shown here]. Inspection of these microdimples by scanning electron microscopy, optical microscopy, optical profilometry, and stylus profilometry reveals that the dimple walls are smooth and their dimensions are highly reproducible. All of these features are evidence for an efficient melting process without fracture. In addition, when laser irradiation occurs in air, one observes the formation of fine streamers or filaments which freeze as they are ejected into the atmosphere, forming fine wool-like structures loosely attached to the surface.

Figure 4 shows the results of laser irradiation of fused silica glass at wavelengths of 4.0, 5.9 and 8.0 μm , and a fluence of approximately 6 J·cm⁻², using the full FEL macro pulse duration of 4 μs . Melting and the development of filamentation is clearly evident at 6 μm . At still longer wavelengths, competition between diffusion and convection due to thermal gradient associated with the development of a vaporization front leads to the formation of a Kelvin-Helmholtz instability, a transition to mesoscopic self-organization over a length scale of many microns.⁹ The length scale of this instability is given by the most probable wave number of the hydrodynamic instability:

$$q_{\max} \approx \left[\frac{\alpha_0(1-R)N_0}{2\sigma\kappa} \cdot \frac{\Delta E_v(\infty)}{T_s} \right]^{1/3} \quad (3)$$

Moreover, the transition between the regime of fracture and the regime of melting, surface instability, filamentation and evaporation is more or less continuous, indicating that the issue in question is indeed the relative sizes of thermal diffusion

length and optical absorption depth in the material. Importantly, in this case, since the Si-O stretch is being pumped and it is the single bonding type available in the material, all of the energy deposited by the FEL goes through this channel.

The cause of all this disparate phenomenology is that, as wavelength increases toward the absorption maximum at 9.6 μm , the absorption length becomes comparable to the diffusion depth. The thermal conductivity of fused silica is sufficiently poor that one can assume that there is negligible diffusion on the time scale of the inter-micropulse spacing (approximately 350 ps). Hence, for a laser macropulse duration of 4.0 μs the thermal diffusion length is

$$\mu = \sqrt{D \cdot \tau_{\text{laser}}} = \sqrt{\left(\frac{\kappa}{\rho C_p} \right) \tau_{\text{laser}}} \approx 1.8 \mu\text{m} \quad (2)$$

where D is the thermal diffusivity; $\kappa = 1.38 \text{ W} \cdot \text{m}^{-1} \cdot \text{K}^{-1}$ is the thermal diffusion coefficient; $\rho = 2200 \text{ kg} \cdot \text{m}^{-3}$ is the density; and $C_p = 728.4 \text{ J} \cdot \text{kg}^{-1} \cdot \text{K}^{-1}$ is the heat capacity at constant pressure for fused silica.⁽⁷⁾ Hence, the thermal diffusion length ($\sim 1.8 \mu\text{m}$) is of the same order of magnitude as the optical absorption depth ($\sim 2 \mu\text{m}$) around 8 μm . At these wavelengths, surface vaporization and melting are extremely efficient.

Although similar hydrodynamic effects have been observed in the ablation of metal and semiconductor surfaces, this is apparently the first time it has been carried out using dielectric surfaces. This effect is only observable because of the unique characteristics of the free-electron laser as a tunable, mid-infrared, ultrafast-pulse light source with controllable macropulse duration. Changing wavelength makes it possible to control the relative magnitudes of absorption depth and thermal diffusion depth — *i.e.*, to control the degree of thermal confinement — while changing the macropulse duration varies the fluence in the absorption volume, and thereby controls the specific energy deposition.

3.4 Infrared Matrix-Assisted Laser-Induced Desorption and Ionization

Along with electrospray ionization, matrix-assisted laser desorption-ionization (MALDI) mass spectrometry (MS) is becoming the most widely used technique for mass analysis of large biological molecules.¹⁰ In a typical MALDI analysis, the analyte molecules are dispersed at low concentration ($\sim 10^{-4}$) in a liquid solution of a weak organic acid. When dried, this solution typically yields a thin film of microcrystallites, whose size and uniformity can be controlled by the conditions of crystallization. When irradiated in vacuum by an appropriate laser, the matrix disassembles and the entrained analyte molecules are ionized with relatively high efficiency. In spite of its relative simplicity, the technique is astonishingly powerful: proteins with masses in excess of 1 MDa have been measured, albeit it with only modest mass resolution; sensitivities in the attomole range are becoming routine.

Most MALDI mass spectrometers use ultraviolet lasers and aromatic matrix crystals, in which desorption and ionization are triggered by $\pi\text{-}\pi^*$ transitions in the ultraviolet. In UV-MALDI, the matrix is believed to isolate the analyte thermomechanically during the desorption and ionization process, and to provide the charged particles to cationize or protonate the ejected analyte molecules. However, even though the mechanism of UV desorption and ionization is understood in a qualitative way, details are still sketchy. In principle any aromatic matrix should work, but in practice, fewer than a dozen “good” matrix materials are in routine use, in part because the correlation between matrix properties and MALDI mechanisms is poorly understood.

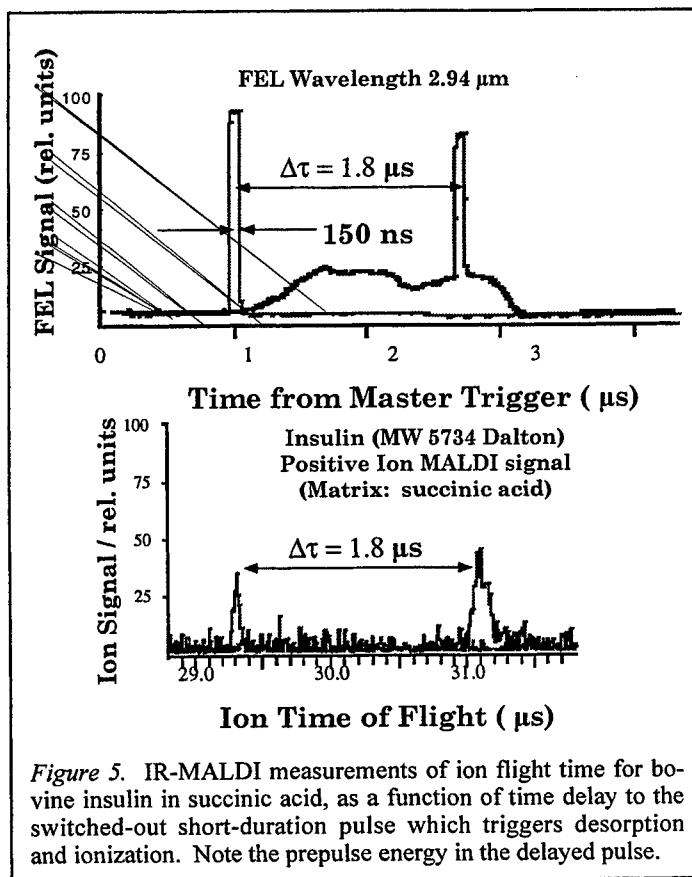


Figure 5. IR-MALDI measurements of ion flight time for bovine insulin in succinic acid, as a function of time delay to the switched-out short-duration pulse which triggers desorption and ionization. Note the prepulse energy in the delayed pulse.

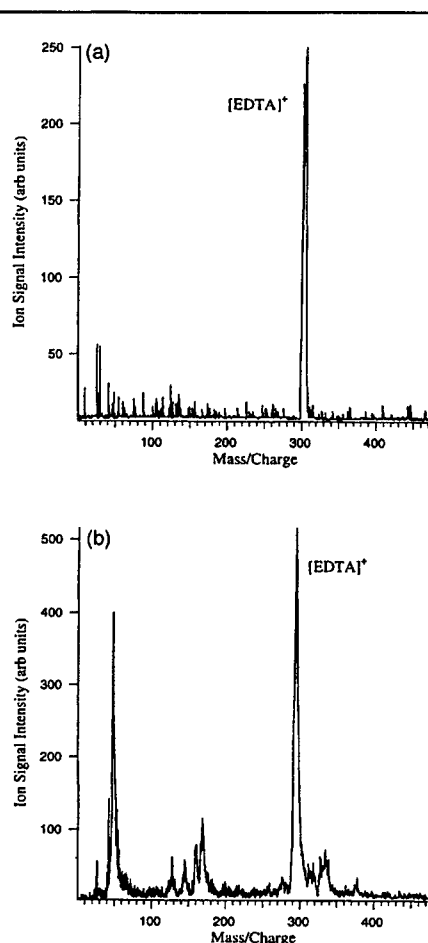


Figure 6. Comparison mass spectra of EDTA⁺ in a succinic acid matrix for FEL irradiation at 2.94 μm (a) and Er:YAG laser-induced desorption and ionization at much higher fluence (b).

the FEL macropulse-micropulse structure which makes it possible to do this.

Another question relevant to the role of irradiance in the mechanism of desorption and ionization is whether the use of a nanosecond laser vs a picosecond laser makes any difference to the mass spectra. In another experiment, the chelating agent EDTA was prepared in the standard way in a succinic acid matrix and irradiated by the FEL at 2.94 μm, near the stretching vibration of the OH group in water, using both the FEL and using the Q-switched pulse from an Er:YAG laser.¹¹ The two mass spectra obtained for the EDTA are shown in Figure 6. Note the virtual absence of background signal and the much better mass spectrum obtained with the picosecond irradiation from the FEL. Moreover, although the peak irradiance in the two cases is essentially identical, the fluence required in the FEL experiment is nearly 10³ times smaller than that required to desorb and ionize EDTA using the nanosecond Er:YAG laser, with a corresponding increase in the amount of MALDI sample used up on each laser shot. This direct comparison suggests that the ultrashort pulses of the FEL in fact have an important and beneficial effect on desorption and ionization of this small molecule from its microcrystalline host.

This apparent dependence on irradiance or intensity rather than on fluence is perfectly understandable if we recall that the quantum-mechanical transition probability for any event triggered by an optical excitation with intensity I takes the form

$$\frac{dN}{dt} = \eta N_o \sigma_{(n)} I^n \quad (4)$$

In contrast, many potentially desirable matrix materials have richly structured mid-infrared absorption bands which have been shown to be suitable for IR-MALDI. For example, succinic acid, an aliphatic open-chain carboxylic acid employed successfully in IR-MALDI, exhibits a richly structured mid-infrared spectrum, with significant absorption bands on the O-H, C-H, C-O and C-N stretching modes. Moreover, liquid matrices with nearly neutral pH , such as glycerol — which would be very desirable for many biochemical analyses — do not generally work in UV-MALDI. Were it not for the scarcity of appropriate infrared laser sources, the spectral richness of the vibrational infrared region would surely make IR-MALDI appear an exciting and versatile analytical technique.

The question of the ion generation mechanism is central not only for MALDI, but also for materials modifications in which it is desirable to take advantage of ions to, for example, deliver additional energy in thin-film growth. We have carried out an experiment which shows quite clearly that the ionization mechanism for ultrashort, mid-infrared pulses is intensity-dependent. Bovine insulin (mass 5,287 Da) was prepared in a succinic acid matrix according to the standard recipe. The Pockels cell was set to switch out a 150-ns slice of the FEL macropulse near the onset of the pulse, approximately 1 μs after the time “zero” determined by the RF trigger signal sent out by the FEL master clock. The position of the insulin peak was then recorded in the time-of-flight spectrum, in this case, occurring at 29.3 μs after the zero time. The polarizers in the Pockels cell were then reoriented to permit the formation of a pre-pulse lasting about 2 μs and containing approximately five times the energy as the switched out 150-ns pulse; at the end of this period, the Pockels cell voltage was switched on to produce a 150-ns pulse at a time 1.8 μs later in the macropulse. Figure 5 on the preceding page shows the results of the experiment: in both cases, the insulin ion appears in the time-of-flight spectrum only when the high-intensity, 150 ns pulse is switched out. Although the time-of-flight spectrum is slightly broadened compared to the case in which there is no prepulse, there is no hint of a leakage of insulin ions caused by the extended, high-energy prepulse. This we interpret to mean that the ionization event is controlled by IR intensity, not by fluence, which was much higher during the prepulse. It should also be noted that such an experiment is hardly possible with conventional lasers; it is clearly the unique properties of

where η is a quantum efficiency, dN/dt is the transition probability, N_0 is the number of absorbing species per unit volume, $\sigma_{(n)}$ is the n -photon cross section for the event in question, and I is the laser intensity. This basic principle suggests that the fluence plays a dominant role primarily because of thermal or diffusive processes occurring during nanosecond laser pulses.

4.0 MECHANISMS OF ENERGY TRANSFER

Surface modification using visible or ultraviolet lasers usually is initiated by an electronic excitation which leads to alterations in the electronic structure of the constituent atoms, mesoscale movement of atoms or defects (that is, nuclear motion), or both. To understand the dynamics of these processes, consider the schematic in Figure 1. Depending on laser wavelength, electronic or vibrational transitions are excited, creating excited states which are initially quite localized and highly anharmonic. As these initial excitations are relaxed, the high-frequency vibrations gradually couple to the low-frequency phonon bath states, leading to a thermal equilibrium. With ultrashort pulses in the vibrational infrared, as with the picosecond pulse structure of the FEL, we suggest that it is possible in many cases to initiate these modifications without going through an initial stage of electronic excitation.

To understand how this conjecture might apply to the surface-modification phenomena observed in our mid-infrared experiments, it is appropriate to consider both the materials and laser properties that bear on the interaction. There are two keys to the interaction physics. First, the fact that an ultrashort laser pulse can deposit energy on a time scale which is comparable to the vibrational frequencies of the solid; second, that the bandwidth of an ultrashort pulse makes possible multiphoton and/or multiple-photon vibrational transitions even where the anharmonicity of the potential is substantial. In addition, the thermal and optical properties of the material will play a significant role by determining the relationship between absorption depth and thermal diffusion length.

In the case of the molecular crystals, such as CaCO_3 , the energy absorbed from the laser as delivered to a resonant mode near $7\text{ }\mu\text{m}$ is dissipated both by vibrational relaxation to the surrounding molecular groups, and by diffusion to the phonon "bath" of the solid. For any given temperature T , the Debye frequency is a good benchmark of the highest phonon frequencies which are effective in the thermal diffusion process. At room temperature, this frequency is

$$\nu_{\text{Debye}} = \frac{k_B T}{h} \sim 6 \cdot 10^{12} \text{ Hz} \quad (5)$$

This is substantially lower in frequency than the asymmetric carbonate stretch vibration excited by the laser light (200 cm^{-1} vis á vis 1400 cm^{-1}), and therefore it couples weakly, hence relatively slowly, to the phonon "bath" states.

In the specific case of the FEL excitation around the $7\text{ }\mu\text{m}$ band ($\sim 1400\text{ cm}^{-1}$), there is competition between the localized anharmonic vibrational relaxation mechanisms in the carbonate or nitrate groups and the delocalized harmonic vibrations in the phonon spectrum. There are nine normal modes in the carbonate group which are either infrared- or Raman-active.¹² To illustrate the relative densities of these levels, Figure 8 shows the resonant and non-resonant modes at $7.1\text{ }\mu\text{m}$. These levels were calculated assuming Morse potentials and equal binding energies for all modes. On the basis of these energy-level densities, energy deposited in the asymmetric stretch is much more likely to couple to other vibrational modes of the carbonate group than to the non-resonant modes of the phonon bath.

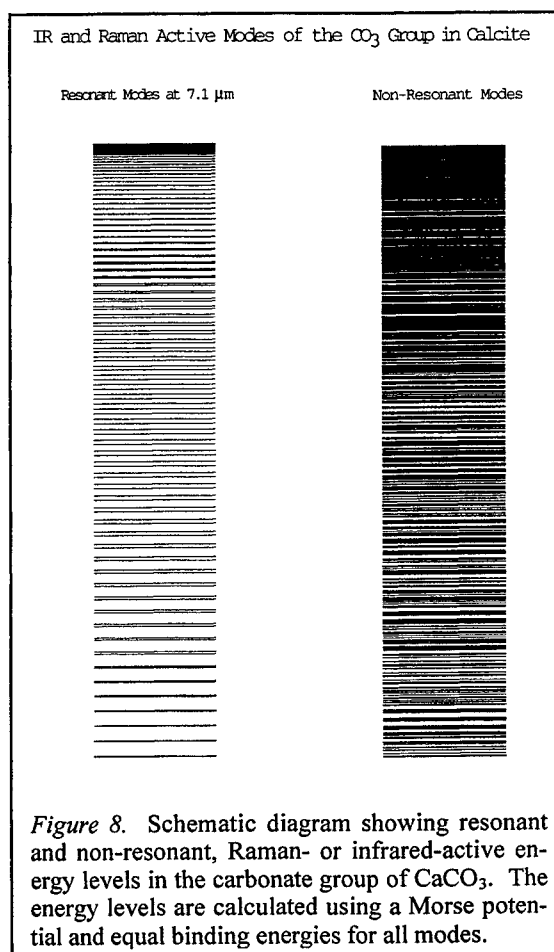


Figure 8. Schematic diagram showing resonant and non-resonant, Raman- or infrared-active energy levels in the carbonate group of CaCO_3 . The energy levels are calculated using a Morse potential and equal binding energies for all modes.

Vibrational relaxation times are not very well known in the mid-infrared, but the handful of measurements which have been performed provide a very broad range of plausible values. Relaxation times of CO bound to heme protein are between 10 and 50 ps.¹³ For the CO stretch of Cr(CO)₆ and W(CO)₆ dissolved in carbon tetrachloride and chloroform, the vibrational relaxation times were between 300 and 800 ps.¹⁴ The measurements shown in Section 3.2 suggest a relaxation time of order 10 ps, although this time may not represent a true thermalization time. Since there are other infrared-active modes with energies near 1400 cm⁻¹, the measured times may represent a combination of intramode relaxation to the other resonant frequencies and intermode relaxation to the thermal bath states. Therefore, we can reasonably guess that the carbonate group makes something like 10³-10⁴ vibrations before it equilibrates to the surrounding thermal environment of the crystal.

Thus the energy in the highly excited carbonate group, even though the excitation is vibrational in character, does not yet constitute fully equilibrated thermal energy. Because of the large frequency mismatch between the resonant and Debye frequencies, the only coupling can be through the anharmonicity of the potential generated by the driving electromagnetic field. This anharmonicity can be substantially increased by using the ultrashort pulses of the FEL, which can drive the carbonate molecular vibration "up the vibrational ladder" even when the potential is quite anharmonic, thanks to the large bandwidth of the picosecond FEL micropulses (as much as ~20 cm⁻¹).

For small perturbations of a quantum anharmonic oscillator (QAHO), the well-known result of closer spaced energy levels as the number of vibrational quanta increases makes so called "ladder climbing" very difficult given the narrow bandwidth of typical nanosecond lasers. However at some higher intensity, this can no longer be the case; moreover, for ultrashort pulses such as the micropulses of the FEL, the bandwidth is large enough to compensate for anharmonicity. Examining classical solutions to the driven AHO should then give a general idea about the behavior of the QAHO at high optical intensities. We are presently carrying out calculations based on the exact solution to the QAHO, including the effects of finite bandwidth. However, even an inspection of the energy spectra of the resonant and non-resonant states of the QAHO can give an idea about energy transfer possibilities between the two kinds of states.

Resonant optical pumping of a strongly absorbing vibrational mode leads to the deposition of energy in a very small volume of material. The absorption depth of CaCO₃ at the asymmetric stretch is approximately 100 nm.¹⁵ This value was calculated from the density of absorbers in calcite at 7.1 μm and assumes a typical vibrational cross section of 10⁻¹⁸ cm². Taking into account the reflectivity of calcite (~50% at 7.1 μm), assuming an absorption depth of 100 nm and a spot diameter of 100 μm, a single 2 μJ FEL micropulse deposits an average of 1.76 quanta of vibrational energy into every carbonate group in the absorption volume (7.1·10⁻¹⁶ m³), or 0.3 eV per group. Near the surface, the occupation is roughly twice the average. Given the vibrational relaxation time and the spacing of the FEL micropulses, we are not depositing enough energy into the CO bond to break it. However, if the energy of narrow-pulse, high-bandwidth lasers can be increased, a completely different regime of laser ablation might be reached.

To increase the temperature of the absorption volume from 300 K to 1240 K requires 2.6 μJ. Since the thermal diffusion time for an insulator such as CaCO₃ is much longer than the interval between micropulses (~350 ps), the FEL is capable of rapidly heating the absorption volume to very high temperature in a few micropulses.

CaCO₃ decomposes by sublimation into CaO_(s) and CO_{2(g)} at approximately 1000 K (T_{dec}) instead of melting. Decomposition of calcite in vacuum at T_{dec} results in a porous layer of CaO with a volume equal to that of the original sample.¹⁶ However, evidence of ejected molten CaCO₃ droplets during ablation at 7.1 μm has been observed.¹⁷ Furthermore, ablation craters produced in vacuum (Figure 2) are relatively smooth and do not show significant retention of solid CaO on the surface. Tapping-mode atomic-force microscopy (TMAFM) indicates that the particles at the bottom of the crater in Figure 2 are loosely attached, as they are easily moved about by scanning the tip over them. We presume that they are either CaO or solidified droplets of CaCO₃. Regardless, the morphology of the crater is not consistent with what is expected from the normal thermal decomposition of calcite. This anomaly indicates that the calcite reaches a temperature sufficiently higher than T_{dec} before the sublimation reaction can take place. There is also no evidence of melting in Figure 2 — as there is with the fused silica — and very little debris is visible at the rim or outside of the crater. In previous work, the shock wave produced by ablation of calcite at 7.1 μm was shown to be nearly planar, in contrast to off-resonance ablation which had a more nearly spherical character.¹⁸

The evidence points to an ablation mechanism that involves rapid heating and is not consistent with simple melting or decomposition of calcite. Molecular dynamics simulations by Zhigilei *et al.* Of the ablation of solids by energy deposited into vibrational modes shows the ejection of material by an explosive process; the ablation products are a mixture of vapor, liquid and solid particles.¹⁹ An explosive mechanism for the ablation of metal is described by Martynyuk,²⁰ A related process called *phase explosion* or *explosive boiling* has been described by Kelly.²¹ This mechanism involves rapid heating to a critical temperature T_{tc} at which the internal pressure is greater than the tensile strength of the material. This mechanism is apparently consistent with what we have seen during the ablation of calcite. Calcite ablation, as observed experimentally, involves the ejection of solid, liquid and vapor. Rapid heating is made possible by the high power and tunability of the FEL,

as well as by control of the fluence which is achieved by shortening or lengthening the FEL macropulse. Further work, such as characterizing the plume gas dynamics, measuring velocity distributions, and determining ablation threshold, will be necessary to confirm that the phase explosion is in fact the primary mechanism responsible for ablation calcite at the 7.1 μm vibrational resonance.

5. SUMMARY AND CONCLUSIONS

We have seen that the "molecular fingerprint" region of the mid-infrared spectrum, wavelength selectivity, laser ultrashort pulse duration, irradiance and fluence can all play distinctive roles in laser ablation, surface modification, and matrix-assisted desorption and ionization. These experiments, and the calculations of the energy deposition and relaxation which we have carried out, suggest several general conclusions

- For any given wavelength, shorter laser-pulse duration leads to greater deposition of energy in the material and less into the ablation plume and/or material heating.
- For ultrashort pulses, longer wavelengths produce greater energy deposition directly into vibrational degrees of freedom and rather less into diffusive and dissipative processes.
- Resonant excitation into selected electronic or vibrational degrees of freedom is more effective in surface modification than either nonlinear or non-resonant excitation.

Targeted mesoscale materials modification can then be achieved by having micropulse trains whose overall length governs total deposited energy and therefore the total volume of modified material.

An understanding of laser-surface interactions at the mesoscale is central to laser processing and analysis of complex materials, such as oxides, polymers and compounds semiconductors — the building blocks of smart structures and devices. The combination of ultrashort pulses, broad tunability and continuous or quasi-continuous pulse trains will make it possible to target specific materials modifications while minimizing unwanted collateral effects (e.g., thermomechanical damage, remnant debris, defect generation and plume ionization or excitation).

Beyond that, many potential technological applications in research, medicine and industry require sophisticated control of energy flow during laser-induced surface modifications. A major difficulty in most laser-surface processing or analysis using visible, near-infrared or ultraviolet laser is, that the energy goes initially into highly energetic electronic state, the generation of a plasma plume, or the creation of unwanted debris or, after electron-phonon coupling, collateral thermal damage. Many of these problems can be ameliorated or eliminated by the use of ultrashort pulse, high-duty-cycle lasers depositing energy in specific vibrational infrared bands. In principle, such lasers could facilitate higher production speed, reduced tool wear, greater ease in modifying processes, and reduced collateral damage. While the free-electron laser is probably too complex and expensive to become a routinely available light source for such work, the increasing availability of tunable mid-infrared femtosecond sources suggests that solid-state coherent sources may be able to do many of the same kinds of surface modifications as those reported here.

Ultrafast, high average-power, broadly tunable mid-infrared light sources, such as the free-electron laser, can help develop the basic scientific understanding needed for such a "designer" approach to materials modification and analysis. It cannot be emphasized too strongly that even in the mid-infrared, the blanket assumption that the laser-materials interaction can be characterized simply as "thermal." Even such simple questions as the relationship between strongly localized vibrational excitation and delocalized thermal excitation of a solid challenge our commonly held viewpoints about thermal vs non-thermal interactions of laser light with materials.

5. ACKNOWLEDGEMENTS

This work was supported by the Office of Naval Research under the Medical Free-Electron Laser program administered by the Office of Naval Research (Contract N00014-94-1-1023), and by the United States Department of Energy, Office of Science (Contract Grant Number DE-FG07-98ER62710).

6. REFERENCES

1. R. F. Haglund, Jr., "Mechanisms of Laser-Induced Desorption and Ablation," in *Laser Ablation and Desorption*, eds. J. C. Miller and R. F. Haglund, Jr. (Boston: Academic Press, 1998), pp. 15-138.
2. Hee K. Park and R. F. Haglund, Jr., "Laser Ablation and Desorption from Calcite from Ultraviolet to Mid-Infrared Wavelengths," *Appl. Phys. A* **64**, 431-438 (1997).
3. C. A. Brau, *Free-Electron Lasers* (New York: Academic Press, 1990). C. A. Brau, "Free-Electron Lasers," *Science* **239**, 115-1121 (1988).
4. G. S. Edwards, D. Evertson, W. Gabella, R. Grant, T. L. King, J. Kozub, M. Mendenhall, J. Shen, R. Shores, S. Storms and R. H. Traeger, "Free-Electron Lasers: Reliability, Performance, and Beam Delivery," *IEEE J. Sel. Top. Quantum Electron.* **2**, 810-817 (1996).
5. M. Alam, T. DebRoy and R. Roy, "Laser-Induced Calcite-Aragonite Transition," *J. Am. Ceram. Soc.* **73**, 733-735. (1990).
6. O. Yavas, E. L. Maddocks, M. R. Papantonakis and R. F. Haglund, Jr., "Planar and Spherical Shock-Wave Generation During Infrared Laser Ablation of Calcium Carbonate," *Appl. Surf. Sci.* **127-129**, 26-32 (1998).
7. O. Yavas, E. L. Maddocks, M. R. Papantonakis and R. F. Haglund, Jr., "Shock-Wave Generation During Rear- and Front-Side Ablation of Calcite," *Appl. Phys. Lett.* **71**, 1287-1289 (1997).
8. Edward D. Palik, *Optical Constants of Solids* (John Wiley,), p.
9. For detailed discussion of the origins of this instability, see D. Bäuerle, *Laser Processing and Chemistry*, 2nd Edition (Berlin: Springer Verlag, 1996), §28.4.
10. For a review and extensive bibliography, see J. A. Carroll and R. C. Beavis, "Matrix-Assisted Laser Desorption and Ionization," in *Laser Ablation and Desorption*, eds. J. C. Miller and R. F. Haglund, Jr. (Boston: Academic Press, 1998), pp. 413-448.
11. W. P. Hess, H. K. Park, O. Yavas and R. F. Haglund, Jr., "IR-MALDI of low molecular weight compounds using a free-electron laser," *Appl. Surf. Sci.* **127-129**, 235-241 (1998).
12. Gerhard Herzberg, *Infrared and Raman Spectra*, 1st Edition (New York: Van Nostrand-Reinhold, 1945).
13. J. R. Hill, D. D. Dlott, C. W. Rella, K. A. Peterson, S. M. Decatur, S. G. Boxer and M. D. Fayer, "Vibrational Dynamics of Carbon Monoxide at the Active Sites of Mutant Heme Proteins," *J. Phys. Chem.* **100**, 12100-12107 (1996).
14. A. Tokmakoff, B. Sauter and M. D. Fayer, "Temperature-dependent vibrational relaxation in polyatomic liquids: picosecond infrared pump-probe experiment," *J. Chem. Phys.* **100**, 9035-9043 (1996).
15. K. K. Kelley, *Contributions to the data on theoretical metallurgy: X. High-temperature heat content, heat capacity and entropy data for inorganic compounds*, (United States Department of the Interior, Washington, 1949).
16. D. Beruto, L. Barco and A. W. Searcy, "Rearrangement of Porous CaO Aggregates during Calcite Decomposition in Vacuum," *J. Am. Cer. Soc.* **66** (12), 893-896 (1983).
17. O. Yavas, unpublished results (1997).
18. O. Yavas, M. R. Papantonakis, E. L. Maddocks and R. F. Haglund, Jr., "Planar and spherical shock-wave generation during infrared laser ablation of calcium carbonate," *Appl. Surf. Sci.* **127-129**, 26-32 (1998).
19. L. V. Zhigilei, P. B. S. Kodali and B. J. Garrison, "Molecular Dynamics Model for Laser Ablation and Desorption of Organic Solids," *J. Phys. Chem. B* **101**, 2028-2037 (1998).
20. M. M. Martynyuk, "Mechanism for metal damage by intense electromagnetic radiation," *Sov. Phys. Tech. Phys.* **21** (4), 741-746 (1975).
21. R. Kelly and A. Miotello, "On the mechanisms of target modification by ion beams and laser pulses," *Nucl. Instrum. Meth. In Phys. Res.* **B122**, 374-400 (1997).

Material Processing of Dielectrics with Femtosecond Lasers

David Ashkenasi*, Arkadi Rosenfeld

Max-Born-Institut für Nichtlineare Optik und Kurzzeitspektroskopie, 12489 Berlin, Germany

ABSTRACT

Ultrashort laser pulses have considerable potential for micron and sub-micron structuring of several materials. The lower energy impact, the reduction of thermal damage, the elimination of laser-plume interaction, and the exploitation of nonlinear optical effects all contribute to a strong improvement when compared to results using pulse widths in the nanosecond range. Depending on the choice of fluence compared to the damage threshold, with ultra-short laser pulses one is able to generate different types of structures, minimizing the heat affected zone. The damage threshold drops dramatically during the first laser shots, due to defect incubation. This has important consequences for applications, such as laser machining and for the lifetime of optical components. At a fluence below surface damage threshold we were also able to generate bulk modifications of different size and location in a controllable fashion by variation of laser pulse width, energy and number of shots, utilizing the beam narrowing effects during self focusing. A study of the dependence of the structure depth on the square root of the laser power for a given pulse length provides a straightforward method for determining the non-linear index of refraction.

Keywords: Ultrashort laser pulses, transparent materials, ablation threshold behavior, surface micro-structuring, self-focusing, non-linear index of refraction, three-dimensional bulk objects.

1. INTRODUCTION

There is strong evidence that fs and ps laser pulses are advantageous for micron and sub-micron structuring of several (not necessarily all) materials for many applications¹⁻⁷. However, a broad introduction of ultrashort-pulse lasers for industrial manufacturing still suffers from the present complicated and costly arrangement of these systems. The development of new compact laser systems designed also for industrial needs and the advances made in material processing with ultrashort laser pulses (in many cases even under atmosphere conditions) will stimulate the use of the femtosecond technology outside research and development. In this paper we confine the discussion to the ultrashort-pulse laser-induced processing of transparent materials in a pulse width range from 100 fs to a few ps, where we see considerable potential for applications.

The quality and type of the laser-induced structures in wide band-gap transparent materials with ultra-short pulses in the near infra-red (i.e. 800 nm) depends strongly on the choice of the operating laser fluence F relative to the (varying) surface damage threshold level F_{th} ; or to be more precise: $F_{th}(N, \tau_p)$ as a function of laser shot number N and pulse duration τ_p . Investigations of the surface damage threshold under laser irradiation have been the subject of numerous studies over many years. Recently, the pulse duration dependence of laser induced damage on dielectrics for infrared laser pulses from the nanosecond to the sub-picosecond range have been outlined in several publications⁸⁻¹¹. However, one has to be very careful when comparing experimental threshold levels from different groups. There are severe differences in the criteria of defining surface damage threshold and in the techniques of determination. Stuart et al., for example, exposed their samples to 600 laser shots at many different fluence levels for a given pulse duration to identify the threshold value, which they defined as irreversible modification on the surface observable by a Normarski microscope⁸. There is no discussion as to what degree the number of laser shots between 1 and 600 change the threshold. This data is very important for applications, such as for estimating the lifetime of optical components and for laser processing. In a preliminary study we demonstrated that the single-shot damage thresholds for α -SiO₂ and CaF₂ in a pulse duration range of 0.2 to 5 ps are at least a factor of two higher¹⁰ than the multi-shot thresholds presented by Stuart et al.

* Correspondence: Email: ashke@mbi-berlin.de; WWW: <http://www.mbi-berlin.de>; Telephone: +49.30.63921214; Fax: +49.30.63921229

2. EXPERIMENT

The laser used in our experiments is a Ti:sapphire oscillator-amplifier system based on chirped pulse amplification. The linearly polarized laser pulses of a wavelength of 800 nm were focused by a quartz lens (focal length 25 and 75 mm) onto the sample surface. The experiments were carried out in rough vacuum (10^{-3} mbar). The repetition rate of irradiation on the sample was ca. 2 Hz at shot numbers $N = 1$ to 100, and 20 Hz for $N > 100$. The polished samples, α -SiO₂, Al₂O₃, CaF₂, MgF₂ and LiF, 10 mm in diameter and 2 mm thick, were mounted on a metal target holder such that the laser processed area was not backed. The sapphire and fluoride samples (UV-windows) were obtained from Crystal GmbH. We received the fused silica samples from Steeg & Reuter GmbH. The mean roughness of the samples, which were cleaned in an ultrasonic bath of acetone prior to mounting, was typically between 10 and 20 nm.

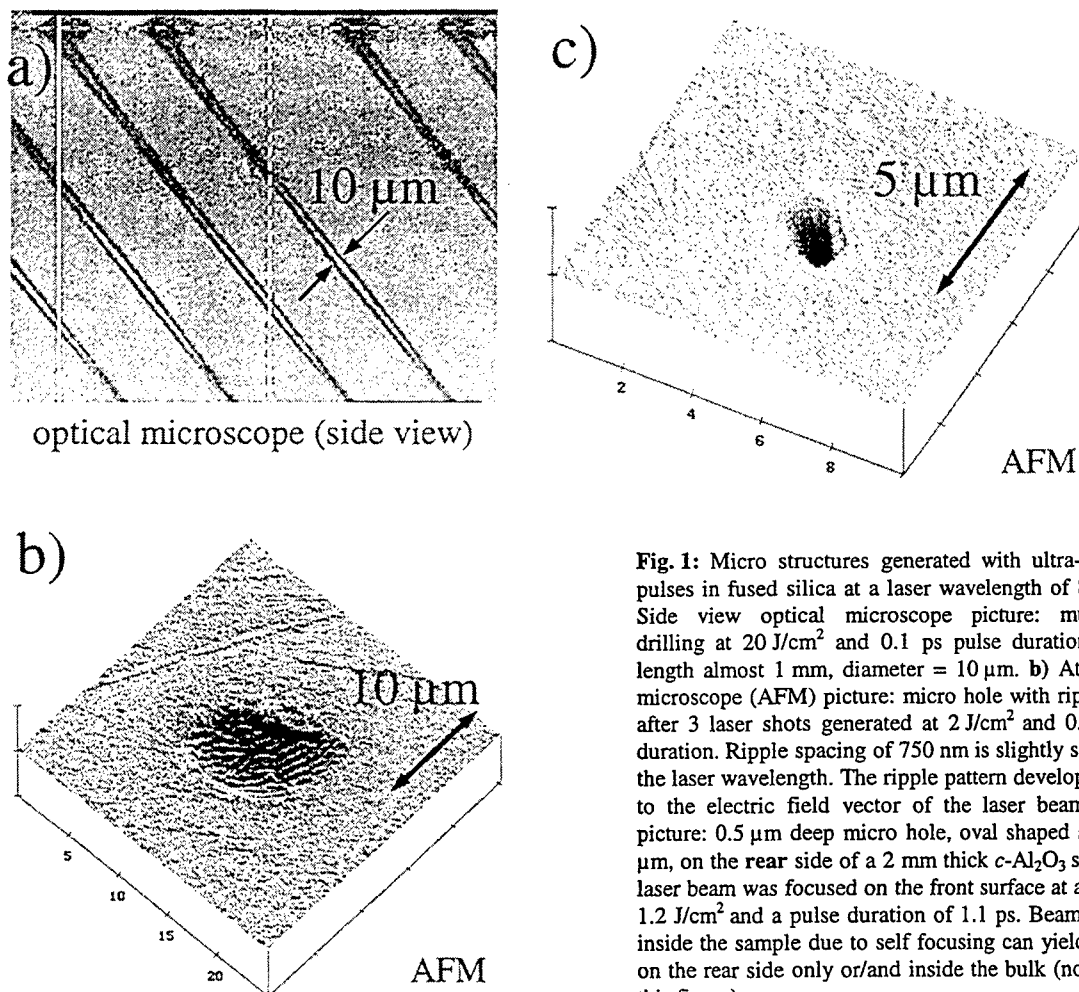


Fig. 1: Micro structures generated with ultra-short laser pulses in fused silica at a laser wavelength of 800 nm. a) Side view optical microscope picture: multiple-shot drilling at 20 J/cm² and 0.1 ps pulse duration. Channel length almost 1 mm, diameter = 10 μm. b) Atomic force microscope (AFM) picture: micro hole with ripple pattern after 3 laser shots generated at 2 J/cm² and 0.1 ps pulse duration. Ripple spacing of 750 nm is slightly smaller than the laser wavelength. The ripple pattern developed parallel to the electric field vector of the laser beam. c) AFM picture: 0.5 μm deep micro hole, oval shaped size of 1x2 μm, on the rear side of a 2 mm thick c -Al₂O₃ sample. The laser beam was focused on the front surface at a fluence of 1.2 J/cm² and a pulse duration of 1.1 ps. Beam narrowing inside the sample due to self focusing can yield structures on the rear side only or/and inside the bulk (not shown in this figure)

Our interest is in applying laser pulses of picosecond and sub-picosecond pulse duration and investigating material and pulse-width dependencies of the surface damage threshold for different number of laser shots N . On the basis of multiple-shot threshold studies for $N \leq 1000$ we should also be able to estimate the expected maximum lifetime of optical components for laser shot numbers of many magnitudes higher. The structuring of micro-pockets and grooves with depths of several μm will make multiple-shot processing on the same area of the surface necessary. Depending on the size and depth of the laser generated structure, N will range somewhere between 2 and several 1000 shots. Basically, the laser processing of dielectrics

with ultra-short pulses in the infrared can be divided into three major fluence regimes for the following applications¹²: 1. the high fluence regime, $F/F_{th} \gg 1$ to drill channels with a high aspect ratio²; 2. the intermediate fluence regime $F/F_{th} > 1$ to generate pockets and surface (periodic) patterns^{1,4}, and 3. the low fluence regime $F/F_{th} < 1$ to produce micro structures inside the sample or on the rear side^{5,6}. A few examples of recently generated micro structures in fused silica (α -SiO₂) and sapphire (c -Al₂O₃) are depicted in Fig. 1. Fig. 1a shows (side view perspective) thin channels drilled at an angle of approx. 40° using 100 fs laser pulses in the high fluence regime, Fig. 1b is an atomic force microscope picture of periodic structures with a spacing of 800 nm obtained also with 100 fs laser pulses the intermediate fluence regime, and finally Fig. 1c illustrates a micro hole generated on the rear side of the sample. The laser wavelength was around 800 nm and the laser diameter of the focused beam on the front surface ranged between 25 and 30 μ m. Note that all examples show little or no signs of stress induced modifications outside the processed region.

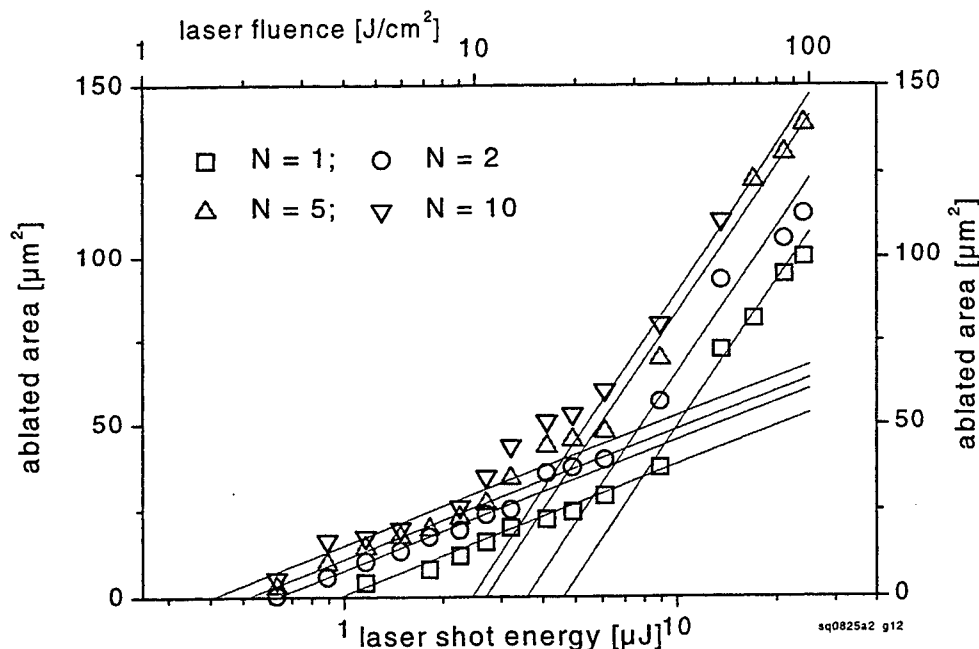


Fig. 2: Semi-logarithmic plot of the ablated area vs. laser energy (fluence) for α -SiO₂ for laser shot numbers of $N = 1, 2, 5$ and 10 at a wavelength of 800 nm and a pulse duration of 100 fs. Solid lines are linear fits in the fluence regime 1 to 20 J/cm² and in the fluence regime 20 to 100 J/cm², see text.

To determine the surface damage threshold at a given pulse duration and number of laser shots we used the following two step method: 1. We viewed the surface using optical Normarski and scanning electron microscopy to determine the fluence interval between the cases where no modification was observable and the (sudden) on-set of visible damage. 2. For several laser fluence levels above an obvious damage threshold we determined the ablated area. A semi logarithmic plot of the ablated area versus the fluence leads to a linear dependency^{11,13}, from which the ablation threshold can be estimated. These threshold levels were in all cases inside the uncertainty intervals determined in the first step. This is illustrated in Fig. 2, where the ablated area is plotted semi-logarithmically over the laser fluence for $N = 1, 2, 5$ and 10 laser shots. The laser spot size ($1/e^2$) on the surface was determined to be 25 μ m². The data does not follow the expected single linear dependency but rather two lines with different slopes. Therefore, the linear fit of the data in the fluence regime $F = 1$ to approx. 20 J/cm² was used to determine the surface damage threshold that identifies the minimal fluence level at which ablation starts. The origin of the second slope is still unclear. It is possible that the fluence of 20 J/cm² marks the transition from a gentle to a strong etch phase at low shot numbers. For c -Al₂O₃ the different etch phases can easily be discriminated without much doubt¹.

3. RESULTS AND DISCUSSION

3.1. Surface Processing

Fig. 3a illustrates the surface damage threshold in α -SiO₂ plotted semi-logarithmically over laser shot numbers N and determined at a pulse duration of 0.1 ps and two different focal spot sizes ($1/e^2$) on the surface: 25 and 450 μm^2 , depending on the focal length of the two lenses used in this study. Within the experimental uncertainty the fluence threshold levels are spot size independent. This behavior is expected for ultra-short laser pulses, since the energy deposition remains strongly localized, in contrast to ns laser pulses. During the first 50 laser pulses we obtain a dramatic 70 % decrease in damage threshold: $F_{th}(1; 0.1 \text{ ps}) = 3.7 \text{ J/cm}^2$ reduces to $F_{th}(50; 0.1 \text{ ps}) = 1.0 \text{ J/cm}^2$.

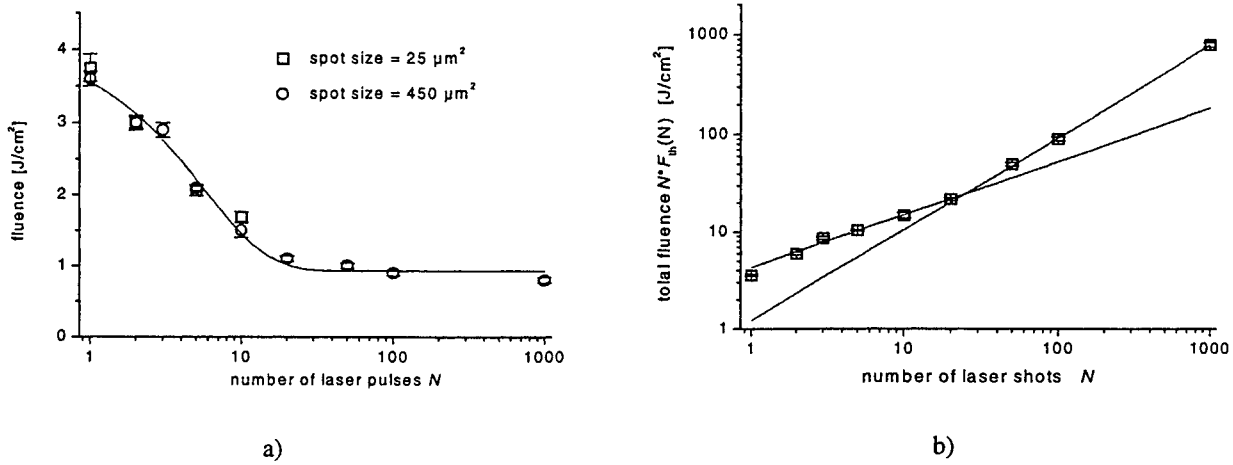


Fig. 3: a) Semi-logarithmic plot of the surface threshold versus shot numbers in fused silica determined at a laser wavelength of 800 nm and at a pulse duration of 0.1 ps. Solid line from fit following Eq. 1 yielding $F_{th}(1) = 3.6 \pm 0.2 \text{ J/cm}^2$, $F_{th}(\infty) = 0.9 \pm 0.2 \text{ J/cm}^2$ and $k = 0.18$. b) Double logarithmic plot of multi-shot damage threshold versus shot numbers. Solid lines are fits to the data following Eq. 2 with $S = 0.55$ and $F_{th}(1) = 3.6 \pm 0.2 \text{ J/cm}^2$ at $N \leq 20$ and $S = 0.95$ for $N > 20$.

Incubation effects in dielectric materials can be greatly influenced by the excitation and generation of conduction band electrons which will eventually lead to an accumulation of defect sites. The primary (resonantly enhanced) multi-photon excitation will lead to a production of electron-hole pairs on a sub-100 fs time-scale. These states have a lifetime between 150 fs and several ps¹⁴ before forming self-trapped excitons and Frenkel-pairs. A small fraction of these Frenkel-pairs may not recombine and stabilize to F -centers¹⁵, introducing additional energy levels and excitation routes for the next laser shot. The relative change in the laser-induced defect concentration will decrease with increasing shot numbers until finally reaching a point of saturation in the dielectric. The reduction in damage threshold is therefore less pronounced while going to higher shot numbers. In such a case, irradiation at a fluence below a minimum level would require an infinite numbers of pulses to initiate the defect accumulation and, hence, activate macroscopic damage. If we assume that the relative change $\Delta F_{th} = F_{th}(N, \tau_p) - F_{th}(N-1, \tau_p)$ is proportional to $F_{th}(N-1, \tau_p)$, N : laser shot numbers and τ_p : pulse duration, we can describe the laser shot number dependency of the surface damage threshold $F_{th}(N, \tau_p)$ in the following straightforward way¹⁶:

$$F_{th}(N, \tau_p) = F_{th}(\infty, \tau_p) + [F_{th}(1, \tau_p) - F_{th}(\infty, \tau_p)]e^{-k(N-1)} \quad (1)$$

Here, $F_{th}(1, \tau_p)$ is the single shot threshold and k characterizes the strength in the defect accumulation. The larger k is, the fewer laser shots are necessary to obtain a minimum damage threshold $F_{th}(\infty, \tau_p)$ at infinite number of laser shots. In Fig. 3a the solid line is the calculated curve obtained from the fit of the threshold behavior of α -SiO₂ based on Eq. 1.

Surface roughening related to the storage of thermal stress-strain energy can not be ruled out completely and may lead to an additional minor reduction in the damage threshold at very high shot numbers, as demonstrated in the surface damage investigations of Cu, Al, and GaAs with ns laser pulses^{17,18}. In this case, the total damage threshold $N \cdot F_{th}(N, \tau_p)$ can be described by the following equation¹⁷:

$$N \cdot F_{th}(N, \tau_p) = F_{th}(1, \tau_p) \cdot N^S \quad (2)$$

For a given pulse duration τ_p , $F_{th}(N, \tau_p)$ is the threshold level after N laser shots, $F_{th}(1, \tau_p)$ is the single shot damage threshold and S characterizes the degree of incubation causing the surface fatigue. The more S approaches 1, the less

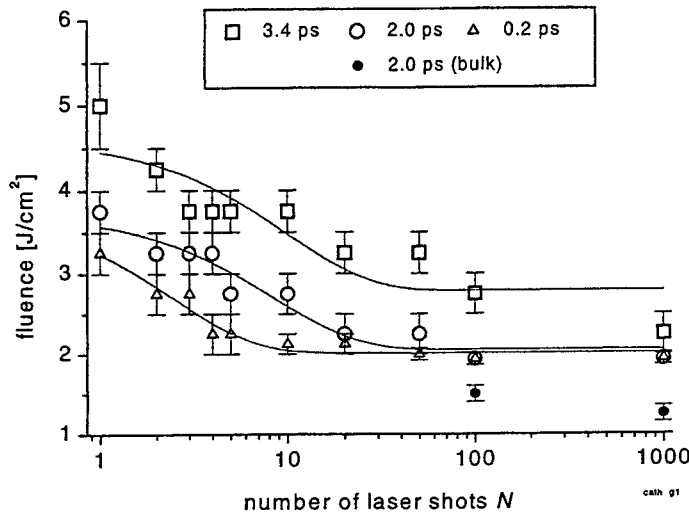


Fig. 4: Semi-logarithmic plot of the surface threshold versus shot numbers in CaF_2 determined at a laser wavelength of 800 nm and at a pulse duration of 0.2 ps, 2.0 ps and 3.4 ps. Solid line from fit following Eq. 1 yielding $F_{th}(1) = 4.5 \pm 0.5 \text{ J/cm}^2$, $F_{th}(\alpha) = 2.8 \pm 0.2 \text{ J/cm}^2$, $k = 0.10$ for 3.4 ps; $F_{th}(1) = 3.6 \pm 0.2 \text{ J/cm}^2$, $F_{th}(\alpha) = 2.0 \pm 0.1 \text{ J/cm}^2$, $k = 0.11$ for 2.0 ps; and $F_{th}(1) = 3.2 \pm 0.2 \text{ J/cm}^2$, $F_{th}(\alpha) = 2.0 \pm 0.1 \text{ J/cm}^2$, $k = 0.40$ for 0.2 ps.

important this accumulation effect will be. Basically, Eq. 2 was developed to explain laser-induced incubation effects in metals. In Fig. 3b the total damage threshold $N \cdot F_{th}(N, \tau_p)$ was plotted double logarithmically against N for $\alpha\text{-SiO}_2$. The data does not follow one single linear dependency but rather two lines with different slopes: $S = 0.70$ for $N \leq 20$ shots and then $S = 0.95$ for $N \geq 20$. The incubation is strongest during the first 20 laser shots. This is not seen in the case of metals¹⁷, where one linear fit with a slope S above 0.9 is totally sufficient to describe the shot number dependency of the threshold. However, for GaAs surfaces¹⁸, the character of incubation did seem to change, illustrated in the transition of $S = 0.7$ to $S > 0.9$ at laser shot numbers N above 10. This leads to the conclusion that the incubation effects in dielectrics based on a possible laser-induced storage of thermal stress-strain energy¹⁷ may actually lower the threshold only after very high number of laser shots. The laser induced accumulation of defect sites (F-centers) is the dominate effect for the strong reduction in the threshold observed for dielectrics, especially during the first laser shots.

Fig. 4 illustrates the surface damage threshold in CaF_2 for $N = 1$ to 1000 shots for three different pulse durations: 0.2, 2.3 and 3.3 ps. The focal spot size on the surface was $700 \mu\text{m}^2$ using the lens with a focal length of 75 mm. The shot number dependency of the surface damage threshold is different for each individual pulse duration. Again, the solid lines illustrate the calculated $F_{th}(N, \tau_p)$ based on the fit using Eq. 1 for each individual pulse duration τ_p . The accumulation parameter k increases with decreasing pulse duration, illustrating the intensity relevance of the saturation effect. Also included in Fig. 4 is the bulk damage threshold obtained at $N = 100$ and 1000 shots for $\tau_p = 2.0$ ps. For a high number of shots, typically in the picosecond pulse duration range, we observe sub-surface damage in most dielectric materials even before surface damage is obtained due to self-focusing of the laser beam in the bulk material. This effect can make the determination of $F_{th}(N > 100, \tau_p)$ in some cases difficult or can even lead to unexpected low surface damage threshold levels. This is probably true in the case of the surface damage threshold determined at 3.3 ps and $N = 1000$ laser shots in CaF_2 , shown in Fig. 4, which may have originated from a sub-surface region. As discussed in the next section, these pulses are short enough that the critical power of self focusing can be reached for laser fluence below the surface damage fluence. However, for even shorter laser pulses, it seems that other non linear effects counteract beam narrowing inside the Kerr media.

Fig. 5 shows two AFM-pictures of micro-holes laser generated in α -SiO₂ after $N = 5$ laser shots at a laser fluence above and below single shot damage threshold : $F > F_{th}(1)$ (Fig. 4a) and $F < F_{th}(1)$ (Fig. 4b). The laser parameters are identical as mentioned in the discussion on Fig. 2 and Fig. 3, confined to spot size (intensity drop to $1/e^2$) of ca. $25 \mu\text{m}^2$. The arrows in the lower part of the figure illustrates the beam diameter ($1/e^2$) of approx. $6 \mu\text{m}$. At 6 J/cm^2 we obtained a very smooth walled micro-hole $0.5 \mu\text{m}$ deep and a diameter under $5 \mu\text{m}$, see Fig. 4a. The heighten circular rim around the hole and also several tracks of material perpendicular to the rim seem to indicate the development of melt near threshold and 100 fs pulse duration. A 50 % reduction in laser fluence to 3 J/cm^2 yields a very shallow $5 \mu\text{m}$ wide crater superimposed by a thin $0.1 \mu\text{m}$ deep pointed void with maximum (base) diameter of $1 \mu\text{m}$. The aspect ratio of 1 to 10 is in both cases the same. However, the choice of laser fluence relative to the damage threshold can lead to micro structures much smaller than the spot size of the focused laser beam, even for brittle materials. This is possible only laser pulses with pulse durations in a time range, where the energy depositions remains strongly localized in the material. In addition, the small single photon energy of 1.6 eV compared to the band gap of ca. 9 eV makes an utilization of non linear absorption possible. Multi photon absorption enhances the localization of energy.

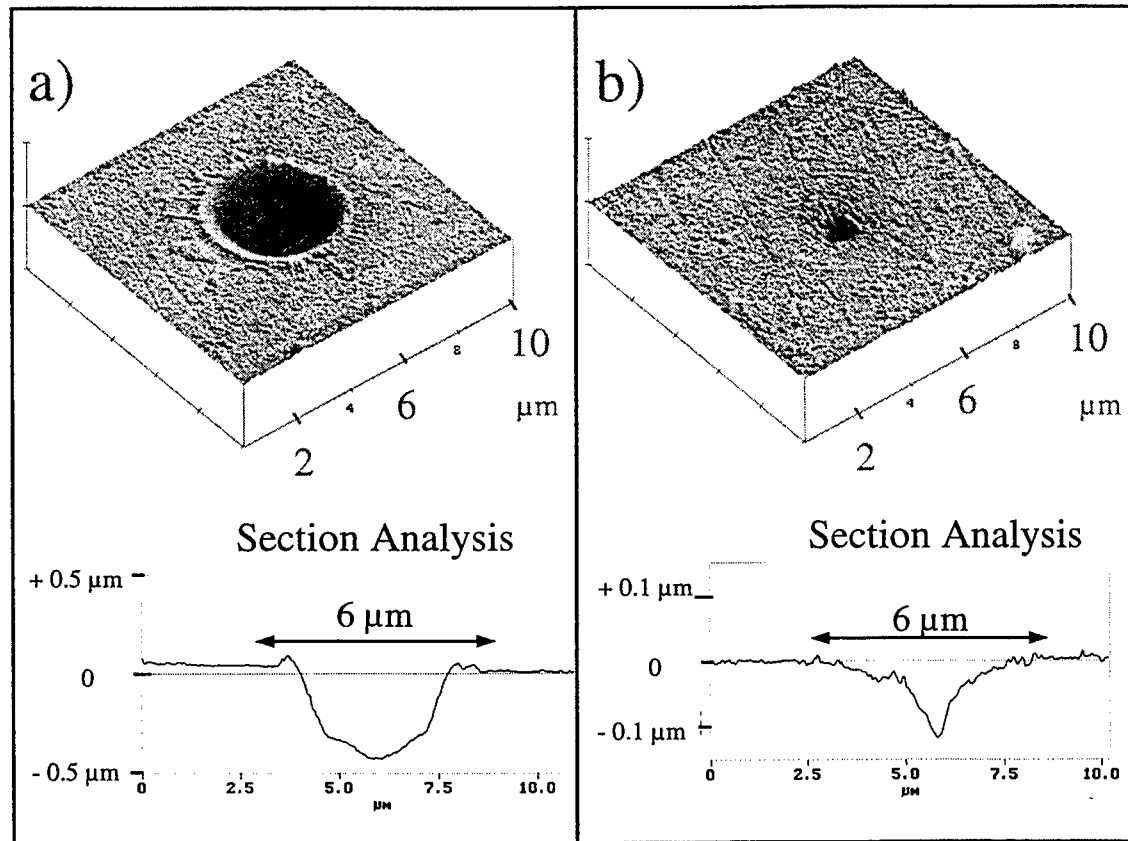


Fig. 5: AFM pictures and section analysis of micro holes in α -SiO₂ after $N = 5$ laser shots at wavelength of 800 nm, pulse duration of 100 fs; laser fluence: a) 6 J/cm^2 b) 3 J/cm^2 . The diameter of the Gaussian laser spot on the surface was determined to be $6 \mu\text{m}$, as indicated by the double arrow included in the section analysis pictures.

3.2. Bulk Processing

When the laser beam is focused on the surface at a fluence below damage fluence, no damage on the entrance surface can be observed even under conditions, where bulk modifications are generated several 100 μm below the surface. Fig. 6 depicts some examples of laser generated bulk structures in $\alpha\text{-SiO}_2$ due to the self-focusing of the laser beam at three different pulse durations, a pulse energy of 13.5 μJ and shot numbers running from $N = 25$ to 500. The modification depth z_M is defined as the distance from the entrance surface at which the modification starts, as indicated by the horizontal thin lines in Fig. 6. As additional laser pulses act on the bulk modification starting at a specific modification depth z_M , the damage adds up forming a damage track with increasing length towards the surface. A very clear dependence of z_M on the laser pulse energy is seen with z_M decreasing for increasing pulse energy and decreasing pulse duration. A similar dependence was obtained for the other samples. In cases, where the first damage point is generated 100-200 μm below the surface, only a few laser shots are necessary to obtain a violent ablation feature at the surface. Additional studies are necessary to unambiguously discriminate between surface and bulk accumulation properties at high shot numbers. A closer inspection of the bulk structures, as to be seen in the insert of Fig. 6, reveals a conglomeration of smaller structures reminiscent of micro-explosions.

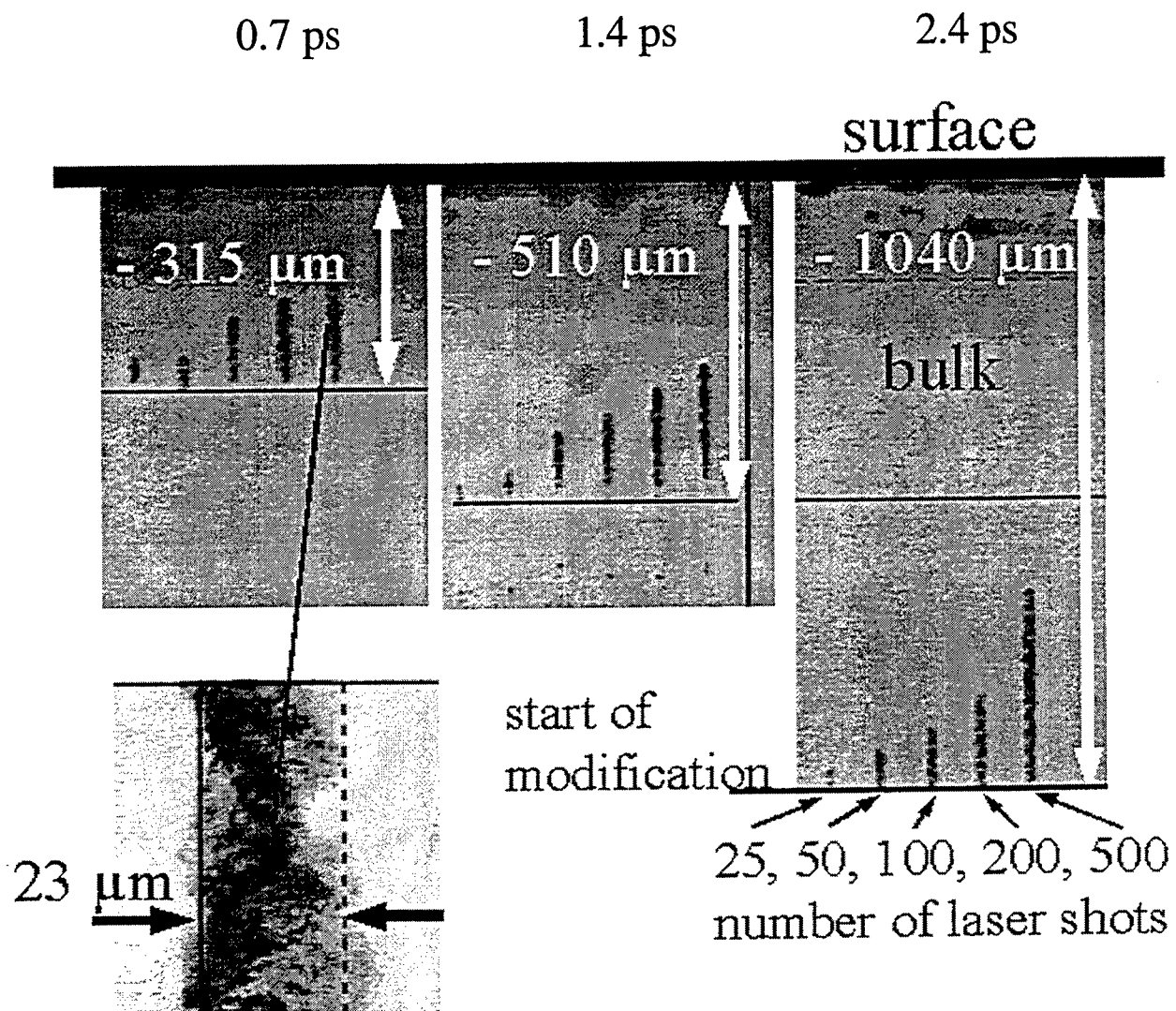


Fig. 6: Microscopic side view of bulk modifications in a 2 mm thick $\alpha\text{-SiO}_2$ sample. The three different pulse widths, 0.7, 1.4 and 2.4 ps, demonstrate different modification depths, 315, 510 and 1040 μm respectively, from which the damage begins after approx. 10 shots. Additional laser pulses contribute to the length of the damage track moving toward the surface.

It is possible to utilize the self-focusing effects to produce controlled micrometer sized modifications in bulk. The size and depth of the structures can be varied by varying the laser pulse duration and/or energy. To determine short pulse laser induced bulk damage thresholds and to investigate the capabilities of nonlinear optical effects to generate controllable bulk microstructures, we conducted this study on self focusing in different wide band-gap materials with picosecond and sub-picosecond laser pulses. Fig. 7 presents the results of the reciprocal modification depths z_M^{-1} versus the square root of the laser power \sqrt{P} for *a*-SiO₂ (a) and *c*-SiO₂ (b) at different pulse widths. For catastrophic self focusing a linear dependency is expected in this kind of plot¹⁹, as it is the case also for the experimental depths of modifications. A linear fit to the experimental data yields the critical laser power for self-focusing, P_{cr} . The value of P_{cr} for *a*-SiO₂ obtained from the fits is practically identical (3.6 MW) for the pulse duration range of 1.4 to 4.2 ps. The same is true for *c*-SiO₂ where $P_{cr} = 1.85$ MW for 1.4 and 2.8 ps. Included in Fig. 7 as dotted lines are the expected dependencies for the catastrophic self focusing depths. For a given pulse duration there seems to be a fixed ration between modification and theoretical catastrophic self focusing depth, for which we at this time can not offer a plausible explanation. For the shortest pulses used in the experiment (0.7 ps) for *a*-SiO₂ we see a clear increase in the value of P_{cr} extracted using this procedure (7 MW). We observed a similar increase in the critical self focusing power at sub ps laser pulses for CaF₂, and LiF. First estimations demonstrate that the group velocity dispersion above 0.1 ps is not strong enough to influence the self focusing significantly⁶. It is possible that the behavior may be explained by invoking the onset of defocusing effects due to the presence of free plasma electrons produced by multi-photon ionization. This will give a lower non-linear refractive index giving a larger value for P_{cr} and should be highly non-linear for our conditions (photon energy much lower than the band gap). The reason for the increasing gradients with increasing laser pulse width for ps pulses, seen in Fig. 7, is also unclear. Further work is in progress to determine the underlying physical mechanisms for the observed behavior.

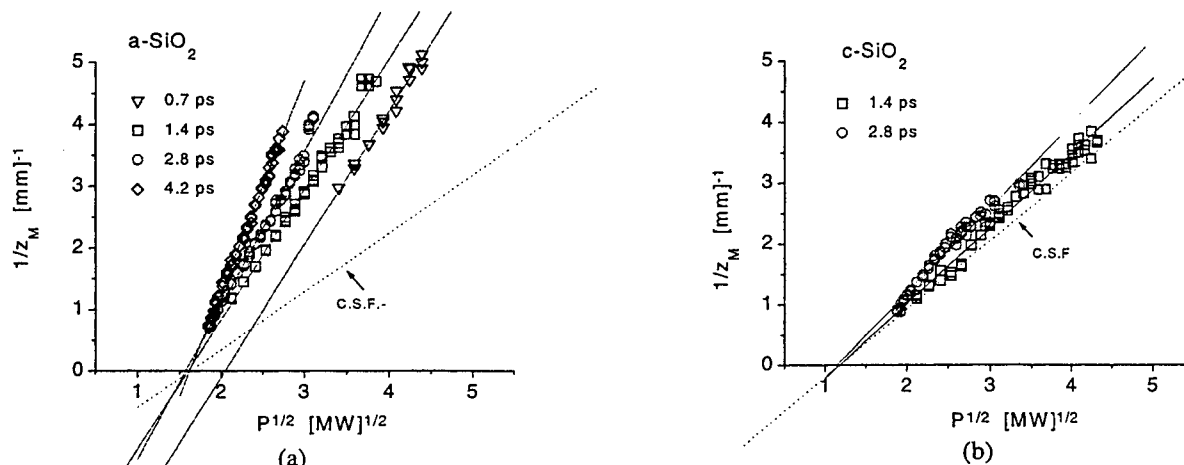
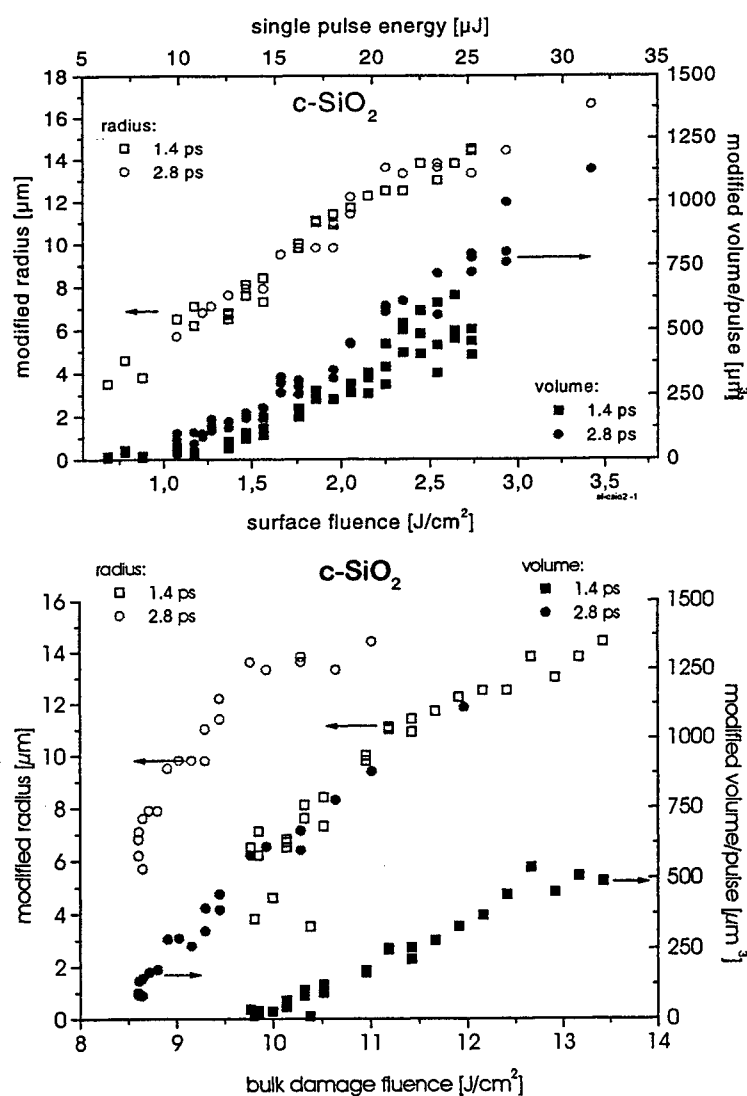


Fig. 7: Plot of reciprocal modification depth vs. square root of laser power for (a) *a*-SiO₂ and (b) *c*-SiO₂. Lines are linear fit to the experimental data. The dotted line represents the expected catastrophic self focusing depth assuming (a) $P_{cr} = 3.6$ MW for *a*-SiO₂ and (b) $P_{cr} = 1.85$ MW for *c*-SiO₂.

We take the average of the P_{cr} values found, using the above procedure, for pulse duration's greater than 1 ps and use this to determine n_2 . The results are summarized in Table 1 for four different materials (*a*-SiO₂, *c*-SiO₂, *c*-Al₂O₃, CaF₂) and compared with literature values obtained by determination of beam distortion in the far field²⁰ and degenerate three-wave mixing²¹. The results we obtain are in excellent agreement with the literature values. The only discrepancy we find is for *a*-SiO₂. The value we obtain is about a factor of 1.5 smaller than from degenerate three-wave mixing²¹ but agrees excellently with the value obtained from the beam distortion measurements²⁰. One possible explanation for the differences in the literature values for *a*-SiO₂ is that small Kerr contributions of resonant origin could increase the measured n_2 reported from the three-wave mixing experiments which employed ns pulses²¹.

MATERIAL	P_{cr} (MW)	$n_2 / (10^{-20} \text{ m}^2 \text{ W}^{-1})$	$n_2 / (10^{-13} \text{ esu})$	$n_2 / (10^{-13} \text{ esu})$ LIT.
<i>a</i> -SiO ₂	3.6 ± 0.14	1.72 ± 0.04	0.61 ± 0.02	0.85 ± 0.13 ²¹ 0.60 ± 0.15 (a) ²⁰ 0.62 ± 0.15 (b) ²⁰
<i>c</i> -SiO ₂	1.85 ± 0.12	3.11 ± 0.19	1.14 ± 0.07	o: 1.12 ± 0.17 ²¹ e: 1.16 ± 0.17 ²¹
<i>c</i> -Al ₂ O ₃	2.2 ± 0.4	2.4 ± 0.4	1.0 ± 0.2	o: 1.23 ± 0.18 ²¹ e: 1.30 ± 0.20 ²¹
CaF ₂	5.54 ± 0.26	1.15 ± 0.23	0.39 ± 0.08	0.43 ± 0.06 ²¹

Table 1: Critical self-focusing power thresholds P_{cr} and Kerr coefficients n_2 determined from straight line fits to plots of the inverse modification depth z_M^{-1} vs. square root of the laser intensity $P^{1/2}$ (averaged over the results for pulse durations > 1 ps) for different dielectric materials⁶. The last column compiles the Kerr coefficients n_2 from the literature determined by beam deflection²⁰ ((a) 1.06 μm ; (b) 0.53 μm) and by degenerative three-wave mixing²¹ (1.06 μm). o: ordinary and e: extraordinary orientation.



In Fig. 8a the radius and volume modified per laser pulse in the bulk of *c*-SiO₂ versus the input single pulse energy are shown for pulse widths above one ps. The minimal radius is ca. 4 μm and increases with pulse energy (or surface fluence). The modified volume is lowest for short pulses and low energy and demonstrates a similar increase with the pulse energy as for the radius. Fig. 8b then presents the bulk damage fluence in the oxides derived after the self focusing analysis¹⁹ of the experimental results in Fig. 8a. The bulk damage thresholds (in J/cm^2) are not constant and increase with the radius (and the volume) of modification. In this picture pulse duration dependencies are even more obvious, where a „zero volume“ multiple-shot bulk damage threshold can be estimated to be ca. 8.5 J/cm^2 for 2.8 ps and ca. 9.8 J/cm^2 for 1.4 ps. Similar result of an increase in bulk damage threshold with decreasing pulse duration was obtained for *a*-SiO₂. To be able to discuss these first results there are at least two important factors that need to be further addressed and investigated: 1. incubation effects that play a stronger role at low energy, 2. normalization of threshold to the volume of laser absorption.

Fig. 8: radius and volume of bulk modification at 1.4 and 2.8 ps pulse duration averaged per laser pulse in *c*-SiO₂ vs. (a) the input single pulse energy/surface fluence; (b) the estimated bulk damage fluence.

Utilization of self focusing of ps laser pulses is one possible way to generate bulk micro structures. Another approach is focusing ultra-short laser pulses directly into the sample by use of a micro objective of high numerical aperture⁷. Fig. 9 illustrates a few examples of micro traces obtained after $N = 1$ to 5 laser shots focusing a 100 fs laser beam of a wavelength of 800 nm inside fused silica. The modification arise at the position where we expect the beam focus to be inside the bulk (without self focusing). They develop after the first laser shot, are long and thin, whereby rather increasing in diameter (instead of length) from shot to shot.

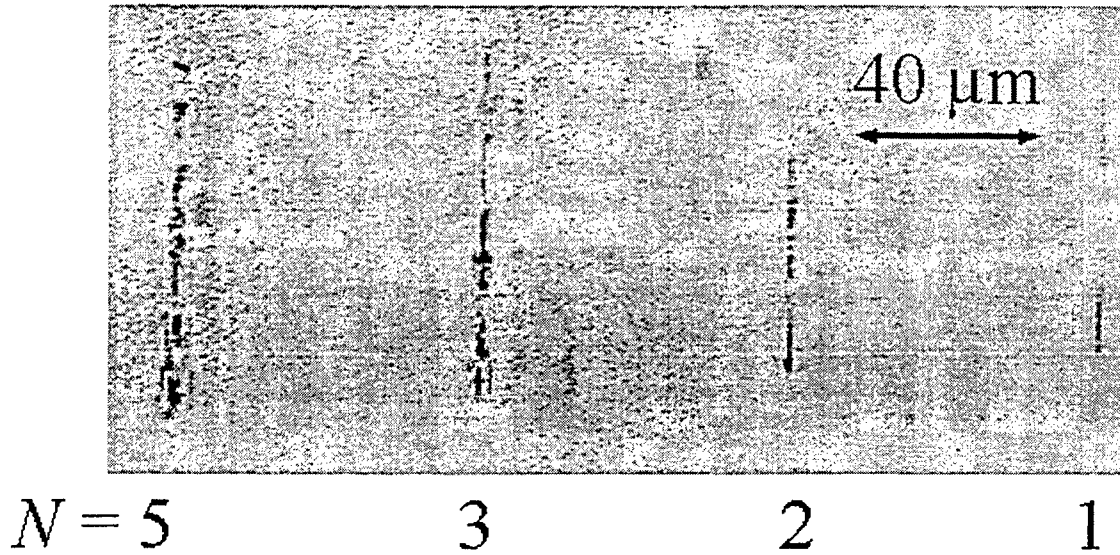


Fig. 9: Side view microscope picture of structures in α -SiO₂ obtained by direct focusing 2 mm inside the bulk at a wavelength of 800 nm, 100 fs pulse duration and a single pulse energy of 18 μ J. (focal length of used lens: $f = 25$ mm). Shot numbers from right to left: 1, 2, 3 and 5. Laser beam propagated from the top into the bulk.

In Fig. 10 we plotted semi-logarithmically the bulk modification diameter (Fig. 10a) and the length (Fig. 10b) vs. the single shot energy for the case $N = 5$ laser shots. Also included are the expected beam diameter in the focus and Rayleigh length (determined as 2 times the length between minimum waist and position where the beam waist is increased by $\sqrt{2}$), however, without taking beam distortions of non-linear nature (i.e. beam filamentation, defocusing, self focusing effects) into account.

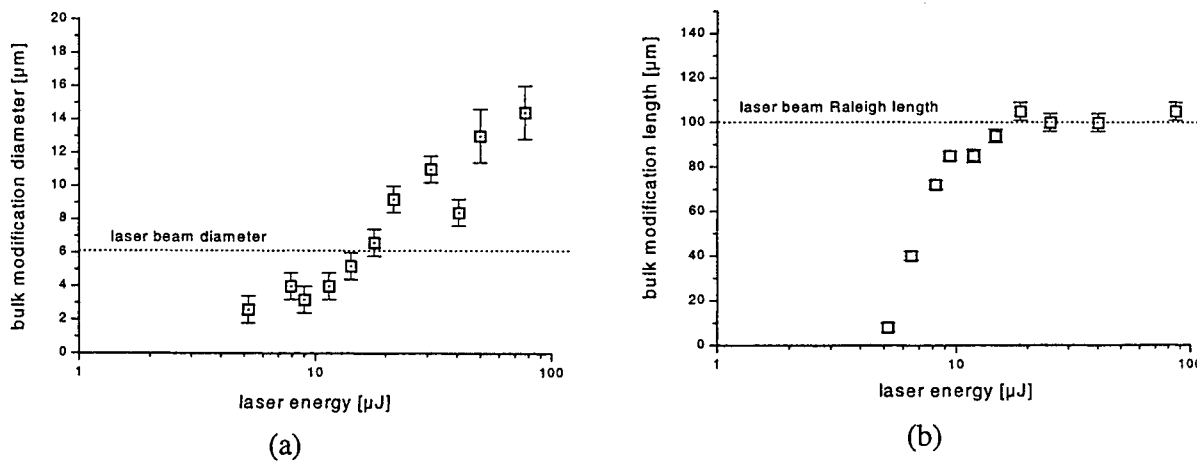


Fig. 10: Semi-logarithmic plot of **a)** the diameter and **b)** the length of bulk modifications laser generated inside fused silica vs. the single shot laser energy. Wavelength = 800 nm, pulse duration = 0.1 ps. Dotted lines characterize **a)** expected beam waist diameter in focus (6 μ m); **b)** Rayleigh length (100 μ m).

The control of the modification diameter is easier than for the modification length. This can be seen in the smaller slope of Fig. 10a. As in the examples shown in the section on surface processing, one is able to confine the diameter of the micro trace inside the size of the beam profile. A confinement of the length below 5 μm while using this type of lens with a focal length of 25 mm is much more difficult. It can be seen in Fig. 10b that the modification length increases dramatically inside an energy interval of a few μJ reaching a maximum level comparable to the Raleigh length. Bulk modifications from self focusing of ps laser pulses are more difficult to control in diameter but easier in length. However, here multiple-shots were necessary to introduce a micro dot inside the bulk, so that incubation effects have to be taken into account. From our experience, writing inside the bulk (i.e. complex arrangements of lines, etc.) by simply moving the sample is more straightforward with fs pulses, since bulk modifications can be generated with a single-shot.

4. CONCLUSION

We have demonstrated the applicability of femtosecond laser systems for the micro machining of dielectric materials, showing different examples of highly localized and fairly stress-free micro structures generated in fused silica and sapphire, such as thin channels, periodic patterns, micro holes and bulk modifications. The surface damage threshold is not only related to the pulse duration but demonstrates strong laser shot number dependencies which we relate to an increase in the absorption cross section due to the accumulation of laser induced generation of defects and successfully describe with a very simple model. We have shown that it is possible to produce controlled micrometer-sized modifications in bulk transparent materials using ps laser pulses at laser fluence in the focused spot size at the entrance surface which are lower than the surface damage threshold. The size and depth of the structures can be varied by varying the laser pulse duration and pulse energy. The effects are shown to be due to self-focusing of the laser beam. The experimental determination of the modification depths as a function of the laser power provides a very straightforward method of obtaining the value of the non-linear Kerr coefficient, n_2 which is independent of the laser focus size. We compare these results with those obtained by direct focusing of fs laser pulses inside the bulk material, where incubation and self focusing effect play a less important role.

ACKNOWLEDGEMENTS

We would like to thank Prof. Eleanor E.B. Campbell from the Gothenburg University & Chalmers University of Technology for her interest and support of this study. We are also greatly indebted to our Ph.D students, Razvan Stoian and Markus Lorenz. Financial aid from the BMBF is gratefully acknowledged.

REFERENCES

1. D. Ashkenasi, A. Rosenfeld, H. Varel, M. Wähmer, E.E.B. Campbell, „Laser processing of sapphire with picosecond and sub-picosecond pulses, *Appl. Surf. Sci.* 120, pp. 65-80, 1997
2. H. Varel, D. Ashkenasi, A. Rosenfeld, M. Wähmer, E.E.B. Campbell, „Micromachining of quartz with ultrashort laser pulses“, *Appl. Phys. A* 65, pp. 367-373, 1997
3. B.N. Chikov, C. Momma, S. Nolte, F. von Alversleben, A. Tünnermann, „Femtosecond, picosecond and nanosecond laser ablation of solids“, *Appl. Phys. A* 63, pp. 109-115, 1996
4. D. Ashkenasi, A. Rosenfeld, H. Varel, E.E.B. Campbell, „Laser-induced microstructuring of dielectrics using ultrashort laser pulses“, *CLEO'97 Conference on Lasers and Electro-Optics*, 1997 Technical Digest Series 11, CTuR3, p. 161, 1997
5. H. Varel, A. Rosenfeld, D. Ashkenasi, S. Henz, J. Herrmann, E.E.B. Campbell, „Bulk modifications in transparent materials induced by ultrashort laser pulses“, *CLEO'97 Conference on Lasers and Electro-Optics*, 1997 Technical Digest Series 11, CThL4, pp. 358-359, 1997
6. D. Ashkenasi, H. Varel, A. Rosenfeld, S. Henz, J. Herrmann, E.E.B. Campbell, „Application of self-focusing of ps laser pulses for 3D microstructuring of transparent materials“, *Appl. Phys. Lett.* 72, 12, pp. 1442-1444, 1998
7. E.N. Glezer, E. Mazur, „Ultrafast-laser driven micro-explosions in transparent materials“, *Appl. Phys. Lett.* 71, 7, pp. 882-884, 1997
8. B.C. Stuart, M.D. Feit, A.M. Rubinchik, B.W. Shore, and M.D. Perry, „Laser-induced damage in dielectrics with nanosecond to subpicosecond pulses“, *Phys. Rev. Lett.* 74, pp. 2248 (1995)
9. B.C. Stuart, M.D. Feit, S. Herman, A.M. Rubinchik, B.W. Shore, and M.D. Perry, „Optical ablation by high-power short-pulse lasers“ *J. Opt. Soc. Am. B* 13, pp. 459 (1996)

10. H. Varel, D. Ashkenasi, A. Rosenfeld, R. Herrmann, F. Noack, E.E.B. Campbell, „Laser-induced damage in SiO₂ and CaF₂ with picosecond and femtosecond laser pulses“, *Appl. Phys. A* **62**, 293 (1996)
11. W. Kautek, J. Krüger, M. Lenzner, S. Satania, C. Spielmann, and F. Krauz, „Laser ablation of dielectrics with pulse durations between 20 fs and 3 ns“ *Appl. Phys. Lett* **69**, 3146 (1996)
12. D. Ashkenasi, G. Herbst, A. Rosenfeld, H. Varel, M. Lorenz, R. Stoian, and E.E.B. Campbell, „Laser ablation and structuring of transparent materials with ultrashort laser pulses“, *SPIE Proc. of High Power Laser Ablation*, Santa Fe, Vol. 3343, pp. 400-410 (1998)
13. J.M. Liu, „Simple technique for measurements of pulsed Gaussian-beam spot sizes“ *Opt. Lett.* **7**, 196 (1982)
14. G. Petite, P. Daguzan, S. Guizard, P. Martin, „Ultrafast processes in laser irradiated wide bandgap insulators“, *Appl. Surf. Science* 109/110, pp. 36-46, 1997; P. Martin, S. Guizard, P. Daguzan, G. Petite, „Sub-picosecond study of carrier trapping in wide band-gap crystals“, *Phys. Rev. B* **55**, pp. 5799-5810, 1997
15. R.T. Williams, „Optically generated lattice defects in halide crystals“, *Opt. Eng.* **28**, 1024; N. Itoh and K. Tanimura, „Effects of photoexcitation of self-trapped excitons in insulators“, *Opt. Eng.* **28**, 1034 (1989)
16. D. Ashkenasi, R. Stoian, A. Rosenfeld, „Incubation effects in the ablation of transparent materials with ultrashort laser pulses“ (in preperation) 1999
17. D.K. Sardar, M.F. Becker, R.M. Walser, „Auger Analysis of elemental depth profiles correlated with multi-pulse laser damage of GaAs surfaces“, *J. Appl. Phys.* **62**, 3688 (1987)
18. Y. Jee, M.F. Becker, and R.M. Walser, „Laser-induced damage on single-crystal metal surfaces“, *J. Opt. Soc. Am. B* **5**, 648 (1988)
19. J.H. Marburger, „Self-focusing: Theory“, *Prog. Quantum Electron.* **4**, 35 (1997)
20. M.J. Soileau, W.E. Williams, N. Mansour and E.W. Van Stryland, „Laser-induced damage and the role of self-focusing“, *Opt. Eng.* **28**, 1133 (1989)
21. R. Adair, L.L. Chase and S.A. Payne, „Nonlinear refractive index of optical crystals“, *Phys. Rev. B* **39**, 3337 (1989)

Micromachining with Ultrashort Laser Pulses

J.-X. Zhao⁺, B. Hüttner, and A. Menschig⁺⁺

Deutsches Zentrum für Luft- und Raumfahrt e.V., Institut für Technische Physik

Abstract

Practical high precise and efficient micromachining can be realized with computer controlled ultrashort laser pulses suppressing the thermal diffusion effect inside the material to be ablated. A direct translation from solid to the vapor state takes place at sufficient intensity levels. Experimental results of micromachining of different materials (Al, Si, InP and fused silica) with femtosecond laser pulses at wavelengths of 800 nm and 267 nm from a commercial Ti:sapphire laser are presented. Holes down to a diameter below 1 micron have been drilled with 800 nm pulses into aluminum as an interesting metal with an absorption peak in the IR-range nearby 800 nm. Because of their low energy band gap semiconductors have a strong absorption at UV wavelengths. Arrays of holes down to 1 micrometer in diameter have been drilled into silicon and InP using 267 nm pulses. Results of fused silica as an example for transparent insulator materials are compared to results of semiconductors. The hole array manufacturing process takes only a few seconds. Precision can be improved by matching laser parameters to the processed material.

Keywords: micromachining, Ti:sapphire laser, UV beam, metal, semiconductor, insulator, ultrashort laser pulses

1. Introduction

Micromachining with femtosecond laser pulses is of growing interest for the fabrication of microsystems or semiconductor devices. Due to the progress in the development of lasers with ultrashort pulses the very high flexibility and high repeatability of patterning, well known from other laser systems, can be combined with high resolution, high precision and high ablation efficiency. Therefore necessary conditions are met for the practical application of ultrashort laser pulses (< 20 ps) in material microprocessing.

The thermal diffusion inside the ablated material, which reduces the micromachining quality of lasers which nanosecond laser pulses, is effectively suppressed due to the use of ultrashort pulses^[1]. By means of femtosecond pulses a direct solid-vapor translation takes place. At high enough intensities the peak power reaches the terawatt regime which allows the patterning even of transparent, crystalline materials^{[2],[3]}.

In the last years many papers about micromachining with femtosecond laser pulses were published^{[1]-[8]}. To our knowledge only a few results have shown real practical machining

⁺ Present address: Universität der Bundeswehr Hamburg, Holstenhofweg 85, D-22043 Hamburg

⁺⁺ Correspondence: DLR, Institut für Technische Physik, Dr. A. Menschig, Pfaffenwaldring 38-40, D-70569 Stuttgart
Tel.: +49 711 6862 493; Fax: +49 711 6862 555; Email: a.menschig@dlr.de

applications in the real micron range. Most of the work shows hole diameters and structure sizes between tens and hundreds of micrometers or single micro-holes without repeatability (e.g. array arrangements).

In contrast the excimer laser is a better known tool to achieve microstructures due to its short wave length^{[9]-[11]}. But the excimer laser has two main disadvantages: the laser medium is based on poisonous gas and the laser beam profile is far away from a gaussian one. Therefore the microstructuring is done with a homogenized beam in an imaging arrangement and not with a focusing method. The normal optical demagnification of excimer patterning systems is between 1/10 and 1/40. Therefore even the fabrication of a mask for real micromachining with an excimer laser is a difficult task.

In our paper we present microdrilling results on different materials (metal, semiconductor and insulator) using a femtosecond Ti:sapphire laser with 800 nm and 267 nm wavelength. The microablation of different materials will be discussed. We show for the first time hole arrays with high precision and good repeatability to lower than 1 μm in diameter on different materials (aluminum, silicon, indium phosphide and fused silica).

2. Experiment

In figure 1 the scheme of our working station for micromachining is shown. The Ti:sapphire laser is a commercial laser system (Clark-MXR CPA 1000), which provides pulses from 100 fs to 10 ps duration. Its maximal pulse energy is 0.7 mJ at 800 nm. The Ti:sapphire oscillator is pumped by a cw argon ion laser with a power of 6 W. The self-modelocked oscillator generates pulses with a pulse duration of about 100 fs, a repetition rate of 91 MHz and an average power of 300 mW. In a stretcher the pulses were extended to a pulse duration of about 200 ps.

Then the pulses were amplified to an average power of 0.7 W at a repetition rate of 1 kHz (0.7 mJ pulse energy) in a regenerative amplifier pumped by a frequency-doubled Nd:YAG laser with an average power of 8 W. Finally the pulse duration is reduced to 100 fs by a compressor. The final pulse duration is controlled with an optical autocorrelator.

The laser average power can be reduced with the help of a $\lambda/2$ wave plate rotated by DC motor and a beam splitter cube arranged between the amplifier and the compressor. Single pulse and pulse train operation together with a variation of the repetition rate from 1 kHz to 1 Hz and the on/off switching of the laser beam for the micromachining is realized by a second pockels cell and a specially designed electronic set-up under computer control. The laser beam at 800 nm wave length can be converted into an UV-beam (267 nm) by two nonlinear crystals. The

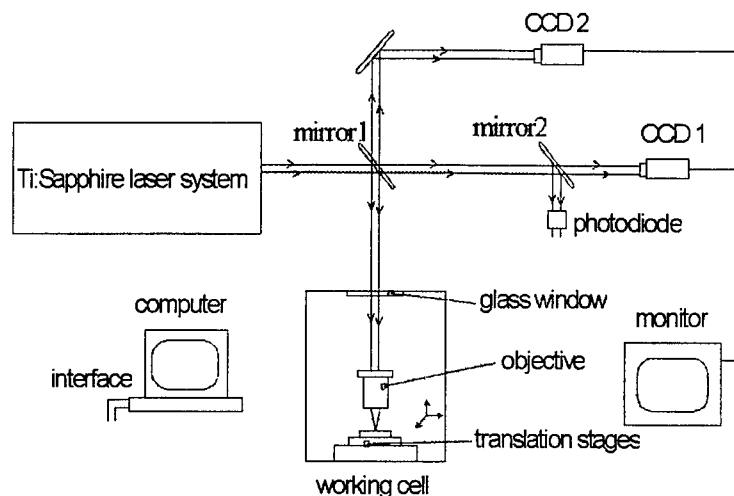


Figure 1: Schematic illustration of the working station for micromachining.

conversion efficiency is about 6 %, so that the maximal pulse energy of the UV - beam is about 0.04 mJ.

In the optical beam propagation set-up an in-process characterization of the medium laser power and the beam profile is realized. The semi-permeable mirror 1 transmits about 5 % of the pulse energy which is distributed by mirror 2 (50 % transmission) to a first CCD-camera for observing the laser beam profile and to a photodiode for measuring the laser power. The second CCD-camera is used to optimize the beam path through the optics and to observe the working surface to control the micromachining results. All the measuring elements are shielded by gray filters to avoid damage.

For our micromachining experiments a high flexibility together with a high resolution is required. Therefore a direct focusing method is favorable. A glass lens with a short focus length is not useable for ultrashort pulses because of its geometrical and chromatic aberrations due to the small radius, the damage problem because of the self-focusing effect^[3] and the pulse broadening caused by the nonlinear dispersion.

Therefore we used a reflecting Schwarzschild-objective to focus laser beam directly on the sample surface. An additional advantage of some reflecting objectives is a working distance greater than the focal length. For example the Ealing 15 x reflecting objective has a focal length of 13,5 mm , but its working distance is 24 mm. This is an advantage for the optical adjustment of the focusing optic.

The translation stages for the xyz-motion and the objective are mounted in a working cell. A sample holder arrangement fixes the material to be processed with high precision in x-, y- and z-direction on the translation stages. The whole system is semi-automatically controlled with a personal computer.

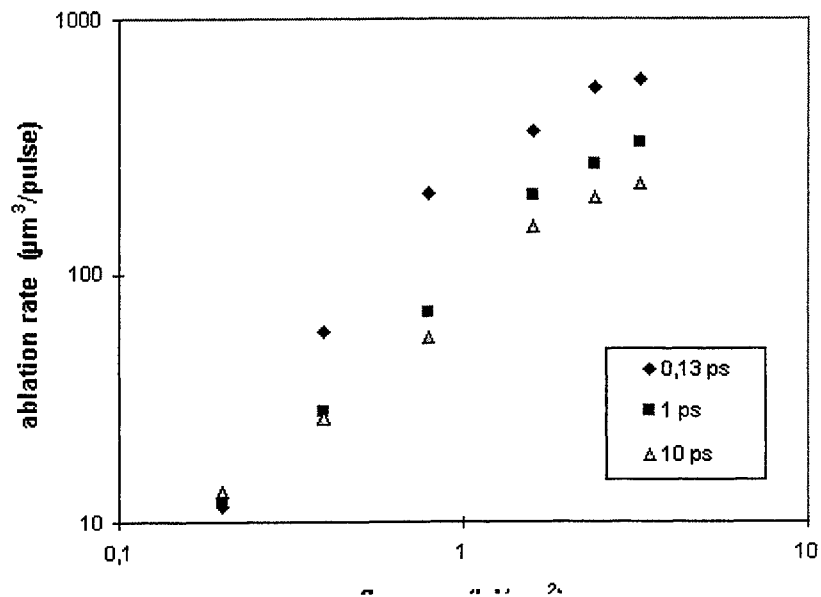


Figure 2: Ablation rate per laser pulse for polished aluminum targets as a function of the fluence at different pulse widths (Ti:sapphire 800 nm, 10 pulses).

3. Results and Discussion

For our experiments we use substrates with a surface roughness of about 10 nm (RMS) to measure even the smallest holes in the sample surface. For the determination of the ablated volume or the ablation depth an interference microscope was used. General characterizations were done with an optical and an electron microscope. All the photographs at the optical microscope were taken at a 1000 x magnification.

a. Microablation of aluminum at 800nm

Aluminum is an interesting material for the ablation at 800 nm due to its special absorption peak in the near infrared. Therefore an effective ablation should be possible.

For the experiments we focused the Ti:sapphire laser with a 15 x reflecting objective (focus length: 13.5 mm, NA = 0.28) to a calculated spot size of 3 μm .

In figure 2 we demonstrate microablation results for a polished aluminum target drilled with a series of 10 laser pulses at 1 kHz repetition rate. We plotted the ablation rate as the ablated volume per laser pulse as a function of the laser fluence for the pulse widths 130 fs, 1 ps and 10 ps. Close to the ablation threshold a single laser pulse ablates small volumes of about 10 μm^3 independent of the pulse width. With increasing fluence the ablation rate increases linearly. At the highest fluence values the ablation rate starts to develop a saturation behavior. For smaller pulse widths a clearly higher ablation rate was achieved compared to the longest pulse width examined. At 130 fs the ablation close to the saturation value is about 3 times as effective as at 10 ps.

This is due to the changed thermal regime^[12]. For fs-pulses the energy is transported from the electron subsystem to the phonon one in about a volume given by spot size times the electron penetration depth $L_e \equiv (\lambda \cdot \tau_L / c_e)^{1/2}$, where λ is the thermal conductivity, $c_e = \gamma \cdot T_e$ the specific heat of the electrons and τ_L the pulse duration. For energy densities above the threshold this leads to a fast heating up of this volume almost without the usual energy loss caused for longer pulses by the thermal transport of the phonons inside the material. Consequently, a larger part of the absorbed energy is used for the evaporation which increases the ablation rate.

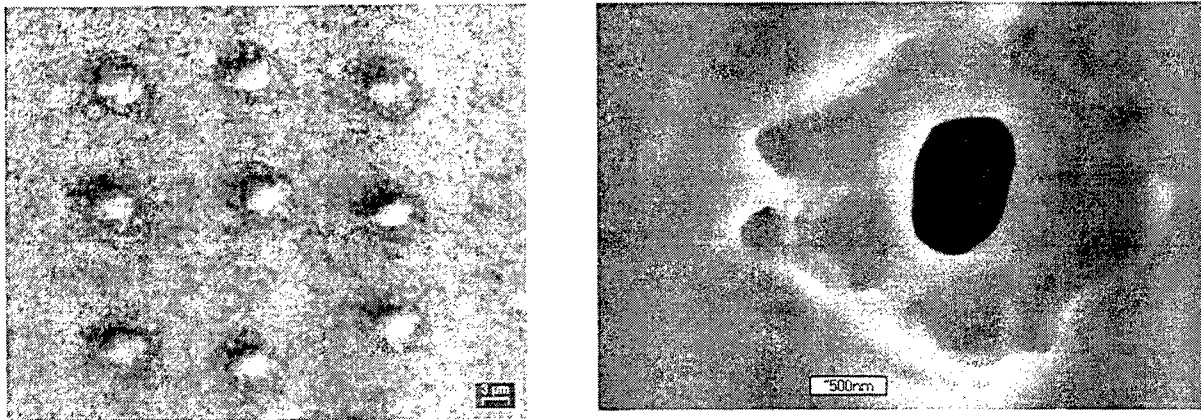


Figure 3: Microablation of aluminum at two different fluences. Left: Well above threshold (280 J/cm²). Right: Above threshold only in the center of the laser spot (11,2 J/cm²).

In figure 3 (left) a photograph taken via an optical microscope is depicted. It shows a series of small holes fabricated by single shot ablation at a pulse energy of 25 μJ (fluence: 280 J/cm²) and a pulse width of 150 fs. This fluence was chosen to demonstrate hole diameters of about 3 μm as the resolution limit expected from the calculated spot size. The high precision of the hole formation (the positioning of the xy-stages was not acceptable at this moment) and the good repeatability even for this single shot drilling clearly can be seen.

The energy density distribution of the laser beam profile is in a good approximation a gaussian type. Therefore a strong local inhomogeneity over the spot size exists. A certain energy density

value defines the ablation threshold within the spot size. We have determined the microablation threshold of aluminum to about 0.4 J/cm^2 . To smaller energy density values a small boundary region, typically $<1 \text{ }\mu\text{m}$, with melted aluminum is obvious.

This inhomogeneity of the energy density distribution can be used to drill even smaller holes than the resolution of the optical set-up. The laser fluence can be reduced to values where the ablation threshold is reached only in the center region of the laser spot. Figure 3 (right) shows an electron beam microscope photograph of a microablation result drilled in a thin aluminum film ($\sim 100 \text{ nm}$) on a glass carrier. Using a single laser shot of about $1 \text{ }\mu\text{J}$ the total film was removed within a center region of about 600 nm in diameter. Whereas in an area of about $3 \text{ }\mu\text{m}$ in diameter a surface modification due to the thermal influence can be seen.

The control of the ablation parameters for the holes with sizes smaller than the wavelength is quite difficult. Small changes have strong influences on the process due to the rapid variation of the energy density due to the gaussian distribution. The ablation depth typically is smaller than the hole diameter. The irregularities are due to a non-circular beam profile and a non-perfect gaussian energy density distribution of the Ti:sapphire laser. Both can be observed viewing the laser beam with CCD 1.

b. Microablation of semiconductors at 267 nm

As semiconductor materials we have examined silicon and indium phosphide. Both materials are nominally undoped and therefore the concentration of free electrons at room temperature should be $< 10^{17} \text{ cm}^{-3}$ (compared to $> 10^{22} \text{ cm}^{-3}$ in metals). Nevertheless, the ablation process is similar to that in metals in the second stage. In the first stage, however, the laser has to produce a high enough electron density for effective absorption. This can be realized for lower intensities by the avalanche process and for higher ones by multi-photon absorption. No matter which mechanism is dominant, it needs some time leading to a reduced ablation efficiency for semiconductors compared to metals.

For these experiments we focused the laser with a $52\times$ reflecting objective (focus length: 3.5 mm , $\text{NA} = 0.65$) to a calculated spot size of $2 \text{ }\mu\text{m}$. For the following experiments a constant value of the pulse width at 150 fs was chosen.

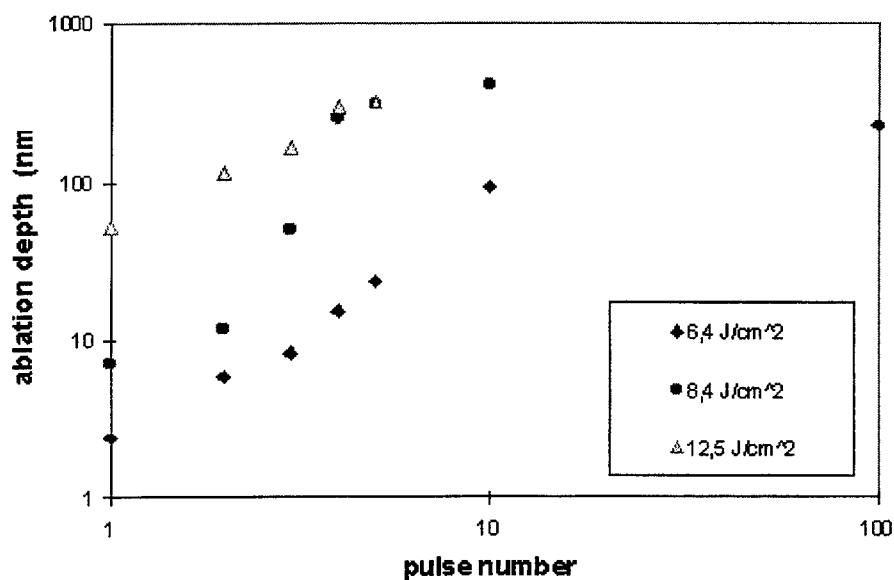


Figure 4: Microablation depth for silicon in dependence of the pulse number at different laser fluences (Ti:sapphire 267 nm , pulse duration 170 fs).

The hole depth for this single shot microablation is in the nanometer regime as can be seen in figure 4. With an increasing number of pulses also an increase in the ablation depth can be found. With ten times the pulses typically over ten times the depth can be achieved. At a depth of about 300 nm a saturation behavior independent of the laser fluence was found.

Figure 5 (left) shows the optical microscope photograph of three rows of a pulse number variation from 1 to 5 pulses from right to left. We used a constant value of the pulse energy at $0.3 \mu\text{J}$ (fluence: 12.5 J/cm^2) for drilling these holes. The hole diameter changes from about $2 \mu\text{m}$ for a single shot to about $4 \mu\text{m}$ for five shots. The minimal hole diameter at this fluence corresponds with the calculated spot size.

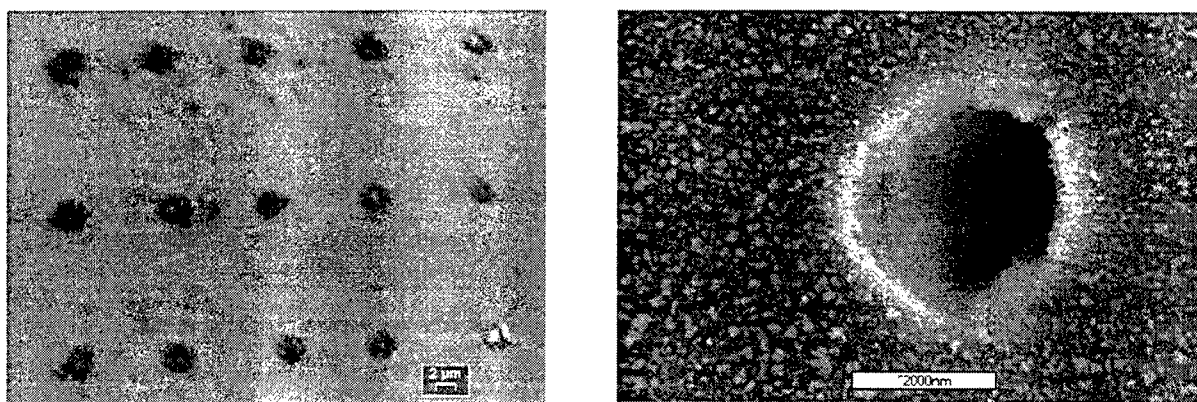


Figure 5: Three series of an identical pulse number variation in silicon (left) and a 100 shot drilling into InP (right).

An example of a hole about $3 \mu\text{m}$ in diameter and $1 \mu\text{m}$ in depth is depicted in figure 5 (right, SEM photo). It was drilled into InP with 100 pulses at a pulse energy of $0.13 \mu\text{J}$ (fluence: 7.4 J/cm^2) and a pulse width of 170 fs. The debris around the hole can be removed with a kind of duster or an ultrasonic bath. According to our experience up to now the aspect ratio of microablated holes will not exceed 1:1 in semiconductors.

c. Microablation of insulators at 267 nm

The optical arrangement was the same as for the semiconductor microablation experiments. The thickness of the fused silica sample (1mm) was chosen to a value much larger than the depth of focus ($0.6 \mu\text{m}$) to avoid ablation at the backside of the sample known from other experiments in transparent dielectrics^[5].

For comparison to the hole in InP (figure 5 right) we show a hole in figure 6 (left, SEM photo) of comparable size in fused silica. For this microablation 100 pulses with a pulse energy of $2.6 \mu\text{J}$ (fluence: 127 J/cm^2) at 150 fs were used. Even in a transparent material a high quality drilling of micron size holes can be achieved. It is self evident that a much higher fluence is necessary. The holes have a clear conical shape with well defined sidewalls. The high quality boundary at the surface is not disturbed by the sprout of melted material. The debris on the surface can be removed as described for the semiconductors.

With a reduced number of pulses even smaller holes can be fabricated. In figure 6 (middle) five series of a pulse number variation with 1, 2, 3, 4, 5 and 10 shots from right to left are depicted

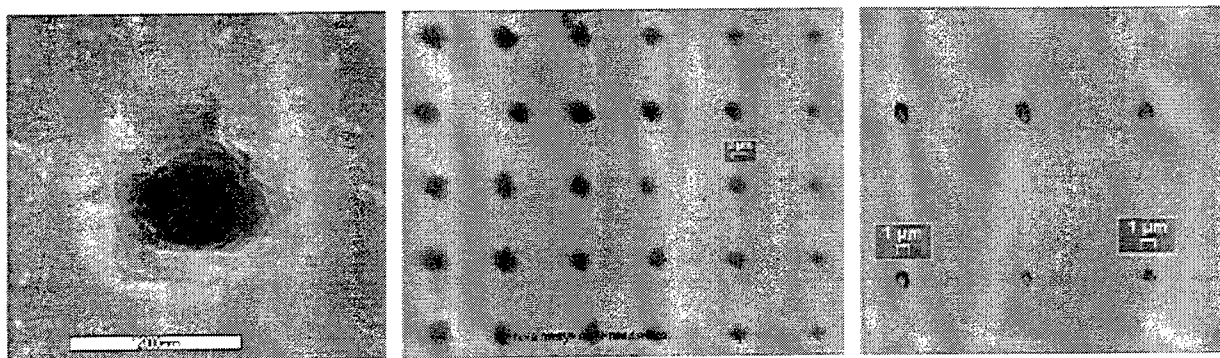


Figure 6: Microablation of fused silica.. Left: Hole drilled with 100 pulses at 127 J/cm². Middle: Holes fabricated by a variation of the pulse number at 127 J/cm². Right: Low fluence drilling at 50 J/cm².

(laser parameters as above). A clear reproducibility of high quality openings is visible. The sizes range from about 2 μm for a single shot to about 3 μm for ten shots. A reduction of the laser fluence can be used to a further shrinking of the hole size. As described for the aluminum ablation (see above) the ablation threshold can be used to ablate only in the center region of the laser spot. In figure 10 we show holes of about 1 μm in diameter at a fluence of about 50 J/cm².

4. Summary and conclusions

A micromachining method with high precision, high flexibility, high repeatability, high resolution, and high efficiency was presented. Ultrashort laser pulses as a key issue to minimize material melting effects during the machining allow the fabrication of micron size structures in a wide range of materials. Hole arrays and single holes with diameters to below 1 μm in aluminum, silicon, fused silica and indium phosphide were shown.

For a satisfying reproducibility of the microablation results many parameter must be controlled and optimized as the focus position relative to the sample surface, the laser fluence, the pulse duration, the number of pulses, or the mode of the laser beam. For some applications also an aspect ratio value >1 is desirable which seems to be possible through a relative movement between sample and objective.

The combination of ultrashort laser pulses with the computer control for the laser source and the machining set-up opens up new opportunities for material microprocessing. At least it can be used as a very short-term prototyping method for new semiconductor devices and complex microsystems.

5. Acknowledgments

This work was financially supported in part by the Bundesministerium für Bildung, Wissenschaft, Forschung und Technologie under contract number 13N7047. The authors are indebted to Dr. T. Kurosawa of the Panasonic Technologies, Inc. for his support of materials.

6. References

- [1] B.N.Chichkov, C.Momma, S.Nolte, F.von Alvensleben, and A.Tünnermann, „Femtosecond, picosecond and nanosecond laser ablation of solids", Appl. Phys. A63, pp. 109-115 (1996)
- [2] X.Liu, D.Du, and G.Mourou, „Laser ablation and micromachining with ultrashort laser pulses", IEEE, J.Quantum Electron., 33, pp. 1706-1716 (1997)
- [3] D.Ashkenasi, A.Rosenfeld, H.Varel, M.Wähmer, and E.E.B.Campbell, „Laser processing of sapphire with picosecond and sub-picosecond pulses", App. Surf. Sci. 120, pp. 65-80 (1997)
- [4] P.P.Pronko, S.K.Dutta, J.Squier, J.V.Rudd, D.Du, and G.Mourou, „Machining of sub-micron holes using a femtosecond laser at 800 nm", Opt. Commun. 114, pp. 106-110 (1995)
- [5] C.Momma, B.N.Chichkov, S.Nolte, F.von Alvebsleben, A.Tünnermann, H.Welling, and B.Wellegehausen, „Short-pulse laser ablation of solid targets", Opt. Commun. 129, pp. 134-142 (1996)
- [6] J.Krüger, W.Kautek, M.Lenzer, S.Sartania, C.Spielmann, and F.Krausz, „Laser micro-machining of barium aluminium borosilicate glass with pulse duration between 20 fs and 3 ps", App. Surf. Sci. 127-129, pp. 892-898 (1998)
- [7] S.Ameer-Beg, W.Perric, S.Rathbone, J.Wright, W.Weaver, and H.Champoux, „Femtosecond laser microstructuring of materials", App. Surf. Sci. 127-129, pp. 875-880 (1998)
- [8] A.Menschig, J.Oberfell, and H.-E.Swoboda, „Präzise Mikrofertigung", Laser-Praxis, Okt, pp. 32-35 (1997)
- [9] P.Simon and J.Ihlemann, „Ablation of submicron structures on metals and semiconductors by ultrashort UV-laser pulses", App. Surf. Sci. 109-110, pp. 25-29 (1997)
- [10] I.Zergioti, S.Mailis, N.A.Vainos, C.Fotakis, S.Chen, and C.P.Grigoropoulos, „Excimer laser micro machining of inorganic dielectrics", App.Surf.Sci. 127-129, pp. 601-605 (1998)
- [11] S.Preuss, A.Demchuk, and M.Stuke, „Sub-picosecond UV laser ablation of metals", Appl. Phys. A61, pp. 33-37 (1995)
- [12] B.Hüttner and G.Rohr, „On the theory of ps and sub-ps laser pulse interaction with metals: II. Spatial temperature distribution", App.Surf.Sci. (1998) (in print)

Second Harmonic of Ti: Sapphire femtosecond laser as a possible tool for point-like 3D optical information recording

Nikita M. Bityurin^a, Alexey I. Korytin^a, Sergey V. Muraviov^a, and Alexander M. Yurkin^b

^a Inst. Appl. Phys. RAS, Nizhnii Novgorod, 603600, Russia

^b Inst. Mineral. & Petrography Sib. Branch RAS, Novosibirsk, Russia

ABSTRACT

We show that irradiation by the second harmonic (SH) of Ti:Sapphire femtosecond laser provides well-defined spots with micrometer diameter by controllable manner in pure PMMA. Combined effect of SH and fundamental frequency (FF) radiation of Ti:Sapphire laser yields significant decrease in recording time. These results relate to 3D bitwise optical information storage. Usually in order to produce irreversible detectable changes, either single amplified Ultra-Short Laser Pulse (USLP) irradiation of pure matrix or multi-shot irradiation of matrix with dyes by nonamplified USLP is employed. In our present experiments the 1.5% transformation of nonamplified Ti:Sapphire laser radiation (wavelength 770nm, repetition rate 70MHz, pulse duration 200fs, pulse energy 2nJ) into the SH has been obtained by means of BBO crystal with thickness of 300 μ m. The SH beam was then focused within the PMMA matrix by a lens with N.A.=0.55. The onset of emission corresponds to the onset of detectable irreversible changes in PMMA detected by optical microscope. The SH provides two-photon electronic transition to the absorption band of PMMA. Theoretical analysis of experimental data shows that preliminary matrix excitation by SH is followed by a self-developing process. This process can be driven not only by SH radiation but by potentially more powerful FF radiation as well.

Keywords: Ultra-Short laser pulses, second harmonic, optical damage, information recording, experimental data, theoretical modeling

1. INTRODUCTION

Optical data recording in photopolymers¹, photochromic materials² and photorefractive crystals³ has met some difficulties related to a short lifetime or low contrast in optical properties of recorded information. On the other hand femtosecond lasers exhibit outstanding capabilities in material microfabrication⁴. Ultrashort laser damage not only may be confined in submicrometer-sized volume, but also demonstrates a large contrast in refraction index as well as high durability. All these features are suitable for 3-D optical information recording. In previous papers optical recording was demonstrated in pure materials by single near-IR 0.3- μ J pulse from a femtosecond laser system with chirped-pulse-amplification⁵ or in doped polymers⁶ by near-IR high-repetition-rate femtosecond pulses with a moderate pulse energy (3 nJ).

In this communication we report optical recording in pure PMMA by train of 30-pJ pulses of second harmonic of Ti:Sapphire laser. Doubled photon energy of the SH corresponds to PMMA chromophore absorption band that provides a nonlinear coupling of laser pulse with matter by means of a two-photon transition. The simultaneous irradiation of the sample by SH and fundamental frequency radiation (FF) leads to significant acceleration of the recording process.

The simple models are suggested which explain the main features of the experimental data and clarify the possible role of FF radiation.

2. EXPERIMENTAL

In our experiments we used the second harmonic (SH) of a femtosecond Ti:Sapphire master-oscillator (2nJ, 200 fs, 70 MHz, 770 nm). 1-mm TEM₀₀ beam of fundamental frequency (FF) of the laser was focused in a nonlinear crystal (300- μ m BBO) by a lens with a focal length of 30 mm. Maximum conversion efficiency was 1.5% that corresponds to about 2 mW in SH. The second harmonic beam yielded some ellipticity with aspect ratio about 1.5 due to the fact that the NA of focused light exceeded a phase-matching angular width of the nonlinear crystal. SH radiation was collimated by a 150-mm lens and then was focused into the bulk of a sample by an aspheric lens with NA=0.55. The sample, a polished cube of pure PMMA, was obtained from methylmethacrylate by thermal free radical polymerization in mass. The sample was placed on 3-D positioner combined with an optical microscope. We illuminated the sample at various SH power levels and exposure times. The power alteration was performed by tilting of the nonlinear crystal around the SHG phase-matching angle and the exposure time was controlled by a mechanical shutter.

Illumination of the sample by SH femtosecond pulses caused bulk damage of PMMA. It took several seconds before the sample modification occurred. Typical sideview optical microscope pictures of the optical damage in bulk of the sample are shown in Fig. 1 for the exposure time slightly more than the damage delay time. Further exposure caused a damage region growing and a bright glow of white color in the focus region. It was found that the moment of the damage emergency coincides with the glow beginning within experimental error of tenths of a second. Note that illumination of the sample only by the FF radiation of the Ti:Sapphire laser only at the maximally available power yielded no material modification.

Fig. 2 shows experimental data of measurements of the delay time between the exposure beginning and the glow ignition vs. SH power for the case of illumination by the SH only (circles) and by both harmonics simultaneously (triangles). In the former case the FF was rejected by a color optical filter that is transparent for the SH except Fresnel losses.

3. MODELS AND DISCUSSIONS

If we assume that the damage is related to a simple accumulation of products of two-photon photochemical reaction, then the inverse delay time should depend on the SH power as a parabolic function. The corresponding fit is shown as a curve 1 in Fig.2. However, the power function fit $1/t_s \propto P^\beta$ provides $\beta = 1.23$ rather than $\beta = 2$.

One explanation of this fact is provided by the assumption that a self-developing process of some kind is involved here:

$$\frac{\partial N}{\partial t} = (\delta N_0 I_2^2 + \sigma_A^{(2)} N I_2) t_p f - N/\tau \quad (1)$$

Here N is the number density of produced species, N_0 is the number density of chromophore, δ is the product of two-photon absorption coefficient and the quantum yield of two-photon photochemistry-like reaction. This reaction provides the initial amount of N - species, whereas subsequent chainwise reaction, described by the second term, is accounted for the multiplication of these species, $\sigma_A^{(2)}$ being the corresponding cross-section. The superscript (2) stands for the values at the SH wavelength. The mentioned above processes occur during laser pulse. I_2 is the SH intensity at the waist of the SH beam. It is measured in $\text{Photon}/\text{cm}^2 \cdot \text{s}$. The laser pulse is assumed to be rectangular, t_p and f are laser pulse duration and repetition rate, correspondingly. The amount of species decays with the characteristic time τ as it is seen from the third term in r.h.p. of Eq. (1). When writing (1) we suppose that $N \ll N_0$. Equation (1) can describe the photochemical chainwise reaction as well as the accumulation of free electrons. In the latter case the first term yields the preliminary ionization process. The I^2 dependence reveals the saturation of single-photon transitions, which follow the two-photon limiting step (see Ref. 7). The linear intensity term reads for multiplication of amount of free electrons by impact ionization. It is understood that after the pulse a part of free electrons are captured by traps, the next pulse resulting in ionization of these traps thus allowing these captured electrons to participate in multiplication process. The relaxation time τ is related here to annealing of captured electrons between laser pulses. Within the framework of the model (1) it is assumed that the significant damage occurs when concentration N reaches some appropriate value N^* (See e.g. Ref.8).

The model (1) yields the dependence of the delay time, t_s , between the start of irradiation and the onset of significant damage.

$$\frac{t_A}{t_s} = \frac{(\tilde{p} - t_1/\tau)}{\ln(1 + (\tilde{p} - t_1/\tau)/\tilde{p}^2)} \quad (2)$$

$$\text{Here } t_A = \frac{s \hbar \omega_2}{\sigma_A^{(2)} P_A}, \quad n^* = N/N_0, \quad \tilde{p} = P^{(2)}/P_A.$$

$$P^{(2)} \text{ is the SH average power; } P^{(2)} = I_2 t_p f \hbar \omega_2 \cdot s,$$

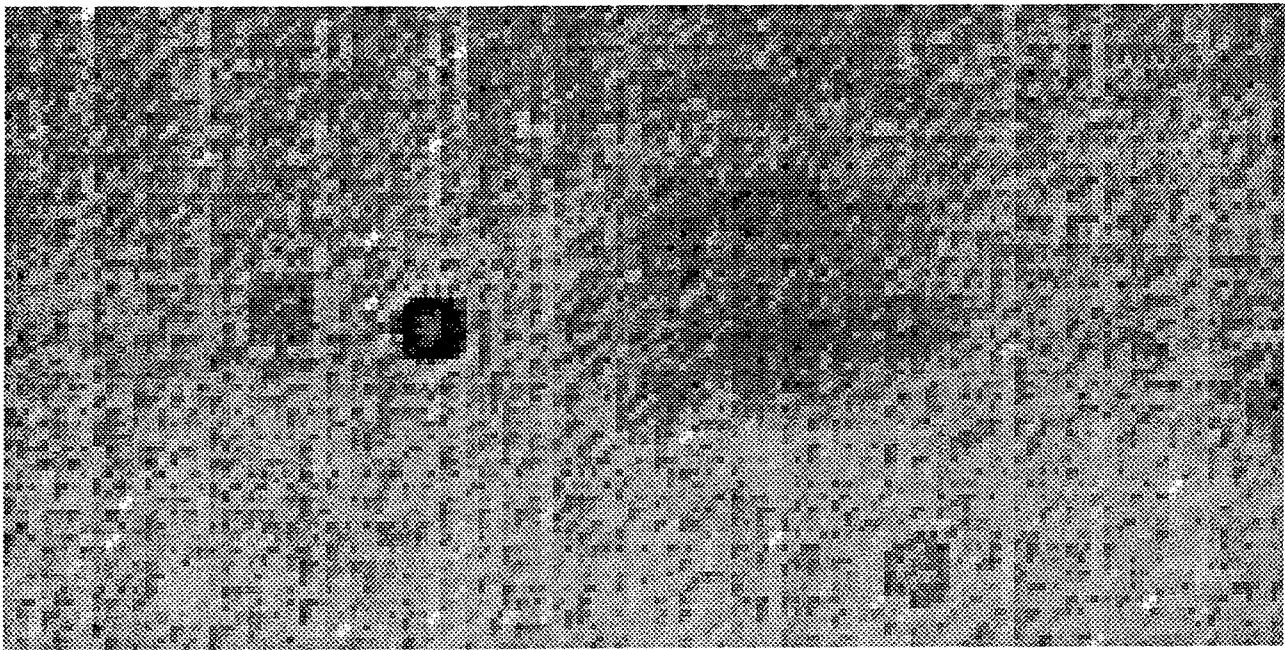
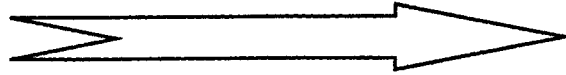
s is the beam waist area, $\hbar \omega_2$ is the photon energy, ω_2 is the SH frequency,

$$P_A = n^* \sigma_A^{(2)} t_p f \delta^{-1} \hbar \omega_2 \cdot s$$

It is evident that (2) is valid if $\tilde{p} > t_1/\tau$, otherwise $t_1/t_s = 0$.

The fitting of the experimental data by the model (1) is shown in Fig.2 (curve 2). The appropriate values of parameters involved are as follows:

LASER



10 μm

Fig.1 Typical sideview optical microscope picture of the optical damage in bulk of the sample for the exposure time slightly more than the damage delay time.

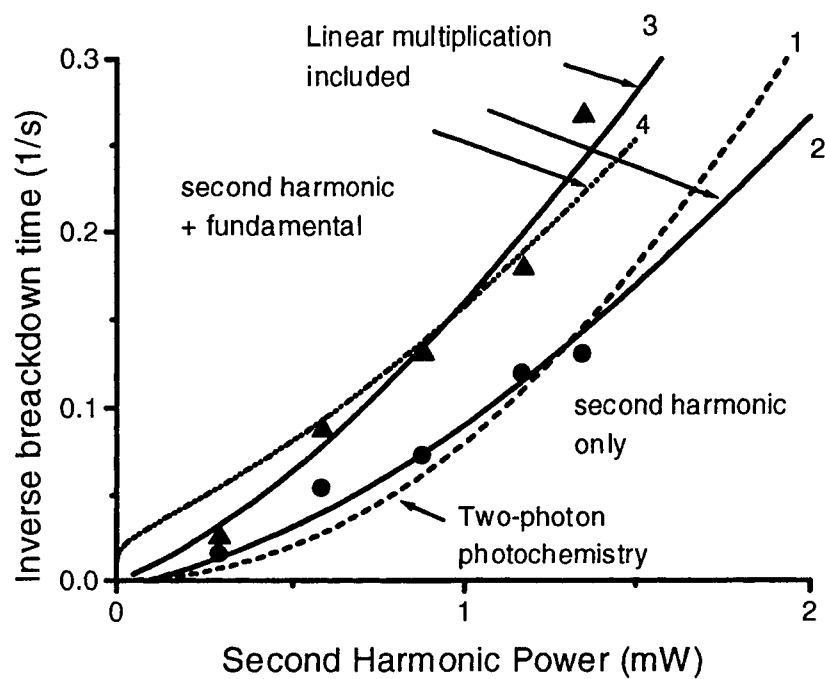


Fig.2 Experimental data of measurements of the inverse delay time between the exposure beginning and the glow ignition vs. SH power for the case of illumination by the SH only (circles) and by both harmonics simultaneously (triangles). Curves 1,2,3,4, - fitting of experimental data by different models (see text).

$$\delta/n^* \leq 10^{-53} \text{ cm}^4 \text{ s}; \quad \sigma_A^{(2)} = 0.8 \cdot 10^{-24} \text{ cm}^2; \quad \tau \geq 50 \text{ s}.$$

Another criterion of the damage of material can be connected with the appropriate heating of the irradiated region.

The simplest model can be formulated as follows. The small linear absorption initiates the photochemical reaction resulting in formation of strongly absorbing species. This induced absorption accounts for the heating of the material. In what follows we suppose that the temperature can be estimated by its quasistationary value. Temperature estimation in the waist region can be performed by calculating a stationary increase in temperature (ΔT) in the center of the evenly absorbing sphere with the radius equal to the waist radius. While doing this we slightly overestimate the influence of heat conductivity.

$$\frac{dN}{dt} = (N_0 - N)\sigma_A^{(2)} I_2 t_P f \quad (3)$$

$$\Delta T = \frac{I_2 t_P f \sigma_H^{(2)} N \hbar \omega_2 \cdot s}{2\pi \chi c \rho} \quad (4)$$

Here N is the number density of products of photochemical reaction, $\sigma_A^{(2)}$ is the product of absorption cross-section of initial absorbing species (with the number density N_0) and the quantum yield of photochemical reaction, $\sigma_H^{(2)}$ is the absorption cross-section of the reaction products. χ is the thermal diffusivity, c is the specific heat, and ρ is the material density. The model (3), (4) yields the relation

$$\frac{t_H}{t_s} = \frac{p}{\ln\left(\frac{1}{1-1/p}\right)} \quad (5)$$

$$\text{Here } p = P^{(2)}/P_H, \text{ and } P_H = \frac{2\pi\chi c \rho \Delta T^*}{\sigma_H^{(2)} N_0}; \quad \Delta T^* = T^* - T_{\infty}; \quad t_H = \frac{s \hbar \omega_2}{\sigma_A^{(2)} P_H}$$

It is understood that (5) is valid only if $P^{(2)} > P_H$. Otherwise, the stationary temperature cannot reach its critical value $T = T^*$ needed for the onset of damage. Fitting of experimental data by the model (5) provides $t_H = 10^3 \text{ s}$, $P_H = 10^4 \text{ W}$. In our experiments $s \sim 10^{-8} \text{ cm}^2$, $\hbar \omega_2 = 4.7 \cdot 10^{-19} \text{ J}$, This allows estimating $\sigma_A^{(2)} \cong 4.7 \cdot 10^{-26} \text{ cm}^2$.

It is interesting to estimate the value of induced absorption coefficient. In all the models that attribute the damage to heating of material up to the appropriate temperature, the effective absorption coefficient, which is needed to reach this temperature can be estimated as follows.

$$\alpha_{\text{eff}} = 2\pi\chi c \rho \Delta T^* (P^{(2)})^{-1} \quad (6)$$

If $P^{(2)} = P_H$ where P_H is the minimal laser power providing damage, then α_{eff} is the maximum effective absorption coefficient. In our case $P_H \cong 10^4 \text{ W}$. If we suppose that $\Delta T^* = 300 \text{ K}$, then, taking the values of parameters close to those of PMMA at room temperature, $\chi = 1.2 \cdot 10^{-3} \text{ cm}^2 \text{ s}^{-1}$, $c = 1.26 \text{ J/(gK)}$, $\rho = 1.19 \text{ g/cm}^3$, we obtain: $\alpha_{\text{eff}} \sim 3.4 \cdot 10^4 \text{ cm}^{-1}$.

As it was mentioned above, in Eq. (5) $p > 1$. When $p \gg 1$, the Eq. (5) yields

$$t_H/t_s \cong p^2$$

It means that this model provides results that are very close to the predictions of the simple two-photon photochemical model (curve 1, Fig. 2). Thus, the both corresponding curves practically coincide. Hence, the model of single-photon photochemistry plus heating cannot explain the almost linear character of experimental dependence $1/t_s (P^{(2)})$.

Contrary, in (2) there is no such restriction on \tilde{p} . If $\tilde{p} \ll 1$ and simultaneously $\tilde{p} \gg t_A/\tau$, then Eq. (2) reads:

$$t_A/t_s \cong \frac{\tilde{p}}{\ln(1/\tilde{p})}$$

Thus, Equation (2) can demonstrate almost linear dependence of $1/t_s$ on $P^{(2)}$ measured experimentally. Moreover, it follows from the above consideration that by fitting the experimental data by the formula (2) we can estimate product $t_A \cdot P_A$ rather than t_A and P_A separately. This yields the estimation of $\sigma_A^{(2)}$. The condition $\tilde{p} \ll 1$ allows estimating the upper limit of δ . (See above estimations after Formula (2)).

We also study the model which comprises the kinetic equation (1) yielding the accumulation of absorbing species of number density N and Eq. (4) which reads the increment in temperature provided by heating of those absorbing species. The onset of damage corresponds to heating up to the appropriate temperature ΔT^* .

This model yields:

$$\frac{t_{AH}}{t_s} = \frac{(\tilde{p} - t_2/\tau)}{\ln(1 + (\tilde{p} - t_2/\tau)/\tilde{p}^3)} \quad (7)$$

Here

$$\tilde{p} = P^{(2)}/P_{AH}$$

$$t_{AH} = \frac{s\hbar\omega_2}{\sigma_A^{(2)} P_{AH}}$$

$$P_{AH} = \sqrt{\frac{2\pi\chi c\rho\Delta T^* \sigma_A^{(2)} \cdot t_p f \cdot s \cdot \hbar\omega_2}{\delta \sigma_H^{(2)} N_0}} = \sqrt{P_A P_H}$$

The last equality is valid if in determination of P_A we take $n^* = 1$. It is understood that (2) is valid if $\tilde{p} > t_{AH}/\tau$, otherwise $t_{AH}/t_s = 0$.

Analogous to the above model (1), (2), the experimental points can be fitted by formula (7) if $\tilde{p} \ll 1$. The fitting curve is very close to the curve 2 in Fig. 2. The corresponding asymptotic reads:

$$t_{AH}/t_s \cong \frac{\tilde{p}}{2 \ln(1/\tilde{p})}$$

The fitting of experimental data yields the relation $t_2 \cdot P_2 \approx 2 \cdot 10^{-3} J$; $P_2 \geq 5mW$. Together with the consideration based on relation (6) that is valid for all models including heating through the induced absorption, these relations provide the estimation $\sigma_A^{(2)} = 0.8 \cdot 10^{-24} \text{ cm}^2$; $\delta < 10^{-55} \text{ cm}^4 \text{ s}$.

The fitting of experimental data by the last model provides estimations that are close to that following from the model (1).

Let us consider now the combined effect of the second harmonic and the fundamental frequency radiation. This combined effect within the framework of the model (1) provides the additional multiplication of absorbing species (electrons) by the FF radiation whereas the initial two-photon initiation (ionization) is performed by the SH only. The generalization of equation (1) reads:

$$\frac{\partial N}{\partial t} = (\delta N_0 I_2^2 + N(\sigma_A^{(1)} I_1 + \sigma_A^{(2)} I_2)) t_p f - N/\tau \quad (8)$$

Here I_1, I_2 are the intensities of the FF and the SH at the SH beam waist. $\sigma_A^{(1)}, \sigma_A^{(2)}$ are the corresponding cross-sections. The relation analogous to (2) reads:

$$\frac{t_A}{t_s} = \frac{(\tilde{p} - t_1/\tau + t_1/t^{(1)})}{\ln(1 + (\tilde{p} - t_1/\tau + t_1/t^{(1)})/\tilde{p}^2)} \quad (9)$$

Here $t^{(1)} = \frac{s\hbar\omega_1}{\sigma_A^{(1)} P^{(1)}}$; s being the waist area of SH beam, and

$$P^{(1)} = I_1 t_p f \hbar\omega_1 \cdot s, \omega_1 \text{ is the fundamental frequency.}$$

In the model (3), (4) the Eq. (3) remains unchanged because we assume that photochemical reaction is driven by the SH only, while the generalized Eq. (4) reads:

$$\Delta T = \frac{t_P f N (\sigma_H^{(1)} I_1 \hbar \omega_1 + \sigma_H^{(2)} I_2 \hbar \omega_2) \cdot s}{2\pi \chi c \rho} \quad (10)$$

Eq.(5) now looks like

$$\frac{t_0}{t_s} = \frac{p}{\ln \left[\frac{1}{1 - (p + \frac{\sigma_H^{(1)} P^{(1)}}{\sigma_H^{(2)} P_H})^{-1}} \right]} \quad (11)$$

At least the last model comprising Eqs. (8) and (10) leads to the following relation:

$$\frac{t_{AH}}{t_s} = \frac{(\tilde{p} - t_2/\tau + a)}{\ln(1 + (\tilde{p} - t_2/\tau + a) \tilde{p}^{-2} (p + h)^{-1})} \quad (12)$$

$$\text{Here } a = t_{AH}/t^{(1)} = \frac{\omega_2 \sigma_A^{(1)} P^{(1)}}{\omega_1 \sigma_A^{(2)} P_{AH}} \quad \text{and} \quad h = \frac{\sigma_H^{(1)} P^{(1)}}{\sigma_H^{(2)} P_{AH}}.$$

Let us consider the last model. From the point of view of the studied dependence $1/t_s (P^{(2)})$ the effect of FF radiation is taken into account by terms a and h . The term a describes participation of the FF radiation in multiplication of absorbed species, while the term h accounts for the additional heating provided by the FF radiation. If we fix the value of h and increase gradually the value of a from 0, then we obtain the gradual decrease of the offset of the curve caused by the term t_{AB}/τ . Increasing the value of a beyond t_{AB}/τ results in onset of a sharp increase of the curve just near the value $P^{(2)}=0$. ($1/t_s = 0$ at $P^{(2)} = 0$). This sharp increase is followed by almost linear dependence of $1/t_s$ on $P^{(2)}$ as shown in Fig.2, curve 4. The parameter h regulates the slope of the curve. Curve 3 in Fig.2 corresponds to the values $a=0.01$,

$h = 0.45$. It provides a good fit but yields the inequality $\frac{\sigma_H^{(1)}}{\sigma_H^{(2)}} \gg \frac{\sigma_A^{(1)}}{\sigma_A^{(2)}}$. This means that the contribution of FF radiation

to heating is significantly greater than to multiplication of absorbing species. It hardly could be understood within the framework of the plasma model. Contrary, curve 4 in Fig.2 corresponds to $a=0.06$, $h = 0.09$. Here the mentioned above ratios of cross-sections are close to each other. This is inherent to the ionization model of damage.

The fitting of experimental curve by the formula (9) also leads to curve 4. Curve 3 can be obtained here only by the additional assumption that the FF radiation changes the value of $\sigma_A^{(2)}$. At the moment we cannot choose between different models because of lack of experimental data. Our estimations show the value $P^{(1)} \cong 10^{-4} W$. Such small value is connected with mismatching of focuses of FF radiation and SH due to chromatic aberration of the lens. It should be noted that all the models considered above predict an essential decrease in breakdown time with an increase in FF intensity at the SH beam waist area.

4. CONCLUSIONS

We have shown that it is possible to produce a controllable bulk damage of pure PMMA by low-average-power second harmonic of a high-repetition-rate femtosecond Ti:Sapphire laser. The fact that optical damage may be confined in volume with micrometer dimensions demonstrates an attractive feature of the proposed method for high-density optical recording and microfabrications.

It is shown that the combined effect of SH and FF radiation provides a decrease in breakdown time, while irradiation by FF does not affect the material.

Theoretical models are derived which attribute almost linear dependence of inverse breakdown time on the second harmonic power to some kind of self-developing process. The SH radiation initiates this process while the FF radiation together with the SH can participate in multiplication of absorbing species and in heating of the material. These models allow estimating the main parameters involved.

ACKNOWLEDGEMENTS

The authors are grateful to Dr. A.P.Alexandrov for providing with the PMMA sample and to Prof. A.M.Sergeev for helpful discussions. This work was supported in part by the Russian Foundation for Basic Researches.

REFERENCES

1. J. H. Strickler, W.W.Webb, "Three- dimensional optical data storage in refractive media by two-photon point excitation", *Opt. Letters*, **16**, pp. 1780-1782, 1991.
2. A.S.Dvornikov, J.Malkin, and P.M.Rentzepis, "Spectroscopy and Kinetics of Photochromic Materials for 3D Optical Memory Devices," *J.Phys.Chem.*, **98**, pp. 6746-6752, 1994.
3. R.M. Shelby, J.A. Hoffnagle, G.W. Burr, C.M. Jefferson, M.-P. Bernal, H. Coufal, R.K. Grygier, H. Günther, R.M. Macfarlane, G.T. Sincerbox, "Pixel-matched holographic data storage with megabit pages", *Opt. Letters*, **22**, pp. 1509-1511, 1997.
4. X. Liu, D. Du, G. Mourou, "Laser ablation and micromachining with ultrashort laser pulses", *IEEE Journal of Quantum Electronics*, **33**, pp.1706-1716, 1997.
5. N. Glezer, M. Milosavljevic, L.Huang, R.J.Finlay, T.-H.Her, J.P.Callan and E.Mazur, "Three-dimesional optical storage inside transparent materials", *Opt. Letters*, **21**, pp. 2023-2025, 1996.
6. A.I.Korytin, N.M.Bityurin, A.P.Alexandrov, N.A.Babina, L.A.Smirnova, and A.M.Sergeev, "High-contrast bitwise three-dimensional optical data storage in doped polymers", *Optical Memory and Neural Networks*, **7**, pp. 11-18, 1998.
7. M.Castillejo, S.Couris, E.Koudoumas, M.Martin, "Subpicosecond ionization of benzene and cyclic alkanes at 800and 400nm", *Chem. Phys. Letters*, **289**, pp. 303-310, 1998
8. B.C.Stuart, M.D.Feit, S.Herman, A.M.Rubenchik, B.W.Shore, and M.D.Perry, "Optical ablation by high-power short-pulse lasers", *J.Opt.Soc.Am.B*, **13**, pp. 459-468, 1996.

SESSION 4

Laser-induced Modification of Surface and Subsurface Properties of Materials

Photoinduced and grating alignment of polyimide using excimer lasers for liquid crystal displays

Christopher J. Newsome^a, Mary O' Neill^{*a} and Guy P. Bryan-Brown^b

^aDepartment of Physics, The University of Hull, Hull, HU6 7RX, UK,

^bDefence Evaluation and Research Agency, St. Andrews Rd., Malvern, Worc. WR14 3PS, UK

ABSTRACT

Recently there has been renewed interest in the grating alignment of liquid crystals because of its application in bistable nematic displays. In this paper, grating and photoinduced liquid crystal alignment techniques based on excimer laser exposure of thin polyimide films are discussed. Gratings are etched into the alignment film using a KrF laser illuminated through a phase mask. These give homogeneous liquid crystal alignment with the liquid crystal directors aligned along the grooves of the grating. The observed azimuthal anchoring strength is compared with that predicted using Berreman theory. No pretilt is observed because of the grating symmetry. When a polarized excimer laser beam is incident on the film with a fluence below that required for ablation, an anisotropy is photoinduced which results in liquid crystal alignment perpendicular to the polarization direction. This anisotropy is created photochemically by selective depletion of the polymer chains. Exposure of the polyimide with elliptically polarized light at non-normal incidence gives pretilted alignment. Grating etching followed by photoinduced alignment can be used to obtain pretilted grating alignment with a pretilt angle of 3°.

Keywords: excimer laser; laser ablation; gratings; phase mask; polyimide; liquid crystals; alignment; pretilt; azimuthal anchoring; photoinduced alignment;

1. INTRODUCTION

Gratings etched into thin films have been known to homogeneously align liquid crystals for many years and have attracted renewed interest recently because of their application in novel nematic displays. For example, gratings coated with a low energy surfactant show two surface anchoring states that can be exploited in bistable nematic¹ and voltage-controlled twist² devices. The grating alignment mechanism was first studied by Berreman³, who showed that elastic strain is minimized when the molecular director aligns parallel rather than perpendicular to the grating grooves. Since then reactive-ion etching^{4,5}, photolithographic^{6,7} and stamping⁸ methods have been used to etch gratings onto liquid crystal alignment layers. Pretilted liquid crystal alignment, where the director axis is uniformly displaced by a small angle out of parallelism with the substrate, is essential for displays as it prevents the development of reverse tilt domains on switching. Using the latter method⁸, such alignment was achieved with a double grating topology: a weaker tilted grating was formed with wave-vector parallel to the micro-grooves of the grating that dominates the anchoring. Niino et al. first investigated liquid crystal alignment using ripples etched into polyethersulfone films by polarized excimer laser ablation⁹. These ripples, with period $\sim 1 \mu\text{m}$ and amplitude $\sim 0.04 \mu\text{m}$, spontaneously develop because of interference between the transmitted and diffracted waves in the expanding plume of ablated products above the polymer¹⁰. They found that a dye-doped liquid crystal in a grating aligned cell showed an absorbance ratio of 3.2:1 for polarization parallel and perpendicular to the direction of the gratings. Excimer laser irradiated phase masks provide a more convenient and controllable method to etch gratings into polymer layers¹¹. This alignment technique would be particularly useful for multi-domain displays with large viewing angles since phase masks can be designed to produce microscopic variations in the alignment direction. Using unpolarized light from a KrF laser, we reported alignment of twisted nematic cells by gratings ablated into polyimide¹². Azimuthal anchoring energies of $3.5 \times 10^{-6} \text{ Nm}^{-1}$ were found in agreement with the Berreman theory.

* Correspondence: Email: M.Oneill@physics.hull.ac.uk; Telephone: +44 1482 465246; Fax: +44 1482 465606

Prolonged exposure of polyimides to linearly polarized light from a UV lamp can also achieve liquid crystal orientation^{13,14}. The alignment results from the anisotropic depolymerisation of the polyimide chains along the polarization direction of the incident light. The alignment direction, therefore, is usually perpendicular to that of the incident polarization although parallel alignment has been found using some polyimides containing sidechains^{15,16}. The threshold UV fluence required to achieve photoalignment is generally high ($> 10 \text{ J cm}^{-2}$) compared to that required for polyvinyl coumarin derivatives¹⁷ ($< 0.02 \text{ J cm}^{-2}$) although a threshold of 0.72 J cm^{-2} was found for an oxydiphenylene polyimide¹⁶. Small pretilt angles have been reported with the oblique exposure of polyimides which give alignment parallel to the polarization direction^{18,19}. Higher pretilt angles, from 0° to homeotropic, can be achieved by increasing the degree of imidization of the polyimide²⁰. Varying the temperature of the hard bake prior to exposure does this. Recently, we found that a photoinduced alignment results from exposure of polyimide to a polarized excimer laser at 248 nm ²¹. Ten shots of fluence 13 mJ cm^{-2} give alignment with a saturated azimuthal anchoring energy $> 10^{-5} \text{ J m}^{-2}$. Pretilt angles of about 1° were also found for oblique exposures.

Excimer lasers are currently used to anneal defects in amorphous silicon thin film transistors that are used as backplates for twisted nematic displays. Hence, laser technology is accepted by the liquid crystal industry and the excimer laser processing of alignment layers has many advantages. For example, grating alignment by laser ablation is a non-contact alignment technology that avoids the mechanical and electrostatic damage to transistors, which currently limits the yield of rubbed active matrix displays. Furthermore laser etching is a one step process and avoids the wet chemistry required for grating production by photolithography. The laser-induced photoalignment of polyimides occurs on a timescale of seconds, i.e. at least three orders of magnitude shorter than typical UV lamp exposure times.

In this paper we discuss recent developments in both grating and photoinduced alignment of polyimide films using excimer lasers. We measure the azimuthal anchoring energy of grating aligned nematic cells for a wide range of grating amplitudes and compare them with the Berreman predictions. We also show that the photoinduced alignment effect can be combined with grating alignment to give pretilted anchoring.

2. SAMPLE PREPARATION AND MEASUREMENT

Commercial polyimide films (Nissan SE130) on InSnO coated glass were prepared by spin-casting followed by baking at 180° for 30 minutes. These films were illuminated with light from a KrF laser at 248 nm with a pulse duration of 25 ns. The films were placed about $180 \text{ }\mu\text{m}$ behind a phase mask of period $\lambda = 1.1 \text{ }\mu\text{m}$, and gratings were etched onto the polyimide using one or two shots from the laser operating above the threshold fluence for ablation. The grating amplitude was calculated from measurements of first order diffraction efficiency of light from a HeNe laser²². Atomic force microscopy was used to calibrate these measurements and also to obtain the grating period. An anisotropy was photoinduced in the alignment layers on exposure to the UV beam operating below or just above threshold. In this case, the KrF laser was polarized using a "pile of plates" so that its output polarization was elliptical with a s:p ratio dependent on the numbers of Brewsters plates. The s:p ratio also varies with angle of incidence of the beam onto the polymer because of the different reflection coefficients for s and p polarized light. Typically, a polarization ratio of about 20:1 was achieved for the laser emission. The angle of incidence of the UV light was varied to achieve pretilted alignment. 90° twisted nematic cells of thickness $17 \text{ }\mu\text{m}$ filled with the nematic liquid crystal E7 (Merck) were constructed using one grating/exposed alignment surface and one rubbed polyimide layer with perpendicular alignment directions. On observation through crossed polarizers, the cells appear white because of the waveguiding effect. In these cells, the actual twist angle, ϕ , may be less than the constructed twist angle, because of competition between surface and bulk forces. The cells were mounted on a polarizing microscope with the input polarizer arranged parallel to the rubbed direction. ϕ was measured by rotating the analyzer to achieve maximum extinction. Assuming infinite anchoring at the rubbed polyimide surface, the azimuthal anchoring energy can be found from the equation²³

$$W_\phi = \frac{2K_{22}\phi}{d \sin 2\phi} \quad (1),$$

where K_{22} is the twist elastic constant and d the cell spacing measured before filling using a spectrophotometer. The pretilt angle of antiparallel nematic cells, constructed with two photo-aligned surfaces exposed with equal UV fluence, was

determined by the crystal rotation method^{24,25}. Both the azimuthal anchoring energy and pretilt angles were measured at room temperature.

3. GRATING FORMATION WITH NONPOLARIZED LASER ABLATION

An ideal phase mask, where the zero order is fully suppressed, produces a sinusoidal distribution of transmitted irradiance with period $\lambda/2$ and 100% modulation between the peaks and troughs, because of first order interference. If there is perfect spatial beam coherence, efficient grating ablation can occur independently of the distance between the mask and sample. This is particularly useful since the non-contact processing of alignment layers is desirable to avoid damage to large display substrates. In our experiments, the phase mask shows some zero and second order diffraction at 248 nm resulting in an ablated grating period of λ , as predicted by a numerical calculation²⁶. Furthermore, the excimer laser has a beam divergence of 1.5 mrad so that the contrast between the maxima and minima of the irradiance pattern decreases with distance from the phase mask. It is this difference, rather than the laser fluence alone, which determines the etch depth.

In a previous publication¹² we reported that, for a limited range of grating amplitudes (60 nm to 80 nm), the azimuthal anchoring energy measured using equation one agrees with that predicted with the Berreman theory, expressed as

$$W_B = \frac{2\pi^3 a^2 K}{\lambda^3} \quad (2),$$

where a is the grating amplitude and K the geometric average of the bend and splay elastic constants. We now extend this investigation to grating depths between 0.01 μm and 0.15 μm . The gratings were formed by ablation with a single shot of unpolarized light from the laser. Twist nematic cells were constructed using one rubbed and one grating-etched polyimide surface and the azimuthal anchoring energy was measured as a function of grating amplitude.

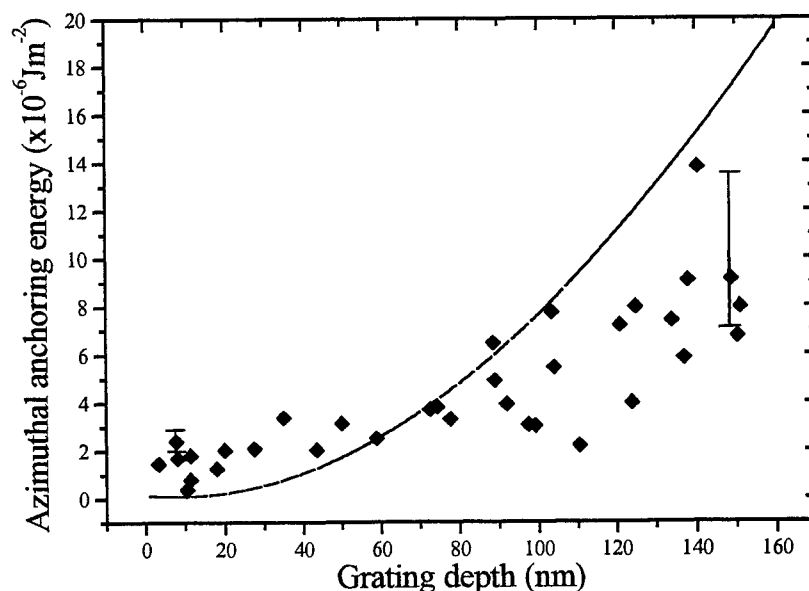


Figure 1. Variation of azimuthal anchoring energy of twisted nematic cells with grating amplitude. The cells were prepared using one rubbed and one grating aligned anchoring surface. The diamonds and solid line indicate the anchoring energies, W_ϕ and W_B , calculated using equations one and two respectively. Unpolarized light was used to etch the gratings.

In calculating W_ϕ from equation one, the error in the twist angle is taken to be $\pm 1^\circ$. This uncertainty reflects the error in obtaining the angle of extinction as well as spatial variations in the twist. Hence the error in W_ϕ increases with ϕ . In the

computation of W_B , the error in the grating amplitude is taken as $\pm 10\%$. Figure one shows that for grating amplitudes between 60 nm and 90 nm, the measured anchoring energies agree with the Berreman theory. Smaller grating amplitudes provide anchoring that is consistently greater than that predicted from the Berreman calculation whereas larger grating amplitudes give weaker than expected alignment. Although the cells were filled in the isotropic phase of the liquid crystal, there may be residual flow alignment along the grating grooves that may explain the larger than expected anchoring at small grating amplitudes. Flow alignment would be expected to give an anchoring independent of grating amplitude but its effect would be not be significant for bigger grating depths. The weak anchoring observed with larger grating depths has many possible explanations. The derivation of equation two assumes sinusoidal gratings whereas laser ablation can produce a variety of grating profiles, depending on the laser fluence and its periodic variation. We are currently investigating the variation of W_B with grating shape and the results will be reported elsewhere. As Faetti points out²⁷, if the assumption of infinite polar anchoring used in the derivation of equation 2 is invalid, periodic variations of the surface pretilt angle can occur at the grating surface to reduce the azimuthal surface anchoring. Taking finite polar anchoring into account, equation 2 can be modified so that W_B becomes

$$W_B = \frac{2\pi^3 a^2 K}{\lambda^3} \left[\frac{1}{1 + \frac{\pi K}{\lambda W_p}} \right] \quad (3),$$

where W_p is the polar anchoring energy. A polar anchoring energy of $1 \times 10^{-4} \text{ Jm}^{-2}$ would reduce W_B by a factor of 1.4, leading to agreement with the measured W_p at the larger grating amplitudes. We have yet to measure W_p of grating aligned polyimide layers but values $\approx 10^{-3} \text{ Jm}^{-2}$ are found for rubbed polyimide²⁸. However, the process of laser ablation may influence the polar anchoring energy of the grating layers. Wood et al.²⁹ suggest that the calculations of W_B and W_p should use elastic constants appropriate to the temperature at which the liquid crystal molecules first take up a minimum energy configuration at the grating surface on cooling. This changes the results by about 10%, which is too small to explain the discrepancy in our measurements.

4. POLYIMIDE EXPOSURE WITH POLARIZED LASER RADIATION

4.1 Photoinduced alignment

We have previously reported²¹ that the exposure of polyimide layers with polarized light from a KrF laser photoinduces an optical anisotropy which gives liquid crystal alignment with azimuthal anchoring energies in excess of $1 \times 10^{-5} \text{ Jm}^{-2}$. The laser fluences used were below the threshold for ablation. The alignment direction is perpendicular to the polarization direction of the incident radiation. Hence, the alignment can be explained by the anisotropic depolymerisation of the polyimide chains, as occurs by prolonged illumination with continuous UV lamps. We found that oblique exposure to elliptically polarized light with a s:p ratio >1 resulted in pretilted alignment whereas no pretilt was observed when the s:p ratio was <1 . Pretilt occurs because the distribution function of the polyimide chains become tilted on illumination. The probability of a photochemical reaction is proportional to $\mathbf{m} \cdot \mathbf{e}$ where \mathbf{m} is the polarization vector of a photosensitive bond, assumed parallel to the polyimide chain direction, and \mathbf{e} the electric field direction of the optical wave. Hence the angular distribution of photosensitive bonds varies with time during a photochemical reaction according to

$$N(\theta, \phi) = N_0(\theta, \phi) \exp(-\alpha t \cos^2 \theta \cos^2 \phi) \quad (4),$$

where α is a constant, θ is the out-of-plane tilt angle and ϕ the azimuthal angle measured from \mathbf{e} . Since s:p >1 , the s polarized component dominates the azimuthal depolymerisation so that the azimuthal polyimide distribution is maximized perpendicular to its electric vector. However, symmetry considerations dictate that only the p polarized component can generate a tilted polyimide number density. We found that when an unexposed isotropic distribution is assumed before exposure, the polymer inclination angle measured from the surface is equal to $(\pi/2 - \theta_t)$, where θ_t is the angle of refraction of the laser beam on the polyimide during exposure: i.e. the polymer number density is maximized parallel to the direction of the refraction ray. This is illustrated in figure two.

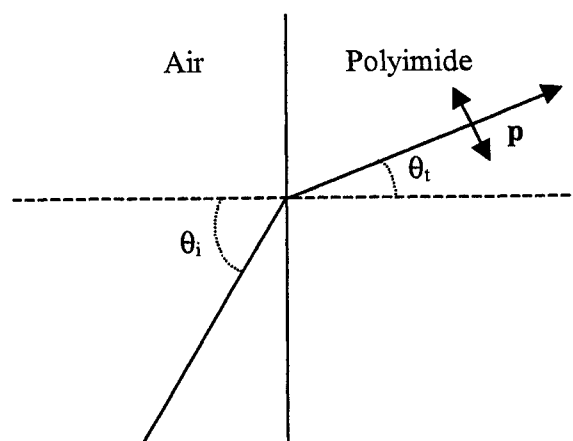


Figure 2. The solid lines show the incident and transmitted rays across the air-polyimide interface at oblique incidence. The electric field direction of \mathbf{p} polarized light is indicated. Assuming an initial isotropic distribution, the depolymerisation of the polyimide chains is maximized along this direction. Hence the maximum polyimide density is achieved along the ray direction giving a polymer tilt angle of $(\pi/2 - \theta_t)$.

However, spin-cast polyimide layers orient parallel to the substrate with a polar distribution which can be described by a Gaussian, so that the polymer tilt angle would not be as large as given above: for example a standard deviation of 15° gives a polymer inclination angle of only 1.5° . A more sophisticated approach is required to relate the polymer inclination angle to the liquid crystal pretilt angle and this has not been attempted. A polarized infra-red analysis shows that the liquid crystal pretilt angle is linearly dependent on the polymer inclination angle for rubbed polymer layers³⁰. Galabova et al. use the Landau de Gennes theory to relate the pretilt angle to the irradiation conditions of polyimide photoaligned with two UV exposures³¹.

In a previous publication we reported pretilt angles between 0.7° and 1.1° when polyimide layers of thickness 2000 \AA were used. Figure 3 shows the transmitted intensity as a function of incident angle (θ) through a nematic cell having the alignment layers, which were exposed using identical conditions, in an antiparallel configuration. These polyimide layers were 5000 \AA thick and were exposed at an incident angle of 75° with 40 shots of fluence 6 mJ cm^{-2} . The transmission is not symmetric about $\theta = 0$ indicating that pretilt is achieved. The liquid crystal pretilt angle, θ_p , is found from the equation,

$$\sin 2\theta_p = \frac{2 \sin \alpha}{n_o + n_e \sqrt{1 + (\sin \alpha / n_o)^2}} \quad (5),$$

where α corresponds to the angle which gives maximum transmission. θ_p is found to be 2.7° which is over twice as large as that measured previously. Larger pretilt angles are consistently obtained when thicker polyimide layers are used. These are expected to have a broader Gaussian distribution and, on exposure, would give a larger polymer inclination angle as explained above. All of the polyimide layers used were cured at the same temperature. Hence the difference in pretilt angle is not due to differences in the degree of imidization which is known to affect the pretilt angle²⁰.

4.2 Grating alignment with polarized light

Grating alignment was examined using laser ablation with polarized light at normal incidence and the azimuthal anchoring energy of twisted nematic cells was measured as a function of grating depth. Figure four shows that, when the

grating amplitude is small, the measured azimuthal anchoring energy is much greater than that calculated on the basis of grating alignment alone. The difference is too big to be explained on the basis of flow alignment. However, the

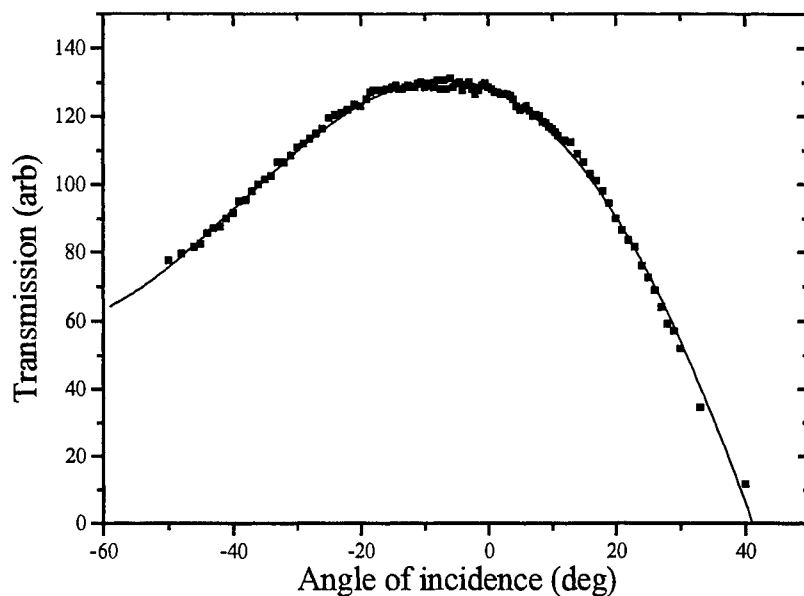


Figure 3. Transmitted intensity versus incident angle through an antiparallel aligned nematic cell using the crystal rotation method. The solid is a fitted curve to obtain the pretilt angle.

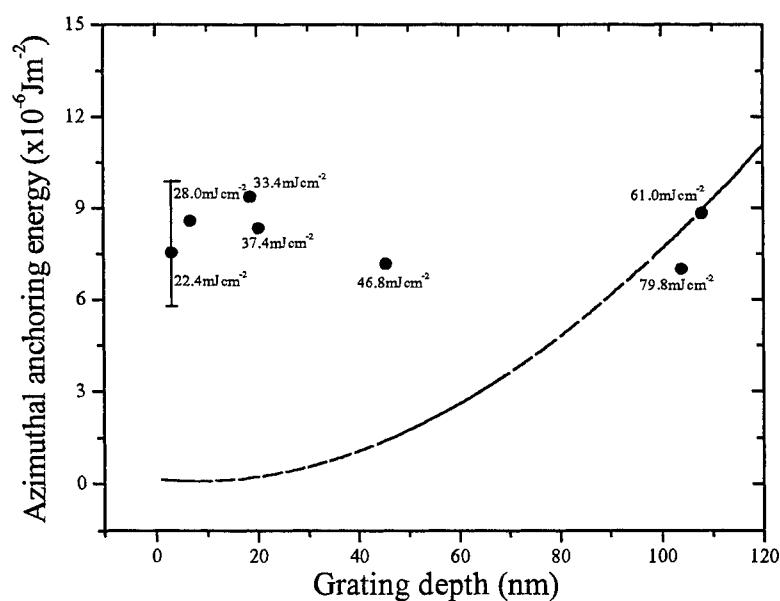


Figure 4. Azimuthal anchoring energy versus grating amplitude for TN cells with alignment layers etched using polarized light. The circles and solid line indicate the anchoring energies, W_ϕ and W_B , calculated using equations one and two respectively. The laser fluence used for ablation is indicated for each point.

polarization vector of the incident light was perpendicular to the grating grooves so that the alignment due to the photoinduced effect should add to that resulting from grating formation. When deeper gratings are etched, the measured anchoring energy could be explained on the basis of the grating only: no extra anchoring due to the photoinduced effect is apparent. The threshold for laser ablation is $I_{th} = 22 \text{ mJ cm}^{-2}$, so that the latter gratings were formed with fluences $> 2.5I_{th}$. These results suggest that when high fluences are used a surface polarization memory is not retained possibly because the ablation occurs by a photothermal rather than a photochemical reaction. However, in view of the smaller than expected grating alignment discussed in section three, a more detailed analysis is required to quantify the relative contribution of the grating and photoinduced alignment.

4.3 Pretilted grating alignment

Grating alignment has the disadvantage that the achievement of pretilt requires complex processing. For example, pretilted grating alignment has been obtained using a double grating topography⁸. In this configuration a weak blazed grating is formed perpendicular to a symmetric grating which determines the azimuthal alignment direction. Blazed gratings are difficult to obtain using a phase mask so that the photoinduced effect was investigated in conjunction with laser ablation in order to achieve pretilted grating alignment. For this experiment, the grating was etched onto the polyimide alignment layer by ablation using unpolarized light through the phase mask. This was followed by exposure with polarized light from the laser at a fluence below the ablation and with an incident angle of 75° . A pretilt angle of 3° was found for nematic cells, which were prepared using two identical alignment layers arranged in an antiparallel configuration. The azimuthal anchoring energy of the obliquely exposed grating layers is dependent on the grating depth, with typical values being $\approx 1 \times 10^{-5} \text{ Jm}^{-2}$.

5. DISCUSSION AND CONCLUSIONS

The azimuthal anchoring energy achieved by grating alignment with nonpolarized light is small but large improvements can be made by optimization of the phase mask. As shown in equation two, the azimuthal anchoring energy is inversely proportional to the cube of the grating period, so that much stronger anchoring would be obtained using smaller periods. This would also decrease the influence of a finite polar anchoring energy. Furthermore, the sinusoidal energy distribution of the UV light behind the phase mask has a contrast ratio between the peaks and troughs of only about two. The profile of the etched grating depends on this contrast as well as the absolute laser fluence relative to the ablation threshold. The novelty of our approach towards achieving grating and photoinduced alignment is the use of excimer lasers. This gives the advantages discussed in section one, and both alignment methods can be combined in the one device as illustrated in section four above. Preliminary spectroscopic studies of the laser-induced photoalignment suggest that anisotropic depolymerisation is involved as occurs with UV lamp illumination. However, the total fluence required for the laser-alignment process is much less than that typically used with lamp exposure, although quantitative comparisons are impossible since the exact chemical composition of SE130 is unknown. The excellent match of the excimer laser wavelength to the absorption peak of SE130 may be the explanation. Alternatively, nonlinear effects are involved in the laser-induced photoalignment and these are being investigated.

In conclusion, gratings etched onto polyimide thin films can be used to align nematic liquid crystals. When unpolarized laser light at 248 nm is used to ablate the gratings, a modified Berreman model is required to explain the variation in the azimuthal anchoring energy with grating amplitude. Exposure with polarized light below the fluence required for ablation gives a photoinduced alignment. Pretilt angles up to 3° have been obtained using an oblique exposure with elliptically polarized light. A convenient method is developed to achieve pretilted grating alignment: this involves grating formation followed by oblique exposure. This technique could be developed for use in bistable nematic devices.

ACKNOWLEDGEMENTS

We acknowledge The Engineering and Physical Sciences Research Council and DERA for providing a studentship. We thank A. J. Pidduck is thanked for carrying out the AFM measurements and P. E. Dyer for use of the laser.

REFERENCES

1. G. P. Bryan Brown, E. L. Wood, C. V. Brown, J. C. Jones, I. C. Sage and P. Brett, "Grating aligned bistable nematic devices", *Proc. IDW 97 (SID)*, pp. 261, (1997).
2. G. P. Bryan Brown, C. V. Brown, I. C. Sage and V. C. Hui, "Voltage dependent anchoring of a nematic liquid crystal on a grating surface" *Nature*, **392** pp. 365, (1998).
3. D. W. Berreman, "Alignment of liquid crystals by grooved surfaces", *Mol. Cryst. Liq. Cryst.*, **23** pp. 215-231, (1973).
4. D. C. Flanders, D. C. Shaver and H. I. Smith, "Alignment of liquid crystals using submicrometer periodicity gratings", *Appl. Phys. Lett.* **32** pp. 597-598, (1978).
5. J. Cheng and G. D. Boyd, "The liquid crystal alignment properties of photolithographic gratings", *Appl. Phys. Lett.* **35** pp. 444-446, (1979).
6. G. P. Bryan-Brown, J. R. Sambles and K. R. Welford, "Grating coupled liquid crystal waveguides using nematics and smectics" *J. Appl. Phys.* **73** pp. 3603-3607, (1993).
7. Y. Kawata, K. Takatoh, M. Hasegawa and M. Sakamoto, "The alignment of nematic liquid crystals on photolithographic micro-grooves patterns". *Liq. Cryst.* **16** pp. 1027-1036, (1994).
8. E. S. Lee, P. Vetter, T. Miyashita, T. Uchida, M. Kino, M. Abe and K. Sugawara, "Control of liquid crystal alignment using stamped morphology method", *Jpn. J. Appl. Phys.* **32** pp. L1436-L1438, (1993).
9. H. Niino, Y. Kawabata and A. Yabe, "Application of excimer laser ablation to alignment of liquid crystals: Periodic microstructure on polyethersulfone", *Jpn. J. Appl. Phys.* **28** pp. L2225-L2227, (1989).
10. P. E. Dyer and R. J. Farley, "Periodic surface structure in the excimer laser ablative etching of polymers", *Appl. Phys. Lett.*, **57** pp. 765-767, (1990).
11. P. E. Dyer, R. J. Farley and R. Giedl, C. Ragdale and D. Reid, "Study and analysis of submicron period grating formation on polymer ablated using a KrF laser-irradiated phase mask" *Appl. Phys. Lett.* **64** pp. 3389-3391, 1994.
12. C. J. Newsome, M. O' Neill, R. J. Farley and G. P. Bryan Brown "Laser etched gratings on polymer layers for alignment of liquid crystals", *Appl. Phys. Lett.* **72** pp. 2078-2081, (1998).
13. M. Hasegawa and Y. Taira, "Nematic homogeneous photo alignment by polyimide exposure to linearly polarized light" *J. Photopol. Sci. Tech.*, **8**, pp. 241, (1995).
14. J. L. West, X. Wang, Y. Ji and J. R. Kelly, "Polarized UV-exposed polyimide films for liquid crystal alignment", *SID 95 Digest*, pp. 703-705, (1995).
15. H. Endo, T. Shinozaki, H. Fukuro, Y. Imura and S. Kobayashi, *IDW96* (1996).
16. M. Nishikawa, B. Taheri and J. L. West, "Mechanism of unidirectional liquid crystal alignment on polyimide with linearly polarized ultraviolet light exposure", *Appl. Phys. Lett.*, **72**, pp. 2403, (1998).
17. P. Hindmarsh, G. J. Owen, S. M. Kelly, P. O. Jackson, M. O' Neill and R. Karapinar, "New coumarin polymers as non-contact alignment layers for liquid crystals" accepted by *Mol. Cryst. Liq. Cryst.* (1999).
18. T. Yamamoto, M. Hasegawa and H. Hatoh, "Liquid crystal alignment by slantwise irradiation of non-polarized UV light on a polyimide layer", *SID 96 Digest*, pp. 634, (1996).
19. D.-S. Seo, L.-Y. Hwang and S. Kobayashi, "Generation of pretilt angles in a nematic liquid crystal by transcription alignment of a polyimide surface" *Liq. Cryst.*, **23** pp. 923, (1997).
20. W. Wang, D. Subacius, O. Lavrentovich and J. L. West, "Four domain LCD using high pretilt photoaligned substrates", *SID 96 Digest*, pp. 655, (1996).
21. C. J. Newsome and M. O' Neill, "Photoinduced alignment of liquid crystals using polyimide irradiated with a polarized excimer laser" accepted by *Mol. Cryst. Liq. Cryst.* (1999).
22. C. J. Newsome, M. O' Neill, R. J. Farley and G. P. Bryan-Brown, "Azimuthal anchoring energy of liquid crystals aligned using laser ablated gratings on polyimide", *Proc. SPIE 3297* pp. 19, (1998).
23. G. P. Guy-Bryan and I. C. Sage, "Photoinduced ordering and alignment properties of polyvinylcinnamates", *Liq. Cryst.* **20** pp. 825-829, (1996).
24. T. J. Scheffer and J. Nehring, "A new highly multiplexable liquid crystal display", *Appl. Phys. Lett.*, **45**, pp. 1021, (1984).
25. M. P. Cuminal and M. Brunet, "A technique for measurement of pretilt angles arising from alignment layers", *Liq. Cryst.* **22** pp. 185, (1997).
26. P. E. Dyer, R. J. Farley and R. Giedl, "Analysis of grating formation with excimer laser irradiated phase masks", *Opt. Comm.* **115** pp. 327-334, 1995.

27. S. Faetti, "Azimuthal anchoring energy of a nematic liquid crystal at a grooved interface", *Phys. Rev. A*, **36** pp. 408, (1987)
28. D. Shenoy, K. Gruenebergm J. Naciri and R. Shashidhar, "Photo-dimerized monolayer versus rubbed polyimide: a comparison of electro-optical properties", *Jpn. J. Apl. Phys.* **37** pp. L1326, (1998)
29. E. L. Wood, G. W. Bradberry, P. S. Cann and J. R. Sambles, "Determination of azimuthal anchoring energy in grating-aligned twisted nematic liquid crystal layers", *J. Appl. phys.* **82** pp. 2482-2487, (1997).
30. R. Arafune, K. Sakamoto, S. Ushioda, S. Tanioka and S. Murata, "Importance of rubbing-induced inclination of polyimide backbone structures for determination of pretilt angle of liquid crystals", *Phys. Rev. E*, **58** pp. 5914, (1998).
31. H. G. Galabova, D. W. Allender and J. Chen, "Pretilt angle generation on photoreactive polymer films", *Phys. Rev. E*, **58** pp. 3295, (1998).

Three-dimensional microscopic modifications in glasses by a femtosecond laser

Kiyotaka Miura^{a*}, Jianrong Qiu^a, Tsuneo Mitsuyu^a, Kazuyuki Hirao^{a,b}

^aHirao Active Glass Project, ERATO, Keihanna Plaza,

1-7 Hikaridai, Seika-cho, Kyoto 619-0237, Japan

^bDivision of Material Chemistry, Faculty of Engineering,
Kyoto University, Sakyo-ku, Kyoto 606-8501, Japan

ABSTRACT

We examined the feasibility of making various microscopic modifications in glasses by ultra-short pulses. It was confirmed that permanent refractive index changes, photo-reduction of samarium ions, the phenomenon of long-lasting phosphorescence, and creation of microcrystals with second-order nonlinear optical functions can be produced with a femtosecond pulse laser only in selective internal areas in glasses. By using a femtosecond laser with a high repetition rate, permanent optical waveguides can be successfully written in various glasses, where refractive index changes are continuously induced along a path traversed by focal point. We also confirmed that only rare earth ions of the core region in the waveguides are reduced by the laser irradiation.

Keyword : three-dimensional, femtosecond laser, refractive index, waveguide, glass, photo-reduction, long lasting phosphorescence, nonlinear optical crystal

1. INTRODUCTION

The reactions between light and glass in photochromic, photosensitive, and polychromatic glasses have been well researched.¹⁻³ There have also been considerable research on the writing of Bragg gratings inside optical fibers and on photochemical hole burning.⁴⁻⁶ The reaction between light and glass has been put to practical use in phase-change-type memories using a heat-mode scheme.⁷ Such reactions are usually produced by exciting an absorption area on the glass to achieve various types of light-induced structural changes. Continuous-wave lasers and pulse lasers having pulse widths of nanosecond order and greater are used as light sources, and the laser wavelengths are mostly in the ultraviolet regions. As a consequence, light-induced reactions are more active on or near the surface layer of the glass; it is difficult to achieve light-induced effects only in selective internal areas of the glass.

In general, it is difficult to produce an interaction effect between glass and light by one photon process when the excitation wavelength does not agree with the wavelength of absorption region of the glass. However, various types of interactions with glass can be produced by using an ultrashort-pulse laser operating at the nonresonance wavelength with pulse widths of femtosecond order.^{8, 9} Ultrashort light pulses are useful for observing and evaluating at a very high time resolution the dynamics of the phenomena that occur within materials at speeds ranging from pico- to femtosecond. Such phenomena include the direct interaction between light and atoms or molecules, the saturation process associated with the coherent state of materials, and the elementary process of chemical reactions. A short pulse width also means that extremely high peak power can be obtained and that high intensity light (up to 10^{14} W/cm²) can easily be achieved by focusing the laser. The development of high-energy-density femtosecond pulse lasers has prompted us to investigate the unexplored potential for inducing multiphoton photochemical reactions. There is therefore considerable interest in using femtosecond lasers to generate various types of microscopic which are of scientific and practical interest.

We recently discovered that refractive index changes of the order from 10^{-2} to 10^{-3} can be induced within various types of glass by irradiating the glass with focused femtosecond laser pulses.¹⁰ By using a femtosecond laser with a high repetition rate, permanent optical waveguides can be successfully written in various glasses, where refractive index changes are continuously induced along a path traversed by focal point.^{11, 12} We have also discovered the long lasting phosphorescence phenomenon which can be observed with naked eye even 10 hours after the removal of the exciting.¹³

*Correspondence : Email : kiy@hap.jst.go.jp; Telephone : 81 774 95 5205; Fax : 81 774 95 5206

More recently, it was confirmed that photo-reductions of rare earth ions in a few glasses can be produced by the irradiation of femtosecond laser pulses. Up to now, to our knowledge, no creation of permanent photo-redox reactions in the glass have been reported with the laser, although several investigations have been conducted on the transient creation of the divalent rare earth ions in solutions and halide crystals by laser irradiation.^{14, 15} In this paper we describe a variety of microscopic modifications which are permanent or metastable at room temperature can be made only in the laser focusing area inside transparent glasses by using femtosecond laser pulses. We also introduce the preparation and optical characterization of photo-written optical waveguides formed in bulk glasses by a ultrashort pulse laser in femtosecond region.

2. EXPERIMENTAL ARRANGEMENT

By using the apparatus shown in Fig. 1, we tightly focus femtosecond laser pulses inside a bulk glass to create localized microscopic modifications. The irradiation sources employed were a regeneratively amplified 800-nm Ti:sapphire laser that emitted 1 mJ, 140 fs, 1-kHz mode-locked pulses, or 4 μ J 130 fs, 200-kHz mode-locked pulses. The pulse width of the laser was continuously adjusted from 110 to 250 fs by changing the dispersive path length of a pair of prisms. The peak energy of laser pulses at the sample location was approximately controlled between 10 nJ and 1 mJ by using neutral-density filters inserted between the laser and the prism compressor.

We used a microscope system to tightly focus the laser pulses inside various types of glasses to create localized microscopic modifications. A 10-mm laser beam was focused at a diameter of 10 μ m or less through microscope objectives and injected into a polished sample placed on an XYZ stage. To write optical waveguides in the glasses, we used 200-kHz mode-locked pulses in the Gaussian-profile mode to form a continuous pattern of photo-induced refractive-index changes. By using a computer to control the position of the stage, the waveguides were written by translating the sample either parallel or perpendicular to the axis of the laser beam at a rate of 20 to 1,000 μ m/s.

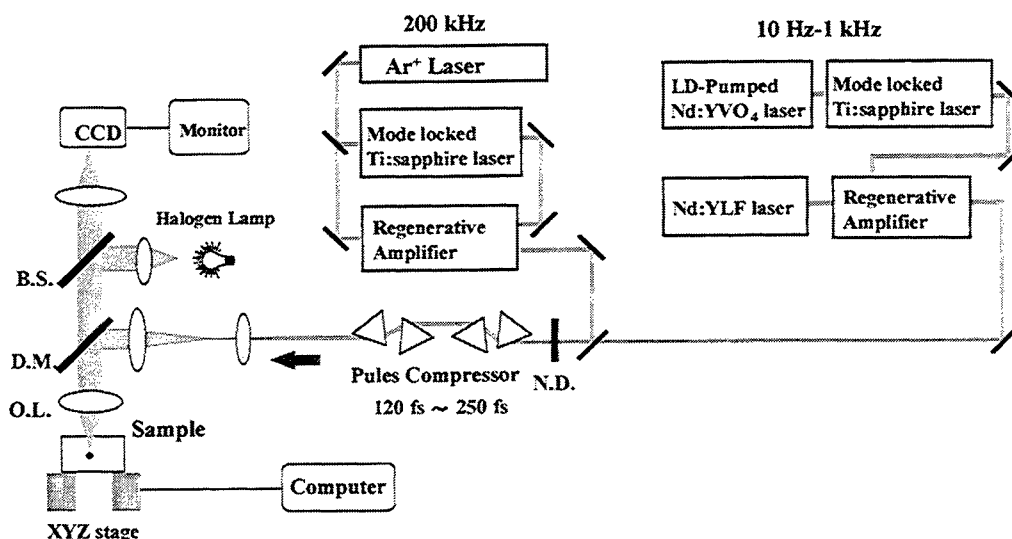


Figure 1. Schematic diagram of three-dimensional microscopic modifications writing by a femtosecond laser.

3. LASER INTERACTION WITH GLASSES

In general, it is difficult to produce an interaction between glass and a laser when the pulse energy is not absorbed by one photon absorption process. However, an ultrashort-pulse laser can produce various types of interactions with glasses through the nonlinear optical process. In practice, white-light generation due to the self-phase modulation and second-harmonic generation were observed from the focal point of the laser beam inside the glass. A typical emission spectra of fluoride glass and Ge-doped silica glass during the irradiation of laser is shown in Fig. 2; the laser wavelength and average power were 800 nm and 200 mW at 200 kHz, respectively. It shows that various nonlinear processes occur at a focal point. After the irradiation of the focused femtosecond laser, a variety of microscopic modifications was formed in the glass samples. AFM observation of a damage caused by focusing laser pulses on the surface of the glass samples are shown in Fig. 3 (a), and the damages caused by focusing in the interior of the samples are shown in Fig. 3 (b) (c) (d). Each sample received 200,000

pulses/spot through a microscope objective. Ablation or cracking (a) due to thermal shock occurred at high power when the ultra-short laser pulse was focused on the near surface of the glass samples, but when the laser beam was focused in the interior of the glasses, no cracking was detected and only visible damages resulting from various phenomena such as the formation of color centers or lattice defects (b), local densification (c) or melting of very small area (d) were observed in the glasses. By use of the photosensitivity attributed to the nonlinear optical process, visible laser damages could only be formed inside the focused region, because nonlinearity only occurs in regions with high optical intensity above the damage threshold. Moreover, the threshold of each microscopic modification is different and dependent on the type of glass. Varying the type of glass and laser-irradiation conditions can therefore produce various types of microscopic modifications inside glass. The following describes typical examples of microscopic modifications by a femtosecond laser.

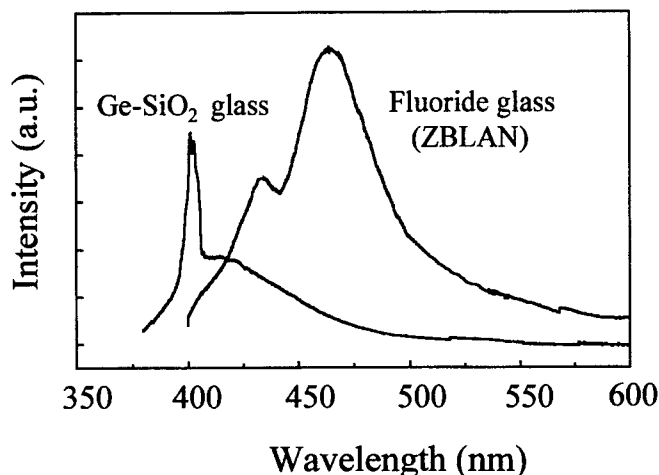


Figure 2. Typical emission spectra of fluoride glass and Ge-doped silica glass during the irradiation of a femtosecond laser.

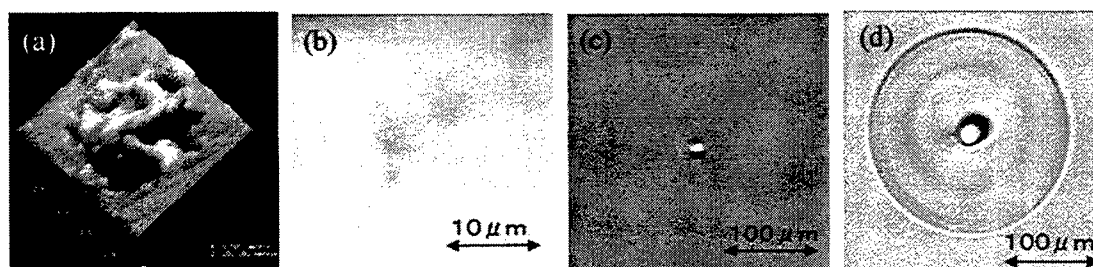


Figure 3. Various types of damage formed by the irradiation of the focused femtosecond laser (130-fs, 200-kHz).

- (a) Damage on the surface caused by 50- μ J pulses focused through a 10X objective lens
- (b) Damage in the interior caused by 1- μ J pulses focused through a lens of 100-mm focal length
- (c) Damage in the interior caused by 1- μ J pulses focused through a 10X objective lens
- (d) Damage in the interior caused by 4- μ J pulses focused through a 50X objective lens

3.1. Photo-reduction

The sample used in this study was prepared with composition of 35AlF₃-14YF₃-10MgF₂-20CaF₂-10SrF₂-10BaF₂-1SmF₃ (mol%) in an Ar+NF₃ (5 mol%) atmosphere by the induction heating method. High purity fluorides containing impurity transition metals at 10 ppb by weight was used as starting materials. The laser beam with an average power of 200 mW was focused by a 100-mm focal length lens in the interior of the samples. The irradiation condition of laser is correspondent to Fig. 3(b). Figure 4 shows the absorption spectra for a laser-irradiated area (a) and non-irradiated area (b) in fluoride glass containing Sm³⁺ ions. For the comparison, the absorption spectrum of a glass which contains Sm²⁺ ion prepared in a reducing atmosphere (Ar + H₂) was shown in (c). As can be seen, the (a) and (c) spectra are remarkably similar, confirming

that the valence of samarium ions in the laser-irradiated area was changed from three to two by photo-reduction. No creation of permanent photo-reduction in the glass have been reported with the laser, although several investigations have been conducted on the transient creation of the divalent rare earth ions in solutions¹⁴ and halide crystals¹⁵ by laser irradiation. Photo-reduction by femtosecond laser pulses exhibits almost no change over time at room temperature. ESR measurements of the laser-irradiated area showed the creation of defects in which holes are captured. It is inferred that the electrons and holes generated by the irradiation of femtosecond laser are captured in Sm^{3+} ions and defects in the glass structure, respectively. Sm^{2+} ions in the fluoride glass reduced by femtosecond laser pulses can be easily oxidized to Sm^{3+} ions by CW laser such as the dye laser. The found phenomenon in this study is inferred to be useful to fabricate rewritable three-dimensional optical memory with an ultrahigh storage density.

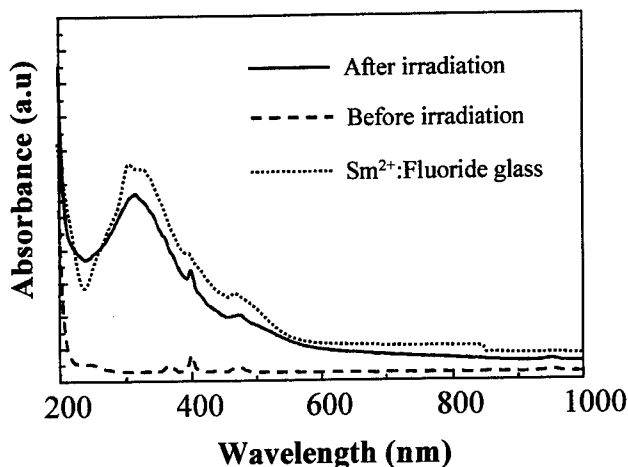


Figure 4. Absorption spectra of Sm^{3+} -doped fluoride glass before and after

3.2. Long lasting phosphorescence

We prepared glass samples with compositions of $53\text{ZrF}_4\text{-}20\text{BaF}_2\text{-}1\text{LaF}_3\text{-}4\text{AlF}_3\text{-}20\text{NaF-}3\text{LnF}_3$ ($\text{Ln}=\text{Tb}^{3+}, \text{Pr}^{3+}$). The laser beam with an average power of 400 mW was focused by a 100-mm focal length lens in the interior of the samples. With the help of an XYZ stage controlled by a computer, the samples were translated at rate of 1,000 $\mu\text{m/s}$ perpendicular to the axis of the incident laser beam. After irradiation by the focused laser, bright and long lasting phosphorescence from focused area was observed in the dark after removal of the laser. Figure 5 shows a photograph of the emission states of phosphorescence in Tb^{3+} -(green) and Pr^{3+} -(red) doped glasses.

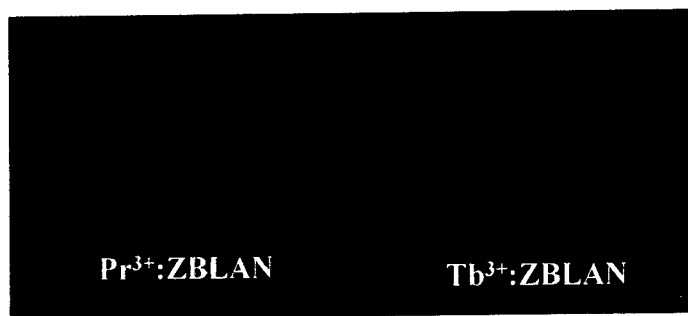


Figure 5. Photograph of the emission states of long lasting phosphorescence.

As shown in Figure 6, the emission spectrum of the phosphorescence (b) of the Tb^{3+} -doped glass has same appearance as observed in the photoluminescence spectrum (a) excited by 250 nm UV light. The emission peaks in the wavelength region from 350 to 700 nm can be ascribed to the $^5\text{D}_J \rightarrow ^7\text{F}_{J'}$, ($J=3,4$, $J'=3\sim 6$) transitions of Tb^{3+} ions. Figure 7 shows the decay curve of phosphorescence at 543 nm in a Tb^{3+} -doped glass. The emission intensity of phosphorescence decreases quickly at

first and then slowly. The phosphorescence can be seen with the naked eye in the dark even 10 hour after the removal of the activating laser. Based on the absorption spectra, the long lasting phosphorescence is considered to be due to the thermostimulated recombination of holes and electrons at traps induced by the femtosecond laser irradiation, which leave holes or electrons in a metastable excited state at room temperature. Like green and red light emissions of long lasting phosphorescence in Tb^{3+} and Pr^{3+} doped fluoride glasses, we also observed blue light emission of Ce^{3+} ions doped into a calcium aluminosilicate glass. These results indicate that optional three-dimensional image patterns emitting long lasting phosphorescence in various colors are possible by selecting appropriate glass compositions and species of rare earth ions.

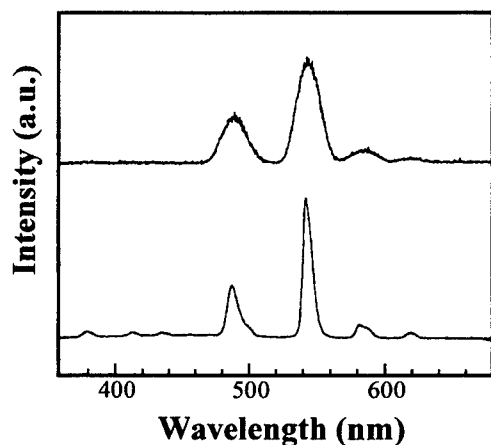


Figure 6. Photoluminescence and phosphorescence spectra of a Tb^{3+} -doped glass.

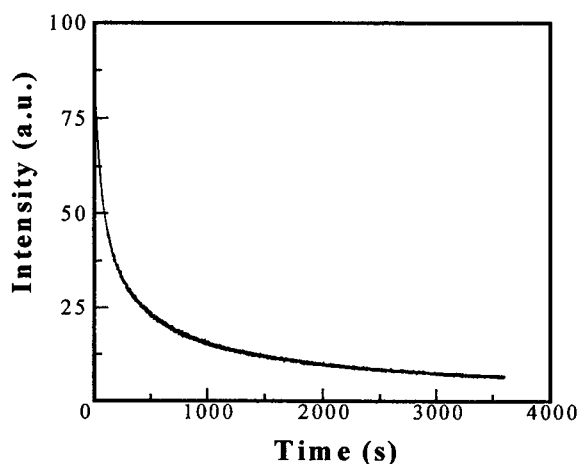


Figure 7. Decay curve of phosphorescence at 543 nm in a laser irradiated Tb^{3+} -doped glass.

3.3. photo-induced refractive index change

Figure 8 shows an array of the refractive index changes inside silica glass induced by a single pulse for each, where peak power was 10^9 W/cm^2 . These spots have diameters of roughly 400 nm, as measured with a confocal laser scanning microscope. This was significantly smaller than the focal-beam size and the wavelength of the laser (800 nm). This may be due to the self-focusing of the laser and non-linear effect of the glass, which resulted from the interaction between the laser and the glass. The spot size of refractive index change increases with increasing number of irradiation pulse and peak power of each pulse. Using a microellipsometer, we measured refractive index profiles across the cross sections of refractive index change lines that were formed perpendicular to the laser beam with a 10X lens, 470 mW, 130 fs and 200 kHz. For the pure silica and the Ge-doped silica glasses, the laser irradiation produced refractive index increases of approximately 0.015 and 0.01, respectively, at the center. The refractive index increases observed here are large enough for the creation of optical devices or three-dimensional memory.

We observed a densification phenomenon in the silica glass irradiated by the femtosecond laser from the measurement of Raman spectra. Figure 9 shows Raman spectra of a laser-irradiated area (a) and non-irradiated area (b) in a silica glass. The wide band centered at 430 cm^{-1} is attributed to the symmetrical stretching vibration mode (ω_1) of SiO_4 . In the laser-irradiated area, ω_1 band is shifted toward the high-frequency side. It is known that the ω_1 band of silica glass shifts in relation to density. The amount

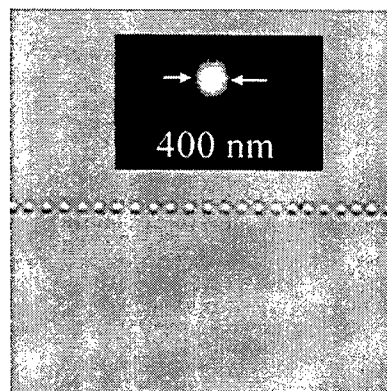


Figure 8. Refractive index changes inside silica glass induced by a single pulse for each.

of ω_1 band shift in this figure is $3\text{--}5\text{ cm}^{-1}$ corresponding to an increase in density of about 1%. Therefore, the increases in refractive index can be related to local densification which finally occurred inside the glass, though the initial process of refractive index changes may be accompanied by various phenomena such as the formation of color centers or lattice defects, or melting of very small area. However, there have been no reports of the densification for optical reactions that participate in both glass bonding and defects with the exception of pure silica and Ge-doped silica glasses. Although it is possible to increase the refractive index in various types of glass other than silica glass by a femtosecond laser, the mechanism behind this process must be studied in more detail.

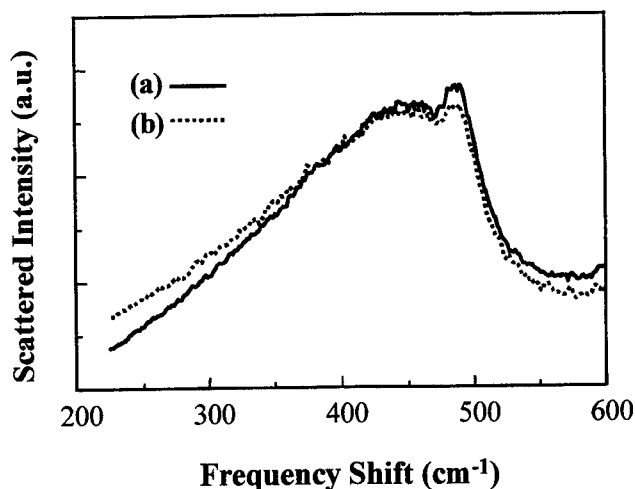


Figure 9. Raman spectra of a silica glass before (b) and after (a) the laser irradiation.

3.4. Creation of second-order nonlinear optical crystals

Second-order nonlinear optical crystals can be generated near the focal point of a laser beam under the irradiation conditions such as Fig. 3(d). Figure 10 shows microscopic photographs near the focal point directly after focused irradiation (a) and 30 minutes after irradiation (b) of the laser (wavelength: 800 nm, repetition frequency: 200 kHz, average output: 600 mW) in a $\text{BaO-TiO}_2\text{-B}_2\text{O}_3$ glass via an 50X objective lens. A polarizing microscope is used here to facilitate observation of the crystallization. A spectrum of second harmonic generation from laser irradiation area (b) obtained by incidence of a 800 nm nanosecond laser pulses is shown in Fig. 11. From the measurement of X-ray diffraction patterns, it was confirmed that β -BBO crystals were generated in the laser focused area. In a similar way, it is possible to generate LiNbO_3 crystals for a $\text{Li}_2\text{O-K}_2\text{O-Nb}_2\text{O}_5\text{-SiO}_2$ glass by a femtosecond laser. In addition, just as the single crystal can be formed by Czochralski method, it may also be possible to form a single crystal by continuously moving the melting area. Forming a single crystal inside glass should enable an optical confinement effect to be achieved that makes use of the difference of refractive indices of the glass and the crystal, which in turn should make it possible to achieve a high-efficiency wavelength converter.

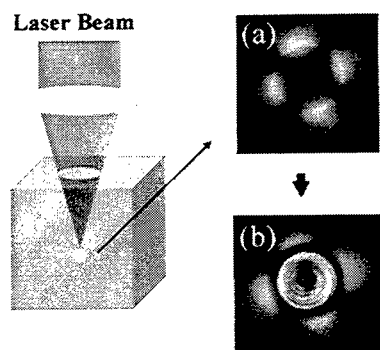


Figure 10. microscopic photographs near the focal point directly after focused irradiation (a) and 30 minutes after irradiation (b) of the laser in a $\text{BaO-TiO}_2\text{-B}_2\text{O}_3$ glass

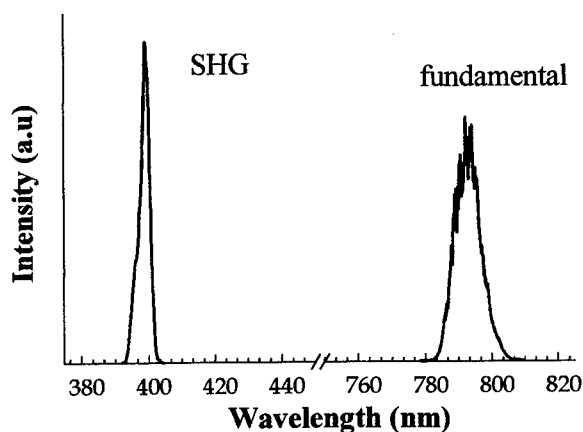


Figure 11. Second harmonic generation from laser irradiation area (b)

4. LASER-INDUCED OPTICAL WAVEGUIDES

By using a femtosecond laser with high repetition rate, it is possible to write waveguides, where laser damage spots are continuously induced along a path traversed by the focal point. Waveguides could be written inside various glasses such as fused and synthetic silica, Ge-doped silica, borosilicate, borate, phosphate, fluorophosphate, fluoride, and chalcogenide glasses. Typical photo-written waveguides formed inside fluoride glass are shown in Fig. 12; they were created using 800-nm, 120-fs, 200-kHz mode-locked pulses. The waveguides were written by translating the sample (a) parallel or (b) perpendicular to the axis of the laser beam at a rate of 20 $\mu\text{m/s}$ and focusing the laser pulses through a 10X or 50X microscope objective, respectively. A cross section of a waveguide written by translating the sample parallel to the axis of the laser beam is shown in Fig. 13 (a); that written by translating the sample perpendicular to the axis of the laser beam is shown in Fig. 13(b). Both cross sections are almost circular. When the samples were translated parallel to the laser beam, the shapes of the cross sections remained unchanged despite changes in the average laser power or the magnification of the objective, with diameters of approximately 7 to 30 μm . The core of the waveguides produced when the samples were translated perpendicular to the laser beam became more elliptical as the numerical aperture was decreased because of the self-focussing. Therefore, a high-numerical-aperture objective should be used to form waveguides with a circular core. Writing waveguides perpendicular to the incident laser beam provides the most flexibility for writing planer patterns and allows one to create multiple-pattern layers by simply changing the focus depth of the beam.

To obtain information on the densification due to structural changes in the laser-irradiation region, we observed the unpolished surface of the core-end on a waveguide by using atomic force microscopy. We found that the shrinkage of the surface gradually increased from outside the core towards the center, leading us to conclude that the densification of a glass occurs in the laser irradiated region.

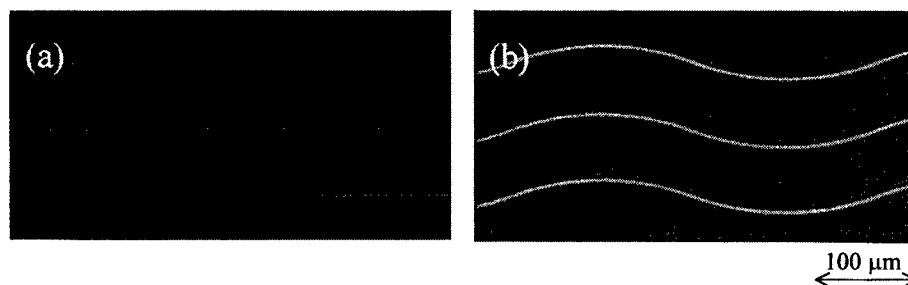


Figure 12. Photo-written waveguides in fluoride glass formed using 800-nm 200-kHz mode-locked pulses. The waveguides were written by translating the sample (a) parallel or (b) perpendicular to the axis of the laser beam at a rate of 20 $\mu\text{m/s}$ and focusing the laser pulses through a 10X or 50X microscope objective, respectively.

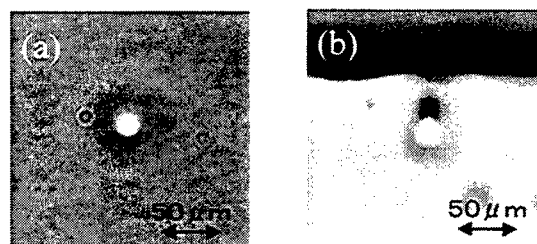


Figure 13. Cross sections of waveguides written by (a) translating the sample parallel to the axis of the laser beam, and (b) translating the sample perpendicular to the axis of the laser beam.

We examined the effects of the average power, the pulse width, and the number of laser passes on the refractive index and core size of optical waveguides. The relationship between the diameter of a core formed by translating the sample parallel to the axis of the laser beam and the average power of the laser is shown in Fig. 14. The core diameters increased

with increasing average laser power at a constant pulse width. The intensity profiles of the guided light for waveguides produced at different pulse widths at a constant average power are shown in Fig. 15. The peak intensity increased as the pulse width decreased at a constant average power. This shows that the change in the refractive index increases as the pulse width is decreased. That is, the refractive-index change increases with the peak power, which is equal to the average power over the pulse width. Note that the core diameters decreased as the peak power was increased. As shown in Fig. 16, the intensity profiles of the guided light varied with the number of laser pass over the same area. The core diameters remained unchanged despite the number of passes, although increasing the number of passes increased the guided-light intensity due to increasing the refractive index of the core area. These results indicate that the refractive-index difference and the core diameter can be controlled by adjusting the writing conditions. We observed the field-intensity distributions of the guided light in waveguides written in fluoride glass at different average powers by using a CCD camera. The intensity distributions of the far field at 800 nm for 15-mm-long fluoride-glass waveguides are shown in Figs. 17 (a) and (b), where the core diameters were 8 and 27 μm , respectively. At a core diameter of 8 μm , it was possible to propagate only a fundamental mode that was nearly Gaussian, while a complicated intensity distribution resulting from the overlap of several modes was observed at a core diameter of 27 μm . The cut-off wavelength of the waveguide in Fig.17 (a) was found to be around 800 nm by examining the wavelength dependence of the mode profiles at several wavelengths ranging from 633 nm to 1 μm . For the waveguide in Fig. 16 (a), on the assumption that the refractive index of the core decreases in proportion to the square of the distance from the center, the result of Hermite-Gaussian fitting for the intensity distributions of the near field is shown in Fig. 18. The calculated result is in good agreement with the experimental data, indicating that this waveguide is a graded-index one with a quadratic refractive-index distribution. The refractive indices of the core center and base glass calculated from the result of the fitting were 1.502 and 1.499, respectively. Although our knowledge of the mechanisms behind the formation of the optical waveguide in various glasses is still insufficient, our findings have opened up new possibilities in the field of integrated optics. They show that it may be possible to form three-dimensional optical integrated circuits in bulk glass by using laser writing.

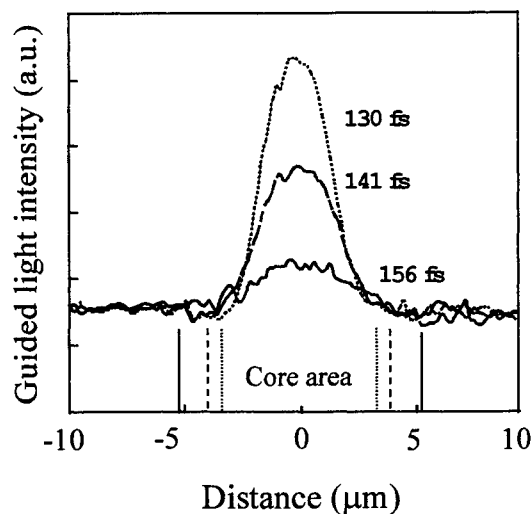


Figure 15. Intensity profiles of the guided light for waveguides produced at different pulse widths. Average

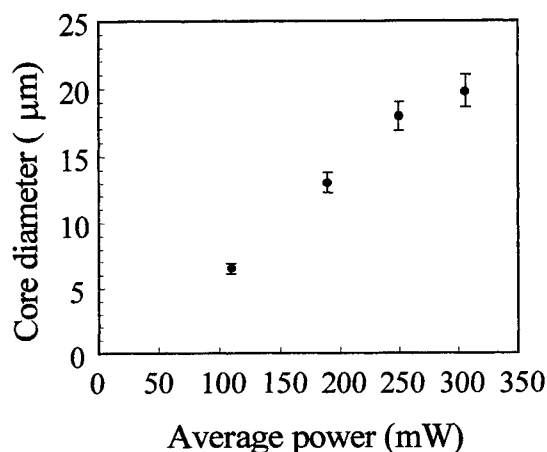


Figure 14. Relationship between the diameter of a core formed by translating the sample parallel to the axis of the laser beam and the average power of the laser.

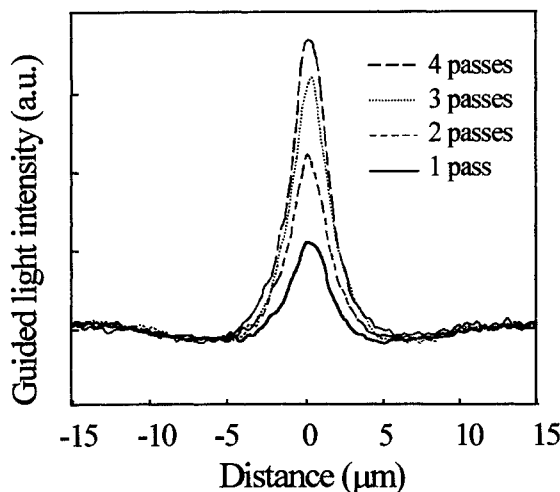


Figure 16. Intensity profiles of the guided light varied with the number of laser passes over the same area. Average power and pulse width were 170 mW and 120 fs, respectively.

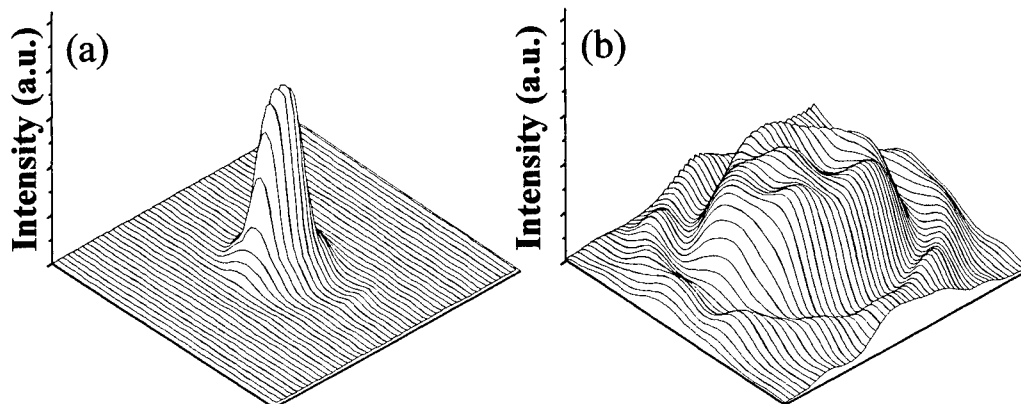


Figure 17. Intensity distributions of the far field at 800 nm for 15-mm-long fluoride-glass waveguides where the core diameters were (a) 8 μm and (b) 27 μm , respectively.

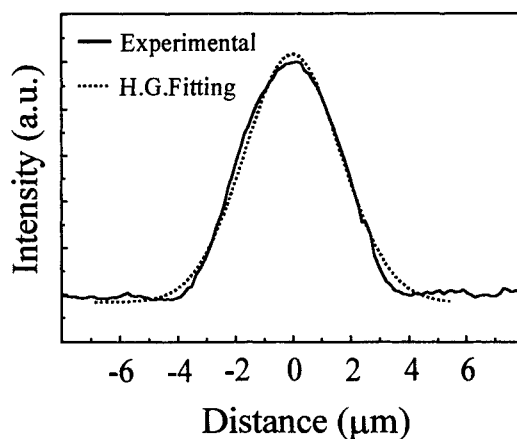


Figure 18. Result of Hermite-Gaussian fitting for the intensity distributions of the near field. The sample was the same as that observed in (a).

5. COMPOSITE FORMATION OF PHOTO-INDUCED STRUCTURES

With microscopic modifications in glass by the femtosecond laser, multiple photo-induced structures can be formed in the same area by the use of differences of thresholds for various types of photo-reactions. For example, by making use the difference of thresholds for the refractive index change and for photo-reduction, it is possible to reduce only rare earth ions in the core area of the optical waveguide written by a femtosecond laser. Figure 19 shows an example of photo-reduction of samarium ions in a core area at an average laser power of 90 mW after writing an optical waveguide within samarium-doped glass with a 10X objectives and an average laser power of 200 mW. Figure 20 shows the emission spectra exited by an 514-nm argon ion laser of a laser-irradiated area (a) and non-irradiated area (b) correspond to (a) and (b) in figure 19, respectively. Broad bands observed around 560, 600, and 645 nm can be attributed to the $^4G_{5/2} \rightarrow ^6H_{5/2,7/2,9/2}$ transitions, respectively, of the Sm^{3+} ions. On the other hand, emissions at 680, 700, and 725 nm that are attributed to the $^5D_0 \rightarrow ^7F_{0,1,2}$ of Sm^{2+} ions were observed from the core area in the laser induced optical waveguide. Thus, these spectra implies a photo-reduction of Sm^{3+} ions into Sm^{2+} ions in only the core area. By the combination of photo-induced refractive index change

and photo-reduction, it is possible to fabricate composite structure of microscopic modifications in which the emission and absorption characteristics of low refractive-index area and high refractive-index area are completely different. Composite formations of microscopic modifications by femtosecond laser pulses are an effective means of giving new functions to glass materials.

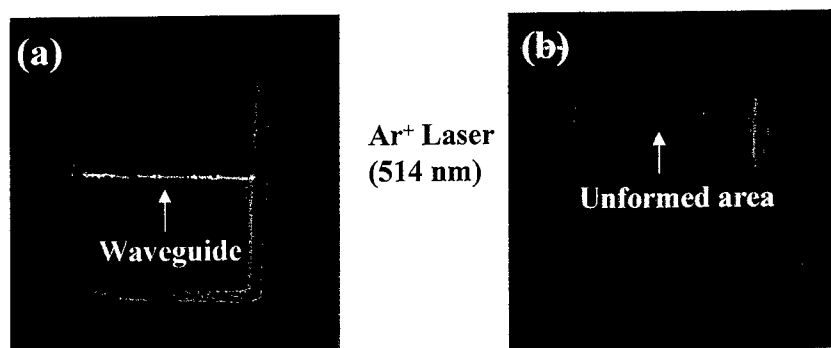


Figure 19. shows an example of photo-reduction of samarium ions in a core area at an average laser power of 90 mW after writing an optical waveguide within samarium-doped glass with a 10X objectives and an average laser power of 200 mW.

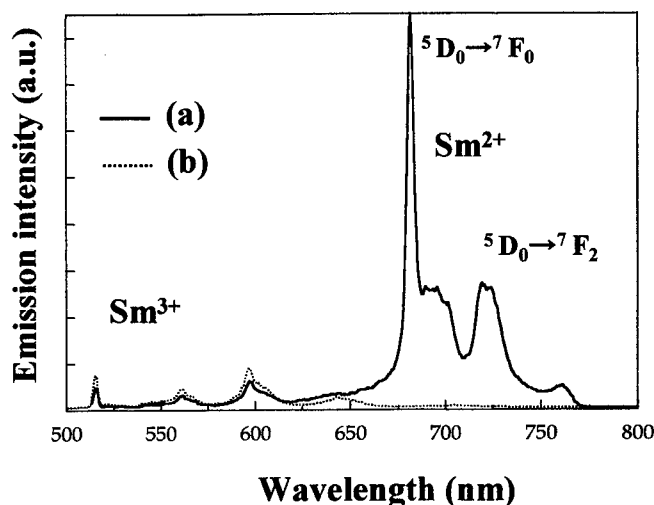


Figure 20. Emission spectra of (a) the waveguide formed by the laser irradiation and (b) the non-irradiated area in a Sm^{3+} doped fluoride glass. The excitation wavelength is 514 nm. This shows that the photo-reduction of Sm^{3+} to Sm^{2+} was occurred simultaneously with the refractive index change.

6. CONCLUSIONS

In an attempt to form three-dimensional microscopic modifications in bulk glasses, we have investigated various photo-induced structures produced by focusing an ultra-short laser pulse through a microscope objective. It was confirmed that permanent refractive index change, photo-reduction of samarium ions, long lasting phosphorescence phenomenon and precipitation of micro-crystals with excellent nonlinear optical functions can be produced only in selective internal areas with a femtosecond pulse laser. We investigated optical waveguides formed by using photo-induced refractive index change produced with an ultra-short pulse laser in the femtosecond region, and demonstrated that permanent optical waveguides

could successfully be formed in various types of glass through our novel method. Because of the presence of a threshold for photosensitivity of each modifications, it is possible to make microscopic modifications three-dimensionally in glasses by using a nonresonant femtosecond laser. In addition, it was confirmed that multiple photo-induced structures can be formed in the same area by the use of the difference of thresholds. Our findings have opened up new possibilities in the production of novel functional optical materials and devices.

ACKNOWLEDGEMENTS

We acknowledge helpful discussions with Y. Kondo, H. Inouye, S. Fujiwara and T. Suzuki of the Hirao Active Glass Project, ERATO, JST, Japan. We thank N. Nishimura of Central Glass Co., Ltd. for his help in fluoride glass fabrication.

REFERENCES

1. N. F. Borrelli and B. Wedding, *J. Appl. Phys.* **63**, 15, 1988.
2. D. C. Boyd and J. F. MacDowell, *Commercial Glasses, Advance in Ceramics* **18**, 165, 1986.
3. N. F. Borrelli, J. B. Chodak, D. A. Nolan, and T. P. Seward, *J. Opt. Am.* **69**, 1514, 1979.
4. K. O. Hill, Y. Fujii, D. C. Johnson, and B. S. Kawasaki, *Appl. Phys. Lett.* **32**, 647, 1978.
5. P. Cordier, J. C. Doukhan, E. Fertein, P. Bernage, P. Niay, J. F. Bayon, and T. Georges, *Opt. Commun.* **111**, 269, 1994.
6. K. Hirao, *J. Non-Cryst. Solids* **196**, 16, 1996.
7. M. Terao, T. Nishida, Y. Miyauchi, S. Horigome, T. Kaku, and N. Ohta, *Proc. SPIE* **695**, 105, 1986.
8. E. N. Glezer, M. Milosavljevic, L. Huang, R. J. Finlay, T.-H. Her, J. P. Callan, and E. Mazur, *Opt. Lett.* **24**, 2023, 1996.
9. Y. Kondo, T. Suzuki, H. Inouye, K. Miura, T. Mitsuyu, and K. Hirao, *Jpn. J. Appl. Phys.* **37**, 94, 1998.
10. K. M. Davis, K. Miura, N. Sugimoto and K. Hirao, *Opt. Lett.* **21**, 1729, 1996.
11. K. Miura, J. Qiu, H. Inouye, T. Mitsuyu and K. Hirao, *Appl. Phys. Lett.* **71**, 3329, 1997.
12. K. Miura, H. Inouye, J. Qiu, and K. Hirao, *Nuclear Instruments and Methods in Physics Research B* **141**, 726, 1998.
13. J. Qiu, K. Miura, H. Inouye, Y. Kondo, T. Mitsuyu and K. Hirao, *Appl. Phys. Lett.* **73**, 1763, 1998.
14. M. Kusaba, N. Nakashima, Y. Izawa, C. Yamada, and W. Kawamura, *Chem. Phys. Lett.* **221**, 407, 1994.
15. Y. Yamada and S. Ohno, *Chemistry Lett.* 465, 1991.

Fiber Bragg Grating Writing by Interferometric or Phase Mask Methods Using High Power Excimer Lasers

Eric E. Mayer, David A. Gillett, and Sergei Govorkov
*Lambda Physik Inc., 3201 West Commercial Boulevard, Suite 110,
Fort Lauderdale, Florida 33309, USA*

ABSTRACT

This paper reports the development of high power excimer lasers with enhanced spatial and temporal coherence. These excimer lasers are applicable to writing fiber Bragg gratings by interferometric or phase-mask techniques. An excimer laser with a novel unstable resonator will be analyzed with respect to its suitability to the production of passive fiber optic components and in terms of production flexibility, efficiency, and reliability. A survey of applicability of this tool to short and long period fiber Bragg gratings will be presented.

Keywords: excimer laser, optical fiber, fiber Bragg grating, interferometry, phase mask

1. INTRODUCTION

The emergence of fiber technologies in the telecommunication and sensor industries has made fiber Bragg grating (FBG) production economically important. The demand for FBGs in step-indexed, germanosilicate-core fibers has seen exponential growth in the telecommunication industry. FBGs are applicable to band pass filters and wavelength division multiplexers (WDM) as well as used for gain flattening in amplifiers and dispersion correction. FBGs have also been applied as pressure, temperature, and stress sensors. This large demand has fueled growth in the development of passive optical devices and laser technology.

A FBG is a longitudinal index modulated diffractive element, which selectively reflects a design wavelength. The FBG is produced by patterning the zones of refractive index change along the fiber core. For the reflection of a set of harmonically related wavelength the core is patterned with a period that satisfies the Bragg condition,

$$\lambda_b = 2\Lambda n_{\text{eff}}/N, \quad N=1, 2, 3 \dots, \quad (1)$$

where λ_b is the wavelength, Λ is the period, and n_{eff} is the effective index of refraction, and N is the order of the reflection. For instance, a typical design wavelength would be 1.55 μm . The reflectivity of the grating is a function of the length of the fiber and the wavelength dependent coupling strength of the light to the grating,

$$R = \tanh^2(\kappa L), \quad (2)$$

where R is the reflectivity, L is the length of grating, and κ is coupling strength.

The photoinduced refractive index change in germanium doped fibers to produce a FBG was first observed over 20 years ago.¹ Standing wave interference features were produced with the 488 nm line of an Argon ion laser. It was later shown that the photoinduced change was the result of a two-photon process.² Further work has shown the process has a photosensitivity between 240 nm and 260 nm.

There has been a continual growth in understanding of the mechanisms of photoinduced change in index of refraction. These models are important in understanding the photosensitivity, permanence of index change, and mechanical stability of FBGs. Additionally, accurate models offer further strategies of FBG production, such as hydrogen loading of fibers. One theory is the color center model.³ In the color center model, oxygen deficit sites are ionized to produce free electrons. These electrons then relocate to produce new absorption bands. These new absorption bands produce a wavelength-specific change in the

index of refraction. Another theory is the stress relief model.^{4,5} In the stress relief model, stress is induced in the fiber core by photolytic bond breaking. Although one model may describe the dominant mechanism under moderate illuminations, another model may better describe the mechanisms involved in high power density illuminations.

2. METHODS OF FGB FABRICATION

The required beam qualities and degree of coherence needed for writing fiber Bragg gratings depends upon the method. For example, amplitude mask-imaging techniques have little need of well-correlated photons. On the other hand, a high degree of coherence is needed for writing fiber Bragg grating with interferometric techniques or techniques that diffract the beam. In amplitude-division interferometric techniques, the beam is split and recombines at a selected angle to produce an interference pattern on the target. The requirements of coherence for these techniques depend upon the experimental setup. The temporal coherence requirements depend upon the precision of beam path compensation, and the spatial coherence requirements depend upon the symmetry of the beam paths and precision of overlap alignment. Additionally, factors such as air current induced refractive index changes and optics induced wavefront distortions need to be accounted for. Amplitude-division methods require a homogeneous laser beam profile, high spatial coherence (~1 mm desirable), high temporal coherence (~10 mm desirable), high pulse-to-pulse energy stability, and high beam pointing stability.

Another common interferometric method involves wave-front division. In this method a phase-mask is used to diffract the beam to produce a designed-interference, intensity modulation at the target. Usually the first orders of diffraction (-1 and +1) are recombined at the target to produce the specific interference pattern. The simplicity and less critical dependence on alignment makes phase-mask methods the most applicable to production level demands. Phase-mask methods require a homogeneous laser beam profile, high spatial coherence (~1 mm desirable), high pulse-to-pulse energy stability, and high beam pointing stability. The quality or contrast of the interference pattern behind the mask is a function of the spatial coherence of the laser. Additionally, higher spatial coherence allows the interference pattern to persist further behind the mask. This allows for the fiber to be moved away from the mask to minimize the fluence on the mask, minimize the contamination of the mask, and minimize the cross contamination of the fiber. These factors contribute to high quality gratings, increased reliability and consistency.

3. LASER PERFORMANCE AND APPLICABILITY OF FBG PRODUCTION

3.1. Experimental

In our experiments, we used a LAMBDA 1000 excimer laser with a krypton fluoride (KrF) gas mixture. The LAMBDA 1000 was optimal due to its external resonator optical design, high long-term stability, high power, and reliability. The krypton fluoride mixture delivers high peak power, pulsed, 248 nm output, which is in the appropriate range to produce an index of refraction change in step-indexed, germanosilica-core fibers. The peak power delivered is in the order of 10^6 Watts, while the average power is on the order of 15 Watts. This allows short fiber exposure times (from one shot to a few minutes) with large induced effects and with a minimal amount of fiber heating.

Spatial coherence properties of the excimer lasers were measured using shearing interferometer (Figure 1a). In the shearing interferometer, the entire laser output was split by a beam splitter and recombined with independent control of the temporal delay and temporal displacement of the beams. The contrast of fringes (Figure 1b) was measured and quantified in terms of visibilities. Visibility of the interference fringes was defined as $(I_{\max} - I_{\min}) / (I_{\max} + I_{\min})$. We defined spatial and temporal coherence length or radius as a displacement or a path length difference at which the visibility of the interferometric pattern drops to 0.5.

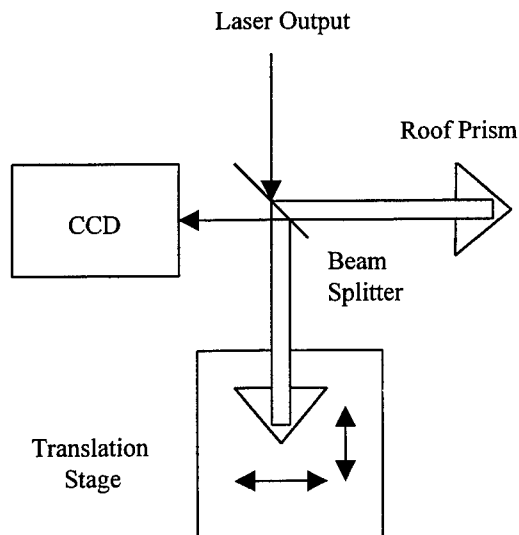


(Figure 1a)

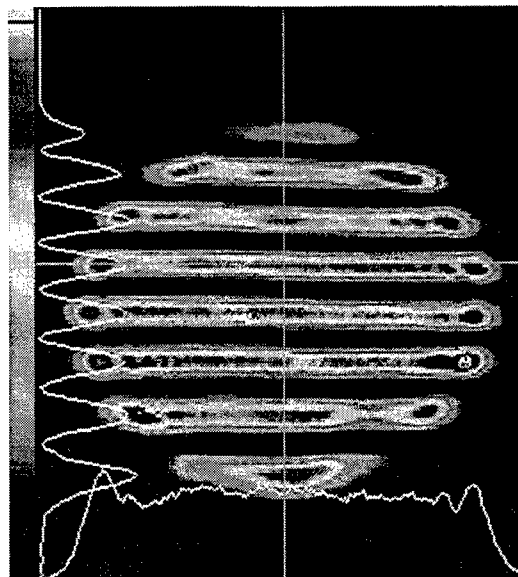


(Figure 1b)

Figure 1a: The shearing interferometer used in used to measure the interference fringe contrast. Translation of the lower roof prism provides the differential in path length and displaced overlap. Figure 1b shows typical fringes generated with a shearing interferometer.

3.2. Spatial Coherence

High spatial coherence is critical for producing high contrast interference features and is needed to increase the offset between the fiber and phase-mask. Unstable resonators are commonly used to reduce divergence and increase spatial coherence in lasers with large-volume gain media, such as in excimer lasers. The high gain of the excimer can sustain the high loss per round trip, and the short pulse limits the number of attainable round-trips. However, typical unstable resonators may still have deficits in low conversion efficiency, low pulse-to-pulse energy stability, high levels of amplified spontaneous emission (ASE), and poor beam profiles. A detailed study of spatial coherence of the beam produced by conventional unstable resonators reveals negative effects of amplified spontaneous emission (ASE) on spatial coherence. The interference fringe contrast variation of a conventional unstable resonator with the lateral displacement of the two beams of the shearing interferometer (Figure 2) shows the negative effect of high ASE. The sharp drop in the contrast of interference fringes at displacements greater than ± 0.2 mm in this conventional, unstable-resonator laser is indicative of ASE.

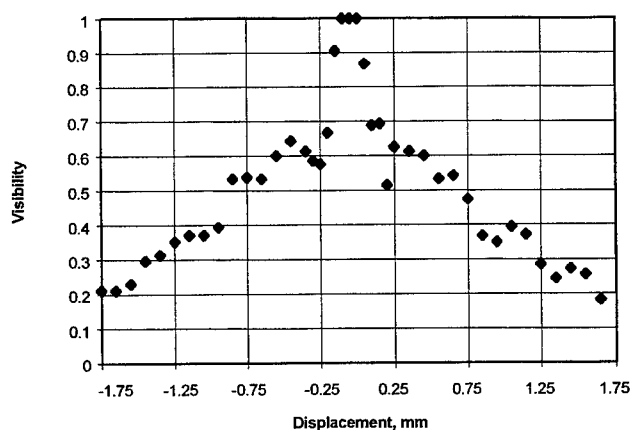


Figure 2: Spatial coherence of laser with conventional unstable resonator yields a much lower spatial coherence radius.

This indicates a need to remove the ASE from the excimer laser output. However, classical spatial filtering of the beam by focusing the beam and bounding the beam waist at the focal point is not easily applied to a high-energy excimer laser system. The difficulty in classical spatial filtering is that the high power densities at the focal point may lead to air break down and damage to the aperture. Given the single dimensional requirement of the modulated periodicity of the FBG, we chose a similar single axis approach in resonator design and spatial filtering (Figure 3). We chose the long axis of the laser to be the critical axis for this application. The long axis offers a stable, flat-top beam intensity profile that is independent of discharge conditions and aging of the electrodes. We chose a cylindrical unstable-resonator oscillator (CUR) design to provide a high degree of spatial coherence along the long critical axis, while minimizing gain losses. The CUR oscillator reduces losses by an order-of-magnitude when compared with a spherical unstable resonator of the same magnification. Consequently, the CUR oscillator achieves gain saturation. This efficient design combined with an integrated single axis spatial filter provides unsurpassed pulse-to-pulse energy stability, a superior beam profile, and a minimum of ASE.

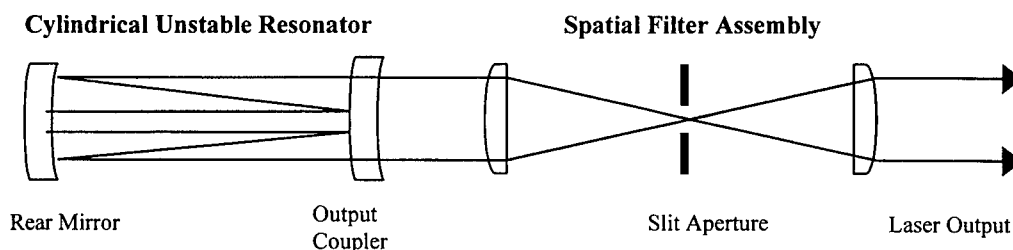


Figure 3: Schematic of the laser resonator and beam processing.

Measurements of the visibility for known beam displacements in a shearing interferometer (Figure 4) show a radius of spatial coherence is more than 1 mm in the long (critical) axis of the beam and approximately 0.25 mm in the short (non-critical) axis. The divergence was measured to be less than 0.3 mrad along the critical-long axis of the beam and 1.5 mrad along the short (non-critical) axis.

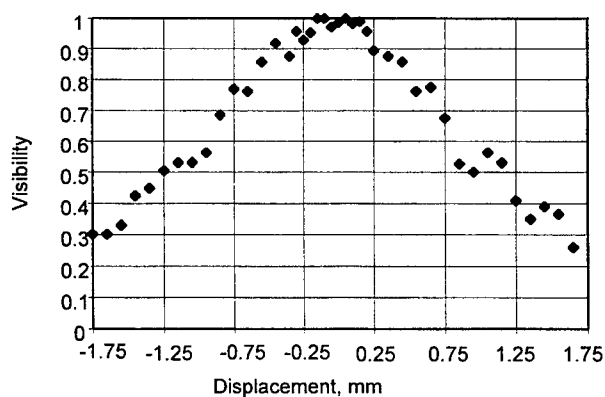


Figure 4: Spatial coherence of the spatially filtered CUR laser along critical (long) axis of the beam. The visibility is plotted as a function of the lateral beam displacement in a shearing interferometer. Note that the coherence radius is greater than 1 mm.

3.3. Uniformity of Beam Intensity Distribution

The uniformity or the beam homogeneity is important for producing even illumination along the exposed fiber. The intensity distribution of the beam (Figure 5) shows that the beam intensity is nearly constant along critical (long) axis. The choice of the long axis as the coherently enhanced axis allows for the most consistent homogeneity with regards to the laser's gain or

tube aging. This offers a very reproducible beam intensity profile along the long axis, which is important in insuring a minimal variation in the illumination envelope along the fiber. The long-term consistency of the beam profile is essential for a highly reproducible writing process. A 48-hour continuous run test showed no observable change in the intensity distribution.

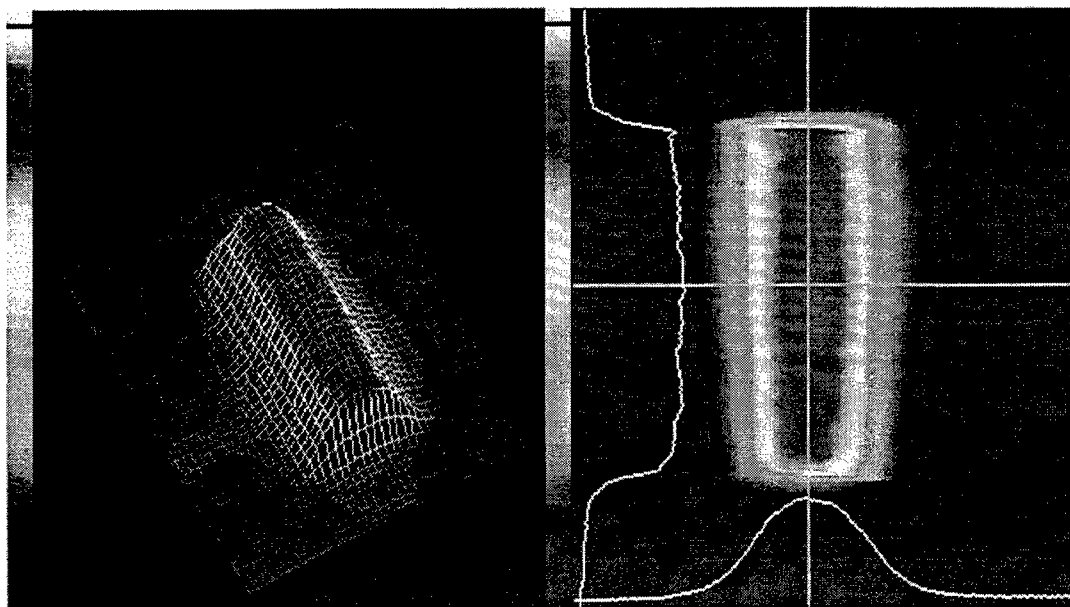


Figure 5: Near field beam intensity distribution of the beam after spatial filtering.

3.4. Short- and Long-Term Pointing Stability

Pointing stability is important for minimizing the shot-to-shot interference variation and for maintaining sensitive optical alignments. High pointing stability can increase contrast in FBG and improve reproducibility of FBGs. Figures 6 and 7 show measurements of pointing stability of the spatially filtered laser. In Figure 6, the standard deviation of the far field center of gravity (centroid) of the beam (calculated within the sample of 256 pulses) is plotted against time in 48-hour continuous run. This short term pointing stability test shows that the sigma stays within 0.02 mrad. Long term beam pointing stability is plotted in Figure 7. In this extended 48-hour test, the center of the beam remained within an angle of ± 0.04 mrad.

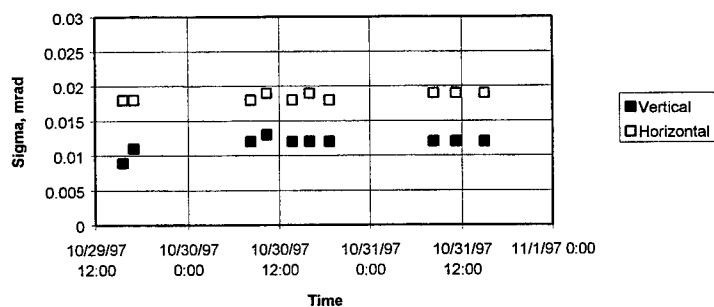


Figure 6: Short term pointing stability of the CUR resonator with spatial filtering. Each point represents the standard deviation within a sample of 256 laser pulses.

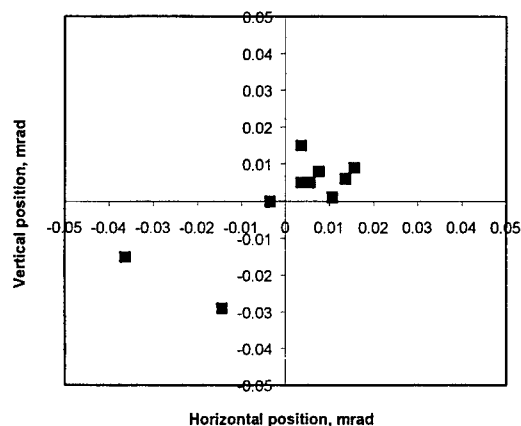


Figure 7: Long term pointing stability of the CUR resonator with spatial filtering. Each point represents the average position of 256 laser pulses. These points were taken at even intervals over a 48 hour period.

3.5. Pulse-to-Pulse Energy Stability

High pulse-to-pulse energy stability is important for maintaining strict dose tolerances. The laser was operated at a repetition rate of 50 Hz and with a servo-controlled, constant pulse-energy of 130 mJ. Figure 8 shows that the standard deviation of the pulse energy (in samples of 1000 pulses) remained below 2.5% over 48 hours, whereas the standard deviation of moving average over 50 pulses was as low as 0.1%. Additionally, a 5.5 hour test of the laser power with time shows a peak-to-peak variation of $\pm 1.2\%$ (Figure 9). This data shows extremely high reproducibility of the representative dose of radiation accumulated in 50 pulses.

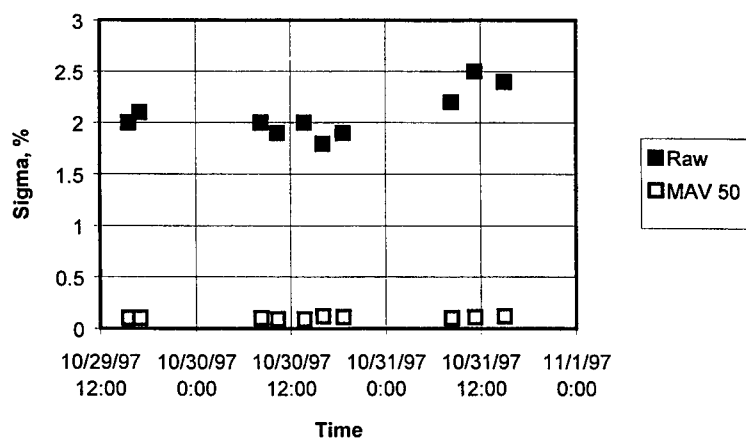


Figure 8: Pulse-to-pulse energy stability in 48 hours run. Each solid point represents the standard deviation of 1000 laser pulses. Each hollow point represents the standard deviation of a moving average of 50 pulses within a sample of 1000 laser pulses.

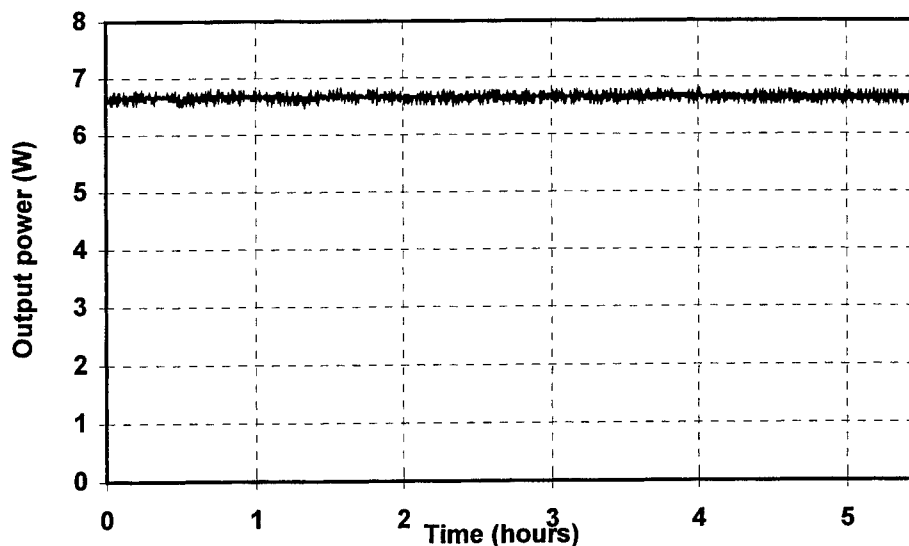


Figure 9. Long-term power stability of the spatially filtered CUR excimer laser recorded at 50 Hz with a servo-controlled constant pulse energy of 130 mJ.

4. PERFORMANCE AND APPLICABILITY OF LINE NARROWED CUR EXCIMER LASER TO FBG PRODUCTION

An additional advantage of the cylindrical unstable resonator (CUR) design described above is the possibility of line narrowing the output. The single axis aspect of the CUR resonator provides high spatial coherence along the long, critical axis while allowing for intracavity line narrowing of the beam on the short, non-critical axis. This offers the possibility of using single axis beam processing elements such as lenses, prisms, and gratings. We line narrowed the cavity by expanding the short axis of the beam onto a Littrow-orientated, retroreflecting grating with two fused silica, 37° prisms. The prisms provided a magnification of 8 times, a beam deviation of 35.5 degrees per prism, and an effective aperture of 3 mm.

This line-narrowed configuration of the CUR with spatial filtering delivered both high spatial coherence and high temporal coherence. Figure 7 shows that the high spatial coherence of more than 1 mm of the spatially filtered CUR oscillator is maintained with the addition of the line-narrowing components. Figure 8 shows that the line-narrowing produces an observed temporal coherence of more than 10 mm. The addition of the line-narrowing optics produces additional output characteristics, such as a highly linearly-polarized output, which may be beneficial in the production of certain FBGs. A summary of these characteristics can be found in Table 1.

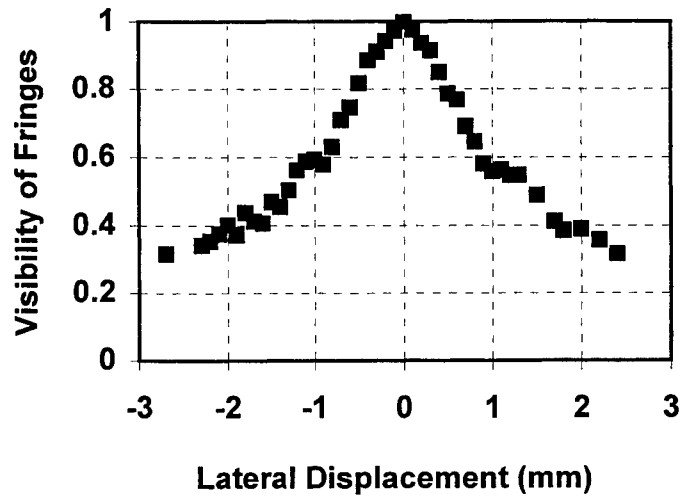


Figure 7: Spatial coherence of the spatially-filtered, line-narrowed CUR oscillator. The visibility is plotted as a function of the lateral displacement in a shearing interferometer.

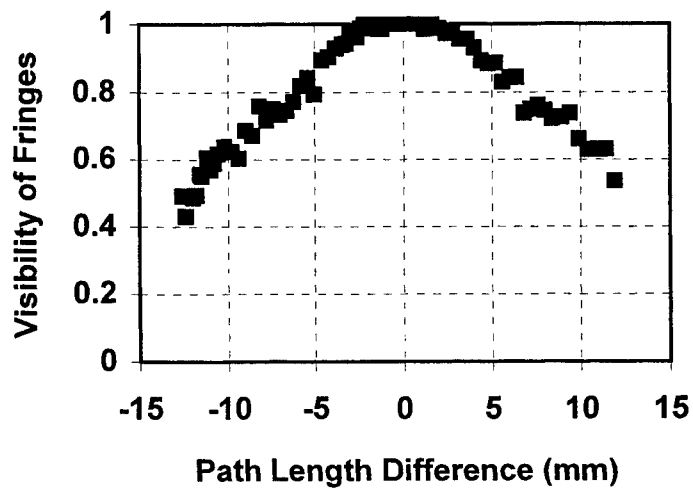


Figure 8: The temporal coherence of spatially-filtered, line-narrowed CUR oscillator. The visibility is plotted as a function of the optical path length difference in the Michelson interferometer.

Wavelength.....	248 nm
Temporal coherence length (at 50% visibility).....	>10 mm
Spatial coherence radius (at 50% visibility)	> 1 mm
Maximum energy per pulse	> 50 mJ
Maximum repetition rate	50 Hz
Divergence (long x short axis).....	<0.5 mrad x 2.0 mrad
Beam size.....	22 mm x 5 mm
Pulse width	40 ns typical
Polarization ratio (short axis / long axis)	>60:1
FWHM bandwidth).....	< 1 cm ⁻¹

Table 1 Summary of line-narrowed CUR excimer laser characteristics

5. CONCLUSION

A spatially-filtered, cylindrical unstable resonator, krypton fluoride, excimer laser has been designed for the production of fiber Bragg gratings in an industrial environment. The spatially-filtered CUR provides low divergence and high spatial coherence in the critical long-axis dimension. The laser output has a homogeneous, flat-top, intensity distribution along the long axis of the beam profile. This laser possesses long-term stability of key parameters, such as the beam intensity distribution, pulse energy, and power. These features, along with the high pointing stability, make this system optimal for FBG production with phase-mask methods. A spectral line-narrowed version of the spatially-filtered CUR has been shown to increase the temporal coherence by several orders of magnitude while maintaining high spatial coherence. This line-narrowed system is optimal for FBG production with interferometric techniques.

ACKNOWLEDGMENTS

Special thanks to: D. Rodham, V. Pfeufer, and D. Basting.

REFERENCES

1. Hill, K. O., Fujii, Y., Johnson, D. C., Kawasaki, B. S., *Appl. Phys. Lett.* **32**, p. 647, 1978.
2. Lam, D. W. K., Garside, B. K., *Appl. Opt.* **20**, p. 440, 1981.
3. Hand, D.P., Russell, P. St. J., *Opt. Lett.* **15**, p.102, 1990.
4. Sceats, M. G., Atkins, G. R., Poole, S. B., *Ann. Rev. Mat. Sci.* **23**, p. 381, 1993.
5. Mihailov, S. J. , Gower, M. C., *Appl. Phys. Lett.* **65**, p. 2639, 1994.

Modification in optical fibers using high-intensity femtosecond lasers

Sung-Hak Cho*, Hiroshi Kumagai, Katsumi Midorikawa and Minoru Obara*

Laser Technology Laboratory, The Institute of Physical and Chemical Research (RIKEN)
2-1, Wako, Saitama 351-01, Japan

* Permanent address

Department of Electronics and Electrical Engineering, Faculty of Science and
Technology, Keio University
3-14-1, Hiyoshi, Yokohama 223, Japan

Keywords: Refractive index modification, Channeling, Self-focusing, Femtosecond laser, Optical fibers, Double cladding structure, Color center

Abstract

Refractive index modification in optical multimode fibers was firstly demonstrated, as a fabrication method of double cladding structure, using plasma channeling excited by a high intensity femtosecond (110fs) Ti: sapphire laser ($\lambda_p=790\text{nm}$). The induced refractive index modification in a pure silica multimode fiber (step index) with 100/110 μm core/cladding diameter was reached to the length of approximately 9~10 mm from the end of optical fiber with the diameters ranging from 5 to 8 μm at more than input intensity of $1.5 \times 10^{12} \text{ W/cm}^2$. It had graded refractive index profile that was a symmetric form from the center of a multimode fiber and the maximum values of refractive index change (Δn) was 1.6×10^{-2} . According to the ESR spectroscopic measurement, it was observed that the concentration of defect of SiE' center was heavily increased in refractive index modification refer to that of non-modification region. It was suggested that the defect was induced by the multiphoton absorption process through plasma channeling. Near-field pattern and beam intensity profile of a modified multimode fiber showed that bulk modification played a role as a double cladding structure. The fabrication method of double cladding structure in the end of multimode fiber can be useful tool for mode converter and single-mode connector in the fields of optical communication and optical sensor.

Further information

Sung-Hak, CHO: E.mail: cho@obara.elec.keio.ac.jp, Tel.: +81-45-563-1141 (ex.3315), Fax.: +81-45-563-2773

1. Introduction

Several type structures of silica glasses based optical fibers with high efficiency, high functionality have been developed in the fields of optical communication, medicine, optical sensor because of their high transmission from UV to IR.[1] Among one of them, much attention has been paid to the multimode optical fiber with double cladding structure as powerful tools for fiber lasers, fiber amplifiers with high pumping efficiency, and sensitive mode interferometer in optical fiber sensors.[2-4] In particular, single-mode structure in the end of multimode optical fibers has been expected as a useful device of mode-converter from propagated multimode beam to single-mode one in an multimode fiber.[5-7] Therefore, it is heavily favored to connect to single mode fiber with high single-mode coupling efficiency in the fields of optical amplifier and optical sensor because of their capability of an essentially propagating diffraction-limited optical beam. [8] Although it was used with the methods of MCVD (Modified Chemical Vapor Deposition, OVD (Outside Vapor Deposition), VAD (Vapor-phase Axial Deposition) to fabricate the double cladding structure of optical fibers at fiber deposition stage, it was known a little problem to make double cladding structure in the limited end of optical fibers in view of high cost and fabrication technologies.[9] And, to date it have not been reported for the fabrication methods of the double cladding structure in the preformed optical fibers. If it can be easily fabricated the refractive index modification with single-mode waveguide structure in the end of preformed multimode optical fibers, it can be used with low cost in the various application of mode-interferometers, mode-converters in multimode fibers, and optical connectors between multimode fiber and connected single-mode optical fiber with high mode coupling efficiency.

In recent, it was reported that the plasma-induced bulk modification occurred at tightly focused laser beam spot of bulk silica glasses in sub-picosecond laser applied experiments for three-dimension optical memories and micro-structurings.[10-12] If the stable plasma channeling, the nonlinear phenomenon of interaction between propagating beam and matter occurred when high intensity laser beam was propagated into transparent materials[13], were formed following the axis of an optical fiber, double cladding structure could be obtained in multimode fibers by change of refractive index induced by the interaction between the plasma and the core.

In this letter, as a new simple fabrication method of double cladding structure, we demonstrate the plasma-induced refractive index modification in the end of optical multimode fibers using a stable plasma channeling excited by a high peak-intensity femtosecond laser. In experiment, step index optical multimode fibers composed of pure silica usually used in the fields of optical communication and optical sensor are used to study the properties of the plasma channeling-induced modification.

2 Experimental

The schematic diagram of experimental setup for plasma channeling-induced refractive index modification is shown in Fig. 1. The laser used in our experiment was a Ti:sapphire oscillator-amplifier laser system ($\lambda_p=790\text{nm}$) based on the chirped pulse amplification technique with 110 fs pulse duration, 1W output power, and 1 kHz repetition rate, as a pumping source. The linearly polarized laser beam with

gaussian profile was focused through a quartz lens with focal length of 60 mm and incident onto the end of the optical fiber located away from breakdown point to avoid optical damage at input surface. The step index optical multimode fiber composed of pure silica core with 100/110 μm core/cladding diameter (Newport F-MCB-T, NA: 0.22) was used. The transmitted power was recorded by the optical power meter connected to the computer. The various formations of plasma channeling and plasma-induced refractive index modification were observed by the microscope with CCD camera.

3. Experimental results and Discussion

Intense ultrashort laser excitation into optically transparent materials cause a change in the refractive index of the intensity-dependent material, which is written as $n = n_0 + n_2 E^2$, and thus influences self-focusing. n_0 is a linear refractive index, n_2 is a Kerr coefficient. It was generally known that self-focusing in pure silica glass occurred at input intensity of $1 \times 10^{12} \text{ W/cm}^2$. [14]

In our experiment, the first plasma spot was observed at 70 μm from the end of optical fiber by self-focusing effect at input intensity of $8 \times 10^{11} \text{ W/cm}^2$ on the input surface of optical fiber. The first self-focusing point could be controlled by the change of input beam angle on the fiber end surface using the different focal range lenses. When input intensity exceeds $1.5 \times 10^{12} \text{ W/cm}^2$, stable plasma channeling with a diameter of 10~12 μm was observed and reached to the length of 10 mm from the first self-focusing point in a multimode fiber. (Fig. 2) Beam intensity at where self-channeling occurred in an optical multimode fiber would be reached to $\sim 10^{14} \text{ W/cm}^2$, approximately 10^2 times higher than the input intensity on the end surface of an optical fiber. Those plasma channeling was attributed to the balance of refractive index profile between self-focusing caused by the optical kerr effect and self-defocusing due to diffraction from created plasma within single-shot laser irradiation. [15] Some visible modification was observed in the center of optical fiber after plasma channeling occurred and it proceeded to the deep distance from the first self-focusing point as the number of laser pulses was increased. No more procedure was observed at more than approximate 1×10^4 irradiation shots. Modification was formed onto the distance of 9 mm with a diameter of approximately 5 μm after laser shot of 1×10^4 irradiated. (Fig. 3(a),(b)) When Input intensity was $2.0 \times 10^{12} \text{ W/cm}^2$, the refractive index modification that had the diameter of 6 μm and a length of 10 mm was obtained. The bulk modification with a diameter 8 μm and the length of 10 mm was also formed at input intensity of $3.0 \times 10^{12} \text{ W/cm}^2$. The diameter of induced-modification was dependent on input intensity, however, almost no variance of length was observed at more than input intensity of $3.0 \times 10^{12} \text{ W/cm}^2$. The variance of induced-modification profile related to distance was within 5 % in the diameter of refractive index modification. The observation of bulk modification by the use of microscope showed that stable, uniform refractive index change occurred by the infrared femtosecond laser. (Fig. 3(b))

However, when input intensity exceeded $3.5 \times 10^{12} \text{ W/cm}^2$, the induced modification which have cracks, so called the optical damages, occurred. In this case, the transmitted beam power was decreased to 35% because of the scatter and diffraction from cracks.

In order to measure refractive-index change of bulk modification induced by plasma channeling, the perpendicular Fresnel reflection was chosen. This technique, as devised by Eickhoff and Weidel, relies on

the Fresnel relation between the materials refractive index and its reflectivity.[16]

At normal incidence we have

$$R = \left(\frac{n_{\text{fiber}} - n_{\text{air}}}{n_{\text{fiber}} + n_{\text{air}}} \right)^2.$$

A linearly polarized He-Ne laser incident upon a 10x beam expander and is focused on the end surface of a cutted fiber of bulk modification by a 20x microscope objective. Approximately minimum spot of focused beam on the end surface of fiber are 2 μm . Reflective beam was detected by a photodiode and its signal was recorded by computer through a lock in amplifier. Refractive index profile was shown in Fig. 4 obtained by the use of parabolic fit.[17] The refractive index in the center of induced modification was increased to 1.479, referred to 1.457 in non-induced modification. The maximum value of reflective index change was 1.6×10^{-2} and it had a symmetric graded index profile around the center of a multimode optical fiber. The facts of center location of induced refractive index profile suggested that plasma channeling was a little effected by waveguide structure of an optical multimode fiber. Uniform photoinduced refractive index change in pure silica glass after plasma channeling occurred appears to be new observation.

From the ESR (Electron Spin Resonance) spectroscopic measurement[18], before laser irradiation, no defect was observed in an optical fiber (Fig. 5(a)), however as a result of plasma channeling, the defect concentration of SiE' ($\equiv \text{Si}^\cdot$, E' center) was heavily increased in refractive index modification (Fig. 5(b)). Another types of defects beside E' center were not observed in refractive index modification.

When plasma channeling occurred within single laser shot, free electrons were generated by energy coupling from the ultrashort laser pulse into optical fiber through a combination of multiphoton absorption and avalanche ionization. However, after laser pulse was passed, those were shortly recombined with surrounding atoms caused by the plasma rapid quenching. It was explained that the concentration of SiE' defect was increased around the regions formed of plasma channeling.

The ultrafast energy deposition under plasma channeling also would induce high temperature and pressures inside the region. It was suspected that main reasons of the increase of refractive index are the heavily increase of defects concentration in bulk modification region by rapid plasma quenching and structural rearrangement to different state by localized melting and pressing although we do not yet direct evidence of densitification. More studies for the physical mechanism of structural rearrangement induced by plasma formation in transparent materials are needed.

Fig. 6 showed the NFPs (near field pattern) and beam intensity profiles of transmitted laser beam of 800 nm measured before laser irradiation and after induced bulk modification in an optical multimode fiber. It was found that the mode coupling from high-order multimodes beam into low-order multimodes one in an multimode fiber during the propagation through refractive index modification occurred. Beam intensity was increased around the center of a modified multimode fiber (Fig. 6 (a),(b)), referred to an unmodified multimode one. (Fig. 6 (c),(d)) It means that double cladding structure was formed and refractive index modification could play a role as a single mode coupler from propagated multimode

beams. The beam diffraction range from the end of an optical fiber was found that the measured NA of transmitted beam of 800nm through a modified fiber was 0.11 that it was smaller than that of unmodified multimode one with the NA of 0.22. It is expected that more high mode coupling can be happened in a refractive index modified fiber, if a multimode fiber with relative small core diameter is used.

In general, single-mode fibers have a core diameter with the range from 4 to 10 μm , according to the applied laser wavelength regime. By the consideration of the diameter of plasma channeling-induced refractive index modification, from 5 μm to 8 μm , it could be used as a double cladding structure in the end of a multimode fiber that has a single-mode waveguide in the range of applied laser wavelengths from visible to infrared of 1.3-1.5 μm for light communication.

4. Conclusion

In conclusion, uniform refractive index modification with the length of 9~10 mm, 5~8 μm diameter induced by the plasma channeling was demonstrated in pure silica multimode fibers as a new fabrication method of double cladding structure in the end of an multimode fiber. The double cladding structures with a single-mode waveguide enable to make high coupling from multimodes beam into single-mode one during the propagation in a multimode fiber and will be useful tools for various application in optical sensors and optical communications.

Reference

- [1] S. L. W. Meardon, *The Elements of Fiber Optics* (Prentice Hall, New Jersey, 1993) pp. 28-56
- [2] J. Canning and A. L. G. Carter, *Opt. Lett.* **22** (1997) 561
- [3] L. Goldberg, J. P. Koplow, Moeller, and D. A. V. Kliner, *Opt. Lett.* **23** (1998)
- [4] B. A. Malomed, G. D. Peng, and P. L. Chu, *Opt. Lett.* **21** (1996) 330
- [5] M. E. Fermann, *Opt. Lett.* **23** (1998) 52
- [6] D. Donlagic and M. Zavrsnik, *Opt. Lett.* **22** (1997) 837
- [7] Z. J. Chen, A. B. Grudinin, J. Porta, and J. D. Minelly, *Opt. Lett.* **23** (1998) 454
- [8] U. Griebner, R. Koch, H. Schonngel, R. Grunwald, *Opt. Lett.* **21** (1996) 266
- [9] J. M. Senior, *Optical Fiber Communications: Principles and Practices -2nd.* (Prentice Hall, New York, 1992) pp. 160-206
- [10] K. M. Davis, K. Miura, N. Sugimoto, and K. Hirao, *Opt. Lett.* **21** (1996) 1729
- [11] E. N. Glezer, M. Milosavljevic, L. Huang, R. J. Finlay, T. -H. Her, J. P. Callan, and E. Mazur, *Opt. Lett.* **21** (1996) 2023
- [12] D. Ashkenasi, H. Varel, A. Rosenfeld, S. Henz, J. Herrmann, and E. E. B. Cambell, *Appl. Phys. Lett.* **72** (1998) 1442.
- [13] S. H. Cho, H. Kumagai, I. Yokota, K. Midorikawa, and M. Obara, *Jpn. J. Appl. Phys.* **37** (1998) L737
- [14] O. M. Efimov, K. Gabel, S. V. Garnov, L. B. Glebov, S. Grantham, M. Richardson, and M. J. Soileau, *J. Opt. Soc. Am. B.* **15** (1998) 193
- [15] A. B. Borisov, O. B. Shiryayev, A. McPherson, K. Boyer, and C. K. Rhodes, *Plasma Phys. Control.*

Fusion. **37**, 569 (1995)

[16] W. Eickoff and E. Weidel, *Opt. Quant. Electron*, **7** (1975) 109

[17] J. H. Sharp, R. Illingworth, and I. S. Ruddock, *Opt. Lett.* **23** (1998) 109

[18] D. L. Griscom, *J. Non-Crystal. Solids* **73** (1985) 51

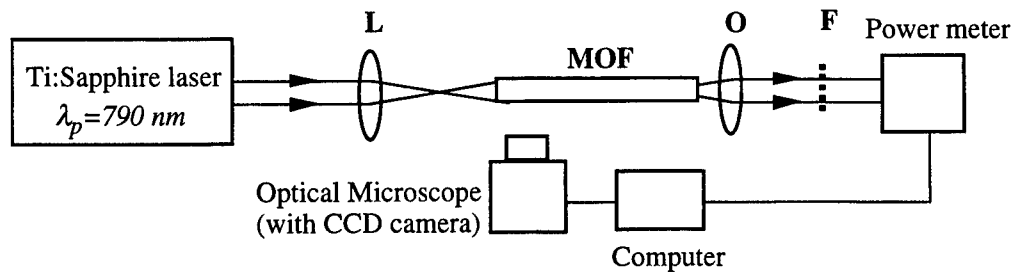


Fig. 1. Schematic of the experimental setup for laser-induced plasma channeling and refractive index modification in an optical fiber. L: Focal lens, MOF: Multimode optical fiber, O: Objective lens, F: Filter

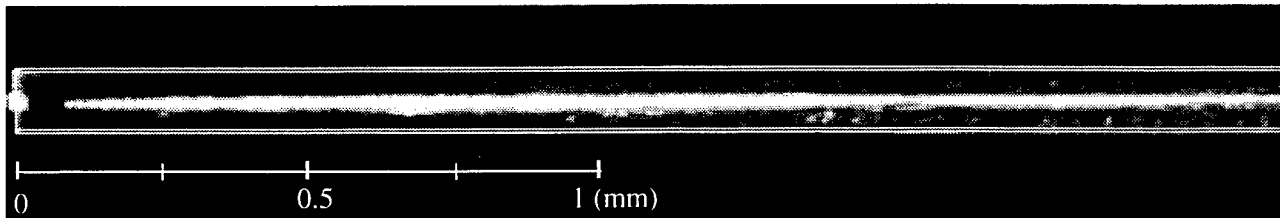
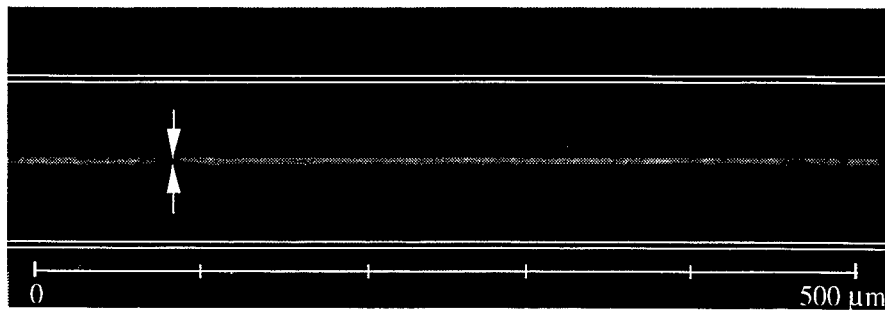
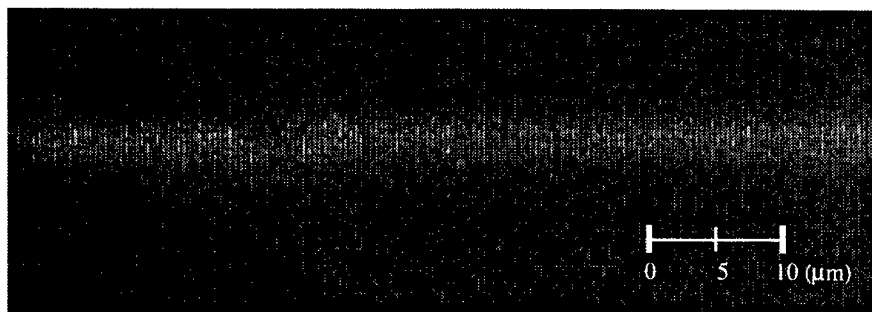


Fig. 2. Microscopic side view during plasma channeling in a multimode fiber with 100/110 μm core/cladding diameter excited by input intensity of $1.5 \times 10^{12} \text{ W/cm}^2$.



(a)



(b)

Fig. 3. Microscopic side view of refractive index modification induced by stable plasma channeling in a multimode fiber with 100/110 μm core/cladding diameter. (a) $\times 150$ (b) $\times 1500$ magnified views. The diameter of refractive index modification is 5 μm .

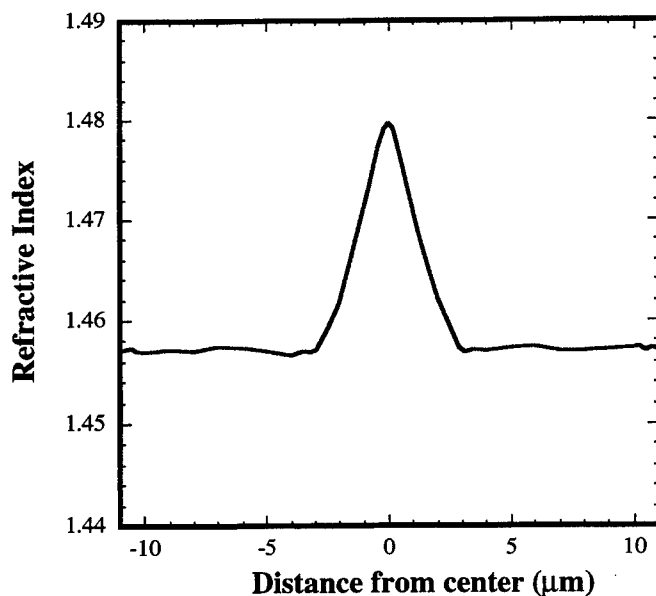


Fig. 4. The profile of laser-induced refractive index in a multimode fiber. After laser irradiation of the pulses of 1×10^4 at 1.5×10^{12} W/cm², the maximum value of increase refractive index was 1.479 and the refractive index of unmodified region was 1.457. The laser-induced refractive index modification have a graded index profile which is symmetric from the center in a multimode fibers.

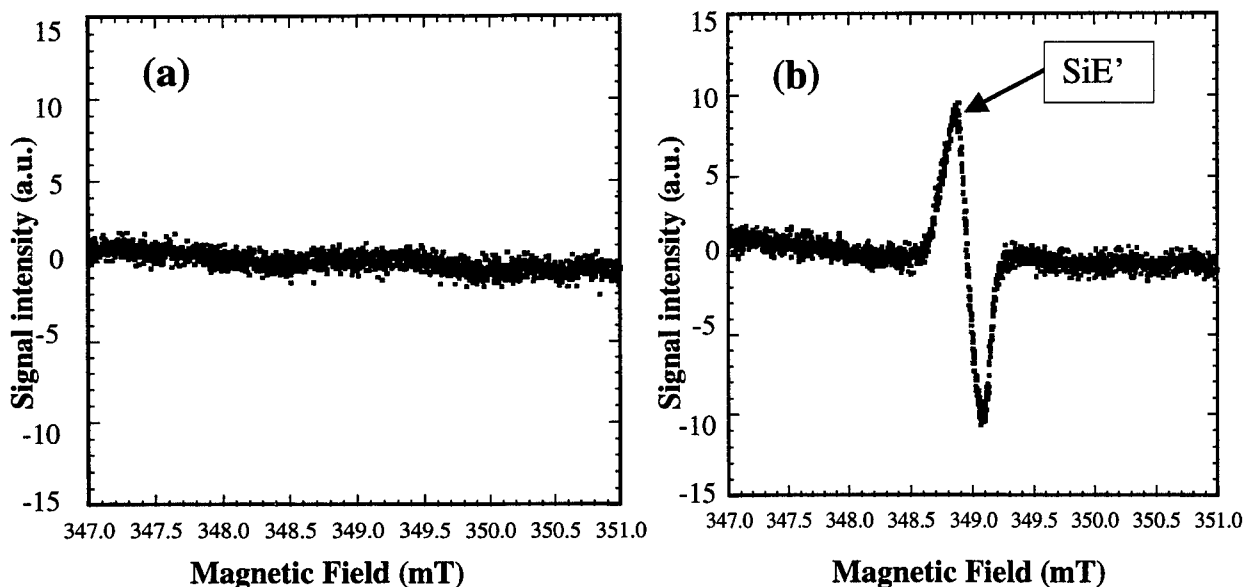


Fig. 5. ESR spectroscopic measurement of optical fiber (a) before laser irradiation (b) after laser irradiation in laser-induced modification. SiE' ($\equiv si \bullet$) center was paramagnetic defects, where \equiv represents a silicon atom bonded to three separated oxygens and \bullet represents a nonbridged electron.

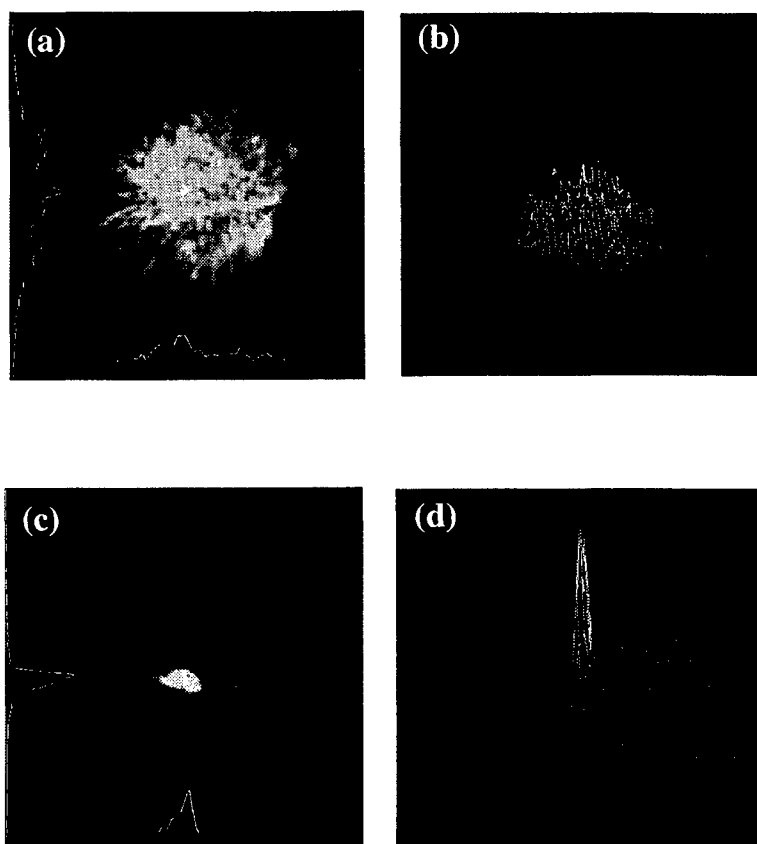


Fig. 6. The output properties of transmitted laser beam of 800nm. (a) near-field pattern and (b) beam intensity profile of an unmodified multimode fiber, (c) near-field pattern and (d) beam intensity profile of a modified multimode fiber. The sample was the same as that observed in Fig. 3.

Laser Induced Non-Thermal Surface Modification of Aluminum

David P. Taylor ^a and Henry Helvajian ^b

^a Mechanics and Materials Technology Center

^b Center For Microtechnology

The Aerospace Corporation

2350 El Segundo Blvd.

El Segundo, CA 90245, USA

ABSTRACT

Low fluence UV laser stimulated desorption of ions from metal surfaces leads to the production of high kinetic energy species and also modifies the surface left behind. Both of these effects are small for an individual laser shot. The number density of the desorbed ions by the laser is very low -- much less than a monolayer per pulse. The changes in the crystal surface are also subtle. However, in both cases there are cumulative effects after many laser shots which cannot be attributed to thermal or plasma plume laser interaction processes. There is no evidence for thermal ions in the TOF mass spectrum. A laser ionization experiment was performed to measure the kinetic energy distribution of the desorbed neutral aluminum species (and thereby ascertain the attained peak surface temperature). The high kinetic energy Al^+ ions were used as monitor for insuring that the laser induced desorption process was always in the non-thermal regime during the surface modification experiments. We observe, via SEM, surface modification only after exposure to a large number of laser shots ($>10K$). Examination of the laser exposed surface with electron microscopy reveals quasiperiodic patterns made up of sub-micron scale ridges. After exposures to more than 100K laser shots, the quasiperiodic patterns break-up into irregular nodule-like shapes. Our data indicates the surface modification occurs without desorbing significant amounts of material.

Keywords: Non-Thermal Surface Modification, Laser, Sputtering, Sub-micron Texturing, Aluminum

1. INTRODUCTION

Lasers have increasingly been used as a processing tool in the modification of materials. The ability to focus the laser and precisely control the deposition of energy offers desirable processing capabilities over many different energy regimes, from industrial cutting or welding through the melt texturing of hard drive surfaces to the direct write "editing" of integrated circuits. In general, aside from photolithography, laser texturing of surfaces can usually be regarded as a thermal phenomenon. Thermal processes leading to the modification of surfaces include cratering [1] associated with laser ablation, the build-up of ejected material on the surface analogous to sand dune formation [2] and the patterning of melt zones. [3]

"Desorption Induced by Electronic Transition" (DIET) stimulated desorption behavior has been observed for photons (PSD), electrons (ESD) and ions (SIMS). Some laser desorption experiments exhibit a product yield which is linear with the laser power -- as is usually the case for Photon Stimulated Desorption (PSD). On the other hand, many other laser desorption experiments exhibit a superlinear laser power dependence which commonly results in the desorption of high kinetic energy ions via a non-thermal process. [4,5]

Relatively little work has been done which evaluates the surface changes in morphology which might accompany low fluence laser desorption experiments. One reason for this is that it can be difficult to do these experiments in the non-thermal regime. Exposure to the laser can often build up defects near the surface and reduce the power threshold for laser ablation and thermal effects, so a superlinear absorption experiment can easily shift from the non-thermal to thermal regime. Another reason is that the known applications drive the practical research into other areas, such as catalysis or thermal processing. Laser experiments on metal surfaces have tended either to study the low-fluence linear behavior characteristic of MGR-type processes involving adsorbates or the high-fluence thermal behavior characteristic of laser ablation. Intuitively, one would not expect a laser stimulated desorption process, which produces only a few ions per laser shot, could also result in a significant change in the surface structure -- but yet it does.

Our UV laser stimulated desorption experiments at 355nm, 266nm and 248nm produced desorption of high kinetic energy (most probably $KE = 15\text{eV}$, 4 eV FWHM) aluminum ions from a single crystal polished aluminum sample (<111> orientation). [6] We have also observed that there are cumulative changes in the surface morphology as a result of the non-thermal laser stimulated desorption process. The modified aluminum surface had a quasiperiodic pattern of ridges and nodules of on a scale of about 400nm. The surface morphology change was noticeable to the unaided eye after the surface had been exposed to almost a million laser shots..

The experiments reported here were designed to investigate the observed surface modification process in two ways. First, the desorbed species were monitored. At the laser fluences we employed, the kinetic energy of the aluminum ions was always found to be in the non-thermal regime. It was initially presumed that the observed number of aluminum ions was small relative to the number of neutral atoms desorbed from the surface by the laser. The kinetic energy distribution of the neutrals desorbed by laser ablation from an aluminum surface has been reported several times and we anticipated that the kinetic energy profile of the neutral desorbates would provide a good indication of the peak surface temperature. Second, the number of laser shots applied to a region of surface was systematically reduced as a UHV manipulator moved the region of the sample surface exposed to the laser.

2. EXPERIMENT

1. Laser Ionization of Neutral Desorbates

The Time of Flight (TOF) UHV experimental apparatus used in this work has only been slightly changed from the system reported previously. [7] The TOF mass spectrometer has been lengthened, the ion extraction region has been modified to allow for zero field extraction and the accelerator plate stack was modified so that a pulse extraction mode could be used. This feature was not used, since the kinetic energy of the desorbed ions observed is higher than we anticipated and isotope separation problems are not an issue.

The UV stimulated desorption laser was an MPB PSX-100 operating at 248nm. It was loosely focused to about a 300 micron diameter spot on the surface and the laser fluence was typically $100\text{ mJ/cm}^2 \pm 50\text{ mJ/cm}^2$. The kinetic energy profile of the desorbed neutral species was measured with a time delayed Quantel 581C Nd:YAG laser pumping a TDL dye laser mixed with the IR fundamental to reach 394 nm. Aluminum atoms could be ionized at this wavelength by using a (1+1) Resonance Enhanced Multiphoton Ionization scheme through the $Al(4s)$ excited state. [8,9] Wavelength calibration was done using a hollow cathode lamp and a 1/3 meter monochromator. The two laser beams were aligned using HeNe lasers and fast photodiodes were used to set the time delay between the laser pulses. Using this pump-probe technique with a variable time delay, it is possible to measure the kinetic energy distribution of the desorbed neutral aluminum species. From the measured kinetic energy distribution an estimate can be made of the attained peak surface temperature. [10,11]

The TOF ion signal is detected by a microchannel plate stack and recorded using a 100MHz dsp Transiac 2001 transient digitizer in a CAMAC system under PC control. The laser power was measured by a Laser Precision Rj-7200 Energy Radiometer or a Molecron P3 pyroelectric detector which could be digitized though a boxcar system and recorded by the PC. All though most of this experiment was conducted at

248nm laser irradiation, the kinetic energy of the desorbed aluminum ions is the same for laser stimulated desorption at 355nm, 266nm and 248nm. [12]

2. Evaluation of the surface

The aluminum sample is a single crystal about 1cm in diameter and about 1mm in height cut to the (111) crystallographic direction. The aluminum crystal was polished with aluminum oxide and washed with acetone. In an antechamber of the of the vacuum system, the Al(111) sample was cleaned by sputtering with 3kV Argon. This cleaning process for aluminum had previously been evaluated by taking an Auger spectrum showing less than 1% oxygen just after the sample had been transferred to the main chamber. The experiment was conducted at a background pressure between 2×10^{-10} Torr and 2×10^{-9} Torr and as a result of the duration of the experiment (hours) some oxidation is expected.

A sequence of adjacent spots were irradiated. The sequence began with the largest number of laser shots applied ($\sim 10^6$). Although the laser fluences were commensurate with ion desorption, the high dose exposure spot leaves a mark which is visible to the unaided eye. Using a UHV manipulator, the sample was displaced a fixed distance and the process was repeated. After two spots were visible, the UHV manipulator was used to move the sample the same amount and $\sim 3 \times 10^5$ laser shots were applied to the surface. This process was repeated with progressively smaller numbers of laser shots applied across the surface. The sample was removed from the chamber, exposed to the atmosphere for about an hour, and moved to another vacuum chamber where the surface was examined by a Scanning Electron Microscope.

3. RESULTS

1. Neutral Desorbates

Figure 1 shows the nascent kinetic energy distribution of the desorbed aluminum ions measured by the TOF mass spectrometer. The data clearly shows that the ions are desorbed with high kinetic energy which cannot be described by a thermal desorption process. In our experiment this KE distribution served as the probe of the non thermal photodesorption process. The laser fluence was set all the while monitoring the desorbed ion kinetic energy distribution.

Laser ionization is a sensitive scheme for detection of atomic species and it can even be used to detect specific quantum state populations. In gas phase photochemistry, laser ionization schemes can be problematic in the case of neutral atoms with several electron volts of kinetic energy, particularly if their number density is low. In this experiment, the ejected neutral species are primarily forward directed and, by orienting the ionization laser normal to the velocity vector of the desorbed species, the effects arising from Doppler broadening are minimized. The rate limiting step in a (1+1) experiment is the initial excitation. Because of the size of the UHV chamber, we are forced to use a lens with a half meter focal length. Another issue in the laser ionization detection efficiency is that our 1.8 meter TOF design has a relatively small solid angle of acceptance. Although there is an extraction plate only about 2.5cm from the sample, the multichannel plate stack is only 18mm in diameter. We use an estimate that our TOF apparatus allows us to detect perhaps one tenth of the ions produced simply because of the length of the flight tube, the number of grids and the efficiency of the multichannel plate stack. Our collection efficiency is further reduced if the initial angular distribution of the neutrals is a $\cos \theta$. The expected signal from the laser ionization of the neutral aluminum desorbates depends linearly on their number density in the laser focus region. We can roughly estimate the ion yield using a single photon absorption cross section of 10^{-19} cm^2 and 10ns for ionization laser pulse of about 3mJ. For a local pressure of about 10^{-7} Torr, we would expect on the order of 10^3 neutral species Torr in the ionization laser focus. This leads to an estimate of about one ion count collected per laser shot under these conditions. We would have to change the conditions of this experiment to have a good signal to noise below about 10^{-7} Torr local pressure in the ionization region.

There are two other issues which further complicate the TOF pump - probe measurement of the kinetic energy distribution. Stimulated desorption experiments are sensitive probes of certain trace species on the surface. Ion signals from K^+ and other trace species are often observed -- even from freshly cleaned surfaces. There is also always a background electronic noise in the experiment. If the ion peaks produced by the ionization laser are separated in time from the ion peaks produced by the desorption laser, there is little change in the noise of the TOF experiment. However, the time delay to firing the ionization laser is

scanned in order to map out the velocity distribution of the neutrals. For very small ionization laser signals, the trace background ion peaks from desorption laser can degrade the signal to noise. This is most troublesome when the signal time-window passes through these background ion peaks as the relative delay of the ionization laser is scanned. Moreover, scanning the ionization laser significantly decreases the average signal collected. Although it is possible to increase the length of time the experiment runs, there is still a practical constraint on maintaining operations over longer times.

It was possible to detect a signal we could attribute to aluminum ions produced by the ionization laser. However, although we observed a signal, the signal to noise ratio was too small to produce a meaningful kinetic energy distribution. Confirmation that the correct laser wavelength was being used is provided by the ion signal wavelength dependence of the ionization laser. (Refer to Figure 2.) From these results we can conclude that a very small fraction of a monolayer is desorbed as neutral aluminum species. This result is consistent with the very low peak temperature increase expected in the sample for the desorption laser fluences used in this work. It also supports the contention that the laser spatial intensity profile on the sample does not contain intensity "hot spots" which could induce local thermal melting since the evaporated products from these sites would have been detected.

2. Changes Surface Morphology (SEM and White Light Interferometer)

The UV laser induced surface modification has been previously observed in our other desorption experiments. The unaided eye could find the spots on the polished crystal which had been exposed to a million laser shots, regardless of the laser wavelength used (e.g., 266 nm or 248 nm). Under magnification, the altered region of the laser is also identifiable by a color change. This visible change in the crystal associated with the laser surface modification is currently under study. The apparent diameter of the altered surface associated with this color change is more than two times larger than the spot diameter measured using the electron microscope. If the laser spot area estimate from the optical microscope is used, then the laser fluences of this experiment are about 4 times lower than the numbers reported above.

Figures 3 through 5 are scanning electron micrographs (SEMs) of the 248 nm irradiated Al(111) surface. The SEMs shown under several magnifications show a progression in the surface topology as a function of laser shot. An SEM image of the polished Al(111) crystal is also shown in Figure 3A. For the lowest exposures the SEM images show long narrow "solitary wave" features between 5 and 10 μm in length and about 0.4 μm in width. These features as well as a quasiperiodic structure in the surrounding region can be seen in Figure 3B. The small dark rectangular region in the center of Fig. 3B is a consequence of surface charging during the SEM scan. Similar dark boxes appear in other electron micrographs.

Figure 4 shows a clear progression of changes with increasing laser exposure. The SEM image in Figure 4A indicates that the surface is modified in the upper right corner after about 50K shots. The bottom part of Figure 4A is also covered in the SEM of Figure 4B where the surface had been exposed to about 100K laser shots. The region imaged by Figure 4C was exposed to about 200K shots while the heavy surface texturing shown in Figure 4D is the result of 1000K shots.

Figure 5 shows a sequence of SEM images taken at 10,000X magnification. Again, an image of the polished aluminum surface taken far from the part exposed to the laser is shown in Figure 5A. Figure 5B shows a modified area on the surface exposed to the lowest number of laser shots that we were able to locate with the SEM (15K shots). The SEM reveals significant surface modification after only 15 K shots. This change in surface morphology occurred even though *surface melting should not have been possible* at the laser fluences used. At 50K shots a pattern appears which is shown in Figure 5C. With more laser shots (100K shots) this pattern becomes more complex as that shown in Figure 5D and after 200K shots (Figure 5E) all surface regularity is lost. No new pattern emerges even after 1000K shots have been delivered (Figure 5F). This progressive change in the surface topology from what appears to be a pattern, to a more complex pattern and finally to disorder is not only prevalent for 248 nm excimer laser irradiation but also for 266 nm Nd-Yag radiation. Figure 6 shows a set of SEM images taken with progressively higher magnifications following 1000K shot 266nm irradiation.

In an effort to get a handle on the depth of the features observed with the SEM, we used a WYKO white-light interferometer to take 3D images of the various regions. An interferometric processed image of both

the polished crystal surface and a region subject to $>10^6$ shots at 248nm is shown in Figure 7A and with increased magnification in Figure 7B. The WYKO gives an estimate of about $2\mu\text{m}$ as the total height of the features within the laser spot and only about 300nm (including scratches) for the polished region on the right of the image.

From the 100K shot region, we observe that the ridge structures are quasiperiodic. The SEM indicates the width between wave-like features to be in the 300nm to 400nm range. The WYKO indicates that the total height across the image in the 100K shot region is 200nm, while adjacent triangular features seem to differ by about 50nm in depth. This set of WYKO white light interferometer images for the 100K shot region appears in Figure 8 at different magnifications.

Figure 9 provides WYKO white light interferometer images at 100X from two other regions after exposure to the pulses from the 248nm laser. Figure 9A is believed to be a region of the Al(111) surface exposed to $>200\text{K}$ laser shots and the WYKO (VSI) estimates the structures to be $2\mu\text{m}$ to $3\mu\text{m}$ in height. Figure 9B is believed to be a region exposed to 50K laser and the WYKO (PSI) estimates the central feature to be 300nm in height and other features to be about 50 nm to 80 nm in height.

4. DISCUSSION

1. Non-Thermal Laser Interaction With the Surface

The laser fluence provides an indication of the sort of peak temperature increase we can expect in this experiment. For a 20 ns pulse of 248 nm light at about $150\text{mJ}/\text{cm}^2$, a one dimensional calculation indicates that the peak rise in surface temperature of aluminum should only be about 25K. [14] This calculation ignores the possible presence of an oxide layer on the sample. Since our crystal was polished to $\lambda/2$ and the polishing process introduces scratches and other defects, it is also possible that there are local variations ignored by a 1D calculation.

Both the calculated estimate of peak surface temperature and the fact that no significant neutral species desorption is measured make it unlikely that the changes we observe in the surface morphology are due to a thermal process or melting. Another piece of supporting evidence is that high kinetic energy ions are observed. The measured Al^+ ion kinetic energy distribution is narrow, about 3 eV, has a most probable KE at 15eV and does not fit a Maxwell-Boltzmann distribution. Since, the ion desorbates were monitored throughout the experiment it would have been evident if a thermal or a plasma process ensued on a particular laser shot.

2. Surface Changes

The surface changes imaged in Figures 5B, 5C and 5D in the sample show a quasi-periodic pattern. This suggests, though does not prove, that a cooperative process might be at work. If we rule out melting and other thermal processes as we have argued above, then the rearrangement of the surface must be explained in some other way.

The atoms on the surface can be displaced in two ways. First, patterning could occur by removing the metal atoms from the surface and then redepositing them. We reject this picture outright based on the failure to observe neutral desorbates, the low estimated peak temperature of the sample and the rather high cohesive energy ($3.4\text{eV}/\text{atom}$) to form separated neutral aluminum atoms in their ground state.[K] The second and remaining alternative is that the changes in surface morphology can occur without removing atoms and redepositing them on the surface.

The simplest way to arrive at a quasi-periodic structure is if the lattice is somehow distorted. The observed $5\mu\text{m}$ to $10\mu\text{m}$ long "solitary wave-like" structures are 300 to 400 nm in width. These structures appear to have formed via a cooperative process. Again, one immediately thinks of melting and related local stress relief to produce surface texturing. However, the estimated peak rise in temperature here does not support this physical picture and another process must be found which could lead to surface rearrangement. The "plucked lattice model" might explain our results [15]. The model describes the dynamics for a hard

stretch and soft-compression anharmonic potential lattice subject to local impulses. This mathematical model permits soliton wave solutions. This picture depends on assuming soliton-like waves can freeze out as vertical displacements and that they can annihilate each other. Over a number of repeated impulses (>10K shots) these small vertical displacements could be additive to produce a macroscopically measurable alteration of the surface. In this "plucked lattice" picture, the apparent patterning in the surface could be associated with surface crystallographic orientation. Although these results are preliminary, the patterning exhibited in Figure 5C has some of the same symmetry to the (111) surface. In a more careful experiment we plan to evaluate if there is a coincidence between the crystallographic axes and the observed three-fold pattern.

5. CONCLUSION

Low fluence pulsed UV laser irradiation can texture a metallic surface on the sub-micron scale without resorting to the removal of a large density of matter. Our estimate is that less than 0.1% of the surface atoms are removed for the large surface topology changes observed. From the material processing perspective, this surface texturing is done with a minimal "heat affected zone" and without the need for surface annealing. This work suggests that it is possible to pattern a surface with a laser in a non-thermal manner. The "plucked lattice" model comes closest to explaining all our experimental results. The model provides a convenient scheme by which surface morphology may be altered without the need for a large density surface migration. A set of experiments are planned using different crystal faces.

The laser-induced surface textures generated on the aluminum surface open an interesting area of future material processing applications. Cooperative-effect low fluence laser patterning of a surface could be useful for generating a patterned "seed" layer for a sub-micron atomic/molecular self-assembly process. Alternative applications could exploit enhanced chemical reactivity at modified specific sites. Perhaps the most interesting potential application of this work is that non-thermal laser processing might present an entirely new set of approaches to future materials processing.

6. ACKNOWLEDGEMENTS

This work has been funded by A.F.O.S.R. under contract F04701-93-C-0094. The support of program manager Dr. Howard Schlossberg AFRL/AFOSR/NE is gratefully acknowledged. The authors also wish to thank William Hanson and Joseph Uht.

7. REFERENCES

1. A. Peterlongo, A. Miotello, and R. Kelly, **Phys. Rev. E**, **50**, 4716, (1994).
2. L. K. Ang, Y. Y. Lau, R. M. Gilgenbach, H. L. Spindler, J. S. Lash, and S. D. Kovaleski. **J. Appl. Phys.**, **83**, 4466 (1998).
3. F. Vega, C. N. Afonso, W. Szyszko, J. Solis. **J. Appl. Phys.**, **82**, 2247 (1998).
4. R. Welle and H. Helvajian, **J. Chem. Phys.**, **91**, 2616, (1989).
5. M. A. Schilbach and A. V. Hamza. **Phys. Rev. B**, **45**, 6197 (1992).
6. *In preparation*, D. P. Taylor and H. Helvajian.
7. D. P. Taylor and H. Helvajian, "Nonlinear Photon Stimulated Desorption From and Oxidized Tungsten Surface," in **SPIE Proceedings Vol. 3274, Laser Applications in Microelectronic and Optoelectronic Manufacturing III**, Eds, J. J. Dubowski, Peter E. Dyer, p 25-33, (1998).
8. W.C. Martin and R. Zalubus, **J. Phys. Chem. Ref. Data** **8**, 817 (1979).
9. C. E. Moore, **Atomic Energy Levels**, Nat. Bur. Stand. (US GPO, Wash. DC, 1971).
10. R.A. Lindley, R.M. Gilgenbach, C.H. Ching, and J.S. Lash, G.L. Doll. **J. Appl. Phys.**, **76**, 5457 (1994).
11. I. Borthwick, C.T.J. Scott, K.W.D. Ledingham, and R. Singhal. **AIP Conf. Proc.**, **288**, 414, (1993).
12. *In preparation*, D. P. Taylor and H. Helvajian.
13. K. M. Beck, D. P. Taylor, and W. P. Hess, **Phys. Rev. B**, **55**, 13253, (1997).
14. C. I. H. Ashby, **Photons and Low Energy Particles in Surface Processing**, **Materials Res. Soc. Symp. Proc. V236** (1992). or J. Y. Tsao and D. J. Ehrlich. **Laser Microfabrication Thin Film Processes & Lithography**, Academic Press, (1989).
15. E. A. Jackson, **Perspectives in Nonlinear Dynamics, Vol. 2**, Cambridge University Press, (1991).
16. P. S. Bagus, C. R. Brundle, F. Illas, F. Parmigiani and G. Polzonetti. **Phys. Rev. B**, **44**, 9025 (1991).

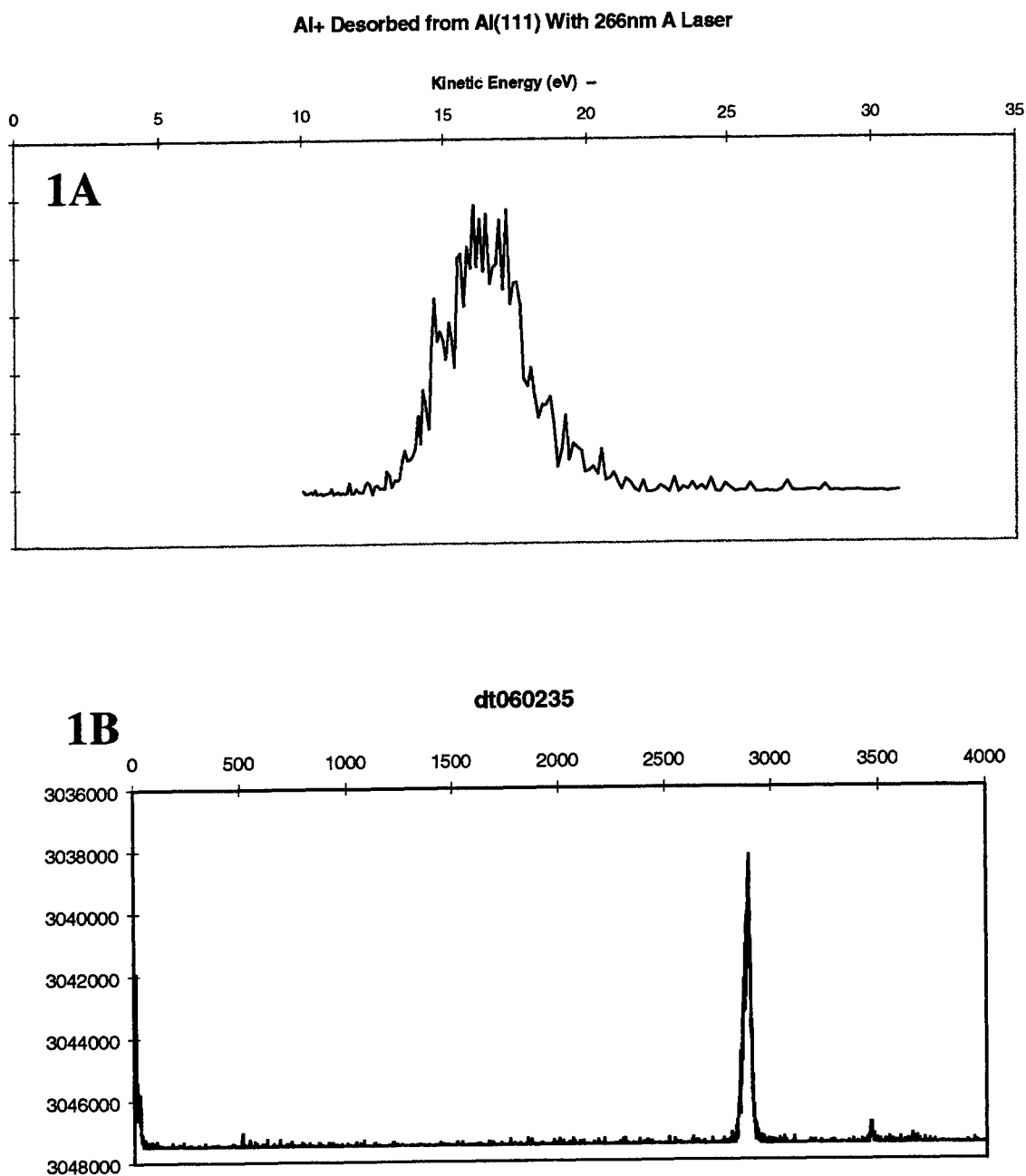


Figure 1: A. Kinetic Energy Distribution of Al⁺ from Al(111)
B. Time of Flight Raw Data (2.5V Extraction and 10ns/channel). The large peak at about 2800 channels is Al⁺.

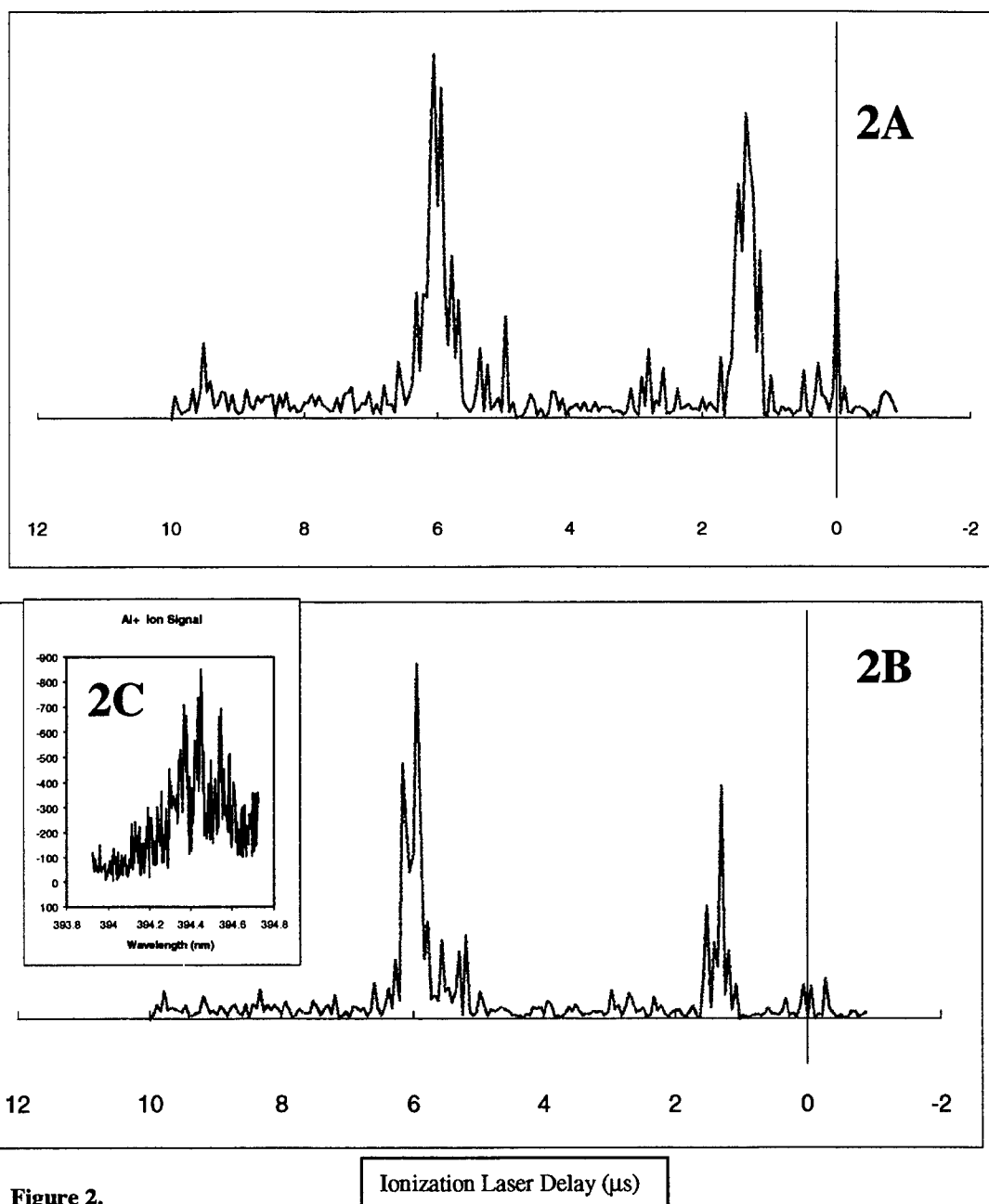


Figure 2.

- A. Ionization laser delay spectrum. The time indicated is the delay between the desorption laser and the ionization laser. The small difference between this spectrum and the background indicates that the number of neutral aluminum atoms ionized by the laser was too low to construct a kinetic energy distribution.
- B. Background laser delay spectrum. The peaks depend only on the desorption laser and appear as the time gate is scanned through the arrival time of background ions in the laser stimulated desorption experiment.
- C. The wavelength dependence of the small signal associated with the ionization laser signal is included in the insert.

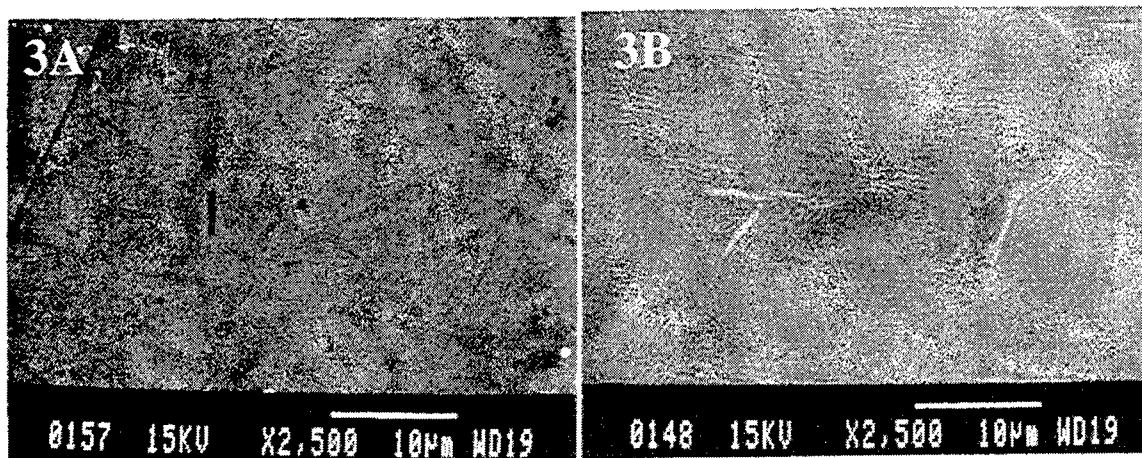


Figure 3.

- A. The polished Al(111) surface without exposure to the laser. SEM magnification is 2,500X.
- B. The same Al(111) surface after modification by exposure to approximately 50,000 laser shots at 248nm. SEM magnification is 2,500X.

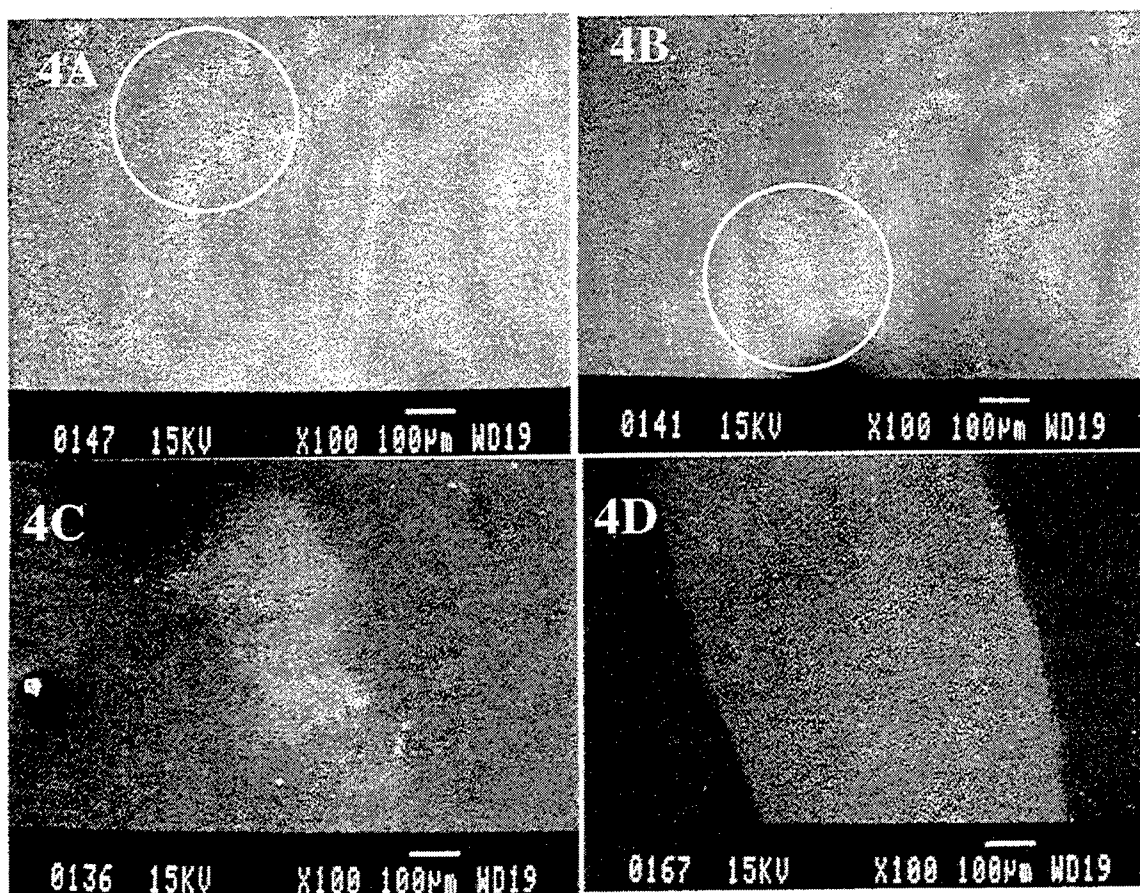


Figure 4.

- A. Al(111) exposed to 50,000 laser shots @248nm SEM magnification 100X, affected zone circled.
- B. Al(111) exposed to 100,000 laser shots @248nm SEM magnification 100X, affected zone circled.
- C. Al(111) exposed to 200,000 laser shots @248nm SEM magnification 100X.
- D. Al(111) exposed to >1,000,000 laser shots @248nm SEM magnification 100X.

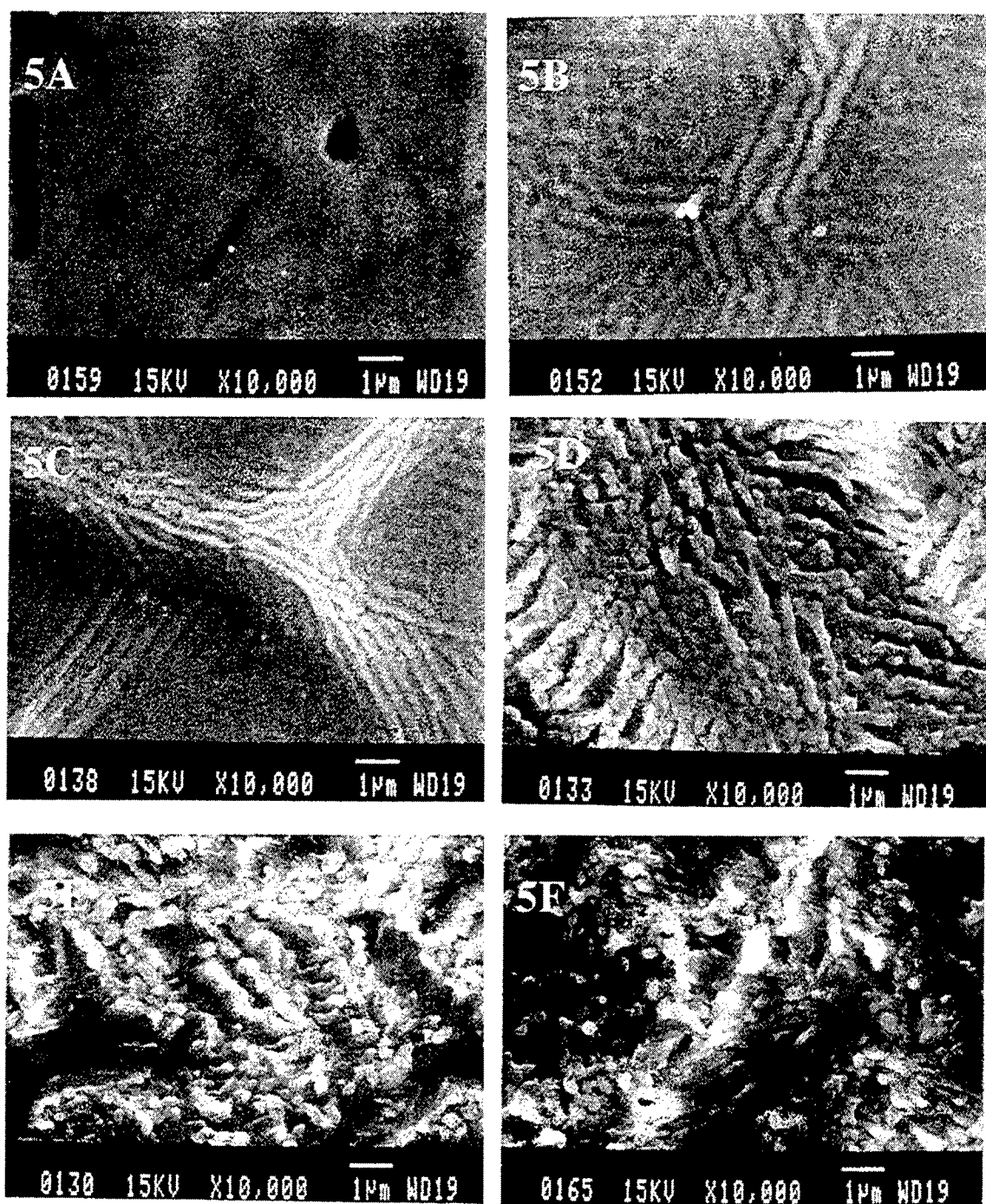


Figure 5.

- A. Polished Al(111) surface, 0 laser shots (10,000X SEM image).
- B. Al(111) surface after approximately 15,000 laser shots @ 248nm (10,000X SEM image).
- C. Al(111) surface after approximately 50,000 laser shots @ 248nm (10,000X SEM image). The features appearing in B and C are typical of quasiperiodic patterning over a larger region.
- D. Al(111) surface after approximately 100,000 laser shots @ 248nm (10,000X SEM image).
- E. Al(111) surface after approximately 200,000 laser shots @ 248nm (10,000X SEM image).
- F. Al(111) surface after $>10^6$ laser shots @ 248nm (10,000X SEM image). The quasiperiodic structures which appeared in Figures B and C, break up in D and in E feature periodicity almost completely lost.

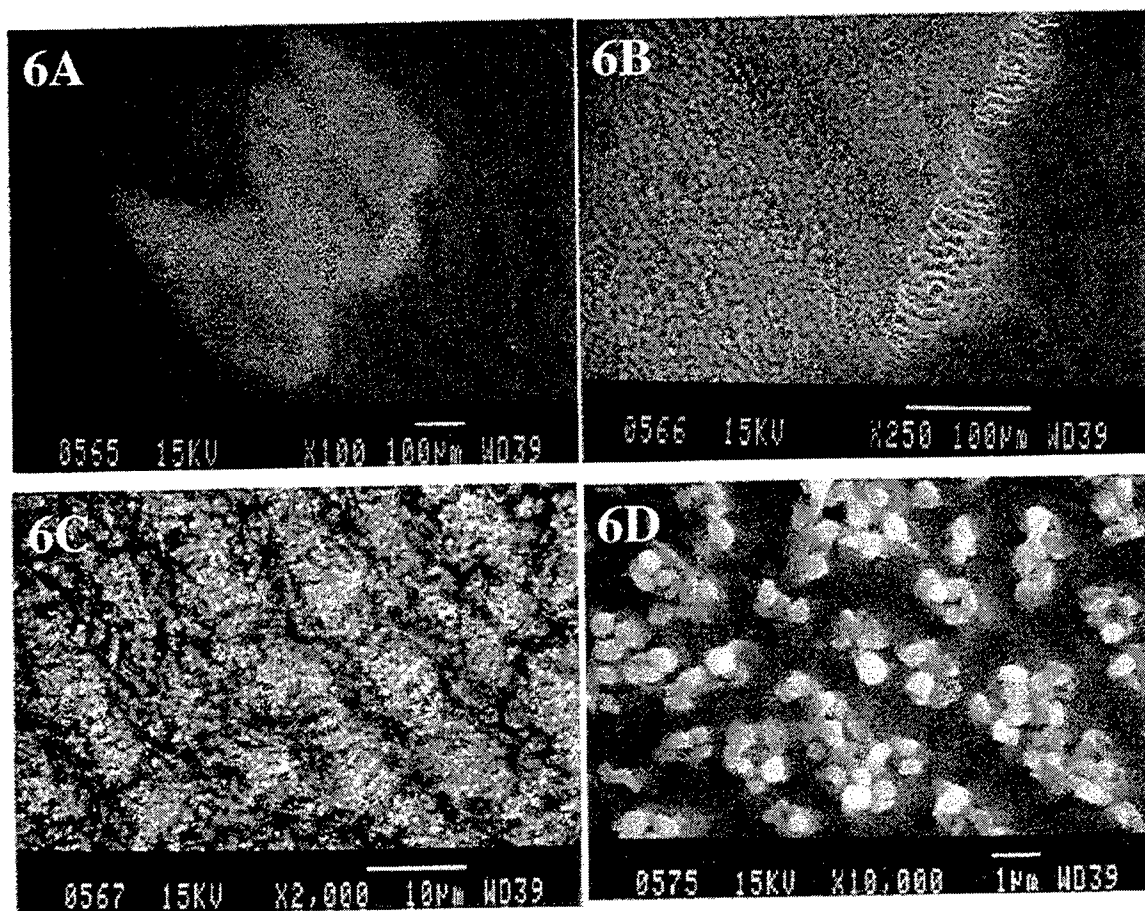


Figure 6.

- A. Similar behavior for Al(111) exposed to more than 10^6 shots at 266nm and imaged with an SEM at 100X. Al(111) exposed to more than 10^6 shots at 266nm and imaged with an SEM at 250X.
- B. Al(111) exposed to more than 10^6 shots at 266nm and imaged with an SEM at 2,000X.
- C. Al(111) exposed to more than 10^6 shots at 266nm and imaged with an SEM at 10,000X.

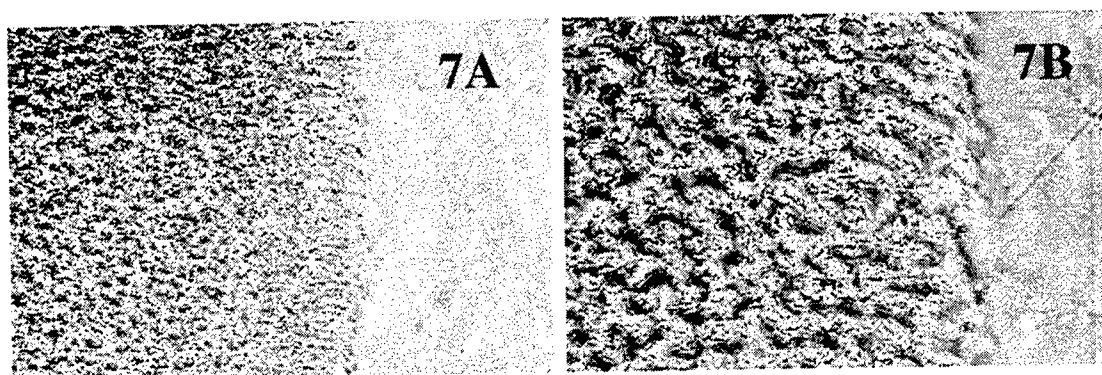


Figure 7

- A. Wyko white light interferometer (VSI) image of the laser affected region of the Al(111) crystal at 25x magnification. The region on the left side of the image has been exposed to $>10^6$ laser shots at 248nm and the total feature height is $2\mu\text{m}$. The region on the right side of the image is consistent with the polished Al(111) crystal, which was determined to have better than $\lambda/2$ roughness using this instrument.
- B. Wyko white light interferometer (VSI) image of the same region at 50X magnification.

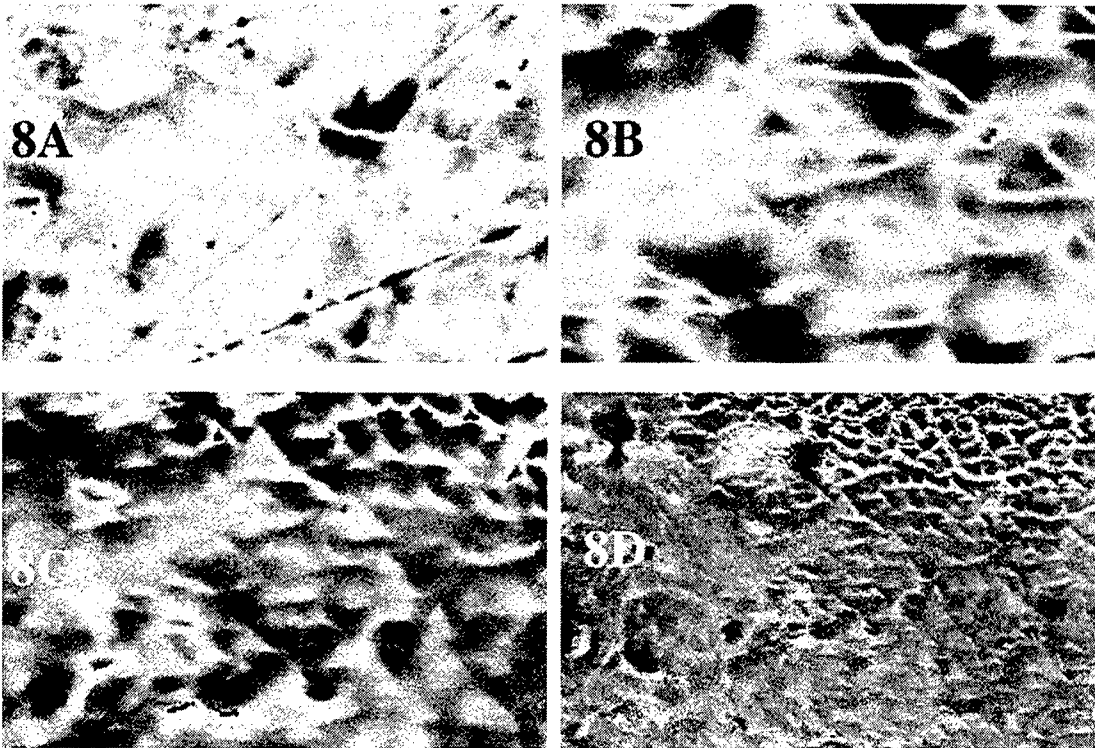


Figure 8.

- A. The white light interferometer (PSI) image of the polished Al(111) crystal surface at 100X.
- B. Another (PSI) image at 100X magnification, this time of a region on the same surface processed by exposure to about 100K shots with the 248nm laser.
- C. Same region at 50X magnification. Adjacent triangular features typically differ in height by about 50nm, while the maximum height difference is estimated to be 200nm in this image.
- D. Same region at 25X magnification. The laser processed region is in the upper right hand corner.

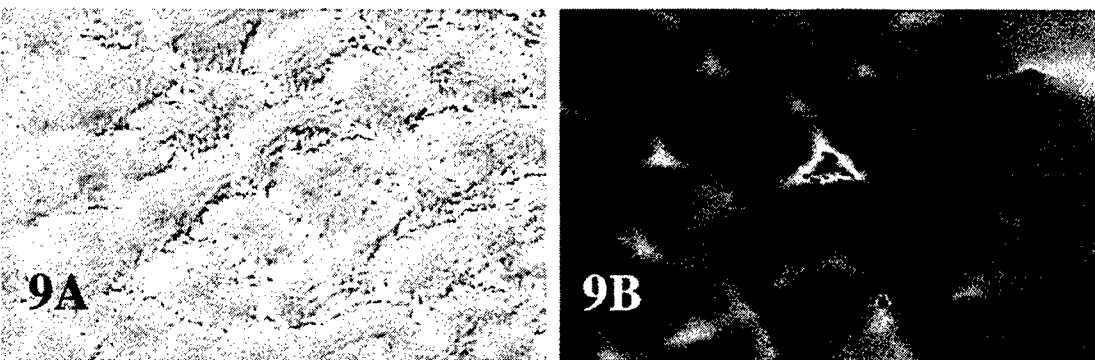


Figure 9.

- A. White light interferometer (VSI) 100X image of another region of the Al(111) crystal exposed >200K laser shots at 248nm. The total height of the surface features is estimated to be 2 to 3 μm .
- B. White light interferometer (PSI) 100X image of a region of the Al(111) crystal believed to be exposed to 50K laser shots at 248nm. The central feature is estimated to be about 300nm in height and the other triangular features are 50nm to 60nm in height.

Time- and space-resolved imaging and numerical simulation of laser zone texturing of Ni-P disk substrates

Shaochen Chen, Mengqi Ye and Costas P. Grigoropoulos¹⁾

Department of Mechanical Engineering, University of California, Berkeley, CA 94720-1740

ABSTRACT

This work investigates the transient process of melting and microscale surface deformation upon pulsed Nd:YLF (FWHM=15 ns, $\lambda=1,047$ nm) laser heating of Ni-P hard disk substrates. The laser pulse energy is in the range of 1.0 μ J to 5.0 μ J. The features produced by laser heating have a diameter of approximately 15 μ m and height in the tens of nanometers range. A laser flash photography system is developed to visualize the transient topography development during the laser texturing process. The system has a nanosecond time resolution and sub-micron spatial resolution. A numerical analysis based on finite difference method is conducted to simulate the microscale energy transport and fluid flow. Comparison between the numerical and the experimental results helps to understand the physical mechanism of the process.

Keywords: Laser flash photography, transient melting and deformation, imaging, surface tension, numerical simulation.

1. INTRODUCTION

Laser zone texturing (LZT) of Ni-P hard disk substrates has attracted a lot of interest both in academic research and industrial development.¹⁻³ Extensive research has been focused on developing various shapes of feature ("Bump") such as a single-crater, sombrero, and double-rimmed-crater to meet a specific tribology requirement.⁴⁻⁵ The mechanism of the feature formation was investigated by numerical simulation.³ However, all these studies were based on the final topography. To well understand the mechanism of bump formation in the LZT process, time and space-resolved experimental investigations and numerical simulation are necessary.

In the LZT process, a laser pulse is delivered to the target to initiate melting. The molten pool has a diameter of several micrometers and the melting duration lasts only several hundred nanoseconds. Since the heating laser beam has a Gaussian profile, a temperature gradient is established in the laser affected zone. The temperature gradient-induced surface tension, which increases as temperature decreases, drives a fluid flow outward from the center of the molten pool, causing the free surface deformation.

In this paper, a laser flash photography (LFP) system is developed to visualize the transient topography development during the laser texturing process. The system has a nanosecond time resolution and a sub-micron spatial resolution. LFP has been an efficient tool to study the transient process of laser materials interaction, such as pulsed laser ablation of absorbing liquid,⁶ laser melting and ablation of solid thin film.⁷⁻⁸ One advantage of this technique is that it is able to visualize the transient growth process of the entire feature.

In the numerical simulation of unsteady, incompressible, free surface fluid flow problems, the location of the free boundary is not known a priori. Therefore, in addition to including a method for solving the Navier-Stokes equations, any solution procedure for free surface fluid flow problems must also include methods for locating and advancing the free surface, as well as for treating the free surface boundary conditions. In this paper, a numerical analysis based on finite difference method was conducted to simulate the microscale energy transport and fluid flow. A highly simplified marker and cell method is used to deal with the free surface deformation.⁹

¹⁾ Electronic mail: cgrigoro@me.berkeley.edu

2. EXPERIMENTAL PROCEDURES

A Nd:YLF laser ($\lambda=1,047$ nm, FWHM=15 ns) is used as the heating beam. The beam is expanded, attenuated and focused onto the Ni-P sample (12 wt. % of P) with a focal diameter of approximately $17\text{ }\mu\text{m}$ measured using knife-edge profiling. The pulse energy is adjusted to create smooth bumps with similar sizes and shapes to those used in the disk industry.

In order to visualize the dynamic process of bump growth, a LFP system is developed as shown in Fig. 1. A pulsed nitrogen laser-pumped dye laser ($\lambda=650$ nm, FWHM=4 ns) provides illumination on the sample surface through a long-working distance objective lens. The reflected heating beam is blocked out by a filter. The time-resolved images are captured in the CCD camera. Since the technique can produce only a single image for each firing of the heating laser pulse, the image sequences are obtained by repeating the experiment under the same conditions based on the fact that the pulse-to-pulse instability of the heating laser is small, and the sample is uniform, thus yielding highly reproducible laser texture. A function generator externally triggers both the Nd:YLF laser and the dye laser. The time interval between the two lasers is varied by the pulse generator. The spatial resolution of the imaging system is limited by the numerical aperture of the microscope objective lens and the pixel size of the CCD camera. The time resolution is within several nanoseconds, limited mainly by the pulse width of the dye laser.

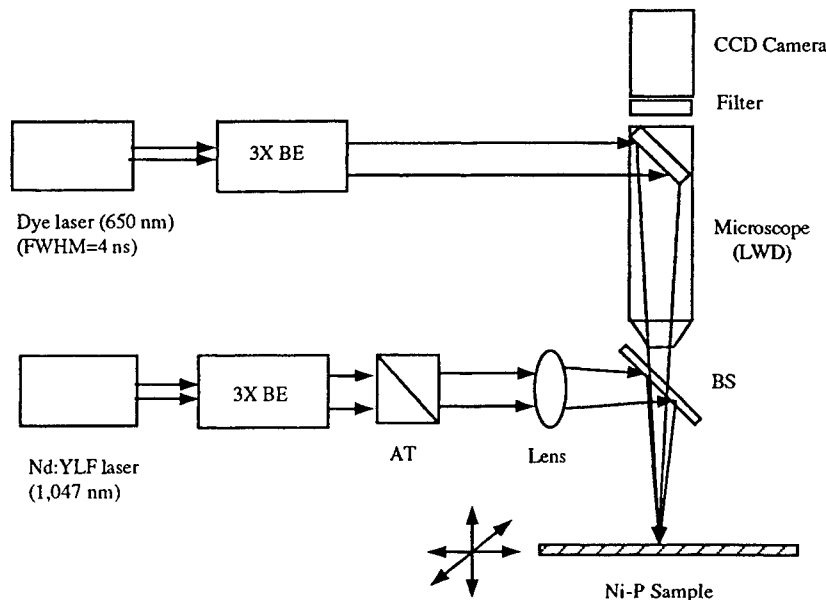


Fig. 1 Experimental setup of the laser flash photography system
(AT: attenuator, BE: Beam Expander, BS: Beam Splitter, LWD: Long-Working Distance)

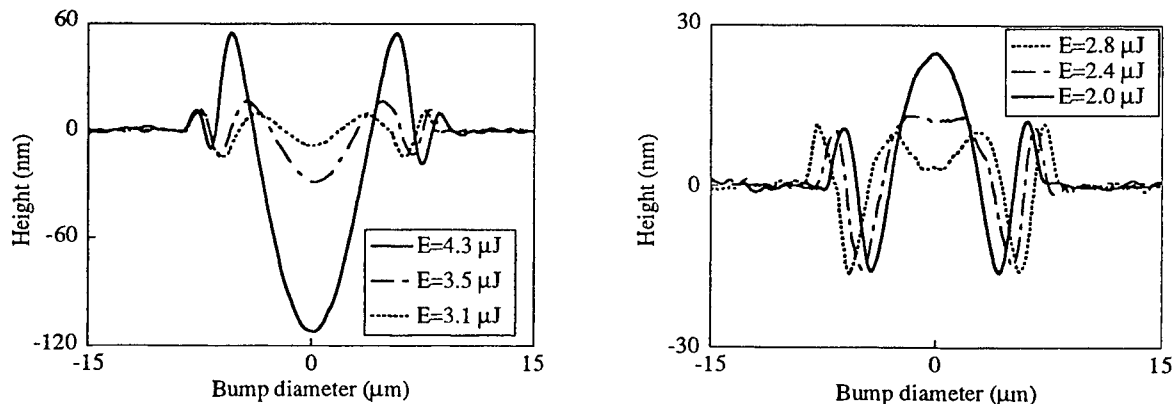


Fig. 2 Bump shape (cross section, measured by AFM) variation due to the incident heating beam energy change

3. EXPERIMENTAL RESULTS

The dependence of the bump shape (measured by AFM) on the incident energy of the IR heating beam is shown in Fig. 2. The diameter of the bumps is about $15\text{ }\mu\text{m}$, and the bump height varies from 50 nm to 10 nm . When the incident heating beam energy is $4.3\text{ }\mu\text{J}$, the bump has a deep crater at the center and a low peripheral rim. As the pulse energy decreases, the center of the crater starts to move up, forming shapes of "double ring" or "W". When the laser energy reaches $2.0\text{ }\mu\text{J}$, a rounded, smooth central bump is formed, which is called 'Sombrero' shape. At even lower laser intensity, the central dome shrinks and decreases in height to eventually disappear, forming a bowl type of bump.

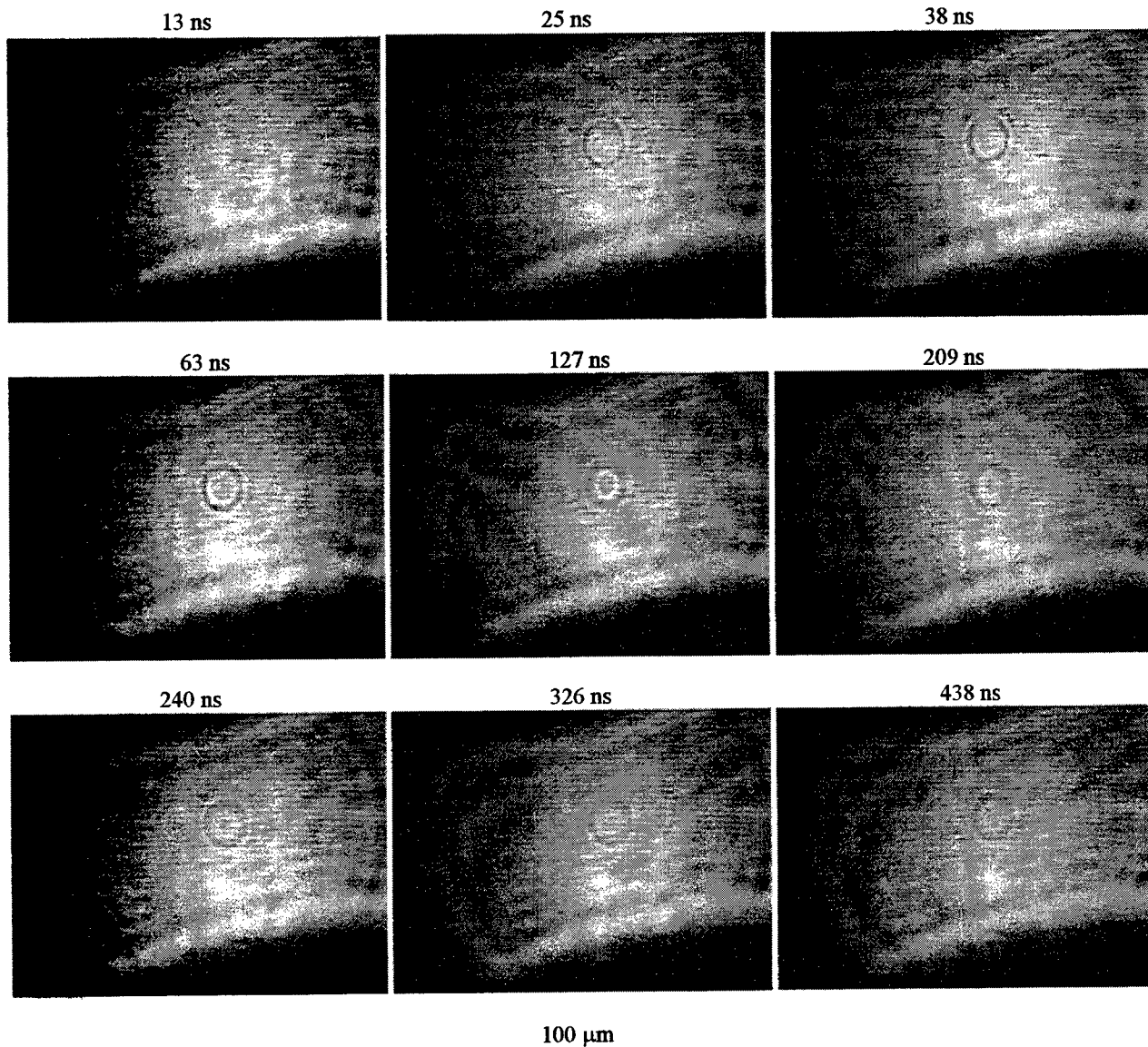


Fig. 3 A sequence of images of bumps at laser pulse energy of $3.3\text{ }\mu\text{J}$ produced by the LFP system

The visualization of the entire bump growth has been conducted for various pulse energies. As an example, Fig. 3 shows the sequence of images for the case with laser pulse energy equal to $3.3\text{ }\mu\text{J}$. A rim and a central hole become visible in the early stage, having formed right after melting. The melt pool expands and the hole diameter keeps increasing and

deepening until 127 ns. The photos from 127 ns to 438 ns show that there is some recovery at the central hole. After 438 ns, no change is discernible and the solidification process has concluded.

Thermal emission contribution to the images has been examined by blocking the dye laser illumination. No significant thermal emission image can be captured even at the pulse energy of 6 μ J. Therefore, images in Fig. 3 are mainly due to the reflection of the dye laser beam.

4. NUMERICAL MODELING

A numerical model, solving the finite difference form of the governing equations with the Highly Simplified Marker and Cell method, is conducted to study the surface deformation of materials under pulsed laser heating (Fig. 4). The incident laser power is assumed to have a Gaussian distribution in the radial direction and is absorbed in the region very close to the surface. The surface evolution is determined by solving the kinematically derived equation for height function.

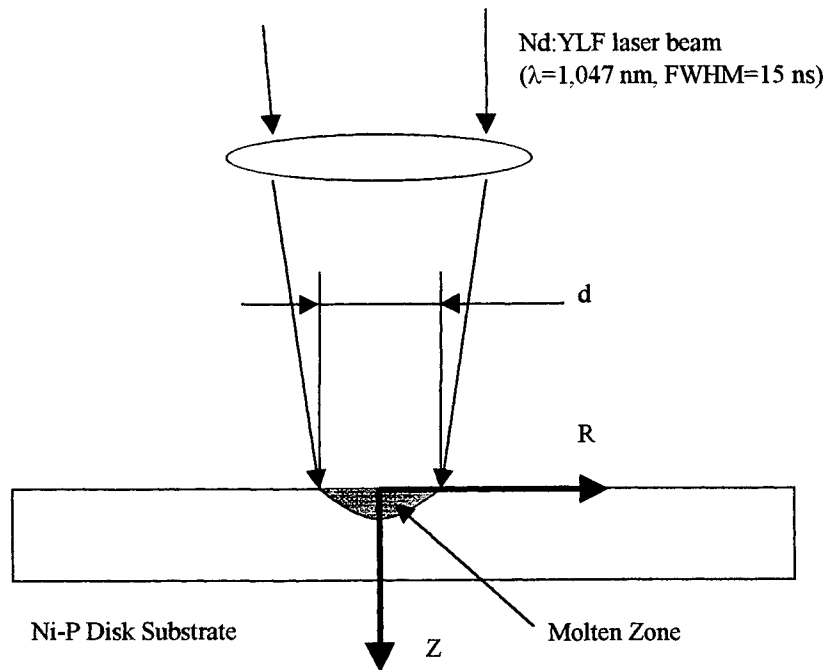


Fig. 4 A schematic representation of the pulsed laser melting system

The governing equations consist of the continuity equation, the momentum equations and the energy equation. Assuming two-dimensional flows, the system of equations in non-dimensional form in cylindrical system is stated as followings:

$$\frac{1}{R} \frac{\partial}{\partial R} (RU) + \frac{\partial W}{\partial Z} = 0 \quad (1)$$

$$\frac{\partial U}{\partial \tau} + U \frac{\partial U}{\partial R} + W \frac{\partial U}{\partial Z} = -\frac{\partial P}{\partial R} + P_r \left[\frac{\partial}{\partial R} \left(\frac{1}{R} \frac{\partial}{\partial R} (RU) \right) + \frac{\partial^2 U}{\partial Z^2} \right] \quad (2)$$

$$\frac{\partial U}{\partial \tau} + U \frac{\partial W}{\partial R} + W \frac{\partial W}{\partial Z} = -\frac{\partial P}{\partial Z} - P_r Ra T + P_r \left[\frac{1}{R} \frac{\partial}{\partial R} \left(R \frac{\partial W}{\partial R} \right) + \frac{\partial^2 W}{\partial Z^2} \right] \quad (3)$$

$$\frac{\partial T}{\partial \tau} + U \frac{\partial T}{\partial R} + W \frac{\partial T}{\partial Z} = A_1 \left[\frac{1}{R} \frac{\partial}{\partial R} \left(R \frac{\partial T}{\partial R} \right) + \frac{\partial^2 T}{\partial Z^2} \right] + A_2 Q_v \quad (4)$$

where W and U are dimensionless components of velocity in the axial and radial directions, Pr is the Prandtl number, τ is the dimensionless time, Ra is the Rayleigh number, $Q_v = q_v / q_0 = (1 - R_s) I(r, t) dA / dV / q_0$, R_s is the surface reflectivity, $A_1 = A_2 = 1$ in the molten zone, and $A_1 = a_s / a_m$, $A_2 = (a_s / a_m)(\lambda_m / \lambda_s)$ in the solid zone, a_s and a_m are thermal diffusivity of the solid and the melt while λ_m and λ_s are the thermal conductivity. The incident laser power intensity is assumed to be of Gaussian distribution:

$$I(r, t) = I_0(t) \frac{8}{\pi d^2} \exp \left(-\frac{8r^2}{d^2} \right), \quad (5)$$

where $I(r, t)$ is the laser intensity distribution, $I_0(t)$ is the total incident laser energy, d is the laser beam diameter.

The radial velocity and pressure boundary conditions in the molten zone are determined from the surface stress condition, and are given by the following equations:

$$\frac{\partial V_\tau}{\partial N} = -M_a \frac{\partial T}{\partial \tau} - \frac{\partial V_N}{\partial \tau} \quad (6)$$

$$P_{int} = P_m - P_g = 2P_r \frac{\partial V_N}{\partial N} - \frac{M_a P_r}{C_a(T)} \kappa \quad (7)$$

where V_τ and V_N are the tangential and normal velocities on the melt surface, M_a is the Marangoni number, C_a is the Capillary number, κ is the curvature, and P_{int} is the interface pressure. The axial velocity boundary condition on the molten zone is determined from the continuity equation. At the solid-liquid interface, U and W are zero. At the center ($R=0$), U and $\partial W / \partial R$ are zero.

It is assumed that all of the laser energy is absorbed on the surface, and that heat loss on the surface by radiation and convection is negligible. At the solid-liquid interface, the temperature is equal to the melting point of the material. At the gas-solid interface, the temperature of the side and bottom disk walls is equal to the ambient temperature, 300K. At the center ($R=0$), $\partial T / \partial R$ is zero.

Table 1 Thermophysical properties of Ni-P

Item	Physical properties	Units
Density	8000	[kg/m ³]
Viscosity	1×10^{-3}	[Pa·s]
Thermal conductivity	18.5	[W/(m·K)]
Specific heat	600	[J/kg·K]
Melting point	1200	[K]
Volumetric expansion coefficient	1.51×10^{-4}	[1/K]
Surface tension constants γ	-1.0×10^{-3}	[N/(m·K)]
σ_0	-0.7667	[N/m]
Reflectivity	0.65	[-]

The Highly Simplified Marker and Cell method is used to deal with the free surface deformation. The surface height is determined from:

$$\frac{\partial h}{\partial t} = W_s - U_s \frac{\partial^2 h}{\partial R^2} \quad (8)$$

where W_s and U_s are the axial and radial velocities on the surface.

The computational results are obtained for a thin Ni-P disk (P: 12% by weight) heated by a Nd:YLF laser ($\lambda=1,047$ nm). The physical properties of Ni-P are shown in Table 1.

Figure 5 shows the radial variation of the surface temperature for the laser pulse energy $E=3.3 \mu\text{J}$. The initial disk temperature is uniform at ambient temperature (300 K). The peak temperature is 3450K, which occurs at 30 ns. The transient velocity vectors are shown in Figure 6. The higher melt temperature results in lower surface tension near the center region. The gradient of the surface tension across the disk induces the melt to flow outward from the center. The resulting mass deficit near the center results in a crater with a downward velocity component. The melt flow turns upward when approaching the edge of the molten zone. Figure 7 shows the transient surface deformation. Significant surface movement begins at about 40 ns. The molten duration is about 150 ns, which is consistent with the experimental observation.

The laser energy dependence of peak surface temperature, molten duration, rim height, rim diameter and crater depth is shown in Figure 8. The numerical simulation helps to optimize the design of the LZT process, for instance, the choice of the laser peak heating time and diameter of the heating laser beam. A parametric study in Figure 9 shows the dependence of the bump rim height and crater depth on the heating laser beam diameter and the peak heating time.

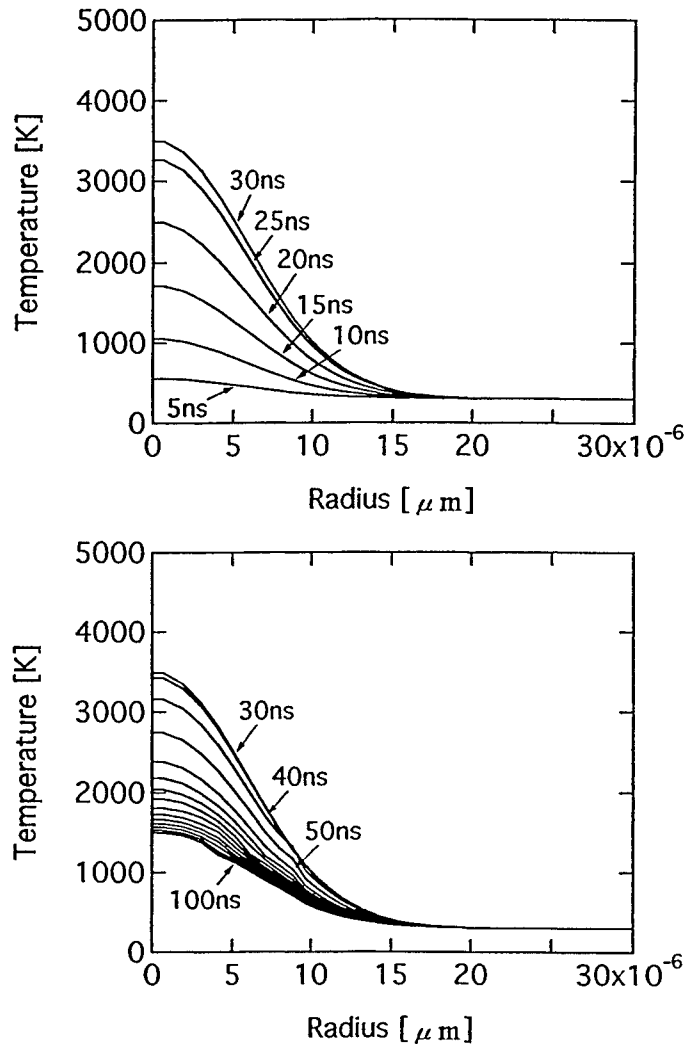


Fig. 5 Radial variation of the surface temperature at $E=3.3 \mu\text{J}$

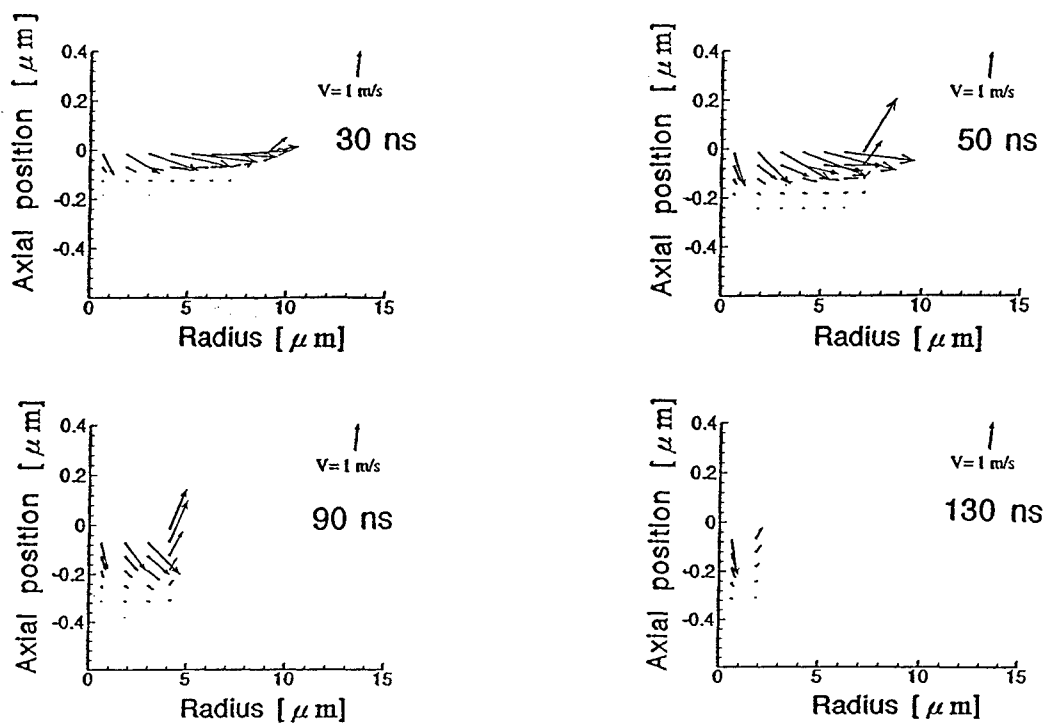


Fig. 6 The computed transient velocity vectors at $E=3.3 \mu\text{J}$

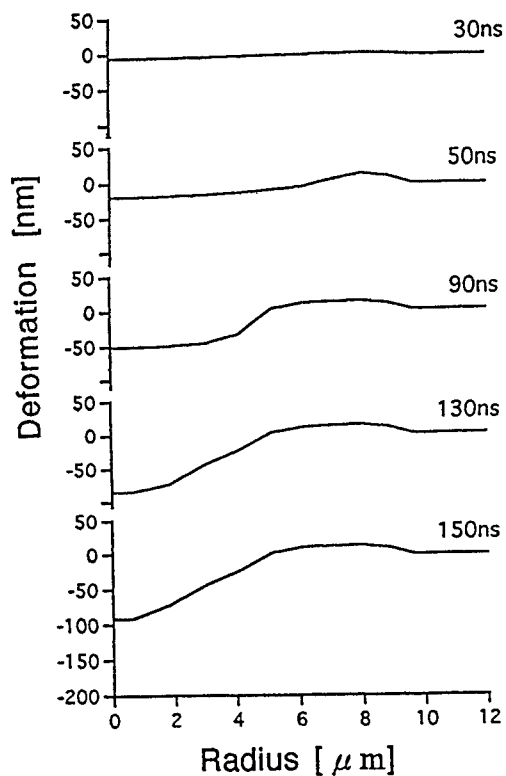


Fig. 7 The computed transient surface deformation at $E=3.3 \mu\text{J}$

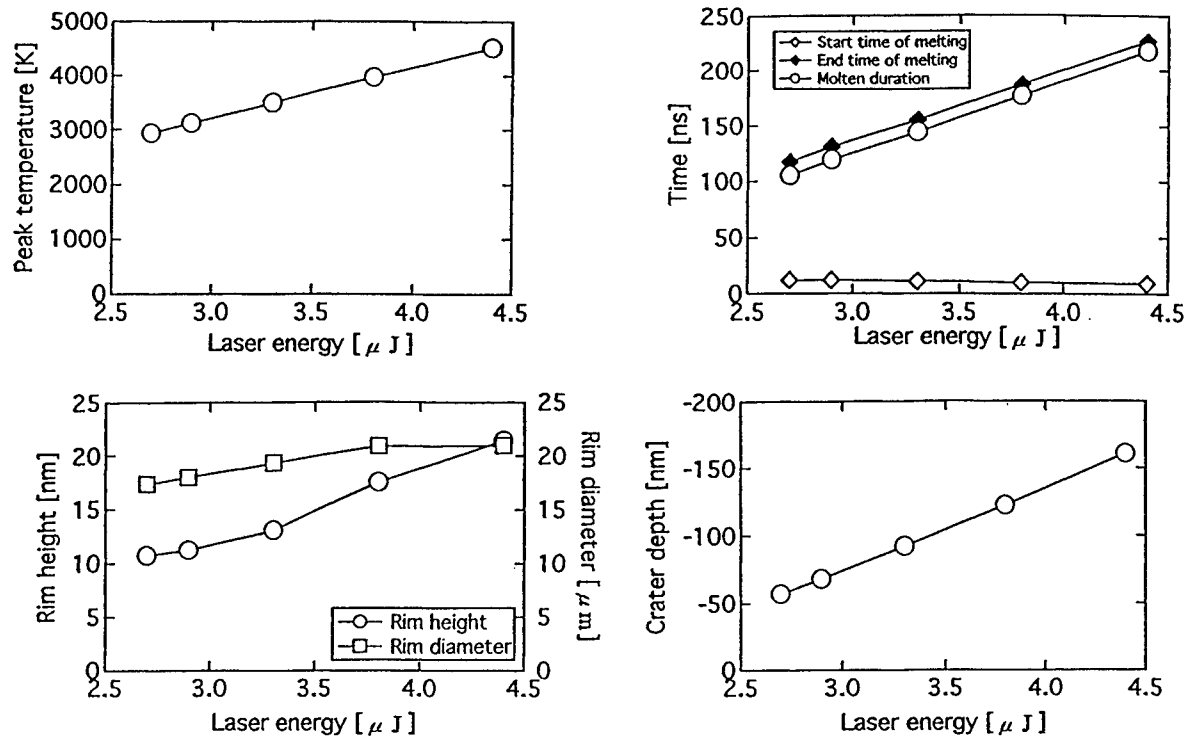


Fig. 8 The laser energy dependence of peak surface temperature, molten duration, rim height, diameter, and depth

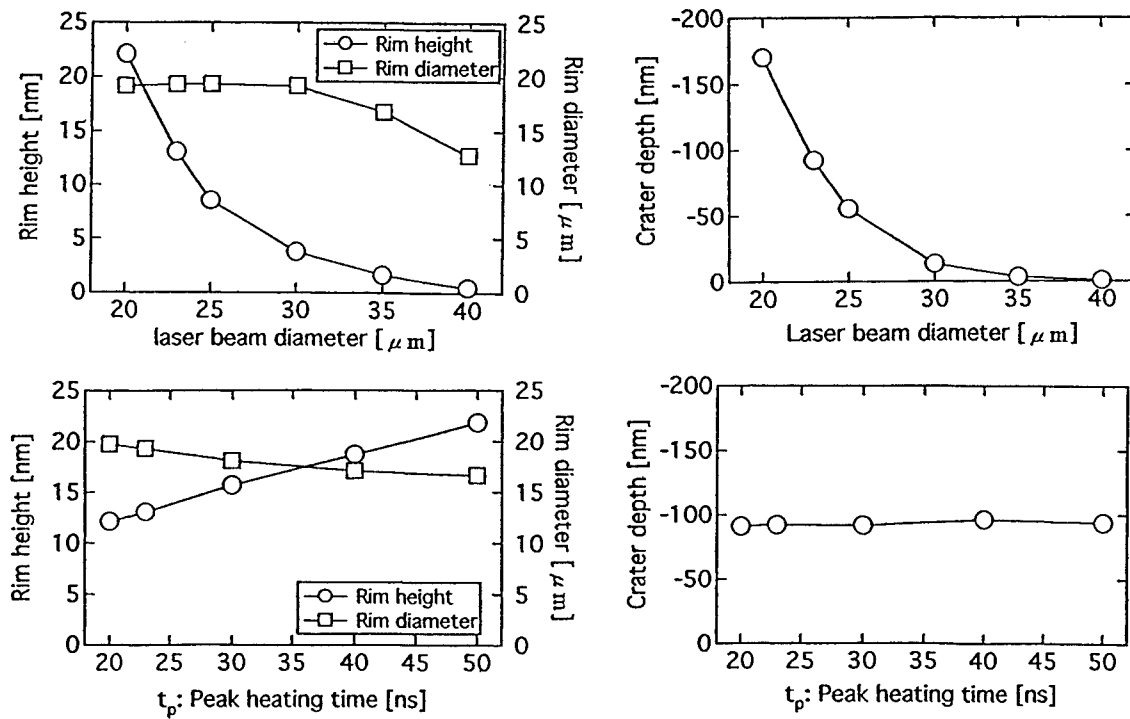


Fig. 9 The rim height and crater depth versus the laser beam diameter and the peak heating time at $E = 3.3 \mu\text{J}$

5. CONCLUDING REMARKS

The transient process of pulsed laser-induced melting and surface deformation in LZT process has been investigated experimentally and theoretically. The nanosecond-time-resolution laser flash photography system is able to visualize the transient melting, surface deformation, and resolidification process of the Ni-P disk substrates upon nanosecond laser heating. A numerical model has been developed to solve the energy transfer and fluid flow in a nanosecond timescale within several micrometers. Both the melting time and surface deformation predicted in the model are comparable to the experimental results.

ACKNOWLEDGEMENTS

This work was conducted at the Laser Thermal Laboratory of the University of California at Berkeley.

REFERENCES

1. R. Ranjan, D.N. Lambeth, M. Tromel, P. Goglia, Y. Li, "Laser texturing for low-flying-height media," *J. Appl. Phys.* **69**, pp. 5745-5747 (1991).
2. P. Baumgart, D.J. Krajnovich, T.A. Nguyen, and A.C. Tam, "A new laser texturing technique for high performance magnetic disk drives," *IEEE Trans. Mag.*, **31**, pp. 2946-2951 (1995).
3. T.D. Bennett, D.J. Krajnovich, C.P. Grigoropoulos, P. Baumgart, and A.C. Tam, "Marangoni mechanism in pulsed laser texturing of magnetic disk substrates," *J. Heat Transfer*, **119**, pp.589-593 (1997).
4. D. Kuo, J. Gui, B. Marchon, S. Lee, *et al.*, "Design of laser zone texture for low glide media," *IEEE Trans. Mag.*, **32** (5), pp. 3753-3758 (1996).
5. A.C. Tam, I.K. Pour, T.A. Nguyen, D.J. Krajnovich, and P. Baumgart, "Experimental and theoretical studies of bump formation during laser texturing of Ni-P disk substrates," *IEEE Trans. Mag.*, **32** (5), pp. 3771-3773 (1996).
6. D. Kim, and C.P. Grigoropoulos, "Phase-change phenomena and acoustic transient generation in the pulsed laser induced ablation of absorbing liquids," *Appl. Surf. Sci.*, **127-129**, pp. 53-58 (1998).
7. J. Jandeleit, P. Russbuldt, G. Urbasch, D. Hoffmann, and others, "Picosecond imaging of laser-induced ablation processes and production of microstructures by picosecond laser pulses," *Proc. of the SPIE*, **3092**, pp. 481-484 (1997).
8. D. A. Willis, X. Xu, C.C. Poon, A.C. Tam, " Laser-assisted surface modification of thin chromium films," *Optical Engineering*, **37** (3), pp. 1033-1041 (1998).
9. C.W. Hirt, B.D. Nichols, and N.C. Romero, "Sola - A numerical solution algorithm for transient fluid flow," Technical Report, Los Alamos Scientific Laboratory (1975).

Semiconductor laser array fabricated by Nd:YAG laser-induced quantum well intermixing

J.J. Dubowski, G. Marshall, Y. Feng, P.J. Poole, C. Lacelle, J.E. Haysom, S. Charbonneau and M. Buchanan

National Research Council of Canada, Ottawa, Ontario K1A 0R6, Canada

ABSTRACT

Selective area CW Nd:YAG laser annealing of GaInAsP/InP quantum well (QW) structures has been investigated as a possible route towards the fabrication of monolithically integrated photonic circuits. Laser irradiation of a 5 QW laser structure, originally designed to yield lasers emitting at 1.5 μm , yielded material having a continuously changing band-gap ranging from 1.5 to 1.38 μm over the distance of about 3 mm. Bars with arrays of broad area lasers, having lengths from 300 to 600 μm , were fabricated from the processed material. An individual bar (2 to 3 mm long) comprised lasers operating typically between 1.4 and 1.5 μm . The lasers showed stable threshold current density and quantum efficiency as function of the operating wavelength. This demonstration indicates that the applied technology has the potential to realize the cost-effective fabrication of advanced photonic devices and photonic integrated circuits.

Keywords: photonic integrated circuits, quantum well intermixing, laser processing

1. INTRODUCTION

Selective area post-growth processing of semiconductor heterostructures is the subject of intense investigations due to the potential of this approach in the fabrication of advanced devices and photonic integrated circuits (PIC). For quantum well (QW) microstructures, the spatially selective intermixing of the QW and barrier material, referred to as quantum well intermixing (QWI), has been suggested as a feasible route to this end. This approach has the potential to enable device engineers to realize monolithic integration of optical devices with different functions and properties on a common substrate.¹ The most frequently investigated methods of QWI include impurity induced intermixing, impurity-free vacancy diffusion and ion implantation induced QWI. There is also an increasing interest in QWI induced with powerful lasers (Laser-QWI). Lasers, such as KrF excimer ($\lambda = 248$ nm), Ar-ion ($\lambda = 514.5$ nm) and Nd:YAG ($\lambda = 1064$ nm) have been successfully applied for the purpose of demonstrating QWI in microstructures consisting of GaAs/AlGaAs,^{2,4} InP/GaInAs,^{5,6} GaInP/AlGaInP,⁷ and Si/SiGe.⁸ Since high-temperature annealing is the basis of any QWI technique, the choice of lasers as a heating source is highly attractive due to the ease with which a laser beam can be delivered to a well defined spot. Generally, the lateral resolution of Laser-QWI is expected to depend on the geometry of both the target microstructure and the laser beam used for processing. It has been claimed that this approach makes it possible to modify band-gap structure on a lateral scale better than 25 μm .⁵ Other results demonstrate the successful use of laser annealing for writing 100 μm -wide lines of QWI material in InP/GaInAs,⁶ lateral modulation of band levels with a 380-nm period in GaAs/AlGaAs,⁹ and writing 70 nm-diameter dots of p-doped GaAs/AlGaAs heterostructures.¹⁰ Fabrication of lasers blueshifted from 1.59 μm by up to 160 nm has been demonstrated following Nd:YAG laser annealing of InP/GaInAs QW microstructures.¹¹ Those results were illustrated with individual semiconductor lasers, each fabricated from a sample processed in a separate laser annealing experiment. The value of any technology investigated for manufacturing monolithically integrated devices

can only be assessed if it is used for demonstration of a truly integrated device. This issue has been addressed by our experiments. In this paper, we discuss results of the successful application of the Laser-QWI technology for the fabrication of a monolithically integrated array of lasers emitting between 1.5 and 1.4 μm .

2. EXPERIMENTAL DETAILS

The investigated sample, which was grown by chemical beam epitaxy, comprises 5 $\text{In}_{0.53}\text{Ga}_{0.47}\text{As}$ QWs (6 nm thick) separated by $\text{In}_{0.74}\text{Ga}_{0.26}\text{As}_{0.57}\text{P}_{0.43}$ barriers (20 nm thick), a confining layer of $\text{In}_{0.74}\text{Ga}_{0.26}\text{As}_{0.57}\text{P}_{0.43}$ (70 nm thick), a cladding layer of InP (1.59 μm thick), a contact layer of $\text{In}_{0.53}\text{Ga}_{0.47}\text{As}$ (0.2 μm thick), and an InP cap (0.2 μm thick). The composition of QWs was chosen to have the as-grown material suitable for the fabrication of lasers operating at room-temperature at the wavelength of 1.5 μm . Other details concerning the sample structure are given in Table 1.

Table 1. Parameters of QW semiconductor laser structure used for the fabrication of monolithically integrated arrays of lasers.

Sample	Substrate	Buffer	Well	Barrier/Confining	Cladding	Cap
98029	(001)InP S-doped	InP $\text{Si:}6 \times 10^{17}$ 0.6 μm thick	$\text{In}_{0.53}\text{Ga}_{0.47}\text{As}$ undoped	$\text{In}_{0.74}\text{Ga}_{0.26}\text{As}_{0.57}\text{P}_{0.43}$ undoped	InP $\text{Be:}1 \times 10^{18}$	InGaAs $\text{Be:}1 \times 10^{19}$

The surface of a rectangular sample, approximately 15 x 6 mm, used in this experiment was coated with a 200 nm thick layer of SiO_2 to protect it from decomposition (desorption) during laser irradiation.

The annealing was carried out with a CW Nd:YAG laser (Quantronix 116) operating at the wavelength of 1064 nm. The near-Gaussian laser beam, 0.8 mm in diameter, was shaped with the use of an optical expander to give a 10 mm in diameter spot on the sample. The surface temperature induced with the laser power density of 0.5 W/mm^2 was about 800 $^\circ\text{C}$ and the annealing time was 120 sec. Sample temperature was monitored with an infrared pyrometer (Mikron Instrumentes M680) using a focussing lens, which gave an estimated 2 mm diameter detection area.

The extent of QWI was measured with a FTIR-based room-temperature PL mapping system. A CW Nd:YAG operating at 1064 nm was focus on the sample to spot with a diameter of ~ 0.25 mm, with a power density of ~ 0.15 W/mm^2 . Sample luminescence was analysed using an FTIR spectrometer with an InGaAs detector. The sample was placed on a computer-controlled x-y stage, which was moved in 0.5 mm steps, such that one PL spectrum was acquired for each 0.5 mm square of the 15 x 6 mm sample. The computer software then analysed each spectrum and created a 2-dimensional map for peak wavelength as a function of x-y position (the software was also capable of analysing multiple peaks, as well as creating maps of peak intensity, FWHM of a peak and other useful spectral information).

The fabrication of an array of broad area lasers started with metalization (Ti 25 nm /Pt 55 nm /Au 300 nm) of p-type contact stripes with widths, w, ranging from 40 μm to 200 μm . The sample was thinned

and polished to about 100 μm thick, and a n-type metal (Ni 25 nm / Ge 55 nm / Au 80 nm) was then deposited at the back side of the sample. A rapid thermal annealing at 350 $^{\circ}\text{C}$ for 30 seconds was carried out to ensure good ohmic contact on both top and bottom surfaces. Finally the sample was cleaved into laser bars with cavity lengths ranging from 300 μm to 600 μm .

The lasers were characterized using a 1 kHz current source that could operate at bias voltages up to 50 volts. The laser light output was detected by a InGaAs photodiode, the signal from which was input into a boxcar integrator. In the second configuration that was dedicated for spectral measurements, a fiber tip was positioned close to the laser aperture and captured light pulses were transmitted to a high-resolution spectrometer with lock-in amplifier detection.

3. RESULTS AND DISCUSSION

QWI is a strong function of local temperature since it is a thermally activated diffusion process. Following laser irradiation, PL mapping measurements showed that the central area of the sample, 5 mm along the longer axis and its entire 6 mm width, displayed varying degree of band-gap shifting. The band-gap of the intermixed material gradually changed over a distance of 2.5 mm along the longer axis of the sample from 1380 nm, in the center of the laser annealed zone, to about 1500 nm, the latter of which compares to the band-gap of the as-grown material. A moderate temperature gradient applied in this experiment was necessary for the preparation of a sufficient area of material to be used for the fabrication of the integrated laser arrays.

A separate experiment indicated that no band-gap shifting for similar QW microstructures takes place at 720 $^{\circ}\text{C}$ and annealing times of ~ 60 sec. This suggests that in the current experiment, material at distances greater than 2.5 mm from the center of the laser annealed zone (along the longer axis of the sample) was at temperature of less than ~ 700 $^{\circ}\text{C}$. It should be noted that background wafer heating, in addition to the laser beam shaping approach, offers increased control over laser-induced temperatures. If needed, more moderate temperature gradients could easily be obtained with this technique. A distribution of the wafer area as a function of the material band-gap, determined by the PL signal corresponding to QW, is shown in Fig. 1. It illustrates that the QWI material, characterized by $1380 \leq L_g < 1480$ nm, constitutes about 39% of the wafer area. The result also indicates that in this particular case $1490 \leq L_g \leq 1510$ nm characterizes most of the as-grown material.

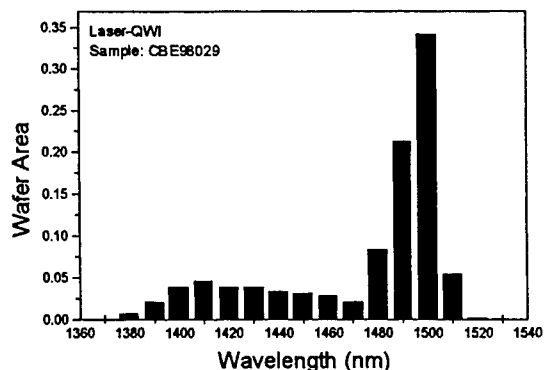


FIG. 1. *Distribution of the wafer area as a function of the material band-gap following Nd:YAG laser irradiation.*

Several bars of broad area lasers operating between 1400 and 1500 nm were fabricated from this material. Figure 2a shows the location of a series of lasers on the 500 μm cavity length bar. As an illustration, normalized spectra of 4 lasers from this bar are shown in Figure 2b. The spectrum from laser A corresponds to as-grown material ($\lambda_{\text{max}} = 1498 \text{ nm}$, $w = 100 \mu\text{m}$), while spectra B ($\lambda_{\text{max}} = 1476 \text{ nm}$, $w = 40 \mu\text{m}$), C ($\lambda_{\text{max}} = 1440 \text{ nm}$, $w = 60 \mu\text{m}$) and D ($\lambda_{\text{max}} = 1405 \text{ nm}$, $w = 40 \mu\text{m}$) were obtained from the QWI

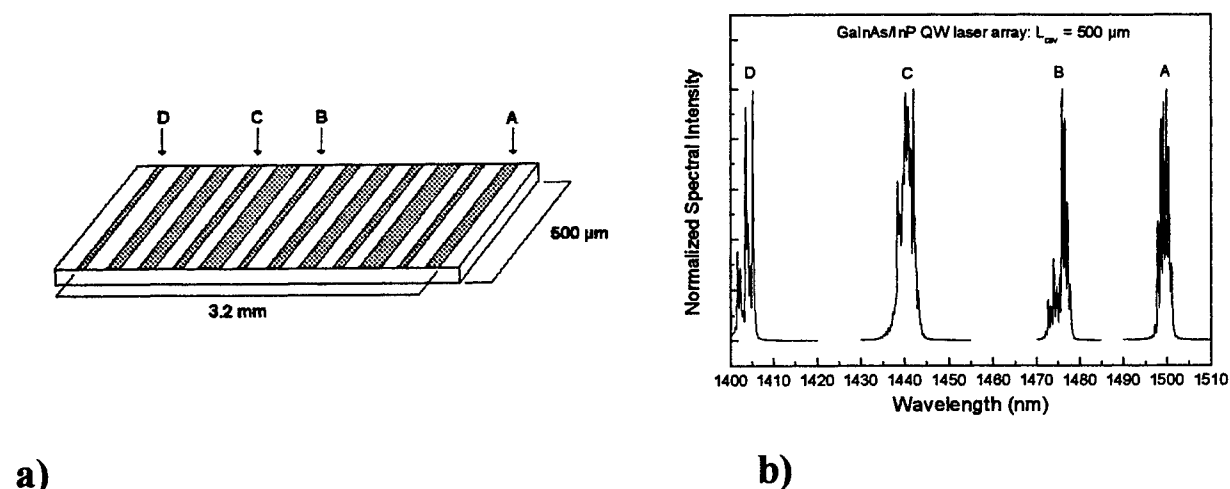


FIG. 2. A schematic drawing illustrating positions of broad area 500 μm cavity lasers on a 3.2 mm long bar (a), and corresponding emission spectra for the indicated lasers (b).

material. Lasers B to D are located at distances of 1.9, 2.4 and 3.2 mm from the laser A. In addition, an example of a bar with 400 μm cavity lasers is shown in Figure 3a. Spectra characteristic of the lasers indicated in this figure are shown in Figure 3b. Spectrum from laser A ($w = 60 \mu\text{m}$) exhibits maximum emission at $\lambda_{\text{max}} = 1494 \text{ nm}$. Other lasers located to the right from A (not shown in Fig. 3a) were characterized by $\lambda_{\text{max}} \approx 1496\text{--}1498 \text{ nm}$, which is close to the expected value for such lasers made from the

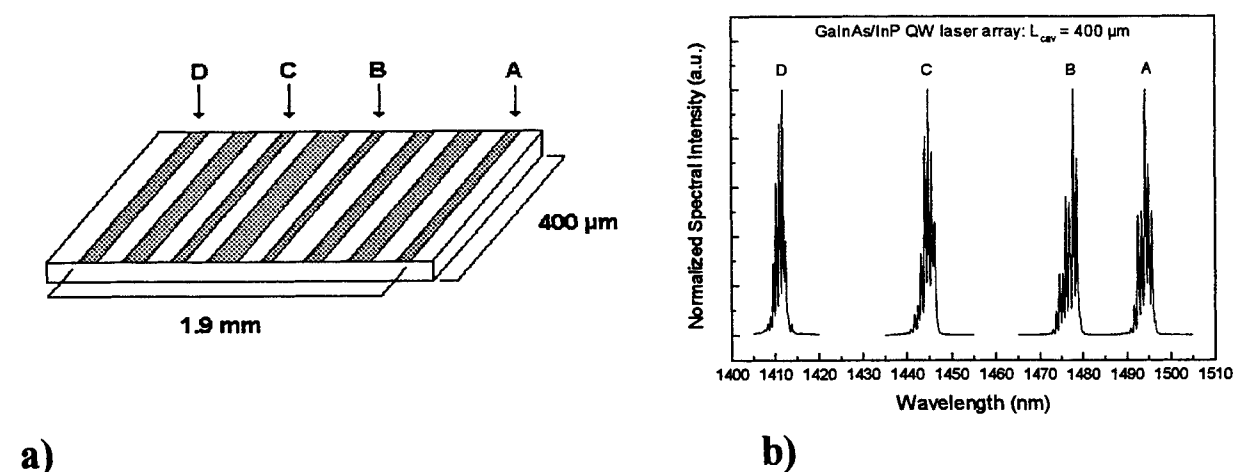


FIG. 3. A schematic drawing illustrating positions of broad area 400 μm cavity lasers on a 1.9 mm long bar (a), and corresponding emission spectra for the indicated lasers (b).

as-grown material. Spectra B ($\lambda_{\text{max}} = 1478 \text{ nm}$, $w = 40 \text{ }\mu\text{m}$), C ($\lambda_{\text{max}} = 1445 \text{ nm}$, $w = 60 \text{ }\mu\text{m}$) and D ($\lambda_{\text{max}} = 1412 \text{ nm}$, $w = 100 \text{ }\mu\text{m}$) were obtained at distances of 0.8, 1.4 and 1.9 mm to the left from the laser A. Similar results, with lasers emitting between 1.5 and 1.40 μm , were obtained for 300 and 600 μm cavity length bars. Typically, the laser emission spectra were 6 nm wide irrespective of the blueshift. An example of the laser emission spectrum obtained for the as-grown material is shown in Figure 4.

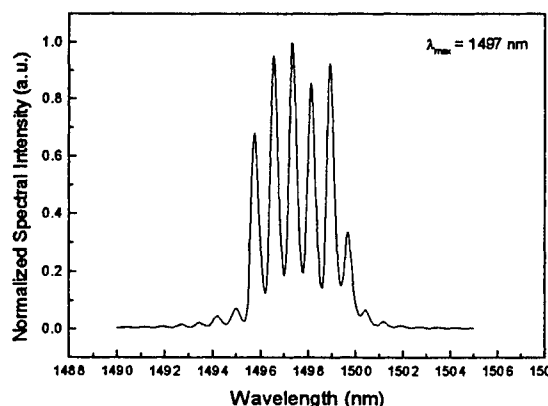


FIG. 4. Emission spectrum for a broad area laser ($L_{\text{cav}} = 400 \text{ }\mu\text{m}$, $w = 100 \text{ }\mu\text{m}$) fabricated from as-grown material.

An investigation of the threshold current density, J_{th} , and quantum efficiency for the fabricated lasers (about 40 lasers were tested) was carried out to provide a more qualitative analysis. The analysis was made based on the results limited to the lasers with lowest threshold current values and highest quantum efficiencies. After this qualification process we were left with several lasers that operated in the range of $1400 < \lambda \leq 1500 \text{ nm}$ for each cavity length. The laser quantum efficiency was found to be constant, and equal to about 0.33. For 300, 400 and 500 μm cavity lasers the threshold current density increased by 11-13 % for lasers operating at $\lambda_{\text{max}} \sim 1400 \text{ nm}$. The initial values of J_{th} corresponded respectively to 1970, 1550 and 1330 A/cm^2 . Given the uncertainty of these measurements, it is difficult to conclude if the increase in the threshold current concerns all the lasers fabricated from the QWI material, or only those made from the most blueshifted material. Although it could only be qualitatively assessed, it is worth of mentioning that for comparable bias conditions the spectra of lasers obtained from the material shifted up to 60 nm did not show any measurable differences in their intensity. However, the most blueshifted ($\lambda_{\text{max}} \sim 1400 \text{ nm}$) lasers showed reduced emission intensity to about 50-30 % of the intensity characteristic of the lasers made from the as-grown material. Below 1400 nm, lasers were observed to emit semi-coherent light exhibiting weak mode structure over roughly a 20 nm band width. It seems reasonable to expect some increase in the threshold current density of a QW laser made from the QWI material, mainly due to the well shape changing and resulting reduced confinement of the electrons/holes. Reported earlier results⁶ showed a 20% increase in J_{th} (from 500 A/cm^2) for lasers blueshifted by 141 nm from 1585 nm. For a 1263 nm laser, made from the 30 nm blueshifted material (made by ion-implantation induced QWI), the predicted device lifetime was reported to be in excess of 25 years.¹² Lasers that were made from more blueshifted material, exhibited higher degradation rates and shorter lifetimes. The increased functionality and/or reduced manufacturing costs of an integrated circuit are key issues addressed by the QWI technology. Clearly, it remains to be shown what would be the maximum allowable blueshift, for a particular material system, without compromising the performance of integrated devices made from such material.

An increase in threshold current from 1100 to 2200 A/cm^2 was observed for the 600 μm cavity laser blueshifted to $\lambda_{\text{max}} \approx 1410 \text{ nm}$. Non-uniformity of as-grown material and/or surmountable but currently present limitations in controlling the temperature gradient along the short axis of the sample,

which coincided with the direction of laser cavities, are feasible reasons behind such behavior. Those issues should easily be addressable at the more advanced stages of introducing the Laser-QWI technology for practical applications.

The Laser-QWI approach offers the possibility of fabricating QWI material with continuously changing band-gap (~ 1 nm blueshift per $15\ \mu\text{m}$ of lateral distance) along one direction. This feature, which seems to be unique to Laser-QWI can find applications in, e.g., the fabrication of broad-spectrum light-emitting diodes. Of particular relevance to manufacturing PICs is that the slow continuous grading of the QW band-gap (e.g., $36\ \text{nm}$ across a region of $550\ \mu\text{m}$ as it can be seen in Fig. 2) would make it possible to chose, by purely geometrical means, any wavelength of a laser in that spectral range. It could also be used to produce a dense array of ridge lasers ($w < 5\ \mu\text{m}$) with wavelengths covering the full range in a single bar. The usefulness of such a device for DWM applications has yet to be demonstrated: its success will mostly depend on the ability to fabricate different pitch gratings within small areas.

4. CONCLUSIONS

- A Nd:YAG laser-induced quantum well intermixing approach was investigated for selective modification of the band-gap of semiconductor quantum well laser structures. A small portion of as-grown GaInAsP/InP material, which was designed to yield lasers emitting at $1.5\ \mu\text{m}$, was successfully intermixed into a material with a uniaxial band-gap gradient of about $1\ \text{nm}$ wavelength per $15\ \mu\text{m}$ distance.
- Broad area lasers were fabricated on four bars, each 300 to $600\ \mu\text{m}$ wide and 2 - $3\ \text{mm}$ long, from the laser-processed material. Each bar comprised a series of lasers operating between 1.5 and $1.4\ \mu\text{m}$. To the best of our knowledge, this is the first demonstration of a successful use of the laser-induced quantum well intermixing process for manufacturing of a single device consisting of monolithically integrated multi-wavelength semiconductor lasers.
- The analysis revealed that the laser threshold current for 300 , 400 and $500\ \mu\text{m}$ cavity lasers increased by 11 - $13\ \%$ for the most blueshifted ($\lambda_{\text{max}} \approx 1410\ \text{nm}$) lasers. However, a $100\ \%$ increase in the threshold current density, from 1100 to $2200\ \text{A}/\text{cm}^2$, was observed for the $600\ \mu\text{m}$ cavity laser operating at near $1410\ \text{nm}$. The increase of J_{th} for the longer cavity laser may be an indication of non-uniform properties of material along the cavity of the device.
- It remains to be shown what would be the maximum allowable blueshift, for a particular material system, without compromising the performance of integrated devices made from such material.
- Laser-QWI offers a possibility to fabricate QWI material with its band-gap continuously changing along one direction. This feature appears to be unique to Laser-QWI. It can find applications in, e.g., the fabrication of broad-spectrum light-emitting diodes.
- It is suggested that the investigated Laser-QWI technology could be applied for the manufacturing of densely packed arrays of multiwavelength ridge waveguide lasers at a rate of approximately 100 lasers per $1\ \text{mm}$ long bar. Each laser would operate at a fixed wavelength from the spectral range available within the bar. The usefulness of such an array of lasers for DWM applications has yet to be demonstrated, as it will depend mostly on the ability to fabricate different pitch gratings within small areas.

- The ability to address individual semiconductor lasers, as well as laser facets, with a Nd:YAG laser has the potential application for fine tuning of the lasers optical properties (an analog to, e.g., laser trimming of resistors applied in microelectronics).

REFERENCES

1. E. Herbert Li, editor, "Selected papers on quantum well intermixing", SPIE milestones series, Vol. MS 145 (1998).
2. J. Ralston, A.L. Moretti, R.K. Jain and F.A. Chambers, *Appl. Phys. Lett.* **50**, 1817 (1987).
3. J.E. Epler, R.L. Thornton and T.L. Paoli, *Appl. Phys. Lett.* **52**, 1371 (1988).
4. B.S. Ooi, C.J. Hamilton, K. McIlvaney, A.C. Bryce, R.M. De La Rue and J.H. Marsh, *IEEE Photonics Technol. Lett.* **9**, 587 (1997).
5. J.H. Marsh, A.C. Bryce, R.M. De La Rue, C.J. McLean, A. McKee and G. Lullo, *Appl. Surf. Sci.* **106**, 326-334 (1996).
6. J.J. Dubowski, S. Charbonneau, P.J. Poole, A.P. Roth, C. Lacelle and M. Buchanan, *Proc. SPIE*, vol. **3274**, 53-59 (1998).
7. C.J. Hamilton, O.P. Kowalski, K. McIlvaney, A.C. Bryce, J.H. Marsh, C.C. Button, *Electronics Lett.* **34**, 665 (1998).
8. J.J. Dubowski, N. Rowell, G.C. Aers, H. Lafontaine and D.C. Houghton, *Appl. Phys. Lett.* **74**, 1948 (1999).
9. M.K. Kelly, C.E. Nebel, M. Stutzman and G. Böhm, *Appl. Phys. Lett.* **68**, 1984 (1966).
10. P. Baumgartner, W. Wegscheider, M. Bichler, G. Schedelbeck, R. Neumann and G. Abstreiter, *Appl. Phys. Lett.* **70**, 2135 (1997).
11. McKee, C. J. McLean, A. C. Bryce, R. M. De La Rue, J. H. Marsh and C. Button, *Appl. Phys. Lett.* **65**, 2263 (1994).
12. J.-P. Noël, D. Melville, T. Jones, F.R. Shepherd, C.J. Miner, N. Puetz, K. Fox, P.J. Poole, Y. Feng, E.S. Koteles, S. Charbonneau, R.D. Goldberg and I.V. Mitchell, *Appl. Phys. Lett.* **69**, 3516 (1996).

Thermal and optical properties of semitransparent ceramics: laser induced high temperature modifications

O. G. Tsarkova^{*a}, S. V. Garnov^a, V. I. Konov^a, E. N. Lubnin^a, F. Dausinger^b

^aGeneral Physics Institute of Russian Academy of Sciences, Vavilov 38, Moscow, 117942, Russia

^bInstitut für Strahlwerkzeuge, Pfaffenwaldring 43, 70569 Stuttgart, Germany

ABSTRACT.

The laser combined express technique has been applied to high temperature ($T \leq 3000$ °C) measurements optical (reflectivity, transmission, absorptivity, volume absorptivity) and thermal (heat capacity, temperature conductivity and heat conductivity) properties of different ceramics (AlN, Si₃N₄, SiC, Al₂O₃). It was found that the ambient atmosphere (neutral, oxidizing or reduced pressure) noticeably affects the physical properties of the heated ceramics that marks a noticeable structural and chemical modification of the material.

Keywords: reflectivity, transmission, absorptivity, heat capacity, temperature conductivity, heat conductivity, high temperatures, CW Nd:YAG laser heating

1. INTRODUCTION.

Due to the unique resistance to high temperatures (thousands of degrees) and harsh environmental conditions, ceramics are widely used in modern technologies. Therefore, it is quite important to know how the intrinsic physical properties of the ceramics vary with temperature and how the thermal action in conjunction with aggressive ambient atmosphere influences the structure and chemical composition of the materials. Besides, being very hard stuff, ceramics are usually processed with "thermal" tools, e.g. with different pulsed or CW lasers. Hence, the information on optical (e.g. absorption coefficient, reflection coefficient) and thermal (e.g. heat capacity, heat conductivity) properties is the clue point in the development of laser processing technologies.

Meanwhile, there are quite limited and fragmentary data on physical properties of the ceramics at high temperatures. Moreover, as a rule, there is no information at all concerning newly made ceramic materials. Basically, this lack of information is explained by the essential experimental difficulties arisen at extremely high temperature measurements when the conventional methods either do not provide the reasonable accuracy or can not be applied at all.

Therefore, the development of the relevant methods and techniques permitting such measurements is a very important task.

2. EXPERIMENTAL SET-UP.

We present here a laser based express technique and results of investigations of optical and thermal properties of semitransparent scattering solids - ceramics - heated by an intense laser radiation to high temperatures (up to melting/sublimation points) in the presence of different ambient atmospheres: argon, air at 1 atm and 0.5 Torr pressure.

The designed set-up for high speed (10^3 – 10^4 K/s), high temperature measurements (800 °C–3000 °C) allowed us to record simultaneously reflectivity R_λ , transmission J_λ and absorptivity A_λ as a function of surface temperature T , so as their heat capacity C_p , temperature conductivity a and heat conductivity χ . Namely the simultaneous measurements of the physical parameters of the materials provide valid and reliable data obtaining and its unambiguous interpretation.

A principal scheme of the experimental set-up is shown at Fig.1. CW Nd:YAG laser operated at 1064 nm wavelength with the output power up to 100 Watt is applied to heat the tested specimens. The same laser radiation is used also as a probing beam, i.e. the reflection and transmission of the same high power laser beam were recorded during the heating processes.

The diameter of multimode top-flat laser beam onto a target surface was about 5 mm. The tested specimens (5 mm in diameter and 100-500 μm in thickness, depending on the particular task) were placed into the integrating sphere (for reflectivity measurements). The integrating device designed for transmission measurements is mounted exactly under the specimen. Because the tested ceramics are the high-melting-point materials, tungsten wires were applied for the samples fixing.

The measurements of temperature were performed with the optical pyrometer.
A computer acquisition/processing system was used for data control.

3. STRUCTURAL AND CHEMICAL MODIFICATION OF THE CERAMICS.

A wide variety of different ceramics (AlN , Si_3N_4 , SiC , Al_2O_3) and CVD diamond films [1] have been tested. For majority of ceramics the ambient atmosphere (neutral, oxidizing or reduced pressure atmosphere) strongly affects the optical properties of the heated ceramics that marks a noticeable structural and chemical modification of the material (mainly the specimen surface, but also its bulk). As an example, Fig.2 demonstrates the temperature/chemical induced modifications of the AlN ceramics in "specific points" of its reflectivity temperature curve.

At the analysis of the dependences one should pay attention on the variations of the chemical composition of irradiated surfaces. We undertook an elementary analysis of AlN ceramic using a method of X-ray-electron spectroscopy allowing to record spatial-energy distribution of electrons being emitted from a surface under X-ray irradiation. The obtained electron spectra provide one with information on: an element presence; its concentration and its chemical form. It allows fairly sensitive and informative diagnostic of tested objects.

Four main elements composing the AlN ceramic have been traced - Aluminum (Al), Nitrogen (N), Oxygen (O) and Yttrium (Y). The point #1 at the plot exhibits the non-irradiated surface. The subsequent heating to about 1600-1700 $^\circ\text{C}$ (point #2) leads to a noticeable change of element concentration. Thus, Y contamination increased in ten times, so as N decreased by an order of magnitude. As to aluminum, its atomic concentration was changed and the chemical form was modified. Instead of being bounded with N it became bounded with oxygen in the form of aluminum oxide. The heating to the temperature close to (point #3) and equal to the melting point (point #4) led to further noticeable increase in Y concentration (in times) and also caused essential nitrogen contamination growth.

4. EXPERIMENT.

4.1. Method of the heat capacity determination.

The proposed optical method of heat capacity $C_p(T)$ measurements consists in recording the target temperature behavior, when the heating laser radiation is periodically turned on and off, so that the target starts to be repeatedly heated and cooled (look at Fig.3). The slope of the corresponded temperature curve (growth /fall) depends on: i) the laser power $P(t)$, ii) the thermal energy accumulated in a specimen body (that is proportional to the C_p and the mass) and iii) the total value of heat losses.

To evaluate the heat capacity $C_p(T)$ one need to measure the slopes of the temperature curve at "heating" and "cooling" periods just before and just after the laser radiation is blocked and to use the following relationship:

$$m C_p(T) [(dT/dt)_{\text{heat}} - (dT/dt)_{\text{cool}}] = [1 - R_\lambda(T, t) - J_\lambda(T, t)] P(t). \quad (1)$$

Here, $(dT/dt)_{\text{heat}}$ is the slope of the temperature curve, when both heating and cooling processes take place; $(dT/dt)_{\text{cool}}$ is the slope, when only cooling occurs.

The estimated accuracy of $C_p(T)$ determination in our experiments was about 5-10%.

More detailed description of the heat capacity determination is presented in reference [2].

4.2. Results of heat capacity and optical properties measurements for SiC ceramics in different atmospheres.

As is seen, both the temperature and the oxidizing ambient atmosphere can influence optical and thermal properties even for such resistant material as SiC (Figs.4-5). Chemical and structural modifications of surface layers result in heat capacity decreasing of the whole specimen.

It is interesting to note that the reducing of the ambient gas pressure from 1 atm to 0.5 Torr causes the temperature shift of the phase transition (see the typical peak at the C_p curve) associated with material melting in according with the Klaproune-Klasius law:

$$dT/dP = T \cdot (\Delta V / \Delta H), \quad (2)$$

where T and ΔH are, respectively, the temperature and the heat of phase transition; ΔV - the change of substance volume at the transition; P - the pressure.

4.3. Method of the temperature conductivity and the heat conductivity determination.

We propose also optical method of temperature conductivity and heat conductivity measurements (Fig.6). It is based on the recording the temperature respond onto the back surface. Indeed, just after the beam is blocked, the temperature of the back surface of a "thick" target continues to increase because of heat flowing through the sample (heat conductivity); reaches the maximum and only after that begin to fall due to the heat losses. The time interval Δt between the moment of blocking of the laser beam and the temperature reaching the maximum, depends on i) the temperature conductivity $a(T)$; ii) the specimen thickness x ; and iii) the heat (radiation) losses L as:

$$\Delta t = f(L) \cdot x^2 / a(T), \quad (3)$$

where, $f(L)$ is a function of heat losses and geometrical parameters of the target. Taking into account that in our experiments the temperature gradient along the sample thickness is quite small (specimens are still thermally and geometrically thin) and the heat losses are linearly dependent on time within the short "cooling" interval, we can evaluate $f(L)$ within the whole range of the experimental parameters and to determine the temperature conductivity $a(T)$.

Besides, we can determine the heat conductivity χ :

$$\chi(T) = a(T) \cdot C_p(T) \cdot \rho, \quad (4)$$

where ρ is the density.

Fig.7 demonstrates a heat conductivity decrease about 4 times in the range from 1200 °C to 2000 °C.

5. CONCLUSIONS.

1. We presented the optical combined express method for investigation of optical (reflectivity $R(T)$, transmission $J(T)$ and absorptivity $A(T)$) and thermal (heat capacity $C_p(T)$, temperature conductivity $a(T)$ and heat conductivity $\chi(T)$) properties of ceramics at high temperatures. The advantages of the applied method are:

- simultaneous detection of optical and thermal properties of materials;
 - broad range of investigated temperatures (up to 2500°C);
 - convenience in the data obtaining;
 - high temporal resolution (0.5 microsecond).
2. Optical and thermal properties of ceramics (AlN, Si₃N₄, SiC, Al₂O₃) have been investigated.

3. It was shown that the ambient atmosphere (neutral, oxidizing or reduced pressure) noticeably affects the physical properties of the heated ceramics that marks a considerable structural and chemical modification of the material.

6. REFERENCES.

1. Konov, S.V. Garnov, O.G. Tsarkova, E.D. Obratsova, E.N. Lubnin, and F. Dausinger, "Laser measurements of optical and thermal properties of CVD diamond at high temperatures", *Proc. SPIE*, **3484**, pp. 230-240, 1999.
2. Garnov, V.I. Konov, A.S. Silenok, O.G. Tsarkova, V.N. Tokarev, and F. Dausinger "Experimental study of temperature dependence of reflectivity and heat capacity of steels and alloys at continuous wave by Nd:YAG laser heating", *Proc. SPIE*, **3093**, pp.160-175, 1997.

* Correspondence: Email: olga@kapella.gpi.ru; Telephone: 007 095 132 8146; Fax: 007 095 135 0270.

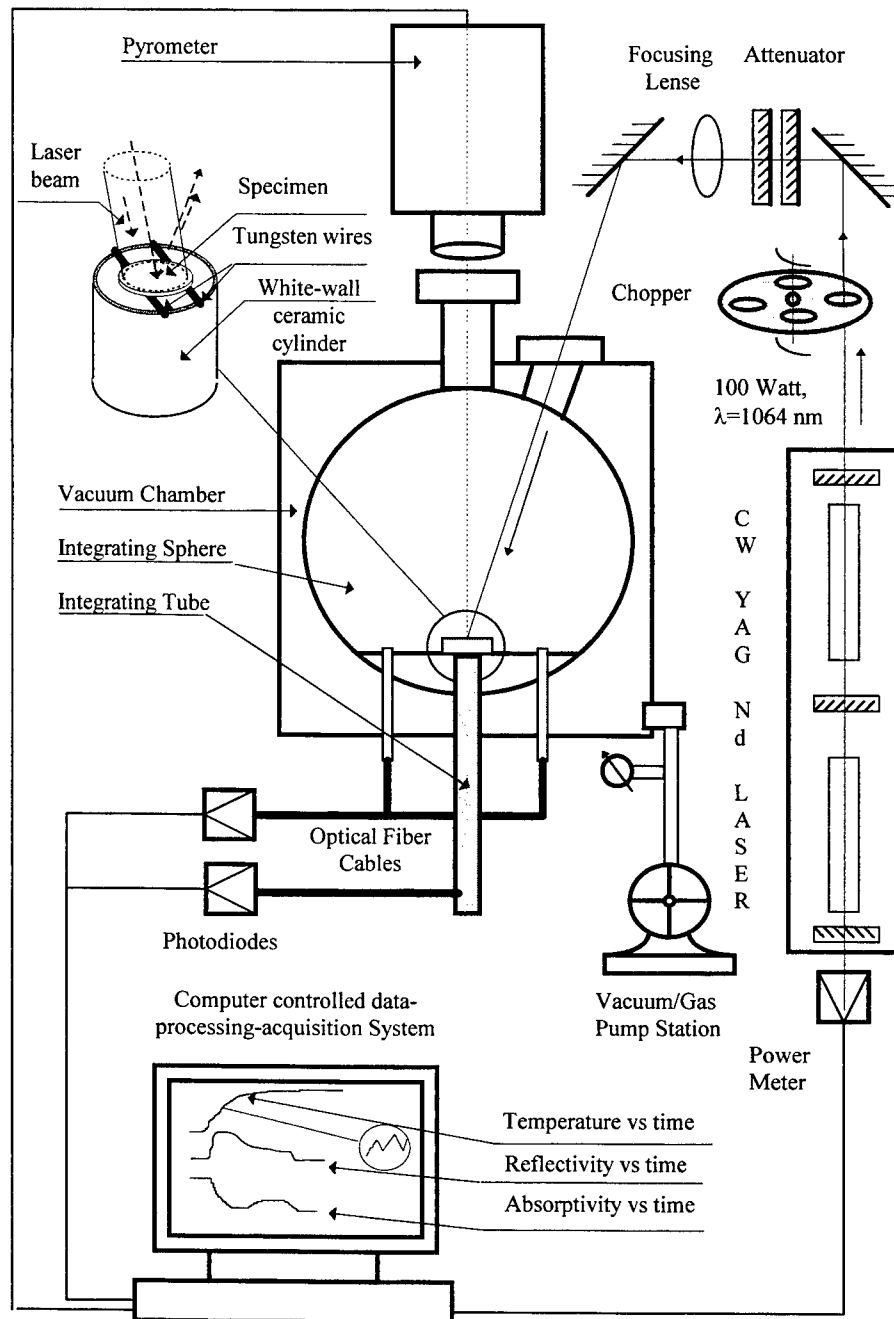


Fig.1. Experimental set-up for physical properties measurements.

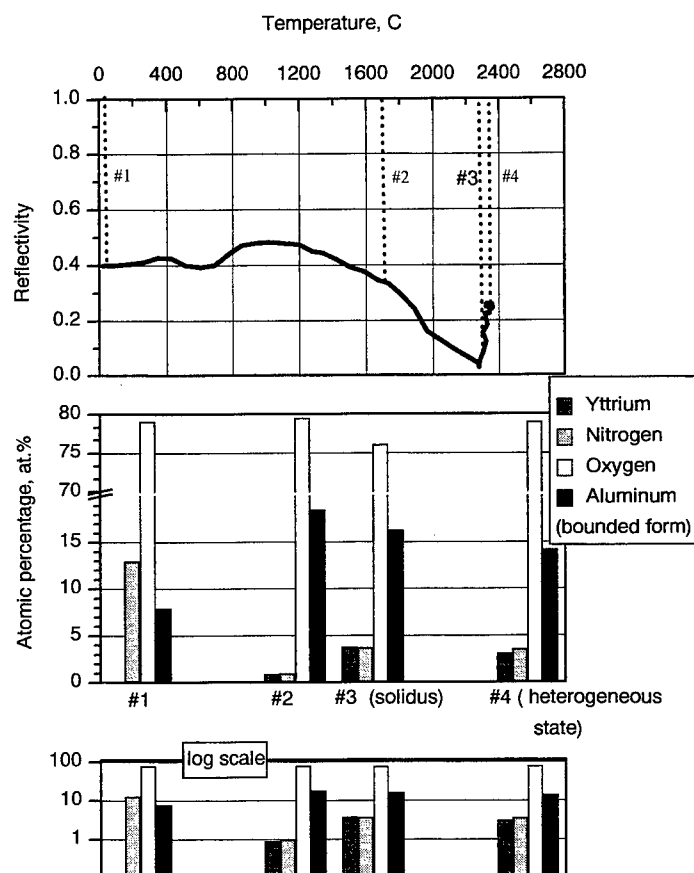


Fig. 2. X-ray-electron spectroscopy: variation of basic elements concentration (Y, N, O, Al) in the surface layer with temperature for AlN ceramics (white). Air 1 atm.

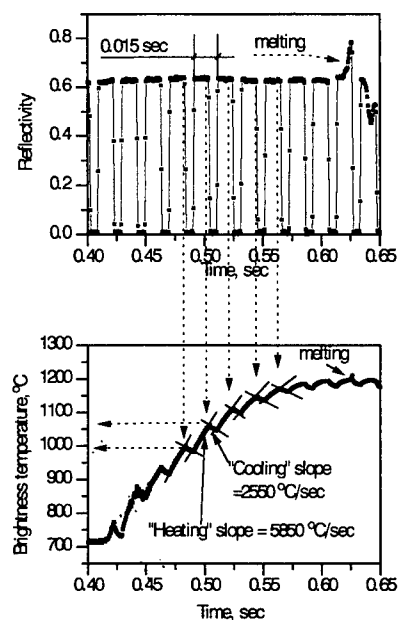


Fig.3. Modeling to obtain the heat capacity temperature evaluation $C_p(T)$.

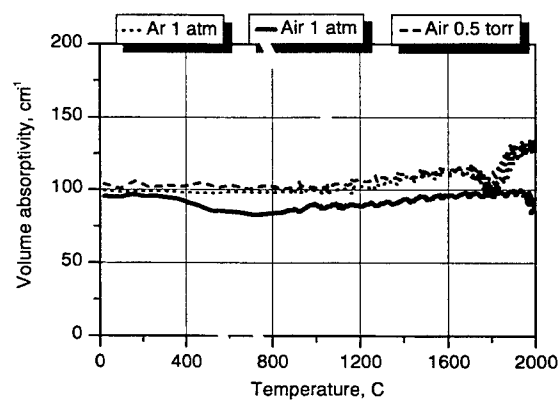


Fig. 4. Volume absorptivity temperature dependence for SiC (semitransparent) sample in different ambient atmospheres.

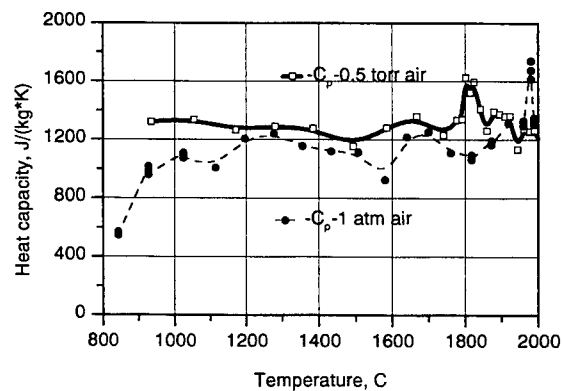


Fig. 5. Heat capacity temperature dependence for SiC (semitransparent) sample. Air 0.5 torr and 1 atm.

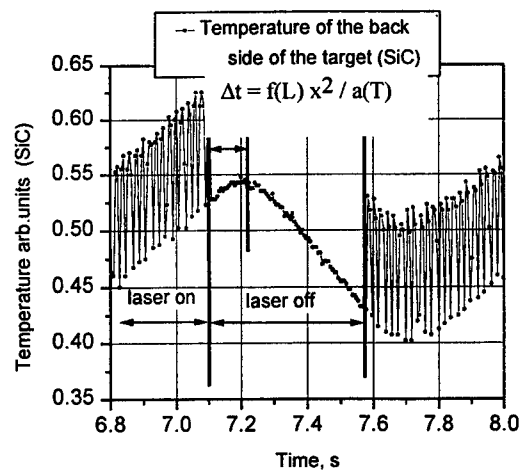


Fig. 6. Temperature signal of the back side of the target (SiC, $x = 2.6$ mm).

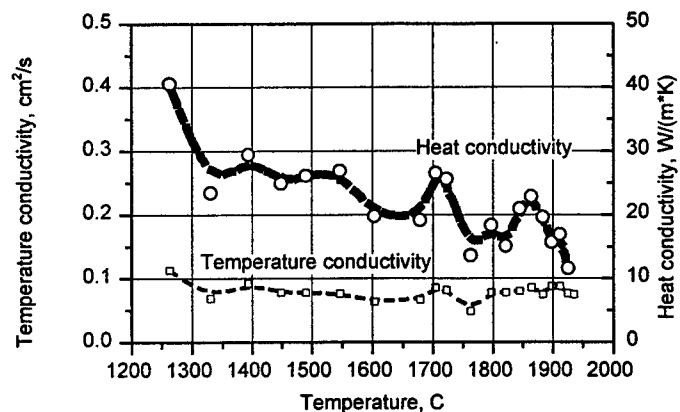


Fig. 7. Temperature conductivity and heat conductivity temperature dependences for SiC (black, opaque) sample. Air 0.5 torr.

A study of laser texturing processes by reflected light detection

W.J. Wang, Y.F. Lu, and M.H. Hong

Laser Microprocessing Laboratory of Electrical Engineering Department and Data Storage Institute
National University of Singapore, 10 Kent Ridge Crescent Singapore 119260

ABSTRACT

Laser texturing technique has been established to provide low flying height and low stiction required for manufacturing high storage density media. The characteristics of the laser bumps can be precisely controlled, and are critically important for the excellent tribological performance. In the study, the hard disks have been textured successfully using the argon ion laser with the aid of an acoustic-optic modulator in the optical path. Alternative laser bumps can be formed with various bump shape and bump height. The topography of the laser bumps are observed using AFM. Laser bumps are formed because of the modification of laser beam on the substrate surface during the heating and cooling processes. In attempt to study the bump formation mechanisms, a photodiode was employed to detect the reflected and scattered laser light, which irradiates on the hard disk surface to form laser bumps. The detected signals were studied under various laser power and pulse duration. It was found that there is a good correlation between the detected signal and the laser bump characteristics. The system has been proved to be an effective and convenient method to study the laser bump formation processes, and to *in situ* diagnose the laser bump characteristics.

Keywords: Laser texturing, topography, tribology, photodiode.

1. INTRODUCTION

Laser texturing has been proved to be an effective way to improve the tribological problem of hard disk drive for higher recording density. Several studies have been reported on the laser bump formation processes, the dependence of laser bump on laser parameters and the tribological behavior of the laser textured surface^[1-5]. The bump diameter is usually around 4 to 25 μm , and bump height of 10 to 40 nm. The stiction performance depends on the bump characteristics, including the bump shape, bump diameter, bump height, and bump distribution. The control of the laser parameters is critically important for the excellent tribological performance. The characteristics of the laser bumps depend on the laser energy and the material properties of the disk substrate. It is known that the laser bumps are formed because of the micro capillary wave during the laser-induced surface modification processes^[6-7]. The local area of the hard disk surface absorbs the laser energy when the laser beam irradiates the hard disk surface, and is melted to become a melting pool when the laser energy reaches the melting point of the substrate material. The permanent surface deformation is caused when the molten material resolidifies during the cooling process. The final bump characteristics, including the bump shape, bump height and bump diameter depend on the laser energy and the substrate material properties. The surface deformation will cause the scattering of the probing light, and the intensity of the reflected probing light from the deformed local area will vary with the deformation features. The intensity of the reflected probing light varies with the laser bump formation processes. Therefore, the laser bump characteristics are expected to be presented by the detected light. The reflected light in the cooling process is critically important, and presents the final bump characteristics. By *in situ* monitoring the reflected laser beam, the laser bump formation processes can be studied and the laser bump quality can be diagnosed.

The objective of the study is to develop a real time inspection system to study the laser modification processes and to *in situ* diagnose the laser bump quality. The zero order diffraction of the laser beam from the acoustic-optical modulator (AOM) is used as the heating and detecting source. Since the diffraction rate is adjustable, we set the pulse off energy at the level of 15 to 20% of the pulse on energy level. The laser beam of the high energy level is used as working light to modify the substrate surface. While, the laser beam at the low energy level is used as the probing light, which should be low enough to avoid surface deformation. A photodiode is used for high-resolution (nanosecond time scale) detection of the reflected laser

* Email: W.J. Wang, wangwj@dsi.nus.edu.sg
Y.F. Lu, eleluyf@nus.edu.sg

beam during the laser texturing processes. The bump shape and bump height changes in nanometer range can be detected. The detected signals will be presented, and the correlation between the laser bump characteristics and detected signals will be studied. The conventional photodiode detection method to study and *in situ* diagnose the laser modification processes is to use an additional CW light source, such as He-Ne laser etc., as the probing light [8]. The probing light must be well aligned and focused on the local area where the working light irradiates on, so as to make sure the true signal is detected. While, the argon ion laser is the only light source used in the established system as both the working and probing light, which makes the light alignment easy and accurate. Mean while, the detected signal contains rich information, such as the absorption information during the heating process, and reflection and scattering information during the cooling process. It is expected to be an effective and convenient way to study and monitor the laser texturing processes.

2. EXPERIMENTAL SETUP

The schematic of the experimental setup is shown in Fig. 1. A TEM₀₀ mode output of a CW Ar⁺ laser with a wavelength of 514.5 nm is employed to rapidly melt microscopic areas on hard disk substrate surface, and to detect the bump characteristics. The hard disks are aluminum-magnesium substrates coated with a 10 to 20 μm thick nickel-phosphorous (90-10wt%) layer to improve its surface hardness and smoothness. The coated surface is polished with a surface roughness of 2 to 3 nm rms.

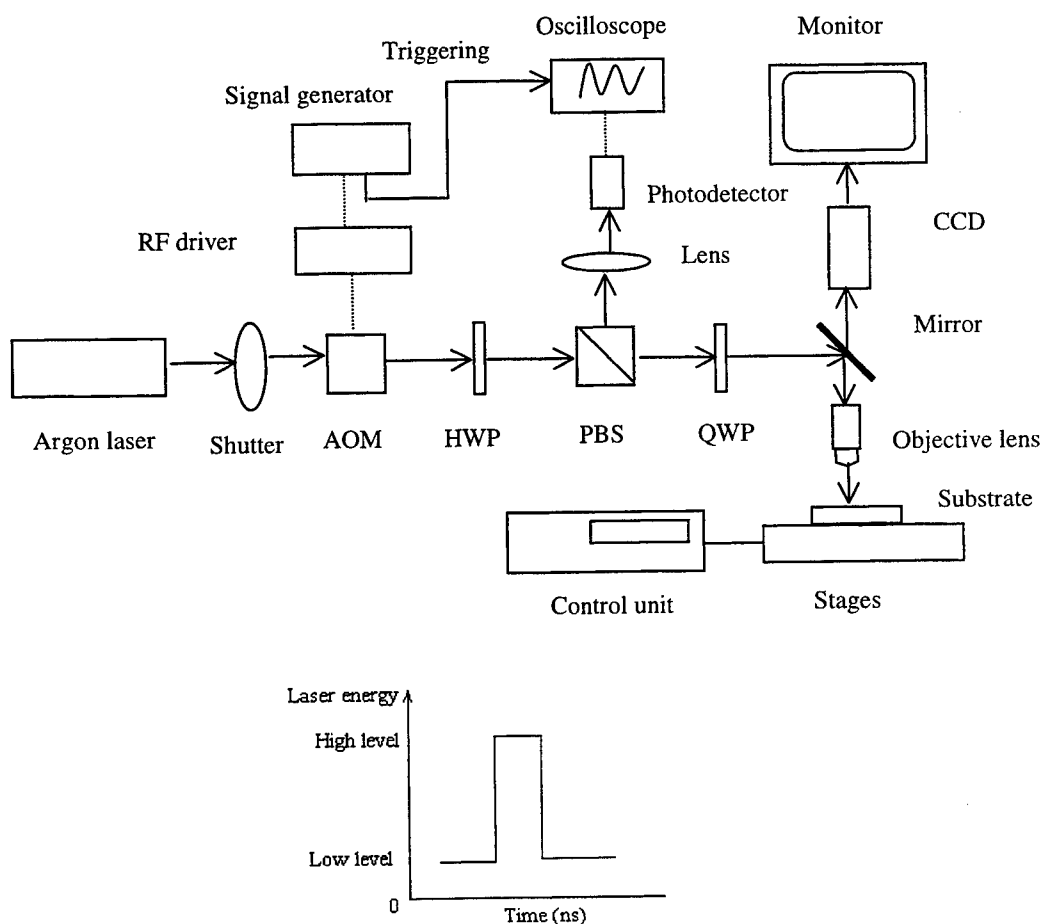


Fig. 1 Schematic of experimental setup for laser texturing and optical detection and modulated laser pulse profile
AOM: acoustic-optical modulator; HWP: half wave plate; QWP: quarter wave plate; PBS: polarizing beam splitter.

An acoustic-optical modulation is used to generate pulsed laser beam with flexibly controlled pulse duration and pulse frequency. The diffraction efficiency is around 85% at a wavelength of 514 nm. The acoustic wave from the FR driver is modulated by a signal generator to control the laser energy, pulse frequency and pulse duration of the laser beam irradiated on the substrate surface. The zero order and the first order of the diffraction light can be used as the energy source to irradiate on the substrate surface. The zero order diffraction light was selected in our experiment. By adjusting the voltage level of the TTL modulating signal, the diffraction efficiency is controlled. The high and low energy level of the laser pulse can be controlled as shown in Fig. 1. The substrate surface is modified by high pulse energy, which is defined as the working light, with adjustable pulse duration and pulse frequency. The low energy pulse is defined as the probing light, and its energy level should be lower enough so that the surface deformation is avoided. It is expected to detect the intensity variation of the reflected light during the laser bump formation processes. We will concentrate more on the study of the probing light at the falling edge of each laser pulse. The vertical polarized CW laser beam is modulated by the AOM, and becomes pulsed. The modulated laser passes through a half wave plate, a beam polarizing splitter, a quarter wave plate, a mirror, and finally is focused on to the substrate surface by an objective lens. The reflected light from the substrate surface passes back through the same objective lens, the mirror to the quarter wave plate where the polarization of the laser beam is changed with 90 degrees. The reflected laser beam is deflected by the beam polarizing splitter, and reaches to the photodiode detector. The intensity of the reflected laser light is then detected and the detected signal is sent to a digital oscilloscope, which is triggered by the synchronization TTL signal. The resolution of the detection system is 1 ns. The deformation of the substrate surface will cause the scattering effect, and therefore, the intensity of the reflected laser beam will be varied. It is known that the bump characteristics vary with the laser energy and/or substrate surface properties. The dependence of the detected signal on the topography of the laser bumps, including bump height, bump diameter and bump shape, will be studied. By the analysis of the detected signals, we can study the bump formation processes and the signal can also be used for the real time monitoring of the laser texturing processes. It is noticed that the detected signal has an offset at the rising and falling edge, correlating to the laser bump characteristics.

The hard disk substrate is mounted on a motorized stage. When the stage reaches the desired speed and position, the shutter is opened for a certain time interval so that the laser beam irradiates on the disk surface. A video camera is mounted on the top of the optical system, and the video image is sent to a monitor for focusing adjustment and real-time monitoring. The landing zone texturing processes can be carried out by mounting a rotation stage on the linear stage. Therefore, a series of laser bumps with spiral distribution are formed. The textured surface is observed by using atomic force microscope (AFM). By adjusting the laser parameters, alternative bumps can be produced with various bump characteristics. The reflected laser light is probed in the real time by the photodiode detecting system, and the signal is recorded. By the analysis of the detected signal, it is found that there is a well correlation between the laser bump characteristics and the probing signals. It has been proved to be an effective and convenient method to study the laser modification processes and diagnose the laser bump quality.

3. DISCUSSION AND RESULTS

Alternative laser bump features are observed by atomic force microscope (AFM) as shown in Fig. 2. The dome-like bumps as shown in Fig. 2(a) are formed when the laser pulse duration is 400 ns with a laser power of 0.5 W. The bump diameter and bump height is around 5 μm and 10 nm respectively. With the increase of the laser power, the top of the bump is depressed with its rim growing up, resulting in the formation of the crater bump as shown in Fig. 2(b) with bump diameter of 5 μm , bump height of 15 nm. The sombrero bump, with 4 μm in diameter and 25 nm in height, is formed when the laser pulse duration is 1 μs and laser power of 0.5 W. With the increase of the laser power, the top of the central peak is depressed lower and lower. The double-rim crater bump, with 5 μm in diameter and 30 nm in height, is formed when the laser power is 0.65 W. The AFM images of the sombrero bump and double-rim crater bump are shown in Fig. 2 (c) and (d) respectively. The bump shape is sensitive to the laser power at some energy levels. The surface profile changes of the laser bump profile are responsible for the scattering effect, resulting in the intensity variation of reflected laser beam.

The probing light alignment is carried out before the measurement on a flat substrate surface with low laser energy to avoid the surface deformation. The detected signal shows the same energy level at the rising and falling part of the laser pulse. The signal profile is similar to that of the signal generator, which is used to modulate the AOM FR driver. When the laser pulse energy reaches the threshold of the substrate material, the local area of the substrate surface is molten. At the falling edge of the laser pulse, the molten material is cooling down to resolidify, causing the deformation of the substrate material. The probing light is scattered by the surface deformation. The dependence of the laser bump profile on laser pulse duration

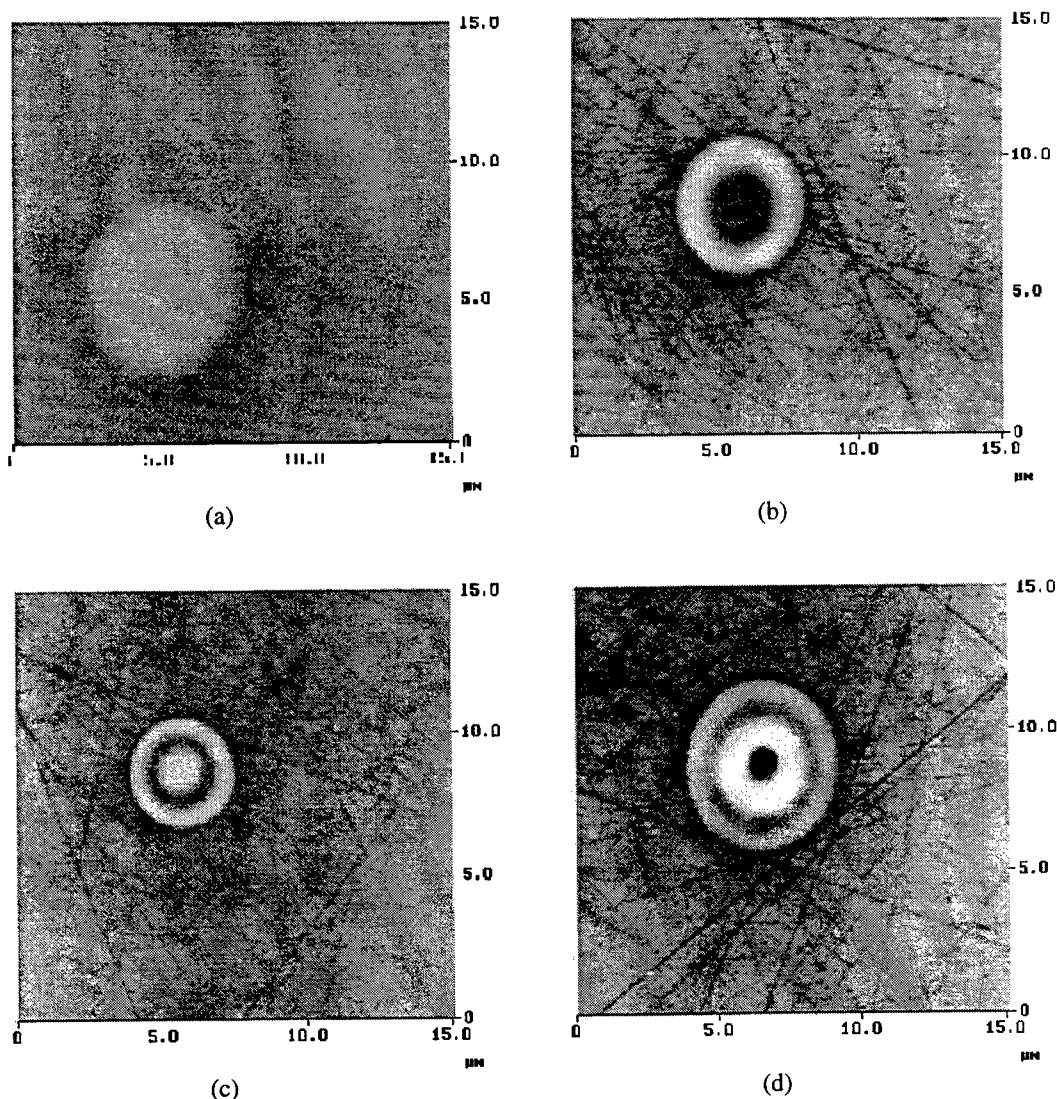


Fig. 2 Two-dimensional AFM images of laser bumps on hard disk surface. (a) dome-like bump with central peak, produced with laser power of 0.5 W and laser pulse duration of 400 ns (laser pulse energy 0.2 μJ); (b) crater bump with a peripheral rim, produced with laser power of 0.65 W and laser pulse duration of 400 ns (laser pulse energy 0.24 μJ); (c) sombrero bump with central peak and a peripheral rim, produced with laser power of 0.5 W and laser pulse duration of 1 μs (laser pulse energy 0.5 μJ); (d) double-rim crater bump, produced with laser power of 0.65 W and laser pulse duration 1 μs (laser pulse energy 0.65 μJ).

and the laser power is shown in Fig. 3. The laser bumps in Figs. 3(a), (b), (c), (d) are produced with laser pulse duration of 400 ns, and laser power of 0.5, 0.55, 0.6, and 0.65 W respectively. The bump (a) exhibits dome-like profile with bump diameter around 4 μm and bump height of 10 nm. The probing light is scattered away from the beam center by the bump slop, the intensity of the reflected light is therefore reduced. It is noticed from the signal profile, as the solid line shown in Fig. 4 (a), that the voltage level of the detected signal is lower at the falling edge of laser pulse than at the rising edge. The flat tops are depressed lower and lower with the increase of laser power, as shown in Figs. 3 (b) and (c). The depressed center may enhance the intensity of the probing light. Therefore, the detected signals have higher signal voltage level as the dash and the dot lines respectively, as shown in the Fig. 4 (a). The crater bump is formed with the further increase of

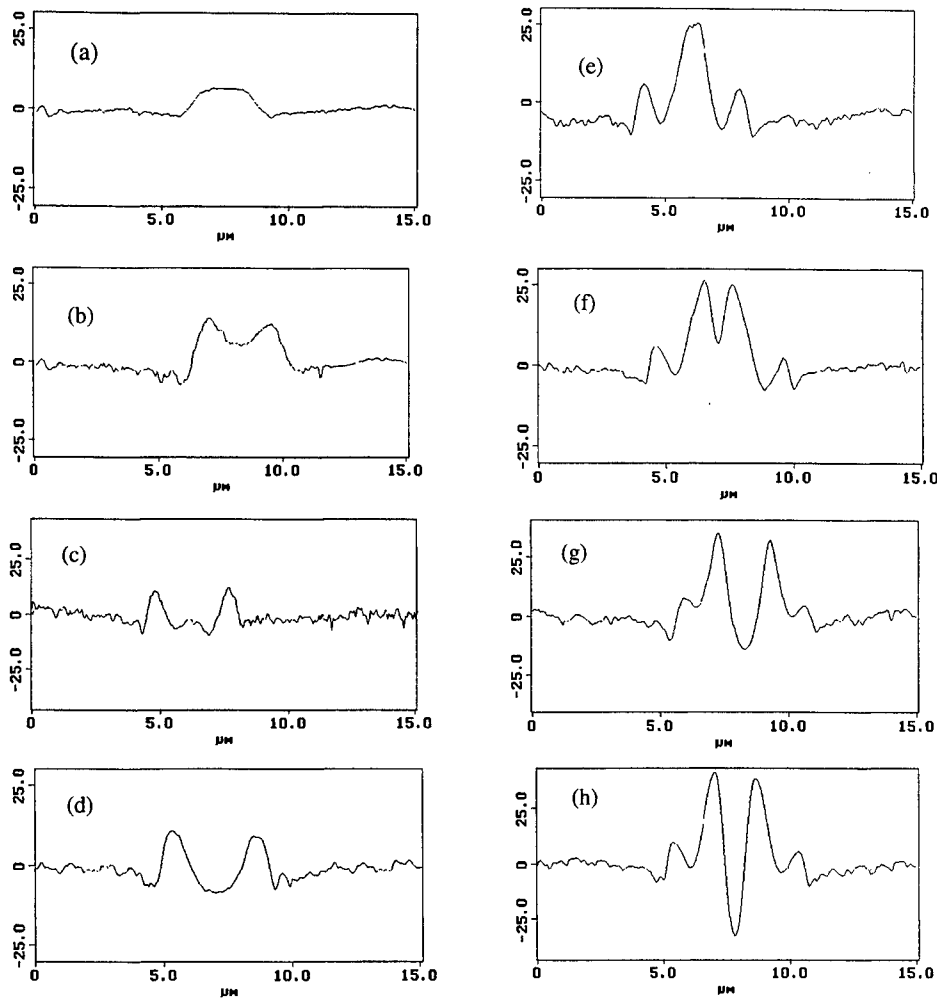
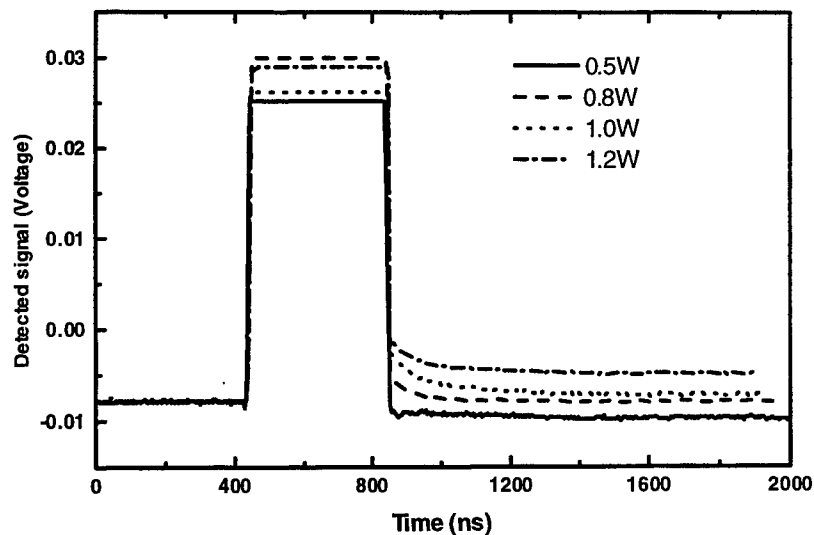
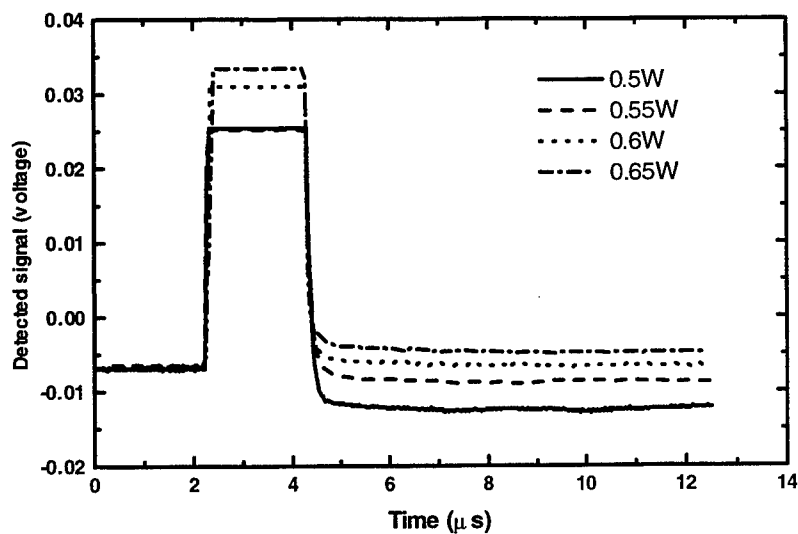


Fig. 3 The dependence of the laser bump profiles on laser pulse duration and laser power.
 (a), (b), (c), (d) laser pulse duration 1 μ s with laser power of 0.5W, 0.55W, 0.6W, 0.65W respectively.
 (e), (f), (g), (h) laser pulse duration 400 ns with laser power of 0.5W, 0.8W, 1.0W, 1.2W respectively.

the laser power as shown in Fig. 3(d). The bump diameter is 4.5 μ m and bump height of 15 nm. The detected intensity is higher, since the profile of the crater bump has a sharper slop. The dash-dot-dash line shown in the Fig. 4(a) shows the detected light profile of the crater bump. The dependence of the bump profile on laser power at laser pulse duration 1 μ s is shown in Fig. 3 (e), (f), (g), (h) with laser power of 0.5, 0.8, 1.0, and 1.2 W respectively. The sombrero bump with diameter of 6 μ m and bump height of 25 nm as shown in Fig. 3(e) causes the scattering effect to the probing light. The voltage level of the detected signal is the lowest as solid line shown in Fig. 4(b). With the increase of the laser power, the central peak of the sombrero bump is depressed. The slop of the bump profile is reduced, resulting in the weak scattering effect as the dash line shown in Fig. 4(b). Figures 3 (g) and (h) show the double-rim crater bumps with sharper profile slop, the scattering light intensity is increased as the dot line and dash-dot-dash line shown in Fig. 4(b). The detected signal is well correlated with the bump profile. It is known that there may have variations of the substrate material, substrate morphology, and laser energy, which will induce the variation of the bump characteristics. By monitoring the profile of the detected signal, the bump quality can be diagnosed easily with the setup.



(a)



(b)

Fig. 4 The dependence of detected signals on laser power (a) pulse duration 400 ns, with laser power of 0.5W, 0.8W, 1.0W, and 1.2W respectively; (b) pulse duration 2 μ s, 0.5W, 0.55W, 0.6W, and 0.65W respectively.

The signal offset is defined as the deflection of the probing signal at the falling edge to the probing signal at the rising edge of the laser pulse. Figure 5 shows the dependence of the signal offset on the laser power at the pulse duration 1 μ s. It is found that the signal offset varies with the laser power. The negative offset refers to the sombrero bumps with central protrusion. The positive offset refers to the crater bumps with depressed bump center. The bigger offset refers to sharper slope of the bump profile, due to greater surface deformation. When the rim height of the bump is irregular as shown in Fig. 6, which may be caused from the unsymmetry of the beam profile. The offset of the probing light will shift away from where it should be in the Fig. 5.

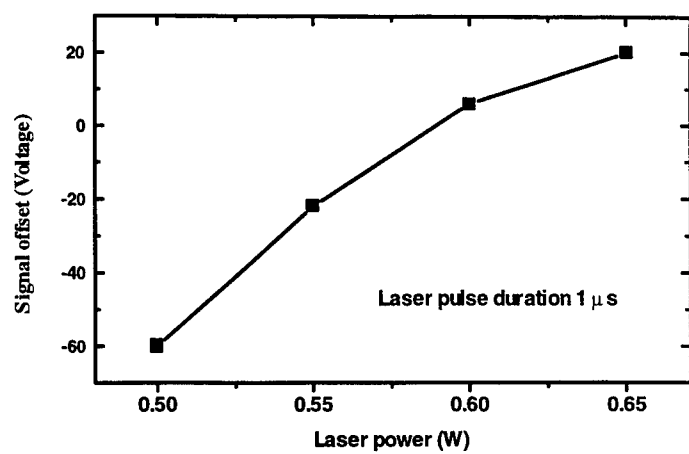


Fig. 5 The dependence of the signal offset on the laser power at pulse duration 400 ns.

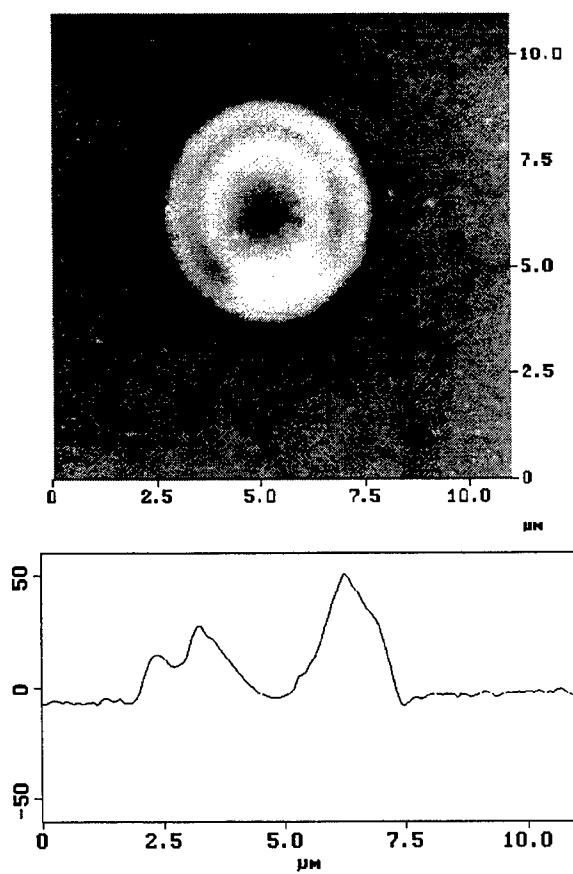


Fig. 6 Two dimensional AFM image and profile analysis of laser bump produced by laser beam with irregular profile

4. CONCLUSIONS

The experimental setup has been proved to be an effective and convenient method to study the processes of the laser modification, and the real time monitoring of the laser texturing processes. The hard disk can be textured successfully with the system and the topography was measured by AFM. Alternative bumps can be formed with the dome-like bumps, sombrero bumps, crater bumps, and double-rim crater bumps. The bump height, bump diameter, and bump distribution can be varied flexibly by the control of the laser parameters. The argon ion laser is the only light source used in the system as both working light and probing light. The detected signal profile depends on the features of the surface deformation. The detected signal profiles and the bump characteristics present good correlation.

5. ACKNOWLEDGEMENTS

The authors would like to express their thanks to Dr. W.D. Song, Dr. D.M. Liu, Dr. C.W. An, Mr. K.D. Ye for their help and collaboration.

6. REFERENCES

1. R. Tanjan, D.N. Lambeth, M. Tromel, "Laser texturing for low-flying-height media" J. Appl. Phys. Vol. 69, No. 8, pp5745-5747, 1991.
2. P. Baumgart, D.J. Krajnovich, "A new laser texturing technique for high performance magnetic disk drives" IEEE Trans. On Magn. Vol. 31, No. 6, 1995.
3. T. R. Anthony, H.E. Cline, "Surface rippling induced by surface-tension gradients during laser surface melting and alloying", J. Appl. Phys., Vol. 48, No. 9, pp3888-3894, 1977
4. J. Gui, B. Marchon, "A stiction model for head disk interface of a rigid disk drive", J. Appl. Phys., Vol. 78, pp4206-4217, 1995.
5. W. J. Wang, Y.F. Lu, "Formation and tribological behavior of NiP surface textured by argon ion laser", IEEE Trans. On Magn. Vol. 31, No. 6, 1998.
6. J.F. Yong, J.E. Sipe, H.M. van Driel, "Laser-induced periodic surface structure, II. Experiments on Ge, Si, Al, and Brass" Phys. Rev. B, Vol. 27, No. 2, pp1155-1172, 1983.
7. J.F. Yong, J.E. Sipe, H.M. van Driel, "Laser-induced periodic surface structure, III. Fluence regimes, the role of feedback, and details of the induced topography in Germanium" Phys. Rev. B, Vol. 30, No. 4, pp2001-2015, 1984.
8. S. Chen, C.P. Grigoropoulos, H.K. Park, P. Kestens, A.C. Tam, "Photothermal displacement measurement of transient melting and surface deformation during pulsed laser heating", Appl. Phys. Lett., Vol. 73, No. 15, pp2093-2095, 1998.

Fabrication of True 3D Microstructures in Glass/Ceramic Materials by Pulsed UV Laser Volumetric Exposure Techniques

Peter Fuqua*, S. W. Janson, W. W. Hansen, and H. Helvajian

Microtechnology Center

*Mechanics and Materials Technology Center

The Aerospace Corporation

Los Angeles, CA 90009-2957

ABSTRACT

A pulsed UV laser based technique has been developed which permits the transfer, by direct-write exposure, of 3D images into a photosensitive glass/ceramic material. The exposed latent image volume is developed via temperature programmed bake process and then etched away using HF in solution. The height of the 3D microstructures is controlled by the initial laser wavelength used during the exposure and the time duration of the etching cycle. Using this technique we have fabricated large arrays of microstructures which have applications to microfluidics, microelectromechanical systems and optoelectronics. The resulting master copy can be used either as is or by use standard injection molding techniques converted into a metallic or plastic copies (i.e. LIGA). We present these results and others which have specific applications to miniature 1Kg class satellites – nanosatellites.

Key Words: MEMS, Nanosatellite, Laser Micromachining, Glass-Ceramics, Direct-Write

1. INTRODUCTION

It has been over 40 years since the Russian Sputnik satellite was launched¹ heralding the strategic possibilities of space. Given its simple mission, that of broadcasting a simple signal, Sputnik, with its primitive technology, still has one commonality with modern satellites. Both are assembled the same way, one custom made piece at a time. There is now a move afoot in the aerospace industry to modernize satellite production and manufacturing operations by implementing a standardization of parts protocols and assembly-line methods. There is also the intent to integrate more of the satellite sub-systems, thereby saving the excess mass. One outcome of this exercise is that particular space missions can be accomplished with a constellation of very small earth orbiting satellites. The mission of such tiny satellites might require various degrees of coordination. It might operate as a companion to a much larger satellite like the Space Shuttle or International Space Station. Such a unit would move about and providing images of damaged or questionable components and aid in repairs. In larger numbers, a constellation in low earth orbit might provide global coverage, perhaps mapping cloud cover for civilian applications. Furthermore, a local cluster properly coordinated could form a sparse synthetic aperture with a baseline of many kilometers.

The Nanosatellite or the "silicon" satellite is an Aerospace Corporation concept whereby all the subsystems are fabricated using microelectronics processing and advanced packaging techniques and are assembled as an integrated unit². The result is a 1 kilogram satellite which should be mass-producible to the exacting standards set by the microelectronics manufacturing industry. Initially, the Aerospace Corporation Nanosatellite will be assembled using multi-chip module (MCM) packaging techniques; however, future generations will integrate sub-systems using wafer-scale monolithic packaging techniques. Since most of the nanosatellite subsystems are electronic in nature, the fabrication, integration and packaging issues have been

addressed already by the microelectronics industry. However, propulsion and attitude control systems are unique to space systems and the miniaturization, integration and packaging aspects require further study and development.

The development of a micropropulsion system is required for nanosatellite production. This will require technology development in the area of processing of non-silicon materials including ceramics, glass, metal and specific space qualified polymers. There is also a need to fabricate true 3 dimensional (3D) microstructures most of which would be difficult, if not impossible, using LIGA or DRIE techniques. For the specific case of micropropulsion systems, many elements may also have heights larger than 100 microns. For this reason, The Aerospace Corporation is developing direct-write laser material processing techniques. Aerospace has developed a CAD/CAM laser based tool for rapid prototyping of micropropulsion components. The laser tool uses both ablative and volumetric exposure techniques³ to fabricate needed true 3D microstructures. Presently, the Corporation is both evaluating and developing prototype micropropulsion concepts for application to nanosatellite class spacecraft. The thruster types being considered here include the cold gas thruster and the "one-shot" micro-solids array. We are also investigating micro- ion propulsion, but that will not be discussed here. Laser material processing plays an important role in the fabrication of all these devices.

2. EXPERIMENTAL

The primary material used in this work is a photostructurable glass ceramic available in wafer form from Schott glass under the trade name Foturan⁴. This material is composed of a lithium aluminosilicate glass doped with trace amounts of silver, cerium and antimony⁵. The cerium is a photosensitizer. In the presence of ultraviolet light, the Ce^{3+} ion gives up an electron to become Ce^{4+} and the free electron finds a silver ion and then reduces Ag^+ to Ag^0 . In this work, pulsed UV laser light was introduced into our laser micromachining station. The beam was focused by a 10x objective into the work where it was moved by a computer controlled xyz stage. The computer also controls several shutters allowing the use of more than one illumination source. If the sample is exposed to a sufficient fluence of ultraviolet light, a latent image in the form of neutral silver atoms is recorded in the amorphous glass. If the density of neutral silver species is too small, the latent image will not "develop" sufficiently to enable mass removal.

The latent image is developed thermally. The sample is placed in a furnace and the temperature is ramped at $5^{\circ}C/min$ to $500^{\circ}C$ and held for an hour. At this temperature, neutral silver atom diffusion permits the formation of silver clusters in the UV exposed regions. The temperature is then raised again to $605^{\circ}C$ at $3^{\circ}C/min$ and held for an hour. At this higher temperature, the glass can devitrify, nucleating a crystalline phase at the silver clusters. It is important to note that the crystalline phase (also called ceramic phase) is slightly less dense than the amorphous phase, so there is a small expansion associated with the devitrified regions. The temperature is sufficient for softening of the amorphous phase, so the glass warps slightly to accommodate the expanded volume. In some applications, after cooling to room temperature, the sample would be polished to remove any unwanted texture.

After completing the nucleation and growth steps, the sample has a latent image consisting of crystalline regions in an amorphous matrix. It is a property of the crystalline phase that it is more rapidly soluble in hydrofluoric acid than the surrounding phase. In a 5% solution of HF, the etch ratio is 20 to 1. Typically, 5% HF at $40^{\circ}C$ will dissolve through a 1 mm thick polycrystalline region in under an hour.

Fabrication of true 3D microstructures is achieved by varying the exposure conditions. In one strategy, we take advantage of the varying bulk absorption of Foturan. Figure 1 shows the UV transmission curve with the calculated penetration depth overlaid. Here the penetration depth is defined as the depth at which the intensity has

fallen to $1/e$ of the incident intensity. A one millimeter thick sample exposed to 355nm light would result in a latent image that is uniform through the thickness of the sample (assuming the incident fluence exceeds the minimum value for exposure.) On the contrary, if this sample were to be exposed to 248nm light the image will develop to only a depth where the critical fluence is maintained. Clearly, since exposed regions etch more rapidly than the surrounding areas, true 3D machining can be achieved by varying the photon flux and wavelength over different parts of the workpiece.

Another strategy to 3D micromachining involves illuminating the sample with a laser beam and shaping the beam. Structures with straight walls are obtained with a columnated laser beam. Hyperboloids are formed with light that focuses or defocuses as the light passes through the material. One can also place the focus at the center of the material to create an hour-glass shaped latent image. Moving the workpiece in the XYZ direction during exposure increases the possible complexity of the produced part.

An interesting consequence of the unique processing of Foturan, is the texture of the resultant parts. Because the crystalline phase nucleates and grows into the glass and then is etched away, one can achieve widely varying morphologies. In figures 2 below, the remaining structures look as if material is scooped out of the side surfaces. In fact, the surface conforms to the growth of the crystal into the glass. Where grains intersect and etch away, the amorphous phase that remained in the interstices can possess very sharp edges, which we hope to exploit in field emission devices.

3. THRUSTER CONCEPTS

3.1. Cold Gas Thruster

The cold gas thruster is the most common. It typically consists of a pressurized gas chamber (propellant tank), a gas metering valve, a cavity chamber (gas plenum) and an hour-glass shaped exit nozzle. Cold gas thrusters usually possess low specific impulse and as a consequence great care is exercised in their design to insure the efficient conversion of the pressurized fuel to thrust. The miniaturization of the cold gas thruster poses significant challenges in maintaining efficiency. As fluidic devices are miniaturized, the surface area to volume ratio increases which can result in larger drag forces. The proper design of the exit nozzle is key to providing maximum thrust. A true 3D axis symmetric hour-glass shape nozzle is more efficient than an extruded 2D hour glass nozzle. The use of photostructurable glass and laser direct-write processing permits the fabrication of 3D nozzles to a wide range of dimensions and an expansion ratios defined as the exit plane cross-sectional area divided by the throat cross-sectional area.⁶ The processing variables include beam shape and position in the workpiece as well as laser fluence metering. It is important to choose a laser fluence that enables the exposure of the sample, but not initiate thermal effects within the volume of the beam. The Aerospace laser prototyping center was used to fabricate 3D axisymmetric micronozzles in 1mm thick Foturan with a throat diameter of 100 microns and area expansion ratio of 10. Two nozzles, along with a laser fabricated gas plenum and a commercial silicon MEMS valve (IC sensors), were assembled into a bi-directional 1mN class cold gas thruster. Figure 3 shows a picture of the thruster and figure 4 shows the thrust data. The largest measured specific impulse was 50% of the ideal specific impulse expected for argon with a 10:1 expansion ratio. Without the MEMS valves, the thruster efficiency approached 80%. Comparison of the two configurations clearly shows that the gas flow is choked at the MEMS valve. This problem is mitigated by the use of a MEMS valve with a larger throat opening.

3.2. Digital Thruster

Another Nanosat propulsion concept is that of the digital single-shot thruster. Here MEMS technologies could be used to create an array of miniature single use thrusters. One might imagine 10,000 single shot thrusters on a single wafer. Each thrust chamber would be independently addressable and each propellant chamber would be sealed. This approach mitigates the use of valves that add complexity and are prone to leakage. Satellite

trajectory calculations show that a large array of single-shot thrusters can be used to maintain attitude or maneuver 1kg class nanosatellites⁷

Our embodiment of this concept involves 3 layers. The first layer is a silicon die with an array of heating elements or fuses which ignite the fuel. The second layer is the propellant array chamber, fabricated from Foturan. The propellant cylinders are fabricated by direct-write patterning with the UV laser and etched. The arrays of fuel cavities can be filled with any one of a number of fuels. The propellant chamber is capped with the third wafer layer. This layer contains an array of silicon expansion nozzles that are sealed at the throat by a silicon nitride diaphragm. The diaphragm array is produced from a silicon wafer coated on both sides with 5000Å of silicon nitride. Laser ablation is used to create an array of breaches in the nitride film on one side of the wafer. The other side is left unpatterned. The breaches form the perimeter of the nozzle exit. The wafer is anisotropically etched in 35% KOH (60C) for a day leaving a silicon nitride membrane at the bottom of a truncated pyramidal pit. The square membrane forms the throat of the expansion nozzle. The fuel is ignited by delivering a pulse of electrical current to the heating element, which explodes a patterned wire. The pressure in the microchamber builds until the silicon nitride diaphragm bursts, producing a single pulse of thrust.

In figure 5 we show the three layers of the prototype thruster array. The first is the array of resistive polysilicon elements. The second figure is the Foturan propellant chamber. There are 15 chambers, each is 700 microns in diameter. The four smaller holes are for alignment with fiducials on the wafer below. Lastly is the array of laser patterned and KOH etched die.

Figure 6 shows frames from a high-speed video tape of a single cell ignition. In this experiment the 15 element array thruster is mounted on an IC flatpack chip and placed in a test fixture to measure thrust. The visual burn time is just over a 1 millisecond. Thrust measurements show that an average of 80 millinewtons is achieved for a propellant chamber 1mm long and 900 microns in diameter. The single ignition produces an equivalent power of 60 W.

The use of direct-write laser processing for the fabrication of the digital thruster chip provides several advantages, given below.

Table 1. Beneficial capabilities of direct-write laser processing for digital thrusters

- Rapidly prototype test chips with various chamber diameters.
- Individually alter the fuel chamber shapes and positions.
- Rework prior fuel chambers.
- Laser direct-write techniques can selectively seal individual chambers.
- Fabricate non cylindrical chamber shapes and circular nitride membranes.

4. CONCLUSION

A direct-write laser micromachining volume exposure technique has been developed to fabricate true 3D microstructures in a photostructurable glass. This new technique, in conjunction with traditional direct-write ablation techniques, has been used to fabricate two types of microthrusters for applications to 1Kg class satellites. The results of the thrust measurements are promising and they open the door for fabricating microthrusters out of glass/ceramic materials that have certain advantages for space use. Laser based processing offers the rapid prototyping capability that is advantageous in the development of microthrusters, where the physics of fluids in

microchannels is still an exploratory science. Another advantage is that this processing is relatively clean with minimal debris for contamination. Further experiments will be conducted to refine the volumetric exposure technique and to develop microtextured surfaces which are amenable to ion emission thruster applications.

ACKNOWLEDGEMENTS

We gratefully acknowledge the support provided by the Aerospace Corporation through the Corporate Research Initiative program, the Air Force Office for Scientific Research and DARPA through the MEMS Microthruster Program.

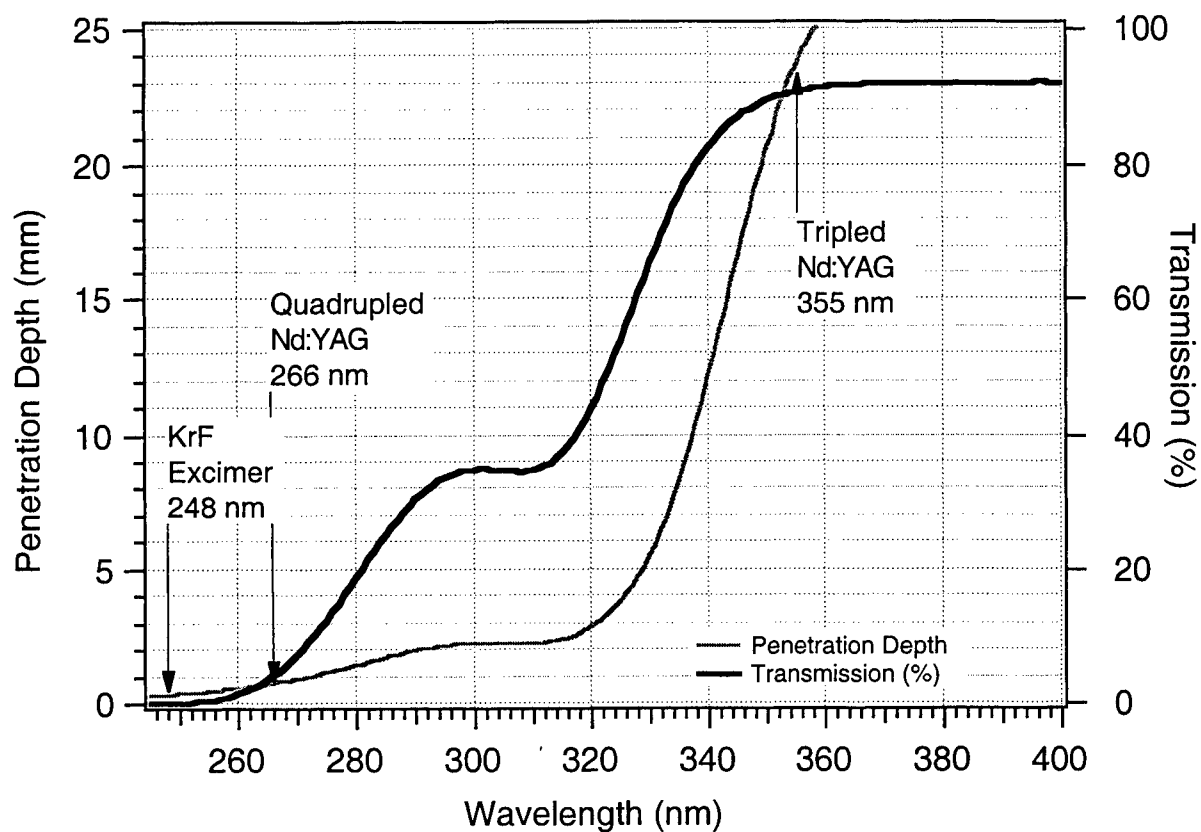


Figure 1: Transmission curve and penetration depth versus wavelength for Foturan.

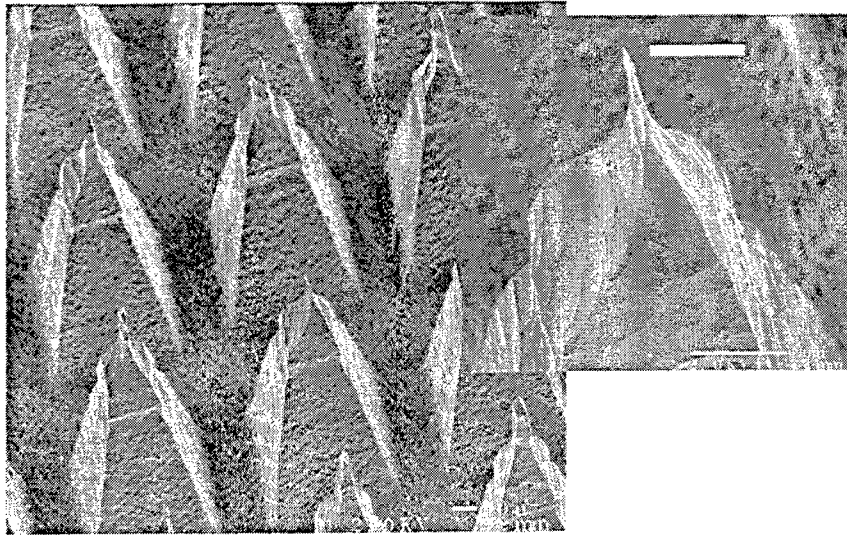


Figure 2: Etched Foturan microstructures. Note the tip's tight radius of curvature.

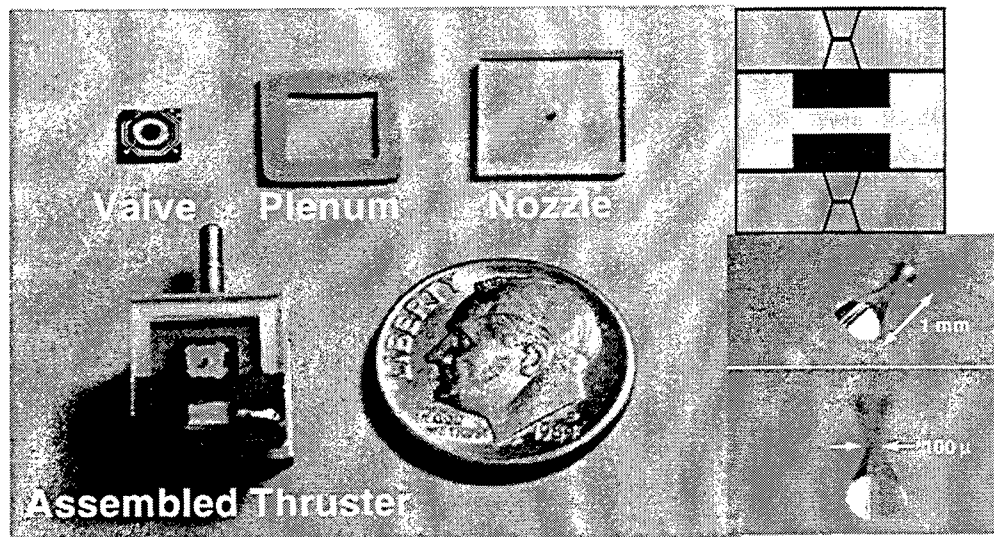


Figure 3: Cold gas thruster

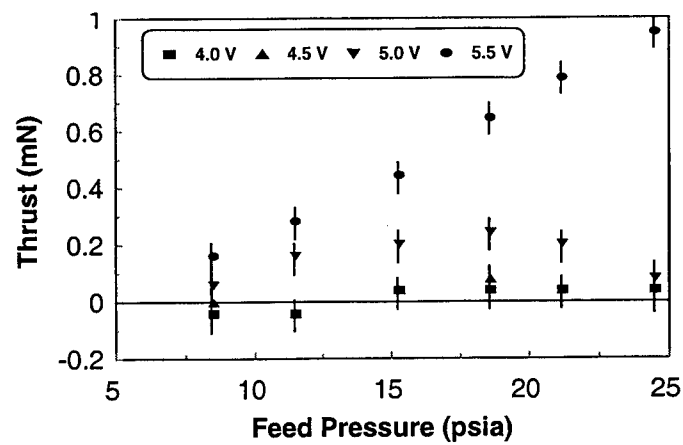


Figure 4: Measured data for thrust versus feed pressure for a bi-directional mN thruster.

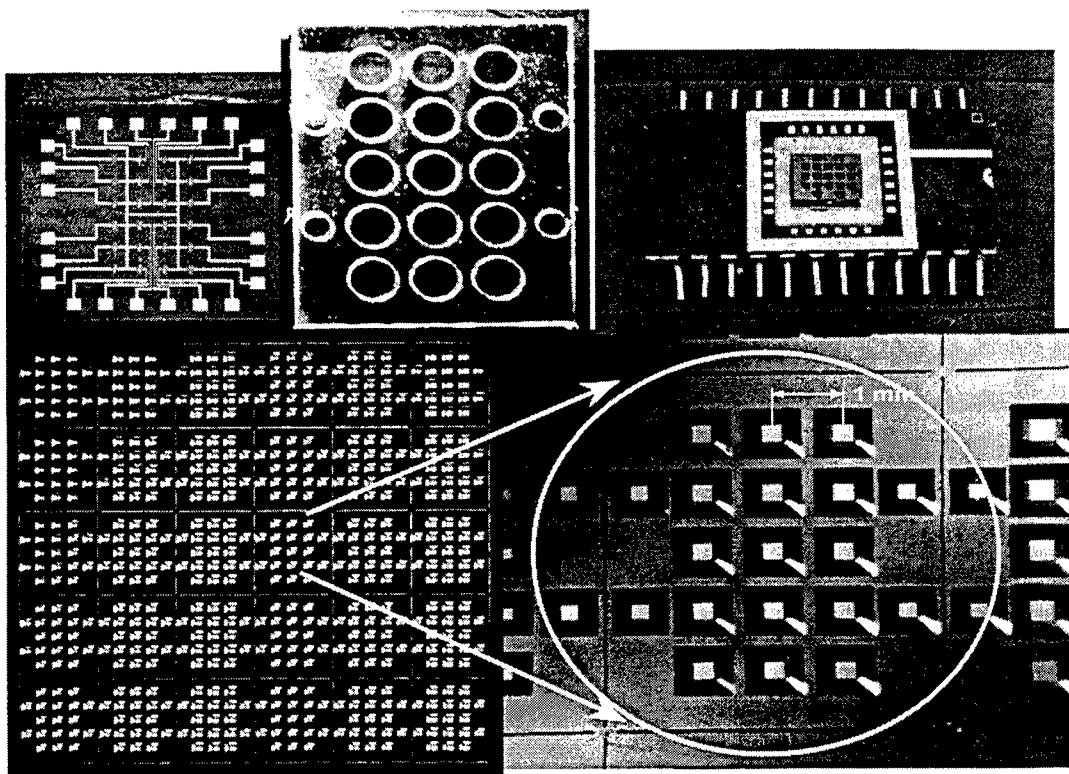


Figure 5: Digital thruster array. 1)Resistor wire igniter bottom wafer, 2)Laser fabricated propellant chambers typically 700 dia by 1 mm deep. 3)Silicon nitride membranes (0.15 microns) fabricated by laser ablation patterning and KOH bulk silicon etching. 4)Final package of the 3 wafer package wire bonded in a silicon-die chip holder package.

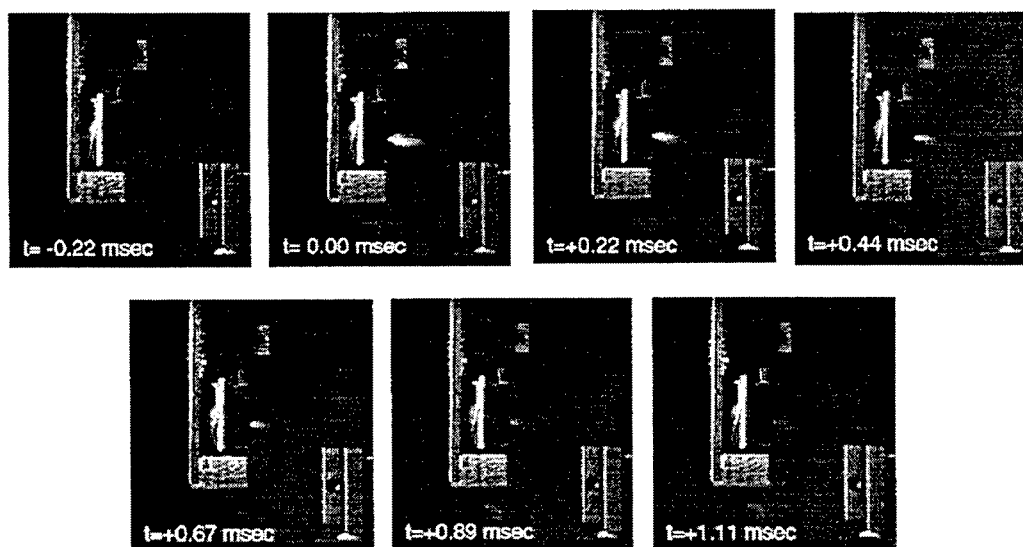


Figure 6: Video frames of solid propellant digital thruster firing on a thrust stand. Average thrust is 80mN; equivalent power is 60W.

REFERENCES

1. Sputnik was launched October 4, 1957.
2. S. W. Janson, *Chemical and Electric Micropropulsion Concepts for Nanosatellites*, Proceedings of the 30th AIAA Joint Propulsion Conference, AIAA-94-2998 (1994) and S. W. Janson, *Spacecraft as an Assembly of ASIMs*, in *Microengineering Technology for Space Systems*, H. Helvajian Ed., Aerospace Technical Report ATR-95(8168)-2, 1995
3. W.W. Hansen, S.W. Janson, H. Helvajian, "Direct-Write UV Laser Microfabrication of 3D Structures in Lithium-Alumosilicate Glass," Proceedings of the SPIE, Vol. 2991 1997
4. D. Hülsenberg, R. Brunsch, K. Schmidt, F. Reinhold, *Mikromechanische Bearbeitung von fotoempfindlichem Glas*, Silikattechnik, Vol. 41 (1990), 364.
5. Foturan - A Material for Microtechnology, technical literature by Schott Glaswerke Optics Division and IMM Institut für Mikrotechnik GmbH Mainz Germany.
6. S. Janson, H. Helvajian, K. Breuer "Micropropulsion Systems for Aircraft and Spacecraft" in *Microengineering Aerospace Systems*, ed. H. Helvajian, (Aerospace Press El Segundo, CA) 1999, p 657
7. D. H. Lewis, Jr. S. W. Janson, R. B. Cohen and E. K. Antonsson, "Digital Micropropulsion", IEEE MEMS'99 Orlando, FL, paper 46 IEEE 99CH36291C

Planarization of hexagonal-GaN(0001) by KrF excimer-laser ablation followed by hydrochloric acid treatment

T. Akane ^a, K. Sugioka ^a, H. Ogino ^b, H. Takai ^b and K. Midorikawa ^a

^a The Institute of Physical and Chemical Research (RIKEN),
Hirosawa 2-1, Wako, Saitama 351-0198, Japan

^b Department of Electrical Engineering, Faculty of Engineering,
Tokyo Denki University,
Kanda 2-2, Chiyoda, Tokyo 101-8457, Japan

ABSTRACT

GaN surface is clear etched by combination of KrF excimer laser irradiation and post chemical wet treatment using hydrochloric acid. KrF excimer laser irradiation ablates GaN surface and turns the ablated surface to Ga-rich layer. The Ga-rich layer is etched off by the hydrochloric acid treatment. X-ray photoelectron spectroscopy (XPS) analysis reveals that the chemically etched surface has similar composition and chemical bonding to untreated GaN. The average roughness amazingly decreases to ~48 % compared to the untreated GaN sample at the laser fluence increases beyond 1.5 J/cm².

Keywords: GaN, KrF excimer laser, ablation, planarization, X-ray photoelectron spectroscopy (XPS), Atomic force microscope (AFM)

1. INTRODUCTION

III-V nitride semiconductor crystals (GaN, InN and AlN) have Wurtzite structure at normal state and these materials show direct band-gap. Alloys can be formed with same crystal structures, By changing alloy composition, band-gap can be changed in the range of 1.95–6.0 eV continuously, these materials are most promising for light emitting devices covering from infrared to ultraviolet. In recent year, the processing techniques for III-V nitride such as GaN are successfully established especially on crystal growth, while the etching method is not still concrete because of their chemical stability or high hardness. Plasma etching¹ and reactive ion etching (RIE),^{2, 3} are mainly applied for etching of III-V nitride crystals. In those manners, damages by ion or plasma bombardment will be serious problems. Photoassist wet etching,^{4, 5} and electrochemical etching,^{6, 7} based on conventional wet etching method, and melt-back etching⁸ based on technique of liquid phase epitaxy (LPE) is reported.

Laser processing has the advantages in preventing damages and contaminations, and has the spacial selectivity with high resolution while there is few report on laser processing of III-V nitride crystals. ArF excimer laser-assisted ablation using HCl gas,⁹ microfabrication using multiwavelength light source for direct machining of GaN.¹⁰ Excimer laser is thought to have the advantages of photon-cost and processing speed. Recently, KrF excimer laser etching of GaN and AlN¹¹ was demonstrated to show high efficiency of the direct-laser etching, where the etching rate was ~ 1400 Å/pulse, high surface roughness was obtained. Obtaining flat surface at the etching area is an important issue,

Corresponding author: T. Akane, E-mail: akane@postman.riken.go.jp, Fax: +81 48 462 4683; Phone: +81 48 462 1111 ex. 4454

for example, in the pre-treatment for homoepitaxial growth or metalization, however, it is difficult to obtain with high etching rate. In this paper, we characterize KrF excimer laser ablation of GaN, and report the planarization effect.

2. EXPERIMENTAL

Samples used were Mg-doped 700 nm-GaN/10 nm-AlN/Al₂O₃(0001) grown by gas-source molecular beam epitaxy (GSMBE) using Ga metal, RF plasma-cracked N₂ and Mg metal as Ga, N and Mg source, respectively. Hall concentration of GaN epilayer was $1 \times 10^{18} \text{ cm}^{-3}$.

The experimental setup are depicted in Fig. 1. Base pressure of the chamber was $\sim 1 \times 10^{-6}$ Torr. KrF excimer

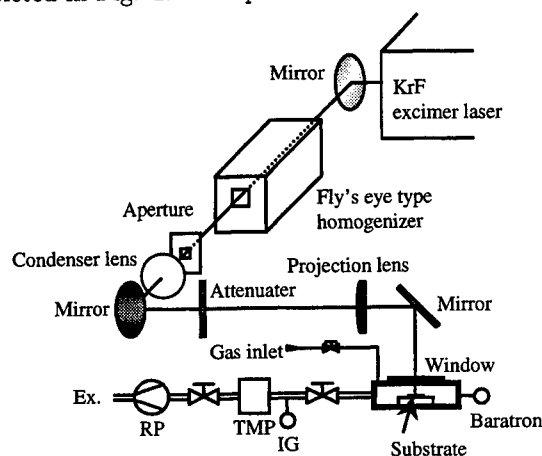


Fig. 1. Schematic diagram of the experimental setup.

laser ($\lambda=248 \text{ nm}$, FWHM=34 ns, Lambda Physik: LPX200) was employed for a light source. The laser beam was homogenized and projected into $2.2 \times 2.2 \text{ mm}^2$ area. Ambient was 760 Torr N₂. The laser fluence (E_d) was ranged from 0.2 to 3.5 J/cm^2 and number of laser pulse was set at 1. After laser irradiation, damaged layer at the ablated area was etched by 35 %-hydrochloric acid for 5 min-dipping. Etched depth was measured by stylus profiler. Surface morphology was observed by optical microscope and atomic force microscope (AFM) in the tapping-mode operation. Surface state of laser-irradiated area was evaluated by X-ray photoelectron spectroscopy (XPS).

3. RESULTS AND DISCUSSION

As-irradiated samples exhibited metallic color and soft surface with cracks, which infers that nitrogen effuse from the ablated surface and forming of Ga-rich layer (crystal decomposition).

Ablation of GaN surface was confirmed above the laser fluence of 0.3 J/cm^2 . Figure 2 shows the laser fluence dependence of the ablation/Etched depth. The filled triangles and opened squares represent the ablation depth of as-irradiated sample and total etching depth after hydrochloric acid treatment, respectively. High etching rate of $\sim 130 \text{ nm/pulse}$ (nm/s) was attained at 3.5 J/cm^2 .

Generally, laser fluence penetration depth profile is given by

$$I(z) = I_0 \exp(-\alpha z), \quad (1)$$

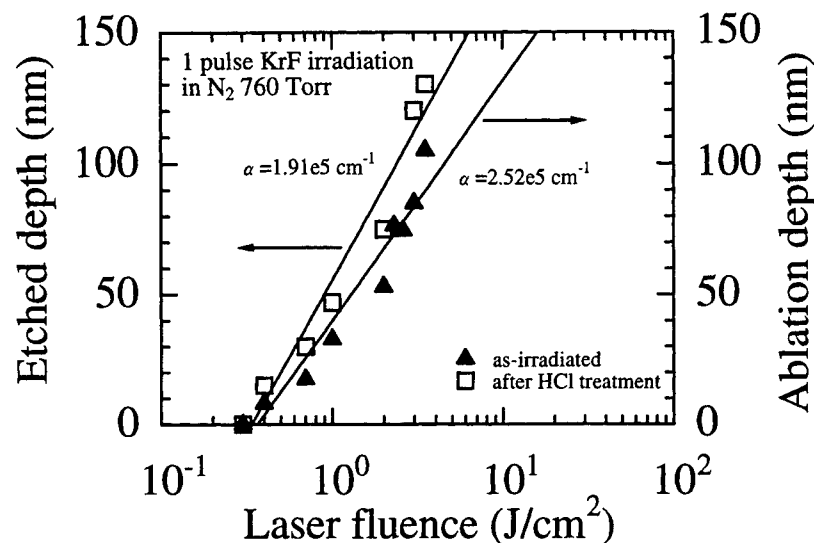


Fig. 2. Laser fluence dependence of the ablation/Etched depth. irradiated number of pulse is 1.

where $I(z)$ is the laser fluence at depth z , I_0 is the laser fluence at surface and α is the absorption coefficient. Since the ablation depth z_{ab} gives ablation threshold fluence $I(z_{ab})$, the laser fluence at ablation depth is expressed by

$$I(z_{ab}) = I_0 \exp(-\alpha z_{ab}), \quad (2)$$

therefore,

$$\begin{aligned} z_{ab} &= \frac{1}{\alpha} (\ln I_0 - \ln I(z_{ab})) \\ &= \frac{1}{\alpha} \ln \left(\frac{I_0}{I(z_{ab})} \right). \end{aligned} \quad (3)$$

thus, z_{ab} linearly depends upon $\ln I_0$ with the slope $1/\alpha$. Equation (3) is fitted to plots in Fig. 2 to evaluate α . The α was obtained to be $1.91 \times 10^5 \text{ cm}^{-1}$ and $2.52 \times 10^5 \text{ cm}^{-1}$ for plots of after hydrochloric acid treatment and as-irradiated, respectively. Recently, absorption coefficient of GaN film was determined to be $2.0 \times 10^5 \text{ cm}^{-1}$ for 5 eV-photon by transmission measurement.¹² Absorption coefficient obtained from samples after hydrochloric acid treatment shows well agreement with the reported value ($\alpha = 1.91 \times 10^5 \text{ cm}^{-1}$), i.e., the crystal decomposition proceeds with 1 photon absorption. While, absorption coefficient obtained from the as-irradiated samples ($2.52 \times 10^5 \text{ cm}^{-1}$) shows slightly large value compared to the reported value ($2.0 \times 10^5 \text{ cm}^{-1}$). This may mean that the ablation of GaN proceeds with 1 photon absorption and attached thermal effect.

Figure 3 shows Ga3d XPS narrow-scan spectra obtained from as-irradiated samples (as-ablated surface) with the (b) $E_d = 0.4 \text{ J/cm}^2$, (c) 1.0 J/cm^2 , (d) 1.5 J/cm^2 , (e) 2.0 J/cm^2 and (f) 3.0 J/cm^2 . Spectrum (a) was obtained from an unirradiated sample. As the E_d increase ($> 0.4 \text{ J/cm}^2$), XPS spectra of ablated surfaces can be deconvoluted by GaN and off-stoichiometric (Ga-rich) peaks, which indicating that an increase of laser fluence causes Ga-N bond dissociation at the ablated surface. At laser fluences over 2.0 J/cm^2 , peaks corresponding to metal-Ga are detected.

XPS spectra in Fig. 4 obtained from the samples after dipping in hydrochloric acid showing with some E_d as a parameter, (a) $E_d = 1.0 \text{ J/cm}^2$, (b) 2.0 J/cm^2 and (c) 3.0 J/cm^2 . It is obvious that the Ga-rich layer is completely

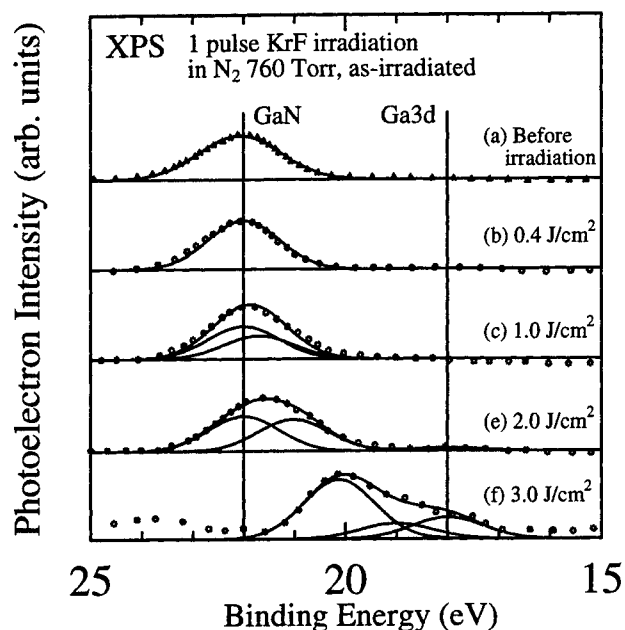


Fig. 3. Ga3d XPS narrow-scan spectra obtained from as-irradiated samples with the various E_d , (a) before irradiation (b) 0.4 J/cm², (c) 1.0 J/cm², (d) 1.5 J/cm², (e) 2.0 J/cm² and (f) 3.0 J/cm².

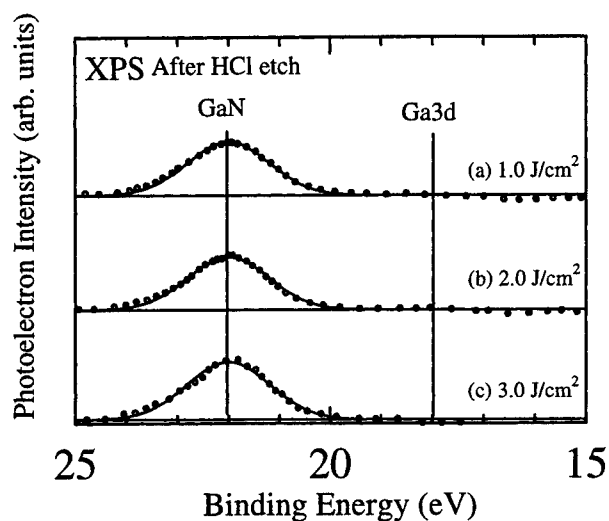


Fig. 4. XPS spectra around the Ga3d level obtained from the samples after dipping in hydrochloric acid. (a) $E_d = 1.0$ J/cm², (b) 2.0 J/cm² and (c) 3.0 J/cm².

removed by 5 min hydrochloric acid treatment at the every E_d .

Figure 5 (a)–(d) illustrate AFM images of the samples after hydrochloric acid treatment, with (a) no laser irradiation, (b) $E_d = 0.7$ J/cm², (c) 2.0 J/cm² and (d) 3.5 J/cm². The scanning area was 5 μm^2 . From these AFM images, it can be said that the surface of GaN is flattened with the increase of E_d . The E_d dependence of average roughness (R_a) is summarized in Fig. 6. R_a saturates with the E_d increase beyond 1.5 J/cm², and R_a is lowered to ~ 4.9 nm from 10.2 nm for the untreated sample, i.e., ~ 48 %, at $E_d = 3.5$ J/cm². Thus, higher E_d is desirable for

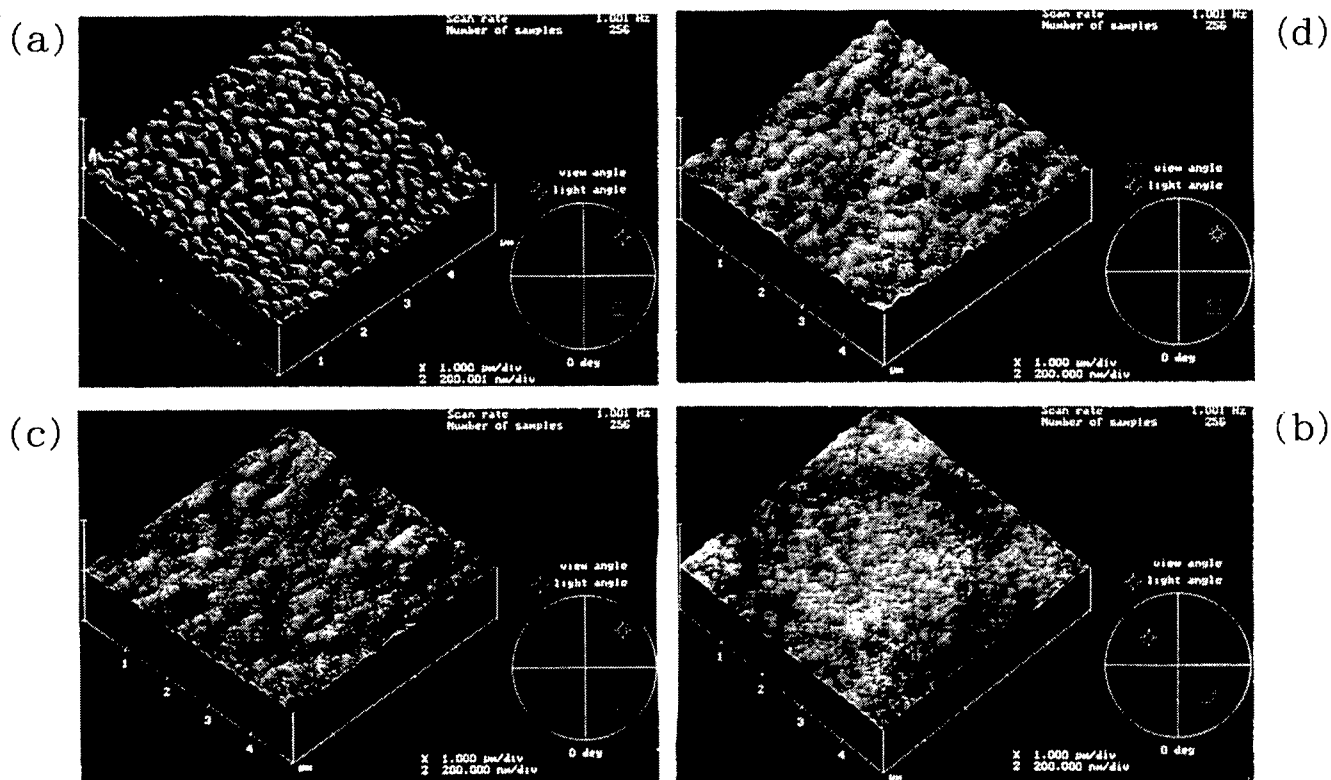


Fig. 5. AFM images of surfaces after hydrochloric acid treatment, with (a) no laser irradiation, (b) $E_d = 0.7 \text{ J/cm}^2$, (c) 2.0 J/cm^2 and (d) 3.5 J/cm^2 . The scanning area is $5 \mu\text{m}$. 1 div. of vertical axis represents 200 nm.

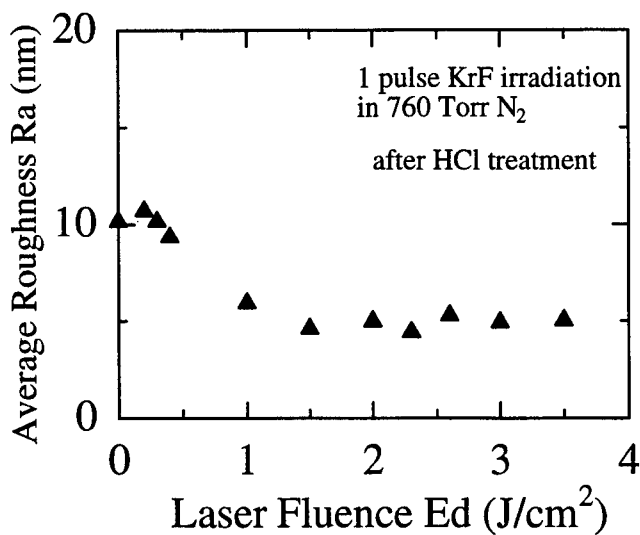


Fig. 6. E_d dependence of average roughness (R_a).

obtaining flat surface. Higher fluence irradiation usually causes surface roughening, however, in this case, the Ga-rich layer is considered to disperse heat with higher conductivity compared to GaN, which may average the distribution of heat penetration depth in GaN caused by the roughness of an as-grown surface.

Here, we define the successive process of 1 pulse irradiation and post 5 min-hydrochloric acid dipping as "one cycle". Fig. 7 shows R_a reduction with the number of the cycles increases in case of $E_d = 1.5 \text{ J/cm}^2$. This result

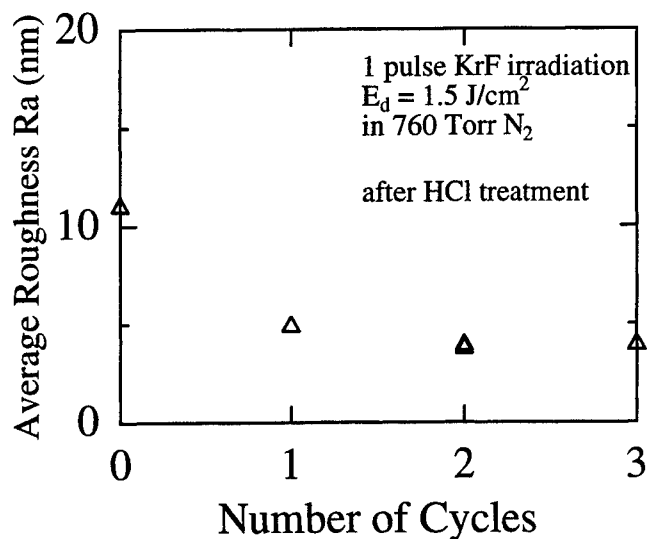


Fig. 7. R_a as a function of the cycles. $E_d = 1.5 \text{ J/cm}^2$.

reveals that the repetition of KrF-irradiation and hydrochloric acid treatment can also make GaN surface flat.

Crystal quality is evaluated by five crystals X-ray diffraction. E_d dependence of FWHM of GaN(0002) locking curve is shown in Fig. 8. Distribution of the unirradiated crystal's FWHM is shown as an error bar at $E_d = 0 \text{ J/cm}^2$.

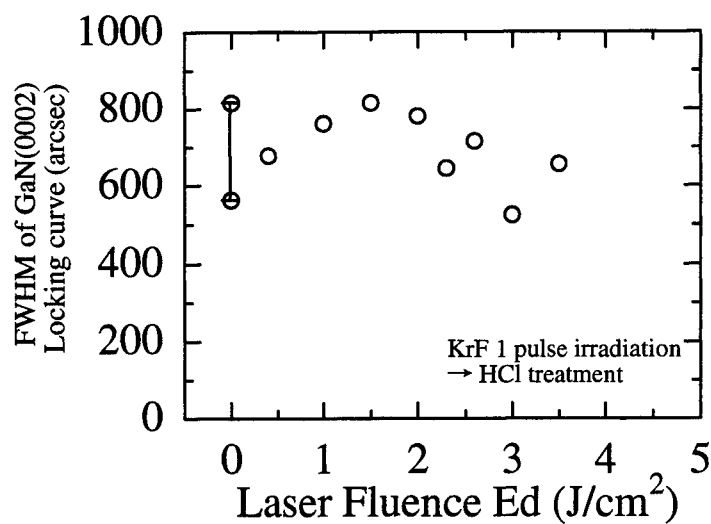


Fig. 8. FWHM of GaN(0002) locking curve as a function of the E_d .

No increase of FWHM is observed with increase of E_d . Thus, crystal structure was maintained with increase of E_d at the range of 0.4–3.5 J/cm^2 .

4. CONCLUSION

In conclusion, surface of GaN crystals was successfully flattened by the combination of KrF excimer laser irradiation and post hydrochloric acid treatment. GaN is ablated by KrF excimer laser irradiation and ablated surface was changed to off-stoichiometric Ga-rich layer. The Ga-rich layer is completely removed by the hydrochloric acid treatment and etched surface is flattened dramatically with the E_d increasing. No severe degradation of crystal structure was found in samples irradiated with high laser fluence (3.5 J/cm^2). This method should be proposed for high quality etching and planarization of GaN surface.

ACKNOWLEDGMENTS

The authors would like to acknowledge TRICHEMICAL Lab., Inc. for obtaining GaN epi-wafer. They would also like to thank Y. Iimura and M. Otake in RIKEN for experimental support.

REFERENCES

1. S. A. Smith, C. A. Wolden, M. D. Bremser, A. D. Hanser, R. F. Davis and W. V. Lampert, "High rate and selective etching of GaN, AlGaIn, and AlN using an inductively coupled plasma", *Appl. Phys. Lett.* **71**, pp. 1631–1633, 1997.
2. D. Basak, M. Verdu, M. T. Montojo, M. A. Sanchez-Garcia, F. J. Sanchez, E. Munoz and E. Calleja, "Reactive ion etching of GaN layers using SF_6 ", *Semicond. Sci. Technol.* **12**, pp. 1654–1657, 1997.
3. J. B. Fedison, T. P. Chow, H. Lu and I. B. Bhat, "Reactive ion etching of GaN in BCl_3/N_2 plasmas", *J. Electrochem. Soc.* **144**, pp. L221–L224, 1997.
4. M. S. Minsky, M. White and E. L. Hu, "Room-temperature photoenhanced wet etching of GaN", *Appl. Phys. Lett.* **68**, pp. 1531–1533, 1996.
5. C. Youtsey, G. Bulman and I. Adesida, "Dopant-selective photoenhanced wet etching of GaN", *J. Electronic Materials* **27**, pp. 282–287, 1998.
6. S. Yoshida, "Electrochemical etching of a conductive GaN crystal for patterning", *J. Crystal Growth* **181**, 293–296, 1997.
7. C. Youtsey, G. Bulman and I. Abesida, "Photoelectrochemical etching of GaN", *Mat. Res. Soc. Symp. Proc.* **468**, pp. 349–354, 1997.
8. Y. Kaneko, N. Yamada, T. Takeuchi, Y. Yamaoka, H. Amano and I. Akasaki, "Melt-back etching of GaN", *Solid-State Electronics* **41**, pp. 295–298, 1997.
9. R. T. Leonard and S. M. Bedair, "Photoassisted dry etching of GaN", *Appl. Phys. Lett.* **68**, pp. 794–796, 1996.
10. J. Zhang, K. Sugioka, S. Wada, H. Tashiro, K. Toyoda and K. Midorikawa, "Precise microfabrication of wide band gap semiconductors (SiC and GaN) by VUV-UV multiwavelength laser ablation", *Appl. Surf. Sci.* **127–129**, pp. 793–799, 1998.
11. H. Chen, R. D. Vispute, V. Talyansky, R. Enck, S. B. Ogale, T. Dahmas, S. Choopun, R. P. Sharma, T. Venkatesan, A. A. Iliadis, L. G. Salamanca-Riba and K. A. Jones, "Pulsed laser etching of GaN and AlN films", *Mat. Res. Soc. Symp. Proc.* **482**, pp. 1015–1020, 1998.
12. J. F. Muth, J. H. Lee, I. K. Shmagin, R. M. Kolbas, H. C. Casey, Jr., B. P. Keller, U. K. Mishra and S. P. DenBaars, "Absorption coefficient, energy gap, exciton binding energy, and recombination lifetime of GaN obtained from transmission measurements", *Appl. Phys. Lett.* **71**, pp. 2572–2574, 1997.

SESSION 5

Innovative Laser Technology for Industrial Applications

Laser applications in electronics and optoelectronics industry in Japan

Kunihiko Washio

Control Systems Operations Unit, NEC Corporation, Sagamihara 229-1198 Japan

ABSTRACT

This paper explains current status and technological trends in laser materials processing applications in electronics and optoelectronics industry in Japan. Various laser equipment based on solid state lasers or gas lasers such as excimer lasers or CO₂ lasers has been developed and applied in manufacturing electronic and optoelectronic devices to meet the strong demands for advanced device manufacturing technologies for high-performance, lightweight, low power-consumption portable digital electronic appliances, cellular mobile phones, personal computers, etc. Representative applications of solid-state lasers are, opaque and clear defects repairing of photomasks for LSIs and LCDs, trimming of thick-film chip resistors and low resistance metal resistors, laser cutting and drilling of thin films for high-pin count semiconductor CSP packages, laser patterning of thin-film amorphous silicon solar cells, and laser welding of electronic components such as hard-disk head suspensions, optical modules, miniature relays and lithium ion batteries. Compact and highly efficient diode-pumped and Q-switched solid-state lasers in second or third harmonic operation mode are now being increasingly incorporated in various laser equipment for fine material processing. Representative applications of excimer lasers are, sub-quarter micron design-rule LSI lithography and low-temperature annealing of poly-silicon TFT LCD.

Keywords: repairing, trimming, cutting, drilling, patterning, welding, lithography, annealing, laser equipment

1. INTRODUCTION

Laser materials processing has several excellent features, which are increasingly satisfying industry's requirements such as for high-speed, high-precision, clean and flexible processing technologies for swift delivery of high-value added innovative products with reasonable or minimized costs. According to the questionnaire survey conducted in the summer of 1998 in Japan, the number of lasers installed per manufacturing company has considerably increased during recent ten years¹. Exceeding ten thousand laser systems are estimated to be currently in operation in electronics industry.

Various laser materials processing technologies have been developed and been applied for manufacturing electronic and optoelectronic devices, because of their widely different requirements for treating thin-films, thick-films, metals, ceramics, polymers, etc. Owing to the recent increased demands for light-weight, high-speed portable electronic appliances, such as cellular phones, digital still cameras, note PCs (personal computers), PDAs (portable digital assistants), fine laser materials processing based on short-wavelength- or short-pulse lasers are becoming vital and indispensable technologies for the development and manufacturing leading-edge products in electronics and optoelectronics industry. Compact and highly efficient diode-pumped and Q-switched solid-state lasers in second or third harmonic operation mode as well as in fundamental wave mode are now being increasingly incorporated in various laser materials processing systems such as for repairing, marking, drilling and patterning. Excimer lasers are being extensively utilized in lithography and annealing.

This paper briefly summarizes what parts or devices are utilizing what kinds of laser materials processing and what kinds of lasers are currently preferably utilized. Detailed explanation will be given on the technological state of the arts and trends in some representative application fields in electronics and optoelectronics industry in Japan.

2. SUMMARY OF REPRESENTATIVE APPLICATIONS

Some representative applications of laser materials processing in electronics and optoelectronics industry are summarized in Table 1. With a glance at Table 1, it can be safely said that almost all present-day leading-edge portable or multimedia electronic appliances are at least utilizing some devices treated with laser material processing. For example, key devices such as LSIs, TFT(thin-film transistor)-LCDs, multi-layer build-up circuit boards, lithium ion batteries, are increasingly utilizing some kinds of laser materials processing.

* Correspondence: E-mail: washio@lam.sgm.nec.co.jp; Telephone: +81-42-771-0655; Fax: +81-42-771-0823

Table 1. Representative applications of laser materials processing in electronics and optoelectronics industry

Classification	Components or devices	Applications of laser materials processing	Typical lasers used
Semiconductor devices	Photomasks (reticles) Si wafers LSIs DRAMS Optical modules IC Packages CSP IC packages	LSI photomask repairing Wafer marking Excimer laser lithography Memory repairing High precision spot welding IC package marking Interposer micro-via drilling	Q-switched solid-state lasers Q-switched solid-state lasers KrF or ArF excimer lasers Q-switched solid-state lasers Pulsed Nd:YAG lasers Q-switched solid-state lasers Q-switched solid-state lasers
Display devices	Photomasks for LCDs TFT-LCDs Poly-Si TFT-LCD TV tubes	LCD photomask repairing TFT-LCD repairing Low temperature excimer laser annealing High precision electron-gun spot welding	Q-switched solid-state lasers Q-switched solid-state lasers XeCl excimer lasers Pulsed Nd:YAG lasers
Circuit components	Chip resistors Quartz oscillators Printed circuit boards Relays Component packages	Resistor trimming Quartz oscillator tuning Build-up circuit board via drilling Assembling by laser spot welding Component package marking	Q-switched solid-state lasers Q-switched solid-state lasers Pulsed CO ₂ lasers Pulsed Nd:YAG lasers Nd:YAG or CO ₂ lasers
Peripheral devices	Hard disks Hard disk sliders Ink-jet printer heads Key boards, key pads	Hard disk (HD) laser texturing HD slider suspension spot welding Ink-jet printer nozzle drilling Laser marking	Q-switched solid-state lasers Pulsed Nd:YAG lasers KrF or ArF Excimer lasers Q-switched solid-state lasers
Energy devices	Lithium ion batteries Amorphous silicon solar-cell modules	Seam welding of battery cases Laser patterning of amorphous silicon solar cell modules	Pulsed Nd:YAG lasers Q-switched solid-state lasers

3. TYPICAL LASERS USED IN ELECTRONICS AND OPTOELECTRONICS INDUSTRY

Figure 1 shows typical lasers used in electronics and optoelectronics industry and relevant applications in accordance with their typical average power. Solid state lasers used are either Nd:YAG, Nd:YLF, or Nd:YVO₄ lasers. They are used either

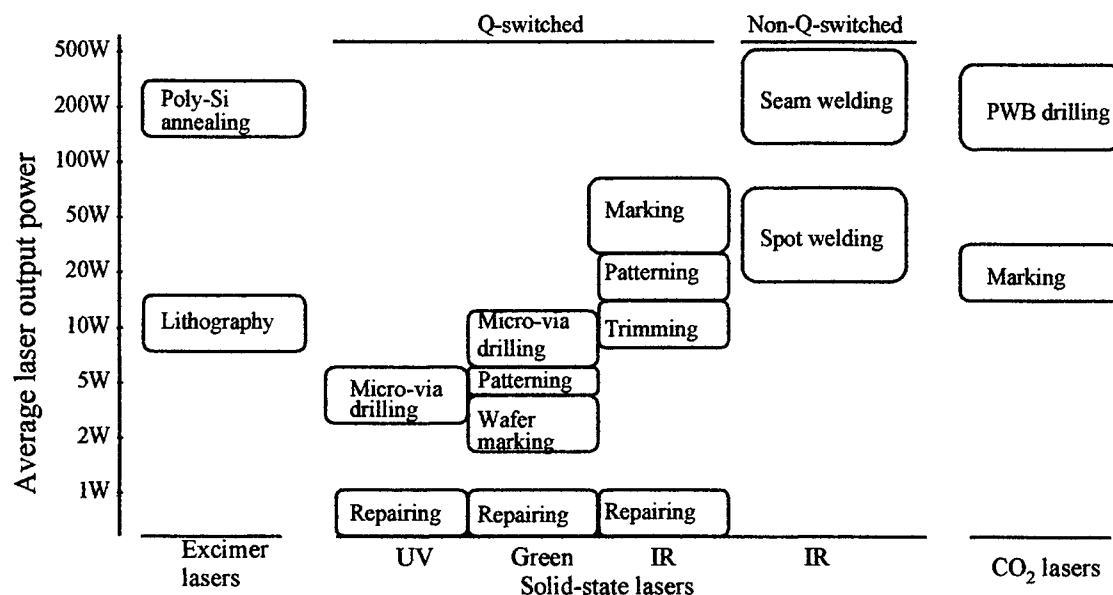


Fig. 1 Typical lasers used in electronics and optoelectronics industry and relevant applications in accordance with their typical average power. Solid state lasers are either Nd:YAG, Nd:YLF, or Nd:YVO₄ lasers.

in fundamental (IR) operation mode or in second -harmonic (green) , or third and higher harmonic (UV) operation mode. For Q-switched laser applications with average laser power less than 20W, compact and highly efficient diode-pumped solid-state lasers in second or third harmonic operation mode as well as in fundamental wave mode are now being preferably utilized than lamp-pumped lasers. For low power application of CO₂ lasers, RF-excited waveguide type lasers are dominantly utilized.

4. REPRESENTATIVE APPLICATIONS AND TECHNOLOGICAL TRENDS

4.1 Photomask Repairing

The masks used for lithography are required to be entirely defect-free. There are mainly two different application fields for masks, namely, LSIs and LCDs. Minimum feature sizes for LSI masks are becoming very small. For 0.25 μ m design rule devices such as 256M DRAM, for example, minimum line and space of 1 μ m and linewidth accuracy of 0.04 μ m are required for a mask to be used with a stepper having four times magnification. Therefore, high-precision repairing is absolutely necessary for LSI masks. For LCD applications, mask sizes are becoming larger and larger, well exceeding 600mm. Therefore, high-throughput repairing is necessary for large size defects in LCD masks. Table 2 shows trends of key specifications of NEC's mask repairs for LSIs and LCDs since 1983 ².

Table 2 Trends of key specifications of NEC's mask repairs for LSIs and LCDs

Year of product release	1983	1991	1995	1998
Product models for LSIs	SL452 A	SL453C	SL453X	SL458A
Accuracy (μ m)	± 0.3	± 0.2	± 0.1	± 0.1
Repairing function	Opaque defect repair	Opaque defect repair	Opaque defect repair	Opaque and Clear defect repair
Laser wavelength (nm)	1064	532	532	355 and 349
Pulse width (ns)	~ 6	~ 4	Subns.	Subns. (Zapping) 50 ns (4kHz, CVD)
Product models for LCDs		SL465B	SL465C	SL465D
Substrate size (mm)		610 \times 510	900 \times 870	900 \times 870
Lasers for zapping		532nm, 4ns	355nm, 4ns	355ns, 4ns
Lasers for CVD		532nm, 6kHz	266nm, 4kHz	355nm, 4kHz
Methods of CVD		Chamber type	Chamber type	Gas curtain type (Chamberless type)

Figure 2 shows an external appearance of a recently developed LSI mask repair SL458A, capable of repairing both opaque and clear defects². In order to obtain high throughput for clear defect repair by laser CVD (Chemical vapor deposition), a unique gas curtain type scheme has been developed to eliminate bulky and time consuming gas chamber.

Examples of observed mask patterns, before and after repairing, for repairing clear and opaque defects are shown in Fig.3. Average operating times required for repairing a defect are about 2 seconds for opaque repair (zapping) and about 6 seconds for clear defect repair (laser CVD), respectively.

To completely eliminate glass substrate transmission deterioration due to laser-caused surface damage during opaque-defect repair and to improve edge sharpness of opaque defect repair, lasers having shorter pulsewidths are strongly preferred. Recently commercialized mask repairs are incorporated with sub-nanosecond Q-switched lasers. Experiments are in progress to investigate for the capability of ultrashort pulses for repairing chromium masks and comparisons are being made on quality of repairing for pulses in the range from 30 ps to 150fs³.

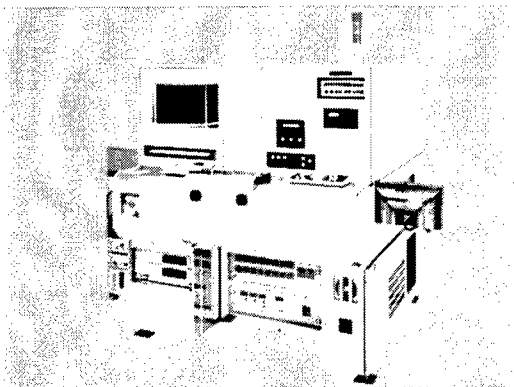


Fig. 2 External appearance of LSI mask repair SL458A.

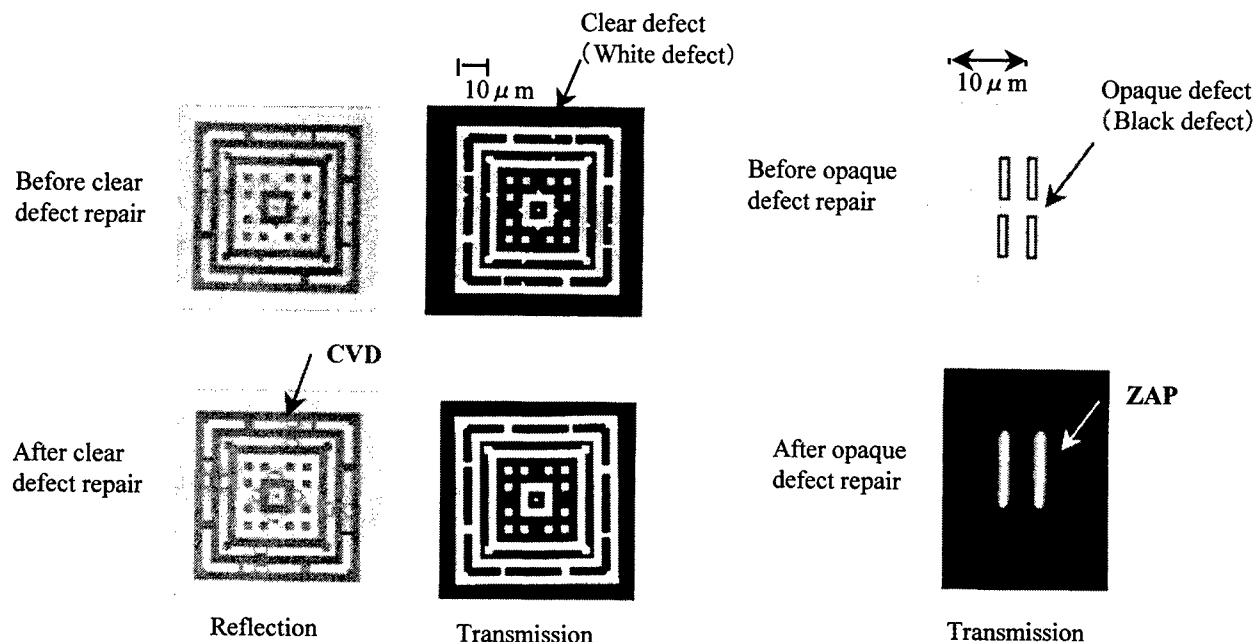


Fig. 3 Examples of observed mask patterns, before and after repairing, for repairing clear and opaque defects.

4.2 Excimer Laser Lithography

Today's dominant DRAM (Dynamic random memory) in market size is 64Mbit DRAM. Owing to recently attained significant progress in 248nm KrF excimer laser lithography technologies, share of shipment of KrF excimer laser exposure systems is rapidly increasing world-wide and seems to have exceeded 60% in 1998 as shown in Fig. 4⁴. With introduction of KrF excimer laser exposure systems, minimum design feature size has shrunk to $0.25 \mu\text{m}$ or below and sample production of 256Mbit DRAM has already started. Figure 5 shows example of NEC 256Mbit SDRAM (Synchronous DRAM)⁵. With introduction of upgraded exposure systems in 1998 having large NA (Numerical aperture) around 0.68-0.7 and KrF excimer laser spectral bandwidth of less than 0.6pm, mass production of LSIs having $0.18 \mu\text{m}$ design rule is expected to start in 1999. Mass production of $0.13 \mu\text{m}$ devices by using 193nm ArF excimer laser lithography is expected to start by 2001. Line and space patterns as narrow as $0.09 \mu\text{m}$ has been already demonstrated by using an ArF excimer laser exposure system⁶⁻⁷.

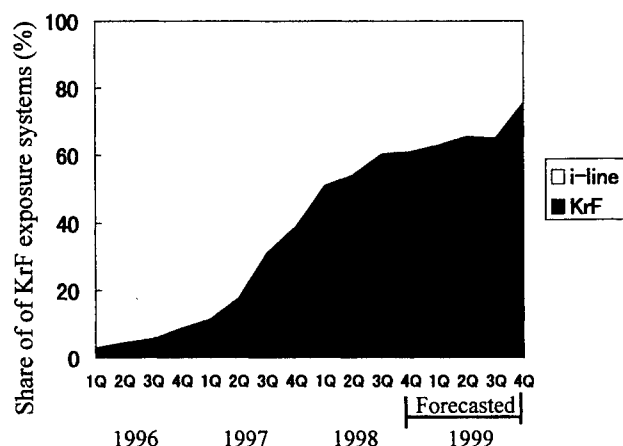


Fig. 4 Trends of world-wide quarterly shipment market share of KrF excimer vs. i-line exposure systems. After Nikkei Market Access, © 1998 NIKKEIBP.

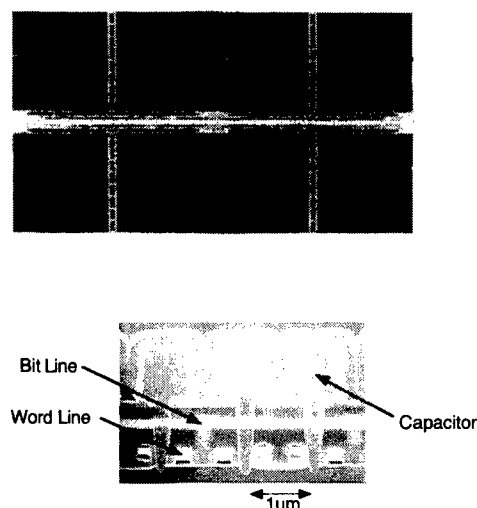


Fig. 5 Example of 256Mbit SDRAM⁵. Design rule: $0.22 \mu\text{m}$. Die size: 244.6mm^2 . Cell size: $0.55 \mu\text{m}^2$. KrF scanner was used.

4.3 Memory Repairing

Memory repair system is becoming increasingly necessary for improving yields of highly-integrated memory devices designed with shrunk feature sizes and having large number of bits per chip, such as 64Mbit DRAM and 256Mbit DRAM. Figure 6 shows an external view of NEC's novel memory repair system SL550A in development. This equipment is incorporated with a diode-pumped and high-repetition Q-switched Nd:YVO₄ laser and is capable of cutting fuses on the fly with maximum pulse rate up to 20kHz, realizing high throughput for wafers up to 300mm in diameter. Throughput depends on fuse layout. Minimum laser beam spot size on the wafer surface is 2 μ m. Overall positioning accuracy ($|X| + 3\sigma$) is equal to or better than 0.3 μ m for 200mm diameter wafers. Figure 7 shows arrays of fuses before and after laser cutting.

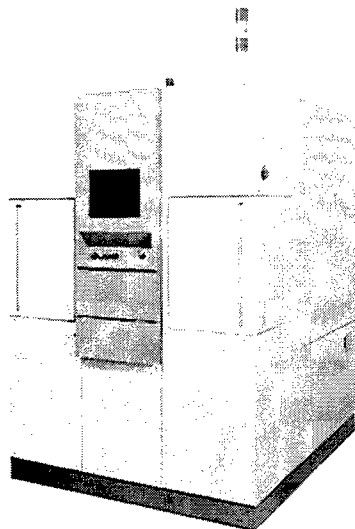


Fig. 6 External view of memory repair system SL550A

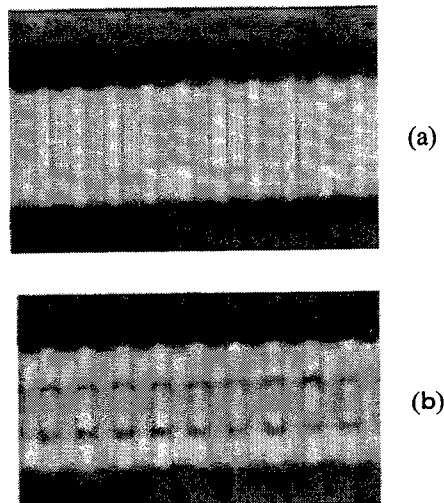


Fig. 7 Arrays of fuses before (a) and after (b) laser cutting.

4.4 Excimer Laser Annealing

Low-temperature poly-Si (LTPS) TFT LCD has several advantages of capability of integrating a peripheral driver circuit, achieving higher pixel density and realizing larger aperture ratio as compared with amorphous silicon TFT LCD, owing to its higher electron and hole mobility realized by excimer laser annealing (ELA) process⁸⁻⁹. ELA can convert amorphous Si layer to polycrystalline Si at low substrate temperature under 430°C, much lower than high-temperature poly-Si (HTPS) technology which requires quartz substrates, thus enabling use of inexpensive, large-size glass substrates. LTPS TFT LCD has found rapid and wide spread application such as digital still cameras and digital video camcorders. Figure 8 shows an example of digital still camera having 2-inch LTPS TFT LCD. Figure 9 shows a B5 size note notebook computer having 10.4-inch XGA (1024 \times 768) LTPS TFT LCD.

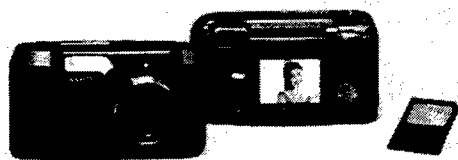


Fig. 8 Digital still camera (SANYO DSC-SX1Z) incorporated with 110,000 pixel 2-inch light collecting LTPS TFT LCD.

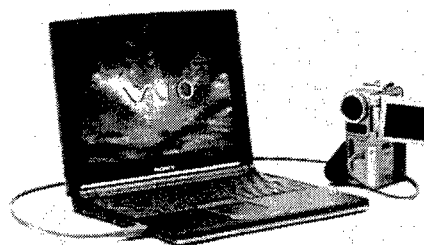


Fig. 9 Notebook computer (SONY VAIO [PCG-505RX]) incorporated with 10.4-inch XGA (1024 \times 768) LTPS TFT LCD and separately sold digital video camera [DCR-PC1].

4.5 Laser Marking

Laser marking seems to be the largest application segment in electronics industry, if installed number of laser systems are compared among various laser material processing applications. Continuously pumped and Q-switched Nd:YAG lasers are preferably utilized for marking various IC molded packages than CO₂ lasers because of their capability of fast and flexible marking with good visibility. For example, Nd:YAG laser based package marker NEC SL575CL has realized marking speed exceeding 330 characters per second for 1mm height alphanumeric characters on plastic molded packages. New types of package markers, CSP (chip size package) markers, have recently been commercialized by several manufacturers by incorporating diode-pumped and frequency-doubled Nd:YAG lasers. Figure 10 shows examples of CSP marking obtained with a CSP laser marker NEC SL576A. Laser markers incorporated with RF (radio-frequency) excited waveguide-type CO₂ lasers are separately finding wide range of applications such as marking colored plastic packages and printed circuit boards. Scanning type laser markers incorporated with galvano-mirrors are preferably utilized than mask type markers because of their ease and flexibility in changing marking contents swiftly

There are two types of laser marking methods, namely, soft marking and hard marking, for marking silicon wafers. For hard marking, 1.06 μ m fundamental wavelength Nd:YAG lasers are used to obtain deep engraved marking exceeding 100 μ m. For soft marking without splash and debris, frequency converted green (0.53 μ m) laser beams are utilized. Diode-pumped Nd:YAG lasers have been preferably utilized because of their excellent beam quality, reliability and compactness.

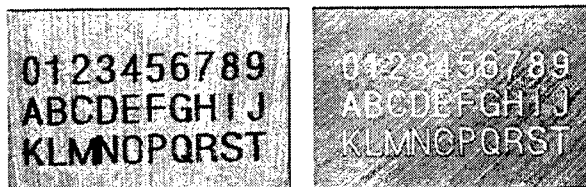


Fig. 10 Examples of CSP marking: Enlarged photos of black character marking and white character marking.

4.6 Laser Trimming

Owing to the increased demands for portable and compact electric appliances such as cellular mobile phones, digital cameras, notebook PCs, etc. laser trimming markets such as for smaller chip size resistors, ultra-low resistance chip resistors for current monitoring, and VCOs (Voltage controlled oscillators) are steadily expanding. Currently, dominantly mass-produced thick-film resistor chip size seems to have shifted from 2012 (2mm \times 1.2mm) toward 1608 (1.6mm \times 0.8mm) size and the production share of 1005 (1mm \times 0.5mm) size is also increasing considerably. A high speed and high precision laser trimmer NEC SL436G has been developed for small chip size resistors¹⁰. This laser trimmer is capable of trimming resistance as low as 10m Ω (optional)¹⁰. Figure 11 shows a SEM (scanning electron microscope) photograph of laser trimmed thick-film 1005 type resistor.

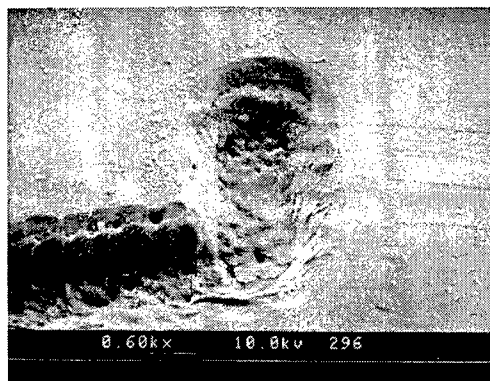


Fig. 11 SEM photograph of laser trimmed thick-film 1005 type chip resistor. Kerf width: ca. 30 μ m. Trimming speed: 50mm/s. Q-switched pulse repetition frequency: 10kHz.

4.7 Laser Via Drilling

Adoption of CSP packages and build-up printed circuit boards is preferable for both miniaturization and performance enhancement of electronic appliances. Build-up printed circuit boards are extensively utilized in portable and personal digital electronic appliances such as cellular mobile phones, digital video cameras (DVC) and digital still cameras (DSC)¹¹.

Figure 12 shows an example of compact cellular mobile phone Digital MOVA N206S for NTT DoCoMo and printed board NEC's DV-MULTI used in it¹¹. Laser process and photographic process are two methods practically utilized for drilling small vias less than 150 μ m in diameter, which are too small to drill mechanically¹². Laser process has advantages in flexibility for selection of materials to be drilled and ease in obtaining excellent cross sectional via shape. Laser via drilling is increasingly and preferably utilized for drilling smaller vias less than 100 μ m in diameter¹³. Figure 13 shows example of

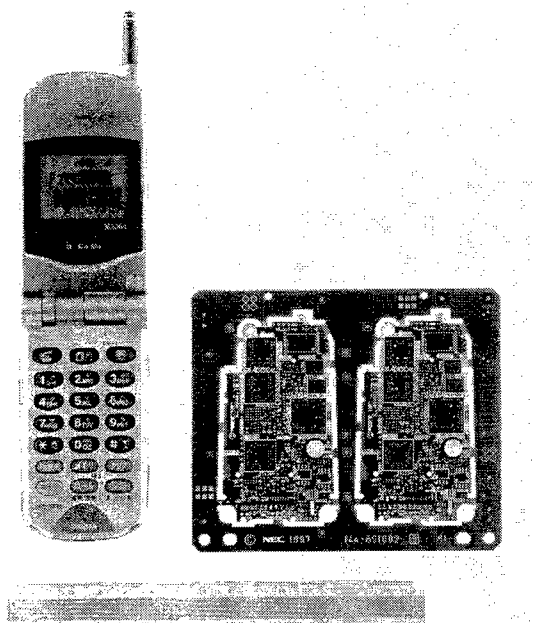


Fig. 12 Digital MOVA N206S for NTT DoCoMo and NEC DV-MULTI printed board¹¹ with vias drilled by laser process.

Cross-sectional view of blind via by laser process¹². Currently, pulsed CO₂ lasers are mainly utilized for drilling vias having diameter in the range 75-150 μ m because of their high power availability above 100W average power for obtaining high throughput allowing drilling exceeding 500 holes per second¹⁴.

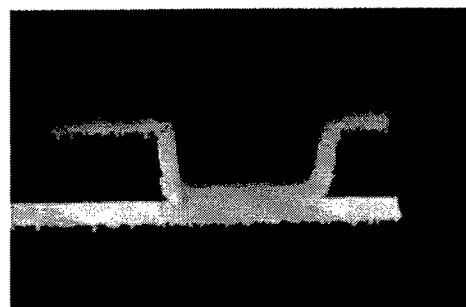


Fig. 13 Cross sectional view of blind vias by laser process¹².

For CO₂ lasers, it becomes very difficult to drill micro-vias smaller than 50 μ m, because of occurrence of strong diffraction for 9.4 μ m or 1.06 μ m infrared laser beams. For high pin count fine-pitch LSI packages, such as CSPs, substrates having build-up layers and having micro-vias holes with diameter much smaller than 50 μ m, are increasingly being incorporated as interposers for interconnecting signal lines from LSI chips to ball grid arrays. To make such micro-via holes, the drilling scheme employing repetitively pulsed UV lasers such as frequency tripled (THG) or frequency quadrupled Nd:YAG Q-switched lasers are well suited¹⁵⁻¹⁶, owing to their excellent focusability and higher absorption coefficients of metal film and organic substrate materials. Continuously diode-pumped and repetitively Q-switched Nd:YAG lasers can emit much shorter pulses with higher peak power than relevant lamp pumped lasers if compared at the same average power. Therefore, diode-

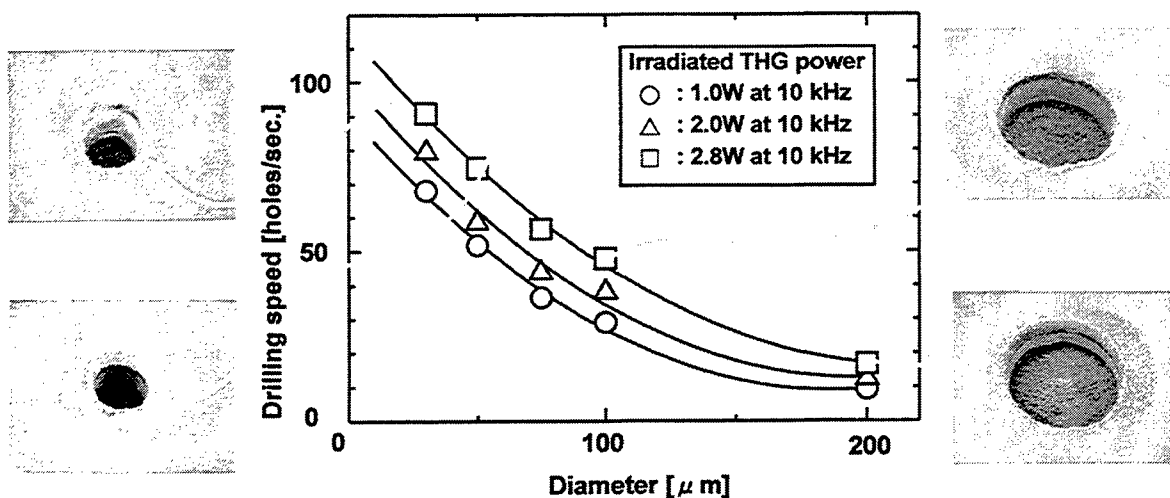


Figure 14 Blind via drilling speed dependence on via diameter and irradiated THG power measured for copper-laminated 25 μ m thickness polyimide films having 18 μ m thickness copper layer and 20 μ m thickness adhesive epoxy resin layer for both sides of polyimide films¹⁶.

pumped and Q-switched Nd:YAG lasers are desirable pumping sources for efficient generation of higher harmonic coherent waves.

355nm THG beam as high as 4.5W maximum average power has been obtained from 20W average power fundamental beam at Q-switch repetition rate of 10kHz¹⁶. Pulsewidth is about 35ns. Drilling characteristics of copper-laminated polyimide films have been extensively studied by using such UV laser beams. Figure 14 shows blind via drilling speed dependence on via diameter and irradiated THG power measured for copper-laminated 25 μ m thickness polyimide films having 18 μ m thickness copper layer and 20 μ m thickness adhesive epoxy resin layer for both sides of polyimide films¹⁶. Clean blind vias with very little smear have been obtained, enabling subsequent smear removal processing much simpler as compared with vias drilled by CO₂ lasers. In case of making blind via-holes with 50 μ m diameter, drilling speed of 76 holes per second has been so far obtained at an average power of 2.8W at 10kHz¹⁶. Efforts to increase drilling speed is in progress.

4.8 Laser Patterning of Solar Cells

Solar cell technology for generating electric power is a promising technology for alleviating so-called greenhouse problem caused by infrared light absorbing gases exhausted when fossil fuels are burnt. NEDO (New Energy and Industrial Technology Development Organization) is conducting research and development on thin-film solar-cells, focusing on the improvement of energy conversion efficiency and the development of mass production technology. Figure 15 shows an example of building-integrated solar cell modules for private housing¹⁷.

Amorphous silicon thin-film solar cells have several advantages over conventional crystalline silicon solar cells. For, example, they require a small amount of silicon and less energy in manufacturing, they can be fabricated into modules with large surface area¹⁷⁻¹⁸. Amorphous silicon thin-film can be deposited on various materials such as glass, polyimide, etc. Therefore, they are also suitable for obtaining see-through and flexible solar cell modules¹⁸ to be utilized for building windows, car sunroofs, etc.

Laser patterning is becoming a standard technology for realizing large area thin-film solar cell modules¹⁸. Repetitively Q-switched Nd:YAG lasers at 1.06 μ m fundamental wavelength is used to scribe TCO (transparent conductive oxide) thin-film made of SnO₂. Repetitively Q-switched and frequency-doubled Nd:YAG laser is used to selectively scribe amorphous silicon thin film on TCO without causing any damage on TCO thin film.

4.9 Laser Welding

Laser welding is well suited for assembling precise electronic or optoelectronic components accurately with high throughput. Laser welding is useful not only for miniaturization but also for accurate and secure connection. Laser spot welding has been extensively utilized for assembling electronic guns for TV tubes, fiber-optical devices¹⁹⁻²⁰ such as LD (laser diode) modules, miniature power relays²¹, ultra-light and thin suspensions for hard-disk head sliders, etc. Figure 16 shows an example of optical module assembled by laser spot welding. In assembling optical modules to efficiently couple diode laser power into a single-mode optical fiber, average coupling loss due to misalignment caused by pulsed laser irradiation for spot welding has been reduced to within

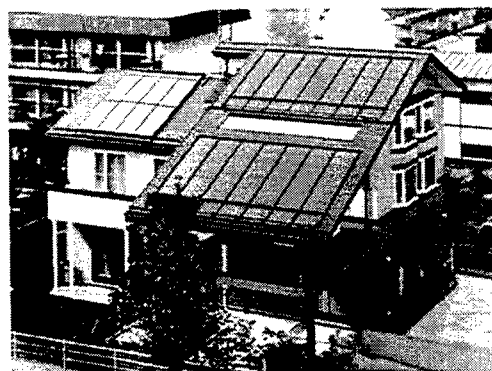


Fig. 15 Building-integrated solar cell modules for private housing¹⁷. (Photo: courtesy of NEDO)

0.1dB²⁰. Compact pulsed Nd:YAG lasers with average power in the range from 20W to 100W are predominantly used for these high precision spot welding.

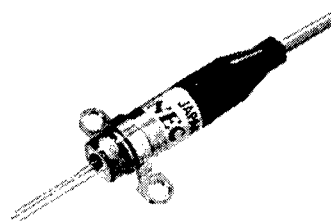


Fig. 16 Optical module for fiber-optic communications.

High-power, high-repetition rate pulsed-Nd:YAG laser enables high-precision seam welding. Pulsed Nd:YAG laser based seam welding has been extensively utilized in assembling rectangular lithium ion battery cells, fuel injectors, pressure sensors, etc. Figure 17 shows an example of seam welding of rectangular battery cell. Leak-free, excellent welding quality has been obtained with good surface bead appearance, without causing any serious deterioration of heat sensitive chemical components. Methods for penetration instability prevention has been investigated for seam welding of A3003 aluminum alloy²². For seam welding for joining various electronic parts, Nd:YAG lasers having average power in the range from 200W to 1200W are dominantly utilized.

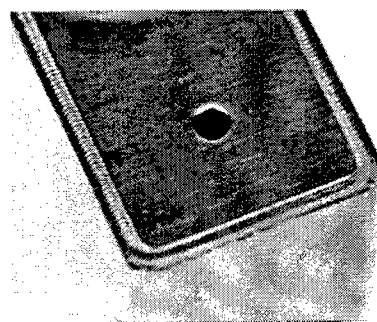


Fig.17 Seam welding of rectangular battery cell

5. CONCLUSION

This paper presented a review on current status and technological trends in laser materials processing applications in electronics and optoelectronics industry in Japan. Various laser systems based on solid state lasers or gas lasers such as excimer lasers or CO₂ lasers have been developed and applied in manufacturing electronic and optoelectronic devices to meet the strong demands for high-performance, lightweight, low power-consumption portable digital electronic appliances, cellular mobile phones, personal computers, etc. Representative applications of excimer lasers are sub-quarter micron design-rule LSI lithography and low-temperature annealing of poly-silicon TFT LCD. Representative applications of solid-state lasers are opaque and clear defects repairing of photomasks for LSIs and LCDs, trimming of thick-film chip resistors and low resistance metal resistors, laser cutting and drilling of thin films for high-pin count semiconductor CSP packages, laser patterning of thin-film amorphous silicon solar cells, and laser welding of electronic components such as hard-disk head suspensions, optical modules, miniature relays and lithium ion batteries.

Progress in high-average power light-sources capable of generating high-repetition-rate, short wavelength or short optical pulses, together with advancement in optics for high-precision materials processing, is expected to increasingly play a vital role for electronic and optoelectronic device performance improvement and manufacturing technology innovation.

ACKNOWLEDGMENT

The author would like to thank NEDO (New Energy and Industrial Technology Development Organization), ASET (Association of Super-advanced Electronics Technologies), Nikkei Business Publications, Inc., various companies in Japanese electronics industry and colleagues of NEC Corporation for lot of valuable information and stimulating discussions.

REFERENCES

1. I. Miyamoto, "Recent status of laser materials processing in Japanese Industry," *Proc. 45th Laser Materials Processing Conf.*, pp.111-119, 1998.
2. Y. Morishige and T. Kajikawa, "Laser mask repair," presented at the Laser Energy Applied Equipment Study Meeting, OITDA (Optoelectronic Industry and Technology Development Association), 19th June, 1998.
3. H. Kouta, Y. Kondo, K. Akagawa and K. Hirao, "Repairing of Cr-photo-mask by ultrafast-pulse laser," to be presented at the 19th Annual Meeting of the Laser Society of Japan, 22-23 Jan. 1999.
4. NIKKEI Market Access Report, No. 27 Supplement pp.17, December 1998. (<http://www.nikkeibp.co.jp/MA/>)
5. T. Saeki et al, "A 2.5ns clock access 250MHz 256Mb SDRAM with a synchronous delay", *Digest of Technical Papers of 1996 IEEE International Solid-State Circuits Conference*, pp.374, 1996.
6. M. Sasago, "Present status of ArF excimer laser lithography", *Optronics*, No.9, pp.106-111, 1997.
7. A. Ishitani, "Evolution of semiconductor technology", *J. Institute of Electronics, Information and Communication Engineers*, **81**, pp.1087-1092, 1998.

8. K. Yoneda, "State-of-the-art low temperature processed poly-Si TFT technology," *Proc. Society for Information Display (SID) IDRC97*, pp. M-40~M47, 1997.
9. K. Yoneda, Y. Segawa, T. Yamada, K. Kihara and R. Yokoyama, "A smart arrangement of TFTs in low-temperature poly-silicon circuitry for achieving higher effective yield in production," *Proc. Society for Information Display (SID) IDRC97*, pp. L-1~L-4, 1997.
10. K. Ohta, S. Horikoshi and Y. Saito, "Laser trimmer SL436G", *NEC Technology Journal*, **50**, No. 4, pp.14-17, 1997.
11. S. Noguchi, "Build-up printed board technology and its future," *NEC Technology Journal*, **51**, No. 10, pp.37-39, 1998.
12. S. Kuramata, T. Ito and S. Nakajima, "Production technology of build-up PWB," *NEC Technology Journal*, **51**, No. 10, pp.45-48, 1998.
13. Y. Matsumoto, "Application of build-up printed board and it's latest design standard trend," *NEC Technology Journal*, **51**, No. 10, pp.40-44, 1998.
14. S. Takeno, M. Moriyasu and M. Kukimoto, "Laser drilling of epoxy-glass printed circuit boards," *Proc. Laser Materials Processing Conference, Section B-ICALEO '97*, pp.63-72, 1997.
15. D. B. Noddin, E. Swenson and Y. Sun, "Solid-state UV-LASER technology for the manufacturing of high performance organic modules", *Proc. 48th Electronic Components and Technology Conference*, pp.822-827, 1998.
16. Y. Kyusho, M. Yonekawa, Y. Miyauchi, M. Tateno and H. Hatanaka, "THG-YAG laser drilling of micro-via holes in copper-laminated polyimide film," *Proc. 45th Laser Materials Processing Conf.*, pp.139-147, 1998.
17. NEDO home page, <http://www.nedo.go.jp>
18. K. Murata and S. Tsuda, "Features and applications of amorphous Si solar cells —See-through and flexible modules —," *Oyo Butsuri*, **67**, pp.1192-1196, 1998.
19. T. Shibuya, T. Shiga, K. Sato, K. Matsumoto and K. Hara, "Highly reliable LD modules," *NEC Res. & Develop.*, **32**, No.1, pp.76-81, 1990.
20. Y. Odagiri, F. Yoshimura, T. Siga and M. Tsukame, "YAG laser spot welding technique for fiber optics devices," *Optronics*, No.1, pp.49-53, 1994.
21. T. Ide, A. Kaito, K. Ichikawa, and K. Chiba, "Miniaturization of twin relay for automotive applications," *Proc. 42nd relay conference*, pp.23-1~23-6, Boston, May 9-11, 1994.
22. N. Nakamura, T. Togawa, K. Okino, S. Watanabe and K. Washio, "Seam welding of A3003 aluminum alloy using high-brightness pulsed slab YAG laser," *Proc. Laser Materials Processing Conference, Section G-ICALEO '97*, pp.130-139, 1997.

Advanced-laser processing of photonic and microelectronic components at Photonics Research Ontario

Peter R. Herman^{*a}, Gregory Goodno^b, Xijia Gu^c, Jeff B. Kalbfleisch^c, John Long^a, Marc Lukacs^d, Robin S. Marjoribanks^b, R.J. Dwayne Miller^b, Marc Nantel^{b,c}, Sola Ness^a, and Anton Oetti^b

^aDepartment of Electrical and Computer Engineering, ^bDepartment of Physics

^cPhotonics Research Ontario and University of Toronto
Toronto, ON, Canada, M5S 3G4

ABSTRACT

Photonics Research Ontario (PRO) is an Ontario Provincial Center of Excellence supporting a broad range of laser-processing activities within its photonics program. These activities are centered at the University of Toronto, and split between an industrial-user facility and the individual research programs of principal investigators. The combined effort furnishes forefront laser systems and advanced optical tools to explore novel processing applications in photonic, biomedical, and microelectronic areas. Facilities include laser micromachining stations, excimer-based mask-projection stations, extremely short wavelength lasers such as the molecular fluorine laser (157 nm), and ultrafast laser systems (100 fs – 1 ps). The latter two advanced lasers offer interesting advantages and contrasts in processing ‘difficult’ materials through linear and nonlinear absorption processes, respectively. These laser systems provide fine precision and strong interaction with a wide range of materials, including ‘transparent’ glasses, and also ceramics and metals. Applications fall broadly into several areas: wafer-level circuit trimming (electronics), high-resolution ultrasonic transducers (biomedical devices), and the shaping of optical waveguides and Bragg-gratings for photonic components (telecommunications). This paper summarizes the laser-processing infrastructure and research activities at PRO.

Keywords: laser micromachining, ablation, laser trimming, photonics, Bragg gratings, photosensitivity, ultrafast lasers.

1. INTRODUCTION

Laser systems and optical tools for laser-material processing are advancing rapidly on several evolutionary fronts. Both diode-pumped lasers and direct-diode lasers are now firmly entrenched in industrial processing. Sub-micron optical-tool beds routinely offer 1- μ m accuracy, key for new application areas in electronics, photonics, and micro-electromechanical structures (MEMs). Compact laser systems offer a wide assortment of wavelengths (ultraviolet to infrared), pulse durations (femtoseconds to continuous), and power levels to precisely control laser-matter interactions and provide the special capabilities needed for exploiting a much broader base of industrial applications. Short-wavelength excimer lasers (248, 193, and 157 nm) define the smallest features (200 nm) on today’s electronics semiconductor wafers. Science developments in the last decade have also brought reliable ultrafast lasers, and affordable electro-optical controls to shape pulses arbitrarily and adjust their duration. With both these advanced technologies, we now have the option of choosing between ‘multi-photons’ and ‘big photons’ in driving physical or chemical processes on material surfaces. These, and many other developments, have been instrumental in shaping a new generation of laser processing tools.

Photonics Research Ontario¹ (PRO) is an Ontario Centre of Excellence committed to enhancing the competitiveness of Ontario’s industrial sector by focusing R&D on specific and defined industry needs, and with the objective of transferring key photonics technology to industry. PRO supports a broad base of research activities at Ontario’s universities that include biophotonics, laser source development, light-matter interaction, optical communications, and nano-optics and materials. PRO also supports three resource facilities that interface with both industry and academic researchers: the Biomedical Facility, the Photonics Facility, and the Laser Micromachining Facility. Laser processing is a rapidly expanding activity at PRO, emerging from many years of basic studies in laser-matter interactions and laser source development at the University

^d Department of Physics, Queen’s University, Kingston, ON, Canada, K7L 3N1

* Correspondence: Email: hermanp@ecf.utoronto.ca; WWW: <http://www.ece.utoronto.ca/~hermanp>;
Telephone: 416-978-7722; Fax: 416-971-3020

of Toronto. The goals in this program are to capitalize on these early developments and create a center of forefront laser systems and tools for emerging new applications in processing photonic, electronic, and biomedical devices.

This invited paper provides a broad overview of the laser-processing activities and infrastructure supported, in part, by PRO. Conventional laser-processing systems include CO₂, Nd:YAG, diode-pumped lasers, and excimer lasers. Diode-pumped-laser applications offer general micromachining capabilities with $\sim 1\text{-}\mu\text{m}$ precision. One application area is the ablation of micron-size aluminum conductors, in order to trim microwave electronic circuits. In another, contact masks are laser-cut, and then used in an excimer-laser process to imprint long-period fiber gratings that flatten the gain of fiber-laser amplifiers. An excimer-laser mask-projection system has been optimized for cutting arrays having 10–15- μm slots on piezoelectric ceramic surfaces. The array provides ~ 40 MHz ultrasonic imaging for high-resolution medical applications.² At the cutting edge of laser technology, ultrafast lasers and very short-wavelength F₂ lasers have been developed at the University of Toronto to exploit novel material-processing applications. These lasers offer two 'extreme' approaches — multiple photons and big photons, respectively — to micromachining and to controlling the refractive index in glass. The advantages and limitations of these approaches are considered here for shaping photonic devices in fused silica.

2. LASER PROCESSING AS A TOOL

In the PRO facilities, staff scientists and a variety of academic and industrial partners have developed state-of-the-art laser-processing tools. This section describes three currently active project areas that involve laser trimming, laser-write cutting, large-area projection etching, and laser-induced refractive-index changes in glass fibers. These are prime examples of the use of mature laser technologies as tools to conduct research and development projects

2.1 Circuit Trimming

Laser micromachining finds widespread use in trimming and isolating electronic components on silicon-based integrated circuits. High-speed and microwave circuits are often laid out in a versatile architecture with test points, and several extra connections to optional components such as capacitors and resistors. During circuit testing and tuning, connections must be severed and/or others made, to better address the specific functionality of the final product. Laser processing is often used for this. Laser micromachining has the following attributes in severing connectors: 1) it is a non-contact and gentle etching process well-adapted to fragile chips, 2) features as small as a few microns can be ablated on highly convoluted surfaces with a tightly focussed laser beam, 3) precise-depth control of the ablation can be exercised, and 4) ablation plumes carry away much of the etched material, minimizing surface debris and contamination.

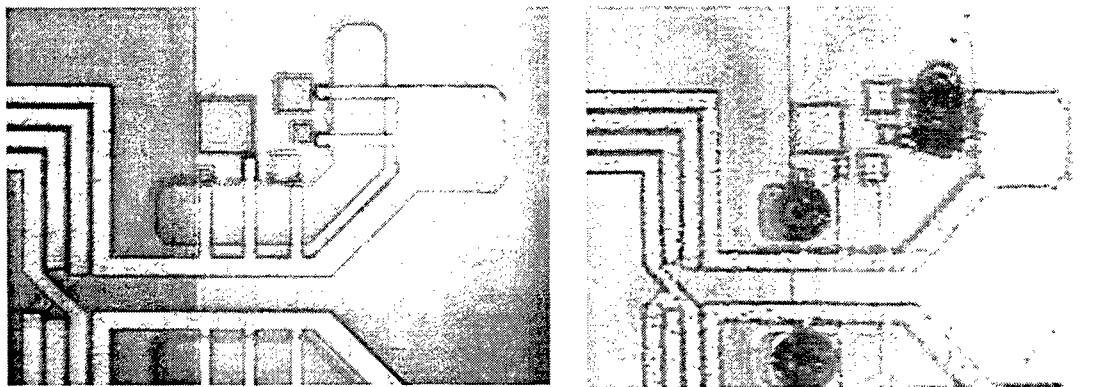


Figure 1: Enlarged detailed view of a radio-frequency mixer circuit on a silicon wafer before (left) and after (right) laser trimming. The aluminum wires (smallest are 3- μm wide) linking the coil to a series of five capacitors of different values (darker squares) can be selectively cut by the laser (four holes of $\sim 15\text{-}\mu\text{m}$ dia. on right) without affecting nearby structures. (The poorer resolution on right was due to lower lens magnification.)

Figure 1 shows part of a high-frequency mixer circuit containing several capacitors (squares of various sizes) initially connected to the circuit with 3- μm wide aluminum conductors (left photo). By selectively cutting the aluminum lines,

individual capacitors can be isolated and the total capacitance of this part of the mixer circuit tuned to the desired value. On the right is shown the same circuit with four lines ablated by the laser while neighboring structures remain untouched. The laser used in this case was a diode-pumped, air-cooled Nd:YAG (Spectra-Physics T40-X30-106QA) at 1.06- μm wavelength. In this particular exercise, each ablation hole was produced using 50-mW power in a 500-ms burst of 30-ns pulses at 4-kHz repetition rate. The etched holes are larger than the 3- μm wide connectors and collateral damage extends to $\sim 7\text{-}\mu\text{m}$ radius—less than the 10- μm spacing between adjacent aluminum lines (5- μm diameter spots were also produced). Collateral damage consists mainly of microcracked surfaces in the underlying 5- μm thick silicon-oxide layer. The laser pulse-train removed the entire 2- μm thickness of aluminum and $\sim 2\text{ }\mu\text{m}$ of silicon oxide. Depth control was particularly important to ensure complete electrical isolation of the capacitor without breaking into a buried conducting layer below the silicon-oxide insulator. A laser fluence of $\sim 10\text{ J/cm}^2$ was found to be optimal in maximizing the etching rate ($\sim 2\text{-nm}$ per pulse) without generating debris or substantial collateral damage. Circuits were successfully laser trimmed both before and after packaging.

2.2 Ultrasonic Transducers

Small high-frequency ($>30\text{ MHz}$) ultrasonic transducers, made from piezoelectric ceramics, are used in medicine to resolve small tissue-features in the skin and eye, and in intravascular imaging applications. Normally, a fixed-focused single-element transducer is physically scanned to capture a 2D-depth image. Linear-array transducers are more attractive, offering features such as variable focus, variable beam steering, and permitting more advanced image construction algorithms. For $>30\text{ MHz}$ array-transducers, this means structuring the surface of 50- μm thick ceramic slabs into 20- μm wide rectangular ribs with $\sim 15\text{-}\mu\text{m}$ wide grooves — sizes that separate the fundamental lateral and thickness resonance modes while also suppressing side lobes of the acoustic beam. Excimer lasers supply high-energy photons that drive photochemical decomposition during ablation of many materials. Such short wavelengths readily etch ‘difficult’ ceramic materials such as the lead zirconate titanate (PZT) used in such transducers. This beneficial process supports good surface morphology and high resolution without deleterious microcracking and incubation effects. Further, the large and uniform output beam of the excimer laser is most advantageous for beam-projection applications. PRO has established a 248-nm laser micromachining station for large-area etching ($\sim 3\text{ mm} \times 10\text{ mm}$) of $\sim 3\text{-}\mu\text{m}$ resolution — ideal characteristics for shaping small array structures on high-frequency ultrasonic transducers.

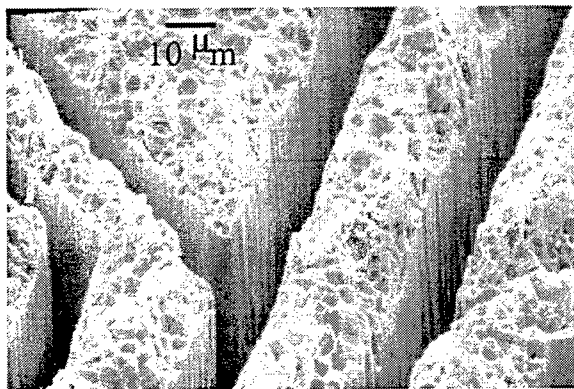


Figure 2: An angled close up view of the surface of an unpolished PZT ceramic etched with a first-generation 17-element laser micromachined array pattern. The width and depth of the cuts is 15 and 60 μm , respectively. The sides are straight with sharp edges. The sample was cleaned in an ultrasonic bath.

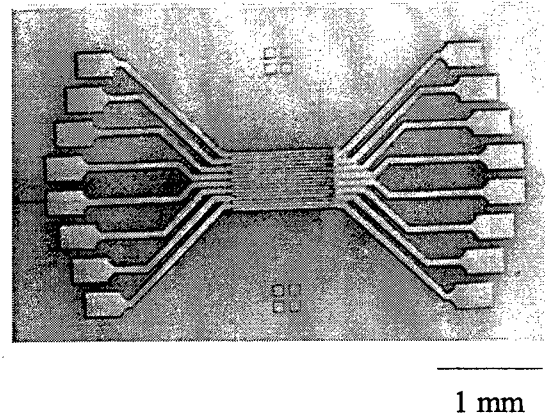


Figure 3: A second-generation 16-element linear-array structure designed with a single-wavelength pitch for use at 40 MHz. Each array element (in the center) fans back to a large bond pad on one side of the device. The array elements are 23- μm wide separated by 15- μm wide laser-cut trenches.

The projection-etching system at PRO applied a 50-Hz excimer laser (Lumonics Pulsemaster 844; 248 nm) delivering a pulse energy up to 350 mJ to a 10:1-demagnification optical-tool bed. To prevent damage to the Cr-quartz mask the incident fluence was reduced to 65 mJ/cm² providing on-target fluence of 6.5 J/cm². The beam was smoothed and collimated with a beam homogenizer and field lens, respectively, in order to provide a uniform etch depth of $\sim 6\text{ }\mu\text{m}$. Since the whole mask

could not be illuminated at once, the mask and the sample were moved synchronously with sub-micron precision such that the complete ceramic array could be machined in a seamless fashion. This approach permits the complete fabrication of a complex array-structure in ~5 minutes, with minimal thermal and mechanical collateral damage. The SEM photograph in Figure 2 shows the high aspect-ratio slots milled into the PZT ceramic; the full transducer array is shown in Figure 3. Such devices are now being tested for medical applications.

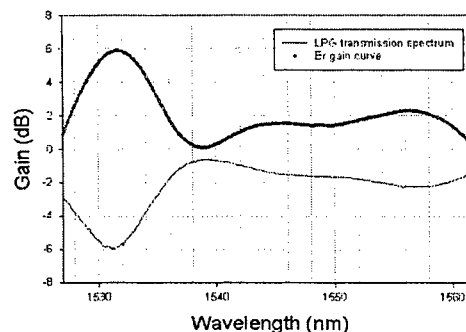
2.3 Long-Period Fiber Gratings

In this example, a combined laser process is applied to fabricate long-period gratings (LPG) in photosensitive fibers. Such gratings serve an important function in long-haul optical networks, by spectrally attenuating the output of Er-doped fiber amplifiers (EDFAs) in order to maintain equal gain across many different wavelength-channels.³ The gain flattening is achieved by laser-inducing a refractive-index modulation of 100's-of-microns period along a few centimeters of optical fiber. This period spacing permits the use of a contact amplitude-mask to pattern an ultraviolet-excimer-laser beam in a side-writing geometry. The design of a LPG involves the interplay between a number of dynamic variables, including the photosensitivity response of the fiber, the laser beam intensity, the shape of the loss peak, and the wavelength shift after fiber annealing. As such, the production of a particular grating to meet specific criteria often results in an iterative procedure, where a number of variables need to be optimized, including the period and shape of the amplitude mask.

The LPG amplitude masks were fabricated with the diode-pumped laser-micromachining station described in Section 2.1. For this, a 2000-Hz repetition rate was used to cut through 26- μm -thick brass strips. The 1.75-W laser beam was beam-expanded 10 \times to 10-mm dia. before being focused to a spot <10- μm diameter, by a 60-mm focal-length Gradium lens. Individual slots were excised at 1-mm/s cutting speed, moving the sample with an x-y pair of linear-motor stages (Newport PM500). A 10-cm travel range and 0.1- μm resolution were essential for generating the appropriate stop-band in each optical fiber. The mask was laser-cut in 2 min and then lightly etched in acid solution to remove ablation debris and dross.

These amplitude masks were then illuminated with a 248-nm KrF laser (Lumonics Pulsemaster 844) to induce refractive-index patterns in optical fibers. The laser beam (8-mm V x 20-mm H) was tightly focussed onto a static mask/fiber pair with a cylindrical lens. A second cylindrical lens expanded the beam to up to 50-mm length for full-length exposures of the fiber. Laser exposures of 1-2 minutes duration were applied, while simultaneously monitoring the reflection spectrum of the developing grating with an optical spectrum analyzer. Figure 4 shows the spectral gain of an EDFAs plotted together with the spectral loss of a LPG. Gain flattening with the EDFAs-LPG pair to ± 0.20 dB can be obtained across the full 1530–1560-nm optical-communication band. This dual laser-processing procedure supports design, creation, and testing of amplitude masks with ~30-min. turnaround times, correcting for subtle changes in period or duty cycle that cannot be fully controlled in a manufacturing environment.

Figure 4: Spectral gain of an EDFA plotted with the spectral loss of a LPG. The LPG loss compensates the non-uniform gain of the EDFA to provide uniform amplification in wavelength-division multiplexing optical networks.



3. SHAPING PHOTONIC DEVICES: ULTRAFAST PULSES VS. ULTRASHORT WAVELENGTH

Optical systems are rapidly evolving to incorporate more complex miniature optical components that directly accelerate the speed of our long-distance communication networks. This optical technology is also pushing into traditional electronic-based communication applications such as local area networks, computer back planes, and chip-to-chip links. Demand for low-cost and more functional optical devices is pressuring the photonics industry to integrate more optical components into smaller packages. The analogy is similar to the early development stage of the planarization and integration of electronic components onto the silicon wafer in the 1950's, out of which was born today's formidable microelectronics industry.

In the photonics industry today, the miniaturization and integration of many optical devices is only just beginning—requiring brand new approaches in fabrication, packaging, and assembling of components. Rapidly growing demand for photonic components is also adding pressure to develop high-volume manufacturing techniques on a scale never before experienced by this industry. Laser technology will be key to many aspects of this development, enabling high-volume manufacturing of precision optical circuits, components, and opto-electronic assemblies, paralleling the widespread use of lasers in current electronic and semiconductor manufacturing industries.

Meeting the increasing need to laser-process optical materials is fundamentally difficult simply because these are *optical* materials, having high transparency to radiation from traditional laser sources. The future evolution of photonics processing applications is therefore centered on emerging discoveries in laser science. At the University of Toronto, a decade of F_2 -laser-interaction studies with optical materials⁴⁻⁸ has shown exceptional promise in micromachining smooth and precise surface structures and in inducing rapid changes to refractive index. The key here is the F_2 -laser's short 157-nm wavelength, or 7.9-eV photon energy, which encroaches on the absorption band edge of fused silica materials, driving new absorption channels in this most important optical material. Ultrafast lasers are another promising approach where high fields access a new and unusual realm of physical and chemical interactions. Laser energy can be deposited into exceptionally small ($\sim 1\text{-}\mu\text{m}^3$) volumes, affording an unprecedented degree of control and precision in sculpting material surfaces⁹⁻¹³ or changing the refractive index of optically transparent materials^{14,15}. We have recently shown¹⁶ that moderately smooth and shallow holes of 1.7- μm diameter can be reproducibly etched with a 1-ps laser, offering excellent prospects for 3-D-surface-structuring applications. In 100-fs laser interactions with microscope slides, we have demonstrated¹⁷ the rapid imprinting of volume holograms with 20% efficiency into the both first orders. In the sections below, we present examples of laser processing as a science, using these leading-edge laser technologies to develop new processes and devices in photonics.

3.1. Micromachining Photonic Materials

In past work, this laboratory demonstrated⁴ that 157-nm F_2 -laser radiation couples strongly into amorphous silica and other wide-bandgap materials, furnishing smoothly etched surfaces free of microcracks or significant ablation debris. Etching proceeds at much lower fluences than with longer-wavelength ultraviolet lasers and 'incubation' processes were not observed. Deep-ultraviolet photochemical decomposition provides precise depth control to $\sim 20\text{-nm}$, more than adequate for shaping optical surfaces or photonic devices to better than $\lambda/20$ -figure accuracy. This strong optical coupling involves radiation-induced defects since the small-signal absorption coefficient of 10 cm^{-1} is too weak to directly account for the ablation. One defect candidate with absorption near 157 nm is the Si-Si wrong bond, known to form in vitreous silica under prolonged exposure to VUV lamp radiation.¹⁸ Sugioka et al.¹⁹ have also observed the critical role played by vacuum-ultraviolet (VUV) radiation for smooth etching of fused silica with a multi-wavelength laser source. Radiation at 160-nm was pivotal in dissociating Si-O and creating excited-state absorption centers that coupled the longer-wavelength laser radiation into the silica. The single-pulse etch depth, D , for uv-grade fused silica (Corning 7940) follows a logarithmic fluence dependence, $(1/\alpha_{\text{eff}}) \ln(F/F_{\text{th}})$, where the effective absorption coefficient, α_{eff} , has a value of $1.7 \times 10^5\text{ cm}^{-1}$ —17,000 times larger than the small-signal absorption coefficient. The threshold ablation fluence, F_{th} , is 1 J/cm^2 . In contrast, ablation studies⁴ at 193-nm have shown poor surface morphology, swelling phenomena, substantial ablation debris, susceptibility to microcracking, and the need for much higher laser fluence to remove material.

One promising platform for the development of two-dimensional photonic circuits is germanium-doped glass, from which waveguides may be produced. These optical circuits offer low loss and efficient coupling into optical communication fibers. Deep-ultraviolet laser ablation is one approach to smoothly structuring or trimming miniature optical components for use in optical communication networks. Typically, one begins with a single-mode planar-slab waveguide (PIRI SMPWL; 8- μm

germanosilicate on 20- μm fused silica) overgrown on a silicon wafer. Smooth two-dimensional structures with sub-micron resolution are then etched in relief, to define optical 'wires', filters, interconnects, multiplexers, etc. Figure 5 compares 193-nm laser etching of a PIRI waveguide with 157-nm etching. In the 193-nm case, a 28- μm deep hole of $\sim 225 \times 225\text{-}\mu\text{m}^2$ area was ejected by a single pulse at 3.6 J/cm^2 fluence. High transparency of the underlying glass led to substantial heating of the silicon-silica interface, mechanically lifting the complete glass coating in the laser irradiated area. In contrast, the 157-nm etching proceeded linearly with pulse number, yielding a smooth surface uniformly 6- μm deep after 100 pulses at similar fluence. No damage to the underlying silicon substrate was observed beneath the smooth $\sim 125 \times 180\text{-}\mu\text{m}^2$ depression. The 60-nm/pulse etch rate offers excellent control in precisely shaping photonic components. As an example, Figure 6 shows a microscope photograph of a single-mode rib waveguide of 8- μm width etched into the planar glass waveguide—the first such demonstration⁵ with any laser source. The 1-cm long rib waveguide provided a modest loss of 4 dB/cm to 0.635- μm laser light, losses attributed to a $\sim 40\text{-nm}$ surface roughness. Further refinements to the 157-nm laser source and optical tools promise decreased losses and numerous additional applications in shaping optical and photonic components.

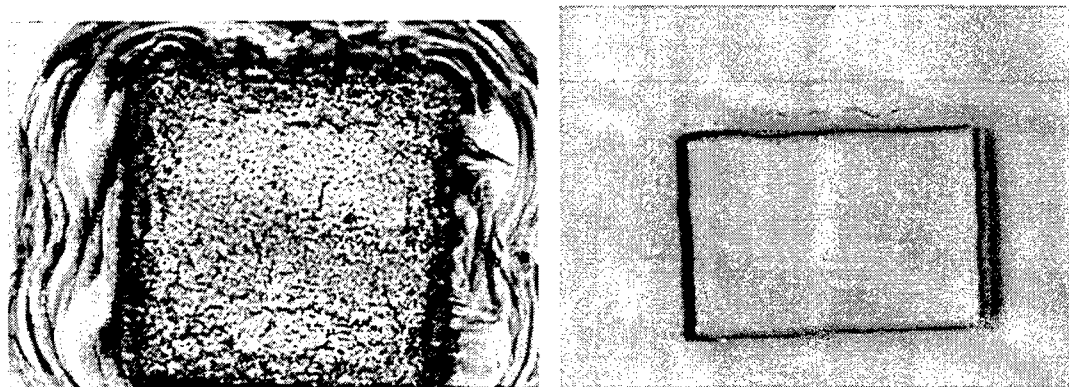
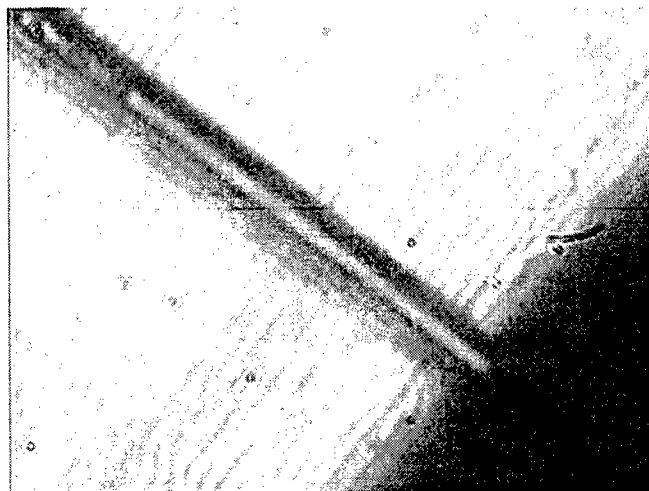


Figure 5: Optical microscope photograph of a planar-optical waveguide etched by 193-nm (left) and 157-nm lasers (right). A single pulse at 3.6 J/cm^2 fluence applied on the left mechanically ejected the whole 28- μm thick glass layer leaving a damaged silicon surface and gross cracks in the adjacent glass coating. An optically smooth, 6- μm deep recess was formed with 157-nm radiation (right) with 100-laser pulses at 3.0-J/cm^2 fluence. Hole sizes are $\sim 225 \times 225\text{ }\mu\text{m}^2$ on left and $\sim 180 \times 125\text{ }\mu\text{m}^2$ on right.

Figure 6: Microscope photo of top view of a single-mode rib waveguide etched by 157-nm laser radiation. The glass rib is 8- μm wide and $\sim 3\text{-}\mu\text{m}$ high with a side wall resolution of $\sim 2\text{ }\mu\text{m}$. The fine parallel lines (perpendicular to rib) are $\sim 40\text{-nm}$ diffraction ripples projected by mask edge as the sample was stepped 15- μm each laser pulse. See Ref. 5 for further details.



Ultrafast lasers are a promising alternate source for micromachining transparent materials by inducing opacity through nonlinear high-field interactions. Several groups^{12,20,21} have demonstrated smooth etching on various optical materials, although reproducibility and control over debris, surface rippling, and microcracking are not yet well characterized. We have examined etch rates and surface morphology in 1-ps micromachining of $\sim 1\text{-}\mu\text{m}$ diameter holes on uv-grade fused-silica cover slips (Corning 7940; 160- μm thick). A Nd:glass laser oscillator and amplifier system operating at 1 Hz provided a mode-

locked train of 430 pulses with pulse-to-pulse separation of 7.5 ns. Single pulses of 1.2-ps duration and 1-Hz repetition rate could be selected with an external Pockels cell. The beams were focussed to $\sim 1.5\text{-}\mu\text{m}$ spot diameter (FWHM) with a GRIN lens, and variable amplifier gain provided on-target laser fluences in the range of 2–170 J/cm². Samples were irradiated by 1 to 60 pulses at various fluence values, and examined with an optical microscope, atomic-force microscope (AFM), and scanning emission microscope (SEM) to study the surface morphology and to determine etch rates. A more complete discussion is provided in Reference 16.

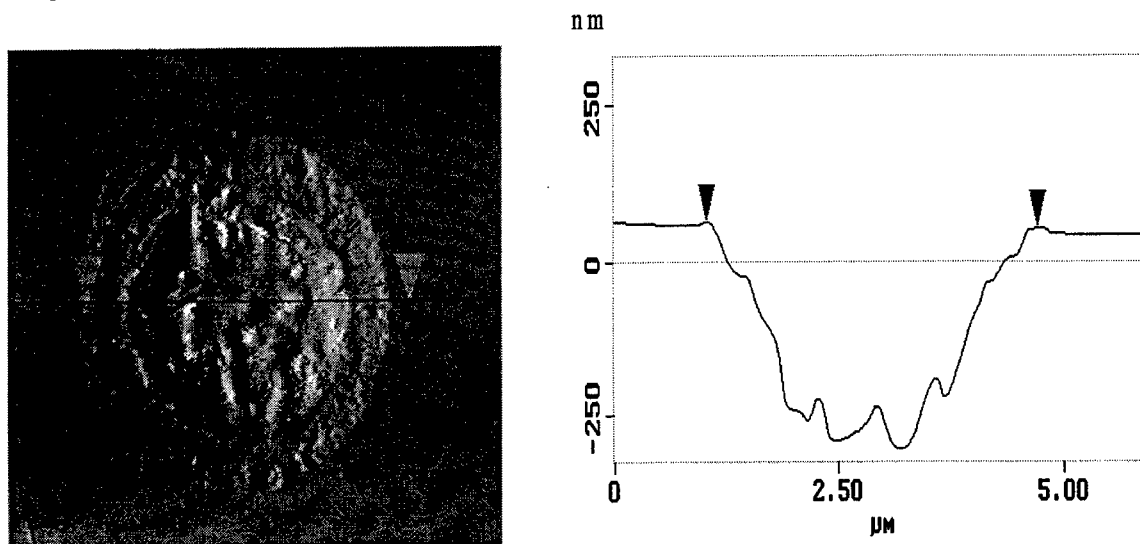


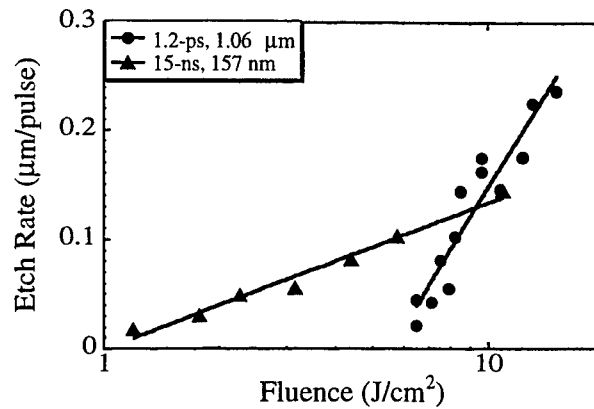
Figure 7: AFM image (left) and depth profile (right) of a micro-hole in fused silica, drilled by a single 1.2-ps laser pulse with a peak fluence of 38 J/cm². The 2.3- μm diameter hole (FWHM) shows a 25-nm surface roughness (rms).

Surface morphology for a 2.3- μm diameter hole (FWHM) is shown in the AFM photograph in Figure 7. A single 1.2-ps pulse of 38-J/cm² fluence produced a 250-nm deep hole having $\sim 25\text{-nm}$ (rms) surface roughness. Surface swelling and/or microcracks typically developed after several laser pulses, restricting precise laser micromachining to depths of less than $\sim 3\text{ }\mu\text{m}$. Microcracking generally appears after an onset number of laser pulses, N , that approximately follows $N = 1.1 + 96/F$ where F is the fluence in J/cm². However, by operating in the region below this fluence-dependent number of pulses, 1-ps lasers offer good prospects in microstructuring smooth and precisely controllable etch features in fused silica.

Single-pulse etch rates are plotted in Figure 8 as a function of fluence. Etch depth follows a logarithmic dependence from the ablation threshold of $\sim 5.5\text{ J/cm}^2$ to 20 J/cm², and increases more rapidly to a rate of $\sim 2\text{ }\mu\text{m/pulse}$ at 170 J/cm² (off range in graph). The inverse of the slope also provides an effective single-photon absorption coefficient of $4 \times 10^4\text{ cm}^{-1}$ —a surprising response considering the nonlinear mechanisms that underlie absorption in the transparent glass. For comparison, single-pulse etch rates are also plotted in Figure 8 for 157-nm laser ablation of fused silica with much longer, 15-ns pulses. Single-photon absorption mechanisms are primarily responsible for material removal at this short wavelength, reducing the ablation threshold fluence by a factor of 5. Nevertheless, the similarity in etch depths (i.e. at $\sim 10\text{ J/cm}^2$) is astonishing for these two extreme approaches in laser micromachining.

Overall, 157-nm laser ablation typically provides better surface morphology, presumably owing to the strong photochemical interaction. The absence of shock-induced microcracking, swelling, and rippling phenomena are important additional advantages. However, Kruger et al.¹³ have noted much improved surface morphology in borosilicate glasses when ultrafast-laser pulse duration was reduced from 3 ps to 20 fs. Further, our group has discovered¹⁶ an alternative approach to control surface microcracking during ultrafast-laser micromachining of fused silica. By applying the full oscillator pulse train—430 pulses of 1.2-ps duration at $\sim 100\text{ J/cm}^2$ fluence each—smooth symmetric holes of 10- μm diameter and up to 30- μm deep were generated by one pulse train. No evidence of surface microcracking or swelling was found. Heating effects associated with the 133 MHz repetition rate may improve the ductility of the surrounding glass. Multi-pulse etching is therefore attractive as a new parameter to eliminate undesirable microcracking phenomena in glass materials.

Figure 8: Etch rates of fused silica comparing 1.2-ps 1.06- μm laser pulses with the 15-ns 157-nm F_2 laser. The solid lines are fitted by $D = (1/\alpha_{\text{eff}}) \ln(F/F_{\text{th}})$, where F_{th} is the ablation threshold fluence and α_{eff} is effective single-photon absorption coefficient. For 1.2-ps ablation, α_{eff} is $4 \times 10^4 \text{ cm}^{-1}$ and F_{th} is 5.5 J/cm^2 . For 157-nm ablation, α_{eff} is $1.7 \times 10^5 \text{ cm}^{-1}$ and F_{th} is 1.1 J/cm^2 .



3.2. Refractive Index Profiling

Ultraviolet lasers are widely employed in defining miniature photonic structures inside the core of optical waveguides through laser-induced index-of-refraction changes ('photosensitivity'). However, weak photosensitivity responses have prompted the development of enhancement techniques such as hydrogen loading²², high-germanium concentration²³, and ion implantation²⁴ that boost index-processing speed and increase the magnitude of the index change. Our group is exploring an alternate approach, applying record short-wavelength laser radiation to access new absorption channels near the bandedge of pure forms of glass. Also promising are ultrafast lasers which have produced^{14,15} large index changes of $\Delta n = 0.1$ in fused silica. Such lasers offer exciting prospects for forming 3-dimensional structures internally in glass—a difficult feat for short-wavelength lasers.

Single-mode slab waveguides (3% GeO_2 ; PIRI Model SMPWL) and bulk fused silica (Corning 7940) were irradiated with 157-nm radiation at a various dose levels using a nitrogen-purged beam line. No enhancement techniques were employed to increase the photosensitivity response. Index changes were measured using a prism-coupler technique (for waveguides) or by monitoring the diffraction efficiency of laser-induced Bragg gratings ($1.55 \mu\text{m}$) with a He-Ne laser probe beam. Surfaces were also examined by optical microscopy and atomic-force microscopy (AFM).

The accumulated index change for the slab waveguide is shown in Figure 9 as a function of the number of laser pulses, N , for fluences, F , between 30 and 150 mJ/cm^2 . The large unsaturated index change of 8.5×10^{-4} was obtained after 25,000 laser pulses and a total dose of 2.5 kJ/cm^2 —a ~ 10 -fold more rapid and larger-index change in comparison with longer wavelength sources. However, a larger index change was precluded for this sample by the onset of surface ablation, presumably due to material incubation (defect generation) during the 25,000 laser-pulse exposures. This sets an upper limit for the total index change, for single-pulse fluences above 100 mJ/cm^2 .

The photosensitivity responses for all three fluences are re-plotted as a function of FN in Figure 10. The data follow an identical relationship, $\Delta n = 9.67 \times 10^{-6} (NF)^{0.57}$ (F in J/cm^2), where index change is only dependent on the accumulated fluence, NF . This graph demonstrates for the first time that the photoinduced-index change in germanosilicate glass follows a universal relationship well-known in compaction studies of ultraviolet-irradiated fused silica (i.e., solarization damage). For example, Allen *et al.*²⁵ observed a nonlinear compaction response of $\sim (NF^2)^{0.53}$ for 193-nm laser irradiation of fused silica. However, a fluence-squared (F^2) response has been noted by Albert *et al.* for index changes induced in germanosilicate waveguides with 193-nm radiation.²⁶ The single-photon response in our work suggests that the 157-nm radiation is directly accessing new photosensitivity channels associated with bandgap or near bandedge states.

Ultrafast lasers offer high-field strength with minimal thermal loading to rapidly induce refractive-index changes in transparent glasses. However, the wide bandwidth inherent to short pulses makes difficult the formation of periodic structures by conventional beam-interference techniques. The formation of complex refractive-index structures requires the locking of phases in two beams to several 10 's-of-nm path difference. Spatio-temporal overlap of tilted wavepackets was achieved here¹⁷ by a novel optical system offering extremely high phase stability of $< \lambda/50$ for periods of hours—progress which is key in forming 'coherent' refractive-index structures that require large accumulations of shots. The interferometer

employed here consisted of a diffractive optical beamsplitter and a spherical mirror, which system had a 1:1 conjugate ratio to eliminate the effects of angular dispersion at the sample.

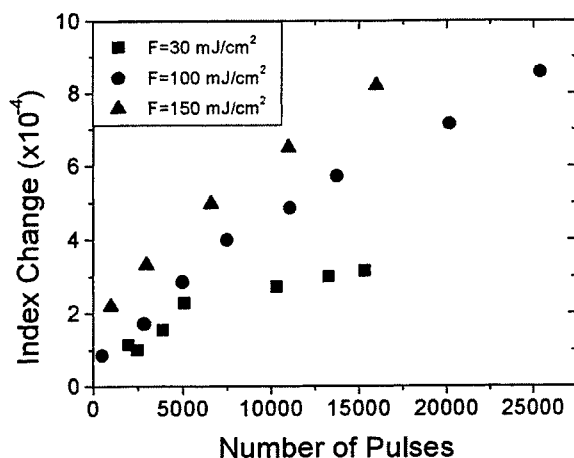


Figure 9: Index-of-refraction changes induced in germanium-doped planar waveguides (PIRI - SMPWL) by 157-nm laser irradiation. Index values were inferred from using a prism-to-waveguide coupler.

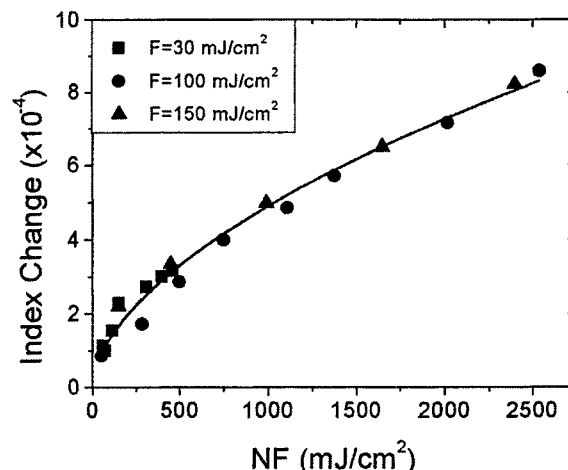


Figure 10: Refractive-index change in 157-nm irradiated germanosilicate as a function of the product of fluence and number of pulses. The data closely follow a universal compaction scaling, $9.67 \times 10^{-6} \cdot (NF)^{0.57}$ (F in J/cm^2), indicating a single-photon mechanism.

A 1-kHz Ti:sapphire laser system provided 100- μJ pulses of 100-fs duration at 800-nm wavelength. The output beam was split and recombined as above, producing a 30- μm period sinusoidal intensity pattern at 10^{12} – 10^{13} W/cm^2 on glass microscope slides. Diffraction efficiency of the evolving volume hologram was monitored with a 488-nm probe laser beam normally incident on the sample. The diffraction efficiency saturated at 30% into all orders, or 10% each for the first orders, after 100,000 pulses or ~ 1 -min. exposure. A large index change (0.01–0.1) is anticipated although a precise value could not be determined without knowing the depth of the volume hologram. Also, it is not clear what fraction of the diffraction is due to material bulk index change and what contribution arises from surface relief and damage. Nevertheless, such rapid formation of permanent volume holograms in optical-grade glasses is highly attractive for manufacturing robust diffractive-optical elements. Other applications include the formation of couplers and WDM-Bragg filters for optical communication systems.

Both F_2 and ultrafast lasers offer excellent prospects in micromachining and imprinting refractive index structures in glass. Although each laser type holds special advantages in processing photonics, manufacturing applications are most likely to fall into large-area projection processing for the large-beam F_2 laser—useful in high volume applications—and direct-write processing by scanning the Gaussian-profiled ultrafast laser—ideal in a flexible-manufacturing environment.

4. LASER MICROMACHINING FACILITY

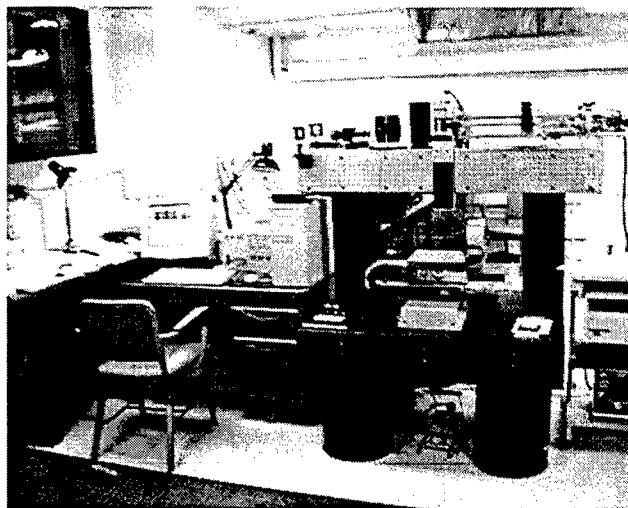
In an effort to draw together and build on the laser processing efforts described in this paper, PRO has recently established the Laser Micromachining Facility (LMF).¹ The LMF is an advanced laboratory facility designed to address growing industrial and academic demand for high-precision laser-optical tools that can machine, shape, and mark features down to the scale of microns. The Facility partners include the University of Toronto, McMaster University, Materials and Manufacturing Ontario (MMO), and several Ontario-based companies.

At the heart of this Facility is a high-precision micro-positioning system, shown in Figure 11, supporting sub-micrometer resolution over a long-range x–y translation stage (30 cm x 30 cm). This precision is essential to a wide range of applied-

research projects including the large-area patterning of refractive-index changes in glass, and in corneal sculpting. The focussing optics are mounted on a z-axis translation stage to support three-dimensional structuring of surfaces. A rotation stage with better than 1 arc-min accuracy further extends the micromachining capability to cylindrical geometry, for such projects as shaping arterial stents and catheters for biomedical research. The lasers and stages are fully interfaced to state-of-the-art CCD-camera alignment systems and computer-aided motion controls, to aid user operation.

Several lasers will be coupled to the micro-positioning system to further enhance the versatility of the Facility. Notably, these laser sources will feature the most advanced solid-state designs for user-friendly operation, and will operate at wavelengths in the infrared, visible, near- and deep-ultraviolet, allowing for processing of the widest possible gamut of materials. The laser already installed is a Lumonics 8–40-kHz repetition-rate diode-pumped Nd:YLF laser, with pulse duration adjustable from 150 to 600 ns. The laser produces 12 W at 1.053- μm wavelength; 8 W of green and 4 W of ultraviolet light are anticipated upon frequency doubling and tripling, respectively, with new periodically poled nonlinear crystal technology. A 30-ns pulse duration option is also planned. A new and important addition for exploring new frontiers in laser processing is the integration of an ultrafast laser system into the LMF-positioning station: a diode-pumped solid-state Cr:LiSGaF ultrashort-pulse laser will provide 5-ps and 100-fs options at kHz-repetition rates for study of photosensitivity responses in photonic materials and for developing a submicron-scale machining capability.

Figure 11: Laser microprocessing station at the PRO LMF: granite table, linear-motor positioning stages, computer-driven controller, and a Lumonics SIGMA-400 laser overhead on the horizontal crossbar.



5. CONCLUSIONS

A new generation of laser systems and optical tools are emerging that promise to broaden the base of today's laser processing applications. PRO is actively pursuing several facets of this evolution, especially in the areas of photonics, electronics, and biology, by broadly supporting a host of research activities from basic science through to collaborative university-industry projects.

ACKNOWLEDGMENTS

Funding for many programs and student stipends has been provided by Photonics Research Ontario, the Natural Sciences and Engineering Research Council of Canada, the Canadian Foundation for Innovation, the Ontario R&D Challenge Fund, Materials and Manufacturing Ontario, Micronet, and the Canadian Microelectronics Corp. Industrial partners include: Nortel Networks, Lumonics, JDS Fitel, Alcan Aluminum, ISG Technologies, A & K Technologies.

REFERENCES

- 1 <http://www.pro.on.ca/>; (formerly Ontario Laser & Lightwave Research Centre—OLLRC)
- 2 M. Lukas, Ph.D Thesis, Dept. of Physics, Queen's University, Kingston, ON, Canada, to be published in 1999.
- 3 A.M. Vengsardar, J.R. Pedrazzani, J.B. Judkins and P.J. Lemaire, *Optics Lett.* **21**, 336 (1996).

- 4 P.R. Herman, K. Beckley, B. Jackson, K. Kurosawa, D. Moore, T. Yamanishi, and J. Yang, *SPIE Proc.* **2992**, 86-95 (1997).
- 5 P.R. Herman, J. Yang, K. Kurosawa, and T. Yamanishi, *SPIE Vol.* **2991**, 170-174 (1997).
- 6 K. Kurosawa, P.R. Herman, and W. Sasaki, *J. Photopolymer Sc. & Tech.*, **11**, 367-373 (1998).
- 7 B. Jackson and P.R. Herman, *Appl. Surf. Sci.* **127-129**, 595-600 (1998).
- 8 P.R. Herman, K. Beckley, and S. Ness, in *Bragg Gratings, Photosensitivity, and Poling in Glass Fibers and Waveguides: Appl'ns and Fundamental*, Vol. **17**, OSA Tech. Digest (1997) p. 159
- 9 S. Press & M. Stuke, *Appl. Phys. Lett.* **67**, 338 (1995); S. Kuper & Stuke, *Appl. Phys. B* **44**, 199 (1987).
- 10 D. Du, X. Liu, G. Korn, J. Squier, & G. Mourou, *Appl. Phys. Lett.* **64**, 3071 (1994).
- 11 P.P. Pronko, S.K. Dutta, J. Squier, J.V. Rudd, D. Du, & G. Mourou, *Optics Comm.* **114**, 106 (1995).
- 12 B.C. Stuart, M.D. Feit, A.M. Rubenchik, B.W. Shore, and M.D. Perry, *Phys. Rev. B* **53**, 1749 (1996).
- 13 J. Kruger, W. Kautek, M. Lenzner, S. Sartania, C. Spielmann, and F. Krausz, *Appl. Surf. Science* **127-129**, 892 (1998).
- 14 K.M. Davis, K. Miura, N. Sugimoto, and K. Hirao, *Opt. Lett.* **21**, 1729 (1996).
- 15 E. N. Glezer, M. Milosavljevic, L. Huang, R. J. Finlay, T.-H. Her, J. P. Callan, and E. Mazur, *Opt. Lett.* **21**, 2023 (1996).
- 16 P.R. Herman, A. Oettl, K.P. Chen, and R.S. Marjoribanks, 'Laser micromachining of 'transparent' fused silica with 1-ps pulses and pulse trains,' appearing in *SPIE Vol.* **3616**, (1999).
- 17 G. D. Goodno, G. Dadusc, and R. J. D. Miller, *J. Opt. Soc. Am. B* **15**, 1791 (1998); G. D. Goodno, V. Astinov, and R. J. D. Miller, *J. Phys. Chem. B*, in press (1999).
- 18 Y. Morimoto, T. Igarashi, and T. Okanuma, *J. of Non-Crystal. Solids* **179**, pp. 260-275, 1994.
- 19 K. Sugioka, S. Wada, Y. Ohnuma, A. Nakamura, H. Tashiro, and K. Toyoda, *Appl. Surf. Sci.* **96-86**, pp. 347-351, 1996.
- 20 H. Varel, D. Ashkenasi, A. Rosenfeld, M. Whamer, E.E.B. Campbell, *Appl. Phys. A* **65**, 367 (1997).
- 21 D. Ashkenasi, A. Rosenfeld, H. Varel, M. Wahmer, E.E.B. Campbell, *Appl. Surf. Sci.* **120**, 65 (1997).
- 22 P.J. Lemaire, R.M. Atkins, V. Mizrahi, and W.A. Reed, *Electron. Lett.* **29**, 1191-1193 (1993).
- 23 E. Fertein, S. Legoubin, M. Douay, S. Canon, P. Bernage, P. Niay, F. Bayon, and T. Georges, *Electron. Lett.* **20**, 1838-39 (1991).
- 24 J. Albert, B. Malo, K.O. Hill, D.C. Johnson, J.L. Brebner, and R. Leonelli, *Opt. Lett.* **17**, 1652 (1992).
- 25 D.C. Allan, C. Smith, N.F. Borrelli, and T.P. Seward III, *Opt. Lett.* **21**, 1960-62 (1996).
- 26 J. Albert, B. Malo, K.O. Hill, F. Bilodeau, D.C. Johnson, and S. Theriault, *Appl. Phys. Lett.* **67**, 3529-31 (1995).

EXCIMER LASER MICROMACHINING: A 15 YEAR PERSPECTIVE

Malcolm C Gower
Exitech Ltd
Hanborough Park
Long Hanborough
Oxford OX8 8LH
United Kingdom¹

ABSTRACT

Reports in 1982 of polymers ablated and etched by excimer laser radiation mark the founding of laser micromachining as a technology that in the intervening period has matured into a manufacturing process used by a diverse range of industries. This paper describes some of these industrial applications.

Keywords: *Micromachining, excimer lasers, laser ablation, industrial applications, MEMS*

1. INTRODUCTION

Although material ablation by pulsed light sources has been studied since the invention of the laser^(1,2), reports in 1982 of polymers etched by uv excimer laser radiation stimulated widespread investigations in using the process for micromachining^(3,4). In the intervening years scientific and industrial research in this field has proliferated to a staggering extent – probably spurred on by the remarkably small features that can be etched and replicated with little or no apparent damage to surrounding unirradiated regions of the material. Excimer laser micromachined features in human hairs has long been a standard party trick used to illustrate these features.

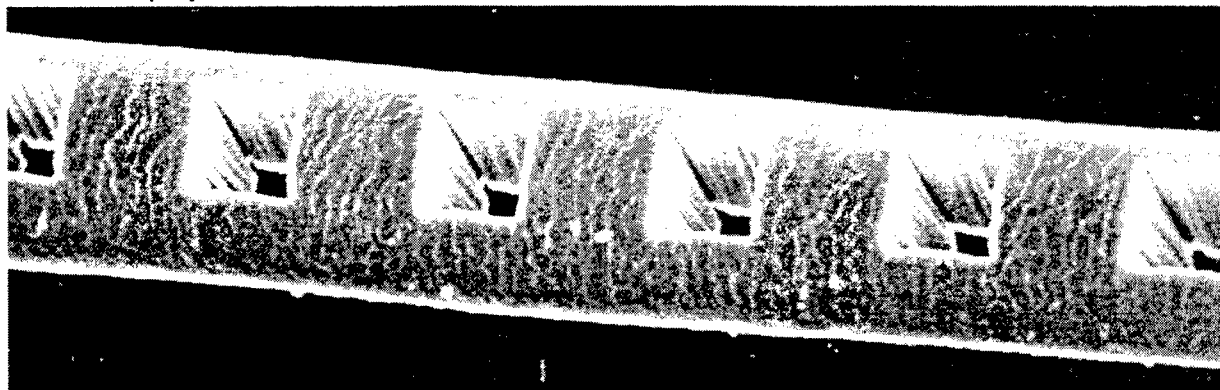


Figure 1. ArF laser-micromachined 40 μ m square holes through a human hair

¹Further author information:

Exitech Limited: Tel: 44-1993-883324; Fax: 44-1993-883334; e-mail: m.gower@exitech.co.uk

A more practical illustration is obtained when comparing the hole drilling capabilities of mechanical twist drill bits and excimer lasers. Figure 2 compares 100 μm diameter holes drilled in 75 μm thick high-density polyethylene with a drill bit and a KrF excimer laser. While the mechanically hole is close to the minimum size that can be drilled, the improved quality of this and much smaller holes drilled by excimer lasers is obvious.

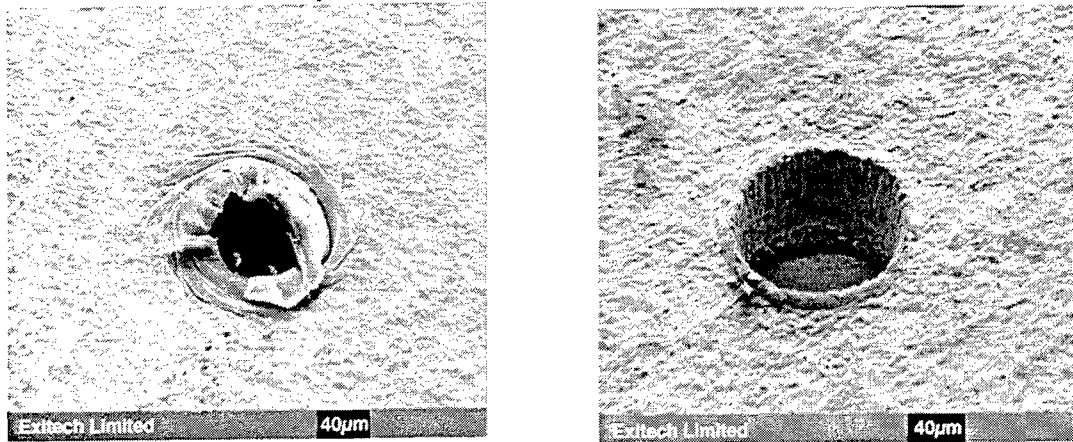


Figure 2. Holes drilled with: (a) Twist drill bit

(b) KrF laser

Once the hallmark of excimer laser ablation, it is now known that such clean ablative etching can also be achieved with pulsed laser sources at other wavelengths⁽⁵⁾. Provided laser photons are absorbed strongly in the material in submicron depths at the surface and on timescales less than the time it takes for heat to diffuse away from the irradiated region, then pulsed lasers like CO₂, copper vapor, Nd:YAG and its harmonics can be as effective for ablative micromachining⁽⁶⁾. Indeed lasers providing ultrafast durations of < 10psec (10^{-11} sec) based on diode-pumped solid-state gain media have in recent years demonstrated remarkably clean micromachining of many materials. For a particular micromachining application the choice of laser type is now judged as much by criteria such as process speed, part throughput, reliability, service intervals, capital and operating costs of the overall machine tool rather than solely by the quality of the processed part. Despite initially gaining a poor reputation for reliability, over the past 15 years excimer lasers have developed into mature industrial tools.

The degree of industrial takeup of a technology is a good yardstick for assessing its utility and state of maturity. This paper reviews the background and market importance to several industries which use excimer laser ablation for micromachining. In this context '*industrial application*' is taken to mean a process proven to add value to a manufactured product. Not included are areas which use excimer lasers for non-ablative surface treatment applications like photolithography, marking, annealing, hardening; secondary ablative processes like pulsed laser deposition of thin films; medical micromachining applications like photorefractive keratectomy (PRK) of the cornea.

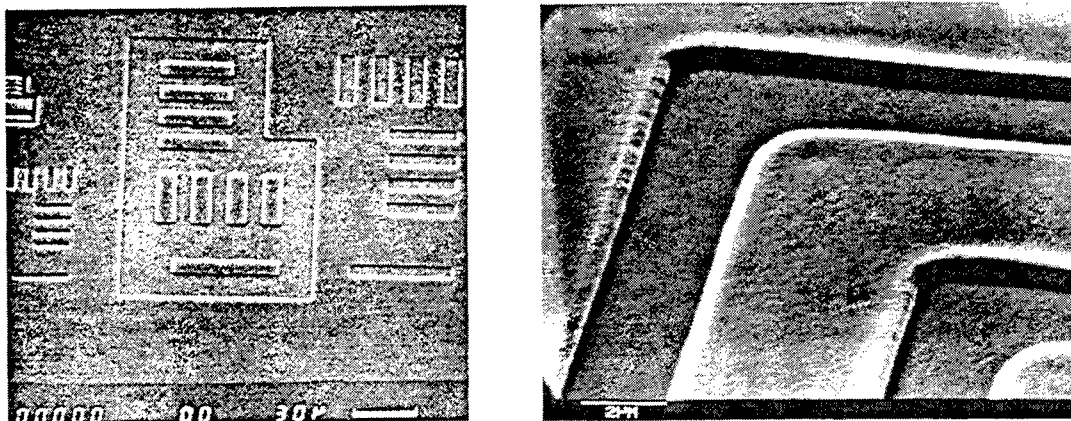


Figure 3. Mask test patterns ablated in 1 μm thick PMMA electron beam resist by ArF laser. From Ref 7.

During evaluations of its use for submicron deep-uv lithography as used in the production of integrated circuits, the high-resolution capability of excimer laser ablation of polymer photoresist materials was soon recognized⁽⁷⁾. Indeed as early as 1983 excimer laser micromachining was being used to fabricate specialist targets in laser-fusion implosion experiments⁽⁸⁾. Figure 4 shows ArF laser machined polystyrene microshell targets used for studying Rayleigh-Taylor plasma instabilities.

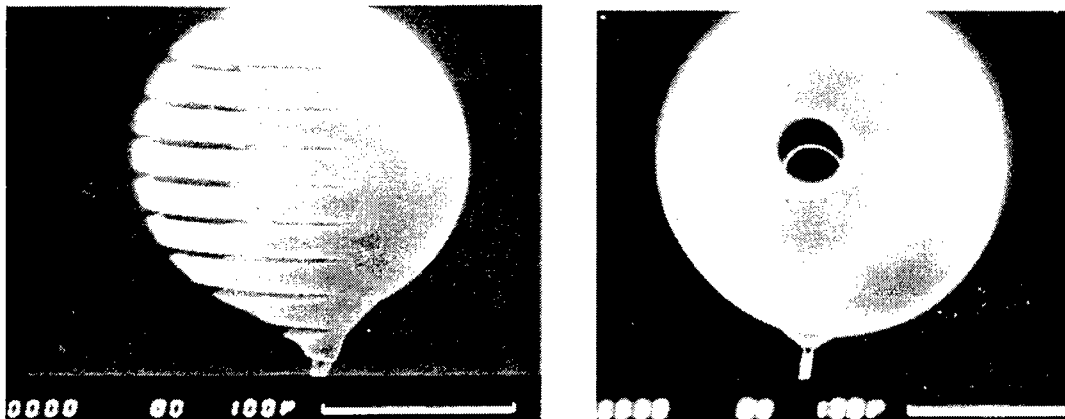


Figure 4. ArF laser machined features in 150µm diameter polystyrene laser targets. From Ref 8.

Nevertheless for large-scale manufacturing the first use of excimer laser ablation occurred some five years later when Siemens introduced the drilling via holes in multichip module (MCM) circuit boards⁽⁹⁾. With fewer process steps than other methods, such drilling is now regarded as the most versatile, robust, reliable and high-yield technology for creating microvias in these packages.

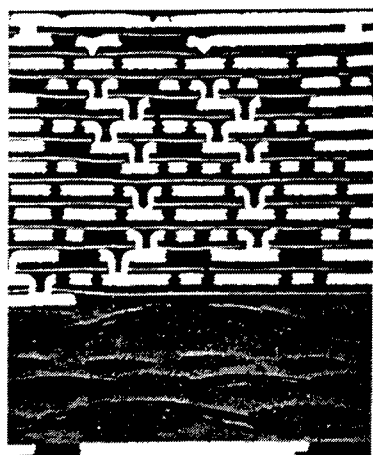
The ability to drill ever smaller holes - down to $\sim 1\mu\text{m}$ diameter, is an underpinning technology in many other industries which manufacture high-tech products. For example, the nozzle hole arrays in most of the ink jet printers currently sold in the world are now drilled by excimer lasers on production lines in Asia, Europe and the US. By providing solutions to critical problems in manufacturing integrated circuits, hard disks, displays, interconnects, desk top printers and telecommunication devices, excimer laser materials processing is a key enabling technology allowing the current revolution in information technology to continue. Precision excimer laser microdrilling is now routine for making some of the delicate medical probes that measure *in situ* properties of blood in human arteries. The requirement for material processing with micron or submicron resolution at high-speed and low-unit cost is an underpinning technology in nearly all industries that manufacture high-tech products. The combination of high-resolution, accuracy, speed and flexibility has allowed excimer laser materials processing to gain acceptance in many industries⁽¹⁰⁻¹²⁾.

2. EXCIMER LASER DRILLING OF VIA HOLES IN INTERCONNECTION PACKAGES

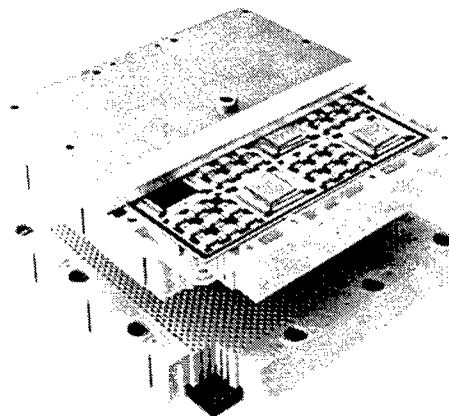
Almost as important as the rapid improvements in speed and memory of IC's are the parallel developments in interconnection packaging made during the last 20 years. So speed, power and area (real estate) are not compromised, packages on which chips are mounted for connection to other devices have had to keep pace with the rapid advances made in IC's. There are now more than a dozen generic types of chip interconnection packages which include *multichip-modules* (MCM's), *chip-scale-packages* (CSP's) like *ball-grid-arrays* (BGA's), *chip-on-boards* (COB's), *tape-automated-bonds* (TAB's). Generally these consist of multilayer sandwiches of conductor-insulator-conductor with electrical connection between layers made by drilling small holes (vias) through the dielectric and metal plating metal down the hole. Such blind via holes provide high-speed connections between surface-mounted components on the board and underlying power and signal planes while minimizing valuable real estate occupation. For example, due to difficulties in soldering IC's with greater than ~ 200 pins, peripheral lead mounting packages like TAB's must be made larger than the chip. By placing microvia connections in the package at the base of the chip instead of around its periphery, a BGA is no larger than 20% the

size of the chip. Typically then the requirement is to drill $100\mu\text{m}$ diameter microvias on $\sim 500\mu\text{m}$ centers. The cost for drilling these vias on such high-density packages can represent 30% of the overall cost of the board.

Drilling microvias by ablation was first investigated in the early 1980's using pulsed Nd:YAG and CO_2 lasers^(13,14). Excimer lasers led the way in applying it to volume production when the Nixdorf computer plant of Siemens introduced polyimide ablative drilling of $80\mu\text{m}$ diameter vias in MCM's - as used to connect silicon chips together in high-speed computers⁽⁹⁾. Figure 5 shows the Siemens MCM and the KrF laser drilled microvias in the acrylic resin-polyimide dielectric material. Other mainframe computer manufacturers such as IBM rapidly followed suite and installed their own production lines for this application⁽¹⁵⁾.



(a) Cross-section of 14-layer copper-plated MCM board showing $80\mu\text{m}$ diameter microvias.



(b) Populated and assembled MCM package

Figure 5. KrF laser drilled microvias in MCM's. *Courtesy of Siemens AG, Germany*

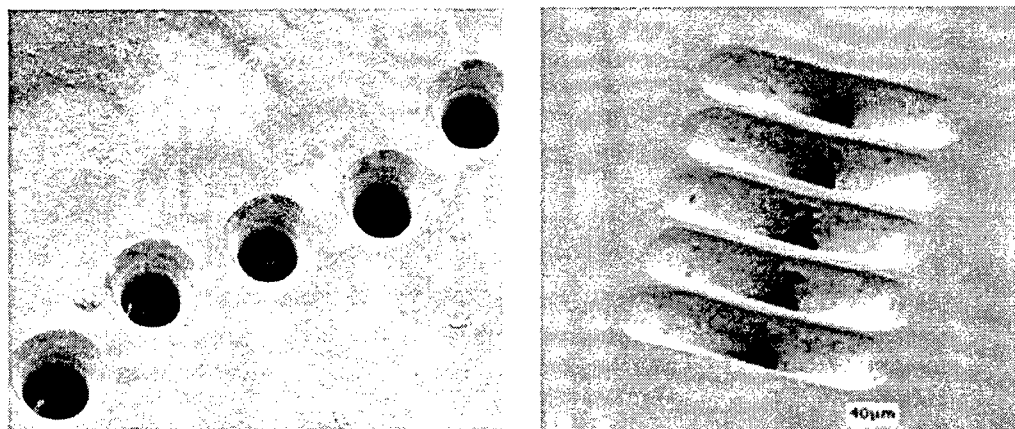
With fewer process steps than other methods, laser-drilling is regarded as the most versatile, robust, reliable and high-yield technology for creating microvias in thin film packages. Trillions of vias have now been drilled with excimer lasers at yields $>99.99\%$ whose *mean time between failure* (MTBF) has been logged at $>1,000$ hours.

Interconnection densities on rigid and flexible *printed circuit and wiring boards* (PCB's, PWB's and FPC's) are also increasing - driving the requirement for drilling ever-smaller vias in these packages⁽¹⁶⁾. Thus there is a demand for an ever-increasing packing density of interconnections - for example mountings in current mobile phones and camcorders have around 1200 interconnections/ cm^2 . Such packages have much lower fabrication costs than MCM's and the current common practice is to mechanically drill the vias. However as diameters decrease to $< 100\mu\text{m}$ it is generally recognized pulsed CO_2 and/or Q-switched Nd:YAG lasers will displace mechanical drills - for such low cost packages excimer lasers are too slow and their running costs are too high. For these boards, holes must be drilled at speeds of several hundred per second at costs of $< 1¢/1,000$ holes. At present excimer lasers are only used to drill microvias in high-value packages such as MCM's and BGA's⁽¹⁷⁾.

3. EXCIMER LASER DRILLING OF INK JET PRINTER NOZZLES

Inkjet printers comprise a row of small tapered holes through which ink droplets are squirted onto paper. Adjacent to each nozzle, a tiny resistor rapidly heats and boils ink forcing it through the orifice. Increased printer quality is achieved by simultaneously reducing the nozzle diameter, decreasing the hole pitch and lengthening the head. Modern printers like HP's Desk Jet 800C and 1600C have $300 \times 28\mu\text{m}$ input diameter nozzles giving a resolution of 600 dots-per-inch (dpi). Earlier 300dpi printers consisted of a 100 nozzle row of $50\mu\text{m}$ diameter holes made by electroforming thin nickel foil. Trying to fabricate more holes with smaller diameters reduced even further the already low 70-85% production yield. Laser-drilling

of nozzle arrays allowed manufacturers to produce higher performance printer heads at greater yields. At average yields of >99%, excimer laser mask projection is now routinely used for drilling arrays of nozzles each having identical size and wall angle⁽¹⁸⁾. Most of the ink jet printer heads sold currently (e.g by HP and Canon) are excimer laser drilled on production lines in the US and Asia. Figure 6(a) shows an excimer laser drilled nozzle array in a modern printhead.

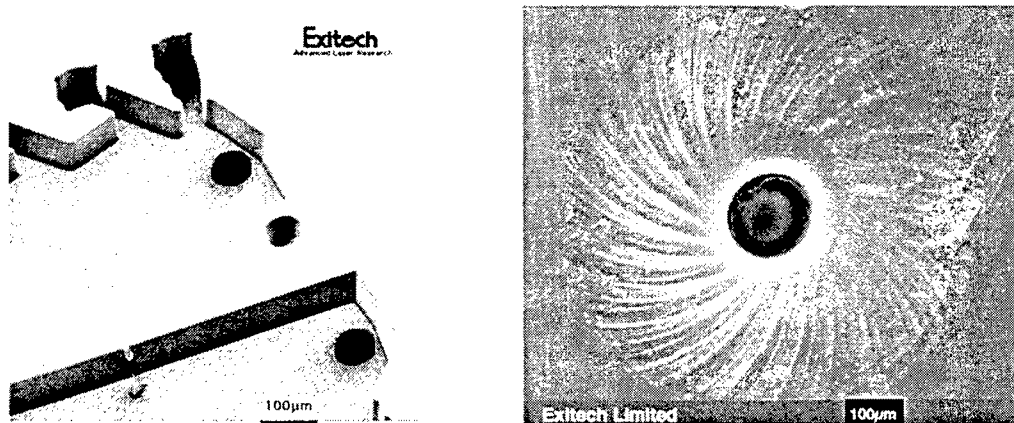


(a) 30µm diameter nozzle array

(b) Nonlinear tapered nozzles to aid laminar flow

Figure 6. KrF laser-drilled ink jet printer nozzles in polyimide

Figure 6(b) shows nozzles with nonlinear tapers to aid the laminar flow of the droplet through the orifice. More advanced printers sometimes use piezo-actuators. Rather than being constrained to give shapes characteristic of the process, excimer laser micromachining tools with appropriate CNC programming can readily engineer custom-designed reverse-tapered, 2¹/₂D and 3D structures. Figure 7(a) shows an array with ink reservoirs machined behind each nozzle while Figure 7(b) shows an example of a rifled tapered hole which spins the droplet to aid its accuracy of trajectory.



(a) Nozzle array with ink reservoirs

(b) Tapered nozzle with rifling

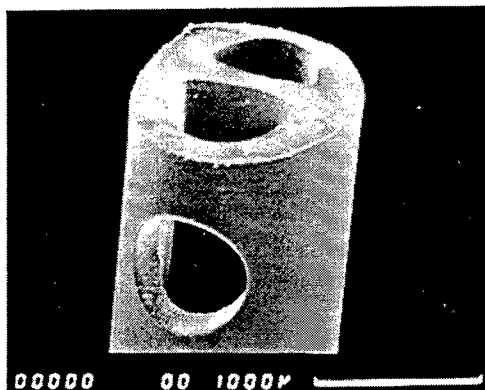
Figure 7. KrF laser-micromachined nozzle structures in polyimide

4. EXCIMER LASER MICROMACHINED BIOMEDICAL DEVICES

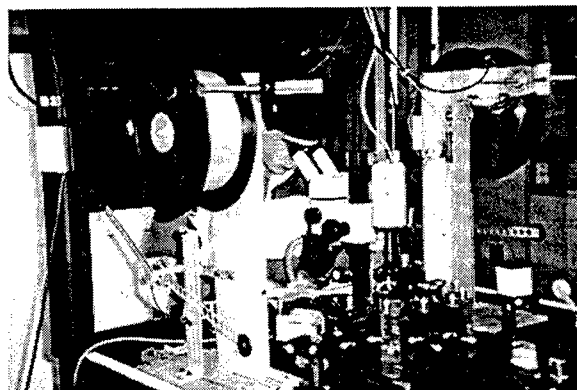
As in microelectronics and its associated technologies, the drive for increasing miniaturization with improved device functionality is crucial to the rapid progress being made in the biomedical industry⁽¹⁹⁾. Precision microdrilling with excimer lasers is routine when making delicate probes used for analyzing *arterial blood gases* (ABGs)⁽²⁰⁾. ABG sensors measure the partial pressures of oxygen (PaO₂), carbon dioxide (PaCO₂) and hydrogen-ion concentration (pH) used for monitoring the acid-base concentration essential for sustaining life. In intensive care units, ABG results are used to make decisions on

patient's ventilator conditions and the administration of different drugs. The use of fiber-optic sensors for ABG analysis provide clinical diagnostics at the patient's bedside without the need for taking blood samples and doing remote analysis⁽²¹⁾.

Figure 8(a) shows an example a ABG catheter for monitoring blood in prematurely borne babies. The hole at the side of the PVC bilumen sleeving tube through which blood is drawn is machined using a KrF laser. In this case the clean cutting capability of the laser provides the necessary rigidity that prevents kinking and blockage of the tube when inserted into the artery.



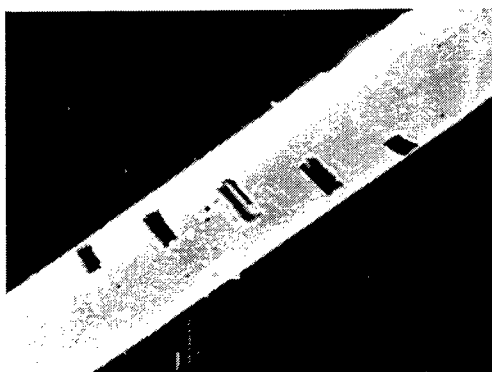
(a) KrF laser-drilled hole in side of PVC bilumen catheter.



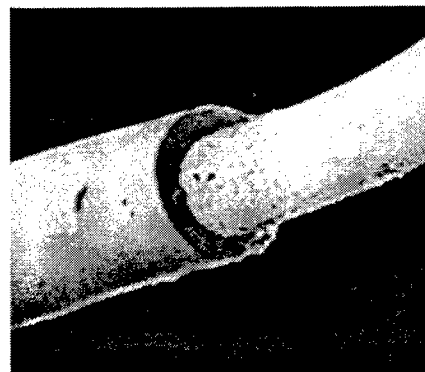
(b) Automated reel-to-reel fibre hole-drilling system

Figure 8. Excimer laser manufacture of blood gas sensor

More important components of this catheter are the PaO_2 and PaCO_2 sensors. These consist of a spiral of up to five $\sim 50 \times 15 \mu\text{m}$ rectangular holes machined in a $100 \mu\text{m}$ diameter acrylic (PMMA) optical fiber with an ArF laser. The holes are filled with a reagents whose optical transmission depend on the PaO_2 and PaCO_2 levels of the surrounding blood. Using a fully-automated workstation shown in Figure 8(b) that has computer-controlled reel-to-reel fiber feeding and laser-firing, all five holes shown in Figure 9(a) are drilled in the fiber. By spatially-multiplexing a single excimer beam into five smaller ones, holes are drilled simultaneously through the fiber.



(a) ArF laser-drilled holes in PaO_2 and PaCO_2 acrylic fibres



(b) KrF laser-stripped insulation from pH-sensor wire

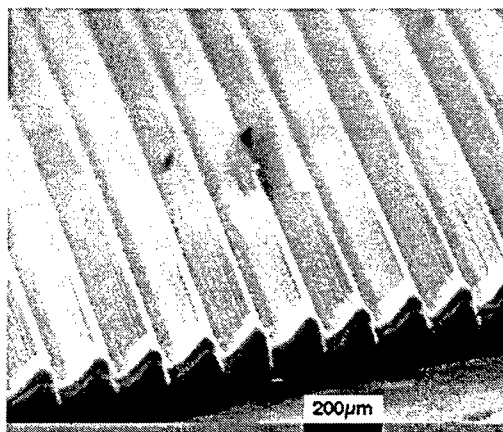
Figure 9.

Preferential excimer laser etching of plastics compared to metals is applied to the stripping of insulation from $100 \mu\text{m}$ diameter wires prior to soldering connections. The process relies on the threshold for excimer laser ablation of the polymer being much lower than for damaging the copper or silver core. As shown in Figure 9(b), excimer lasers are used to cleanly strip away the polyurethane insulation sleeving of wires which form the pH resistivity sensor in the ABG catheter above. Such pulsed laser wirestripping is also in widespread use for preparing connection wires to computer hard-disk reader heads.

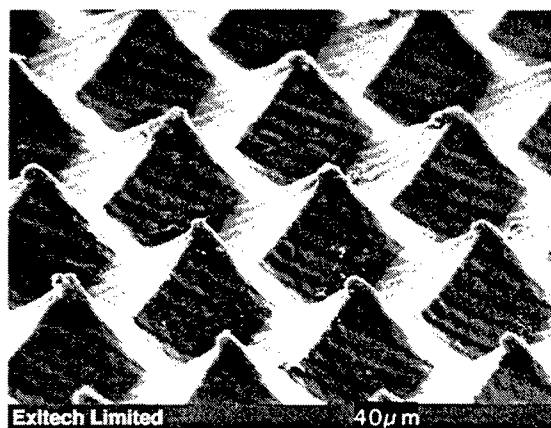
5. EXCIMER LASER MICROMACHINED MICRO-ELECTRO-MECHANICAL SYSTEMS

'Micro-electro-mechanical systems' (MEMS) bring together mechanical, electrical and optical technologies to create an integrated device that employs miniaturization to achieve high-complexity in a small volume⁽²²⁾. This generally involves fabricating mm- μ m size structures with μ m-nm tolerances. In Europe MEMS is referred to as '*Microsystems technology*' (MST), in the UK as '*Microengineering*' and in Japan as '*Micromachines*', and is predicted to be a \$4B/year industry by the end of the century. The success of microengineering comes from miniaturization and its consequences: high-sensitivity, short-measurement times, low-energy consumption, good-stability, high-reliability, self-calibration and testing. Microsensors detecting local parameters like pressure, flow, force, acceleration, temperature, humidity, chemical content etc, have in the last decade been engineered into the engine and performance management systems of cars and aircraft. They also provide the key to electromechanical microcomponents such as ink jet printer nozzles, gas chromatographs, gyroscopes, galvanometers, microactuators, micromotors, micro-optics etc. Devices like implantable drug delivery systems containing sensors, valves and control system with power source capable of operating for many years are being developed. There is no doubt microengineering will be a key underpinning technology of the 21st century.

Examples of the types of surfaces that can be structured by excimer laser ablation are shown in Figure 10. Blazed grating and pyramid-like structures can be readily fabricated on surfaces by mask-dragging techniques⁽²³⁾.



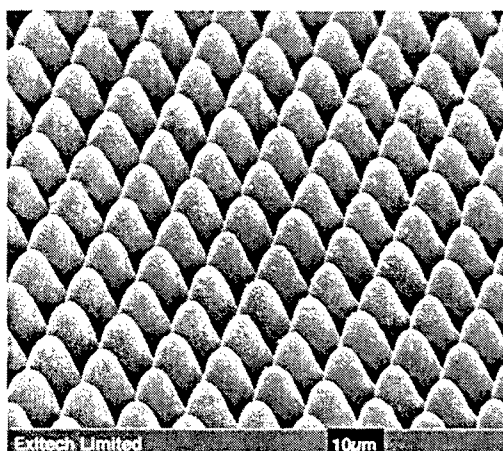
(a) Blazed grating



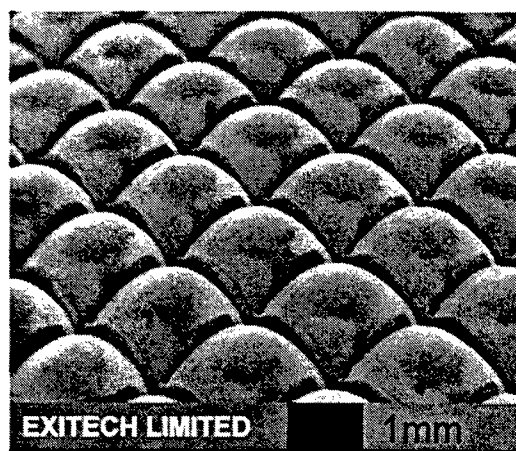
(b) Pyramids

Figure 10. KrF laser produced surfaces in polycarbonate produced using mask-dragging techniques

Such methods can be used for making micro-optical surfaces like those shown in Figure 11. The 'black' anti-reflective



(a) Cesium Iodide far-infrared optical crystal



(b) Polycarbonate

Figure 11. Micro-optical surfaces fabricated by KrF laser micromachining and orthogonal mask-dragging

property of the 'moth's-eye' type of surface machined on the CsI crystal shown in Figure 11(a) is being used to prevent ghost images in very large infrared optical telescopes. The microlens array shown in Figure 11(b) is used for shaping beams from laser diodes. Each lenslet in this array has a focal length of 1mm.

Adaption of silicon lithography and etch batch-processing as developed by the semiconductor industry is currently the dominant MEMS fabrication method. However being restricted to just one material (silicon) surface and bulk etched in only 3 directions- along (110), (100) and (111) crystallographic-planes, other more flexible micromachining methods including pulsed uv-laser ablation are being evaluated for MEMS. The perceived advantages of uv-laser micromachining are many: (i) few processing steps, (ii) highly-flexible CNC programming of shapes for engineering prototyping, (iii) capable of serial and batch-mode production processing, (iv) no major investment required in large clean-room facilities and many expensive process tools, (v) can be applied to a wide range of polymers, ceramics, glasses, crystals, insulators, conductors, piezomaterials, biomaterials, non-planar substrates, thin and thick films, (vi) compatible with lithographic processes and photomask making.

Excimer laser ablation is being used to manufacture '*biofactory-on-a-chip*' (BFC) travelling-wave dielectrophoresis cell-sorters and sensors that consist of $2\frac{1}{2}$ D laminations of channels, chambers and electrode conveyor tracks⁽²⁴⁾. Figure 12 shows examples of microfluidic channels and ramps being used in this device as well as in medical sensors such as pregnancy testers.

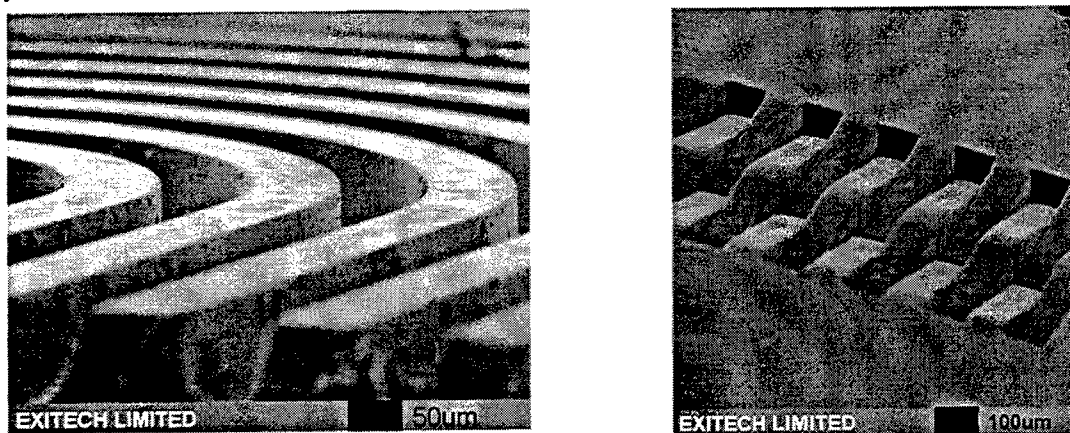


Figure 12. KrF laser micromachined microfluidic channels in polyester

Flat and ramped channels such as those shown in Figure 13 are being used for securing small cylindrical objects like fiber optic cable.

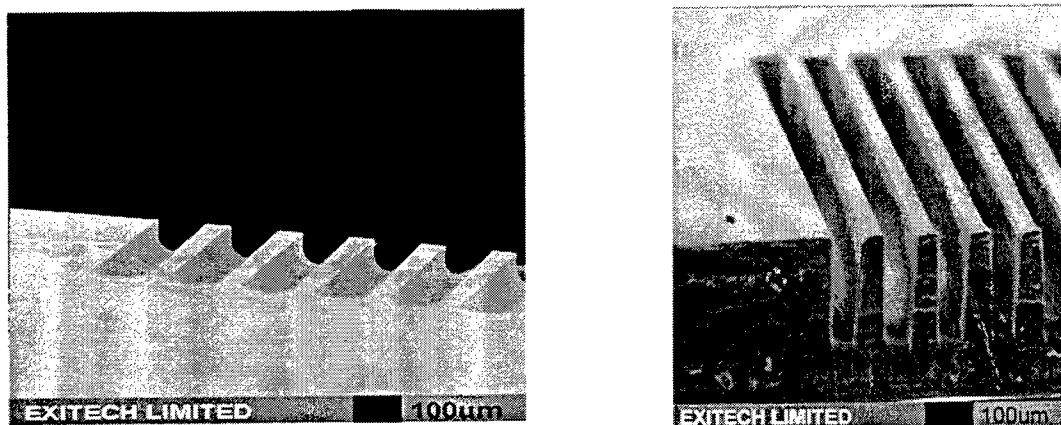


Figure 13. KrF laser micromachined fiber holders in polyester

As illustrated in Figure 14, controlled 3D-structuring of materials by excimer laser etching⁽²³⁾ can produce the basic building blocks of bridges, diaphragms, pits, holes, ramps, cantilevers, etc needed for microengineering devices like gyroscopes, galvanometers, gas chromatographs, microactuators, micromotors, etc.

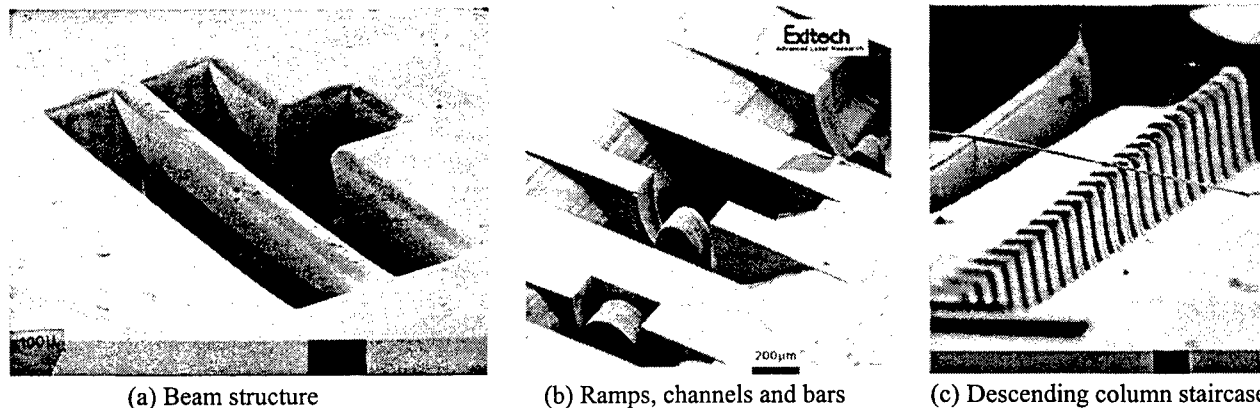
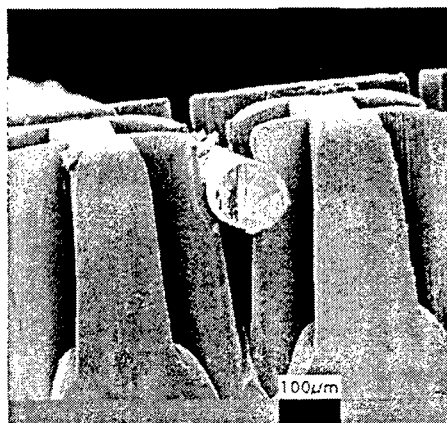
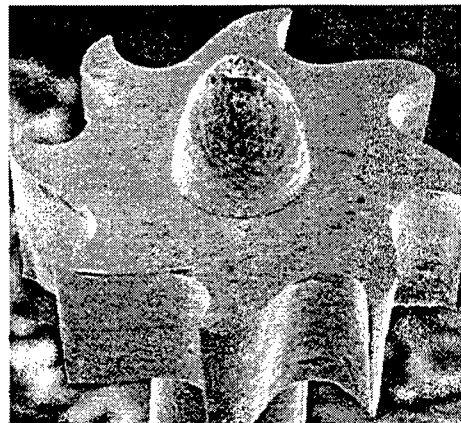


Figure 14. KrF laser-machined 3D-structures in polycarbonate using Exitech Series 7000 CNC-controlled micromachining system. (c) was fabricated using a half-tone mask to produce a grey-scale image that controlled the etch depth.

Figure 15 shows examples of uv-laser micromachined 3D-structures in polymers which when used with the LIGA (from



(a) KrF laser machined 100µm fiber clamp



(b) 470µm diameter, 130µm height nickel intravascular rotor microturbine. Replicated by electroplating from ArF laser machined PMMA master. *Courtesy of the Rutherford Appleton Laboratory*

Figure 15. MEMS devices fabricated by excimer laser micromachining

the German acronym: *lithographie galvanofornung abformung*) process of electroforming, can be replicated in metal - a process now known as Laser LIGA⁽²⁵⁾. Once a master has been made by excimer laser micromachining such methods allow high volumes of replica parts to be manufactured at low unit costs.

Already recognized by government-supported initiatives in Japan and the European Union, laser micromachining will be a key manufacturing tool in emerging nanotechnologies⁽²⁶⁾. The economic advantages of mass production at low unit cost is of the highest importance and will open up many new industrial application areas.

6. ACKNOWLEDGEMENTS

It is a pleasure to thank P Rumsby, N Rizvi, E Harvey and D Thomas of Exitech Ltd who contributed much to the original experimental material contained in this paper.

7. REFERENCES

1. N Bloembergen, 'Laser-material interactions, fundamentals and applications', in 'Laser Ablation: Mechanisms and Applications II', AIP Conference Proceedings, eds J C Miller & D B Geohegan, Vol 288 (1994)
2. J C Miller. 'History, scope and the future of laser ablation', in 'Laser Ablation, Principles and Applications', ed J C Miller, Springer-Verlag (1994)
3. Y Kawamura, K Toyoda and S Namba, 'Effective deep ultraviolet photoetching of polymethyl methacrylate by an excimer laser', Appl Phys Letts **40**, 374, (1982)
4. R Srinivasan and V Mayne-Banton 'Self-developing photoetching of poly(ethylene terephthalate) films by far ultraviolet excimer laser radiation', Appl Phys Letts **41**, 576, (1982)
5. J H Brannon and J R Lankard 'Pulsed CO₂ laser etching of polyimide', Appl Phys Letts **48**, 1226 (1986)
6. M C Gower 'Industrial applications of pulsed lasers to materials processing', in 'High-Power Laser Ablation' SPIE **3343**, 171 (1998)
7. G M Davis, A F Gibson, M C Gower, R A Lawes and R A Moody 'Direct photoetching of resist materials using excimer lasers', Microcircuit Engineering '83, Conference Summary, Cambridge, UK.
8. P T Rumsby et al, 'Target production and development', p1.26, Central Laser Facility Annual Report, SERC Rutherford Appleton Laboratory (1983).
9. F Bachman. 'Excimer lasers in a fabrication line for a highly integrated printed circuit board'. Chemtronics **4**, 149 (1989).
10. M C Gower. 'Excimer lasers: current and future applications in industry and medicine' in 'Laser Processing in Manufacturing', eds R C Crafer & P J Oakley, Chapman & Hall, (1993)
11. D J Elliott 'Ultraviolet laser technology and applications', Academic Press (1995)
12. W W Duley 'UV lasers - Effects and applications in materials science', Cambridge University Press (1996)
13. S D Allen, M Bass and M L Teisniger 'Comparison of pulsed Nd:YAG and pulsed CO₂ lasers for hole drilling in printed circuit board materials', CLEO '82 Conference Summary
14. M N Watson. 'Laser drilling of printed circuit boards', Circuit World, **11**, 13 (1984)
15. J R Lankard & G E Wolbold. 'Laser ablation of polyimide in a manufacturing facility'. Appl Phys. **A54**, 355 (1992)
16. H Holden. 'Microvia PCB's: the next generation of substrates & packages', Future Circuits International **1**, 71, (1997)
17. R S Patel, T F Redmond, C Tessler, D Tudryn and D Pulaski, 'Via production benefits from excimer laser tools', Laser Focus World (Jan 1996)
18. C Rowan. 'Excimer lasers drill precise holes with higher yields', Laser Focus World (Aug 1995)
19. A South. 'Miniaturization of Medical Products: The Development Challenge'. Medical Device Technology, **9**, 30, (1998)
20. M C Gower. 'Excimer lasers for surgery and biomedical fabrication' in Nanotechnology in Medicine and the Biosciences, eds R R H Coombs & D W Robinson, Gordon & Breach (1996)
21. R S Gifford & D J Bartnik. 'Using optical sensors to measure arterial blood gases', Optics & Photonics News, **9**, 27, (Mar 1998)
22. A B Frazier, R O Warrington and C Friedrich 'The Miniaturization Technologies: Past, Present and Future', IEEE Trans. on Industrial Electronics, **42**, No5, 423 (1995)
23. E C Harvey & P T Rumsby. 'Fabrication techniques and their application to produce novel micromachined structures and devices using excimer laser mask projection' in 'Micromachining and microfabrication process technology III' SPIE **3223**, 26, (1997)
24. M C Gower, E C Harvey, N H. Rizvi, P T. Rumsby, J P H Burt, M S. Talary, J A. Tame, R Pethig. 'Manufacture of Miniature Bioparticle Electromanipulators by Excimer Laser Ablation', in 'Laser Applications in Microelectronic and

- Optoelectronic Manufacturing III', SPIE **3274**, 152 (1998)
25. W Bacher, W Menz and J Mohr, '*The LIGA Technique and its potential for Microsystems – A Survey*', IEEE Trans. on Industrial Electronics, **42**, No5, 431 (1995)
 26. P McKeown. '*Nanotechnology*'. Emerging Technology Series: New and Advanced Materials, UN Industrial Development Organization **1** (1997)

Laser welding of functional and constructional ceramics for Microelectronics

Horst Exner*, Anne- Maria Nagel

Laserinstitut Mittelsachsen e.V. – Mittweida – Germany

* Dir.

ABSTRACT

We are presenting a very successful new method of a laser welding technology developed in the Laser Institute of Mittelsachsen. It allows us to join parts of alumina without any changes of their properties based on an additive free procedure. Furthermore it enables us to carry out the procedure without furnaces and in natural atmosphere within only a few minutes. In order to avoid thermally induced stresses two laser beams are used.

We will describe this procedure of laser welding of ceramics including the manner of preheating: their limits and advantages. The thermal influence on the welding bath and the grain structure will be discussed.

High pure laser welded Al_2O_3 - ceramic parts of various shapes will be presented.

This new method of Laser welding of ceramics opens up a wide field of new applications. Almost now a lot of branches of industry have already shown their interest in this promising technique. Most applications are expected with sensor elements generally, and in the protection of electronic elements against high temperatures, abrasion and / or chemical attacks.

Keywords: Laser welding, joining, ceramics, alumina

1. INTRODUCTION

Ceramics are working materials produced by a special process. They can have characteristics like high temperature resistance, extremely high hardness, low electrical conductivity and high thermal insulating properties, high chemical resistance and also lower density, compared with metals.

These excellent properties are the reason for applying technical ceramics in wide fields of electronics, automotive and chemical industries.

Later there was an appreciation of the procedure setting limits to the variation of shapes, and a stagnation of the development began. The conventional procedures involve disadvantages like not exactly definable shrinkage during sintering, for example in case of plastic forming, limitations to the ratio between base and height of the geometries, for example in case of nonplastic forming, a higher porosity, for example in case of pouring forming, or they are very expensive.

Methods, of joining ceramics direct, without intermediate bonding materials, require either a high expenditure of preparation of joining parts, for example in case of diffusion welding, and/or they are connected with a high expenditure of equipment, for example in case of electron beam welding. Joining techniques using additives like stick or braze often not advisable because the ceramics lose their specific superior properties.

Our investigations to the theme: "Precision material processing of ceramics by solid- state lasers" under supervision of Prof. Dr.- Ing. H. Exner at the Laserinstitut Mittelsachsen e.V. demonstrate that the limits mentioned above may be overcome by a technique using two laser beams. For first time now it is possible to produce geometries previously not realisable.

The further development of this technology will be a good prospect for an enormous expansion of the application of ceramics.

2. PROBLEM DISCRIBTION

The advantage of laser material processing: the very local energy input means an important problem for welding ceramics. Because of the relatively small thermal conductivity compared with the high thermal expansion, stresses in the material can occur leading to its destruction inevitably. The cause can be found in the structure of crystal lattice. A comparison to metals may show it: in metals the crystal lattice only consists of positive metal ions, the gabs between them being filled with flexible, negatively charged electron gas. It is characterised by a high density of misalignments . In case of an extern mechanical force this structure enables a migration of the misalignments.

Ceramics are characterised by a lattice consisting of alternating positive and negative ions with high binding forces. This constellation effects in case of an external force that the ions are driven towards fields of same charge. They react with high repulsion. This leads to high stresses, especially in the cooling phase.

The amount of the resulting stresses depends on the temperature gradient, on the physical properties of the material, and also on the procedure requirements.

The knowledge of this basic behaviour is a precondition for the development of a laser welding technology of ceramics that represents a combination of the difficult behaviour of ceramics and the advantages of laser material processing.

3. INTERNATIONALE STATE OF DEVELOPMENT

The investigations in laser welding of ceramics are mostly referred to welding with additives or to ceramics with a high proportion of fluid phases.

The varying technologies differ in the use of laser devices and in the kind of heating the ceramics. Essentially pulsed CO₂-lasers are used for welding because of the very good absorption behaviour. The most important thing is the preheating and postheating of the material in the correct manner. Therefor mostly furnaces are used. The application of gas burners is known, too[1,2,3].

All in all they generated all known join geometries like butt welding, lap welding and flanged welding. The joints resulted in I-, L-, and T- pieces up to a thickness of 20 mm. Welding of tubes could only be realised with a high concentration of silicium [3].

A disadvantage of all technologies mentioned above is a very long time (some hours) for processing. It is also necessary to use a long focal length because of the distance between target, furnace and optical system, and to use special optical windows that are transparent for the laser wave length. Another problem is to position the ceramical parts during temperatures of 1500°C or above.

The members of the Laser Application Centre Mittweida developed a technology that uses two laser beams to avoid thermally induced stresses [4,5]. One laser beam of 10.6 µm wave length is deflected by two scanner mirrors. Like the programmed scan geometry on the surface of the material a temperature field appears that minimises the temperature gradients on the complete area during the welding process. Some minutes later the welding laser beam of a wavelength of 1.06 µm can join the parts crackfree. The complete procedure only takes a few minutes and can be performed in natural atmosphere. As a result of the investigations it is possible to fasten longer parts of the material by metal fixtures. The principal set-up is shown in figure 1.

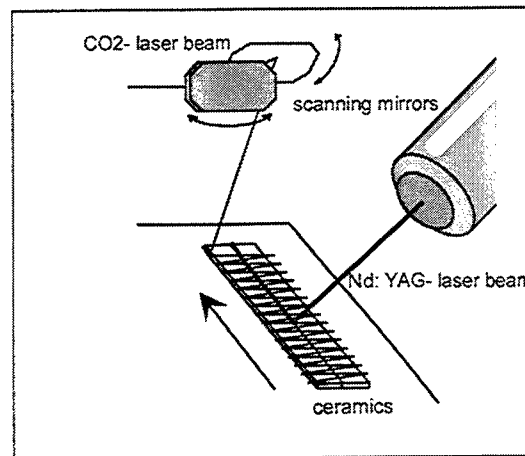
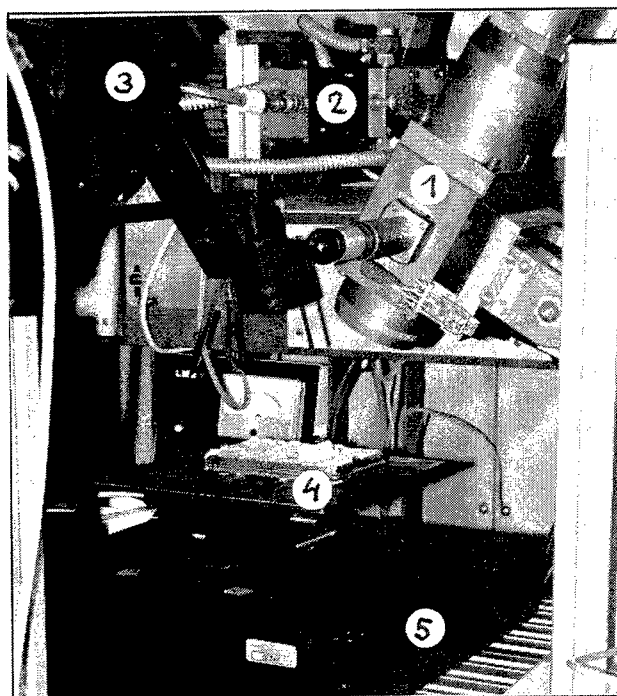


figure 1: principal set-up of the experimental procedure for welding ceramics developed in the Laser Application Centre of Mittweida

4. EXPERIMENTAL SET-UP

For the welding experiments a 400 W CO₂- laser was used for preheating. The laser beam was deflected by two scanner mirrors to create define scanning geometries. The material was positioned in the laser beam below the mirrors that was highly defocused. The welding laser beam was a 1,2 kW cw- Nd: YAG laser- his beam was applied through a fibre to the target. An acoustic emission analysis was used for controlling and checking the process in order to detect energy discharges during crack development. A pyrometer was used to record the temperatures during preheating , welding and postheating in a range from 500°C to 2500°C with a wavelength between 7,5µm and 8,3µm. The spot diameter of less than 1mm makes it possible to control the welding bath. The pyrometer is able to control the laser power, but therefore important investigations mentioned later are necessary.

The process proceeds without protective gases. The parts are held in place by ceramical supports, and bigger materials are fastened metallic holders. A picture of the test equipment is shown in figure 2.



- 1 Nd: YAG- laser head
- 2 CO₂- scanning mirrors
- 3 pyrometer
- 4 specimen
- 5 X - Y table

figure 2: picture of the used testing equipment

The material used is a typical substrate ceramics for electronic circuits. It has a purity of 97% alumina and a bending strength of 400 MPa.

It is important to notice the manner of separating. Investigations showed the important influence of this pretreatment. Figure 3 illustrates the comparison of three possibilities: cutting by CO₂- laser, scribing by Nd: YAG- laser and mechanical cutting.

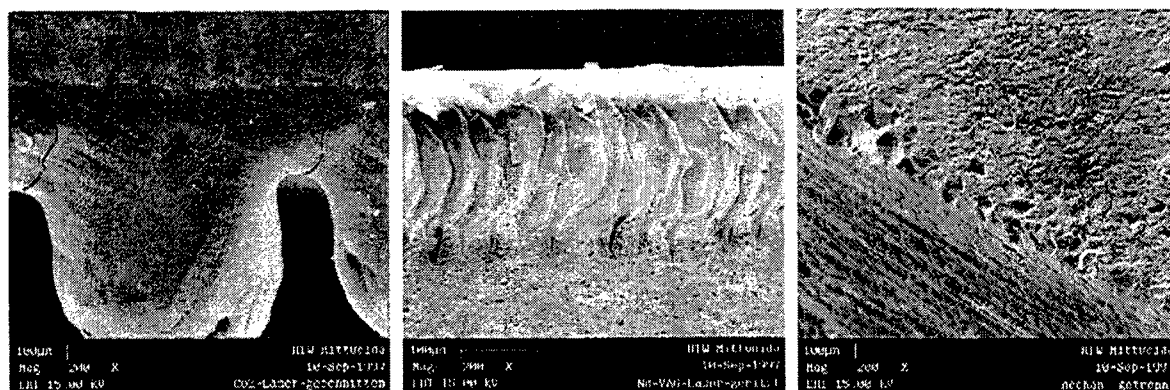


Figure 3: Comparison of three possibilities of dividing: on the left by CO₂- laser, in the middle by Nd: YAG- laser, on the right mechanical

Exactly every CO₂- cut face shows micro cracks that works as germs for new cracks immediately. In the picture on the left is easy to see the molten beard on the bottom, the mentioned cracks of some μm width are located between them running over the hole cut face. In the middle the scribed track of a Nd: YAG -laser can be seen with a depth of $\approx 200\mu\text{m}$ (around 1/7 of the depth). Neither in the track nor in the broken surface cracks can be found. In the right picture the side of a mechanical divided and ground ceramics is illustrated. No cracks can be found, but they often tend to break during the welding process and it is assumed that there are stresses in the material.

A tempering process can avoid this phenomenon and it is reasonable to do it.

5. RESULTS

Development of suitable parameters

The first step to join ceramics was to use the right heating conditions by varying the scanning geometries, scanning parameters like velocity, laserpower, and the distance from the focal plain. The dimensions named are a function of the geometry of the ceramic parts, and cannot be generalised. In comparison to the results achieved by other scientists using furnaces for preheating, a higher temperature of $\geq 1600^\circ\text{C}$ is necessary. This is because of the relatively short time for the transport of the substances surrounding the grains. This transport is important to avoid stresses.

The main aspect of investigations was focused on getting an optimum quality of welded joints. Therefore a lot of parameters was varied. The most important influence can be found in a change of the laser power and the welding velocity. After investigations of the welding zone by light microscopy, scanning electron microscopy and grinding tests, interesting tendencies were obtained as shown in figure 4. All the specimens were joined under same conditions of preheating regime, in the focal plain of the welding laser beam and without assisting gases.

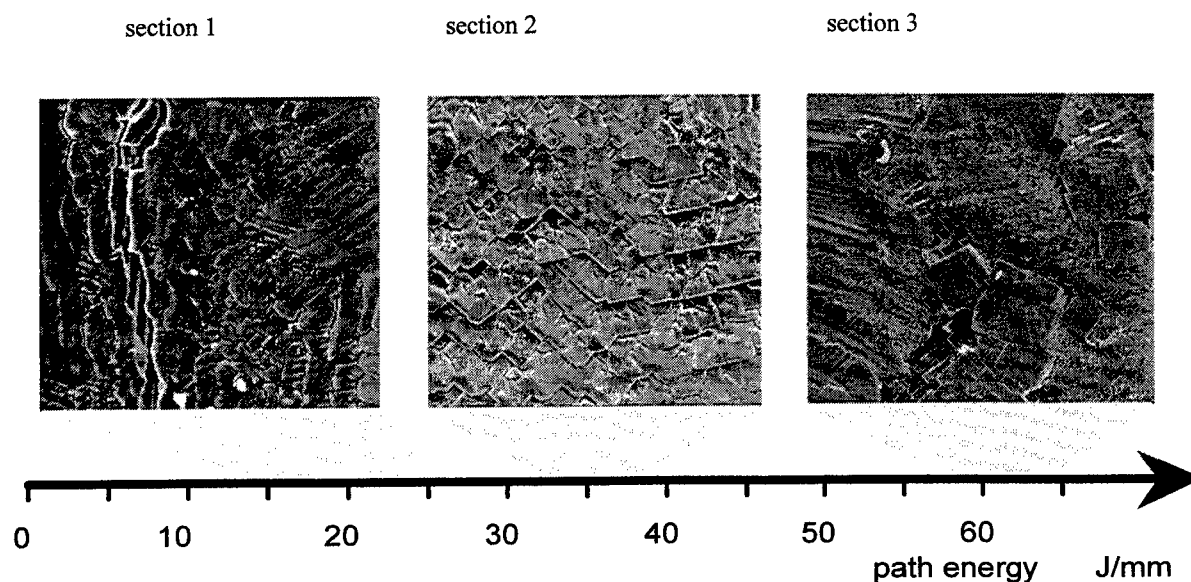


figure 4: trend behaviour of the welding quality as a function of laser path energy

section 1

In the first section a lot of dendrites were obtained, that met in the middle of the welding joint. Often the joint was cracked. It was assumed, that there appeared a hot cracking like in metals. During the recrystallisation of the molten mass impurities are pushed in front of the solidification front. In the centre of the welding bath these polluted substances of the lower melting point are collected. Because of the shrinkage during the solidification at the moment of a still existing liquid centre this area tears up apart. This behaviour is typical for section 1.

section 2

In the second section optimal qualities were found. This area is characterised by dense welding zones without bigger pores and dendrites. The surface shows equal crystals on the complete cross section arranged in a disordered state. This shape is favourable to be effective against a crack propagation. Tests of the bending strength showed that the joined parts are of the same strength as the basis material. The quality of this joint is illustrated as a grinding test in figure 5.

section 3

The third section is characterised by a progressive increase of big pores along the border area. In the centre of the recrystallised mass big grains are growing. On the edges long dendrites occurred. The system is very friable and not resistant.



Figure 5: grinding test of a high quality laser welded angle of Alumina

Investigations of Temperature Fields

Investigations of the temperature distribution on the surface of thin materials or of the whole body, respectively, are very important. For welding small parts it is possible to heat the complete material with the same temperature.

For bigger parts it is favourable to heat the material selectively. That means to have temperatures higher than 1600°C near the welding point, and to create a special temperature gradient for the surrounding fields, considering the stress distribution as established [4]. Consequently it is important to find the maximum temperature gradient for the neighbouring fields. The result is shown in figure 6.

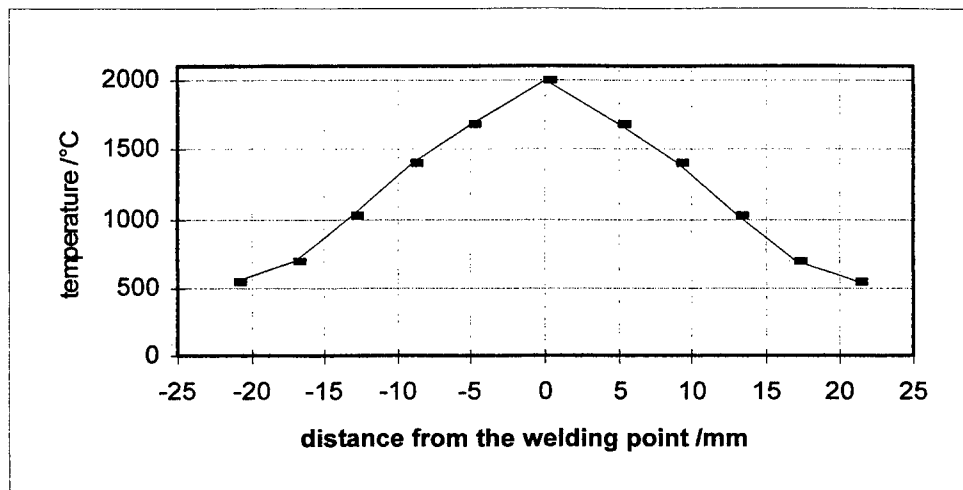


figure 6: temperature distribution over two ceramic stripes during laser welding of highest temperature gradients

This model shows the temperature distribution along two 10 x 50 mm stripes that are joined in the middle. A temperature gradient of 70 K/mm in two-dimensional direction was found as a meaningful course to guarantee a crackfree and also economic process. The importance of this statement is in the possibility of fastening the material by metals at a distance of about 25 mm from the welding point.

As already mentioned the investigations described referred to material with a thickness of 1 mm. But even with such dimensions it is necessary to think about temperature gradients into the depth. Although the temperature conductivity for ceramics is relatively good it sets limits to this technology. Calculations revealed that at a maximum temperature of 2000°C on the surface the temperature decreased to 1600°C in a depth of 3,5 mm. That means, still thicker materials would have temperatures below the critical point of 1600°C on the underside warranting a crackfree welding joint. Additional energy courses have to be considered.

Welded Geometries

In the following (figure 7) some examples welded during the investigations are demonstrated. Some welded hollow bodies like squares and cubes are shown. They reveal the possibility of including systems completely.

The wave structure is to demonstrate a possible application as a highly temperature insulating structure. After an inquiry some tubes for high temperature sensors were closed by laser welding.

All these figures show high quality joints and high strengths.

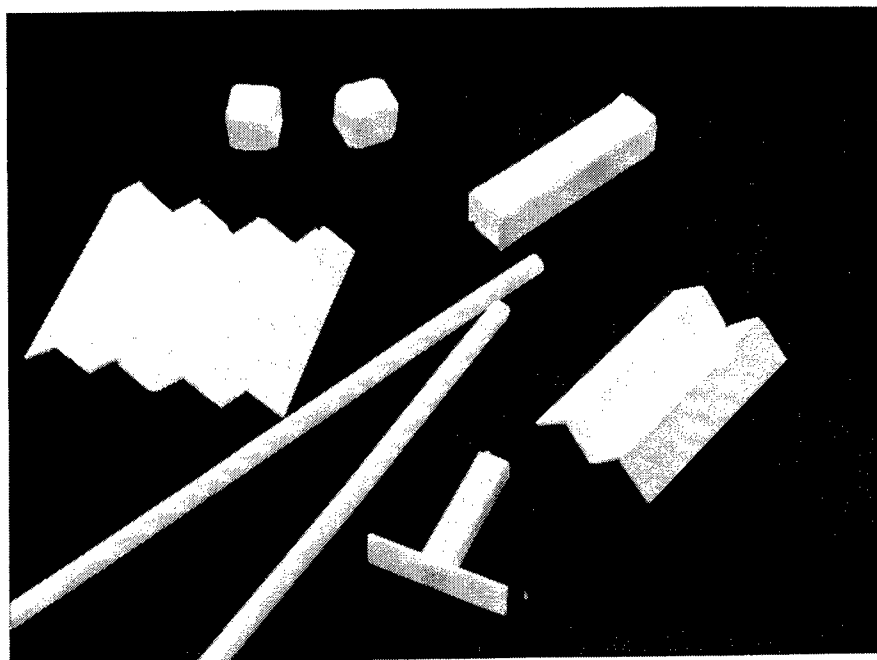


Figure 7: different laser welded geometries

6. CONCLUSIONS

The investigations of alumina laser welding with a purity of 97% showed that in general the technology is suitable. It was established, that high quality welding joints are realisable. The structure is homogeneous and leads to no losses of strength. Also, losses of material properties are not known. The technology allows to join up to a thickness of 3.5 mm. By using selective preheating it is possible to fix the material by metals. The shortest distance to the welding zone is more than 25 mm.

The technology performed expands the application of ceramic enormously. All the outstanding advantages of the laser material processing are useful: precision, touchlessness, flexibility and high velocity.

The investigations described are the basis for an industrial application. The knowledge about suitable temperature gradients makes it possible to automate the process generally. The next step will be the computer controlling of the laser heating parameters.

REFERENCES

- [1] Tomie, M.; Abe, N.; Noguchi, S.; Arata, Y.; Oda, T. (1995) Characteristics of weld bead and strength of joint by laser welding of 87% Al_2O_3 - Ceramics; Quarterly Journal of the Japan Welding Society, 13: 71- 76
- [2] Gedrat, O.; Emmelmann, C. (1991) Machining of Ceramics with Laser Radiation; 10. International Symposium on Electromachining: 52- 66
- [3] De Paris, A.; Robin, M.; Fantozzi, I.G (1992) CO_2 - Laserwelding of SiO_2 - Al_2O_3 - Tubes; ECLAT'92, Laser Treatments of Materials, DGM- Verlag: 131- 136
- [4] Exner, H.; Gerber, B.; Kimme, T.; Seifert, U.; Straube, R. (1993) Further Progress in Laser Welding of Ceramics, Proceedings ICALEO'93: 611- 619
- [5] Nagel, A.- M. (März, 1996) Untersuchungen zum Laserschweißen von Keramik, Diplomarbeit an der Hochschule für Technik und Wirtschaft Mittweida (FH)

Concurrent in-line inspection system for CO₂ laser drilling machine

Makoto Kato^a, Nobuhiro Araki^a, Kazuhide Isaji^b, Hidehiko Karasaki^b

^aMatsushita Research Institute Tokyo, Inc.,
3-10-1 Higashimita, Tama-ku, Kawasaki 214-8501, Japan

^bMatsushita Industrial Equipment Co., Ltd.,
3-1-1 Inazu-cho, Toyonaka, Osaka 561-0854, Japan

ABSTRACT

We describe the concurrent in-line inspection system, which controls the CO₂ laser drilling machine for printed wiring boards. The performance of a CO₂ laser drilling process was improved drastically by the introduction of this inspection system. The principle of this inspection system is based on the relationship between the exposed bottom area of the inner layer copper foil in via hole and the intensity of the reflected laser beam. The end of drilling process is detectable by the saturation of the reflected laser beam intensity generated at the copper foil surface of the blind via hole. We have carried out the drilling process for glass-cored epoxy substrate and have observed that the productivity of the drilling process is increased by 30% due to this inspection system.

Keywords: in-line inspection, CO₂ laser, drilling

1. INTRODUCTION

The reduction of the weight and size of electronic equipment, such as personal handy phones and notebook PCs, has become the trend in the market. The importance of high-density interconnection technology of electrical parts, especially BGA (ball grid array) and CSP (chip size package) mounting technology is well-known for manufacturing compact electronic products. In particular, interstitial via holes fabricated on printed wiring boards should follow new design rules by reducing the wiring route and the mounting space of electrical devices. Interstitial via holes of over 300,000 holes/m² are drilled on printed wiring boards, because a fine design rule of silicon chip has led to the reduction of the chip size. Currently, as the I/O pin pitch of CSP has decreased to 0.3mm, it is required that the lines and spaces are less than 50 μ m and the diameters of the via holes and pads are less than 150 μ m.

The currently used drilling method, mechanical drilling, is not suitable for making small via holes. Recently, several drilling methods, for example, laser-drilling, plasma-drilling and photo-etching methods, have been examined. Since it is easy to change the laser irradiation conditions to control the shape of the via hole and it is capable of drilling various kinds of resin (epoxy, glass-cored epoxy, polyimide and BT resin), the laser-drilling method has become the subjects of extensive research.

Wrenner of IBM Corp. was the first to develop a CO₂ laser drilling system with two sets of mechanical synchronous choppers and a 150W CW CO₂ laser, which has the capability to generate several millisecond-order laser pulse.¹ He demonstrated the system's ability to drill through-holes into a 0.006-inch-thick glass-cored epoxy substrate at a rate of 57,000 holes/hr. Then, Seraphim, also of IBM Corp., developed the chip-module package and the printed wiring module of 3081's CPU unit.^{2,3} He was able to get good results from the thermal cycle test of the laser-drilled printed wiring boards, and verified it useful for practical industrial use.

In 1995, Matsushita Electric Industrial Co.Ltd., developed the new concept of the multi-layer printed wiring board "ALIVHTM" for personal handy phone.⁴ For this purpose, a new CO₂ laser drilling system consisting of a two-dimensional galvanometric scanner and a telecentric scan lens was developed. The drilling speed of this system is about 200 holes/sec, which is ten times that of a typical four-axis mechanical drilling machine. We have developed a CO₂ laser drilling system whose performance is improved by real-time process control using concurrent in-line inspection system. In this paper, the principle and the advantages of concurrent in-line inspection system for glass-cored epoxy substrate are described.

2. OPTICAL SYSTEM FOR DRILLING VIA HOLES WITH CONCURRENT IN-LINE INSPECTION SYSTEM

The schematic diagram of the CO₂ laser drilling system is shown in Fig.1. The system consists of a CO₂ laser, collimating unit, a mask changer, an optical isolation unit, a two-dimensional galvanometric scanner and a telecentric scan lens.

The CO₂ laser resonator (located on the right side in Fig.1) outputs a linearly polarized laser light of 9.3 μm wavelength. In general, the absorption coefficient of the resin at the 9.3 μm band is higher than that at the 10.6 μm band. Therefore, the wavelength of 9.3 μm was chosen from the viewpoint of drilling quality, especially to avoid the carbonization of the drilled via hole and the smear after the drilling process. The Kepler-type collimating unit converts the diameter and the divergence angle of the laser beam for optimizing to each optical mask mounted on the mask changer. The laser beam transmitted through the mask propagates through several optical components (described below) and is irradiated on the workpiece on the processing table. The drill data of the CAD are converted into the galvanometric scanner command in the divided scan field, and the galvanometric scanner precisely locates the laser beam on the workpiece. Then, the processing table is moved to the next scan field after the scanning. With the scan lens, the shape of the optical mask is projected on the workpiece with predetermined magnification.

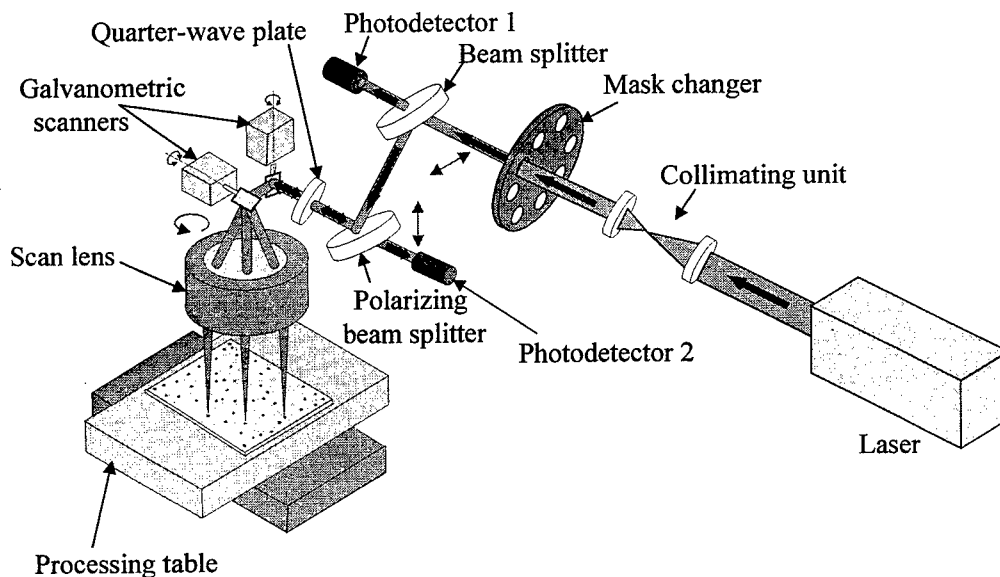


Fig.1 The optics of CO₂ laser drilling machine

We developed two kinds of the inspection systems. The first one is the laser pulse monitoring system. Photodetector 1 detects a part of the incident laser beam. When it detects the lack or the incompleteness of the laser pulsing, the control unit of the drilling machine controls the laser pulsing according to the results. The second one is the concurrent in-line inspection system, which consists of an optical isolation unit and a photodetector. The principle of the optical isolation unit is based on the polarization of the laser beam. Laser beam with linear polarization is incident onto the polarizing beam splitter (PBS) with an S-polarized angle and is reflected. The laser beam reflected from the PBS surface propagates through the quarter-wave plate, where the beam is converted to circular polarization. At the first stage of the drilling process, the laser beam is absorbed by the resin substrate. When the copper foil of the inner layer is exposed, laser light is reflected from the bottom surface of via hole. By this reflection, the direction of the rotation of the circular-polarization is inverted. The reflected laser beam propagates through the quarter-wave plate again. The polarization of the transmitted laser beam is converted into the

linear polarization perpendicular to the incident beam, P polarization. Then, the returning laser beam propagates through the PBS and is detected by the photodetector 2.

We designed both the scan lens and the galvanometric scanner head to minimize the difference of the optical axes of the incident laser beam and the returning reflected laser beam.

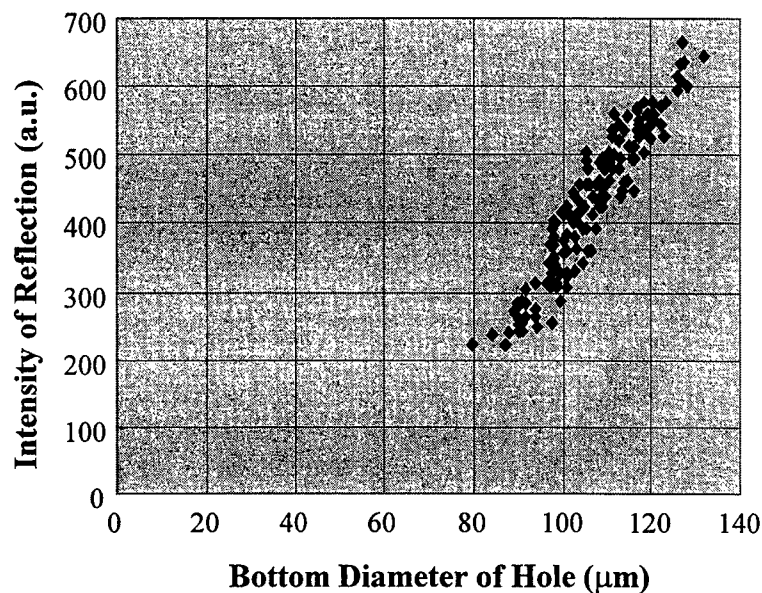


Fig.2 The relationship between the bottom diameter of drilled hole and the intensity of reflected beam

3. CHARACTERISTICS OF THE REFLECTED BEAM DETECTION

Figure 2 shows the relationship between the bottom diameter of the exposed area on the inner layer copper foil in the via hole and the intensity of the reflected laser beam measured by the mercury cadmium telluride (MCT) photodetector. In principle, the relationship between the bottom diameter and the intensity of the reflection shows a parabolic curve because the laser beam has a top-hat distribution of the intensity. From measured data, there is a linear relationship between them in the range of the diameters from 80 μm to 150 μm . With this relationship, we can determine the diameter of each hole. Because this system uses the reflection of the laser beam for the processing, we can know the diameter of the via hole immediately. We call this system "concurrent in-line inspection system".

The cause of the distribution of the plots are the slope of the inner layer copper foil (about ± 1 deg.), the surface treatment (e.g., back oxides and no hollowing treatment) and the effect of the surface roughness of the inner layer copper foil.

4.COMPENSATION OF THE DETECTED SIGNAL AND CONTROL ALGORITHM

For precise inspection, we adopted three kinds of signal compensation for concurrent in-line inspection system. With this compensated signal, the drilling process is controlled. Details are described below with a reference to Fig.3.

4.1. Signal compensation

4.1.1. Compensation of temperature of photodetectors

During the laser drilling process, both the photodetector 1 and the photodetector 2 are irradiated by laser beam at random. The photodetector consists of MCT, which is heated by the laser beam. Of course, the room temperature is not stable. As the result, the responsivity of the photodetector changes according to its temperature, and the gain of the output signal should change.

In this system, we measure the gain of the output signal in advance as a function of the temperature for each photodetector, and the measured output signal is compensated according to the temperature of the photodetector. The measured relationship between them is pre-installed as a compensation data to the control unit of the drilling machine.

4.1.2. Scan field mapping

The practical axis of the laser beam between the telecentric scan lens and the processing table is not vertical, because X- and Y- galvanometric scanner mirrors can not be positioned at the scanning point of the scan lens simultaneously. The difference of the angle between the vertical axis and the practical one increases with the increase of the distance from the center of the scan lens. Therefore, the axis of the reflected laser beam differs from that of the incident beam and the intensity of the reflection decreases geometrically. To compensate such a geometric error, the scan field mapping data are measured using a high-reflection mirror and a compensation data is created in advance. During the drilling process, each compensation data is read out from the mapping data in the control unit according to the position that the two-dimensional galvanometric scanner is positioning. Then, each output signal of the photodetector is calculated using the compensation data.

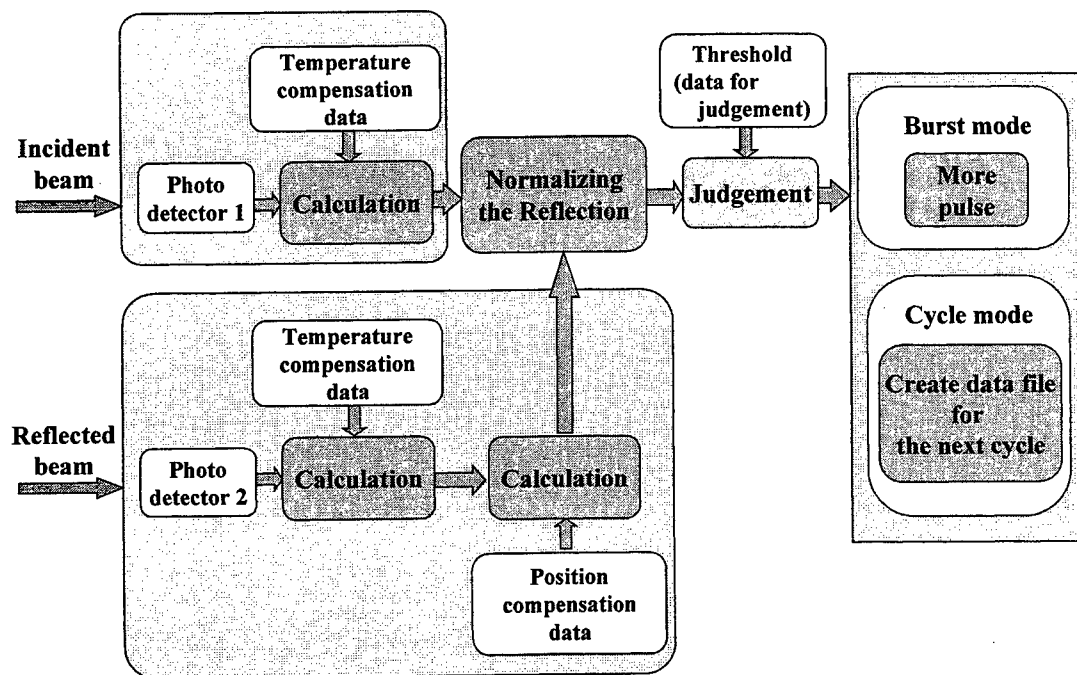


Fig.3 Signal compensation and control algorithm of concurrent in-line inspection system

4.1.3. Normalization of the reflected laser beam

Laser beam emitted from the resonator fluctuates between the range of less than $\pm 5\%$. Therefore, for precise measurement, the signal of the reflected laser beam should be normalized by the intensity of the incident laser beam. In addition, two A/D converters work simultaneously for both incident and reflected laser beams for the precise sampling in the concurrent in-line inspection system.

4.2. Control algorithm

We have utilized the concurrent in-line inspection system for the drilling process. We call it "active-control processing". This drilling system has two kinds of processing mode, the cycle mode and the burst mode. In the cycle mode, the scanning of the galvanometric scanning mirrors repeats several times till finishing all the holes. In the burst mode, the laser beam is pulsed continuously till the end of the processing of each via hole. The suitable processing mode depends on the thermal damage of the drilled via holes. The active-control system works in each mode as follows.

4.2.1. Control algorithm of the cycle mode

In both modes, the threshold of the compensated signal should be decided in advance. The value of the threshold depends on the quality of the drilled via holes. In the processing, if the compensated signal from a hole does not exceed the threshold, the control unit adds the position of the hole to the position-file for the next cycle. In the next scanning cycle, the control unit fires the laser pulse according to the position-file. This process repeats till finishing all the holes.

The maximum number of the scan time is predetermined. In the case that the signal does not exceed the threshold at the last laser beam, we consider the processing to the hole is not good and the PWB should be checked in detail.

4.2.2. Control algorithm of the burst mode

In the burst mode, if the compensated signal from a hole does not exceed the threshold, the control unit fires one more pulse to the same hole immediately. And this process repeats till exceeding the threshold. The maximum number of the laser pulse is predetermined, too.

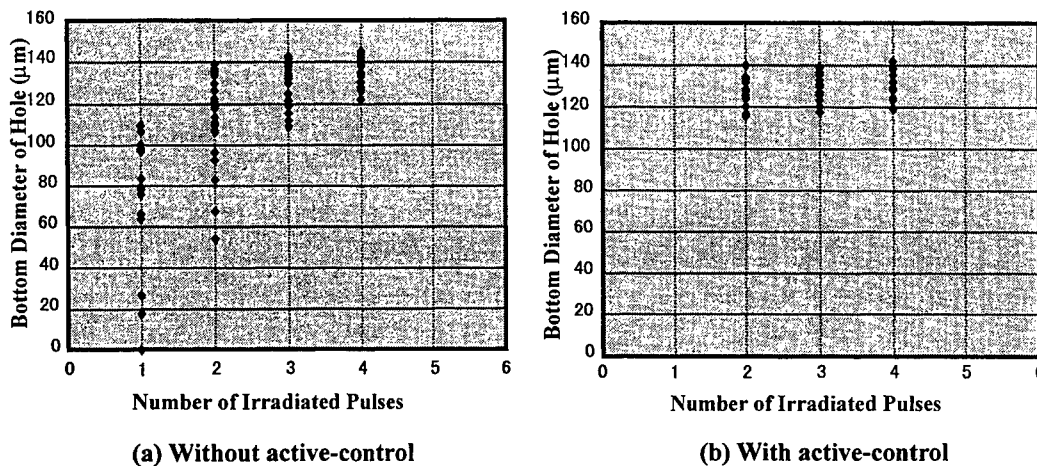


Fig.4 Task time of laser drilling without / with active-control processing

5. EFFECT OF THE ACTIVE-CONTROL PROCESSING

Figure 4 (a) shows the distribution of the bottom diameter of the via hole as a function of the number of the laser pulses without the active-control processing in the cycle mode for the glass-cored epoxy substrate. There is large distribution of the bottom diameter with 1 shot processing. It depends on the density of the glass-cloth. The distribution becomes smaller with the increase of the number of the laser pulses. And with 4 laser pulses, every via hole has the diameter of more than 120 μm . In the conventional drilling process without the active-control for hybrid materials, e.g., glass-cored epoxy substrate, we selected 4 laser pulses. However, in some area with low-density glass-cloth, drilling was completed with 2 or 3 laser pulses. In this process, because the number of the laser pulses is predetermined to finish the highest-density glass-cloth, all the holes are drilled with 4 laser pulses. Figure 5 (a) shows a photo of an example of the cross-section of a via hole without the active-control processing. This photo shows that an extra laser pulse irradiation has a possibility to induce liquefied resins flow to the bottom area during laser irradiation. This barrel-shaped via hole is not suitable for the plating.

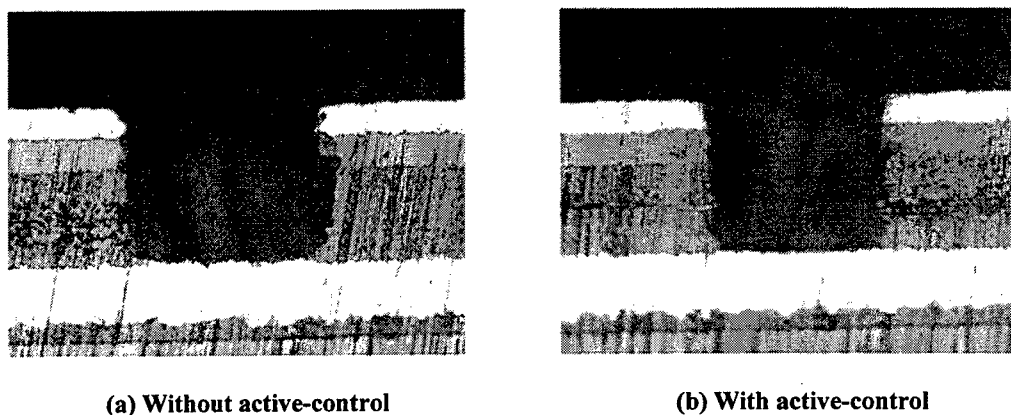


Fig.5 Cross-section of via hole without / with active-control processing

Figure 4 (b) and Figure 5 (b) show the results of the drilling with the active-control processing. The active-control processing can detect the bottom area of the exposed copper foil at each laser pulse irradiation, and can control the drilling process in real time. In Fig.4 (b), the distribution of the bottom diameter remains narrow consistently with the increase of the number of the laser pulses from 2 to 4. We measured the average number of the irradiation and found it equivalent to about 2.8 shots, which is shorter by about 30% than the case without the active-control processing. With the active-control processing, the task time for inspection is not required because of the in-process monitoring technology.

The finished via hole was easily transformed into a barrel-shaped one by extra laser pulses. Figure 5 (b) shows an example of the cross-section of a via hole with active-control processing. We verified that there were no barrel-shaped via holes in the absence of extra laser irradiation. Therefore, the active-control system reduces the task time and keeps drilling quality stable, since the irradiation condition is optimized for each via hole.

6. CONCLUSIONS

We have developed a CO_2 laser drilling system controlled by concurrent in-line inspection system using in-process monitoring technology. This inspection system requires no additional task time and we found the following results.

(1) For hybrid materials, for example, glass-cored epoxy substrate, the active-control processing is better than the conventional drilling process from the viewpoint of the quality of the drilled via holes.

(2) The number of the laser pulses is optimized to each via hole using the active-control system, and the task time in the active-control processing is reduced about 30% in comparison with the case without the active-control processing.

REFERENCES

1. W.R.Wrenner, "CO₂ laser drilling system for computer circuitry", *Circuit Manufacturing*, pp. 29-32, 1977.
2. D.P.Seraphim, "Chip-module package interfaces", *IEEE transaction on components, hybrids and manufacturing technology*, CHMT-1, No.3, pp. 305-309, 1978.
3. D.P.Seraphim, "A new set of printed circuit technology for IBM 3081 processor unit", *IBM journal of research and development*, vol.26, No.1, pp. 37-44, 1982.
4. United States Patent, No.5,690,846

SESSION 6

Laser Surface Cleaning and Crystallization

Laser surface cleaning of electronic materials

Y.F. Lu, W.D. Song, Y. Zhang, and Y.W. Zheng

Laser Microprocessing Laboratory,
Department of Electrical Engineering and Data Storage Institute,
National University of Singapore, 10 Kent Ridge Crescent, Singapore 119260

ABSTRACT

Laser cleaning was demonstrated both theoretically and experimentally to be an effective cleaning technique for removing particulate and thin film contaminants from electronic materials. Two types of laser cleaning techniques have been discussed, relying on pulsed laser of the surface without or with the presence of a thin liquid coating. For dry and steam laser cleaning, cleaning models were established for removal of particles from substrate surfaces without or with a thin liquid layer by taking adhesion forces and cleaning force into account. The models not only explain the influence of laser fluence on cleaning efficiency, but also predict the cleaning thresholds. The laser-induced removal of organic thin film contaminants is considered due to laser ablation of the contaminants. Applications of laser cleaning to clean magnetic sliders, magnetic media surfaces, IC mold and PCB (Printed Circuit Board) will also be addressed.

KEYWORDS: Laser cleaning, quantitative modelling, cleaning mechanisms, cleaning applications.

1. INTRODUCTION

There have been significant efforts to develop effective techniques to remove surface contaminants,^{1,2} such as high-pressure jet; mechanical wiping and scrubbing; etching and ultrasonic cleaning. Some of them such as ultrasonic cleaning require the immersion of a sample into a liquid bath, which has a number of serious drawbacks. Firstly, it is widely known that wet techniques could add contaminants due to insufficient cleaning and filtering of the liquid at the submicron level. Secondly, the bulk usage of hazardous chemicals and solvents becomes undesirable for environmental and industrial reasons such as causing cancers in humans and depleting ozone layer. Other problems associated with the wet techniques are rinsing/drying difficulties and incompatibility with other processes. Hence, dry cleaning techniques have emerged in order to overcome these drawbacks.

Recently, laser cleaning was demonstrated to be an efficient cleaning method for removal of particulate and organic film contamination from solid surfaces.³⁻²⁰ Two types of laser cleaning have been reported in the literature, relying on pulsed laser heating of the solid surfaces without or with the presence of a thin liquid coating. We shall refer to these two types as dry laser cleaning and steam laser cleaning, respectively. For dry laser cleaning, particles can be ejected from particulate-contaminated surfaces by short-pulse laser irradiation. The proposed mechanism of the ejection is fast thermal expansion of the particle and/or solid surfaces, which induces large cleaning force to overcome the adhesion force between particles and solid surfaces.¹⁶⁻²⁰ Another mechanism is laser ablation of particles as particulate materials have smaller ablation threshold than that of solid surfaces.⁹ The laser cleaning of organic film contaminants is considered due to laser photo-ablation and thermal-ablation of the contaminants.⁷ For steam laser cleaning, the proposed mechanism is supposed to be the momentum transfer from the laser-heated and suddenly evaporating liquid film to the particles on the solid surfaces.³⁻⁵ Compared with wet cleaning, it has several advantages such as dry process without using organic solvents, area-selective cleaning and cleaning samples on line. The following will focus on laser-induced removal of particulate and organic thin film contaminants from electronic materials. The cleaning models, cleaning efficiency and several industry applications will be discussed in detail.

Y.F. Lu: Email: elehuyf@nus.edu.sg; Telephone: 65-8742118; Fax: 65-7791103

2. REMOVAL OF PARTICLES FROM ELECTRONIC MATERIALS

2.1 Cleaning model

Several important forces exist and can cause strong adhesion of a tiny particle on a solid surface.¹ These include Van der Waals force, capillary force, and electrostatic forces, which easily exceed gravitational forces on small particles.

2.1.1 Adhesion Forces

For a dry system, a capillary force will not be taken into the consideration while calculating the adhesion force of particles on substrate because there is no liquid film layer between the particulates and substrate (assuming negligible atmospheric moisture). In a dry system, Van der Waals force predominates for tiny particles with a particle size less than a few microns and electrostatic forces predominate for large particles, i.e. greater than about 50 microns in size.¹ In semiconductor, disk drive and other microelectronic industries, particles are usually much smaller than 50 μm , Van der Waals force is dominant for these tiny particles on dry solid surfaces. Therefore, the adhesion force between a tiny particle and a solid surface F is

$$F = \frac{hr}{8\pi z^2} + \frac{h\delta^2}{8\pi z^3} \quad (1)$$

where r , h , δ and z are the particle radius, the material-dependent Lifshitz-Van der Waals constant, the radius of the adhesion surface area and the atomic separation between the particle and surface. Typical values of h range from a low value of ~ 0.6 eV for polymer/polymer interaction to a large value of ~ 9.0 eV for gold/gold interaction. For Van der Waals-bonded crystals, the atomic separation z is approximately 4 angstroms.^{1,2}

For a wet system, a capillary force and Van der Waals force will act to hold a tiny particle. The adhesion force between a tiny particle and a solid surface F is

$$F = \frac{hr}{8\pi z^2} + \frac{h\delta^2}{8\pi z^3} + 4\pi\gamma r \quad (2)$$

where γ is the liquid surface tension and r is the radius of the particle.¹

2.1.2 Temperature distribution

Since cleaning forces induced by laser irradiation, discussed in the following, depend on temperature distribution in a substrate or a particle, it is needed to know the temperature distribution in order to calculate the cleaning force. When a pulsed laser irradiates a substrate surface, the temperature distribution in the substrate can be described by the one-dimensional heat equation. The temperature at any point inside the substrate $T(x,t)$ is a function of depth below the substrate surface x and time t , and is governed by the one-dimensional heat equation^{21,22}

$$\rho c \frac{\partial T(x,t)}{\partial t} = k \frac{\partial^2 T(x,t)}{\partial x^2} + (1-R)\alpha I_0 \exp(-\alpha x) \quad (3)$$

where ρ , c , K , R , α and I_0 are density, specific heat, thermal conductivity, reflectivity, absorption coefficient of the substrate material and laser intensity on the substrate surface, respectively.

For a cylindrical, a rectangular, a square, or a plate particle with a thickness of d , or a spherical particle with a diameter of d , the temperatures at the irradiated surface of the particle and at the bottom of the particle are approximately

estimated to be those at the substrate surface of the same bulk material and at the depth of d below the substrate surface, respectively. This approximation causes the final result to be less accurate. Nevertheless, it is still a reasonable approximation to the real case.²⁰

2.1.3 Dry Cleaning Forces

Due to the short pulse laser irradiation, there is a rapid increase in temperature of the particles and/or substrate. This increased in temperature will indirectly generate a cleaning force which opposes to the adhesion force. And it is this cleaning force that causes cleaning phenomena, ejecting particles from the substrate surface.

For transparent particles on an absorbing substrate, majority of the laser energy is absorbed by the substrate, which results in temperature rise in the substrate. When the substrate surface under the particle experiences a fast expansion due to temperature rise induced by pulsed laser irradiation, the expansion will be restrained by the particle. Therefore, an action force per unit area to the particle due to the thermal expansion of the substrate surface is produced, which is defined as the cleaning force per unit area f_l . That is

$$f_l = \gamma E \Delta T(0, t) \quad (4)$$

where γ and E are the linear thermal expansion coefficient and the elastic modulus of the substrate, respectively. The $\Delta T(0, t)$ is the temperature rise at the substrate surface and time t , which is given by $\Delta T(0, t) = T(0, t) - T_0$, where T_0 is the initial temperature at substrate surface.

For a transparent substrate, only particles are absorbing the energy from the laser beam. Similarly, the temperature rise in the particles will also result in thermal expansion which is restrained by the substrate below it. Therefore, an action force to the substrate surface due to the thermal expansion of the particles is produced. Meanwhile, the substrate surface impose a reacting force to the particles given by $\gamma E \Delta T(d, t)$, where γ and E are the linear thermal expansion coefficient and the elastic modulus of the particles, respectively. The $\Delta T(d, t)$ is the temperature rise of the particle at the interface between the particle and substrate.

If the cleaning force (per unit area) exceeds the adhesion force (per unit area), the particle may be detached from the substrate surface. Therefore, the cleaning condition will be cleaning force (per unit area) larger than the adhesion force (per unit area).

2.1.4 Steam laser cleaning force

For laser with enough intensity irradiating on a solid surface coated by non-absorption liquid film, a sheet of liquid near the liquid/substrate interface can be superheated through thermal diffusion. The growth of vapor bubbles on the interface can be generally observed over a range of temperature.^{24,25} During the process of bubble growth, the pressure and temperature inside the bubble will lie in the ranges:²⁵

$$\begin{aligned} P_\infty \leq P_v \leq P_{\text{sat}}(T_\infty) \\ T_{\text{sat}}(P_\infty) \leq T_v \leq T_\infty \end{aligned} \quad (5)$$

where P_∞ , P_v , P_{sat} , T_{sat} , T_v , T_∞ are the ambient liquid pressure, vapor pressure inside the bubble, saturation vapor pressure, saturation temperature, temperature inside the bubble and ambient liquid temperature, respectively.

The process of bubble growth is divided into two regimes: inertial-controlled growth and heat-transfer-controlled growth. In cases of quickly imposed heat flux by laser irradiation and highly wetting liquid, inertial-controlled growth is more likely to occur. In this regime $T_v \cong T_\infty$, and with the constraint of local thermodynamic equilibrium, $P_v = P_{\text{sat}}(T_v) \cong P_{\text{sat}}(T_\infty)$.

The upper limit for velocity of bubble growth in inertial-controlled process has been theoretically described as below:^{25,26}

$$v(T) = \left(\frac{2}{3} \frac{P_v(T) - P_\infty}{\rho_l(T)} \right)^{1/2} \quad (6)$$

where $v(T)$ and $\rho_l(T)$ are the velocity of bubble growth, liquid density at temperature of T . P_v and P_∞ are defined as before. The size of bubbles cannot be larger than the thickness of the superheated liquid.

It has been known that coating of a thin water layer on metal surface can enhance the laser-generated pressure of stress wave by up to 20 dB.²⁷ The enhancement of pressure has been attributed to plasma formation, rapid evaporation and bubble expansion. The plasma formation occurs only for high-intensity laser irradiation due to optical breakdown. For laser intensity below the breakdown threshold, the pressure of stress wave is dominated by the rapid evaporation and bubble expansion.

Based on the results of other studies,²⁸ we can deduce the pressure of stress wave by assuming that: (1) in the region near liquid/substrate interface, the vapor layer created by evaporation of liquid acts as a plane piston, compressing its adjacent liquid layer and generating stress wave, although the value of volume fraction of vapor inside the superheated liquid layer is less than 1;²⁹ (2) due to the non-uniform temperature distribution in the liquid film, the vapor pressure inside bubbles is approximately considered to be the average saturation vapor pressure of the superheated layer; (3) the expansion velocity of vapor layer is equal to the growth velocity of the bubbles which is shown in Eq. (6). Then the average energy on unit area vapor/liquid interface obtained through the expansion of vapor layer is $\int (P_v - P_\infty) v f dt$, where v and f are expansion velocity and volume fraction of vapor. For the generated stress wave, its energy per unit area is calculated by:³⁰

$$E = \int \frac{P^2}{2\rho c} dt \quad (7)$$

where ρ , c and P are the liquid density, transmit speed and pressure of stress wave. According to energy conservation, the pressure of stress wave at the vapor/liquid interface is:

$$P = [2\rho c(P_v - P_\infty)vf]^{1/2} \quad (8)$$

The cleaning force caused by this pressure on adhesion particles with radius of r can be obtained by Eq. (8). The threshold of laser cleaning is defined as the laser fluence at which the cleaning force is equal to the adhesion force.

2.2 Experimental results and discussion

The schematic diagram of laser cleaning system was described elsewhere.⁹ A KrF excimer laser and a YAG laser are used as light sources for laser cleaning. The particles on solid surfaces were introduced by coating the solid surfaces with methanol suspension of fine powders. The substrates with particles were dried by a heater to evaporate the methanol. Then a strong air jet was applied to remove all "loose particles". The contaminated samples were observed under an optical microscope before and after laser cleaning. The cleaning efficiency is defined as the ratio of the number of particles removed by laser irradiation to that on the same area before laser cleaning.

2.2.1 Dry laser cleaning

Quartz particles as non-absorbing particles and single crystal silicon as absorbing substrates were chosen for examining above cleaning model. Laser fluence dependence of cleaning efficiency at 100 pulses and 10 Hz for removal of quartz particles from Si substrate surfaces is shown in Fig. 1(a). From Fig. 1(a), it was found that the cleaning threshold for laser removal of quartz particles from Si surfaces is about 135 mJ/cm², and the cleaning efficiency increases with increasing laser fluence. The peak cleaning force (per unit area) and adhesion force (per unit area) at different laser fluences are shown in Fig. 1(b). From Fig. 1(b), it was observed that the cleaning force (per unit area) is smaller than adhesion force (per unit area) below 125 mJ/cm², which means quartz particles on Si substrate surfaces cannot be removed by laser irradiation. At a laser fluence of 125 mJ/cm², the cleaning force (per unit area) is equal to the adhesion force (per unit area) between quartz particles and Si surfaces. Therefore, the cleaning threshold is 125 mJ/cm². With increasing laser fluence above 125 mJ/cm², the difference between the cleaning force and the adhesion force increases, which leads to

easier removal of the particles from Si surfaces or a higher cleaning efficiency at higher laser fluence. Thus the experimental results in Fig. 1(a) can be predicted by above theoretical analysis.

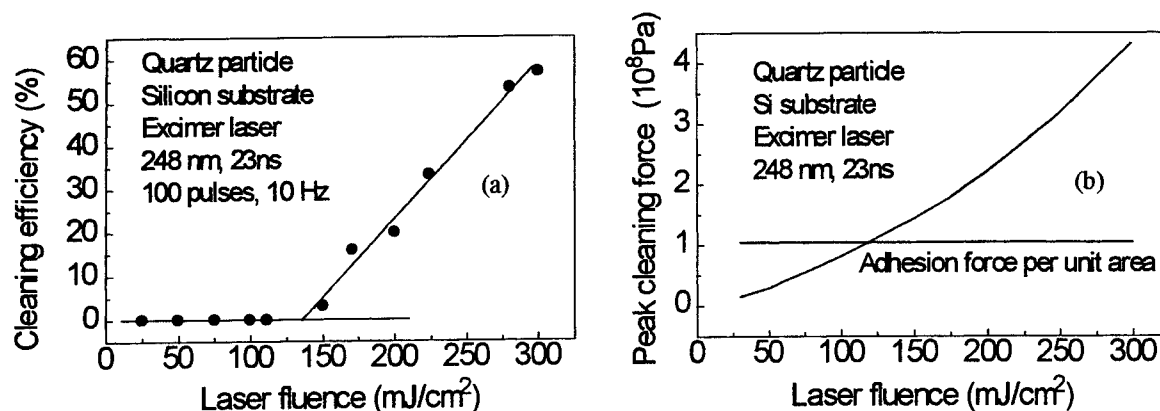


Fig. 1 (a) Laser fluence dependence of cleaning efficiency for removal of quartz particles from Si substrate surfaces; and (b) the peak cleaning force (per unit area) and adhesion force (per unit area) at different laser fluences

Copper particles as absorbing particles and quartz as a non-absorbing substrate were elected for examining above cleaning model. Comparison of laser cleaning efficiency for three different wavelengths at 500 pulses and 10 Hz for removal of copper particles from quartz surfaces is shown in Fig. 2(a). From Fig. 2(a), it was observed that the cleaning efficiency increases with increasing laser fluence for all three different laser wavelengths and is higher for the shorter wavelength at a particular laser fluence for removing copper particles from quartz surfaces. The experimental cleaning thresholds for removal of copper particles from quartz surfaces are 80 mJ/cm^2 at 1064 nm, 40 mJ/cm^2 at 532 nm and 20 mJ/cm^2 at 266 nm, respectively. These show that the experimental thresholds become smaller for the shorter wavelength.

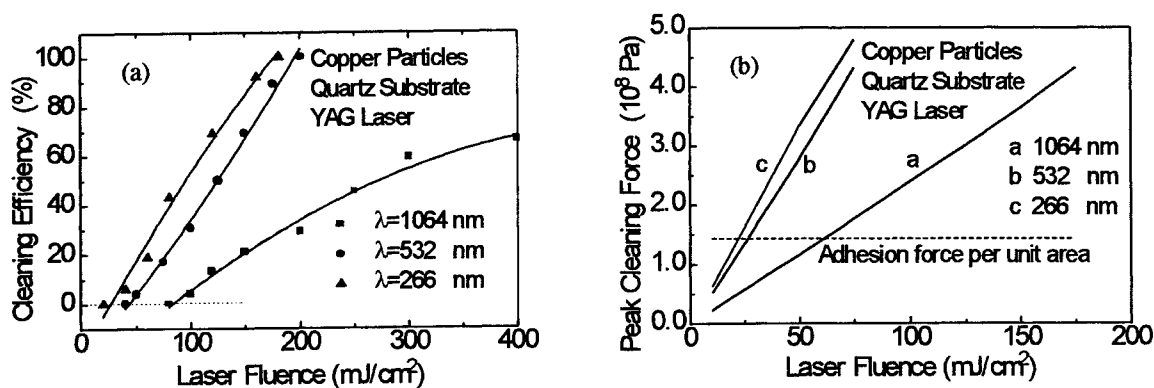


Fig. 2 (a) Comparison of laser cleaning efficiency for three different wavelengths at 500 Pulses and 10 Hz for removal of copper and aluminum particles from quartz surfaces; and (b) the peak cleaning force per unit area of copper and aluminum particles on a quartz substrate as a function of laser fluence at different wavelengths of 1064 nm, 532 nm and 266nm

Above wavelength effects can be explained by the following theoretical analysis. The peak cleaning force per unit area of copper particles on a quartz substrate as a function of laser fluence at different wavelengths of 1064 nm, 532 nm and 266nm is shown in Fig. 2(b). From Fig. 2(b), it was found that for all three different laser wavelengths, as laser fluences increases, the peak cleaning force per unit area increases too. As the peak cleaning force increases, it is easier to overcome the adhesion force between the particles and substrate. Therefore, it is expected that the cleaning efficiency

will increase with increasing laser fluence. Due to the fact that shorter laser wavelength can generate greater change in temperature which result in larger cleaning force, hence leads to higher cleaning efficiency. By plotting the peak cleaning force per unit area and the adhesion force per unit area as a function of laser fluence, the laser fluence at the intersection of these two curves will be the point where the cleaning force is equal to the adhesion force. This will be the theoretical cleaning threshold. The results show that the cleaning thresholds for removal of copper particles from quartz substrates decrease with shorter wavelength. This is because wavelength decreases, it is easier to bring a large temperature rise in the particle which results in a generation of a greater cleaning force. The theoretical cleaning thresholds for removal of copper particles from quartz surfaces are 65 mJ/cm^2 at 1064 nm , 27 mJ/cm^2 at 532 nm and 23 mJ/cm^2 at 266 nm , respectively. Comparing theoretical and experimental thresholds, the same trends for both theoretical and experimental cleaning thresholds were observed. The theoretical cleaning thresholds are quite close to those of the experimental cleaning thresholds. Thus it can be seen that above the theoretical analysis successfully predicts and explains the experimental results.

2.2.3 Steam laser cleaning

For steam laser cleaning, nickel-phosphorus (NiP) coating with a typical thickness $20 \mu\text{m}$ on aluminum-magnesium alloy was elected as a substrate, which is most commonly used as undercoat in the thin film recording media. Alumina particles with size of $1 \mu\text{m}$ were applied as contaminants. The thin liquid film was constructed simply through the diffusion and evaporation of isopropanol alcohol (IPA) drop on NiP surface as IPA immerses on it.

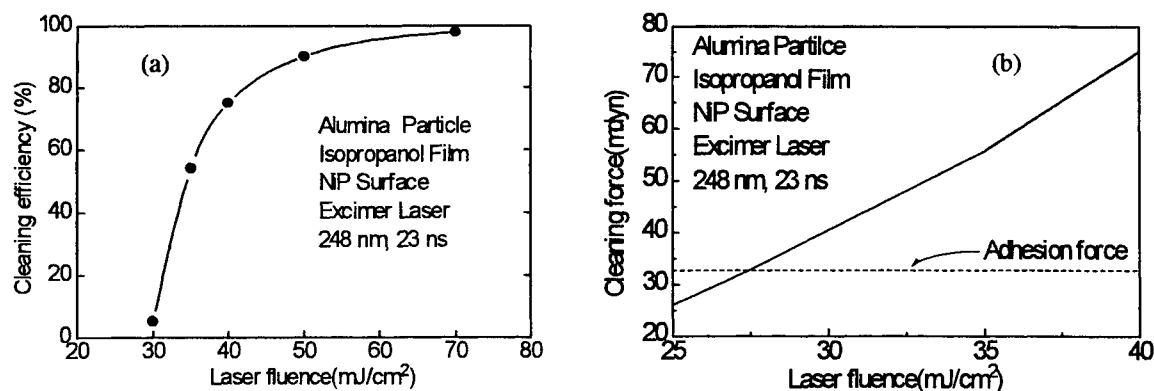


Fig. 3 (a) The laser fluence dependence of cleaning efficiency for removal of $1 \mu\text{m}$ alumina particles from NiP surfaces with deposition of the IPA film; and (b) the cleaning forces as a function of laser fluence

Figure 3(a) shows laser fluence dependence of cleaning efficiency for removal of $1 \mu\text{m}$ alumina particles from NiP surface with deposition of the IPA film. It is found that the cleaning threshold is about 30 mJ/cm^2 and the cleaning efficiency increases rapidly with laser fluence. In the theoretical model, we calculated the pressure of stress wave induced by laser irradiation on IPA coated NiP surface. This pressure causes cleaning force on the adherent particles. The cleaning forces on $1 \mu\text{m}$ particle caused by this pressure at different laser fluence are shown in Fig. 3(b) together with the adhesion force. It indicates that the theoretical cleaning threshold of laser fluence is 27.5 mJ/cm^2 for removal of $1 \mu\text{m}$ alumina particles from IPA coated NiP surface. By comparing the cleaning force and adhesion force, we can predict the cleaning threshold of laser fluence.

2.3 Applications in disk drive industry

In a hard disk drive, head flying height, the distance between read-write head and disk surface, has been continually reduced to increase the recording density. At present the flying height is about or below $0.1 \mu\text{m}$, this implies that even

submicron particles can damage both the slider and disk surfaces, hence lead to failure of the disk drive system. Thus, the cleanliness of disk and slider surfaces becomes very critical. Above discussions indicate laser cleaning being an efficient cleaning method for removal of particles from solid surfaces. The following shows that laser cleaning can be used in hard disk drive industry. Figures 4 and 5 show typical optical micrographs of laser cleaning of magnetic disk and sliders. It was found that particles on disk and slider surfaces can be efficiently removed by laser cleaning.

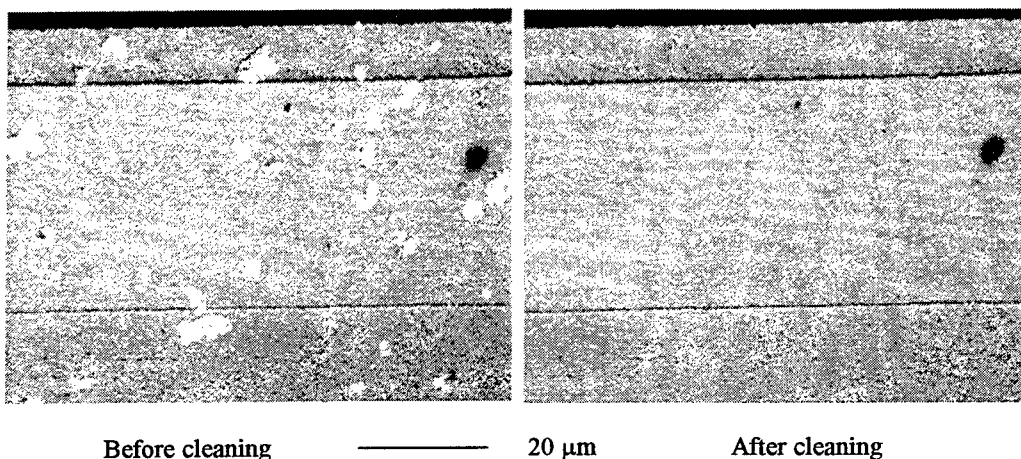


Fig. 4 The typical optical micrographs of magnetic sliders before and after laser cleaning

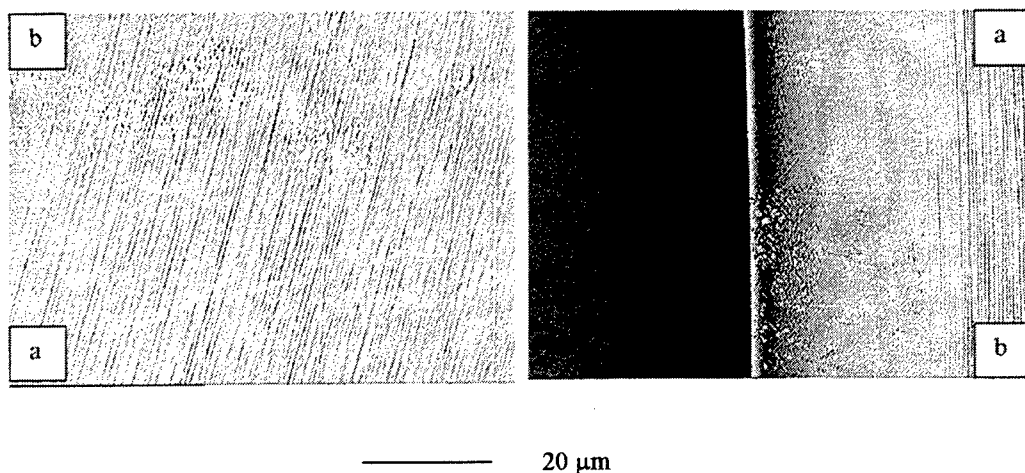


Fig. 5 The typical optical micrographs of magnetic disk surfaces with (a) and without (b) laser cleaning

3. REMOVAL OF FILM CONTAMINANTS FROM ELECTRONIC MATERIALS

3.1 Cleaning mechanism

The mechanisms of laser-induced removal of thin film contaminants are laser photo-ablation and thermal-ablation.⁷ If the binding energies of molecules of thin film contaminants are within the range of photon energies of laser irradiation, photo-decomposition or photo-ablation is possible. For example, the photon energy of a KrF excimer laser is 5 eV. This energy can break the O-O, H-H, O-H, C-C, C-H, N-H chemical bonds. When superfluous energy is irradiated, simultaneous thermal-ablation will occur.

3.2 Applications in semiconductor industry

3.2.1 Cleaning IC mold

Traditionally, surface contaminants such as oil, grease, wax and other organic and inorganic compounds on IC mold are removed from the surfaces by injecting a substance called melamine into the empty molds, exposing it to intense heat and pressure to melt the substance, and then let it solidify. During this process, the contaminants react with the melamine compound and bond to its surface of the solidified melamine compound. Once solidified, the melamine compound is removed. However, this method has a number of shortcomings such as long time processing, low cleaning efficiency and containing toxic fumes being harmful to human beings. Therefore, a new cleaning process is needed to overcome above shortcomings. We demonstrated that laser cleaning is a good cleaning method to remove these contaminants from IC mold surfaces.

Figure 6 shows a typical optical micrograph of a IC mold with and without laser cleaning. In Fig. 6, the left half surface of the IC mold are processed by excimer laser irradiation, whilst the right one retain the contaminated originals. The experimental results show that grease and wax contaminants on IC mold surfaces can effectively be removed by laser irradiation. It was also found that there is an obvious cleaning efficiency for laser-induced removal of organic contamination such as grease and wax at laser fluence larger than 100 mJ/cm².

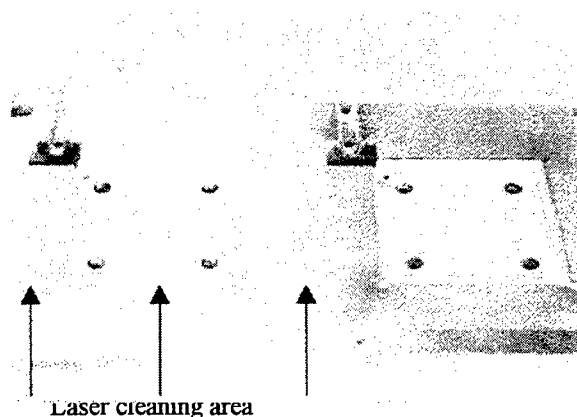


Fig. 6 The optical micrograph of IC mold with and without laser cleaning

In order to investigate laser cleaning efficiency, AES measurements were performed for IC mold surfaces before and after laser cleaning. Figures 7 (a) shows the AES spectra of the IC mold with grease and wax contamination before laser cleaning. As shown in Fig. 7(a), there are strong C and O peaks in the spectrum recorded for the original surface. Only very weak Cr peak of the IC mold coating materials can be observed. Since the contamination such as greases and waxes are composed predominantly of carbon, hydrogen and oxygen, the quantity of the resident carbon species on IC mold surfaces is believed to be in proportion to the level of contaminating and the carbon C signal represents the contamination while Cr is the IC mold surface itself. Therefore, this high C-peak intensity represents that the surface is heavily contaminated. With sputtering time increasing, Cr-peak intensity increases and C-peak intensity decreases correspondingly. It is only after 130 min Ar-ion sputtering that strong peaks for Cr can be observed and C and O peaks

become very weak. The surface composition became the same as that of the bulk material. This result also provided the information for the thickness of the contaminant layer. Because the Ar-ion sputtering rate is of the order of nanometer per minute, the thickness of the contaminant layer should have about 130 nm.

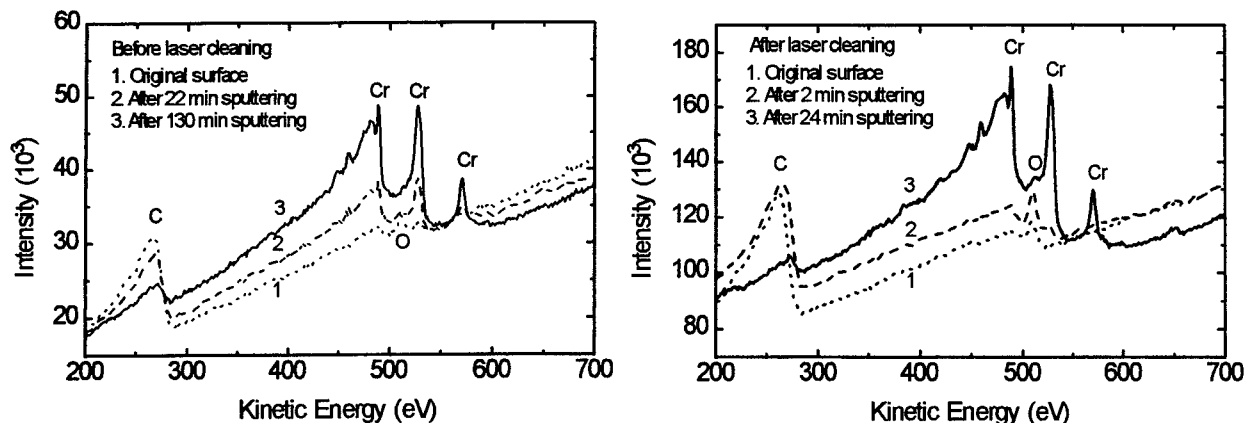


Fig.7 The AES spectra of IC mold with grease and wax contamination before (a) and after (b) laser cleaning with a laser fluence of 250 mJ/cm² and a pulse number of 10

Figure 7(b) shows the AES spectra of IC mold surfaces with grease and wax contamination after laser cleaning. Again there are strong C and O peaks in the spectrum measured for the original surface after laser cleaning. However only 24 min sputtering, the surface composition became the same as that of the bulk material. This means that there is a thin layer of contamination on the IC mold surfaces after laser cleaning, but only about 24 nm thickness of contamination exists. Therefore, the cleaning efficiency is about 80% based on the contamination thickness. It can be seen that the excimer laser cleaning can effectively remove the surface contaminants. In order to obtain higher cleaning efficiency, it is necessary to increase laser fluence or pulses.²

3.2.2 Cleaning PCB

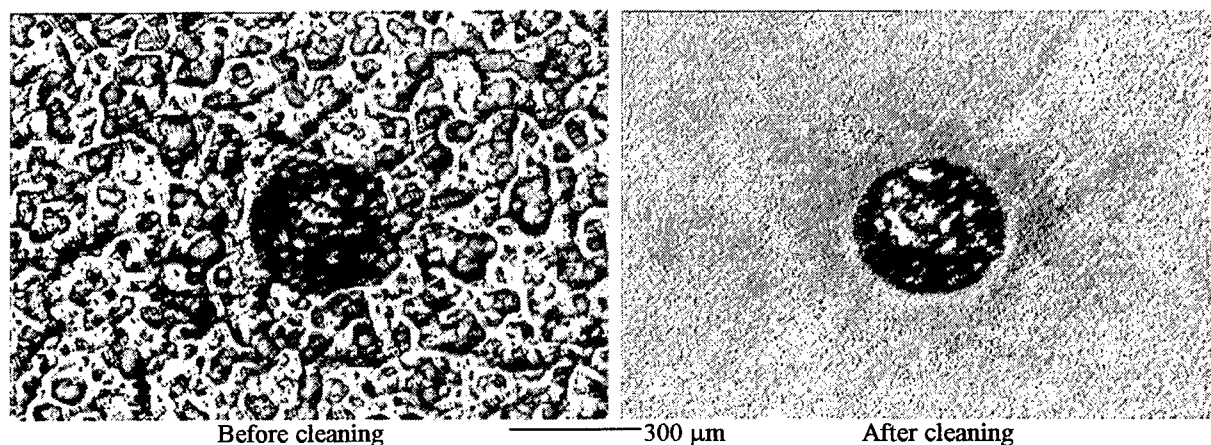


Fig. 8 The typical optical micrographs of PCB before and after laser cleaning

Resin contaminants around holes are produced in manufacturing of PCB. Usually, these contaminants are removed by inserting PCB into chemical. Although this method is widely used in industry, it has some drawbacks such as waste chemical solutions. Laser cleaning was demonstrated to be a powerful cleaning tool to remove those resin contaminants from PCB surfaces without other new pollution.

Figure 8 shows the typical optical micrographs of PCB surfaces with resin contaminants around holes before and after laser cleaning. It was observed that there is a thin layer of resin contaminants around holes before laser cleaning of PCB surfaces. The fresh surfaces come out after laser cleaning, which is shown in Fig. 8(b). In order to confirm cleaning efficiency, we made a group of Raman spectra. Figure 9 shows Raman spectra of PCB surfaces with resin contaminants around holes before and after laser cleaning. As a reference, Raman spectrum of the PCB surface far away holes without resin contaminants is also shown in Fig. 9. The Raman spectrum in Fig. 9(a) can be deconvoluted into two Gaussian peaks at 1459 and 3104 cm^{-1} . The peak at wavenumber of 3104 cm^{-1} belongs to PCB itself, which can be confirmed by Raman spectra in Figs. 9(b) and 9(c). The peak at wavenumber of 1459 cm^{-1} belongs to resin contaminants, which has been annihilated in the spectrum after laser cleaning. Comparing Figs. 9(b) and 9(c), it was found that two Raman spectra are in good agreement, which means that the contaminants have been removed and fresh surfaces come out after laser cleaning.

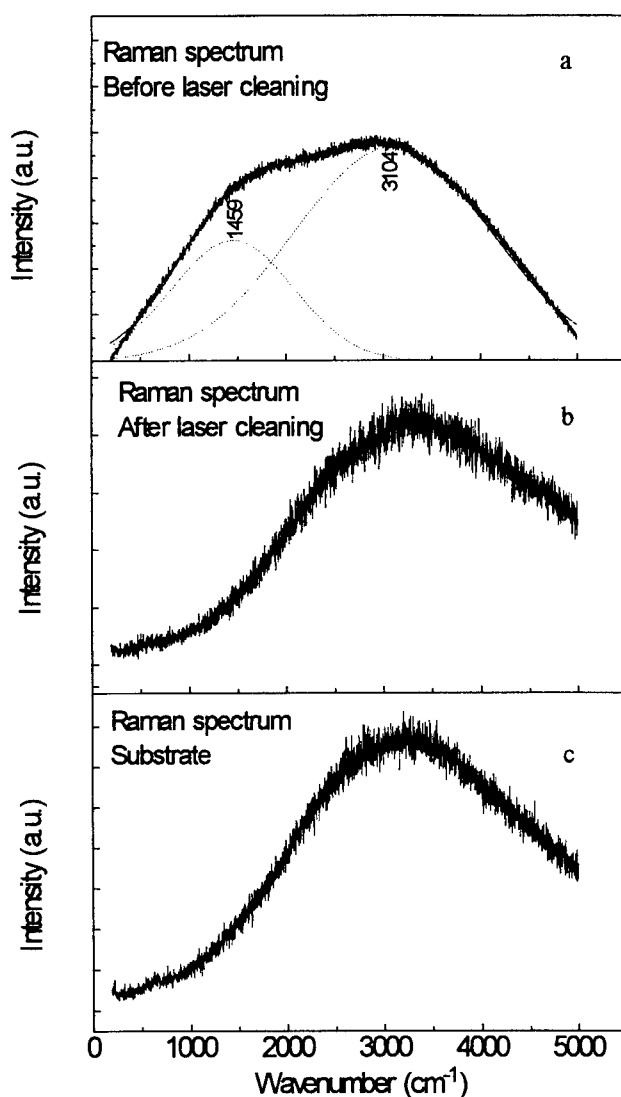


Fig. 9 The Raman spectra of PCB surfaces with resin contaminants around holes (a), after laser cleaning (b) and PCB itself (c)

4. CONCLUSION

In summary, dry and steam laser cleaning was demonstrated to be an efficient cleaning tool for removing particles and thin film contaminants from electronic materials both theoretically and experimentally. Cleaning models were established for laser-induced removal of particles from solid surfaces by taking adhesion forces and cleaning force into account both for dry and steam laser cleaning. Laser cleaning forces are induced by fast thermal expansion of particles and/or solid surfaces irradiated by laser for dry laser cleaning and by evaporating liquid film heated by laser irradiation for steam laser cleaning, respectively. With increasing laser fluence, the difference between the cleaning force and the adhesion force increases, resulting in easier removal of particles from substrate surfaces or a higher cleaning efficiency. Comparing theoretical and experimental thresholds, the same trends for both theoretical and experimental cleaning thresholds were observed. The theoretical cleaning thresholds are quite close to those of the experimental cleaning thresholds, which means that the theoretical analysis can successfully predict and explain the experimental results. The mechanism of laser-induced removal of organic film contaminants are laser photo-ablation and thermal-ablation. The organic film contaminants on electronic materials are easily removed by laser cleaning. Applications for laser-induced removal of particles from magnetic sliders and disk surfaces, and organic film contaminants from IC mold and PCB surfaces are available in the near future.

5. ACKNOWLEDGEMENTS

This study was financially supported by National Science and Technology Board (Singapore). The authors would like to thank K.D. Ye, M.H. Hong, C.K. Tee, D.M. Liu, W.J. Wang, Z.M. Ren, C.W. An and Y.W. Goh of the Data Storage Institute of Singapore for their valuable participation and contributions to this work.

6. REFERENCES

1. K.L. Mittal, *Particles on Surfaces*, vol.1, Plenum Press, New York, pp.3-400, 1988.
2. K.L. Mittal, *Particles on Surfaces*, Marcel Dekker, New York, pp.1-45, 405-417, 1995.
3. W. Zapka, W. Ziemlich, and A.C. Tam, "Efficient pulsed laser removal of 0.2 μm sized particles from a solid surface," *Appl. Phys. Lett.*, pp. 2217-2219, 1991.
4. K. Imen, S.J. Lee and S.D. Allen, "Laser-assisted micron scale particle removal," *Appl. Phys. Lett.*, 58(2), pp. 203-205, 1991.
5. A.C. Tam, W.P. Leung, W. Zapka and W. Ziemlich, "Laser-cleaning techniques for removal of surface particles," *J. Appl. Phys.* 71(7), pp. 3515-3523, 1992.
6. J.D. Kelley and F.E. Hovis, "A thermal detachment mechanism for particle removal from surfaces by pulsed laser irradiation," *Microelectronic Engineering* 20, 159-170, 1993.
7. Y.F. Lu, M. Takai, S. Komuro, T. Shiokawa and Y. Aoyagi, "Surface cleaning of metals by pulsed-laser irradiation in air," *Appl. Phys. A* 59, 281-288, 1994.
8. H.K. Park, C.P. Grigoropoulos, W. P. Leung and A.C. Tam, "A Practical excimer laser-based cleaning tool for removal of surface contaminants," *IEEE Transactions on Components, Packaging, and Manufacturing Technology Part A*, 17(4) 631-643, 1994.
9. Y.F. Lu, W.D. Song, M.H. Hong, B.S. Teo, T.C. Chong and T.S. Low, "Laser removal of particles from magnetic head sliders," *J. Appl. Phys.*, 80(1), pp. 499-504, 1996.
10. K. Mann, B. Wolff-Rottke and F. Muller, "Cleaning of optical surfaces by excimer laser radiation," *Appl. Surf. Sci.*, 98, pp. 463-468, 1996.
11. R. Oltra, O. Yavas, F. Cruz, J.P. Boquillon and C. Sartori, "Modelling and diagnostic of pulsed laser cleaning of oxidized metallic surfaces," *Appl. Surf. Sci.*, 98, pp. 484-490, 1996.
12. D.A. Wesner, M. Mertin, F. Lupp and E.W. Kreutz, "Cleaning of copper traces on circuit boards with excimer laser radiation," *Appl. Surf. Sci.*, 98, pp. 479-483, 1996.
13. M. Afif, J.P. Girardeau-Montaut, C. Tomas, M. Romamd, M. Charbonnier, N.S. Prakash, A. Perez, G. Marest and J.M. Frigerio, "In situ surface cleaning of pure and implanted tungsten photocathodes by pulsed laser irradiation," *Appl. Surf. Sci.*, 98, pp. 469-473, 1996.

14. I. Gobernado-Mitre, J. Medina, B. Calvo, A.C. Prieto, L.A. Leal, B. Perez, F. Marcos and A.M. de Frutos, "Laser cleaning in art restoration," *Appl. Surf. Sci.*, 98, pp. 474-478, 1996.
15. J.B. Heroux, S. Boughaba, I. Ressejac, E. Sacher and M. Meunier, "CO₂ laser-assisted removal of submicron particles from solid surfaces," *J. Appl. Phys.* 79(6), 2857-2862, 1996.
16. W.D.Song, Y.F.Lu, K.D.Ye, C.K. Tee, M.H. Hong, D.M. Liu and T.S.Low, "Cleaning force in laser cleaning of silicon substrate", *SPIE Vol.3184*, 158(1997).
17. Y.F.Lu, W.D.Song, B.W. Ang, M.H.Hong, D.S.H.Chan and T.S.Low, "A theoretical model for laser removal of particles from solid surface", *Appl. Phys.* A65, 9(1997).
18. Y.F.Lu, W.D.Song, K.D.Ye, Y.P.Lee, D.S.H.Chan and T.S.Low, "A cleaning model for removal of particles due to laser-induced thermal expansion of substrate surface", *Jpn. J. Appl. Phys.*, 36(10A), L1304(1997).
19. Y.F.Lu, W.D.Song, K.D. Ye, M.H.Hong, D.M. Liu, D.S.H.Chan and T.S.Low, "Removal of submicron particles from nickel-phosphorus surfaces by pulsed laser irradiation", *Appl. Surf. Sci.* 120, 317(1997).
20. Y.F.Lu, W.D.Song, C.K. Tee, D.S.H.Chan and T.S.Low, "Wavelength effects in dry laser cleaning of particles on solid surfaces", *Jpn. J. Appl. Phys. Part 1*, No.3A, 840(1998).
21. D. Bhattacharya, R.K. Singh and P.H. Holloway, "Laser-target interactions during pulsed laser deposition of superconducting," *J. Appl. Phys.* 70(10), 5433-5439, 1991.
22. J.R. Ho, C.P. Grigoropoulos and J.A.C. Humphrey, "Computational study of heat transfer and gas dynamics in the pulsed laser evaporation of metals," *J. Appl. Phys.* 78(7), 4696-4709, 1995.
23. D. Burgreen, *Elements of thermal stress analysis*, C.P. Press, Jamaica, New York, pp.1-91, 1971.
24. W. Zapka, W. Ziemlich, W. P. leung and A. C. Tam, "Laser cleaning removes particles from surfaces", *Microelectron. Eng.* 20, p.171, 1993.
25. V. P. Carey, *Liquid-Vapor Phase-Change Phenomena*, Hemisphere Publishing Corporation, 1992.
26. A. Prosperetti and M. S. Plesset, "Vapour-bubble growth in a superheated liquid", *J. Fluid. Mech.* 85(2), p.349, 1978.
27. D. A. Hutchins, R. J. Dewhurst and S.B. Palmer, "Laser generated ultrasound at modified metal surfaces", *Ultrasonics* 19, p.103, 1981.
28. C. J. Knight, "theoretical modeling of rapid surface vaporization with back pressure", *AIAA J.* 17, p.519, 1979.
29. O. Yavas, A. Schilling, J. Bischof, J. Boneberg and P. Leiderer, "Bubble nucleation and pressure generation during laser cleaning of surfaces", *Appl. Phys.* A64, p.331, 1997.
30. P. D. Edmonds and F. Dunn, *Methods of Experimental Physics-Ultrasonics*, Vol. 19, Academic, New York, 1981.

Excimer laser cleaning for microelectronics: Modeling, applications and challenges

M. Meunier, X. Wu, F. Beaudoin, E. Sacher and M. Simard-Normandin *

École Polytechnique de Montréal, Département de Génie Physique and Groupe de recherche en physique et technologie des Couches Minces (GCM) C. P. 6079, Succursale Centre-Ville
Montréal (QC), H3C 3A7 Canada

* Nortel, Centre for Microanalysis, P.O Box 3511, Station C, Ottawa (ON) K1Y 4H7, Canada

ABSTRACT

Chlorofluorocarbon-free laser cleaning techniques, compatible with cluster tool processing, have been developed for application to microelectronics processing. A KrF excimer laser (248 nm) is directed toward the wafer to be cleaned and rastered over the surface which might be intentionally covered by a thin liquid layer. It is demonstrated that various types of submicrometer-sized particles including polystyrene latex (PSL), silica and alumina, can be efficiently removed, by laser cleaning, from the front sides of silicon wafers. These results are explained by a particle adhesion model, including van der Waals forces and hydrogen bonding, and a particle removal model involving rapid thermal expansion of the substrate due to the thermoelastic effect and the pressure shock due to bubble generation in the condensed water film. The results of the calculations of the adhesion and removal models are consistent with the experimental observations. In addition, the excimer laser technique was successfully used to remove micrometer-sized metallic particles (iron oxide) from the backsides of silicon wafers; such a removal represents a challenging task in today's integrated circuit technology.

Keywords: excimer laser, laser cleaning, microelectronics, metallic contamination

1. INTRODUCTION

Surface microcontamination is recognized as the main source of yield loss in integrated circuit (IC) manufacture¹⁻⁴. It also affects device performance and reliability³⁻⁶. Contaminants may be particles, metallic impurities, organic materials, native oxides and adsorbed gases^{2,3}. Because the total elimination of contamination sources during IC processing operations is presently not achievable⁵, surface cleaning is a frequently applied after each step during circuit fabrication. The most widespread cleaning techniques in the industry are wet-chemical processes⁷, which are usually based on dilute mixtures of H₂O₂ and NH₄OH, HCl or H₂SO₄³. Since these liquids are, themselves, potential sources of contamination, costly ultrapure, low particulate grade chemicals and water must be used. The processing of liquids and hazardous waste disposal further increases operating costs⁸, especially now that environmental issues impose more and more stringent constraints. Moreover, wet cleaning methods are not compatible with the in-situ processing trend in which cluster tools play a major role. Another important limitation of these techniques is their inability to efficiently remove particles 0.1 μ m and smaller. The removal of such particles is one of the most challenging tasks the microelectronics industry has to meet in today's sub-half-micrometer IC technology.

Over the last few years, several liquid-chemical-free cleaning techniques have been developed⁹. Among these vapor- or vacuum-based methods, laser cleaning has demonstrated promising potential¹⁰⁻²⁶. Its high efficiency in the removal of 0.1 μ m particles has attracted great interest because of the simplicity of the technique, both conceptually and experimentally. It must be emphasized that this lower limit in particle size corresponds to the detection limit of currently available laser particle counters; laser cleaning might still be efficient at even lower particle dimensions.

In the present article, we give a short overview of the different approaches to the laser-cleaning of surfaces and we present a review of our work on the removal of various types of particles from silicon wafer front surfaces using an

excimer laser. Modeling of the excimer laser particle removal will be discussed in terms of the various forces involved. An application of the laser cleaning technique to the removal of metallic contamination from silicon wafer back surfaces will also be presented.

2. PRINCIPLES OF LASER CLEANING

Two laser cleaning techniques have been investigated, to date. The first, called "steam" laser cleaning, makes use of either a CO₂ (10.6 μm)^{10-12, 26} or a pulsed excimer (248 nm)¹³⁻¹⁶ laser, coupled to a liquid energy transfer medium, which is condensed on the surface. The transfer medium consists of water or a mixture of water and alcohol. The laser beam serves as a fast, localized heating source to bring the liquid film to its critical point, provoking its explosive vaporization. The forces generated are sufficient to remove the contaminant particles. The main difference between the use of a CO₂ or an excimer laser lies in the heating mechanism of the liquid film. In the former, the laser beam is partially, but directly absorbed by the liquid layer. Using an excimer laser, the medium is transparent to the radiation and the beam is strongly absorbed by the substrate surface; the latter is heated and transfers energy to the liquid film. In the work of Zapka and co-workers¹³⁻¹⁶, it was demonstrated that the energy density required for efficient cleaning was far smaller using an excimer laser than a CO₂ laser. This was attributed to the fact that, when using UV radiation, explosive evaporation occurs at the interface and is, thus, more effective.

The second approach is dry laser cleaning, where no intermediate medium is used. A short-pulse (a few tens of nanoseconds) laser beam is either strongly absorbed by the substrate surface or the contaminant particles; fast thermal expansion of either the surface or the particles results in a strong acceleration of the particles outward from the surface^{15, 24}. The beam radiation could be in either the UV (e.g., KrF excimer at 248 nm²⁵) or the IR (e.g., Nd:YAG at 1.06 μm²⁴) range. However, at the shortest wavelengths permitted by excimer lasers (ArF at 193 nm, KrF at 248 nm), the photons are strongly absorbed by the surface, leading to a very efficient thermoelastic removal force. This permits the removal of a wide variety of contaminants, not only particles but organic and inorganic films¹⁷⁻¹⁹, by direct bond breaking.

Both "steam" and "dry" approaches are presently being investigated as potential cleaning alternatives to the conventional liquid chemicals methods. As explained above, the excimer laser is the most appropriate laser for high efficiency cleaning. It must be emphasized that microelectronics is not the only field in which laser cleaning can assert itself. The cleaning of optical components and air bearing surfaces of magnetic head sliders was successfully achieved^{25, 27}. Art restoration is another field where laser cleaning has demonstrated strong capabilities²⁸.

3. EXPERIMENTAL

The experimental set-up has already been described elsewhere and is schematically presented in Figure 1²⁹⁻³⁰. Very briefly, a KrF excimer laser (248 nm, with a pulse energy of 200 mJ and a duration of 22 ns) was focused onto the substrate surface. The substrate was mounted facing down on the underside of a computer-controlled XYZ stage. The XY axes permitted the scanning of the surface to perform the cleaning of large areas, while the Z axis was used to vary the laser beam energy flux in the range of 0.05 - 1 J/cm² with an estimated error of 10 %. In the case of steam cleaning, a pulsed vapor generator was used to controllably deposit a liquid film at the spot to be irradiated, immediately before the laser pulse is triggered. The generator consisted in a heated (37-40 °C) nozzle and stainless steel container half-filled with deionized (DI) water. A nitrogen gas input of 4700 ml/min, connected to a flowmeter and valves, was used to generate a controlled volume of water vapor near the surface to be cleaned. Upon reaching the colder surface, the vapor condensed to a liquid film. A pulse-timing unit controlled the open time of the valves in the range between 0.1 and 3.5 s. After a vapor burst, several laser pulses were triggered at intervals to assure that all the water had been evaporated. In order to perform a cleaning over a sufficiently large area, the wafer was linearly stepped between 0.4 and 3 mm after each vapor burst sequence. The area cleaned was a square 50 X 50 mm², whose center corresponded to that of the wafer.

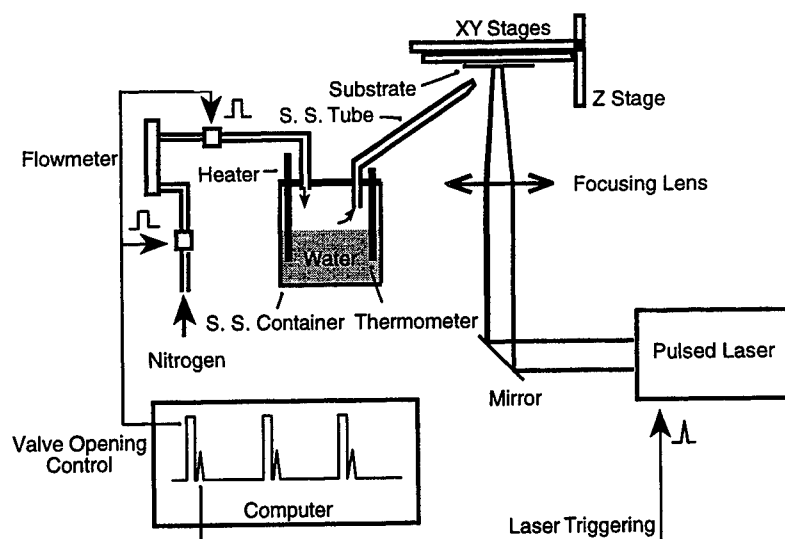


Figure 1 Schematic of the experimental set-up; S.S.: stainless steel.

The substrates were 100-mm-diameter <100> silicon wafers. Some were used as received, while others were first cleaned and made hydrophilic, using a modified RCA recipe^{2, 22, 23}. Front side surfaces were artificially contaminated by various types of particles (polystyrene latex or PSL, Al_2O_3 and SiO_2) using a particle generator (Particle Measuring Systems, Inc.)^{22, 23}. Similarly, back surfaces were contaminated by Fe_2O_3 particles. A dedicated particle generator, composed of a nebulizer, drying tube, chamber, and output nozzle, was used for each type of contaminant particle. To evaluate the cleaning efficiency, a laser scanning surface inspection system (Particle Measuring Systems Inc., SAS 3600) was used to classify particles according to their spherical PSL equivalents, from 0.1 to 10 μm . Inside the cleaned square area, the surface inspected was a circle of 30 mm diameter. It must be emphasized that this scanning system can only be used for the polished front surface. However, since the roughness of the wafer back side is very important, the surface photovoltage (SPV) technique was used as a cleaning evaluation tool of metallic contaminants³¹⁻³⁸. Rapid thermal annealing (RTA), at 1050 $^\circ\text{C}$ for 4 min., was first performed to allow metallic contaminants to diffuse into the silicon wafers. SPV was then used to evaluate the iron bulk concentrations.

4. EXCIMER LASER CLEANING EFFICIENCIES

The particle densities (the number of particles divided by the area of the 30 mm diameter analyzed circle) as a function of size are shown in Figure 2. Dry excimer laser cleaning was very efficient in removing 0.1 μm PSL particles from silicon. However, for Al_2O_3 (0.2 μm) particles, only those with diameters >0.5 μm were removed with some efficiency. By using steam excimer laser cleaning, most of Al_2O_3 particles are removed. Fig. 3 summarizes the overall particle densities for various types of particles, before and after laser irradiation, for both dry cleaning and steam cleaning.

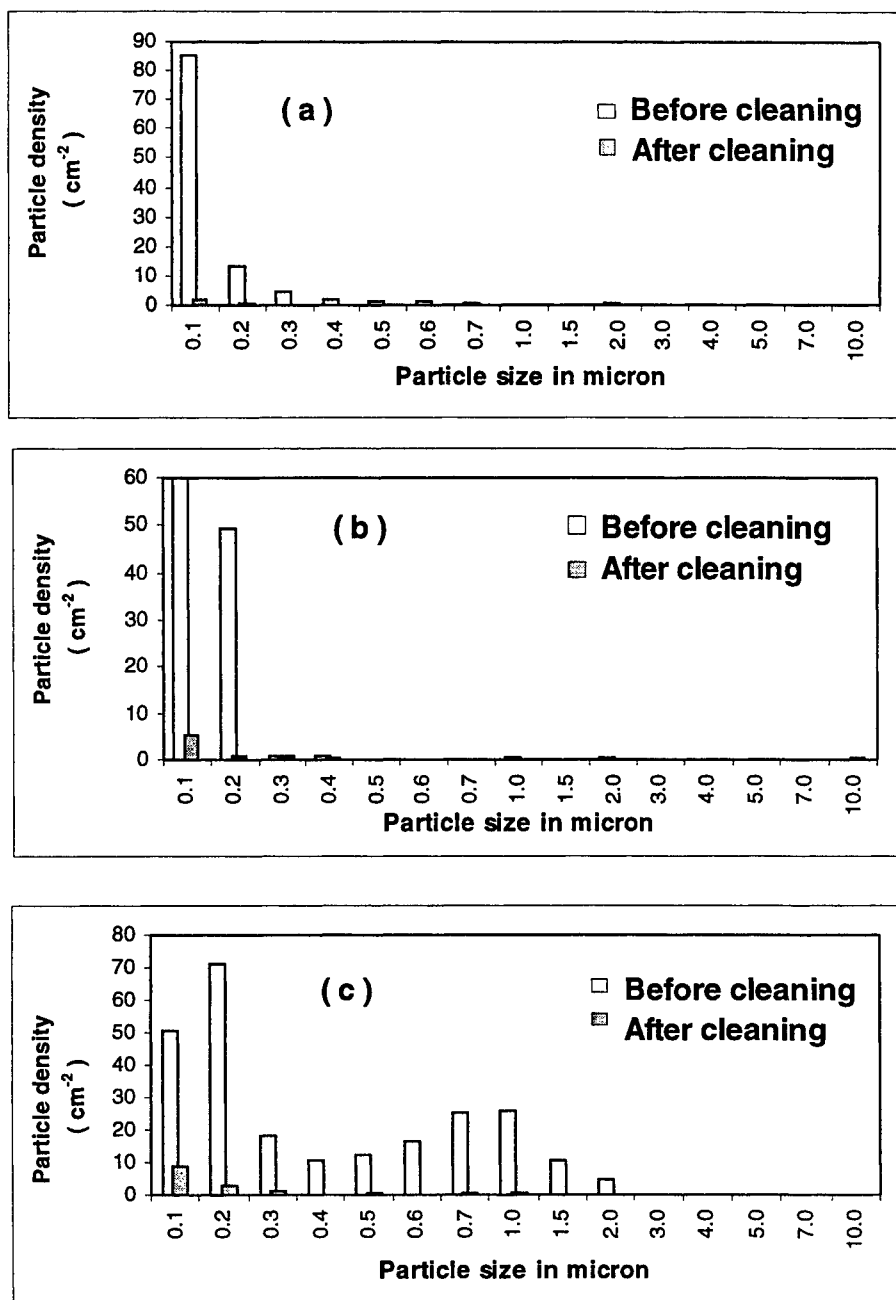


Figure 2(a) Size distribution of PSL before and after a dry excimer laser cleaning with a laser fluence of 326 mJ/cm^2 ; (b) and (c) Size distribution of silica and alumina particles before and after steam excimer laser cleaning with an energy beam density of 154 mJ/cm^2 and a water vapor burst duration of 0.2 s. The analyzed surface is a circle of 30 mm in diameter.

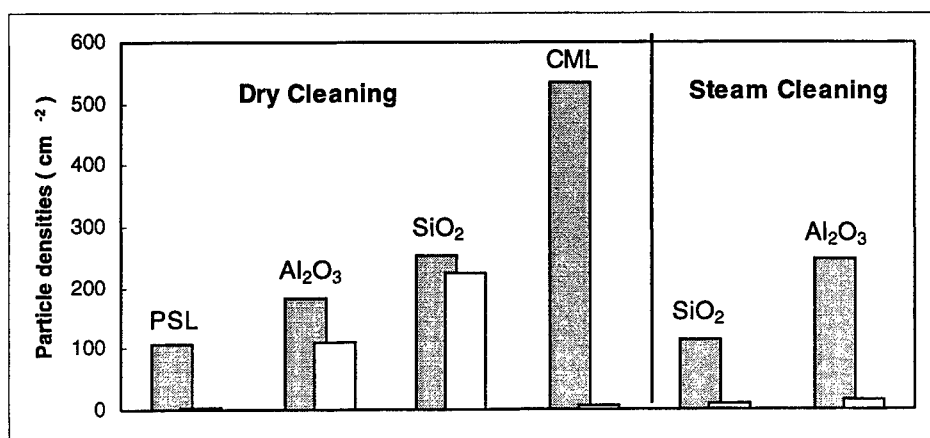


Fig. 3. Particle densities before (gray bar) and after (white bar) laser cleaning. During dry laser cleaning, the laser fluences for PSL, SiO₂, Al₂O₃ and CML were 326, 314, 326 and 353 mJ/cm², respectively, and 2, 4, 4 and 2 cleaning scanning cycles were used, respectively. During steam cleaning, the laser fluences for SiO₂ and Al₂O₃ were 180 and 154 mJ/cm², respectively, and 5 and 4 cleaning scanning cycles were used, respectively.

5. MODELING THE EXCIMER LASER PARTICLE REMOVAL TECHNIQUE

High efficiency cleaning requires that the removal forces be greater than the particle adhesion forces. To explain the large differences between dry and steam cleaning, and between organic with inorganic particles, we quantitatively analyzed the adhesion and removal forces between particles and surfaces.

5.1 Adhesion model

The interaction forces between solids which cause the adhesion of particles to substrate surfaces can be classified into long- and short-range³⁹. Long-range forces include van der Waals, capillary, electrostatic and double-layer forces. Short-range forces include the various types of chemical bonds: metallic, covalent and ionic, as well as hydrogen bonds. In our previous study²⁹⁻³⁰, it was demonstrated that, for submicron-sized particles on hydrophilic silicon surfaces, the dominant long-range adhesion force is the van der Waals interaction, while hydrogen bonding is the most important short-range contribution to inorganic particles.

Van der Waals attractive forces can be calculated using a macroscopic approach⁴⁰, in which the material properties are related to the Lifshitz-van der Waals constant. For a spherical particle and a smooth substrate surface, it can be expressed as⁴¹:

$$F^v = F_0^v + F_{Deformation}^v = \frac{h\varpi_{132}r_p}{8\pi z_o^2} + \frac{h\varpi_{132}a^2}{8\pi z_o^3} \quad (1)$$

The first term of equation (1) is the van der Waals forces between a sphere and a plane before deformation, and the second term is the force acting on the contact area due to elastic or plastic deformation. $h\varpi_{132}$ is the Lifshitz-van der Waals constant, r_p is the particle radius, z_o is the atomic separation distance between particle and substrate, which is not measurable but assumed to range from 0.4 to 1 nm [8] (we used $z_o = 0.4$ nm), a is the radius of the deformation area on the particle which can be calculated using the JKR model⁴² for rigid particles (SiO₂ and Al₂O₃). For PSL particles, a is given by Rimai and Demejo⁴³. During steam cleaning, particles were covered with a condensed water film. The shielding effect of the liquid greatly reduces the van der Waals forces³⁹; for example, the Lifshitz-van der Waals constant of Al₂O₃ particles on silicon surfaces is reduced from 5.62 eV to 2.23 eV⁴⁴.

The adhesion force due to hydrogen bonding between inorganic particles and the hydrophilic silicon surface was discussed in our previous study³⁰. It was given by:

$$F_{H-bond} = DE_{bond}(\pi a^2 + 2\pi r_p \Delta z b) / d_{bond} \quad (2)$$

where D is the OH group density on the particle surface (12.5 OH/nm^2 for Al_2O_3 ⁴⁵) and E_{bond} is the hydrogen bonding interaction energy between particle and substrate. E_{bond} depends on the natures of the surfaces, in particular on their degrees of hydroxylation and on the electronic structures of the materials⁴⁶. The average energy of the O-H...O hydrogen bond is about 5 kcal/mole ($\sim 0.48 \text{ eV/bond}$)⁴⁶, πa^2 is the deformation area of the particles and $2\pi r_p \Delta z$ is the ring area taken to a height Δz near the contact point with the probability b that particle and surface are bonded by a chain of water molecules. For Al_2O_3 on dry cleaning, $\Delta z b$ is $\sim 0.38 \text{ nm}$ ^{30,47,48}. During steam cleaning, free water molecules may replace and break the hydrogen bond chain connecting the particle to the surface, so the probability b is reduced by that probability. d_{bond} is the hydrogen bond dissociation distance, which is assumed to be half the length of a hydrogen bond, $\sim 0.1 \text{ nm}$ ⁴⁹. For PSL particles, there are no surface groups capable of participating in hydrogen bonding, so only van der Waals forces play a role.

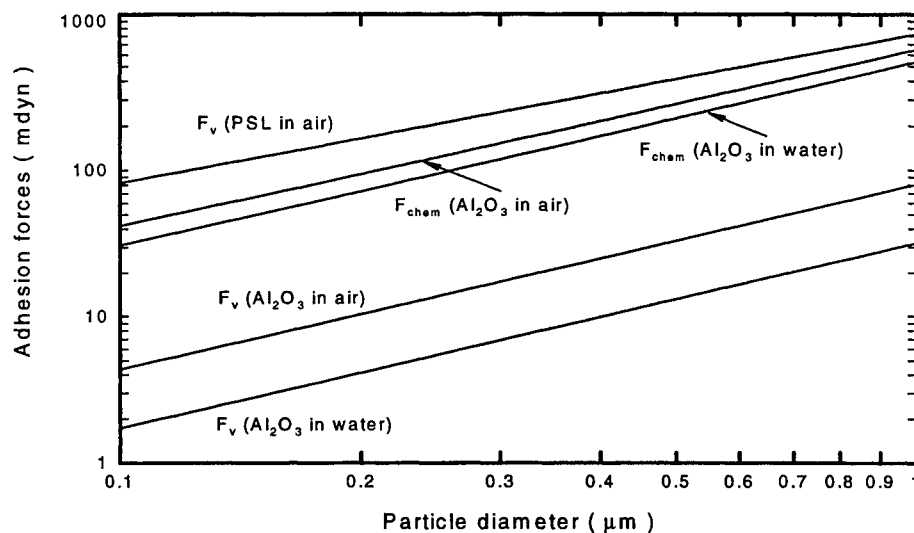


Figure 4 Adhesion forces of PSL and Al_2O_3 particles on hydrophilic silicon surface during dry and steam cleaning, as a function of particle diameter.

Using equations (1) and (2), we calculated the adhesion forces versus particle diameters for a typical organic particle, PSL, and for a typical inorganic particle, Al_2O_3 , contacting a hydrophilic silicon surface; this was done for both dry and steam cleaning, as shown in Fig. 4. It appears that the adhesion forces are almost a linear function of particle diameter; they are greatly reduced during steam cleaning, and hydrogen bonding between Al_2O_3 particles and hydrophilic silicon surfaces becomes much stronger than van der Waals interactions. The van der Waals forces of Al_2O_3 particles are already much less than those of PSL particles due to their smaller deformation.

5.2 Laser cleaning model

During laser pulse irradiation, the particle and silicon substrate absorb laser energy and are heated rapidly. Due to the thermoelastic effect⁵⁰, an extremely rapid thermal expansion of the substrate ejects the particles from the surface. In order to calculate the removal forces, we must first know the temperature increase of both particles and silicon substrate due to the laser irradiation.

Since the dimension of the 248 nm excimer laser beam (0.8 mm × 18 mm) on silicon, is much larger than the light absorption length α^{-1} of 5.5 nm⁵¹ and the heat diffusion length of 4.3 μm ^{52,53}, the semi-infinite, one-dimensional heat equation is a good approximation⁵². Heat losses at the substrate surface may be neglected, because heat conduction from the substrate surface to the ambient air is very slow, and the radiation losses are much smaller than the laser energy. The one-dimensional conductive heat transfer equation was solved numerically by an implicit finite difference algorithm. The peak surface temperature of the silicon substrate as a function of laser fluences is shown in Fig. 5.

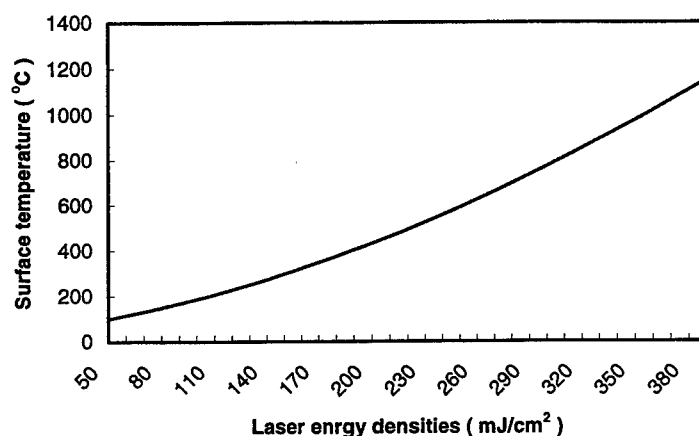


Fig. 5 Surface temperature of silicon substrate as a function of laser fluences.

The calculation of the temperature distribution in particles is a very complex problem because of non-uniform surface absorption due to small particle Mie-type scattering⁵⁴ and the difficulty of solving the three-dimensional, spherical coordinate, heat diffusion equation. Fortunately, the optical absorption lengths α^{-1} of the particle considered are 10–10² μm , much larger than the dimensions of the particles. This means that the particles absorb laser energy weakly, the temperature increase in the particle during laser irradiation is not large, and we can assume that the submicron-sized particles maintain a constant temperature during laser irradiation.

The rapid temperature rise in the substrate, induced by the laser pulse, generates stresses and strains in the irradiated area. These strains cause some particle displacement. From the point of view of the particles, their resistance of these strains subjects them to ejection forces from the substrate surface, equal to the stresses in the substrate⁵⁵. If the particles are to be detached from the surface, they must experience a real displacement. Based on the relationship between stresses and strains⁵², an expression for the thermal removal force on the particles produced by the thermal expansion of the substrate can be obtained:

$$F_{thermal} = \gamma E \pi a^2 \Delta T \quad (3)$$

where γ , E , ΔT are the linear thermal expansion coefficient, the elastic modulus and the temperature increase at the substrate surface. πa^2 is the deformation area of the particle. The equation shows that the thermal removal forces

depend on the deformation area of the particle. Soft particles such as PSL should suffer much stronger removal forces from the substrate than hard particles, such as SiO_2 and Al_2O_3 . Fig. 6 shows the removal forces on PSL and Al_2O_3 particles due to the thermoelastic effect during dry cleaning (the incident laser energy density is about 320 mJ/cm^2) as a function of the particle diameter. The dominant adhesion forces are also included in Fig. 6 for comparison purposes. It is apparent, in Fig. 6, that the thermal removal force is large enough to overcome the adhesion forces for PSL particles, but is much less than hydrogen bonding forces in the case of the Al_2O_3 particles. These predictions are in consistence with the laser cleaning experiments.

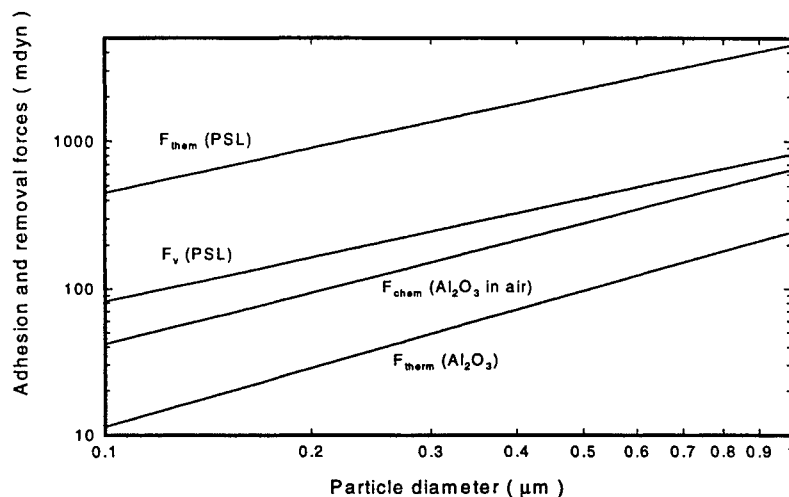


Fig. 6 Thermal removal forces and dominant adhesion forces, as a function of particles diameter, for PSL and Al_2O_3 particles during dry cleaning with a laser flux of 320 mJ/cm^2 .

During steam cleaning, the water film is transparent to the excimer laser. The laser energy is absorbed only by the substrate. The rapidly heated substrate surface induces the water layer adjacent to it to be superheated before nucleation sets in⁵⁶; this is followed by the creation of a layer of bubbles at the water/substrate interface, called film boiling. A detailed description of the explosive evaporation of the water film is extremely difficult, due to the formation of a superheated liquid, the thermal instability of the bubble and the development of nucleation centers⁵⁷. The incident laser energy density (10^2 J/cm^2) is much larger than the heat energy density needed to heat liquid water to boiling (10^3 J/cm^2) or to vaporization (10^2 J/cm^2)⁵⁸. The heat isolated by the vapor layer continues to transfer from substrate to liquid water, so that the temperature distribution in the substrate is approximately the same as during dry cleaning. The rapid bubble layer formation creates a pressure shock on the particles attached to the surface, with the removal force acting on the particles given by:

$$F_{\text{bubble}} = \pi r_p^2 [P_v(T) - P_v(T_0)] \quad (4)$$

where r_p is the radius of the particle, $P_v(T)$ is the vapor pressure at temperature T , and $P_v(T_0)$ is the ambient liquid pressure⁵⁸. The removal forces due to bubble generation and the thermoelastic effect, and the dominant adhesion forces due to hydrogen bonding, as functions of the particle diameter, are shown in Fig. 7 under steam cleaning conditions (the incident laser energy density is about 150 mJ/cm^2). During steam cleaning, as shown in Fig. 7, the explosive evaporation of the water film generates a strong removal force, much higher than the thermal expansion

force, which is also much greater than the adhesion force due to hydrogen bonding. This model appears to interpret the high cleaning efficiencies of steam cleaning for Al_2O_3 particles.

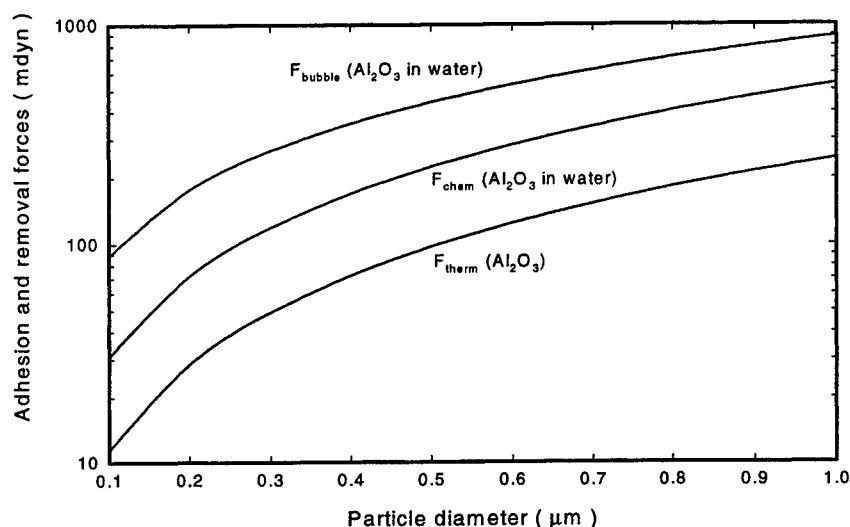


Fig. 7 Thermal removal forces, bubble removal forces and dominant adhesion forces, as a function of the particle diameter, for Al_2O_3 particles during steam cleaning with a laser flux of 150 mJ/cm^2 .

6. APPLICATION OF EXCIMER LASER CLEANING TO THE REMOVAL OF BACK SIDE METALLIC CONTAMINATION

Metallic contaminants that are present during semiconductor processing introduce deep recombination levels in the bandgap. Such contamination affects the device reliability and performance by reducing the lifetime of minority carriers and by increasing the leakage current at p-n junctions³¹⁻³⁸. For example, the presence of 10^{12} cm^{-3} of iron, as measured by surface photovoltage (SPV)³⁸, reduces the electronic diffusion length to a value as low as $60 \mu\text{m}$. This problem of metallic contamination will become more important as critical device dimensions are reduced. The SIA Roadmap has determined that metallic contamination must decrease from 10^{12} cm^{-3} for $0.8 \mu\text{m}$ technology to 10^{10} cm^{-3} for $0.35 \mu\text{m}$ technology. Among the various metallic contaminant sources, equipment and vacuum systems fabricated from stainless steel appear to be the primary sources: handling the wafers in these systems may generate particulates which deposit on either side of the wafer. Much care is presently taken to prevent the particles from interfering with the lithographic processes performed on the front side. Unfortunately, particles on the back side are generally ignored³⁸. These particles come from the different chucks and holders which the wafers contact during the various steps of integrated circuit fabrication. The most critical steps are those carried out at the front-end of the fabrication, before the high-temperature annealing processes. Such thermal processes permit the metallic contaminants at the back side to diffuse through the wafer and reach the sensitive front side, reducing device performance. To avoid these adverse effects, the particles deposited on the back side during handling must be removed before any important thermal budget step at the front-end of the line, such as thermal oxidation or RTA.

Due to the fact that iron has a relatively high diffusivity and is the most troublesome contaminant, we have investigated the use of an excimer laser-based cleaning technique to eliminate it. Our preliminary results on the removal of Fe_2O_3 particles ($0.2 - 2 \mu\text{m}$) from both sides of the wafer⁵⁹ are shown in Table 1. In these experiments, it is clear that deliberate contamination by iron oxide led to a significant Fe bulk contamination level after RTA at

1050 °C for 4 min.. However, when the surface was first laser-cleaned, the Fe concentration was reduced by more than an order of magnitude. Note that the cleaning efficiency is independent of the roughness. Improvements are being performed on our laser cleaning system to increase its efficiency in the removal of such metallic contamination.

TABLE 1: Steam excimer laser cleaning of Fe₂O₃ particles (at a fluence of 200 mJ/cm²) from the front- and back sides of a silicon wafer. Diffusion lengths and iron concentrations were obtained from SPV measurements at the center of the wafer.

	Fe ₂ O ₃ particle density (>0.3µm) (cm ⁻²)	Diffusion length (center point) (µm)	Iron concentration (center point) (X 10 ¹² cm ⁻³)
Front side			
Before laser cleaning	243	63	16
After laser cleaning	17	171	1.1
Back side			
Before laser cleaning	NA	82	7.3
After laser cleaning	NA	138	1.3
Not contaminated	no contamination	136	1.6

NA : impossible to measure due to extensive surface roughness

7. CONCLUSIONS AND CHALLENGES

The removal of particles as small as 0.1 µm from silicon surfaces can be achieved using the excimer laser-based cleaning technique. Cleaning efficiency may be optimized by controlling various parameters such as the beam energy density and the use (or not) of an energy transfer liquid. The application of this cleaning technique to the removal of back side metallic contamination has also been demonstrated.

Theoretical models of particle adhesion and removal were used for the purpose of explaining our excimer laser cleaning results. The dominant adhesion force holding organic particles, such as PSL, to the surface is the van der Waals force with deformation. Hydrogen bonding between inorganic particles, such as Al₂O₃, and the substrate is the dominant contribution to adhesion forces. A deposited water film greatly reduces the adhesion forces, due to the shielding effect of the van der Waals force and the breaking of the hydrogen bond chain between particle and surface. The laser pulse-generated thermoelastic effect of the heated substrate gives rise to the removal force on the particles attached on the surface during dry and steam cleaning. An additional removal force, due to bubble pressure during steam cleaning, is larger than that due to the thermoelectric effect.

Development of the excimer laser cleaning technique involves many challenges. A real integration of this technique into a cluster tool will probably require *dry* excimer laser cleaning. While the transfer medium, such as water, seems to be necessary for the removal of inorganic particles, research should be done to improve the cleaning efficiency of the dry approach. Most of the development so far was done on bare silicon substrates for which this technique is very appropriate. However, cleaning real circuits with this technique sometimes causes the breaking metallic lines, probably because these lines have poor adhesion to the substrate. The scaling up of this technique will involve the use of a larger and uniform excimer laser beam. Investigations should be made to develop a "find and clean" system in which an appropriate system will find a particle and the excimer laser will be use to remove it. This cleaning approach will probably be simpler and faster that the approach presently used.

ACKNOWLEDGMENTS

The authors thank S. Boughaba, J. P. Lévesque, M. Curcio, J.B. Héroux and D. Landheer for their help. This work was supported by the Natural Sciences and Engineering Research Council of Canada.

REFERENCES

1. T. Hattori, *Solid State Technol.* 33 (7), S1 (1990).
2. W. Kern, *J. Electrochem. Soc.* 137, 1887 (1990).
3. W. Kern, in *Handbook of Semiconductor Wafer Cleaning* edited by W. Kern (Noyes Publications, 1993), p. 3
4. W. Kern, in *Handbook of Semiconductor Wafer Cleaning* edited by W. Kern (Noyes Publications, 1993), p. 595.
5. D. Tolliver, in *Handbook of Semiconductor Wafer Cleaning Technology. Science, Technology and Applications*, edited by W. Kern (Noyes Publications, 1993), p. 68.
6. J. R. Mankowski, in *Treatise on Clean Surface Technology*, Vol. 1, edited by K. L. Mittal (Plenum, 1987), p. 123.
7. D. C. Burkman, D. Deal, D. C. Grant, and C. A. Peterson, in *Handbook of Semiconductor Wafer Cleaning Technology. Science, Technology and Applications*, edited by W. Kern (Noyes Publications, 1993), p. 111.
8. A. C. Engelsberg and J. A. Dehais, *Proceedings, SEMICON Korea 95*, (1995) p. 63.
9. J. Ruzyllo, in *Handbook of Semiconductor Wafer Cleaning Technology. Science, Technology and Applications*, edited by W. Kern (Noyes Publications, 1993), p. 201.
10. K. Imen, S. J. Lee, and S. D. Allen, *Appl. Phys. Lett.* 58, 203 (1991).
11. S. J. Lee, K. Imen, and S. D. Allen, *Appl. Phys. Lett.* 61, 2314 (1992).
12. S. J. Lee, K. Imen, and S. D. Allen, *J. Appl. Phys.* 74, 7044 (1993).
13. W. Zapka, W. Ziemlich, and A. C. Tam, *Appl. Phys. Lett.* 58, 2217 (1991).
14. A. C. Tam, W. Zapka, and W. Ziemlich, in *Lasers in Microelectronics Manufacturing*, SPIE Proc., Vol. 1598 (SPIE, Bellingham, WA, 1991), p. 13.
15. A. C. Tam, W. P. Leung, W. Zapka, and W. Ziemlich, *J. Appl. Phys.* 71, 3515 (1992).
16. W. Zapka, W. Ziemlich, W. P. Leung, and A. C. Tam, *Adv. Mater. Opt. Electr.* 2, 63 (1993).
17. A. C. Engelsberg, *Mater. Res. Soc. Proc.*, Vol. 315, edited by G. S. Higashi, E. A. Irene and T. Ohmi (Materials Research Society, 1993), p. 255.
18. A. C. Engelsberg, in *Optical System Contamination : Effects, Measurements and Control IV*, SPIE Proc., Vol. 2261, edited by A. P. M. Glassford (SPIE, Bellingham, WA, 1994), p. 312.
19. A. C. Engelsberg, 40th Proc. Annual Institute of Environmental Sciences Meeting, Chicago, Illinois, May 1-6 (1994).
20. J. B. Héroux, S. Boughaba, I. Ressejac, E. Sacher, and M. Meunier, *J. Appl. Phys.* 79, 2857 (1996).
21. J. B. Héroux, S. Boughaba, E. Sacher, and M. Meunier, *Can. J. Phys (suppl)* 74, S95 (1996)
22. S. Boughaba, E. Sacher, and M. Meunier, *Mater. Res. Soc. Proc.*, Vol. 397, edited by R. Singh et al. (Materials Research Society, 1996), p.497.
23. S. Boughaba, X. Wu, E. Sacher, and M. Meunier, *J. Adhesion* 61, 293 (1996)
24. J. D. Kelley, M. I. Stuff, and F. E. Hovis, *SPIE Proc.*, Vol. 1415, 211 (1991).
25. Y. F. Lu, W. D. Song, M. H. Hong, T. C. Chong, and T. S. Low, *Mater. Res. Soc. Proc.*, Vol. 397, edited by R. Singh et al. (Materials Research Society, 1996), to be published.
26. S. Boughaba, J.B. Héroux, M. Curcio, E. Sacher and M. Meunier, to be published in the Proceedings of the symposium on particles and solid surfaces, Chicago (August 6-9, 1996)
27. Y. F. Lu and Y. Aoyagi, *Japan. J. Appl. Phys.* 33, L430 (1994).
28. K. G. Watkins, J. H. Larson, D. C. Emmony, and W. M. Steen, in *Laser Processing : Surface Treatment and Film Deposition*, edited by J. Mazumder et al. (Academic, 1996), p. 907.
29. X. Wu, E. Sacher and M. Meunier, submitted to *Surf. Scien.*
30. X. Wu, E. Sacher and M. Meunier, submitted to *J. Adhesion*
31. W.B. Henly, L. Jastrzebski, N. F. Haddad, *J. Non-Cryst. Solids* 187, 134 (1995)
32. W. Bergholz, et al. ECS-Symposium on 'Crystalline Defects and Contamination: Their Impact and Control in Device Manufacturing', Grenoble, 17 Septembre (1993).
33. L. Jastrzebski, W. Henley and C.J. Nuese, *Solid State Technol.*, 12., p. 27-35 (1992).
34. J. Lagowski, P. Edelman, M. Dexter, W. Henley, *Semicond. Sci. Technol.*, 7, A185, (1992)
35. G. Zoth and W. Bergholz, *J. Appl. Phys.*, 67, 6764 (1990)
36. J. Lagowski, et al. *Appl. Phys. Lett.*, 63, 3043 (1993)

- 37 L. Jastrzebski, W. Henley, O. Milic, Proceedings of the Institute of Environmental Sciences, 1994, p. 316-324.
- 38 M. Simard-Normandin, F. Beaudoin and M. Meunier, Proceeding of the 27th annual meeting of the Fine Particle Society, August 96
- 39 H. Krupp, *Advan. Colloid Interface Sci.* **1**, 111 (1967).
- 40 E. M. Lifshitz, *Sov. Phys. JETP*, **2**, 73 (1956).
- 41 R. A. Bowling, *J. Electrochem. Soc.* **132**, 2209 (1985)
- 42 K. L. Johnson, K. Kendall and A. D. Roberts, *Proc. R. Soc. London* **A324**, 301 (1971).
- 43 D. S. Rimai and L. P. Demejo, *Annu. Rev. Mater. Sci.* **26**, 21 (1996).
- 44 M. B. Ranade, *Aerosol Sci. Tech.* **7**, 161 (1987).
- 45 J. J. Kipling and D. B. Peacall, *J. Chem. Soc.*, **182**, 834 (1957).
- 46 P. K. Iler, *The Chemistry of Silica* (Wiley-Interscience, New York, 1970), p. 387.
- 47 CRC Handbook of Chemistry and Physics, D. R. Lide and H. P. R. Frederikse Ed. (CRC Press, New York, 1996), pp. 6-12.
- 48 R. G. Greenler, *J. Chem. Phys.*, **37**, 2094 (1962).
- 49 J. Israelachvili, *Intermolecular and Surface Forces* (Academic, New York, 1991), Chap. 8.
- 50 D. Burgreen, *Elements of Thermal stress Analysis* (C. P. Press, Jamaica, New York 1971). Pp. 77, 129, 179.
- 51 D. E. Aspnes and A. A. Studna, *Phys. Rev.* **B 27**, 985 (1983).
- 52 P. Baeri and S. U. Campisano in *Laser Annealing of Semiconductors*, (Academic Press, Now York, 1982), J. M. Poate and J. W. Mayer Ed., chap. 4.
- 53 Y. S. Touloukian Ed. *Thermophysical Properties of Matter*, (IFI/ Plenum, New York-Washington, 1970, 1973, 1977), vol. 4, 5, 13.
- 54 H. Hulst, *Light Scattering by Small Particles* (Wiley, New York, 1957).
- 55 Y. F. Lu, W. D. Song, K. D. Ye, Y. P. Lee, D. S. H. Chan and T. S. Low, *Jpn. J. Appl. Phys.* **36**, L1304 (1997).
- 56 S. V. Stralen and R. Cole, *Boiling Phenomena* (Hemisphere, Washinton, 1979), vol. 1.
- 57 L. M. Lyamshev and K. A. Naugol'nykh, *Sov. Phys. Acoust.*, **27**, 357 (1982)
- 58 D. R. Lide and H. P. R. Frederikse Ed. *CRC Handbook of Chemistry and Physics*, (CRC Press, New York, 1996), pp. 6-10, 6-16.
- 59 F. Beaudoin, M. Meunier, M. Simard-Normandin and D. Landheer, *J. Vac. Sci. Technol.* **A16**, 1976-1979 (1998).

Transient temperature measurement of amorphous silicon thin films during excimer laser annealing

Seungjae Moon^a, Minghong Lee, Mutsuko Hatano^b,
Kenkichi Suzuki^c, and Costas P. Grigoropoulos^{*a}

^aDepartment of Mechanical Engineering, University of California, Berkeley, CA 94720

^bHitachi Ltd., Central Research Laboratory, Tokyo 185-8601, Japan

^cElectron Tube & Devices Division, Hitachi Ltd., Mobara 297, Japan

ABSTRACT

The excimer laser annealing of amorphous silicon thin films has been investigated via optical diagnostics. Amorphous silicon films of 50 nm thickness are used in laser annealing. To obtain the transient temperature variation in the laser annealing process, the thermal emission and near-infrared optical properties are measured. The front transmissivity and reflectivity are measured to obtain the emissivity at the 1.52 μm wavelength of the probe IRHeNe laser. Significant undercooling of the liquid silicon is observed during the cooling stage. The emissivity is almost constant during the melting period, but increases during the melting and solidification transformations.

Keywords: amorphous silicon thin film, laser annealing, reflectivity, transmissivity, emissivity, undercooling, and crystallization

1. INTRODUCTION

Excimer laser crystallization has recently emerged as a promising new method for fabricating polycrystalline thin film transistors (TFTs) on glass for applications to active matrix flat panel displays used in advanced multi-media.¹ Excimer laser annealing has been shown superior to other techniques in terms of fabrication cost and efficiency. In Excimer laser annealing, the ultraviolet laser beam is absorbed at the surface of the amorphous silicon thin film, which is heated up within a few tens of nanoseconds, melts and then crystallizes into polycrystalline silicon. The substrate remains unaffected during this process.² This fact is crucial, because it allows use of inexpensive and large size glass as substrate instead of quartz. In laser crystallization, it is very important to obtain high quality (low defects and uniform grain size) polycrystalline silicon, which yields high performance thin film transistors.³ However, the mechanism of recrystallization is not well known, especially in the nanosecond time scale and under nonequilibrium phase-change conditions. To understand these phenomena, optical diagnostic methods are considered appropriate.⁴ Since the optical properties are dependent on temperature and state of phase, the reflectivity and transmissivity are good indicators for monitoring the laser annealing process. For example⁴ analysis of time-resolved reflectivity data during the laser heating of silicon and germanium was used to determine the onset of melting and the melting duration time. For understanding the solidification mechanism, it is very important to obtain the temperature distribution. Development of *in-situ*, noncontact, and fast time response methods is therefore necessary. A nanosecond-time resolution pyrometer was developed to study the transient temperature field in the pulsed laser melting of polycrystalline silicon thin films on transparent substrates⁵.

In this study, the emission signal is captured using a fast InGaAs detector to measure the transient temperature data. To accurately extract the temperature information, the emissivity is needed. Since the silicon thin film is semitransparent, *in-situ* reflectivity and transmissivity is measured to obtain

* Electronic mail: cgrigoro@newton.me.berkeley.edu

the emissivity and determine the temperature. Significant change in optical properties during the phase-change process and notable undercooling during the cooling stage are observed.

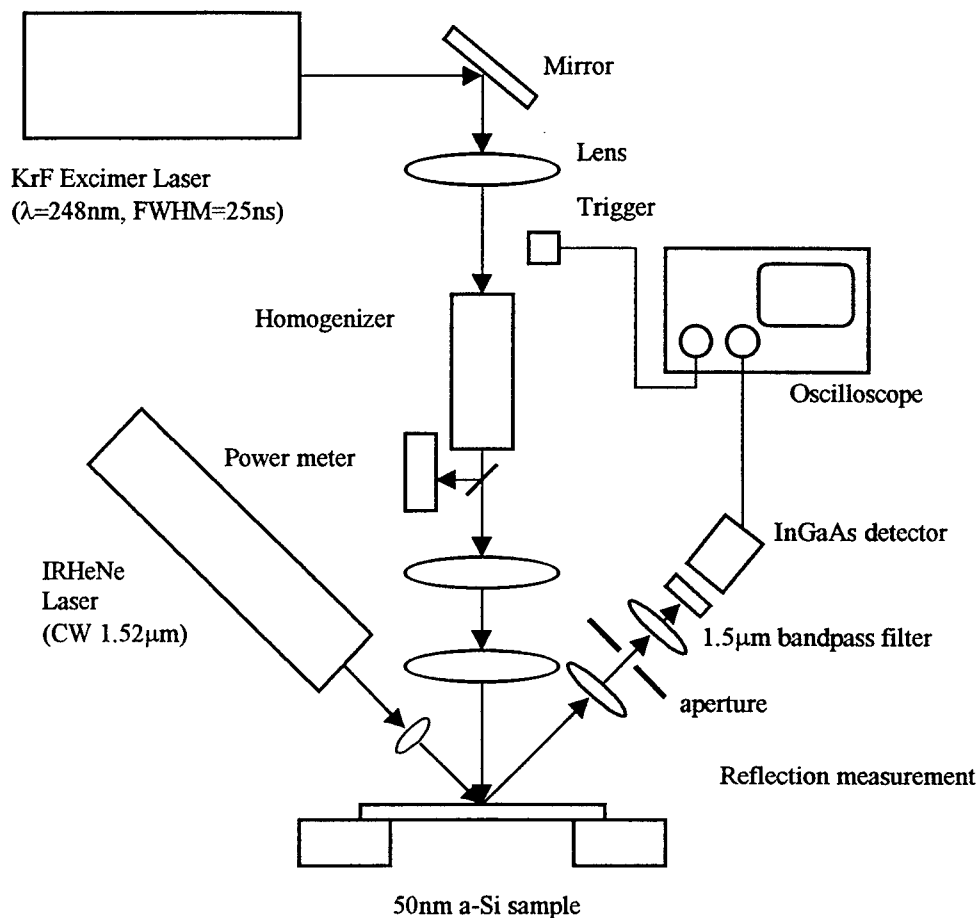


Fig. 1. Schematic diagram for experimental setup for measuring front reflection at the wavelength of $1.52\mu\text{m}$.

2. EXPERIMENTAL SETUP

Undoped amorphous silicon thin film was deposited on a quartz substrate by low pressure chemical vapor deposition technique (LPCVD). A schematic of the experimental setup for measuring front reflectivity is shown in Fig. 1. The amorphous silicon thin film is heated by a KrF excimer laser beam ($\lambda=248\text{ nm}$). A tunnel type beam homogenizer is used to ensure spatial uniformity of the laser beam. A quartz beam splitter is used to reflect 10 % of the laser beam to an energy meter in order to measure the laser pulse energy. The Excimer laser beam is focused onto the sample surface to a spot size of $6\text{mm} \times 2\text{mm}$ by two UV lenses. Focused $1.52\mu\text{m}$ IRHeNe laser beam is used for measuring reflectivity and transmissivity. Reflectivity and transmissivity measurements are conducted separately. For transmissivity measurement, the same detection optics is aligned against the sample backside at an angle of 45° with respect to the normal direction. Also, backside reflectivity is measured at the angle of 45° to investigate the solidification mechanism. The role of the aperture is to reduce the solid angle of emission signal and possible scattering from the roughened target surface. The aperture allows the detector to capture only the reflected IRHeNe laser beam from the sample. A $1.5\mu\text{m}$ narrow bandpass filter with half

band width of $0.05\mu\text{m}$ is also used to eliminate contribution to the IR signal from emission of other wavelengths. The IRHeNe laser has inherent fluctuation and noise. In addition, it is noted that $1.52\mu\text{m}$ probe laser intensity is modulated with high frequency oscillation, which could be effectively eliminated by fast Fourier transforming the optical signal, filtering out the spurious oscillation, and then Fourier transforming back to acquire the filtered optical signal. The measured reflectivity and transmissivity signal is then normalized with room temperature values obtained from thin film optics calculations and measurement. When the emission signals are measured, the aperture is removed in the detection part to maximize the signal. The collected and focused emission signal by two short focal lenses is captured by the InGaAs photodetector. To distinguish the spectral thermal emission and enhance the accuracy of the measurement, four bandpass filters of the wavelengths of $1.2\mu\text{m}$, $1.4\mu\text{m}$, $1.5\mu\text{m}$, and $1.6\mu\text{m}$ are respectively employed. In this study, only the optical properties at the wavelength of $1.5\mu\text{m}$ are measured. For other wavelengths, the optical properties at $1.5\mu\text{m}$ are used within 10 % error.⁶

3. EMISSION CALCULATION

The derivation of temperature from thermal emission measurement is based on Planck's blackbody radiation intensity distribution law. The blackbody emissive power is as follows.⁷

$$e_{\lambda b} = \frac{2\pi C_1}{\lambda^5} \cdot \frac{1}{\exp(C_2 / \lambda T) - 1}, \quad (1)$$

where $C_1 = 3.740 \times 10^8 \text{ W}\mu\text{m}^4/\text{m}^2$, $C_2 = 1.438 \times 10^4 \text{ K}\mu\text{m}$. It is assumed that the thermal emission from the target material during the nanosecond pulsed laser heating obeys Planck's Blackbody radiation intensity distribution law. The thermal emission signal collected by the detector can be expressed by⁵:

$$v_e(T) = \frac{R_\Omega A}{\pi} \int_{\lambda_1}^{\lambda_2} \int_{\phi_1}^{\phi_2} \int_{\theta_1}^{\theta_2} \varepsilon'_\lambda(\lambda, \theta, \phi, T) \tau(\lambda) G(\lambda) e_{\lambda b}(\lambda, T) d\theta d\phi d\lambda, \quad (2)$$

where T is the temperature, θ and π are the polar and azimuthal angles, λ is the wavelength, R_Ω is the impedance of the oscilloscope (50Ω), A is the area on the sample which is sensed by the detector, $\varepsilon'_\lambda(\lambda, \theta, \phi, T)$ is the directional spectral emissivity, $\tau(\lambda)$ is the transmissivity of the two lenses, $G(\lambda)$ is the responsivity (A/W) of the InGaAs detector at different wave lengths, and $e_{\lambda b}$ is the black body emissive power which follows Planck's black body intensity distribution law. The transmissivity of lenses in the infrared regime is taken to be constant values between $1.2\mu\text{m}$ and $1.6\mu\text{m}$.

In order to enhance the accuracy of the measurement, four different wavelengths signals as discussed above are measured and the compared by the following equation:

$$F(T) = \left| \frac{v_{o,1.6\mu\text{m}}}{v_{o,1.2\mu\text{m}}} - \frac{v_{e,1.6\mu\text{m}}}{v_{e,1.2\mu\text{m}}} \right| + \left| \frac{v_{o,1.5\mu\text{m}}}{v_{o,1.2\mu\text{m}}} - \frac{v_{e,1.5\mu\text{m}}}{v_{e,1.2\mu\text{m}}} \right| + \left| \frac{v_{o,1.4\mu\text{m}}}{v_{o,1.2\mu\text{m}}} - \frac{v_{e,1.4\mu\text{m}}}{v_{e,1.2\mu\text{m}}} \right|, \quad (3)$$

where $v_{o,1.2}$, $v_{o,1.4}$, $v_{o,1.5}$, and $v_{o,1.6}$ are the measured oscilloscope readings at these four wavelengths, and $v_{e,1.2}$, $v_{e,1.4}$, $v_{e,1.5}$, and $v_{e,1.6}$ are the corresponding temperature-dependent values from equation(2). The peak surface temperature can be determined by minimizing equation(3).

The transient temperatures at other times are compared with the peak temperature and derived from the following equation.

$$\frac{v_o(t)}{v_{o,\max}} = \frac{v_e(T)}{v_e(T_{\max})} \quad (4)$$

The measured emissivity at the wavelength of $1.52\text{ }\mu\text{m}$ is used in the transient temperature calculation through the whole wavelength range.

4. RESULTS AND DISCUSSION

Figure 2 shows the relationship between laser fluence and averaged temperature. In the liquid region, the absorption depth of infrared light is about 20 nm on the basis of the optical property data for liquid silicon measured by Shavarev, et al.⁶ The calculated temperature corresponds to the averaged temperature over the absorption length. It is known that the thermal conductivity of liquid silicon is in the range of the thermal conductivity of metals. Thus, the temperature gradient across the liquid layer is flat, compared to that in the solid amorphous silicon layer. The emission signal in the liquid region therefore emanates from an essentially uniform temperature distribution across the absorption length. A flat region is clearly shown in the figure. This region corresponds to the duration of the partial melting. Also this region indicates that the phase-change of amorphous silicon from liquid to solid occurs within a certain temperature range, in the neighborhood of 1510 K . It is known that the melting temperature of amorphous silicon is lower than that of crystalline silicon, 1685 K , by about $100\text{--}200\text{ K}$.⁸ In the case of emission measurement of metal samples, the surface temperature of sample can be obtained due to the high value of the extinction coefficient. However, for the solid semitransparent amorphous silicon material, and in the near infrared range, the emission signal corresponds to the integrated radiation over the absorption depth, $\lambda/4\pi k$, which exceeds the film thickness. Therefore, the emission signal includes the temperature information of solid thin film and some part of substrate.

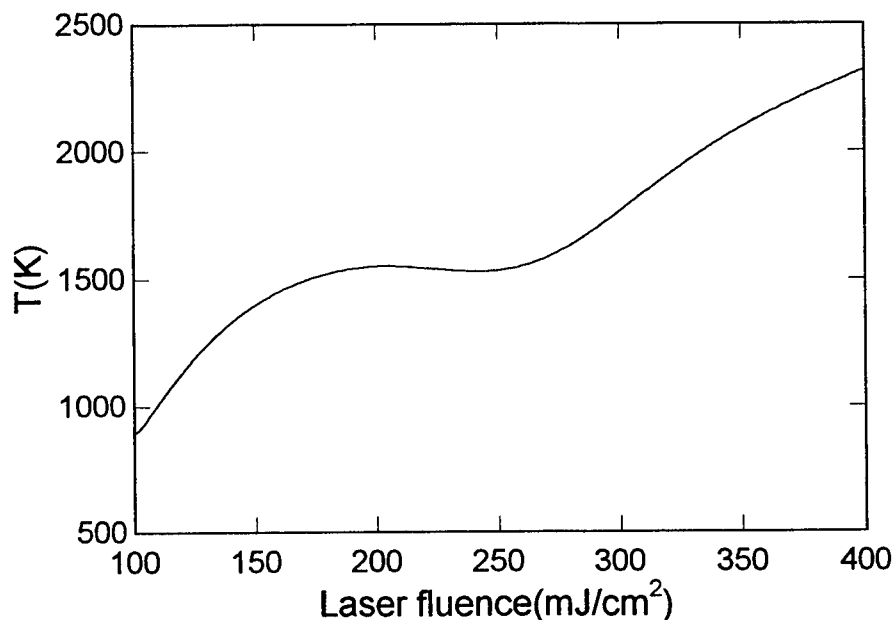


Fig. 2. The peak integrated temperature versus incident excimer laser fluence

The transient variations of optical properties measured at the IRHeNe laser wavelength of $1.5\text{ }\mu\text{m}$ (reflectivity, transmissivity, emissivity, and back reflectivity), the emission signal, and averaged temperature are presented in Fig. 3 to Fig. 6 for various laser fluences. Solid silicon is highly transparent in the infrared range. However, when the liquid silicon thickness exceeds the absorption depth, it turns to opaque. The film reflectivity increases and the transmissivity decreases upon melting. In the emissivity

plot, shown in thin solid line, two peaks are distinguished in the melting and solidification periods, correspondingly. These features are attributed to the phase-change process and the accompanying optical property change. In the emission measurement, the emissive power is actually acquired. As shown in Equ. (2), the data include information on the optical properties and the radiation intensity. The first and larger in magnitude peak is generated by the temperature rise during the laser heating. The duration of the second bump coincides with the change of the optical properties captured by the reflectivity and transmissivity signals that is due to solidification process. The front reflectivity measurement is carried out without the aperture in order to evaluate the effect of scattering by evolving surface morphology. However, no appreciable scattering was detected during the phase change process. It also appears that the emissivity increases during the phase-change process. This phenomenon requires further investigation. The transient temperature distribution is calculated using Equ. (2) & Equ. (4). The emissivity data are used in the temperature calculation. Supercooling is clearly observed in the transient temperature plot as the cooling process occurs under nonequilibrium conditions. Nuclei form in the supercooled liquid, releasing latent heat. Eventually, the liquid pool solidifies, and the cooling process continues via the conductive loss to the substrate.

Figure 3 shows the results at the laser fluence of 212 mJ/cm^2 , which drives partial melting. In this figure, V and $b\rho$ represent captured emission and back reflection signals. The reflectivity of silicon at the $1.52 \text{ }\mu\text{m}$ wavelength increases monotonically with time during the laser heating until the surface melts, resulting in a large increase of the reflectivity. The transmissivity exhibits reverse behavior compared with the reflectivity. In the partial-melting regime, the maximum temperature is still lower than the equilibrium crystalline silicon melting point and crystallization originates from unmelted silicon seeds.

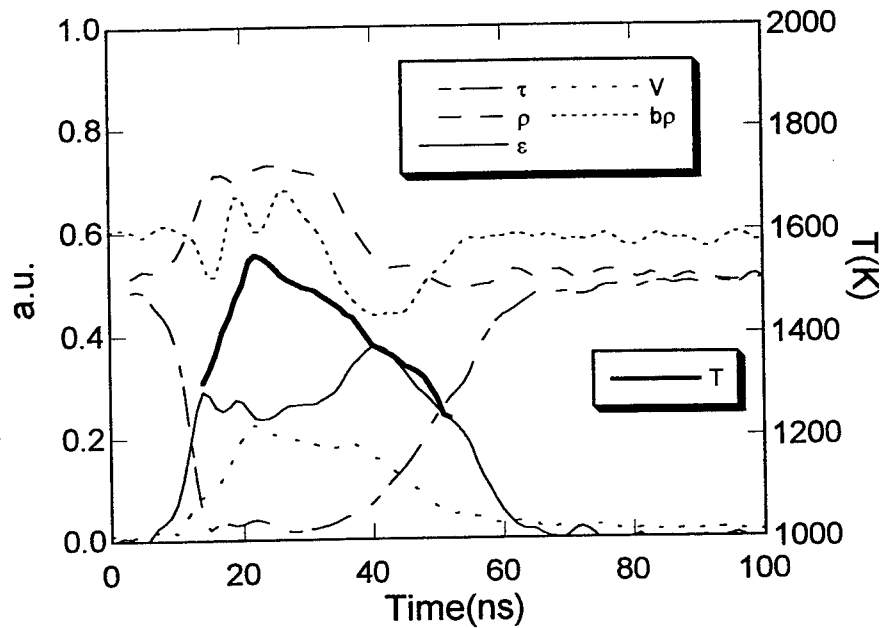


Fig. 3. Transient variations of front reflectivity, ρ , transmissivity, τ , emissivity, ε , emission signal, V , back reflection, $b\rho$, at the angle of 45° , and the wavelength of $1.52 \text{ }\mu\text{m}$, and integrated temperature, T . The Excimer laser fluence is 212 mJ/cm^2 .

Figure 4 presents the results at the laser fluence of 262 mJ/cm^2 , which is just past the full melting threshold. Some undercooling effects are noted in this graph. Results for full melting are shown in Fig. 5 and Fig. 6 for laser fluences of 301 mJ/cm^2 and 318 mJ/cm^2 .

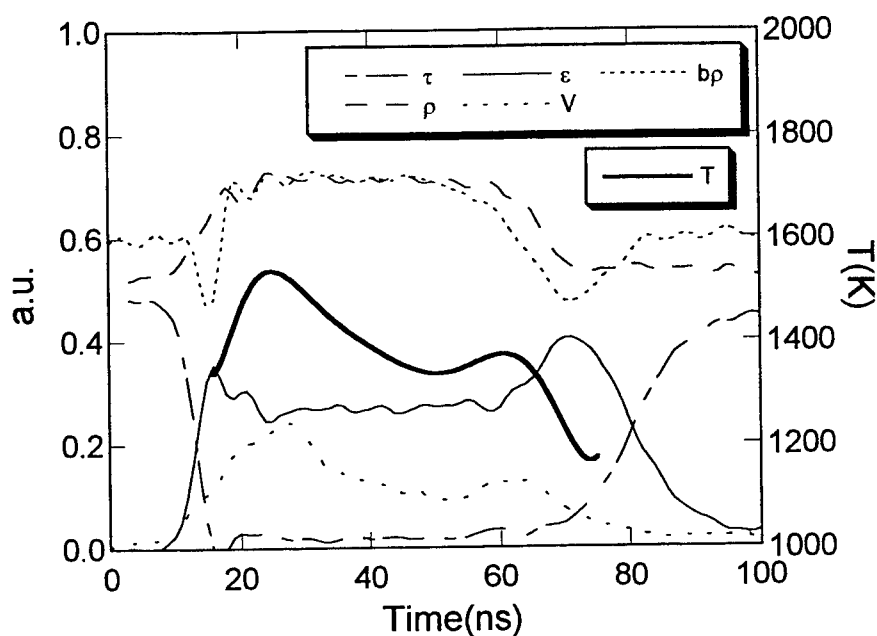


Fig. 4. Transient variations of front reflectivity, ρ , transmissivity, τ , emissivity, ε , emission signal, V , back reflection, $b\rho$, at the angle of 45° , and the wavelength of $1.52 \mu\text{m}$, and integrated temperature, T . The Excimer laser fluence is 262 mJ/cm^2 .

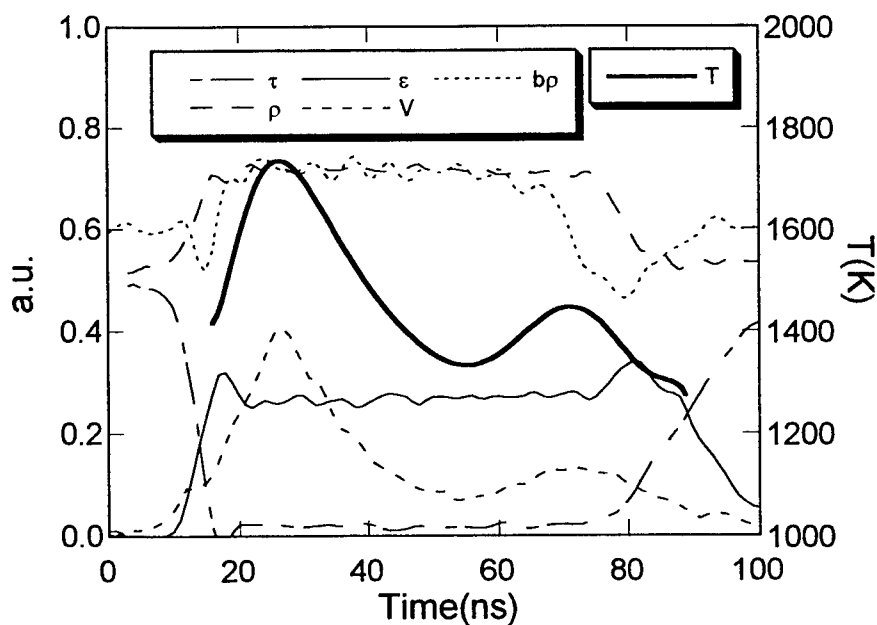


Fig. 5. Transient variations of front reflectivity, ρ , transmissivity, τ , emissivity, ε , emission signal, V , back reflection, $b\rho$, at the angle of 45° , and the wavelength of $1.52 \mu\text{m}$, and integrated temperature, T . The Excimer laser fluence is 301 mJ/cm^2 .

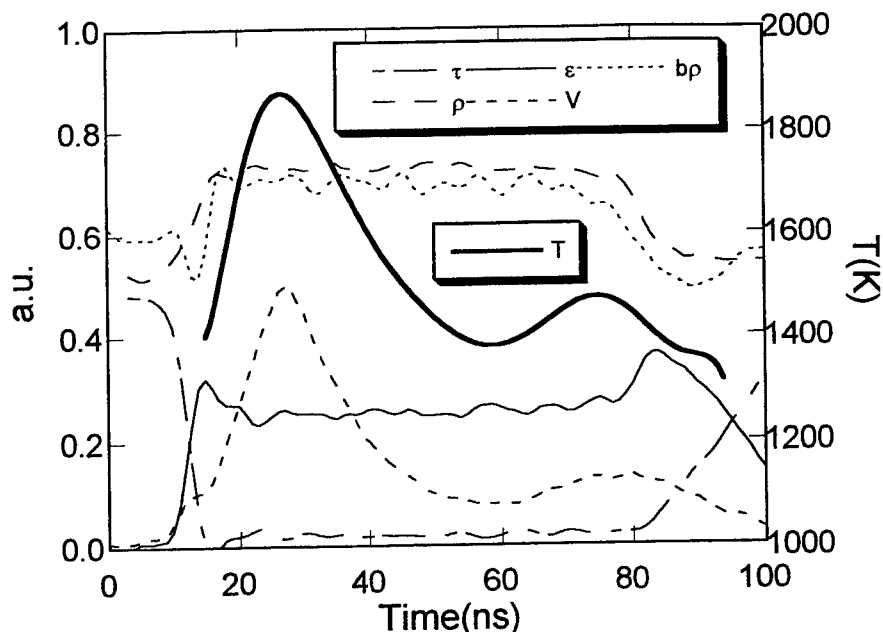


Fig. 6. Transient variations of front reflectivity, ρ , transmissivity, τ , emissivity, ε , emission signal, V , back reflection, $b\rho$, at the angle of 45° , and the wavelength of $1.52 \mu\text{m}$, and integrated temperature, T . The Excimer laser fluence is 318 mJ/cm^2 .

Cooling of the liquid layer occurs in the nanosecond time scale, and without the presence of inhomogeneous nucleation sites at the interface with the glass substrate that could readily promote crystallization. The assumption of equilibrium phase-change is no longer valid. Thus, in dealing with laser-induced crystallization, nonequilibrium phase change model should be adopted.⁸⁻⁹ Significant undercooling exists in the laser recrystallization process, as the laser irradiation energy increases.

5. CONCLUSION

The transient temperature and the dependence of temperature on laser fluence are quantified by measuring the emission signal during the laser annealing process. The transient emissivity at the wavelength of $1.52 \mu\text{m}$ was measured *in-situ*. By analyzing the experimental information, the physical mechanism of the phase-change phenomena could be understood. Due to the rapid cooling rate, (of the order of several m/s), significant undercooling was observed for laser fluences exceeding the full melting threshold. Further study is necessary in order to analyze the increase of absorptivity during the phase transformation process and the relation of the cooling mode to the mechanism of polycrystalline grain formation.

ACKNOWLEDGMENT

This work is sponsored by Hitachi Ltd., Tokyo, Japan.

REFERENCES

1. T. E. Dyer, J. M. Marshall, W. Pickin, A. R. Hepburn, and J. F. Davies, "Polysilicon produced by excimer (ArF) laser crystallization and low-temperature (600°C) furnace crystallization of hydrogenated amorphous silicon (a-Si:H)," *Journal of Non-Crystalline Solids*, 164-166, pp.1001-1004, 1993.
2. W. Staudt, S. Borneis, and K.-D. Pippert, "TFT annealing with excimer laser technology and market outlook," *Phys. Stat. Sol. (a)*, 166, pp.743-749, 1998.

3. J. S. Im and R. S. Sposili, "Crystalline Si films for integrated active-matrix liquid-crystals displays," *MRS Bulletin*, Vol. 11, No. 3, pp. 39-48, 1996.
4. G. E. Jellison, Jr., D. H. Lowndes, D. N. Mashburn and R. F. Wood, "Time-resolved reflectivity measurements on silicon and germanium using a pulsed excimer KrF laser heating beam," *Physical Review B*, Vol. 34, No. 4, pp. 2407-2415, 1986.
5. X. Xu, C. P. Grigoropoulos and R. E. Russo, "Nanosecond time resolution thermal emission measurement during pulsed excimer laser interaction with materials," *Appl. Phys. A*, 62, pp.51-59, 1996.
6. K. M. Shavarev, B. A. Baum, and P. V. Gel'd, "Optical properties of liquid silicon," *Sov. Phys. Solid State*, Vol. 16, No. 11, pp. 2111-2112, 1975.
7. R. Siegel, and J. R. Howell, *Thermal radiative heat transfer*, 3rd ed., Hemisphere, Bristle, 1992.
8. R. F. Wood, and G. A. Geist, "Theoretical analysis of explosively propagating molten layer in pulsed-laser-irradiated a-Si," *Physical Review Letters*, Vol. 57, No. 7, pp. 873-876, 1986.
9. R. F. Wood, and G. A. Geist, "Modeling of nonequilibrium melting and solidification in laser irradiated materials," *Physical Review B*, Vol. 34, No. 4, pp.2606-2620, 1986.

Correlation between power density fluctuation and grain size distribution of laser annealed poly-crystalline silicon

Kenkichi Suzuki^a, Masakazu Saitou^a, Michiko Takahashi^a, Nobuaki Hayashi^a,
and Takao Terabayashi^b

^aElectron Tube & Devices Div., Hitachi, Ltd.

3300 Hayano, Mobara, Chiba 297 Japan

^bProduction Engineering Research Laboratory, Hitachi, Ltd.,

292 Yoshida-cho, Totsuka-ku, Yokohama 244 Japan

ABSTRACT

The grain size of polycrystalline silicon (p-Si) by the excimer laser annealing (ELA) is primarily determined by the fluence, and the distribution uniformity is strongly influenced by the intensity fluctuation. Instead of the conventional CCD profiler, an resist film is used to monitor the light intensity distributions over whole illumination area in submicron resolution. The high resolution measurements show speckle patterns with 0.1~0.15 μm spacing with maximum 10mJ/cm² variation. The fluctuation does not influence the grain size variation in the lateral growth region over 1~2 μm area, however, the undulation of intensity about 10mJ/cm² over 10 μm distance produces an appreciable changes in the grain sizes. Such a local temperature distribution corresponds to the envelop obtained by averaging small area, and is maintained during crystallization process.

Keywords: Polycrystalline silicon, Excimer laser annealing, Resist, Beam profiler.

1. INTRODUCTION

Many of the TFT-LCD manufacturers have launched production of the low temperature p-Si (LTP)TFT-LCD, as the performances of MOS transistors of p-Si become applicable to integration of the peripheral circuitries of some types of the displays. This is mainly due to qualities of ELA-p-Si⁽¹⁾ and PE-CVD-SiO₂ which enable to realize usable TFT performances, e.g. the field effect mobility of more than several tens, sometimes 300 cm²/Vs in experimental level. The crystallinity of ELAp-Si has rather high quality inherent to liquid phase solidification, and the performances are considered to be degraded mainly by the grain boundaries. Larger grain size assures better performance. Actually a transistor with a single grain over 1 μm short channel shows more than 400 cm²/Vs. This stimulates developments of single crystallization techniques, and ultimately realization of a system-on-glass of high definition TFT-LCD, which is sole advantage of p-Si over the current a-Si TFT-LCD. There are so many experiments aiming larger grain sizes, new and mostly revised from '80s⁽²⁾, however, they are a little far from practical applications because of lack of uniformity and reproducibility.

* Correspondence: E-mail: ksuzuki@cm.mobara.hitachi.co.jp; TEL:+81-475-25-9062;FAX:+81-475-24-2463

The uniformity and the reproducibility in the present LTP-TFT mass production is considered to be assured by smaller sized grains than a characteristic length, sacrificing higher performances. Typical characteristic length is usually a channel length (L), and is now $3\text{ }\mu\text{ m}$ at most due to the current production equipments for large area substrates. So a reasonable grain size is no more than $0.3\text{ }\mu\text{ m}$. This is primary condition of ELA process in manufacturing at present. The secondary condition comes from requirement from the device structure. The precursor film thickness should be less than 100nm, preferably near 50nm, as the LTP-TFT device is fundamentally SOI and the film thickness should be less than the depletion layer. The preferred film thickness is reasoned by less fluence resulting less throughput time and less production cost.

Thus the basic technology of ELA crystallization is to produce uniform and high graded p-Si film under these two conditions. For this purpose, it is essential to understand the mechanisms of ELA crystallization. More clearly we have to understand to what extent we can control the non-equilibrium phenomenon of ns time scale. From huge volume of the investigations hitherto, we can deduce some qualitative models for the grain growth, however, for mass production we need to know quantitatively what working parameters are effective and how they can be controlled. All these parameters seems to be classified into three categories; those related directly to ELA, the precursor film, and the interface. The first ELA parameters are fluence, shot numbers or repetition rate and the stage scanning speed, substrate temperature, atmosphere, and illumination uniformity. The second category includes film thickness, morphology and the concentration of hydrogen in the film. The third is difficult to define, but is related directly to crystallization dynamics, such as heterogeneous nucleation and lateral grain growth. At present the contributions of some of the parameters are considered to be almost established, however quantitative data necessary to the mass production are not necessarily sufficient, because the explicit technical parameters above are somehow coarse to control submicron grain growth. An example is CCD beam profiler, of which spatial resolution is usually $10\text{ }\mu\text{ m}$ and monitors only confined region of the illumination area.

This paper presents a concept of the resist profiler which is possible to evaluate light intensity distribution over whole illumination area with submicron resolution. Such a profiler is essential because we are observing only intensity distribution in rather rough resolution at present although there may be microscopic fluctuations inherent to gas laser, and the grain size used is in submicron region. In the second chapter, the relationship between the ELA crystallization and the fluence and shot numbers are described according to our observations. The third chapter is devoted to the description of the technique of the resist profiler. The fourth and fifth are for discussions and conclusion.

2. FEATURES OF ELA POLYSILICON CRYSTALLIZATION

As a standard precursor Si film, we adopted a-Si film by LP-CVD of 50nm thick on quartz substrates. The deposition gas is monosilane (SiH_4) and the substrate temperature is $550\text{ }^\circ\text{C}$. ELA experiments are performed both by 248nm, $4\text{ x }8\text{ mm}^2$ and by 308nm, $0.3\text{ x }150\text{ mm}^2$ illumination area with nominal uniformity of $\pm 5\%$. The former is used mainly for examining the effects of temperature and atmosphere, and the latter is mainly for beam scanning.

The relationships between laser fluence and grain size are depicted in Fig. 1. The shot number is an fundamental factor for grain growth. One shot means solidification from precursor to polycrystalline, and the multi-shot corresponds to poly-to-poly transformation. The feature of grain growth is similar to both situations, that is, small grains at low fluence and

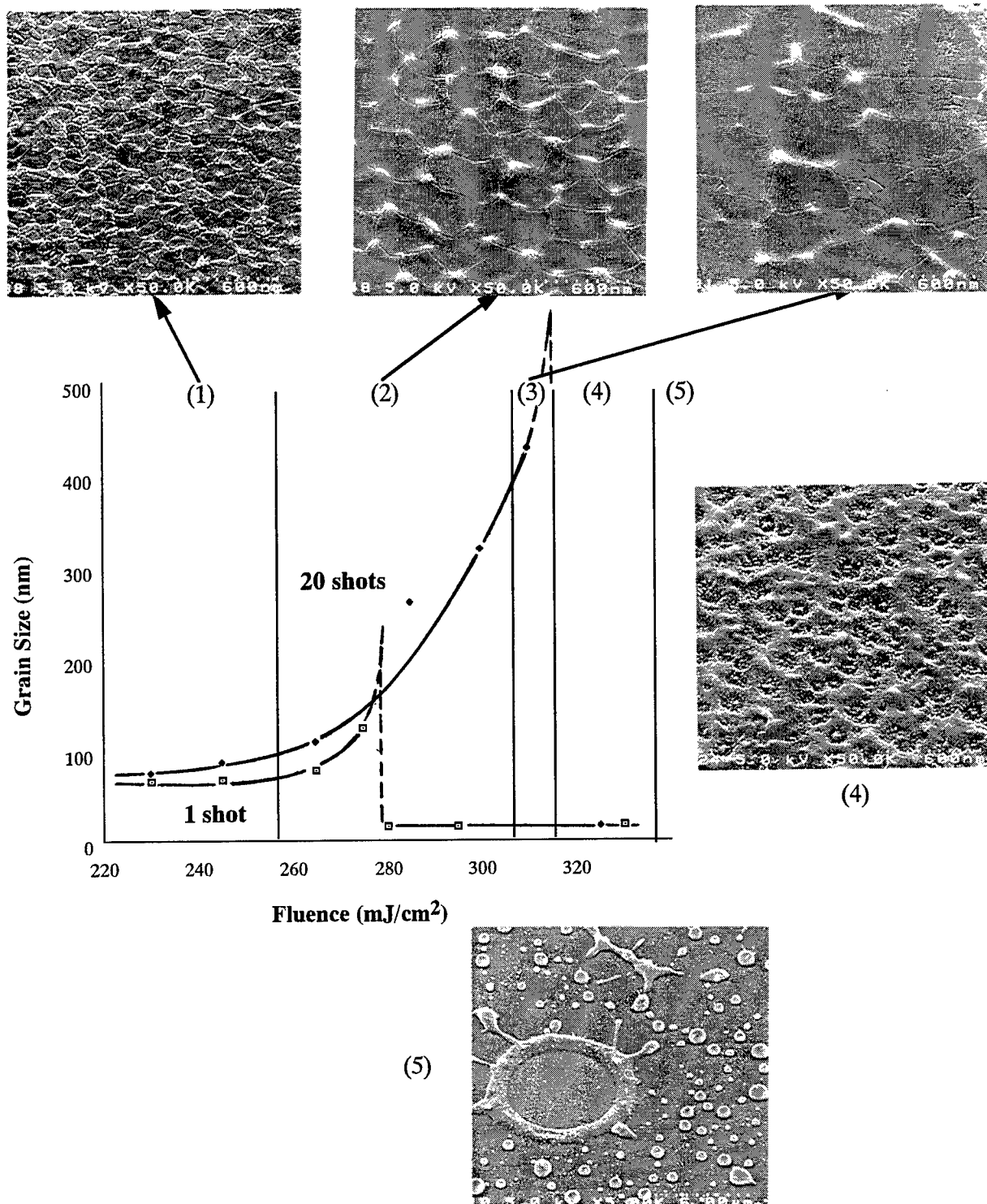


Fig.1 Relationship between fluence and grain size(average).

The grain growth is divided into 5 stages (here for 20 shots' case) , and the grains in each stage are shown in SEM picture.

becomes larger with fluence. The growth ends abruptly at a certain critical fluence, above which it becomes microcrystalline and amorphous mixture. Further increase of fluence results ablation. The fundamental difference between one- and multi-shot condition is the grain size and the uniformity of its distribution. The multi-shot grain size increases with shot number above a certain fluence, from which lateral growth starts. Improvement of the uniformity by the multi-shot seems to be also related to the lateral growth and is essential to practical applications. The grain growth is characterized by five stages according to the fluence, and SEM picture of typical grain structure at each stage is shown in Fig. 1. These pictures are results of 20 shots-LA in vacuum and at room temperature.

The first stage is vertical growth of small grains. When the size becomes nearly equal to the film thickness, the lateral growth is started. For 50nm film thickness, there is a particular size of the grain, approximately $0.3 \mu\text{m}$, which shows rather uniform distribution. This feature is very prominent when we use small pitch overlapping of scanning, e.g. $10 \mu\text{m}$, over wide area. The third stage is of rather larger grain size, but not uniform. It looks that the larger sized grains are constructed by merging smaller grains. The fluence of the abrupt transition to microcrystalline is different between one- and multi-shot, which is due to the differences of the melting point and the latent heat between amorphous and polycrystalline. The fourth stage is microcrystalline due to rapid bulk nucleation. The fifth is ablation. AFM data in Fig.2 show quantitative aspects of the grain growth. The bumps are created at the grain boundaries, and it is higher at a triple or sometimes quadruple junction. A grain corresponds to the valley between the peaks. The positions of the bottom of the valley, that is, the height of the grains, change randomly for the smaller grain region, but it becomes rather longer undulation when the grain size becomes larger.

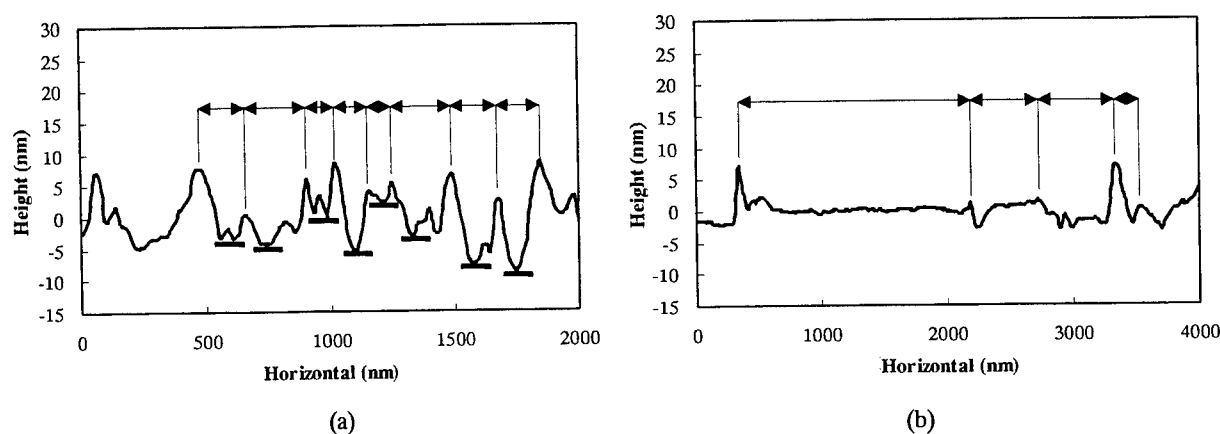


Fig. 2 AFM profiles of p-Si surfaces. (a) small grain size, (b) large grain size

The crystallization processes are qualitatively explained by a simple nucleation and crystal growth model, but the details are varied with different types of precursors. The most prominent is the onset fluence of ablation. This is apparently correlated to hydrogen contents in the case of amorphous Si by PE-CVD. The larger the hydrogen content, the smaller the ablation fluence. Sometimes the film is ablated without the pass of microcrystalline phase. The PE-CVD precursors are mostly amorphous, and the morphology is strongly influenced by H contents, making various types of Si-H bonds³⁾. The various bonding structure makes it difficult to dehydrogenate completely, and results fluctuation in crystallization process. Even the

films by sputtering sometimes show very low ablation threshold, although H concentration is very low. It seems that morphology, microcrystallinity or defects, irrelevant to H are also the cause of such a behaviour. Higher substrate temperature results lower fluence to make same supercooling than r.t., and sometimes it improves the uniformity.

3. RESIST BEAM PROFILER

The most common beam profiler makes use of CCD camera. The pixel size is $5 \mu\text{m}$ square in minimum, and the number of pixel is 1M (XGA) usually. Accordingly with 1:1 image system, the resolution is just $5 \mu\text{m}$. It is improved by a magnified optics. A conventional magnifier is the objective lens of the microscope, and we can obtain ideally $0.2 \mu\text{m}$ resolution with an adequate optics($\times 100$) corresponding to a CCD pixel at minimum resolution. The drawback is reduction of the objective field. In the case of the highest resolution above it is $0.2\text{mm}\phi$. The field spreads upto $1.0\text{mm}\phi$ when $\times 20$ objective lens is used. However the resolution is reduced to $0.5 \mu\text{m}$.

Our objective is to measure the intensity distribution with submicron resolution over all beam area. Only resist film can realize such a high spatial resolution over wide area. The principle of the resist beam profiler is very simple. The light incident into a resist film react with the material, producing insoluble or soluble region according to the types of resists, proportional to light intensity. The following development process removes or fixes the reacted region, and the light intensity is mapped as surface undulation. The configuration of the resist profiler system is shown schematically in Fig. 3(a). The homogenized beam is splitted by the mirror, and illuminates the resist film through a conjugate optics. The resist film is moved by X-Y stage to be exposed with each shot. The surface profiles are measured by various types of high resolution profilers and by AFM. Resist sensitivity should be linear in low light intensity. There must be a base plane flat

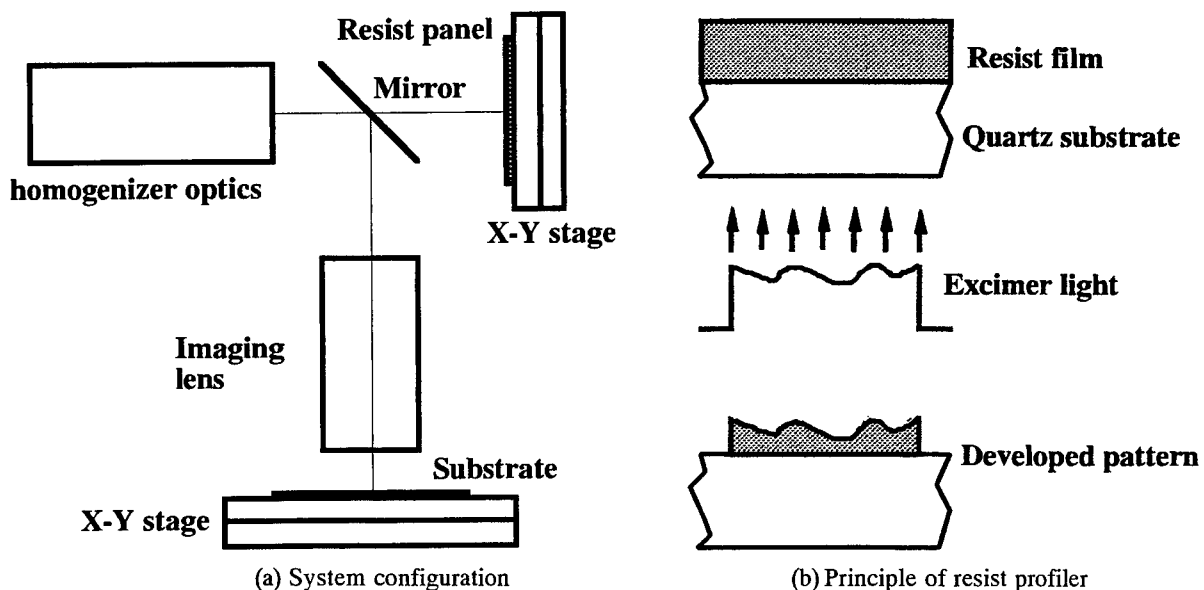


Fig. 3 Resist profiler system

enough to measure the roughness produced by light intensity distribution. Such a flat basis is obtained only by a substrate surface. It follows that the light should be illuminated from the substrate side, and thus to use a negative type resist film as shown in Fig. 3(b). This configuration prevents also LIPSS structure⁴⁾.

Phenol-azido system⁵⁾ is selected as resist material. The matrix resin is poly(p-vinylphenol), and the chromophore is 3-3'-diazidodiphenyl sulfone. This material was synthesized originally for the resist sensitive to ultraviolet region. The photochemical reaction scheme is depicted in Fig. 4. Ultraviolet light activates azido radicals of the chromophores, which subsequently release nitrogen, and are changed to an intermediate nitrene. The nitrenes extract hydrogens at aryl-carbons in the resin monomers, which are polymerized and become insoluble. The sensitivity and linearity is controlled by the concentration of the chromophore and the molecular weight of the matrix.

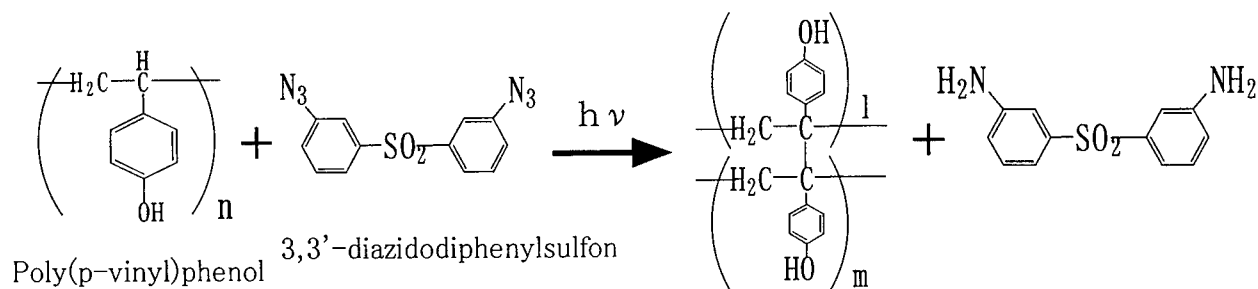


Fig. 4 Photochemical reaction scheme of the resist

The relationship between fluence (1 shot) and developed film thickness is shown in Fig. 5. The dynamic range (defined by the ratio of average film thickness after development and minimum variation from the average) is conditioned by the concentration of the developer chemicals and developing time. The resist film is coated on a quartz plate, and baked 1 hour at 100°C. The light is illuminated from the rear of the plate and developed. An average film thickness is measured by a profiler (DEKTAK) and the surface undulation is measured by an optical type of profiler (Wyko TOPO-3D) and AFM. The flatness of the substrate surface is finished to $\lambda/10$, and the Ra of the substrate surface is less than 0.15nm for $2\ \mu\text{m}$. This value assures the accuracy to measure the local variation of the resist surface.

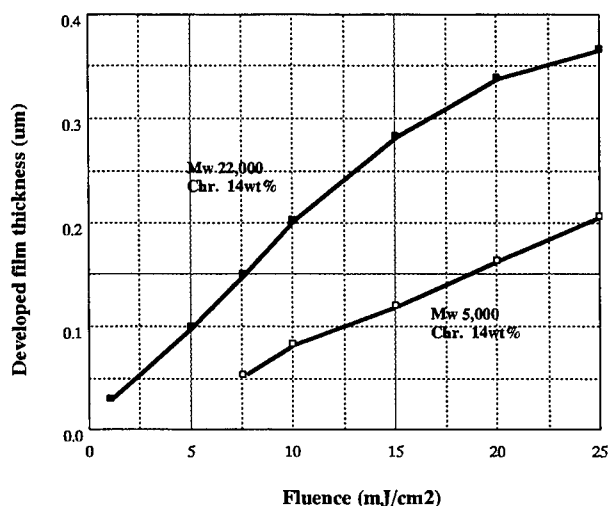


Fig. 5 γ -characteristics of the resist

The sensitivity is strongly dependent upon molecular weight, rather than the concentration of the chromophore.

4. RESULTS AND DISCUSSIONS

Comparison between the profiler(WYKO) picture and p-Si micrograph (Nomarski) is shown in Fig. 6. To distinguish the variations of illumination, a little deteriorated homogenizer optics are used. The spatial resolution of the profiler(WYKO) is $0.5 \mu\text{m}$. The measurement area is 1mm^2 , a part of whole illumination region $4 \times 8 \text{mm}^2$. The average film thickness is approximately 300nm , and is corresponding to 180 scales. The variations are ± 38 scales. From Fig.5 and taking into account of 20:1 attenuation of the intensity on the resist film, the profiler maps about $\pm 20 \text{mJ}/\text{cm}^2$ variation of the light intensity.

The Nomarski micrograph of Fig. 6(b) is corresponding to the same area of p-Si surface, obtained by 10 shots. The change of the intensity distribution at each shot supposed to be small owing to the homogenizer optics. The colours in the micrograph come from Rayleigh scattering by the roughness due to the bumps on the surface. The averaged height of the bumps is proportional to the grain size, and thus the colours represent the grain sizes; black at starting amorphous, pale green at small grains, green at $0.1\text{--}0.3 \mu\text{m}$, blue at $0.3\text{--}0.5 \mu\text{m}$, white at more than $0.5 \mu\text{m}$, and again black at microcrystalline. There is no one-to one correspondence between details in two pictures, because the relationship between fluence and the grain size is not similar to the relationship between colour and the grain size. However there are close resemblance between two figures. It should be also noticed that the resolution is limited by the measurement method and instrument. As the whole profile of the illumination region is mapped on the resist profiler, there are two possibilities to utilize the profile data; improvement of homogenizer optics by rather coarse resolution, and the analyses of local grain growth mechanisms by fine resolution.

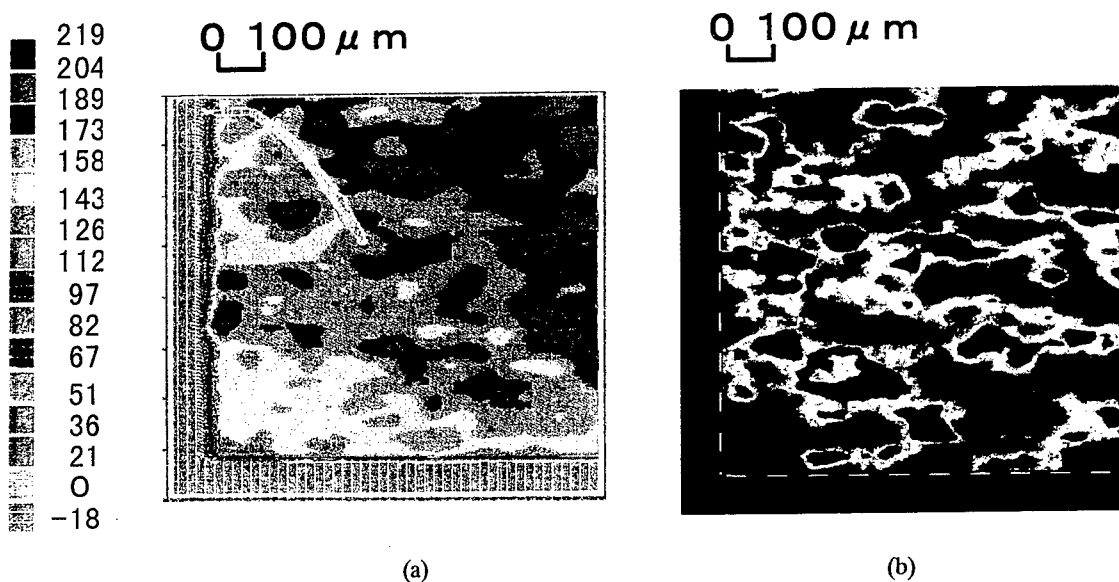


Fig. 6 Comparison between the profiler chart of the resist (a) and Nomarski micrograph of p-Si (b)

The base of the resist profiler is a gamma characteristics, which is the relationship between fluence and developed film thickness. The absolute resolution is defined as minimum thickness or volume removed by development for minimum light exposure (in the case of negative resist). Experimentally it is very difficult to define minimum light intensity, as the fluence of the excimer laser changes more than $\pm 10\%$ shot by shot. Besides, the profile is not always uniform due mainly to homogenizer optics. Each point on the gamma curve in Fig. 5 is an average determined from measurements of the thickness of ten one-shot profiles for each nominal fluence by the profiler (Wyko) at the same point. The minimum resolution is inferred from comparison among ten profiles. It is 3nm for $0.2\text{mJ}/\text{cm}^2$ at averaged total thickness 300nm for $15\text{mJ}/\text{cm}^2$. The rms roughness of the substrate surface is less than 0.15nm over $2\text{ }\mu\text{m}$, which is far less than minimum resolution of the resist. As stated previously monitoring light is reduced to 1:20. Accordingly at $300\text{mJ}/\text{cm}^2$ illumination to a sample, $\pm 2\text{mJ}/\text{cm}^2$ variation can be detected. The absorption coefficient of the resist is $2.2 \times 10^4\text{cm}^{-1}$ at 248nm. This value does not change appreciably with the concentration of the chromophor. The developed film thickness is 300nm in average, and upto the thickness from the substrate, the exponential decay curve of the intensity is well approximated to be linear. This means there is no truncation in the details of the profile. The result of higher resolution measurement by AFM is shown in Fig. 7. The speckle pattern is clearly recognized. The high spots in the speckle are about 10nm at most, that is, $10\text{mJ}/\text{cm}^2$. Although almost all the values are near to the resolution limit and not so accurate, there are intensity fluctuations with nearly half wave length period over whole illumination area.

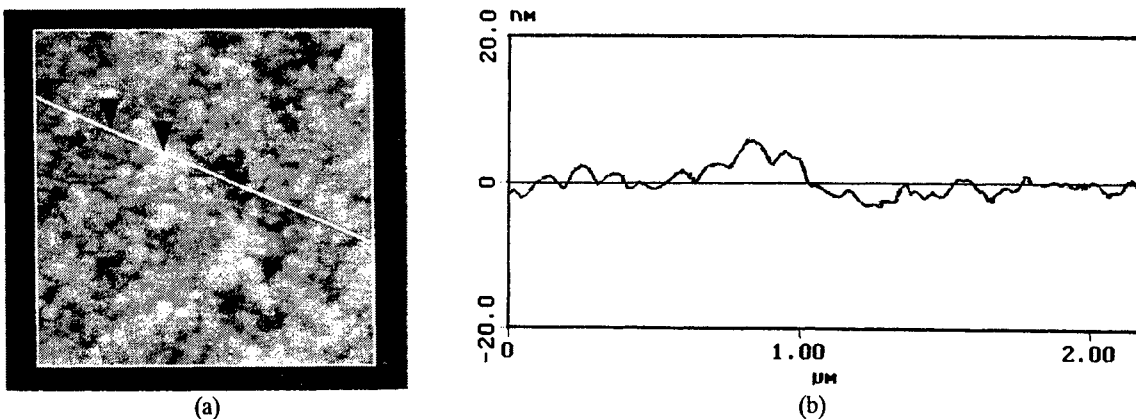


Fig. 7 AFM picture of the resist surface. (a) speckle patterns, (b) scanning chart

From Fig. 1 it is pointed out that the variation $10\text{mJ}/\text{cm}^2$ produces about two times differences of the grain size at $0.3\text{ }\mu\text{m}$ region. However SEM pictures show that the distribution of the grain size does not vary appreciably over $1\sim 2\text{ }\mu\text{m}$ area, although the speckle spacing are 1/10 of the region and the lateral grain growth is considered to start from $0.05\text{ }\mu\text{m}$. Such uniformity is enhanced when shot number is increased, and it is most prominent at $0.3\text{ }\mu\text{m}$ region. This suggest some factors other than fluence are equally essential for the grain growth. Multi-shot ELA is a process of repetition of melt and recrystallization. In the course of the repetition, smaller grains tend to disappear, as they are melted faster than the larger owing to the ratio of boundary area and volume. There is higher probability that a nucleation appears at the larger grain site. Repetition seems to multiply the probabilities. However intensity variation about $10\text{mJ}/\text{cm}^2$ over more than $10\text{ }\mu\text{m}$ area

is clearly observable as the change of the grain size. The larger distance variation is effectively an envelop of the intensity distribution averaged over $1\sim 2\ \mu\text{m}$ area. From observations of optical micrographs (Nomarski) of p-Si surface, it is reasonable to assume that the pattern of the averaged distribution is maintained during the crystallization period. The grain distribution is regarded to be preserved even during multi-shot illuminations. The localization of temperature distribution during crystallization period is prominently exhibited in the SEM picture in Fig. 8 of the region where area of the larger grains are adjacent to the microcrystalline region.

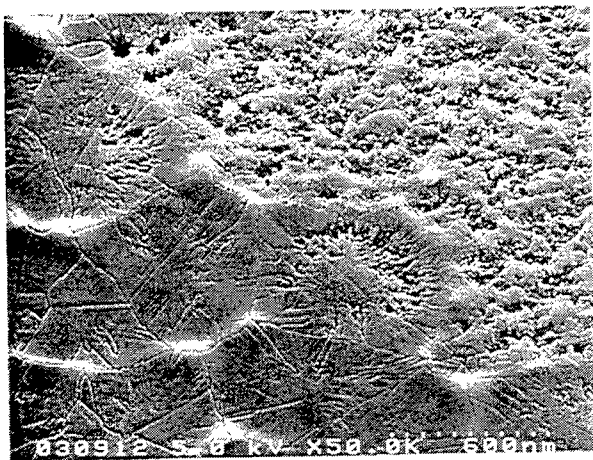


Fig. 8 SEM picture of the boundary between large grain region and microcrystalline region

Smearing out of light intensity fluctuation over $1\sim 2\ \mu\text{m}$ area is explained by thermal diffusion length $\sqrt{2Dt}$ in the liquid phase of Si film. D is thermal diffusion coefficient, and t is a full pulse duration. In the liquid phase, D is $0.07\ \text{cm}^2/\text{s}$ ⁶⁾, and the diffusion length is $0.8\ \mu\text{m}$ for 50 ns full pulse duration. It is inferred that the lateral growth is confined within the locally uniform temperature region. The duration staying in liquid phase is approximately proportional to the incident fluence. Accordingly the smearing area will be proportional to square root of the fluence. However the grain size increases much faster as shown in Fig. 1. It is evident that the large sized grain is resulted by lateral grain growth, and larger grain is obtained by faster lateral motion. According to the theory of the interface response function⁷⁾, there is a maximum at a certain supercooling. The supercooling in our experimental conditions always exists at the lower side of the maximum, as the higher fluence produces the larger grains as shown in Fig. 1. Over the maximum toward higher temperature, it does not result any reduction of the interface velocity but bulk nucleation producing microcrystalline. This may be a characteristic feature of the heterogeneous nucleation and thin film.

The bumps at the grains is another feature to be elucidated. It is an important phenomenon to understand the mechanisms of grain growth, and at the same time, it is very obstructive structure for TFT performances and is needed to be reduced. This structure suggests an upheaval of viscous liquid thrust between solid plates. This leads a simple model; a nucleus is created at the centre of locally uniform temperature region, and it grows initially vertically and next laterally. If there are such nuclei situated at equidistance and grow equally, then they collide side by side and at junction according to the growing crystallographic axis. The middle part of the grains stays liquid, as the latent heat is released. The exothermic process also prevent small grain growth according to the velocity of the interface.

5. CONCLUSION

The resist beam profiler can map whole illumination area with high resolution. The effective resolution is limited by the resolution power of measurement equipments. High resolution measurements reveal existence of speckle patterns with 0.1~0.15 μ m spacing. The fluctuation over 1~2 μ m area does not influence the grain growth. On the other hand, the undulation of temperature distribution over 10 μ m area obtained by averaging the small scale fluctuation maintains its distribution pattern during crystallization period, and thus it determines the grain sizes and the distribution. The localization of intensity envelop is on the one hand owing to the homogenizer optics which reduce spatial variations of the beam profile if it does not change substantially. On the other hand, it suggests that cooling speed and resulting nucleation is much higher than the lateral thermal diffusion time, as is pointed out by many investigations. Accordingly accurate design of the homogenizer optics and control of cooling process through the buffer layer and the substrate over 10 μ m area is essential to realize uniform grain distribution. The resist beam profiler gives quantitative data necessary for the purpose.

REFERENCES

1. T. Sameshima et al., IEEE EDL 7 (1986) 276 ; H. Kuriyama et al., Jpn. J. Appl. Phys. 31 (1992) 4550
H. Kuriyama et al., Jpn. J. Appl. Phys. 32 (1993) 6190
2. E.I. Givargizov, "Oriented Crystallization on Aborphous Substrates", Plenum Press, New York (1991)
H. Kuriyama et al., Jpn. J. Appl. Phys. 30 (1990) 3700 ; H. Kuriyama et al., MRS Symp. Proc. 321 (1993) 657
K. Shimizu et al., IEEE T-ED 40 (1993) 112 ; D.H. Choi et al., Jpn. J. Appl. Phys. 33 (1994) 70 ; R. Ishihara et al., Jpn. J. Appl. Phys. 34 (1995) 1759 ; R. Ishihara et al., Elect. Lett. 31 (1995) 1956 ; J.S. Im et al., MRS Bulletin vol 21 [3] (1996) 39 ; K. Ishikawa et al., Jpn. J. Appl. Phys. 37 (1998) 731
3. M.H. Brodsky, "Properties of Amorphous Silicon", Chapter 2 in "emis data review series #1", ed. by J.M.D. Thomas INSPEC (1985) ; R.A. Street, "Hydrogenated Amorphous Silicon", pp44 - 61, Cambridge Univ. Press (1991) ; E.A. Davis, J. non-Crystall. Solids, 198 - 200 (1996) 1 ; C.G. van de Walle, ibid. 227 - 230 (1998) 111
4. S.E. Clark and D.C. Emmony, Phys. Rev. B 40 (1989) 2031
5. T. Iwayanagi, et.al., IEEE Trans. Electron Devices, ED-28 (1976) 1306 ; T. Iwayanagi, et.al., J. Electrochem. Soc., 127 (1980) 2759
6. A. Goldsmith, "Handbook of Thermodynamic Properties of Solid Materials", MacMillan, New York (1961)
7. D. Turnbull, J. Phys. Chem. 66 (1962) 609 ; M.D. Kluge and J.R. Ray, Phys. Rev. B 39 (1989) 1738 ; S.R. Stiffler et al., Acta Metall. Mater. 40 (1992) 1617

Lattice Strain in Excimer Laser Crystallized Poly-Si Thin Films

Hiroshi Okumura^{*a}, Akio Tanikawa^b, Kenji Sera^a, Fujio Okumura^a

^aNEC Electronic Component Development Div., Sagamihara 229-1198, Japan

^bNEC Silicon Systems Res. Labs., Tsukuba 305-8501, Japan

ABSTRACT

The lattice strain in excimer laser crystallized polycrystalline Si (poly-Si) thin films reflects the grain growth induced by the laser irradiation. In this report, the measurement of the lattice strain is made by using the energy-dispersive grazing-incidence X-ray diffraction with synchrotron radiation. The excimer laser crystallized poly-Si thin films show tensile lattice strain in the directions parallel to the substrate surface. The {111} strain increases from 2.2×10^{-3} to 5.0×10^{-3} when the grain size increases from 40 to 200 nm. The strain is anisotropic between the {111} strain and the {220} strain in the layer near the substrate interface when the grain size is small. Carrier mobility in a thin film transistor tends to increase when the strain increases and the anisotropy decreases.

Keywords: polycrystalline silicon, excimer laser crystallization, lattice strain, energy dispersive grazing incidence diffraction, lateral grain growth

1. INTRODUCTION

Polycrystalline silicon (poly-Si) is a promising material for the active layer of thin film transistors (TFTs) to be used in liquid crystal displays¹⁻³ and contact type image sensors⁴⁻⁶ with integrated driving circuits on glass substrates. The excimer laser crystallizing method plays a key role in lowering the process temperature. The carrier mobility of excimer laser crystallized (ELC) poly-Si thin films is higher than that of as-deposited or solid phase crystallized poly-Si thin films, and this feature of the ELC poly-Si thin films comes from films' structure with less defects density. Lattice defects result from grain growth and relaxation of the total amount of internal energy, i.e. surface energy, interfacial energy, strain energy and so forth, therefore lattice defects, grain growth and lattice strain correlate to each other. The excimer laser crystallization process of a melt and regrowth process hardly achieves a thermal equilibration with extremely rapid and large heat hysteresis, so that the ELC poly-Si thin films contain less density of lattice defects, larger lattice stress⁷ and larger lattice strain. Moreover, the grain growth of the ELC poly-Si films strongly depends on the laser energy density changing the melting depth of the film,⁸⁻¹⁰ and the heat flow induced by the laser irradiation generates the distribution of lattice defects and lattice strain in the direction perpendicular to film surface. Therefore, it is worth investigating the lattice strain in the ELC poly-Si thin films to comprehend not only the laser-induced grain growth process but the electronic properties. In this experiment, we have carried out energy-dispersive grazing incidence diffraction with synchrotron-radiation white X-ray (SR-EDGID) measurement. The SR-EDGID method with wide energy-band SR is newly developed for crystallographic analysis of thin films less than 100 nm thick in a very short time.¹¹ In this paper, we report the laser-

* Correspondence: Email: hok@ecd.sgm.nec.co.jp; Telephone: +81 42 771 0984; Fax: +81 42 771 0826

energy-dependent and the thickness-dependent lattice strain change of the ELC poly-Si thin films.

2. EXPERIMENT

The ELC poly-Si thin films were fabricated by the room temperature irradiation of a KrF excimer laser on 75-nm-thick amorphous Si (a-Si) films deposited on glass substrates by using low-pressure chemical vapor deposition (LPCVD). A square laser beam $3 \times 15 \text{ mm}^2$ was focused on the Si surface through a beam homogenizer. The laser energy density (E) was varied from 300 to 550 mJ/cm^2 and the beam was shot 3 times. The films were observed by scanning electron microscopy (SEM) after Secco-etching treatment. As-deposited (AS) poly-Si and solid phase crystallized (SPC) poly-Si were also fabricated for comparison. The 110 nm thick AS samples were deposited by using LPCVD at 620 °C, and the SPC samples were annealed from the a-Si thin films described above at 600 °C.

The lattice strain (ϵ) of the samples was evaluated by the deviation of the X-ray energy at the SR-EDGID peak for the samples from that for powder Si reference, as equation (1),

$$\epsilon = (\epsilon_r + 1) E_r/E_s - 1, \quad (1)$$

where, E_s , E_r , and ϵ_r are the peak X-ray energy for the samples, the peak X-ray energy for the reference, and the lattice strain existed in the reference (-2.3×10^{-4}) which was determined by using the conventional X-ray diffractometry, respectively. Plus and minus signs on ϵ define tensile and compressive, respectively. Two dominant diffraction peaks from {111} and {220} were used to evaluate ϵ , and the accuracy of ϵ was evaluated to the exist of 5×10^{-4} by cyclic measurements. It should be noted that the glancing angle of the incidence white X-ray of the SR-EDGID was set at 0.5 degree at which total reflections could be ignored, and that the SR-EDGID patterns come from lattice planes perpendicular to the substrate surface. The obtained ϵ represents the average value through the whole sample thickness. For the thickness-dependent ϵ analysis, the samples were etched to 40 nm thick by $\text{HF}+\text{HNO}_3$ acid solution.

Planer TFTs were then fabricated at temperatures below 600 °C, using these poly-Si thin films as the active layer. A SiO_2 insulating film 40 nm thick was deposited by LPCVD at 400 °C. The source and drain regions were prepared by ion-doping method in the self-align process after fabricating a double-layered gate electrode of WSi_2 and doped (n^+) poly-Si. Post-hydrogenation was performed by hydrogen plasma.

3. RESULTS

3.1. Laser Energy Dependence of Lattice Strain

Figure 1 shows the SR-EDGID pattern for the excimer laser crystallized (ELC) poly-Si thin film irradiated at 500 mJ/cm^2 . The SR-EDGID peaks for the sample appear at lower energies than those of the powder Si reference as indicated by lines, and this reveals that the lattice strain is tensile in the planer directions. Figure 2 shows the laser energy dependence (E) of the {111} strain (ϵ_{111}) and the {220} strain (ϵ_{220}) evaluated by the {111} peak and the {220} peak, respectively. This figure also shows the data for as-deposited (AS) and solid phase crystallized (SPC) poly-Si thin films. The ELC poly-Si thin films contain much larger tensile strain as compared to the others, in this E range.

When E increases from 300 to 500 mJ/cm^2 , ϵ_{111} increases from 2.2×10^{-3} to 5.0×10^{-3} . Then ϵ_{111} turns to decrease to 4.6×10^{-3} with further increasing E to 550 mJ/cm^2 . ϵ_{220} shows the similar value to ϵ_{111} with the measurement accuracy

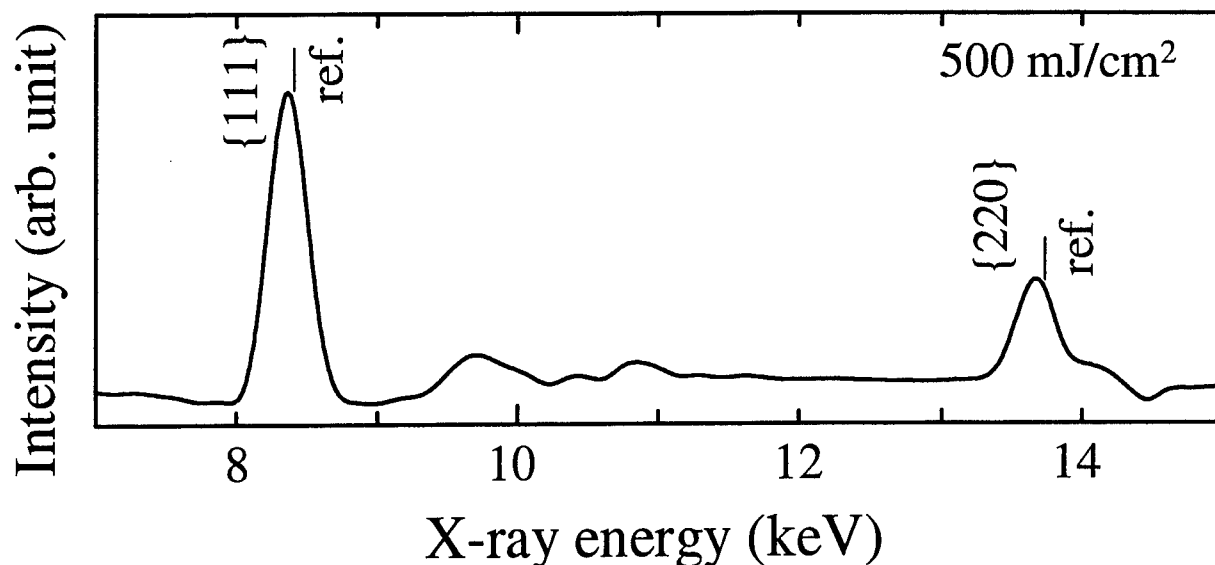


Fig. 1 SR-EDGID pattern for the ELC poly-Si thin film irradiated at 500 mJ/cm².

The peak positions for the ref. are also indicated by lines.

considered, and the similar E dependence with a maximum of 4.4×10^{-3} at 500 mJ/cm². Theoretically the evaluation of the thermal expansion coefficient should make the tensile lattice strain of 5.5×10^{-3} in the cooling process from the melting point of Si to a room temperature. The less amount of ϵ indicates the relaxation by the lattice defects and the lower maximum temperature.

The ϵ change observed here indicates that the films' structure changes depending on E . Figure 3 shows the scanning electron micrographs with varied E for the ELC poly-Si thin films. The average grain size (d) increases first from 40 to 200 nm when E increases from 300 to 500 mJ/cm². The laterally grown columnar grains with d larger the film thickness are observed in the energies over 400 mJ/cm². However, the d decreases to 20 nm at 550 mJ/cm², which is similar with the ϵ - E curve. This behavior has been reported for the ELC poly-Si thin films as the high energy micro-crystallization or amorphization.⁸⁻¹⁰ The degradation of grains has been considered to change in the nucleation process from the inhomogeneous nucleation at the substrate interface to the

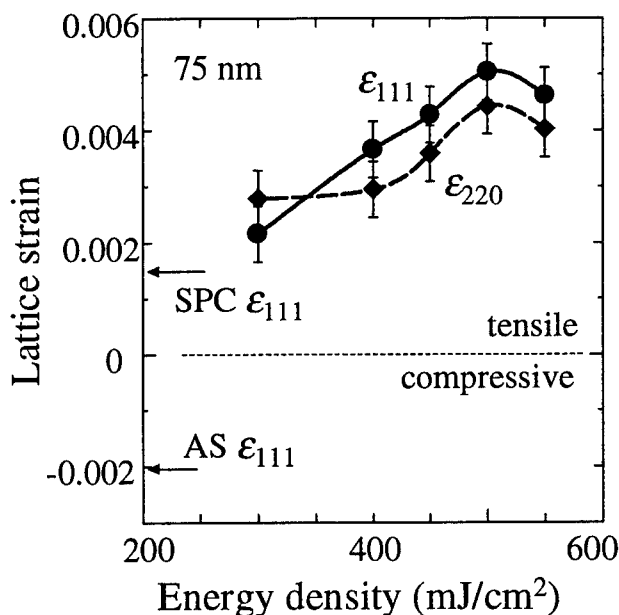


Fig. 2 Laser energy density dependence of the {111} strain (ϵ_{111}) and the {220} strain (ϵ_{220}).

AS and SPC represent as-depo. and solid phase crystallized poly-Si thin films, respectively.

homogeneous nucleation, depending the melting depth. The relation between ϵ and d is summarized as shown in fig. 4. Both ϵ data tend to increase when d increases, except for those of the micro-crystallization poly-Si indicated by open symbols in fig. 4. The data for the micro-crystallization poly-Si locate higher value for its d .

3.2. Thickness Dependence of Lattice Strain

To investigate the ϵ in the lower layer of the films, the samples were etched to 40 nm thick and measured the SR-EDGID patterns. Figure 5 shows the ϵ - E curves for the etched films. In the case of the smaller d at 300 and 550 mJ/cm², the difference between ϵ_{111} and ϵ_{220} becomes 1.3×10^{-3} and 1.1×10^{-3} , respectively, being larger than the measurement accuracy. From the data of Figs. 2 and 5, all ϵ data except ϵ_{111} at 300 mJ/cm² decrease when the film thickness (t) decreases. Figure 6 shows the ϵ_{111} - t change.

The ϵ change with t indicates the ϵ distribution during the vertical grain growth (solidification), and the increase or the decrease with decreasing t reveals the existence of smaller or larger strain, respectively, in the etched region. The thin films consisted of granular grains with d smaller than t involve the grain boundary traversing the vertical grain boundary. The traversing boundary causes discontinuity in the ϵ - t change. Moreover, the effect of the substrate should be not negligible as compared with free solidification. Therefore, ϵ in the lower part of thin films behaves differently depending on their d . In this result, the anisotropy between ϵ_{111} and ϵ_{220} characterizes the ELC poly-Si thin films of small d .

3.3. Lattice Strain and TFT Mobility

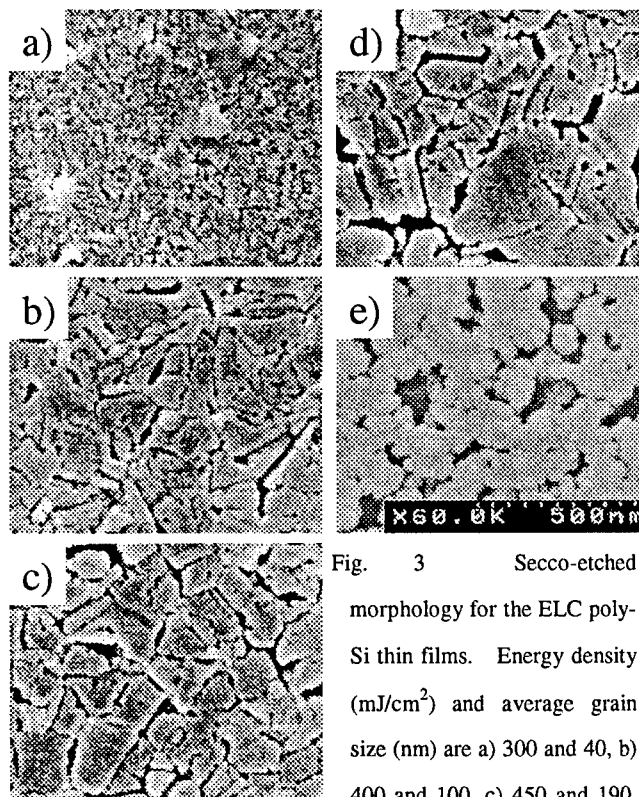


Fig. 3 Secco-etched morphology for the ELC poly-Si thin films. Energy density (mJ/cm²) and average grain size (nm) are a) 300 and 40, b) 400 and 100, c) 450 and 190, d) 500 and 200, and e) 550 and 20, respectively.

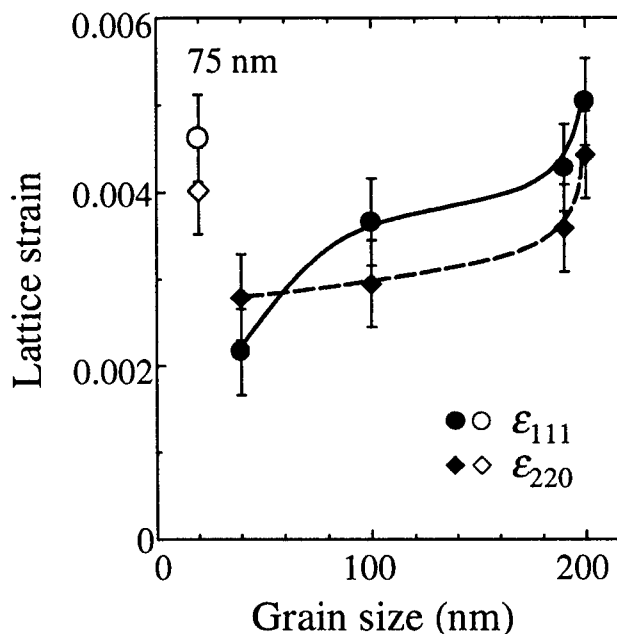


Fig. 4 Grain size dependence of ϵ_{111} and ϵ_{220} . Open symbols are for the micro-crystallization at 550 mJ/cm².

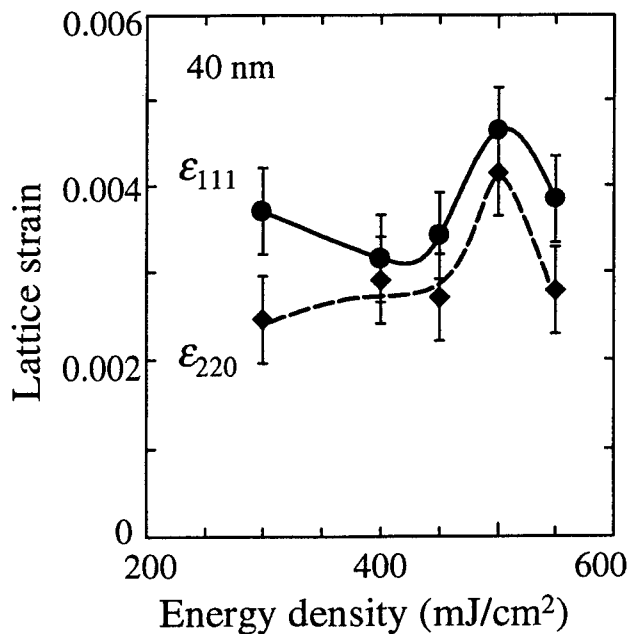


Fig. 5 Energy density dependence of ϵ_{111} and ϵ_{220} for the etched films to 40 nm.

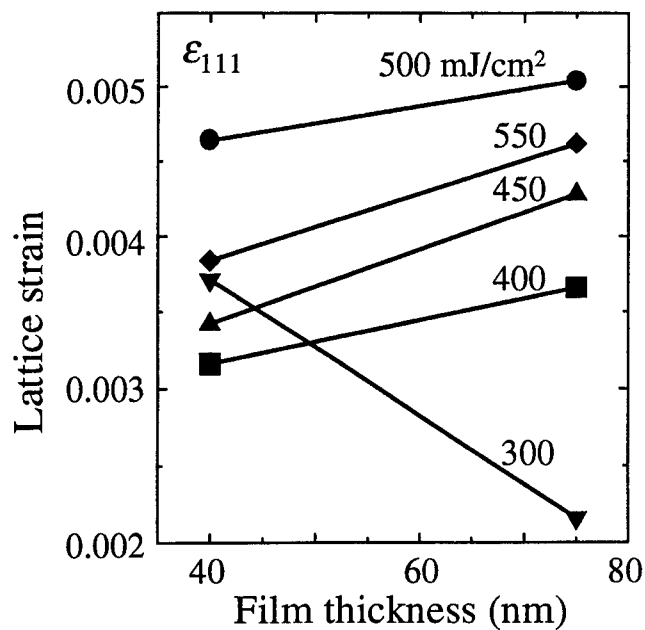


Fig. 6 Film thickness dependence of ϵ_{111} .

Electronic property of these ELC poly-Si thin films was evaluated as a carrier mobility of n-channel TFTs. Figure 7 shows the relation between ϵ_{111} and n-ch. TFT mobility (μ). The μ shows a maximum value of 149 cm²/Vs at E of 500 mJ/cm². The ϵ_{111} - μ change at 75 nm shows good linearity except the data for the micro-crystallization poly-Si at 550 mJ/cm², shown by the open symbols. The TFT characteristic reflects lattice defects in the whole channel region and the active layer/the insulator interface trap density. Therefore, μ is well correlated with ϵ_{111} at 75 nm rather than that at 40 nm.

4. DISCUSSION

The ELC poly-Si thin films change films' structure from granular grains, through columnar grains, to granular grains again when the laser energy increases, as shown in fig. 3. The structural change indicates the change in the maximum temperature and the temperature distribution in vertical direction. Figure 8 summarizes schematically the

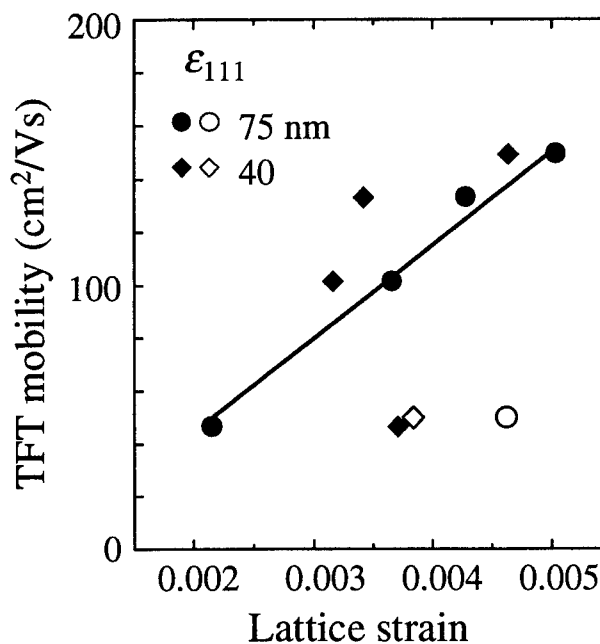


Fig. 7 ϵ_{111} dependence of TFT mobility. Open symbols are for the micro-crystallization at 550 mJ/cm².

correlation among the films' structure, the grain growth and the lattice strain.

In the case of the lower energy granular structure at 300 mJ/cm^2 , the lattice strain shows complex behavior. It is anisotropic at 40 nm caused by increasing ϵ_{111} when the film thickness decreases. The lattice strain should decrease when the film thickness decreases, in consideration of the heat flow induced by the laser irradiation. Therefore, this complex behavior comes from the effect of the substrate, which suggests the difference in ϵ between the grains located in the upper and the lower layer with the different nucleation sites.

The higher energy granular structure at 550 mJ/cm^2 also shows the anisotropic lattice strain at 40 nm. However, the lattice strain at 75 nm is large for its grain size as compared to that of the lower energy granular structure. This suggests the higher maximum temperature suppressing the inhomogeneous nucleation at the substrate interface and too rapid crystallization through large supercooling⁹ to form the additional defects relaxing strain. From the viewpoint of the electronic property of TFTs, the carrier mobility decreases when the anisotropy increases.

The columnar structure at the energy range from 400 to 500 mJ/cm^2 shows the isotropic lattice strain, and the lattice strain at 75 nm depends on the grain size well. The low nucleation density and the high lateral growth rate suppress the anisotropic effect of the substrate. This growth feature of the columnar grains results in the high carrier mobility in TFTs.

The vertical distribution of the lattice strain of the columnar structure is rather uniform, suggesting the continuous grain growth from the nucleation at the substrate interface. The lateral grain growth has been considered to proceed prominently at the upper layer as the vertical growth. This feature is thought to bring about the enhanced tensile lattice strain in the upper layer.

The SPC poly-Si thin films contain the smaller tensile lattice strain than that of the ELC poly-Si thin films, caused by the lower crystallization temperature and the higher defect density with an anisotropic dendritic structure. The SPC proceeds

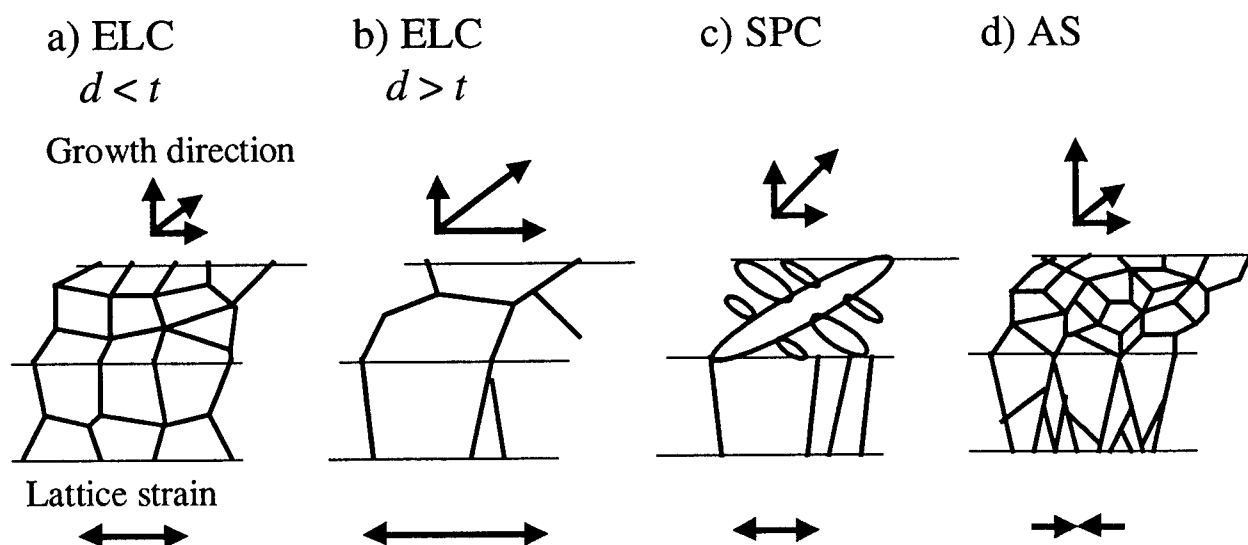


Fig. 8 Schematic illustrations for the correlation among the films' structure, the grain growth and the lattice strain for various poly-Si thin films.

laterally by utilizing the twin planes,^{12,13} and the lateral motion of atoms is thought to generate a part of tension. It is another interest for comprehending the SPC process that the planer distribution of the lattice strain can be found among the different-order dendritic arms.

The AS poly-Si thin films contain the compressive lattice strain. This fact suggests that the crystallization process correlates the production of the lattice strain. The AS poly-Si thin films were formed by the deposition of the vertical grain growth, contrary to the ELC and SPC poly-Si thin films formed by the lateral grain growth. The deposition seems to make the vertical lattice elongation by high defect density and by changing the oriented structure along the growth direction.¹¹

5. SUMMARY

We have measured the lattice strain in the poly-Si thin films by using the energy-dispersive grazing-incidence X-ray diffraction with synchrotron radiation. The excimer laser crystallized poly-Si thin films show the large tensile lattice strain in the directions parallel to the substrate surface. On the other hand, the solid phase crystallization poly-Si thin films show the small tensile lattice strain by the lower crystallization temperature and the higher defect density of the dendritic structure, and the as-deposited poly-Si thin films show the compressive lattice strain by the different crystallization process of the deposition.

The lattice strain for the excimer laser crystallized poly-Si thin films increases when the grain size increases depending on the laser energy density. The {111} strain reaches to the maximum value of 5.0×10^{-3} around the value evaluated by the thermal expansion coefficient. The lattice strain is anisotropic between the {111} strain and the {220} strain in the layer near the substrate interface, when the grain size is smaller than the film thickness. Carrier mobility in a thin film transistor increases when the lattice strain increases and the anisotropy decreases by the increased lateral grain growth.

ACKNOWLEDGMENTS

The authors wish to thank Messrs. K. Okada and I. Sasaki for their support and encouragement.

REFERENCES

1. S. Inoue, M. Matsuo, K. Kitawada, S. Takenaka, S. Higashi, T. Ozawa, Y. Matsueda, T. Nakazawa, and H. Ohshima, "425 °C poly-Si TFT technology and its application to large-size LCDs and Integrated digital data drivers," *Asia Display '95 Digest*, pp. 339-442, 1995.
2. F. Okumura, H. Asada, K. Sera, K. Hirata, K. Kurakagi, Y. Hirai, S. Kaneko, K. Hamada, N. Kodama, A. Mineji, S. Saito, K. Ikeda, K. Miyakoshi, and M. Imajo, "A 76-mm (3-in.) driver-integrated poly-Si TFT-LCD light valve," *SID '94 Digest*, pp. 79-82, 1994.
3. S.D. Brotherton "Polycrystalline silicon thin film transistors," *Semicond. Sci. Technol.* **10**, pp. 721-738, 1995.
4. S. Morozumi, H. Kurihara, T. Takeshita, H. Oka, and K. Hasegawa, "Completely integrated contact-type linear image sensor," *IEEE Trans. Electron Devices* **ED-32**, pp. 1546-1550, 1985.
5. K. Sera, H. Asada, F. Okumura, H. Tanabe, K. Nakamura, H. Sekine, I. Fujieda, S. Tsujimura, and S. Kaneko, "Integrated contact-type linear image sensor with excimer laser annealed poly-Si TFT driver," *SID '93 Digest*, pp. 356-

359, 1993.

6. H. Sekine, H. Asada, I. Fujieda, K. Sera, H. Tanabe, F. Okumura, and S. Kaneko, "A high-speed linear-image sensor with integrated poly-Si TFT drivers," *SID '95 Digest*, pp. 315-318, 1995.
7. H. Okumura, H. Tanabe, K. Sera, and F. Okumura, "Residual stress in excimer laser annealed poly-Si thin films," *Extended Abstracts (41st Spring meeting, 1994); Jpn Soc. Appl. Phys. and Related Soc.*, pp. 749, 1994.
8. J.S. Im, and R.S. Sposili, "Crystalline Si films for integrated active-matrix liquid-crystal displays," *MRS Bulletin* **21**, pp. 39-48, 1996.
9. J.S. Im, H.J. Kim, and M.O. Thompson, "Phase transformation mechanisms involved in excimer laser crystallization of amorphous silicon films," *Appl. Phys. Lett.* **63**, pp. 1969-1971, 1993.
10. H. Okumura, H. Tanabe, and F. Okumura, "Effect of grain growth process on the characteristics for the excimer laser crystallized poly-Si thin film transistor," *Mat. Res. Soc. Symp. Proc.* **403**, pp.315-320, 1996.
11. A. Tanikawa, and K. Akimoto, "Energy dispersive grazing incidence diffraction with synchrotron radiation white X-rays of very thin polycrystalline silicon films," *Jpn. J. Appl. Phys.* **36**, pp. 5759-5763, 1997.
12. T. Noma, T. Yonehara, and H. Kumomi, "Crystal forms by solid-state recrystallization of amorphous Si films on SiO₂," *Appl. Phys. Lett.* **59**, pp. 653-655, 1991.
13. D. Girginoudi, S. Girginoudi, A. Thanailakis, N. Georgoulas, J. Stoemenos, and J. Antonopoulos, "Stability of structural defects of polycrystalline silicon grown by rapid thermal annealing of amorphous silicon films," *Thin Solid Films* **268**, pp. 1-4, 1995.

SESSION 7

Laser Microfabrication and Micromachining

Laser Direct Writing of circuit elements and sensors

A. Piqué^{a*}, D.B. Chrisey^a, R.C.Y. Auyeung^b, S. Lakeou^c, R. Chung^d, R.A. McGill^a,
P.K. Wu^e, M. Duignan^f, J. Fitz-Gerald^a, and H. D. Wu^b

^aNaval Research Laboratory, Washington, DC 20375

^bSFA, Inc. Largo, MD 20774

^cUniv. of the District of Columbia, Washington, DC 20008

^dGeo-Centers, Inc., Ft. Washington, MD 20744

^eSouthern Oregon Univ., Ashland, OR 97520

^fPotomac Photonics, Inc, Lanham, MD 20706

ABSTRACT

A novel approach for maskless deposition of numerous materials has been developed at the Naval Research Laboratory. This technique evolved from the combination of Laser Induced Forward Transfer (LIFT) and Matrix Assisted Pulsed Laser Evaporation (MAPLE), and utilizes a computer controlled laser micromachining system. The resulting process is called MAPLE-DW for MAPLE Direct Write. MAPLE-DW can be used for the rapid fabrication of circuits and their components without the use of masks. Using MAPLE-DW, a wide variety of materials have been transferred over different types of substrates such as glass, alumina, plastics, and various types of circuit boards. Materials such as metals, dielectrics, ferrites, polymers and composites have been successfully deposited without any loss in functionality. Using a computer controlled stage, the above mentioned materials were deposited at room temperature over various substrates independent of their surface morphology, with sub-10 μ m resolution. In addition, multilayer structures comprising of different types of materials were demonstrated by this technique. These multilayer structures form the basis of prototype thin film electronic devices such as resistors, capacitors, cross-over lines, inductors, etc. An overview of the results obtained using MAPLE-DW as well as examples of several devices made using this technique is presented.

Keywords: Direct Write, Rapid Prototyping, Laser Induced Forward Transfer, Matrix Assisted Pulsed Laser Evaporation, MAPLE Direct Write

1. INTRODUCTION

The ever increasing role played by electronic systems in our everyday life shows no signs of slowing down. However, the demand for new products has placed an enormous emphasis towards miniaturization and increased functionality. These trends call for the ability to produce electronic assemblies with reduced weight, volume and cost as well as the rapid fabrication of prototypes for testing new designs and architectures. Considerable progress has been achieved with the use of surface mounted electronic components. This progress, however, still relies on the old strategy of first designing, then patterning, and finally mounting each of the system components on a circuit board. Any changes to the design usually require a start over from the patterning phase. In order to completely sidestep the above described process, a totally new approach is needed. One such approach would be to employ rapid prototyping techniques. The application of rapid prototyping processes to the fabrication of electronic assemblies would make it possible to directly write over any surface all the elements and components called for in the circuit design. Moreover, the time that will be saved would have a great impact in reducing the long delay between concept, design and production.

* Correspondence: Email: pique@nrl.navy.mil; Telephone: (202) 767 5653; Fax: (202) 767 5301

Rapid Prototyping (RP) techniques have offered some of these advantages for the manufacture of mechanical components for some time, where it is now possible to generate an actual 3-dimensional "working part" from a CAD drawing using CAM tools. The development of RP techniques for the fabrication of electronic devices is only recent. They offer the capability to deposit or pattern the different types of materials that make an electronic device without the use of masks or patterns, and as such they are known as direct write processes. Direct write technologies do not compete with photolithography for size and scale, but rather complement it for specific applications requiring rapid turnaround and/or pattern iteration, conformal patterning, or for modeling difficult circuits. Current technologies are either subtractive, i.e. they remove material from the part or additive, i.e. material is added instead. Examples of direct write technologies for fabricating or modifying metallic interconnects and/or other passive elements include laser trimming, ink jet printing, laser chemical vapor deposition (LCVD), Micropen[®] and laser engineered nano-shaping (LENS). However, none of these techniques is yet capable of operating in air and at room temperature while maintaining sub-10 μm resolution as well as being compatible with the broad classes of materials required for electronic assemblies and not requiring *ex situ* processing. In addition, none of these techniques is capable of operating in both additive and subtractive fashion.

By combining some of the major positive advantages of laser induced forward transfer (LIFT) and matrix assisted pulsed laser evaporation (MAPLE), a novel laser driven direct write technique has been developed. This technique has been called MAPLE Direct Write (MAPLE-DW). This paper will outline the approach to the MAPLE-DW process, and some of its advantages, such as the ability to perform *in situ* laser micromachining, surface pretreatment and annealing. In addition, details on the fabrication of gold interconnect lines and nichrome thin film resistors using LIFT will be provided. Finally, examples of ferroelectric single layer capacitors as well as a ferrite core inductor fabricated using the newly developed MAPLE-DW technique will be shown.

2. BACKGROUND

2.1. LIFT

Over the past decade, a several direct write techniques based on laser-induced processes have been developed for depositing electronic materials for a variety of applications. Among these techniques, laser induced forward transfer or LIFT has shown the ability for direct writing of metals for interconnects and mask repair and also dielectric materials such as simple metal oxides. The LIFT process utilizes the focused beam of a pulsed laser to remove a thin predeposited film from a laser transparent substrate, called the ribbon. The removed material is then redeposited over a second substrate placed in close proximity ($\approx 25 \mu\text{m}$) to the ribbon. The area coated per laser pulse depends on the size of the laser spot striking the ribbon as well as the gap between both substrates. LIFT was first demonstrated using metals such as Cu and Ag over substrates such as silicon and fused silica utilizing excimer or Nd:YAG lasers^{1,2}.

There are several experimental requirements for LIFT to produce useful patterns including: 1) the laser fluence should exceed the threshold fluence for removing the thin film from the transparent support, 2) the target thin film should not be too thick i.e., less than a few 1000 Å, 3) the target film should be in close contact to the substrate, and 4) the absorption of the target film should be high. Operating outside these regime results in problems with morphology, spatial resolution, and adherence of the transferred patterns. Repetitive transfer of material can control the film thickness deposited on the substrate. Laser induced modification of the transferred material can occur through the transparent substrate after deposition. Overall, LIFT is a simple and powerful technique that can be used on a wide variety of target films.

2.2. MAPLE

A new vacuum deposition technique, known as Matrix Assisted Pulsed Laser Deposition, or MAPLE³ has been developed at NRL for depositing thin and uniform layers of chemoselective polymers^{4,5,6} as well as other organic materials, such as carbohydrates⁷. This technique is a variation of the conventional Pulsed Laser Evaporation process in that it provides a more gentle mechanism for transferring complex organic molecules from the solid to their vapor phase. In MAPLE, a matrix consisting of a frozen solution of the organic compound dissolved in a relatively volatile solvent is used as the laser target. When the laser strikes the surface of the target, it causes the rapid vaporization of the solvent molecules. Part of the thermal energy acquired by the solvent is transferred to the organic molecules. When these molecules become exposed to the gas-target interface, they are transported into the gas phase with sufficient kinetic energy to be desorbed from the target surface without being denatured in the process. A film will be formed on a substrate placed opposite to the target, while the solvent is pumped away.

2.3. MAPLE Direct Write

The MAPLE-DW⁸ process combines several of the advantages of LIFT with MAPLE in order to produce a novel laser driven direct write technique capable of transferring all kinds of materials such as metals, ceramics and polymers. The MDW process has been used successfully to deposit numerous types of materials in air and at room temperature. The resolution with which these materials have been deposited is of the order of $10\mu\text{m}$ over a variety of substrates such as silicon, fused silica, polyimide and several types of circuit board materials. Because the MAPLE-DW process uses a highly focused laser beam, it can easily be utilized for micromachining, drilling and trimming applications, by simply removing the ribbon from the laser path. Thus MAPLE-DW is both an additive as well as subtractive direct write process.

The key to the MAPLE-DW process is the development of a suitable matrix containing the material to be transferred. This matrix is then used to form a very uniform coating on the surface of a transparent substrate, i.e. the ribbon. The matrix is chosen so it absorbs strongly the laser wavelength being used. Laser fluences below the ablation threshold of the matrix are used. The purpose of the matrix is to hold the material in place until heating from the laser pulse causes the matrix to decompose resulting on the material being ejected from the ribbon and transferred to the nearby substrate. Because the laser fluences employed are lower than the ablation thresholds of the materials being transferred, no decomposition ever takes place, so the functionality of the transferred material is never affected. Similarly to LIFT, MAPLE-DW requires that the ribbon be held in close proximity to the substrate. In MAPLE-DW, the area coated per laser pulse also depends on the size of the laser spot striking the ribbon as well as the gap between the ribbon and the substrate. Figure 1 shows a simple schematic diagram of a MAPLE-DW system.

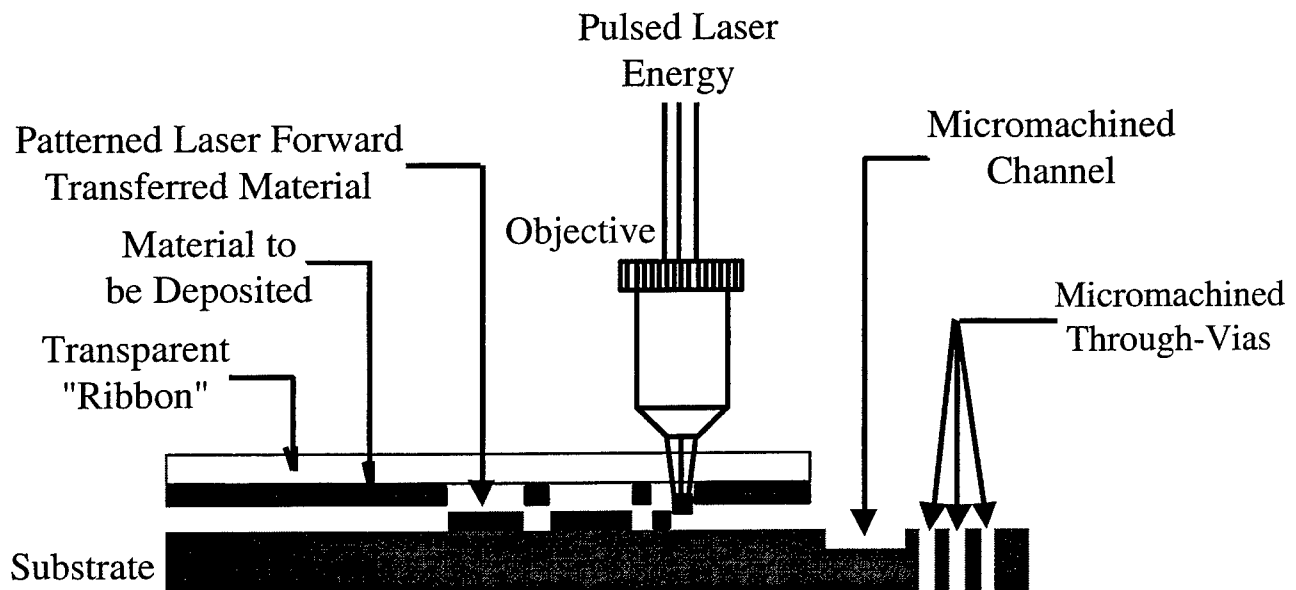


Figure 1. Schematic diagram showing the basic elements of a MAPLE-DW system.

3. RESULTS AND DISCUSSION

Fused silica quartz discs 5.0 cm dia. of various thickness were used as ribbon supports. These discs were coated by e-beam evaporation with 150 nm thick layers of gold for the LIFT of conducting lines and with 150 nm thick layers of nichrome for the LIFT of the resistors. For the MAPLE-DW experiments, a matrix containing the materials to be transferred was used to coat the discs. Various substrates were used for the transfer experiments including silicon, glass, polyimide and various types of circuit boards such as FR-4 and Rogers RO4003. In all the transfer experiments a 25 micron spacer was used to separate the coated side of the ribbons from the substrates. Both the substrate and ribbons were held in place using a vacuum chuck over an X-Y translation stage. The output from an excimer laser operating with a KrF mixture (248 nm, 10 ns pulse) was directed through a circular aperture and then through a 10x UV grade objective. By changing the aperture size, beam spots from 8 to 50 microns were generated. The laser fluence was estimated by averaging the total energy of the incident beam over the irradiated area.

A simple test pattern containing examples of passive circuit elements such as metal lines for interconnects, single layer capacitors, coplanar resistors and inductors with a rectangular cross section core was developed for testing purposes. The test pattern was prepared in the form of a CAD file which was then translated into machine code using a software package developed by Potomac Photonics, Inc². The machine code routines were then used to control the substrate position as well as the laser firing during the fabrication of each of the structures described on this work. These routines contained information about the laser spot size in use, the relative shift required between laser pulses, as well as the required overlap between layers. Figure 2 shows the layout that was used.

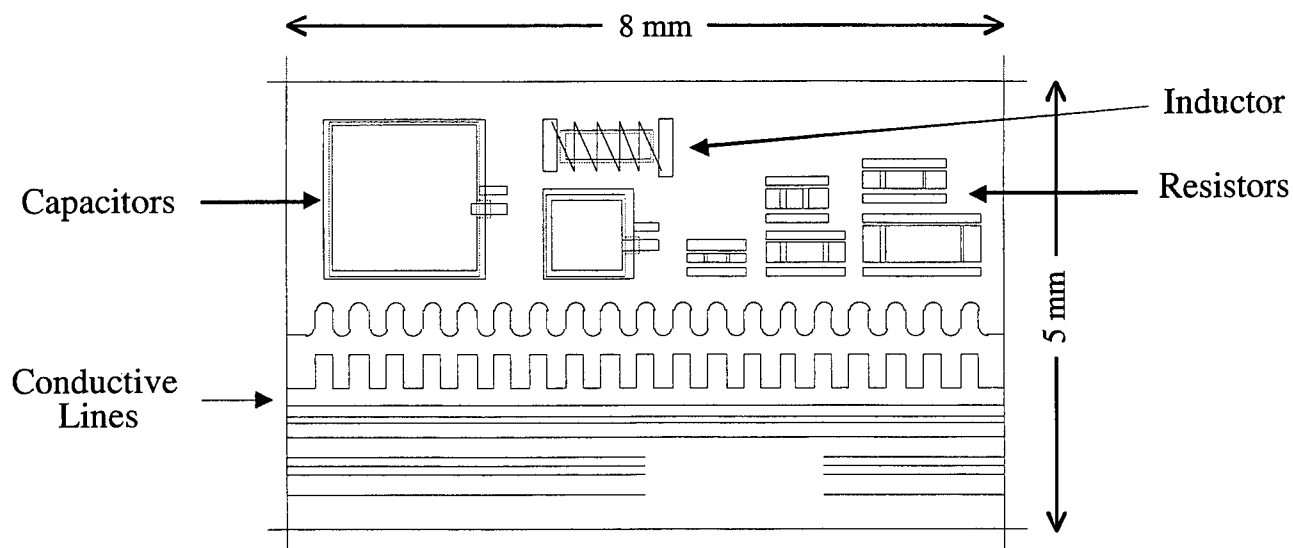


Figure 2. CAD design pattern comprising of typical circuit elements used for evaluating the MAPLE-DW process.

3.1. Conductive lines

Using the gold coated ribbons, Au conducting lines were deposited following the patterns indicated in Figure 2. A 25 micron laser spot size was selected. It was found that in order to improve the morphology of the transferred gold it was necessary to operate at laser fluences only slightly above the ablation threshold of the gold films. At higher fluences, any part of the laser pulse which is not absorbed by the Au layer on the ribbon can interact with the gold already transferred over the substrate and ablate it. Furthermore, multiple passes were required in order to build the gold lines to the desired

thickness of 10 microns. The overlap between those passes also had a marked effect on the morphology of the final line. Figure 3 shows SEM images comparing two gold lines made by LIFT. In the first one, neither the laser fluence nor the overlap between passes had been optimized. The second line clearly shows the improvement achieved after optimization. The best results were obtained for laser fluences between 550 and 600 mJ/cm² and 12.5 μm overlap between passes. Once the entire pattern of interconnect lines from Figure 2 was completed, any debris which might have accumulated on the sides of the lines during the transfer was removed by rastering the laser along the edges of the lines using the same 25 μm spot with the ribbon removed. Microscope images of the resulting conductive gold lines are shown on Figure 4. The surface roughness of the lines reflect largely the underlying roughness of the substrate on which they were transferred. The average conductivity of these lines was measured to be $7.5 \times 10^{-7} \Omega\text{m}$ at room temperature which is about 30 times higher than that of bulk Au ($2.4 \times 10^{-8} \Omega\text{m}$).

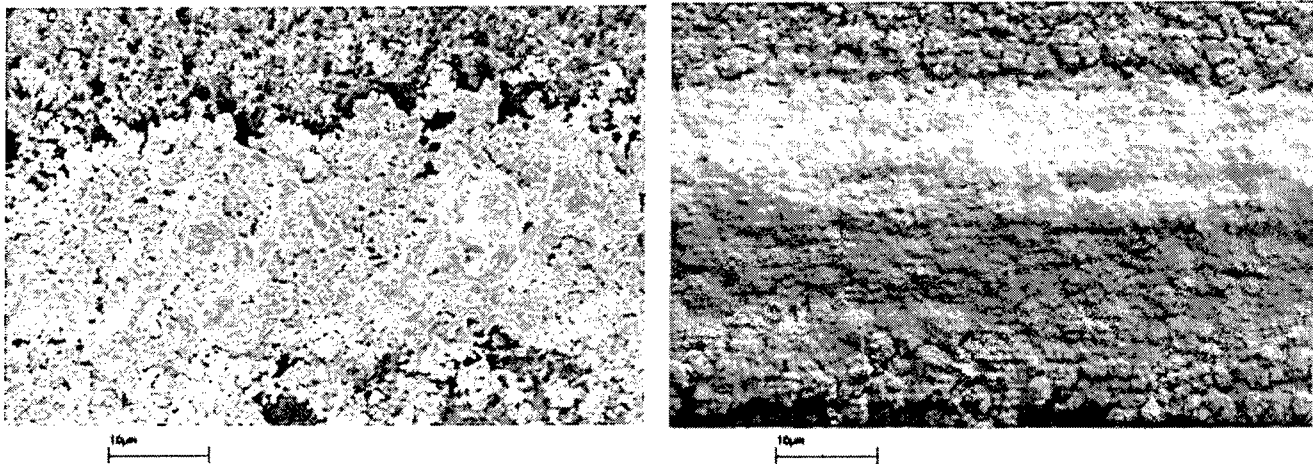


Figure 3. SEM images showing the effect of varying the fluence and the overlap between passes in the fabrication of Au conducting lines. The fluence was too high and the overlap did not provide good uniformity for the line shown in the left image. The right image shows a line made after both these parameters had been optimized. The scale bar indicates 10 μm.

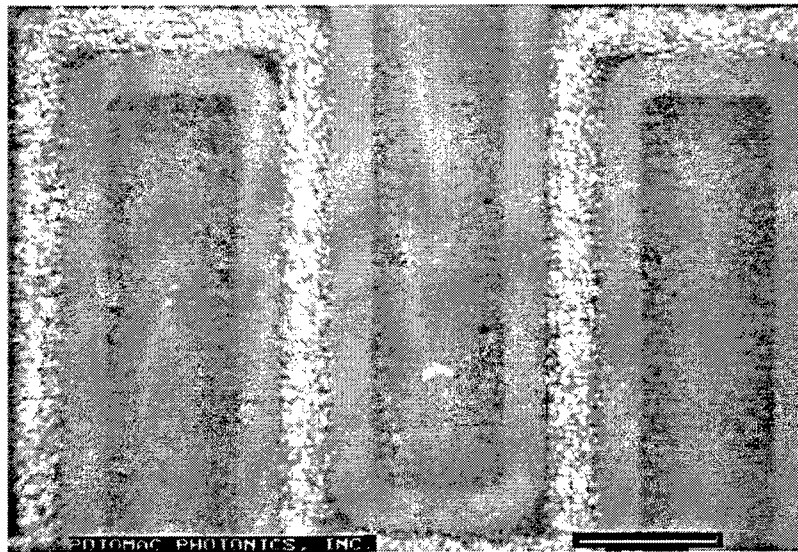


Figure 4. Au lines deposited by LIFT on RO4003 circuit board using the tests pattern of Fig. 2. The Au linewidth is approximately 30 μm. A final laser trimming pass was performed along both sides of the line. The scale bar indicates 125 μm.

3.2. Coplanar Resistors

The 5 coplanar resistors shown in Figure 2 were made by using nichrome ribbons. A $25\text{ }\mu\text{m}$ laser spot was used at a fluence of 1.5 J/cm^2 to generate the rectangular resistor pads. The overlap between successive passes was optimized in order to improve the uniformity of the nichrome structures. The thickness of the nichrome was about $10\text{ }\mu\text{m}$. The measured resistances ranged from 65 to $190\text{ }\Omega$ and they scaled with respect to cross section and length as expected. The resistivity of the transferred nichrome was considerably larger than that of bulk and is likely due to the high degree of porosity present in the transferred nichrome as well as oxidation of the alloy during transfer. Figure 5 shows a micrograph of the resistors.

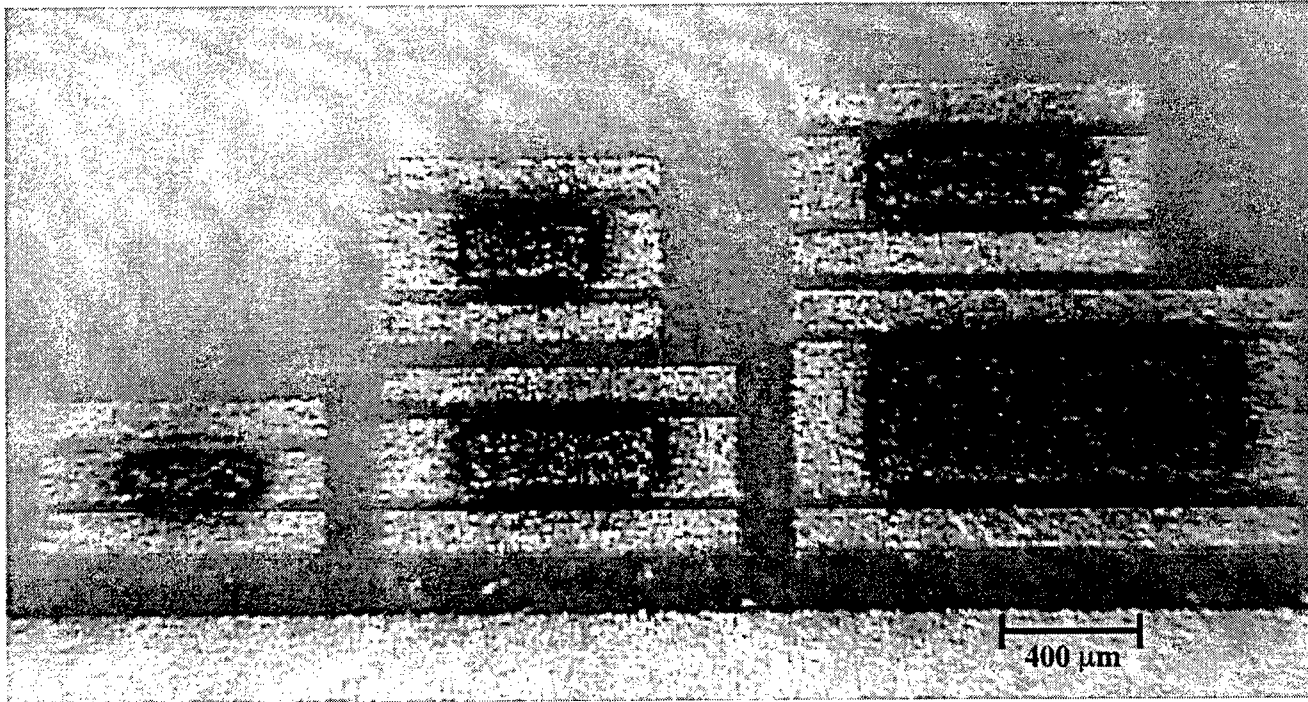


Figure 5. Various size nichrome coplanar resistors fabricated by LIFT.

3.3. Capacitors and Inductors

For the fabrication of the capacitors and inductor a hybrid approach was used. First, a $3\text{ }\mu\text{m}$ thick gold layer was e-beam deposited over bare Rogers RO4003, a hydrocarbon ceramic composite circuit board used for RF applications. The bottom electrodes were then patterned with the laser. Using a $25\text{ }\mu\text{m}$ laser spot and a fluence of 3 J/cm^2 the gold was ablated in order to generate the bottom electrode patterns shown in Figure 2. Then a ferroelectric layer consisting of BaTiO_3 (BTO) in the case of the capacitors or a ferrite layer consisting of $\text{Y}_3\text{Fe}_5\text{O}_{12}$ (YIG) in the case of the inductor was deposited by MAPLE-DW. Finally, the top Au electrodes were deposited by LIFT using the same conditions employed for making the conduction lines. Figure 6 illustrates the above steps schematically.

For the capacitors, a $25\text{ }\mu\text{m}$ laser spot at a fluence of 400 mJ/cm^2 was used to fabricate 20 to $30\text{ }\mu\text{m}$ thick BTO layers. For the inductor, similar parameters were used to fabricate a $20\text{ }\mu\text{m}$ thick YIG core. In both cases the morphology and thickness of the BTO and YIG layers was quite uniform, and the surface roughness variations observed with a profilometer were due primarily to the imperfections of the underlying substrate. Figure 7 shows the profilometer scan from one of the capacitors made.

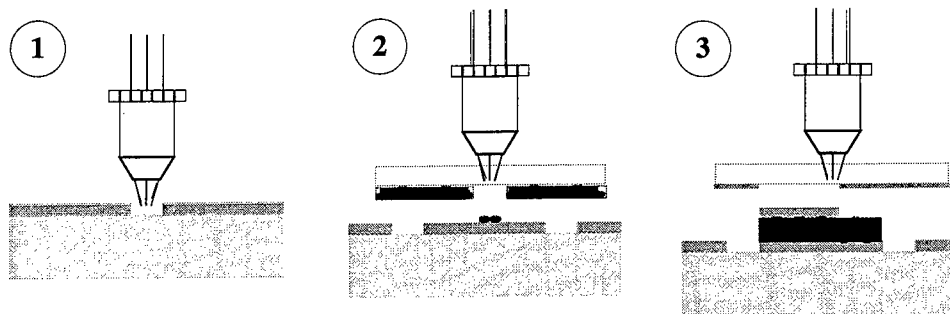


Figure 6. Schematic showing the fabrication steps for the parallel plate capacitors. (1) Patterning of the bottom Au electrode, (2) MAPLE-DW of the dielectric layer, (3) LIFT of top Au electrode.

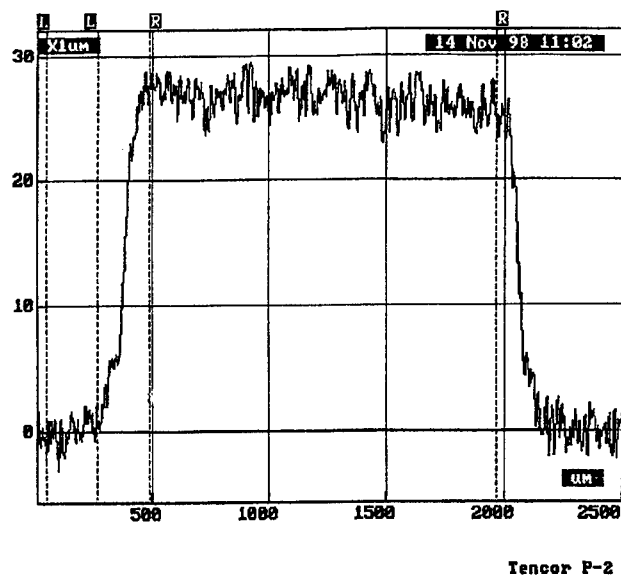


Figure 7. Profilometer scan showing the uniformity across the capacitors fabricated by MAPLE-DW.

The parallel plate capacitors were evaluated from frequencies ranging from 1 MHz up to 1.8 GHz using a HP4291A impedance analyzer. The capacitance ratio between the large and small capacitors was close to their area ratio (4:1) as expected with some variations attributed to non-uniformities on the BTO transfers. All the capacitors made showed capacitances between 2 and 40 pF and dissipation factors between 0.11 to 0.17. These capacitors were then annealed on a furnace at 200 °C for two hours. After the annealing step, the capacitances dropped by about 40% while the dissipation

factors decreased by an order of magnitude. From these results, the effective dielectric constant of the capacitors was estimated to be around 25 after the annealing step. Figure 8 shows a micrograph of one of the BTO capacitors pairs made.

The inductance of the four turn YIG core inductor was 9 nH at 1 MHz. The inductor exhibited very high losses and the effective permeability was estimated to be about 70. This result can be attributed to the fact that the inductor made had a very small YIG core with a large number of air gaps. Figure 9 shows a micrograph of the inductor.

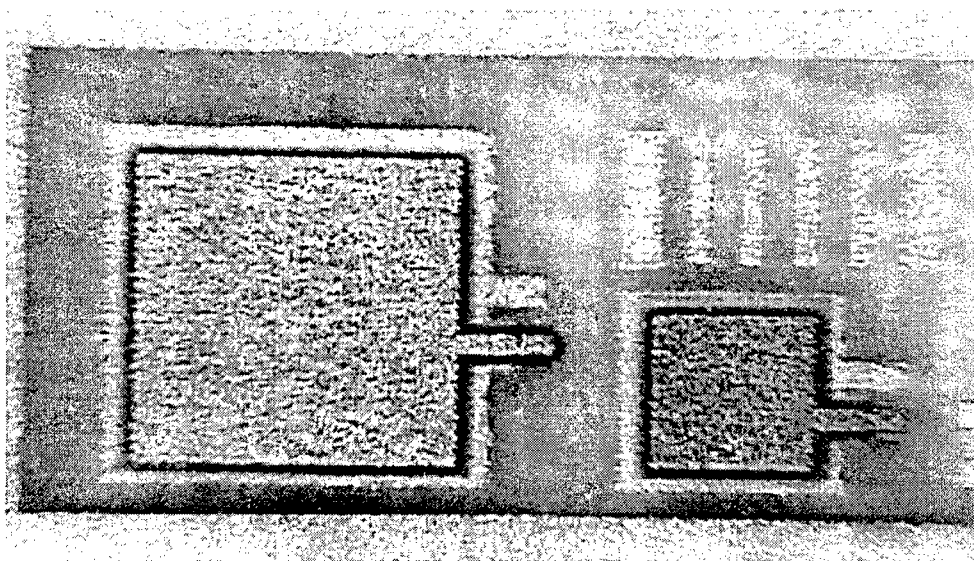


Figure 8. BaTiO_3 capacitors with Au electrodes made by MAPLE-DW. The larger capacitor was 1.6 mm x 1.6 mm other is 25% smaller.

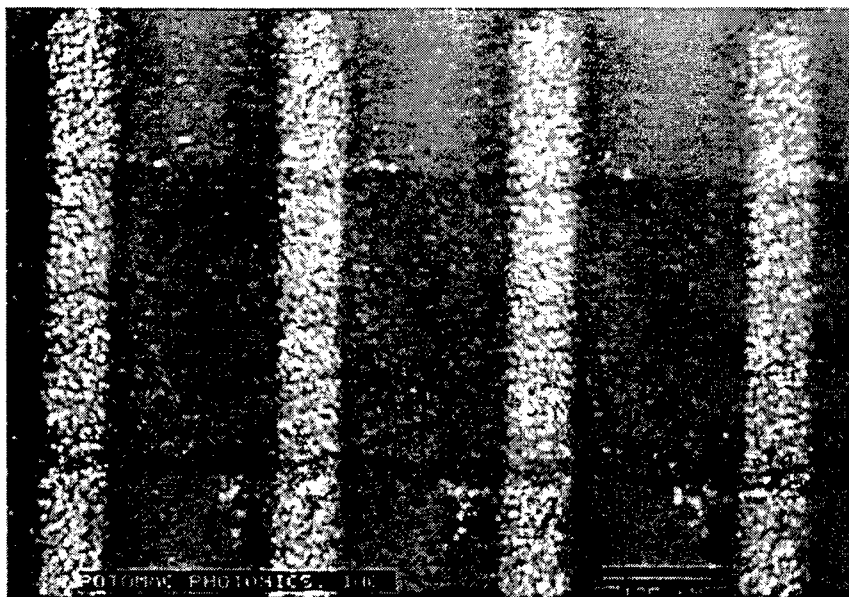


Figure 9. Four turn inductor with YIG core fabricated by MAPLE-DW.

3.4 Gas Sensors

A new type of gas sensors based on conductimetric techniques^{10,11} can be fabricated using composites made from a dispersion of a conducting material such as graphite and a non-conducting polymer. The resulting matrix is conductive and its resistance will change when exposed to different vapors. A ribbon made with a 4 μm thick layer of Polyepichlorohydrin (a chemoselective polymer) mixed with graphite was used in order to test the ability of the MAPLE-DW process to transfer polymer materials as well as composites¹². A series of conductive patches across gold electrodes were produced. These electrodes showed sensitivities of the order of parts per million (ppm) when exposed to several gases. This work is still in its preliminary stages, and more detailed analysis will follow. However, it clearly demonstrates that MAPLE-DW can also be used for direct writing of functional polymer materials as well as composites. Figure 10 shows an optical micrograph of one of the prototype chemoresistors fabricated by MAPLE-DW.

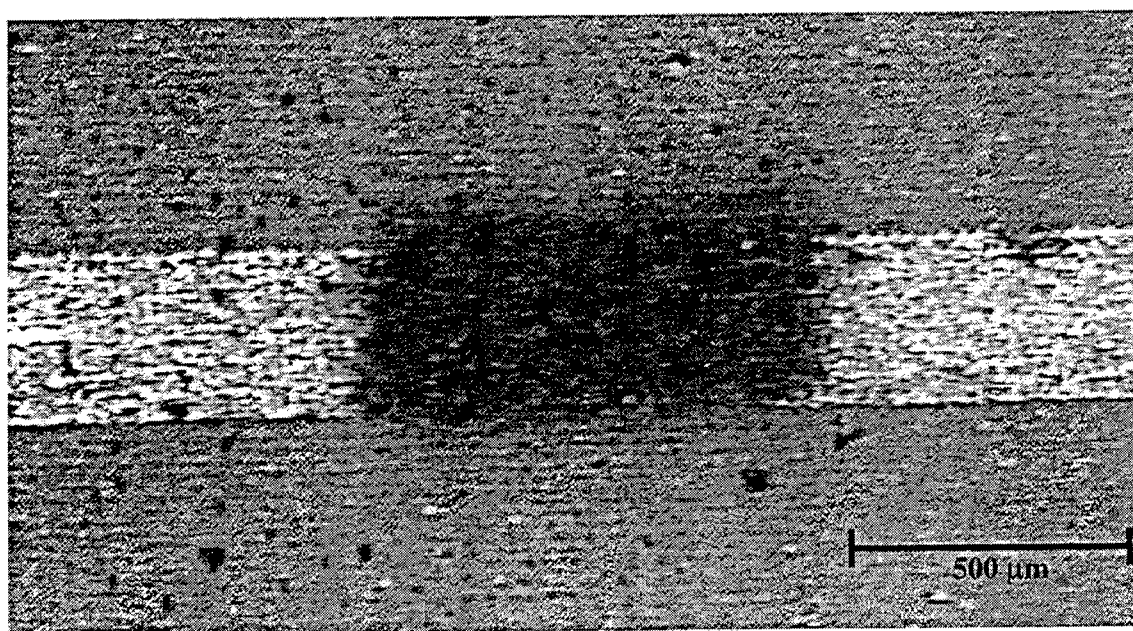


Figure 10. Photograph of a PECH/graphite chemoresistor gas sensor fabricated by MAPLE-DW.

4. SUMMARY

A novel direct write process for rapid prototyping of electronic circuit elements was developed by combining two laser based processes, LIFT and MAPLE. The new technique is called MAPLE Direct Write or MAPLE-DW. Materials such as metals, dielectrics and ferrites, polymers and composites have been successfully deposited without any loss in functionality by this technique. MAPLE-DW was used to fabricate gold interconnect lines, nichrome resistors, Barium Titanate parallel plate capacitors and a YIG core inductor. All these components were fabricated in air and at room temperature with sub-10 μm resolution. Using the MAPLE-DW setup developed for this work both subtractive processes such as laser machining, trimming and cleaning as well as additive processes such as LIFT and MAPLE-DW were demonstrated.

5. ACKNOWLEDGEMENTS

We would like to thank Tim Schaeffer of the Mayo Foundation for the high frequency measurements of the capacitors and inductor made for this work. Financial support for this work was provided by DARPA.

6. REFERENCES

1. J. Bohandy, B.F. Kim, and F.J. Adrian, J. Appl. Phys. **60**, 1538 (1986).
2. J. Bohandy, B.F. Kim, F.J. Adrian and A.N. Jette, J. Appl. Phys. **63**, 1558 (1988).
3. R. A. McGill, D. B. Chrisey, Method of Producing Thin Film Coating by Matrix Assisted Pulsed Laser Deposition, US Navy Case No. 79,214.
4. R.A. McGill, R. Chung, D.B Chrisey, P.C. Dorsey, P. Matthews, A. Piqué, T.E. Mlsna, and J.L. Stepnowski, IEEE Trans. On Ultrasonics, Ferroelectrics and Frequency Control, **45**, 1370 (1998).
5. R. A. McGill, D. B. Chrisey, A. Piqué, T. E. Mlsna, SPIE Proceedings Vol 3274, pp 255-266, 1998.
6. A. Piqué, R.A. McGill, D.B. Chrisey, J. Callahan, T.E. Mlsna, in *Advances in Laser Ablation of Materials*, MRS Proceedings, vol 526, p. 421, 1998.
7. A. Piqué, D.B. Chrisey, B.J. Spargo, M.A. Bucaro, R.W. Vachet, J.H. Callahan, R.A. McGill and T.E. Mlsna, in *Advances in Laser Ablation of Materials*, MRS Proceedings, vol 526, p. 421, 1998.
8. D. B. Chrisey, R. A. McGill, A. Piqué, Matrix Assisted Pulsed Laser Evaporation Direct Write, US Navy Case No. 79,702.
9. Potomac Photonics Inc. 4445 Nicole Drive, Lanham, MD 20706.
10. J.W. Gardner, M. Craven, C. Dow and E.L. Hines, Meas. Sci. Technol., **9**, 120 (1998).
11. J.V. Hatfield, P. Neaves, P.J. Hicks, K. Persaud and P. Travers, Sens. Actuators B: Chem., **18**, 221 (1994).
12. R. A. McGill, D. B. Chrisey, A. Piqué, Fabrication of Patternable Electrically Conductive Thin Films for Chemoresistor Chemical Sensor Applications with Laser Evaporation Techniques, US Navy Case No. 79,708.

Microstructuring of materials by pulsed laser focusing and projection technique

Horst Exner, Bernd Keiper, Peter Meja

Laserinstitut Mittelsachsen e.V., Hochschule Mittweida, University of Applied Sciences,
Technikumplatz 17, 09648 Mittweida, Germany, *

ABSTRACT

Presently, there is a growing demand from the industry for microprocessing of materials. In particular, for applications in the field of microsystems technology it is necessary to produce structures with dimensions down to the micrometer scale in various materials.

We have been investigating the structuring of silicon, anodic bondable PYREX glass, Al_2O_3 -ceramic and PMMA by means of laser microprocessing using an excimer laser (248 nm or 193 nm wavelength, 30 ns pulse duration, 400 mJ pulse energy) and a TEA CO_2 laser (10,6 μm wavelength, 80 ns or 200 ns pulse duration, 6 J pulse energy). Both the mask projection technique and the focusing technique have been employed. We will show the dependence of the ablation thresholds and the ablation rates on the laser parameters and on the physical properties of the materials, i.e. absorption coefficient, melting point and thermal conductivity.

During and after the laser processing of different glasses we observed the formation of cracks in the laser irradiated region and partly in the glass wafer surrounding the drilled holes. Those crack formations should be due to the development of thermally induced mechanical stress in the glass.

We calculated the TEA CO_2 laser ablation process using a half empirical rotation symmetrical model.

Keywords: Laser microprocessing, mask projection technique, focusing technique, temperature field calculations

1. INTRODUCTION

The integration of electronic mechanical and optical functions in single devices gets growing importance with the fast development of the microsystems technology. There is a demand for such special devices with dimensions as small as possible. This trend is noticeable in a number of publications of the last time. Most of the devices for the microsystems technology are produced with the well known microelectronic silicon technology. The development of new devices requires however also the application of other materials e.g. glasses, ceramics and plastics, which couldn't or couldn't be processed with the microelectronic technology.

A obvious possibility to solve that problem is the application of lasers because of the chance to process nearly all materials. Therefore we have investigated the structuring of different materials by the excimer laser and TEA CO_2 laser mask projection technique. Recently a considerable number of authors have reported on the use of lasers for micro material processing for instance of Si_3N_4 ceramics using excimer lasers [1] as well as of ceramics and hard metal [2] and of glasses [3] using Nd:YAG lasers.

2. EXPERIMENTAL DETAILS

Silicon, PYREX glass, Al_2O_3 -ceramic and PMMA were structured by means of TEA CO_2 and excimer laser microprocessing using the mask projection technique with the parameters given in Table 1. The TEA CO_2 laser was used in two different resonator configurations, the short standard resonator and the longer smooth pulse resonator. Therefore we were able to investigate the ablation process using pulses with 90 ns and with 180 ns pulse duration.

Table 1: Processing parameters

Excimer laser				
Wavelength [nm]	Pulse duration [ns]	Repetition rate [Hz]	Laser fluence [J/cm^2]	Reduction scale
248	30	1 to 50	0,2 to 10	1:3,3
248	30	1 to 50	0,2 to 20	Focused beam
TEA CO_2 laser				
10600	180	1 to 30	4 to 12	1:5
10600	90	1 to 30	3 to 8	1:5
10600	180	1 to 30	Over 100	Focused beam

* Correspondence: Email: exner@htwm.de; Telephone: ++49 3727 581413; Fax: ++49 3727 581496

The experiments were carried out with the experimental set-up shown in Fig. 1. We illuminate a mask with the TEA CO₂ laser or the excimer laser beam and project it by a projection lens on to the sample surface. Consequently material of the sample will be removed by the influence of the laser radiation.

The excimer laser radiation shows a vary inhomogeneous energy distribution over the beam cross section. That's why it is necessary to homogenize the excimer laser beam. The used laser beam homogenizer is dividing the laser beam into a number of beam parts by two crossed cylinder lens arrays. Those beam parts are projected to a combined area with homogeneous laser energy distribution in the plane of the mask. Otherwise The assembly is similar for the excimer and for the TEA CO₂ laser processing apparatus.

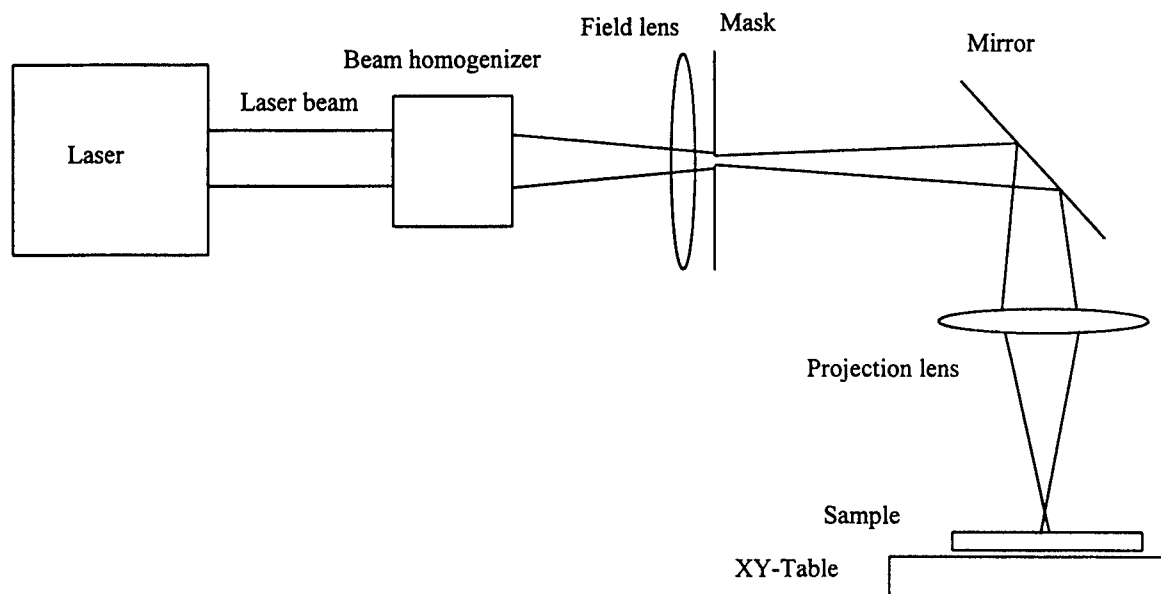


Fig. 1: Experimental set-up for TEA CO₂ laser and excimer laser microprocessing respectively. The beam homogenizer and the field lens are only used for the excimer laser assembly.

Some experiments were carried out using a focussed laser beam too. In the case of TEA CO₂ laser microprocessing with focussed laser beam we observed a breakdown in the air above the sample surface. The air plasma shields the laser energy from the sample and led to relatively low ablation depths. That's why the TEA CO₂ laser focussing technique in air is not suitable for the material processing.

The excimer laser beam was focussed by two cylinder lenses in order to realize the best focus for both directions of the laser beam with different divergence. Nevertheless the ablation crater is irregular formed because of the beam properties of the excimer laser. So we couldn't produce microstructures with the demanded dimensions by the excimer laser focussing technique, but we were able to determine the ablation depths of the investigated materials at higher laser fluences than we could realize with the mask projection technique.

3. RESULTS

1. Excimer laser microprocessing

The ablation thresholds of the materials were determined using the excimer laser mask projection technique (see Table 2). An area of 1 mm² was irradiated with a homogeneous laser energy distribution.

It was found, that the ablation threshold varies with the used number of laser pulses. Subsequent to the laser induced change of the sample surface, e.g. ablation of impurities or water as well as increasing roughness and absorption, much less laser fluence is necessary to remove material from the sample compared to the single pulse ablation threshold.

In the case of PMMA occur a breaking of bonds at low energy fluences below 2 J/cm². With it the surface of the sample becomes white and rough. At laser fluences above 4,5 J/cm² the thermal ablation mechanism is dominant and the ablated surface is smooth and transparent.

Table 2: Excimer laser ablation thresholds of different materials:

Material	Number of pulses	Ablation threshold [J/cm ²]	Comments
PMMA	20...45	0,2...0,4	Breaking of bonds
PMMA	1	1,7	Breaking of bonds
PMMA	1	4,5	Thermal ablation
Silicon	1	2,7	Strong increase of roughness
Silicon	1	3,3	Start of ablation
BK7	10	5,6	Single pulse ablation up to 10 J/cm ² not found
PYREX glass	10	8,9	Single pulse ablation up to 10 J/cm ² not found

The ablation depth per laser pulse of the materials was determined in dependence on the laser pulse repetition rate and on the number of pulses, that means on the total ablation depth. The Figures 2 to 4 are showing the connection between the ablation depth and the repetition rate for a different numbers of pulses: Fig. 2 for PMMA, Fig. 3 for silicon and Fig. 4 for BK7.

The diagram Fig. 2 shows only little variation of PMMA ablation depth with the increasing number of laser pulses, but an increasing ablation depth with increasing repetition rate. The ablation depth of PMMA is generally relatively high compared to the other investigated materials. This behavior can be explained with the low melting point, the low evaporation temperature and the low thermal conductivity. Those properties cause a relatively strong temperature rise near the irradiated sample area. Therefore more material can be ablated with the same laser pulse energy at higher repetition rates. At repetition rates above 20 Hz occur a melting of the PMMA outside of the irradiated area i.e. those parameters are not suitable for material processing.

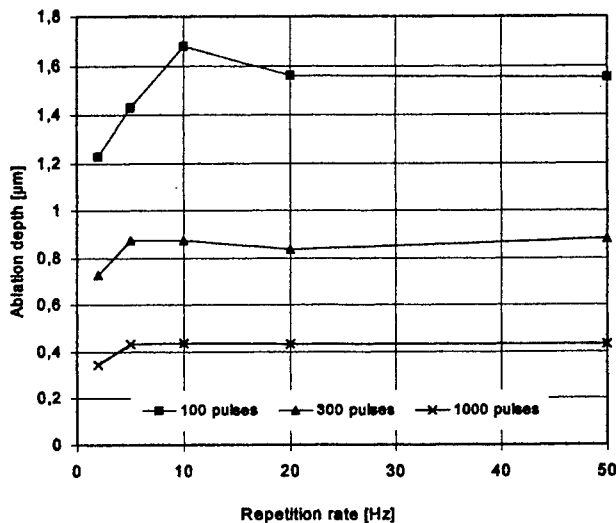


Fig. 3: Ablation depth per pulse in silicon in dependence on the repetition rate for a different number of pulses. Parameters: Excimer laser focusing technique, 1 mm² ablated area, 75 mJ laser pulse energy at the sample surface.

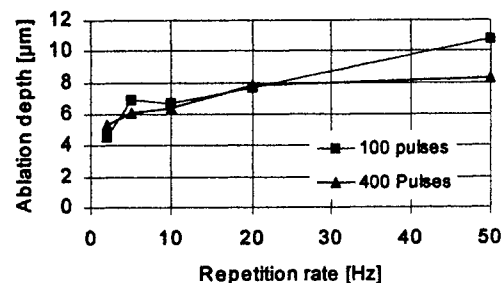


Fig. 2: Ablation depth per pulse in PMMA in dependence on the repetition rate for a different number of pulses. Parameters: Excimer laser focusing technique, 1 mm² ablated area, 75 mJ laser pulse energy at the sample surface.

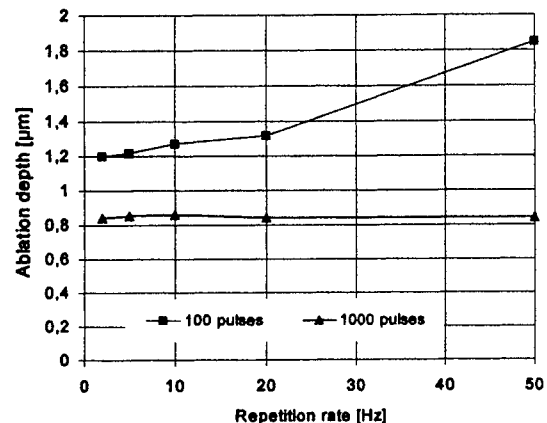


Fig. 4: Ablation depth per pulse in BK7 in dependence on the repetition rate for a different number of pulses. Parameters: Excimer laser focusing technique, 1 mm² ablated area, 75 mJ laser pulse energy at the sample surface.

In the case of silicon (see Fig. 3) the ablation depth increases with the change of the repetition rate from 1 to 10 Hz, at even higher repetition rates a saturation is reached. We assume, the reason for the increase of ablation depth should be the growing absorption due to the increasing mean temperature near the irradiated sample area. Furthermore can be observed in Fig. 3, different to the behavior of PMMA, a strong decreasing ablation depth with the increasing number of pulses. This can be explained as follows: The total ablation depth increases with the number of pulses. Consequently a growing part of the absorbed laser energy will be brought into a larger volume of the sample via thermal conduction. Especially at the edge of the irradiated area is the remaining thermal energy smaller than the ablation threshold and the ablated area decreases with increasing depth. Furthermore the ablated particles have to be ejected from a deeper ablation crater. With it an increasing part of the laser energy will be absorbed by the ablated material and will contribute to the plasma formation. That's why the fraction of the laser energy, that contributes to the material ablation decreases.

In the case of PMMA (see Fig. 2) the loss of energy for the ablation process by thermal conduction doesn't influence the ablation depth since the laser fluence is far above the ablation threshold. Therefore the dependence of the number of pulses on the ablation depth is small.

The ablation depth of BK7 (see Fig. 4) decreases with increasing number of pulses and increases with increasing repetition rate.

The dependence of the ablated volume on the used laser pulse energy for different materials is presented in Fig. 5.

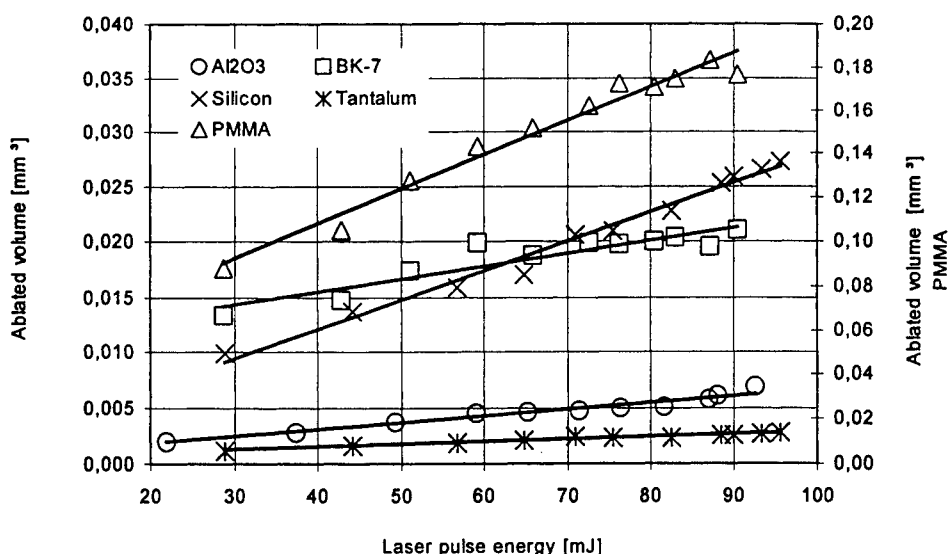


Fig. 5: Ablated volume of different materials in dependence on the laser pulse energy. Parameters: Excimer laser focusing technique, 1 mm² irradiated area, 100 pulses, 2 Hz repetition rate.

We observed the lowest ablation rates for the materials with the highest melting point and thermal conductivity e.g. tantalum and Al₂O₃ ceramics in accordance to our expectations. The ablation rate of PMMA is more than one order of magnitude higher. From Fig. 5 can be seen, that the ablated volume increases nearly linear with the used laser energy in the investigated field of parameters.

2. TEA CO₂ laser microprocessing

The single pulse ablation depth of different materials was determined with the TEA CO₂ laser mask projection technique. The irradiated area was 1 x 1 mm² and the pulse duration was 180 ns respectively 90 ns. The results are shown in Fig. 6. As single pulse ablation thresholds were found at 180 ns pulse duration: PMMA: 4,15 J/cm²; PYREX glass: 3,97 J/cm² Quartz glass: 5,64 J/cm². Surprisingly the ablation threshold of PMMA with the lower melting point is larger than that of PYREX glass. The reason should be the much higher ablation threshold of the unirradiated sample surface compared to the already ablated surface of some materials similar to the results of the excimer laser ablation experiments.

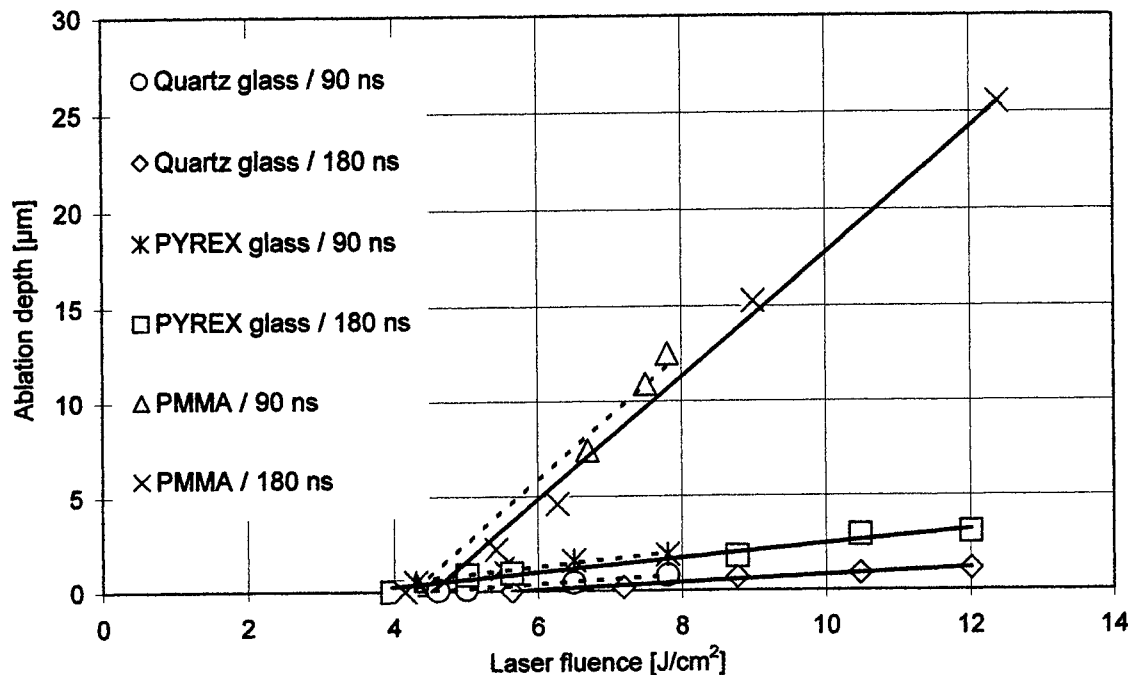


Fig. 6: Single pulse ablation depth of different materials in dependence on the laser fluence. Parameters: CO₂ TEA laser mask projection, 180 ns respectively 90 ns pulse duration (dashed line), 1 mm² ablated area.

Between the single pulse ablation depth and the laser fluence exist in the investigated parameter field a nearly linear connection. Merely the curve of PMMA shows a lower slope near the ablation threshold than at larger laser fluences, where the curve is linear too.

The shorter pulse duration (dashed lines in Fig. 6) resulted in a minor increase of ablation depth at constant laser fluence due to the higher laser peak power.

In the case of Al₂O₃ ceramics nearly no ablation could be observed at the maximum laser fluence of 12,5 J/cm² after thousand pulses and tantalum showed only a cleaning effect of the sample surface.

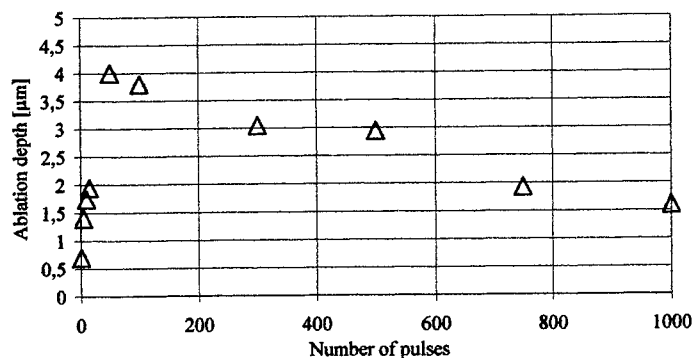


Fig. 7: Dependence of ablation depth per pulse on the number of laser pulses in quartz glass. Parameters: CO₂ TEA laser mask projection, 180 ns pulse duration, 1 mm² ablated area, 12 J/cm² laser fluence.

The diagram (Fig. 7) shows the dependence of the ablation depth on the number of laser pulses in quartz glass. The results are similar to the above described results of the excimer laser ablation process. At the beginning of the ablation process the ablation depth is very small. After changing of the surface i.e. cleaning, melting, increasing roughness and absorption, the ablation depth increases very strong. With the increasing number of pulses and with it the increasing total ablation depth decreases the ablation depth per laser pulse because of the stronger abduction of energy by thermal conduction and the formation of a more intensive plasma as explained in the previous chapter.

During ablation of some materials, particularly BK7 and PYREX glass we have observed the formation of cracks inside of the irradiated sample area (see Fig. 8). The reasons for the crack formation are: The high thermal expansion coefficient and the relatively low thermal conductivity resulting in high temperature gradients and strong mechanical stress in the irradiated area. The mechanical stress causes the cracks in the brittle glass materials. This ablation mechanism influences the ablation depth since solid particles with different size will be ejected. The ablated surface is very uneven and should be not suitable for the most applications. If a hole have to be produced the process can be used, as the cracks are only inside of the irradiated area.

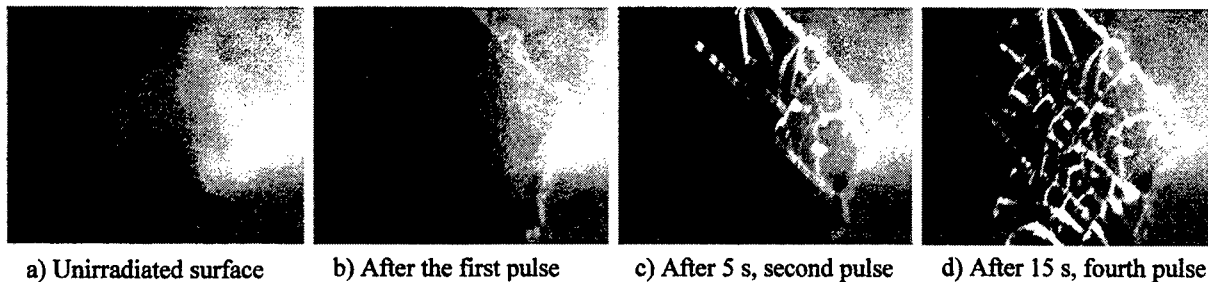


Fig.8: Formation of cracks subsequent to the TEA CO₂ laser ablation in BK-7.

3. Calculation of the TEA CO₂ laser ablation process

For the simulation of the ablation process of PYREX glass we used a half empirical rotation symmetrical model. We have divided the sample in hollow cylinder segments for simulation. The polarization and the angel of incidence of radiation as well as the thermal conduction and the thermal radiation were considered in the model. The convection was included with a constant correction factor. However the temperature dependence of the refractive index was not known for the material and was ignored. The simulation was made through adaptation of the measured to the simulated ablation depth. The optimized parameters were the energy of the ablated particles and the latent heat of the softened glass.

Parameters used for calculation:

- Laser parameters: (flat top profile)
 - Laser fluence: 4 J/cm²
 - Repetition rate: 10 Hz
 - Pulse duration: 180 ns
 - Irradiated area: 1 mm diameter
- Parameters of PYREX glass:
 - Refractive index: 1,4 +0,75i (measured and calculated with spectrophotometer)
 - Evaporation temperature: 2800 K
 - Capacity of heat: 753 J/kgK
 - Mass density: 2230 kg/m³
 - Thermal conductivity: 6,9 10⁻⁷ m²/s
- Geometric parameters:
 - Difference of the neighboring cylinder radii: 25 μm
 - Thickness of elements: 25 μm
 - Thickness of the sample: 0,5 mm

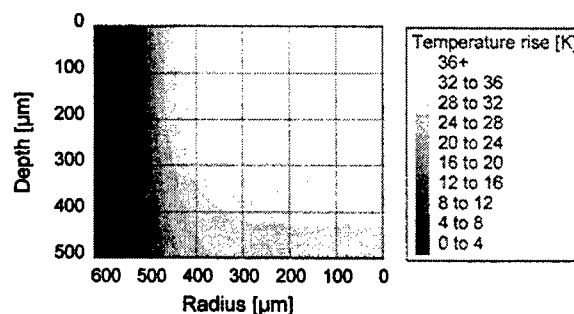


Fig. 9: Calculated temperature distribution in PYREX glass 0.1 second after the fifth laser pulse.

Fig. 9 shows the calculated temperature distribution 0,1 s after the fifth laser pulse. It can be seen that the temperature rise of the sample as result of the laser irradiation at the beginning of the next laser pulse is very small. In accordance with the experimental results no distinct heat remain in the sample after the laser pulse. Neither in the experiment nor in the calculation an increase of ablation depth was observed with increasing number of pulses. Therefore the absorbed energy must leave the sample with the ablated particles nearly completely.

In the previous chapters we reported on the formation of sloping crater walls because of the thermal conduction at the edge of the ablation area. From Fig. 10 we can see that our calculation of the ablation process led us to the same result.

At first the crater wall is nearly perpendicular to the sample surface. After some pulses the wall becomes more and more sloping. The described slope of the walls is in accordance with results of experiments which were made with the same parameters. In the calculation for Fig. 10 was used the mean value for both polarization directions.

We have calculated the ablation process with polarized laser radiation too. The results are shown in Fig. 11. The TEA CO₂ laser produces with the long resonator configuration (180 ns pulse duration) linear polarized radiation. The ablation craters showed indeed different slopes of the wall parallel and perpendicular to the laser beam.

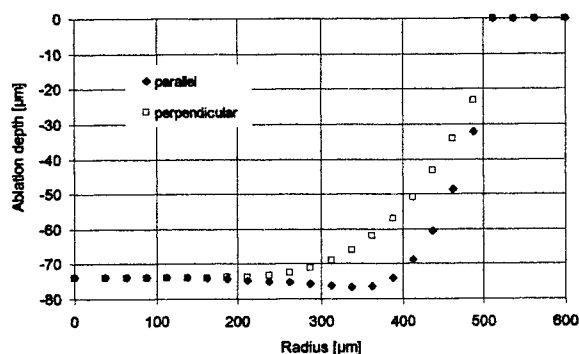


Fig. 11: Calculated ablation geometry in dependence on the polarization of the TEA CO₂ laser beam in PYREX glass after 150 pulses.

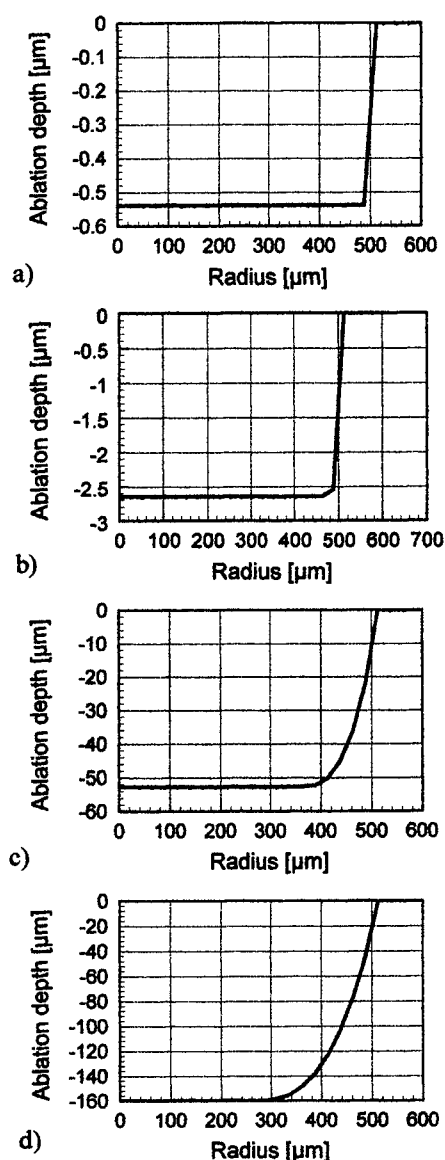


Fig. 10: Calculated ablation geometry in PYREX glass after 1 pulse (a), 5 pulses (b), 100 pulses (c), 300 pulses (d).

SUMMARY

The following influences of the properties of the processed materials on the ablation process were observed:

- Absorptance:
Quartz glass is transparent in the wavelength region from 165 to 4000 nm. Therefore it can only be processed with a good quality using the TEA CO₂ laser if the laser pulse duration is in the order of ns or longer.
- Reflectance:
Metals like tantalum can't be processed with the TEA CO₂ laser in the investigated parameter field because of the high reflectance.
- Melting respectively evaporation temperature:
The ablation depth of materials with high melting and evaporation temperatures like tantalum and Al₂O₃ ceramics is relatively low.
- Thermal conductivity:
A high thermal conductivity of the processed material causes the formation of molten edges and will make the resolution of the projection process worse.
- Thermal expansion coefficient:
Large thermal expansion coefficients cause the formation of cracks in brittle materials with low thermal conductivity like BK7 because of high thermal gradients and high mechanical stress.
- Quality of the Surface:
Smooth unirradiated surfaces possess mostly a lower absorptance than already ablated surfaces, so that for the initialization of the ablation process a higher laser fluence is necessary. Impurities or water films at the sample surface can cause higher ablation thresholds too.

ACKNOWLEDGMENTS

The research project that was the basis for this publication is supported with EFFRE-means of the EU and with means of the Freistaat Sachsen (Projekt-Nr.: 4355/679). The authors would like to thank the Dr. Teschauer & Petsch AG, Chemnitz for the financial support as well.

REFERENCES

1. J. Heitz, J.D. Pedarnig, D. Bäuerle, G. Petzow, "Excimer-laser ablation and micro-patterning of ceramic Si₃N₄", Applied Physics A 65, S. 259-261 (1997).
2. A. Gillner, D. Hellrung, R. Poprawe, „Micro-structuring with Nd:YAG-Lasers“, Laser Assisted Net shape Engineering 2, Proceedings of the LANE '97, eds.: M. Geiger, F. Vollertsen, Meisenbach Bamberg 1997.
3. T. Koyama; K. Tsunetomo, „Laser micromachining of silicate glasses containing silver ions using a pulsed laser“, Japanese Journal of Applied Physics, Part 2, Bd. 36 (1997) 2B, 244-247.

High-accuracy micromachining of ceramics by frequency-tripled Nd:YAG-lasers

Dirk Hellrung*, Li-Ya Yeh, Frank Depiereux, Arnold Gillner, Reinhart Poprawe

Fraunhofer Institute Lasertechnology, 52074 Aachen, Germany

ABSTRACT

Ceramics like Si_3N_4 , Al_2O_3 (sapphire) and ZrO_2 and also diamonds can be hardly machined by conventional methods. Short pulse lasers, especially frequency-tripled, diode pumped Nd:YAG-lasers with a high beam quality offer the possibility to ablate these materials with high quality. With a spot size of about $10\text{ }\mu\text{m}$, high fluences ($> 100\text{ J/cm}^2$) can be achieved, so that the materials are vaporised without or with only a small amount of molten material. This technique is applicable for drilling small holes with diameters $\geq 5\text{ }\mu\text{m}$ (aspect ratio up to 60) and cutting of thin ceramic substrates (thickness $< 0.5\text{ mm}$). The edges are sharp and the face of the cut is very smooth. Furthermore it is possible to ablate three dimensional microstructures. Therefore the laser beam is scanned over the surface and the material is ablated pulse beside pulse. The surface roughness depends on the overlap of the laser pulses, the pulse energy and the scanning strategies. With optimised machining parameters the surface roughness can be reduced to $R_a \leq 0.1\text{ }\mu\text{m}$. Due to the low ablation rate of around $0.05\text{ }\mu\text{g/pulse}$ the ablation depth of a single slice can be controlled very precisely. Depending on the material and the machining parameters the depth is in the range of 1 to $10\text{ }\mu\text{m}$.

Keywords: micromachining, ceramics, laser, sapphire, diamond

1. INTRODUCTION

The machining of hard materials and especially of ceramics and diamonds is very difficult. In most cases, the final structure of a part cannot be produced directly by sintering. The part has to be processed additionally to get the final shape. There are only a few manufacturing methods available, like grinding. But they are not applicable for very small and complex structures. Some developments have produced electrical conductive ceramics, which can be machined by electrical discharge processes, but the material properties have been changed.

The main advantages of ceramics are:

- nonconductivity
- good heat conductivity
- high hardness
- high chemical resistance

These properties make ceramics very interesting for different applications, where furthermore small dimensions are required.

The machining of ceramics with Nd:YAG-lasers is already used. But especially for the fundamental wavelength of the Nd:YAG-laser the absorption of many ceramics is poor. Using very high intensities, this disadvantage can be compensated and melting, vaporization and removal of material is also possible. But the process efficiency and often the machining quality is very low [1]. Furthermore the smallest structure sizes are restricted. Frequency tripled Q-Switch Nd:YAG-lasers as

* For further author information -

email: hellrung@ilt.fhg.de; WWW: <http://www.ilt.fhg.de/>; Telephone: ++49-241/8906-273; Fax: ++49-241/8906-121

well as Excimer-lasers can improve the process because the absorption is higher in the UV-range. Machining parameters and results have been investigated for ZrO_2 , Al_2O_3 , Si_3N_4 , Diamond and WC.

2. LASER AND EQUIPMENT

The laser source is a Q-Switch diode pumped solid state laser (DPSSL) with an extra cavity frequency doubling and tripling [2]. The beam profile can be approximated as a gaussian mode which results in a near-diffraction limited beam quality ($M^2 \leq 1.1$). The laser beam has a high energy stability, which is important for the machining quality. The pulse repetition rate is in the range of 1 to 5 kHz. With different beam guiding and shaping devices the focus diameter can be varied between 3 and 20 μm . The main laser beam parameters are listed up in Tab. 1.

pulse repetition rate	f_p [kHz]	1	5
wavelength	λ [nm]	355	355
average power	P_{av} [W]	0.7	2.1
pulse duration	t_p [ns]	15	25
max. Pulse energy	E_p [mJ]	0.7	0.425
pulse peak power	P_p [kW]	46.6	16.8
max. fluence ¹	F [J/cm ²]	396.1	237.7

¹ for a focus diameter of 15 μm

Table 1: Parameters of the DPSSL

The laser is combined with a 4-axis positioning system where the optic is fixed on the z-axis. The x-y- Θ -axis move the workpiece underneath the focused laser beam. In most cases the laser beam is focused on the surface of the workpiece. The linear drives provide a high dynamic behaviour with a maximum velocity of 500 mm/s. Due to the resolution of 0.1 μm a positioning accuracy of 1 μm can be achieved. The axis motion is controlled by a CNC-interface. Because the laser pulses cannot be triggered on demand but are fixed at a chosen pulse repetition rate, a special logical device synchronizes the laser pulses with the velocity of the axis to avoid grooves at the edges due to the acceleration and deceleration.

A CCD-camera is integrated to observe the process. The machined structures can be directly measured with a white light sensor (CHR 150 N) [3]. This sensor uses the chromatic aberration of a lens and has a measuring range of 300 μm at a resolution of 1 μm and a spot size of 1 μm . The lateral dimensions of the area are only restricted by the maximum way of the positioning tables and with adapted strategies also a larger z-range can be measured. With this sensor single point measurements, line and three-dimensional scans can be recorded and the corresponding roughness R_a will be calculate. The white light sensor is also used in an off-line control loop for the three dimensional laser beam removal process. Additional measurements are done with an optical and a scanning electron microscope (SEM).

3. MACHINING WITH SINGLE LASER PULSES

Figure 1 shows the absorption versus the wavelength in the interesting spectrum from 200 to 1200 nm. The values for the absorption are calculated from the measured reflection and transmission. The measurements are done only at low energies with a white light lamp, so that they cannot give an exact value for the laser process but they figure out the general course. The absorption increases rapidly in the UV-range for Al_2O_3 and ZrO_2 . For Si_3N_4 and hard metal (WC) there is no significant change over the whole spectrum as well as sapphire is nearly transparent. But at high intensities or with a rough surface also sapphire can be machined.

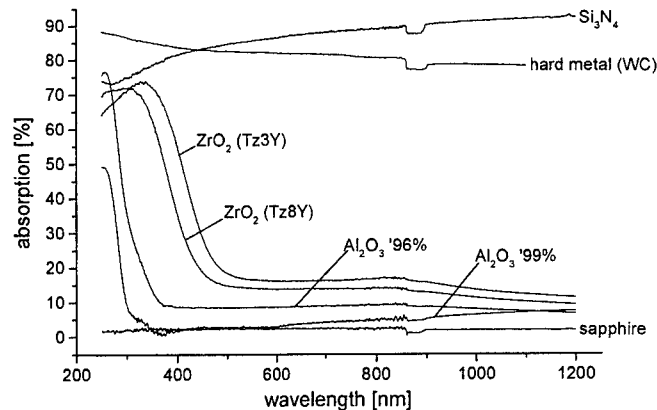


Figure 1: Absorption of different hard materials

The effective working diameter does not need to be equal to the focus diameter but depends directly on the maximum power of the beam profile and the material specific threshold [4,5]. So the effective diameter can be adjusted by the laser power and the beam shaping. Different investigations [6,7] on threshold fluences of ceramics show that the values are in the range of 0.2 up to 1.5 J/cm² which is very low compared to the maximum possible fluences of the used laser source (see Tab. 1). But for the reduction of the surface roughness, the minimization of debris around the machined area and the accuracy of the structure, which are important for the three-dimensional microstructuring and the drilling and cutting, it is necessary to reduce the energy density. This is done by an external reducer, which can vary the laser beam energy from 0 to 100 %.

Vice versa higher energy densities which can be achieved by increasing the laser beam energy or decreasing the focus diameter produce a deeper mould at a single laser pulse. Because of that the machining time will be reduced, but it causes more molten and damaged material. Therefore the energy density has to be adapted for different applications.

Figure 2 shows the mould of different ceramic materials. The amount of molten material varies between different materials and can be reduced to a minimum. The grain sizes also influences the quality of the machined ceramic. During the removal process not only vaporization of material takes place, but also the removal of whole grains, due to the high pressure of the vaporized material. Single grains can be detected in the surrounding area of the moulds.

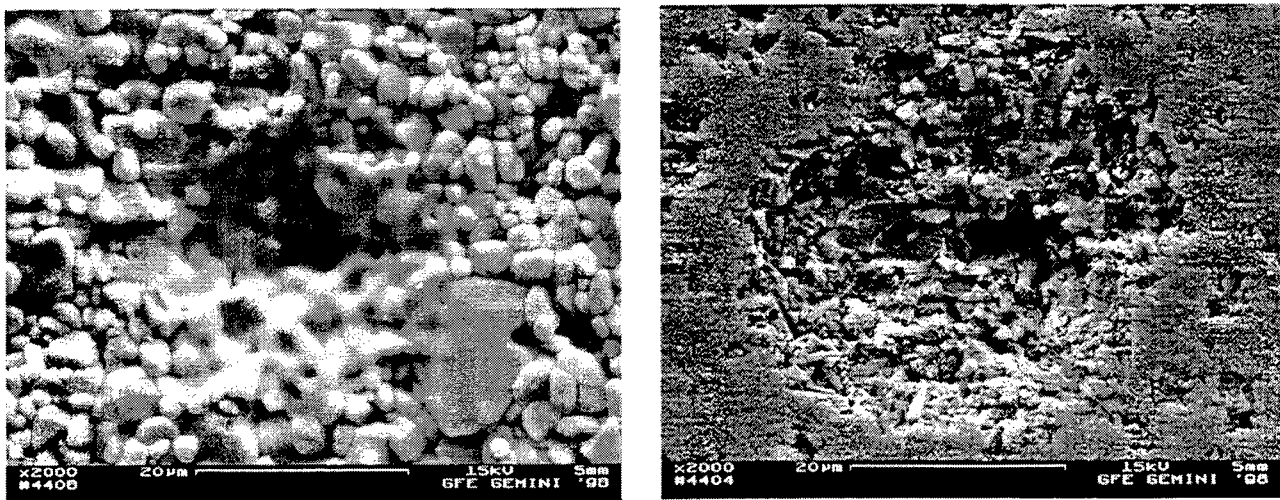


Figure 2: Single laser pulse moulds on Al₂O₃ and Si₃N₄ ($\lambda = 355$ nm, $f_p = 1$ kHz, $E_p = 0.56$ mJ)

4. DRILLING AND CUTTING

The drilling process has been investigated for different ceramic materials. The thickness for all ceramics was 0.25 mm, so that a single pulse drilling was not possible. For small holes the percussion drilling was used. Comparable to results for drilling of metals with a pulsed Nd:YAG-laser the diameter of the holes is dependent of the irradiation time [8]. After a laser parameter and material specific time, which is necessary for drilling through the given material thickness, the hole diameter increases. But at longer irradiation times a pulsation of the hole diameter can be observed. The hole opens and closes again, until it reaches a final diameter (see Fig. 3). This is caused by the production of molten material on the edges of the hole, where the energy density is not high enough, to vaporize the material. The molten material flows to the center of the hole and is removed out of the hole with the following laser pulses. So the hole diameter depends on the irradiation time. This pulsation is independent on the total energy density at the working position.

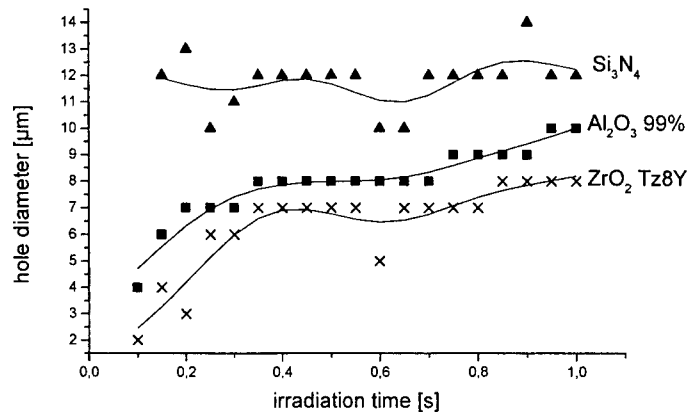


Fig. 3: Hole diameter as a function of time

But the energy density at the focal position influences the maximum diameter, the removal depth per pulse respectively the time for drilling through the material and the maximum depth of a hole. Fig. 4 shows the final hole diameter versus the energy density. The energy density can be easily varied by the pulse repetition rate (see Tab. 1). At higher pulse repetition rates the pulse energy decreases.

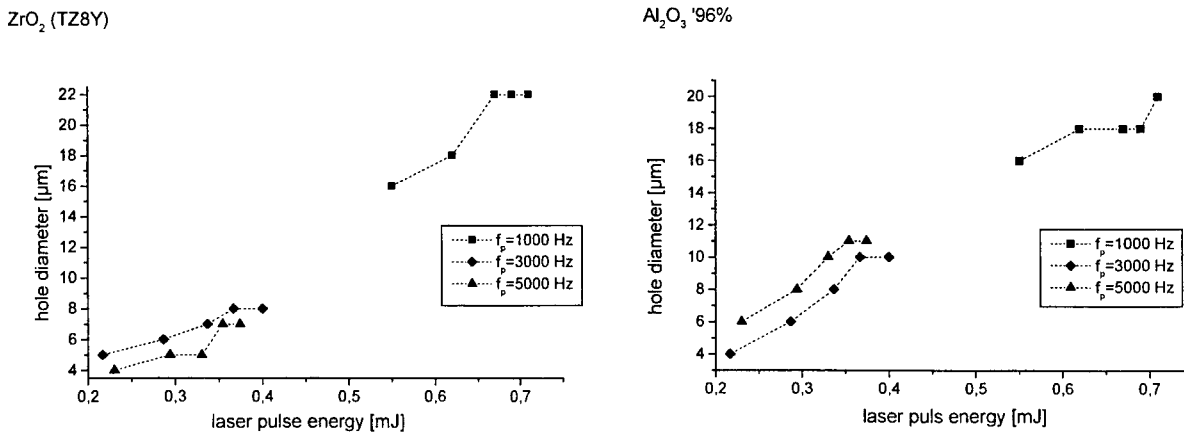


Fig. 4: Hole diameter (exit) as a function of laser pulse energy (ZrO_2 , Al_2O_3)

Similar to the ablation or removal process of an Excimer-laser, the removal depth per pulse has a maximum value at a material specific energy density. After that the amount of removed material decreases. But the best results are achieved at lower intensities, because higher intensities causes a damage of the surrounding material. In the range of investigation a damage of the edges caused by removed grains could only be observed at high energy densities. Furthermore the thickness of the recast layer could be reduced down to $< 5 \mu\text{m}$. Typical holes for Al_2O_3 , ZrO_2 and diamond are shown in Fig. 5 and Fig. 6. The material properties of the recast layer, e.g. the hardness and the existence of micro cracks, have not been investigated due to the small size of the holes. It is possible that due to the thermal shock behaviour of ceramics a small layer of damaged material could exist under the recast layer. Investigations with shorter pulse length show no significant advantage [9]. At higher energy densities also laser pulses in the fs-range can cause a material damage. So the machining quality is dependent on the maximum pressure of the vaporized material. The pulse length influences only the amount of molten material.

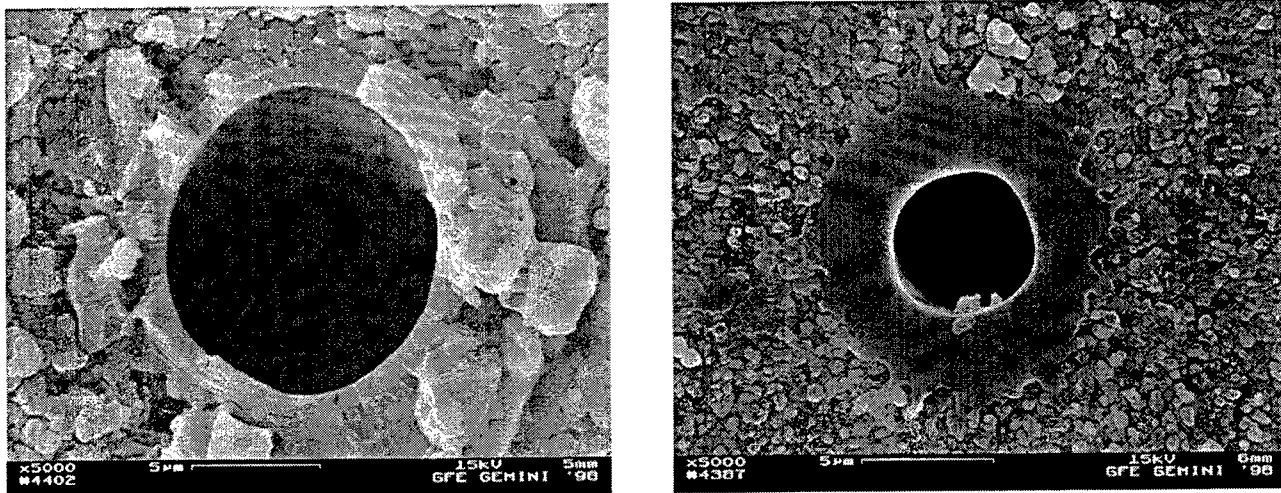


Fig. 5: Hole in Al_2O_3 (thickness $250 \mu\text{m}$): entrance (left) exit (right) ($\lambda = 355\text{nm}$, $f_p = 5 \text{ kHz}$, $E_p = 0.22 \text{ mJ}$)

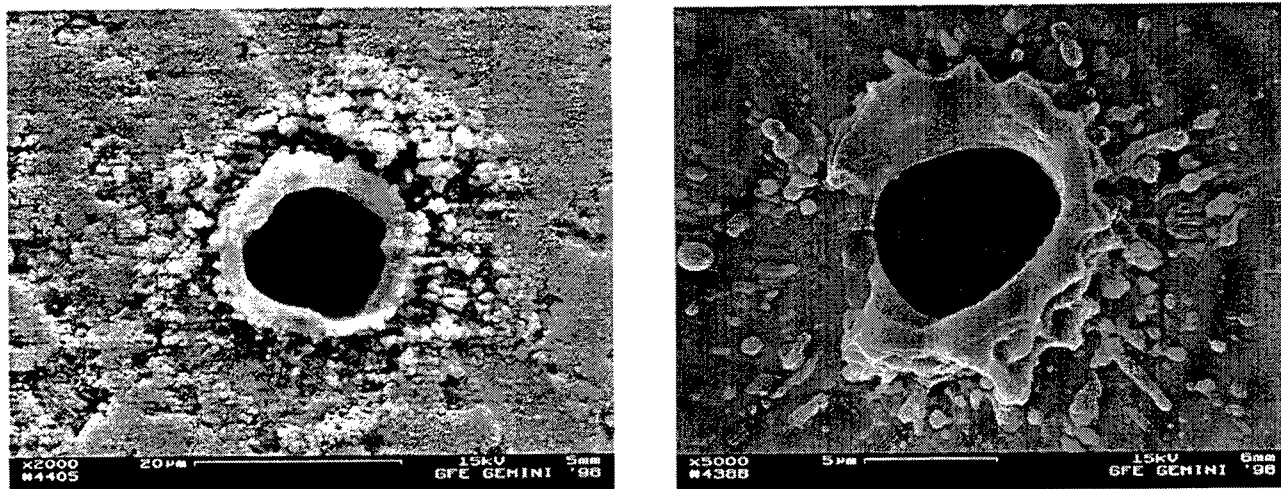


Fig. 6: Hole in ZrO_2 (thickness $250 \mu\text{m}$): entrance (left) exit (right) ($\lambda = 355\text{nm}$, $f_p = 5 \text{ kHz}$, $E_p = 0.23\text{mJ}$)

To produce larger diameters the holes have to be trepanned. Therefore the laser beam is guided over the workpiece several times along the cutting line. Fig. 7 shows the cut edges of Si_3N_4 and diamond. The cut edges are very smooth. For both materials no molten material can be detected. The cutting speed is about $100 \mu\text{m/s}$.

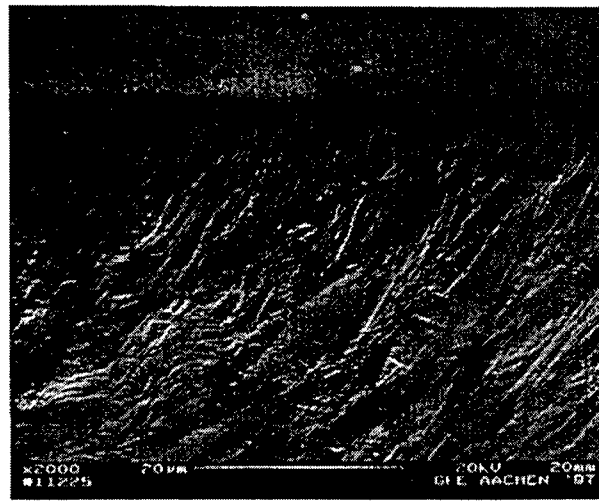
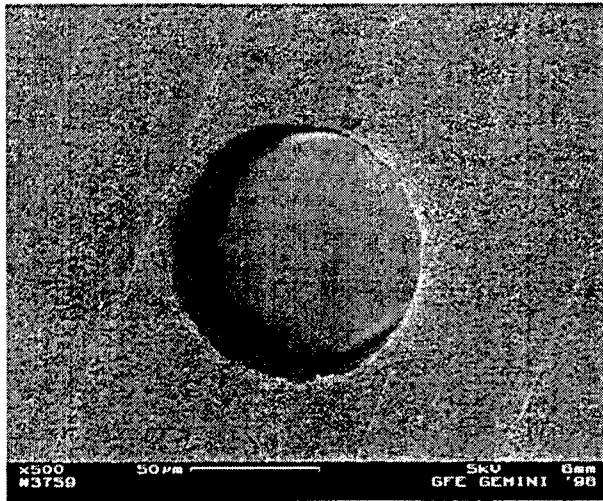


Fig. 7: Cut edge of Si_3N_4 ($\lambda = 355\text{nm}$, $f_p = 5\text{ kHz}$, $E_p = 0.34\text{mJ}$) and polycrystalline diamond ($\lambda = 355\text{nm}$, $f_p = 5\text{ kHz}$, $E_p = 0.34\text{mJ}$)

5. 3D-MICROSTRUCTURING

To produce 3-dimensional microstructures with a direct writing laser beam removal process a relative movement between the laser beam and the workpiece is necessary, which is realized in most cases by straight lines. Several lines side by side produce a removed layer. For a 3-dimensional microstructure the geometry is sliced into several layers comparable to a milling process. This can be done by a CAD/CAM-software. The average depth of a single layer is a needed parameter for the calculation of the toolpath. After removing each layer, the exact depth of the layer is measured with the white light sensor and compared with the desired value. Any deviation can be adjusted by varying the process parameters or recalculating the toolpath. In this way very precise microstructures are produced.

The depth of a single layer and the resulting roughness of the surface depend on the overlap of the single laser pulses. This overlap is defined as

$$O = \left(1 - \frac{m}{d_w}\right) \cdot 100\%$$

with: O = overlap [%]
 m = movement of the axis between two laser pulses
 d_w = effective working diameter of the laser beam

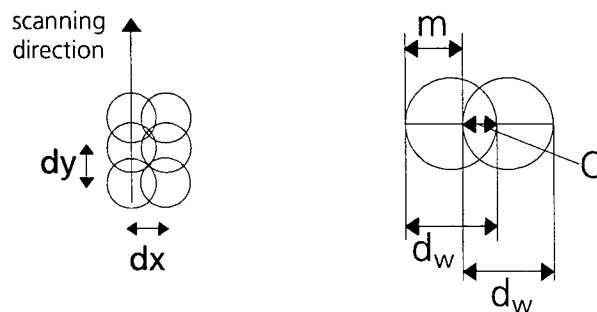


Fig. 8: Definition of the overlap

At an overlap of 30-50 % a good surface roughness can be achieved. Out of this range the roughness increases steep [5]. Furthermore the energy density influences the depth of a single layer and the roughness. The surface roughness increases at higher aspect ratios of a single pulse mould (removal depth of a single laser pulse in comparison to the effective working diameter). A periodic wavy surface is the result, where the period of these waves is not a function of the grid of the laser pulses. Figure 9 shows the surface of ZrO_2 , where the spatial distance between two laser pulses was $10\text{ }\mu\text{m}$ and the period of the waves is around $40\text{ }\mu\text{m}$.

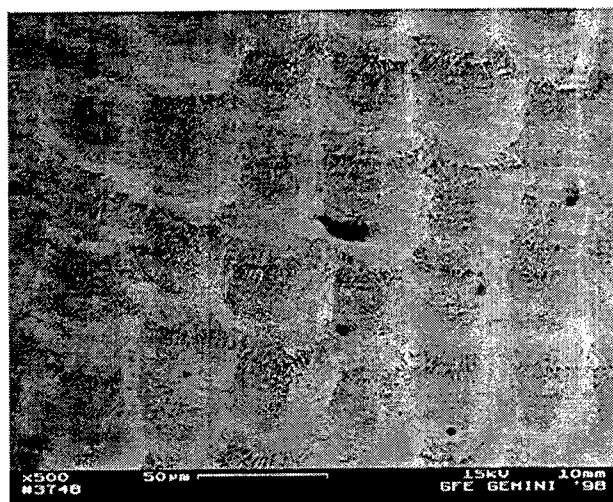


Fig.9: Structure of ZrO_2 surface ($\lambda = 355\text{nm}$, $f_p = 5\text{ kHz}$, $E_p = 0.26\text{mJ}$)

An optimized surface roughness can be achieved with flat removed areas, that means a low aspect ratio of the single pulse mould (see Fig.10). Especially the pyramid made of Si_3N_4 has a very good surface roughness, which is in the range of the raw material. The height of the steps is around $100\text{ }\mu\text{m}$. The quality of the edges is very good. Due to the low energy densities damage caused by removed grains could not be detected. The debris is very low and the removed material has only a very weak adhesion to the basic material, so that the structures can be cleaned in an ultrasonic bath.

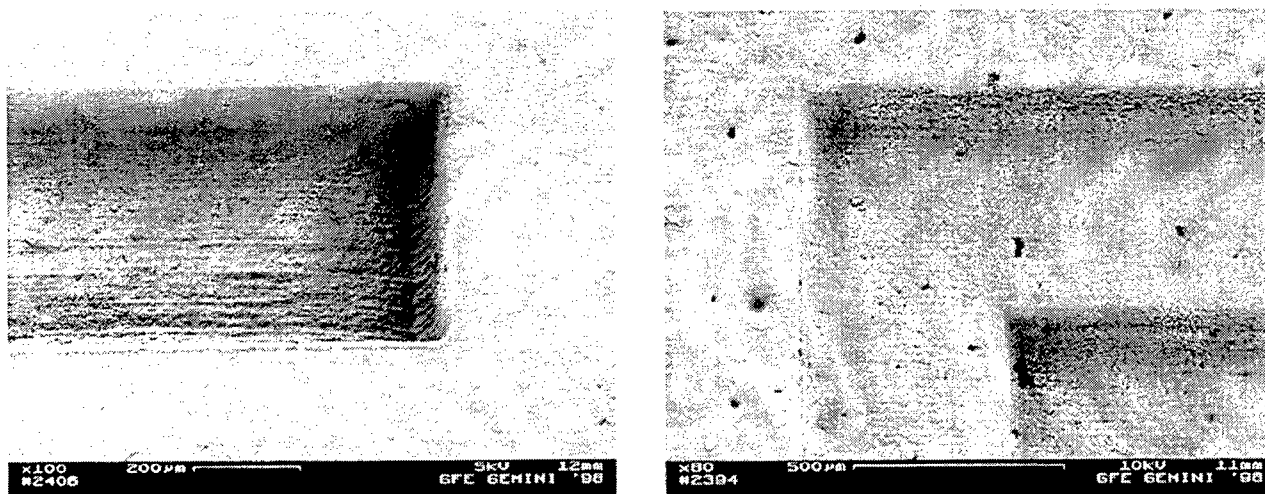


Fig.10: Surface of Al_2O_3 ($\lambda = 355\text{nm}$, $f_p = 5\text{ kHz}$, $E_p = 0.3\text{mJ}$) and Si_3N_4 ($\lambda = 355\text{nm}$, $f_p = 5\text{ kHz}$, $E_p = 0.26\text{mJ}$)

Typical values for the surface roughness and depth of a single layer as well as ablation rates are listed up in Tab. 2.

	R_a [μm]	ablation rate [mm^3/min]	depth [μm]
ZrO_2	0.6	0.01-0.015	2-4
Al_2O_3	0.3	0.02	2-5
Si_3N_4	0.5	0.1	3-20
WC	0.1	0.05	1-10

Tab. 2: Optimized surface roughness R_a , depth of a single layer and ablation rates

Compared to the combined mask and direct writing process with an Excimer-Laser, the direct writing process with a Q-Switch Nd:YAG-laser offers a higher flexibility concerning the possible shapes [10], because curved lines can be generated by the CAD/CAD-system (Fig. 11). The main restrictions are caused by the accuracy of the moving system. With this technique real three-dimensional structures can be produced. The final structures can be used as tools for the production of embossed metal micro parts.

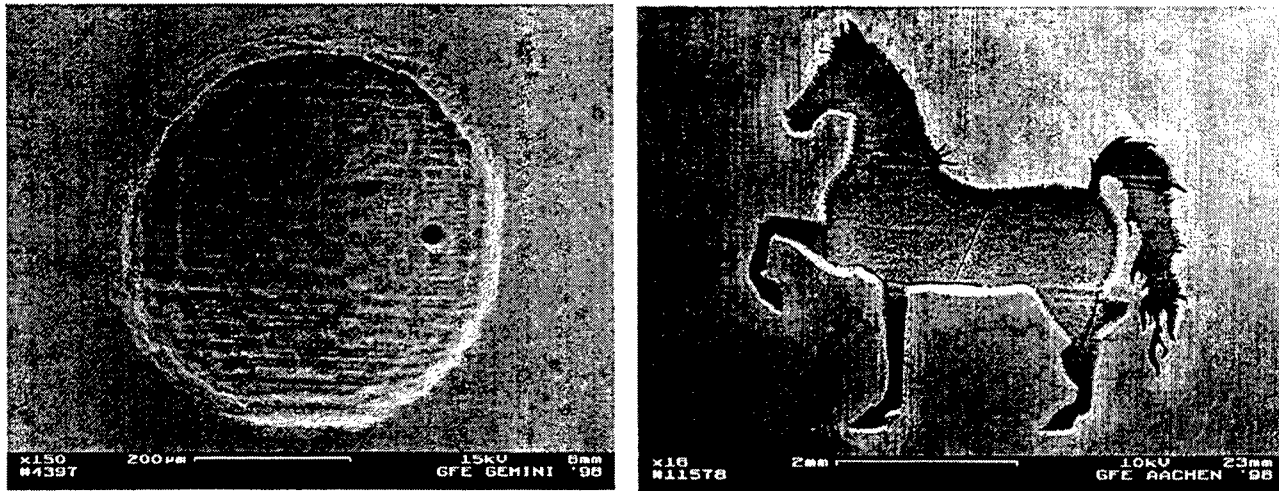


Figure 11: Structured hard metal (WC) ($\lambda = 355\text{nm}$, $f_p = 5\text{ kHz}$, $E_p = 0.34\text{mJ}$; depth = 0.1 mm resp. 1.5 mm)

ACKNOWLEDGMENTS

These investigations were financially supported by the BMBF of the Federal Republic of Germany (code number 02PV76054). The authors are responsible for the contents of this publication.

REFERENCES

1. E. Meiners, M. Wiedmaier, F. Dausinger, K. Krastel, I. Masek, A. Kessler, „Micro Machining of Ceramics by Pulsed Nd:YAG Laser“, *Proc. Laser Material Processing Symposium ICALEO'91*, pp. 327-336, San Jose, 1991
2. R. Koch, T. Schröder, U. Stamm, W. Zschocke, D. Basting, „High Average Power, High Pulse Repetition Frequency Diode Pumped UV Solid-State Laser System“, Paper CWJ5, Cleo/Europe 98, 14.-18. September 1998, Glasgow, UK
3. C. Diez, M. Jurca, „Eine Alternative zum Laser“, *Sensor Magazin* 4, 1997
4. S.S. Charschan, *Lasers in Industry*, Laser Institute of America, Toledo (Ohio), 1984

5. D. Hellrung, A. Gillner, R. Poprawe, „Laser beam removal of micro-structures with Nd:YAG-lasers“, *Proc. Lasers in Material Processing Laser '97, SPIE 3097*, pp. 267-273, Munich, 1997
6. J. Jandeleit, G. Urbasch, D. Hoffmann, H.G. Treusch, E.W. Kreutz, „Mikrostrukturierung von Metallen und Halbleitern durch ultrakurze Laserimpulse“, *Proc. Laser in Research and Engineering, Laser '95*, pp.947-950, Munich, 1995
7. K. Dickmann, C. Lammers, J. Hildenhagen, R. Thiemann, „Mikrostrukturierung von Keramik-Spinndüsen mit Excimer-Laser und hochqualitativem Abbildungssystem“, *Laser und Optoelektronik* **30**(6), pp. 56-63, 1998
8. H. Rhode, F. Dausinger, „The Forming Process of a Through Hole Drilled with a Single Laser Pulse“, *Proc. Laser Material Processing Symposium ICALEO '95*, pp. 331-340, San Diego, 1995
9. J. Kaspar, A. Luft, „Electron Microscopic investigation of Structural Changes in Single Crystalline Silicon Induced by Short Pulse Laser Drilling“, *Proc. Micro Materials*, pp. 539-542, Berlin, 1997
10. H. K. Tönshoff, J. Mommsen, „Process of generating three-dimensional microstructures with excimer lasers“, *Proc. ECLAT'92*, Göttingen, 1992

UV-laser ablation of ultrathin dielectric layers

K. Rubahn^a, J. Ihlemann^a, F. Balzer^b, H.-G. Rubahn^c

^a Laser Laboratorium Göttingen e.V., Hans-Adolf-Krebs-Weg 1, D-37077 Göttingen, Germany

^b present address: Stanford University, Chemistry Department, Stanford, CA 94305-5080, USA

^cMax-Planck-Institut für Strömungsforschung, Bunsenstr. 10, D-37073 Göttingen, Germany

ABSTRACT

Ablation yields and thresholds for 193 nm UV laser ablation of ultrathin HfO₂ layers on bulk SiO₂ are presented. The single shot threshold fluence increases approximately linearly with HfO₂ thickness from 28 nm to 120 nm. Due to the logarithmic dependence of ablation depth on fluence this results with increasing layer thickness in an exponential increase of fluence necessary for clean ablation of the whole layer. The observed ablation depth for fixed HfO₂ thickness can be reproduced phenomenologically by taking ablation from the HfO₂ film as well as the quartz substrate into account. As a first approach to a quantitative understanding we calculate numerically the heat evolution in the layered system and identify ablation with the onset of melting of the absorbing layer. Whereas the ablation curve for a 74 nm thick film can be reproduced that way, this is not the case for the overall thickness dependence of the ablation threshold. This points to possible finite size effects for the phonon-phonon scattering rate in the thin dielectric layers.

Keywords: UV laser ablation; dielectrics; thin films

1. INTRODUCTION

UV laser ablation of dielectric films holds promises as a technological relevant method for the generation of ultrathin structures with a lateral dimension in the micrometer range. For example, recently UV laser ablation of highly reflective HfO₂/SiO₂ dielectric layer stacks on quartz substrates has been reported.^{1,2} In a subsequent step these structured mirrors are used as masks for UV-light to generate well-defined ablation patterns in polymers and quartz. As the layer thickness for interference mirrors is dictated by the wavelength at which high reflectivity is achieved, the primordial laser ablation step has to be optimized as a function of HfO₂ layer thickness. This in turn would enable one to generate in a controlled fashion masks for various wavelengths of light.

In the present work we study 193 nm ablation yields and thresholds for the ablation of ultrathin HfO₂ layers on bulk SiO₂, the HfO₂ thickness ranging between 28 nm and 120 nm. We note that such kind of systematic studies of laser ablation of ultrathin films have concentrated on ultrathin metal films in the past.³ There, a linear dependence between ablation threshold and film thickness was observed as long as the thickness was small compared with the thermal diffusion length L , but larger than $1/\alpha$ ("surface heating source"). Then the visible damage threshold was well described by invoking thermal material constants in order to determine the critical energy density for melting to occur.^{3,4}

For dielectric films (*i.e.*, optical coatings) correlations between laser damage and thermal properties of the coating material have also often been invoked. Due to the largely different methods of film preparation these results did not provide an unique picture. Measurements of the thermal properties of the films show that the thermal conductivity K of thin films is between one and two orders of magnitude lower as compared with the conductivity of the corresponding bulk material.⁵⁻⁷ Due to the resulting concentration of absorbed laser light in the focus region, this lower conductivity is assumed to result in a lower damage threshold (*i.e.*, the temperature increase $\Delta T \propto 1/K$). For HfO₂ and thicknesses larger than 260 nm the thermal conductivity was found to be independent of film thickness.^{5,7} In the present work we use films with thicknesses $d_{film} \leq \lambda_{ph}$, where the phonon mean free pathlength λ_{ph} is of order 100 nm, as estimated by comparison with values for other oxides such as Al₂O₃.⁸ In that case the thermal conductivity might well increase (linearly) with thickness, which would result in an increase of damage threshold with thickness.

E-mail: hrubahn@gwdg.de

As seen from a comparison of the data for metal films an important dimension for the present systems is given by the thermal diffusivity κ of the thin films, which results in a thermal diffusion length $L = 2\sqrt{\kappa\tau}$, over which the initially absorbed energy is smeared out during the laser pulse length τ . If one uses the most probable value of K_{HfO_2} for HfO_2 thin films (however, $d_{film} \gg \lambda_{ph}$!), which is $K_{HfO_2} = 0.052$ W/mK,⁵ and the bulk value for the thermal capacity c_p , then $\kappa_{HfO_2} = 2.1 \cdot 10^{-4}$ cm²/s. For a laser pulse of length 18 ns, this results in $L = 40$ nm, which is at the lower end of the presently investigated range of thickness values. Finally the absorption depth $1/\alpha$ is important. For the two differently prepared dielectric films used in the present work, namely electron beam evaporated ("BAK") and ion assisted sputtered ("APS") these depths amount to 185 nm and 106 nm, respectively, due to the slightly different absorption coefficients. The band gap of HfO_2 is $E_g = 6.5$ eV, which should facilitate single photon absorption at $\lambda = 193$ nm ($h\nu = 6.42$ eV) and room temperature samples.

Obviously, the film thickness in the present case is of the same order as the absorption depth, but also of the same order or larger than the thermal diffusion length. By comparison with the result for thin metal films we would expect to observe no thickness dependence of the ablation threshold in that case. In the following we present the observed characteristic dependencies of the ablation process on the thickness of the dielectric layers and compare our results with data obtained by numerically solving the heat transfer equation for the layered systems.

2. RESULTS

The samples are irradiated under normal incidence by an ArF excimer laser (LPX 315, $\lambda = 193$ nm) from the side of the dielectric HfO_2 layers. Only the homogeneous part of the laser beam behind a rectangular aperture made of four steel blades is applied to the sample. Imaging with a 100 mm focal length quartz lens results in a rectangular spot of typical 180×90 μm^2 size. The generated structures are examined for topographic quality via scanning electron microscopy (SEM) and for depth via stylus profilometry. The energy density of the laser light is determined in a shot-by-shot fashion by reflecting part of the laser beam via a quartz plate onto a UV sensitive photodiode.

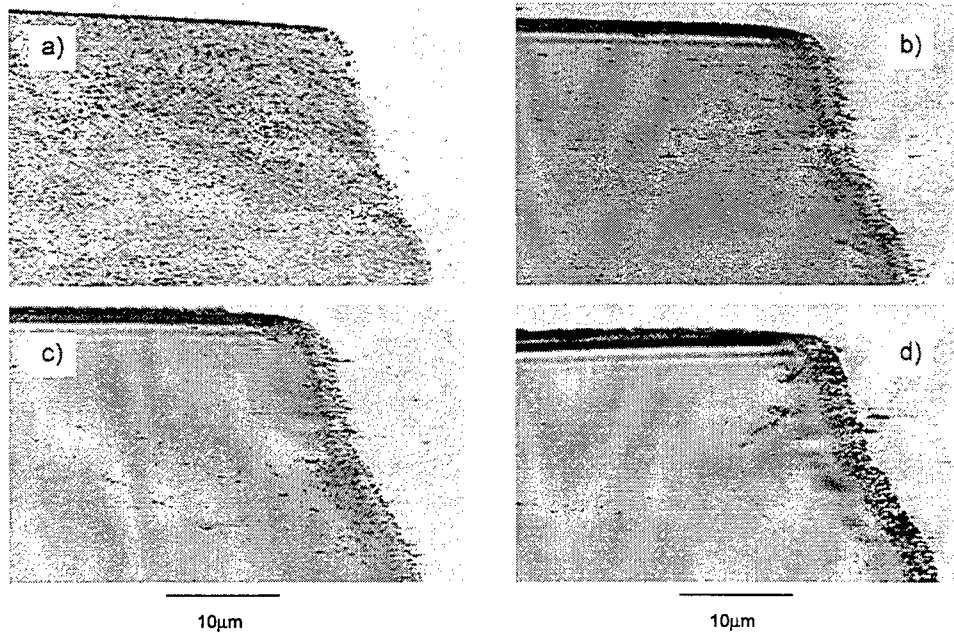


Figure 1. SEM pictures of 74 nm HfO_2 on SiO_2 samples, irradiated by 1.55 J/cm² (a), 3.5 J/cm² (b), 4.6 J/cm² (c) and 7.8 J/cm² (d). The measured depths of the ablation holes are 21.3 nm (a), 73.7 nm (b), 78.7 nm (c) and 133.5 nm (d).

Fig. 1 shows SEM pictures of 74 nm thick HfO_2 layers, which are irradiated with increasing fluence from Fig. 1a to Fig. 1d. All pictures have been taken at an angle of 75° with respect to the electron beam. With fluences close to the ablation threshold (Fig. 1a) a very rough ablated area (arithmetic roughness $R_a = 3.2$ nm over $100\mu\text{m}$) is observed with clear hints for melting. Stylus profilometry results in a depth of ablation of 21.3 nm, *i.e.*, well below the HfO_2 film thickness. At 3.5 J/cm^2 (Fig. 1b) the HfO_2 film has been totally ablated (measured depth 73.7 nm) and the roughness is small ($R_a = 0.9$ nm). We call the fluence necessary for that kind of ablation "optimum fluence" F_{opt} . With further increasing fluence the ablated depth stays approximately constant (measured depth 78.7 nm for 4.6 J/cm^2 (Fig. 1c)), but the roughness is strongly increasing ($R_a = 4.7$ nm in Fig. 1c), until material from the quartz substrate becomes ablated. At 7.8 J/cm^2 the measured depth is 133.5 nm with $R_a = 7.8$ nm. From SEM pictures of that kind we conclude that a precise knowledge of that fluence that leads to ablation of the right depth also results in smooth ablation patterns.

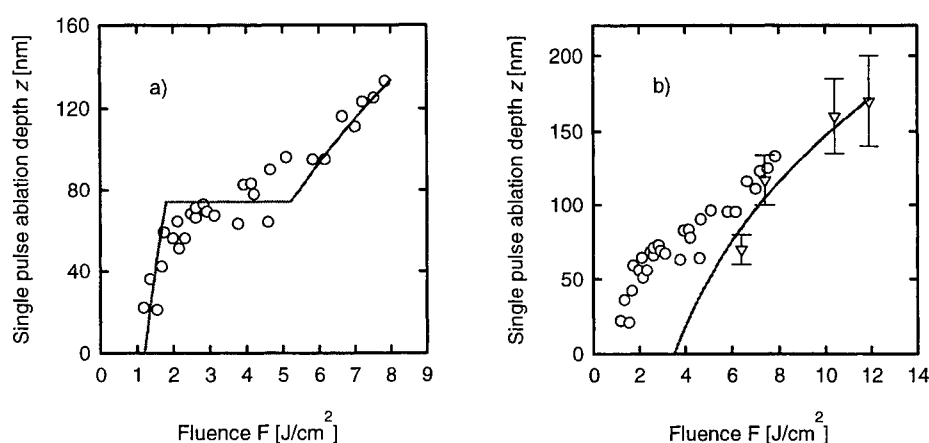


Figure 2. a) Ablation depths for BAK prepared HfO_2 layers (thickness 74 nm) as a function of 193 nm fluence. The solid line is a fit curve assuming logarithmic fluence dependences of ablation rates in HfO_2 and quartz substrate; see text. b) Circles: ablation depths for HfO_2 , triangles: ablation depths for quartz. The solid line is a logarithmic fluence dependence of 193 nm ablation from quartz with $1/\alpha_{eff} = 140$ nm and $F_{thr} = 3.5 \text{ J/cm}^2$.

The measured single pulse ablation depths z are plotted as a function of laser fluence for the 74 nm thick HfO_2 film (BAK made) in Fig. 2. Ablation up to the film thickness can be fitted well with a logarithmic fluence dependence $z = 1/\alpha \cdot \ln(F/F_{thr})$. Using the above noted $1/\alpha$ values we obtain as a fitting parameter the threshold fluence F_{thr} , which in that case is 1.2 J/cm^2 . The solid line in Fig. 2a is calculated using this logarithmic depth dependence up to the thickness of the HfO_2 layer and being constant for higher fluences. In addition to ablation of HfO_2 , ablation from the underlying quartz substrate has been taken into account. For that purpose ablation depths as a function of laser fluence have been determined via stylus profilometry (triangles in Fig. 2b) from the same sample substrate but without the HfO_2 film. As seen, they also obey a logarithmic fluence dependence, albeit with a higher threshold of 3.5 J/cm^2 and an effective absorption coefficient α_{eff} that it is not equal to the linear absorption coefficient α . Next we have used this quartz ablation curve to reproduce the experimentally measured curve in Fig. 2a for the $\text{HfO}_2/\text{SiO}_2$ system. The total ablation depth for fixed fluence is given as ablated thickness of the HfO_2 film (constant value as soon as the film thickness has been ablated) plus ablated quartz thickness. The latter value takes into account that the HfO_2 film reduces the effective fluence at the quartz layer to 67% of the initial value (as determined from HfO_2 thickness and absorption coefficient). With this procedure, the overall agreement between measurement and calculation is quite satisfactory.

In the following Fig. 3 we present data from a systematic investigation of the ablation behaviour of various HfO_2 films of different thicknesses. The solid lines are logarithmic fit curves providing values of the single pulse threshold fluences. Those values are plotted in Fig. 4a as a function of HfO_2 layer thickness for the BAK sample. In Fig. 4b

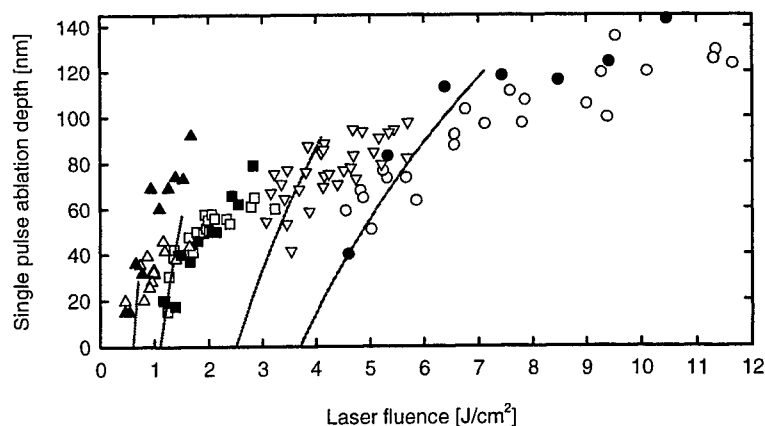


Figure 3. Fluence dependence of single pulse ablation depths for BAK (open symbols) and APS (filled symbols) prepared samples of HfO_2 of thickness 28 nm (Δ), 55 nm (squares), 86 nm (∇) and 120 nm (circles) on SiO_2 substrates. The solid lines are logarithmic fluence dependences with threshold fluences 3.7 J/cm^2 (120 nm), 2.5 J/cm^2 (86 nm), 1.1 J/cm^2 (55 nm) and 0.6 J/cm^2 (28 nm).

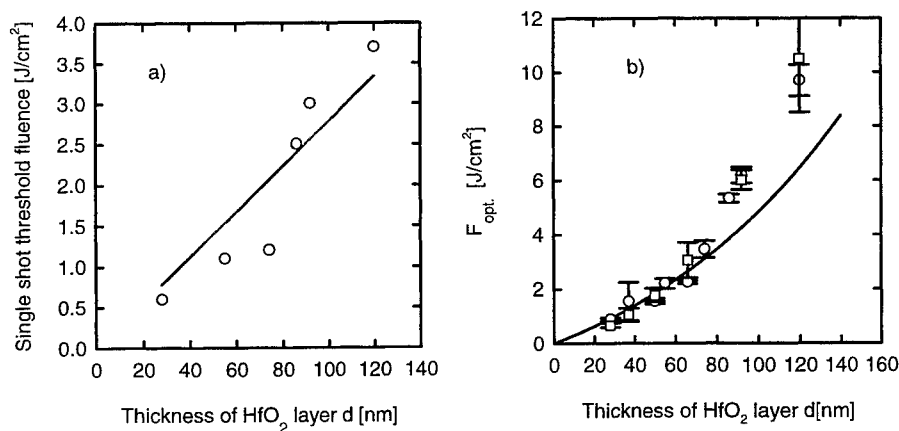


Figure 4. a) Single pulse threshold fluence, derived from Fig. 3 as a function of HfO_2 layer thickness. The solid line is a least squares fit. b) Threshold fluence for optimum layer ablation for BAK (\circ) and APS (squares) films. The solid line is a prediction assuming the linear thickness dependence of 4a.

we plot the optimum fluence values F_{opt} as a function of layer thickness for BAK (circles) and APS (squares) made samples. The solid line is a curve that takes into account the linear thickness dependence presented in Fig. 4a by the linear fit curve $F_{thr}[\text{mJ/cm}^2] = 28 \cdot d [\text{nm}]$, while assuming again a logarithmic dependence of ablated mass on fluence; i.e., $F_{opt} = 28 \cdot d \exp(d/d_{eff})$ with $d_{eff} = 1/\alpha$. As seen, if one accepts the thickness dependence of the single shot threshold, then the thickness dependence for the removal of the total layer is a direct consequence. The deviation between measurements and predictions at high fluences above 6 J/cm^2 might be due to the onset of plasma shielding effects. In addition, there appears to be a non-monotonic step around 80 nm thickness in Fig. 4a that cannot be explained by our simple models.

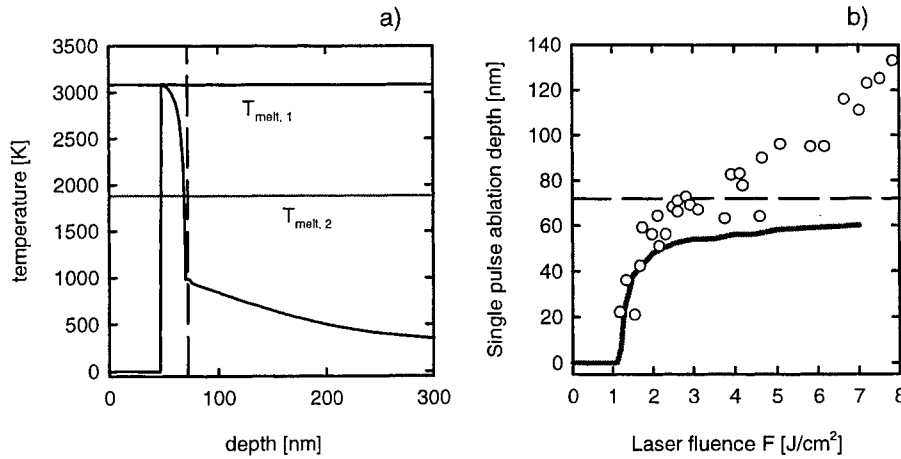


Figure 5. a) Calculated temperature as a function of depth in the layered system at the end of the laser pulse for 74 nm HfO₂ on SiO₂ and a fluence of 2 J/cm². The dashed line denotes the thickness of the HfO₂ layer and $T_{\text{melt},1}$ and $T_{\text{melt},2}$ are the melting temperatures of HfO₂ and SiO₂, respectively. b) Theoretical ablation curve for the 74 nm film in comparison with experimentally determined values. The dashed line denotes the thickness of the HfO₂ film.

Note that within error bars we do not observe differences between BAK and APS prepared samples (open and filled symbols in Fig. 3). Since the method of deposition does not alter significantly the thin film conductivity but affects the interfacial thermal resistance,⁵ this observation suggests that absorption of laser light within the film dominates F_{opt} and not interface properties.

3. NUMERICAL MODEL

We model the ablation process by solving numerically the three-dimensional heat equation for the layered system by the method of finite differences.⁹ The 193 nm laser light is absorbed with an absorption coefficient of $\alpha_{\text{HfO}_2} = 5.4 \cdot 10^4 \text{ cm}^{-1}$. For the quartz substrate ($E_g = 7.8 \text{ eV}$), $\alpha_{\text{SiO}_2} \approx 3 \cdot 10^{-2} \text{ cm}^{-1}$,¹⁰ which we set zero to first approximation. We implement the values of K_{HfO_2} and κ_{HfO_2} given above as well as $K_{\text{SiO}_2} = 1.38 \text{ W/mK}$ and $\kappa_{\text{SiO}_2} = 5.9 \cdot 10^{-3} \text{ cm}^2/\text{s}$. The melting enthalpy for HfO₂ is 17 kcal/mol. The thermal constants are valid for $T = 300 \text{ K}$, but depend strongly on temperature. For bulk SiO₂ the temperature dependences of K_{SiO_2} and κ_{SiO_2} are taken from.¹¹ In view of the fact that at least up to 500 K the temperature dependencies of the thermal conductivities of SiO₂ and HfO₂ thin films are very similar,¹² we use the scaled temperature dependence of SiO₂ for HfO₂, too.

Fig. 5a shows the calculated temperature as a function of depth in the substrate for a 74 nm HfO₂ film and fluence 2 J/cm² immediately after the end of the ablation pulse. Note that the melting temperature of HfO₂ is 3083 K, whereas that of SiO₂ is about 1900 K. As a first approach to the complex ablation behaviour and in view of the SEM pictures we assume that the dielectric film at least has to melt before getting ablated.³ Once the melting temperature has been reached we assume instantaneous ablation, take the loss in melting enthalpy into account and calculate the further evolution of temperature through the system. Hence for the Fig. 5a ablation has occurred over the range where the temperature is zero. Resulting theoretical curves of ablation yield vs. fluence are demonstrated exemplary in Fig. 5b for the 74 nm film. The agreement between experimental data and theoretical curve is good except for an offset of the values of ablation depth close to the film thickness. This might be interpreted as being due to the higher conductivity of the quartz substrate, which decreases the temperature at the interface for given laser fluence. A possible criterion for "optimum" ablation then would be that the melting temperature has been reached at the interface between HfO₂ film and SiO₂ substrate. However, the F_{opt} values calculated that way as a function of film thickness are nearly independent of film thickness, in agreement with the predictions for metal films,³ but in strong contrast with the experimental observations (Fig. 4b).

Possible explanations for this disagreement include part of the energy getting lost in channels that have not been taken into account in the calculation such as plume absorption, or the thermal constants of HfO_2 depending on the film thickness. The permanent increase of threshold fluence with film thickness in the range below and above $\lambda/4$ in Fig. 4a rules out a strong influence of optical interference effects on the ablation characteristics of the thin film system. As noted already in the Introduction, in the present thickness regime the thermal conductivity could well increase with thickness, which would result in a much stronger increase of damage threshold with thickness compared with that expected from the simple thermal absorption mechanism discussed above. Thus from a comparison of calculated with measured values of optimum threshold fluence as a function of film thickness one might deduce the change in thermal conductivity with film thickness.

4. CONCLUSIONS

Ablation yields for 193 nm UV laser ablation of ultrathin HfO_2 layers on SiO_2 are shown as a function of film thickness. Simultaneous scanning electron microscopy observations allow us to find values of those laser fluences that allow an optimum ablation of the total HfO_2 film. These values depend exponentially on film thickness. The yield as a function of laser fluence agrees satisfactorily with simple phenomenological considerations and also - for the 74 nm thick film - with results from a numerical calculation of the heat evolution through the system. Whereas the exact preparation conditions of the films (APS vs. BAK) seem to have no strong influence on the ablation characteristics the thicknesses of the films themselves affect directly the ablation thresholds, which then lead to the observed exponential thickness dependence of the optimum ablation fluence. The simple numerical temperature calculations which implement a thickness-independent thermal conductivity do not agree with the measured thickness dependent ablation thresholds. This indicates that the thermal conductivity in the present thickness range might depend on film thickness.

ACKNOWLEDGMENTS

We are grateful to the coating department of the Fraunhofer Institute, Jena, for preparation of the dielectric coatings. Partial financial support by the BMBF under contract No.13N6925 is also gratefully acknowledged.

REFERENCES

1. J. Ihlemann and B. Wolff-Rottke, "Excimer laser ablation patterning of dielectric layers," *Appl.Surf.Sci.* **86**, pp. 228 - 233, 1995.
2. K. Rubahn and J. Ihlemann, "Graded transmission dielectric optical masks by laser ablation," *Appl. Surf. Sci.* **127 - 129**, pp. 881 - 884, 1998.
3. E. Matthias, M. Reichling, J. Siegel, O. Käding, S. Petzoldt, H. Skurk, P. Bizenberger, and E. Neske, "The influence of thermal diffusion on laser ablation of metal films," *Appl. Phys. A* **58**, pp. 129 - 136, 1994.
4. J. Siegel, K. Ettrich, E. Welsch, and E. Matthias, "UV-laser ablation of ductile and brittle metal films," *Appl.Phys.A* **64**, pp. 213 - 218, 1997.
5. J. Lambropoulos, M. Jolly, C. Amsden, S. Gilman, M. Sinicropi, D. Diakomihalis, and S. Jacobs, "Thermal conductivity of dielectric thin films," *J.Appl.Phys.* **66**, pp. 4230 - 4242, 1989.
6. C. Henager,Jr. and W. Pawlewicz, "Thermal conductivities of thin, sputtered optical films," *Appl.Opt.* **32**, pp. 91 - 101, 1993.
7. M. Grilli, T. Aumann, D. Ristau, M. Dieckmann, F. Alvensleben, and E. Masetti, "Thermal conductivity of e-beam and IBS coatings," *SPIE Proceedings* **2775**, 1995.
8. N. Ashcroft and N. Mermin, *Solid State Physics*, W.B. Saunders Co., New York, 1976.
9. F. Balzer and H.-G. Rubahn, "Size effects and the determination of absolute temperature increases in laser heating of dielectrics," *Chem. Phys. Lett.* **233**, pp. 75 - 80, 1995.
10. E. Eva and K. Mann, "Calorimetric measurement of two-photon absorption and color center formation in UV-window materials," *Appl.Phys.A* **62**, pp. 143 - 150, 1996.
11. Y. Touloukian and C. Ho, eds., *Thermophysical Properties of Matter*, vol. 1, 3 und 10, IFI/Plenum, New York, 1970 - 1973.
12. S.-M. Lee, D. Cahill, and T. Allen, "Thermal conductivity of sputtered oxide films," *Phys.Rev.B* **52**, pp. 253 - 257, 1995.

Micromachining of glass materials by laser-induced plasma-assisted ablation (LIPAA) using a conventional nanosecond laser

Jie Zhang*, Koji Sugioka, Katsumi Midorikawa

Institute of Physical and Chemical Research (RIKEN), Wako, Saitama, 351-01, Japan

ABSTRACT

We report precision micromachining of fused quartz and Pyrex glass by laser-induced plasma-assisted ablation (LIPAA) using a conventional nanosecond UV (248nm or 266nm) or visible (532nm) laser. High-quality micrograting structures with periods of 1.06 and 20 μ m using a phase mask and a mask projection technique, respectively were fabricated by LIPAA. The Fresnel zone pattern was also produced in fused quartz. The hole with the size of 700 μ m in diameter was fast drilled in fused quartz and Pyrex glass. A possible ablation mechanism was discussed based on the dependence of ablation rate and ablation threshold of laser fluence on the distance between metal target and glass substrate.

Key words: Micromachining, Laser ablation, plasma and fused quartz

1. INTRODUCTION

It is well-known that fused quartz and related silicate glass are one of the most important materials in the fields of optoelectronics and microelectronics, due to their high transmission from UV to IR, high hardness values, excellent thermal properties, high electrical insulation and high chemical stability. On the other hand, such excellent properties make precision microfabrication of the materials with high speed difficult, though development of the fabrication technique is strongly demanded in various industrial fields. Reactive ion etching (RIE) is the most popular method for micrometer size machining of glass. However, RIE requires a resist process based on photolithography, and the etched rate is as small as several Angstrom per second¹. Recently, much attention has been paid to pulsed laser ablation as a powerful tool for surface micropatterning and structuring of materials². Laser ablation has a large number of advantages for micromachining; it is a single-step process, has high flexibility, direct patterning without the resist process, high etch rate, and unnecessary of etchants. Usually nanosecond (ns) UV lasers, such as excimer (193 and 248nm) and higher orders of

harmonics of Nd⁺: YAG (213, 266 and 355nm) lasers, which are commercially available and provide large pulse energy, are widely used for ablation. It is generally known that the laser beam must be strongly absorbed by the materials to achieve high-quality ablation and that ablation of transparent materials generates severe damage and cracks^{3, 4}. Due to the wide band gap (9.0eV) and the large bond strength (9.3eV), high quality ablation of pure fused quartz has not been realized by use of a ns laser. Thus, the use of either a short wavelength in the VUV region or a short pulse width in the sub-picosecond range has been first attempted⁵⁻⁸, while such lasers have many difficulties for practical use, i.e., small pulse energy, high photon cost, and difficult optics for micropatterning. In fact, for research as well as industrial purposes the development of precision microfabrication techniques using a conventional nanosecond laser is desirable. Thus, new ablation methods, based on tripartite-interaction-system of laser, fused quartz and another medium were developed. Table 1 lists a summary of recent reports about the micromachining of fused quartz by use of ns laser.

In this paper, we report precision micromachining of fused quartz and Pyrex glass by laser-induced plasma-assisted ablation (LIPAA) using a conventional nanosecond UV or visible laser. Additionally, the interesting applications of LIPAA method in optical elements are demonstrated.

* Correspondence: Email: jzhang@postman.riken.go.jp; Fax: 081-48-462-4703

Table 1. Summary of micromachining of fused quartz by Hybrid ns laser ablation

No	Hybrid ns-laser ablation of fused quartz	
1	355nm laser ablation photomachinable glass (PMG)	T. Toyama et al. ⁹
2	1.06 μ m YAG laser ablation in an inorganic solution	J. Ikeno et al. ¹⁰
3	248nm laser ablation in an organic solution	J. Wang et al. ¹¹
4	266nm-VUV(133-184nm) multiwavelength ablation	K. Sugioka et al. ⁶ ,
5	248, 266 or 532nm laser ablation assisted by laser-induced metallic plasma	J. Zhang et al. ¹²⁻¹⁴

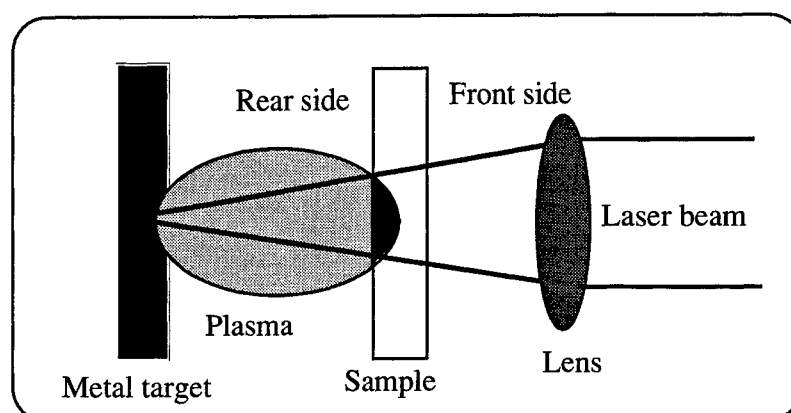


Fig. 1. Schematic diagram of the experimental principle

2. EXPERIMENTAL

Optical grade fused quartz substrates (Viosil 600mm thick, Shinetsu Quartz Co., Ltd) and normal Pyrex glass were employed in our experiments. Before beginning the experiment, the substrates were ultrasonically cleaned with trichloroethylene, acetone and ethanol, followed by rinsing with DI water. The schematic diagram of experimental principle is shown in Fig. 1. A great success in the experimental design is that a single laser beam can be used for both generation of the metal plasma and ablation on the rear side of sample. A commercial KrF excimer laser (Lambda Physik LPX-200, 248nm, 34ns) and a Q-switched Nd⁺: YAG laser (Spectra-Physics, GCR-100, 266nm and 532nm, 6ns) were used as light source both for the generation of plasma from a metal target and ablation of fused quartz. The KrF laser beam is homogenized using a couple of 5x5 microlens arrays (Exitech Fly's Eye Type). The spatial uniformity of intensity is more than 95%. The repetition rate of laser irradiation is kept constant at 1Hz. The phase mask made of fused quartz manufactured by QPS Technology Inc., Canada, for a 248nm wavelength is used for fabrication of micrograting. The mask has a 1.065 μ m period and the measured energy transmissions of ~2.7% for the zero order and ~38.6% for the \pm 1st-orders for 248nm wavelength. The stencil mask possessing a period of 130 μ m is used for projection printing as well. 99.99% pure Ag and Stainless steel foils were used as target for plasma generation. The ablation process was performed in a vacuum chamber (10^{-4} Torr). After laser ablation, the samples were cleaned in an acidic solution such as HNO₃ to remove metallic residues.

3. RESULT AND DISCUSSION

3.1. Surface patterning of fused quartz

Figure 2a shows a three-dimensional SPM image of the grating fabricated in fused quartz by KrF laser ablation using the phase mask at the distance (d) of 0.2mm between metal target and sample. The laser fluence (F) and the number of laser pulses (N) are $1.3\text{J}/\text{cm}^2$ and 40, respectively. The $1.06\text{ }\mu\text{m}$ period of the grating agrees well with that of the mask. The cross-sectional profile of the grating has a sine wave-like structure with a depth of 100nm.

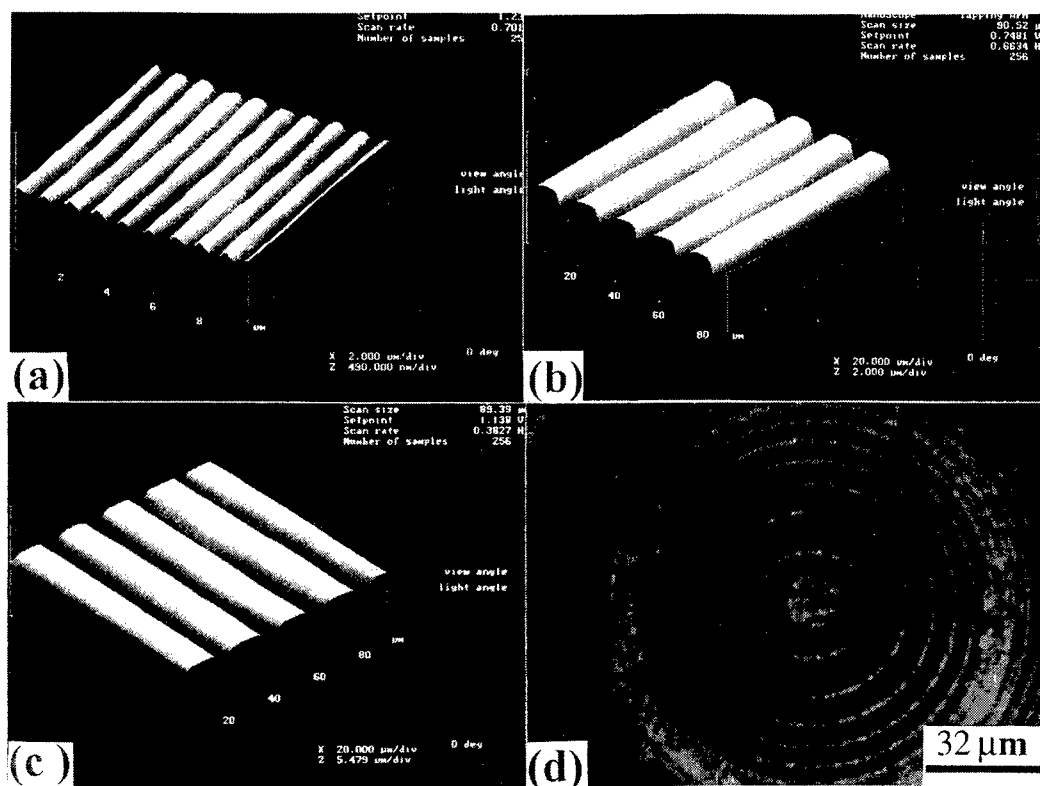


Fig. 2. Three-dimensional SPM images of grating fabricated by 248nm laser ($F=1.3\text{J}/\text{cm}^2$, $N=40$) using a phase mask at $d=0.2\text{mm}$ (a) and by 266nm ($F=1.5\text{J}/\text{cm}^2$, $N=10$) and 532nm laser ($F=4.0\text{J}/\text{cm}^2$, $N=60$) using a projection mask at $d=1.5\text{mm}$ (b, c) and two-dimensional optical image of Fresnel zone pattern by 266nm laser ($F=1.5\text{J}/\text{cm}^2$, $N=10$) at $d=1.5\text{mm}$ (d)

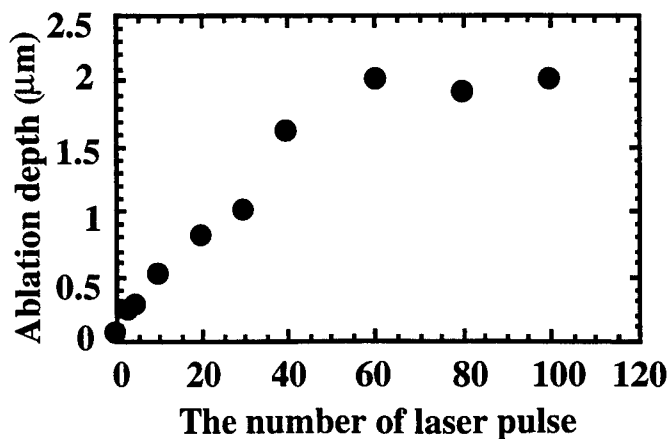


Fig. 3. The dependence of ablation depth on the number of laser pulse at $d=2.0\text{mm}$ and $F=1.5\text{J}/\text{cm}^2$.

A clean and well-defined grating structure with a period of $20\mu\text{m}$ and depths of 0.6 and $0.9\mu\text{m}$ fabricated in fused quartz using a mask projection technique at $d=1.5\text{mm}$ was also observed by 4th (266nm , $F=1.5\text{J}/\text{cm}^2$ and $N=10$) and 2nd (532nm , $F=4.0\text{J}/\text{cm}^2$ and $N=60$) harmonic $\text{Nd}^+:\text{YAG}$ laser ablation, respectively, (in Fig. 2b and c). Besides the microgratings, a Fresnel zone pattern can be also fabricated in fused quartz by 266nm laser ablation ($F=1.5\text{J}/\text{cm}^2$, $N=10$) using an in-line holography technique at $d=1.5\text{mm}$ (in Fig. 2d).

An interesting phenomena of ablation self-limitation was observed in the ablated depth as a function of the number of laser pulses (in Fig. 3). That is; the depth monotonically rises up to 60 pulses, and is then saturated around $2.0\mu\text{m}$ beyond 60 pulses. The saturation is probably due to scattering or refraction of the incident laser beams by the fabricated grating with large depth, leading to self-limitation of ablation. The ablation rate is estimated to be about $33.0\text{nm}/\text{pulse}$ at less than 60 pulses.

3.2. Hole-drilling of fused quartz and Pyrex glass

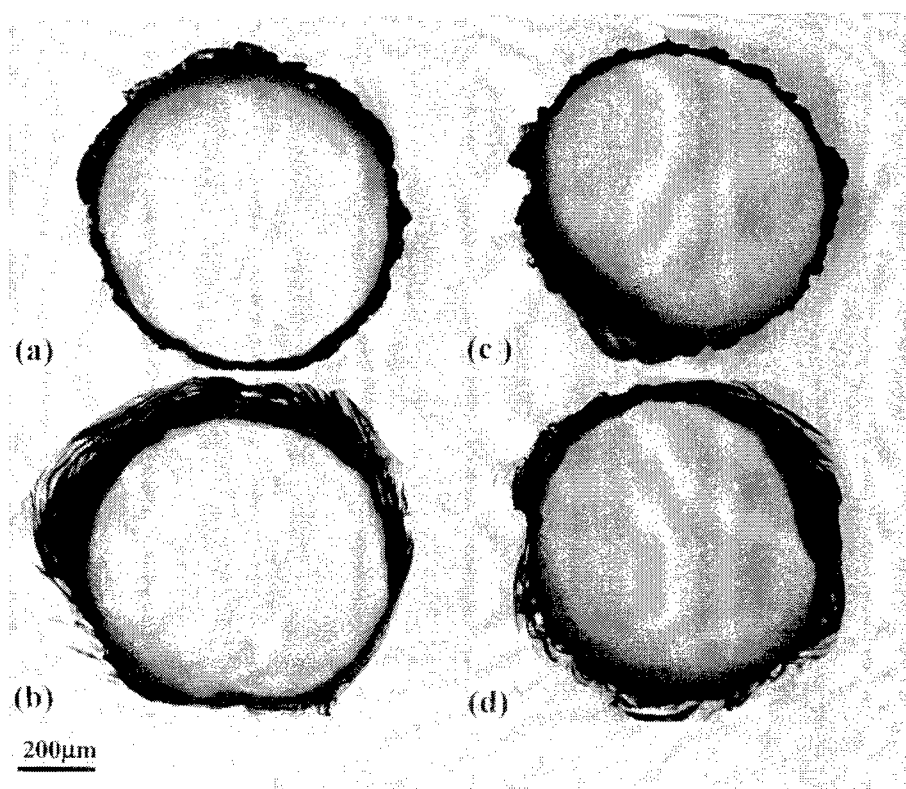


Fig. 4. Optical microscopy image of holes in fused quartz (a: rear surface, b: front surface) and Pyrex glass (c: rear surface and d: front surface) drilled by 532nm laser at $d=1.5\text{mm}$, $F=7.7\text{J}/\text{cm}^2$ and $N=300$

The through holes (about $700\mu\text{m}$ in diameter) were produced for both 0.5mm thick fused quartz and Pyrex glass by 532nm laser ablation at $d=7.7\text{J}/\text{cm}^2$ and $N=300$ (in Fig. 4.). For both fused quartz and Pyrex glass, a basically well-defined hole without large cracks was formed at the rear surface of the sample. But at the front surface, the hole is somewhat distorted with cracks. This is due to the fact that the influence of plasma on the ablated front becomes weaker as channel is being grown.

3.3. Ablation mechanism

A simple model of tripartite-interaction-system of photon ($h\nu$), energetic species (M) and substrate (SiO_2) is proposed to

understand the ablation mechanism (in Fig. 5). It was already reported that the laser produced metal plasma can expand several hundreds μm during the pulse duration, which contains high energetic species such as ions, radicals and electrons (in region *a*). The expansion continues up to several mm after pulse, which leads deposition of metal atoms on the sample surface. (in region *b*). Thus, when ablated sample is set in the region *a*, the interaction of laser, energetic species (ions, radicals, electrons) and sample takes place simultaneously to produce ablation by the first laser pulse. In this case, transfer of energy or charge to the sample surface resulting in formation of transient absorption site to the laser beam, may play the dominant role in the process. When the sample is set in region *b*, the thin metal film was first formed on the rear side of sample by the first laser pulse and then the ablation takes place by the subsequent pulse. Since the deposits may have strong absorption to the incident laser beam, heat transfer from the deposits to the sample leads the ablation¹⁵,

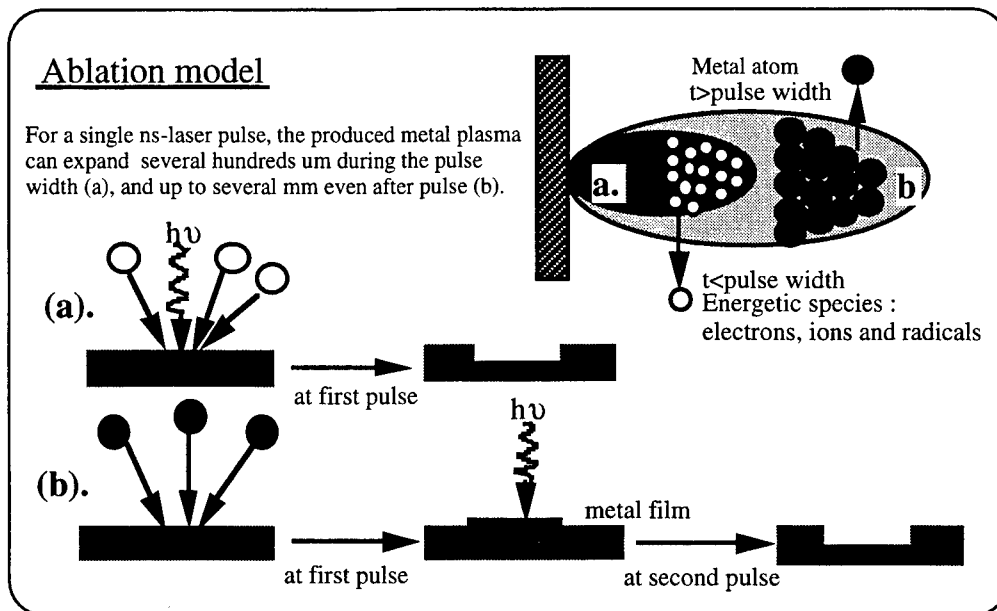


Fig. 5. A simple model of LIPAA of fused quartz

A series of experimental results from a single pulse ablation provides a direct evidence. Figure 6 shows the ablation depth produced by the first single laser pulse as a function of the distance between metal target and fused quartz substrate.

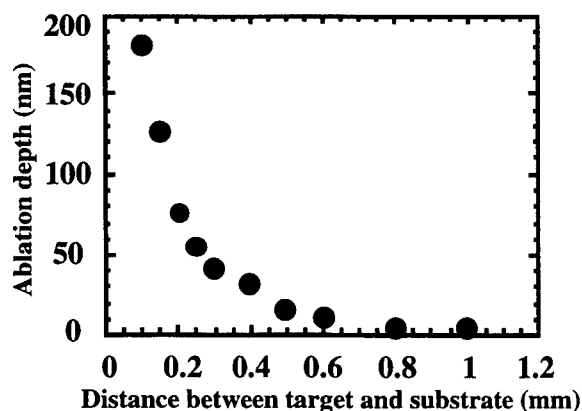


Fig. 6. The dependence of ablation depth on the distance between target and substrate at $F=6.55\text{J}/\text{cm}^2$ and $N=1$ (the first pulse).

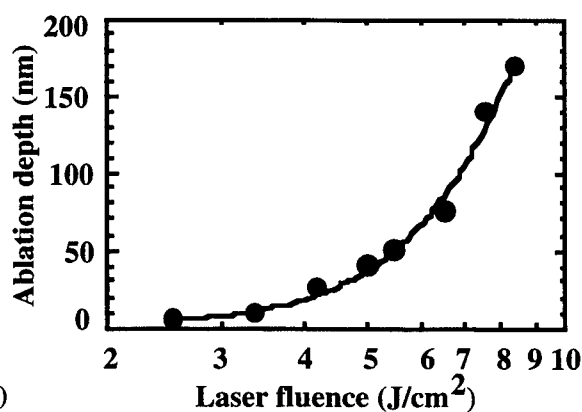


Fig. 7. The dependence of ablation depth on the laser fluence at $d=0.2\text{mm}$ and $N=1$ (the first pulse).

A ablation threshold of distance (d_{th}) of 0.6mm was obtained, which basically agrees with the expansion length of plasma. From the variation of ablation depth produced by the first pulse as a function of laser fluence, a ablation threshold of laser fluence (F_{th}) of about 3.0J/cm² was also obtained (in Fig. 7). Thus, when the distance is longer than $d_{th}=0.6$ mm or the laser fluence is lower $F_{th}=3.0$ J/cm², the ablation is produced by the second pulse. In this case, two ablation processes are expected. (1) At the shorter distance than $d_{th}=0.6$ mm and the lower laser fluence than $F_{th}=3.0$ J/cm², a compound, which is formed by the interaction between SiO₂ and the high-energetic-species produced by the first-pulse, mainly contributes to the ablation. Furthermore, the formation of the compound depends on the laser fluence on the metal target. In this case, the ablation process depends not only the laser fluence on the sample, but also that on the metal target. Thus, a nonlinear increase of ablation depth as a function of laser fluence (similar to Fig. 7) was observed, as shown in Fig. 8.

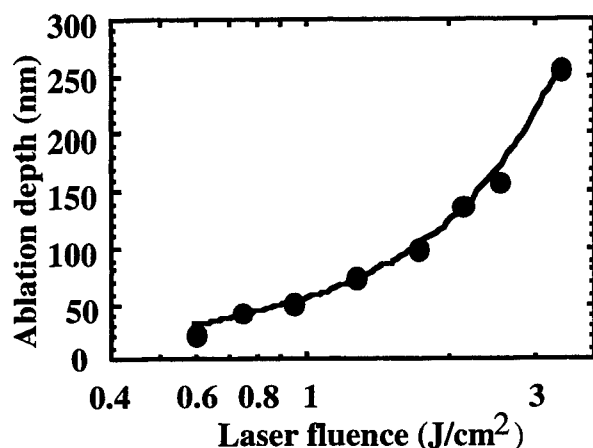


Fig. 8. The dependence of ablation depth on the laser fluence at $d=0.2$ mm and $N=2$.

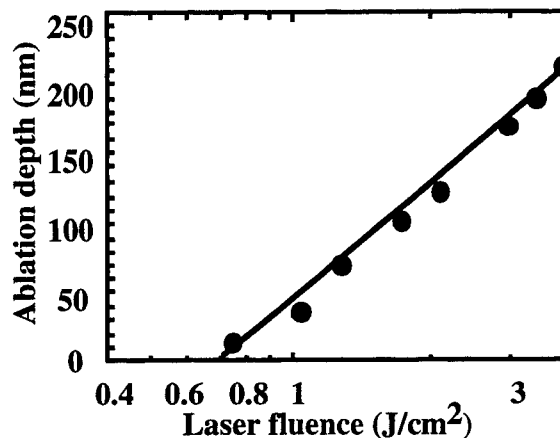


Fig. 9. The dependence of ablation depth on the laser fluence at $d=1.0$ mm and $N=2$.

(2) At the longer distance than $d_{th}=0.6$ mm and the lower laser fluence than $F_{th}=3.0$ J/cm², only the metal-deposits produced by the first-pulse mainly induce the ablation, since the energy of species in plasma at this distance may not be large enough to form the compound. In addition, a variation of deposit thickness in the range of several tens nm due to the change of the laser fluence on the metal target seems to be not effective to markedly influence the ablation process. The ablation process mainly depends on the laser fluence on the sample. Thus, a linear increase of ablation depth as a function of laser fluence at $d=1.0$ mm was observed (in Fig. 9.).

4. CONCLUSION

we demonstrate precision microfabrication optical elements in fused quartz and Pyrex glass by LIPAA technique, using conventional nanosecond lasers. The investigation on the LIPAA mechanism indicates that either energetic species in the plasma or thin metal film can induce the laser ablation of glass materials. We believe that the novel ablation technique presented here has great potential for precision microfabrication of optical elements and optoelectronic devices.

ACKNOWLEDGMENTS

J. Zhang would like to acknowledge the Japan Science and Technology Agency (STA) Fellowship for his support.

REFERENCES

1. L.M. Ephraïm, and E.J. Petrillo, "Parameter and reactor dependence of selective oxide RIE in CF₄ + H₂", J. Electrochem. Soc. 129, pp. 2282-2287 1982.
2. D. Bauerle, *Laser processing and chemistry*, (Springer-Verlag, Berlin Heidelberg), pp. 191-207, 1996.

3. B. Braren, and R. Srinivasan, "Controlled etching of silicate glasses by pulsed ultraviolet laser irradiation" J. Vac. Sci. Technol. B6, pp. 537-541, 1988.
4. J. Ihlemann, B. Wolff, and P. Simon, "Nanosecond and femtosecond excimer laser ablation of fused silica", Appl. Phys. A54, pp. 363-368, 1992.
5. P. R. Herman, K. Beckley, B. Jackson, D. Moore, T. Yamanishi, and J. Yang, "Processing application with the 157-nm fluorine excimer laser", SPIE Proc. 2992, pp. 86-94, 1997.
6. K. Sugioka, S. Wada, A. Tsunemi, T. Sakai, H. Takai, H. Moriwaki, A. Nakamura, H. Tashiro, and K. Toyoda, "Micropatterning of quartz substrates by multi-wavelength vacuum-ultraviolet laser ablation", Jpn. J. Appl. Phys. 32, pp. 6185--6189, 1993.
7. J. Zhang, K. Sugioka, S. Wada, H. Tashiro, and K. Toyoda, "Dual-beam ablation of fused quartz using 266nm and VUV laser with different delay-times", Appl. Phys. A 64, pp. 477-481, 1997.
8. H. Varel, D. Ashkenasi, A. Rosenfeld, M. Wahmer, and E. E. B. Campbell, "Micromachining of quartz with ultrashort laser pulses", Appl. Phys. A 65, pp. 367-373, 1997.
9. K. Tsunetomo, and T. Koyama, "Direct formation of a surface-relief grating on glass by ultraviolet-visible laser irradiation", Opt. Lett. 22, pp. 411-413, 1997.
10. J. Ikeno, A. Kobayashi and T. Kasai, "YAG laser processing of fused silica glass with the aid of solution", Proc. of Laser Materials Processing Conference (WG), pp. 93-98, 1997.
11. J. Wang, H. Niino, and A. Yabe, "One-step microfabrication of fused quartz by laser ablation of an organic solution", Appl. Phys. A (in press).
12. J. Zhang, K. Sugioka, and K. Midorikawa, "Laser-induced plasma-assisted ablation of fused quartz using the fourth harmonic of a YAG⁺ laser", Appl. Phys. A 67, pp. 545-549, 1998.
13. J. Zhang, K. Sugioka, and K. Midorikawa, "High-speed machining of glass materials by laser-induced plasma-assisted ablation using a 532-nm laser", Appl. Phys. A 67, pp. 499-501, 1998.
14. J. Zhang, K. Sugioka, and K. Midorikawa, "Direct fabrication of microgratings in fused quartz by laser-induced plasma-assisted ablation with a KrF excimer laser", Opt. Lett. 18, pp. 1486-1488, 1998.
15. J. Ihlemann, and B. Wolff-Rottke, "Excimer laser ablation patterning of dielectric layers", Appl. Sur. Sci. 86, pp. 228-233, 1995.

A study on laser direct dry etching of GaAs/AlGaAs multi-layer

Se-Ki Park^a, Cheon Lee^a, Eun-Kyu Kim^b

^aDept. of Electrical Engineering, Inha University, Incheon, Korea

^bSemiconductor Materials Research Laboratory, Korea Institute of Science and Technology

ABSTRACT

It has been studied the direct dry etching of GaAs/AlGaAs multi-layer using argon ion laser. To analyze etching characteristics at an interface between GaAs and AlGaAs, local temperature profiles on the surface by a laser irradiation were calculated through three dimensional heat transfer equation. Etching profiles obtained in this study were somewhat different from that of GaAs bulk obtained in our previous study. Etch width of GaAs/AlGaAs interface was larger than that of the AlGaAs/GaAs.

Now until, accurate mechanism of the dry etching for multi-layer has not been reported. But, it is assumed that the mechanism has to do with thermal characteristics such as thermal conductivity, absorption coefficient, and melting point of materials. The phenomenon result from the fact that laser direct dry etching is dominantly thermal reaction. The maximum etching rate was 32.5 $\mu\text{m}/\text{sec}$ and the aspect ratio of etched groove on multi-layer was 0.5 (3 μm / 6 μm). This special etching profiles obtained in this study are expected to apply for a waveguide of optoelectronics and cantilever of MEMS.

Keywords : direct dry etching, GaAs/AlGaAs multi-layer, local temperature profiles, etch width, thermal conductivity, absorption coefficient, melting point, etching rate

1. INTRODUCTION

Various techniques have been developed for fabricating optoelectronic and microelectronic devices and circuits including wet-chemical, ion beam, and plasma etching.^{1,2} Laser direct dry etching is a relatively new technique in semiconductor processing which possesses³⁻⁵ many of the advantages including lack of etch-induced damages as well as material selectivity. A conventional wet-etching technique has uniform etching rates across the wafer and requires a photoresist mask for patterning. Laser direct dry etching allows resistless light-defined patterning as well as light-contoured etching.

Laser direct dry etching of GaAs/AlGaAs multi-layer with CCl_2F_2 provides self-aligned device processing by removal of GaAs on AlGaAs with a high selectivity in etching rates⁶, superior to that obtained with wet-chemical etching procedures.⁷⁻⁸ For example, selective dry etching has been demonstrated for micro-lenses, waveguide devices, and diffraction gratings.⁹⁻¹⁰ For applications the dependences of selectivity in etching rates between GaAs and AlGaAs on the etching conditions is crucial.¹¹ Therefore, we examined variations of the etching profile correspond on varying the etching conditions.

In this study, we present the characteristics of direct dry etching for GaAs/AlGaAs multi-layer by a single scan of laser. The etching characteristics using $\text{C}_2\text{H}_2\text{F}_4$ gas of CFC alternatives have been also investigated to compare with that using CCl_2F_2 gas.

2. EXPERIMENT

Laser direct dry etching of GaAs/AlGaAs multi-layer was carried out in the setup shown in Fig. 1. The arrangement consist of an argon ion laser, optical system, and processing chamber fixed on an electrically controlled X-Y-Z stage. The irradiation was carried out with an argon ion laser operating at 514.5 nm and was focused by a microscope objective lens ($\text{NA}=0.4$) down to a spot diameter of about 1.2 μm (at 1/e intensity) on the sample surface. The laser power density was varied from 13.3 MW/cm^2 to 29.1 MW/cm^2 . The focused laser beam was scanned on the sample by moving the chamber with speed ranges from 8 $\mu\text{m}/\text{sec}$ to 80 $\mu\text{m}/\text{sec}$. The samples were mounted in a vacuum chamber with a quartz window. The chamber was evacuated down to 10^{-3} Torr by a rotary pump and etching gas was introduced through a needle valve at a pressure of 760 Torr to the chamber. In order to compare etching characteristics, two gases, CCl_2F_2 and $\text{C}_2\text{H}_2\text{F}_4$ were used as ambient gases. The etching rate was defined as the depth divided by the laser beam dwell time, which is defined as the laser beam diameter divided by the beam scan speed. The physical characteristics of the etched patterns such as their shape, size and cross sectional view were obtained using scanning electron microscope (SEM). The chemical compositions of the residues nearby etched area were analyzed by Auger electron spectroscopy (AES). The local temperature rising on the sample surface by laser irradiation has been calculated with three dimensional heat equation to investigate etching characteristics for GaAs and AlGaAs.

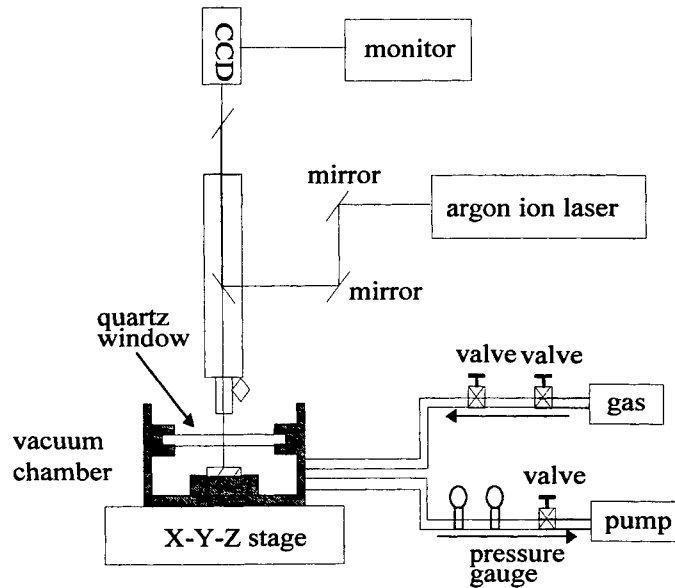


Fig. 1. Schematic diagram of laser direct dry etching system.

3. GaAs- AND AlGaAs-SURFACE LASER-INDUCED HEATING

The modeling of temperature distributions induced by laser irradiation in solids was pioneered by Lax^{12,13} for stationary spots and by Cline and Anthony¹⁴ for moving spots. With the growing interest in laser processing, these models have been developed further. Very recently, melting has been incorporated into the calculation for stationary circular spots.¹⁵

We present calculations of the temperature profiles induced by a stationary cw laser beam with a Gaussian intensity distribution for GaAs and AlGaAs, respectively. Temperature-dependent thermal conductivity, optical absorption coefficient and surface reflectivity are incorporated in our calculation. In the case of stationary beam, thermal conductivity is not considered in calculation.¹⁵ The heat equation¹⁵ can be written as

$$\frac{K(T)}{D(T)} \frac{\partial T}{\partial t} - \nabla \cdot [K(T) \nabla T] = Q(x, y, z, t) \quad (1)$$

where the first term represents the time development of the temperature T , the second term describes the spatial dependence of T , and the third is the incident source term. The $K(T)$ is the temperature-dependent conductivity of the irradiated material, $K(T)$ is an energetic term with dimension $W/(cm \cdot K)$. $D(T)$ is the thermal diffusivity of the material and is a kinetic term with dimension cm^2/sec , $D(T)$ becomes important whenever scanned beams are to be incorporated in the model. The temperature-dependent thermal conductivity $K(T)$ can be eliminated from the heat equation by performing a Kirchhoff transform.¹⁵ The Kirchhoff transform requires the introduction of a linearized temperature θ , which is defined as

$$\theta(T) = \theta(T_0) + \int_{T_0}^T \frac{K(T)}{K(T_0)} dT \quad (2)$$

where $\theta(T_0)$ and $K(T_0)$ are constants.

The heat equation can now be written in terms of the linearized temperature θ as

$$\frac{1}{D(T(\theta))} \frac{\partial \theta}{\partial t} - \nabla^2 \theta = \frac{Q(x, y, z, t)}{K(T_0)} \quad (3)$$

For GaAs, $K(T)$ and $D(T)$ can be modeled with approximate $1/T$ by a least-square fit to experimental data¹⁶

$$K(T) = \frac{k}{T - T_k} \quad k = 98 \text{ W/cm}, T_k = 91 \text{ K} \quad (4)$$

$$D(T) = \frac{1}{1.6} \times \frac{k}{T - T_k}$$

The terms $\theta(T)$ and $T(\theta)$ can now be expressed analytically[Eq.(2)] :

$$\theta(T) = \int_{T_o}^T \frac{K(T)}{K(T_o)} dT = (T_o - T_k) \ln\left(\frac{T - T_k}{T_o - T_k}\right) \quad (5)$$

$$T(\theta) = T_k + (T_o - T_k) \exp[\theta / (T_o - T_k)] \quad (6)$$

The term T_o is the substrate temperature of the sample that is to be irradiated. The θ and T can be calculated directly by numerical iteration. Figure 2 shows a local temperature rise characteristics on the surfaces of GaAs and AlGaAs by a laser irradiation were calculated.

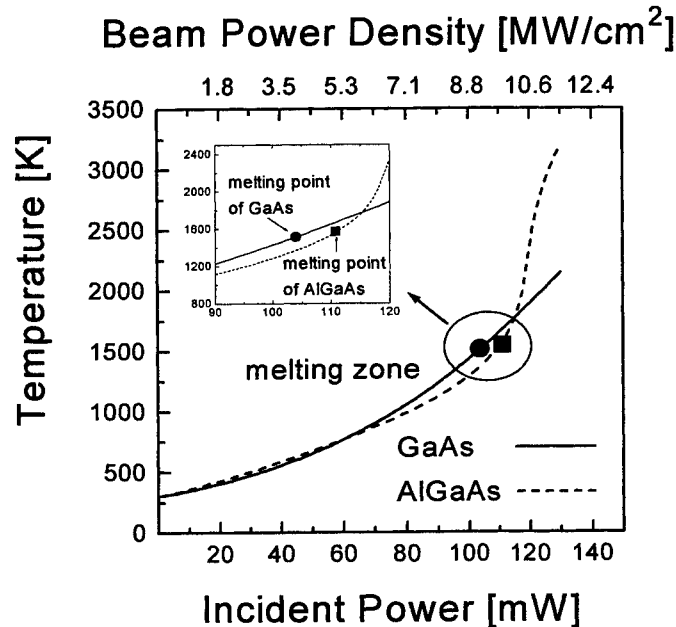


Fig. 2. Local temperature rise characteristics on the surfaces of GaAs and $\text{Al}_x\text{Ga}_{1-x}\text{As}$ ($x=0.3$) by a laser irradiation were calculated with three dimensional heat transfer equation.

4. RESULTS AND DISCUSSION

In order to find the best conditions for highly selective laser direct dry etching, the behavior of the two materials GaAs and $\text{AlGaAs}(x=0.3)$ was investigated under two etching gases and various laser power densities. Samples with 1 μm thick of GaAs and AlGaAs on top of the semi-insulator(S.I.) GaAs substrate were used. Figure 3 shows the etching profiles of the sample under the conditions from laser power density of 16.8 to 20.3 MW/cm^2 , scan speed of 13 $\mu\text{m/sec}$, and CCl_2F_2 pressure of 760 Torr.

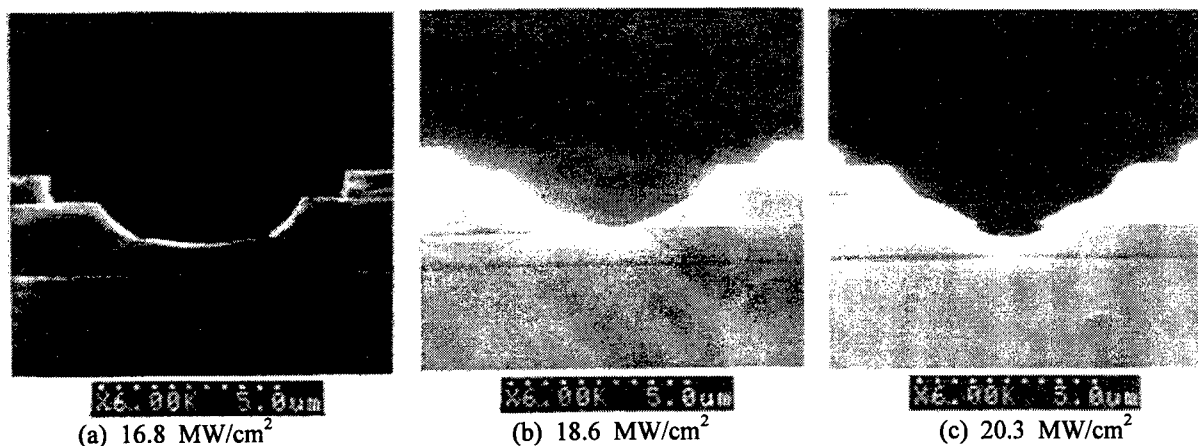


Fig. 3. Cross-sectional views of etching profile of the multi-layer obtained by a beam scan speed of 13 $\mu\text{m}/\text{sec}$, CCl_2F_2 pressure of 760 Torr, and different incident laser power densities ; (a) 16.8 MW/cm^2 (b) 18.6 MW/cm^2 (c) 20.3 MW/cm^2 .

The etch width of GaAs located in top layer and 3th layer from the top layer increase with the increase of laser power density. The reason is because etching rate of GaAs is larger than that of AlGaAs. As shown in Fig. 2 and as known in the numerical calculation, this is also due to the higher temperature rise of GaAs compared to that of AlGaAs.

In order to observe the differences of etching rate for two materials, samples with different thickness of GaAs and AlGaAs were also used. The sample is consist of capping layer of 30 nm, AlGaAs layer of 1 μm , sandwiched GaAs layer of 0.4 μm , and AlGaAs buffer layer of 3.0 μm . Figure 4 shows the expected schematic plot of etching process in the multi-layer structure.

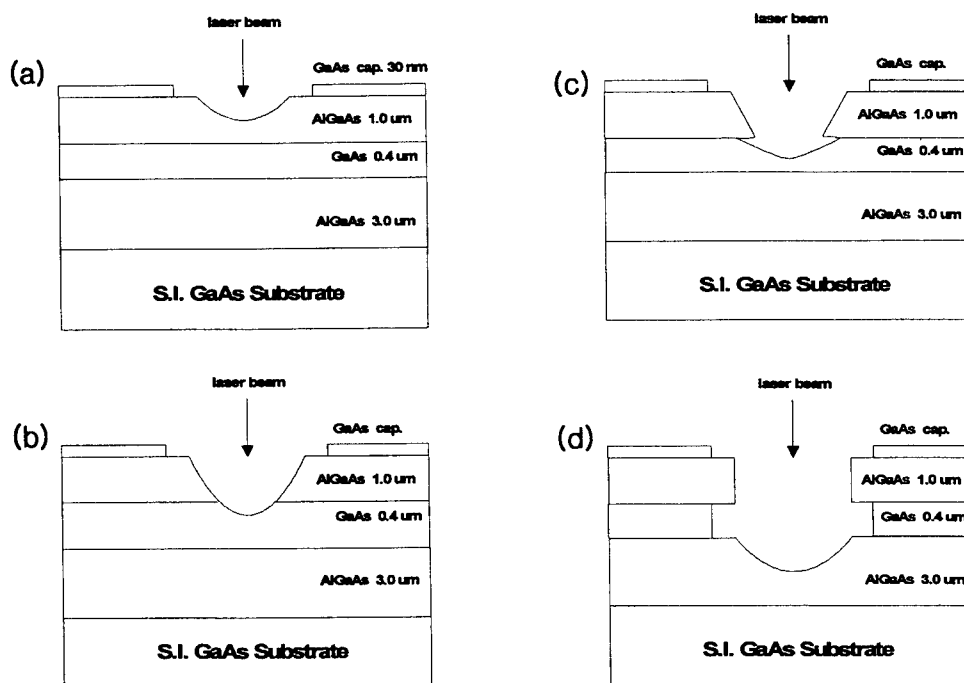


Fig. 4. The expected schematic diagram of laser direct dry etching process in the multi-layer structure.

If the thickness of GaAs or AlGaAs is changed, etching profiles also are changed as shown in Fig. 4. Therefore, we can control an etching profile with the variations of the thickness of multi-layer.

Figure 5 shows the cross sectional view of etching profile was expected in Fig. 4. By these results, it was found that the mechanism of laser direct dry etching for multi-layer is related closely with differences of etching rate

and thermal effects ; thermal conductivity, optical absorption coefficient, melting point and so on.

In this structure, we obtained the etching rate of $32.5 \mu\text{m}/\text{sec}$ and the aspect ratio of about 0.5. These results of the etching rate and aspect ratio for GaAs/AlGaAs multi-layer were lower than those for GaAs bulk¹⁷. On the other hand, it is interesting that the etch width of GaAs layer is wider than that of AlGaAs layer in the GaAs/AlGaAs multi-layer structure. The reason results from difference in the temperature rise characteristics and in the etching rate between GaAs and AlGaAs as mentioned in previous.

The etch width ratio of GaAs to AlGaAs can be enhanced with good thermal confinement of GaAs/AlGaAs interface which caused by lower thermal conductivity ($0.106 \text{ W}/\text{cm} \cdot \text{K}$) of AlGaAs than that ($0.44 \text{ W}/\text{cm} \cdot \text{K}$) of GaAs¹⁵. The maximum etch width ratio of GaAs to AlGaAs was obtained about 1.7 at a laser power density of $20.4 \text{ MW}/\text{cm}^2$, a scan speed of $13 \mu\text{m}/\text{sec}$, and a CCl_2F_2 pressure of 760 Torr.

Etching profiles for $\text{C}_2\text{H}_2\text{F}_4$ gas (CFC alternative) to compare etching characteristics showed in Fig. 6. In this figure, deposition of reaction products on and nearby etched groove was appeared. This phenomenon mainly appeared in using $\text{C}_2\text{H}_2\text{F}_4$ gas and the reason is that CFC alternative has no chlorine which is important components in conventional dry etching reactions.

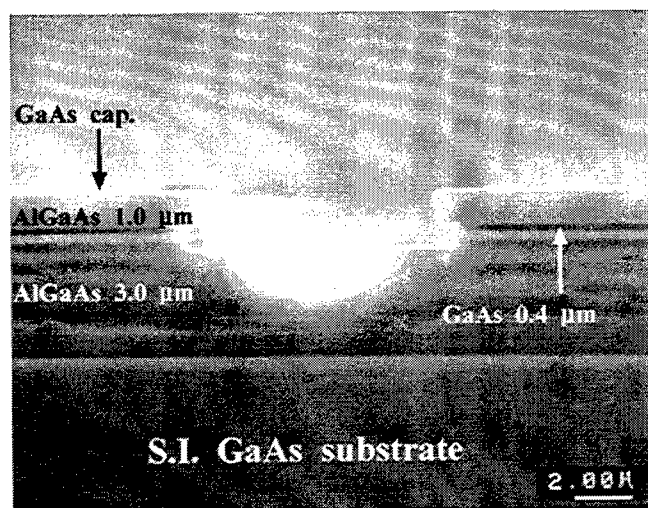


Fig. 5. Cross sectional view of the etching profile for the structure as shown in figure 4. The etching conditions are a beam scan speed of $13 \mu\text{m}/\text{sec}$, a CCl_2F_2 pressure of 760 Torr, and an incident laser power densities of $15.9 \text{ MW}/\text{cm}^2$.

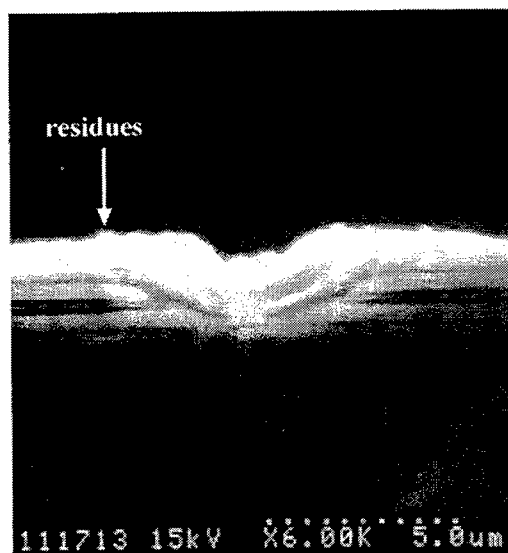


Fig. 6. Cross sectional view of the etched groove obtained in $\text{C}_2\text{H}_2\text{F}_4$. Conditions are a gas pressure of 760 Torr, a beam

scan speed of 13 $\mu\text{m}/\text{sec}$, and an incident laser power densities of 29.2 MW/cm^2 .

AES profiles for the residues on etched surface are measured to obtain the stoichiometry of the reaction products. As shown in figure 7, there were not only As and Ga peaks but C and F peaks in the AES spectra for the reaction products. This figure indicates also that the residues include carbides and fluorides of Ga and As after laser-induced thermochemical etching under $\text{C}_2\text{H}_2\text{F}_4$ ambience. Therefore, it is suggested that there are too much carbides and fluorides to be imperfectly vaporized. However, the residues on etched surface can be controlled with an incident laser power, a scan speed, and an etching gas pressure as shown in our previous study.¹⁷

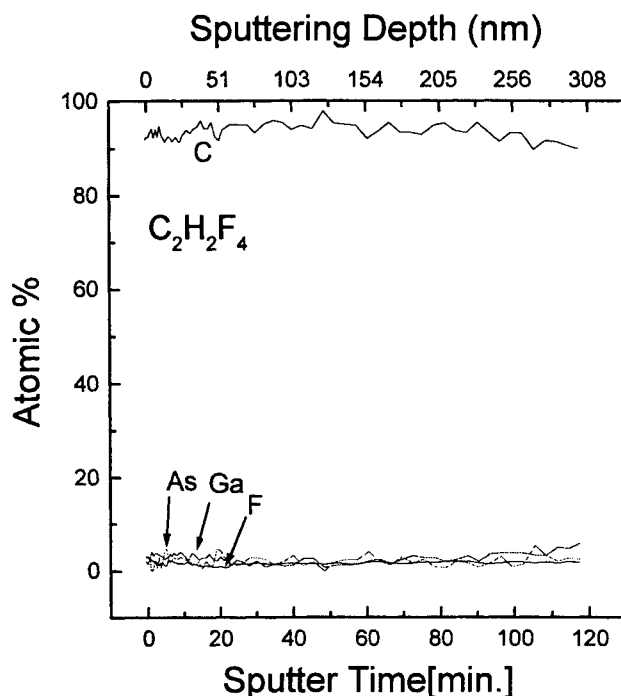


Fig. 7. AES depth profiles of elementary composition in the near surface region of sample in Fig. 6.

Figure 8 shows the etch depth (a) and etch width (b) as a function of laser power density in CCl_2F_2 pressure of 760 Torr and a scan speed of 13 $\mu\text{m}/\text{sec}$. The etch depth increases with increasing the laser power density up to 17.7 MW/cm^2 . However, the etch depth decreases with increasing the laser power density above this value as shown in Fig. 8 (a).

The decrease of etch depth in higher power range is because that the etch width of GaAs layer on AlGaAs layer tends to enlarge and etching process can be suppressed by the reaction products deposited on and nearby the etched groove (Fig. 8(b)). Also the deposition of residues in the etched surface during etching process occurs with a weak light guiding effect¹⁸ which the focused laser beam is reflected repeatedly between the two side walls and laser beam is guided to the bottom of the groove with very small loss.

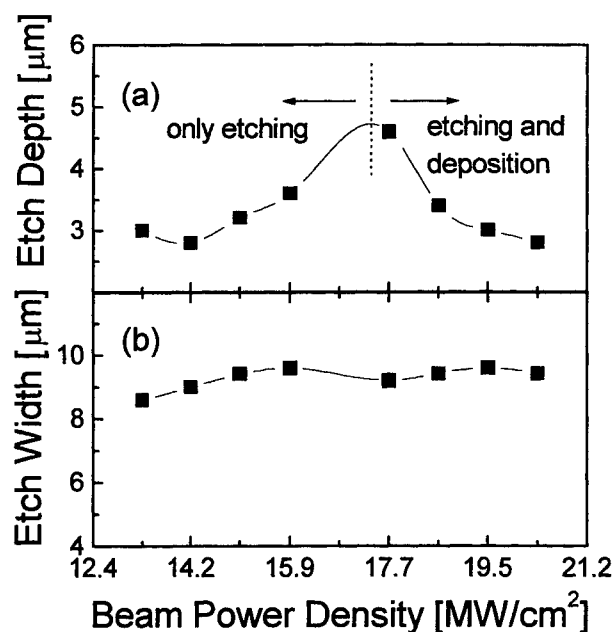


Fig. 8. Etch depth (a) and etch width (b) as a function of laser power density at a scan speed 13 $\mu\text{m}/\text{sec}$ and a CCl_2F_2 pressure of 760 Torr.

5. CONCLUSIONS

The laser direct dry etching of GaAs/AlGaAs multi-layer, which is useful for fabrication of three dimensional micro-structure, have been investigated with etching gas such as CCl_2F_2 and $\text{C}_2\text{H}_2\text{F}_4$ (CFC alternative). We have obtained the unique profiles which etching activity in horizontal higher than in vertical with CCl_2F_2 . The maximum etching rate 32.5 $\mu\text{m}/\text{sec}$ and the maximum etch width ratio of GaAs to AlGaAs was about 1.7 in this study.

When the thermochemical etching occurred on the sample surface by laser beam, the reaction products were deposited simultaneously on and nearby the etched groove in case of higher laser power density. These reaction products appeared dominantly in the samples etched with $\text{C}_2\text{H}_2\text{F}_4$ gas of CFC alternatives, which is less active than CCl_2F_2 gas. The residues were clarified to the carbides of Ga and As or fluorides of them by AES measurements.

The special etching profile obtained in this study, are expected to apply for a waveguide of optoelectronics and cantilever of MEMS.

ACKNOWLEDGEMENTS

This work is supported by the Korea ISRC (Contract No. 97-E-4033)

REFERENCES

1. S. D. Mukherjee and D. W. Woodard, in *Gallium Arsenide*, M. J. Howes and D. V. Morgan, Editors, p.119, John Wiley & Sons, Inc., New York, 1985.
2. J. J. Kelly, J. E. A. M. van den Meerakker, P. H. L. Noten, and R. P. Tijburg, *Philips Tech. Rev.* **44**, 61, 1988
3. F. Kuhn-Kuhnenfeld, *J. Electrochem. Soc.* **119**, 1063, 1972
4. F. W. Ostermayer, Jr., and P. A. Kohl, *Appl Phys. Lett.* **39**, 76, 1981
5. M. N. Ruberto, X Zhang, R. Scarmozzino, A. E. Willner, D. V. Podlesnik, and R. M. Osgood, Jr., *J. Electrochem. Soc.* **138**, 1174, 1991
6. K. Hikosaka, T. Mimura, and K. Joshin, *Jpn. J. Appl Phys.* **20**, L847, 1981
7. J. J. Le Pore, *J. Appl. Phys.* **51**, 6441, 1980
8. C. Jung, K. J. Kuhn, and R. B. Darling, *J. Vac. Sci. Technol.* **B8**, 1122, 1990
9. D. V. Podlesnik, H. H. Gilgen, R. M. Osgood, Jr., and A. Sanchez, *Appl. Phys. Lett.* **43**, 1083 1983
10. J. E. Bowers, B. R. Hemenway, and D. P. Wilt, *Appl. Phys. Lett.* **46**, 453 1985
11. C. M. Knoedler and T. F. Kuech, *J. Vac. Sci. Technol.* **B4**, 1233, 1986
12. M. Lax, *J. Appl Phys.* **48**, 3919, 1977
13. M. Lax, *Appl Phys. Lett.* **33**, 786, 1978
14. H. E. Cline and T. R. Anthony, *J. Appl. Phys.* **48**, 3895, 1977
15. J. E. Moody and R. H. Hendel, *J. Appl. Phys.* **53**(6), 4364, 1982
16. D. J. Ehrlich and J. Y. Tsao, *Mat. Res. Soc. Symp. Proc.* **17**, 3, 1983
17. M. S. Kim, S. K. Park, C. Lee, E. K. Kim, and S. K. Min, *J. Elec. Mater.* **26**, 436, 1997
18. C. Arnone, M. Rothschild, and D. J. Ehrlich, *Appl. Phys. Lett.* **48**, 736, 1986

Correspondence: E-mail: skpark@kistmail.kist.re.kr; Telephone: 81-2-958-5742; FAX; 81-2-958-5739

Maskless laser-induced deposition of Cu film patterns from copper formate

Jae-Kwon Kim^a, Cheon Lee^a

^aDept. of Electrical Engineering, Univ. of Inha, Incheon 402-751, Korea

ABSTRACT

Laser direct writing using thin solid films of metallo-organic precursors offers some unique advantages in terms of materials design, process control, and safety over gas phase or solution processes. Micro patterned copper films were obtained by laser-induced deposition using $\text{Cu}(\text{HCOO})_2 \cdot 4\text{H}_2\text{O}$ films as a precursor. Then the new applicabilities for interconnection of integrated circuits were preliminary studied by the estimation of physical and electrical properties of copper films after annealing. The growth kinetics of these Cu films was investigated as a function of the laser power and the scan speed which were varied in the range of 70 to 600 mW and 0.1 to 20 mm/s, respectively. The high-purity of the deposit was also confirmed by Auger electron spectroscopy (AES) analysis. The resistivity of the patterned copper films was a factor of about 20 higher than that of bulk value however, the resistivity decreased due to changes in morphology and porosity of the deposit and was about $10 \mu \Omega \text{ cm}$ after annealing at 300°C for 5 minutes.

Keywords: Laser direct writing, Metallo-organic precursors, Laser-induced deposition, Copper formate, Annealing, Interconnection

1. INTRODUCTION

The field of laser direct writing is expanding rapidly as the potential for accomplishing one-step pattern definition and metallization. Current investigations in this area include laser-induced photochemical, photothermal, and photoelectrochemical reactions, in the gas, liquid, or solid state¹⁾. Major issues being addressed relate to characterization of the final deposits, namely, spatial resolution, chemical composition, and electrical properties. Optimization of direct-write processes, however, requires an understanding of the reaction chemistries involved and the ability to tailor precursors for specific applications. Most of the studies reported to date have used gas phase precursors for decomposition, though some results on the use of solid metallo-organic films have been recently reported. Here we describe results based on a new approach, namely, scanned cw laser writing of room-temperature stable metallo-organic films. These materials offer the potential for patterned deposition of a wide variety of metals from uniform films that can be developed by methods compatible with standard lithographic techniques. Precursors must meet certain requirements to be of practical use. These include (1) homogeneous film formation and (2) high metal content, i.e., sufficient to form continuous metal features after (3) complete volatilization of organic components at (4) decomposition temperatures low enough to prevent substrate damage²⁾.

In addition, either the film or the substrate must have enough optical absorption at the laser wavelength to initiate the decomposition of the metallo-organic film.

In this paper, we focus on the reaction profiles generated in a direct-write process for copper as a means of understanding and optimizing the process. We report the deposition of copper by pyrolytic decomposition of copper formate films using a focused argon ion laser beam (514.5 nm). We have also investigated the contents of the deposited material and the resistivity of the copper patterns.

2. EXPERIMENTAL

2.1. Apparatus

The laser-induced deposition equipment consisted of an Ar^+ laser, a translation stage and an optics. The experimental setup is schematically shown in Fig. 1. The focused output of the 514.5 nm beam from an argon ion laser (Spectra-Physics model *stabilite 2017*) was used to decompose the metalorganic film to metal for selective area. The laser beam was focused using a microscope with a $20\times$ objective ($\text{NA}=0.4$) onto substrates positioned on a translation stage. The focused minimum spot size on the substrate was about $1 \mu\text{m}$. The sample was rastered with respect to the laser spot by computer-controlled DC servo-motor-driven translation stages.

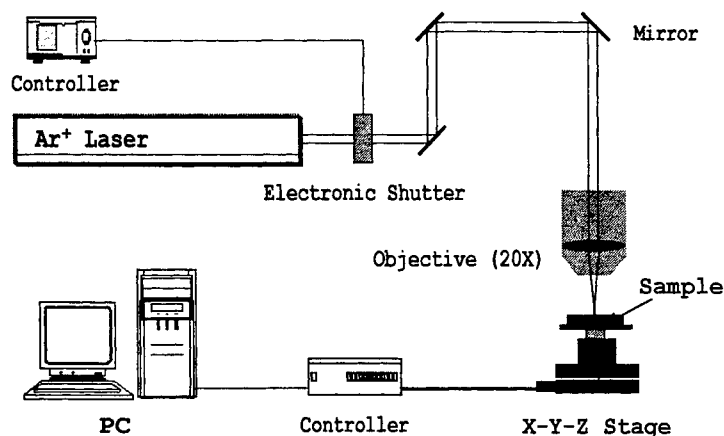


Figure 1. Scheme of experimental setup for laser-induced deposition.

2.2. Experimental procedure

Copper formate should be decomposed to metallic copper when locally heated with a laser³⁾. We used the tetrahydrated copper formate ($\text{Cu}(\text{HCOO})_2 \cdot 4\text{H}_2\text{O}$) as a more simple copper precursor in terms of ligand complexity. This precursor contains only Cu, O, C and H. In addition, the thermal decomposition byproducts (CO_2 , CO, H_2 and H_2O) are harmless to the environment⁴⁾.

The substrate preparation for deposition from copper formate is as follows :

The substrates, which are used for the all experiments, are slide glass and silicon wafer covered with thermal oxide film with a thickness of $0.6 \mu\text{m}$. They are cleaned with acetone and isopropyl alcohol (IPA) before coating of copper formate films. The films were sprayed onto the substrate from an aqueous solution of copper formate and are subsequently dried at $70 \sim 80^\circ\text{C}$ to remove the water. We obtained smooth and semitransparent films of composition. The sample should be used quickly after spraying because crystallization sets in following water loss. The samples were fixed on a three-dimensional scanning translation stage and were irradiated with the focused laser beam through a microscope objective. After the local decomposition step, the laser-written samples were developed in deionized water to remove unirradiated metalorganic film.

To investigate the effects of annealing on the surface roughness, the structural properties of the deposits, and the influence of annealing temperature on the resistivity of the copper film, the samples were heated in a tube furnace at a rate of $3^\circ\text{C}/\text{min}$ in air to the designated temperature of $200 \sim 300^\circ\text{C}$ for 5 minutes.

2.3. Characterization methods

The thickness and width of the deposited material were evaluated by scanning electron microscope (SEM) and stylus profilometer (Alpha Step 500, Tencor Instruments). The composition of it was observed by Auger electron spectroscopy (AES). Scotch-tape tests performed on these films after development to demonstrate good adhesion.

The deposition rate of deposits was obtained from the ratio of film thickness, measured with the stylus profilometer, to beam dwell time.

The resistivities are obtained from the copper line profiles measured with the stylus profilometer and the line resistance measured with a multimeter. Dots of silver paste were deposited on both ends of the lines to improve the electrical contacts. After annealing, morphological changes in copper films are observed by atomic force microscopy (AFM).

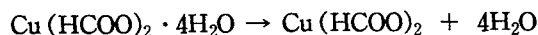
3. RESULTS & DISCUSSION

3.1. Copper deposition from copper formate

The choice of a suitable copper formate is based on the search for a molecule which is fairly transparent to the laser radiation and decomposes rapidly to volatile and stable reaction products at relatively low

temperatures. The compound should be easy to dissolve for spin-on, spray-on, or paint-on purposes, and should give a homogeneous gel-like layer after drying. Rapid crystallization of the metalorganic in the drying procedure should be avoided because it leads to inhomogeneities in the metallization step. In the case of copper, several compounds were considered among copper formate, copper oxalate, and copper acetate. These were tested for laser metallization in different solvents (water, formic acid, acetone, pyridine, acetonitrile, THF, glyme, and diglyme). Copper formate sprayed from aqueous solution was the only one which did not crystallize immediately through solvent evaporation⁵⁾.

The kinetics and products of thermal decomposition of copper formate have been reported⁶⁾. The overall decomposition may be satisfactorily represented as



The decomposition behavior is quite complicated and the rate depends to some extent on the method of preparation of the original formate and its water of crystallization. The fractional decomposition of the film during laser writing is determined by the temperature-time relation in the film, which is controlled by the laser power and scan speed.

Typical films deposited on glass and silicon substrates are shown in Fig. 2. The laser power was 90 mW for deposition on glass and 300 mW for the silicon substrate with a 200 $\mu\text{m/s}$ scan speed. The power required for decomposition on silicon is in general of a factor of 3~4 higher than a glass. For a glass substrate, the central region reaches a temperature high enough to melt and evaporize the copper film. These results can be qualitatively understood by considering the thermal properties of the deposit and substrate. The thermal conductivity of copper is similar to that of glass at room temperature. Thus, the heat is lost primarily through the copper film in the case of glass substrate, leading to strong coupling between temperature distribution and deposit geometry. In the case of silicon most of the heat loss is through the substrate and the temperature distribution is relatively insensitive to the geometry of the deposit^{7) 8)}.

As proved by tape tests, the lines show a sufficient adhesion to the glass substrate but not silicon substrate.

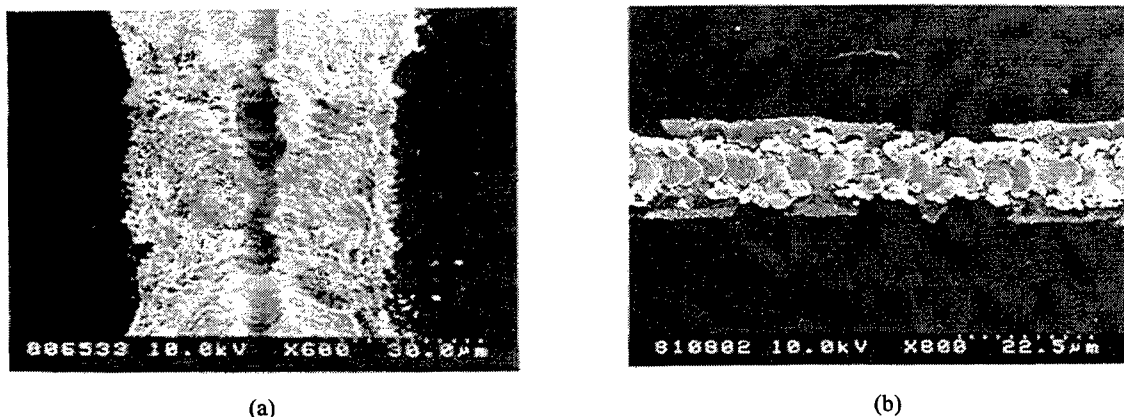


Figure 2. SEM micrographs of Cu film on glass (a) and silicon substrate (b).

The dependence of the linewidth for the copper lines deposited on glass substrate on laser power density is shown in Fig. 3. This result confirms that laser-induced deposition occurs via a local heating of the substrate. For a given scan speed, the linewidth varies almost linearly with laser power density.

As thickness profiles of the copper lines were measured with a stylus profilometer, it is found that Gaussian profiles are produced at low power density, giving way to volcano-like profiles at high density.

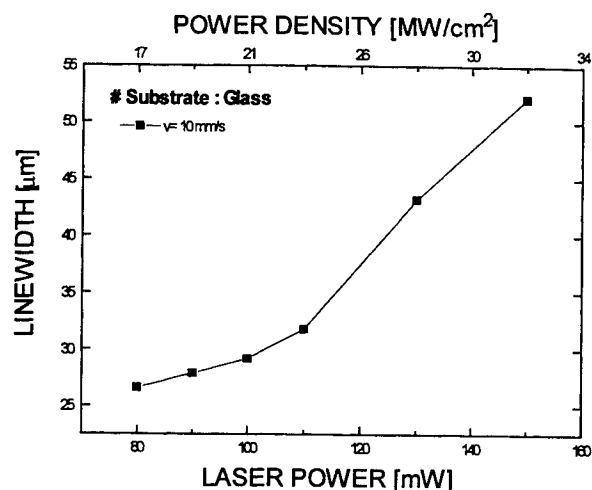


Figure 3. Linewidth of Cu films as a function of laser power density.

The linewidth of the copper films as a function of scan speed for a range of laser power (80~150 mW) is plotted in Fig. 4. The linewidth is observed to decrease with increasing scan speeds, and is varied from 25 to 78 μm .

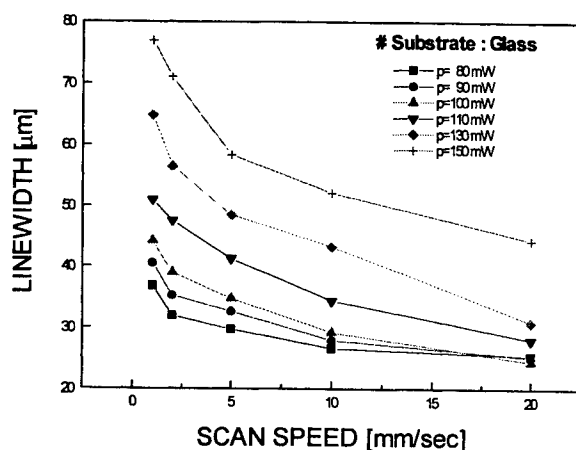


Figure 4. Linewidth of Cu films as a function of scan speed.

While the linewidth increases approximately linearly with the laser power, the thickness of the film presents a more complicated behavior. Fig. 5 shows the average thickness of the copper films as a function of scan speed. The thickness of the film was approximately independent of scan speed for above 90 mW laser power. This behavior is due to the different temperatures reached at the center and at the edge of the films, both of which determine respectively the vertical and the lateral growth rates. At high power densities the central region reaches a temperature high enough to melt and evaporize the copper film, so that the height of the edge is higher than that of the center of the film. The thickness therefore is smaller than that of the film deposited at 80 mW laser power.

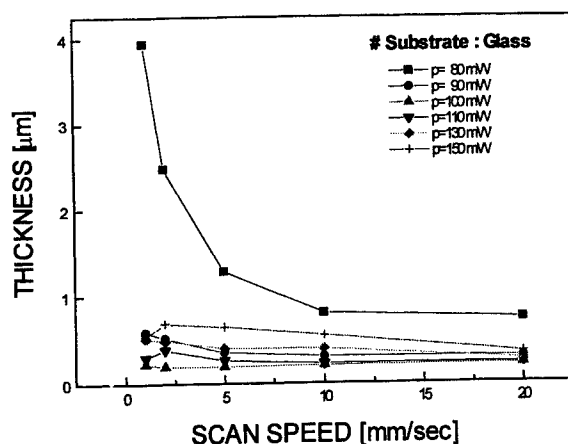


Figure 5. Thickness of Cu films as a function of scan speed.

Fig. 6 shows scanning electron microscope image of a copper line, which was approximately $4\text{ }\mu\text{m}$ thick and $40\text{ }\mu\text{m}$ wide on the glass substrate. The laser output power was 80 mW and the scan speed was 1 mm/s.



Figure 6. SEM micrograph of Cu line deposited under 80 mW laser power and 1 mm/s scan speed.

3.2. Deposition rate

The deposition rate can be determined by the height of written lines and the residence time of the laser beam. Fig. 7 shows the deposition rate as a function of laser power density for various scan speeds. Once the deposition rate is seen to decrease until, at about 100 mW. For fast writing speeds and hence short residence times, the thickness is almost constant under laser powers are above 100 mW. For this reason, deposition rate increases slightly with scan speeds of 2~20 mm/s and laser powers in the range of 100~150 mW.

From the deposition rate point of view, laser-induced deposition process is excellent in comparison with conventional chemical vapor deposition (CVD) processes. However, the wafers coming from a large-area process such as conventional CVD is more than those coming out from the laser direct writing technique. The laser technique is a serial process in which connection lines are drawn one by one.

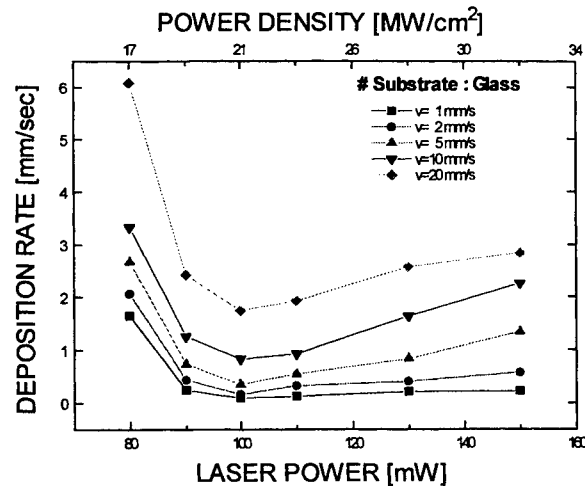


Figure 7. Deposition rate as a function of laser power density.

3.3. Film properties

3.3.1. Purity

Auger analysis of the laser written features reveals little oxygen as shown in Fig. 8. The origin of O at the surface is due to a post-deposition contamination when the processed sample surface was exposed to air before the AES measurements. We conclude that oxide in the laser-written features is not the primary formate decomposition product but formed by reaction of copper with the air ambient. The every spectrum is almost same for films deposited over a wide range of scan speeds (0.1~20 mm/s) and laser power (70~600 mW) and for deposits on silicon substrate.

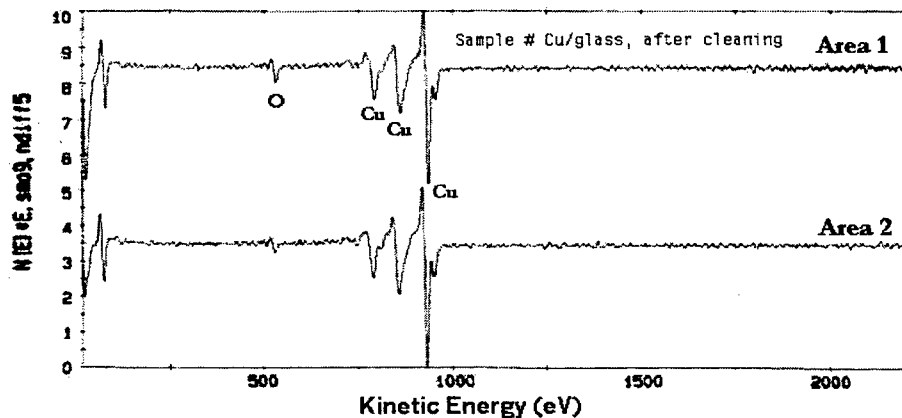


Figure 8. Auger electron spectra of copper features written at laser power of 80 mW and a scan speed of 1 mm/s.

3.3.2. Morphology

SEM images of the film morphology are given by Fig. 9. The overview in Fig. 9 (a) shows that the surface of as-deposited film is very rough and porous. This results from incomplete sintering of formed copper particles and volatilization of organic by-products during decomposition of the copper formate. Rapid cooling of the reaction area then limits the extent of sintering. Films contain a significant degree of porosity, which can be partially eliminated by subsequent annealing.

Fig. 9 (b) and (c) show that the morphology of the films which annealed at 200 °C and 300 °C for 5

minutes, respectively. As shown in Fig. 9 (b) and (c), it is observed that the grains tend to grow with formation of agglomerates and decrease in porosity. This is to be expected considering the known strong tendency of copper particles to sinter together.

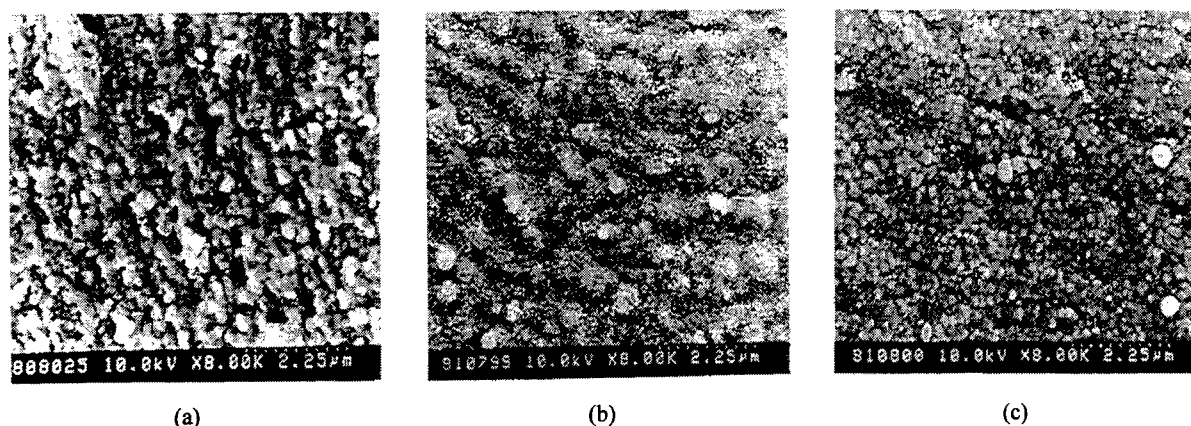


Figure 9. Morphology of Cu films as a function of annealing temperature.
(a) as-deposited, (b) 200 °C, (c) 300 °C.

Fig. 10 shows that atomic force microscopy images of surface morphology as a function of annealing temperature. After annealing, the surface roughness of the films are more smooth in comparison with as-deposited surface. Therefore, these structural changes probably affect the electrical properties of the films.

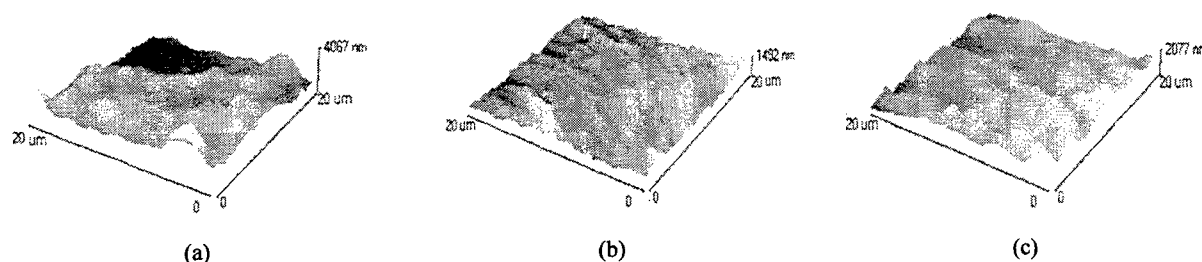


Figure 10. AFM images of surface morphology as a function of annealing temperature.
(a) as-deposited, (b) 200 °C, (c) 300 °C.

3.3.3. Resistivity

Because AES analysis of the samples resulted in essentially 100 % copper composition for all the samples, the variations in resistivity could only be explained as being due to the differences in morphology of the deposited lines. The resistivity of the patterned copper films was a factor of about 20 higher than that of bulk value ($\rho = 1.67 \mu\Omega\text{cm}$). The films however were annealed at 300 °C for 5 min., the resistivity decreased with annealing temperature until about $10 \mu\Omega\text{cm}$. The resistivity drop is due to changes in morphology and porosity of the deposit.

3.4. Applications

For the purpose of microelectronics repairing and pattern direct writing applications of electronic circuits, it is necessary to beam scanning technique, which can be automatically rastered the laser spot toward a random direction. In experiment, desired copper patterns (frequently lines) were created by moving the sample using computer controlled translation stages with a lateral resolution of $0.1 \mu\text{m}$. Examples of the micro patterned copper films with various shape are shown in Fig. 11.

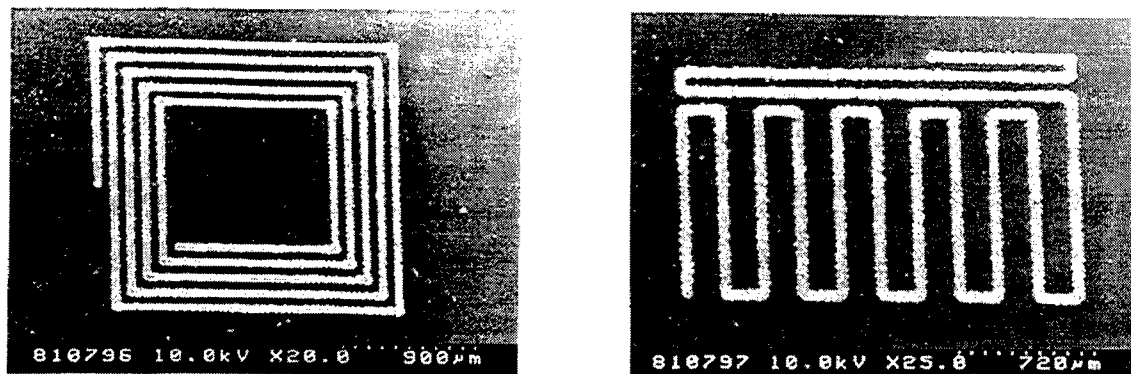


Figure 11. Examples of micro patterned copper films.

4. CONCLUSION

We have characterized copper films that were deposited by laser decomposition of copper formate film. The dependence of the laser power and the scan speed on the geometry, the morphology and the resistivity of lines has been studied. The principal conclusions drawn from this study can be summarized as follows :

- (1) The temperature rise induced by absorbed radiation explains the different influence of the laser power and the scan speed on the width and height of the lines.
- (2) AES data indicates that the decomposition can be carried out in air since the rapid heating and fast cooling during laser-induced pyrolytic decomposition prevents oxidation of the copper.
- (3) Copper films have an average as-deposited resistivity value of $30 \mu\Omega\text{cm}$. The high resistivity may be caused by film morphology with porosity and poor roughness.
- (4) Annealing the films at 300°C for 5 minutes reduces the resistivity by less than $20 \mu\Omega\text{cm}$.

The major conclusion of this work is that reducing the resistivities to values much closer to the bulk resistivity is considered essential for a copper laser-induced deposition process to become a viable manufacturing technology.

REFERENCES

1. D. J. Ehrlich and J. Y. Tsao, *Laser Microfabrication : Thin film processes and lithography*, Academic Press, San Diego, pp. 385-439, 1989.
2. M. E. Gross, A. Appelbaum, and K. J. Schnoes, "A chemical and mechanistic view of reaction profiles in laser direct-write metallization in metallo-organic films. Gold.", *J. Appl. Phys.* **60**(2), pp. 529-533, 1986.
3. A. Gupta and R. Jagannathan, "Laser writing of copper lines from metalorganic films", *Appl. Phys. Lett* **51**, pp. 2254-2256, 1987.
4. M. Mouche, J. Mermet, M. Romand , and M. Charbonnier, " Metal-organic chemical vapor deposition of copper using hydrated copper formate as a new precursor", *Thin Solid Films* **262**, pp.1-6, 1995.
5. P. Hoffmann et al., "Fast laser writing of copper and iridium lines from thin solid surface layers of metal organic compounds", *Applied Surface Science* **43**, pp. 54-60, 1989.
6. A. G. Galeway, D. M. Jamieson, and M. E. Brown, "Thermal decomposition of three crystalline modifications of anhydrous copper(II) formate", *J. Phys. Chem.* **78**(26), pp. 2664-2670, 1974.
7. K. Piglmayer, J. Doppelbauer, and D. Bäuerle, "Temperature distributions in cw laser induced pyrolytic deposition", *Mat. Res. Soc. Symp. Proc.* **29**, pp. 47-54, 1984.
8. D. Bäuerle, *Chemical Processing with Laser*, Springer, Berlin, Vol.1, pp. 69-134, 1986.

SESSION 8

Novel Methods and New Tools for Photon Processing

An Overview of the User Program for the Jefferson Lab Free Electron Laser

H. F. Dylla
Jefferson Laboratory
12000 Jefferson Ave.
Newport News VA 23606

ABSTRACT

Jefferson Lab is commissioning a high-average-power infrared IR FEL during 1998. When driven with its superconducting linac operating in a recirculated mode, the IR Demo FEL is capable of producing kilowatt-level average power in the mid-infrared (2–7 microns) range. With operational experience and hardware changes involving primarily change-out of the optical cavity mirrors, the FEL is capable of covering a wide range of the infrared (1–16 microns) at power levels exceeding 100 watts. This tuning range combined with a unique pulse structure (ps micropulses at 37 MHz) makes the Jefferson Lab FEL a versatile research and development tool for a wide variety of laser applications. A core group of industrial partners has been involved in planning applications using the FEL since 1991. This initial user group was augmented with university partners in 1993 and with participants from several national laboratories in 1996–1997. With the initiation of construction of the FEL and the associated 600 m² user facility laboratory in 1996, a number of topical user groups were formed to plan and implement the first series of user experiments. The industrial partners have formed user groups planning applications in polymer surface processing, metal surface processing, microfabrication, and electronic materials. University partners have submitted proposals on basic science topics which complement the planned applied research topics, in addition to proposing experiments in atomic physics, chemical physics and materials science which take advantage of one or more of the unique characteristics of the FEL. A synopsis of the proposed user experiments for the first phase of operation of the Jefferson Lab FEL will be presented.

*This work is supported by US DOE Contract No. DE-AC05-84ER40150, the Office of Naval Research, the Commonwealth of Virginia, and the Laser Processing Consortium.

1. INTRODUCTION

A versatile high-power, infrared (IR) free electron laser (FEL) user facility was recently completed at the US DOE Thomas Jefferson National Accelerator Facility (Jefferson Lab) campus in Newport News, Virginia. The FEL is driven by a dedicated 50 MeV, recirculated, superconducting linac^[1] based on the technology in Jefferson Lab's much larger 5 GeV linac (CEBAF) used for the nuclear physics research community. This linac technology provides a high-average-power, high brightness, short pulse electron beam driver for FEL applications. The first FEL to be built in the facility began lasing in June 1998^[2] and is capable of producing kilowatt-level average powers in the mid-infrared (2–7 microns) and 0.2 kW power output over a wide range of the infrared (1–16 microns). A planned upgrade to the linac extending the electron beam energy to 200 MeV would allow the mid-infrared power to be increased by an order of magnitude and would extend the kilowatt-level power through the visible to the deep ultraviolet (230nm).

The FEL Facility at Jefferson Lab is the result of a public-private partnership organized by the Laboratory and key users of the facility who formed a consortium in 1993, the Laser Processing Consortium (LPC), to develop applications and solicit support for construction and use of the high-average-power FELs. Given the large potential for industrial applications with the successful development of cost effective, high-average-power FELs, industry members of the consortium have played a key role in the specifications of the Jefferson Lab FELs and in the identification of relevant applications of industrial interest.^[3] Unique aspects of the FEL output (high-average power, tunability and time structure) have attracted university members to the consortium who have proposed basic science applications of the light source. In 1996, the U.S. Department of Navy joined the consortium because of defense interests in the propagation of high-average-power laser light through mid-infrared atmospheric windows in the maritime environment.^[4] The consortium has held biannual workshops since 1993 to plan the use of the FELs and to identify user equipment and infrastructure which could be shared among the project stakeholders in the industrial, university and national lab research communities.

The consortium was successful in attracting sufficient support and funding for the construction of a 600 m² User Facility and the first FEL (the "IR Demo FEL") by June 1996. Construction was completed and FEL commissioning began in

September 1997. Completion of commissioning of the IR Demo will be interleaved with the start-up of the first experiments in the User Facility during 1999. Funding for FEL hardware came from the US DOE, the US Dept. of Navy and the Northrop Grumman Corporation. Funding for the User Facility building came from the Commonwealth of Virginia. Initial outfitting of the User Facility laboratories is being provided by DuPont, Armco, Virginia Power, Northrop Grumman and Aerospace Corporation.

Figure 1 shows the power spectrum for the IR Demo FEL under various operational scenarios and Table 1 lists output characteristics that would be of interest to light source users. The fundamental operating range of the IR Demo FEL is in the mid-infrared range from 2–7 microns, where kilowatt-level average powers can be delivered. Third harmonic operation would extend the short wavelength limit of operation to near 1 micron at power levels in the 100 watt range. When the linac is operated in a non-recirculated mode, the electron energy can be dropped to 18 MeV extending the long wavelength limit out to 16 microns. The IR Demo has an evolutionary upgrade plan that involves adding a second and third cryomodule to the superconducting linac. The second cryomodule would extend the short wavelength limit to the mid-visible range and the third cryomodule would extend the short wavelength limit to 230 nanometers in the deep UV. The FEL accelerator vault in the User Facility building has been designed to accommodate this upgrade path.

The use of a cw superconducting linac results in a unique time structure for the FEL output. Similar to many linac driven FELs, the micropulse length is a very useful, short period of the order of a picosecond (chirping may allow pulse lengths as short as 200fs). Because of the cw capability

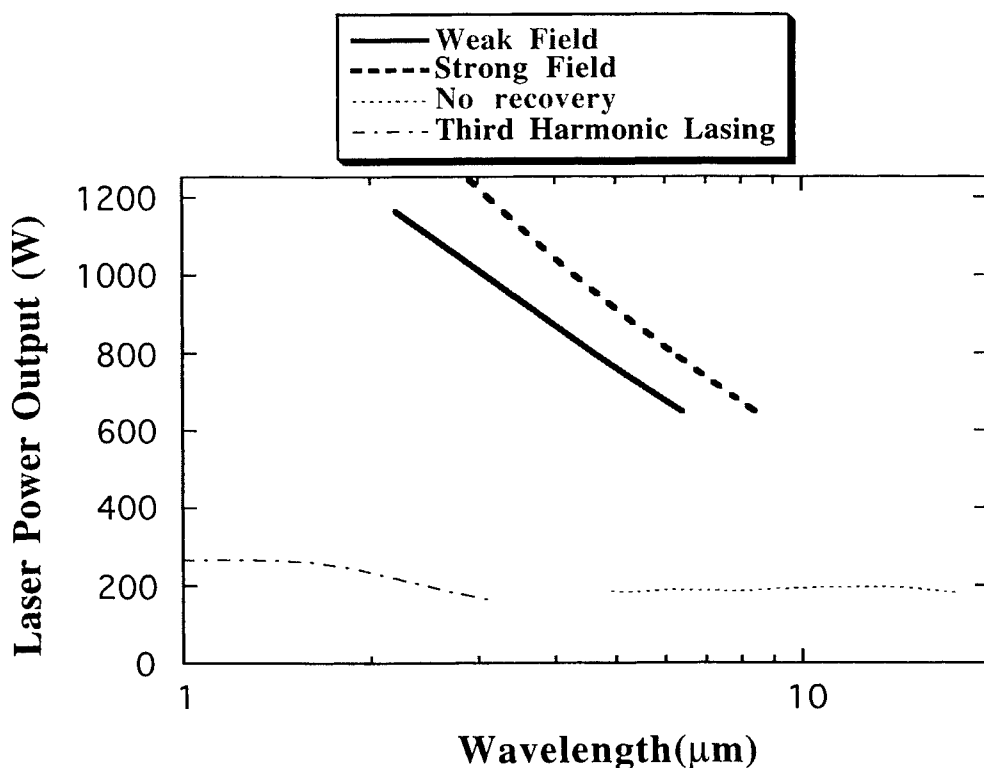


Figure 1. Performance of the IR Demo FEL. The installed hardware is capable of delivering kilowatt level power mid-infrared (2–7 microns) at two field positions (weak/strong) of the wiggler. With third harmonic operation, the short wavelength emit can be extended to 1 micron operation. With the use of long wavelength optics and no energy recovery the long wavelength limit can be extended to 16 microns.

2. FEL CHARACTERISTICS OF INTEREST TO USERS

Table 1. IR Demo FEL Output Characteristics
(see www.jlab.org/FEL/sciencap.html for further details)

Average Power	(see Figure 1)
Wavelength range	(see Figure 1)
Micropulse energy	15-30 μ J
Pulse length	~2 ps FWHM nominal
PRF	37.425 MHz, 18.7125 MHz
Bandwidth	<1.2 times Fourier transform limit
Timing jitter	< 0.2 ps RMS
Amplitude jitter	< 5% peak-to-peak
Amplitude drift	<20%/hour
Wavelength jitter	0.08% RMS
Polarization	linear, > 100:1
Transverse mode quality	< 2X diffraction limit

of the linac, the micropulse repetition rates are high, in the range of a few megahertz to 37 megahertz at the full average-power output rating. The combination of the short micropulse and high-average power gives the laser significant advantage for materials processing. In the basic science arena, this FEL offers new capabilities for sensitive spectroscopic measurements in selected condensed matter systems and almost all gas phase systems.

3. FEL INDUSTRIAL APPLICATIONS

A number of industrial partners have played a key role in the specification of the FEL and the subsequent development of applications with industrial relevance. Working groups led by industrial partners have been formed in four application areas: polymer surface processing, metal surface processing, microfabrication, and electronic materials. These working groups have been planning initial experiments and fit-up of user lab areas with relevant equipment. Table 2 lists some of the applications developed by the working groups. Most of these applications have been benchmarked using conventional Nd-YAG or excimer lasers. Processing capabilities will be extended by taking advantage of one or more of the characteristics of the IR Demo FEL, i.e., the high-average-power can enable large area processing, and the tunability and short pulse structure can enhance absorption. A description of many of the industrial applications proposed by industry members of the consortium is given in Reference.^[3] A brief summary of several of the applications is presented here.

Table 2. Illustrative Applied Research and Industrial Applications of the IR Demo FEL
Topic Participants

• polymer surface modification amorphization, texturing	DuPont/UVA
• metal processing amorphous metals texturing cutting/welding	Armco, VA Power Northrop Grumman Univ. of Mass.
• microfabrication non thermal processing ceramics/glasses	Aerospace, 3M Northrop Grumman
• photovoltaics defect analysis annealing	NREL, Solarex

Conventional lasers have been used to modify the surface of industrially important polymers to enhance a surface property that has commercial value. Examples include surface texturing and amorphization at relatively low laser fluences ($> 0.5 \text{ J/cm}^2$), and ablation and chemical transformation at higher laser fluences. This work could largely be done with excimer lasers. However, the typical long pulse length (ns) of these lasers decreases the efficiency of coupling the laser energy to the surface.

Secondly, the average power limits (200 watts) and pulse repetition rates (a few KHz) of available industrial excimer lasers prevents processing of production quantities at affordable rates.

With the availability of a high-power, tunable, infrared FEL, many of these surface modification demonstrations can be repeated at infrared wavelengths where there are significant absorbencies for commercially important polymers such as nylon (6.1 microns) and PET (5.9 microns). The first experiments in this area are planned by the polymer working group leader from DuPont who will investigate surface amorphization effects in PET. One of the FEL User Labs has been outfitted by DuPont with polymer film exposure equipment to enable the FEL beam to be rastered over an area of polymer film with a variable flux and variable transport rate. This work is an extension of experiments that were first performed at both the Stanford and Vanderbilt FEL user facilities. A complementary study of the fundamentals of energy transfer that occur during rapid thermal processing of polymers is being planned by a University of Virginia/DuPont collaboration.

A metals working group has planned similar large area, surface processing applications. Surface modification effects on metals surfaces benchmarked by conventional lasers include: surface amorphization, surface texturing,^[7-10] surface alloying, and surface ablation.^[11] A consortium led by Armco, Virginia Power and Northrop Grumman has outfitted one of the User Labs with a general purpose apparatus for varying the FEL exposure on sheet metal stock accurately positioned on a scanning work table. An important application from the metals working group is Virginia Power's interest in modifying the surface of the high strength steels used in the manufacturing of turbine blades to improve corrosion and wear resistance.^[8] This process has been benchmarked with YAG lasers, but again because of the time structure and the low average-power of these sources, the process is not commercially viable. Proposals have been prepared by several university groups (University of Mass. and Old Dominion University) to investigate the more fundamental aspects of laser material interactions on metal surfaces, particularly emphasizing the nature of laser-induced amorphization and surface alloy formation.

A microfabrication working group comprised of 3M, Aerospace Corporation and Northrop Grumman Corporation is planning to install several laser-micromachining workstations in the User Facility laboratories. One workstation will be dedicated for investigating fundamental aspects of laser ablation that can be used to optimize microfabrication tasks.^[12, 13] Given the broad tunability of the FEL, these studies will emphasize a wide variety of materials, including materials that are difficult to machine, such as glasses and ceramics. The second workstation will accommodate much larger samples to test production scale-up issues.

The most recently formed working group is a collaboration of industry and university partners in the LPC interested in electronic materials processing. This team is planning to use the IR Demo for pulse laser deposition^[11] and laser assisted chemical vapor deposition^[14] studies. The tunability of the source allows novel precursor materials to be used and the available power will enable processing rates and processing areas to be scaled over a larger range than can be studied with conventional lasers.

4. BASIC SCIENCE APPLICATIONS

Because of the expense, size and limited capabilities of FELs, these light sources have not yet had wide impact on scientific studies. The situation is changing rapidly with the availability of several FEL user facilities in the U.S. (Stanford, Duke, Vanderbilt, and Santa Barbara) and Europe (FOM, Orsay). In general, the scientific market is well served with the availability of Ti-sapphire pumped, optical parametric oscillators (OPOs) that can provide short pulse (~100 fs), widely-tunable radiation (350 nm–3 μ m) with sufficient micropulse energies (mJ) and average powers (milliwatts) for most scientific investigations. However, if considerably more average power and access to the mid-to-far IR or deep UV is required, than FELs provide the only available sources. Secondly, if an FEL is operated as a user facility, with appropriate attention to availability and user needs, then the facility costs can be easily amortized over a modest user base (10–20 users) such that the cost-per-user experiment is much less than the comparable cost of state-of-the art bench top lasers.

The university community that is involved with the Laser Processing Consortium has proposed a number of experiments that take advantage of the unique properties of the Jefferson Lab FEL. As noted in the previous section, some of these experiments examine a basic science problem associated with one of the FEL industrial applications, while others have no particular connection to one of the established applications. From the initiation of the LPC workshops in 1993, consortium members have benefited from, and encouraged a healthy mixture of applied science and basic science interests as the user program developed.

During the Spring of 1997, a specific call for basic science proposals for the FEL was issued through the consortium and several workshops sponsored by DOE's Basic Energy Science program office. The topics that were addressed in these proposals are listed in Table 3 and a brief description of several of the most promising proposals is given below.

Table 3. Basic Science Proposals for the IR Demo FEL

short pulse laser ablation physics	Vanderbilt, U. Mich., PVD, Aerospace
laser deposition	NCSU, ODU, NSU, FSU
photophysics at buried semiconductor interfaces	OSU, Vanderbilt, NCSU, Aerospace
amorphous layers on metals	Univ. of Mass., ODU, Stony Brook
rapid thermal processes in polymers	UVA, DuPont
laser synthesis of ferroelectric nanoparticles	ODU, Kodak
spectroscopy of molecular and cluster beams	Princeton, UVA
characterization of photovoltaic films	NREL, Solarex, Inc.
kinetics of carbon nanotube formation	Univ. of KY, Univ. of PA, DuPont

Many scientific applications of the FEL will take advantage of the significant increase in source brightness when the FEL is compared to existing scientific sources in the mid-infrared. Fig. 2 plots the average brightness of the FEL relative to a standard laboratory IR source (a 2000K blackbody radiator or "glowbar") and with the strength of the IR synchrotron emission extracted at the IR beamlines at the National Synchrotron Light Source at Brookhaven National Laboratory.^[15] In the mid-infrared (~5 microns) the Jefferson Lab FEL is 5 orders of magnitude brighter than the NSLS synchrotron emission and 8 orders of magnitude brighter than a glowbar source. Scientific measurements that are signal limited by the IR source average brightness can take particular advantage of the FEL.

An example of such a class of experimental measurements is the spectroscopy of silicon surfaces and embedded interfaces in silicon microelectronic structures. Silicon is reasonably transparent in the mid-infrared which means that average powers in the 0.1-1 kW range could be used on clean silicon samples for enhanced spectroscopy in either absorbing or reflecting modes. Basic science proposals have been submitted^[16-18] which address the nature of diatomic bonds (e.g., Si-O, Si-H, Si-D, Si-N) at the Si/SiO₂ interface; this bond structure strongly effects the electronic behavior across the interface. An understanding of this important interface has impact on the performance of gate electrodes in silicon microelectronics. All of the diatomic pairs noted above have stretch transitions in the mid-infrared that are weak and difficult to observe with conventional sources especially when the interface is buried. There is sufficient source brightness with the FEL to detect these transitions with standard spectroscopic techniques without relying on multiple internal reflection geometries. The average power in the FEL would enable surface defects to be analyzed

Average Brightness vs. Photon Wavelength

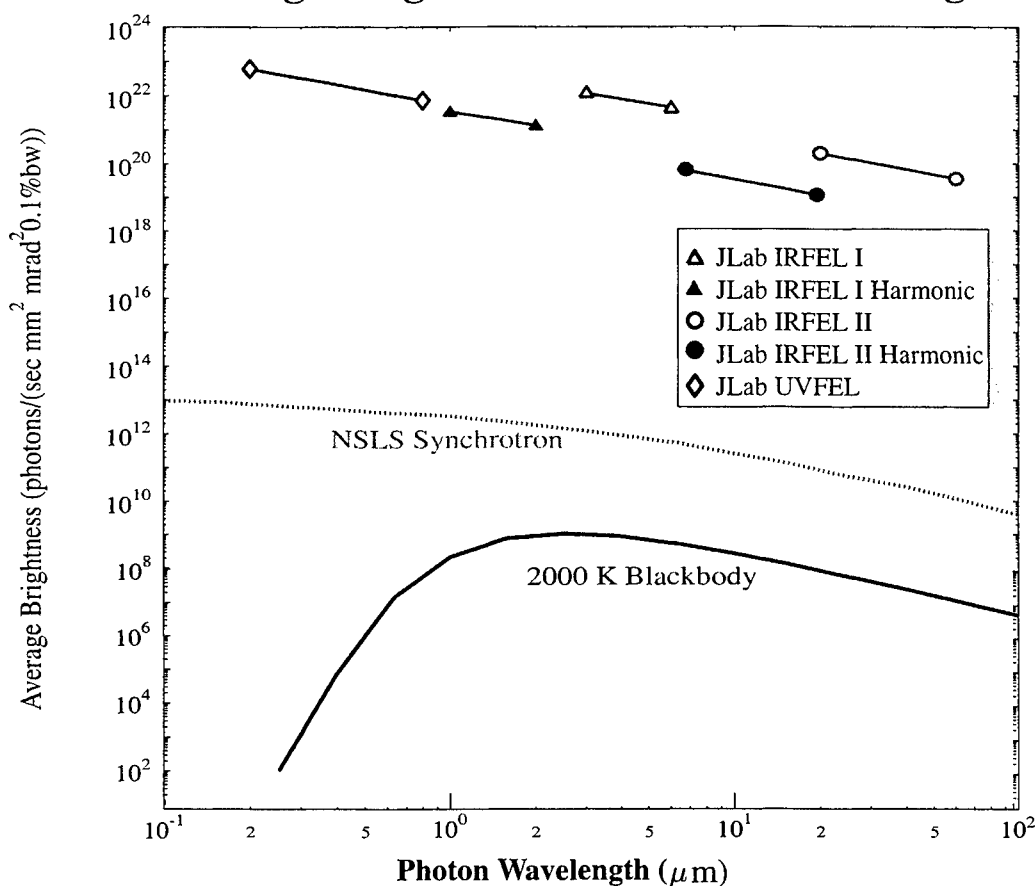


Figure 2. Average Brightness vs. Photon Wavelength

at buried interfaces well below the sub-monolayer level ($< 10^{10} \text{ cm}^{-2}$), and may also afford the possibility of selective annealing of problematic defects at buried interfaces.

A related study on silicon has already been performed using IR radiation from the Vanderbilt FEL. Feldman et al.^[19] have detected the presence of silicon-hydrogen vacancy complexes, some of which can be induced by the FEL radiation. This work will continue at Vanderbilt^[20] and migrate to the Jefferson FEL to take advantage of the higher power and expanded tuning range.

Both polycrystalline and amorphous silicon films are the primary materials incorporated in solar photovoltaic panels. A collaboration involving DOE's lead laboratory in solar photovoltaic development (NREL) and the largest manufacturer of commercial solar panels (Solarex) has proposed using the FEL for characterization of impurities and defects in silicon PV films and for the development of large area laser processing techniques for panel materials.^[21]

Proposals have been submitted from a number of university groups (NCSU, Norfolk State University, Old Dominion University and Florida State University) that would use the FEL IR radiation both as a source for laser assisted chemical vapor^[14, 22] deposition and a probe of growth conditions and growth kinetics.^[23-24] This group is aligned with the electronic materials working group mentioned previously under the heading of industrial applications.

Conventional short pulse lasers (excimers and YAGs) have been used for laser ablation of difficult to melt or multicomponent target materials and for laser deposition of thin films from the resulting laser-produced plasma plumes.^[11]

High quality films of complex materials (alloys, high Tc superconductors, ferroelectrics, etc.) have been produced by pulsed laser deposition that are unrivaled with other high purity deposition techniques. The high-average power of FEL enables extrapolation of the technique to significantly larger substrate geometries than the typical (~10 cm) substrates. The tunability of the FEL may improve the efficiency of the technique by taking advantage of specific absorbencies in the laser target materials. Proposals are under development that explore many uses of the FEL for laser ablation and deposition. A group from Vanderbilt University is interested in the fundamentals of the interaction of short pulse (ps) laser radiation with oxides and metals.^[25] A collaborating group from the University of Michigan would analyze the characteristics of the resulting plasma plumes to connect plume properties to incident laser conditions and the resulting quality of the deposited films.^[26] A collaboration involving the University of Kentucky, the University of Pennsylvania and DuPont^[27] has proposed using the FEL to optimize the laser ablated growth of carbon nanotubes.^[28] The laser ablation technique has been demonstrated^[29] to make significant quantities of carbon nanotubes which promises to be very useful for a wide variety of scientific and technical applications (q.v., a host material for 1D quantum confinement studies, a building block for nanoelectronics and extremely high strength fibers).

Laser ablation is also useful for producing useful quantities of nanoparticles^[30] which can be used to characterize materials properties at nanoscale dimensions and for source material for synthesis studies. A collaboration involving Old Dominion University and Cornell University^[31] is developing a proposal for laser ablation and laser-assisted CVD production of ferroelectric nanoparticles.^[32]

The high-average-power, relatively high peak power, and broad tunability of the FEL open up an array of scientific studies involving gas phase chemical systems. The FEL will be particularly attractive for detection of dilute species in plasmas, flames and molecular beams. Such applications were first proposed in one of the first workshops on FEL applications,^[33] and most recently provided the scientific justification for a high-average-power IR FEL that was to be built as a major scientific tool for combustion research at the Lawrence Berkeley National Laboratory.^[34] The first proposal in this area for implementation at Jefferson Lab involves a collaboration between Princeton University and the University of Virginia. Recent work by Lehmann and Scoles^[35] has shown the value of ⁴He cluster beams for high sensitivity spectroscopic analysis of molecules encapsulated in the ⁴He clusters. The ⁴He clusters provide a weakly interacting host for the test molecule: the translational temperature of the clusters is of the order of 0.4K and there is no spin coupling to the host atoms because of the lack of spin in ⁴He. The existing spectroscopic studies performed with low repetition rate conventional lasers are severely count-rate limited. The use of a high average power IR FEL can saturate IR transitions in the test molecules allowing determination of: (1) true homogeneous line widths; (2) rotational and vibrational population relaxation; and (3) dissociation and recombination times.

In the beginning of this discussion of scientific applications of FELs, it was noted that most scientific applications of lasers are well served by the current generation of Ti-sapphire or YAG laser-pumped OPOs. These laser systems have found wide application in chemical physics, atomic, molecular and optical physics, and surface physics. Most of these studies would benefit from having several (2-3) OPOs synchronized and available for interrogation of the system under study with variable time delays between the separate OPOs. The expense mounts considerably and the time synchronization problem is non-trivial as OPO systems are multiplexed. A collaboration involving the University of Virginia, the College of William and Mary, and Old Dominion University has proposed a novel solution to this problem.^[36] The FEL can be used as the drive laser for multiple OPOs, thus providing in one user lab a unique spectroscopic tool for atomic, chemical and surface physics studies.

Several options for such an "OPO Farm" are being evaluated by the collaboration and the FEL design team. One possible version uses the third harmonic laser radiation (100-200 watts at 1-2 microns), which is first beam split to the power handling limits of harmonic conversion crystals for converting the IR to UV for driving the OPOs. The OPOs would be synchronized because of the use of the identical drive laser. Downstream pulse compression techniques could be used to provide ultrashort pulses in one or more of the OPO channels. Potential uses for a facility with multiple, time-synchronized OPOs include: (1) coherent control studies of chemical reactions in atomic/molecular beam scattering experiments; (2) pump-probe studies of gas-phase and surface phase reactions; (3) preparation of ultra-pure chemical reactants.

SUMMARY AND ACKNOWLEDGEMENTS

The specification, design and development of the Jefferson Lab FEL User Facility has been strongly coupled to a user community interested in the use of high-average-power laser light. After commissioning of the first FEL in the User Facility,

a versatile infrared FEL, the first user experiments will be executed in the Winter of 1999. The preceding document was a brief description of several of the experiments planned by industrial, university and national laboratory participants in the user programs. Further details are available in the proceedings of the Laser Processing Consortium workshops and directly from the principal investigators. The author thanks the principle investigators for granting permission to summarize their proposed experiments and for their strong support of the Jefferson Lab FEL program. The author is indebted to his colleagues on the FEL team, in the Accelerator Division, and our funding agencies (Dept. of Energy, Dept. of Navy, Commonwealth of Virginia) who have made the Jefferson Lab FEL a reality.

REFERENCES

1. C. L. Bohn, Proc. 1997 Particle Accelerator Conference (IEEE Piscataway, NJ, 1997) 82
2. S. Benson, Proc. 20th International Free Electron Laser Conference, Williamsburg (1998) (in press)
3. M. Kelley, Lasers as Tools for Manufacturing of Durable Goods and Microelectronics, SPIE Proc. Vol. 2703 (1996) 15-20; Nucl. Instr. Meth. B144 (1998) 186-192
4. B. Jannery, J. Electronic Defense, (1997) 37-63
5. D. S. Dunn and A. J. Ouderkirk; Macromolecules 23 (1990) 770-774
6. W. Kesting, D. Knittel, T. Bahnners and E. Schollmeyer; Appl. Surf. Sci. 69 (1993) 330-335
7. H. B. Singh, S. M. Copley and M. Bass; Met. Trans. 12A (1981) 138-140
8. B. Brenner, E. Wiedmann and B. Winderlich in "Laser Treatment of Materials", B. Mordike (ed.) DGM Informationsgesellschaft Verlag, Munich, (1992) 199-204
9. D. R. Baer, D. J. Frydrych and T. R. Jervis in "Environmental Degradation of Ion and Laser Beam Treated Surfaces", G. S. Was and K. Grabowski, eds., (The Metallurgical Society, Warrendale, PA 1989)
10. Thomas R. Jervis, James P. Hirvonen and Michael Nastasi; Lubric. Eng. 48 (1991) 141-146
11. John D. Miller and Richard F. Haglund, eds., "Laser Ablation and Desorption", (Academic Press, San Diego 1998)
12. H. Helvajian, L. Wiedeman, and H.-S. Kim, SPIE Proc. Vol. 2045 (1994) 2
13. H. Helvajian, L. Wiedeman, and H.-S. Kim, Adv. Mat. for Opt. and Electr. 2 (1993) 31
14. F. A. Houle, et al., Appl. Phys. A49 (1989) 189
15. G. P. Williams, Brookhaven National Laboratory Report, BNL-26947 (Nov. 1979)
16. B. J. Hinds, F. Wang, D. M. Wolfe, C. L. Hinkle and G. Lucovsky, J.Vac.Sci.Technol. B16 (1998) 217
17. A. P. Young, J. Schafer, G. H. Jessen, R. Bandhu, L. J. Brillson, G. Lucovsky and H. Niimi, J.Vac.Sci.Tech Vol. B16 (1998) 22177
18. B. Bech Nielsen, L. Hoffman, and M. Budde, Mat. Sci. and Eng. B36 (1996) 259
19. L. Feldman (Vanderbilt University), private communication
20. N. H. Tolk, R. G. Albridge, A. V. Barnes, B. M. Barnes, J. L. Davidson, V. D. Gordon, G. Margaritondo, J. T. McKinley, G. A. Mensing and J. Sturmann, Appl. Surf. Sci. 106, (1996) 205
21. L. Kazmerski (NREL), private communication
22. D. Brachotte and H. van den Bergh, Appl. Phys. A49, (1989) 189
23. N. Dietz, N. Sukidi, C. Harris, and K. J. Bachmann, J. Vac. Sci. Technol. A15, (1997) 807
24. D. E. Aspnes, J. Vac. Sci. Technol. A14, 960 (1996)
25. R. Haglund (Vanderbilt University), private communication
26. R. Gilgenbach (University of Michigan), private communication
27. P. Eklund (University of Kentucky), J. Fischer and G. Lavin, private communication
28. A. Thess, R. E. Smalley, et al., Science 273 (1996) 483
29. S. Bandow, Inst. of Molecular Science (Okazaki) private communications
30. A. S. Edelstein and R. C. Cammarata, Nanometals: Synthesis Properties and Applications (IOP Publishing, London 1996)
31. M. Gupta (Old Dominion University), private communication
32. E. V. Colla, A. V. Fokin and Yu A. Kumzerov, Nanomaterials: Synthesis, Properties and Applications, Solid State Comm. 103, (1997) 127
33. V. Scoles, Workshop on FEL Applications (1979)
34. Combustion Dynamics Research Facility Proposal, Lawrence Berkeley National Laboratory, (1994)
35. K. Lehmann and V. Scoles, Science 279,/ (1998) 2065
36. W. Cooke (College of William and Mary), R. Jones, T. Gallagher, C. Sukenik, private communication

High Power Ultraviolet All-Solid-State Laser for Industrial Applications

Ch. Mehlmann, Th. Schröder, P. Klopp, R. Koch, U. Stamm, D. Basting, LP US
Lambda Physik GmbH, Hans-Böckler-Str. 12, D-37079 Göttingen, Germany
Phone: (+49)-(0)551-6938-0, Fax: (+49)-(0)551-68691, e-mail: randd@lambdaphysik.com

ABSTRACT

A diode-pumped laser system is described operating at 1 Hz - 7 kHz pulse repetition frequency. Average powers of more than 5 W at 355 nm are achieved. With it's beam quality of M^2 better than 1.1 it is excellently suitable for micro-machining applications generating smaller spot sizes with rather simple imaging systems. Laser parameters such as pulse duration, average power as well as energy stability are investigated. Long term test results above 4.0×10^{10} shots are presented.

KEY WORDS

Micro-Machining, Micro-Drilling, Diode-Pumped Laser, UV Solid-State Laser, High Pulse Repetition Frequency

1. INTRODUCTION

Industrial applications of ultraviolet (UV) lasers include micro-lithography, ablation, micro-hole-drilling, micro-adjustment, and micro-welding. While at highest UV average power levels production systems employ excimer lasers, progress in UV solid-state laser technology and nonlinear materials has widened their potential impact on low power applications in microengineering and optoelectronic manufacturing. The required throughput of flexible industrial processes often demands high pulse repetition frequencies (PRF). The paper discusses achievements in all-solid-state UV lasers. Prospects of applications in microelectronic and optoelectronic manufacturing are discussed and examples of micromachining are presented.

2. LASER OSCILLATOR

Fig. 1 depicts a schematic outline of a diode-pumped Nd:YAG laser that is commercially available as the Lambda StarLine and meanwhile well established in applications in science and industry [1, 2]. The laser oscillator is a hermetically sealed-off electro-optic Q-switched diode-pumped Nd:YAG laser with stable resonator. The laser rod is side-pumped by 100 W average power quasi-cw laser diode bars with 25% duty-cycle. An advanced imaging arrangement of the diode-bars into the Nd:YAG rod has been developed. Optimum overlap of the pumped gain volume and the transverse fundamental mode of the resonator is obtained while thermal distortions are minimized.

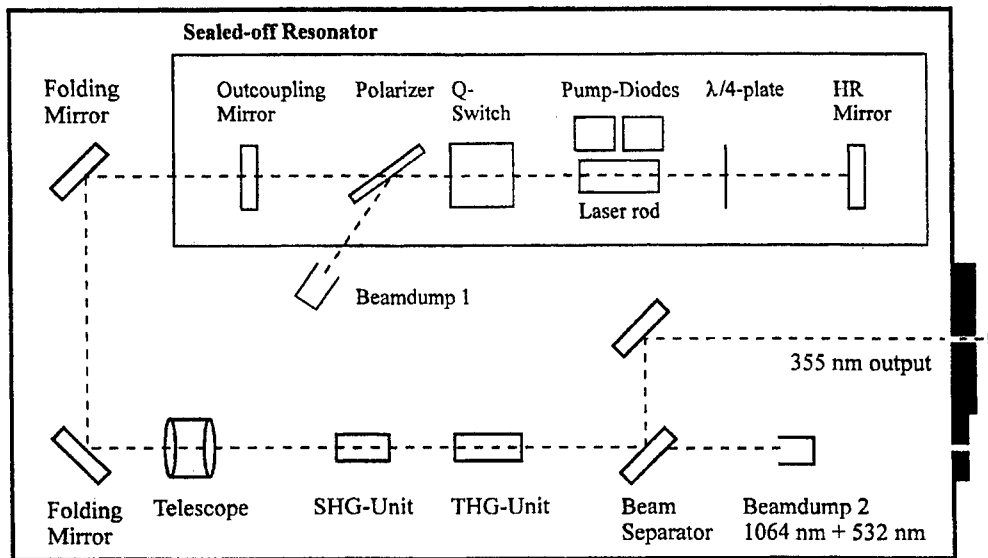


Fig. 1 Diode-pumped Nd:YAG laser oscillator – schematic view.

Additionally, the use of a quarter wave-plate and the electro-optical Q-switch on opposite sides of the laser rod results in a twisted-mode arrangement which provides significant advantages. Spatial hole burning is prevented and the quarter-wave plate compensates for thermally induced birefringence.

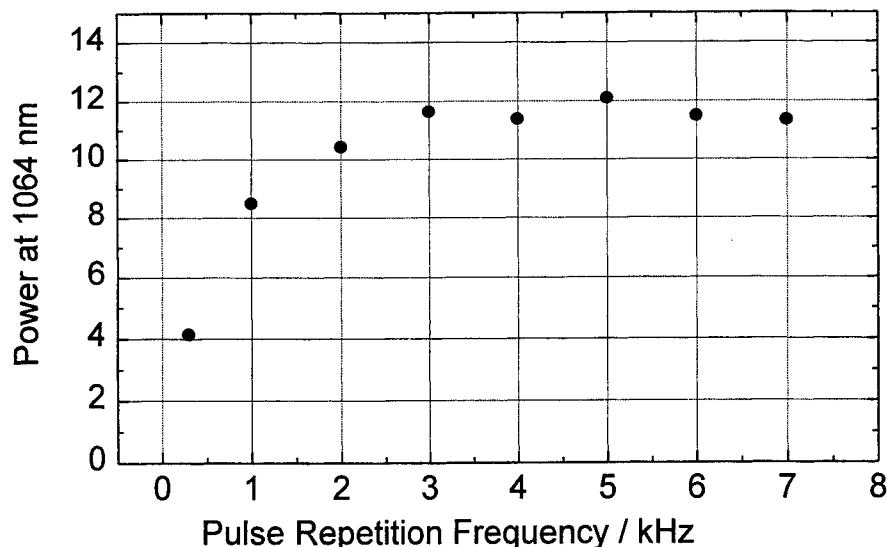
In the following we present first results of the next generation prototype system. The output beam of more than 10 W for operation in a range of PRF between 1 Hz and 7 kHz is nearly diffraction limited ($M^2 < 1.1$). The fast rise-time of the electro-optical Q-switch in combination with the high laser gain

results in a pulse duration of less than 10 ns at 1 kHz PRF. At 5 kHz a pulse length below 28 ns is achieved. Extraordinary beam quality, high intensity and short pulse length qualify this system for efficient external generation of harmonics.

For a variety of applications it is desirable to adjust the pulse energy without changing other beam parameters such as spatial beam profile and divergence. Furthermore, it is often necessary to vary the pulse repetition rate depending on the specific process. The resonator design and software meet these requirements. The laser output power can be continuously adjusted between 50% and 100% without changes in mode quality. The repetition rate can be varied to any integer value between 1 Hz and 7 kHz without affecting mode quality.

Fig. 2 illustrates the performance of the laser between 300 Hz and 7 kHz repetition rate. At 5 kHz more than 11.5 W of average power (pulse energy > 2.4 mJ) are obtained at 1064 nm with excellent beam quality ($M^2 < 1.1$, demonstrated in fig.3). A shorter resonator has been developed to reduce the pulse length. At 1 kHz the system generates 10 ns pulses and even at 5 kHz the pulse length is less than 28 ns. This is of particular importance for efficient external harmonic generation and for special high peak power applications.

Fig. 2 Average output power at 1064 nm versus pulse repetition frequency.



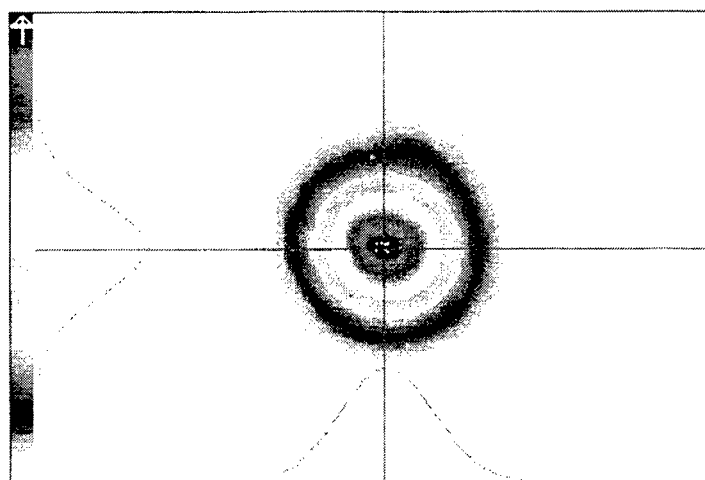


Fig. 3 Beam profile of laser at 1064 nm, running at 5 kHz.

The excellent energy stability for different pulse repetition frequencies from 1 Hz to 5 kHz is illustrated in Fig. 4.

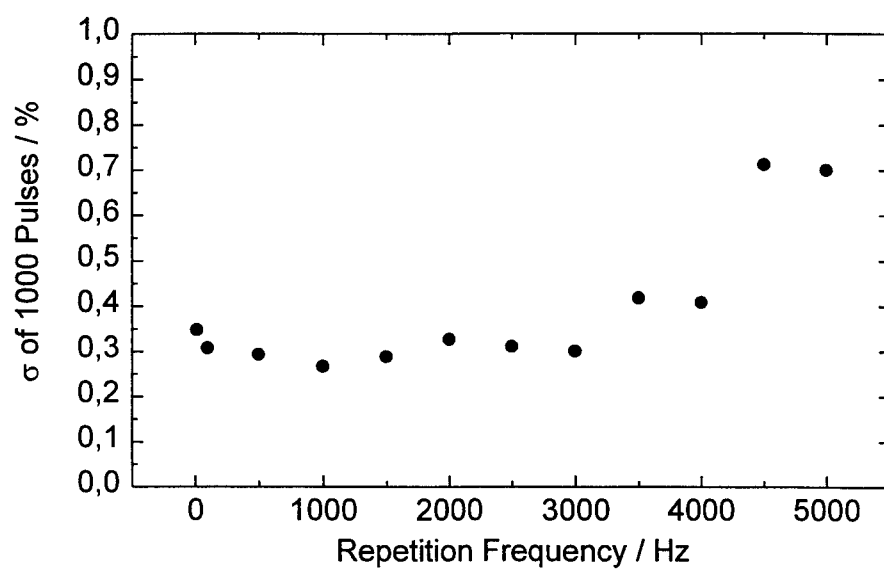


Fig. 4 Pulse energy fluctuations (standard deviation) at 1064 nm using different pulse repetition frequencies.

3. HARMONICS GENERATION

The demands of specific applications and materials require different laser wavelengths for optimum results. Additionally, shorter wavelengths provide higher spatial resolution and may be preferred therefore. The laser has been tested with SHG (532 nm) ,THG (355 nm) and 4HG (266 nm). This paragraph summarizes some main results on frequency conversion.

Superior beam quality and pulse energies are the key to highly efficient external harmonic generation, even at pulse repetition frequencies up to 7 kHz. External conversion schemes have the advantage of higher stability as they do not affect the fundamental frequency of the laser. Therefore then, the stability of the harmonic output is superior to that of intracavity frequency conversion schemes. Additionally, it is much easier to switch between different wavelength if requested.

Frequency tripling is performed in two consecutive doubling / mixing crystals. Fourth harmonic generation is performed by frequency- doubling of the 532 nm radiation using a proprietary second frequency converter [3]. At 5 kHz PRF the laser delivers average powers well above 11.5 W at 1064 nm, 6 W at 532 nm, 5 W at 355 nm and almost 2.5 W at 266 nm. Fig. 5 depicts the dependence of the harmonics' average power on the average power of the fundamental wave.

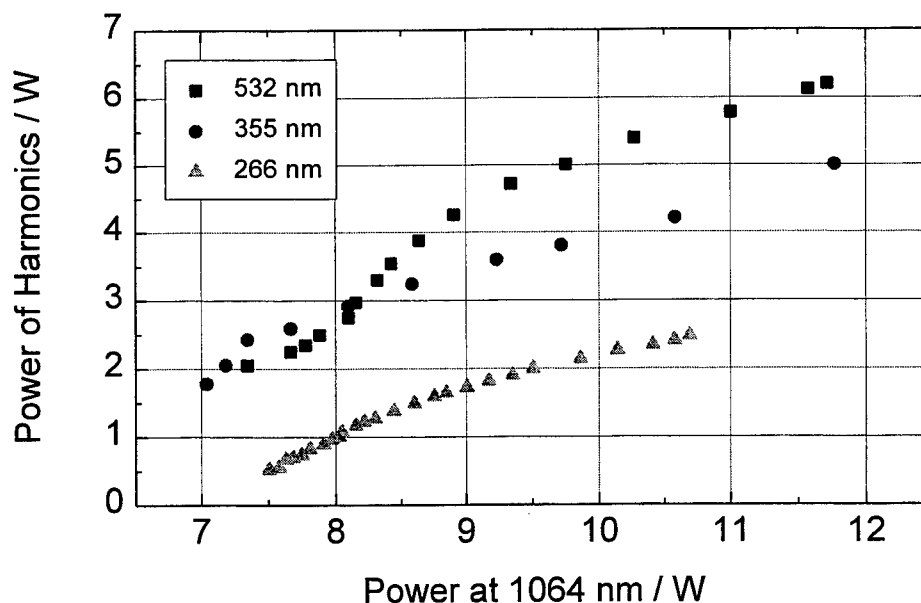


Fig. 5 Average output power of second, third and fourth harmonic versus average power at 1064 nm at 5 kHz.

At 7 kHz PRF the system produced 4.7 W in the second harmonic (532 nm) using 11.4 W in the fundamental wave (1064 nm) with a corresponding pulse length of 30 ns for the SHG (32 ns at 1064 nm).

Generating the third harmonic with this laser system the beam quality is absolutely excellent. As shown in Fig. 6. the beam quality is measured as to $M^2 < 1.1$.

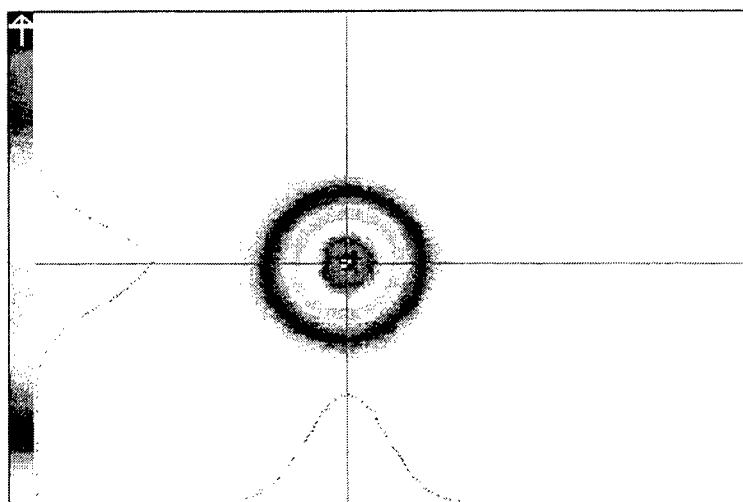


Fig. 6 Beam profile of the 355 nm beam and cross-section with Gaussian fit.

4. PROMISING APPLICATIONS IN MANUFACTURING

The unmatched performance as reported above opens new prospects for the application of diode-pumped solid state lasers in manufacturing. Besides obvious applications in nonlinear optical processes for diagnostic studies, material processing itself benefits from the average power levels available, the beam quality and the intensity in the UV. Typical applications are hole drilling and manufacturing of

three dimensional structures. Figure 7. shows an example of a three dimensional structure of 1.5 mm depth, manufactured by using Lambda Physik's StarLine at 532 nm, running at 1 kHz.

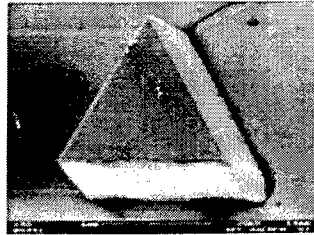


Fig. 7 three dimensional pyramid in TSM 30, 532 nm. Source ILT Aachen.

5. CONCLUSIONS

We have developed a diode-pumped laser system that is operating at pulse repetition frequencies from 1 Hz to 7 kHz. At 5 kHz PRF the laser delivers average powers well above 11.5 W at 1064 nm, 6 W at 532 nm, 5 W at 355 nm, and almost 2.5 W at 266 nm. Laser parameters such as pulse duration, average power and energy stability are investigated.

Prospects of applications in microelectronic and optoelectronic manufacturing have been discussed. Beam quality is better than $M^2 = 1.1$ and so forth excellently suitable for micro-machining applications generating smaller spot sizes. An example on micro machining structures has been shown.

ACKNOWLEDGEMENTS

Parts of this work were supported by the Bundesministerium für Bildung, Wissenschaft, Forschung und Technologie (BMBF) under contract # 02PV76041. The contributions of S.Govorkov and A.Wießner to the development of the 4 HG cell are gratefully acknowledged.

REFERENCES

1. Patent StarLine
2. U. Stamm et al., CLEO 1997
3. Patent 4 HG-Cell

Efficiency increase for laser structuring using mask projection

Knut Jasper, Peter Berger, Helmut Hgel

Institut fr Strahlwerkzeuge (IFSW), University of Stuttgart, Germany

ABSTRACT

Mask based structuring in excimer laser applications is costly if masks with a small ratio of the hole pattern area compared to the whole illuminated area are used. In this case, the major part of the laser beam is reflected or absorbed at the mask. The herein presented system shapes the reflected part of the beam and guides it onto the mask again. This principle has been realized for up to eight irradiations of the mask. In order to achieve high quality ablation results both the beam divergence as well as the homogeneity play an important role. Therefore, a special homogenizer was developed which converts the excimer laser beam efficiently into a flat-top profile with negligible influence on the beam quality. The achieved optical resolution keeps within 2µm and the homogeneity is sufficient to achieve nearly the same structure quality over the entire image field. Providing that the transmitting areas of the mask do not exceed a few per cent of the total irradiated area, an efficiency enhancement by more than a factor of five was achieved for eight mask irradiation passes compared to a single irradiation.

Keywords: Micro machining, structuring of polyimides, excimer laser ablation, homogenizer, efficiency enhancement

1. INTRODUCTION

Excimer lasers are suitable for structuring different polymers, e.g. polyimides, which are used in electronics industry. The typical properties of excimer lasers, e.g. the pulse duration in the order of nanoseconds and the short wavelength, in combination with the material properties of polymers, e.g. short absorption length and low thermal diffusivity, allow to generate high precision structures with a well controlled depth.

Due to the poor beam quality of the excimer laser usually a mask projection technique is employed. On the one hand, the result of the ablation is determined by the quality of the optical components which are used for the projection and on the other hand it is highly dependent on the homogeneity of the mask irradiation. One method to generate homogeneity in the plane of the mask is to cut off the inhomogeneous sections of the beam's cross-section with an aperture. Another possibility is to employ a so-called homogenizer to obtain a large homogeneous part of the beam profile. In the first case, the efficiency is drastically reduced due to the usually large fraction of the cross-sectional area that is cut away and thereby absorbed or reflected at the aperture. In the second case, a homogeneous beam profile can only be achieved in one single plane and the beam quality is usually worse compared to that of the original laser beam. The poor beam quality after homogenization requires top quality projection lenses to achieve structures without the influence of optical aberrations. From an optical point of view this method ensures structure resolutions down to a sub µm scale.

If the structure density is low compared to the entire irradiated area of the mask, the overall efficiency of the system is poor even if a homogenized beam is used. In order to increase the efficiency of the process, a system was developed at the IFSW which consists of an excimer laser, a new homogenizer concept, and an arrangement of mirrors and lenses that allows to use that part of the laser beam which is reflected at the mask to irradiate the mask several times.

2. SYSTEM LAYOUT

In order to explain the function of each component as well as their interaction, an overall view of the system is presented in Fig. 1. An excimer laser (Lambda 4000) operating with KrF at 248nm serves as laser beam source. In many systems the laser beam is shaped by two telescopes consisting of pairs of cylindrical lenses in order to achieve a beam with a square cross-section to be sent into a conventional fly-eye homogenizer¹. In contrast to that, in the presented system the homogenizer is adapted to the output beam of the excimer laser and consequently the telescopes are located after the homogenizer and are used to adapt the cross-section and the divergence angle of the homogenized beam to the mask-irradiation system.

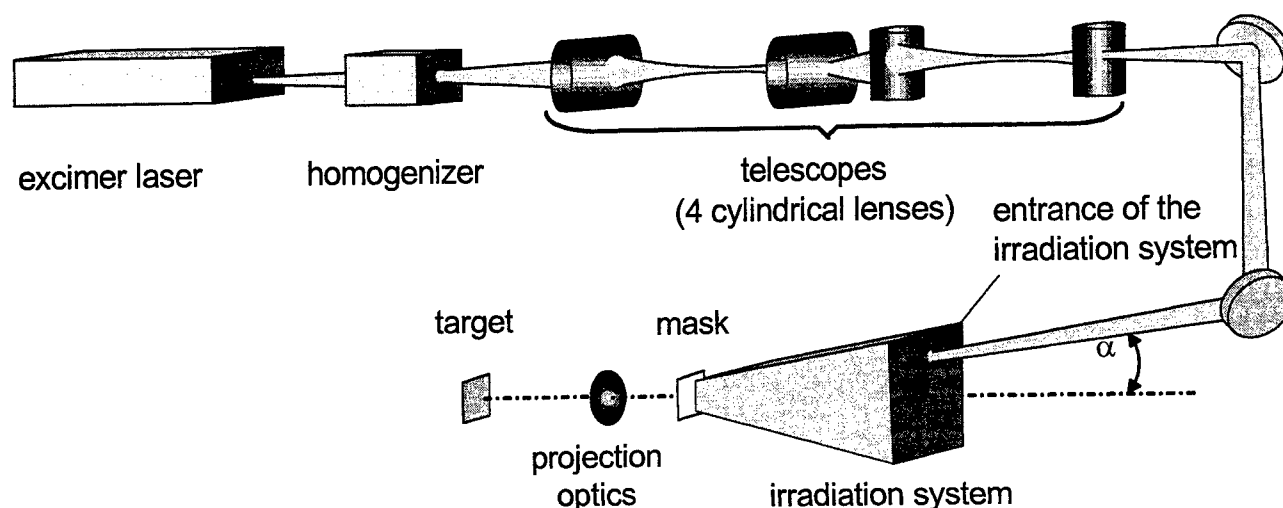


Fig. 1 System layout with excimer laser, homogenizer, telescopes, irradiation system, and mask projection

The irradiation system reshapes that part of the laser beam which is reflected at the mask and guides it back onto the mask that can be repeated several times. The actually used set-up generates eight illuminations (shown in detail in Fig. 7). Each illumination meets the mask at a slightly different angle of incidence. The largest angle of incidence occurring at the mask can be considered as the divergence angle α (see Fig. 1) of the total illumination. This divergence angle α is small enough that the mask structures can be imaged onto the target using conventional projection optics.

3. PRINCIPLE OF A NEW HOMOGENIZER

The realization of a multi irradiation system with small divergence angles at the mask requires that a homogeneous beam profile is maintained over a beam path of several meters. Conventional homogenizers^{1,2}, however, have a homogeneous beam profile only within a range of about 10 mm to 50 mm. Therefore, a homogenizer³ was developed that satisfies the required specifications.

Many excimer lasers have a rectangular beam cross-section with a nearly flat-top profile along the long beam axis. Therefore, this beam axis does not need to be altered by the homogenization. Along the short beam axis, however, the profile is similar to a Gaussian profile which is to be homogenized.

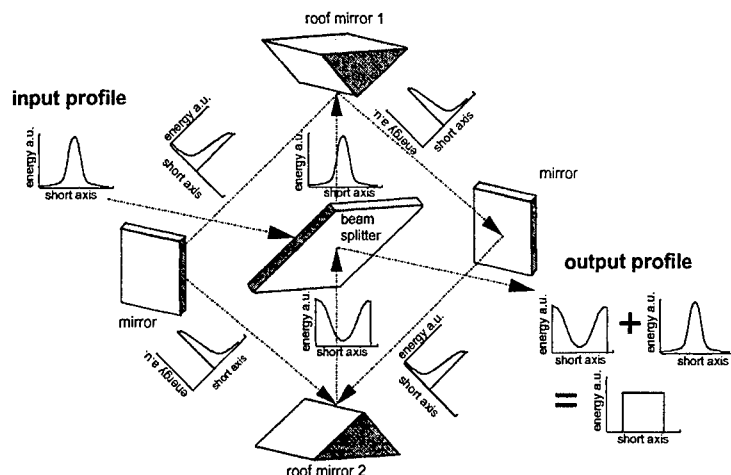


Fig. 2 Principle of the homogenizer and beam profiles for the first round trip

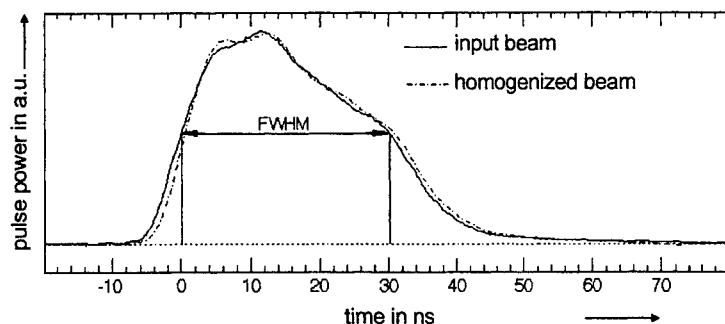


Fig. 3 Pulselength of the input beam and the homogenized beam

homogenizer in comparison to the beam profile at the laser output. The beam profiles measured in the distances of 500 mm and 2500 mm resemble each other. The slightly change of the shape is caused by the divergence of the laser. The measured beam parameter product of the homogenized laser beam is nearly equal to the original beam.

The laser beam is divided by the beam splitter into two beams, see Fig. 2. The transmitted beam leaves the homogenizer with the original beam profile whereas the reflected beam is guided to the first roof mirror. It divides the beam in half along the long beam axis. Each half beam is reflected separately onto the second roof mirror which recombines the two beams. The recombined beam now has an inverted-shaped Gaussian-like beam profile, having its minimal intensity at the center and the maxima at the edges. At the back of the beam splitter this beam profile is coaxially superimposed with the originally transmitted beam. The other part of the shaped beam profile, that is transmitted through the beam splitter after the first round trip, is inverted once more by the roof mirrors during the next round trip which leads to a Gaussian-like profile similar to the original one. For further round trips the beams leaving the homogenizer alternate between an inverted Gaussian and a Gaussian profile. After four round trips 90 % of the pulse energy has left the homogenizer. Due to the short beam paths a prolongation of the pulse width can not be observed (see Fig. 3).

When an adequate transmission ratio of the beam splitter is chosen the beams which leave the homogenizer after several round trips add up to a homogeneous beam profile. Fig. 4 shows the beam profiles at different distances behind the

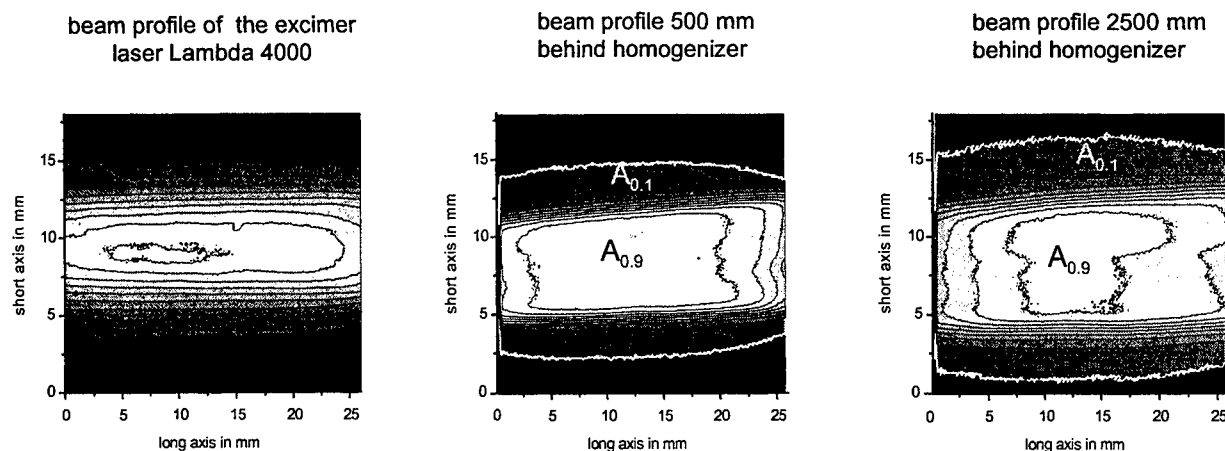


Fig. 4 Original beam profile and homogenized beam profiles at the distances of 500 mm and 2500 mm behind the homogenizer with area $A_{0.1}$ (framed white) wherein all energy densities amount to more than 10 % of the maximal energy density and area $A_{0.9}$ (central white area) wherein all energy densities amount to more than 90 % of the maximal energy density (the beam profiles are cut off on the left and right side by the camera chip)

The homogeneity can be characterized according to the ISO 13964 standard¹ by the edge steepness and the plateau uniformity. The plateau uniformity can be illustrated by the statistical energy density distribution of the spatially resolved energy densities of the entire beam profile. That means that the cross-section of the beam is divided into small cells (here 240x240 according to the pixels of the camera frame grabber which was used for the measurement) and all cells with an energy density within a certain interval are counted. These numbers of pixels can be assigned to the mean energy density of each interval. The numbers of pixels for each energy density included in the beam profiles measured at distances of 500 mm and 2500 mm behind the homogenizer are displayed in Fig. 5. The FWHM of the peak short below the maximum energy density is characteristic for the homogeneity of the measured beam profile. The plateau uniformity which is defined as

$$U_p = \frac{\Delta H_{FWHM}}{H_{max}} \quad (1)$$

amounts to 5,0 % at the distance of 500 mm and to 11.1 % at the distance of 2500 mm. Both values are limited by the inhomogeneities along the long beam axis which was not affected by the homogenization. For an optimal top-hat profile the plateau uniformity U_p approaches 0. The results depend in detail on the shape of the input beam profile and hence of the laser. The other criterium, the edge steepness s , is defined as the normalized difference between the area $A_{0.1}$ (framed white in Fig. 4) wherein all energy densities amount more than 10 % of the maximum intensity and area $A_{0.9}$ (central white area in Fig. 4) wherein all energy densities amounts at above 90 % of the maximal intensity. Equation (2) shows that an optimal top-hat profiles approaches 0.

$$s = \frac{A_{0.1} - A_{0.9}}{A_{0.1}} \quad (2)$$

The measured edge steepness at the distance of 500 mm amounts to 0.67 and to 0.82 at the distance of 2500 mm.

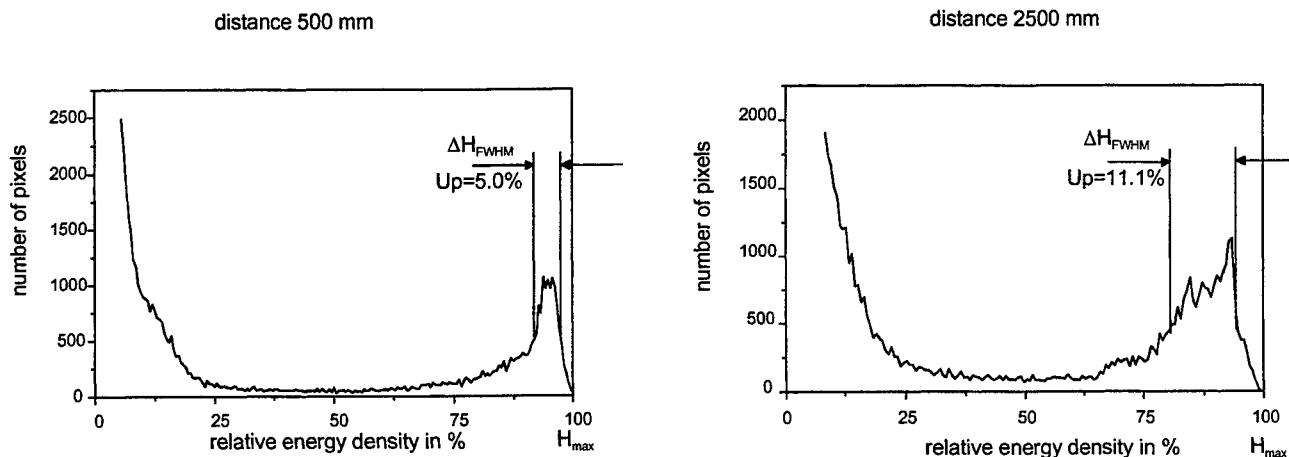


Fig. 5 Statistically spatially resolved energy density distribution of the homogenized beam profiles measured at the distances 500 mm and 2500 mm behind the homogenizer

Many other types of homogenizers have apertures determined by the homogenizing system itself, e.g. microlens-arrays or prisms, which usually cut off the inhomogeneities of the beam and decrease the efficiency of the homogenizer. But the ISO standard cited above does not take into account the efficiency of the homogenization. Note that all beam profiles are displayed without cutting off parts of the beam profile by using an aperture. The total efficiency of the presented homogenizer that means output divided by the input power depends on the shape of the input profile and ranges in the scale between 75 % to 95 %.

This homogenizer cannot be easily compared to fly-eye homogenizers which achieve a plateau uniformity of 2.5% and a edge steepness of 0.1. It has to be taken into account that the efficiency of those systems depend on the demagnification which is used for the mask projection due to the high divergence angles which usually occur in the mask plane.

The presented homogenizer may be useful for many other applications beside the presented multi-irradiation concept due to the sum of the properties. The most advantage, the low beam parameter product after homogenization, makes the presented homogenizer particularly well suited for set-ups employing a mask projection with a high demagnification.

By choosing the transmittance of the beam splitter, the energy density distribution of the output beam can be controlled. The use of a mirror, for example, would lead to an inverted Gaussian profile. In the system presented in this paper the output beam profile is adapted to the needs of the multi-irradiation system.

4. EFFICIENCY INCREASE USING MULTIPLE IRRADIATIONS

The basic idea of the multi-irradiation system⁴ is to capture the part of the beam which is reflected at the mask, to shape it, and to guide it back onto the mask. In order to achieve a high structure quality on the target and a large depth of focus a low divergence of the total irradiation at the mask is required. The beam quality provided by the homogenizer plays an essential role for the divergence angles at the target. Other multi-irradiation systems^{5,6,7} suffer from high divergence angles at the target due to the chosen design of homogenization or beam superpositioning at the mask. Some of these systems may be useful for laser marking but their use may be problematic for laser structuring due to the small depth of focus at the target.

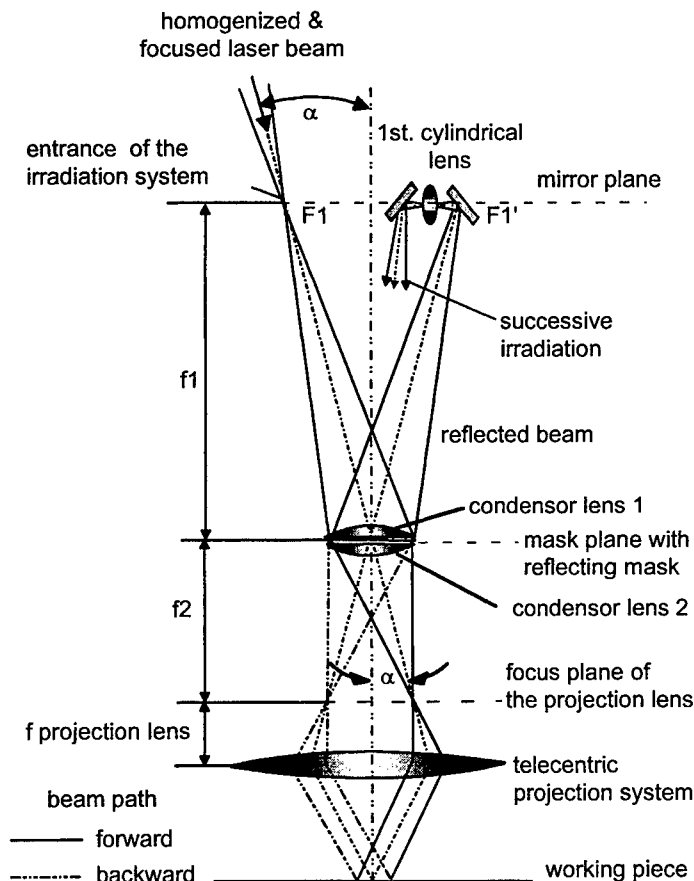


Fig. 6 Principle of the multi irradiation system

The homogenized laser beam is shaped by the telescopes (see Fig. 1) such that a focus $F1$ (having the cross-section of 14 mm x 2 mm as will be shown at the end of this chapter, see also Fig. 9) occurs in the mirror plane at the entrance of the irradiation system (see Fig. 6). The focal length of the condensor lens 1 is equal to the distance between the mask and the mirror plane, and, consequently, the divergent ray pencil of each irradiation which passes through the mask is collimated. Condensor lens 2, located directly behind the mask, focuses each ray pencil into the focus plane of the projection lens such that a telecentric projection is achieved. The projection lens images the mask onto the work piece with a demagnification by a factor of four.

The part of the laser beam which is reflected at the mask is refocused by condensor lens 1 into the mirror plane which means an imaging of $F1$ to $F1'$. A small inclination of $\alpha = 25$ mrad of the incoming laser beam with respect to the normal of the mask and the distance of 1000 mm between mirror plane and mask plane allow the incoming beam to be separated from the reflected beam. A flat mirror reflects the beam to cylindrical lens 1 which shapes the beam for the successive irradiation. The following mirror guides the beam onto the mask again.

In order to achieve eight irradiations with the low divergence angle $\alpha = 25$ mrad at the mask, a three dimensional packing of the optical components for the mirror arrangement has been realized (see Fig. 7). The laser beam is focused through the entrance of the irradiation system and irradiates the mask for the first time. After reflection at the mask and focusing by condensor lens 1, as described above, mirror 1 guides the reflected part of the laser beam to the cylindrical lens 1 which shapes the beam. Via mirror 2 the beam is directed onto the mask for the second irradiation. The reflected part of the laser beam is guided to the cylindrical lens 2 by mirror 3, consequently by means of mirror 4 the third irradiation is generated. Mirror 5 guides the reflected beam through the cylindrical lens 3 to mirror 6 in order to realize the fourth irradiation. The focusing mirror 7 reflects the laser beam onto itself such that the whole beam path is reversed. When at least the laser beam leaves the mirror arrangement, the mask has been irradiated eight times. The cylindrical lenses 1 and 3 have to be inclined to account for the orientation of the long beam axis, which occurs when the astigmatic laser beam is guided three-dimensionally by the mirrors 1,2 and 5,6.

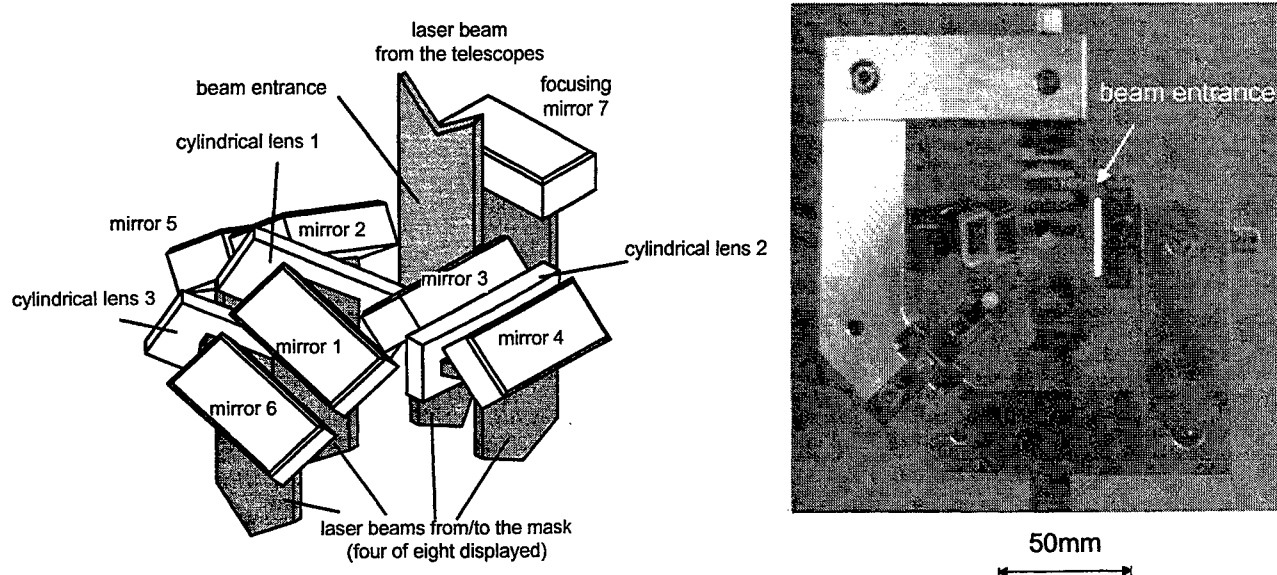


Fig. 7 Left: Three-dimensional scheme of the optical elements in the mirror plane, right: design of the arrangement of the mirror plane (viewed from the mask in direction to the mirror plane)

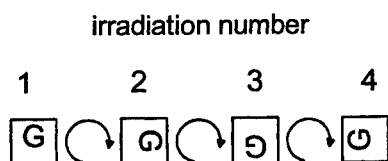


Fig. 8 Irradiation of the mask

Due to the arrangement of the mirrors, the beam cross-section on the mask turns 90° during consecutive illuminations (see Fig. 8). Therefore, the system was optimized for a square cross-section at the mask which is illuminated full sized. The turning of the laser beam on the mask leads to an additional homogenization of the total irradiation.

The cross-sections of the laser beam cannot be calculated in detail using ray optics presented in Fig. 6 due to the different beam parameter products of the laser axes. Therefore, in Fig. 9 the calculated cross-sections of the irradiation system are presented unwrapped along the beam propagation. Due to the beam parameter product of the homogenized beam which is nearly the one of the original laser beam, the beam cross-sections are calculated using the ABCD-formalism^{8,9} for four mask irradiations. The inclination of the mask is neglected and the calculated result is optimized for a cross-section of 15 mm x 15 mm square in the mask plane in respect to the properties of the projection lens. Depending on the aperture of the projection lens and in combination with the required energy density on the target larger or smaller irradiation fields can be realized. The cylindrical lens in the mirror plane images the mask upon itself along the long beam axis to correct for its bad beam quality. Along the short axis the beam propagates freely without imaging and reaches the required size at the mask. In principal it is possible to image the short beam axes upon itself, too. But it should be taken into account that the parts of the laser beam which fall on transmittive areas of the mask cover no energy. If for the successive irradiations those parts are imaged onto transmittive parts of the mask, no efficiency enhancement will occur. By choosing a free-space propagation along the short beam axis, as was done in this case, the intensity structures of the mask vanish in the reflected beam.

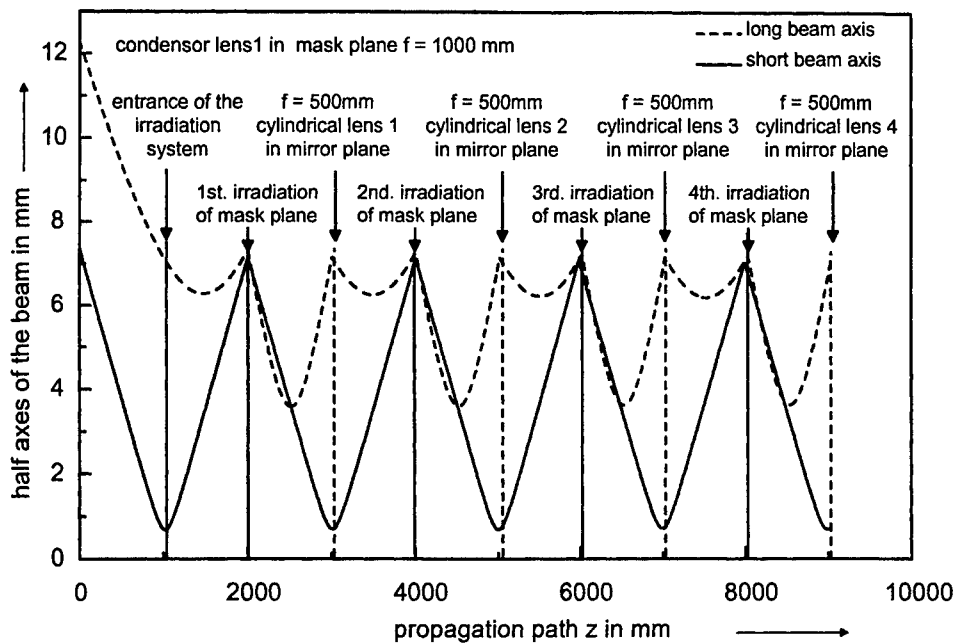


Fig. 9 Unwrapped presentation of the beam propagation for four illuminations of the mask. Along its short axis the laser beam is propagated freely between each illumination while along the long axis a cylindrical lens is used for imaging the mask upon itself

Therefore, an efficiency enhancement is ensured.

It can also be seen in Fig. 9 that the focal cross-sections on the surface of the cylindrical lenses in the mirror plane are rectangular having a size of 14 mm x 2 mm. The combination of demagnification (here 1:4), eight mask irradiations, and the common energy density used for structuring polyimides which ranges usually between 0.5 J/cm² and 2.5 J/cm² leads to a maximal energy density of 20 mJ/cm² on the surface of the cylindrical lenses. The threshold of destruction of the optical components and coatings is higher by at least a factor of ten.

5. EFFICIENCY AND OPTICAL RESOLUTION

Considering the losses of the optical components the theoretical efficiency of this system amounts to a factor of 6.2 for a structure density of 1 % on the mask. Experiments show that an efficiency increase of 5.5 can be achieved easily. With high precision adjustment a further improvement is possible and a maximum efficiency of 5.8 was obtained.

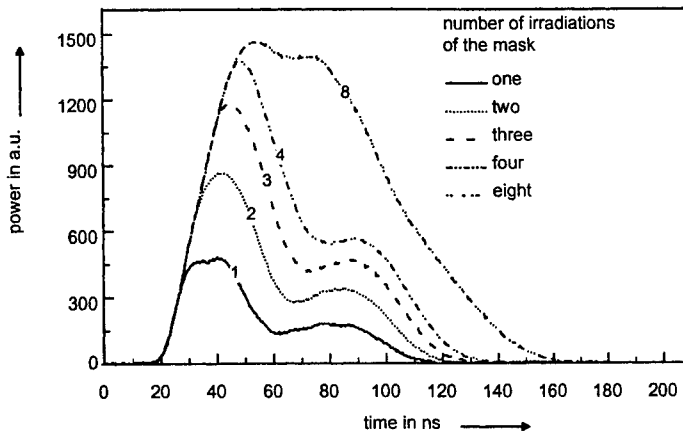


Fig. 10 Puls duration in dependence of the number of illuminations performed experiments no effects have been observed.

The efficiency increase can be also seen at the area below the temporal power distribution for eight irradiations (see Fig. 10). Due to the distance of 1000 mm between the mask plane and the mirror plane the time between two successive irradiations extends up to 6.6 ns. Therefore, the efficiency enhancement can be separated in an enhancement of the pulse peak power by a factor of 4 and a theoretical prolongation of the pulse duration by 46 ns.

After four irradiations the pulse peak power increases underproportionally with respect to the number of irradiations. For each successive illumination the laser pulse is prolonged. An effect of the pulse prolongation on the quality of the laser induced structures, therefore, may be suspected. Within the time scale in the

Furthermore, two other features of the irradiation system could influence the quality of the ablated structures. On the one hand, neither the projection lens nor the target are irradiated perpendicularly (see Fig. 6 and Fig. 7) since the mirror arrangement leads to an inclination of the irradiation directions. On the other hand, in contrast to common systems, the placement of the condensor lens 2 (see Fig. 6) between the mask and the projection lens is determined by the system principle, and this may have a negative influence on the quality of the projection. In order to examine the influences of these features the optical resolution over the entire image field was measured in detail. In doing this, a mask containing lines of various widths and different line spacings was imaged onto the surface of the target. The ablation result displayed in Fig. 11 does not show any effects of optical aberrations at a structure size of $2\text{ }\mu\text{m}$ which is the maximal optical resolution of the employed projection lens. The demagnification amounts to 1:4, the Numerical Aperture (NA) at the working piece is 0.1, and the pulse length (FWHM) is 80 ns. These structures were obtained with 0.3 J/cm^2 at the target and 30 pulses in polyimide. The laser-manufactured structures match the structures of the mask exactly.

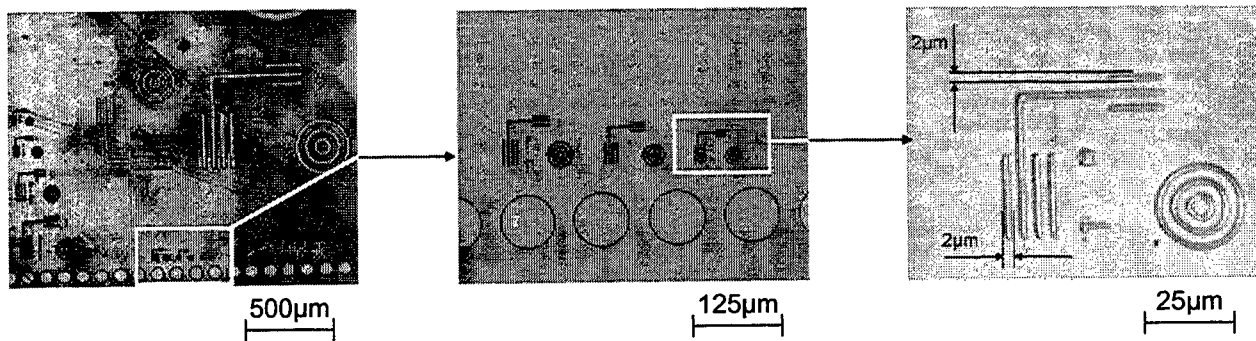


Fig. 11 Optical resolution achieved on polyimide after 30 pulses with $H=0.3\text{ J/cm}^2$ using the mirror arrangement of Fig. 7

6. ABLATION RESULTS

The efficiency and the quality of the laser produced structures depend essentially on the homogeneity achieved by the entire system. In order to examine the homogeneity, a mask with 9×9 holes was used for drilling 81 holes within an image field of $3.8\text{ mm} \times 3.8\text{ mm}$ (see Fig. 12).

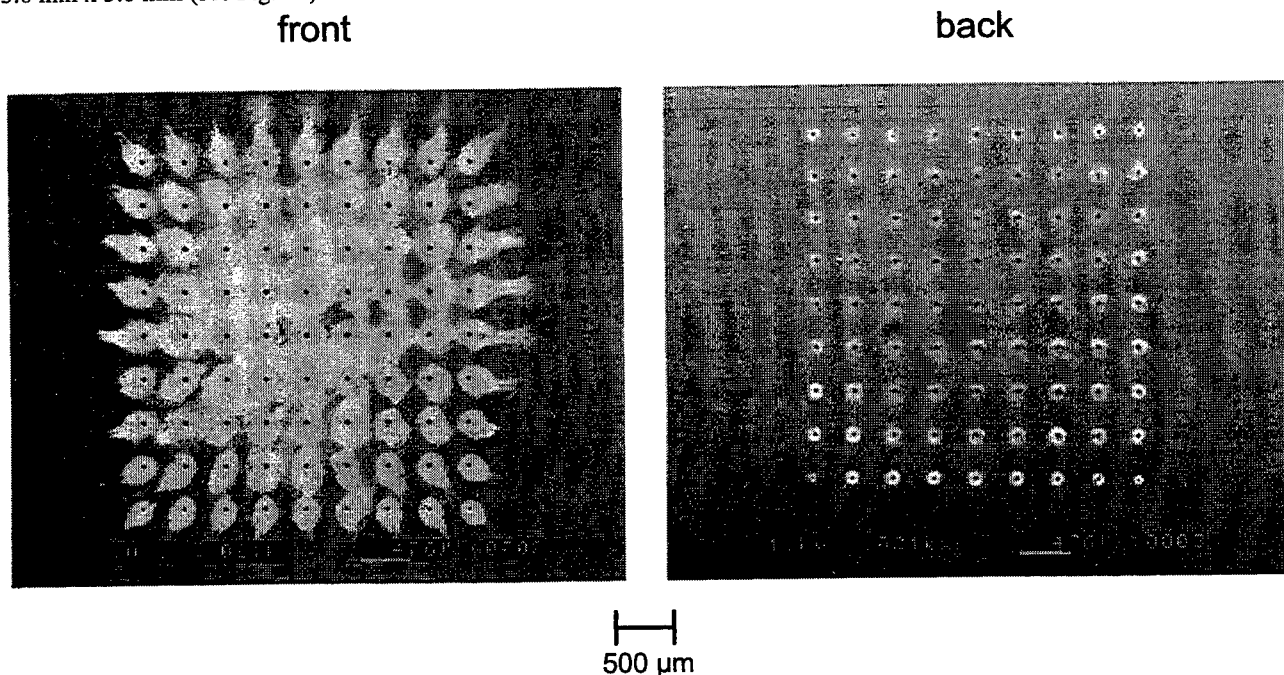


Fig. 12 Test matrix with 9×9 holes drilled in polyimide, $H = 0.5\text{ J/cm}^2$, 390 pulses

The structure density on the mask was 1.3 % of the entire irradiated area. Taking into account all losses at optical components the required energy for the whole structure amounts to 34 mJ per pulse. For drilling the test matrix without the irradiation system an energy of 187 mJ would be required. The light-coloured structures around the holes consist of ablation products which are deposited on the surface of the target, they can easily be removed.

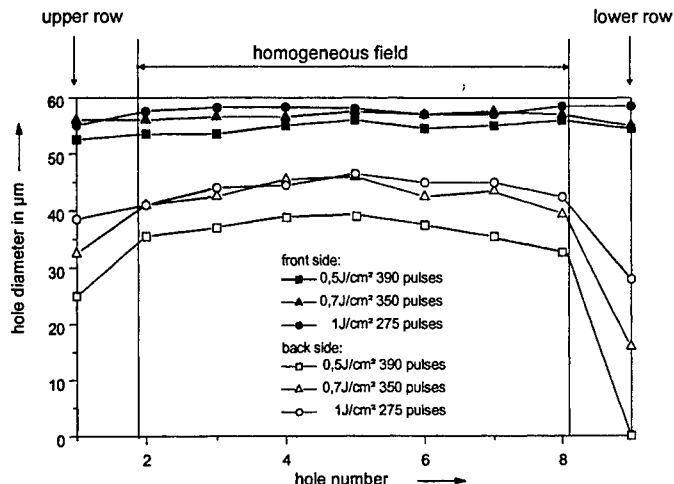


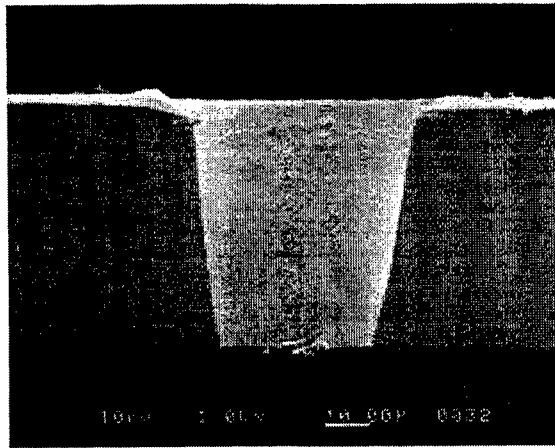
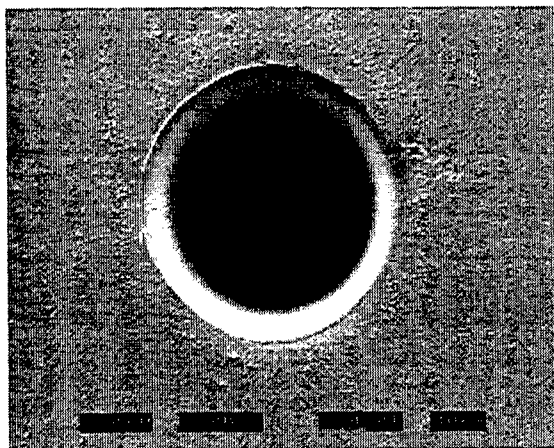
Fig. 13 Hole matrix diameters along the diagonal of the matrix

Along the vertical direction the mask was not fully illuminated by the irradiations, consequently, the upper and lower rows of holes do not have the same quality as the rest of the holes. This can also be seen in Fig. 13 where the hole diameters along the diagonal of the matrix are shown. The front diameters vary only within the range of the measurement accuracy of the equipment used. The missing energy density at the upper and lower rows of the matrix can be recognized considering the hole diameters on the rear of the sample. These rows show a quite small rear diameter. For an energy density of 0.5 J/cm² in the homogeneous field the corresponding wall angles are $12.9^\circ \pm 1.6^\circ$. For higher energy densities of 0.7 J/cm² and 1 J/cm² the wall angles amount to $9.4^\circ \pm 1.6^\circ$. Choosing other energy densities and demagnifications allows to influence both the wall angles as well as the size of the hole diameter¹⁰.

The overall hole geometry may not satisfy the required quality for e.g. ink jet printers but is sufficient for many other applications. The quality of a single hole of the matrix with respect to the described limits is shown in Fig. 14. The cross-section on the right hand side of Fig. 14 is not exactly through the middle of the hole. However, it can be seen that the hole is perpendicular and the difference between the minimal and maximal front diameters varies within the scale of the measurement accuracy. Similar properties can be observed at the back of the target.

front view

cross-sectional cut



10 μm

Fig. 14 Hole quality of a single hole of the test matrix in PI, $H = 0.7 \text{ J/cm}^2$, 390 pulses

7. SUMMARY

In this contribution a system is presented which increases the efficiency of mask based laser ablation using multiple irradiations of the mask. The increase in efficiency is based on a mirror arrangement which guides that part of the laser beam that is reflected at the mask back onto the mask again. A specially developed homogenizer which does not influence the beam quality of the laser beam ensures small divergence angles and a good beam quality for projection. The presented homogenizer is characterized according to ISO 13694. The achieved optical resolution of the entire system was below 2 μm corresponding to the resolution limit of the projection optics used. This system was applied to structuring hole matrices as well as lines and spaces. The homogeneity of the total irradiation of the mask is sufficient to achieve nearly the same structure quality over the entire image field. Providing that the transmitting areas of the mask do not exceed a few per cent of the total area, an efficiency enhancement by more than factor five was achieved for eight mask irradiation passes compared to a single irradiation.

ACKNOWLEDGEMENTS

The authors wish to express their sincere thanks to Martin Vogt for his support in measuring the homogeneity and the divergence of the homogenizer, to Markus Reile for his support testing the mirror arrangement, to Yalcin Yarimca for technical support, to Hans Jürgen Kahlert of Microlas GmbH for supplying test masks, and to Siegfried Dippon of Hewlett Packard Stuttgart, for the supply of polyimide samples. The development of the mirror arrangement was supported by the BMBF Germany, project no. 13N6774.

REFERENCES

1. K. Mann, J. Ohlenbusch, V. Westphal, *Normgerechte Charakterisierung von Excimerlaserstrahlung*, Laser und Optoelektronik, 1/98, p. 66.
2. Coherent Inc., *Apparatus for creating a square or rectangular laser beam with uniform intensity profile*, International patent no. WO95/18984, 1995.
3. Institut für Strahlwerkzeuge (IFSW), *Verfahren zur Erzeugung eines homogenen, über den gesamten Strahlquerschnitt im wesentlichen konstante aufweisende Energiedichte sowie Vorrichtung zur Durchführung des Verfahrens*, patent registration 1997.
4. Institut für Strahlwerkzeuge (IFSW), *Mehrfach-Maskenbeleuchtung mit definierter Abbildung*, patent registration 1997.
5. J. Bastue, O. F. Ohlsen, *Energy enhancer for mask based laser materials processing*, XI International Symposium on Gas Flow and Chemical Lasers 1996, SPIE Volume 3092, p. 131, 1996.
6. Cymer Inc., *Full field mask illumination enhancement methods and apparatus*, United States patent no. 5,601,733, 1997.
7. Mitsubishi Denki K.K., *Laserbearbeitungsvorrichtung*, German patent no. DE 4106 423 C 2, 1995.
8. F. K. Kneubühl, M. W. Sigrist, *Laser*, Stuttgart, Teubner, 1988 (Teubner Studienbücher Physik).
9. H. Kogelnik, T. Li, *Laser beam and resonators*, Appl. Optics 5, p. 1550, 1966.
10. H. Endert, *Excimerlaser als neue Werkzeuge zur Feinbearbeitung*, VDI Berichte Nr. 1031, p. 81, 1993.

Microstructuring with 157 nm laser light

Heinrich Endert*, Michael Kauf, Eric Mayer, Michael Scaggs, John Fair and Dirk Basting
Lambda Physik Inc., 3201 W. Commercial Blvd. Ste.110
Fort Lauderdale, FL 33309-3431 USA

ABSTRACT

The use of fluorine (F_2) lasers, emitting at 157 nm, offers new possibilities for key applications demanding very high resolution (e.g. microlithography for chip production) and/or higher photon energy to expand the laser-processable material spectrum (e.g. nanotechnology). Promising results have been achieved using F_2 lasers at 157 nm for micromachining of various materials that are very difficult to process at other laser wavelengths.

This paper reports about new F_2 laser source developments and their efficiency in processing Teflon®/Polytetrafluoroethylene (PTFE) and fused silica under moderate, uniform illumination conditions. Ablation rates and threshold parameters have been investigated. Scanning electron micrographs of the produced microstructures are presented.

Keywords: Excimer Laser, Fluorine, F_2 , 157nm, Microlithography, Nanotechnology, Micromachining, Teflon, Quartz, Fused silica, Diffractive optics

1. INTRODUCTION

Excimer laser sources working at 308 nm, 248 nm and 193 nm are established tools for high precision micromachining of materials such as polymers, ceramics and glass. The combination of unique features, such as a short wavelength and a high peak power, have established excimer lasers as the tool of choice in many different manufacturing applications, such as microlithography, microstructuring, surface modification and marking.¹⁻³

However, there is a strong interest to achieve shorter wavelengths to yield higher resolution and higher photon energy. The next step will be commercially available F_2 lasers operating at a wavelength of 157 nm. Recently, a study was published using 157 nm laser exposure in optical microlithography to achieve a line resolution of 80 nm.⁴ On the other hand, applying direct laser structuring, many refractory and high band-gap materials (such as PTFE, silicon, fused silica, and silicone polymers) require a shorter wavelength for effective ablation. Therefore the interest in the 157 nm laser output with a photon energy as high as 7.9 eV is strongly increasing.

2. DEVELOPMENT OF F_2 LASER SOURCES

Although the F_2 laser has many similarities to the excimer laser, the mechanism of the emission is distinctly different.⁵ In an excimer laser, emission occurs when a loosely-bound, excited-state dimer undergoes a radiative transition to an unbound or weakly bound lower state. The exciplex ArF^* decays, for example, to atomic Argon and Fluorine ($Ar + F$). In contrast, F_2 laser emission occurs in a transition between two bounded states, resulting in a much lower bandwidth. The natural emission spectrum of the fluorine laser shows two lines (157.5233 nm and 157.6299 nm, respectively) with individual line bandwidths of about 10 pm.

Industrial applications require F_2 laser sources with high performance, reliability and efficiency. Since cost of ownership is a major criteria, lifetime of the laser tube, laser gas and optical components are crucial factors, especially for F_2 lasers. The shorter the laser wavelength, the stronger its interaction with matter, from the internal laser tube surfaces to all optical materials encountering the 157 nm radiation. Therefore we developed, based on our NovaTube® metal ceramic technology,¹ a special laser series for 157 nm radiation: the LPF™ 100 and LPF™ 200 laser series. These lasers deliver the shortest commercially available laser wavelength and offer the state-of-the-art in Deep UV (DUV) laser technology. With pulse energies exceeding 25 mJ, repetition rates of 300 Hz, and output power greater 5 W, the LPF laser series creates new fields of application studies.

In our R&D laboratories we have developed F_2 laser prototypes with 25 W average output power and pulse repetition rates of 1000 Hz. The three graphs in figure 1 represent the average output power versus repetition rate. There are two individual laser lines with corresponding output power (157.523 and 157.629 nm). The top graph is result of the broadband emission spectrum (both lines without selection). Figure 2 demonstrates the output power as a function of repetition rate to 1 kHz (broadband). An energy of 17 mJ per pulse is reached at the maximum repetition rate.

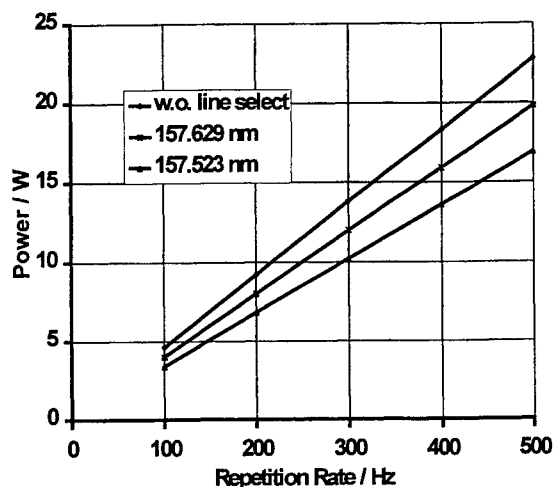


Figure 1: Output power of prototype F_2 laser (157 nm) running at 600 Hz

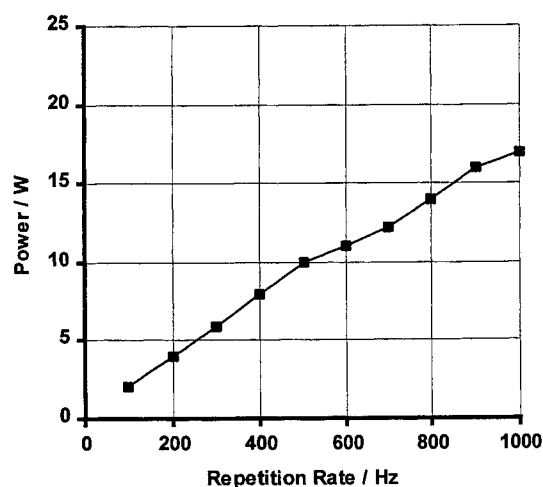


Figure 2: Output power of prototype F_2 laser (157 nm) running at 1000 Hz

3. EXPERIMENTAL SETUP FOR APPLICATION STUDY

A Lambda Physik fluorine laser LPF 210, incorporating NovaTube® technology and Magnetic Switch Control (MSC®) was used to produce 157 nm pulsed laser output. NovaTube technology, a complete metal/ceramic laser tube design, assembled under clean room conditions, greatly extends gas lifetimes, optics cleaning intervals, and component lifetimes. The MSC protects the electrical circuitry from reversal currents of the plasma discharge. The rear resonator mirror was a dielectrically coated, normal-incidence, high-reflection MgF_2 flat optic. The laser produced pulse energies in excess of 30 mJ, a beam profile of 8 mm by 23 mm and a pulse length of 18 ns. All experiments were run at a repetition rate of 50 Hz.

Figure 3 shows a schematic of the experimental layout including laser, focusing optics, contact-mask and substrate. The samples were placed within a 1.5 m distance of the laser and were machined either in the focal point or using a contact mask. Due to the absorption of oxygen at 157 nm, the complete optical beam path from the laser output-coupler to the sample was enclosed and purged with helium. The laser is equipped with a purge gas connection, check valve, and purge tube leading out of the laser housing. The remaining purge system consisted of a polycarbonate tube and a flexible plastic enclosure.

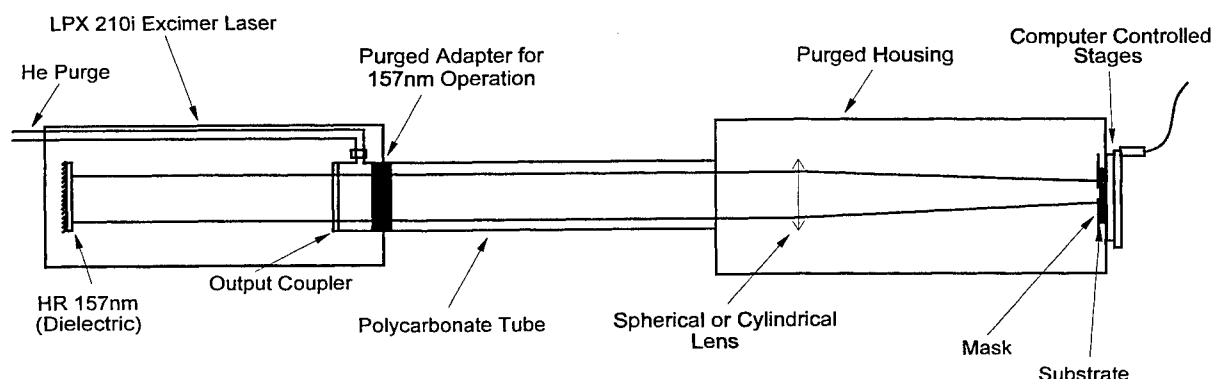


Figure 3: Schematic of the experimental setup.

A contact mask setup allowed for quick, space efficient, and reliable adjustment of the fluence delivered to the substrate. All experiments using a contact mask were completed with a flat rear-mirror and flat output-coupler for the laser resonator. Focal point machining was either done with the flat/flat resonator configuration or an unstable-resonator configuration. The unstable-resonator configuration consisted of a flat rear-mirror and a meniscus output-coupler.

The contact mask as well as focal point machining setups focused the beam with a 50.6 mm focal length, biconvex, $\lambda/10$, MgF_2 , spherical lens. Line features were produced by positioning substrates at the line focus of a 62.1 mm focal length, plano-convex, $\lambda/2$, MgF_2 , cylindrical lens. Substrates were positioned axially with a 0.25 μm resolution, Aerotec ATS 100 positioning stage. The sample was translated laterally with another ATS 100 and an Aerotec AVSO 100 stage.

4. RESULTS

4.1. Ablation rate

The use of a contact mask permitted a simple approach to characterize the ablation rates and threshold levels. The fluence was easily adjusted by varying the distance between the lens and substrate and determined by measuring the energy throughput of a known aperture area. A contact mask with a hole diameter of 400 μm yielded an ablation rate for PTFE of 0.47 $\mu\text{m}/\text{pulse}$ at a fluence of 1.4 J/cm^2 . The ablation rate for fused silica was determined in a similar way to be 0.15 $\mu\text{m}/\text{pulse}$ at a fluence of 2.0 J/cm^2 .

4.2. Resulting Geometry

A sheet of PTFE (0.52 mm thickness) was placed before the focal point of a spherical lens with a focal length of 50.6 mm to increase the fluence delivered to the substrate to 1.4 J/cm^2 . A mask with an array of 300 μm diameter apertures on 600 μm center distance, was placed directly in front of the sample. The mask and sample were scanned across the beam-waist (788 μm diameter) to produce a 1 cm by 0.5 cm array of holes. The holes produced had a sharp edge quality, minimal taper angle, and clean exit (Figure 4). This sample had no surface preparation and no post process modification of any kind.

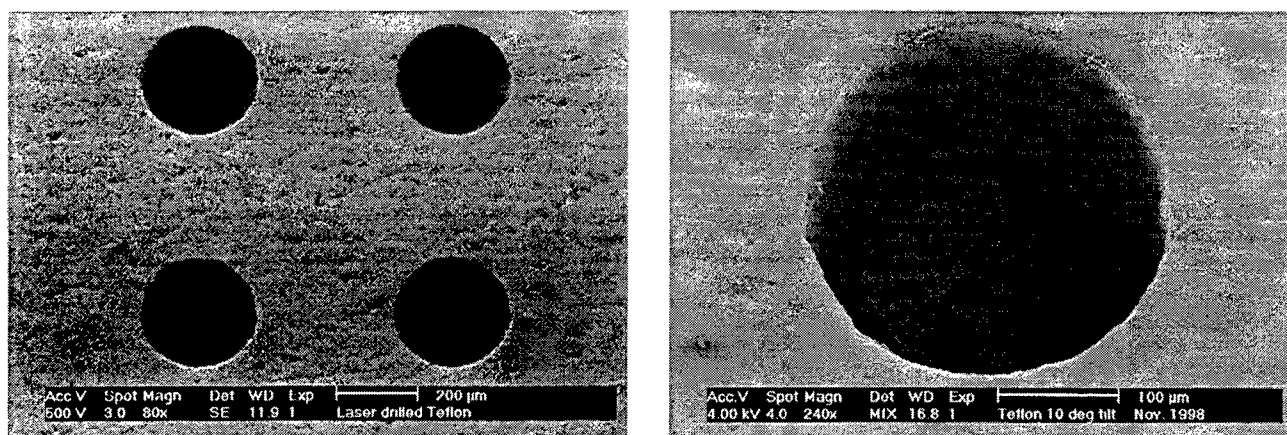


Figure 4: Front view of a Teflon/PTFE sample, machined before the focal point of a biconcave lens ($f = 50.6 \text{ mm}$) using a contact mask

In another setup, fused silica was focal point machined with a spherical lens ($f=50.6 \text{ mm}$). The central portion of the raw beam was selected by placing a round aperture ($\varnothing=5 \text{ mm}$) directly at the output of the unstable resonator configured laser. Grooves of 25 μm were cut in a pattern of concentric circles to produce a crude, Fresnel-type lens (Figure 5).

Micromachining of fused silica opens up interesting possibilities for producing direct-write, rapid prototype, diffractive optics.⁶ Clearly the F_2 laser could be used to produce diffractive optical elements.

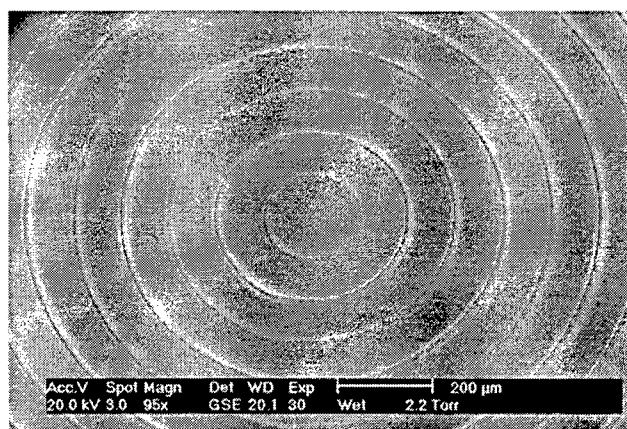


Figure 5: Focal point scribing of concentric circles in fused silica with an unstable flat/convex resonator to simulate a Fresnel lens.

5. CONCLUSION

The use of F₂ lasers, emitting at 157 nm, will allow an essential further step towards higher resolution in DUV microlithography and in material processing by direct laser ablation. The high photon energy expands the spectrum of processable materials and allows more efficient material removal.

ACKNOWLEDGEMENTS

SEM Images provided by: Dr. Mathew Lynn, University of Miami Center for Advanced Microscopy.

REFERENCES

1. H. Endert, M. Scaggs, D. Basting and U. Stamm, "New ultraviolet lasers for material processing in industrial applications", J. of Laser Applications, vol. II, Feb. 1999 (in print)
2. H. Endert, B. Becker -deMos, U. Stamm, S. Borneis, F. Voss, D. Basting, "Optimization of high power excimer laser for TFT annealing", Proc. of SPIE, vol. 3343, pp. 432-439, 1998.
3. R.S. Patel, T.F. Redmond, C. Tessler, D. Tudryn and D. Pulaski, "Via production benefits from excimer laser tools", Laser Focus World, Jan. 1996, pp. 71ff.
4. D. Basting "Progress towards sub-100 nm lithography at MIT's Lincoln Laboratory", Lambda Physik Highlights, vol. 54, pp. 1-5, Jul. 1998.
5. D. Basting, "Breakthrough in F₂ Laser Technology", Lambda Physik Highlights, vol. 22, pp. 1-4, Apr. 1990.
6. E.J. Lerner, "Durable excimer lasers find new applications", Laser Focus World, vol. 34, pp. 131-136, Jul. 1998.

*Correspondence: email: hendert@lambdaphysik.com; home page: www.lambdaphysik.com;
phone: (954) 486-1500; fax: (954) 486-1501

Electrical and optical properties of ITO films deposited by excimer laser assisted EB method

Tetsuo Yano^{*a}, Masafumi Yoneda^a, Toshihiko Ooie^a, Munehide Katsumura^a,
Yoshifumi Suzaki^b and Tomokazu Shikama^b

^a Shikoku National Industrial Research Institute, AIST, MITI,
2217-14 Hayashi, Takamatsu 761-0395, Japan

^b Takamatsu National College of Technology
355 Chokushi, Takamatsu 761-8058, Japan

ABSTRACT

In-situ excimer laser irradiation to growing films is expected to progress the surface reaction i.e. oxidation and surface migration of adatoms. This method therefore will be adequate for the low temperature formation of oxide semiconductor films showing a wide band energy gap. We studied the effect of in-situ excimer laser irradiation on the electron beam(EB) deposited Indium-Tin-Oxide(ITO) films and evaluated the electrical and optical properties. The ITO films deposited without laser irradiation at room temperature were opaque and had an amorphous structure, and its resistivity was higher than $0.04\Omega\text{cm}$. On the other hand, the ITO films deposited with in-situ laser irradiation at room temperature showed good transparency and electric properties. The low resistivity, smaller than $9\times 10^{-4}\Omega\text{cm}$, and high transparency, more than 90%, were achieved simultaneously at room temperature. The films crystallized with in-situ laser irradiation had a cubic crystalline structure. The Hall mobility and carrier density of the ITO film were $12\text{ cm}^2/\text{Vs}$ and $5.5\times 10^{22}\text{ cm}^{-3}$, respectively. These results suggested that the in-situ excimer laser irradiation progressed the surface oxidation and eliminated the unstable adatoms on the surface of growing ITO films.

Keywords: Indium Tin Oxide, Thin film, Excimer laser, EB deposition, resistivity, transparency

1. INTRODUCTION

The band gap energy of oxide semiconductors, such as an Indium-Tin-Oxide (ITO), 3.7eV, is smaller than the photon energy of ultraviolet light, $\sim 5\text{eV}$. Therefore, when oxide semiconductors are irradiated with UV light, the materials will be activated electrically and electron-hole pairs will generate¹. Such electrical activation in materials surface is expected to give the selective desorption of adatoms that exist at surface defects and also promote oxide reactions¹.

ITO films of transparent conductive oxides are highly degenerated wide gap semiconductors with high conductivity and high transparency in the visible region of the spectrum. They are widely used in information displays, such as LCDs. ITO films is usually deposited at the substrate temperature of $350\sim 400^\circ\text{C}$ by the sputtering method². The films used for STN type color LCD are required to be deposited on a resin film substrate with the substrate temperature lower than 200°C and have low resistivity.

In this study we examine the formation of ITO films at room temperature (R.T.) by using the excimer laser assisted electron-beam(EB) deposition method. The resistivity, transparency and surface morphology of the films were evaluated. The effect of laser irradiation on crystallization of EB-deposited ITO films was a special focus of investigation. We made crystallographic analysis of ITO films deposited on glass and single crystal plates.

2. EXPERIMENTAL

Figure 1 shows a schematic illustration of the excimer laser assisted electron-beam(EB) deposition apparatus. The deposition chamber has an EB source at the bottom and a quartz window through which an excimer laser beam (wave length: 248nm) was irradiated on a substrate at the incident angle of 45° . The laser beam was rectangular and $15\text{mm}\times 35\text{mm}$. The deposition chamber is first evacuated to a vacuum $\sim 6\times 10^{-4}\text{Pa}$ using a conventional oil-diffusion pump system

* Correspondence: Email: yano@sniri.go.jp; WWW: <http://www.sniri.go.jp/index.html>; Fax: +81-87-869-3551

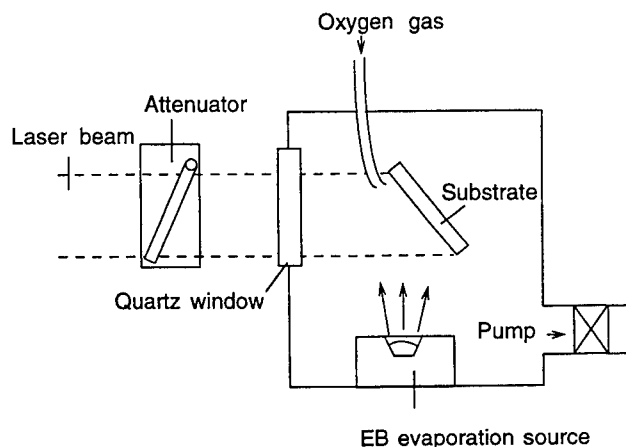


Fig.1 A schematic illustration of the excimer laser assisted electron-beam (EB) deposition apparatus.

with a liquid nitrogen trap, and then back-filled with high purity oxygen gas (99.99 mass %) at a pressure of about 0.13Pa. In the oxygen atmosphere ITO films were deposited by using EB-evaporation of In_2O_3 -5 mass% SnO_2 tablets, and an excimer laser beam was simultaneously irradiated on the depositing film. The laser fluence was varied in the range of 0~46mJ/cm², and the laser repetition rate was a constant of 40Hz. The laser power was obtained by a product of laser fluence and repetition rate; 0~1.8W/cm².

3. RESULTS AND DISCUSSION

3.1. ITO Films Deposited on Glass Substrates

Figure 2 shows the electrical properties of the ITO films deposited at the laser fluence of 0~46mJ/cm² and with the other deposition conditions held constant. The resistivity of the films formed without laser assist was 0.04Ωcm. With increasing laser fluence the resistivity of the films first decreased, and reached the minimum value, $9 \times 10^{-4} \Omega \text{cm}$, at the laser fluence of 22mJ/cm², and then increased again. The resistivity, ρ , of semiconductors is known to be inversely proportional to the

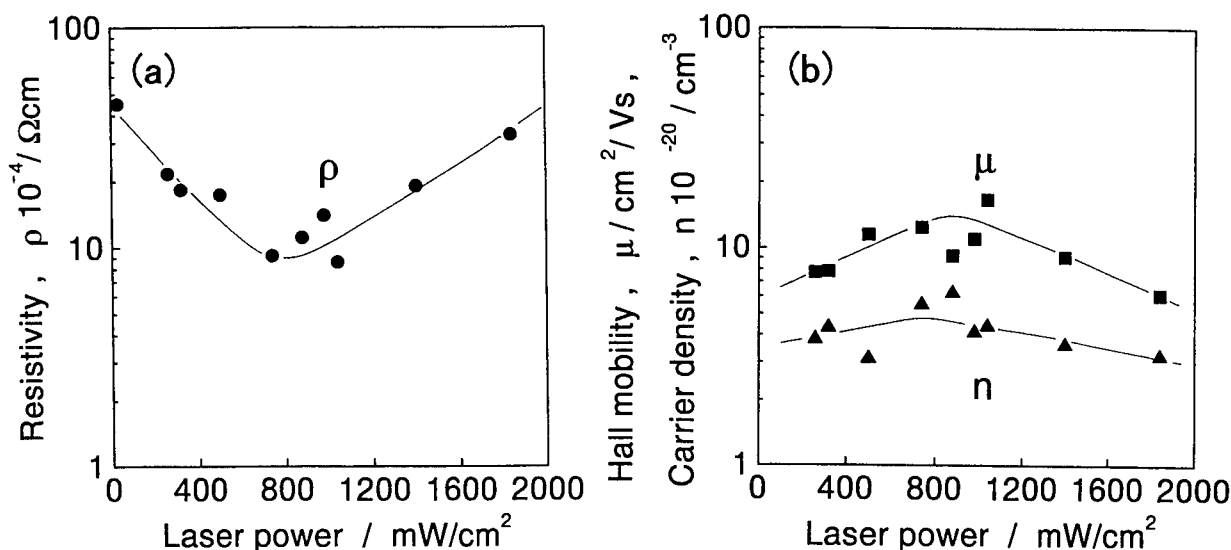


Fig.2 The electrical properties of the ITO films deposited at the laser fluence of 0~46mJ/cm²

product of mobility, μ , and free-carrier density, n . The measured mobility and free-carrier density showed the maximum values at the resistivity reaching the minimum. The maximum mobility, μ , and free-carrier density, n , were $\mu = 12 \text{ cm}^2/\text{Vs}$ and $n = 5.5 \times 10^{20} \text{ cm}^{-3}$, respectively.

The typical electrical properties of ITO films formed by the sputtering method (2) at a substrate temperature of 400°C are $\rho = 1.3 \times 10^{-4} \Omega \text{ cm}$, $\mu = 43 \text{ cm}^2/\text{Vs}$ and $n = 1 \times 10^{21} \text{ cm}^{-3}$. By comparing the properties of both film, we find that the carrier density is nearly equal, but that our films also have moderate oxygen vacancies and form a sufficient substitutional solution of Sn.

This result suggests that the high resistivity of our film derives from the low mobility of carrier electrons in the films. The film grown on a substrate at 400°C is thought to be crystallized under thermally equivalent conditions and so contains relatively low point defect density causing a decrease in mobility. On the other hand, the film grown on a R.T. substrate with laser assist will crystallize under non-thermal equivalent condition, and therefore may contain some defects in the films that will give centers of scattering for carrier electrons and increase carrier electron mobility.

This laser assisted EB- deposition process has the potential to produce better electrical properties by further changing the deposition parameters.

Figure 3 shows the transparency of the ITO films deposited at the laser fluence of $0 \sim 46 \text{ mJ/cm}^2$ and with the other deposition conditions held constant. The transparency of the films formed without laser assist was 20%. With increasing laser fluence, the transparency of the films increased, reached more than 90% at the laser fluence of larger than 12 mJ/cm^2 (laser power is larger than 0.5 W/cm^2), and then slightly decreased to 80%. The film formed without laser assist is black

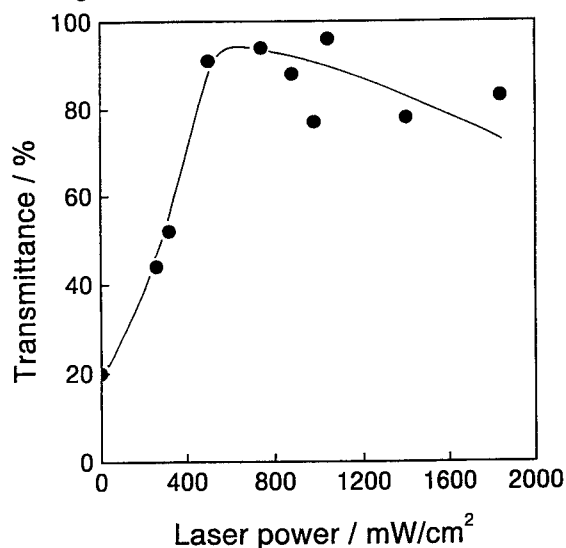


Fig.3 The transparency of the ITO films deposited at the laser fluence of $0 \sim 46 \text{ mJ/cm}^2$

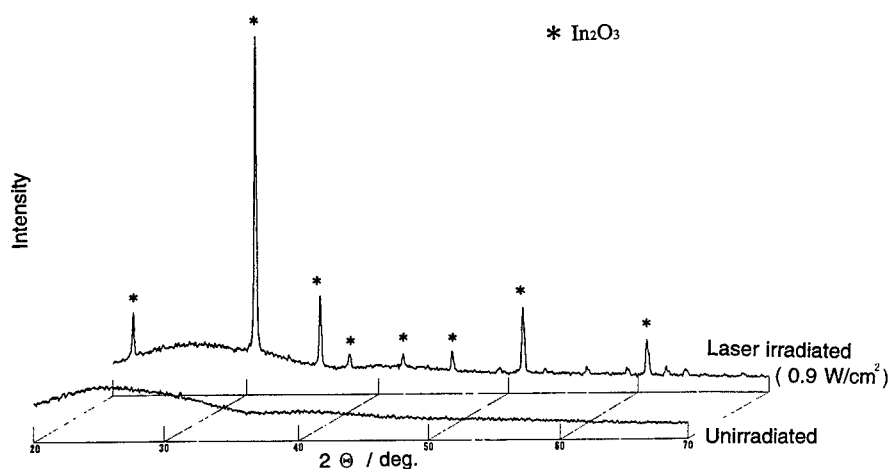


Fig.4 X-ray diffraction patterns of the ITO films formed on glass substrates.

and opaque, whereas the film formed with laser assist became transparent in the visible region of the spectrum, 400~800nm. The color centers based on oxygen vacancies in the films are thought to absorb light and make films opaque³.

Adequate oxygen vacancies are necessary for ITO films to have high electrical conductivity. However too many vacancies make films opaque by increasing absorption of light at color centers. The oxygen vacancies tend to form when the substrate temperature is low, such as at R.T., when oxidation reactivity at the film surface will be low. However, in this experiment the laser assisted EB- deposition process produced transparent ITO films on a R.T. substrate. This result indicates that the laser assist promotes the oxidation reaction at the film surface.

Figure 4 shows X- ray diffraction patterns of the ITO films formed on glass substrates. The film formed without laser assist shows a broadening X- ray diffraction pattern and is therefore thought to be an amorphous structure. The film formed with laser assist is a crystalline form of ITO, because the X- ray diffraction peaks coincide with the peaks of an In₂O₃ standard crystal. Excimer laser irradiation of the EB- deposited film surface changes an amorphous structure to a polycrystalline structure. The crystallization of ITO films will decrease the resistivity of the films. By way of explanation, it has been mentioned that Sn atoms dissolved in In₂O₃ crystal as substitutional atoms increase free- electron carrier density and decrease the scattering centers for carrier electrons⁴.

Figure 5 shows the lattice constant of the films estimated from the (111) peak of X- ray diffraction patterns. The solid line in this figure shows the lattice constant of an In₂O₃ standard crystal. At the laser fluence of larger than 12mJ/cm² (laser

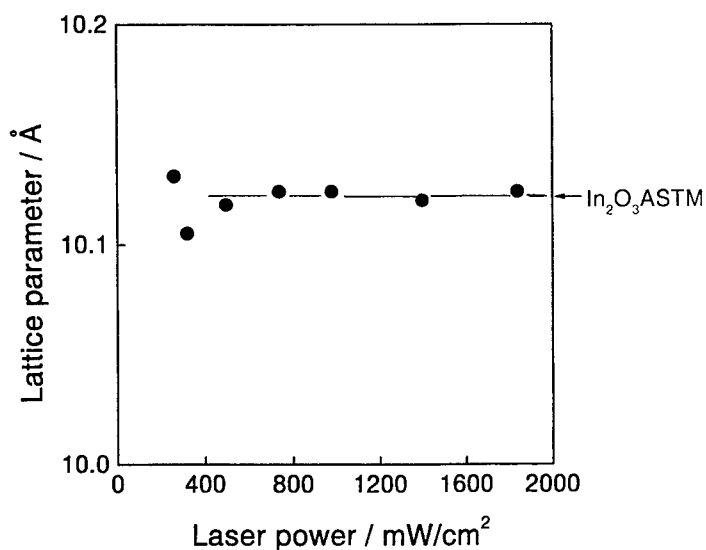
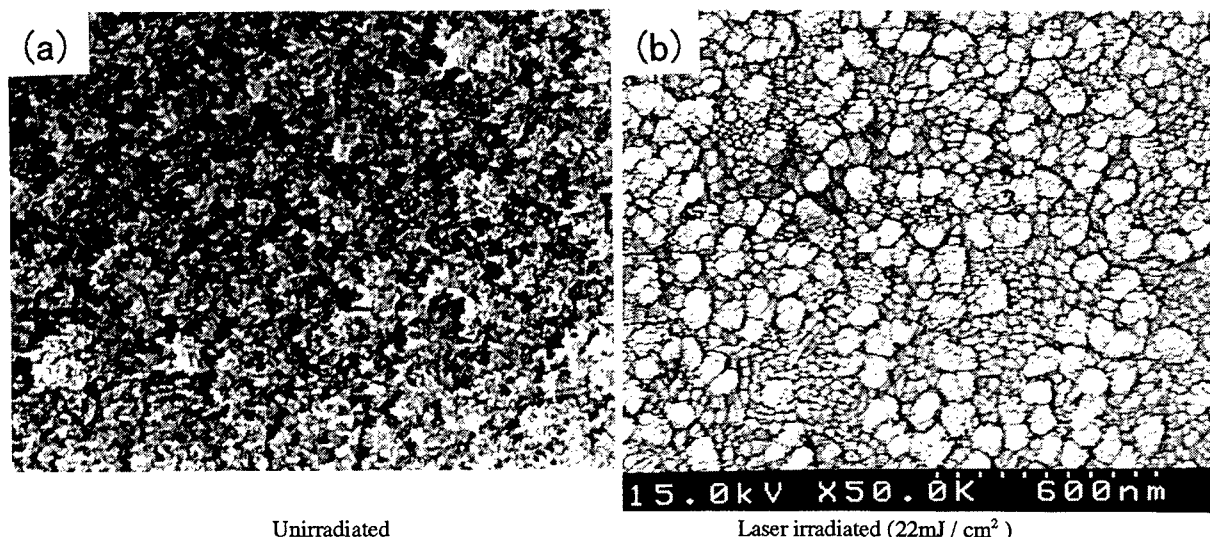


Fig.5 The lattice constant of the films estimated from the (111) peak of X- ray diffraction patterns



Unirradiated Laser irradiated (22mJ / cm²)
Fig.6 FE- SEM images of the surface morphology of ITO films formed on glass substrates.

power is larger than $0.5\text{W}/\text{cm}^2$, the lattice strain of the film is less than 0.1%. This value is smaller than that of the ITO films formed by the sputtering method (4), that is 1.0~1.4%, and so our film has a very small lattice strain. The half value width of the (111) diffraction peak, 0.25° , is also relatively small and thus our film is confirmed to have good crystalline structure. The X-ray diffraction pattern of the film with laser assist coincides with the diffraction pattern of sintered ITO tablet with respect to both peak position, 2θ , and peak ratio. It means that the film has no orientation and has an equiaxial polycrystalline structure.

Figure 6 shows FE- SEM images of the surface morphology of ITO films formed with or without laser assist. The film formed without laser assist, Fig6(a), has the smooth and featureless morphology which coincides with an amorphous structure. The surface of the films formed with laser assist, Fig6(b), shows both cup-like structures of 100nm in diameter, and a finer structure, leading us to believe that the film grows in a columnar manner. The sputtering method at the substrate temperature of 400°C gives a smoother surface than that obtained in our films ⁴. In the sputtering process, ion species having higher kinetic energy pater the film surface ⁴. The film produced by such pattering has a smoother surface and larger lattice strain than our film.

3.2. ITO Films Formed on Single Crystal Substrates

As mentioned above, the best properties of resistivity and transparency are obtained at the laser fluence of $22\text{mJ}/\text{cm}^2$. By using this deposition condition, ITO films were formed on yttrium stabilized zirconia (YSZ) single crystal and magnesium oxide (MgO) single crystal plates. X-ray diffraction patterns of these films are shown in Fig.7. The diffraction pattern for an YSZ substrate, Fig.7(a), has two large peaks deriving from (002) planes of the YSZ substrate and (004) planes of the ITO film. The other peaks are very weak. This result shows that the space between the (002) plates of the substrate is close to the space between the (004) planes of the film, and the oriented c- axis of the film is perpendicular to the YSZ substrate. On the other hand, the diffraction pattern for a MgO single crystal substrate, Fig.7(b), shows no- orientation and has an equiaxial polycrystalline structure the same as the film formed on a glass substrate.

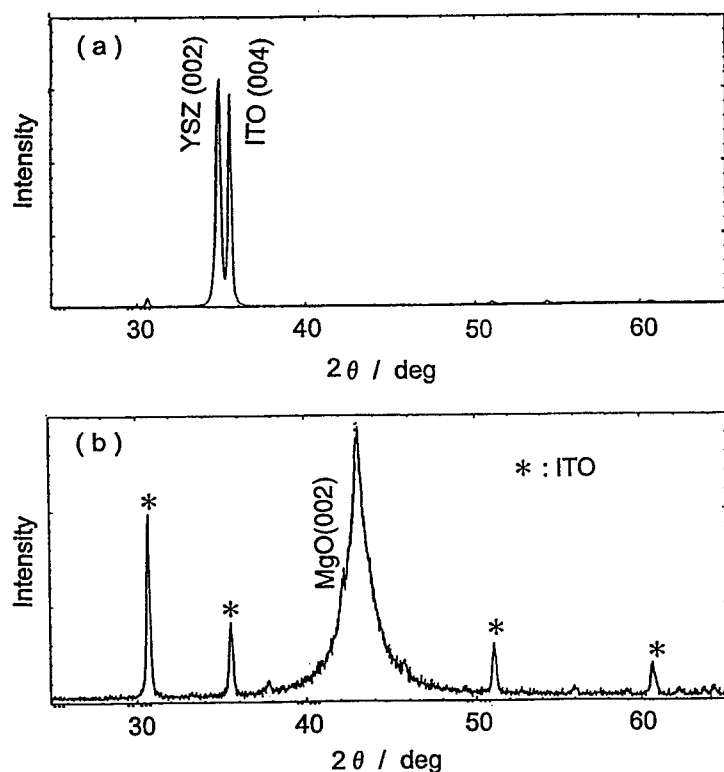


Fig.7 X-ray diffraction patterns of the ITO films formed on yttrium stabilized zirconia (YSZ) single crystal, (a), and magnesium oxide (MgO) single crystal plates, (b).

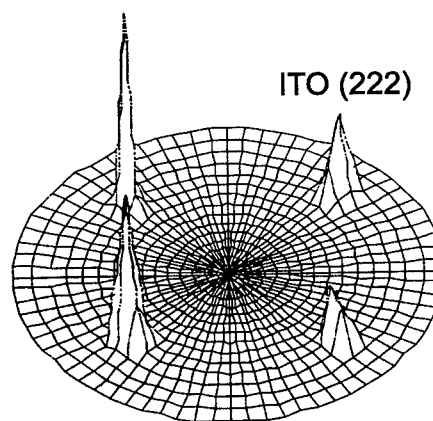


Fig.8 The pole figure diagram from (222) Lattice planes of the ITO film formed on an YSZ substrate.

The misfit strain between YSZ substrate and ITO film is -1.7%, whereas the misfit between MgO substrate and ITO film is 19.6%. The value of the misfit strain between substrates and films is suggested to influence intensely the growth orientation of films.

Figure 8 shows the pole figure diagram from (222) lattice planes of the c- axis oriented ITO film formed on an YSZ substrate. There are four diffraction peaks from (222) lattice planes of the ITO film, at $\alpha = 35\text{deg.}$ and at $\beta = 90\text{deg.}$ intervals, but no other peaks. It is suggested that the film is hetero- epitaxially grown on an YSZ single crystal substrate. In the pole figure measurement, the fixed 2θ angle is set at 30.432deg. , which is close to the 2θ value for (222) planes of ITO film, whereas the 2θ value for (111) planes of YSZ substrate is 30.56deg. Considering that the half- value width of these diffraction peaks is about 0.25deg. , the diffraction pattern of the pole figure in Fig.6 is not derived from (111) planes of the YSZ substrate, but only from (222) planes of ITO film.

Figure 9 and 10 shows FE- SEM images of surface and section morphology of ITO films formed on YSZ crystal and glass substrates. The film formed on a YSZ substrate, which is hetero- epitaxially grown, also has a cup-like structure. Compared with the surface of the ITO film formed on glass, the cup-like surface of that on YSZ seems to be equal in size and also lined up. The half- value width of the diffraction peaks in the pole figure in Fig.8 is about 10%, and therefore this wide peak corresponds to the disorder of crystal at the cup-like surface of the film.

Kamei M. et al ⁵ report that ITO films are hetero- epitaxially grown on a YSZ single crystal substrate at 200°C by using conventional dc magnetron sputtering apparatus. Taga N. et al ⁶ also get the hetero- epitaxially grown ITO films on an YSZ single crystal substrate at 300°C with a conventional EB evaporation method.

As mentioned above, using excimer laser assisted EB- deposition system we formed the hetero- epitaxially grown ITO film on a YSZ single crystal substrate at R.T. for the first time.

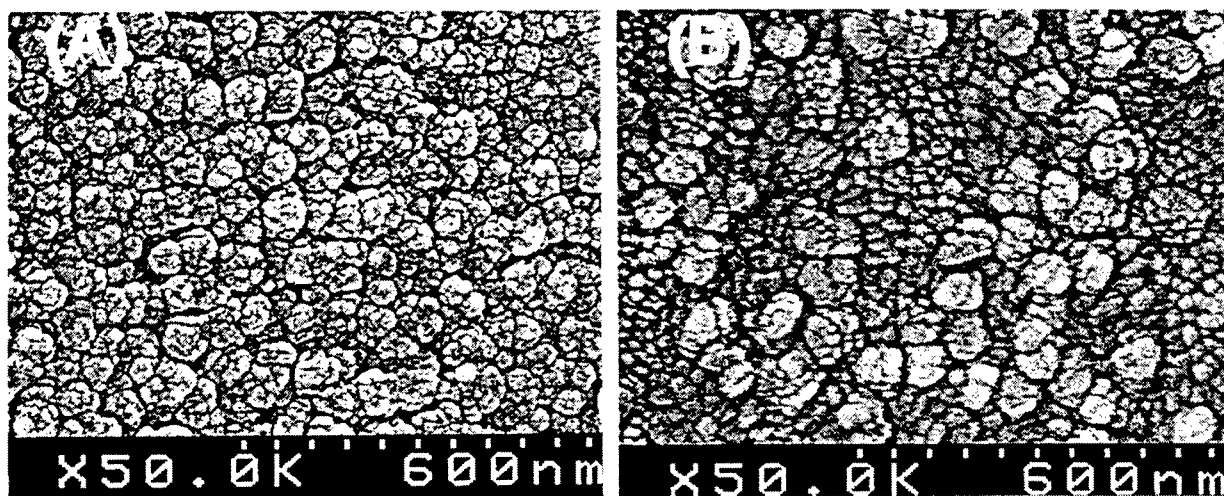


Fig.9 FE- SEM images of surface morphology of the ITO films formed on YSZ (a) and glass(b) substrates.

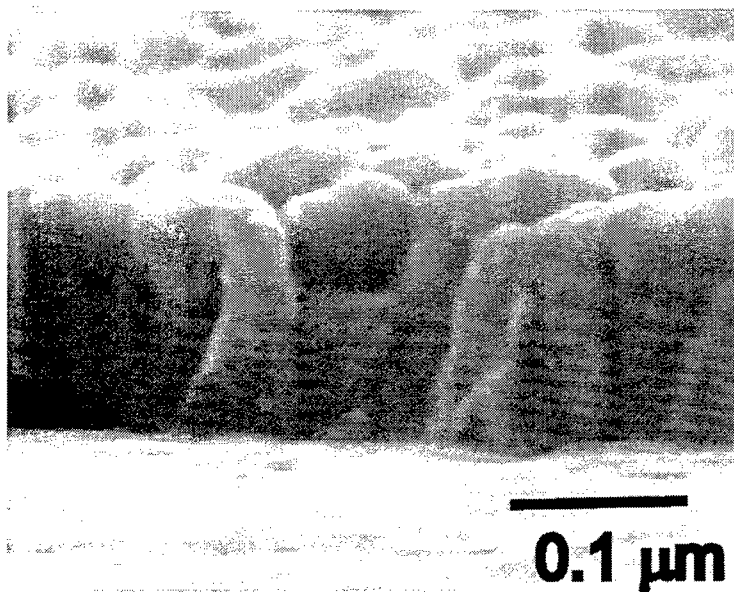


Fig.10 FE- SEM images of cross section of the ITO film formed on YSZ substrates

4. CONCLUSION

We examined the formation of ITO films at room temperature by using the excimer laser assisted electron- beam(EB) deposition method.

The best resistivity and transparency were obtained for ITO films deposited on R.T. substrates at the laser fluence of $22\text{mJ}/\text{cm}^2$, resistivity, ρ , mobility, μ , and free-carrier density, n , being $\rho = 9 \times 10^{-4} \Omega \text{cm}$, $\mu = 12 \text{cm}^2/\text{Vs}$ and $n = 5.5 \times 10^{20} \text{cm}^{-3}$, respectively. The film formed without laser assist is black and opaque, whereas the film formed with laser assist is transparent in the visible region of the spectrum, $400 \sim 800 \text{nm}$, with transparency higher than 80%.

The effect of laser irradiation on crystallization of EB-deposited ITO films was a special focus of investigation. The crystallographic analysis of ITO films deposited on glass and single crystal plates was performed. By using an excimer laser assisted EB- deposition method, ITO film was hetero- epitaxially grown on a YSZ single crystal substrate at R.T.. The value of the misfit strain between substrates and films is suggested to intensely influence the growth orientation of films.

REFERENCES

1. N. Itoh and T. Nakayama, Physics Letters. **92A**, p471-, 1982.
2. Y. Shigesato, S. Takaki, and T. Haranoh, J.Appl.Phys. **71**, p3356-, 1992.
3. Y. Shigesato, D.C. Paine, and T.E. Haynes, Jpn. J. Appl. Phys. **32**, p L1352-, 1993.
4. Y. Shigesato and Paine D.C., Thin Solid Films. **238**, p 44-, 1994.
5. M. Kamei, T. Yagami, S. Takaki, and Y. Shigesato, Appl. Phys. Lett. **64**, p 2712-, 1994.
6. N. Taga, H. Odaka, Y. Shigesato, I. Yasui, M. Kamei, and T.E. Haynes, J.Appl.Phys. **80**, p 978-, 1996.

Reliability and Lifetime of UV Excilamps Pumped by Glow, Barrier and Capacitive Discharges

Victor F. Tarasenko^a, Evgenii B. Chernov^b, Michail V. Erofeev^a,
Alexei N. Panchenko^a, Victor S. Skakun^a and Eduard A. Sosnin^a

^aHigh Current Electronics Institute, SB Russian Academy of Sciences,
4, Akademicheskii Ave., 634055, Tomsk, Russia

^bTomsk State University, 36 Lenin str., 634050, Tomsk, Russia.

ABSTRACT

In the recent years, great progress in development of spontaneous UV and VUV sources, radiating on the transitions of excimer and exciplex molecules has been achieved. However, practical use of sealed-off excilamps is limited by low lifetime of gas mixture. In this paper, stability of output parameters of the excilamps pumped by glow, barrier and capacitive discharges is studied and the mechanism of chlorine losses in low pressure halogencontaining excilamps made of quartz is determined.

Key words: glow, barrier and capacitive discharges, ultraviolet, excilamp, lifetime.

1. INTRODUCTION

In the recent years, significant progress in development of excilamps is achieved. Excilamps represents relatively new subclass of discharge lamps, radiating in the UV and VUV spectral ranges on the transitions of exciplex and excimer molecules¹⁻⁴.

Operating parameters of powerful excilamps with different discharge geometry pumped by glow discharges, high-pressure volume discharge with UV-preionization and barrier discharge were investigated in our early works^{2,4-6}. Intense radiation of Ar₂^{*}, Kr₂^{*}, Xe₂^{*}, ArF^{*}, KrBr^{*}, Cl₂, KrCl^{*}, KrF^{*}, XeI^{*}, XeBr^{*}, XeCl^{*}, XeF^{*}, I₂ and IBr molecules was obtained in rare gases or in rare gas - F₂ (CH₃Br, Cl₂, HCl, I₂, NF₃) mixtures. Excilamps with high spatial uniformity of the output and narrow emission line were developed. It was shown that the efficiency of KrCl^{*} exciplex molecules luminescence of about 30% can be obtained in a high-voltage glow discharge and positive column of a glow discharge. Output at $\lambda \sim 222$ and 308 nm up to 200 W from single excilamp and 500 W from three excilamps operating in parallel was demonstrated. It was shown that efficiency of the barrier discharge excilamps pumped by sinusoidal pulses several tens microseconds in duration can be sufficiently improved.

For practical use of the excimer molecules radiation sealed-off excilamps with long lifetime are required. The present work is devoted to experimental study of radiation parameters of glow, barrier and capacitive discharges in rare gas - halogen mixtures for the purpose to stabilize the excilamp output parameters.

2. EXPERIMENTAL RESULTS AND DISCUSSION

2.1. Experimental setup and measurement procedure

Design of the cylindrical discharge tube is presented in Fig.1(a,b). Inner diameter of the tubes were varied from 1.5 to 6 cm and its length was up to 55 cm. The gap between ring (Fig.1(b)) electrodes was varied from 1 to 30 cm. All excilamp tubes were made of high quality quartz with the transmittance coefficient in the 200-300 nm spectral region no less than 80%.

When investigating glow discharge tubes (Fig.1(a)) the electrodes and flanges for inlet and evacuation of gases were fastened to the tube faces. These electrodes had the cylindrical form with a diameter of 40 mm and were made of stainless steel or nickel. Positive potential was applied to the anode from a DC power supply, the cathode was grounded.

Two excilamp designs were used in the study of a capacitive discharge. Classical capacitive discharge¹¹ was realized in cylindrical tubes with ring electrodes 0.5-10 cm in width placed on the tube walls (Fig.1(b)). Other form of a capacitive discharge, which now is very widely used for development of excilamps^{3,5,12} (so-called "barrier discharge") was realized, using a coaxial design (Fig.1(c)). With diameter of outer tube 4 cm, the inner gap between tubes was 8 mm, and working length coated by solid (1) and perforated (2) electrodes did not exceed 15 cm. The perforated electrode 2 had a transmittance of 82 %.

Let us underline, that capacitive discharge excitation is used both in barrier excilamps and cylindrical excilamps with capacitive discharge. However, operating conditions of the excilamps are differ. A barrier discharge lamp is characterized by relatively high pressure of working mixture and the discharge itself consists in a number of separate filaments. In cylindrical capacitive discharge excilamps the discharge in its appearance is similar to glow one and occurs at small operating pressures. Therefore below we shall distinguish these two types of capacitive discharge. It should be also noted, that probably, we have originally begun to use cylindrical capacitive discharge for development of exciplex lamps.

Excitation of the capacitive discharge excilamps was carried out from a sinusoidal voltage pulse generator, which was assembled on the two-stroke scheme. The generator provided current pulses of about $1.2 \cdot 10^{-5}$ s in duration (FWHM) with frequency up to 22 kHz. Voltage amplitude of the pulses did not exceed 6 kV.

Average output UV power was measured by a FEK-22SPU photodiode. The photodiode has peak sensitivity at wavelengths near 300 nm and is insensitive to the radiation at wavelengths over 600 nm. Besides, calibrated light filters transparent only in the UV placed in front of the photodiode were used to separate UV radiation in the excilamp output. These measurements were made in the following way. An aperture with diameter d was placed directly against the excilamp surface. The photodiode was located at a distance $L \gg d$ from the aperture. Next, the aperture was considered to be a point source, emitting uniformly in solid angle of 4π . In this case the part of the UV output that enters into the photodiode can be calculated as $k = \sin^2(a/2)$, where $a = \arctg(A/2L)$, A is the input aperture of the photodiode. Next, total output power was calculated taking into account the area of radiating surface as well as angular and axial distributions of the UV radiation. Validity of this procedure was tested using a DRL-400 industrial mercury lamp with specified UV output. Measurement results obtained agreed to the specified UV output of the mercury lamp with an accuracy of 15%.

Emission spectra were recorded by a MUM monochromator with inverse linear dispersion of 3.2 nm/mm.

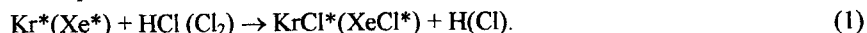
The working mixtures were prepared just in the lamp volume with successive inlet of halogen (Cl_2 , HCl), inert (Xe , Kr) and buffer (Ne , He) gases.

Eighteen diffusion and kinetic models⁷ were used for calculation of isothermal kinetics (formal and nonformal) of heterophase reactions. The choice of optimum model was carried out on the minimum of the root-mean square deviation of calculated dependencies from those obtained experimentally using a program of choosing the best kinetic model of solid state reaction. The calculations were carried using the minimum mean-square error method (MMSE).

2.2. Glow Discharge Excilamps

For obtaining stable output parameters of the lamps it is necessary to reduce a rate of working gas abandon from discharge volume. This rate depends on the medium and walls temperature, envelop and electrodes material, presence of contaminations and lamp design.

The main mechanism reducing life-time of a halogencontaining glow discharge excilamps is chemical interaction of halogen with electrodes. Fig.2 shows the UV radiation efficiency in binary mixture $\text{Xe}/\text{Cl}_2 = 5/1$ versus gas pressures. One can see that Cl_2 concentration decrease in the mixtures with optimal in terms of radiation efficiency pressure results in noticeable drop both efficiency and UV radiation power of the excilamp. Pure chlorine with the greatest reaction ability under low pressure conditions appears in the harpoon reaction:



It is known, that the HCl recovery rate in the reaction $\text{H} + \text{Cl} \rightarrow \text{HCl}$ is much higher than that of reaction atomic chlorine - metal electrode. Therefore, similarly to⁹, the excilamp operation time could be improved by small hydrogen additions into the volume during operation. Unfortunately, as it was shown in^{2,4}, the use of HCl instead of Cl_2 the lamp reduces noticeably average radiation power.

Chlorine losses can be reduced by another way when the electrodes are made from a metal with high chemical resistance, for example, from nickel. So, life-time t_{it} of $\text{Xe}/\text{Cl}_2 = 5/1$ binary mixture (total pressure of 4.5 mmHg) in glow discharge XeCl -excilamp with stainless still electrodes did not exceed one hour at specific input power 0.29-1.1 W/cm^3 . The use of nickel electrodes results in ten-fold extension of t_{it} , other condition being the same. For instance, t_{it} was as long as 15 hours at the specific input power of about 0.15 W/cm^3 (see Fig. 3). The 70 hours pause in the operating of this lamp did not

reduce the ultraviolet output. It indirectly testifies that operation stability of glow discharge excilamp was determined by concentration of chlorine atoms, which formed in reaction (1).

2.3. Cylindrical Capacitive Discharge Excilamps

Design of capacitive discharge excilamps allows to avoid a problem of contact between working mixture and electrode material. Nevertheless, this does not automatically provide significant extension of the working mixture life-time as compared to that of glow discharge excilamps. One of the reasons leading to the radiation power drop of the capacitive discharge lamps can be absorption of d atoms and molecules contained in gas mixture by the wall. When the discharge envelope is filled by a mixture of inert gases at pressure over several tens of mmHg the absorption did not usually lead to noticeable variations of the device operational mode during a long period. However, absorption processes in low-pressure mercury or hydrogen lamps can appreciably reduce longevity of the lamps, and in this case it is necessary to compensate⁷ the gas losses. The same problem is actual for electrodeless chlorine containing excilamps, as well.

Longevity of the cylindrical excilamp excited by capacitive discharge (Fig. 1(b)) directly depends on the engineering process of its preparation to work. Two dependencies of a KrCl-excilamp average power versus its operation time are shown in Fig. 4. The inner diameter and the gap between the ring electrodes were 3.8 and 10 cm, respectively. In the first case (Fig. 4(1)) before test we have prepared a lamp envelope by several cycles of krypton inlet and evacuation. In the second case (Fig. 4(2)) these cycles were supplemented by addition of 15 mmHg Cl₂ just after the preparation and then the system was passivated during two days. As a result, ten-fold improve of the excilamp mixture lifetime was achieved. Further extension of t_{fl} can be achieved using an active passivation by discharge in the gases, which will be further filled the lamp. A small-size sealed-off XeCl-excilamp was prepared according to this procedure. The inner diameter and the gap between the ring electrodes were 1.8 and 1 cm, respectively. Input power density was as high as 0.35 W/cm³ (it is higher, than that in the above examples). As it is shown in Fig. 5, further 100-fold improvement of the excilamp lifetime was achieved after the active passivation.

2.4. Barrier Discharge Excilamps

Optimization of pumping conditions and working mixture composition carried out for barrier discharge excilamps allow us to obtain efficiencies of XeCl and KrCl excilamps up to 10%⁸. However, lifetime of these lamps in our experiments usually did not exceed 100 hours.

As in the case of a glow discharge, the UV radiation output power in a barrier discharge depends critically on Cl₂ content in gas mixtures. Average radiation power in the spectrum region around $\lambda \sim 308$ nm in Ne-Xe-Cl₂ mixture as a function of Cl₂ pressure is shown in Fig. 6. Noticeable reduce of the UV radiation intensity is observed at chlorine pressure lower 1.5 mmHg. It is explained by the shortage of molecular chlorine for formation of molecules XeCl*. It is clear, that steady contact of chlorine with the walls reduces its concentration in the discharge region and leads to a drop of the radiation output power.

We have tried to find out the mechanism responsible for chlorine losses in electrodeless quartz excilamps.

To indirect judge about chlorine losses it is necessary to record emission power on Cl₂* ($\lambda \sim 258$ nm) spectral band. It is known that this band is clearly detected in a KrCl-excilamp spectra and has much lower intensity in XeCl-excilamp spectra. The Ne/Kr/Cl₂ = 750/75/1.5 (mmHg) mixture was taken for this experiment. Output power up to 0.9 W (7 mW/cm³) and ultraviolet radiation efficiency of about 2 % were obtained during first minutes of operation.

Radiation power on KrCl molecules as a function of the lamp operating time is presented in Fig. 7(a). Sharp drop of the intensity on a stage I of the given curve, can be explained by a number of phenomena:

1) adsorption and absorption of Cl₂ molecules during the phase, when quartz micropores do not contain significant portions of gas;

2) adsorption, absorption and chemical interaction of atomic chlorine formed in the process of dissociative electron attachment:



3) release of oxygen from quartz walls of the lamp. Though the last reaction



is energetically favorable, the probability of simultaneous local cooperation of four chlorine atoms with a quartz lattice is extremely low due to low volume concentration of Cl.

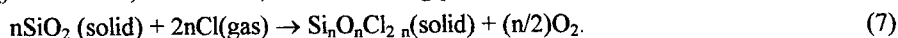
Formation of radiating RCl* molecules (where R is a rare gas tom) occurs in reactions





If molecular chlorine is not regained completely, contribution of reactions (4 - 6) decreases with time. The stage II of the given curve represents slow fall of the radiation intensity and corresponds to normal work of the discharge device. Under the conditions of sufficient micropores filling by portions of a gas absorption and desorption processes occur simultaneously. Therefore the fall of the average power on this stage is slowed down.

Besides it is possible to speak about chemical heterophase reaction of atomic chlorine with a quartz wall, which results in a chlorinesiloxane $(Si_nO_nCl_{2n})_x$ formation, for instance, in the following process:



The thermodynamic calculations done indicate that this reaction is more favorable energetically than (3).

Fig. 7(b) gives emission power of Cl^*_2 molecules ($\lambda_{max} \sim 259 \text{ nm}$) as a function of the lamp operating time. The power behavior is indirect evidence that the decrease of $KrCl^*$ molecules emission power occurs as a result of Cl_2 concentration decrease via the interaction with α - SiO_2 and formation of chlorinesiloxanes. Curves presented in Fig. 7(a) and Fig. 7(b) correlate well.

The mechanism of reaction (7) was determined using the program choosing the best kinetic model of solid state reaction. We reasoned that the radiation intensity is proportional to the degree of chlorine transformation $\alpha(t)Cl$ in the process of interaction with quartz walls. It was also supposed that $\alpha(0)Cl = 1$ at the moment of the lamp triggering and $\alpha(t_k)Cl = 0$ by the moment t_k when Cl_2^* emission intensity in discharge decays to 5 % of its initial value. Eighteen kinetic and diffusion models were taken into account and the anti-Yander model gives minimal dispersion (from 10 up to 6) of $\alpha(t)Cl$ for Therewith the following kinetic equation is valid:

$$[(1+\alpha(t)Cl)^{1/3} - 1]^2 = k \cdot t. \quad (8)$$

This means, that in the conditions of our experiments atomic chlorine displaces oxygen atoms from a quartz crystal lattice and forms chlorinesiloxane skin-deep layer. Mobility of oxygen atoms are higher than that of chlorine atoms (this is due to their different sizes). Therefore, O atoms being superseded from the lattice diffuse to the quartz surface through the chlorinesiloxane layer and form O_2 molecules in the reaction with O atoms accumulated in the surface layer. Then O_2 molecules interact with rare gas atoms R and form chemically neutral compounds RO , RO_2 . Therewith R losses from the excilamp has volume effects insignificantly on the RCl^* formation kinetics.

It can be assumed that the role of the above mechanism has stronger effect in a barrier discharge as compared to that in a classical glow and capacitive discharges realized in cylindrical tubes. This is due to the coaxial barrier excilamp design (see Fig. 1(c)) when the gap between the quartz tubes is usually less than 1 cm. Therewith such parameters as free run length of chlorine ions and high field strength across the gap are favorable for the chlorinesiloxane film formation.

From the above reasoning it follows that for lifetime extension of barrier discharge excilamps containing chlorine in a working media the period of discharge passivation should be longer than in the case of classical capacitive discharge. This assumption was tested using a coaxial excilamp identical to that described in Section 2.1. The excilamp was filled by a mixture of $Xe/Cl_2 = 8/1$ composition at $p = 2 \text{ mmHg}$. Therewith the stage I responsible for the active passivation process (as in Fig. 7) was not observed and the excilamp lifetime above 1000 hours was achieved (Fig. 8).

3. CONCLUSION

The study done showed, that in addition to their high average power and efficiency $XeCl$ and $KrCl$ excilamps can have a long operation period and development of sealed-off samples with a gas mixture lifetime over 1000 hours is possible. The longest lifetime is most easily to obtain in electrodeless excilamps excited by various types of capacitive discharge (barrier, classical low pressure capacitive discharges in cylindrical tubes). Reliability of the capacitive discharge excilamps is determined by the heterophase chemical reaction mechanism of interaction chlorine atoms with a quartz wall with formation of polymeric chlorinesiloxane products. Besides the lifetime extension can be obtained in excilamps with inductive discharge, as well.

ACKNOWLEDGMENTS

This work has been made under partial financial support from the Russian Foundation for Fundamental Research (project No. 96-02-16668a). The authors would like to thank D.V. Shitz for assistance in the execution of the experiment.

REFERENCES

1. M. Obara, "Recent progress of excimer radiation - Research, Development and Application", *Proc. 7th Int. Symp. "Science & Technology of Light Sources"*, Kyoto, 27th-31st August, 1995. - pp. 149-200.
2. A.N. Panchenko, V.S. Skakun, E.A. Sosnin, V.F. Tarasenko, and M.I. Lomaev, "Powerful coaxial excilamps with average output power over 100 W", *Pisma v Zh. Tech. Fiz.* **21**, pp. 77-80, 1995.
3. E. Arnold, R. Dreiskemper, and S. Reber, "High-Power Excimer Sources", *Proc. 8th Intern. Symp. on Science and Technology of Light Sources, Greifswald*, 30.08 - 3.09, 1998. - pp.90-98
4. M.I. Lomaev, A.N. Panchenko, V.S. Skakun, E.A. Sosnin, and V.F. Tarasenko, "Cylindrical Glow Discharge Excilamps", *Zh. Tech. Fiz.* **68**, pp. 64-68, 1998.
5. E.A. Sosnin, M.I. Lomaev, A.N. Panchenko, V.S. Skakun, and V.F. Tarasenko, "Glow and Barrier Discharge Efficient Excilamps," *SPIE Proceedings* **3403**, pp. 732-741, 1998.
6. M.I. Lomaev, A.N. Panchenko, V.S. Skakun, E.A. Sosnin, V.F. Tarasenko, M.G. Adamson, B.R. Myers, and F.T. Wang, "Excilamp Producing up to 130 W of Output Power and Possibility of its Applications", *Laser and Particle Beams* **15**, pp. 241-246, 1997
7. Y.D. Tretyakov, *Solidstate reactions*, Moscow, Chemistry, 1978.
8. I.L. Kaganov, *Ionic Devices*, Moscow, Energy, 1972.
9. E.A. Sosnin, V.S. Skakun, and V.F. Tarasenko, "Coaxial and planar excilamps pumped by barrier discharge", *Proc. 8th Intern. Symp. on Science and Technology of Light Sources, Greifswald*, 30.08 - 3.09, 1998. - pp.240-241.
10. T.J. Mckee, D.J. James, and W.S. Nip, "Lifetime extension of XeCl and KrCl lasers with additives", *Appl. Phys. Lett.* **36** pp.943-945, 1980.
11. Y.I. Raizer, M.N. Sneider, and N.A. Yatsenko, *Radio-frequency Capacitive Discharges*, N.Y., CRC Press, 1995.
12. B. Gellert, and V. Kogelschatz, "Generation of Excimer Emission in Dielectric Barrier Discharges", *Appl. Phys. B.* **52**, pp. 14-21, 1991.

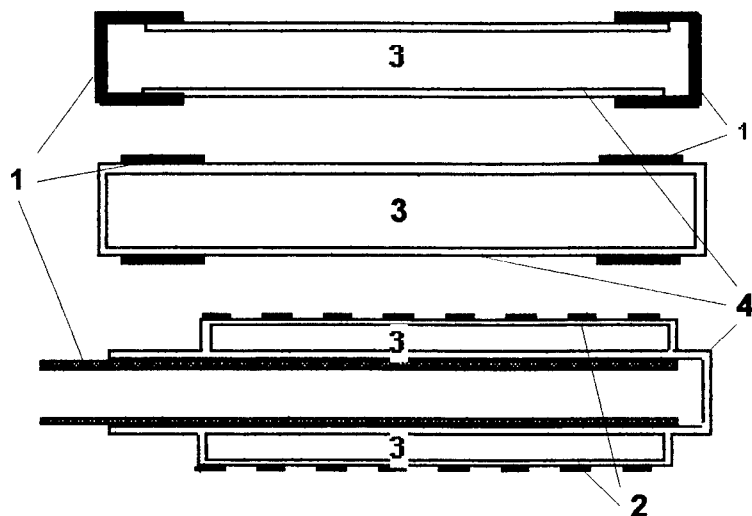


Fig.1. Schematic of glow (a) and capacitive (b,c) discharge excilamps. 1 - solid electrodes, 2 - perforated electrode, 3 - discharge volume, 4 - quartz envelopes.

Fig.2. UV efficiency ($\lambda \sim 308$ nm) of a XeCl-excilamp versus total pressure in mixture Xe/Cl₂ = 5/1. 1 - input power density $P_d = 0.43$ W/cm³, 2 - input power density $P_d = 0.64$ W/cm³.

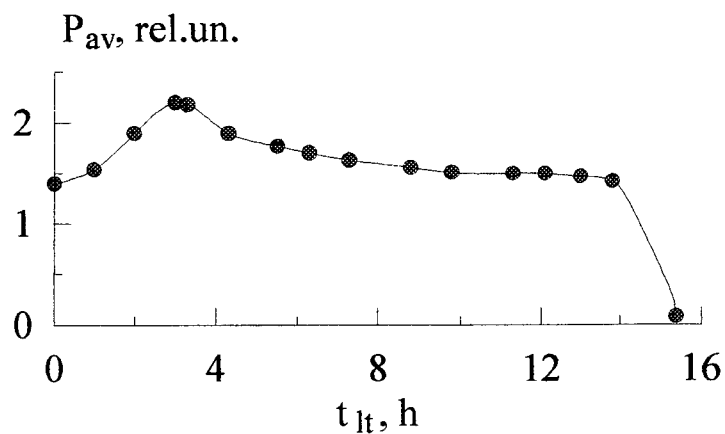
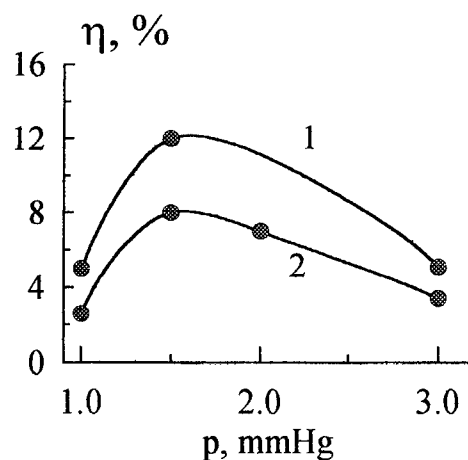
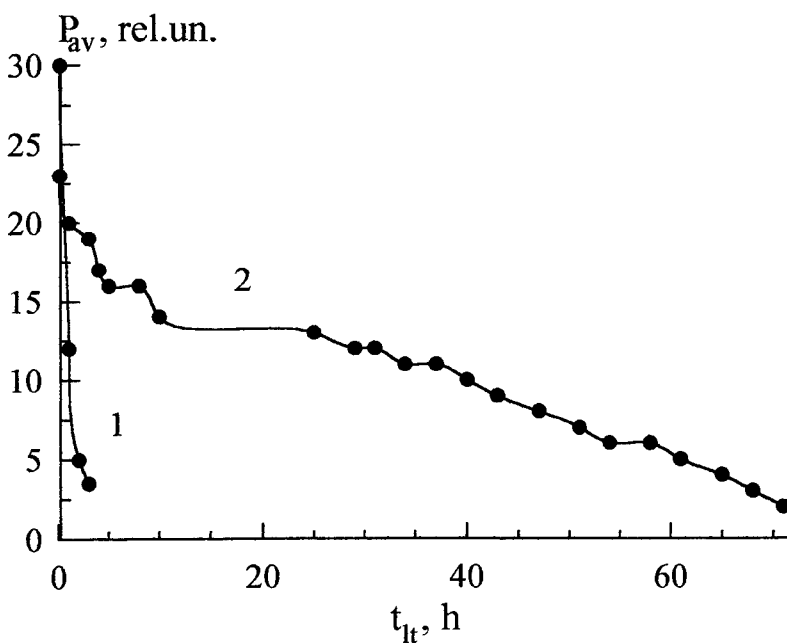


Fig.3. Output average power of glow discharge XeCl* excilamp versus operation time for Xe/Cl₂ = 5/1 mixture. Total pressure was fixed at 4.5 mmHg, input power density is $P_d \sim 0.15$ W/cm³.

Fig.4. Output average power of a capacitive discharge KrCl-excilamp versus operation time for mixture Kr/Cl₂ = 6/1. 1 - without preliminary passivation, 2 - with passivation by 15 mmHg of Cl₂ during 50 hours. Total pressure was fixed at 1 mmHg, input power density is $P_d \sim 0.2$ W/cm³.



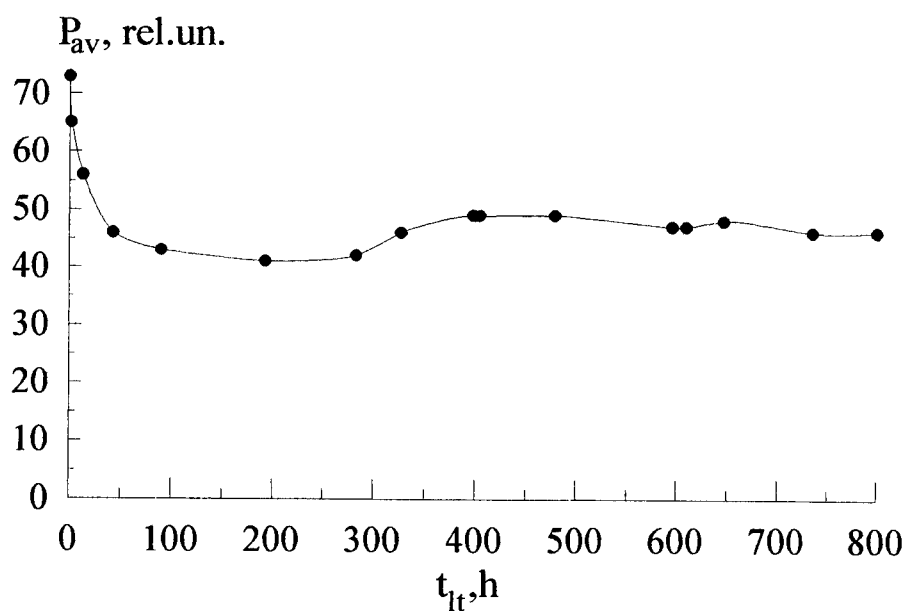
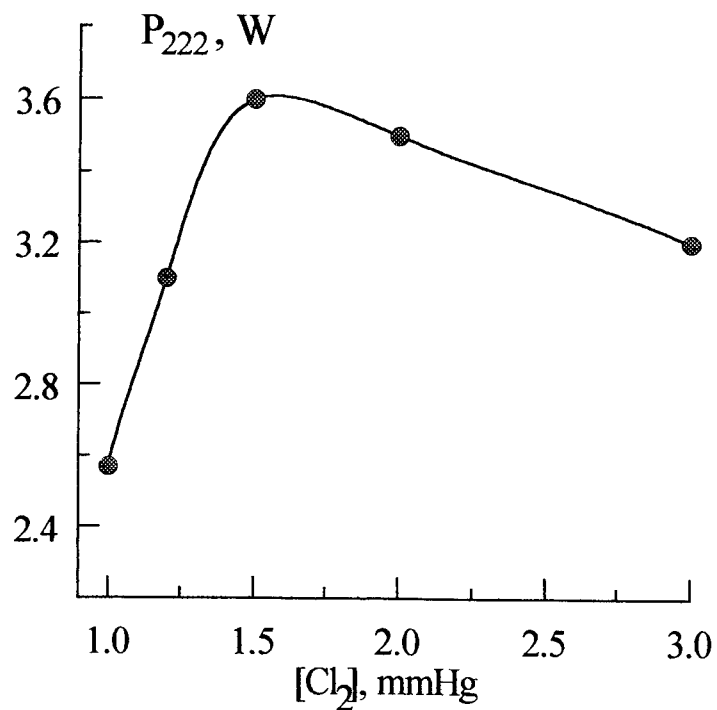


Fig.5. Output average power of a capacitive discharge XeCl-excilamp versus operation time in mixture $\text{Xe}/\text{Cl}_2 = 8/1$. Total pressure was fixed at 3.3 mmHg, $P_d \sim 0.35 \text{ W/cm}^3$.

Fig.6. Output average power of barrier discharge KrCl-excilamp versus Cl_2 pressure in mixture $\text{Ne}/\text{Xe}/\text{Cl}_2 = 750/60/1.5$ (mmHg).



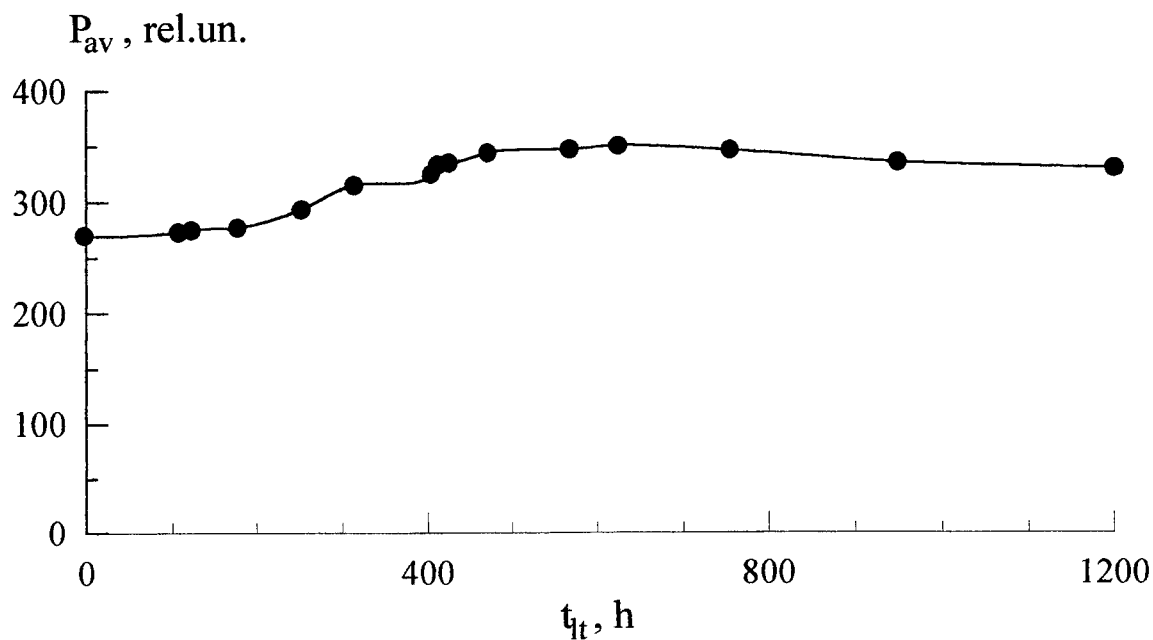
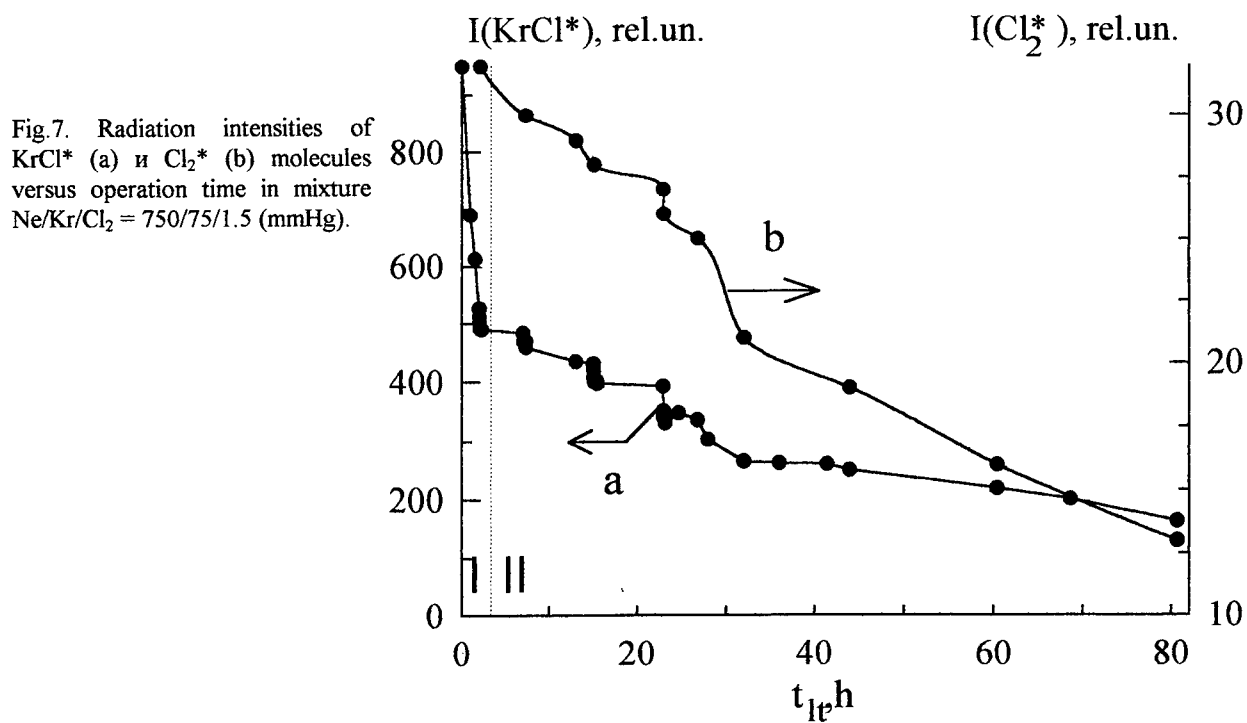


Fig.8. Output average power of a barrier XeCl^* -excilamp versus operation time in mixture $\text{Xe/Cl}_2 = 8/1$ at total pressure ~ 2 mmHg.

SESSION 9

Pulsed Laser Deposition, Nanoclusters, Tribological and Diamond Films

Condensation of vapor and nanoclusters formation within the vapor plume, produced by ns-laser ablation of Si, Ge and C

B. S. Luk'yanchuk ^{a*}, W. Marine ^b, S. I. Anisimov ^c, G. A. Simakina ^a

^a General Physics Institute, Russian Academy of Sciences, 117942 Moscow, Russia

^b UMR CNRS 6631, Faculte des Sciences de Luminy, 13288 Marseille, France

^c Landau Institute for Theoretical Physics, Russian Academy of Sciences, 117940 Moscow, Russia

ABSTRACT

The condensation of vapor within the expanding plume produced by ns-laser ablation is discussed in the frame of Zeldovich and Raizer theory of condensation. The calculations have been performed for Si, Ge and C -vapors. It is shown that the size of clusters formed during the condensation is very small, typically of the order of few nanometers. The averaged cluster radius is calculated for different temperatures and densities of the initial plume. The generalisation of the theory is made for inhomogeneous plume where the rates of nucleation as well as condensation times are different at different parts of the plume. The size distribution function is calculated for the plume expansion into vacuum. For the clusters moving together with vapor one can distinguish three different waves propagating through the plume: (1) The saturation wave, where the vapor becomes saturated, (2) The supercooling wave, where the highest supercooling is reached, and (3) The quenching wave, where the growth of cluster stops. The last stage of cluster formation is related to cooling of clusters and their crystallisation. This leads to delay in photoluminescence signal with typical delay time from 0.1 to 7 ms depending on the type of the background gas and its pressure.

Keywords: Laser ablation; Silicon clusters; Nanocrystals; Theory of condensation; Photoluminescence.

1. INTRODUCTION

Formation of nanoclusters during a fast expansion of vapor, produced by laser ablation is a promising technique for synthesis of new optoelectronic materials [1-5]. The nanoclusters occupy an intermediate position between the quantum objects (atoms, molecules) and macroscopic objects (bulk materials), thus, many properties of nanoclusters differ from both, the quantum objects and bulk materials, this is of great practical and scientific interest [6-8]. There are many problems, which should be clarified to optimize the synthesis of quantum-confined nanomaterials by laser ablation. Condensation of vapor during its fast expansion occurs in strongly nonequilibrium conditions. Characteristic cooling rates for the plume expanding into vacuum reach 10^{10} - 10^{11} K/s. It exceeds many times characteristic rates which physics of phase transitions conventionally treated in explosion problems, impact of meteorite on the surface of planet, etc. Thus, some fundamental problems of fast condensation are still under discussion.

Recently, both, the theoretical [9] and experimental [10] studies of characteristic temporal and spatial scales were done for Si-nanoparticles forming within the vapor produced by excimer laser ablation of c-Si. The basic question is how fast the nuclei are formed within the expanded vapor. According to theoretical study formation of nanocluster is completed at the moment of quenching (when the collisions are terminated) which at typical conditions expansion into vacuum consists

* Correspondence: E-mail: lukyanch@kapella.gpi.ru; Telephone: ++7 095 132 83 42; Fax: ++7 095 135 82 34

of a few μs ($\approx 2 \mu\text{s}$ for the example, shown in [9]). The experimental study of nanoclusters formation by time-resolved imaging of photoluminescence (PL) reveals that the first luminescence signal appears with significant delay time which depends on the pressure and type of the background gas [10]. This time consists of $\Delta t \approx 200\text{--}400 \mu\text{s}$ (in He at 10 Torr) and $\Delta t \approx 3 \text{ ms}$ (in Ar at 1 Torr). Thus, the time of luminescence appearance is two or three orders of magnitude longer than the cluster formation time. Approximately the same delay time was found in [10] for Rayleigh-scattered light (RS).

There are three reasons for this delay time. First of all, the plume expansion in the presence of the background gas occur slower than in vacuum, thus, cluster formation and growth processes are also slower. Second, the nonisothermal effects in nucleation related to the gas and nuclei temperatures difference may be important. Third, the delay time in PL should be also caused by the long stage of cooling and crystallization of nanoclusters [11]. Effects in the melting temperature decrease for small clusters [12, 13], as well as the variation in dielectric constant [14] are also important.

At the same time the classical theory of nucleation yields a reasonable estimation for characteristic size of formed nucleus and we believe that it shows a correct direction of variation in size distribution function versus parameters. Thus, we shall concentrate on this side of calculations and compare results that were found for different materials (nucleation from silicon, germanium and carbon vapors).

2. KINETICS OF CONDENSATION PROCESS.

The theory of first-order phase transitions (see, e.g. [15-18]) agrees that the condensation process is governed by supercooling

$$\theta = \frac{T_{eq} - T}{T_{eq}}, \quad (1)$$

where T_{eq} is the equilibrium temperature along the binodal curve (many features of the real gas behavior can be qualitatively understood from the Van der Waals equation, see in Fig. 1). If one forms instantaneously the metastable homogeneous system with $\theta|_{t=0} = \theta_0$, then the further evolution of the system to the equilibrium state occurs by means of nucleation and further growth of overcritical nuclei. This is the starting point for the understanding of cluster formation. If the supercooling is smaller than critical, $\theta < \theta_c$, where θ_c is supercooling along the spinodal curve, then the dynamics of cluster follows through the well-defined stages as it is shown schematically in Fig. 2. The nucleus of critical size $r = r_c$ is formed with latent time $t_c \propto w^{-1}$ (w is the probability for the formation of a nucleus with radius r_c). The process is initiated by localized (droplet-like) fluctuation of finite amplitude, which develops further as the instability. The rate of formation of such droplets is described by homogeneous nucleation theory. The "classical" nucleation theory is based on the kinetic equation of the Fokker-Planck type, which is written in the "space of sizes"

$$\frac{\partial f}{\partial t} = -\frac{\partial J}{\partial g}, \quad J = -D_s \frac{\partial f}{\partial g} + B_s f, \quad (2)$$

where f is the size distribution function, D_s is the "diffusion coefficient" in the space of sizes g . The coefficient B_s follows from the condition that the flux J goes to zero for equilibrium distribution function $f_0 \propto \exp[-R_{\min}(g)/k_B T]$ (here $R_{\min}(g)$ is the minimal work necessary to produce the nucleus of the size g [15]).

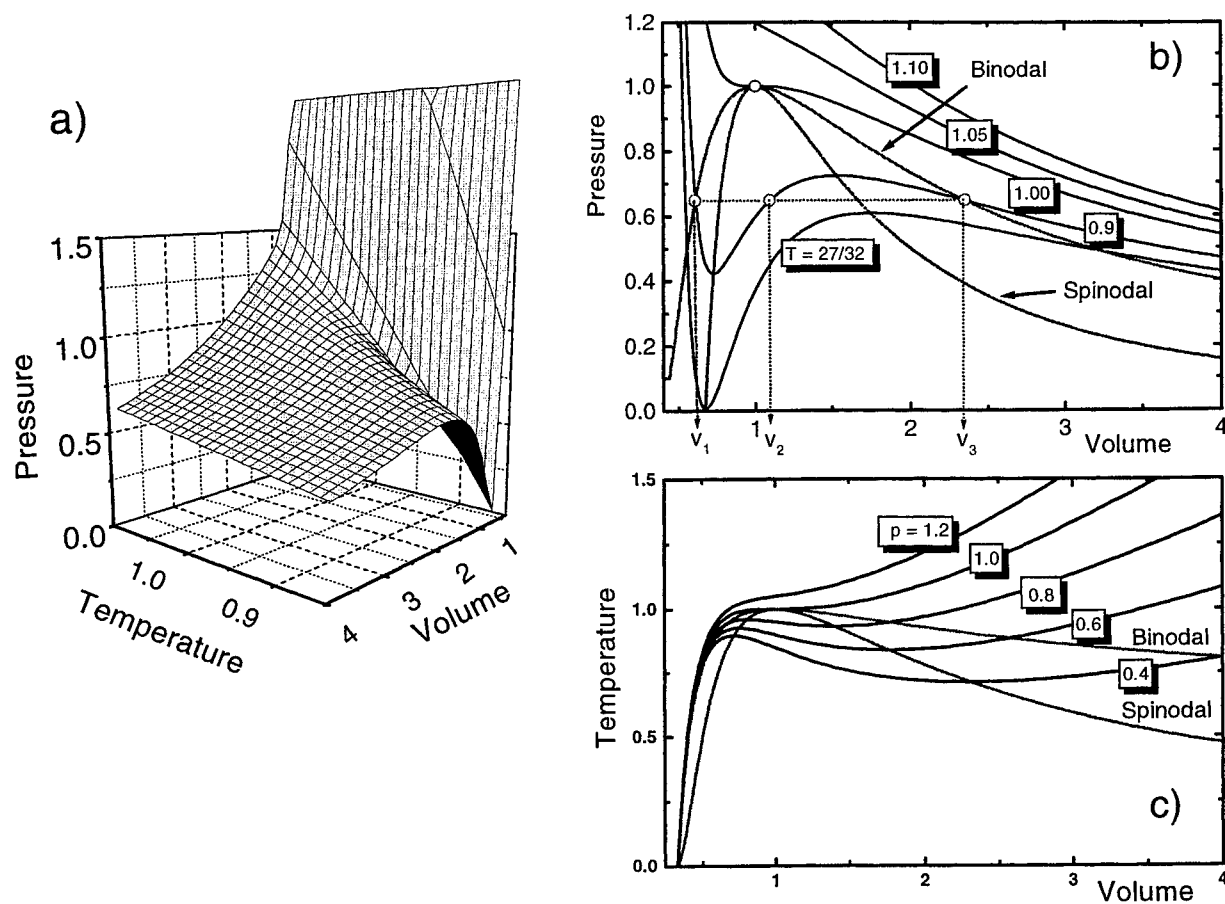


Fig.1. a) 3D surface, given by Van der Waals equation $p = \frac{8\tau}{3v-1} - \frac{3}{v^2}$, where p , τ , v are specified reduced pressure, temperature and specific volume. b) Van der Waals isotherms. The equilibrium phase transition occurs at pressure when the phase trajectory of the system crosses the binodal curve. Equation for binodal follows from the "Maxwell rule" $\int_{v_1}^{v_3} p dv = 0$, where v_i are corresponding roots of the equation. The spinodal curve is given by $p_s = \frac{3}{v^2} - \frac{2}{v^3}$. c) Van der Waals isobars.

Kinetic equation (2) permits to describe the rate of production of "vital clusters" whose size is larger than the critical size. This equation was found by different methods in the classical papers of Becker and Döring [19], Kramers [20] and Zeldovich [21]. The condensation theory based on equation (2) (Becker-Zeldovich equation [18]) is often called as Becker-Döring theory [17] or Zeldovich theory [15]. Having in mind the importance of Kramers contribution [18], it is justified to call the classical theory of nucleation as BDKZ-theory.

If one considers that the establishment of size distribution for subcritical clusters arises sufficiently fast then the production rate of nuclei is given by stationary solution of equation (2). This stationary solution needs special "source and sink" boundary conditions [17] (they are also called Becker-Döring boundary conditions [18]). It assumes that once a cluster

grows to a specified large size (greater than critical), it is removed from the system and replaced by equivalent amount of vapor. This production rate has a clear physical sense, it describes a thermally activated process similar to tunneling of a Brownian particle across a potential barrier [17]. At small supercooling (it means that $\theta < \theta_c$, and θ is not very close to θ_c) the activation energy has a sharp maximum at $x = r_c$. This permits to present the nucleation rate in the following form

$$\frac{dv}{dt} = k_v \exp \left[-\frac{T_v}{T} \frac{1}{\theta^2} \right], \quad T_v = \frac{16\pi\sigma^3 m^2}{3k_B q^2 \rho_\ell^2}, \quad (3)$$

where $v = v(t)$ is the number of condensation centers (per atom of vapor), σ is the surface tension, m is the mass of atom, ρ_ℓ is the density of liquid, q is the heat of vaporization given in Kelvin, and the preexponential factor k_v is proportional to the density of vapor and expressed through the thermodynamic parameters (see, e.g. [15]).

When one uses equation (3) a theoretical description of the condensation process is clearly separated into the nucleation itself and further growth of overcritical nuclei. The latter can be described on the kinetic or macroscopic (diffusion equation) level. This consideration shows that the growth of the overcritical nucleus firstly (when the radius of nucleus is smaller than the mean free path in the vapor) occurs in the kinetically controlled region, where the rate of volume growth is proportional to the number of collisions, i.e. nucleus cross-section, $dr^3/dt \propto r^2$. It leads to linear law, $r \propto t$ (see in Fig. 2).

When the size of cluster becomes comparable to mean free path within the vapor, the flux of condensed particles, J , is related to diffusion (diffusion controlled regime, $J \propto D/r$, where D is diffusion coefficient.). At this stage $dr^3/dt \propto r^2 J$, thereby $r \propto t^{1/2}$. As the supercooling is decreased during the condensation, then the latest stage of condensation occurs at the condition when the sizes of nuclei are close to critical. The rate of volume growth at this stage is constant. It leads to the law $r \propto t^{1/3}$ (Lifshitz-Slyozov or "Ostwald ripening", or coalescence stage, see details of this theory, e.g. in [15, 22, 23]). During the Lifshitz-Slyozov stage the size distribution function varies due to increase of the big clusters and decrease of small ones. However, in the beginning of coalescence stage the clusters (droplets) are practically of the same size, thus, the rate of atom exchange between the clusters is low. This leads to the long transition stage where the condensation is "frozen". The transition stage is characterized by law $r \propto t^\varepsilon$, $\varepsilon \ll 1$, as it was recently suggested in [24, 25].

The specific features of cluster production within the expanding vapor plume is related to dynamics of supercooling $\theta = \theta(t)$, which is governed simultaneously by the plume expansion and release of the heat of phase transition. This self-consistent consideration of the cluster formation was made firstly by Raizer [26]. Raizer discussed the inertial stage of the vapor expansion and solved equation (3) together with equation for the rate of droplet growth and the adiabatic equation in the condensation region. The analysis was done for the problem of cosmic dust production during a collision (and further vaporisation) of a large meteorite with the surface of a planet without an atmosphere. It was found that the degree of condensation, number of clusters and their size strongly depend on the velocity of the vapour expansion which, in turn, depends on the initial size of the vapour cloud, evaporated mass, and internal energy. It was also shown in [26, 27] that condensation stops because of the phenomenon of quenching. We call this theory the Zeldovich - Raizer theory (ZR theory) attributing its origin to papers [21, 26] and monograph [27]. Location of this theory on the kinetics diagram in Fig. 2 corresponds to nucleation and kinetic controlled region.

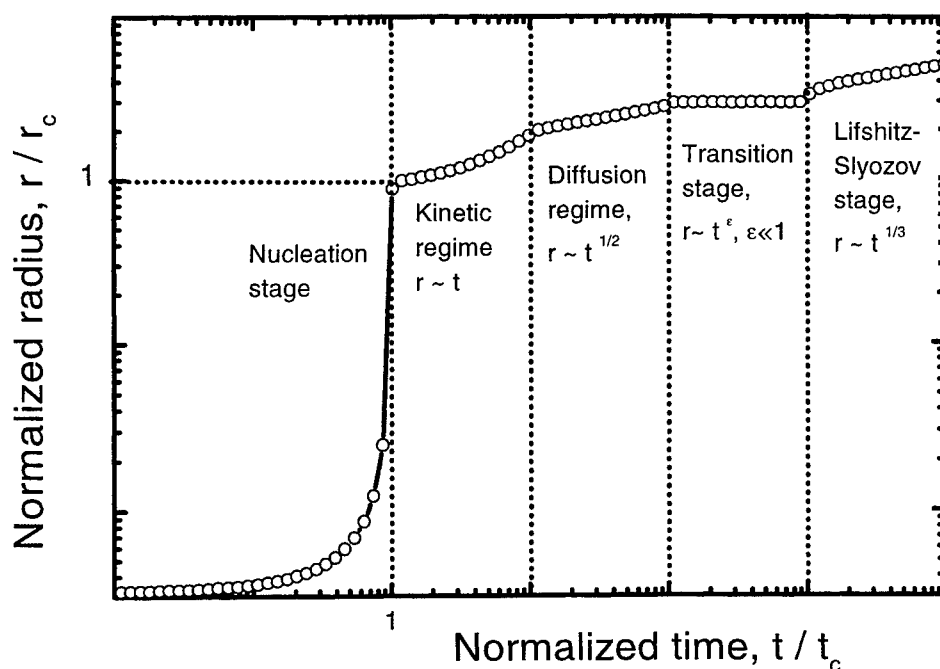


Fig. 2. The schematic for the changes in kinetics of condensation versus normalized time.

An important problem for many applications is to control the size distribution function of clusters generated during the laser ablation. It is desirable to generate clusters with very narrow size distribution. However, this is impossible because the laser plume is strongly nonuniform, and the conditions for vapor condensation vary from place to place within the plume. In the recent paper [28] the assumption is made that the distribution function of clusters is formed due to coalescence. Thus, the authors of [28] described the cluster growths on the basis of Lifshitz - Slyozov theory, i.e. very late stage on the kinetics diagram in Fig. 2.

On the contrary, in paper [9], we neglect the coalescence and discuss an effect related to the formation of the size distribution function due to the difference in condensation time for different parts of the plume. Roughly speaking large clusters are formed in the centre of the plume, while the smaller ones are formed near the plume edge. For the theoretical analysis we used ZR theory of condensation, which was generalised to describe the nonuniform plume and introduce a few corrections related to the special features of the vapour plume produced in laser ablation experiments. Although ZR theory does not contain any fitting parameter it is applicable (with minor corrections) to the description of condensation under wide variety of conditions (it is sufficient to mention a tremendous difference, sixteen orders of magnitude, between evaporated mass in the case of meteorite impact discussed in [26,27] and typical evaporated mass in laser ablation experiments, as well as a great difference in many other parameters).

We mentioned above the problem of a significant delay time of the luminescence signal. This delay time can be attributed, at least, partially, to the long stage of nanocluster cooling and crystallization [11]. There is, however, another reason for the delay in nanocluster formation. The nucleation process is nonisothermal [18], which is not taken into account in the ZR theory. As a result ZR-theory yields overestimated values of the nuclei formation time [18]. In the frame of ZR-

theory the nuclei and atoms within the vapor plume have the same temperature. The latest is calculated in adiabatic approximation. In reality the entropy is changed and the temperatures of nuclei and vapor are different. The experiments [29] shows that even at sufficiently slow variations in the vapor pressures the Becker-Döring theory yields the nucleation rate overestimated by one or two orders. The assumption that the temperature of an embryo is slightly higher than the gas temperature can compensate this discrepancy [18]. As it was pointed out in [9], the condition for isothermal nucleation is broken on some stage of the nucleation process. It means that an adequate description of the condensation process should be based on the nonisothermal nucleation theory (the corresponding equations are given, e.g. in [18]).

We see thus that because of the problem complexity the description of nanocluster formation needs both, the new experiments and corresponding theoretical analysis. Although at the present stage this theory is not completed, some estimation can be made on the basis of ZR-theory. It predicts, as we see below, the size distribution of nanoclusters, which is in a reasonable agreement with experimental data.

3. THE PLUME EXPANSION AND CHARACTERISTIC WAVES

Following [9] we use a simplified model of spherical plume expansion

$$\left(\frac{R}{R_0}\right)^2 \equiv \Psi(t) = 1 + 2\frac{u_0}{R_0}t + \left[\left(\frac{u_0}{R_0}\right)^2 + \frac{16}{3}\frac{E}{MR_0^2}\right]t^2, \quad (4)$$

where M is the total mass of the vapor, E is the initial internal energy of the plume, R_0 is the initial radius of the plume and u_0 is the initial velocity of plume expansion. This solution follows from the special solution of the gas dynamic equations [9, 30] and holds for monatomic gas with adiabatic exponent $\gamma = c_p / c_v = 5/3$.

The density and temperature profiles within the plume are given by

$$\rho(t) = \rho_0 \left(1 - \xi^2\right)^{3/2} \Psi(t)^{-3/2}, \quad \rho_0 = \frac{8}{\pi^2} \frac{M}{R_0^3}, \quad (5)$$

$$T(t) = T_0 \left(1 - \xi^2\right) \Psi(t)^{-1}, \quad T_0 = \frac{\mu}{R_g} \frac{16}{15} \frac{E}{M}, \quad (6)$$

where $\xi = r/R(t)$ is the Lagrangian coordinate ($0 \leq \xi \leq 1$), R_g is the gas constant, and μ is atomic weight of the vapor.

We shall assume that small droplets of condensed vapor *move together with the vapor*. For this case, the condensation process can be considered independently for each fluid particle with Lagrangian coordinate ξ . According to the assumption of the ZR theory, the condensation process does not influence the plume expansion. For arbitrary value of ξ one can write the change of specific volume as

$$\frac{1}{V} \frac{dV}{dt} = \frac{3}{2} \frac{1}{\Psi} \frac{d\Psi}{dt}. \quad (7)$$

The condensation starts when the vapor in the plume becomes saturated, and stops when the plume expansion becomes collisionless (free-molecular regime). If a plume is inhomogeneous, the saturation and free-molecular regime are reached for different places at the different points of time, i.e. the saturation and quenching waves propagate through the expanding vapor.

Before the condensation starts, the expansion of the plume occurs along the Poisson adiabetic, $PV^\gamma = \text{const}$. This expansion regime lasts for as long as the Poisson adiabetic intersects the saturated vapor curve given by Clapeyron-Klausius equation. This intersection occurs at condensation temperature T_c , given by $T_c = q \cdot \Phi(a)$, where $\Phi(a)$ is the smaller root of the transcendental equation

$$\Phi^{-3} \exp\left[\frac{1}{\Phi}\right] = a, \quad a = \frac{B}{V_0} \left(\frac{q^2}{T_s T_0} \right)^{3/2}. \quad (8)$$

Here q is the heat of vaporization given in Kelvins, $T_s = 300$ K, $B = R_g T_s / \mu P_s$, P_s is the preexponential factor in the equation for saturated vapor pressure. It should be noted that T_c depends on initial parameters V_0 and T_0 but it does not depend on Lagrangian coordinate ξ , i.e. we obtain the same condensation temperature for different parts of the given plume. This condensation temperature T_c is shown for germanium vapor in Fig. 3 (we made calculations for three materials- Si, Ge and C; the main results for Si are presented in [9] and for carbon in [31]). Parameters of materials [32, 33] that have been used in calculations are presented in Table 1.

The moment t_c when condensation starts, depends on the Lagrangian coordinate: the saturation wave propagates through the plume from the periphery to the center. The front of this wave $r = r_c(t)$ moves according to

$$\frac{r_c(t)}{R(t)} = \sqrt{1 - \frac{T_c}{T_0} \Psi(t)}. \quad (9)$$

The plot of this function is shown in Fig. 4. For calculations we used parameters of vapor given in Table 2.

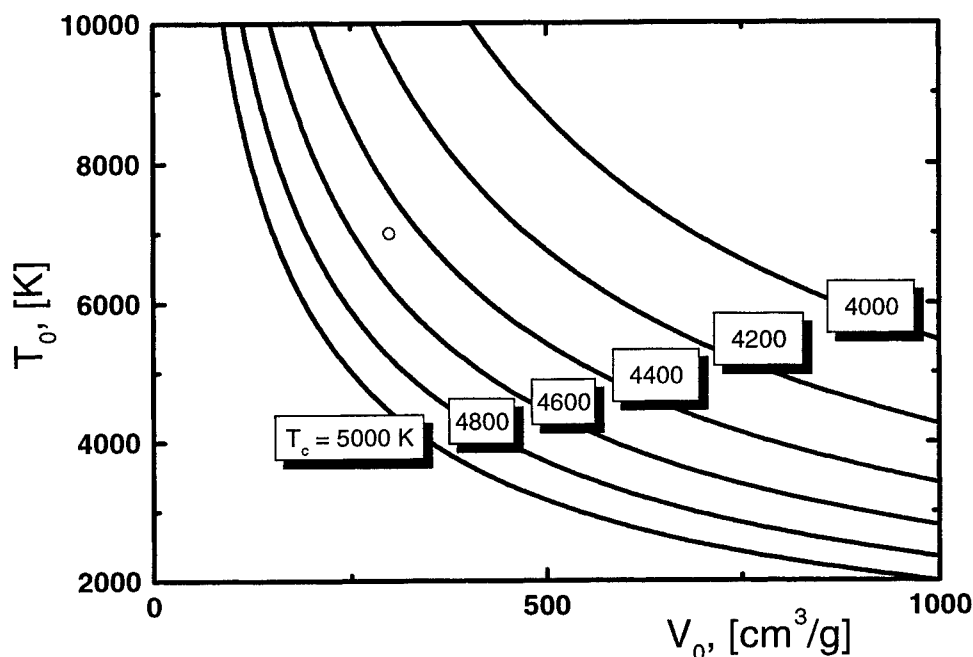


Fig. 3. Condensation isotherms T_c on the plane of parameters T_0 , V_0 for Ge-vapor. The point with $T_0 = 7000$ K and $V_0 = 300 \text{ cm}^3/\text{g}$ corresponds to $T_c = 4481$ K.

Table 1 Parameters of materials [32, 33] which have been used in calculations.

Parameter	Si	Ge	C
Density of condensed phase, ρ_c [g / cm ³]	2.4	5.323	2.25
Atomic weight, μ [g / mole]	28	72.59	12
Heat of vaporization, q [K]	50615	43655	93957
Normalization temperature, T_s [K]	300	300	300
Preexponential factor, P_s [atm]	$6.72 \cdot 10^6$	$5.76 \cdot 10^6$	$2.78 \cdot 10^{10}$
B , [cm ³ / g]	$1.31 \cdot 10^{-4}$	$5.96 \cdot 10^{-4}$	$7.36 \cdot 10^{-8}$
Surface tension, σ [erg / cm ²]	750	604.5	1500 (?)
Cross-section of collisions, σ_g [cm ²]	$4.37 \cdot 10^{-16}$	$6.07 \cdot 10^{-16}$	$1.86 \cdot 10^{-16}$
Melting temperature, T_m [K]	1685	1210.4	4200 [12]

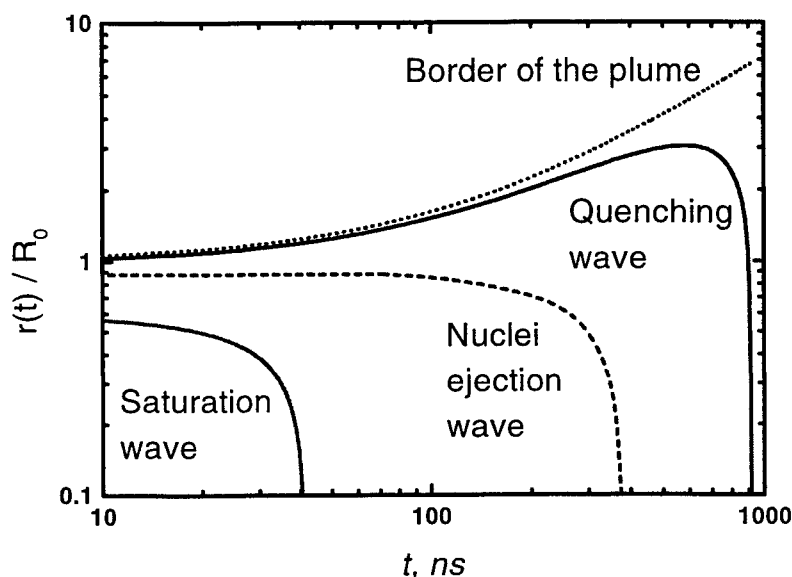


Fig. 4. Propagation of saturation, quenching and “ejection” waves through the Ge-vapor plume with parameters of vapor given in Table 2.

Table 2 Initial parameters of the plumes used in the calculations.

Initial parameters of the plume	Si	Ge	C
Initial temperature, T_0 [K]	7000	7000	8000
Initial specific volume, V_0 [cm ³ /g]	300	300	200
Initial size, R_0 [cm]	0.1	0.1	0.1
Initial pressure, P_0 [atm]	68.4	26.4	273.5
Initial velocity of expansion, u_0 [cm/s]	$6 \cdot 10^5$	$6 \cdot 10^5$	$6 \cdot 10^5$

Condensation stops due to the so called "quenching effect". It occurs because the collisions within the expanding vapor stop at some stage of plume expansion (see [27] for details). To find the boundary $r = r_q(t)$ between the collisional (hydrodynamic) and collisionless (free-molecular) regions of the plume we use the criterion $\ell \nabla v = v_s$. Here $\ell = 1/\sigma_g N = m/\sigma_g \rho(r)$ is the mean free path within the hydrodynamic region (σ_g is the collision cross-section), and v_s is the sound velocity at given point. Then the equation for the radius of quenching wave is given by [9]:

$$\frac{r_q}{R} = \sqrt{1 - \left(t_k \Psi \frac{d\Psi}{dt} \right)^{1/2}}, \quad \text{where} \quad t_k = \frac{mV_0}{2\sigma_g} \sqrt{\frac{3m}{5k_B T_0}}. \quad (10)$$

The third wave refers to the trajectory where the maximum supersaturation is reached. At this condition the nuclei are formed ("ejected" into the saturated vapor). The equation for this wave was found in [9]:

$$\frac{1}{T_{eq}} \frac{dT_{eq}}{dt} = \frac{1}{\Psi} \frac{d\Psi}{dt} + \left[\frac{2}{3} \frac{q}{T_p} - 1 \right] \left(\frac{\alpha}{\theta_p} \right)^3 \frac{dv}{dt}, \quad \text{where} \quad \alpha = \frac{2\sigma m}{k_B q \rho_\ell} \left(\frac{4\pi \rho_\ell}{3m} \right)^{1/3}. \quad (11)$$

Here T_{eq} is the equilibrium temperature and (dv/dt) is the rate of nucleation given by equation (3). The quantities within this equation will be defined below. The derivative (dv/dt) in (11) is taken along the Poisson adiabat, $T = T_p$. The propagation of the saturation, nuclei ejection and quenching waves through the plume is shown in Fig. 4. The plot is given in Euler's coordinates, the border of the expanding plume is shown in Fig. 4 as well.

4. THERMODYNAMICS OF TWO-PHASE REGION.

When the vapor becomes saturated and condensation starts, the state of matter within the plume is presented by two-phase system "liquid + vapor". One can define the degree of condensation, x , as the ratio of number density of molecules in liquid phase to the total number density. If one supposes that the system is in thermodynamic equilibrium, then the evolution of the system follows the equilibrium adiabat of "two-phase" region. This adiabat can be found from the energy balance for adiabatic process [27]. This consideration yields the equation [9]

$$(1+x) \frac{dT}{dt} + (1-x) \frac{T}{\Psi} \frac{d\Psi}{dt} = \left(\frac{2}{3} q - T \right) \frac{dx}{dt}, \quad T|_{t=t_c} = T_c. \quad (12)$$

We denote the temperature along the equilibrium adiabat as equilibrium temperature T_{eq} . If the specific volume varies with time according to (4), then the variation of equilibrium temperature $T_{eq}(t)$ can be found as

$$V_0 \Psi^{3/2} = \left\{ 1 - \frac{2q}{2q - T_{eq}} \left[\frac{T_c - T_{eq}}{T_c} + 3 \frac{T_{eq}}{q} \ln \left(\frac{T_{eq}}{T_c} \right) \right] \right\} B \left(\frac{T_{eq}}{T_s} \right)^{3/2} \exp \left[\frac{q}{T_{eq}} \right]. \quad (13)$$

The variation of equilibrium degree of condensation is given by

$$x_{eq} = \frac{2q}{2q - T} \left[\frac{T_c - T}{T_c} + 3 \frac{T}{q} \ln \left(\frac{T}{T_c} \right) \right], \quad (14)$$

where $x_{eq}(t) = x_{eq}[T_{eq}(t)]$. One can see from (11) that at unrestricted vapor expansion under the conditions close to equilibrium (i.e. when the expansion proceeds rather slowly) the vapor should completely condense, $x_{eq}|_{T \rightarrow 0} \rightarrow 1$. In the case of fast expansion, complete condensation does not occur due to quenching effect.

5. KINETICS OF CONDENSATION

For the example shown in Fig. 5 the cooling rate in the beginning of the condensation process is very high, thus, vapor continues to expand some time "by inertia" along the Poisson adiabat. As a result the vapor becomes supersaturated and the nucleation starts. Later the supersaturation falls down because of the formation of critical nuclei and their further growth. The change of supersaturation is caused by the interplay between the rate of cooling (due to the work of vapor expansion) and the rate of heating (due to latent heat release).

The condensation kinetics is governed by the degree of supercooling (1). We can write now the kinetic equations assuming that for given Lagrangian coordinate all the condensed clusters (nuclei) have the same size. Let us assume that each cluster consists of $g = g(t)$ atoms. We denote $v = v(t)$ the number of condensation centers (per atom of vapor). Then the degree of condensation is given by $x(t) = v(t)g(t)$. Correspondingly, the rate of condensation can be presented as

$$\frac{dx}{dt} = g \frac{dv}{dt} + v \frac{dg}{dt}, \quad x|_{t=t_c} = 0. \quad (15)$$

The first term in (15) describes the change of condensation degree due to the formation of nuclei, while the second term describes the change of condensation degree caused by cluster growth.

The rate of nucleation according to equations (3) and (5) is given by

$$\frac{dv}{dt} = k_{v0}(1-x) \left(1-\xi^2\right)^{3/2} \Psi^{-3/2} \exp\left[-\frac{T_v-1}{T\theta^2}\right], \quad v|_{t=t_c} = 0, \quad (16)$$

where

$$k_{v0} = \frac{\rho_0}{\rho_\ell} 4 \sqrt{\frac{2\sigma}{\pi m}}. \quad (17)$$

The equation for cluster growth can be written under the assumptions that the growth of nuclei occurs in kinetically controlled regime, the accommodation coefficient is equal to unity, and the temperatures of gas and droplet are equal. This consideration yields (see [9])

$$\frac{dg}{dt} = k_g g^{2/3} \sqrt{T} (1-x) \left(1-\xi^2\right)^{3/2} \Psi^{-3/2} \left\{1 - \exp\left[-\frac{q}{T} \left(\theta - \alpha g^{-1/3}\right)\right]\right\}, \quad g|_{t=t_e} = g_0, \quad (18)$$

where α is given by (11) and

$$k_g = \frac{\pi \rho_0}{m} \left(\frac{3}{4\pi \rho_\ell} m\right)^{2/3} \sqrt{\frac{8k_B}{\pi m}}. \quad (19)$$

The initial value of g_0 and the "ejection time", t_e , should be found in self consistent way, using the criterion that cluster formation starts at the moment when supercooling reaches its maximum, and the critical nuclei are ejected at this moment. Thus, $g_0 = g(t_e) = g_{min} = (\alpha/\theta_{max})^3 \gg 1$, where g_{min} is the number of atoms within the smallest critical nuclei. Recall, that kinetic equation (2) considers g as a continuous variable, and it is applicable for macroscopic description, i.e. $g \gg 1$.

To find time t_e we used the following procedure. During the initial stage the temperature T follows very close to the Poisson adiabat $T = T_p(t)$, and one can put the supercooling $\theta_p = 1 - T_p(t)/T_{eq}(t)$. The degree of condensation is also

very small, and one can neglect x in Eq. (16). The latter assumption allows to calculate the instant of time t_e , when the supercooling reaches its maximum, $(d\theta/dt)|_{t=t_e} = 0$. This consideration yields the given above equation (11) for t_e .

It is also convenient to recalculate other initial conditions to the time instant t_e :

$$\begin{aligned} T|_{t=t_e} &= T_p(t_e), & g_0 &= g(t_e) = g_{min}, \\ v|_{t=t_e} &= v_0 = \int_{t_c}^{t_e} \frac{dv}{dt} \Big|_{T=T_p(t)} dt, & x|_{t=t_e} &= x_0 = g_0 v_0. \end{aligned} \quad (20)$$

Thus, the condensation process is described by a set of four ordinary differential equations (ODE) for four unknown functions $T(t)$, $x(t)$, $v(t)$ and $g(t)$ together with corresponding initial conditions at the point in time $t = t_e$.

6. NUMERICAL SIMULATION AND DISCUSSION

It should be noted that the "prehistory" of the system, for $t_c < t < t_e$, can not be described well by the model. Calculations show that, with initial condition $g_0 < g_{min}$ a subcritical nucleus decays, while at $g_0 > g_{min}$ it starts to grow. At the limit case $g_0 = g_{min}$ we observed an effect of the numerical instability - perturbations pushed the system either into the dissociation or condensation regions. In order to relieve these instabilities, and taking into account that kinetic equation (3) describes the production of slightly overcritical nuclei we use the following approximation: $g_0 = g_{min} + 1.5$.

Time dependence of the temperature $T(t)$, supercooling $\theta(t)$ and the degree of condensation $x(t)$ resulting from numerical solution of the set of ODE is presented in Fig. 5. Integration was performed using the "Mathematica" software package [34]. The temperature $T(t)$ (see Fig. 5a) follows initially the Poisson adiabatic, then, on the stage of nuclei formation, it approaches the equilibrium temperature T_{eq} , and finally deviate from T_{eq} due to the quenching. This behavior is typical for ZR theory [27]. Correspondingly, the supercooling (see Fig. 5b) reaches its first maximum at $t = t_e$, then it falls down, and finally increases up to the quenching time $t = t_q$. Time dependence of the degree of condensation is shown in Fig. 5c. Actual degree of condensation is lower than the equilibrium one.

One can see in Fig. 5d that the number of clusters is practically a step-like function. Such behavior is in good agreement with the assumption that clusters within the vapor are practically of the same size (for given Lagrangian coordinate). A Ge-cluster starts to grow when it contains 16 atoms (for Si-cluster $g_0 \approx 18$ [9]). The growth is terminated when the cluster contains approximately 180 atoms. The radius of a growing cluster versus time is shown in Fig. 5e.

The resulting size of growing cluster depends on the initial parameters of the plume, its mass, volume and temperature. The plots given in Fig. 6 illustrate the dependencies of the cluster size on the plume temperature and specific volume.

The calculations presented above were made for the center of the plume, $\xi = 0$. In the same way calculations can be carried out for arbitrary Lagrangian coordinate. This investigation shows that the size of clusters decreases (see in Fig. 7), while the number of clusters (per atom) increases when the Lagrangian coordinate changes from the center of plume to its edge. The degree of condensation therewith slowly decreases. To calculate the dependencies $g(\xi)$ and $v(\xi)$ near the plume edge we use a smooth extrapolation of $g(\xi)$ and $v(\xi)$ by the best fitting cubic polynomial functions.

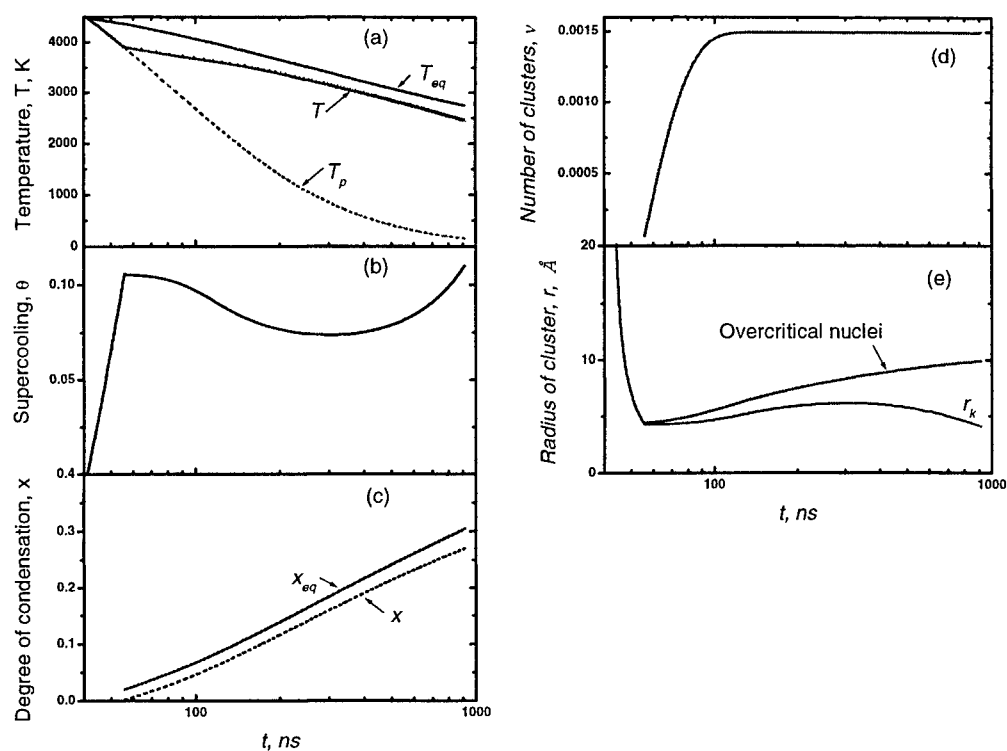


Fig. 5. Kinetics of condensation process at adiabatic Ge-vapor expansion at $\xi = 0$: (a) Temperature of the vapor, symbol T_p denotes the temperature along the Poisson adiabat, and T_{eq} is equilibrium temperature. (b) Calculated supercooling, θ . (c) Degree of condensation. x_{eq} denotes the equilibrium quantity. (d) Number of clusters $v(t)$ per atom in Ge - vapor. (e) Radius of growing cluster $r = r(t)$ versus time; r_k is the critical radius for corresponding supercooling.

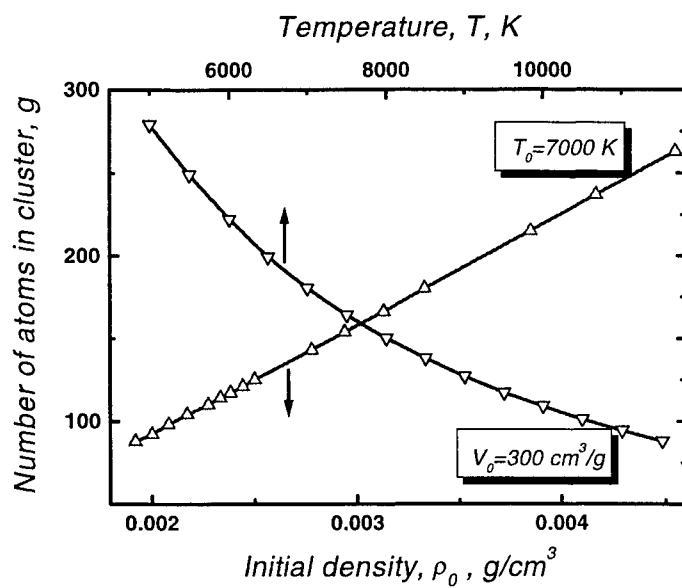


Fig. 6. Numbers of atoms within the Ge-cluster versus temperature at fixed specific volume (upper axis) and versus density at fixed temperature (bottom axis).

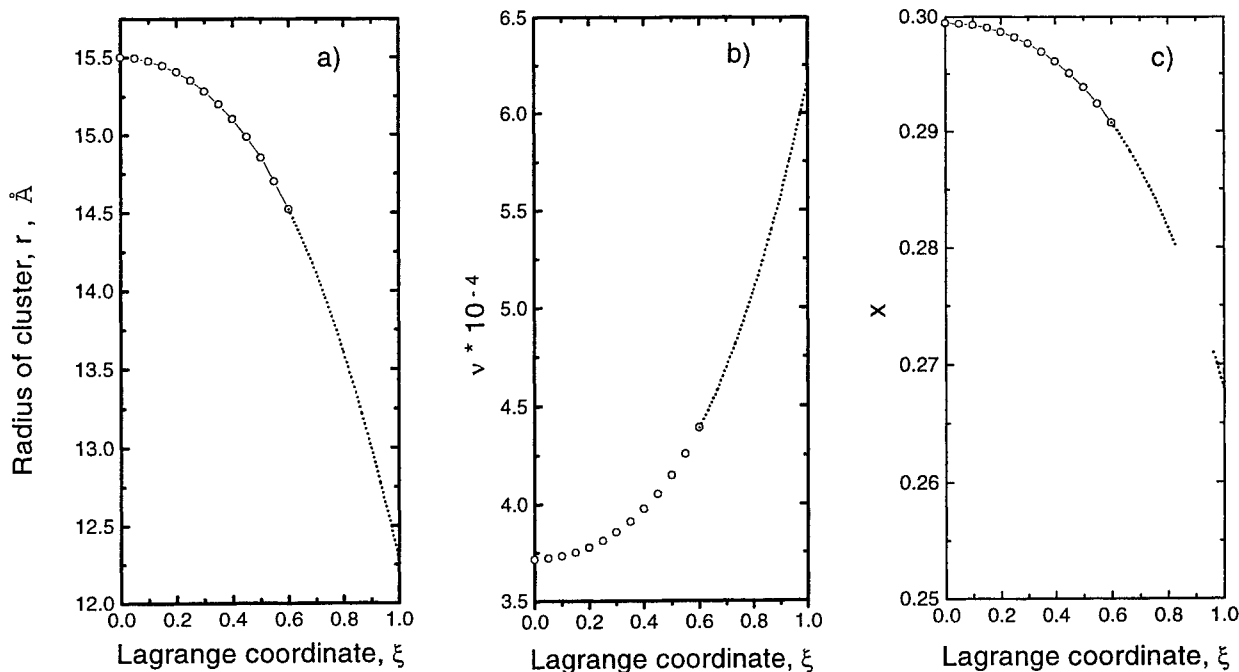


Fig. 7. The spatial distributions of clusters radius (a), number of condensation centers (b) and condensation degree (c) versus Lagrange coordinate for Si-vapor at $T = 7000$ K and $V = 300$ cm³/g. Circles show the results of integration and dotted lines are smooth extrapolations to the plume edge.

Having the dependencies $g(\xi)$ and $v(\xi)$, one can plot the cluster size distribution function $f(r)$ (see Fig. 8). The number of clusters produced within the interval $d\xi$ is given by

$$dN = 4\pi \frac{\rho_0 R_0^3}{m} (1 - \xi^2)^{3/2} v(\xi) \xi^2 d\xi, \quad (21)$$

and the variation in their size is $dr = \frac{dr}{d\xi} d\xi$. Thus, the distribution function can be defined as

$$F(r) = -\frac{dN}{dr} = \frac{32 M}{\pi m} \frac{v(\xi) \xi^2 (1 - \xi^2)^{3/2}}{dr/d\xi}. \quad (22)$$

Here $dr/d\xi < 0$, thus $F(r)$ is positive. This distribution function has the usual meaning: $F(r)dr$ represents the probability to find clusters with sizes between r and $r + dr$. The distribution function $F(r)$ is normalized to the total number of clusters produced:

$$\int_0^\infty F(r) dr = N = \frac{32 M}{\pi m} \int_0^1 (1 - \xi^2)^{3/2} v(\xi) \xi^2 d\xi. \quad (23)$$

For the "genetic plumes" whose parameters are given in Table 2 the total number of condensed clusters equals $N = 6.5 \cdot 10^{13}$ (for Ge), $4 \cdot 10^{13}$ (for Si), and $2.7 \cdot 10^{14}$ (for C). Instead of $F(r)$ one can use the normalized distribution function, $f(r) = F(r)/N$. The obtained distribution function has a specific "triangular" shape (see in Fig. 8). The typical sizes (diameters) of clusters for genetic plumes are ≈ 2 nm (Ge), 3 nm (Si), and 4 nm (C).

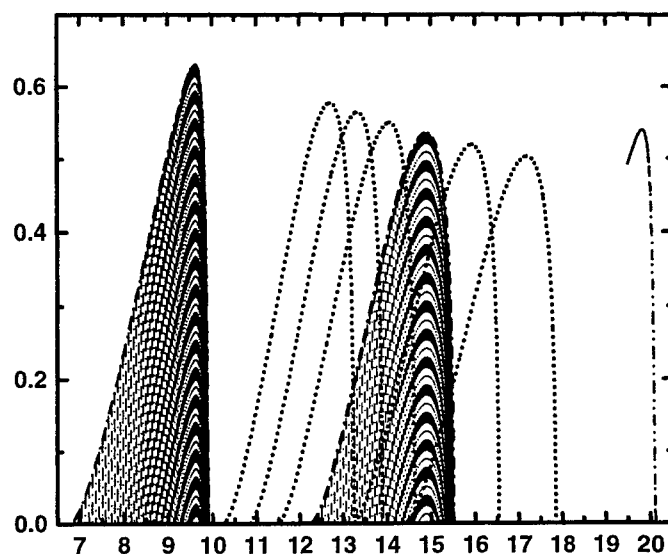


Fig. 8. The normalized distribution function for three materials: Ge (with $T_0 = 7000$ K, $V_0 = 300$ cm³/g), Si ($V_0 = 300$ cm³/g, set of plots with different T_0 - values are written near the curves), and C (with $T_0 = 8000$ K, $V_0 = 200$ cm³/g). Normalization corresponds to $\int_0^\infty f(r) dr = 1$.

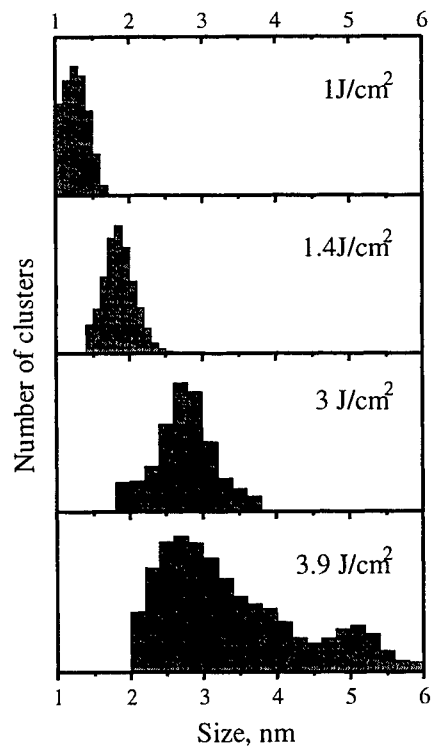


Fig. 9. Si cluster size distribution for deposits prepared at 4 Torr of He and at different laser fluence [35].

The characteristic width of the distribution functions is almost the same for all investigated materials $\Delta d_c \approx 0.6-0.8$ nm. This characteristic size of clusters and the width of the distribution function is close to that which was found experimentally (see example for Si-clusters in Fig. 9). We see, thus, that the model developed in [9] and this paper gives correct size of clusters. It is important to note that the model does not involve any adjustable parameters. We should note that the sharp distribution function found in [9] was resulted from insufficient calculation accuracy.

7. LATE STAGE OF CLUSTER FORMATION: COOLING AND CRYSTALLIZATION

At the quenching temperature clusters are typically still liquid droplets with temperature higher than the melting temperature T_m . At the same time the pronounced PL signal, appears just at sufficiently small temperatures, when all the phase and structural transitions in nanoparticles are completed [36-38]. Thus, the cluster should be cooled up to the corresponding temperatures. In vacuum this cooling (after the quenching) occurs in collisionless regime by radiation heat loss and evaporation. It takes sufficiently long time. Within the background gas clusters also initially have sufficiently big temperature [39], and they also should be cooled.

We shall discuss the cluster cooling on the basis of the energy balance equation for individual cluster

$$\frac{dE}{dt} = -P_R - P_E - P_H + P_C, \quad E = m_c c_\ell T + \sigma S, \quad T|_{t=0} = T_q, \quad (25)$$

Here E is the total cluster energy, which consists of two parts: internal thermal energy $m_c c_\ell T$ and surface energy σS ; $m_c = \rho_\ell V$ is the mass of cluster, $V = \frac{4\pi}{3} r_c^3$ and $S = 4\pi r_c^2$ are, correspondingly, volume and surface of the cluster, r_c is its radius, $c_\ell = 3R_g/\mu$ is the heat capacity of liquid, σ is surface tension. Different terms in the equation (25) present the powers of radiation cooling $-P_R$, heat losses due to evaporation $-P_E$, power of the heat exchange with background gas $-P_H$ and heat release due to crystallization $+P_C$ ($P_C = 0$ at the temperatures above the melting temperature T_m). We consider $t = 0$ as a moment of quenching, thus, T_q is the corresponding initial temperature of the cluster.

After the quenching in condensation a further evolution of cluster temperature in vacuum occurs in collisionless regime (i.e. $P_H = 0$). A similar model (without evaporation, $P_E = 0$) was discussed recently in [40] to analyze the blackbody emission from nanoclusters in silicon nanopowder.

The power of radiation heat losses is given by

$$P_R = 4\pi r_c^2 \varepsilon_R \sigma_0 (T^4 - T_\infty^4), \quad (26)$$

σ_0 is the Stefan-Boltzmann constant, $T_\infty = 300$ K, and ε_R is the total emissivity of cluster. For the small spherical clusters with radius $r_c \ll \lambda$ it can be estimated from formula (see e.g. in [8])

$$\varepsilon_R = 4.9 f \frac{r_c}{\lambda_m}, \quad f = \frac{12\varepsilon''}{(\varepsilon' + 2)^2 + \varepsilon''^2}, \quad (27)$$

where ε' , ε'' are the real and imaginary parts of the dielectric permittivity, and $\lambda_m [cm] \equiv 0.29/T [K]$ corresponds to the maximum spectral intensity of the black body radiation. The function f depends on temperature, because the corresponding values of the dielectric constant should be taken at $\lambda = \lambda_m$. We use the ε frequency dependence found for liquid Si in [41].

The dielectric permittivity depends also on the cluster size [12, 13]. If the size of the cluster is smaller than the mean free path of the electron, then the absorption of radiation occurs due to collisions of the electron with the cluster surface. Roughly speaking, the electron-phonon collision frequency, ν_{ep} , should be replaced by effective collision frequency $\nu_{eff} = \nu_{ep} + \nu_f / r_c$, where ν_f is the velocity of the electron on the Fermi surface [42].

To estimate the evaporation heat losses, we consider that atoms emitted from the surface have the Maxwellian velocity distribution. Using this assumption one can write the equations for evaporation rate and power of evaporation cooling

$$\frac{dr_c}{dt} = -v_s \frac{T_\infty}{T} \exp\left[-\frac{q}{T}\right], \quad P_E = 4\pi r_c^2 \rho_f \nu_s \frac{q R_g T_\infty}{\mu T} \exp\left[-\frac{q}{T}\right], \quad v_s = \frac{P_s}{\rho_f} \left(\frac{m}{2\pi k_B T_\infty}\right)^{1/2}. \quad (28)$$

Here we should mention that this is rather simplified macroscopic picture of the evaporation process. In reality, some collective effects in evaporation may be important for small clusters [43]. Also the dissociation energy depends on the cluster size by nonmonotonous way [44].

To estimate the power of the heat losses, P_H , due to heat exchange with the background gas we shall consider that the mean free path is greater than the cluster size. Then, one can find [40]

$$P_H = 4\pi r_c^2 \frac{m_g c_{vg} \nu_{Tg} P}{4 k_B T_g} \alpha_g (T - T_g), \quad (29)$$

where m_g is the atomic (or molecular) mass of the background gas, c_{vg} is its specific heat, $\nu_{Tg} = \sqrt{8 k_B T_g / \pi m_g}$ is the arithmetic's mean velocity within the background gas, P is the pressure and T_g is the temperature of the background gas. We consider further $T_g = T_\infty = 300 \text{ K}$. The parameter α is the "accommodation coefficient", following to [40] we put $\alpha = 1$.

The last term which we should describe within the equation (25) for the final stage of cluster formation is the power of the crystallization heat release, P_C . Taking into account that the description of the "true" crystallization for small cluster is rather rigorous [13] we applied model (25) just until $T > T_m$ and $P_C = 0$. The melting temperature, T_m , depends on the cluster size as [12]:

$$T_m = T_{m0} \left(1 - \frac{r_v}{2r_c}\right), \quad (30)$$

where T_{m0} is the melting temperature for the bulk material, r_v is parameter of material (for Si $r_v = 18.8 \text{ \AA}$ [12]).

Vaporization at the melting temperature does not play important role, thus, the duration of crystallization can be estimated from the energy balance:

$$\Delta t_m \approx m_c L_m / (P_R + P_H) \Big|_{T=T_m}, \quad (31)$$

where L_m is latent heat of fusion.

The given set of equations describes the cluster cooling either in vacuum or in the background gas.

The results of the calculations with the presented model show that pure radiation cooling in vacuum up to the melting temperature needs a long time $\approx 0.2 \text{ s}$ for 20 \AA Si cluster. Evaporation influenced evaporation process just somewhere above 2000 K. Thus, the heat exchange with the background gas plays the most important role. The necessary cooling time

consists $\approx 70\text{--}80\ \mu\text{s}$ for 10 Torr of He and $\approx 2\ \text{ms}$ for 1 Torr of the Ar. Crystallization process needs, additionally, $\approx 220\text{--}300\ \mu\text{s}$ for 10 Torr of He (depending on the cluster size) and $\approx 7\text{--}8\ \text{ms}$ for 1 Torr of the Ar.

The main error in the given estimations is related to accuracy of the formula (30). This simplified formula was obtained in [12] on the basis of Frenkel's theory of vacancies instability [16] which means the *volume melting* effect. Meanwhile the application of this formula for $T_m/T_{m0} < 0.8\text{--}0.9$ is rather questionable. When the size of cluster will be smaller than some critical one would expect the change in the melting mechanism, where instead of Frenkel's vacancies the Shottky vacancies play the dominant role. In reality, the situation is even more complex, because the collective effects play an important role for small clusters [13].

Finally we should mention problems related to detection of small clusters by the Rayleigh scattering. One can consider that detection threshold corresponds to condition, when the cluster produces at least one scattered photon. At the same time, ratio of absorbed and scattered photons changes in favor of absorption, which can be seen easily from the simplified Lorentz formulae for the cross-section of scattering, σ_s , and absorption, σ_a (more careful estimation can be done with help of the Mie theory)

$$\sigma_s = \frac{8}{3} \left(\frac{\omega r_c}{c} \right)^4 \left| \frac{\varepsilon - 1}{\varepsilon + 2} \right|^2 \pi r_c^2, \quad \sigma_a = 4 \left(\frac{\omega r_c}{c} \right) \text{Im} \left[\frac{\varepsilon - 1}{\varepsilon + 2} \right] \pi r_c^2. \quad (32)$$

Cluster will be completely destroyed if the absorbed energy will be sufficient for its total vaporization. From the energy balance one can write $mL_{eff} = \Phi\sigma_a$, $L_{eff} = c(T_b - T) + L_m + L_v$, where L_{eff} is the total effective enthalpy, which includes the enthalpy of melting, L_m , and vaporization, L_v . The simplified consideration yields the critical size of the cluster which can be detected by Rayleigh scattering.

$$r_c = \left[\frac{9}{8\pi} \frac{\hbar\omega}{\rho L_{eff}} \left(\frac{c}{\omega} \right)^3 \text{Im} \left[\frac{\varepsilon - 1}{\varepsilon + 2} \right] \left| \frac{\varepsilon - 1}{\varepsilon + 2} \right|^2 \right]^{1/6}. \quad (33)$$

It shows that RS signal appears just for sufficiently big clusters.

8. CONCLUSION

In this paper we discussed the peculiarities of fast condensation of vapor and nanoclusters formation on the basis of the Zeldovich-Raizer theory. The calculations were made for Si, Ge, and C vapor plumes produced at typical conditions of excimer ns-laser ablation.

At the parameters used in calculations, a cluster starts to grow when it contains 16 (Ge), 18 (Si), and 20 (C) atoms (within the critical nucleus); the growth is terminated when the cluster contains a few hundred atoms which corresponds to cluster diameters $\approx 20(\text{Ge})$, $30(\text{Si})$, and $40(\text{C})\ \text{\AA}$. The significant stage of the cluster growth occurs near the critical radius, thus, the effects related to nuclei curvature are very important. The size distribution function of clusters demonstrates a typical "triangular" shape with basis $\Delta r_c \approx 0.3 r_{c\text{ max}}$. The size of cluster and the width of distribution function are close to experimentally observed.

The time necessary for the cluster cooling and crystallisation is, typically, long compare to characteristic time of cluster formation.

Acknowledgments:

We wish to thank D. Geohegan and A. Poretzky for valuable discussions and R. Wood and G. E. Jellison Jr. for their assistance with optical constants for liquid Si. We thank the Russian Basic Research Foundation for financial support (grants 98-02-16104 and 97-02-16044).

REFERENCES

1. W. Marine, I. Movtchan, A.V. Simakine, L. Patrone, R. Dreyfus, M. Sentis, M. Autric and N. Merk, "Pulsed Laser Deposition of Si Nanocluster Films", *MRS Symposium Proceedings*, v. **397**, pp. 365-374, ed. by R. Singh, D. Norton, L. Laude, J. Narayan and J. Cheung, (Pittsburgh 1996).
2. I. A. Movtchan, W. Marine, R. W. Dreyfus, H. C. Le, M. Sentis, M. Autric, "Optical Spectroscopy Of Emission From Si-SiO₂ Nanoclusters Formed by Laser Ablation", *Appl. Surf. Sci.* **96-98**, pp. 251-260 (1996)
3. Y. Yamada, T. Orii, I. Umezu, S. Takeyama, T. Yoshida, "Optical Properties Of Silicon Nanocrystallites Prepared by Excimer-Laser Ablation in Inert Gas", *Jpn. J. Appl. Phys.* **35**, Part 1, pp. 1361-1365 (1996)
4. T. Makimura, Y. Kunii, K. Murakami, "Light Emission from Nanometer-sized Silicon Particles, Fabricated by the Laser-ablation Method", *Jpn. J. Appl. Phys.* **35**, Part 1, pp. 4780-4784 (1996)
5. S. Li, S. J. Silvers, M. S. El-Shall, "Surface Oxidation and Luminescence Properties of Weblike Agglomeration of Silicon Nanocrystals Produced by a Laser Vaporization -Controlled Condensation Technique", *J. Phys. Chem. B*, **101**, pp. 1794-1802 (1996)
6. H. Haberland (Ed), "Clusters of Atoms and Molecules", Springer Series in Chemical Physics, vol. **52**, (Springer Verlag, Berlin Heidelberg 1994).
7. P. Melinon, V. Paillard, V. Dupuis, A. Perez, P. Jensen, A. Hoareau, J. P. Perez, J. Tuillon, M. Broyer, J. L. Vialle, M. Pellarin, B. Baguenard, J. Lerme, "From free clusters to cluster-assembled materials", *Int. Journal of Modern Physics B* **9**, pp. 339 - 397 (1995).
8. B. M. Smirnov, "Processes in Expanding and Condensing Gases", *Uspekhi Fiz. Nauk*, **164**, pp. 665-703 (1994).
9. B. Luk'yanchuk, W. Marine, S. Anisimov, "Condensation of Vapor and Nanoclusters Formation within the Vapor Plume, Produced by ns-Laser Ablation of Si", *Laser Physics* **8**, No.1, pp. 291-302 (1998)
10. D. B. Geohegan, A. A. Poretzky, G. Duscher, S. J. Pennycook, "Time-Resolved Imaging of Gas Phase Nanoparticle Synthesis by Laser Ablation", *Appl. Phys. Letts.* **72**, pp. 2987-2990 (1998); "Photoluminescence from Gas-Suspended SiO_x Nanoparticles Synthesized by Laser Ablation", **73**, pp. 371-375 (1998)
11. W. Marine, B. Luk'yanchuk, M. Sentis, "Silicon nanocluster synthesis by conventional laser ablation", *SFV Le Vide*, **287**, (in press - November, 1998); B. Luk'yanchuk, W. Marine, "On the delay time in photoluminescence of Si-nanoclusters, produced by laser ablation " (to be published)
12. M. Wautelet, "Estimation of the variation of the melting temperature with the size of small particles, on the basis of a surface-phonon instability model", *J. Phys. D: Appl. Phys.* **24**, pp. 343-346 (1991)
13. B. M. Smirnov, "Melting of Clusters with a Pair Interaction of Atoms", *Uspekhi Fiz. Nauk*, **164**, 1165 (1994)
14. E. A. Manykin, P. P. Poluektov, Yu. G. Rubeznyi, "Theory of radiation absorption by small particles", *JETP*, **70**, pp. 2117-2125 (1976)
15. E. M. Lifshitz, L. P. Pitaevsky, "Physical Kinetics", (Pergamon, Oxford 1984).
16. Ya. I. Frenkel, "Kinetic Theory of Liquid", (Dover, New York, 1955)
17. J. D. Gunton, M. San Miguel, P. S. Sahni, "The Dynamics of First-order Phase Transitions". In: "*Phase Transitions and Critical Phenomena*", Ed. by C. Domb and J. L. Lebowitz, pp. 267-466, (Academic Press, London, New York, 1983)
18. A. G. Bashkurov, "Nonequilibrium Statistical Mechanics of Heterogeneous Fluid Systems", (CRC Press, Boca Raton London Tokyo 1995)
19. von R. Becker, W. Döring, "Kinetische Behandlung der Keimbildung in übersättigten Dämpfen", *Annalen der Physik*, **24**, pp. 719-752, (1935)
20. H. A. Kramers, "Brownian Motion in a Field of Force and the Diffusion Model of Chemical reactions", *Physica*, **7**, pp. 284-304 (1940)
21. Ya. B. Zeldovich, "Theory of new-phase formation. Cavitation", *JETP*, **12**, pp. 525-538 (1942)
22. I. M. Lifshitz, V. V. Slyozov, "On the kinetics of diffusional decay of supersaturated solid solutions", *JETP*, **35**, pp. 478-492 (1958)
23. P. W. Voorhees, "The Theory of Ostwald Ripening", *J. Stat. Phys.*, **38**, pp. 231-252 (1985)
24. M. Tokuyama, Y. Enomoto, "Dynamics of crossover phenomenon in phase-separating systems", *Phys. Rev. Lett.* **69**, pp. 312-315 (1992)

25. W. Phlügl, U. M. Titulaer, "The size distribution of liquid droplets during their growth from a vapor", *Physica A* **198**, pp. 410-422 (1993)
26. Yu. P. Raizer, "Condensation of a Cloud of Vaporized Matter Expanding in Vacuum", *Sov. Phys. JETP*, **37**, pp. 1229-1235 (1960).
27. Ya. B. Zeldovich, Yu. P. Raizer, "Physics of Shock Waves and High - Temperature Hydrodynamic Phenomena", (Academic Press, New York, 1966).
28. G. Callies, H. Schittenhelm, P. Berger, H. Hüdel, "Modeling of the expansion of laser evaporated matter in argon, helium and nitrogen and condensation of clusters", *Appl. Surf. Sci.* **127-129**, pp. 134-141 (1998)
29. M. Sharaf, R. A. Dobbins, "A Comparison of Measured Nucleation Rates with the Predictions of Several Theories of Homogeneous Nucleation", *J. Chem. Phys.* **77**, pp. 1517-1526 (1982)
30. S. Anisimov, D. Bäuerle, B. Luk'yanchuk, "Gas Dynamics and Film Profiles in Pulsed-Laser Deposition of Materials", *Phys. Rev. B* **48**, pp. 12076-12081 (1993)
31. B. Luk'yanchuk, A. Luches, A. Blanco, V. Orofino, "On the size distribution function of carbon nanoclusters, produced by ns-laser ablation" (to be published)
32. D. E. Gray (Ed), "American Institute of Physics Handbook", 3rd ed., (McGraw-Hill, New York, 1972)
33. I. S. Grigoryev, E. Z. Meilikhov (Eds), "Handbook of Physical Quantities", (Moscow, Energoatomizdat, 1991, in Russian)
34. S. Wolfram, "Mathematica", Second Edition, (Addison-Wesley Publishing Company, Inc., 1991)
35. L. Patrone, D. Nelson, V. I. Safarov, M. Sentis, W. Marine, "Photoluminescence of Silicon Nanoclusters with Reduced Size Dispersion Produced by Laser Ablation", *Journ. of Luminescence* (1998) , (to be published)
36. M. Rosenbauer, S. Finkbeiner, E. Bustarret, J. Weber, M. Stutzmann, "Resonantly excited photo-luminescence spectra of porous silicon", *Phys. Rev. B* **51**, pp.10539-10547 (1995)
37. Y. Kamenitsu, "Slow decay dynamics of visible luminescence in porous silicon: Hopping of carriers confined on a shell region in nanometer-size Si crystallites", *Phys. Rev. B* **51**, pp.10539-10547 (1995)
38. I. Umezu, K. Shibata, S. Yamaguchi, A. Sugimura, Y. Yamada, T. Yoshida, "Effects of thermal processes on photoluminescence of silicon nanocrystallites prepared by pulsed laser ablation", *J. Appl. Phys.* **84**, pp. 6448-6450 (1998)
39. H. C. Le, R. W. Dreyfus, W. Marine, M. Sentis, I. A. Movtchan, "Temperature measurements during laser ablation of Si into He, Ar and O₂", *Appl. Surf. Sci.*, **96-98**, pp.164-169 (1995)
40. J. Costa, P. Roura, J. R. Morante, E. Bertran, "Blackbody emission under laser excitation of silicon nanopowder produced by plasma-enhanced chemical-vapor deposition", *J. Appl. Phys.* **83**, pp. 7879-7885 (1998)
41. G. E. Jellison, Jr., D. H. Lowndes, "Measurements of the optical properties of liquid silicon and germanium using nanosecond time-resolved ellipsometry", *Appl. Phys. Lett.*, **52**, pp. 352-354 (1987)
42. U. Kreibig, M. Quinten, "Electromagnetic Excitation of Large Clusters", In Ref. [6], pp. 321-359
43. D. I. Zhukhovitski, "On the phonon-mechanism of the cluster evaporation", *JETP*, **109**, pp. 839-851 (1996)
44. A. A. Shvartsburg, M. E. Jarrold, B. Liu, Z.-Y. Liu, C.-Z. Wang, K.-M. Ho, "Dissociation Energies of Silicon Clusters: A Depth Gauge for the Global Minimum of the Potential Energy Surface", *Phys. Rev. Lett.*, **81**, pp. 4616-4619 (1998)

Pulsed Laser Deposition of Nanocomposite Thin Films for Photonic Applications

C.N.Afonso^{*a}, J. Solis^a, R.Serna,^a J. Gonzalo^a, J.M.Ballesteros^a and J.C.G. de Sande^b

^aInstituto de Optica, CSIC, Serrano 121, 28006 Madrid, Spain

^bDepartamento de Ingenieria de Circuitos y Sistemas, E.U.I.T.Telecomunicación, UPM, Ctra.de Valencia km7.5, 28031 Madrid, Spain

ABSTRACT

Nanocomposite thin films formed by metal or semiconductor nanocrystals (NCs) embedded in a host exhibit interesting nonlinear optical properties related to the small size of the NCs (typically around 10 nm or below). These properties make these materials potential candidates for the development of all-optical switching devices. The challenge is to produce nanocomposite materials with controlled and suitable characteristics. The present work aims to show that nanocomposite materials produced by pulsed laser deposition (PLD) might have superior structural and non-linear optical properties than those obtained by other techniques. This result will be illustrated in systems formed by metallic NCs (Bi, Cu) embedded in an Al₂O₃ host. Fundamental aspects related to the nucleation and growth mechanisms or the reactivity of the NCs with the host will be discussed. Finally, the excellent nonlinear properties of the PLD synthesized composites will be illustrated in the case of Cu:Al₂O₃ films, in which the dependence of the nonlinear third order optical susceptibility ($\chi^{(3)}$) has been investigated as a function of the NCs size and $\chi^{(3)}$ values as large as 10⁻⁷ esu have been achieved.

Keywords: Pulsed Laser Deposition, Nanocomposites, Metal Nanocrystals, Thin films, Non-linear optics, Third Order Susceptibility.

1. INTRODUCTION

Nanocomposites formed by metallic or semiconductor nanocrystals (NCs) embedded in dielectric hosts show special optical properties. The most striking and easy to observe is the change in coloration undergone by glasses when metal NCs are embedded in them, a property which has been used for centuries to produce artistic objects. More recently the linear optical properties of NCs embedded in glasses have been used for the development of a wide variety of optical filters or sun glasses. These characteristic properties are the result of collective resonances that can qualitatively be understood in the classical frame of the Mie theory.^{1,2}

The study of nanocomposite systems formed by NCs embedded in a host has become lately an active field of research in optics because they exhibit nonlinear optical properties with fast response in the ps time scale, in addition to the well known characteristic linear optical properties. Their nonlinear optical response is determined by dielectric and quantum confinements which are a result of the small dimensions of the NCs compared to both the wavelength of light and the mean free-path of electrons in the bulk material.³ One of the manifestations of the third order nonlinear optical susceptibilities ($\chi^{(3)}$) of these nanocomposites is the optical Kerr effect, which describes the dependence of the refractive index on the intensity of the light propagating in the medium. This effect is the physical basis for the development of all optical switching devices. Figure 1 shows the characteristic values of $\chi^{(3)}$ for several dielectric materials as a function of the wavelength. This figure is an update of the table reported earlier elsewhere⁴ together with the addition of new data for transition metal oxides^{5,6} semiconductor⁷ and metal⁸ NCs embedded in dielectric hosts. Oxide glasses show a moderate value of the third order susceptibility, at least one order of magnitude larger than that reported for fluoride glasses. The oxide glasses are the basic material for optical fibers and since they present extremely low losses, it is possible to use large lengths for switching, and thus their moderate $\chi^{(3)}$ values (10⁻¹³-10⁻¹⁵ esu) might be sufficient. In fact, silica fibres are still

* Correspondance: Email: cnafonso@fresno.csic.es; Telephone: 34 91 590 1617; Fax: 34 91 564 5557

a material of choice for optical switching. The development of integrated devices in waveguide configuration involve much shorter switching lengths and thus the requirement for low losses is less demanding but much larger values of $\chi^{(3)}$ are needed. Chalcogenide glasses show larger values, in the 10^{-12} esu range, that are further improved in the case of transition metal oxides (from 10^{-12} esu to 10^{-10} esu). The larger values reported correspond to nanocomposite systems in which metal and semiconductor NCs are embedded in a dielectric host. Among them, the largest one has been reported for metal NCs systems (10^{-6} esu) over a wide wavelength range in the visible.⁸ It is worthwhile noting in Fig.1 that there are, to our knowledge, no data reported in the wavelength range of interest for optical communications (1.2 μm to 1.6 μm).

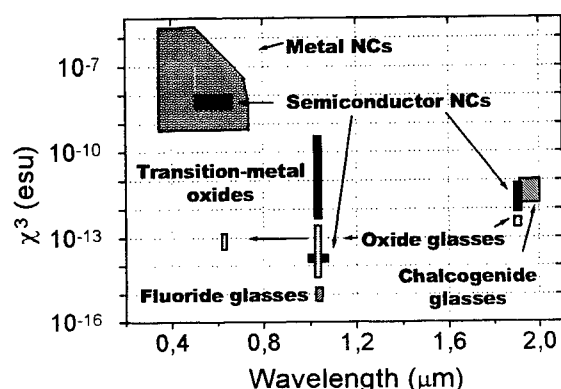


Figure 1. Values reported in the literature for the third order non-linear optical susceptibility χ^3 of several material as a function of the wavelength for which these values have been reported. See text for references. Metal NCs and semiconductor NCs hold for nanocomposite materials formed by nanocrystals embedded in a dielectric host.

The analysis of Fig.1 evidences that nanocomposite materials formed by NCs embedded in a dielectric host are the materials with the larger $\chi^{(3)}$ values. These materials have thus high potential for the development of waveguide all-optical switches, provided that their nonlinear response can be extended into the near IR region, with similar efficiencies to those in the visible, and that the losses are kept low enough at the wavelength of interest. The study of such systems was initiated in the 70's when most of the work was related to the study of the optical properties of NCs immersed in colloidal suspensions or embedded in glass bulk systems.³ Since then, a strong experimental effort has been done in the development of suitable methods for the production of these materials in the form of waveguides. Ion-implantation,^{9,10,11,12} sputtering,^{13,14} and sol-gel,^{15, 16, 17} are among the most commonly used techniques. In all cases, one of the key issues is the control of the size, shape and size distribution of the NCs. Pulsed Laser Deposition (PLD) has been shown to be excellent to produce complex oxide materials such as those typically required to host the NCs.¹⁸ It has, in addition, a high potential for the growth of artificially structured materials due to its flexibility. One of its advantages is that deposition can be done either in vacuum or in a wide range of gas pressures. The first report on the production of NCs embedded in a dielectric host by PLD was, to our knowledge, the production of CdTe NCs in a SiO_2 host.¹⁹ In this case, the films were grown by alternate ablation of the semiconductor and host targets under Ar and O atmospheres respectively. Since then, the works reporting on the production of NCs by PLD took advantage of the possibility of using a background gas pressure, and they showed how the size of Si NCs could be varied by controlling the ambient gas pressure.^{20,21,22}

This work aims to show that PLD is an attractive alternative route to produce nanocomposite materials formed by metal NCs embedded in a host. This technique allows the production of materials with excellent structural and optical (linear and nonlinear) properties, that are in many cases superior to those produced by other techniques. The materials are produced by alternate ablation of the host and the metal targets and the unique feature of this work compared, to the earlier ones reporting the production of nanocrystalline materials by PLD, is the fact that the materials are produced by ablation in *vacuum*. The results here presented correspond to systems formed by Bi and Cu NCs embedded in an amorphous dielectric (Al_2O_3) host. Some results obtained in a system formed by a non-oxide host such as amorphous semiconductor Ge (a-Ge) will also be described in order to discuss the interactions of the metal NCs with an oxide host. The structural properties of the nanocomposite films will be discussed and related to their optical properties, both linear and non-linear. Finally, an updated survey of some of the most promising results reported so far on the nonlinear optical susceptibility of nanocomposites formed by metal NCs embedded in dielectric hosts is provided and discussed.

2. EXPERIMENTAL

Nanocomposite films were produced in vacuum ($<10^{-7}$ Torr) by pulsed laser deposition (PLD), using a system consisting of an ArF laser (193 nm, 12 ns or 20 ns) operating at 5-10 Hz. The UV laser beam was focused alternately on the host target (Al_2O_3 or Ge) and on the metallic target (Bi or Cu) leading to an energy density high enough to ablate the metal ($\approx 2\text{J}/\text{cm}^2$).^{23,24} The targets were set on a computer controlled multi-target holder which allowed both to rotate continuously the targets and to expose independently each one to the laser beam. The substrate was located at 32 mm from the target surface and held at room temperature. The number of pulses on the metallic target was used to control the size of the NCs and it was carefully selected in order to produce metal NCs of sizes of a few nanometers. The number of pulses on the host target was chosen to obtain an in-depth separation between NCs layers from 5 nm to 20 nm. The alternate deposition of the pair of metal NCs and host layers was repeated several times (1 to 10) and a host layer was always deposited at the end of the process in order to protect the metal NCs from reaction with the atmosphere. In order to apply different post-deposition characterization techniques, the films were grown on Si, fused silica, glass and carbon-coated mica substrates. A HeNe laser beam, focused on the substrate at 45° off the normal, was used to follow the evolution of the film reflectivity during growth, which allowed the *in situ* control of the film thickness and deposition rate.²⁵

High resolution transmission electron microscopy (HRTEM) analysis has been used to determine the structural characteristics of the nanocomposite films, mainly the NCs size and size distribution. Whereas the HRTEM images of the NCs show clear lattice fringes indicating their crystalline structure, both the Ge and Al_2O_3 hosts were found to be amorphous.^{23,24} The metal content in the films and its in-depth distribution has been determined by Rutherford Backscattering Spectrometry (RBS).²⁴ The linear optical properties of the films have been determined by absorption and spectroscopic ellipsometry measurements. The ellipsometric parameters, $\tan \psi$ and $\cos \delta$, have been measured by means of a SOPRA spectroscopic rotating polarizer ellipsometer in the 300-800 nm wavelength range, using steps of 10 nm. The Bruggeman effective medium model for three dimensional isotropic systems combined with a standard regression method were used to simulate the measured ellipsometric parameters of the nanocomposite films.²⁶ The nonlinear response has been measured by Z-scan spectroscopy at 590 nm with 30 ps pulses at a repetition rate of 400 kHz. This low repetition rate has been used in order to minimize the thermal contribution to the nonlinear response. The beam was focused by a 150 mm lens, leading to a measured beam waist of 30 μm .²⁷ The resulting data have been analysed in the frame of a model based on a thin lens approximation. This model allows to separate the electronic and thermal contributions to the measured non-linear response, whenever the latter is low enough. This is important because the fast ps nonlinear response comes from the electronic contribution, and this is the one that should be optimized to develop all-optical switching devices.

3. RESULTS AND DISCUSSION

Figure 2 shows HRTEM images of $\text{Cu}:\text{Al}_2\text{O}_3$ films prepared by PLD. In this case the analysed films correspond to trilayer films grown following the sequence $\text{Al}_2\text{O}_3/\text{Cu}/\text{Al}_2\text{O}_3$ and using 160 (Fig.2a) and 240 pulses (Fig.2b) on the metal target. The resulting films have a single metal NCs layer and thus there is no overlapping of images from crystals lying in different layers making it easier the analysis of the shape and size distribution. The images show dark areas with lattice fringes which are the Cu NCs surrounded by an homogeneous amorphous background which is the embedding Al_2O_3 host. The histograms of the NCs size distribution obtained from the HRTEM images included in Fig.2a and 2b are shown in Figs.3a and 3b respectively and clearly show that the average diameter of the NCs increases from 3.0 ± 0.6 nm to 5 ± 1 nm as the number of pulses in the Cu target is increased from 160 to 240 pulses. The NCs size distributions are very sharp, specially for the films having the smaller NCs (Fig. 3a), and it is narrower than those reported for NCs of similar dimensions (≈ 3 nm) produced by other techniques such as sol-gel, or ion-implantation.^{15,28,29} In addition, the images in Fig. 2 show that the NCs are uniformly distributed over the film but their average separation (center to center) also increases (from 6 nm to 7.5 nm) when the number of pulses in the Cu target is increased.³⁰

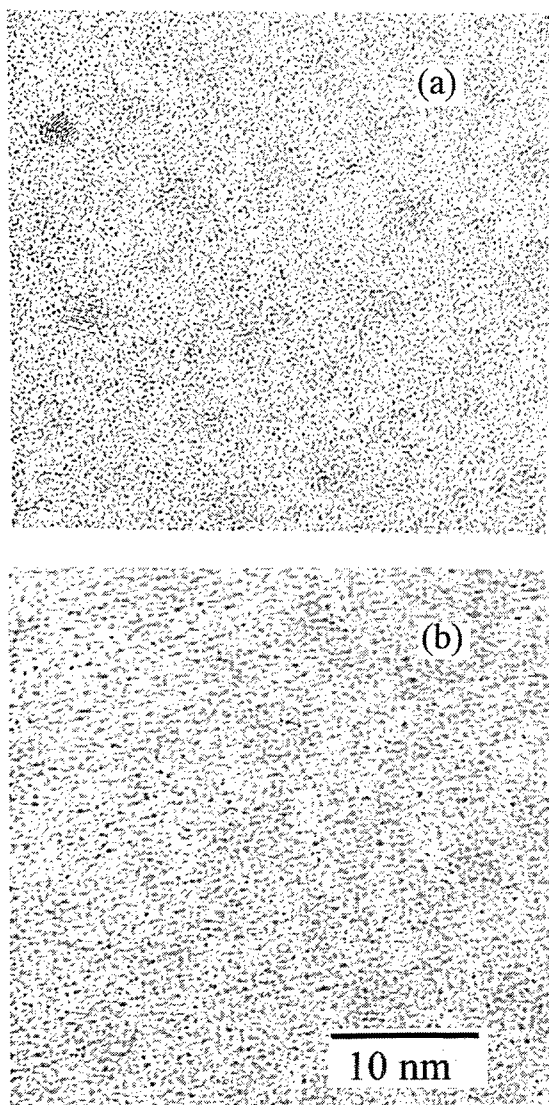


Figure 2. HRTEM images of Cu:Al₂O₃ trilayer films grown by alternate PLD and using (a) 160 and (b) 240 pulses in the Cu target

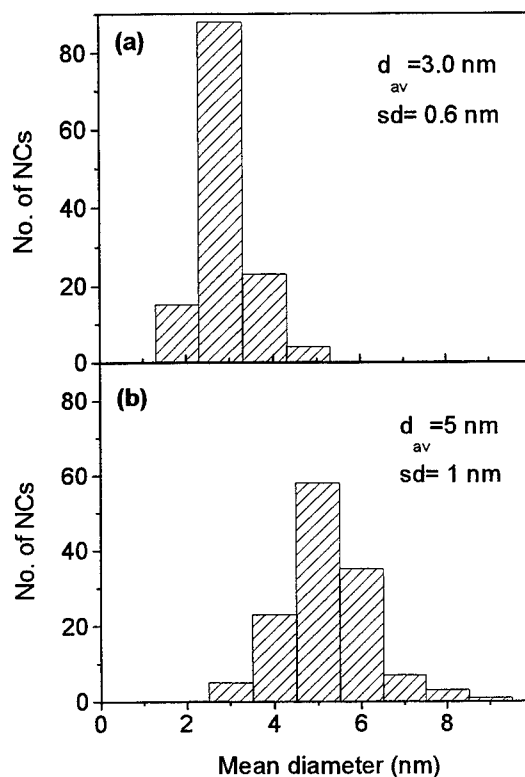


Figure 3. Histogram of the average diameter of the NCs seen in Figs. 2a and 2 b, respectively. d_{av} stands for mean diameter and sd for standard deviation

The image in Fig. 2a shows clearly that the NCs have an in-plane circular shape, this being confirmed by measuring the dimensions of the NCs along two orthogonal directions. The NCs in Fig. 2b have more irregular in-plane shapes with a broader size distribution as it can be seen in the corresponding histogram (Fig. 3b). These results can be interpreted in terms of the nucleation of the NCs at the substrate, followed by their growth and coalescence. The image in Fig. 2a would represent the earlier stages of formation, in which crystalline nuclei have been developed and grown moderately, all the NCs having similar sizes and shapes. At a later stage, the NCs would grow by addition of the new atoms arriving at the surface followed by the coalescence of the NCs which are closer to each other. This process is strongly favored by the conditions in which PLD takes place, since it has been demonstrated that it involves species arriving at the substrate with kinetic energies as high as 150 eV,¹⁸ thus facilitating the mobility of the atoms reaching the substrate and promoting the growth of crystals from pre-existent nuclei.

Spectroscopic ellipsometry measurements are a very powerful non-invasive technique to determine the composition of thin films when combined with effective medium modeling. This technique has been successfully applied to the determination of the stoichiometry of oxide thin films such as SbO_x ³¹ and GeO_x .³² Nevertheless, the potential of spectroscopic ellipsometry to the analysis of nanocomposite thin films has been rarely explored. We have first applied this procedure to a system formed by Bi NCs embedded in an a-Ge host.²⁶ Bi and Ge form an eutectic system with low mutual solubility, even in the liquid phase,³³ and no metastable alloys have been reported. The low mutual solubility of both elements ensures that the Bi will tend to form pure isolated crystals protected against atmospheric oxidation by the Ge matrix. The Bi:Ge films were grown on Si substrates alternating different number of pulses on the Bi target, while keeping a constant number of pulses on the Ge target. The procedure was repeated five times to lead to films with total thicknesses in the range 21 nm to 26 nm. This procedure allowed to obtain films with Bi NCs with diameters ranging from 2.3 ± 0.8 nm to 23 ± 5 nm.²⁴ The optical constants of the films (n and k) were determined from the ellipsometric parameters, assuming an absorbing film on a crystalline Si substrate. The results show that the optical constants continuously evolve from those of pure a-Ge to those of Bi as the number of pulses on Bi, and thus the Bi content in the film and the NCs size, increases. The Bruggeman effective medium model³⁴ was used to simulate the measured ellipsometric parameters, by assuming a three-dimensional isotropic system formed by a-Ge and Bi with the optical parameters (n and k values) reported earlier for PLD films of the pure elements.³⁵ The effective medium model provides the volume fraction of Bi in a-Ge and the film thickness through the use of a standard regression method. Excellent fits of the experimental data were obtained following this procedure. The composition of the films in at.% was then calculated from the Bi volume fraction assuming the density of the bulk materials (2.8×10^{22} at/cm³ for Bi and 4.4×10^{22} at/cm³ for Ge). Figure 4 shows the atomic fraction of Bi determined both from the spectroscopic ellipsometry and RBS measurements as a function of the average size of the NCs. It is clearly seen that the compositions determined by both methods are in excellent agreement.

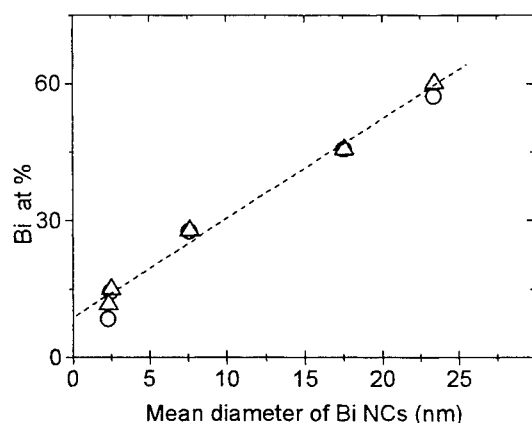


Figure 4. Bi at. % of Bi:Ge films prepared by PLD as a function of the mean diameter of the Bi NCs obtained both from the RBS measurements (O) and from the spectroscopic ellipsometry analysis (Δ).

The same approach was used to determine the Bi content in the case of such NCs embedded in an oxide host, Al_2O_3 . The Bi: Al_2O_3 nanocomposite films were prepared by alternating a number of pulses on the Bi and Al_2O_3 targets and repeating the procedure 10 times, leading to a film with total thickness of ≈ 225 nm and NCs with mean diameter smaller than ≈ 1.5 nm.²⁶ The real part of the refractive index (n) of the composite as a function of the wavelength shows the same behaviour than that of the Al_2O_3 host, the only difference being the slightly larger n value of the nanocomposite film. In contrast, the imaginary part of the refractive index (k) of the nanocomposite behaves quite differently to that of the pure Al_2O_3 film. Whereas the linear absorption is found to be negligible ($k < 1 \times 10^{-3}$) in the whole studied wavelength range for the latter, the result obtained for the Bi: Al_2O_3 nanocomposite film is shown in Fig. 5a. An increase of the overall absorption of the film related to the inclusion of the Bi NCs is observed. A first approach to understand the structure of the k spectrum is its analysis in the frame of the theory of Mie for the diffraction of a conducting sphere in a dielectric, using the electric dipole

approximation.^{1,2} According to this theory, the k value should exhibit an enhancement where the condition $\epsilon_1 + 2n_d^2 = 0$ is satisfied, ϵ_1 being the real part of the dielectric constant of the metal and n_d the real part of the refractive index of the dielectric. The wavelength at which this condition is achieved is known as the surface plasmon resonance of the metal nanocomposite. In our case, this occurs at a wavelength between 370 and 380 nm which is in agreement with the peak structure observed in Fig. 5a for this wavelength range. As described before for the case of the a-Ge host, the Bruggeman effective medium modeling was used to simulate the ellipsometric parameters and to determine the amount of metal embedded in the Al_2O_3 host. The best fit is obtained assuming a mixture of Al_2O_3 with 0.45 % Bi in volume, which leads to 0.14 Bi at.% when taking into account the density of amorphous Al_2O_3 . Figure 5a also includes the calculated k values for such a mixture which reasonably agrees with the experimental data since it shows a maximum at around 360 nm and the absolute k values are similar to the experimental ones. The atomic fraction of Bi atoms was also determined by RBS measurements and the metal content was found to be 0.5 at.%. Even when the absolute differences might seem small, taking into account the uncertainties in the element densities, it should be noted that unrealistically large values of k are obtained using the Bruggeman model for a mixture containing 0.5 at.% Bi. It becomes clear that the analysis of the spectroscopic ellipsometry data underestimate the Bi content in the Bi: Al_2O_3 films, as opposed to the excellent agreement obtained for the Bi:Ge films. This result suggests that part of the Bi is not in metallic form and has most likely undergone some chemical reaction with the matrix.

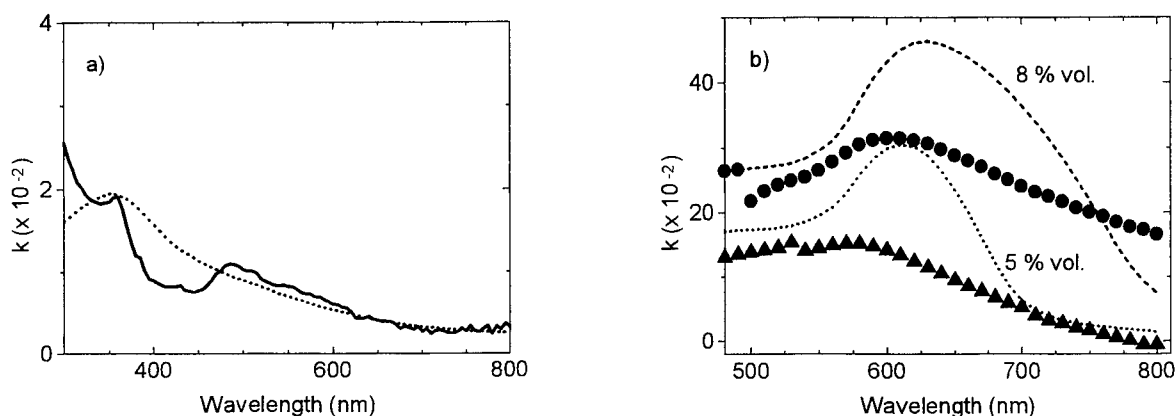


Figure 5. Imaginary part of the refractive index k of (a) Bi: Al_2O_3 films and (b) Cu: Al_2O_3 films as a function of wavelength. The full line in (a) and (▲,●) are the experimental values obtained from spectroscopic ellipsometry and the dashed lines are the curves calculated using the Bruggeman effective medium model with metal contents of (a) 0.14 at.% of Bi and (b) 5 at.% and 8 at.% of Cu. Experimental results for Cu: Al_2O_3 films having metal NCs with average diameters of (▲) 3.0 ± 0.6 and (●) 5 ± 1 nm are both shown.

To analyse further the discrepancies between the absolute determination of the metal content by RBS and by optical measurements in the case of the Al_2O_3 host, the analysis of the absorption of the same host containing a different kind of metal NCs is shown in Fig. 5b. The results correspond to two Cu: Al_2O_3 films prepared by using different number of pulses on the Cu target and thus containing NCs of 3.0 ± 0.6 and 5 ± 1 nm mean diameters each. The size distribution of the NCs in these films corresponds to those shown in Fig. 3. For these films, the surface plasmon resonance condition is achieved at 590 ± 5 nm, in agreement with the experimental results. The RBS measurements provide an atomic Cu content of 7.6 at % and 9.8 at %, respectively and simulations with the Bruggeman model were performed for volume fractions of 5% and 8% (5.4 and 9.3 at.%), the results being also included in Fig. 5b. The comparison of the simulated and experimental values clearly shows that also in the case of Cu: Al_2O_3 films, the metal content is underestimated when determined from optical measurements. Since the agreement for Bi:Ge films is nevertheless excellent as shown in Fig. 4, it has been suggested that

the different reactivity of the semiconductor Ge and the oxide Al_2O_3 hosts with the metal NCs could be responsible of such behavior.²⁶ When embedded in an oxide host, the metal NCs surface could be oxidized or at least covered by a shell of oxygen atoms coming from the host. The optical properties of this oxidized shell are indeed different from those of the metal and the host and thus the assumption of having an homogeneous mixture of the host and the metal would be no longer valid. These results allow us to conclude that some reactions might take place between the metal and the oxide host and that these reactions are most likely to occur no matter the production technique.

The electronic third order non-linear susceptibility (χ^3) and the linear absorption (α) at 590 nm for the $\text{Cu}:\text{Al}_2\text{O}_3$ nanocomposite films are plotted in Fig 6 as a function of the NCs mean diameter. Both parameter follow opposite trends as the size of the NCs increases. Quantum confinement effects have been reported to become important in metal NCs for average diameters smaller than 10 nm due to the contribution of intraband transitions between discrete levels in the metal conduction band.^{3,29} The intrinsic third order susceptibility of the metal NCs associated to these transitions scales as the inverse of the third power of the NCs diameter and it becomes larger for the smaller NCs.^{27,29} The effective susceptibility of the nanocomposite χ^3 is related to the intrinsic one and it is thus expected to be also larger the smaller the NCs as shown in Fig.6. The fact that the linear absorption α at a wavelength close to that of the surface plasmon resonance increases when the mean diameter of the NCs increases is also expected, since the larger the NCs size the higher the metal volume fraction and according to the Mie theory,¹ α is a linear function of the metal volume fraction. Both χ^3 and α are key factors for device development since their ratio has to be optimised in order to produce waveguide devices, the challenge being to produce materials having a large χ^3 with minimal α . The results shown in Fig. 6 evidence that the best figure of merit for optical switching is achieved for the smallest NCs studied (3.0 ± 0.6 nm).

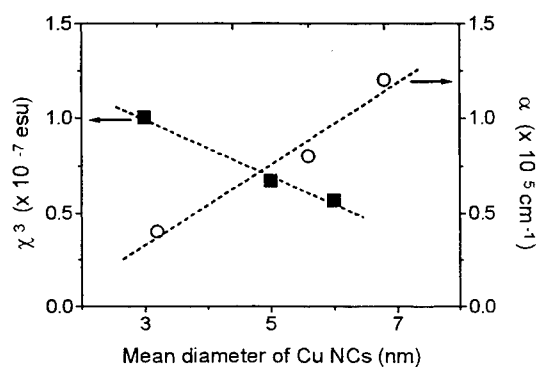


Figure 6. (■) Electronic third order non-linear susceptibility χ^3 and (○) linear absorption α , both at 590 nm, of $\text{Cu}:\text{Al}_2\text{O}_3$ films as a function of the average diameter of the Cu NCs.

Table I presents an updated resume of the works reporting χ^3 values in metal nanocomposite systems,⁸ the data being listed according to the χ^3 value, from larger to smaller ones. The most relevant parameters regarding the nature of the NCs, the method of preparation and the technique used to measure the nonlinear response have been included to facilitate the comparison between the reported χ^3 values. This survey includes experimental results on solid state systems, and studies in colloids have thus been excluded. It can be observed that Au, Cu and Ag are still the most studied metal NCs, although there are few reports on Sn, Bi, and Sb. Regarding the hosts, most of the research has been done in either fused silica or silica glass, a limited number of results are available for Al_2O_3 and other oxides (TiO_2 , Nb_2O_5), and there is one report in which a polymer has been used as host. It is worth noting that the average size of the NCs in metal nanocomposites exhibiting a nonlinear response is in the tenths of nanometer range for a large number of the works. If we compare these sizes to those shown in Fig. 6 (below 7 nm) it is clear that larger sizes imply higher absorption or losses. Furthermore, there are some cases in which the large size of the NCs implies such a high content of metal that brings the metal close to the "percolation threshold",^{13,36,37} and thus close to the formation of a quasi-continuous metal layer.

TABLE I

Summary of the nanocomposite materials formed by metallic NCS embedded in an insulator host which exhibit third order non-linear susceptibility. The columns describe sequentially the kind of metal **NCS**; the **host**; the NCS **size**; the wavelength (λ) at which the optical properties are listed; the linear optical absorption α ; the third order optical susceptibility $\chi^{(3)}$; a column to specify whether the reported $\chi^{(3)}$ value is clearly related to the electronic component (**ec**); the **method** used to measure $\chi^{(3)}$ which includes the method (**m**), the pulse duration (τ) and the frequency (ν) used; the material **synthesis method**; and the reference (**R**).

NCS	Host ^a	size (nm) ^b	λ (nm) ^c	α (cm ⁻¹)	$\chi^{(3)}$ (esu) ^d	ec	Method for $\chi^{(3)}$ m, τ , ν ^e	Synthesis Method ^f	R
Sn	Silica glass	4 - 20	500	10 ⁵	3 x 10 ⁻⁶		D, 5 ns	Ion-impl	9
Au	SiO ₂ glass	80	532	10 ⁵	2.5 x 10 ⁻⁶	Y	D, 70 ps	RF-Sput	13
Au	Al ₂ O ₃	30	532	1.7 x 10 ⁵	1.2 x 10 ⁻⁶	Y	D, 70 ps	RF-Sput	36
Au	TiO ₂	38% (*)	670	3 x 10 ⁵	6 x 10 ⁻⁷	Y	D 200 ps	RF-Sput	37
Au	SiO ₂	34	530	6.7 x 10 ⁴	2 x 10 ⁻⁷		D, 20 ns	RF-Sput	14
Au	Silica glass	3	532	1.9 x 10 ⁵	1.2 x 10 ⁻⁷		D, 7 ns	Ion-impl	10
Cu	Al ₂ O ₃	3	596	4 x 10 ⁴	10 ⁻⁷	Y	Z, 30 ps, 0.4 Mhz	PLD	27
Cu	Glass	48	580	(4 - 5) x 10 ³	10 ⁻⁷		D, 7 ns	Quenching	38
Ag/Sb	Silica glass	10 - 20	596 □	2.5 x 10 ⁴	9 x 10 ⁻⁸	Y	Z, 6 ps, 3.8 Mhz	Ion-impl	39
Au	Nb ₂ O ₅	5	590	2.2 x 10 ⁵	7.3 x 10 ⁻⁸ (**)	Y	D, 1.2 ps	IBADev	40
Ag	Glass	11	420	3 x 10 ³	7 x 10 ⁻⁸		D, 7 ns	Quenching	38
Cu	Silica glass	5 / 50	596 □	-----	6 x 10 ⁻⁸	Y	Z, 6 ps, 15.2 Mhz	Sol-gel	15
Ag	Silica glass	14	596 □	3.2 x 10 ⁴	5.4 x 10 ⁻⁸	Y	Z, 6 ps, 3.8 Mhz	Ion-impl	41
Cu/Ni	Silica glass	10	770 □	4 x 10 ⁴	4 x 10 ⁻⁸		Z, 130 fs, 76 Mhz	Ion-impl	11
Au	Al ₂ O ₃	5	570	4 x 10 ²	3 x 10 ⁻⁸		D, 8 ns	Sol-gel	16
Sb	Silica glass	6	596 □	5.5 x 10 ⁵	2.4 x 10 ⁻⁸	Y	Z, 6 ps, 3.8 Mhz	Ion-impl	41
Au	Silica glass	10	540	2.6 x 10 ³	2.3 x 10 ⁻⁸		D, 10 ns	Sol-gel	17
Cu	Al ₂ O ₃	3	596	4 x 10 ⁴	2 x 10 ⁻⁸	Y	Z, 6 ps, 3.8 Mhz	PLD	23
Cu	Fused silica	5 - 13	570	(0.2-2)x10 ⁴	(0.4-2.2) x 10 ⁻⁸	Y	Z, 6 ps, 3.8 MHz	Ion-impl	12
Ag	SiO ₂	7	390-406 □	5.7 x 10 ⁴	1.6 x 10 ⁻⁸		D, 20 ns	RF-Sput	42
Bi	Fused silica	7	770 □	< 7.5 x 10 ³	1.3 x 10 ⁻⁸		Z, 140 fs, 100Mhz	Ion-impl	43
Au	Al ₂ O ₃	13	570	1 x 10 ²	1.3 x 10 ⁻⁸		D, 8 ns	Sol-gel	16
Cu	Fused silica	5 / 25	563	3.7 x 10 ⁴	10 ⁻⁸	Y	Z, 6 ps,, 3.8 MHz	Ion-impl	28
Sb	Fused silica	7	770 □	< 7.5 x 10 ³	6.3 x 10 ⁻⁹		Z, 140 fs, 100 Mhz	Ion-impl	43
Cu	Fused silica	5 - 13	532	(0.1-3)x10 ⁴	(2.4-8.4) x 10 ⁻¹⁰	Y	D, 35ps	Ion-impl	29
Au	PE	-----	560	1.9 x 10 ⁴	6.3 x 10 ⁻¹⁰	Y	D, 70 fs, 0.3 Mhz	PE dipping	44
Au	Fused silica	5 - 30	532	(0.7-1) x10 ⁴	10 ⁻¹⁰	Y	D, 35 ps, 10 Hz	Ion-impl	45
Au	Fused silica	-----	800 □	-----	6 x 10 ⁻¹²	Y	D, 0.1-1 ps	Ion-impl	46

- ^a PE stands for Polyelectrolyte.
- ^b A range of sizes for the NCS refers either to different specimens with a range of α and $\chi^{(3)}$ values or to a range of NCs size measured in the same specimen. (*) refers not to NCs size but to % volume fraction occupied by the NCs.
- ^c □ indicates that the measuring wavelength is out of the SPR region.
- ^d (**) corresponds to the χ_{xxxx} component of the fourth-rank susceptibility tensor.
- ^e D stands for degenerate four wave mixing and Z for Z-scan measurements.
- ^f "Ion-Impl" stands for ion implantation, "RF-Sput" for RF-sputtering, "IBADev" for ion beam assisted deposition plus co-evaporation, "PE-dipping" for Polyelectrolyte dipping and "PLD" for pulsed laser deposition.

Under these conditions, the thermal load of the material is very high and the discrimination of the electronic component (fast one) in respect to the slow thermal one becomes difficult.²⁷ In this respect, special attention should be taken when comparing results obtained by different authors and/or measuring techniques and that is why a column (ec) has been added to identify the works in which the authors clearly discuss the existence of both components and state they are quoting the electronic component. The possibility of discrimination of the electrical component from the thermal induced effects depends not only on the technique used but also on the experimental conditions used, mainly on the pulse duration and the repetition rate. Note that in the reports in which the electronic component is identified, the measurements have always been performed with laser pulses of ps and fs.

The Table shows that there is a fairly large amount of nanocomposites for which a third order susceptibility value in the range of 10^{-8} esu has been reported, among which our first report on nonlinear response of Cu NCs prepared by PLD is included. There are only four works reporting third order susceptibility values of 10^{-7} esu and above in which the electronic component has been clearly separated. Among these, it is found our Cu:Al₂O₃ nanocomposite prepared by pulsed laser deposition. It should be noted that this result is very promising, specially taking into account that the linear absorption in our film is almost one order of magnitude lower than that for the other films, due to the fact that the NCs size is much smaller (3nm compared to 30-80 nm) in the PLD films.

4. CONCLUSIONS

Alternate pulsed laser deposition in vacuum is a suitable and flexible route to produce nanocomposite films formed by metallic NCs embedded in a dielectric host. The size of the crystals is easily controlled through the number of pulses in the metal target and the size distributions are very sharp, the smaller the diameter the sharper the distribution. The NCs are produced by nucleation, growth and coalescence at the substrate, the latter process leading to broader distributions when the size of the NCs is increased. The linear optical properties of the nanocomposites can be well simulated by effective medium modelling whenever the metal and the host do not interact and the simulation thus provides a very accurate means to determine the metal content. However, interactions between the host and the metal, when the host is an oxide, prevent such determination and lead to an optical behaviour different from that expected, such interactions being most likely leading to the formation of oxide shells surrounding the NCs. Finally, the values for the third order non-linear optical susceptibility $\chi^{(3)}$ of the Cu:Al₂O₃ nanocomposites prepared by PLD are among the larger values reported in the literature. When the absorption is taken into account, the PLD films having the smaller NCs (3.0 ± 0.6 nm) have one of the best figure of merit $\chi^{(3)}/\alpha$ reported so far in the literature for nanocomposite materials formed by metal NCs embedded in a host.

ACKNOWLEDGEMENTS

This work has been partially supported by CICYT (Spain) under TIC96-0467 project and by the EU under BRPR-CT98-0616 project. The authors are grateful to A. K. Petford-Long (University of Oxford, UK) for the HRTEM analysis and very fruitful discussions, and to the GPS (Université de Paris VI et VII, Paris, France) for provision and assistance of RBS facilities. One of the authors (J.G.) acknowledges a Research Contract from the Spanish Ministry of Education and Culture.

REFERENCES

1. G. Mie, "Beiträge zur Optik trüber Medien, speziell kolloidaler Metallösungen," *Ann. Phys.* **25**, 377-455, 1908.
2. M. Born and E. Wolf, *Principles of Optics*, Ch. 13, pp. 633-667, Pergamon Press, Oxford 1983.
3. C. Flytzanis, F. Hache, M. C. Klein, D. Ricard and Ph. Roussignol, "Nonlinear optics in composite materials", in *Progress in Optics*, ed. by E. Wolf, XXIX, 323-311, North Holland, Amsterdam 1991
4. E. M. Vogel, M. J. Weber and D. M. Krol, "Nonlinear optical phenomena in glass," *Phys. and Chem. of Glasses* **32**, 231-254, 1991.
5. M. Ando, K. Kadono, M. Haruta, T. Sakaguchi and M. Miya, "Large third-order optical nonlinearities in transition-metal oxides," *Nature* **374**, 625-627, 1995.
6. T. Hashimoto, T. Yamada, T. Yoko, "Third order nonlinear optical properties of sol-gel derived α -Fe₂O₃, γ -Fe₂O₃, and Fe₃O₄ thin films," *J. Appl. Phys.* **80**, 3184-3190, 1996.
7. G. P. Banfi, V. Degiorgio and D. Ricard, "Nonlinear optical properties of semiconductor nanocrystals," *Adv. in Phys.* **47**, 447-510, 1998.
8. C. N. Afonso, R. Serna, J. M. Ballesteros, J. Solis, A. K. Petford-Long and R. C. Doole, "Nanocrystal composite thin films produced by pulsed laser deposition for nonlinear optical applications," *SPIE* vol. 3404, 74-83, 1998.
9. Y. Takeda, T. Hioki, T. Motohiro and S. Noda, "Large third-order optical nonlinearity of tin microcrystalline-doped silica glass formed by ion implantation," *Appl. Phys. Lett.* **63**, 3420-3422, 1993.
10. K. Fukumi, A. Chayahara, K. Kadono, T. Sakaguchi, Y. Horino, M. Miya, J. Hayakawa and M. Satou, "Au⁺ ion implanted silica glass with non-linear optical property," *Jpn. J. Appl. Phys* **30**, L742-L744, 1991.
11. M. Falconieri, G. Salvetti, E. Cattaruzza, F. Gonella, G. Mattei, P. Mazzoldi, M. Piovesan, G. Battaglin and R. Polloni, "Large third-order optical nonlinearity of nanocluster-doped glass formed by ion implantation of copper and nickel in silica," *Appl. Phys. Lett.* **73**, 288-290, 1998.
12. R.H. Magruder III, R.F. Haglund, Jr., L. Yang, J. E. Wittig and R. A. Zuhr, "Physical and optical properties of Cu nanoclusters fabricated by ion implantation in fused silica," *J. Appl. Phys.* **76**, 708-715, 1994.
13. H. B. Liao, R. F. Xiao, J. S. Fu, P. Yu, G. K. L. Wong and Ping Sheng, "Large third-order optical nonlinearity in Au:SiO₂ composite films near the percolation threshold," *Appl. Phys. Lett.* **70**, 1-3, 1997.
14. I. Tanahashi, Y. Manabe and T. Tohda, "Optical nonlinearities of Au/SiO₂ composite thin films prepared by a sputtering method," *J. Appl. Phys.* **79**, 1244-1249, 1996.
15. G. De, L. Tapfer, M. Catalano, G. Battaglin, F. Caccavale, F. Gonella, P. Mazzoldi and R. F. Haglund, Jr, "Formation of copper and silver nanometer dimension clusters in silica by the sol-gel process," *Appl. Phys. Lett.* **68**, 3820-3822, 1996.
16. Y. Hosoya, T. Suga, T. Yanagawa and Y. Kurokawa, "Linear and nonlinear optical properties of sol-gel derived Au nanometer particle doped alumina," *J. Appl. Phys.* **81**, 1475-1480, 1997.
17. M. Lee, T. S. Kim and Y. S. Choi, "Third-order optical nonlinearities of sol-gel processes Au-SiO₂ thin films in the surface plasmon absorption region," *J. of Non. Cryst. Solids* **211**, 143-149, 1997.
18. C. N. Afonso "Pulsed laser deposition of films for optical applications", in *Insulating materials for optoelectronics: new developments*, ed. by F. Agullo-Lopez, World Scientific Publishing Co. Inc., Chap. 1, 1-28, 1995.
19. S. Ohtsuka, K. Tsunetomo, T. Koyama and S. Tanaka, "Ultrafast nonlinear optical effect in CdTe-doped glasses fabricated by the laser evaporation method," *Opt. Materials* **2**, 209-215, 1993.
20. T. Yoshida, S. Takeyama, Y. Yamada and K. Mutoh, "Nanometer-sized silicon crystallites prepared by excimer laser ablation in constant pressure inert gas," *Appl. Phys. Lett.* **68**, 1772-4, 1996.

21. W. Marine, I. Movtchan, A. Simakine, L. Patrone, R. Dreyfus, M. Sentis, M. Autric and N. Merk, "Pulsed laser deposition of Si nanocluster films," *MRS Symp. Proc.* **397**, 365-374, 1996.
22. D. B. Geohegan, A. A. Puretzky, G. Duscher and S. J. Pennycook, "Photoluminescence from gas-suspended SiO_x nanoparticles synthesized by laser ablation," *Appl. Phys. Lett.* **73**, 438-440, 1998.
23. J. M. Ballesteros, R. Serna, J. Solís, C. N. Afonso, A. K. Petford-Long, D.H. Osborne and R. F. Haglund Jr. "Pulsed laser deposition of Cu:Al₂O₃ nanocluster thin films with high third order non linear susceptibility," *Appl. Phys. Lett.* **7**, 2445-2447, 1997.
24. R. Serna, T. Missana, C. N. Afonso, J. M. Ballesteros, A. K. Petford-Long and R. C. Doole, "Bi nanocrystals embedded in an amorphous Ge matrix grown by pulsed laser deposition," *Appl. Phys. A* **66**, 43-47, 1998.
25. C.N. Afonso, R. Serna, J.M. Ballesteros, A.K. Petford-Long, R. C. Doole, "Synthesis by pulsed laser deposition of metallic nanoclusters embedded in an amorphous host," *Appl. Surf. Sci.* **127-129**, 339-343, 1998.
26. R. Serna, J. C. G.de Sande, J. M. Ballesteros and C. N. Afonso, "Spectroscopic ellipsometry of composite thin films with embedded Bi nanocrystals," *J. Appl. Phys.* **84**, 4509-4516, 1998.
27. J. M. Ballesteros, J. Solis, R. Serna and C. N. Afonso, "Nanocrystal size dependence of the third-order nonlinear optical response of Cu:Al₂O₃ thin films," *Appl. Phys. Lett.* (in press)
28. R. F. Haglund Jr, L. Yang, R. H. Magruder III, J. E. Witting, K. Becker and R. A. Zuhr, "Picosecond nonlinear optical response of a Cu:silica nanocluster composite," *Opt. Lett.* **18**, 373-375, 1993.
29. Li Yang, K. Becker, F. M. Smith, R. H. Magruder III, R. F. Haglund Jr, L. Yang, R. Dorsinville, R. R. Alfano and A. Zuhr, "Size dependence of the third-order susceptibility of copper nanoclusters investigated by four-wave mixing," *J. Opt. Soc. Am. B* **11**, 457-461, 1994.
30. R. Serna, C. N. Afonso, J. M. Ballesteros, A. Naudon, D. Babonneau and A. K. Petford-Long, "Size, shape anisotropy, and distribution of Cu nanocrystals prepared by pulsed laser deposition", *Appl. Surf. Sci.* (in press)
31. J. C. G. de Sande, F. Vega, C. N. Afonso, C. Ortega and J. Siejka, "Optical properties of Sb and SbO_x films," *Thin Solid Films* **249**, 195-200, 1994.
32. F. Vega, J. C. G. de Sande, C. N. Afonso, C. Ortega, and J. Siejka, "Optical properties of GeO_x films obtained by laser deposition and dc sputtering in a reactive atmosphere," *Appl. Optics.* **33**, 1203-1207, 1994.
33. T. Missana, C. N. Afonso and M. F. da Silva, "Interdiffusion studies in Bi-based layered systems with nanosecond laser pulses," *Appl. Phys.* , **59**, 653-658, 1994.
34. D. E. Aspnes, "Optical properties of thin films," *Thin Solid Films* **89**, 249-262, 1982.
35. J. C. G. de Sande, C. N. Afonso, J. L. Escudero, R. Serna, F. Catalina and E. Bernabeu, "Optical properties of laser-deposited a-Ge films: a comparison with sputtered and e-beam-deposited films," *Appl. Optics* **31**, 6133-6138, 1992; J. C. G. de Sande, T. Missana, C. N. Afonso, "Optical properties of pulsed laser deposited bismuth films," *J. Appl. Phys.* **80**, 7023-7027, 1996.
36. H. B. Liao, R. F. Xiao, J. S. Fu and G. K. L. Wong, "Large third-order nonlinear optical susceptibility of Au:Al₂O₃ composite films near the resonant frequency," *Appl. Phys. B* **65**, 673-676, 1997.
37. H. B. Liao, R. F. Xiao, H. Wang, K. S. Wong and G. K. L. Wong, "Large third-order optical nonlinearity in Au:TiO₂ composite films measured on a femtosecond time scale," *Appl. Phys. Lett.* **72**, 1817-1819, 1998.
38. K. Uchida, S. Kaneko, S. Omi, C. Hata, H. Tanji, Y. Asahara, A. J. Ikushima, T. Tokizaki and A. Nakamura, "Optical nonlinearities of a high concentration of small metal particles dispersed in glass: copper and silver particles," *J. Opt. Soc. Am. B* **11**, 1236-1243, 1994.
39. R. A. Zuhr, R. H. Magruder III and T. S. Anderson, "Optical properties of multi-component antimony-silver nanoclusters formed in silica by sequential ion implantation," *MRS Symp. Proc.* **396**, 391-396, 1996.

40. C. M. Cotell, S. Schiestel, C. A. Carosella, S. Flom, G. K. Hubler and D. L. Knies, "Ion-beam assisted deposition of Au nanocluster/ Nb_2O_5 thin films with nonlinear optical properties," *Nucl. Inst. and Methods in Phys. Res. B* **127/128**, 557-561, 1997.
41. R. H. Magruder III, R. A. Weeks, T. S. Anderson and A. Zuhr, "Linear and nonlinear optical properties of metal nanocluster-silica composites formed by implantation of Sb in high purity silica," *MRS Symp.Proc.* **438**, 429-434, 1997.
42. I. Tanahashi, M. Yoshida, Y. Manabe, T. Tohda, S. Sasaki, T. Tokizaki and A. Nakamura, "Preparation and nonlinear optical properties of Ag/ SiO_2 glass composite thin films," *Jpn. J. Appl. Phys.* **33**, Part 2 L1410-L1412, 1994.
43. Z. Pan, S. H. Morgan, D. O. Henderson, S. Y. Park, R. A. Weeks, R. H. Magruder III and R. A. Zuhr, "Linear and nonlinear optical response of bismuth and antimony implanted fused silica: annealing effects," *Optical Materials* **4**, 675-684, 1995.
44. W. Schrof, S. Rozouvan, E. Van Keuren, D. Horn, J. Schmitt and G. Decher, "Nonlinear optical properties of polyelectrolyte thin films containing gold nanoparticles investigated by wavelength dispersive femtosecond degenerate four wave mixing," *Adv. Materials* **3**, 338-341, 1998.
45. R. H. Magruder III, Li Yang, R. F. Haglund Jr, C. W. White, L. Yang, R. Dorsinville and R. R. Alfano, "Optical properties of gold nanocluster composites formed by deep ion implantation in silica," *Appl. Phys. Lett.* **62**, 1730-1732, 1993.
46. R. G. Elliman, B. Luther-Davies, M. Samoc and A. Dowd, "Non-linear optical response of metallic and semiconducting nanocrystals in fused silica," *MRS Symp.Proc.* **438**, 423-428, 1997.

Semiconductor Nanocrystallite Formation Using Inert Gas Ambient Pulsed Laser Ablation and Its Application to Light Emitting Devices

Takehito Yoshida, Yuka Yamada, Nobuyasu Suzuki, Toshiharu Makino,
Takaaki Orii*, and Seinosuke Onai*

Matsushita Research Institute Tokyo, Inc., 3-10-1 Higashimita, Tama-ku, Kawasaki 214-8501, Japan

*Institute of Applied Physics, Univ. of Tsukuba, 1-1-1 Tennoudai, Tsukuba, Ibaraki 305-0006, Japan

ABSTRACT

Pulsed laser ablation (PLA) in inert background gases can synthesize the nanoscaled silicon (Si), for studying its material properties as one of the quantum confinement effects. We report an optimized condition in Si nanocrystallite formation by the PLA in inert background gas, varying processing parameters: pulse energy and width, inert background gas pressure. The optimized process can prepare well-dispersed Si nanocrystallites without any droplets and debris. Furthermore, we investigate the influence of the processing parameters on transition from amorphous-like Si thin films to nanocrystallites. It was found that there is a processing window of the inert background gas pressure where the carrier confinement effects become apparent. Next, we have fabricated electroluminescent (EL) diodes with active layers of the Si nanocrystallites. The structure of the EL diodes was semitransparent platinum electrode/Si nanocrystallite layer/*p*-type Si/Pt electrode. We have observed visible spectra of not only green photoluminescence, but also red EL, at room temperature. Furthermore, we have found that the EL diodes showed strong nonlinear dependence of EL intensity on current density.

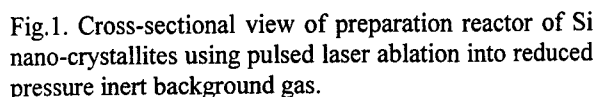
Keywords: silicon, nanocrystallites, pulsed laser ablation, optical properties, electroluminescent diode

1. INTRODUCTION

The group IV elements (Si, Ge) can hardly emit light in the bulk state because they are indirect transition semiconductors, however it is well known that they are capable of emitting strong visible light at room temperature when their size is reduced in the order of several nanometers.¹⁻³ There have been numerous reports concerning light emission from the "porous" Si formed by the liquid phase anodization.⁴ When we study the optical properties of nanoscaled group IV materials as one of the quantum confinement effects, it is significant to adopt another approach using the nanoscaled "spherical" structures which are homogeneous and well-dispersed. However, hitherto it has been difficult to develop nanocrystallites into advanced functional devices because they have a large percentage of surface-exposed atoms (nearly 40% when the diameter is 5 nm), and are extremely sensitive to impurities and/or damage. On the other hand, since the laser processing based on non-equilibrium and the non-mass properties of photons can realize clean and damage-free processing ambients, this processing is very suitable for the nanocrystallite synthesis. In particular, pulsed laser ablation (PLA)⁵⁻⁶ with its capability of maintaining purity in processing ambients has excellent features, notably from the viewpoints of safety and compatibility with the environment. For this purpose, PLA into a background gas has been applied to the preparation of Si nanocrystallites⁷⁻¹⁰. Werwa et al.⁷ reported that the minimum diameter of Si nanocrystallites was about 2 nm in laser ablation into a pulsed inert gas. Yoshida et al.⁹ reported that the size distribution of Si nanocrystallites was controlled by varying the background gas pressure. Deohegan et al.¹¹ confirmed that the ejected species condensed into nanoparticles in the background gases.

Recently, some research groups have focused on electroluminescence (EL) properties as well as on PL properties because the EL of the nanoscaled Si structures is suited to optoelectronic device applications. Most EL Si structures have been thinned to "porous" structures formed by liquid phase anodization.¹² EL of porous Si was first observed during anodic oxidation in an electrolyte solution.¹³ Porous Si EL devices operating in the atmosphere have been studied with solid-state contacts, including semitransparent metal-contacted Schottky junction diodes,¹⁴⁻¹⁶ *p-n* homojunction diodes¹⁷⁻²⁰ and *p-n* heterojunction diodes.²¹⁻²⁴ Besides the porous Si, Qin et al. developed a visible EL device of the low operational voltage (> 4 V) in gold (Au)-contacted extra thin (4 nm) Si-rich Si oxide films deposited by magnetron sputtering.²⁵ Nassiopoulou et al. observed visible EL from Si nanopillars formed using highly anisotropic reactive etching and thinning thermal oxidation.²⁶

* Present address: The Institute of Physical and Chemical Research (RIKEN), 2-1 Hirosawa, Wako-shi, Saitama 351-0198, Japan



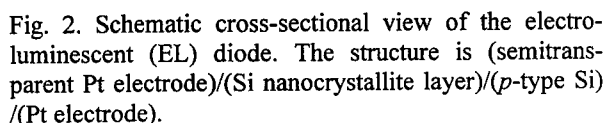
Nd: YAG Laser Parameters

Wavelength	532 nm
Repetition Rate	10 Hz
Pulse Width	<u>0.17</u>, 0.35, 0.54, <u>5.6</u>, 15, 30, <u>42</u> ns
Pulse Energy	1- 100 mJ, typically 10 mJ (~13 J/cm²)

In this work, at first, we study the feasibility of synthesizing such Si nanocrystallites for the device application using the PLA in inert background gas, controlling processing parameters: pulse width and inert background gas pressure. Furthermore, we investigate the influence of the processing parameters on transition from amorphous-like thin films to nanocrystallites. Next, we fabricate EL diodes of which active layers are Si nanocrystallites, using PLA in inert background gas as one of the physical vapor deposition (PVD) methods. Electrical conductivity, dependence of EL intensity on excitation current, and luminescence spectra are characterized to clarify their EL mechanisms. Our fabrication method is compatible with the established Si large scale integrated (LSI) technology because the PVD processing is suitable for successive film stacking and etching of fine patterns.

2. EXPERIMENTAL PROCEDURE

Target : *p*-type (100) Si wafer ($\phi 2$ inch, t 500 μm)
Deposition substrate : Si t 0.625 mm, \square 18 mm or
 $\text{SiO}_2 t$ 1.0 mm, \square 18 mm
He gas flow rate : ~ 200 sccm
He (background) gas pressure : 1.0-20 Torr
T/S distance : 20, 30 mm.



Structural characterization for the as-deposited Si nanocrystallites was carried out using scanning electron microscope (SEM) and high resolution transmission electron microscope (HRTEM). The HRTEM apparatus was Topcon EM002B, 200 keV. We measured optical absorption spectra of the as-deposited Si nanocrystallites, in visible region.

For the EL diode fabrication, the Si nanocrystallite layers were deposited using the PLA in the inert background gas. In this case, we adopted an argon-fluoride (ArF) excimer laser beam (λ : 193 nm, energy density: $1.0 \text{ J/cm}^2 \cdot \text{pulse}$, pulse duration: 12 ns, repetition rate: 10 Hz) as a excitation light source. It was focused onto a *p*-type Si (100) wafer as a target. During the laser ablation of the Si target, He gas was introduced into the vacuum chamber and maintained at a constant reduced pressure using a differential evacuation system. In this fabrication, the pressure of He gas was maintained at 333 Pa where the as-deposited mean diameter and the geometric standard deviation of the Si nanocrystallites were about 10 nm and 1.5, respectively. Other conditions were the same as those reported previously.⁹ A schematic cross-sectional view of the EL diode is shown in Fig. 2. To fabricate the EL diode, (100) oriented *p*-type Si wafers with a resistivity of $12 \Omega \cdot \text{cm}$ were used as substrates. Thermal oxide layers were formed with a thickness of 100 nm for the isolation dielectrics. Electrically active regions with a diameter of 2.0 mm were defined by removing the thermal oxide with $\text{HF} + \text{NH}_4\text{F}$ solution. The Si nanocrystallite layers were deposited using the above PLA method. Thermal annealing was carried out at 800°C for 10 min in N_2 gas to produce the visible PL.¹⁰ In order to form a contact with the Si nanocrystallite layers, semitransparent platinum (Pt) films were deposited with a thickness of 12 nm. The EL active regions were Si nanocrystallite layers with an area of $3.1 \times 10^{-2} \text{ cm}^2$ (2.0 mm diameter circle) and a thickness of about 150 nm.

The current-voltage (*I-V*) characteristics of the EL diodes were measured under forward and reverse bias conditions. The forward bias condition was created by applying a positive voltage to the *p*-type bulk Si substrate with respect to the semitransparent Pt electrode. The photoelectromotive forces were measured using a halogen lamp (150 W) as an excitation

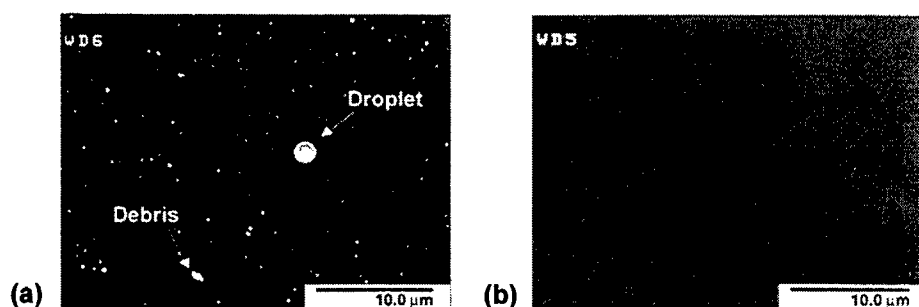


Fig. 3. SEM plane view in low magnification for as-deposited Si species on Si substrate. Wavelength: 532 nm, Pulse number: 2000. (a) Pulse width: 0.17 ns, Pulse energy: 10 mJ, Peak power: 59 MW, (b) Pulse width: 5.6 ns, Pulse energy: 10 mJ, Peak power: 1.8 MW.

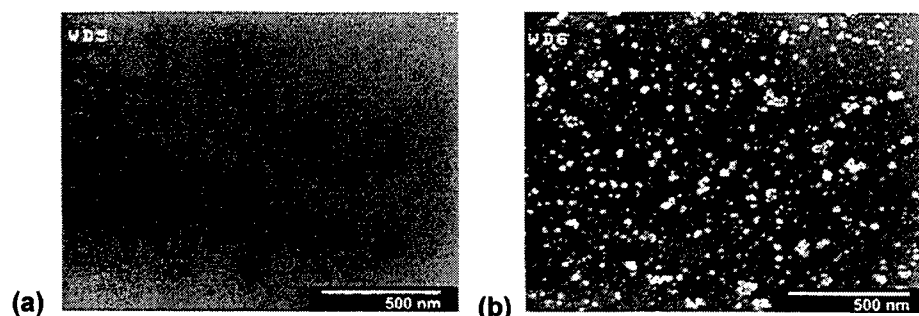


Fig. 4. SEM plane view in high magnification for as-deposited Si species on Si substrate. Wavelength: 532 nm, Pulse number: 1000, Pulse width: 42 ns, Pulse energy: 10 mJ, Peak power: 0.24 MW. (a) Background He pressure: 2.5 Torr, (b) Background He pressure: 5.0 Torr.

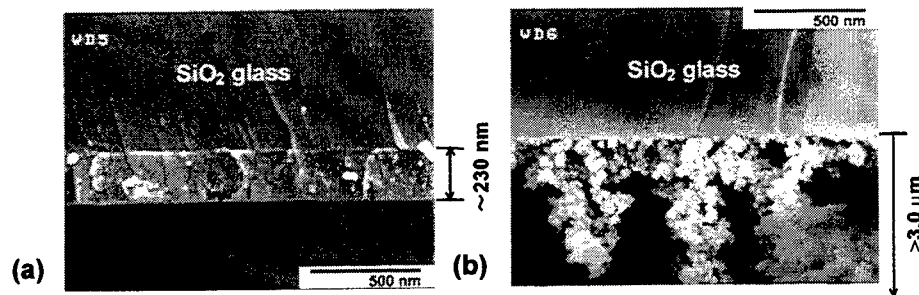


Fig. 5. SEM cross-sectional view in high magnification for as-deposited Si species on Si substrate. Wavelength: 532 nm, Pulse number: 80000, Pulse width: 42 ns, Pulse energy: 10 mJ, Peak power: 0.24 MW. (a) Background He pressure: 2.5 Torr, (b) Background He pressure: 5.0 Torr.

light source. The dependence of the integrated EL intensity on the diode current was investigated at room temperature. The EL intensity was measured by a photomultiplier (Hamamatsu Photonics R3896). The EL and PL spectra were measured at room temperature using a single polychromator system (Jasco CT-25C) with a cooled MOS linear image sensor unit (Hamamatsu C4834-02) as a detector. An Ar^+ ion laser ($h\nu$: 2.54 eV, power: 10 mW) was used as the excitation light source for the PL observation. The spectra were collected by spectral sensitivity of the measurement system obtained using a standard halogen lamp.

3. EXPERIMENTAL RESULTS

We varied the laser pulse width and energy, in order to find appropriate value for suppressing micrometer-sized droplets and debris. **Figure 3** shows low magnification plane views for the as-deposited Si species by the SEM. Two figures (**Fig. 3 (a) and (b)**) describe a typical dependence of the micrometer-sized structure on the laser peak power. In both cases, the laser pulse energies were fixed to be same value: 10 mJ. **Figure 3 (a)** indicates a high peak power case: 59 MW. There are many micrometer-structured droplets and debris. On the other hand, **Fig. 3 (b)** shows results of a low peak power case: 1.8 MW. Formation of the micrometer-structured droplets and debris are completely suppressed. As a result of experiments varying the laser pulse width and energy, we have found conditions to synthesize nanometer-sized Si ultrafine particles without any micrometer-sized droplets and debris. The optimum laser pulse condition is pulse energy: 10 mJ, pulse width: 42 ns, and peak power: 0.24 MW. Under the optimized condition, we varied the He background gas pressure. **Figure 4** shows high magnification plane views of the SEM for the Si species as-deposited by pulse number: 1,000. Two figures (**Fig. 4 (a) and (b)**) describe a typical dependence of the nanometer-sized structure on the He gas pressure. In **Fig. 4 (a)**, the He gas pressure was 2.5 Torr. This image looks a thin film. It was found that at low pressures less than 3.75 Torr, structures of the deposited Si species were plane thin films. On the other hand, in **Fig. 4 (b)**, structure of the Si deposited at 5.0 Torr is well-dispersed nanoparticles. It seems that the

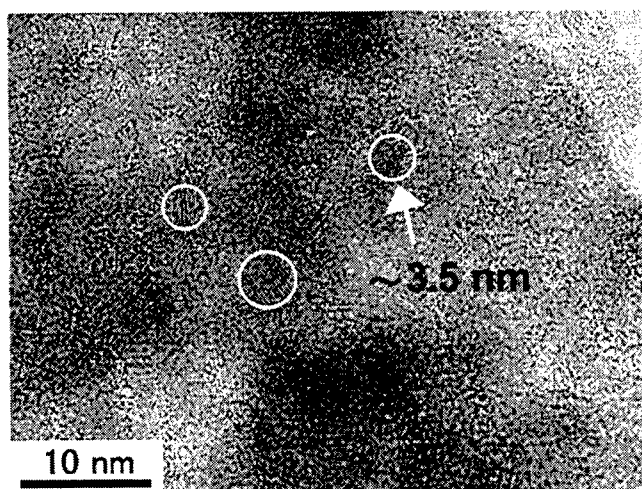


Fig. 6. HRTEM photograph for as-deposited Si nanoparticles on carbon coated micro-grid. Wavelength: 532 nm, Pulse number: 1000, Pulse width: 42 ns, Pulse energy: 10 mJ, Peak power: 0.24 MW, Background He pressure: 5.0 Torr.

nanoparticles of which size distribution is widely ranged from order of one nanometer to ten nanometers were dispersed on the substrate. At high pressure more than 4.0 Torr, Si nanoparticles were deposited. However, agglomeration of the Si nanoparticles become notable with increasing He pressure, especially in higher than 5.0 Torr. **Figure 5** shows a cross-sectional views of the the SEM for much thicker specimen as-deposited by pulse number: 80,000. In a low pressure condition 2.5 Torr (**Fig. 5 (a)**), a thin film structure is observed. Its thickness was 230 nm. On the other hand, in **Fig. 5 (b)**, structure of the Si deposited at 5.0 Torr is nanoparticles mutually agglomerated like cauliflower. This cauliflower structure was porous, fragile, and easily peeled off, these results suggest that mutual binding force is not so strong. Further structural observation was carried out by using the HRTEM. **Figure 6** shows results of the HRTEM observation for the Si nanoparticles deposited on a Cu micro-grid in the same condition as that of **Fig. 4 (b)** and **Fig. 5 (b)**. The droplets and the debris were not observed at all same as the deposition on the Si and SiO₂ substrates. In

Fig. 6, white circles indicate lattice plane image of ball-like single crystalline Si nanoparticles. These lattice plane spacing corresponded to (111) plane of the bulk Si. Their diameters were about 3-4 nm. In the HRTEM observation on the Cu micro-grids, many single crystalline Si nanoparticles were found, and their maximum diameter was around 10 nm. The nanoparticles of which sizes seem order of ten nanometers in **Fig. 4 (b)** and **Fig. 5 (b)**, presumably consist aggregation of the nanocrystallites scaled in the order of one nanometer. **Figure 7** shows the influence of the He gas pressure on optical absorption spectra of the as-deposited Si nanocrystallites. As well known, bulk single crystalline Si has the absorption edge at 1.1 eV. The absorption edges of the Si nanocrystallite are blue-shifted, in comparison with that of bulk Si. Especially at 3.75 and 4.0 Torr, the absorption edges shift remarkably. These results propose that nanometer-sizing of Si caused carrier

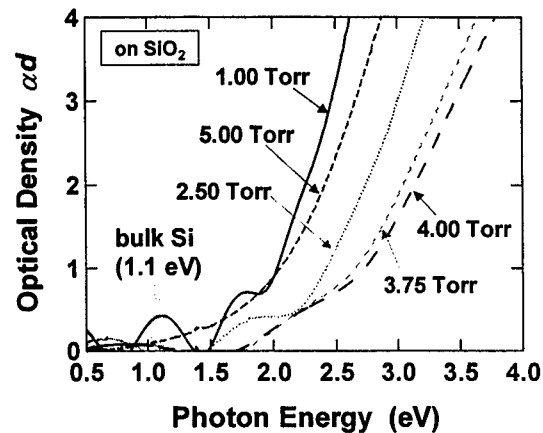


Fig. 7. Optical absorption spectra of as-deposited Si nanocrystallites. Pulse number for deposition was 80000. Influence on He background pressure is indicated.

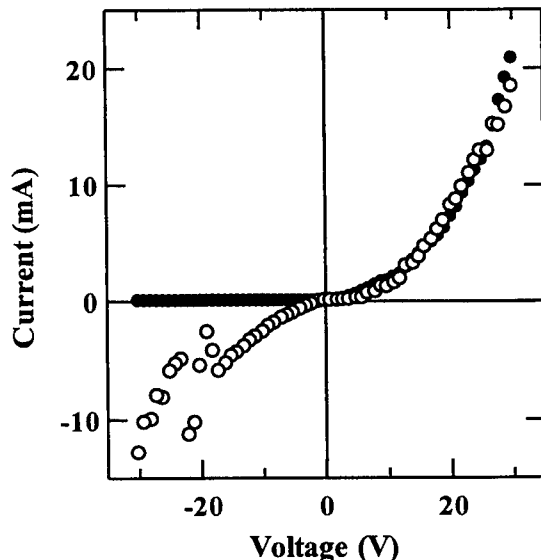


Fig.8 I - V characteristics of the electroluminescence (EL) diode with the Si nanocrystallite layer as the active region. Closed circles mean initial measurement results. Opened circles mean results after current stresses. Linear scale in both forward and reverse bias.

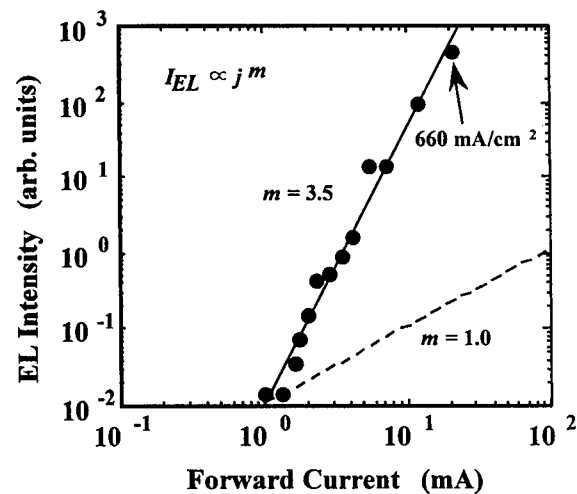


Fig.9 Integrated electroluminescence (EL) intensity (I_{EL}) as a function of the forward current j in a log-log scale. I_{EL} shows a rapid nonlinear dependence on j : $I_{EL} \propto j^m$, $m = 3.5$. The dashed line indicates the case of $m = 1.0$, which appears in the usual EL of a minority carrier injection type.

confinement effects which increase the band gap energy.

Figure 8 shows the I - V characteristics of a typical EL diode in linear scale. A strong rectifying behavior is initially observed, and is indicated by closed circles in Fig. 8. After current stresses, this rectifying behavior was degraded (Fig. 8, opened circles). The series resistance R_s was estimated to be 500 Ω . The open-circuit voltage at the semitransparent Pt electrode was about -0.1 V with respect to the back of the grounded Si substrate, under halogen lamp irradiation. This polarity means that the Si nanocrystallite layer is p -type. Light emission occurred only at forward bias and increased with increasing current. The onset of light emission, measured with the photomultiplier, was at a forward current of 1.0 mA (voltage: 7.0 V). When the forward current and the bias voltage were 15 mA and 25 V, respectively, the light emission could be observed with the naked eye in the dark. The degradation in the rectifying behavior had no bad influence for the forward biased EL properties. Figure 9 shows the integrated EL intensity I_{EL} as a function of the forward current j in a log-log scale. The I_{EL} increases rapidly with increasing j . It is evident that the dependence of I_{EL} on j is according to a power law. The relationship of I_{EL} vs j can be described as follows: $I_{EL} \propto j^m$, $m=3.5$. Integrated external quantum efficiency was roughly estimated using a condenser lens and the photomultiplier operated in dc current amplifying mode, at a forward current of 28 mA and a forward bias of 30.0 V. The result was still extremely low, and remained around 10^{-4} %. We predict that the efficiency can be improved by further optimizing some process parameters, such as the thickness of the nanocrystallite layer, size distribution of the nanocrystallites and thickness of the surface oxide. Furthermore, the formation of a p - n junction by dopant implantation appears to be useful for increasing the external quantum efficiency. Time-dependent degradation of the emission intensity was not observed during five hours of operation at a typical dissipation power of 1.0 W. However, the initial rectifying properties were degraded, showing an increase in the reverse current, whereas the forward current remained unchanged.

The measured EL spectra is shown in Fig. 10 (a). The forward current was varied from 21 mA to 35 mA (power: from 0.55 W to 1.10 W) in this measurement. The PL spectrum of the same sample is superimposed in Fig. 10 (a). Since the as-deposited Si nanocrystallites should have many surface defects, surface oxidation for defect recovering is necessary to realize the PL properties.¹⁰ In the PL spectrum, the main peak of the green band and shoulder of the red band were observed to be similar to that reported previously.¹⁰ In contrast, the EL spectra show a broader main peak around 1.66 eV. The peak positions of the EL spectra shifted slightly to a lower photon energy level with increasing dissipation power of the EL diode. As shown in Fig. 10 (b), it is apparent that

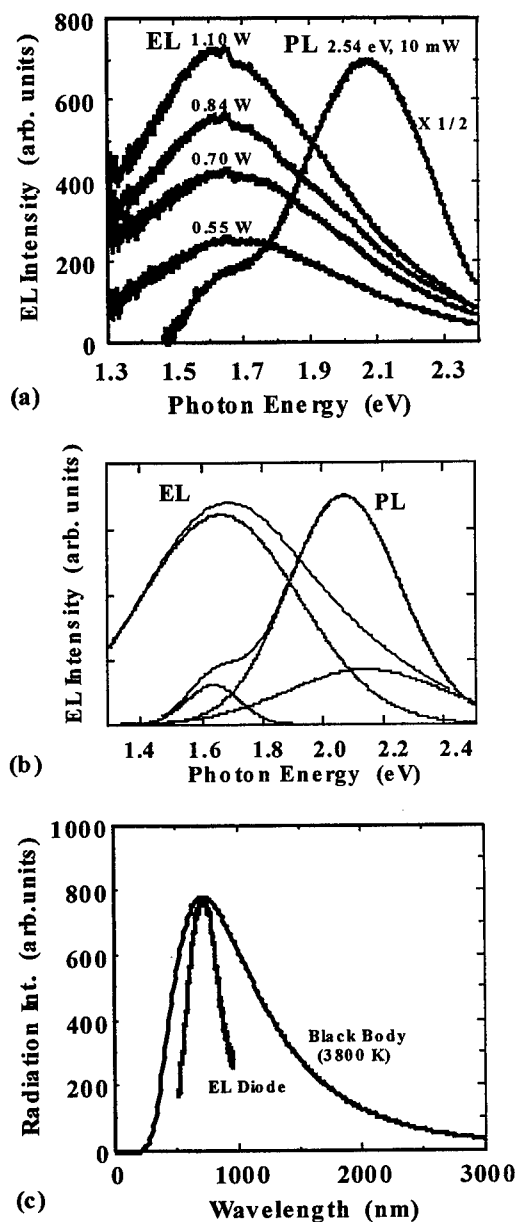


Fig.10 EL spectra for the EL diode at room temperature. (a) Applied forward current varies from 21 mA to 35 mA (power: from 0.55 W to 1.10 W). PL spectrum excited by Ar^+ ion laser ($h\nu$: 2.54 eV, power: 10 mW) of the active region same as that of the EL is superimposed. (b) Deconvolution of the EL spectrum excited at 0.55 W and the PL spectrum excited at 10 mW. Dots indicate experimental data. Solid lines represent Gaussian waveform units and calculated fitting curves composed of the Gaussian units. (c) Calculated black-body radiation spectrum at 3800 K and the EL spectrum excited at 0.55 W.

the PL spectrum is composed of Gaussian waveforms of both the green 2.07 eV band and the red 1.66 eV band. The EL spectra can also be synthesized by the superposition of Gaussian waveforms corresponding to the green shoulder band and the red main peak. Under weak excitation conditions in which the dissipation power was 0.55 W, the calculated fitting curve coincided well with the experimental spectrum. However, each Gaussian waveform in the EL spectra was wider than that of the PL.

4. DISCUSSION

We characterized the influence of He pressure on the structure transition from the amorphous-like thin films to nanocrystallites using SEM and optical absorption spectra (ABS). From the SEM observation it seems that there is a boundary between 3.75 and 4.0 Torr. On the other hand, from the ABS observation, a boundary exist at around 2.5 Torr. In the medium region around 4.0 Torr, we observed the remarkable blue-shifted absorption edge. The reduction of the size of Si to that of the nanometer region brings about carrier confinement effects which increase the band gap energy. Consequently, in the medium region, the quantum confinement effects for carriers become apparent in the Si nanocrystallites. Furthermore, at 5.0 Torr, Si nanocrystallites were coalesced, and were fragiley agglomerated each other. In these, the quantum confinement for carriers become relatively weak.

In the nanometer region of Si more than 3 nm, relation between the band gap energy and the nanocrystallite size can be explained by means of the effective mass approximation.²⁷ In our case (Fig. 7, 3.75 4.0 Torr), average diameter of the Si nanocrystallites was estimated to be about 5.5 nm in accordance with the effective mass approximation. This value corresponds closely to that of the TEM observation.

In the amorphous-like Si films, the absorption edge was around 1.8 eV, a value close to that which had been previously reported. Also we observed interference fringe which is a characteristic of thin films. The absorption curve of the Si nanocrystallites is in a higher photon energy region, in comparison with that of the amorphous-like Si in Fig. 7. The interference fringe hardly appear in absorption curves of the Si nanocrystallites. This result is consistent with the SEM observation in Fig. 4 and 5. From above results, the Si nanocrystalline layers prepared by the PLA in around 4.0 Torr He background gas has different optical properties from both the amorphous-like thin films and the coalesced nanocrystallites. Such optical properties are presumably caused by strong carrier confinement effects characteristic in the well-dispersed Si nanocrystallites.

It is necessary to check the possibility of black-body radiation when we consider the EL mechanism. In general, black-body radiation by Joule's heating shows the following characteristics: 1) Integrated radiation energy is proportional to the forth power of temperature (Stefan-Boltzmann's law), or integrated radiation energy is proportional to the sixth-eighth power of current; 2) The photon energy of the emission peak shifts to a higher region with increasing temperature (Wien's displacement law). In our experimental results, the EL intensity was proportional to a power greater than the cube of the current (Fig. 9). The photon energy of the emission peak shifted slightly to a lower region with increasing dissipation power (Fig. 10 (a)). If black-body radiation emits light with the peak of 1.66 eV, its temperature is estimated to be 3800 K, and would not be attainable. Figure 10 (c) shows both the spectra of calculated black-body radiation at 3800 K and the EL diode. The full width at half maximum (FWHM) of the EL spectrum was about 30% of that of the black-body radiation. Therefore, it can be concluded that our EL mechanism is different from black-body radiation.

Forty years ago, visible light emission was first observed from a reverse-biased avalanche breakdown region (2.0-4.0 A/cm²) of a bulk Si *p-n* junction.²⁸ In our EL diodes, light emission occurred at a forward-biased junction. In addition, the onset of the EL occurred at relatively low current density (30 mA/cm²). Therefore, it is clear that our EL mechanism is different from the highly reverse-biased avalanche breakdown mechanism.

There are several reports on EL diodes fabricated with porous Si, where the EL intensity is nearly proportional to the current in the high current region (above the order of several hundreds mA/cm²),^{15,16,24,29,30} while it is proportional to a value which is larger than the square of the injection current at lower current densities (less than one hundred mA/cm²).^{24,29,30} The linear dependence of the EL intensity on the current density is consistent with a minority carrier injection mechanism.¹⁵ The nonlinear dependence may be ascribed to defect-associated recombination, even though its mechanism is not clear at this time.^{24,29,30}

In our study, the EL intensity dependence, which was a power greater than the cube of the current density, was observed in our experiment. We propose the following mechanism to explain our experimental results. Hot electrons are injected from the Pt-contacted electrode into the surface oxide layer of the Si nanocrystallites at forward bias. In our sample preparation, the residual oxygen could form the surface oxide layers even though the thermal annealing was basically performed in the ambient N₂ gas. Hence, the Si nanocrystallites are isolated from each other by the surface oxide layer. The hot electrons can excite electron-hole pairs by impact ionization at the Si nanocrystallite surface. In the porous Si, the

carriers are most likely transported with relatively long mean free paths because the porous structure can be recognized as wire-like structures. As a result, the minority carrier injection is the dominant mechanism. Nevertheless, in the nanocrystallites isolated by the surface oxide layers, electron-hole pair generation by impact ionization is remarkable because of shorter mean free paths. Chang et al. reported that the quantum efficiency of the impact ionization process by hot electrons passing through the oxide layer increases with increasing kinetic energies of the hot electrons, by applying higher voltage.³⁰ Their result supports our tentative model that the large nonlinearity of the EL intensity is caused by the dependence of the quantum efficiency of the impact ionization process on the hot electron energies. Therefore, the EL of our diode is due to the minority carrier (electron) injection and the electron-hole pair generation by the impact ionization, and successive radiative recombination. The above light-emitting mechanism of our EL diode is schematically described in Fig. 11.

Next, we discuss the reason for the lower peak position and broader width of the EL spectra compared to the PL spectra. First, in the PL measurements, monochromatic radiation (Ar⁺ laser: 2.54 eV) was used as an excitation source. On the other hand, in the EL measurement, the excitation sources were electrons accelerated by electric fields. Hence, in the Si nanocrystallite layer, which is a granular material composed of the oxidized Si nanocrystallites, the kinetic energy distribution of the electrons is presumably very wide, and should show a tail in the lower energy region. Accelerated electrons with kinetic energies of less than the green band photon energy level cause relative enhancement of the red EL band intensity. Second, we previously reported the influence of irradiation time and ambient gas on the green and red PL bands.¹⁰ The peak positions of both green and red PL bands did not shift with laser irradiation. However, the intensity of the green PL peak was quenched by irradiation of the excitation laser in the atmosphere, while the red PL peak intensity remained stable. The EL measurements were performed in the atmosphere. The Si nanocrystallite active layer was exposed to the air via the Pt semitransparent electrode. In addition, higher dissipation powers (more than 0.5 W) were necessary for excitation in the EL measurement, in contrast to that required for the laser irradiation in the PL measurements (10 mW). Therefore, we infer that the intensity of the green EL band was also quenched during accumulation of the emission signal. Third, it can be said that the green band emission (peaked around 2.1 eV) and the red band emission (peaked around 1.7 eV) are associated with "shallow" and "deep" localized states, respectively. Furthermore, in general, the capture cross section of the non-radiative center P_{NR} is described by the following formula:³²

$$P_{NR} = W_0(h\omega_0/kT) \exp(-(2R/R_c) - (E_A/kT^*)) \quad (1)$$

$$T^* = (h\omega_0/2k) \coth(h\omega_0/2kT), \quad (2)$$

where ω_0 , E_A , R , and R_c stand for the phonon frequency, activation energy of a localized state, distance between an electron and a non-radiative center, and extent of electron wave function, respectively. According to equ. (1), the shallower activation energies of the localized states are, the higher probabilities of the non-radiative recombinations are, with increasing temperature. In our experimental conditions, the measuring temperatures of the EL should be much higher than that of the PL, quenching of the light emitting associated with the shallow levels became remarkable in the EL measurements. We suggest that this is also one of the reasons why the EL spectra had 1.7 eV peak and 2.1 eV shoulder in Fig. 10 (a), though the PL spectra had 2.1 eV peaks and 1.7 eV shoulders. For the above reasons, the EL spectra peaks at the red region do not correspond to those of the PL. According to adiabatic approximation, the FWHM of the emission spectrum is proportional to the square root of the absolute temperature. Hence, our experimental results, where the Gaussian waveform width of the

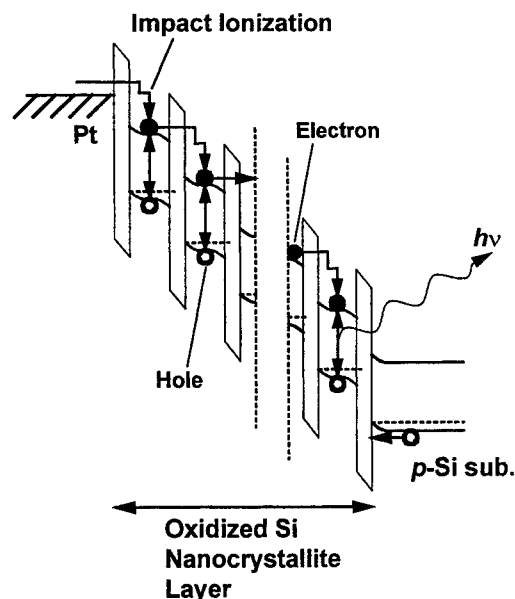


Fig.11 Schematic energy band diagram for the Si nanocrystallite active region of the EL diode.

EL was wider than that of the PL, are reasonable because dissipation powers (0.55-1.10 W) in the EL measurements were extremely high in comparison with the irradiated laser power (10 mW) in the PL measurements.

In the Si nanostructures, it is still under debate as to how the emission photon energies are governed by the quantum confinement effects.^{27,33} In contrast, it is well known that the absorption photon energies increase continuously with the decreasing size of the Si nanostructures, in accordance with the quantum confinement effects.³⁴

5. CONCLUSIONS

In conclusion, we studied an optimized condition in Si nanocrystallite formation by the PLA in inert background gas, varying processing parameters: pulse energy and width, inert gas pressure. The optimized process can prepare well-dispersed Si nanocrystallites without droplets and debris. Furthermore, we have elucidated the influence of the processing parameters on transition from amorphous-like thin films to well-dispersed nanocrystallites or coalesced nanocrystallites. It was found that there is a processing window of the inert background gas pressure where the quantum confinement effects for carriers become apparent.

We have realized visible EL at room temperature from Si nanocrystallite layers prepared by the PLA in reduced pressure inert background gas. In the forward-biased EL diodes, hot electrons are injected from the Pt electrode into the *p*-type Si nanocrystallite active layer. Furthermore, the EL intensity I_{EL} shows a nonlinear dependence on the current density j : $I_{EL} \propto j^m$, $m=3.5$. A possible mechanism of this emission is that the injected minority hot carriers (electrons) induce impact ionization and successive radiative recombination. Our fabrication method is compatible with the established Si VLSI technology because the PVD processing is suitable for successive film stacking and etching off, for the fine patterning process.

6. ACKNOWLEDGEMENTS

The authors would like to express their thanks to Associate Professor. K. Matsuishi (Univ. of Tsukuba) and Professor. T. Arai (Ishinomaki Sensyu Univ.) for their fruitful discussion of the optical properties and spectroscopy of mesoscopic materials. This work was partially conducted in the program "Advanced Photon Processing and Measurement Technologies" of the Agency of Industrial Science and Technology, the Ministry of International Trade and Industry, consigned to the R&D Institute for Photonics Engineering from the New Energy and Industrial Technology Development Organization (NEDO).

7. REFERENCES

1. S. Furukawa and T. Miyasato, Jpn. J. Appl. Phys. 27, L2207 (1988).
2. H. Takagi, H. Ogawa, Y. Yamazaki, A. Ishizaki, and T. Nakagiri, Appl. Phys. Lett. 56, 2379 (1990).
3. L. T. Canham, Appl. Phys. Lett. 57, 1046 (1990).
4. D. J. Lockwood, *Light Emission in Silicon from Physics to Devices*, Academic Press, San Diego, 1998.
5. D. B. Chrisey and G. K. Hubler, *Pulsed Laser Deposition of Thin Films*, John Wiley, New York, 1994.
6. D. H. Lowndes, D. B. Deohegan, A. A. Puretzky, D. P. Norton, and C. M. Rouleau, Science 273, 898 (1996).
7. E. Werwa, A. A. Seraphin, L. A. Chiu, Chuxin Zhou, and K. D. Kolenbrander, Appl. Phys. Lett. 64, 1821 (1994).
8. T. Makimura, Y. Kunii, and K. Murakami, Jpn. J. Appl. Phys. 35, 4780 (1996).
9. T. Yoshida, S. Takeyama, Y. Yamada, and K. Mutoh, Appl. Phys. Lett. 68, 1772 (1996).
10. Y. Yamada, T. Orii, I. Umezu, S. Takeyama, and T. Yoshida, Jpn. J. Appl. Phys. 35, 1361 (1996).
11. D. B. Geohegan, A. A. Puretzky, G. Duscher, and S. Pennycook, Appl. Phys. Lett. 72, 2987 (1998).
12. Z. C. Feng and R. Tsu, *Porous Silicon*, World Scientific, Singapore, 1994.
13. A. Halimaoui, C. Oules, G. Bomchil, A. Bsiesy, F. Gaspard, R. Herino, M. Ligeon, and F. Muller, Appl. Phys. Lett. 59, 304 (1991).
14. A. Richter, P. Steiner, F. Kozlowski, and W. Lang, IEEE Electron Device Lett. EDL-12, 691 (1991).
15. N. Koshida and H. Koyama, Appl. Phys. Lett. 60, 347 (1992).
16. P. Steiner, F. Kozlowski, and W. Lang, IEEE Electron Device Lett. EDL-14, 317 (1993).
17. Z. Chen, G. Bosman, and R. Ochoa, Appl. Phys. Lett. 62, 708 (1993).
18. P. Steiner, F. Kozlowski, and W. Lang, Appl. Phys. Lett. 62, 2700 (1993).
19. J. Linnros and N. Lalic, Appl. Phys. Lett. 66, 3048 (1995).

20. N. Lalic and J. Linnors, *J. Appl. Phys.* 80, 5971 (1996).
21. T. Futagi, T. Matsumoto, M. Katsuno, Y. Ohta, H. Mimura, and K. Kitamura, *Jpn. J. Appl. Phys.* 31, L616 (1992).
22. P. C. Sercel, D. Kwon, T. Vilbrandt, W. D. Yang, J. Hautala, J. D. Cohen, and Hao Lee, *Appl. Phys. Lett.* 68, 684 (1996).
23. F. Namavar, H. P. Maruska, and N. M. Kalkhoran, *Appl. Phys. Lett.* 60, 2514 (1992).
24. H. P. Maruska, F. Namavar, and N. M. Kalkhoran, *Appl. Phys. Lett.* 61, 1338 (1992).
25. G. G. Qin, A. P. Li, B. R. Zhang, and B-C Li, *J. Appl. Phys.* 78, 2006 (1995).
26. A. G. Nassiopoulos, S. Grigoropoulos, and D. Papadimitriou, *Appl. Phys. Lett.* 69, 2267 (1996).
27. Z. H. Lu, D. J. Lockwood, and J.-M. Baribeau, *Nature* 378, 258 (1995).
28. R. Newman, *Phys. Rev.* 100, 700 (1955).
29. J. Xu and J. Steckl, *IEEE Electron Device Letters* 15, 507 (1994).
30. T. Oguro, H. Koyama, T. Ozaki, and N. Koshida, *J. Appl. Phys.* 81, 1407 (1997).
31. C. Chang, C. Hu, R. W. Brodersen, *J. Appl. Phys.* 57, 302 (1985).
32. R. Engelman and J. Jortner, *Molecular Phys.* 18, 145 (1970).
33. H. Mizuno, H. Koyama, and Koshida, *Appl. Phys. Lett.* 69, 3779 (1996).
34. Y. Kanemitsu, H. Uto, Y. Masumoto, T. Matsumoto, T. Futagi, H. Mimura, *Phys. Rev. B* 48, 2827 (1993).

Advances in Pulsed Laser Deposition growth of nitride thin films

Félix E. Fernández, Manuel Pumarol, Antonio Martínez^a, Weiyi Jia,
Yanyung Wang, Edgardo Rodríguez, Houssam A. Mourad

Dept. of Physics, Univ. of Puerto Rico, Mayaguez, PR 00681

^a Dept. of Physics, Univ. of Puerto Rico, Rio Piedras, PR 00931

ABSTRACT

Pulsed Laser Deposition of nitride semiconductor films offers an alternative to more usual techniques, such as MOCVD and MBE. PLD can produce good quality films at reduced growth temperatures. Rapid progress has been achieved in the last few years, including demonstrations of epitaxial growth of GaN directly on sapphire. Work on PLD of direct-transition III-nitrides is briefly reviewed and our recent results for these materials are presented. Growth of these nitrides requires provision of nitrogen in a reactive form, which is usually supplied by NH_3 gas flow. With the approach described here, reactive nitrogen is provided in an atomic beam, which has the advantage of reducing dependence on substrate temperature to surmount the kinetic energy barrier for formation, while eliminating a source of hydrogen during growth. Films grown from ceramic GaN targets are compared with those grown from liquid Ga. The latter method can offer better control of unintentional doping. InN films were also grown directly from In metal targets, with very good results in terms of stoichiometry and crystalline quality. AlN films were grown from ceramic AlN targets, with excellent texture at reduced temperatures. Results are presented for crystal structure (with both in-plane and off-plane XRD), composition, and surface morphology. Optical properties were studied by transmission and luminescence spectroscopy.

Keywords: PLD, nitrides, AlN, GaN, InN, atomic nitrogen, luminescence

1. INTRODUCTION

Of the many techniques which have been employed to date for thin film growth of wide bandgap nitrides, metal-organic vapor-phase epitaxy (MOVPE) and molecular beam epitaxy assisted by reactive nitrogen (RMBE) have produced the best quality materials. Both require the use of fairly high substrate temperatures ($\sim 1,000^\circ\text{C}$ for MOVPE, and over 700°C for RMBE) in order to surmount the kinetic barrier for formation.¹ While MOVPE can produce high quality material and is suitable for large area coverage, the very high temperatures required can limit its applicability. The lower temperatures in RMBE are possible through provision of well controlled reactive-N species. A very recent review of RMBE results for GaN growth has been given by Mohammad et al.² The low (thermal) energies of the evaporated metal species in MBE imply that high substrate temperatures must still be used. An alternative which might allow further lowering of the growth temperature is the provision of higher energy of the metal species, such as can be achieved by pulsed laser deposition (PLD). While PLD growth of AlN in particular has been attempted in the past,^{3,4} these efforts, in which AlN targets were ablated in vacuum or in a N_2 atmosphere, resulted in nitrogen-deficient films with substantial oxygen contamination. More recent work, with improved targets and technique, has led to high quality epitaxial AlN films grown by PLD on sapphire at 800°C .⁵ A more reactive source for the nitrogen could allow further lowering of the growth temperature for AlN and other nitrides, which would be highly desirable. For this purpose, similar approaches to those recently employed in RMBE could be suitable. One of the better alternatives in RMBE appears to be the provision of a low-energy atomic nitrogen beam during growth.^{6,7} One advantage over ion beam sources is that less damage of the growing film should occur. Accordingly, we are exploring wide bandgap nitride growth by PLD assisted with atomic-N beam.

For well known reasons, GaN films are of greater current interest than AlN. While AlN was started earlier with PLD, for the simple reason that ceramic targets were available for AlN and not for GaN, the recent availability of GaN targets has stimulated work by several groups. Epitaxial GaN films have recently been grown directly on (001) sapphire at 950°C .⁸ In this case, a ceramic GaN target was used, and supplementary nitrogen was provided by NH_3 background. The alternative approach

of using a liquid Ga target in PLD has also been used, in this case to grow oriented GaN films on fused quartz substrates via a ZnO buffer layer.⁹

Up to now there has been little interest in indium nitride as a useful semiconductor material, in part due to the difficulty in growing high quality material. As a result, much less is known about InN than about the other III-nitrides. However, very recent Monte Carlo calculations of electron transport properties for InN suggest that these could be better than for GaN and AlN.¹⁰ This has stimulated our interest in growing this material via the approach described here, which appears quite suitable for producing films of adequate quality at low temperatures. The current report offers a summary of our results for AlN, GaN, and InN films. We have used a ceramic AlN target for AlN growth and elemental metal targets for GaN and InN growth.

2. FILM GROWTH

For this work, a dedicated 12" diameter vacuum chamber was built, designed to allow horizontal arrangement of targets, which allows the use of liquid targets, and installation of an atomic nitrogen source (Oxford Applied Research MPD21), which provides reactive nitrogen to the growing film. The source breaks up the nitrogen molecules by coupling RF energy to the N₂ gas flowing through a pyrolytic BN crucible. The crucible has an exit plate with 36 orifices, each 0.5 mm in diameter. In order to maintain stable operation of the source, the RF power is feedback controlled by monitoring the 3s⁴P → 3p⁴S^o nitrogen plasma emission line. This type of source has been shown to generate an appreciable flux on neutral N atoms.¹¹ Furthermore, the ion content of gas exiting the source is very small.¹² Flow of ultra-high purity N₂ into our source is measured through an mass flow controller with digital readout.

The chamber is pumped by a 550 l/s turbomolecular pump, which permits a relatively low working pressure (~ 10⁻⁴ Torr) even at the highest flow rates used for the N source (up to 15 sccm), and background pressures down to the 10⁻⁹ Torr range. Pressure is measured with a nude-type BA ion gauge. Gas composition can be monitored with a residual gas analyzer detecting masses up to 200 amu. A shutter is used to cover the substrate while the target is initially ablated. Substrates can be heated up to 1,000° C using a PID feedback-controlled molybdenum heater. The laser used in our PLD system is an excimer laser (Lambda Physik Compex 110) operating with KrF (248 nm emission), and incident at 45° to the target normal, after passing the focusing lens (f = 350 mm) and chamber window, both of which are fused quartz. In order to further reduce losses, the lens is AR-coated for 248 nm.

A ceramic AlN target (99.99 % pure) was used for most of the AlN depositions. A less pure target (99.8 %) was used for some initial depositions. We experimented also using an Al sputtering target (99.9995% pure). While films with very good composition and structure were obtained for both ceramic and metallic targets, we opted to discontinue use of the Al target due to aluminum droplet inclusion. The high reflectivity of aluminum at the laser wavelength used (248 nm) implies that extremely high intensities must be used.

For the results reported here GaN depositions were executed with a liquid Ga target (99.9999 % purity). We have also used a ceramic GaN target (99.99% purity) with good results in terms of structure and morphology, but fewer particulates at the resulting films were observed when using the liquid Ga target. We also considered that unintentional impurity inclusion could be reduced in this way. The GaN films grown from the ceramic GaN target had a slight yellow coloration, whereas the ones grown from Ga metal were colorless.

For the InN depositions a metallic In target (99.999 % purity) was used. All reported purities are those quoted by the manufacturer and, particularly in the case of ceramic targets, might not include certain organic contaminants which can be deleterious for our application as a source of oxygen. The gallium and indium were kept in alumina crucibles placed directly under the substrate. In all cases the target was rotated by means of a stepping motor. For the solid targets this was done to avoid crater formation. In the case of liquid Ga, we found that more efficient evaporation, and a more stable plume, was obtained when the target was rotated. This was associated with the use of the atomic N source. Our previous experience shows that some nitridation occurs at the Ga target surface, even though it is not in the direct path of the N beam in our setup. Thus we conjecture that a thin GaN layer is forming on the liquid Ga, and that rotation can allow for sufficient time for "renewal" of this layer.

The substrates used for our depositions were (0001) sapphire, (111) Si, and fused quartz. Substrates were cleaned by ultrasonic baths in trichloroethylene, acetone, and methanol, and blow dried with extra-dry nitrogen. Pyrolytic graphite

substrates on which samples for RBS analysis were deposited were used as received. Substrates were attached to the substrate heater with a silver suspension in ethanol. The target-substrate distance was 6 cm for all depositions.

Background pressures for all runs were in the 10^{-8} Torr range. Before each deposition, N_2 was admitted to the N-source, the plasma in the N-source was ignited and stabilized with the RF impedance matching circuit. After this, power control was transferred to the plasma controller. In general, for deposition runs reported here, N_2 flow was 10 sccm, forward RF power was ~ 250 W, and reflected power was ~ 2 W. For some samples deposited more recently, including all GaN films for which we include detailed results here, forward RF power to the N-source was increased to nearly 400 W. Ignition of the plasma causes a discernible drop of the mass 28 signal in the RGA, with a corresponding increase in mass 14, even though in our set-up there is no line-of-sight link between the RGA sensor and the N-source exit apertures. We were also able to observe a decrease in the residual water partial pressure, with a corresponding increase in atomic hydrogen (1) and hydroxyl (17) pressures. Hence it appears that plasma formation is also causing the breakup of residual water molecules. This is unfortunate, since it can lead to formation of trace oxides and hydrides in the growing film. The estimated average laser fluence (and pulse energy) at the targets was 1.8 J/cm^2 (120 mJ pulses) for In, 10 J/cm^2 (180 mJ pulses) for AlN, and over $\sim 25 \text{ J/cm}^2$ (190 mJ pulses) for liquid Ga. These estimates assume a completely clean window, which is not the case particularly near the end of longer deposition runs. The very high values required for Ga are associated with high reflectivity in the uv. Although uv reflectivity for AlN is not as high, after some ablation the exposed surface becomes partially metallized, which explains the high fluences required in this case also. In general, ceramic targets such as AlN and GaN must be ablated prior to deposition in order to obtain stable yields. Ablation of elemental Ga and In produces a deep purple plume in each case. Pulse frequency for all depositions reported here was from 1 to 5 pps. The target-sample distance was kept at 6 cm for nearly all depositions reported here. This relatively long distance (for PLD) results in reduced growth rates, but we opted for it in order to have a larger central area with more nearly uniform thickness, which was preferable for many of the characterization measurements undertaken.

For each of the materials, films were grown at a range of temperatures. Temperatures were measured with a thermocouple attached directly to the heater. Calibrations were performed by placing a second thermocouple directly on substrate surfaces. We estimate that quoted readout temperatures could be in error by as much as 20°C . Temperature stability, on the other hand, is very good, particularly at higher temperatures. AlN and GaN films were grown at temperatures from ambient to 700°C . InN has much higher equilibrium vapor pressures than either GaN or AlN.¹³ InN films were grown at temperatures from ambient to 400°C . At higher temperatures the reported InN vapor pressures in nitrogen ambient are greater than the chamber working pressure for our depositions. In fact, a deposition run with a substrate temperature of $\sim 500^\circ\text{C}$ resulted in no film growth whatsoever. From this observation, growth rates for InN are expected to be strongly affected by temperature.

With our growth method film composition will depend on a number of parameters, including beam fluence and pulse energy, pulse repetition rate, gas flow and RF power for the nitrogen gun, and substrate temperature. Gas pressure itself is not expected to be of consequence because the mean free path at the growth pressures is much longer than the distances involved (\sim few cm). Due to the many factors involved and their interdependence, attainment of conditions for correct film stoichiometry can require many experiments. Film microstructure can depend on all factors affecting adatom arrival rate and kinetic energy, and, of course, substrate properties and temperature. We have attempted mainly to establish conditions suitable for correct stoichiometry, while exploring a range of temperatures which can be considered low for growth of the III-nitrides. At this stage, our efforts include growth directly on common substrates, without use of buffer layers. Clearly, there is ample room for improvement of structural perfection by using substrates more closely matched to the materials, or suitable buffer layers. Our work is continuing using the latter route, and results will be presented in the near future.

For all the target materials used in this work laser fluence levels at the target surface had to be relatively high, due to high reflectivity and/or high heat conductivity. For initial deposition runs we adopted fluences high enough to produce clear plasma plumes, which in any case are much dimmer and smaller than those familiar to PLD practitioners growing ceramic superconductors and ferroelectrics. This is due both to the nature of the target materials themselves and to the chamber growth pressures, which are 2 to 3 orders of magnitude lower in our case than for usual reactive PLD conditions. Considering only film composition, arrival rate of reactive nitrogen species (either to the growing film surface itself or to a nearby interaction region) should limit the growth rate of stoichiometric material. Hence, other conditions being fixed, one can expect deviation from stoichiometry in the direction of excess metal for fluences or beam energies that are too high. When stoichiometric or nearly stoichiometric targets are used this is less of a problem, as the target plume itself will contain reactive nitrogen or metal-nitrogen species. When pure metal targets are used, since all reactive nitrogen must be provided by the N source, the upper limit for

growth rate will be much lower. For AlN and GaN, this implies a choice between the faster growth rate attainable with ceramic targets and the higher target material purity possible with elemental targets. For InN there is currently no choice but In metal targets, as ceramic InN targets are, as far as we know, not available. Metallic targets can offer additional flexibility for alloy deposition. Their cost is much lower than that of ceramic targets of any reasonable purity. Other factors, such as density of particulates which are incorporated in the film during growth, will influence the choice of target. As explained before, we have favored use liquid Ga for GaN growth and of a ceramic AlN target for AlN growth.

3. CHARACTERIZATION RESULTS

3.1. Indium nitride films

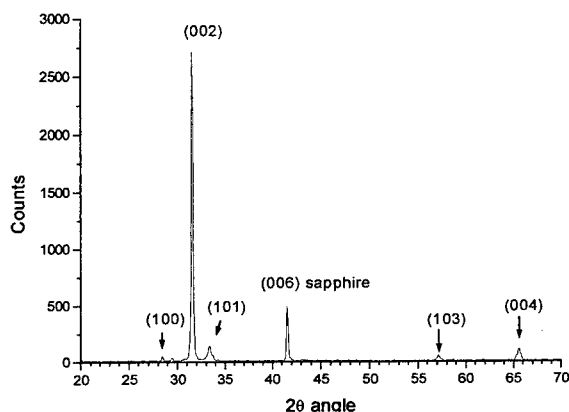


Figure 1 XRD scan for InN/sapphire sample.

for most of the films for which the following results are reported. Repetition rate was maintained at 2 pulses per second, although some samples were grown at 1 pulse per second. Thicknesses of a number of samples were determined from stylus profilometer scans on deposited steps, model fits to light transmission spectra, and from RBS results. From these, average growth rates obtained for the InN films are of $\sim 2 \text{ \AA/pulse}$, which at the repetition rates used translates into $\sim 1.4 \text{ }\mu\text{m/hr}$, a rather high value for nitride growth via PVD.

Indium nitride films were grown on polished sapphire wafers cut along the c plane, (111) oriented silicon wafers, and

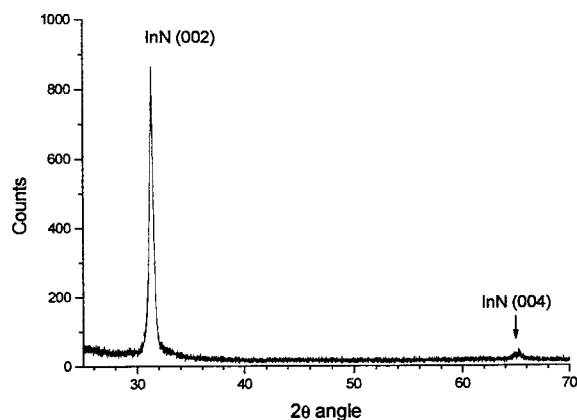


Figure 2 XRD scan for InN film on fused quartz, grown at ambient temperature.

All films were grown from an In metal target, as explained above. Initial films grown at fluences which were too high ($\sim 4 \text{ J/cm}^2$) resulted in deposits which were clearly metallic. Reduced fluences (to $\sim 2 \text{ J/cm}^2$) and increased RF power at the nitrogen cracker produced optical quality films with good transmission in the red part of the spectrum. Very thin films are yellow, and thicker films have a deep brown color, as InN begins to absorb heavily in the orange. Film composition was determined by Rutherford Backscattering Spectroscopy with 2 MeV particles on a film grown at 350°C on pyrolytic graphite. Excluding oxygen content, which appears to be mainly and equally on the substrate and film surfaces, the results show a composition of $50.8 \pm 0.8 \text{ at.\% In}$, and $49.2 \pm 0.8 \text{ at.\% N}$. There is likely some oxygen in the film, however, although it is probably of no more than a few percent. Subsequently, we further reduced the fluence, in order to enhance opportunity for nitridation. Fluence was $\sim 1.8 \text{ J/cm}^2$, and pulse energy $\sim 120 \text{ mJ}$

polished fused quartz. X-ray diffraction scans of the samples were obtained with a Siemens D-5000 θ - 2θ diffractometer. It is found that InN tends to orient rather well with its c-axis parallel to the growth direction, even on severely mismatched substrates, or on an amorphous substrate such as fused quartz. The scan on Figure 1 shows the XRD result for a InN film grown on (001) sapphire at 350°C . The strong (002) reflection, and presence of the second order reflection (004) show clear preferred orientation of the c-axis parallel to the sapphire c-axis. Other orientations are present to a much lesser degree, as indicated by very weak peaks corresponding to other reflections. Even on an amorphous substrate and grown at room temperature, the InN film grows with good preferred orientation with its c axis in the growth direction. This is evidenced in Figure 2, which shows the XRD scan of a sample grown at ambient temperature on fused quartz. Only the (00n) diffraction peaks are observable.

Observation of the InN films with an optical microscope in reflected light and with the Differential Interference Contrast (Nomarski) technique showed smooth surfaces with few particulates. Some films were further examined with an Atomic Force Microscope (Parker Scientific Instruments Autoprobe CP). Surface morphology was revealed as consisting of domes with fairly regular sizes of $\sim 0.1 \mu\text{m}$, possibly due to columnar growth. In some cases the angles between dome sides are clearly indicative of hexagonal geometry. Surface roughness measured for these films (rms values) was $\sim 150 \text{ \AA}$, but can be much lower, as evidenced by a film grown on sapphire at 250°C (Figure 3). In this case surface roughness measured on general areas with sizes of over $0.5 \mu\text{m}$ and line scans of $\sim 1 \mu\text{m}$ was just over 12 \AA rms. This value is essentially the same obtained for scans directly on the dome surfaces. For films grown on fused quartz substrates roughness was greater ($\sim 250 \text{ \AA}$ rms).



Figure 3 AFM image of InN film grown on sapphire at 250°C . Imaged zone is $1.2 \mu\text{m}$ on the side.

Optical transmission and absorbance spectra (190 to $1,100 \text{ nm}$) were obtained with a spectrophotometer for films grown on sapphire and fused glass. In order to avoid thickness variations due to nonuniform coverage common in fixed-spot PLD, these measurements were taken without moving the sample. Using extrema of the transmission spectrum and a model fit calculation to its transparent portion, film thickness and refractive index were determined. The absorption coefficient of the material was then calculated from the absorbance spectra using the thickness value. Approximate corrections for reflection losses were included. Scattering losses are not included in this simple treatment. Results obtained for a $2,700 \text{ \AA}$ film are presented in Figure 4 in

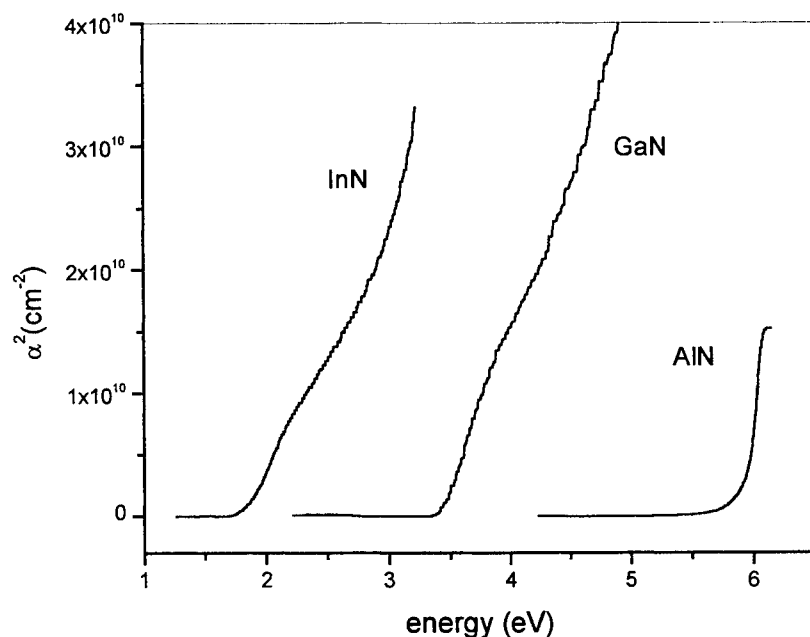


Figure 4 Square of the absorption coefficient as a function of photon energy, calculated from InN, GaN, and AlN thin films. Approximate linearity indicates a direct transition bandgap. Onset of linearity is at bandgap energy value.

terms of the square of the absorption coefficient as a function of the photon energy. The approximately linear behavior for energies over $\sim 1.9 \text{ eV}$ evidences the direct-transition bandgap of the film material, as the absorption coefficient is then proportional to $(E - E_{\text{gap}})^{1/2}$. The result $E_{\text{gap}} \approx 1.9 \text{ eV}$ is in good agreement with the known bandgap for InN (1.89 eV).

Due to the direct-transition bandgap of InN, just as for GaN and AlN, strong band-to-band electronic transitions near the zone center are expected. This is evidenced in the previous results, with the sudden onset of absorption at photon energies over the bandgap value. However, unlike AlN and GaN, for which strong luminescence has been observed, the inverted process, emission from the conduction band to the valence band has not, to our knowledge, been observed for InN. The fact implies that high density of various defects, and therefore high

density of free electrons and holes may exist in currently available material. Elucidation of the existence and nature of those defects, and their elimination or reduction are a key issue in order to improve the quality of this semiconductor and turn it into a commercially interesting material. In order to initiate this study with our films, photoluminescence (PL) experiments were conducted with a variety of samples on all of the different substrates used.

For the spectroscopic studies, a SPEX 1403 double grating spectrometer equipped with a Hamamatsu R 928 photomultiplier and a photon counting system was used. The samples were mounted onto the cooling finger of a He closed cycle refrigerator, providing temperature control from 8K to 300 K. For absorption measurements in this setup, a halogen tungsten lamp was used. For luminescence measurements, the emission line at 488nm of a Coherent Innova 300 Ar laser was used to excite the InN samples. In order to reject plasma lines from the laser, an interference bandpass filter at 488 was used. Great care was taken in order to reduce all possible spurious results from unexpected luminescence. Only well-characterized high quality optics, mirrors, and quartz lenses were used. Luminescence from the oxidized surface of the copper sample mount, cold finger heater varnish, thermal conducting grease, vacuum pump oil, and all substrates used were measured for reference in order to avoid confusion with luminescence signal from samples.

Although the characterization of the InN/sapphire samples previously described showed the films were of good quality, we were unable to clearly identify sample luminescence. Unfortunately, strong emissions from sapphire substrate contamination with Cr (acquired from Insaco) or Ti (acquired from ESCOTE B.V.) impeded us from reaching any meaningful conclusion. The Si substrates did not show any detectable luminescence background. The weak luminescence observed from InN/Si samples was then assigned to emission from the InN thin film. For this measurement, the spectrometer slits were set to 0.5 mm, and integration time for each data point was 5 seconds in order to get a sufficiently high signal-to-noise ratio. The luminescence band observed is very broad, peaking at ~ 650nm and ~ 675nm for spectra taken at 8K and room temperature respectively, as shown in Figure 5. For InN/fused quartz the signal is much weaker; Figure 6 shows the PL signal at 8K. We note that the band edge luminescence for InN, if it was observed, should be near 650 nm.

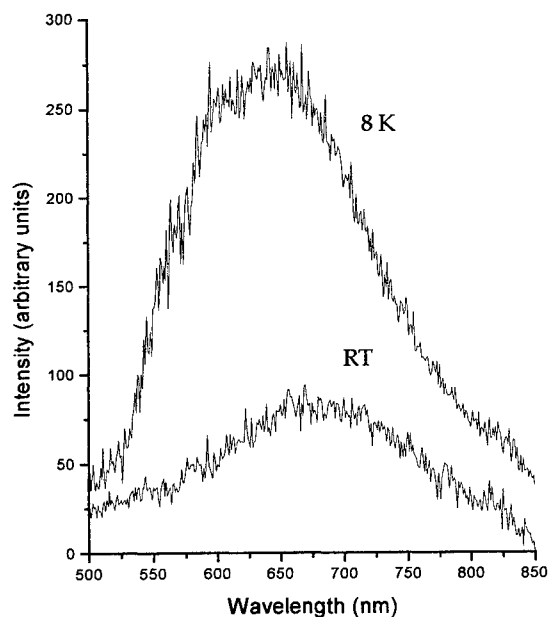


Figure 5 Luminescence spectra for InN/Si sample, taken at room temperature and 8 K.

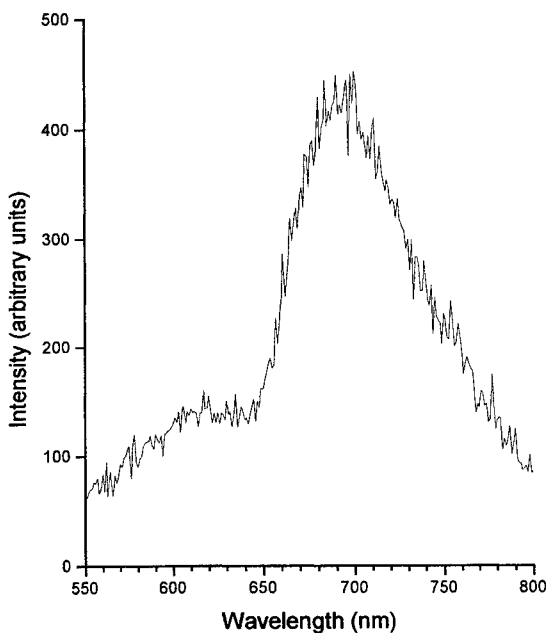


Figure 6 Luminescence spectra for InN/fused quartz, taken at 8 K.

The weakness and broadness of the luminescence for InN are not fully understood. These are certainly associated with high concentrations of various defects, and with the effect of conduction electrons and holes. Recombination from various defect donor-acceptors and their strong coupling with phonon modes is an important physical source responsible for luminescence

broadening and quenching. High density of free carriers is another important physical reason for broadening and quenching of PL, and our InN films do show relatively high conductivity. Up to now this is common with InN films grown by any suitable technique, and is attributed to high concentrations of nitrogen vacancies. It has been reported in investigations of Raman scattering of GaN that LO phonon modes were seriously broadened and barely identified in highly conducting samples.¹⁴ In contrast, sharp and quite intense LO phonon peaks can be easily observed in GaN samples with electron density less than $10^{18}/\text{cm}^3$.¹⁵ Plasmon oscillations have the nature of longitudinal waves, and can strongly couple with LO phonons. It is assumed that similar processes could happen with luminescence from various defect centers. Plasma could efficiently shield the excitation of the bound excitons, or significantly quench the luminescence.

It was found in addition that the luminescence spectrum of our InN/Si samples does depend on position of the excited region on the samples. The samples prepared by PLD are not uniform in thickness, and defect concentration can depend on film thickness. Also, although analytical results may be consistent with overall chemical stoichiometry, this may not be true in microscopic regions.

3.2 Gallium nitride films

We initially grew GaN films trying both liquid Ga and ceramic GaN targets. Use of the former had been our original plan due to unavailability of solid GaN targets, as the material is very difficult to fabricate into sintered powder pieces. However, ceramic GaN targets became commercially available at about the time we started growing GaN films. Growth rates for samples grown from one of these GaN targets were high, but the films had a yellow tinge, probably indicative of highly defective material. Although this could probably be improved, cohesion of the target was not very good and we judged the resulting particulate density over the films not to be very satisfactory. Finally, as unintentional doping of the material is a crucial issue, and the purity of the ceramic GaN targets could not approach that of elemental Ga, we opted to dedicate our efforts for the time being to growth from a liquid Ga target.

Films were grown from a liquid gallium pool, at the conditions described before, and with a repetition rate of 5 pps. Sapphire substrates were used for nearly all samples. The resulting films were transparent, and without any coloration. In some cases samples grown at higher temperature (700°C) showed hazy white portions, possibly associated with uneven heating patterns, but we have not yet done a detailed study of these features. A film grown at 500°C on pyrolytic graphite was analyzed by RBS (Figure 7). The low energy tails are due to thickness non-uniformity in the film, possibly caused by columnar or island growth. Overall composition was determined to be 48.2 ± 0.8 at.% gallium, 48.3 ± 0.8 at.% nitrogen, and 3.4 ± 0.3 at.% oxygen. Most of the oxygen is on the film surface, and, as usual, there must be oxygen at the carbon substrate. However, it was not possible to quantify how much oxygen is at the film interior. A sample grown on sapphire was analyzed by Auger Electron

Spectroscopy. The sample was probed at various depths by sputtering the film with an Ar ion beam. No contaminants other than oxygen and superficial carbon were detected in the sample. However, the oxygen signal, while substantially reduced with respect to that at the surface region, is still clearly present inside the film. This confirms the RBS finding. While the oxygen content is small in the film, possibly of order 1 at.% or less, we are currently attempting to improve on this by further reducing background pressure in the growth chamber. Due to the slow growth rates employed, there is opportunity for oxygen to be included, and a likely source is residual water. On the other hand, increased structural perfection could help reduce oxygen incorporation if this is associated with interstitial regions.

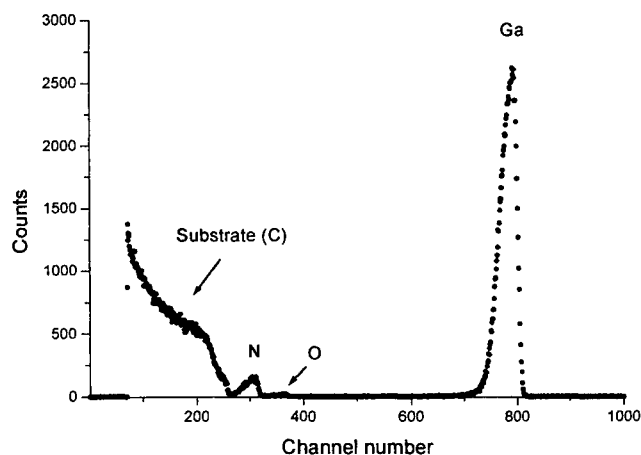


Figure 7 RBS spectrum for GaN sample on pyrolytic graphite. The GaN is nominally stoichiometric.

From the RBS results, light transmission measurements, and profilometer scans on deposited steps, film thicknesses were determined for several samples. From these in turn, we estimate the average

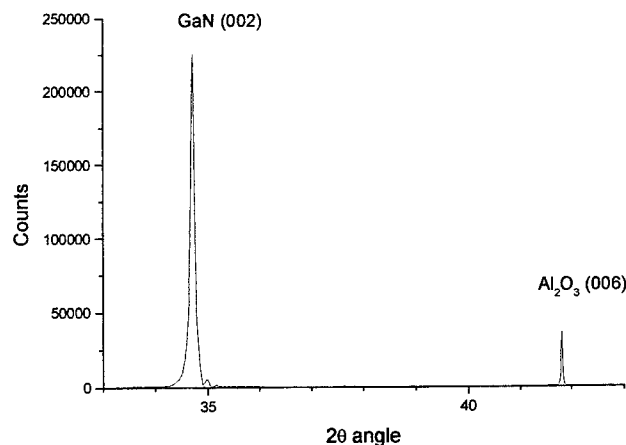


Figure 8 XRD scan for GaN sample grown at 700°C on (001)-cut polished sapphire.

quite clear, particularly for the (101) and (100) reflections. The small spots correspond to the sapphire substrate.

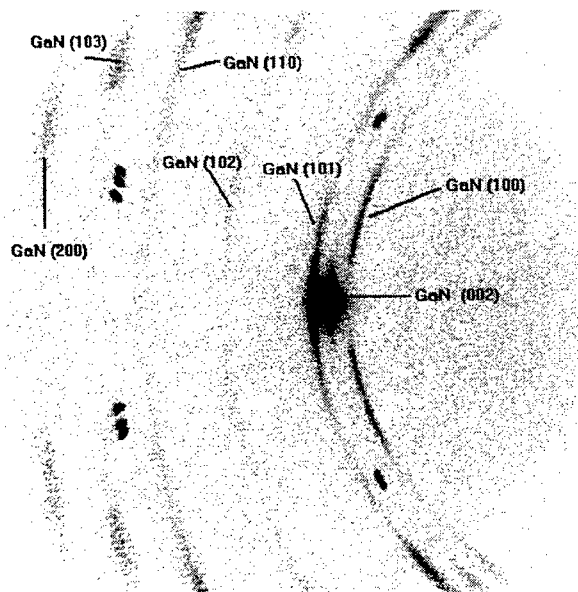


Figure 9 Wide-angle XRD image for GaN/sapphire sample grown at 600°C.

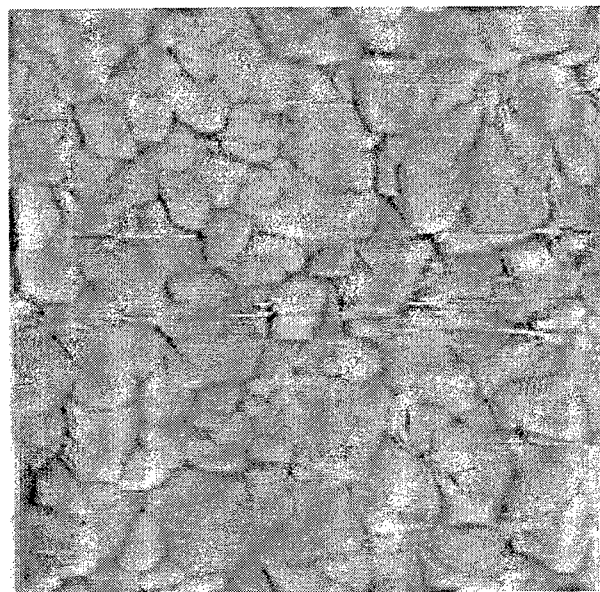


Figure 10 AFM image of GaN/sapphire sample. The image has been field-flattened in order to show angular relationships between domes. Imaged zone side is 1 μm.

deposition rate at our growth conditions to have been ~ 0.07 Å/pulse. At the repetition rate used for the GaN depositions (5 pps) this implies a relatively modest growth rate of 0.12 μm/hr. This is comparable to rates obtained by other PVD techniques.

XRD analysis of films grown on (001) sapphire demonstrate very good orientation, with the film c axis parallel to that of the substrate. As shown in Figure 8 for a sample grown at 700°C the only strong diffraction peak from the film corresponds to the (002) reflection. The sample is polycrystalline, as weak peaks corresponding to other orientations can actually be observed in the θ -2 θ scans, although this is not evident in Figure 8. The film crystallographic texture becomes clearer in a wide-field diffraction image taken with a Siemens General Area Detector diffractometer (Figure 9). The image was taken with Cu K α radiation for a sample grown at 600°C. A strong broad spot for the GaN (002) reflection dominates, but short arcs corresponding to other GaN reflections are

When observed with an optical microscope, the GaN samples showed unremarkable surfaces, except that some of them had a substantial concentration of particulates. This did not consist of gallium droplets, but of irregularly shaped deposits, possibly originating from GaN forming directly on the target surface. At the highest magnifications (X 1000) a few small (sub-micron) hexagonal structures were observed. Examination with the AFM revealed a pattern of domes broadly similar in sizes to that described previously for the InN samples, but much less organized. The sample in Figure 10 was grown at 600°C. Surface roughness (~ 250 Å rms) was higher for the GaN surfaces than for InN.

Optical transmission and absorbance spectra were taken for the GaN samples. Thickness and absorption coefficient were determined as described above for the InN samples, with approximate correction for reflectance losses. Figure 4 shows the result obtained for a sample grown at 600°C, at a portion with a thickness of 2150 Å. The square of the absorption coefficient is given as a function of the photon energy. Approximately linear increase for α^2 after ~3.4 eV is in agreement with the known direct band gap energy of 3.39 eV.

Refractive index for the GaN films was calculated from model fits to the transmission data of one of the samples. The values obtained decrease from 2.51 at 400 nm to 2.18 at 950 nm. These values are lower than published ones.¹⁶ This is to be expected, as the film had a thickness of only 2,150 Å and was polycrystalline.

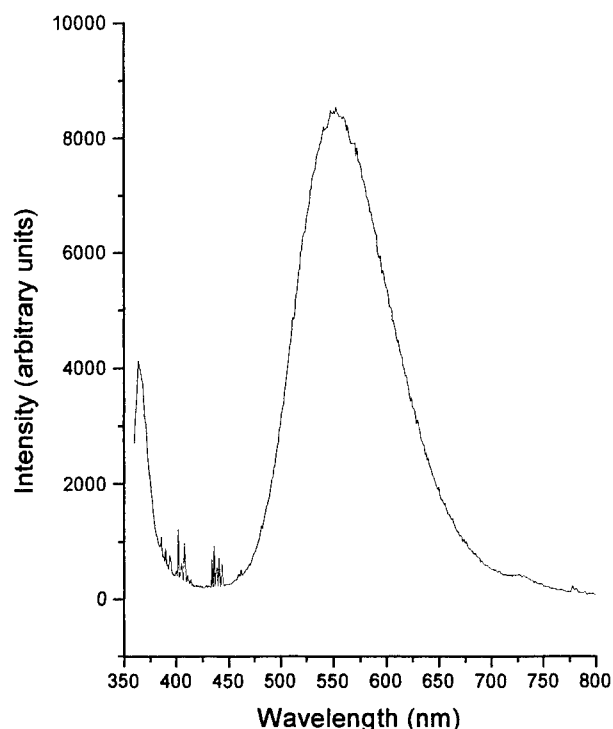


Figure 11 PL spectrum at room temperature for GaN/sapphire sample grown at 600°C. Sharp peaks in the 375 - 450 nm region are laser plasma lines and are unrelated to the sample.

compared to that at ambient temperature. On the other hand, there are variations in both peak position and intensity with probe beam location on the samples. This is associated with slight intensity changes in the uv emission band. The defects causing the yellow-green luminescence may have local density variations, possibly associated with thickness effects. In general, considering that the samples are rather thin, which can be associated with larger defect areal densities, and that all films were grown directly on sapphire substrates (without buffer layers) at relatively low temperatures, the PL results are quite encouraging.

3.3 Aluminum nitride films

Aluminum nitride films were grown from the ceramic AlN target at conditions described above, and with a repetition rate of 3 pps. The resulting films were completely clear and smooth at all growth temperatures, including ambient temperature. It was possible to obtain nominally stoichiometric films (50 ± 1 at. % for both Al and N, excluding oxygen), as determined by RBS of films deposited on pyrolytic graphite. However, composition results varied with different samples which were analyzed, some of which were nitrogen-deficient, while at least one was aluminum-deficient. This variety could be due to target condition, which is difficult to replicate due to the hardness of the material. The RBS results also showed substantial amounts

Luminescence experiments were performed for GaN samples with thicknesses of ~2,000 Å by excitation with the 351.6 nm line of the Ar laser. Essentially the same setup was used as for the InN measurements described before, except that a fused quartz prism had to be used in order to aid in separating the desired exciting line from the very intense plasma lines present. For all samples, a broad emission peaking by 550 to 560 nm (yellow-green) was observed. This was in fact strong enough (unfortunately) to be seen by the unaided eye. Band-edge luminescence was detected in the uv, at 365 nm. The result shown as an example in Figure 11 is the luminescence spectrum taken at ambient temperature for a sample grown at 600°C. The yellow emission appears to be associated with dislocations at crystallite edges, and the emission characteristics we observe in the full spectrum are similar to those known for specular films.¹⁷ For every sample tested, there is little difference in intensity of the uv band between spectra obtained at ambient temperature and at 8K. This is to be expected from the direct-transition nature of GaN. On the other hand, the visible luminescence band does become much more intense at the lower temperature, as radiationless transitions become impeded. Peak position for the band-edge luminescence shifts to shorter wavelengths at 8K, the corresponding energy increase being approximately 65 meV. This is in agreement with the results for bandgap dependence on temperature published by Monemar.¹⁸ There is slight or no shift of the yellow-green luminescence band at 8K,

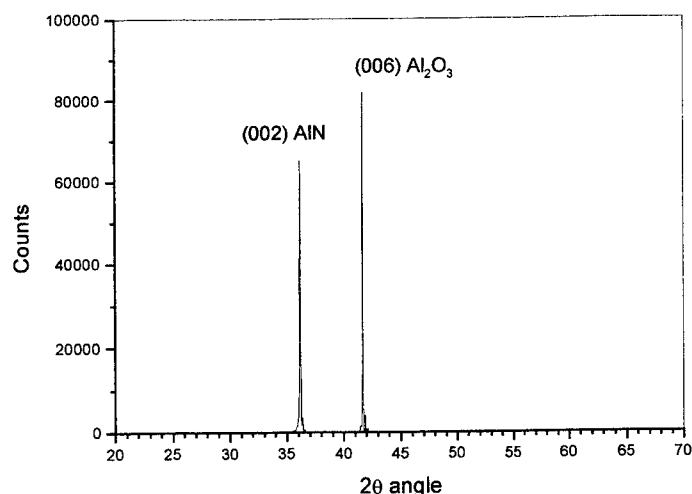


Figure 12 XRD scan for AlN/sapphire sample grown at 600°C.

values of 0.16 $\mu\text{m/hr}$. The yield, at least for thin films, can probably be increased substantially by increasing the repetition rate, but we have not verified this yet. We believe this will be so because of the nitrogen content of the target itself in this case, as opposed to the use of metallic targets for our growth of InN and GaN.

XRD study of the AlN films showed preferred (001) orientation on (111) Si and very strong orientation on (001) sapphire. Figure 12 shows a θ -2 θ scan of a $\sim 2,600$ Å thick film grown on sapphire at 600°C. Only the AlN (002) diffraction peak is observable from the film material. With thicker samples it is possible to observe weaker reflections, particularly those corresponding to (101) and (102). A wide-field diffraction image of the same sample (Figure 13) confirms the small mosaic orientation spread of the AlN film. All diffraction spots corresponding to the film are very short arcs. The smaller spots in the image correspond to the substrate.

Microscopic observation of the AlN films up to X1000 magnification showed surfaces without salient features, except for particulate inclusions attributed to target fragmentation. Observation with the AFM (Figure 14) reveals a domed structure similar to that seen before for the InN films, except that these appear more regular and are larger than in the InN case. Also, for the AlN film, more of the angles between dome interfaces at multiple junctions are 120°, suggesting the underlying hexagonal geometry. The roughness of this film is ~ 280 Å rms: substantially larger than for the InN films, which may be due to the greater height of the domes for the AlN.

As for the other materials grown, transmission and absorbance spectra were obtained for the AlN films deposited on sapphire. The square of the absorption coefficient vs. photon energy for one of the films is presented in Figure 4. As this film is relatively thick (6680 Å), the instrument saturates early in comparison to the InN and GaN results. In any case, the linear portion of the plot begins at ~ 6 eV, not at 6.2 eV,

of oxygen at the top and at the substrate-film interface. Oxygen concentrations of as much as a few atomic percent could be present in the film. This is not unexpected, due to the probability of oxygen-containing impurities in the target, and the large Gibbs free energy of formation for Al_2O_3 ($\Delta_f G^\circ = -1,582.3$ kJ/mol) in comparison to that for AlN ($\Delta_f G^\circ = -287.0$ kJ/mol).¹⁹

From the same variety of thickness measurement techniques as used for the InN and GaN films, plus model fits to multispectral ellipsometry measurements taken with a Woollam M-44 ellipsometer, we estimate the average growth rate for the AlN films to have been ~ 0.15 Å/pulse. However, this is subject to some variability, being as high as 0.2 Å/pulse for very thin ($\sim 1,000$ Å) films, and as low as 0.13 Å/pulse for thicker ($\sim 7,000$ Å) films. We believe this is due to target conditioning. At the repetition rate used (3 pps), the intermediate growth rate implies

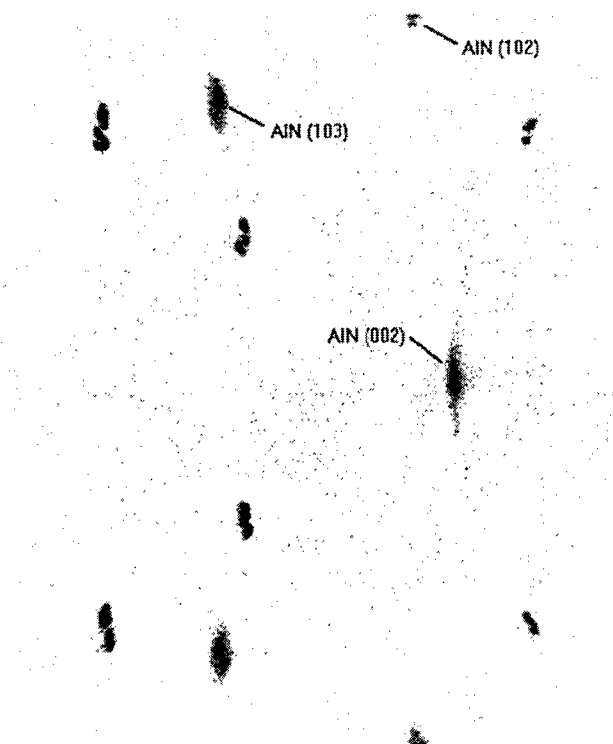


Figure 13 Wide-angle XRD image taken for the same AlN/sapphire as the θ -2 θ scan in Figure 12.

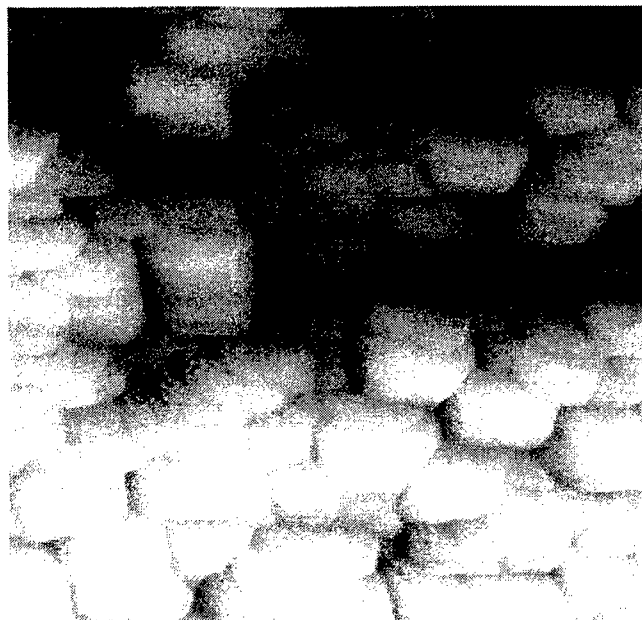


Figure 14 AFM image of an AlN/sapphire sample grown at 700°C. The imaged square has a 1 μm side.

materials. This shows that in fact the GaN film oriented itself on the template provided by the InN film. We expect even better results for similar structures grown on (111) Si or on amorphous materials with a better match to the nitrides in terms of expansion coefficients.

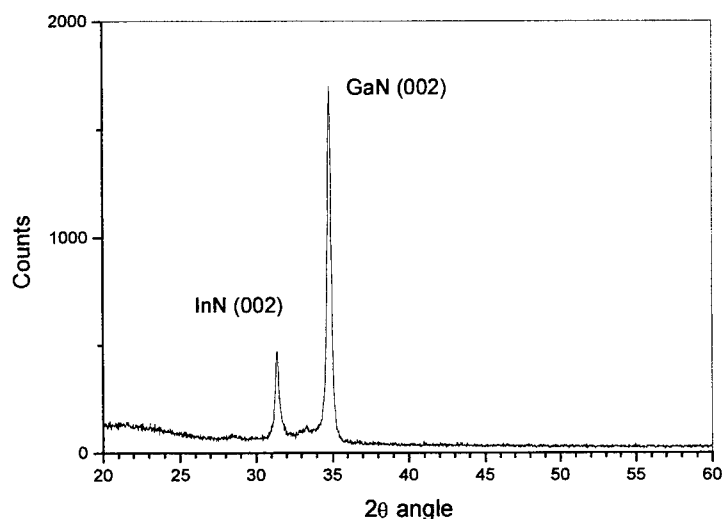


Figure 15 XRD scan for GaN/InN/glass structure. The InN film is $\sim 1,000\text{\AA}$ thick, while the GaN film is $\sim 2,300\text{\AA}$ thick.

which is the commonly accepted value for the AlN bandgap, although values as low as 5.8 eV have been reported. From model fits to the transmission measurements the refractive index for AlN was obtained over its transparent visible and near uv region. The values obtained decrease asymptotically from 2.34 at 275 nm to 2.05 after 800 nm. These are slightly lower than critically reviewed values.²⁰

We were unable to perform luminescence studies for the AlN films due to lack of an intense enough excitation source with wavelength shorter than 200 nm.

3.4 GaN on glass with InN buffer layer

Taking advantage of the ease with which InN orients on (111) Si or SiO_2 , it is possible to use it as a buffer material in order to grow oriented GaN on these substrates. While InN tends to peel on the latter, we grew a 2,300 \AA GaN film directly on a 1,000 \AA InN layer grown on a fused silica substrate. The InN was grown at 350°C, while the GaN was grown at 650°C. The XRD scan for this sample is shown in Figure 15; only the (002) reflections are observed for both

4. CONCLUSIONS

InN, GaN, and AlN thin films were grown by PLD assisted by atomic nitrogen beam. InN and GaN were grown from elemental metal targets. It was proved possible to grow good quality films at reduced temperatures with respect to standard techniques. Growth of InN films in particular was easily accomplished at low temperatures, with the c-axis as the preferred growth direction, on a variety of substrates including amorphous ones. AlN with excellent texture was grown on sapphire at temperatures as low as 600°C. Luminescence properties of GaN films grown directly on sapphire at similar temperatures are satisfactory, and there is a clear route for improvement by using the more readily textured InN or AlN as buffer layers.

ACKNOWLEDGMENTS

We gratefully acknowledge the support for this work by NASA, under Grant NCCW-0088, and by the U.S. Office of Naval Research, under Grant No. N00014-96-1-0929. The RBS measurements were performed at the University of Arizona by L. McIntyre and his associates.

REFERENCES

1. N. Newman *et al.*, Mat. Res. Soc. Symp. Proc. **339** (1994) 483.
2. S.N. Mohammad *et al.*, MRS Bulletin, February 1997, Pag. 22.
3. P. Battacharya and D. Bose, Jpn. J. Appl. Phys. **30** (1991) L1750.
4. G.F. Restrepo, Thesis, Univ. of Puerto Rico-RUM, Mayagüez (1994).
5. R.D. Vispute, H. Wu, and J. Narayan, Appl. Phys. Lett. **67** (1995) 1549.
6. W.E. Hoke *et al.*, J. Cryst. Growth **111** (1991) 1024.
7. H. Liu *et al.*, J. Appl. Phys., **74** (1993) 6124.
8. R.D. Vispute *et al.*, Appl. Phys. Lett. **71** (1997) 102
9. R.F. Xiao *et al.*, J. Appl. Phys. **80** (1996) 4226.
10. S.K. O'Leary *et al.*, J. Appl. Phys. **83** (1997) 1.
11. R.P. Vaudo, J.W. Cook, and J.F. Schetzina, J. Crystal Growth **138** (1994) 430.
12. W.E. Hoke, P.J. Lemonias, and D.G. Weir, J. Cryst. Growth **111** (1991) 1024.
13. T. Matsukoa, H. Tanaka, T. Sasaki, and A. Katsui, International Symposium on GaAs and Related Compounds, Inst. Phys. Conf. **106** (1989) 141.
14. N. E. Christensen and P. Perlin, in "Semiconductors and Semimetals, Vol. 50, J.I. Pankove and T.D. Moustakas (eds.) Chapter 13, Academic Press (1998) p. 409.
15. T. Kozawa, T. Kachi, H. Taga, and M. Hashimoto, J. Appl. Phys. **75** (1994) 1098.
16. E. Ejder, Phys. Stat. Sol. A **6** (1971) 445.
17. F.A. Ponce, in *GaN and Related Materials*, S.J. Pearton (ed.), Gordon and Breach (1997) pag.141.
18. B. Monemar, Phys. Rev. B **10** (1974) 676.
19. *Handbook of Chemistry and Physics*, D.R. Lide (ed.), 77th edition, CRC Press, Boca Raton (1996), pag. 5-4.
20. S. Loughin and H. French, in *Handbook of Optical Constants of Solids*, Vol. III, E. Palik (ed.), Academic Press (1998) pag. 373.

Pulsed laser deposition of high-quality tribological coatings

Gouri Radhakrishnan, Paul M. Adams, and Donna M. Speckman

The Aerospace Corporation, MS M2/271

P.O. Box 92957, Los Angeles, CA 90009

ABSTRACT

Advanced materials are being designed and tested for use on ball bearings that have wide-ranging applications in almost any type of spacecraft. There has been considerable interest in "hard" or wear-resistant coatings for protecting steel surfaces present in bearing components. Titanium carbide (TiC) has received serious consideration as a wear-resistant coating material that could be suitable for use in such applications. At present, the commercially available process for the deposition of TiC involves heating the steel substrates to fairly high temperatures (≥ 1200 K). High-temperature coating deposition is not desirable for applications involving steel substrates as it results in a softening of the steels. This further necessitates post-deposition heat-treatments for re-hardening the steel and re-polishing the coating. This paper will describe the use of *Pulsed Laser Deposition* (PLD) to deposit high-quality thin films of TiC on bearing steels *at room temperature*. Such a process eliminates the problems associated with high temperature deposition, and the costs and complexities involved in the post-deposition heat treatment of steels. To develop an understanding of the deposition process, the plasma generated by laser ablation has been investigated using time-resolved emission spectroscopy. The PLD of TiC films on bearing steels, the material properties of these films, and the spectroscopy of the ablated plume will be discussed.

Keywords: Titanium carbide, pulsed laser deposition, hard coatings

1. INTRODUCTION

Ball bearings are used in a variety of moving mechanical assemblies employed in spacecraft. Typical examples include antennas, scanning mirrors and other optical components, momentum wheels and control moment gyroscopes. Ball bearings have traditionally been manufactured from all-steel components and employ oils or greases for their lubrication. The use of hard coatings on the steel substrates to protect them against wear and provide low friction is an approach that has received serious consideration.¹ Carbides and nitrides of various elements, in particular the transition metals are excellent candidates for hard coatings.² One of the hard materials that has been the focus of numerous groups is titanium carbide (TiC). It has already been used on ball bearings in a few European spacecraft missions,¹ and has drawn wide-spread interest due to its potential applications as a hard coating.

Although a variety of techniques are potentially available for the deposition of thin films of hard materials, the deposition of thin films on steel substrates poses certain specific problems that arise at temperatures exceeding 600 K.³ At these temperatures, diffusion of the alloying elements of the steel into the coating can occur. Additionally, high deposition temperatures cause the steels to soften. This necessitates that the steels be re-hardened, which in turn calls for a high-temperature annealing process. The coated components also have to undergo re-polishing to correct for any dimensional changes that can occur as a result of the residual stress in the coating following the high-temperature deposition step, and the post-deposition heat treatment applied for re-hardening. The numerous corrective process steps that are required because of the elevated temperatures needed for the coating deposition are both expensive and time consuming. Hence, in spite of high growth rates, on the order of 10 $\mu\text{m/h}$, offered by high-temperature deposition processes such as CVD, a low temperature deposition process is very attractive for depositions on steels. In recent years, pulsed laser deposition (PLD) has become increasingly popular as a viable low temperature deposition process for numerous materials including TiC.⁴⁻¹⁰

This study focuses on the room temperature PLD growth of TiC on two commonly used bearing steels, namely 440 C and 52100 steels. The TiC films have been characterized using a variety of analytical techniques. In addition, the plume spectroscopy is being investigated in an attempt to correlate the properties and components of the laser ablated plume to those of the deposited film. In-situ spectroscopic diagnostics can provide valuable information on the generation of reactive species in the ablated plume which subsequently lead to the nucleation and growth of the desired film.

2. EXPERIMENTAL PROCEDURES

An excimer laser (Lambda Physik, LPX 210 I) operating at 248 nm with KrF was used for the ablation of a TiC target. Laser fluences were in the range of 6-10 J/cm². For film depositions, the laser was typically operated at 50 Hz. All depositions were carried out with the substrate at room temperature and in a vacuum chamber which typically had a base pressure in the range of 6×10^{-6} to 1×10^{-5} Pa. TiC films have been deposited on 52100 and 440 C steel flats, as well as on commercially available steel thrust-bearing raceways. The steel flats were polished to an optical quality finish after machining. The substrates were ultrasonicated in heptane twice for 15 min periods, and then dried in dry N₂, prior to being loaded into the vacuum chamber.

A scanning electron microscope (SEM) (JEOL, JSM 840) was used for investigating film morphology over large areas. Information on the morphology over more localized areas was provided by atomic force microscopy (AFM) measurements made with the Autoprobe M5 from Park Scientific Instruments.

The X-ray photoelectron spectroscopy (XPS) system (Surface Science Instruments [SSI] X-probe) used monochromatic Al-K _{α} X-rays. The X-rays were focused to give a spot size of 600 μ m on the sample surface. Analyzer pass energies of 150 and 50 eV were used for wide scans and high-resolution spectra respectively. The XPS analysis chamber was pumped by an ion pump and has a base pressure of 1×10^{-8} Pa. For the XPS analysis, individual high-resolution scans of the C 1s, O 1s, and Ti 2p core levels were used. The core level spectra were deconvoluted into peaks comprising sums of Gaussian and Lorentzian functions. Relative atomic amounts were calculated from estimates of the electron escape depth and Scofield sensitivity factors (for Ti, the 2p_{3/2} component was used). Ar⁺ ions at 2 kV were used for sputter etching the samples to reveal composition information in the bulk of the film. (A sputter rate of 0.25 nm/min was estimated using a reference tantalum oxide sample of known thickness).

Specimens were analyzed by X-ray diffraction (XRD) using copper radiation and a computer controlled Philips Electronics Instruments Model 3720 vertical powder diffractometer equipped with a theta compensating slit and graphite crystal diffracted-beam monochromator.

Sample preparation for plan view transmission electron microscopy (TEM) involved grinding the sample to a thickness of 100 μ m from the back side, punching out 3 mm diameter disks, dimpling from the back side to a small perforation with 20 μ m and 3 μ m Al₂O₃, followed by final polishing with 1 μ m, 0.3 μ m, and 0.05 μ m Al₂O₃. The sample was then ion-milled from the back side, using Ar⁺ ions at 5 kV for 3.5 hours, followed by ion milling from both sides for 10 minutes. The sample was examined with a Philips Electronics EM-420 TEM operated at 120 kV. Selected area electron diffraction (SAED) was performed on approximately 0.3 μ m diameter areas. Dark field TEM was performed on the (111) and the (200) reflections of TiC.

The hardness and modulus of elasticity of the TiC films were measured with a nanoindenter (Nano Indenter II from Nano Instruments) equipped with a Berkovitch diamond tip and capable of employing loads of 50 nN to 500 mN. The nanoindenter was calibrated using a fused silica reference. Using the continuous stiffness capability on this indenter, the film and the substrate could be probed continuously during a single indentation. This mode allows the measurement of hardness as a function of depth and makes it possible to measure the mechanical properties of both the film and the substrate.

A gated, intensified, air-cooled, CCD system (Princeton Instruments) was used to detect the emission from species in the ablated plasma plume. The CCD was mounted at the output plane of a PI 320I, f/4 spectrometer. The spectrometer was equipped with three gratings with 150 grooves/mm, 600 grooves/mm, and 2400 grooves/mm. The first two gratings were both blazed at 300 nm, while the 2400 groove grating was blazed in the UV at 250 nm. One end of a silica optical fiber having a vertical slit was aligned to the entrance slit of the spectrometer, while its other end was mounted on a translation stage and could image different locations of the plume. A UV grade 0.2 m focal length lens (f 0.5) was mounted in front of a quartz window, such that it was parallel to the plane of the plume at the point where the laser was focused on to the target. Measurements reported here were made using 20 μ m slits on the spectrometer. The laser was the master trigger for these experiments and the 5V, 15 μ s, square wave trigger pulse was used to trigger the high-voltage pulse generator (PG-200). The excimer laser light pulse has a FWHM of 30 ns, and is delayed 1330 ns from the leading edge of the laser trigger pulse.

Gate widths of 25 ns were employed. Gate delays were set with respect to the light pulse detected by a fast (2ns) photodiode. In measurements shown here, the CCD accumulated signal from 40 laser pulses.

3. RESULTS AND DISCUSSION

Highly uniform films of TiC were deposited on the different steel substrates (polished flats and curved raceways) at a growth rate of $\sim 0.3 \mu\text{m/h}$. The morphology of the PLD grown TiC films on 52100 steel substrates is shown in Figs. 1 and 2. Fig. 1 shows a large-area SEM photograph of a typical as-grown TiC film on a 52100 steel flat. The film is very smooth over the entire area, and essentially particle-free. A low particle density is very important for wear-resistant applications of hard coatings involving ball bearings. This is because the surface finish of bearings is on the order of $0.1 \mu\text{m}$, and hard particles, if present, can damage the bearing surfaces and induce wear on the surfaces. Shown in Fig. 2 is an AFM image of the as-grown TiC film, that was taken to obtain a quantitative assessment of the surface roughness. The average and RMS surface roughness values of TiC on a 52100 substrate, corresponding to a surface area of $112 \mu\text{m}^2$, were 1.2 nm and 1.6 nm respectively, indicating a very smooth surface for the deposited film.

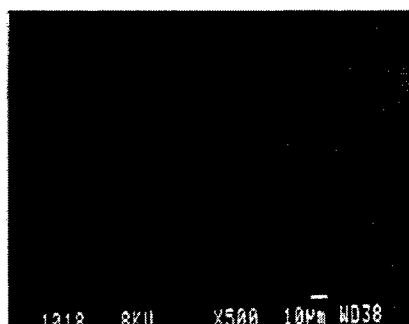


Figure 1 Surface morphology of a 300 nm TiC film deposited on 52100 steel shown by a low-magnification (X500) SEM image.

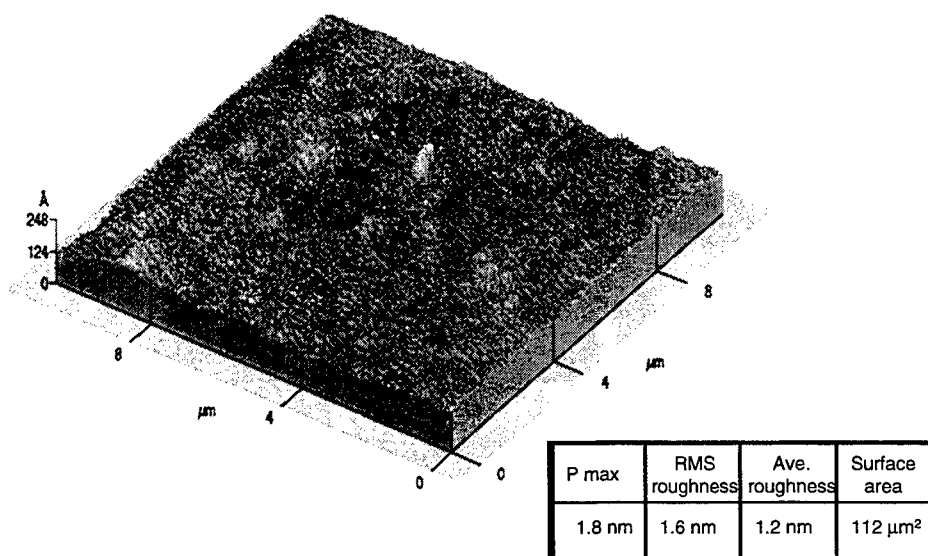


Figure 2 Atomic force microscopy image of a $10.6 \times 10.6 \mu\text{m}$ area of a 300 nm TiC film on 52100 steel. P max defines the height of the highest surface feature in the area investigated.

The chemical composition of these TiC films was established by X-ray photoelectron spectroscopy (XPS). Details are reported elsewhere.¹¹ The results indicate an absence of the TiO₂ features^{11,12} after brief sputtering, which is a clear indication that oxidized Ti on the surface of the film has been removed. In addition, only a single C 1s component at 282.0 eV is observed following sputter-etching the sample. A C/Ti ratio of 0.9, after sputtering, is consistent with the formation of typically sub-stoichiometric TiC² with some preferential sputtering of C relative to Ti. The post-sputter O concentration in these films doesn't quite fall to zero, but approaches the O concentration that has been measured for sputtered and annealed single-crystal TiC using the same XPS system.¹³ There may be some substitution of O for C in the lattice, but no distinct phase of TiO. The TEM data described below lend strong supporting evidence that the bulk of these films indeed consists of pure TiC.

X-ray diffraction (XRD) measurements were conducted on these films. Fig. 3 shows the X-ray diffraction pattern of TiC films on a 52100 steel substrate. A broad (111) TiC peak was observed at a 2θ of 35.5° . Unfortunately, other peaks due to TiC were obscured by the carbide phases in the steel substrates. Similar results were observed for TiC on 440 C steel. The crystallite size of PLD-TiC from both the TiC/52100 and TiC/440 C X-ray diffraction scans was estimated to be ~ 7.5 nm. This calculation was based on the XRD line widths and the Scherrer Equation.

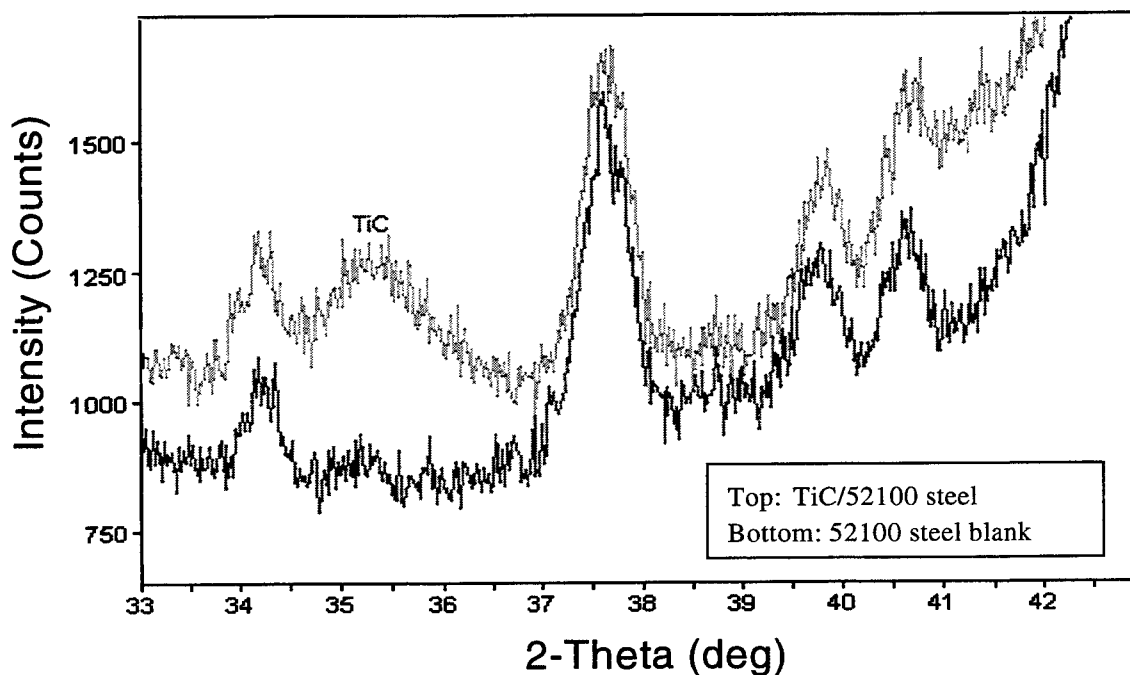


Figure 3 X-ray diffraction of a 300 nm film of TiC on 52100 steel.

To learn more about the crystallinity of the film, plan view TEM was performed on TiC films grown on both 52100 and 440 C steel substrates, as discussed in a previous paper.¹¹ The films are polycrystalline and randomly oriented as discerned from the SAED ring patterns. There are excellent correlations between the observed d-spacings of TiC on 52100 and 440 C, and the reference values from the powder diffraction file (PDF) of TiC. These are listed in Table 1. The relative intensities of the observed and literature values of the diffraction lines are provided in parentheses. The crystallite size was determined from the dark field TEM and was found to be in the range of 3-17 nm. This is consistent with the crystallite size estimated from the X-ray diffraction data.

Table 1 A comparison of the lattice-spacings of PLD-TiC on 52100 and 440 C steel substrates as measured from the SAED patterns in TEM with reference powder diffraction values; relative intensities are shown in parentheses.

Observed d-spacings (Å) TiC/52100 (SAED, this work)	Observed d-spacings (Å) TiC/440 C (SAED, this work)	PDF 32-1383 TiC d-spacings (Å)
2.55 (70)	2.59 (70)	2.499 (78)
2.16 (100)	2.18 (100)	2.164 (100)
1.53 (70)	1.54 (70)	1.530 (60)
1.32 (50)	1.29 (50)	1.305 (30)
1.26 (50)		1.249 (17)
1.10 (40)	1.09 (40)	1.082 (10)
0.98 (50)	0.98 (50)	0.993 (13)

Nanoindentation measurements were taken at multiple locations on TiC films deposited on 52100 steel substrates. The hardness and modulus of a 200 nm TiC film on 52100 steel are 30 ± 3 GPa and 430 ± 30 respectively, as measured at a depth corresponding to roughly 10% of the film thickness. The measured values approach those for bulk TiC.² At depths exceeding 250 nm, the hardness and modulus start approaching those of the respective substrates. A more detailed description of these measurements is provided elsewhere.¹¹

Figure 4 shows a schematic of the experimental set-up used for the spectroscopic measurements. Both the spatial and temporal dependence of the plasma emission generated by ablation of the TiC target are under investigation and some results are discussed below.

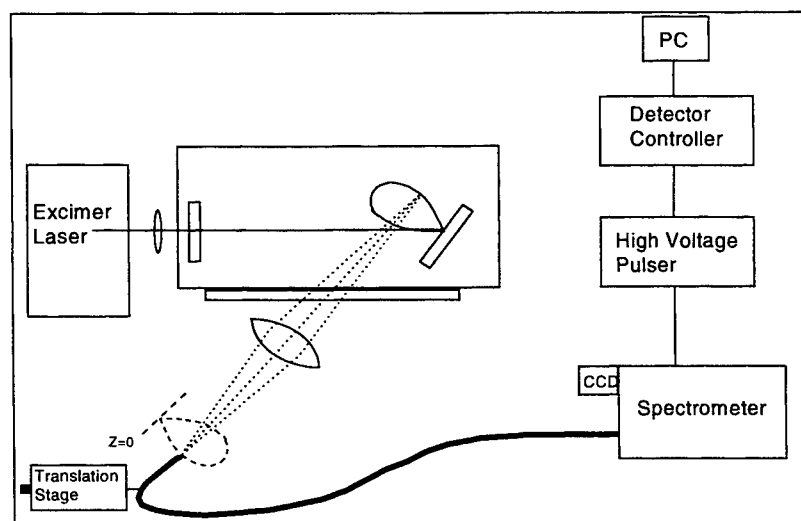


Figure 4 Schematic of experimental setup for in-situ spectroscopic detection during TiC ablation.

The UV emission at the target surface (defined as $z = 0$) consists essentially of a continuum and broad peaks. The plasma emission changes dramatically as a function of distance from the target, and both the onset of emission and the maxima at different distances change, reflecting the velocities of different plume species. At a fixed gate delay, time-resolved emission can be measured as a function of distance from the target. Figure 5 shows a low-resolution spectrum obtained with a 600 groove/nm grating, centered at a wavelength of 350 nm. This spectral region was selected because it contains numerous emission lines due to excited neutrals and ions of Ti.^{14,15} As seen from the spectrum, several of the observed lines originate from singly-charged Ti II ions, but some of the neutral Ti I lines are also observed. High-resolution spectra taken with a 2400 groove/mm grating indicate a significant broadening of emission lines close to the target, which decreases with increasing distance from the target. For the Ti II lines, a spectral linewidth of 0.6 nm was observed at $z \leq 2$ mm.

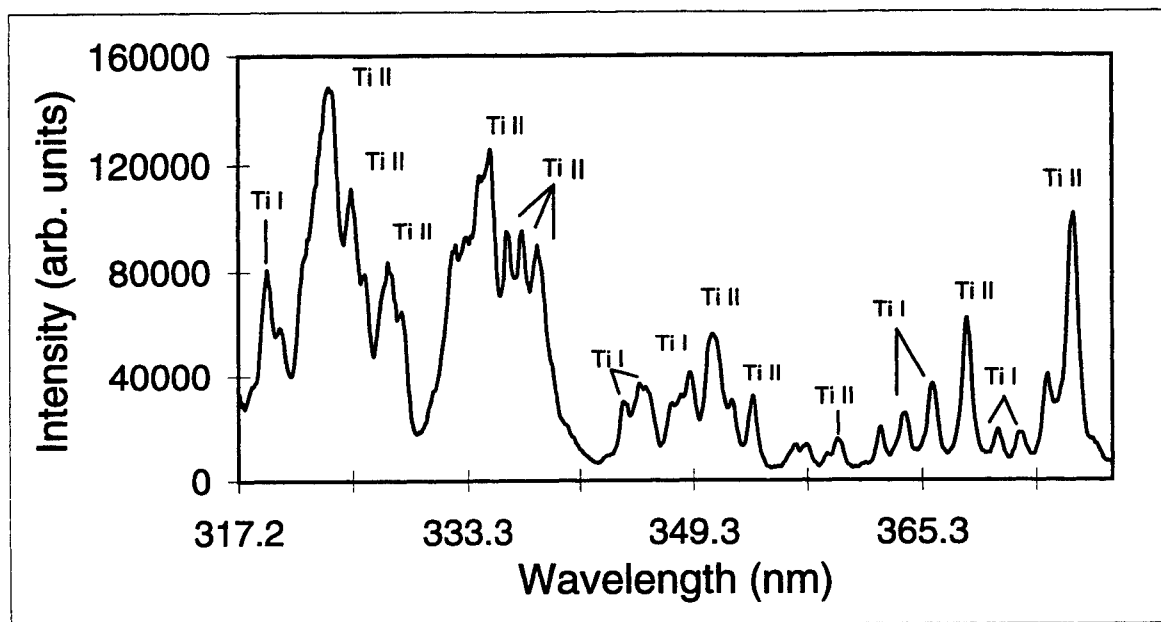


Figure 5 Low-resolution spectra measured using a 600 groove/nm grating showing Ti I and Ti II spectral lines. This spectrum was taken at a distance of 5 mm from the target, and at a delay of 170 ns from the leading edge of the laser pulse. The laser fluence was 6.3 J/cm^2 .

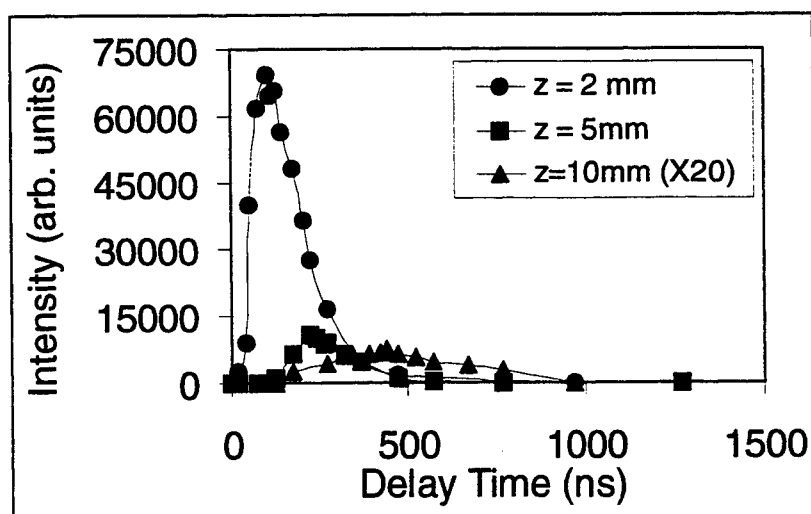


Figure 6 Time-resolved emission from the Ti II line at 368.5 nm measured at distances of 2, 5, and 10 mm from the surface of the TiC target. The laser fluence was 8 J/cm^2 and the repetition rate was 2 Hz.

Time-resolved emission intensity of the Ti II ion at 368.5 nm was measured at distances of 2 mm, 5 mm, and 10 mm from the target surface. The results are shown in Figure 6. From these measurements, an estimate of the plasma axial front velocity (the expansion velocity perpendicular to the target surface) can be made. The velocity of the Ti II ion, calculated using the maxima of emission shown here, is $2.2 \pm 0.1 \times 10^4$ m/s. The accuracy of these measurements is limited by the spatial resolution that can be achieved with the imaging system. It must also be noted that this derivation of velocity is not entirely accurate, as the emission measurements cannot deconvolute contributions from species that are behind, and/or in front of the focal plane. The ion velocities determined here are consistent with measurements made for other PLD-generated ions.¹⁶⁻¹⁸ Emission from neutral and ionic C species in the plume is still under investigation. These data, when available will offer some interesting insight into the chemistry following ablation and the key components in the plume that are responsible for film growth.

4. CONCLUSIONS

Thin films of TiC have been deposited at room temperature on 52100 and 440 C steel substrates using pulsed laser deposition. The films are uniform, essentially particle free, and have a very low average surface roughness of 1.2 nm with an RMS value of 1.6 nm. TEM measurements have shown a precise one-to-one correspondence between measured d-spacings and the literature values for TiC and a crystallite size of 3-17 nm. Nanoindentation measurements indicate that the mechanical properties of these TiC films, namely, their high hardness and elastic modulus, are quite useful for wear protection. In-situ spectroscopic measurements have identified both singly charged Ti ions and Ti neutrals as components of the ablated plume. The axial velocity of the Ti II ion has been estimated from time-resolved emission measurements to be $\sim 2.2 \times 10^4$ m/s. The successful deposition of these coatings at room temperature on bearing steels eliminates the problems that occur during conventional high temperature deposition of coatings on steels and is of tremendous practical value to ball bearings for spacecraft and other applications.

ACKNOWLEDGMENTS

Funding for this work was provided by The Aerospace Corporation's IR&D program.

REFERENCES

1. J. Boving and H.E. Hintermann, "Wear-resistant hard titanium carbide coatings," *Tribology International*, **23**, pp. 129-133, 1990 and references therein.
2. Louis E. Toth, *Transition Metal Carbides and Nitrides*, New York, NY, Academic Press, 1971.
3. G. Radhakrishnan, J.C. Uht, W. Park, M.R. Hilton, P.M. Adams, P.C. Ward, E.G. Herbert, and B.N. Lucas, "Rolling contact fatigue of TiC-coated bearing balls," *Mat. Res. Soc. Symp. Proc.*, **522**, pp. 445-450, 1998.
4. M.S. Donley, J.S. Zabinski, W.J. Sessler, V.J. Dayhouse, S.D. Walck, and N.T. McDevitt, "Low temperature synthesis of carbide thin films by pulsed laser deposition," *Mater. Res. Soc. Symp. Proc.*, **236**, pp. 461-466, 1992.
5. W.J. Sessler, M.S. Donley, J.S. Zabinski, S.D. Walck, and V.J. Dayhouse, "Tribological behavior of TiC thin films grown by PLD," *Surf. Coat. Technol.*, **56**, pp. 125-130, 1993.
6. J.E. Krzanowski and R.E. Leuchtner, "Structure and properties of TiC, VC, and TiC/VC thin films deposited by PLD," *Mater. Res. Soc. Symp. Proc.*, **410**, pp. 301-306, 1996.
7. J.E. Krzanowski and R.E. Leuchtner, "Chemical, mechanical, and tribological properties of pulsed-laser-deposited titanium carbide and vanadium carbide," *J. Am. Ceram. Soc.*, **80**, pp. 1277-1280, 1997.
8. I. Zergioti, C. Fotakis, and G.N. Haidemenopoulos, "Growth of TiB₂ and TiC coatings using pulsed laser deposition," *Thin Solid Films*, **303**, pp. 39-46, 1997.
9. O. Rist and P.T. Murray, "Growth of TiC thin films by pulsed laser deposition," *Materials Lett.*, **10**, pp. 323-328, 1991.

10. A. Kumar, H.L. Chan, and J.S. Kapat, "Deposition and characterization of titanium carbide coatings using laser ablation method," *Appl. Surf. Sci.*, **127**, pp. 549-552, 1998.
11. G. Radhakrishnan, P.M. Adams, and A. Taylor, "Growth and material properties of titanium carbide thin films for ball-bearing applications," *TMS Symp. Proc. "Surface Engineering: Science and Technology I,"* Ed. By A.Kumar, Y.W. Chung, J.J. Moore, and J.E. Smugersky, pp. 155-164, 1999.
12. *NBS Tables of Spectral Line Intensities*, Part I, 2nd ed., 1975.
13. P. Frantz, S.V. Didziulis, P.B. Merrill, and S. S. Perry, " Spectroscopic and scanning probe studies of oxygen and water on metal carbide surfaces," *Tribol. Lett.*, **4**, pp. 141-148, 1998.
14. *MIT Wavelength Tables*, v. 2, prepared by Frederick M. Phelps III, MIT Press, Cambridge, MA, 1969.
15. A.R. Striganov and N.S. Sventitskii, *Tables of Spectral Lines of Neutral and ionized Atoms*, IFI / Plenum, New York, 1968.
16. D.G. Geohegan, "Species-resolved imaging and gated photon counting spectroscopy of laser ablation plume dynamics during KrF and ArF-laser PLD of amorphous diamond films," *Mat. Res. Soc. Proc.* **397**, pp. 55-68, 1996.
17. D.B. Chrisey, J.S. Horowitz, G. Mehlman, R.C.Y. Auyeung, and P.C. Dorsey, "Time resolved vacuum ultraviolet observations of excimer laser-produced YBa₂Cu₃O₇ plasmas," *Mat. Res. Soc. Proc.* **397**, pp. 99-104, 1996.
17. M.L. De Giorgi, J. Hermann, A. Lunches, A. Perrone, and L. Renna, "Spectroscopic studies of XeCl-laser induced plasma on Ti targets in nitrogen containing atmospheres," *Appl. Phys. A* **58**, pp. 595-599, 1994.
18. X.T. Wang, B.Y. Man, G.T. Wang, Z. Zhao, Y. Liao, B.Z. Xu, Y.Y. Xia, L.M. Mei, and X.Y. Hu, "Optical spectroscopy of plasma produced by laser ablation of Ti alloy in air", *J. Appl. Phys.* **80**, pp. 1783-1786, 1996.

Pulsed-Laser Deposited Amorphous Diamond and Related Materials: Synthesis, Characterization, and Field Emission Properties

Vladimir I. Merkulov^a, Douglas H. Lowndes^a, L. R. Baylor^b, G. E. Jellison, Jr.^a,
A. A. Poretzky^a, and D. B. Geohegan^a.

^a Solid State Division

^b Fusion Energy Division

Oak Ridge National Laboratory, Oak Ridge, TN 37831

ABSTRACT

Amorphous carbon films with variable sp^3 content were produced by ArF (193nm) pulsed laser deposition. An *in-situ* ion probe was used to measure kinetic energy of C^+ ions. In contrast to measurements made as a function of laser fluence, ion probe measurements of kinetic energy are a convenient as well as more accurate and fundamental method for monitoring deposition conditions, with the advantage of being readily transferable for inter-laboratory comparisons. Electron energy loss spectroscopy (EELS) and spectroscopic ellipsometry measurements reveal that tetrahedral amorphous carbon (ta-C) films with the most diamond-like properties are obtained at the C ion kinetic energy of ~ 90 eV. Film properties are uniform within a 12 - 15° angle from the plume centerline. Tapping-mode atomic force microscope measurements show that films deposited at near-optimum kinetic energy are extremely smooth, with rms roughness of only ~ 1 Å over distances of several hundred nm. Field emission (FE) measurements show that ta-C does not appear to be a good electron emitter. After conditioning of ta-C films deposited on n-type Si a rather high turn-on voltage of ~ 50 V/ μ m was required to draw current of ~ 1 nA to the probe. The emission was unstable and typically ceased after a few minutes of operation. The FE tests of ta-C and other materials strongly suggest that surface morphology plays a dominant role in the FE process, in agreement with conventional Fowler-Nordheim theory.

Keywords: Diamond, tetrahedral amorphous carbon, pulsed laser ablation, EELS, ellipsometry, field emission

1. INTRODUCTION

Hard amorphous carbon films has drawn significant attention of the industrial and scientific communities since the first reports on their deposition more than two decades ago^{1, 2}. More recent studies have focused on hydrogen-free amorphous diamond films (also known as tetrahedral amorphous carbon, ta-C) that have superior diamond-like properties^{3, 4}, such as high hardness, a large (~ 2 eV) optical (Tauc) band gap and a low coefficient of friction, as well as chemical inertness and excellent thermal stability. In contrast to graphite and diamond, two crystalline forms of C, in which all C atoms have either the sp^2 , three-fold (graphite) or the sp^3 , four-fold (diamond) bonding configuration, a-C is a mixture of sp^2 and sp^3 -bonded C atoms. Conventional amorphous carbon (a-C) prepared by evaporation or sputtering consists mostly of sp^2 -bonded C atoms⁵. In contrast, ta-C films contain a large fraction (up to ~ 75 - 85%) of sp^3 -bonded C atoms and are synthesized using a variety of energetic-beam methods⁶ including filtered cathodic vacuum arc (FCVA), mass-separated ion beam deposition (MSIBD), and pulsed laser deposition (PLD).

The amount of sp^3 bonding in ta-C and consequently its diamond-like properties depend upon the kinetic energy (KE) of the carbon species being deposited. The early work by Pappas et al.⁷ established such a correlation for PLD. Other early experiments using FCVA, PLD, and other methods showed that films with nearly maximal sp^3 content as well as highly diamond-like properties could be produced using carbon ions whose KE ranged from ~ 20 eV to at least several hundred eV⁶. For FCVA it recently was established that the highest sp^3 fraction is obtained for C ions with KE of ~ 80 - 100 eV^{8, 9, 10}. Similarly, recent PLD experiments in our laboratory^{11, 12} show that the sp^3 -bonded fraction, film density, and optical (Tauc) band gap all reach their maximum values for incident carbon ion kinetic energies of ~ 90 eV. In this paper we summarize

the results of our previous work and also report additional data on the systematic study of changes in the bonding, optical properties, and surface morphology of PLD ta-C films as a function of the C⁺ ion KE.

Recently, materials that have electronic conduction-band states with low or negative electron affinity became of great interest as they might be used for fabrication of cold cathodes for flat panel displays and similar applications. It has been established that diamond can possess a negative electron affinity surface^{13, 14} which, in principle, should allow for electron emission under very low electric fields. Unfortunately, n-doping of bulk diamond is problematic and the transport of electrons to the conduction band, required for field emission applications, is difficult to achieve. As a result, despite its low electron affinity, single crystal diamond is not a good electron emitter. Recently, a few studies of FE from ta-C were reported. The results are mixed as some researchers found ta-C to exhibit very good FE properties¹⁵ while the others^{16, 17} do not confirm these results. In this work we report the results of our investigation of field emission properties of ta-C as well as predominantly sp²-bonded a-C films.

2. EXPERIMENTAL

ta-C films were prepared in a high vacuum chamber with a base pressure of 3×10^{-8} Torr using a Lambda Physik Compex 301i pulsed excimer laser operated with ArF (193 nm). ArF PLD is advantageous over longer wavelengths for deposition of ta-C in that it requires lower energy fluences to produce high quality films¹². In addition, the ablated flux in ArF PLD consists mostly of monoatomic C species even at relatively low fluences¹⁸ which allows for simpler characterization of deposition conditions. Maximum laser fluences at the target were $\sim 8 \text{ J/cm}^2$ and produced C⁺ KE $\sim 100 \text{ eV}$. Higher energy carbon ions were produced using a Questek 2960 excimer laser. The Questek has shorter pulse duration, higher pulse energy, and a sharply peaked beam profile which allowed C⁺ ions to be produced with kinetic energies up to 225 eV. 2.54-cm diameter pyrolytic graphite targets containing < 10 ppm total impurities (Specialty Minerals, Inc., Easton, PA) were used. The substrates were kept at room temperature and placed at variable distances (4.8–7.3 cm) from the target. Typical deposition rates were 0.03–0.1 Å/shot. An ion probe¹⁹ was used to determine the kinetic energy of ablated C⁺ ions. It consisted of a bare coaxial-cable tip biased at -100 V and mounted on an arm that rotated it in an arc passing through the center of the ablation plume. The time corresponding to the ion current peak ("icp") was used to calculate a velocity and corresponding kinetic energy of C ions, KE_{icp} .

For spectroscopic ellipsometry (SE) and atomic force microscopy (AFM) measurements ~ 70 –200 nm thick ta-C films were deposited on p- and n-type (001)-oriented Si wafers. Surface roughness studies were carried out using a Nanoscope III AFM (Digital Instruments). A tapping rather than contact mode AFM was utilized because SiN tips used for contact-mode measurements are quickly damaged by the extreme hardness of ta-C films, resulting in degraded image quality. The SE measurements were made using the two-modulator generalized ellipsometer (2-MGE)²⁰ operating from 250 to 850 nm. The SE results were fit using a 5-medium model consisting of air/ surface roughness/ ta-C film/ interface/ Si, where the optical properties of ta-C films were modeled using the 5-parameter Tauc-Lorentz (TL) formulation for the optical functions of amorphous materials²¹. Previous studies²² have shown that this model fits SE data taken on a wide range of amorphous materials, yielding the thickness of each layer, the Tauc (optical) band gap, and the optical functions of the film.

For EELS measurements ta-C was deposited on freshly cleaved NaCl substrates which were subsequently dissolved in DI water and the resultant free-standing ta-C films were placed on folding Ni TEM grids. The thickness of the films was $\sim 30 \text{ nm}$ which is substantially lower than the mean free path for 100 keV electrons ($> 50 \text{ nm}$). In this case the effect of multiple scattering can be neglected. The EELS measurements were carried out using a VG HB501 STEM fitted with a high sensitivity parallel EELS and operated at 100 keV. The energy resolution was 1.1 eV during the measurements, as determined by the FWHM of the zero-loss peak. We did not observe any notable degradation or contamination of the specimens throughout the experiments.

Field emission measurements were carried out in a high vacuum chamber with a base pressure of 10^{-6} Torr. The measurements were taken by applying a positive voltage to a tungsten-carbide current probe (anode) with tip diameter of $\sim 25 \mu\text{m}$ and by collecting electrons emitted from the samples tested (cathode). The current probe stage motion was computer controlled with the minimum step size of 75 nm in x-y-z directions, which allowed for precise control of the distance between the probe and the sample.

3. RESULTS AND DISCUSSION

3.1 EELS and ellipsometry measurements of sp^3 fraction, film density, and optical band gap

The K-edge spectra of ta-C films deposited by ArF PLD with various C^+ ion kinetic energies (KE_{icp}) corresponding to the ion current peak at the ion probe are shown in Fig. 1a. The spectra exhibit two main features: a peak at ~ 285 eV and a broad band with a maximum at ~ 293 eV. These features are due to $1s-\pi^*$ and $1s-\sigma^*$ electronic transitions, respectively²³. The former is associated with sp^2 -bonded C atoms and the latter with both sp^2 and sp^3 C atoms. One can see that the relative intensity of the $1s-\pi^*$ peak changes with the C ion KE_{icp} and becomes the lowest for the films prepared with KE_{icp} in the range of 70–120 eV. This corresponds to the materials with the lowest sp^2 content and hence more diamond-like properties.

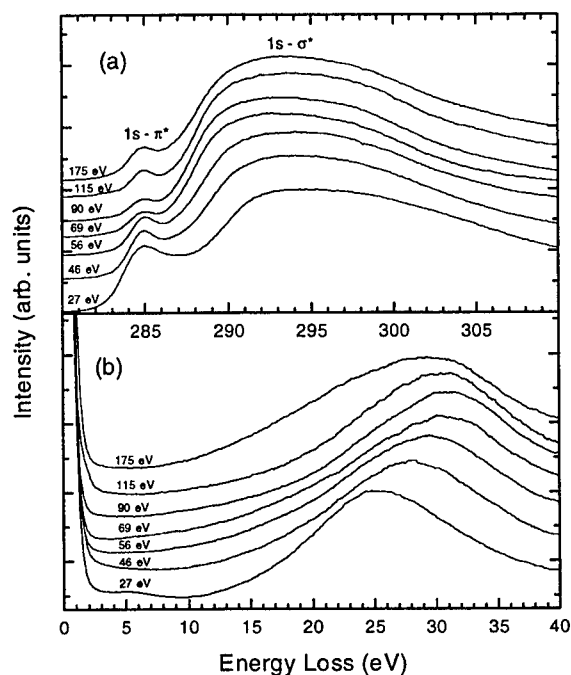


Figure 1. EELS K-edge (a) and plasmon (b) spectra of amorphous C films prepared by ArF PLD at various C ion kinetic energies (KE_{icp}) corresponding to the ion current peak of the ion probe signal.

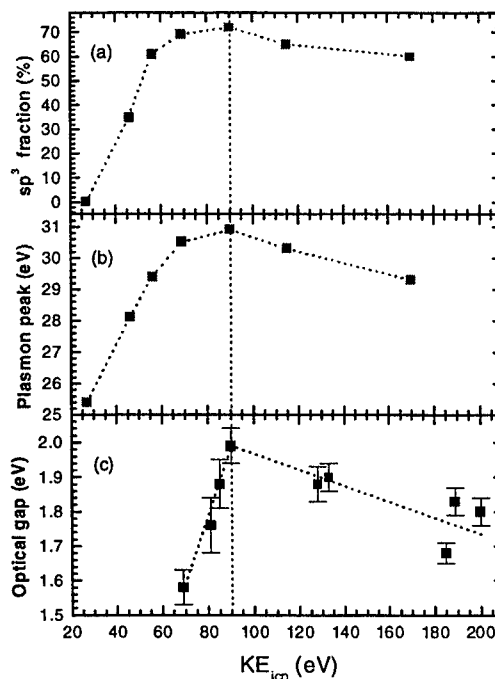


Figure 2. sp^3 content (a) and plasmon peak position (b) extracted from the EELS measurements (Fig. 1) and optical (Tauc) energy gap (c) obtained by scanning ellipsometry, as a function of C ion kinetic energy, KE_{icp} .

EELS spectra also were measured in the low-energy range and are shown in Fig. 1b. The broad peak around 30 eV is associated with collective excitation, or a plasmon, of the valence electrons²³. Using a simple Drude-like model, the energy of this plasmon is proportional to the density of ta-C films²⁴: the higher the plasmon energy, the higher the film density. As two reference points one can use the plasmon peak position of graphite (~ 26.5 eV) and of diamond (33.6 eV).

The analysis of the sp^3 fractions in the ta-C films was performed in a way similar to that of Berger et al.²³. The sp^2 fraction, f_{sp^2} , is calculated by taking the ratio of integrated intensities of the $1s-\pi^*$ and $1s-\sigma^*$ peaks, I_{π}/I_{σ} , and by comparing it to that of arc-evaporated a-C, which is assumed to be entirely sp^2 bonded. The sp^3 fraction is then simply $1-f_{sp^2}$. There are quite a few uncertainties in the data analysis and interpretation associated with this method¹¹. In addition, the difficulty of sample preparation is also an issue for this technique. Yet, in spite of these problems, EELS is currently the most-used tool for analyzing the sp^3 fraction in ta-C. Partly this is due to the absence of any more suitable alternative method, although uv Raman scattering may be a good candidate. In contrast to conventional Raman scattering in the visible, uv Raman scattering directly reveals the presence of sp^3 -bonded C atoms^{25,26} and therefore provides a potential means of simple,

nondestructive characterization of ta-C films. We believe that a combination of techniques, such as EELS, ellipsometry, Raman scattering, and possibly others, is required to fully characterize such a complicated material as ta-C. Nevertheless, EELS provides a reasonable sp^3 estimate suitable for most practical applications.

Briefly, the EELS data analysis includes decomposition of the $1s-\pi^*$ and $1s-\sigma^*$ peaks via a best fit of a Gaussian into the lower energy edge of the latter. The value of I_σ was taken as an integral over the energy range of 290 - 310 eV which is large enough to avoid any significant systematic error. The extracted sp^3 fractions as a function of C ion KE_{icp} are shown in Fig. 2a. The sp^3 fraction clearly exhibits a maximum of $\sim 73\%$ at $KE_{icp} \sim 90$ eV. This is consistent with the optimum KE obtained for FCVA deposition of ta-C.

Fig. 2b shows that the position of the C plasmon peak also reaches its highest value of ~ 30.9 eV at $KE_{icp} \sim 90$ eV. This behavior is expected since higher plasmon peak energy corresponds to higher film density, which is characteristic of more diamond-like films with higher sp^3 content. It should be noted that the plasmon peak position can serve as a useful tool for correlating the sp^3 fractions obtained by different research groups. Inter-laboratory discrepancies in the estimate of sp^3 fractions can arise from various factors, including structural differences in sp^2 calibration samples, variations in the energy ranges and fitting procedures used to define I_π and I_σ , and differences in EELS resolution. The position of the plasmon peak is a more settled parameter and therefore can be used as a reference point for extracting the sp^3 fraction.

The EELS results were correlated with scanning ellipsometry (SE) measurements of the optical properties of ta-C films. The optical energy gaps extracted from the SE measurements are shown in Fig. 2c as a function of the C ion KE_{icp} . The trend is very similar to that observed for the sp^3 fraction and for the position of the plasmon peak. The energy gap is lower for the films prepared at low KE_{icp} , reaches its maximum at $KE_{icp} \sim 90$ eV, and decreases for higher values of KE_{icp} . This is consistent with the variation of the sp^3 fraction in these materials: sp^3 rich films are expected to have a larger optical gap (5.5 eV for pure crystalline diamond) and the gap disappears for predominantly sp^2 -bonded carbon.

3.2 Spatial variation of film thickness and optical band gap of ta-C films

Measurements of the angular distribution of the C^+ KE_{icp} also were carried out since this determines the maximum area within which spatially uniform film properties can be obtained at any given target-substrate separation, D_{ts} . As shown in Fig. 3, KE_{icp} was nearly constant ($\pm 10\%$) within a half-angular range of 12 to 15 degrees on either side of the plume centerline. At $D_{ts} = 10$ cm, for instance, this corresponds to a ~ 20 cm² region of uniform film properties.

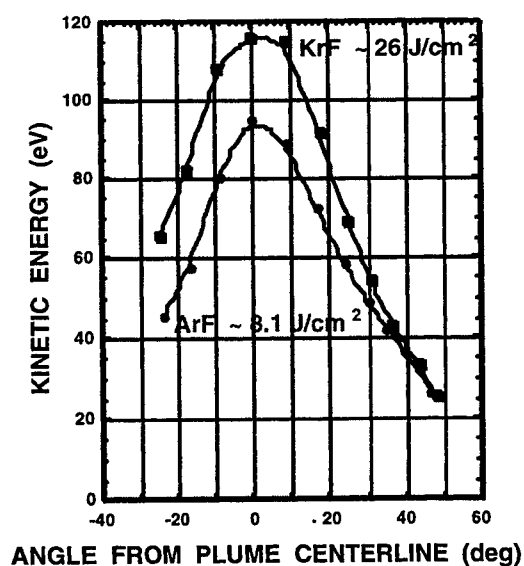


Figure 3. Angular variation of C^+ ion kinetic energy for ArF (193 nm) and KrF (248 nm) laser ablation of pyrolytic graphite.

Also, SE measurements of ta-C films deposited on 7.5 cm diameter Si wafers were employed to study film properties as a function of distance away from the plume center. It was found that not only film thickness but also the optical energy gap (E_g) varied with distance away from the plume center. This is due to the fact that diamondlike properties are a function of C ion KE which, in turn, depends on the angle from the plume centerline (see Fig. 3). If KE_{icp} at the plume center is not substantially higher than 90 eV, as shown in Fig. 4, then uniform diamond-like properties ($E_g \sim \text{constant}$) result over a large central area with properties changing rapidly only further away. However, if a much higher central KE_{icp} is used, such as in the case of $KE_{icp} = 200$ eV presented in Fig. 4, then a *degraded* central area is produced (with E_g increasing away from center) surrounded by a ring of the most diamond-like ta-C, with a rapid fall-off in properties still further away. These angular dependences of E_g are consistent with the energy dependence shown in Fig. 2c and the angular distribution of KE_{icp} in Fig. 3 and again confirm the existence of the optimum KE_{icp} of ~ 90 eV for ta-C film deposition.

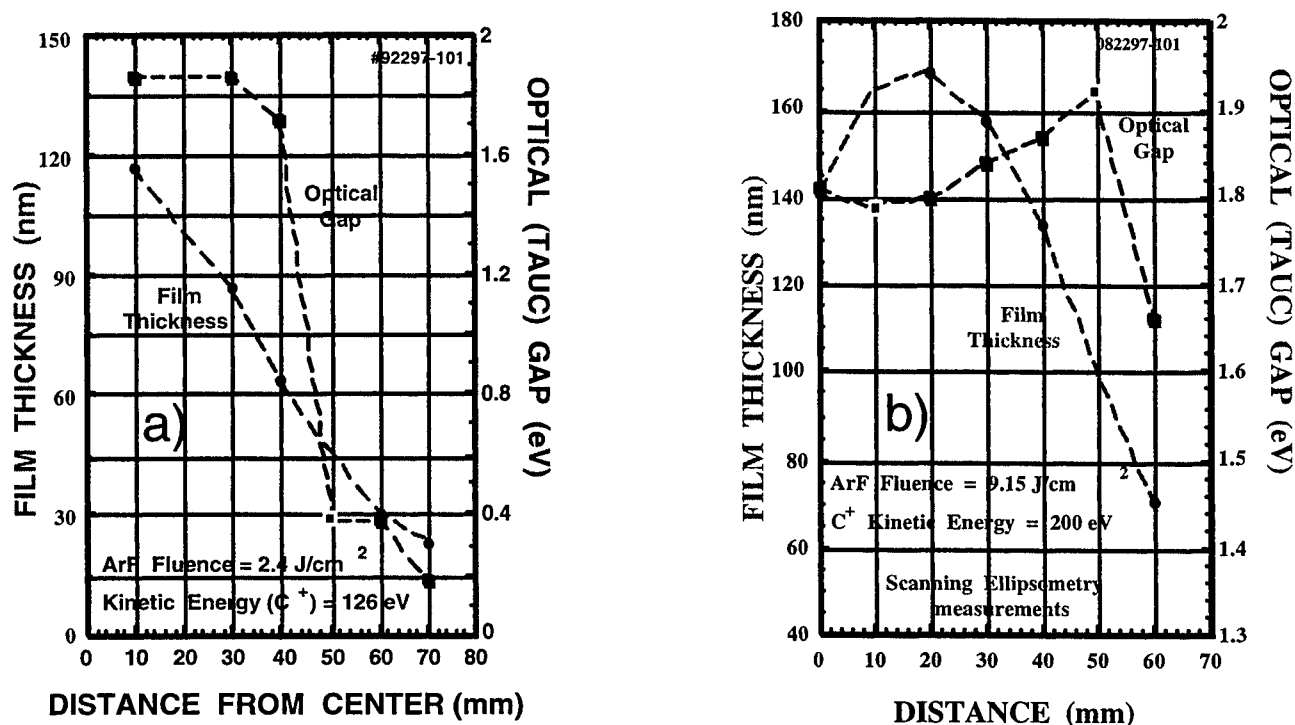


Figure 4. Spatial variation of film thickness and optical (Tauc) energy gap in a ta-C film deposited at the plume-center KE_{icp} of 126 eV (a) and 200 eV (b).

3.3 AFM studies of surface roughness of ta-C films

The AFM images shown in Fig. 5 reveal that ta-C films deposited at KE_{icp} values of 26, 44, and 90 eV all are quite smooth but still display systematic differences in roughness that are correlated with the KE_{icp} of the C ions used for deposition. Films deposited at 90 eV are extremely smooth with an rms roughness of ~ 0.9 Å measured over $(200 \text{ nm})^2$ areas. For 26 and 44 eV the corresponding rms roughness values are ~ 1.6 Å. Similarly, the Z-range of height variation within the $(200 \text{ nm})^2$ area increases from ~ 0.9 Å (at 90 eV) to ~ 1.6 Å (at 26 eV). We note that these energetically deposited carbon films also are relatively free of the large ($\sim \mu\text{m}$ scale) particulates sometimes produced by pulsed laser deposition, with typical and largest particulate diameters of ~ 2 – 10 nm and ~ 100 nm, respectively.

The tapping mode (TM) AFM results of Fig. 5 are in good agreement with the AFM measurements reported by Lifshitz⁶ for ta-C films deposited on silicon substrates by the MSIBD method. Lifshitz found a pronounced increase in roughness for films deposited at a C ion kinetic energy of 10 eV but very smooth films for kinetic energies ranging from 50 eV up to 10 keV.

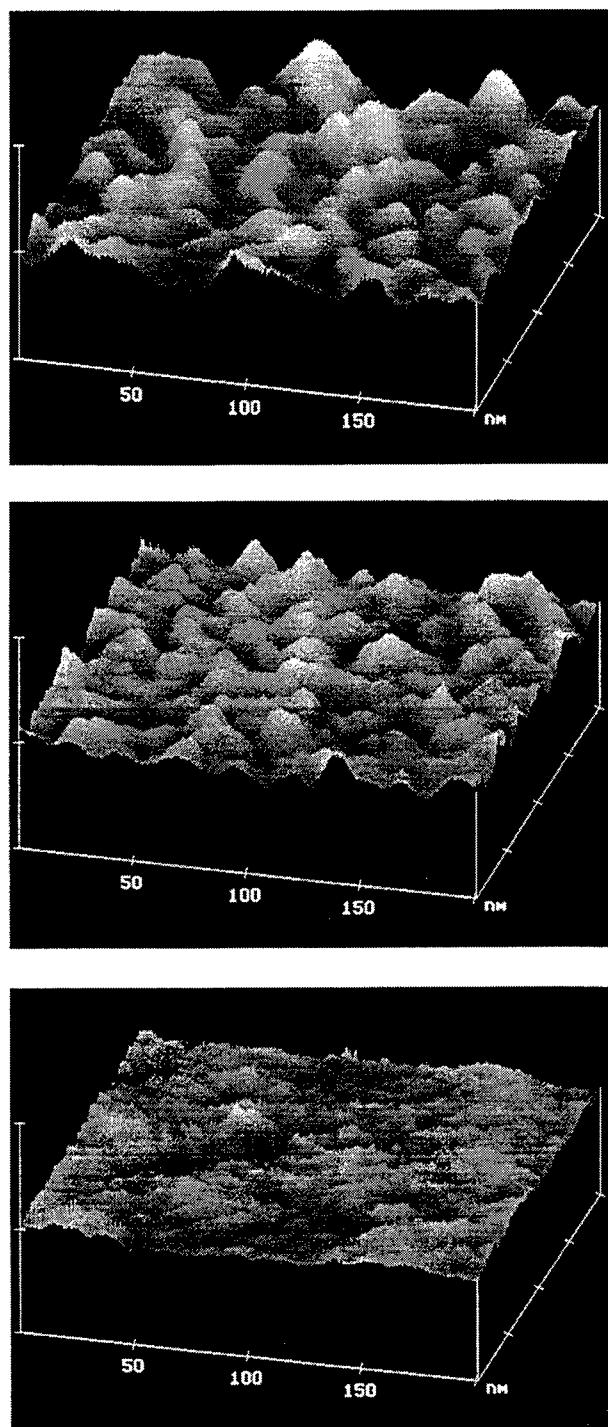


Figure 5. TM-AFM images of the surfaces of amorphous carbon films deposited at kinetic energies (KE_{icp}) of (top) 26 eV, (middle) 44 eV, and (bottom) 90 eV. [z range = 2 nm]

3.4 Field emission properties of amorphous carbon films

The emission current-applied electric field (I-E) measurements were done at a fixed distance between the probe and the sample and are shown in Fig. 6. The macroscopic electric field, E , was simply calculated as the probe voltage divided by the probe-sample distance. A typical turn-on voltage required to draw field emission current of ~ 1 nA from highly sp^3 -bonded C films was found to be ~ 50 V/ μ m. This is substantially higher than that obtained for other forms of carbon materials, such as nanostructured C films¹⁷, CVD diamond²⁷, nanodiamond²⁸, and carbon nanotubes²⁹. In fact, conventional, predominantly sp^2 -bonded a-C prepared by PLD with low C ion kinetic energies exhibits very similar field emission characteristics, with even lower fluctuations of the emission current (see Fig. 6b). The emission curves follow the Fowler-Nordheim (FN) behavior as shown in the insets of Fig. 6a and 6b. Using a simplified FN equation³⁰ and assuming the work function of graphite ($\Phi = 4.6$ eV) for amorphous C films, it is possible to estimate the emission area (EA) and the geometric enhancement factor (β) of the electric field due to sample's surface morphology. The calculations yield high $\beta \sim 100$ -150 and low EA $\sim 10^{-2}$ μ m² for both ta-C and sp^2 -bonded a-C films.

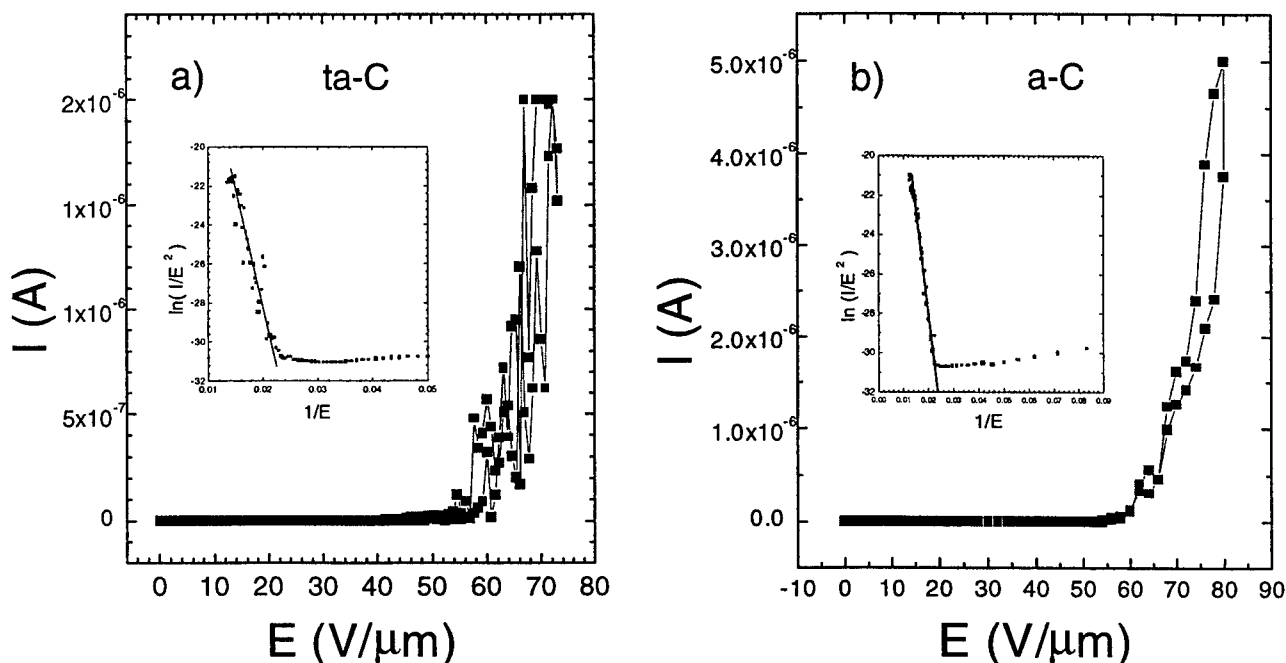


Figure 6. Emission current-applied electric field (I-E) curves and Fowler-Nordheim plots (insets) for 73% sp^3 ta-C (a) and predominantly sp^2 a-C (b) films.

Also, it has to be noted that "conditioning" was required to obtain emission from all samples tested. The conditioning typically resulted in arcing occurred between the probe and the sample as the electric field was increased from 0 to 100 - 200 V/ μ m. SEM was employed to study changes in surface morphology that occurred after the arcing. It was found that at the location where the arcing had taken place a crater of once-molten C film and Si substrate formed (see Fig. 7). Given this fact and the FE characteristics of ta-C films described above, we conclude that FE from ta-C is not due to its low electron affinity but rather should be attributed to the sharp protrusions around the crater formed during the arcing. The protrusions geometrically enhance the electric field around them, thereby providing for electron emission at moderate fields. These results are in good agreement with the observations of Talin et al.¹⁶, Coll et al.¹⁷ and Groning et al.³¹ but differ from that obtained by Satyanarayana et al.¹⁵. However, the latter used parallel plate anode geometry in their experiments. This method has a drawback of "picking-up" the hottest spot on the sample and therefore provides no reliable information about the

average FE properties of the material over large surface areas. Also, in this method the leakage current across the spacers separating the anode from the cathode (sample) is rather difficult to distinguish from the true FE current.

Finally, stability tests of FE from ta-C films were performed and a representative run is shown in Fig. 8. We have found the FE to be typically quite unstable and stop after a few minutes of operation. This can be attributed to the fact of the emission sites being quite sharp. As a result, they draw extremely high current densities and consequently burn out rather quickly. In addition, rather poor vacuum of 10^{-6} Torr may also be an issue as the ion bombardment during the FE measurements may severely damage and consequently terminate the emitting sites.

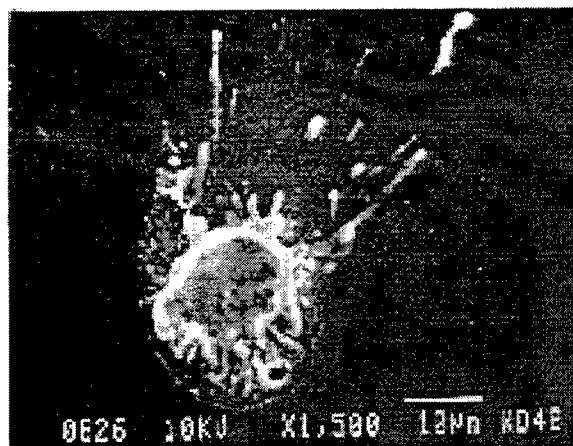


Figure 7. SEM image of a crater formed as a result of the conditioning process (arc discharge) of amorphous C films.

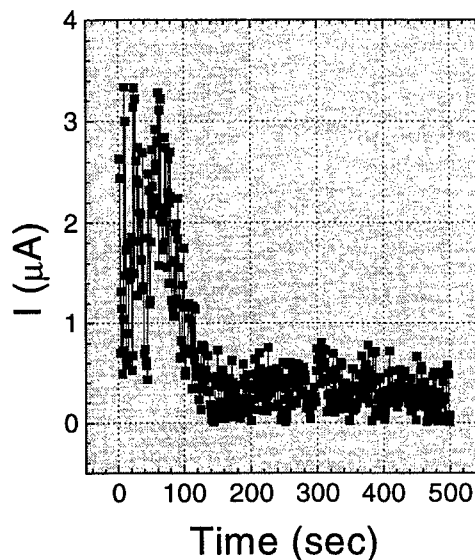


Figure 8. Instability of field emission from ta-C films.

SUMMARY AND CONCLUSIONS

In conclusion, the combination of ArF pulsed laser deposition and in situ ion probe measurements allows for deposition of ta-C films with well-controlled diamond-like properties. EELS measurements show that both the sp^3 fraction and the plasmon peak energy (\sim film density) reach their maximum values of $\sim 73\%$ and 30.9 eV in films deposited at $KE_{icp} \sim 90$ eV. Scanning ellipsometry measurements reveal that the optical (Tauc) energy gap is also maximized (~ 2.0 eV) at $KE_{icp} \sim 90$ eV, consistent with the presence of the highest sp^3 fraction. This combination of independent optical and electronic measurements provides strong evidence of an optimum kinetic energy $KE_{icp} \sim 90$ eV for ArF PLD of ta-C. Measurements of the angular distribution of C^+ kinetic energy show that films with highly uniform ($\pm 10\%$) diamond-like properties are obtained within a half-angular range of at least 12–15 degrees on either side of the plume centerline. Tapping-mode AFM measurements show that films deposited at near-optimum KE are extremely smooth, with rms roughness of only ~ 1 Å over distances of several hundred nm, and are relatively free of particulates. A distinct increase of surface roughness is observed with decreasing C^+ ion KE and is associated with the increase in sp^2 -bonding fraction. Finally, field emission measurements reveal that ta-C does not possess low electron affinity and consequently exhibits rather poor field emission characteristics (high turn-on voltages, strong current fluctuations, short life-time). However, we believe that other kinds of C-based materials, such as nanodiamond, nanotubes, and nanostructured C films, are exceptionally good candidates for various FE applications.

ACKNOWLEDGMENTS

The authors thank S. J. Pennycook for making available the STEM with which the EELS measurements were carried out and P. H. Fleming for assistance with sample preparation. This research was partially sponsored by the Defense Advanced Research Projects Agency under contract DARPA-MIPR-97-1357 with Oak Ridge National Laboratory (ORNL), and by the Office of Basic Energy Sciences, Division of Materials Sciences, U. S. Department of Energy. The research was carried out at ORNL, managed by Lockheed Martin Energy Research Corp. for the U. S. Department of Energy, under contract DE-AC05-96OR22464.

REFERENCES

1. S. Aisenberg and R. Chabot, *J. Appl. Phys.* **42**, 2953 (1971).
2. I. I. Aksenov, V. A. Belous, V. G. Podalka, and V. M. Khoroshikh, *Sov. J. Plasma Phys.* **4**, 425 (1978).
3. J. Robertson, *Prog. Solid State Chem.* **21**, 199 (1991).
4. D. R. McKenzie, Y. Yin, N. A. Marks, C. A. Davis, E. Kravtchinskaya, B. A. Pailthorpe, G. A. J. Amarunga, *J. Non-Crystalline Solids* **164-166**, 1101 (1993).
5. H. Pan, M. Pruski, B. C. Gerstain, F. Li, and J. S. Lannin, *Phys. Rev. B* **44**, 6741 (1991).
6. Y. Lifshitz, *Diamond Relat. Mater.* **5**, 388 (1996).
7. D. L. Pappas, K. L. Saenger, J. J. Cuomo, and R. W. Dreyfus, *J. Appl. Phys.* **72**, 3966 (1992).
8. S. Ravi, P. Silva, S. Xu, B. X. Tay, H. S. Tan, and W. I. Milne, *Appl. Phys. Lett.* **69**, 491 (1996).
9. S. R. P. Silva, S. Xu, B. K. Tay, H. S. Tan, H.-J. Scheibe, M. Chhowalla, and W. I. Milne, *Thin Solid Films* **290-291**, 317 (1996).
10. M. Chhowalla, J. Robertson, C. W. Chen, S. R. P. Silva, C. A. Davis, G. A. J. Amarunga, and W. I. Milne, *J. Appl. Phys.* **81**, 139 (1997).
11. V. I. Merkulov, D. H. Lowndes, G. E. Jellison, Jr., A. A. Puretzky, and D. B. Geohegan, *Appl. Phys. Lett.* **73**, 2591 (1998).
12. D. H. Lowndes, V. I. Merkulov, A. A. Puretzky, D. B. Geohegan, G. E. Jellison, Jr., C. M. Rouleau, and T. Thundat, p. 325 in *Advances in Laser Ablation of Materials* (ed. by R. Singh et al.), Materials Research Society, Warrendale (1998).
13. F. J. Himpsel, J. A. Knapp, J. A. Van Vechten, D. E. Eastman, *Phys. Rev. B* **20**, 624 (1979).
14. J. Van der Weide and R. J. Nemanich, *Appl. Phys. Lett.* **62**, 1878 (1993).
15. B. S. Satyanarayana, A. Hart, W. I. Milne, and J. Robertson, *Appl. Phys. Lett.* **71**, 1430 (1997).
16. A. A. Talin, T. E. Felner, T. A. Friedmann, J. P. Sullivan, and M. P. Siegal, *J. Vac. Sci. Tech. A* **14**, 1719 (1996).
17. B. F. Coll, J. E. Jaskie, J. L. Markham, E. P. Menu, A. A. Talin, P. von All, p. 185 in *Covalently Bonded Disordered Thin-Film Materials* (ed. by M. P. Siegal et al.), Materials Research Society, Warrendale (1998).
18. A. A. Puretzky, D. B. Geohegan, G. E. Jellison, M. M. McGibbon, *Appl. Surf. Sci.* **96-98**, 859 (1996).
19. D. B. Geohegan, p. 124-127 and p. 147-8 in *Pulsed Laser Deposition of Thin Films* (ed. by D. B. Chrisey and G. K. Hubler), John Wiley & Sons, New York, 1994.
20. G. E. Jellison, Jr., and F. A. Modine, *Appl. Opt.* **36**, 8184 (1997); G. E. Jellison, Jr., and F. A. Modine, *Appl. Opt.* **36**, 8190 (1997).
21. G. E. Jellison, Jr., and F. A. Modine, *Appl. Phys. Lett.* **69**, 371 (1996); G. E. Jellison, Jr., and F. A. Modine, *Appl. Phys. Lett.* **69**, 2137 (1996).
22. G. E. Jellison, Jr., D. B. Geohegan, D. H. Lowndes, A. A. Puretzky, and V. I. Merkulov, p. 349 in *Advances in Laser Ablation of Materials* (ed. by R. Singh et al.), Materials Research Society, Warrendale (1998); G. E. Jellison, Jr., F. A. Modine, P. Doshi, and A. Rohatgi, *Thin Solid Films* **313-314**, 193 (1998).
23. S. D. Berger and D. R. McKenzie, and P. J. Martin, *Phil. Mag. Lett.* **57**, 285 (1988).
24. R. F. Egerton, *Electron Energy Loss Spectroscopy in the Electron Microscope* (Plenum, NY, 1986).
25. V. I. Merkulov, J. S. Lannin, C. H. Munro, S. A. Asher, V. S. Veerasamy, and W. I. Milne, *Phys. Rev. Lett.* **78**, 4869 (1997).
26. K. W. R. Gilkes, H. S. Sands, D. N. Batchelder, J. Robertson, and W. I. Milne, *Appl. Phys. Lett.* **70**, 1980 (1997).
27. D. Zhou, A. R. Krauss, T. D. Corrigan, T. G. McCauley, R. P. H. Chang, and D. M. Gruen, *J. Electrochem. Soc.* **144**, 224 (1997).
28. W. Zhu, G. P. Kochanski, S. Jin, *Science* **282**, 1471 (1998).
29. W. A. de Heer, A. Chatelain, and D. Ugarte, *Science* **270**, 1179 (1995).
30. C. A. Spindt, I. Brodie, L. Humphrey, and E. R. Westerberg, *J. Appl. Phys.* **47**, 5248 (1976).
31. O. Groning, O. M. Kuttel, E. Schaller, P. Groning, and L. Schlapbach, *Appl. Phys. Lett.* **69**, 476 (1996).

Pulsed-Laser Deposition of Ti:sapphire Thin Films Using High-Speed Rotating Target

Yoshiki Nakata^{*a}, Hiroshi Uetsuhara^a, Satoshi Goto^a,

Nilesh Vasa^a, Tatuo Okada^a, Mitsuo Maeda^a

^aDept. of Electrical and Electronic Systems, Kyushu University,
6-10-1 Hakozaki, Fukuoka, 812-8581 Japan

ABSTRACT

We describe the deposition of Ti:sapphire thin films by the pulsed-laser deposition (PLD) method for the waveguide laser application, with an emphasis on the reduction of droplets which is inevitably generated during PLD. In order to eliminate the droplets from the film surface, we introduced centrifugal separation of the droplets out of the laser ablation plume using a high-speed rotating target. The behavior of droplets in the ablation plume generated with a high-speed rotating target is presented along with the film properties.

Keywords: pulsed-laser deposition, Ti:sapphire, droplets, thin films, waveguide laser

1. INTRODUCTION

Waveguide lasers are very promising devices which have the advantages of compactness and low oscillation threshold, resulting in an efficient operation. Recently, there is an increasing interest in the development of Ti:sapphire waveguide laser, since Ti:sapphire provides large tunability and ultra-short pulses are also possible. There has been some investigation to fabricate the Ti:sapphire waveguide laser by ion beam implantation,¹ thermal diffusion of titanium into sapphire,^{2,3} and pulsed-laser deposition (PLD).^{4,5} Recently, Anderson et al. achieved the laser oscillation from a Ti:sapphire waveguide laser fabricated by PLD.⁶ PLD is a very powerful method to fabricate waveguides for its high deposition speed, simplicity of apparatus, easy control of the process, etc.. On the other hand, during PLD operation many droplets are deposited on the thin films, which increases the waveguide loss. Different approaches have been tried to avoid the deposition of such droplets fly from the ablation spot, such as spatial filters,⁷ temporal filters and so on. But, some do not have enough effectiveness, and some approaches require complicated apparatus. In this context, another effective and simple method is needed.

In this study we introduced a high-speed rotating target to deflect the flight direction of the droplets to avoid the deposition of droplets onto the film surface. The behavior of droplets generated with a high-speed rotating target is presented. The behavior of emissive atoms or molecules in the gas phase is also imaged. The qualities of deposited thin films, such as the surface of the thin films, photo emission spectra were observed. In this experiment, Ti:sapphire and silicon target were examined.

2. EXPERIMENTAL SETUP

The experimental setup is shown in Fig.1. The chamber was evacuated to 10^{-4} Torr order by a turbo molecular pump. A Ti:sapphire crystal target or a silicon target attached to a high-speed rotary driver was ablated by an ArF excimer laser (Lambda Physik Compex 102) with a energy of 50 mJ and a fluence of 4 J/cm². The distance between the rotation axis and the ablation spot was 22.0 mm for a Ti:sapphire target and 17.7 mm for a silicon target. The maximum speed of the rotation of the target was 8000 rpm. Ejected droplets were deposited on a quartz substrate placed 45 mm from the target surface. The size of the substrate was 10 × 10 × 1 mm. The thermal radiation from the ejected droplets was observed by an image-intensified CCD camera. The image was temporally stored in an image freezer and preserved in a computer.

Correspondence: Email: nakata@ees.kyushu-u.ac.jp; WWW: <http://www.laser.ed.kyushu-u.ac.jp>; Telephone: +81-92-642-3895; Fax: +81-92-642-3965

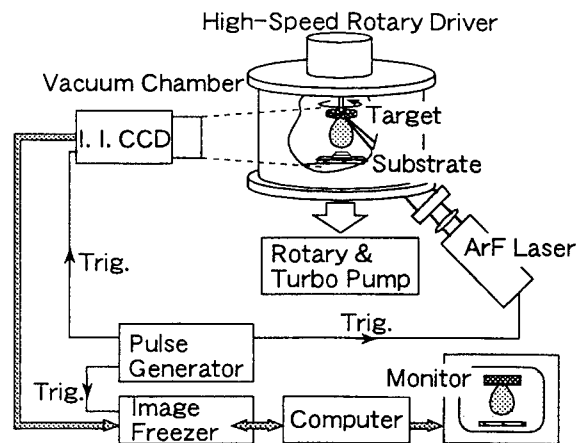


Figure 1. Experimental setup

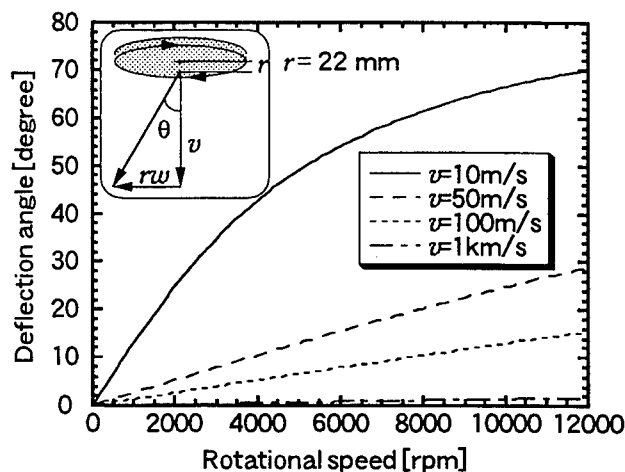


Figure 2. Deflection angle as a function of rotational speed

3. BEHAVIOR OF PARTICLES IN GAS PHASE

3.1. Simulation of the Deflection of the Ejection Angle of Droplets

In the past experiment, the ablated atoms and molecules flew with the velocity over 1 km/s.⁹ On the other hand, the droplets flew with the slower velocity, typically about 50 m/s. The deflection angle due to the rotation of the target is different for the velocity which the species originally have. So by using high-speed rotating target, the directions of the different species can be separated. The deflection angle of the species, which fly vertically to the target surface, can be calculated by the following equation.

$$\theta = \tan^{-1}(rw/v) \quad (1)$$

θ is a deflection angle, v is the normal velocity of the species ejected from the target, r is a distance between the ablation spot and the center of the rotating target, and w is angular speed of the target.

Fig.2 shows the calculated deflection angle as a function of rotational speed. In the calculation, $r = 22$ mm which is the same value in the experiment for Ti:sapphire target.

Usually, for droplets ejected from the target with a velocity of 50 m/s, the deflection angle is about 20 degree with 8000 rpm. On the other hand, most atoms and molecules have the velocity faster than 1 km/s. In this case, the

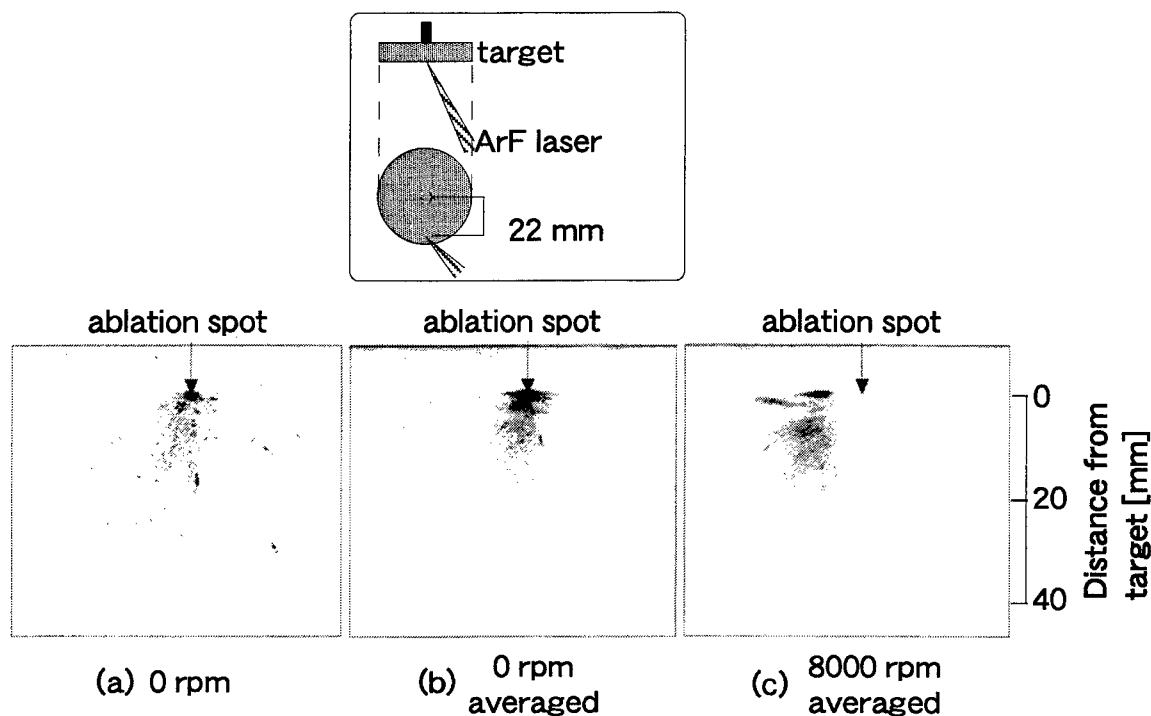


Figure 3. Behavior of the droplets in the gas phase with the ablation of Ti:sapphire. (a) was observed with one shot of ablation and without rotation. (b) shows the image averaged over 10 different images with the same condition of (a). (c) shows the averaged image with rotation of 8000 rpm.

deflection angle is smaller than 2 degree. So, the difference of the deflection angle between droplets and atoms or molecules is around 20 degree. This value becomes larger for the slower droplets.

In actual process, the distribution of droplets in gas phase is as cone shape with an solid angle. So, the rotational speed would change corresponding to the ejection angle and the velocity of the droplets. These values would change with the operating conditions of the ablation laser such as energy, fluence, pulse width, wavelength, and with the condition of the target. Further, the number of the droplets will change by these values, so these should be optimized with the rotation of the target.

3.2. Observation of the Behavior of Droplets by Image-intensified CCD Camera

The droplets ejected by laser ablation are at high temperature, and radiate thermal radiation. By observing this, the behavior of the droplets in the gas phase can be imaged.⁸ Fig. 3 shows the images of droplets observed by image-intensified CCD camera. The observation time was between 200 μ s to 400 μ s after laser ablation, which was controlled by a pulse generator. Fig. 3 (a) was observed with one shot of ablation and without rotation of the target. Fig. 3 (b) shows the image averaged over 10 different images observed at the same condition as (a). Bright points show the thermal radiation from the ablation spot, and the reflection of it by the target holder. Droplets seem to fly with a cone shape. The fastest droplets have the velocity of about 50 m/s. Fig. 3 (c) shows the averaged image observed with a rotation of 8000 rpm. Most droplets seem to fly towards lefthand due to the deflection by rotation. In this condition, the deposition of droplets will be reduced for a substrate placed just below the ablation spot.

Fig. 4 shows the integrated angular distributions of droplets. The signal of the point nearer than 24 mm from the ablation spot is integrated. The signal at around 90 degree is due to the reflection from the target holder. It should be noted that the deflection angle of 13 degree existed without the rotation. This is caused by the incident angle of the ablation laser to the target, which is about 30 degree to the rotation axis as shown in Fig. 4. As the target

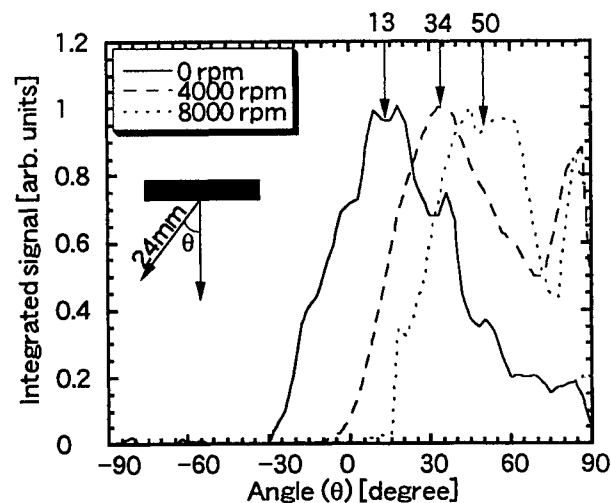


Figure 4. Integrated signal intensity representative angular distributions of droplets with Ti:sapphire target.

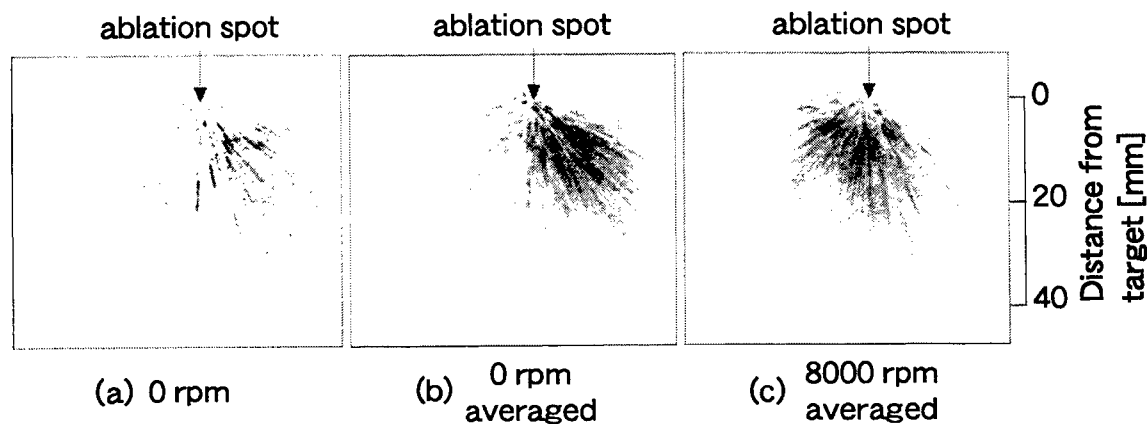


Figure 5. Behavior of the droplets in the gas phase with the ablation of silicon. (a) was observed with one shot of ablation and without rotation. (b) shows the image averaged over 10 different images with the same condition of (a). (c) shows the averaged image with rotation of 8000 rpm.

rotational speed was increased, the deflection angle also increased. The width of distribution in angle is about 50 degree FWHM with any rotational speed. Quite a few droplets flew with 0 degree even with 4000 rpm.

We also observed the behavior of the droplets ejected from a silicon target, as shown Fig. 5. In this case, the observed time region was between 200 and 500 μ s after ablation. The number of droplets seems to be larger than that with the ablation of Ti:sapphire target. The angular distributions of droplets of silicon are shown in Fig. 6. The signal of the point nearer than 26.6 mm from the ablation spot is integrated. The deflection angle without rotation is -45 degree, and this is quite different compared to the case of Ti:sapphire target. As the target rotated faster, the ejection angle became closer to the target normal. For the effective reduction of the droplets, the ablation spot should be on the opposite side of the target, or the direction of rotation should be reversed.

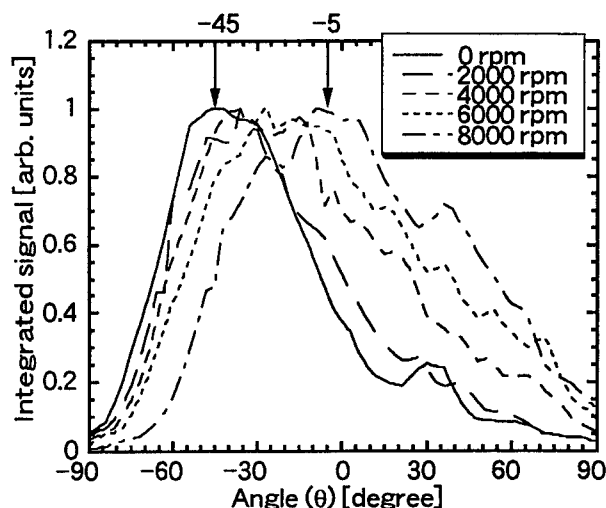


Figure 6. Integrated signal intensity representative angular distributions of droplets with silicon target.

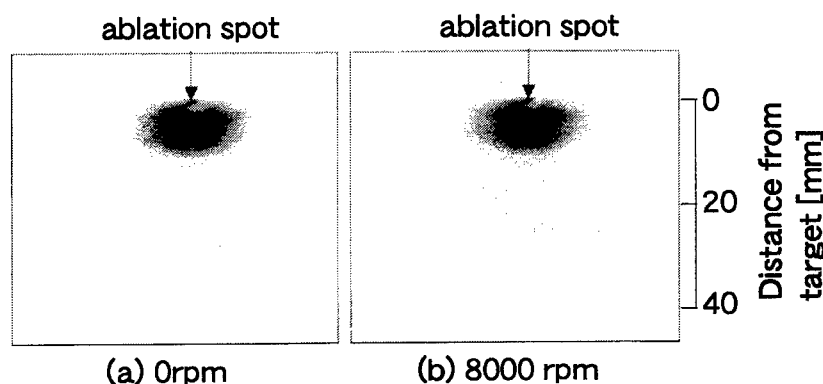


Figure 7. Behavior of atoms and molecules. (a) 0 rpm, (b) 8000 rpm.

3.3. Observation of the Behavior of Atoms and Molecules

Fig. 7 shows the emission from atoms and molecules ejected from the target. This emission can be observed at earlier delay time of some μs .⁹ The delay time was 1 μs and the gate width was 10 ns. No significant difference was observed between 0 and 8000 rpm. This shows that the rotation of the target does not effect the atoms and molecules, which deposit and form a thin film.

4. FILM PROPERTIES

4.1. Images of the Droplets on Substrates

The surface of the substrate was observed by SEM. Fig. 8 shows the examples of observed images of the surface of the deposited Ti:sapphire thin films for the rotation of (a) 0 rpm and (b) 8000 rpm. The films were deposited with 12000 shots of ablation. The films were deposited just below the ablation spot, and the distance between the target surface and the substrate was 45 mm. It is clear that the number of droplets decreased dramatically with the rotation of the target. This clearly shows that high-speed rotation target is quite effective to decrease the deposition of droplets in PLD process.

Fig. 9 shows the number of droplets, of which the diameter was larger than 300 nm, counted from the images observed by SEM. As the target rotated faster, the number decreased. Over 4000 rpm, the number is steady. The droplets which can be seen even with over 4000 rpm are dusts originally adhered at the substrate. Therefore,

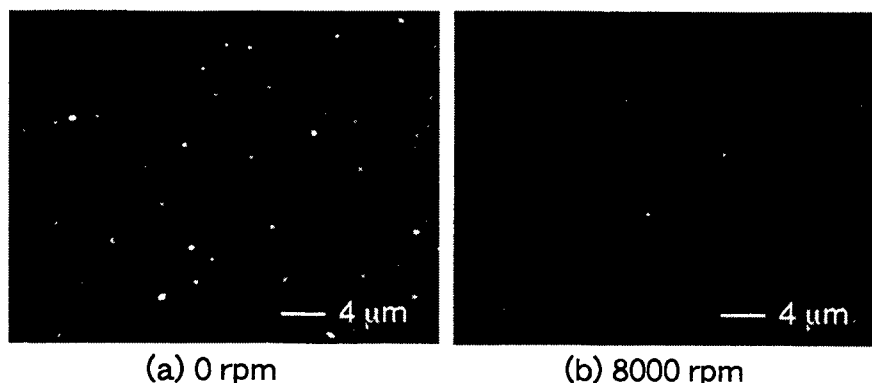


Figure 8. Images of surfaces of thin films for the rotation of (a) 0 rpm and (b) 8000 rpm.

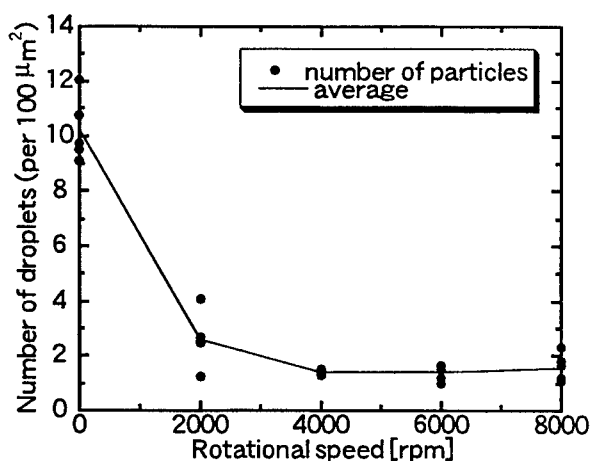


Figure 9. Number of droplets as a function of target rotational speed.

high-quality substrate surface or cleaning is needed for the fabrication of the optical thin films. In addition, in our experiment, the number of ejected droplets decreased as the number of ablation, due to the so called laser cleaning of the surface of the target.

4.2. Photo Emission Spectrum of Ti:sapphire Thin Film

Fig. 10 shows the photo emission spectrum from the deposited Ti:sapphire thin film. In PLD process, the deposition was done in Ar gas at 5 mTorr. The frequency of the ablation laser was 20 Hz, and the deposition time was 1 hour. The substrate was sapphire crystal. In the excitation, the film was irradiated by the second harmonics of a Nd:YAG laser (532 nm). The emission was observed by a photo-multiplier tube attached to a monochromator. Here, the spectrum response of the detector system was not calibrated. A spectrum similar to a bulk target was obtained as shown in Fig. 10. The peak wavelength was about 750nm.

Fig. 11 shows the photo emission intensity as a function of time, observed at 750 nm. The fluorescence lifetime was 3.18 μs , and which is also similar to the value of a bulk crystal.

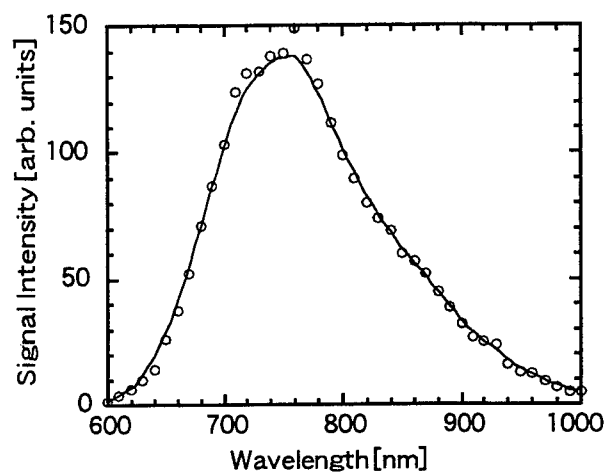


Figure 10. Photo emission spectrum of deposited Ti:sapphire film.

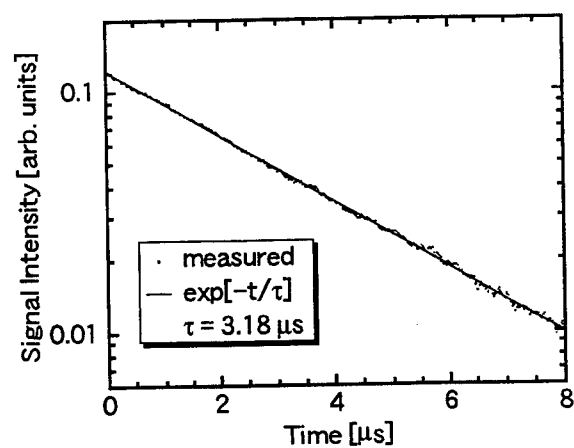


Figure 11. Photo emission intensity as a function of time, which is observed at 750 nm.

5. CONCLUSION

In this paper, we investigated the effect of the high-speed rotating target to the decrease of the droplets on the deposited film. The properties of Ti:sapphire thin films were also investigated.

1. Deflection angle to the flight of droplets was calculated as a function of the rotation of the target. The deflection angle increased as the rotational speed.
2. The behavior of droplets in gas phase was imaged by image-intensified CCD camera. The deflection due to rotation of target was visualized. The angular distributions were calculated by integrating the signal in the observed images.
3. The behavior of emissive atoms and molecules are imaged. No difference was observed for the rotational speed.
4. The surface of deposited films was observed by SEM. The droplets clearly decreased as the rotation of the target.
5. The photo emission spectrum from the Ti:sapphire thin film was observed, and was similar to the bulk Ti:sapphire target.

ACKNOWLEDGMENTS

This work was made collaboration with Fukuoka IST. The SEM observation was performed at the Engineering Branch of the Center of Advanced Instrumental Analysis of Kyushu University.

REFERENCES

1. P. D. Townsend, P. J. Chandler, R. A. Wood, L. Zhang, J. McCallum and C. W. McHargue, "Chemically stabilised ion implanted waveguides in sapphire," *Electron. Lett.* **26**, pp. 1193-1195, 1990.
2. L. M. B. Hickey, E. Martins, J. E. Roman, W. S. Brocklesby and J. S. Wilkinson, "Fluorescence of Ti^{3+} ions thermally diffused into sapphire," *Opt. Lett.* **21**, pp. 597-599, 1996.
3. L. M. B. Hickey, E. Martins, J. E. Roman, W. S. Brocklesby and J. S. Wilkinson, "Titanium diffused waveguides in sapphire," *Electron. Lett.* **32**, pp. 2238-2239, 1996.
4. A. A. Anderson, R. W. Eason, M. Jelinek, C. Grivas, D. Lane, K. Rogers, L. M. B. Hickey and C. Fotakis, "Growth of Ti:sapphire single crystal thin films by pulsed laser deposition," *Thin Solid Films* **300**, pp. 68-71, 1997.
5. H. Uetsuhara, T. Nasu, Y. Nakata, N. Vasa, T. Okada, and M. Maeda, " Ti^{3+} :sapphire thin films fabricated by pulsed-laser deposition," *Jpn. J. Appl. Phys.* **37**, pp. 2530-2531, 1998.
6. A. A. Anderson, R. W. Eason, L. M. B. Hickey, M. Jelinek, C. Grivas, D. S. Gill and N. A. Vainos, "Ti:sapphire planar waveguide laser grown by pulsed laser deposition," *Opt. Lett.* **22**, pp. 1556-1558, 1997.
7. B. Holzapfel, B. Roas, L. Schultz, P. Bauer and G. Saemann-Ischenko, "Off-axis laser deposition of $YBa_2Cu_3O_{7-x}$ thin films," *Appl. Phys. Lett.* **61**, pp. 3178-80, 1992.
8. David B. Geohegan, "Imaging and blackbody emission spectra of particulates generated in the KrF-laser ablation of BN and $YBa_2Cu_3O_{7-x}$," *Appl. Phys. Lett.* **62**, pp. 1463-1465, 1993.
9. Y. Nakata, H. Kaibara, T. Okada, and M. Maeda, "Two-dimensional laser-induced fluorescence imaging of a pulsed-laser deposition process of $YBa_2Cu_3O_{7-x}$," *J. Appl. Phys.* **80**, pp. 2458-2466, 1996.

Crystallinities and Light Emitting Properties of Nanostructured SiGe Alloy Prepared by Pulsed Laser Ablation in Inert Background Gases

Takehito Yoshida, Yuka Yamada, Nobuyasu Suzuki, Toshiharu Makino,
Takaaki Orii*, Kouichi Murakami**,
David B. Geohegan***, Douglas H. Lowndes***, and Michael J. Aziz****

Matsushita Research Institute Tokyo, Inc., 3-10-1 Higashimita, Tama-ku, Kawasaki 214-8501, Japan

*Institute of Applied Physics, Univ. of Tsukuba, Tsukuba, Ibaraki 305-0006, Japan

** Institute of Materials Science, Univ. of Tsukuba, Tsukuba, Ibaraki 305-0006, Japan

***Solid State Division, Oak Ridge National Lab., Oak Ridge, TN 37831-6056

****Division of Applied Science, Harvard Univ., 29 Oxford Street Cambridge, MA 02138

ABSTRACT

For studying the material properties of nanostructured group IV materials, we have developed a pulsed laser ablation method into inert background gases. SiGe alloy nanocrystallites have possibility of novel band structure engineering by controlling not only compositions but also particle sizes. An ArF excimer laser was focused onto the surface of the powder-sintered $\text{Si}_x\text{Ge}_{1-x}$ target. During the laser ablation, He gas was introduced into a vacuum chamber and was maintained at a constant pressure. Size distribution of the $\text{Si}_x\text{Ge}_{1-x}$ ultrafine particles decreases with decreasing composition x under fixed conditions of deposition such as background gas pressure. Raman scattering spectra of the deposited SiGe ultrafine particles show three peaks ascribed to mixed crystalline SiGe after annealing, and the linewidths of these peaks broaden due to the reduced size of the crystallites. The frequencies and intensities of the peaks depend on the composition x . Visible PL spectra have broad peaks from 2.25 eV to 2.10 eV, at room temperature. The peak positions show blue shifts with increasing x . Electroluminescent diodes with the $\text{Si}_{0.8}\text{Ge}_{0.2}$ nanocrystallite active region were fabricated, and emit visible light peaked at around 1.8 eV, at room temperature.

Keywords: silicon-germanium alloy, nanocrystallites, pulsed laser ablation, Raman scattering, electroluminescence

1. INTRODUCTION

Ever since visible photoluminescence (PL) spectra were observed in nanometer-sized silicon (Si) ¹⁻⁴, extensive studies have been carried out on nanometer-sized structures of group IV materials. In particular, the strong PL from porous Si has attracted much attention and much research has been undertaken to clarify its origin ⁵. Furthermore, SiGe alloys have the capabilities of band structure engineering by controlling the composition ⁶, and there have been several reports on optical properties of porous SiGe ^{7,8}. When we discuss the optical properties of nanoscaled group IV materials as one of the quantum confinement effects, it is significant to adopt another approach using the nanoscale "spherical" structures which have well-controlled size and surface chemical structure. For this purpose, pulsed laser ablation (PLA) ⁹ into a background gas has been applied to the preparation of Si ultrafine particles ¹⁰⁻¹³. Werwa et al. ¹⁰ reported that the minimum diameter of Si ultrafine particles was about 2 nm in laser ablation into a pulsed inert gas. Yoshida et al. ¹² reported that the size distribution of Si nanocrystallites was controlled by varying the background gas pressure. Deohegan et al. ¹⁴ confirmed that the ejected species condensed into nanoparticles in the background gases. Furthermore, PLA has the potentialities for use in the deposition of complex materials with congruent transfer of the target composition ^{9,15}, and SiGe thin films have been prepared using this method ¹⁶. However, there have been few studies where alloy nanocrystallites are produced using PLA in background gases.

Recently, some research groups have focused on electroluminescence (EL) properties as well as on PL properties because the EL of the nanoscaled Si structures is suited to optoelectronic device applications. Most EL Si structures have been thinned to "porous" structures formed by liquid phase anodization. ⁵ EL of porous Si was first observed during anodic oxidation in an electrolyte solution. ¹⁷ Porous Si EL devices operating in the atmosphere have been studied with solid-state

* Present address: The Institute of Physical and Chemical Research (RIKEN), 2-1 Hirosawa, Wako-shi, Saitama 351-0198, Japan

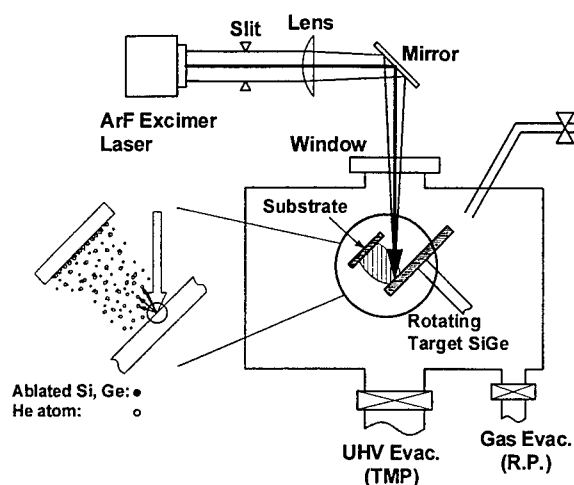


Fig. 1. Schematic of the preparation system of SiGe alloy nanocrystallites using pulsed laser ablation in a reduced-pressure inert background gas.

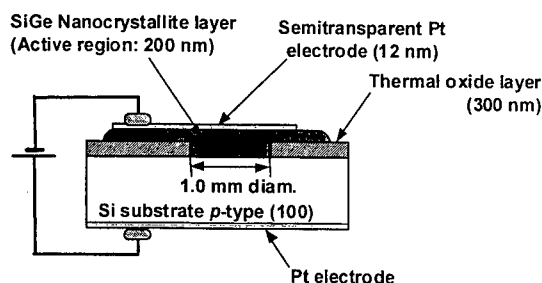


Fig. 2. Schematic cross-sectional view of the electro-luminescent (EL) diode. The structure is (semitransparent Pt electrode)/(SiGe nanocrystallite layer)/(*p*-type Si)/(Pt electrode).

contacts, including semitransparent metal-contacted Schottky junction diodes,¹⁸⁻²⁰ *p-n* homojunction diodes²¹⁻²⁴ and *p-n* heterojunction diodes.²⁵⁻²⁸ Besides the porous Si, Qin et al. developed a visible EL device of the low operational voltage (> 4 V) in gold (Au)-contacted extra thin (4 nm) Si-rich Si oxide films deposited by magnetron sputtering.²⁹ Nassiopoulou et al. observed visible EL from Si nanopillars formed using highly anisotropic reactive etching and thinning thermal oxidation.³⁰

In this work, we adopt the PLA in a constant pressure inert background gas. A sintered mixture of Si and Ge powders is used as a target. We characterize structures and optical properties of SiGe alloy nanocrystallites prepared by the PLA in inert background gas. In addition, we fabricate an EL diode with the $\text{Si}_{0.8}\text{Ge}_{0.2}$ alloy nanocrystallite active region, using the PLA in inert background gases as one of the physical vapor deposition (PVD) methods, aiming reasonable operational voltage (several - 25 V). We characterize electrical conductivity, dependence of EL intensity on excitation current and luminescence spectrum. Our fabrication method is compatible with the established Si large scale integrated (LSI) technology because the PVD-like process is suitable for successive film stacking and etching of fine patterns.

2. EXPERIMENTAL PROCEDURE

In order to deposit Si and Ge, which have different melting points and vapor pressures, at the same time by laser ablation, an appropriate target should be a mixture of Si and Ge with high purity. Thus, sintered SiGe targets were fabricated as follows. Si and Ge powders with the size of μm order and high purity of 6N were mixed without binder and sintered using a hot press system in an inert gas. Then, we could obtain $\text{Si}_x\text{Ge}_{1-x}$ ($x = 0.18, 0.82$) sintered targets of 2-inch diameter with purity over 4N. The alloy composition x of the sintered target was determined using inductively coupled plasma optical emission spectroscopy (ICPS).

SiGe ultrafine particles were prepared using PLA of the sintered SiGe target in an inert background gas at constant reduced pressure. A schematic diagram of the laser ablation apparatus used in this study is shown in Fig. 1. After the vacuum chamber was evacuated to 1.0×10^{-6} Pa, helium (He) gas was introduced into the chamber and was maintained at a constant pressure (333 Pa) using a differential evacuation system. An argon-fluoride (ArF) excimer laser (λ : 193 nm, energy density: $1.0 \text{ J}/(\text{cm}^2 \cdot \text{pulse})$, pulse duration: 12 ns, repetition rate: 10 Hz) beam was focused onto a $3 \times 1 \text{ mm}^2$ rectangular spot at the surface of the sintered SiGe target of 2-inch diameter. Then, a plume of ejected species was created and extended almost perpendicular to the target surface. The target was rotated at 8 rpm. As described above, the size of the mixed powders of the sintered target was of μm order, which is much smaller than the spot size of the irradiated laser beam. Thus, the ejected species can have a mixed composition. A deposition substrate was located at a distance of 10 mm normal to the target. The species ejected from the target condensed during flight in a background gas¹⁴ and then were deposited as ultrafine particles on the substrate¹². The substrate was kept at room temperature during the deposition process. Finally, the deposited substrates were annealed in dry nitrogen (N_2) at 800°C for 10 min., using an usual resistance-heating furnace.

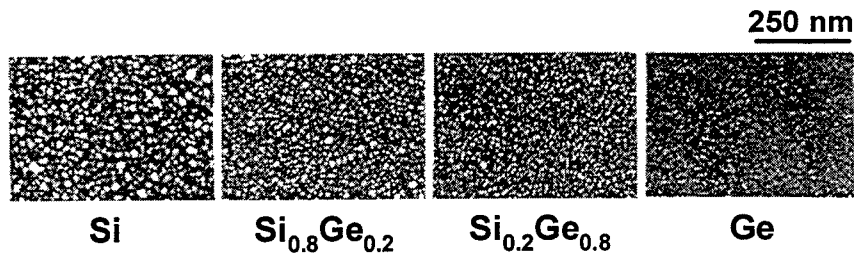


Fig. 3. SEM photographs of as-deposited $\text{Si}_x\text{Ge}_{1-x}$ ultrafine particles. The average size of the ultrafine particles decreases with decreasing composition x .

A schematic cross-sectional view of the EL diode is shown in Fig. 2. To fabricate the EL diode, (100) oriented p -type Si wafers with a resistivity of $0.02 \Omega\cdot\text{cm}$ were used as substrates. Thermal oxide layers were formed with a thickness of 300 nm for the isolation dielectrics. Electrically active regions with a diameter of 1.0 mm were defined by removing the thermal oxide with $\text{HF}+\text{NH}_4\text{F}$ solution. The Si nanocrystallite layers were deposited by the above PLA method. Thermal annealing was carried out at 825°C for 10 min in N_2 , using a rapid thermal annealing system. In order to form a contact with the Si nanocrystallite layers, semitransparent platinum (Pt) films were deposited with a thickness of 12 nm. The EL active regions were Si nanocrystallite layers with an area of $7.9 \times 10^{-3} \text{ cm}^2$ (1.0 mm diameter circle) and a thickness of about 200 nm.

Scanning electron microscope (SEM) observation was employed to evaluate the particle size of the deposits. The average composition of the deposited particles was evaluated using ICPS measurement. Raman scattering spectra were measured with a filtered single monochromator (Jasco TRS-600) system in a backscattering geometry. Excitation was provided by the 514.5 nm Ar^+ ion laser line. A CCD system (Photometrics TK512CB) was used as a detector. To prevent damage of samples by the laser and/or a change of the Raman spectrum during measurements, the laser power was chosen to be less than 4 mW. In the Raman scattering measurement, fused quartz was used for the deposition substrate. Furthermore, PL

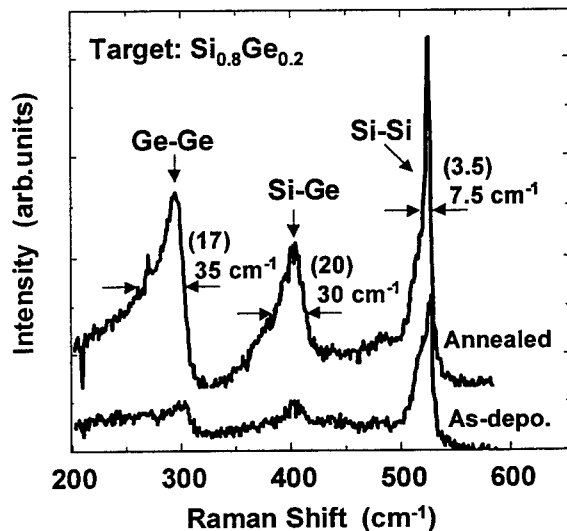


Fig. 4. Raman spectra of $\text{Si}_{0.8}\text{Ge}_{0.2}$ alloy nanocrystallites. Three Raman peaks intrinsic to crystalline SiGe alloys are observed.

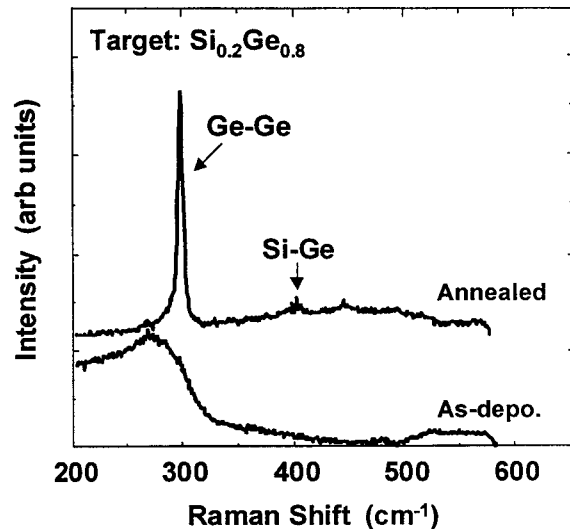


Fig. 5. Raman spectra of $\text{Si}_{0.2}\text{Ge}_{0.8}$ alloy nanocrystallites. Ge-Ge and Si-Ge peaks are observed after annealing.

measurements were performed at room temperature using a single polychromator (Jasco CT-25C) system with a cooled MOS linear-image sensor unit (Hamamatsu C4834-02) as a detector. An Ar⁺ ion laser (λ : 488.0 nm, power: 5 mW) was used as an excitation light source. The spectral sensitivity of the measurement system was calibrated using a halogen standard lamp.

We measured the current-voltage (*I-V*) characteristics of the EL diodes. The dependence of the integrated EL intensity on the diode current was investigated at room temperature. The EL intensity was measured by a photomultiplier (Hamamatsu Photonics R3896). The EL spectra were measured at room temperature using a single polychromator system (Acton SpectraPro-275) with a cooled FET-CCD image sensor unit (Hamamatsu M6296-01) as a detector.

3. EXPERIMENTAL RESULTS

The as-deposited Si_xGe_{1-x} ultrafine particles were observed using SEM to clarify the dependence of the particle size on the composition *x*. These results are shown in Fig. 3. Nanometer-sized ultrafine particles are observed. Furthermore, the average size decreases with decreasing *x* under the fixed processing conditions. The average composition of the ultrafine particles deposited on the Al₂O₃ substrate using the Si_{0.82}Ge_{0.18} target was evaluated by ICPS. The total ratio (at.%) of Si:Ge of the deposited ultrafine particles was obtained as 78.9:21.1. From this result, it is revealed that our PLA process can transfer as a whole the composition of the target to the deposits.

Figure 4 shows Raman scattering spectra of the Si_{0.8}Ge_{0.2} ultrafine particles before and after the annealing. Three Raman peaks ascribed to the vibrations of Ge-Ge, Si-Ge and Si-Si pairs are observed at 292, 400 and 520 cm⁻¹, respectively. These peaks are intrinsic to the crystalline SiGe alloy system.³¹ The intensities of these peaks increase after annealing. This result shows that crystallization progressed after the annealing process. Figure 5 shows Raman scattering spectra of the Si_{0.2}Ge_{0.8} ultrafine particles before and after the annealing. A broad peak appears at 200-300 cm⁻¹ before the annealing, which is associated with amorphous Ge.⁴ After annealing, Ge-Ge and Si-Ge peaks are observed at 298 and 400 cm⁻¹, respectively.³¹ The Si-Si peak cannot be observed. As a result, the Ge-rich ultrafine particles, which are amorphous-like before annealing, are crystallized after the annealing process.

Figures 6 (a), (b), and (c) show the PL spectrum from the SiGe nanocrystallites of which compositions are Si_{0.8}Ge_{0.2}, Si_{0.2}Ge_{0.8}, and pure Ge, respectively. In all of them, broad green PL bands appear at room temperature. The PL intensities increase after the annealing. These PL spectra have broad peaks from 2.25 eV to 2.10 eV, with a low energy shoulder around 1.8 eV. The peak positions showed blue shifts with increasing silicon content *x*. There is a tendency where the shoulder intensity increases with increasing silicon content *x*.

Figure 7 shows the *I-V* characteristics of a typical EL diode in linear scale. In the pure Si nanocrystallite, a weak rectifying behavior is observed. In the Si_{0.8}Ge_{0.2} nanocrystallite, the reverse-biased curve seems a soft-breakdown characteristics. The series resistances *R_s* in the forward bias regions were estimated to be 70 Ω and 170 Ω, in Si_{0.8}Ge_{0.2} and pure Si,

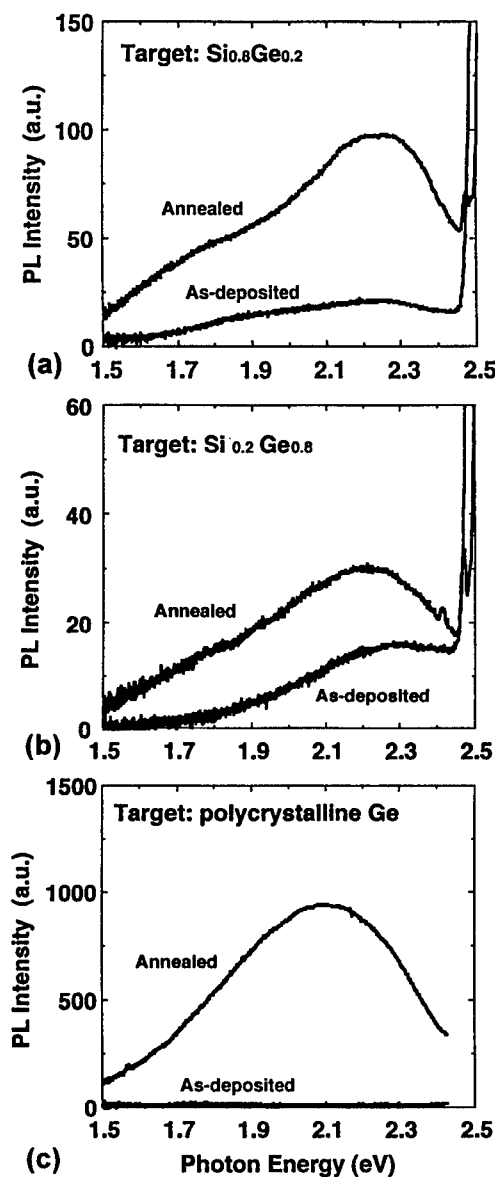


Fig.6. PL spectra from SiGe alloys and pure Ge nanocrystallites. (a) Si_{0.8}Ge_{0.2}, (b) Si_{0.2}Ge_{0.8}, (c) Pure Ge.

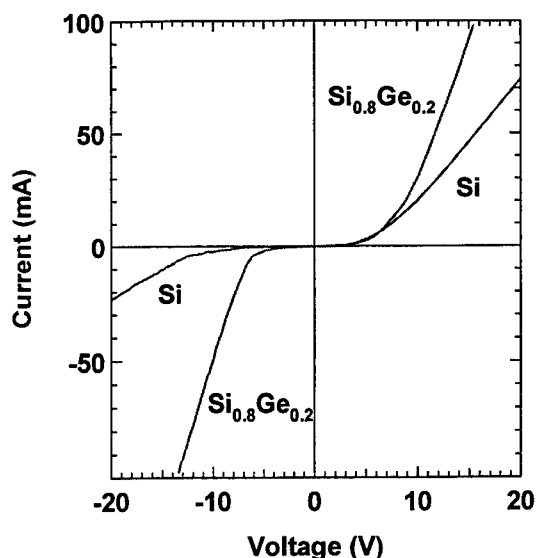


Fig.7. I - V characteristics of the EL diodes with the $\text{Si}_{0.8}\text{Ge}_{0.2}$ alloy and pure Si nanocrystallite layers as the active regions.

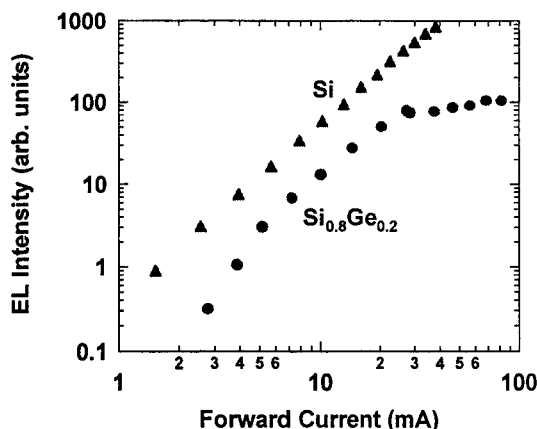


Fig.8. Integrated EL intensity I_{EL} as a function of the forward current j , for the EL diodes with the $\text{Si}_{0.8}\text{Ge}_{0.2}$ alloy and pure Si nanocrystallite active layers.

respectively. The onsets of the light emission, measured with the photomultiplier, were forward-biased dissipation power about 10 mW, in both the pure Si and the $\text{Si}_{0.8}\text{Ge}_{0.2}$ nanocrystallite EL diodes. Figure 8 shows the integrated EL intensity I_{EL} as a function of the forward current j in a log-log scale. In the pure Si, it is evident that the dependence of I_{EL} on j is according to a rapid power law.³² Namely, I_{EL} is proportional to j^m , $m=2.2$. In the $\text{Si}_{0.8}\text{Ge}_{0.2}$, the rapid power law was also observed as a relation between I_{EL} and j . However, I_{EL} saturated in the forward current range more than 3 mA. Figure 9 shows the measured EL spectra of both the pure Si and the $\text{Si}_{0.8}\text{Ge}_{0.2}$ nanocrystallite EL diodes. Dissipation powers of the pure Si and the $\text{Si}_{0.8}\text{Ge}_{0.2}$ were 0.86 W (20 V, 43 mA) and 0.82 W (12 V, 68 mA), respectively. Both spectra have peaks around 1.8 eV and shoulders around 2.2 eV. The peak and shoulder positions of the $\text{Si}_{0.8}\text{Ge}_{0.2}$ looks slightly blue-shifted, in comparison with those of the pure Si.

4. DISCUSSION

There have been several reports on the study of the dependence of the Raman scattering spectra on the composition x of bulk $\text{Si}_x\text{Ge}_{1-x}$ alloys.^{31,33} The frequencies and linewidths (FWHM) of three Raman peaks ascribed to vibrations of Ge-Ge, Si-Ge, and Si-Si pairs strongly depend on the composition x . The frequencies of these peaks in Figs. 4 and 5 correspond well to those of the bulk $\text{Si}_{0.8}\text{Ge}_{0.2}$ and $\text{Si}_{0.2}\text{Ge}_{0.8}$ alloys reported in Ref. 31. This result shows that the composition is maintained in the SiGe alloy nanocrystallites deposited by PLA in an inert background gas.

However, the FWHM of the three Raman peaks in our experiment are about 2 times broader than that of the bulk alloys in Ref. 31. The FWHM values of this work are indicated in Fig. 4. Also the FWHM values in Ref. 31 are indicated in the brackets. According to a spatial correlation model, finite size effects relax the q -vector selection rule and this relaxation of the momentum conservation leads to a broadening and downshift of the Raman spectrum.³⁴ To

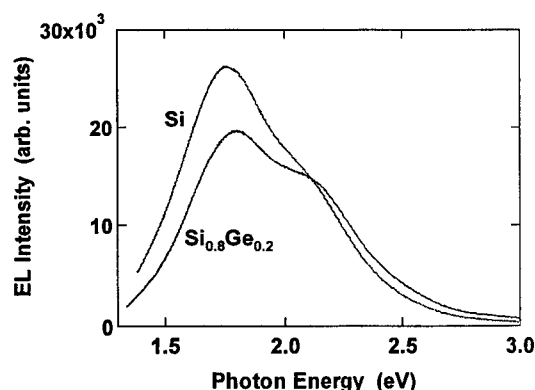


Fig.9. EL spectra at room temperature, for the EL diodes with the $\text{Si}_{0.8}\text{Ge}_{0.2}$ alloy and pure Si nanocrystallite active layers.

clarify the finite size effects shown in the Raman spectrum, Raman scattering measurements were also performed for Si nanocrystallites. **Figure 10** shows Raman scattering spectra of the Si nanocrystallites before and after oxidation annealing.³⁵ The dash-dotted line indicates the peak position of the bulk single-crystalline Si. The Raman peak of the bulk Si was symmetric and had a FWHM of 3.7 cm⁻¹ in this measurement. It was found that the Si nanocrystallites have a broader and lower frequency peak in comparison with the bulk Si. The average diameter of the as-deposited Si nanocrystallites in **Fig. 10** was estimated to be about 11 nm using the strong phonon confinement model.³⁶ This result is in good agreement with the result obtained from high-resolution transmission electron microscopy (TEM).^{12,35} Furthermore, the annealing process causes a much broader shape and lower frequency, as shown in **Fig. 10**. This result proposes that the oxidation annealing caused a size reduction of the core of the Si nanocrystallite.

The broadened FWHMs of the Raman peaks in SiGe alloy nanocrystallites must also be caused by the reduction of the particle size. **Figure 11** shows the Si-Si peak of the Si_{0.8}Ge_{0.2} alloy nanocrystallites after the annealing in **Fig. 4**. The FWHM broadens to 7.0 cm⁻¹, especially to lower frequencies compared to the Si nanocrystallites. This result cannot be explained by only the reduced size of the SiGe nanocrystallites. The inclusion of Ge as impurities in Si should increase lattice disorder which would result in the relaxation of the *q*-vector selection rule. Furthermore, Okada and Iijima indicated the existence of the strong stress in oxidized Si particles from the study of the oxidation properties.³⁷ Such a stress especially in the nanocrystallites can exist in the SiGe nanocrystallites and cause the strain effects, which also results in the broadening of the Raman peaks.

Consequently, Raman scattering spectra of Si_xGe_{1-x} alloy nanocrystallites depend on the composition *x*. The peak shifts of nanocrystalline and bulk SiGe alloys can be explained by the same mechanism. Furthermore, the linewidths broaden to lower frequencies compared to the bulk alloys. This property is considered to be derived from the synergistic effect of the finite size confinement and the lattice disorder.

In **Figs. 6**, the PL spectra have broad peaks from 2.25 eV to 2.10 eV, with a low energy shoulder around 1.8 eV. The peak positions showed blue shifts with increasing composition (silicon content) *x*. This tendency is consistent with bandgap dependence on the composition *x*, in the bulk SiGe alloy.⁶ On the other hand, in the both EL spectra, there are peaks around 1.8 eV and shoulders around 2.2 eV, in **Fig. 9**. The peak and shoulder positions of the Si_{0.8}Ge_{0.2} looks slightly blue-shifted, in comparison with those of the pure Si. It can be said that the green band emission (peaked around 2.2 eV) and the red band emission (peaked around 1.8 eV) are associated with "shallow" and "deep" localized states, respectively. Furthermore, in general, the capture cross section of the non-radiative center P_{NR} is described by the following formula:³⁸

$$P_{NR} = W_0(h\omega_0/kT) \exp(-(2R/Re) - (E_A/kT^*)) \quad (1)$$

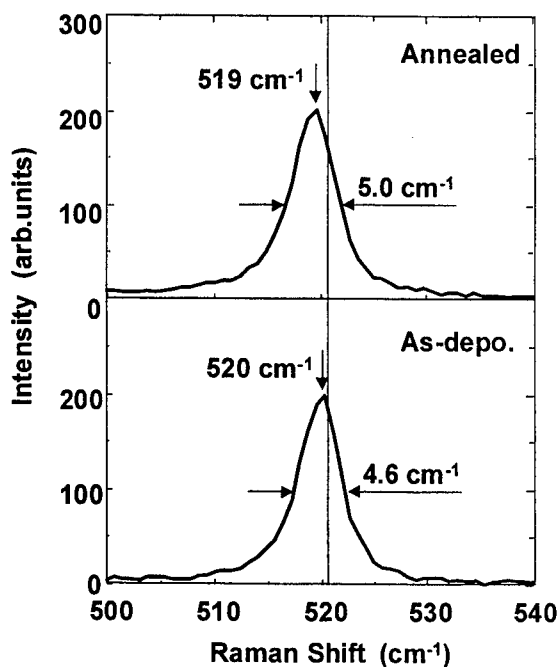


Fig.10. Raman spectra of Si pure nanocrystallites. Dash-dotted line indicates the peak position of the bulk single-crystalline Si. FWHM of the bulk Si was 3.7 cm⁻¹ in this measurement.

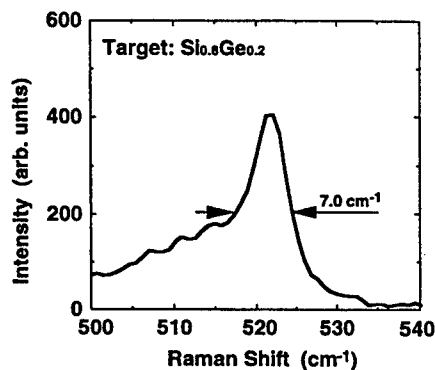


Fig.11. Raman peak ascribed to Si-Si vibration of the Si_{0.8}Ge_{0.2} alloy nanocrystallites after annealing in **Fig. 4**. FWHM broadens to 7.0 cm⁻¹.

$$T^* = (h\omega_0/2k) \coth(h\omega_0/2kT), \quad (2)$$

where ω_0 , E_A , R , and Re stand for the phonon frequency, activation energy of a localized state, distance between an electron and a non-radiative center, and extent of electron wave function, respectively. According to equ. (1), the shallower activation energies of the localized states are, the higher probabilities of the non-radiative recombinations are, with increasing temperature. In our experimental conditions, dissipation power densities in the typical EL measurements were about 40 times higher than that of the PL measurements, because the dissipation power densities of the EL measurements and the PL measurements were about 100 W/cm² and 2.5 W/cm². Since the measuring temperatures of the EL should be much higher than that of the PL, quenching of the light emitting associated with the shallow levels became remarkable in the EL measurements. We suggest that this is the reason why the EL spectra had 1.8 eV peak and 2.2 eV shoulder in Fig. 9, though the PL spectra in Figs. 6 had 2.25-2.10 eV peaks and 1.8 eV shoulders. However, we have not had enough data to discuss dependence of the emission peak position on the composition x .

In Fig. 7, the I - V characteristics of the EL diodes had only weak rectifying behavior. In our previous study, we observed the strong rectifying behaviors, where an usual resistance-heating furnace was used for the nanocrystallites active layer annealing.³² Reactor of the rapid thermal processing system in this work can be evacuated to 1×10^{-3} Pa by a TMP, before introducing pure N₂ ambient gas. On the other hand, the usual resistance-heating furnace was atmospheric pressure operation without evacuation system. Therefore, we propose that the rectifying behaviors were related to residual oxygen or other contaminant gases in the annealing ambient.

According to Fig. 8, in both the pure Si and the Si_{0.8}Ge_{0.2} nanocrystallite EL diodes, the integrated EL intensity I_{EL} had rapid nonlinear dependence on the forward current density j . As we mentioned in previous study,³² it seems that the excitation mechanism for the EL is associated with impact ionization induced by hot carrier injection and successive radiative recombination. However, the I_{EL} saturation phenomenon in the Si_{0.8}Ge_{0.2} nanocrystallite EL diode has not been understood yet. Further study is in progress.

5. CONCLUSION

SiGe alloy nanocrystallites have been obtained using excimer laser ablation of sintered SiGe targets in a constant-pressure inert background gas. The deposited Si_xGe_{1-x} nanocrystallites have the same alloy composition x as the target. The Raman peaks intrinsic to crystalline alloys have broadened to lower frequencies compared with those of bulk alloys. This should be explained in terms of the synergistic effect of the finite size confinement and the lattice disorder. Furthermore, we observed visible PL spectra which had broad peaks from 2.25 eV to 2.10 eV, at room temperature. The peak positions showed blue shifts with increasing x . Electroluminescent diodes with the Si_{0.8}Ge_{0.2} nanocrystallite active region have successfully been fabricated, and have emitted visible light peaked at around 1.8 eV, at room temperature.

6. ACKNOWLEDGEMENTS

The authors would like to express their thanks to Professor. S. Onari and Associate Professor. K. Matsuishi (Univ. of Tsukuba) and Professor. T. Arai (Ishinomaki Sensyu Univ.) for their fruitful discussion of the optical properties and spectroscopy of mesoscopic materials.

This study was partially supported by a Grant in Aid for International Scientific Research Program: Joint Research of the Ministry of Education, Science and Culture.

7. REFERENCES

1. S. Furukawa and T. Miyasato, Jpn. J. Appl. Phys. 27, L2207 (1988).
2. H. Takagi, H. Ogawa, Y. Yamazaki, A. Ishizaki, and T. Nakagiri, Appl. Phys. Lett. 56, 2379 (1990).
3. L. T. Canham, Appl. Phys. Lett. 57, 1046 (1990).
4. Y. Maeda, N. Tsukamoto, Y. Yazawa, Y. Kanemitsu, and Y. Masumoto, Appl. Phys. Lett. 59, 3168 (1991).
5. D. J. Lockwood, *Light Emission in Silicon from Physics to Devices*, Academic Press, San Diego, 1998.
6. R. Braunstein, A. R. Moore, and F. Herman, Phys. Rev. 109, 695 (1958).
7. S. Gardelis, J. S. Rimmer, P. Dawson, B. Hamilton, R. A. Kubiak, T. E. Whall, and E. H. C. Parker, Appl. Phys. Lett. 59, 2118 (1991).

8. A. Ksendzov, R. W. Fathauer, T. George, W. T. Pike, R. P. Vasquez, and A. P. Taylor, Appl. Phys. Lett. 63, 200 (1993).
9. D. H. Lowndes, D. B. Deohegan, A. A. Puretzky, D. P. Norton, and C. M. Rouleau, Science 273, 898 (1996).
10. E. Werwa, A. A. Seraphin, L. A. Chiu, Chuxin Zhou, and K. D. Kolenbrander, Appl. Phys. Lett. 64, 1821 (1994).
11. T. Makimura, Y. Kunii, and K. Murakami, Jpn. J. Appl. Phys. 35, 4780 (1996).
12. T. Yoshida, S. Takeyama, Y. Yamada, and K. Mutoh, Appl. Phys. Lett. 68, 1772 (1996).
13. Y. Yamada, T. Orii, I. Umezu, S. Takeyama, and T. Yoshida, Jpn. J. Appl. Phys. 35, 1361 (1996).
14. D. B. Geohegan, A. A. Puretzky, G. Duscher, and S. Pennycook, Appl. Phys. Lett. 72, 2987 (1998).
15. D. B. Chrisey and G. K. Hubler, *Pulsed Laser Deposition of Thin Films*, Wiley, New York, 1994.
16. F. Antoni, E. Fogarassy, C. Fuchs, J. J. Grob, B. Prevot, and J. P. Stoquert, Appl. Phys. Lett. 67, 2072 (1995).
17. A. Halimaoui, C. Oules, G. Bomchil, A. Bsiesy, F. Gaspard, R. Herino, M. Ligeon, and F. Muller, Appl. Phys. Lett. 59, 304 (1991).
18. A. Richter, P. Steiner, F. Kozlowski, and W. Lang, IEEE Electron Device Lett. EDL-12, 691 (1991).
19. N. Koshida and H. Koyama, Appl. Phys. Lett. 60, 347 (1992).
20. P. Steiner, F. Kozlowski, and W. Lang, IEEE Electron Device Lett. EDL-14, 317 (1993).
21. Z. Chen, G. Bosman, and R. Ochoa, Appl. Phys. Lett. 62, 708 (1993).
22. P. Steiner, F. Kozlowski, and W. Lang, Appl. Phys. Lett. 62, 2700 (1993).
23. J. Linnros and N. Lalic, Appl. Phys. Lett. 66, 3048 (1995).
24. N. Lalic and J. Linnors, J. Appl. Phys. 80, 5971 (1996).
25. T. Futagi, T. Matsumoto, M. Katsuno, Y. Ohta, H. Mimura, and K. Kitamura, Jpn. J. Appl. Phys. 31, L616 (1992).
26. P. C. Sercel, D. Kwon, T. Vilbrandt, W. D. Yang, J. Hautala, J. D. Cohen, and Hao Lee, Appl. Phys. Lett. 68, 684 (1996).
27. F. Namavar, H. P. Maruska, and N. M. Kalkhoran, Appl. Phys. Lett. 60, 2514 (1992).
28. H. P. Maruska, F. Namavar, and N. M. Kalkhoran, Appl. Phys. Lett. 61, 1338 (1992).
29. G. G. Qin, A. P. Li, B. R. Zhang, and B-C Li, J. Appl. Phys. 78, 2006 (1995).
30. A. G. Nassiopoulous, S. Grigoropoulos, and D. Papadimitriou, Appl. Phys. Lett. 69, 2267 (1996).
31. M. Balkanski, *Light Scattering in Solids*, p. 326, Flammarion, Paris, 1971.
32. T. Yoshida, Y. Yamada, T. Orii, J. Appl. Phys. 83, 5427 (1998).
33. W. J. Brya, Solid State Commun. 12, 253 (1973).
34. H. Richter, Z. P. Wang, and L. Ley, Solid State Commun. 39, 625 (1981).
35. T. Yoshida, Y. Yamada, S. Takeyama, T. Orii, I. Umezu, and Y. Makita, Proc. SPIE 2888, 6 (1996).
36. I. H. Campbell and P. M. Fauchet, Solid State Commun. 58, 739 (1986).
37. R. Okada and S. Iijima, Appl. Phys. Lett. 58, 1662 (1991).
38. R. Englman and J. Jortner, Molecular Phys. 18, 145 (1970).

Properties of boron-carbon-nitrogen ternary thin films synthesized by pulsed laser deposition

Z. M. Ren^a, Y. F. Lu^{*a}, Z. H. Mai^a, B. A. Cheong^b, S. K. Chow^b, J. P. Wang^b, T. C. Chong^b

^aLaser Microprocessing Laboratory, Department of Electrical Engineering and Data Storage Institute, National University of Singapore, 10 Kent Ridge Crescent, Singapore 119260

^bData Storage Institute, 10 Kent Ridge Crescent, Singapore 119260

ABSTRACT

Boron-Carbon-Nitrogen $B_xC_yN_z$ thin films were deposited by excimer laser ablation of boron carbide (B_4C) under nitrogen ion-beam bombardment. Thin films were deposited in the intersection of the ablated B-C plasma and nitrogen ion beam on the silicon substrates. The laser pulse energy was selected in the range of 30 ~ 100 mJ with pulse duration of 23 ns. The electronic and compositional properties of the deposited thin films were analyzed by X-ray photoelectron spectroscopy (XPS), Raman and infrared spectroscopy, scanning tunneling microscopy and ellipsometry measurements. The influence of the ion beam bombardment on the optical, electrical and electronic properties of the deposited thin films was studied.

Keywords: Pulsed laser deposition, B-C-N, thin films, STM, ion beam

1. INTRODUCTION

The similarity of layer structure between hexagonal boron nitride (BN) and graphite as show in Fig.1 suggests the possibility of the existence of stable or metastable states of boron-carbon-nitrogen (B-C-N) compounds. This similarity stimulates theoretical studies and experimental research of this new material¹⁻⁷. Most research works of B-C-N system based on synthetic method of chemical vapor deposition (CVD) technology. Recently, the composition ratio in the deposited $B_xC_yN_z$ compound and their electronic and chemical properties were studied by X-ray photoelectron spectroscopy (XPS), Infrared and Raman spectroscopes, X-ray diffract (XRD) etc. measurements. Since graphite has a conductor nature whilst boron nitride (BN) is an insulator, such a new material $B_xC_yN_z$ could be expected to have interesting adjustable electrical and electronic properties between a conductor and a insulator, depending on the compositional ratio: $x:y:z$.

Recent theoretical calculations⁸ have predicted that the hardest materials must be inorganic compound consisting of boron, carbon and nitrogen, such as diamond, cubic boron nitride (c-BN), boron carbide (B_4C), covalent carbon nitride which was recently predicted to be harder than diamond⁹ and $B_xC_yN_z$ with a proper ratio of (x,y,z) ⁸. Experimental synthesis and measurements have supported most of these

* Correspondence author: Email: elcluyf@nus.edu.sg; Telephone: +65 874 2118; Fax: +65 779 1103

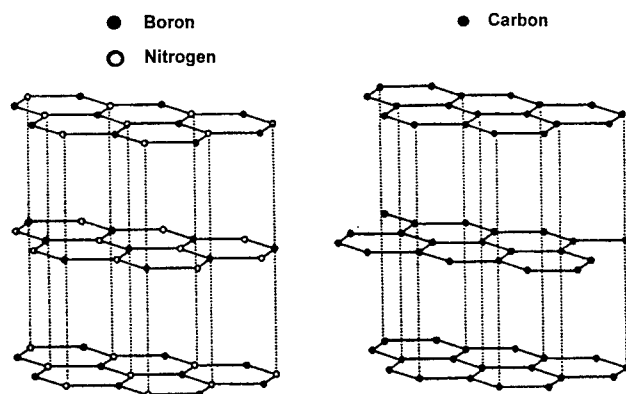


Fig.1. The similarity between hexagonal BN and graphite.

theoretical calculations and predictions, such as the syntheses of diamond, c-BN, B_4C and carbon nitride¹⁰. The research work of B-C-N materials is at its beginning. The synthesis and detailed analyses of $B_xC_yN_z$ have not been carried out, although a few experimental results have been published¹⁻⁷.

In our experiment, we intend to synthesize B-C-N ternary thin film by pulsed laser deposition (PLD) using boron carbide (B_4C) target. The incorporation of nitrogen into the deposited thin films will be characterized by Raman and FTIR spectroscopes, XPS, ellipsometry and scanning tunneling microscopy (STM) measurements. The deposition will be carried out in nitrogen atmosphere or with the assistance of nitrogen ion beam bombardment. The analysis results can be used to make comparison between these two deposition configurations.

2. EXPERIMENTS

Boron-Carbon-nitrogen thin films were deposited in a pulsed laser deposition (PLD) system with a background vacuum of 1×10^{-6} Torr. The experimental set-up is schematically shown in Fig.2. A KrF excimer laser with wavelength of 248 nm and pulse duration of 23 ns was used as light source to ablate B_4C target. The distance between the target and the substrate was 4 cm. The target was rotated by an external motor to provide each pulse with a fresh surface. The target was a piece of B_4C with a purity of 99.5 %. The repetition rate of the KrF excimer laser was 10 Hz. The fluence of the laser ranged from 0.6 to 2.5 Jcm^{-2} . A 1-cm Kaufman-type ion source was mounted on the system which can produce a nitrogen ion beam bombarding on the substrate to assist the deposition process and to incorporate nitrogen into the deposited thin films. The ion flux was 1 mA/cm^2 . The ion beam energy can be selected between 50 and 1000 eV. The working pressure for the ion beam was 1×10^{-4} Torr. The deposition rate was in the range of 10 ~ 20 nm/min. The thickness of deposited thin film was in the range of 200 ~ 400 nm. The substrate temperature was automatically controlled by a digital controller and can be set at deposition temperature up to 900 °C. Before deposition, the silicon wafers were cleaned by acetone in an ultrasonic bath.

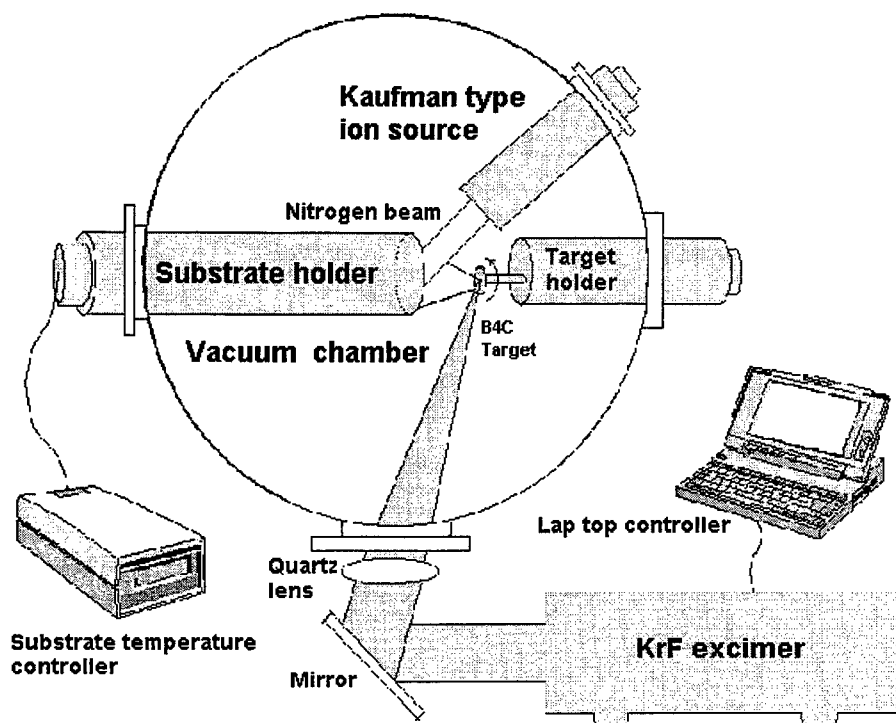


Fig.2. Experimental set-up.

X-ray photoelectron spectroscopies (XPS) were carried out to characterize the electronic and compositional properties of the deposited thin films. XPS measurements were done by using a Mg K_{α} 1253.6 eV X-ray source. Raman spectroscopy measurements were done on a Renishaw Raman Scope. The optical properties of the deposited thin films, the refractive index n , extinction coefficient k and the optical band gap E_{opt} were studied by a JOBIN YVON-SOFIE spectroscopic phase modul and ellipsometer. Scanning Tunneling Microscopy (STM) measurement was performed on an Autoprobe CP Atomic Force Microscopy (AFM) system by Park Scientific Instruments, Co.

3. RESULTS AND DISCUSSIONS

Deposited B-C-N thin films were set for surface profile measurements. Fig. 3 illustrates the surface profile of a deposited B-C-N thin film by STM measurement. The surface morphology is very smooth in general. The surface roughness is about 0.4 nm in the range of $1 \times 1 \mu\text{m}$ sampling area.

Figure 4 shows the XPS survey spectra of a B-C-N thin film deposited by laser ablation of a B_4C target under the bombardment of a 100 eV nitrogen ion beam. According to the XPS analyses based on the signal intensities and sensitivities, the evaluated compositions is $B_{0.63}C_{0.22}N_{0.15}$. It can be seen that the nitrogen ion beam can effectively incorporate nitrogen species into the deposited thin film.

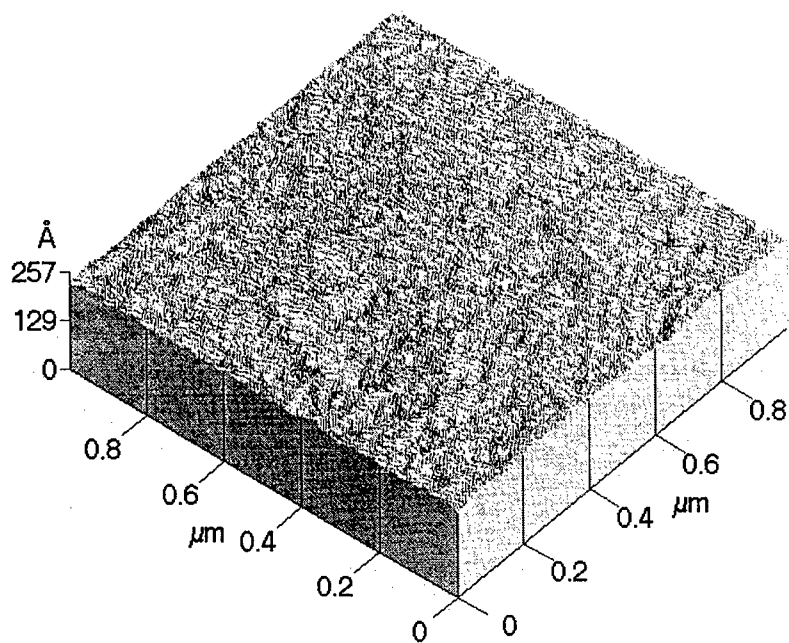


Fig.3. STM surface profile of deposited B-C-N thin film.

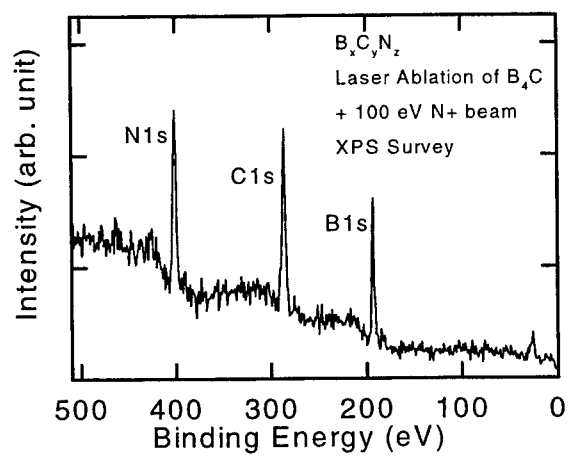


Fig.4. XPS survey of deposited B-C-N thin film.

The results of XPS B 1s, C 1s and N 1s spectra of the deposited thin films are shown in Figs. 5 (a), (b) and (c) respectively. The B 1s peak can be deconvoluted into three Gaussian lines at (I) 186.0, (II) 187.0 and (III) 189.0 eV. The line (I) can be assigned to boron carbide bonds, while line (II) can be assigned to B-B bonds. The B-N bond line (III) implies that nitrogen ion beam bombardment causes breaking of B-C bonds and formation of B-N bonds¹².

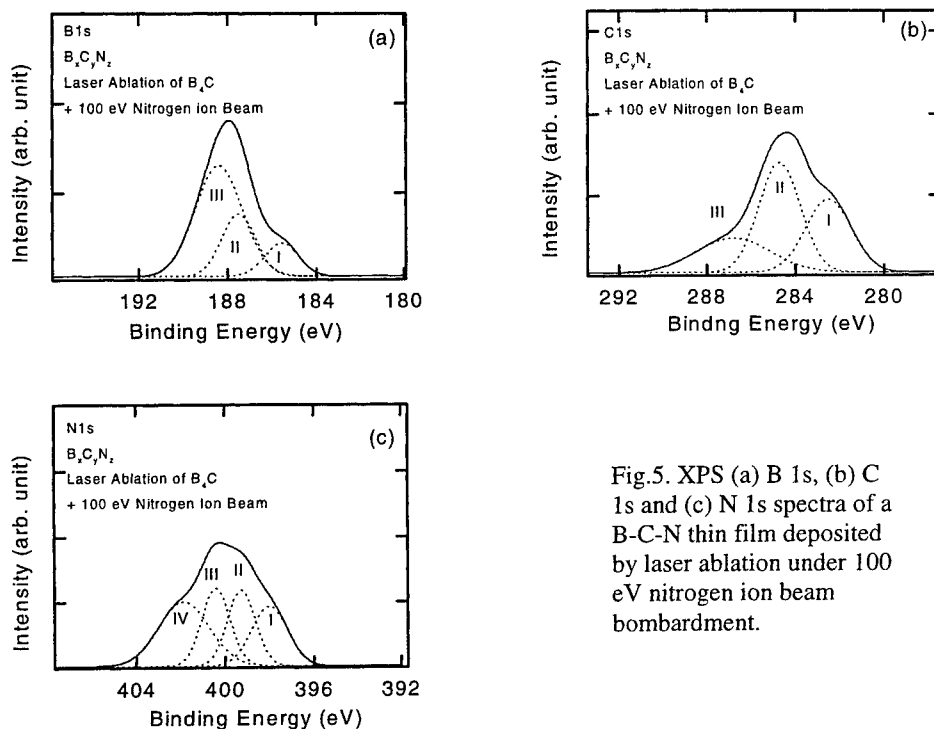


Fig.5. XPS (a) B 1s, (b) C 1s and (c) N 1s spectra of a B-C-N thin film deposited by laser ablation under 100 eV nitrogen ion beam bombardment.

In Fig.5(b), the C 1s peak can be deconvoluted into three Gaussian lines at (I) 282.6, (II) 284.9 and (III) 286.8 eV. The line (II) is corresponding to boron carbide while line (III) is related to carbon nitride binding¹⁰. The line (I) could be amorphous carbon and carbide structures, possibly resulted from ion beam bombardment.

In Fig.5(c), the N 1s peak can be deconvoluted into four Gaussian lines at (I) 397.8, (II) 399.4, (III) 400.0 and (IV) 401.7 eV. The lines (I) and (II) can be assigned to carbon nitride bonds¹⁰ and N-N binding structures respectively. The line (III) and (IV) probably reflect B-N binding structures.

The optical properties of the deposited thin films were measured by an ellipsometer. Figure 6(a) illustrates the (a) refractive index n and (b) extinction coefficient k of a B-C-N thin films deposited by PLD with 100 eV N⁺ bombardment. The refractive index n of the deposited B-C-N thin film is about 1.5 in the photon energy range of 1.5 ~ 4.0 eV, while the extinction coefficient k decreases with the photon energy slightly.

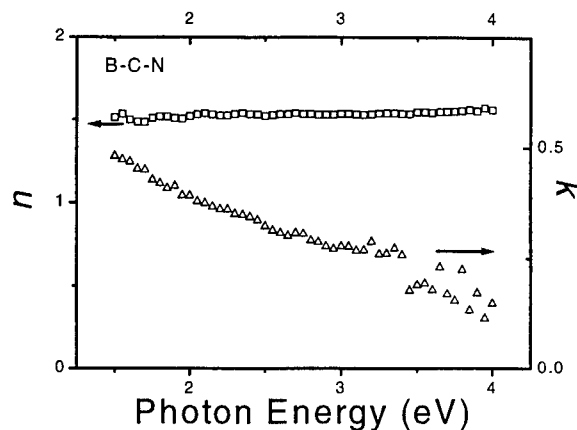


Fig.6(a). Refractive index n and extinction coefficient k of deposited b-C-N thin film

Theoretically, regarding the optical properties, the absorption coefficient α of an amorphous-semiconductor thin film should depend on the photon energy E as¹²:

$$\alpha(E) \propto (E - E_{opt})^2 / E \quad (1)$$

where E_{opt} is defined as the optical band gap of the amorphous-semiconductor. In our experiment, the relation in Eq. (1) of the deposited thin films was studied in order to obtain the value of E_{opt} from the extrapolated zero point. Figure 6(b) illustrates the ellipsometry results for two different samples: a $B_{0.53}C_{0.28}N_{0.19}$ thin film deposited by laser ablation of B_4C under the bombardment of a 50 eV nitrogen ion beam and a $B_{0.63}C_{0.22}N_{0.15}$ thin film deposited by laser ablation of B_4C under the bombardment of a 100 eV nitrogen ion beam. It can be seen that the B-C-N thin films follow the relation of Eq. (1) quite well, implying an amorphous-semiconductor nature. The optical band gaps E_{opt} are 0.48 and 0.31 eV for $B_{0.53}C_{0.28}N_{0.19}$ and $B_{0.63}C_{0.22}N_{0.15}$ thin films respectively. A high energy of nitrogen ion beam gives rise to a low E_{opt} , possibly caused by the high level disorder in the thin films after high energy ion bombardment.

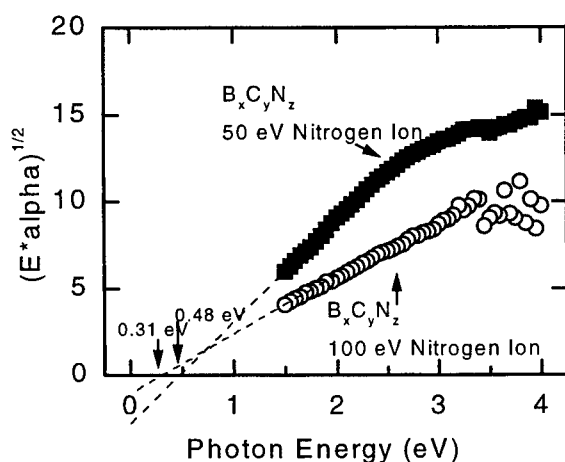


Fig.6(b). The $(E\alpha)^{1/2} \sim E$ relations for B-C-N thin films deposited by laser ablation of a B_4C target under the bombardment of a 50 or 100 eV nitrogen ion beam.

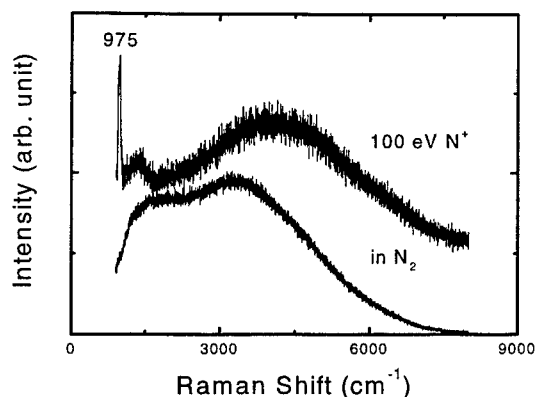


Fig.7. Raman spectra of B-C-N thin films deposited in nitrogen atmosphere or under nitrogen ion beam bombardment.

Different deposition conditions were selected in order to study the influence of nitrogen ion beam bombardment. Two samples were deposited differently. The first was deposited by laser ablation of B_4C target in nitrogen atmosphere with pressure of 100 mTorr. The other was deposited by laser ablation of B_4C target under 100 eV nitrogen ion beam bombardment. Fig.7 gives the Raman spectroscopies of these two samples. The effect of ion beam bombardment is quite obvious. The spectrum of the bombarded sample has a broad peak between 1100 and 1600 cm^{-1} and a sharp peak at 975 cm^{-1} . The broad peak should be resulted from the amorphous carbon or carbide materials in the deposited thin film. The 100 eV N^+ can effectively break B-C bonds and lead to the formation of C-C bonds. The peak at 975 cm^{-1} should be related to B-C-N binding structures, most probably reflects a kind of B-C-N crystalline compound.

The former Raman-measured and described samples are set for FTIR analyses, as shown in Fig. 8. The spectrum of the sample deposited without ion beam bombardment presents a plain feature while that deposited under N^+ co-processing has some peaks as marked in the spectrum. These peaks can be assigned to B-N and C-N stretching¹³, resulted from the incorporation of nitrogen species into the deposited thin films and chemical combination between C-N and B-N. Among the FTIR peaks, C-N stretching is most obvious, implying a high content formation of C-N bonds in the thin films.

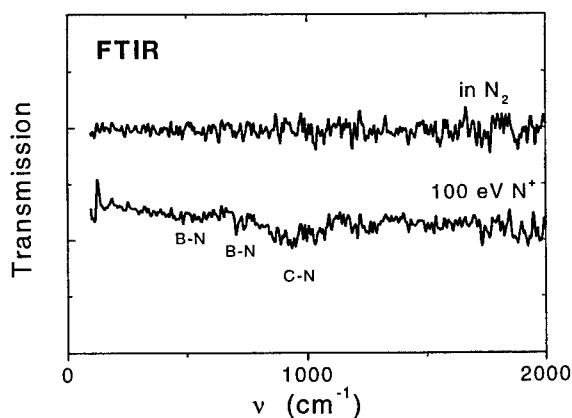


Fig.8. FTIR spectra of B-C-N thin films deposited in nitrogen atmosphere or under nitrogen ion beam bombardment

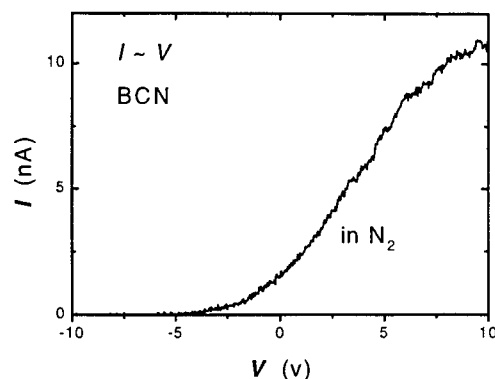


Fig.9. STM tunneling spectra of B-C-N thin films deposited in nitrogen atmosphere.

The electrical properties of the deposited were characterized by STM tunneling spectroscopy. Fig. 9 shows the spectra of a sample deposited in 100 mTorr nitrogen atmosphere. The tunneling spectrum of the sample deposited in nitrogen atmosphere exhibits a perfect relation between tunneling current I (in nA) and bias voltage V , fitting well with the theoretical exponential relation¹⁴:

$$I \propto e^{-2\kappa d}$$

Here:

$$\kappa^2 = (2\pi)^2 2m(E_w - V/2)/\hbar^2$$

where m is the electron mass, \hbar is Planck's constant, E_w is the work function which is the difference between the vacuum level and the Fermi level of the material, d is the distance between STM tip and sample surface (barrier width). The work function calculated from the spectrum of the sample deposited in nitrogen atmosphere is in the range of 3 ~ 6 V.

4. CONCLUSIONS

$B_xC_yN_z$ thin films were deposited by KrF excimer laser ablation of B_4C target in nitrogen atmosphere or under nitrogen ion-beam bombardment. The boron, carbon and nitrogen species have been chemically bound together instead of simple mixture. The optical band gap of the deposited thin film is less than 1 eV. Nitrogen ion beam bombardment can break B-C bonds and lead to the formation of B-N, C-N, C-C and B-C-N amorphous or crystalline structures. The deposited thin films have work functions in the order of 10^1 V.

5. ACKNOWLEDGEMENTS

The authors would like to thank Mr. Y. W. Goh and Miss. H. L. Koh for their technical supports.

6. REFERENCE

1. S. J. Yoon and A. Jha, "Vapour-phase reduction and the synthesis of boron-based ceramic phases", *J. Mater. Sci.* **30**, pp. 607-614, 1995.
2. M. Hubacek and T. Sato, "Preparation and Properties of a Compound in the B-C-N System", *J. Solid State Chem.* **114**, pp. 258-264, 1995.
3. Y. G. Andreev, T. Lundstrom, R. K. Harris, S. W. Oh, D. C. Apperley and D. P. Thompson, "On the nature of boron-carbon-nitrogen compounds synthesized from organic precursors", *J. Alloy and Compounds*, **227**, pp. 102-108, 1995.
4. M. P. Johansson, I. Ivanov, L. Hultman, E. P. Munger and A. Schutze, "Low-temperature deposition of cubic BN:C films by unbalanced direct current magnetron sputtering of a B₄C target", *J. Vac. Sci. Technol.* **A14**, pp. 3100-3107, 1996.
5. E. H. A. Dekempeneer, V. Wagner, L. J. van Ijendoorn, J. Meneve, S. Kuypers, J. Smeets, J. Geurts and R. Caudano, "Tribological and structural properties of amorphous B-N-C coatings", *Surf. and Coatings Technol.*, **86-87**, pp. 581-585, 1996.
6. M. O. Watanabe, T. Sasaki, S. Itoh and K. Mizushima, "Structural and electrical characterization of BC₂N thin films", *Thin Solid Films*, **281-282**, pp. 334-336, 1996.
7. M. Kawaguchi, "B/C/N Materials on the Graphite Network", *Adv. Mater.*, **9**, pp. 615-625, 1997.
8. A. Y. Liu and M. L. Cohen, "Prediction of New low Compressibility Solids", *Science*, **245**, pp. 841-842, 1989.
9. C. M. Sung and M. Sung, "Carbon nitride and other speculative superhard materials", *Mater. Chem. Phys.*, **43**, pp. 1-18, 1996.
10. C. Niu, Y. Z. Lu and C. M. Lieber, "Experimental realization of the Covalent Solid Carbon Nitride", *Science*, **261**, pp.334-336, 1993.
11. *Handbook of X-Ray Photoelectron Spectroscopy*, Physical Electronics Division, Perkin-Elmer, Eden Prairie, MN, 1978.
12. N. F. Mott and E.A. Davis, *Electronic Processes in Non-Crystalline Materials*, 2nd ed., p. 289, Clarendon, Oxford, 1979.
13. K. Nakamoto, *Infrared and raman spectra of Inorganic and Coordination Compounds, part A: Theory and Applications in Inorganic Chemistry*, 5th ed., p. 243 and 261, John Wiley & Sons, Toronto, 1997.
14. D. A. Bonnell, *Scanning Tunneling Microscopy and Spectroscopy, Theory, Techniques, and Applications*, p.32, VCH Publishers, New York, 1993.

Addendum

The following papers were announced for publication in this proceedings but have been withdrawn or are unavailable.

- [3618-01] **Laser-focusing of atoms for nanostructure fabrication**
J. J. McClelland, C. C. Bradley, R. J. Celotta, National Institute of Standards and Technology
- [3618-03] **Forces in the optical near-field**
L. Novotny, R. X. Bian, X. S. Xie, Pacific Northwest National Lab.
- [3618-04] **Tipless near-field infrared microscopy**
D. V. Palanker, T. I. Smith, H. A. Schwettman, Stanford Univ.
- [3618-15] **Black silicon: sharp-spike formation on silicon induced by femtosecond laser pulses**
T.-H. Her, R. J. Finlay, C. Wu, E. Mazur, Harvard Univ.
- [3618-44] **Pulsed laser deposition: recent advances and industry perspectives**
T. Venkatesan, Neocera, Inc.
- [3618-53] **Measurement of quantum efficiency of chalcogenide vitreous semiconductors at sensitization by corona discharge**
B. S. Tice, Advanced Human Design
- [3618-61] **Comparative analysis of silicon wafers micromachining versus nonconventional technology**
D. G. Ulieru, ROMES S.A. (Romania)
- [3618-69] **Pulsed laser deposition of thick piezoelectric films**
J. S. Horwitz, W. Chang, W. Kim, J. C. Rife, Naval Research Lab.; R. W. Smith, Univ. of Nebraska; R. C. Y. Auyeung, Sachs-Freeman Associates; D. B. Chrisey, Naval Research Lab.
- [3618-70] **Nucleation and growth of particles in laser-induced plasma plume**
N. Aya, Shikoku National Research Institute, AIST (Japan); F. G. Shi, Univ. of California/Irvine; H. Shimura, T. Seto, S. Kano, S. Sasaki, Shikoku National Research Institute, AIST (Japan)
- [3618-75] **Picosecond laser pulses induced heat and mass transfer**
E. W. Kreutz, V. Kostykin, M. Niessen, Institute for Laser Technologies (Germany); J. Jandeleit, W. Schulz, R. Poprawe, Fraunhofer-Institut (Germany)

- [3618-76] **Deposition of carbon nitride thin films in a hybrid r.f.-PLD technique**
E. W. Kreutz, T. Klotzbuecher, Institute for Laser Technologies (Germany);
M. Mergens, D. A. Wesner, Technical Univ. Aachen (Germany)
- [3618-77] **DLC thin film growth under energetic particle bombardment, a comparison
between PLD and r.f.-bias enhanced PLD**
E. W. Kreutz, T. Klotzbuecher, J. Gottmann, Institute for Laser Technologies
(Germany); M. Meyer, D. A. Wesner, Technical Univ. Aachen (Germany)

Author Index

- Adams, Paul M., 487
 Afonso, Carmen N., 453
 Akane, Toshimitsu, 221
 Anisimov, Sergei I., 434
 Araki, Nobuhiro, 269
 Ashkenasi, David, 102
 Auyeung, Raymond C. Y., Addendum, 330
 Aya, Nobuhiro, Addendum
 Aziz, Michael J., 512
 Ballesteros, J. M., 453
 Balzer, Frank, 357
 Basting, Dirk, 396, 413
 Baylor, L. R., 495
 Beaudoin, Felix, 290
 Beck, Kenneth M., 37
 Berger, Peter, 403
 Bian, Randy X., Addendum
 Bityurin, Nikita M., 122
 Bosbach, J., 45
 Bradley, Curtis C., Addendum
 Brueck, Steven R. J., 2
 Bryan-Brown, Guy P., 132
 Buchanan, Margaret, 191
 Celotta, R. J., Addendum
 Chang, Jim J., 71
 Chang, W., Addendum
 Charbonneau, Sylvain, 191
 Chen, Shaochen, 182
 Cheong, B. A., 520
 Chernov, Evgenii B., 425
 Cho, Sung-Hak, 161
 Chong, Tow Chong, 520
 Chow, S. K., 520
 Chrisey, Douglas B., Addendum, 330
 Chu, Schubert S., 81
 Chung, Russell, 330
 Cramer, R., 90
 Dausinger, Friedrich, 198
 de Sande, J. C. G., 453
 Depiereux, Frank, 348
 Dickinson, J. Thomas, 37
 Dragon, Ernest P., 71
 Dubowski, Jan J., 191
 Duignan, Michael T., 330
 Dylla, H. Frederick, 388
 Endert, Heinrich, 413
 Ermer, David R., 90
 Erofeev, Michail V., 425
 Exner, Horst, 262, 340
 Fair, John, 413
 Feng, Yan, 191
 Fernández, Félix E., 475
 Finlay, Richard J., Addendum
 Fitz-Gerald, J., 330
 Fuqua, Peter D., 213
 Garnov, Serge V., 198
 Geohegan, David B., 495, 512
 Gillett, David A., 152
 Giller, Arnold, 348
 Gonzalo, Jose A., 453
 Goodno, Gregory, 240
 Goto, Satoshi, 504
 Gottmann, Jens, Addendum
 Govorkov, Sergei V., 152
 Gower, Malcolm C., 251
 Grigor'ev, Dmitry A., 17
 Grigoropoulos, Costas P., 81, 182, 302
 Gu, Xijia, 240
 Haglund, Richard F., Jr., 90
 Hansen, William W., 213
 Hatano, Mutsuko, 302
 Hayashi, Nobuaki, 310
 Haysom, J. E., 191
 Hellrung, Dirk, 348
 Helvajian, Henry, 170, 213
 Her, Tsing-Hua, Addendum
 Herman, Peter R., 240
 Hess, Wayne P., 37
 Hirao, Kazuyuki, 141
 Hong, M. H., 61, 205
 Horwitz, James S., Addendum
 Hügel, Helmut, 403
 Hüttner, Bernd, 114
 Ihlemann, Juergen, 357
 Isaji, Kazuhide, 269
 Ivanitski, Dmitry I., 9
 Jandeleit, Juergen, Addendum
 Janson, Siegfried W., 213
 Jasper, Knut, 403
 Jellison, Gerald E., Jr., 495
 Jia, Weiyi, 475
 Joly, Alan G., 37
 Kalachev, Alexey I., 9
 Kalbfleisch, Jeff B., 240
 Kanasaki, Jun'ichi, 26
 Kano, Seisuke, Addendum
 Karasaki, Hidehiko, 269
 Kato, Makoto, 269
 Katsumura, Munehide, 418
 Kauf, Michael, 413
 Keiper, Bernd, 340
 Khabotov, Andrey V., 17
 Kim, Eun-Kyu., 370
 Kim, Jae-Kwon, 378

Kim, W., Addendum
 Klopp, P., 396
 Klotzbuecher, T., Addendum
 Koch, R., 396
 Konov, Vitaly I., 198
 Korytin, Alexey I., 122
 Kostykin, Vadim, Addendum
 Kreutz, Ernst W., Addendum
 Kumagai, Hiroshi, 161
 Lacelle, Charles, 191
 Lakeou, Samuel, 330
 Lee, Cheon, 370, 378
 Lee, Minghong, 302
 Long, John, 240
 Lowndes, Douglas H., 495, 512
 Lu, Yongfeng F., 61, 205, 278, 520
 Lubnin, E. N., 198
 Luk'yanchuk, Boris S., 434
 Lukacs, Marc, 240
 Maeda, Mitsuo, 504
 Mai, Z. H., 520
 Makino, Toshiharu, 465, 512
 Marine, W., 434
 Marjoribanks, Robin S., 240
 Marshall, G., 191
 Martin, D., 45
 Martinez, Antonio, 475
 Mayer, Eric E., 152, 413
 Mazur, Eric, Addendum
 McClelland, Jabez J., Addendum
 McGill, R. A., 330
 McLean, William, 71
 Mehlmann, Christoph, 396
 Meja, Peter, 340
 Menschig, Arnd, 114
 Mergens, M., Addendum
 Merkulov, Vladimir I., 495
 Meteva, Krassimira, 9
 Meunier, Michel, 290
 Meyer, M., Addendum
 Midorikawa, Katsumi, 161, 221, 363
 Miller, R. J. Dwayne, 240
 Mitsuyu, Tsuneo, 141
 Miura, Kiyotaka, 141
 Moon, Seungjae, 302
 Moskovsky, Victor A., 17
 Mourad, Houssam A., 475
 Murakami, Kouichi, 512
 Muraviov, Sergey V., 122
 Nagel, Anne-Maria, 262
 Nakata, Yoshiki, 504
 Nantel, Marc, 240
 Naumova, Elena V., 17
 Ness, Sola, 240
 Newsome, Christopher J., 132
 Niessen, Markus, Addendum
 Nikonov, Anatoly V., 17
 Novotny, Lukas, Addendum
 O'Neill, Mary, 132
 Obara, Minoru, 161
 Oettl, Anton, 240
 Ogino, Hiroshi, 221
 Okada, Tatsuo, 504
 Okumura, Fujio, 320
 Okumura, Hiroshi, 320
 Onai, Seinosuke, 465
 Ooie, Toshihiko, 418
 Orii, Takaaki, 465, 512
 Palanker, Daniel V., Addendum
 Panchenko, Alexei N., 425
 Papantonakis, M. R., 90
 Park, H. K., 90
 Park, Se-Ki, 370
 Piqué, Alberto, 330
 Poole, P. J., 191
 Poprawe, Reinhart, Addendum, 348
 Pumarol, Manuel, 475
 Puretzky, Alexander A., 495
 Qiu, Jianrong, 141
 Radhakrishnan, Gouri, 487
 Ren, Zhong M., 520
 Rife, Jack C., Addendum
 Rodríguez, Edgardo, 475
 Rosenfeld, Arkadi, 102
 Rubahn, Horst-Guenter, 357
 Rubahn, Katharina, 357
 Sacher, Edward, 290
 Saitou, Masakazu, 310
 Sasaki, Shinya, Addendum
 Scaggs, Michael J., 413
 Schröder, Thomas, 396
 Schulz, Wolfgang, Addendum
 Schwettman, H. Alan, Addendum
 Sera, Kenji, 320
 Serna, R., 453
 Seto, Takafumi, Addendum
 Shi, Frank G., Addendum
 Shikama, Tomokazu, 418
 Shimura, Hirofumi, Addendum
 Simakina, G. A., 434
 Simard-Normandin, Martine, 290
 Skakun, Victor S., 425
 Smirnov, Igor B., 9
 Smith, R. W., Addendum
 Smith, Todd I., Addendum
 Solis, J., 453
 Song, W. D., 278
 Sosnin, Eduard A., 425
 Sovetov, Nikolay M., 17
 Speckman, Donna M., 487
 Stamm, Uwe, 396
 Stietz, F., 45
 Sugioaka, Koji, 221, 363
 Suzaki, Yoshifumi, 418
 Suzuki, Kenkichi, 302, 310
 Suzuki, Nobuyasu, 465, 512

Takahashi, Michiko, 310
Takai, Hiroshi, 221
Tanikawa, Akio, 320
Tanimura, Katsumi, 26
Tarasenko, Victor F., 425
Taylor, David P., 170
Terabayashi, Takao, 310
Tice, Bradley S., Addendum
Träger, Frank, 45
Tsarkova, Olga G., 198
Uetsuhara, Hiroshi, 504
Ulieru, Dumitru G., Addendum
Vasa, Nilesh, 504
Veiko, Vadim P., 9
Venkatesan, T., Addendum
Voronin, Juriy M., 9
Voznessenski, Nikolay B., 9
Wang, J. P., 520
Wang, Wei Jie, 205
Wang, Yanyung, 475
Warner, Bruce E., 71
Washio, Kunihiro, 230
Wenzel, T., 45
Wesner, David A., Addendum
Williams, Richard M., 37
Wolf, Michael, 9
Wu, Claudia, Addendum
Wu, H. D., 330
Wu, P. K., 330
Wu, Xiaoguang, 290
Xie, X. Sunney, Addendum
Yabe, Takashi, 53
Yamada, Yuka, 465, 512
Yano, Tetsuo, 418
Yavas, O., 90
Ye, Mengqi, 81, 182
Yeh, Li-Ya, 348
Yoneda, Masafumi, 418
Yoshida, Takehito, 465, 512
Yurkin, Alexander M., 122
Zaidi, Saleem H., 2
Zhang, Jie, 363
Zhang, Y., 278
Zhao, Jian-Xin, 114
Zheng, Y. W., 278